CONCRETE SOLUTIONS

Michael Grantham
P.A. Muhammed Basheer
Bryan Magee
Marios Soutsos

EDITORS

CRC Press
Taylor & Francis Group
A BALKEMA BOOK

CONCRETE SOLUTIONS

This page intentionally left blank

PROCEEDINGS OF CONCRETE SOLUTIONS, 5TH INTERNATIONAL CONFERENCE ON CONCRETE REPAIR, BELFAST, NORTHERN IRELAND, 1–3 SEPTEMBER 2014

Concrete Solutions

Editors

Michael Grantham
Concrete Solutions, Margate, Kent, UK
Sandberg LLP, London, UK

P.A. Muhammed Basheer
University of Leeds, England, UK

Bryan Magee
University of Ulster, Jordanstown, Northern Ireland, UK

Marios Soutsos
Queen's University Belfast, Northern Ireland, UK

CRC Press
Taylor & Francis Group
Boca Raton London New York Leiden

CRC Press is an imprint of the
Taylor & Francis Group, an **informa** business

A BALKEMA BOOK

Main cover photo
Title of the photograph: UHPFRC Cross Arm for Electrical Transmission Line Towers.
Courtesy of Raafat El-Hacha

Description:
The photo shows a full-scale 11.5m long precast double C-channel cross arm for high voltage electrical transmission lines supported by two poles at 3.0 m from each end. The composite cross arm is made of Ultra High Performance Fibre Reinforced Cementitious (UHPFRC) concrete with short-discontinuous synthetic (poly vinyl alcohol, PVA) fibers and reinforced with two rods of Glass Fibre Reinforced Polymer rebars at the web-flange corner. The concrete has a compressive strength of 200MPa and a tensile strength of 14MPa. The cross arms are tested under in-plane inclined loading at an angle of 60° simulating the worst case scenario of swivelling of the transmission lines. For simplicity of the test set-up in the lab, the cross arm was tested up-side down by pulling upward rather than pulling downward. The photo shows the cross arm after reaching about 1000 mm of vertical deflection at the end of the cantilever at a load of 10kN. The test was stopped due to safety issue.

Small cover photo
Description:
The photo shows the application of electrochemical realkalisation treatment to the reinforced concrete columns of a historical bell tower.
Courtesy of E. Redaelli, M. Carsana, L. Bertolini

CRC Press/Balkema is an imprint of the Taylor & Francis Group, an informa business

© 2014 Taylor & Francis Group, London, UK

Typeset by MPS Limited, Chennai, India
Printed and bound in Great Britain by CPI Group (UK) Ltd, Croydon, CR0 4YY.

All rights reserved. No part of this publication or the information contained herein may be reproduced, stored in a retrieval system, or transmitted in any form or by any means, electronic, mechanical, by photocopying, recording or otherwise, without written prior permission from the publishers.

Although all care is taken to ensure integrity and the quality of this publication and the information herein, no responsibility is assumed by the publishers nor the author for any damage to the property or persons as a result of operation or use of this publication and/or the information contained herein.

Published by: CRC Press/Balkema
P.O. Box 11320, 2301 EH Leiden, The Netherlands
e-mail: Pub.NL@taylorandfrancis.com
www.crcpress.com – www.taylorandfrancis.com

ISBN: 978-1-138-02708-4 (Hardback)
ISBN: 978-1-315-73731-7 (eBook-PDF)

Concrete Solutions – Grantham et al. (Eds)
© 2014 Taylor & Francis Group, London, ISBN 978-1-138-02708-4

Table of contents

Electrochemical repair

Strengthening materials and techniques/Repair with composites

Surface protection methods and materials

Repair of fire damage

NDT and diagnosis of problems

Insitu strength assessment

Structural modelling/finite element analysis

Concrete Solutions – Grantham et al. (Eds)
© 2014 Taylor & Francis Group, London, ISBN 978-1-138-02708-4

Preface

The Concrete Solutions series of International Conferences on Concrete Repair began in 2003 with a conference held in St. Malo, France in association with INSA Rennes. Subsequent conferences have seen us partnering with the University of Padua in 2009 and with TU Dresden in 2011. This conference is being held for the first time in the UK, in association with Queen's University Belfast and brings together delegates from 36 countries to discuss the latest advances and technologies in concrete repair.

Earlier conferences were dominated by electrochemical repair, but there has been an interesting shift to more unusual methods, such as bacterial repair of concrete plus an increased focus on service life design aspects and modelling, with debate and discussion on the best techniques and the validity of existing methods. Repair of heritage structures is also growing in importance and a number of the papers have focussed on the importance of getting this right, so that we may preserve our rich cultural heritage of historic structures.

This book is an essential reference work for those working in the concrete repair field, from Engineers to Architects and from Students to Clients.

Michael Grantham
P.A. Muhammed Basheer
Bryan Magee
Marios Soutsos

This page intentionally left blank

Concrete Solutions – Grantham et al. (Eds)
© 2014 Taylor & Francis Group, London, ISBN 978-1-138-02708-4

About the editors

Professor Michael Grantham is the Director and Chair of Concrete Solutions. He has worked for and in some cases helped to found several of the UK's better known testing consultancies for construction problems. He is also co-author of "Testing of Concrete in Structures," with John Bungey and Steve Millard with a 5th edition in preparation, plus editor of his own book on concrete repair "Concrete Repair, a Practical Guide." He is incoming President of the Institute of Concrete Technology from 2015 and a Council member of the Concrete Society. He is also Editor-in-Chief of Elsevier's "Case Studies in Construction Materials," an open-access on line journal.

Professor Muhammed Basheer holds the chair of Structural Engineering at University of Leeds, England, United Kingdom. He has been an educationalist and researcher in the field of civil (structural) engineering for more than 30 years. His research interests are primarily on the Science, Technology and Performance of Concrete Structures, with special emphasis on non-destructive evaluation, structural health monitoring, performance testing and service life designs of concrete structures. He is an elected Fellow of the Irish Academy of Engineering, Institution of Civil Engineers and American Concrete Institute. He is an Editor of the International Journal of Construction and Building Materials and an Associate Editor of the International Journal of Civil Structural Health Monitoring. He has authored more than 320 refereed technical publications and received the American Concrete Institute's ACI/James Instruments Award for best Non-Destructive Testing Limited in 1990 and 1999. He is also a recipient of best paper awards for his publications in international conferences in Cape Town, South Africa and Edinburgh, Scotland. Professor Basheer has been actively promoting technology transfer of his research to practice, by establishing two University spin-out companies, Amphora Non-destructive Testing Limited and Sengenia Limited. He is also a member of numerous technical committees of both the American Concrete Institute and RILEM. He is a member of the UK Government's Research Excellence Framework 2014 sub-panel on Civil and Construction Engineering.

Dr Bryan Magee is a Lecturer in Construction Materials within the University of Ulster's School of the Built Environment.A chartered civil engineer, Bryan has worked as an educationalist, researcher and policy-maker in the field of civil/structural engineering for over 15 years.Bryan's previous career includes academic posts at the University of Cape Town, Purdue University, University of New Hampshire and Queen's University Belfast, as well as UK-based industry appointments working for TRL Ltd. and The Concrete Centre. His specialist area of interest is the behaviour, performance and advancement of civil/structural materials.

Professor Marios Soutsos is currently Professor of Structures/Materials in Queen's University Belfast. Previously Reader/Lecturer in Engineering at the University of Liverpool since 1995 following two years previous industrial experience relating to concrete repair and quality control of ready mixed concrete. Principal research experience is in construction materials and current interests include: high strength concrete, cement replacement materials, chemical admixtures, concrete rheology, the use of recycled demolition aggregate in concrete products, repair materials as well as heat of hydration effects in concrete structures. Principal Investigator for two EPSRC research grants, Co-Investigator for two EPSRC/EU research grants and Co-Investigator for the DoE funded Cardington concrete frame project. These projects included work on the properties of fresh concrete and non-destructive testing of hardened concrete. A recent EPSRC contract was on promoting greater use of ground granulated blast furnace slag for fast track construction. Author of over 50 relevant technical papers.

Germann Instruments are the leading manufacturer of advanced state-of-the-art Nondestructive Testing Equipment (NDT) for evaluating concrete structures. We are committed to advancing knowledge as well as bringing new technology to market from our companies in Denmark, USA and South America.

Germann Instruments is the developer of the most accurate test systems for measuring the in-place compressive strength of concrete, the LOK-Test and the CAPO-Test.

Germann Instruments was the first to bring to market the DOCter Impact-Echo and the s'MASH Impulse Response systems for nondestructive investigation of concrete structures as well as the MIRA 3D Tomographer.

Germann Instruments offers a complete range of test systems for tensile/adhesion testing, reinforcement location/size/depth, durability, corrosion evaluation, analysis of chlorides and carbonation, and service life estimation. We, as well, are the only producer of a portable ICAR Concrete Rheometer and the Air Void Analyzer for fresh concrete. Download our new 2014 catalog for a complete description of our systems from www.germann.org

NDT Workshops are offered on a regular basis headed by top NDT specialists within the following main areas: Evaluation of the in-place concrete strength, Stress-wave methods for flaw detection, Durability related testing and Advanced test methods.

GERMANN INSTRUMENTS A/S

Emdrupvej 102 - DK-2400 Copenhagen NV - Denmark
Phone: (+45) 39 67 71 17 - Fax: (+45) 39 67 31 67
E-mail: germann-eu@germann.org, Internet: www.germann.org

GI

Test Smart – Build Right

corrPRE engineering

CorrPRE is comprised of two divisions, engineering and special anodes manufacturing for steel in concrete.

The engineering division *(CorrPRE Engineering)* offers the following services :

- Corrosion surveys - specialised in pre-stressed and post-tensioned structures.
- Certified corrosion protection system design
- Non-destructive testing measurements and visual examinations
- Corrosion monitoring
- Custom designed and developed corrosion control products
- Field and Laboratory testing, analysis and evaluation

corrPRE Special Anodes Manufacturing

The special anodes manufacturing division *(CorrPRE - Special Anodes Manufacturing)* is specialised in the manufacturing and distribution of of both sacrificial and impressed current anodes for steel in concrete throughout the world under our own brand names.

Our products are supplied through a carefully selected group of distributors with a specific know-how of this technology to guarantee technical support and full performance of our products after installation.

Our product range :

- Zinc Layer Anode — *A surface applied zinc foil with ion-conductive adhesive.*
- MAS System — *A zinc sacrificial anode system for magnesite based floorings.*
- ZDA ML10/30 — *A zinc discrete concrete embeddable anode.*
- RollAnode — *A zinc discrete anode for pre-drilled holes.*
- Snap-on anode — *A zinc discrete anode designed for precast concrete.*
- CorroDisc 125 — *A surface applied discrete ICCP anode based on MMO coated titanium and acid proof mortar.*
- CorroDisc DI — *An ICCP anode based on MMO coated titanium and acid proof mortar applied in predrilled holes.*

International Qualifications in Concrete Technology & Construction

A four-stage scheme linked to ICT membership

Get qualified!

The Institute of Concrete Technology administers an up-to-date, industry-recognised four-stage qualification scheme, which is directly linked to its professional grades of membership. The Institute offers designatory letters TechICT, AffICT, AMICT, MICT, or FICT to appropriately qualified individuals, either by its own highly regarded examinations or via an alternative qualifications route.

Concrete Technology & Construction

STAGE 1 – Concrete Practice
An entry-level qualification, intended for those starting in the construction industry or for personnel embarking in a career linked to production, use or quality control.

STAGE 2 – General Principles
Designed to provide participants with an in-depth understanding of the fundamentals of concrete. Detailed information is provided on constituent materials, specification, concrete properties, production and performance. Intended for candidates who have some prior knowledge and experience or possess the Institute's Stage 1 qualification.

STAGE 3 – Practical Applications
Provides participants with detailed understanding of the effective application of concrete. Covers the practicalities of materials selection, achievement of quality and performance in site procedures and construction methods. Intended for candidates who have significant knowledge and experience or possess the Institute's Stage 2 qualification.

STAGE 4 – Advanced Concrete Technology
Recognised globally as the leading award in advanced concrete technology, this qualification is designed to provide comprehensive understanding of the subject. Original research is an essential component of the qualification. Intended for candidates who have acquired considerable experience and responsibility.

The Concrete Technology & Construction scheme has been established for more than 40 years to provide graded progression for individuals throughout their career, leading to membership of The Institute of Concrete Technology.

Institute membership status is internationally recognised and highly valued, with its attainment widely viewed as a significant personal achievement and a benchmark of competence and professional standing.

For further information please visit the ICT website: *http://ict.concrete.org.uk* or contact The Executive Officer at: ict@concrete.org.uk, Tel: 01276 607140.

proceq

Portable Non-Destructive
Concrete Testing Instruments

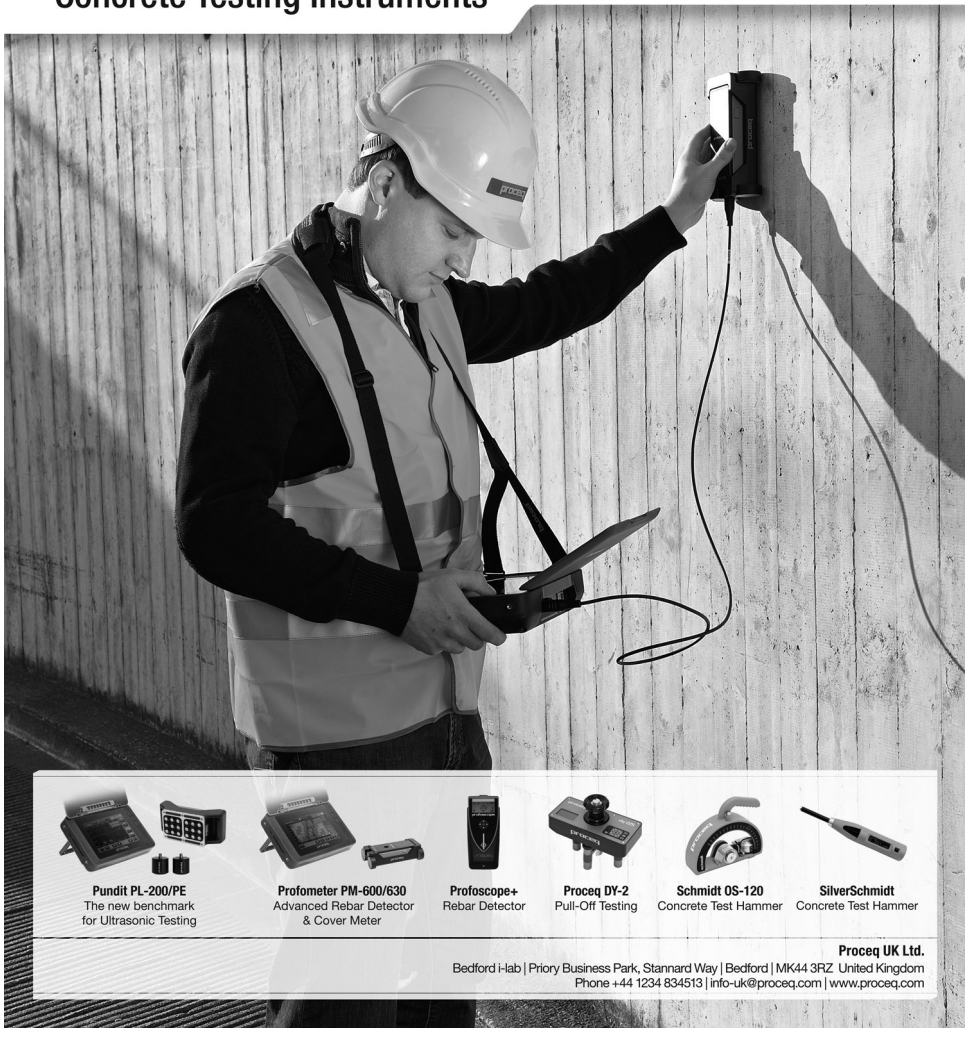

Pundit PL-200/PE
The new benchmark
for Ultrasonic Testing

Profometer PM-600/630
Advanced Rebar Detector
& Cover Meter

Profoscope+
Rebar Detector

Proceq DY-2
Pull-Off Testing

Schmidt OS-120
Concrete Test Hammer

SilverSchmidt
Concrete Test Hammer

Proceq UK Ltd.
Bedford i-lab | Priory Business Park, Stannard Way | Bedford | MK44 3RZ United Kingdom
Phone +44 1234 834513 | info-uk@proceq.com | www.proceq.com

This page intentionally left blank

Keynote papers

This page intentionally left blank

Concrete Solutions – Grantham et al. (Eds)
© 2014 Taylor & Francis Group, London, ISBN 978-1-138-02708-4

Design for concrete durability: From deemed-to-satisfy to dreamed-to-satisfy

J. Gulikers
Ministry of Infrastructure and the Environment, Rijkswaterstaat – GPO, Utrecht, The Netherlands

ABSTRACT: In recent years a clear trend is observed towards the introduction of a performance-based approach in which an overall durability requirement for a complete concrete structure should be met. This overall requirement can be achieved by a variety of alternatives and with respect to reinforcement corrosion ideally such a performance-based durability design is translated into objectively quantified requirements on quality and quantity of the concrete cover. As all alternatives will result into equivalent overall performance of the structure the contractor will thus be given full freedom to choose the most economical solution. In order to derive performance requirements mathematical models on relevant degradation processes are introduced. However, most degradation models include significant pitfalls and limitations which are either not mentioned or not known even to the developer. This paper will critically address these issues regarding design for concrete durability, supplemented by examples based on a Dutch guideline for performance-based durability design. Any future developments on performance-based methods on durability should focus more on a rational, economical and pragmatic approach using common sense as a basis in which the interests and risks of the most important parties involved are seriously and objectively taken into account.

1 INTRODUCTION

Through regional authorities Rijkswaterstaat acts as the asset manager of the Dutch national road network and waterways system. In this role Rijkswaterstaat is responsible for a wide range of structures, e.g. bridges, viaducts, overpasses, tunnels, sluices, and sea defense structures. Given the high economical importance of the national network it is logical that highways agencies will adopt a more conservative approach in the design of new structures in order to minimize major maintenance activities and thus traffic disruption during the full operational service life, see Figure 1. This implies that normally any changes in design solutions from the common approach are treated with serious caution as this imposes a potential and unknown risk for the future availability of the network system.

For most infrastructural facilities it is common to adopt a design service life of 100 years, i.e. much longer than the experience obtained until now based on the stock of existing structures. In practice, defective joints in bridges and viaducts clearly impose most of the maintenance problems necessitating frequent repairs at intervals of 10 to 20 years. Generally, reinforced and pre-stressed concrete are considered the most versatile and economical solution for most infrastructural facilities, resulting in a largely maintenance free service life. However, in literature it is often argued that a significant number of concrete structures suffer from premature corrosion of the embedded reinforcing steel, posing a major threat for serviceability and necessitating vast amounts of money for repair.

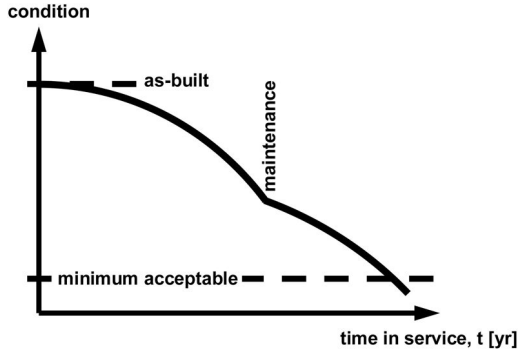

Figure 1. Conceptual model for condition development of infrastructural facilities aimed at a minimum of maintenance during the operational service life.

In the Netherlands, however, until now, damage due to corroding reinforcement is relatively limited although a significant number of structures have reached an age in excess of 50 years. With respect to the infrastructure facilities owned and managed by the Ministry of Infrastructure this is attributed to a combination of conservative design, good quality control during construction, inspections and adequate preventive maintenance at regular time intervals, relative moderate exposure conditions, and the use of concrete based on blast furnace slag cement with a minimum slag content of 50% or fly ash cement having a minimum fly ash content of 25%. In situations where damage has occurred this is limited to specific areas

and most often due to a shallower cover depth than the design cover and poor execution practices (compaction and curing).

In view of the increasing age of existing structures asset managers are becoming more and more interested to have a clearer picture on the actual condition of the complete stock of existing infrastructure so as to anticipate possible maintenance regarding planning and allocation of the financial resources. Consequently, there is also a clear need for prediction of the condition level over time.

Regarding the design of new structures, the current codes are based on traditional options and thus give ample possibilities for alternative solutions. For instance, at present the significantly different performance of binders is often not taken into account in the codes. Therefore it is not surprising that in recent years a clear trend can be observed towards the application of mathematical modelling using a probabilistic approach for durability, e.g. the fib Model Code on Service Life Design (fib 2006) in which a clear distinction is made between types of cement. In the Netherlands, Polder (Polder et al. 2010) developed a CUR Guideline based on the DuraCrete methodology (CUR 2000) to overcome most of the practical problems associated with the use of mathematical models for durability design and especially when a full probabilistic approach is employed. This CUR Guideline (CUR 2009) focuses on a performance-based approach with respect to chloride-induced corrosion.

2 APPROACHES ON DURABILITY DESIGN

The current codes for durability design of new structures are based on empirically derived relationships between concrete mix composition and observed laboratory and field performance. This so-called deemed-to-satisfy approach assumes that the concrete composition selected will result in the desired service life of the structure. One of the major shortcomings is that the significantly different performance of binders is not adequately taken into account. In addition, the durability requirements in the current codes are felt to be illogical regarding cement content and water to cement ratio. Most codes give the impression that a higher cement content will correspond to a higher concrete quality in terms of permeability, however, there is no clear proof that this is generally true. Moreover, a higher cement content will increase the risk of shrinkage cracking which will undoubtedly have an adverse effect on the long-term durability of a concrete structure. It should be appreciated that eventually the achieved properties are relevant rather than the (relative) amount of ingredients used in a concrete mix. In this respect it should be noted that regarding durability the properties of the concrete surface layer (covercrete) are much more important than those of the corecrete. Most of the shortcomings in the codes are felt by concrete producers and contractors as in practice the requirements related to durability may conflict with other requirements, e.g. on strength at a certain age or on workability.

In recent years a clear trend is observed towards the introduction of a performance based approach in which an overall durability requirement for the complete structure should be met. In general, this overall requirement can be achieved by a variety of alternatives and with respect to reinforcement corrosion such a performance-based durability approach will have to be translated into objectively quantified requirements on quality and quantity of the concrete cover. As all alternatives will result in equivalent overall performance of the structure the contractor is then given full freedom to choose the most economical solution.

In order to derive performance requirements mathematical models on relevant degradation processes are introduced. As most model parameters are of a stochastic nature, a probabilistic approach is often advocated. Mathematical modelling allows for prediction of the condition of a structural component over time and can be used to demonstrate equal performance of design solutions. Ideally, degradation models should be mathematically and physically sound, provide logical and realistic results, be understandable and usable for practitioners, and thus be to a considerable extent foolproof. In the literature, a significant number of mathematical models on single degradation mechanisms can be found, ranging from purely empirical, e.g. by employing a simple polynomial approach taking into account parameters considered to be relevant, to models demonstrating a high academic level by using mathematical functions and parameters that remain largely unknown or at least rare to most practitioners.

Whatever method or mathematical model is used the approach adopted should be transparent and consistent, and the outcome should be logical and realistic. However, in practice it is observed that most models include significant pitfalls and limitations which are either not mentioned or not known even to the developer. In addition, in most cases the quantification of the input parameters is not addressed which will undoubtedly result in 'shopping' to obtain suitable input values. In this respect the use of input values based on so-called expert opinion should be treated with serious caution. Moreover, it has to be noted that most mathematical models have been calibrated on results obtained for laboratory experiments that have been performed under ideal conditions not reflecting situations encountered in practice or on a limited number of results from relatively short-term exposure of real structures.

In the Final report of the European project CHLORTEST (CHLORTEST 2006) it was reported that 'a very relevant conclusion is that most of these (chloride ingress) models are still not very accurate in predicting reality'. The results of benchmarking showed that only one model gave a reasonably good prediction on the longer term. However, this cannot be considered a real surprise as this model had been previously calibrated with most of the chloride

profiles available for the benchmark. On the other hand this experience indicates the importance of calibration with reliable long-term data obtained from real structures.

Experience in practice has shown that the use of a probabilistic approach frequently results in a numbers game and checks on the input and the calculations are seldom performed. As the attention becomes more and more focused on the mathematical modeling, there is considerable risk that both the asset manager and the contractor will not be able to check the reliability of the input as well as the output.

In the following the Dutch CUR Guideline developed by Polder et al. (CUR 2009) will serve as an example to demonstrate the pitfalls and shortcomings in a performance-based approach to be used in practice.

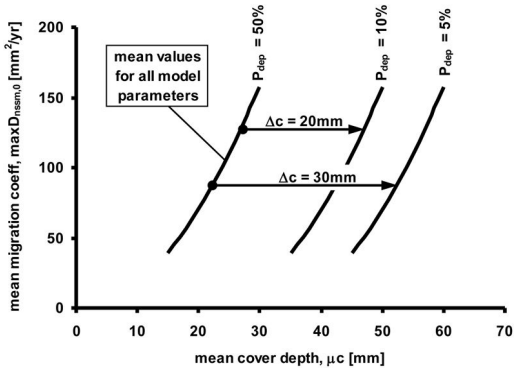

Figure 2. Basic principle of the semi-probabilistic approach as suggested by Polder (CUR 2009, Polder 2010).

3 THE 'DUTCH' APPROACH

The major objective of the Dutch CUR Committee VC81 was to develop a practical methodology for a performance-based approach including criteria for reinforced concrete structures exposed to chlorides comprising exposure classes XD (de-icing salt environment) and XS (marine environment). Such an approach would allow more freedom for the contractor to choose the most economical solution for a given design service life. For the asset manager the advantage is that an objective quantified approach is applied demonstrating that the overall performance requirement as specified by the asset manager will be met for the concrete structure or concrete element for any desired design service life. For reinforcement corrosion the performance requirement is expressed in a maximum probability that depassivation of the steel reinforcement will occur at an age $t = t_{dsl}$, i.e. the specified design service life.

Based on the so-called DuraCrete model (CUR 2000) for chloride ingress, performance criteria related to concrete quality were developed dependent on thickness of concrete cover and type of cement. As a full probabilistic approach was considered too laborious and tricky to be used in practice by the engineering consultant a mathematical simplification was introduced. This resulted in a 'semi-probabilistic' approach (CUR 2009), which was based on a graph presented by Rostam (Rostam 2003). In essence, the underlying reasoning was that the use of mean values for all model parameters would result in an unacceptable probability of depassivation, $P_{dep} = 50\%$, but through the introduction of an increase for (mean) cover depth by $\Delta c = 20$ mm, it was thought that P_{dep} would be reduced to a level of 10%, being the proposed criterion for normal reinforcing steel. For prestressing steel $\Delta c = -30$ mm was chosen considered to correspond to $P_{dep} = 5\%$, see Figure 2. It should be noted that originally in the first draft versions $\Delta c = 15$ mm (reinforcing steel) and $\Delta c = 25$ mm (prestressing steel) were adopted (Polder 2006). These

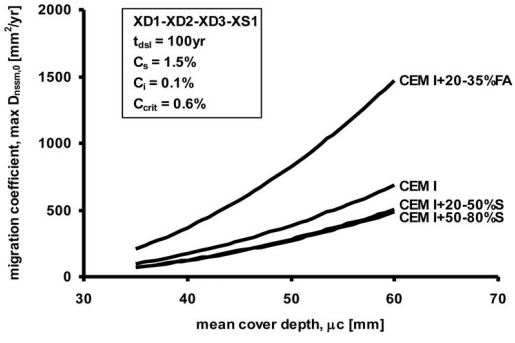

Figure 3. Relationship between mean concrete cover depth, μc, and chloride migration coefficient, $maxD_{nssm,0}$, according to CUR Guideline 1 [10].

values were derived directly from the graphs presented by Rostam, however, without having any information on the statistical quantification of the input parameters that had been used.

Note that the concrete quality is expressed in terms of a chloride migration coefficient, $D_{nssm,0}$, as determined according to NT Build 492 (Nordtest 1999) on laboratory specimens at an age of 28 days. For practical reasons a unit of mm^2/yr has been chosen, with $1 \cdot 10^{-12}$m^2/s being equal to 31.56 mm^2/yr. A higher resistance of concrete to chloride ingress will correspond to a lower value for $D_{nssm,0}$.

For design purposes in CUR Guideline 1, tables for a design service life of 80, 100 and 200 years were established providing data for acceptable combinations of mean thickness of concrete cover, μc, and maximum chloride migration coefficient, $maxD_{nssm,0}$. In each table a clear distinction between 4 groups of cement and 2 groups of environmental exposure conditions was made, thus resulting in 8 design options. In order to simplify a closer evaluation, the results obtained for exposure group XD, comprising exposure classes XD1, XD2, XD3 and XS1, for $t_{dsl} = 100$yr are presented in Figure 3.

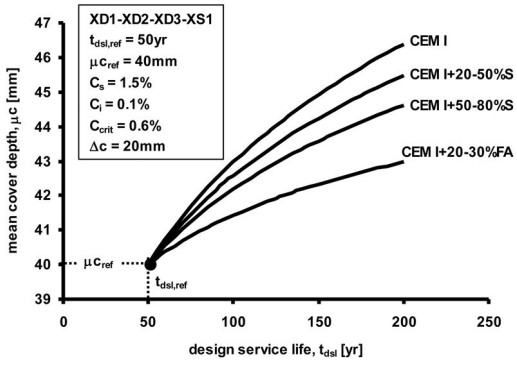

Figure 4. Calculated relationship between design service life, t_{dsl}, and mean concrete cover depth, μc, for a given concrete composition, implicitly assumed by CUR Guideline 1.

It has to be noted that CUR Guideline 1 does not present any graphs on the established relationship μc-$maxD_{nssm,0}$.

CEM I + 20–50%S refers to cement containing 20 to 50% of blast furnace slag, CEM I + 50–80S comprises cement containing 50 to 80% of slag, and CEM I + 20–30FA indicates cement with 20 to 30% fly ash. The group identified by CEM I is not clearly defined but is assumed to comprise all cements not covered by CEM I + 20–50%S, CEM I + 50–80%S and CEM I + 20–30%FA.

4 CRITICAL EVALUATION OF CUR GUIDELINE 1

For the outsider, at first sight the combinations of mean cover depth, μc, chloride migration coefficient, $maxD_{nssm,o}$, as presented in the tables of CUR Guideline 1 seem logical and reasonable. However, when looking in more detail and elaborating some simple calculation examples, the picture becomes completely different. In the following a limited number of findings will be presented.

Logically, the maximum allowable value of $D_{nssm,0}$ will increase as a higher concrete cover depth is chosen. This is indeed the case in the tables as can also be seen from Figure 3.

The semi-probabilistic approach adopted allows to derive a relationship between design service life, t_{dsl}, and required mean cover depth, μc, for any given concrete quality, as expressed by a specific value of $D_{nssm,0}$. As an example, if it is assumed that for a given concrete composition, corresponding to a certain value of $D_{nssm,0}$, a mean concrete cover depth $\mu c = 40$ mm is considered to be acceptable for exposure class XD3, then this can be used as a reference to calculate the mean concrete cover depth needed for any design service life, t_{dsl}.

Figure 4 shows the results based on $\mu c_{ref} = 40$ mm ($t_{dsl,ref} = 50$ yr; XD3) for all groups of cement distinguished in CUR Guideline 1.

Thus, from Figure 4, it can be derived that for concrete made with CEM I + 20–30%FA as little as 3 mm extra cover depth is required to extend the design service life from 50 years to 200 years, whereas for concrete made with CEM I less than 7 mm (6.4 mm) extra thickness in concrete cover would be required to achieve a 4-fold service life. According to the prevailing European standard (EN 1992-1-1 2011) for a design service life $t_{dsl} = 100$ year the nominal cover depth, c_{nom}, has to be increased by 10 mm relative to the nominal cover depth required for $t_{dsl} = 50$ yr. For simplicity the nominal and the mean cover depth can be regarded to be equal. Thus it has to be concluded that according to the approach developed by Polder et al. the European standard has to be considered much too conservative: an extra of 1 mm to 5 mm at the most will already be sufficient to achieve an extension from 50 to 100 years design service life. It will be evident that any respectable and knowledgeable asset manager will never accept such a result, even if this result is said to be the calculated outcome of the mathematical model employed in DuraCrete.

In CUR Guideline 1 it is explicitly written: 'With this (semi-probabilistic) approach it is presumed that at the end of the intended design service life for reinforcing steel, the probability of corrosion initiation will be less than approximately 10% and less than approximately 5% for prestressing steel.' From an owner's perspective this statement raises at least 2 essential questions. Apparently, a probability $P_{dep} = 10\%$ is considered acceptable – however no quantitative physical interpretation of 10% probability of corrosion initiation in terms of amount of corroding reinforcing steel, damage and visual appearance is given. However, for an owner such an interpretation is essential in view of anticipated maintenance and repair activities. The second question relates to the introduction of 'approximately'. Logic would dictate that any mathematical simplification of a full probabilistic approach should result in a conservative estimate and thus the semi-probabilistic approach advocated in CUR Guideline 1 should always result in less than 10% probability of corrosion initiation. As for all model parameters, X, statistical data is provided, i.e. mean value, μX, standard deviation, σX, and type of statistical distribution, e.g. lognormal, for each allowable combination μc-$maxD_{nssm,0}$ the resulting value of P_{dep} can easily be quantified by performing a full probabilistic calculation. Figure 5 presents the detailed results, including the allowed value of $maxD_{nssm,0}$, obtained for concrete made with a cement pertaining to group CEM I ($t_{dsl} = 100$ yr; XD1-XD2-XD3-XS1).

Figure 6 presents the calculated results for all groups of cement with $t_{dsl} = 100$ yr for exposure group XD1-XD2-XD3-XS1, whereas Figure 7 shows the results for exposure group XS2-XS3. Both Figure 6 and 7 clearly demonstrate that the calculated probability of depassivation shows a wide range, for the XD group between 3.6 and 20.6% and for the XS group between 0.5 and 17.2%.

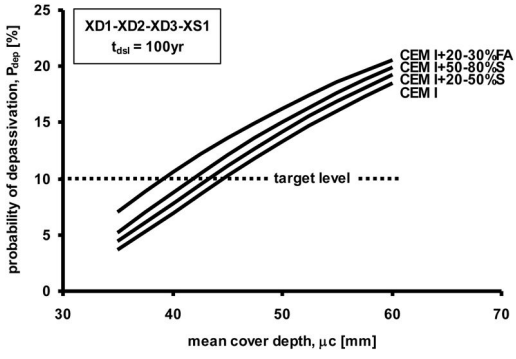

Figure 5. Probability of depassivation as a function of mean cover depth according to a full probabilistic calculation for combinations μc-$maxD_{nssm,0}$ allowed by CUR Guideline 1 (CEM I; $t_{dsl} = 100$ yr, XD1-XD2-XD3-XS1).

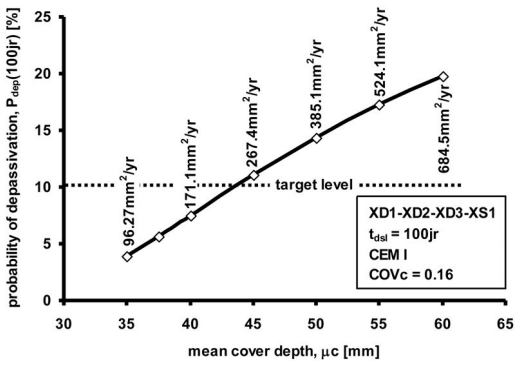

Figure 6. Probability of depassivation as a function of mean cover depth according to full probabilistic calculations for combinations μc-$maxD_{nssm,0}$ allowed by CUR Guideline 1 ($t_{dsl} = 100$ yr, XD1-XD2-XD3-XS1).

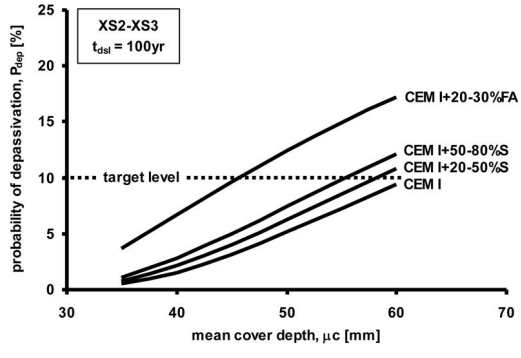

Figure 7. Probability of depassivation as a function of mean cover depth according to full probabilistic calculations for combinations μc-$maxD_{nssm,0}$ allowed by CUR Guideline 1 ($t_{dsl} = 100$ yr, XS2-XS3).

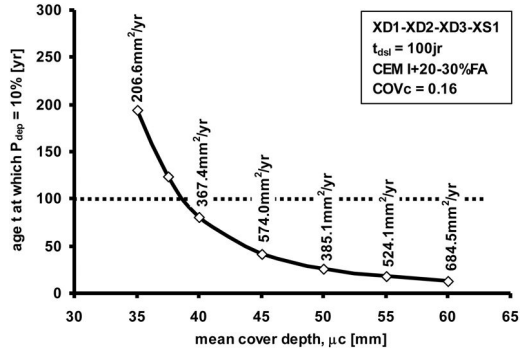

Figure 8. Calculated age at which $P_{dep} = 0.10$ for combinations μc-$maxD_{nssm,0}$ allowed by CUR Guideline 1 (CEM I + 20–30%FA; $t_{dsl} = 100$ yr, XD1-XD2-XD3-XS1).

In CUR Guideline 1 a limited number of case studies are performed to calibrate the semi-probabilistic approach which also result in a serious scatter around the target level $P_{dep} = 10\%$. It is argued that on average the probability will be around 10% and thus it is concluded that the semi-probabilistic approach is an acceptable simplification. However, this line of reasoning is considered to be illogical. Acceptance of CUR Guideline 1 by an assumingly knowledgeable and reliable principal, like Rijkswaterstaat, would imply that design solutions corresponding to $P_{dep} = 0.21$ are considered to be equal as solutions with those corresponding to $P_{dep} = 0.05$. For use in practice such a wide range of P_{dep} claimed to result in equal durability performance is regarded highly undesirable as this would undoubtedly result in misuse by the contractor or concrete producer. Thus it has to be concluded that this so-called semi-probabilistic approach based on an increase of the mean cover depth by 20 mm is an inadequate simplification of full probabilistic calculations and has therefore to be considered a rule of thumb at its best. The predicate 'semi-probabilistic' is highly misleading and it is likely that it is merely introduced as a selling argument to convince owners, contractors and concrete producers.

Another proof of the inadequacy of the mathematical simplification can be demonstrated by calculating the age at which the target level $P_{dep} = 0.10$ will be achieved. Figure 8 shows the results obtained by full probabilistic calculations for concrete made with CEM II/B-V, for the combinations μc-$maxD_{nssm,0}$ allowed by CUR Guideline 1 with $t_{dsl} = 100$ yr and exposure group XD. For $\mu c = 60$ mm the $P_{dep} = 0.10$ will be achieved at $t \approx 15$ yr whereas for $\mu c = 35$ mm, requiring a higher concrete quality, t ≈ 195 yr.

An additional point of discussion is the combining of several exposure classes into one group. As an example, according to EN-1992-1-1 exposure class XD3 has to be considered more severe than XD1, and thus requires a 10 mm higher cover depth. However, according to CUR Guideline 1 XD 1 and XD3 should be treated in the same way.

Although the main authors have indicated they are fully aware of the dramatic errors in the approach, the unrealistic nature of the calculation results, the strong

indications that the theoretical basis of the migration test is questionable, and serious problems will be encountered in practice for concrete producers and contractors. After publication of CUR Guideline 1 they have authored several articles on CUR Guideline 1, presenting it as 'the Dutch approach', see e.g. Polder et al. (2010) and Wegen, van der et al. (2012). However, Rijkswaterstaat has officially rejected this CUR Guideline to be used for their projects (Rijkswaterstaat 2011), and according to Boutz and Van der Wegen (2012) in the Netherlands hardly any projects can be found in which this approach has been applied.

5 DISCUSSION ON SOME CRITICAL APECTS

In order to derive criteria for a performance-based approach, most often mathematical models describing degradation mechanisms are used. It should be appreciated that these mathematical expressions are always based on a simplification of the actual physical and chemical processes using assumptions and introducing boundary conditions. However, these assumptions and boundary conditions are either not known or simply forgotten by the consulting engineer. The most obvious is that most models describe 1-dimensional chloride ingress whereas in reality 2 or even 3-dimensional transport will occur.

The mathematical model generally used for chloride ingress has been modified in the course of time. This has resulted in the fact that results obtained by calculations based on the differential equation will yield different results than those obtained using the analytical solution. The reason for this is that due to these modifications, the mathematical expression does not satisfy the differential equation anymore.

A model can only be used when input values are available. However, there is a considerable lack of sound data obtained from real structures to quantify model parameters. It should be appreciated that most parameters cannot be measured directly but are derived through regression analysis of chloride profiles, e.g. the apparent chloride diffusion coefficient, D_a, and the surface chloride content, C_s. However, based on practice experience the outcome is often dependent on the person performing the analysis.

In CUR Guideline 1 the quantification of most model parameters is based on expert opinion due to a lack of data from practice. In particular, this applies to the ageing exponent, n, used to describe the development of the chloride transport properties over time. It is known that this ageing factor has a pronounced effect on the outcome. In literature, a wide range of values for n can be found and consequently a wide range of output can be calculated. Consequently, the quantification of the ageing exponent is frequently prone to massage and even manipulation in order to achieve the desired and hopefully realistic result.

In all mathematical models implicit assumptions are made on the validity in time. In CUR Guideline 1 the so-called DuraCrete model is used to derive performance criteria for a design service life $t_{dsl} = 200$ yr. However, it is very unlikely that the transport properties of the concrete cover will develop according to the same trend as during the time period up to an age of 50 yr. Figure 4 demonstrates the foolishness of this implicit assumption.

6 CONCLUDING REMARKS

- An objective, sound and rational basis for a performance-based approach for durability design is urgently required.
- However, in most situations a simple and pragmatic approach will be more useful and economical.
- At present there is too much emphasis on mathematical modeling but it should be appreciated that eventually the quality of the concrete cover is achieved on site and not by calculations or through laboratory testing.
- Consequently, for practice it is considered much more effective to pay more attention on quality control on site than to employ complex mathematics.
- The quality of placement, compaction and curing have a significant impact on the cover quality eventually achieved.
- Mathematical models to be used for service life design should be mathematically and physically sound, provide logical and realistic results, understandable and usable for practitioners, and thus to be to a considerable extent foolproof. However, at present most models available do not obey these essential requirements.
- In view of the high uncertainties in the quantification of model parameters, a probabilistic approach is often advocated. However, such an approach will then often lead to unrealistic results and thus input values are prone to manipulation to validate the model.
- Through the introduction of calibration factors most mathematical models are basically empirical in nature and thus the output will only be valid for the conditions employed for calibration. However, such conditions may not prevail in practice for real structures.
- Due to a lack of data, model parameters are often quantified based on 'expert opinion'. However, generally this is not explicitly mentioned. Since calibration factors have been quantified using such model parameters, any change of expert opinion in the course of time should be accompanied by a re-quantification of the associated calibration factors.
- Qualifications like expert opinion, state-of-the-art and semi-probabilistic approach have to be regarded with serious caution as these qualifications are frequently misused to conceal lack of information, knowledge, and responsibility.
- Full and semi-probabilistic approaches for service life design are prone to manipulation of input values

as to achieve the desired result. Neither the principal, asset manager, consulting engineer, concrete producer nor contractor have sufficient knowledge and expertise to validate the input and the output of probabilistic calculations.
- A critical evaluation of the reality level of the output generated by models through graphs is a basic requirement.
- The limitations, constraints and assumptions of any mathematical model should be clearly identified and explicitly indicated. Most mathematical models are considered reliable until an age of 50 years.
- The actual physical meaning of probability of depassivation of reinforcing steel, remains largely unknown. In literature this issue is hardly addressed as the main focus is on the calculation exercise. However, for the asset manager probabilities are less important as he is interested in the associated consequences and thus in his risk. This aspect is often overlooked.
- The asset manager will always suffer from the largest risk. However, this is often not fully appreciated by academics and to a lesser extent by the consulting engineer, the laboratory performing the performance test, the concrete producer and the contractor. In order to prevent too much trial and (t)error in practice it would be beneficial too shift more responsibility and thus risk to other parties advocating (probabilistic) modeling.
- For adequate and realistic design for durability the most important aspect is to use common sense and not to solely rely on what mathematical models dictate.

Any future developments on performance-based methods should focus on a rational, economical and pragmatic approach using common sense as a basis in which the interests and risks of the three most important parties, i.e. the owner, contractor and concrete producer are seriously and objectively taken into account. Therefor these there parties should first describe and the define 'the problem' as well as the boundary conditions. All activities involved in the development of a performance-based approach should be managed and coordinated by these three parties with consultants, scientists and laboratories acting at a supporting level in order to minimize the interference of their self-interest.

REFERENCES

Boutz, M. & Wegen, G. van der 2012 Case studies CUR Guideline. *Cement* **1**: 22–26 (in Dutch).

CHLORTEST 2006. CHLORTEST Final Technical Report. *Resistance of concrete to chloride ingress – from laboratory tests to in-field performance*. EU-Project GRD1-2002-71808.

CUR 2000. DuraCrete – Final Technical Report. Gouda: CUR Document BE95-1347/R17.

CUR 2009. Durability of structural concrete with respect to chloride induced reinforcement corrosion. Gouda: CUR (in Dutch).

EN 1992-1-1 Eurocode 2. 2011. Design of concrete structures –Part 1-1: General rules and rules for buildings.

fib 2006. Model code for service life design. Lausanne, *fib*, Bulletin 34.

Nordtest 1999. Chloride migration coefficient from non-steady state migration experiments. NT Build 492

Polder, R. van der Wegen, G. and van Breugel, K. 2007 Performance based guideline for service life design of concrete for civil engineering structures – A proposal discussed in the Netherlands. In Véronique Baroghel-Bouny et al. (eds), *Performance Based Evaluation and Indicators for Concrete Durability*; *Proc. intern. workshop, Madrid, 19–21 March 2006*. Bagneaux, RILEM, PRO 47.

Polder, R. Wegen, G. van der & Breugel, K. van 2010. Guideline for service life design of structural concrete with regard to chloride induced corrosion – the approach in the Netherlands. In Klaas van Breugel et al. (eds), *Service Life Design for Infrastructure*; *Proc. 2nd intern. symp., Delft, 4–6 October 2010*. Bagneux: RILEM, PRO 70.

Rostam, S. 2004. Long-term performance of concrete structures: The challenge for DuCon to integrate strength, durability and sustainability. *Centre for Durable Concrete Structures*.

Rijkswaterstaat 2011. Position of Rijkswaterstaat Centre for Infrastructure regarding CUR Guideline 1. Utrecht (in Dutch).

Wegen, G. van der, Polder, R. & Breugel, K. van 2012. Guideline for design of structural concrete – A performance based approach with regard to chloride induced corrosion. Delft: HERON, Vol. 57, No. 3: 153–167.

This page intentionally left blank

Concrete Solutions – Grantham et al. (Eds)
© 2014 Taylor & Francis Group, London, ISBN 978-1-138-02708-4

Turkey's grand challenge: Disaster-proof building inventory within 20 years

O. Gunes
Istanbul Technical University, Istanbul, Turkey

ABSTRACT: Turkey is located in a high seismicity region and has suffered extensive losses due to several major earthquakes that struck its various parts in the past two decades. While earthquakes are associated with damage and loss wherever they may occur, the destructive effects of those in Turkey are exacerbated by the large volume of code incompliant buildings constructed with poor materials and workmanship. As a large scale remedial initiative, Turkey has recently embarked upon a grand challenge of retrofitting or renewing all high-risk buildings within the next 20 years. This multi-million building and multi-billion dollar initiative has inevitably raised activity and debates in diverse disciplines regarding all aspects. This paper focuses on the methodologies and developing technologies for rapid condition assessment and structural evaluation of existing buildings in order to identify and prioritize high-risk buildings and for guiding decisions on retrofitting or renewal.

1 BACKGROUND AND INTRODUCTION

Protection of people and the built environment from the destructive effects of natural hazards is a worldwide challenge that faces nations at various degrees of significance based on (1) the type of observed hazards; (2) the size of exposure, i.e. the number of people and structures affected by the hazards; (3) vulnerability of the exposure to the impinging hazards. The prediction and mitigation of damage and losses inflicted by natural hazards are among the most active and invested areas of research participated by all nations in proportion with their exposure and resources (Kidokoro et al. 2008).

A quick survey of the most damaging and deadly natural disasters recorded in history reveals that earthquakes occupy a prominent proportion, especially when followed by resulting hazards such as a large fire or a tsunami (Coburn & Spence 2002). Indeed, earthquakes constitute a primary concern in any country located in a seismic zone. Despite the unceasing attempts to predict earthquakes in more than a hundred years, it is clear that seismic events cannot be predicted accurately enough to issue alarms of imminent damaging earthquakes (Geller 1997). Nevertheless, significant progress made in fault modeling and probabilistic assessment of seismic hazard combined with performance based structural design and evaluation methods provide the necessary tools for engineers to be prepared for earthquakes (Kramer 1997, Bozorgnia & Bertero 2004) although cases of prominent skepticism regarding the validity of probabilistic hazard assessment should be noted (Gulkan 2012). The meaning of preparedness may naturally differ for different nations based on the size of their economy, their level of investment in infrastructures, and their perception of acceptable risk for the population and infrastructure (Coburn & Spence 2002). Although the level of confidence and conservatism used in the aforementioned tools for preparedness may differ in different codes, a generally accepted level of satisfactory performance is (a) for ordinary residential and commercial buildings to survive a design earthquake without collapse; (b) for essential buildings such as schools and hospitals to stay functional after a design earthquake and survive a rare earthquake; and (c) for critical facilities and lifelines to stay fully operational after a design earthquake and stay functional after a rare earthquake.

Turkey is a country known for its unique geography that bridges continents and cultures. It also bridges several tectonic plates including the Eurasian, African, and Arabian plates through the Anatolian plate (Bommer et al. 2002). Interactions between all surrounding plates and the Anatolian plate produce an active seismic region that encompasses most of Turkeyas shown in Figure 1. As a result, earthquakes have been by far the most significant natural hazards in the region. Based on available records, all natural disasters in Turkey since the beginning of the 20th century resulted in 87 thousand casualties, 210 thousand injuries, and 651 thousand heavily damaged or destroyed homes. Earthquakes were responsible for 76% of the damaged or destroyed homes, followed far behind by landslides (10%) and floods (9%) (Ergunay 2007). Several moderate to devastating earthquakes that occurred in Turkey in the past two decades have claimed nearly 20 thousand lives and cost more than $17 billion in direct and indirect losses. The most significant one among these was Kocaeli Earthquake (Aug. 17, 1999, Mw = 7.4) which caused more than 17 thousand casualties and cost around $13 billion; and the most recent one was Van Earthquake (Oct. 23, 2011, Mw = 7.2)

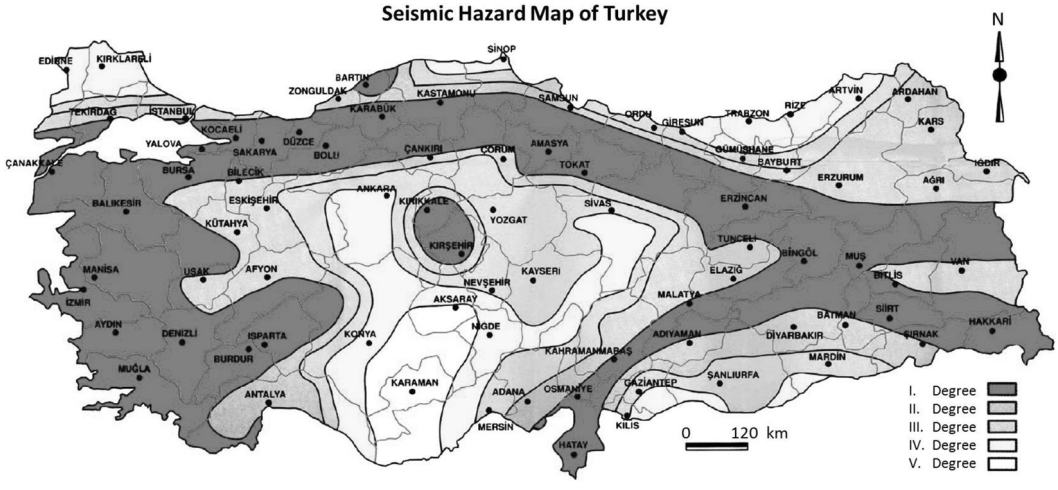

Figure 1. The seismic hazard map of Turkey (Source: Republic of Turkey, Prime Ministry Disaster and Emergency Management Presidency, AFAD).

Table 1. Distribution of various elements within different seismic zones (Ergunay 2007).

Seismic zone (Fig. 1)	Area (%)	Population (%)	Industry (%)	Dams (%)
I (pga = 0.4 g)	42	45	51	46
II (pga = 0.3 g)	24	26	25	23
III (pga = 0.2 g)	18	14	11	14
IV (pga = 0.1 g)	12	13	11	11
V (pga < 0.1 g)	4	2	2	6

which caused more than 6 hundred casualties and cost $1–2 billion (Buyukozturk & Gunes 2002, 2003, Ergunay 2007, Erdik et al. 2012).

Table 1 shows the distribution of various elements such as land area, population, industrial installations and hydroelectric dams within the seismic zones shown in Figure 1 (Ergunay 2007). About half of each element is located in the first degree seismic zone and most of each is located in some degree of seismic zone other than V. Hence, earthquakes affect nearly the entire nation and unless effective mitigation strategies are developed and implemented in a timely fashion, seismic losses will continue to increase in the future.

The concerns highlighted by Figure 1 and Table 1 are exacerbated by the fact that a very large portion of Turkey's building stock does not comply with either the structural/seismic codes that were effective at the time of their construction, or the ever more stringent modern seismic code enforced today. As a matter of fact, it is often reiterated in the daily press and accepted by the government officials that half to three quarters of existing buildings in Turkey lack the design documents and permits required for their construction. Referred to as illegal construction, these buildings are generally constructed with poor materials and workmanship due to insufficient or no supervision or inspections during construction.

An even more concerning development right after the devastating Kocaeli Earthquake in 1999 was the findings of a scientific study which indicated that the probability of occurrence of another severe and destructive earthquake along the North Anatolian Fault, near Istanbul, was $62 \pm 15\%$ within the next 30 years (Parsons et al. 2000). Now almost 15 years after this study, the progress made towards preparing for the next big earthquake has not gone much beyond pilot studies of regional risk assessment and seismic retrofitting of a limited number of essential buildings. Istanbul and the adjacent areas constitute the most densely populated and most industrialized region in Turkey, hence, the heart of Turkish economy. It is impossible to make reliable estimates of seismic losses due to aforementioned complexities but studies based on scenario earthquakes close to Istanbul roughly estimate 30–40 thousand heavily damaged buildings – corresponding to 5% of the building stock in the region – with 5–6 thousand of them collapsed, 30–50 thousand casualties and $11 billion in direct losses due to damage to buildings (Erdik et al. 2003, Strasser et al. 2008).

2 THE GRAND CHALLENGE AND THE SCOPE

The grim picture portrayed by the facts laid out in the preceding section has long called for immediate action in terms of putting greater emphasis and investing more resources on increasing disaster resilience of the building infrastructure in Turkey. During the early years after Kocaeli Earthquake in 1999, the main priority was the recovery of the affected region by means of building housing for those in need of shelter and restoring the interrupted economic activity. In addition to disaster relief funds, the recovery efforts were funded by international aid and special temporary taxes which

later became permanent. In the following years, the above-mentioned call was largely subdued by concerns related to the national economy. Seismic mitigation efforts attracted relatively modest attention and budget for more than ten years during which related research studies were skewed more towards seismic risk assessment than development and implementation of effective retrofit/renewal strategies. Isolated cases of larger scale initiatives such as the Istanbul Seismic Risk Mitigation and Emergency Preparedness Project (ISMEP) must be duly noted (www.ipkb.gov.tr). This ongoing project was initiated in 2005 with a €310 million budget which rose to €1 billion 213 million by 2012, all funded by loans from international funding institutions. Expected to be completed in 2018, main components of the project include (a) enhancing emergency preparedness; (b) seismic risk mitigation for priority public facilities; (c) enforcement of building code. Although a large and comprehensive project, the limited retrofit/renewal content of ISMEP is far from addressing the overall need for seismic mitigation.

Van Earthquake of 2011 turned out to be a major wake-up call for the officials to finally take action on the seismic deficiency of the building stock. The launch of a massive initiative was announced right after the earthquake and six months later Law No 6306 "Transformation of areas under disaster risk," often referred to as the Urban Transformation Law, was approved by the Parliament to be implemented by the Ministry of Environment and Urbanization. The law sets the ground rules and procedures regarding the identification and renewal of high risk buildings as well as high risk areas, the latter of which is a controversial authority given to the cabinet. To facilitate rapid voluntary implementation, the law does not seek consent of all occupants in a building identified as high risk, but rather seeks agreement of two thirds of the occupants sufficient to implement the renewal process. Objections are handled by designated local technical commissions formed by ministry employees and university professors, whose decision is final. Once a building is deemed high risk, the administration has the authority to require its evacuation and demolition even without the consent of the occupants, or to have it demolished for reconstruction. Rent assistance and several fee deductions or waivers as well as financing options are offered to the occupants during the renewal process.

It is estimated that about one third of the nearly 20 million occupancy units in Turkey has insufficient seismic resistance and need retrofitting or renewal. This estimation is in agreement with, or perhaps inspired by, results of regional loss estimation studies (Ansal et al. 2009). The cost of urban transformation is roughly estimated as $500 billion and the time to completion is ambitiously set as 20 years. These figures make this initiative, if adamantly pursued, one of the largest reconstruction projects in history and Turkey one of the largest construction markets for the next two decades.

Besides the natural excitement in the construction industry and the real estate business, the urban transformation initiative has stirred heated discussions and debates in diverse disciplines regarding its all facets. The pros and cons of the urban transformation concept in general and the initiative in particular are scrutinized from sociological, political, legal, environmental, urban planning and human rights perspectives (Kuyucu & Unsal 2010, Ozus et al. 2011, Balaban 2012, Uysal 2012, Colak 2013, Karaman, 2013, Elicin 2014).

The scope of this paper is limited to the civil engineering aspect of the urban transformation initiative. Screening millions of structures to identify those with insufficient seismic resistance requires rapid, reliable and economical tools for condition assessment and structural evaluation. Statistics and important characteristics of the existing building stock in Turkey are presented first, followed by the codes and procedures currently in use. Methodologies and brewing technologies for rapid and reliable condition assessment and structural evaluation are discussed for their potential use in the identification and prioritization of high-risk buildings as well as for providing decision support regarding their retrofitting or renewal.

3 CHARACTERISTICS OF THE BUILDING STOCK IN TURKEY

3.1 *Population and structural characteristics*

Assessment of the size and characteristics of the exposure subjected to the seismic hazard shown in Figure 1 is an important component of seismic risk assessment and mitigation. In this section, brief information is provided about the numbers and important material and structural characteristics of existing buildings in Turkey.

The last comprehensive building census in Turkey was performed in 2000 by the State Institute of Statistics (TSE 2000), now known as the Turkish Statistical Institute (TUIK). Although a more recent 'Population and Housing Census' was performed in 2011, this study involved a sample of the population, albeit a large one, and not the whole population (TUIK 2011) with the objective to produce the population and housing statistics requested by the United Nations that could not be derived from the 'Address based Population Registration System' (APRS) established in 2007. While the 2011 census does not provide accurate information on population and number of buildings, the former can be obtained from APRS and the latter from numbers of building occupancy permits issued since 2000, which obviously exclude those constructed without permits. Figure 2 shows the total number of buildings, occupancy units, and the population in Turkey compiled from population and building census results, the occupancy permit data and the APRS data obtained from TUIK (www.tuik.gov.tr). As of 2010, the average size of households is 3.9 and the average number of occupants in a building is 8.7, where the average number of units per building is 2.25.

Distribution of the occupancy units by building age is shown in Figure 3 for Istanbul and Turkey based on the 2011 Building and Housing Census report (TUIK 2011). The information in the figure combined with the knowledge of seismic code development provides helpful information regarding the expected performance of buildings based on their construction era.

The first national seismic design code in Turkey was published in 1944 which was revised seven times at various dates until the most recent version published in 2007. Early versions of the code included mostly prescriptive rules. The 1975 version was the first to closely resemble modern seismic codes, whereas the 1998 version can actually be considered as one. The currently enforced 2007 version is the first to include state of the art performance based evaluation concepts and it is currently under revision for further improvements.

Possibly influenced by the above knowledge of seismic codes, performance grouping of buildings with respect to age is generally performed as pre- and post-1980 (Erdik et al. 2003, Strasser et al. 2008, Ansal et al. 2010). The latter group can further be divided as pre- and post-2001 considering that Law No 4708 Construction Inspection Law passed in 2001 has led to better quality control of buildings constructed after this date. According to this grouping, 23.4% of the existing occupancy units were constructed in or before 1980, 43.5% in 1981–2000, and 21.8% in or after 2001, while the construction year of 13.1% is unknown (TUIK 2011).

Height of buildings is an important characteristic in that combined with the local soil conditions it may have a strong influence on the level of seismic base shear and hence the level of damage and loss. The distribution of all occupancy units in Istanbul and Turkey by the number of floors in the building is shown in Figure 4 (TUIK 2011). Due to high population density and scarcity of land for construction, more than 40% of the occupancy units in Istanbul are in buildings six floors or higher. The average number of floors in Turkey was determined as 4.0 while that in Istanbul is much higher with an average value of 5.7.

The type of material and structural system of existing buildings are important indicators of their vulnerability under the effects of seismic actions. Vulnerability measures, whether empirical or based on rigorous analyses, are often expressed in conjunction with buildings' materials and structural system type, their age group, and height group (Erdik et al. 2003, Strasser et al. 2008, Ansal et al. 2010). Figure 5 shows the distribution of buildings in Istanbul and Turkey by their structural type. Data for 1984 and 2000 were obtained from the 2000 Building Census report (TSE 2000) while those for 2010 was compiled from building occupancy permits issued between 2000 and 2010, which should be considered as approximate values due to minor discrepancies in data obtained from different tables. Frame type structures, predominantly reinforced concrete frame buildings accounted for more than 90% of buildings constructed in 2000–2010. Hence, the proportion of frame structures in the building inventory is continuously increasing as can be seen from Figure 5. As of 2010, more than half the structures in Turkey were of frame type compared to less than one third in 1984. This ratio is much higher in Istanbul where more than three quarters of all buildings have frame type structural systems.

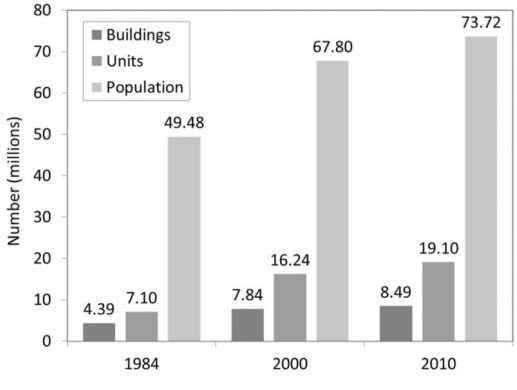

Figure 2. Total number of buildings and occupancy units in Turkey (Source: Turkish Statistical Institute, TUIK).

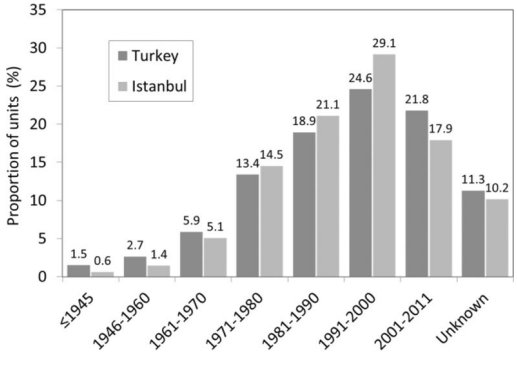

Figure 3. Proportions of occupancy units by the construction year of buildings in Istanbul and Turkey (Source: TUIK).

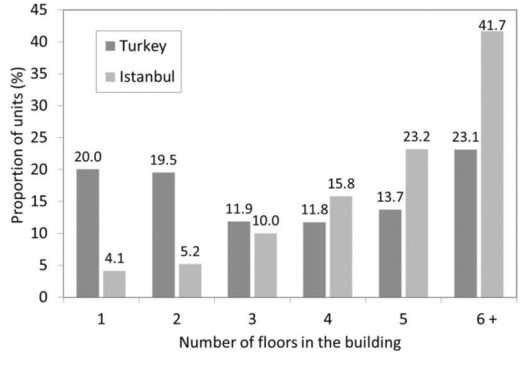

Figure 4. Distribution of occupancy units by the number of floors in the building in Istanbul and Turkey (Source: TUIK).

The information provided in Figures 3–5 about the age, height, and structural systems of existing buildings does not allow generalizations based on these characteristics. Nevertheless, Figure 6 shows sample photos of frequently encountered buildings constructed in different eras in Istanbul's Zeytinburnu district to give the reader a rough idea about the building profile in densely populated urban areas in Turkey.

3.2 *Materials characteristics*

Many factors play a role in the large scale destruction experienced during recent major earthquakes in Turkey. Among these, poor quality of construction materials is almost invariably cited as an important contributing factor in reports of heavily damaged or collapsed buildings. The current seismic code specifies a minimum characteristic compressive strength of 20 MPa for concrete used in buildings in seismic zones. However, the concrete strength in a majority of the existing buildings constructed before 2000,where concrete was mixed on site, falls below this minimum requirement, and values below 10 MPa are not uncommon. Figure 7 shows the characteristic compressive strength distribution of concrete samples obtained from a large number of reinforced concrete buildings in Istanbul and surrounding cities constructed before 2000 mostly using site-mixed concrete (Bal et al. 2008). The results have shown that the characteristic compressive strength of concrete in more than two thirds of the buildings was less than the required minimum (20 MPa). The percentage of buildings with a characteristic concrete strength 8 MPa or less was 21.3% which corresponded to about 135,000 buildings considering the building population in the studied region. Perhaps even more dramatically, the percentage of buildings with a characteristic concrete strength 4 MPa or less was 5.3%, corresponding to nearly 34,000 buildings in the region, which provides a clear indication of the size of destruction that can be caused by a major earthquake in the region.

Use of ready-mixed concrete in construction and improved site supervision enforced by the Construction Inspection Law (Law No 4708) passed in 2001 have improved the quality of concrete in buildings

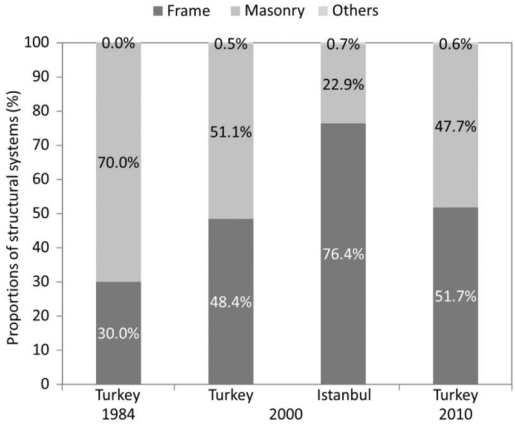

Figure 5. Distribution of buildings in Istanbul and Turkey by their structural system (Source: TUIK).

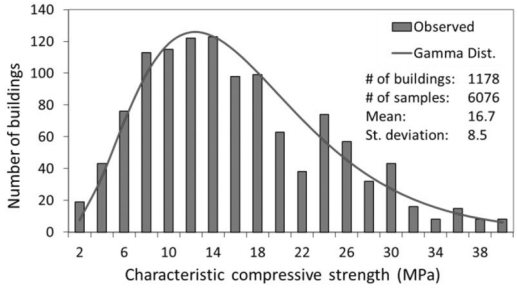

Figure 7. Distribution of concrete strength in buildings constructed before 2000 mostly with site-mixed concrete in Istanbul and surrounding cities (reproduced from Bal et al. 2008).

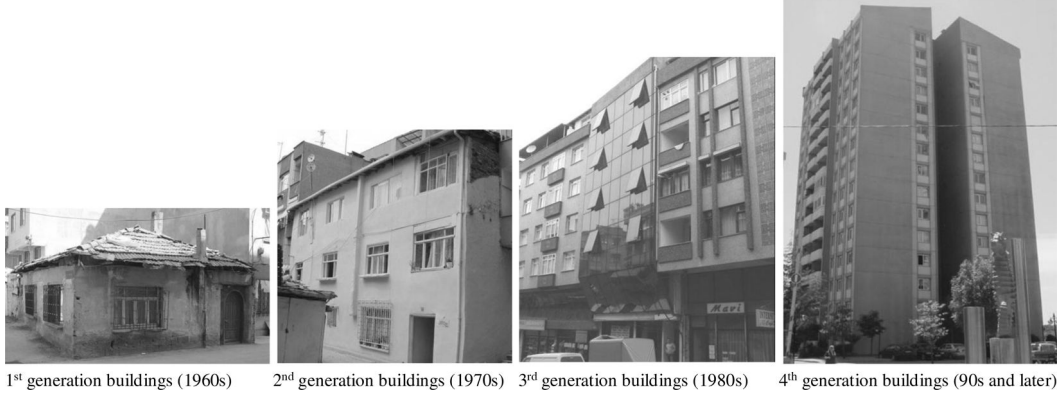

1st generation buildings (1960s) 2nd generation buildings (1970s) 3rd generation buildings (1980s) 4th generation buildings (90s and later)

Figure 6. Representative buildings by their construction era in Istanbul's Zeytinburnu region (Source: Republic of Turkey Ministry of Environment and Urbanization, General Directorate of Infrastructure and Urban Transformation Services, CSB-AKDHGM).

constructed after 2000. Bal et al. (2008) reported that 28-day strength of concrete samples obtained during construction of 433 buildings showed a log-normal distribution with a mean concrete strength of 24.9 MPa and a standard deviation of 2.1 MPa.

(a) S220 type smooth bars (b) S420 type deformed bars produced before and after 1990.

As important as the strength of concrete is the strength and ductility of the reinforcing steel used in buildings. Quality of steel reinforcement receives less attention than that of concrete since it is not produced on site and a relatively higher level of quality control is typically enforced during its production. The current seismic code requires use of deformed steel reinforcement in structures with the exception of shear reinforcement and slab reinforcement where smooth bars can be used. Typical types of deformed and smooth steel bars are S420 and S220, respectively, designations of which indicate their required characteristic yield strength in MPa. Reinforced concrete buildings constructed before the early 1970s involved exclusive use of S220 type steel as the use of S420 steel started with the first publication of the related standard TS 708 (2010) in 1973. Between the 1970s and late 1990s, use of S420 steel increased almost linearly. In buildings constructed after 2000, S420 type steel was used almost exclusively as most major steel manufacturers terminated the production of S220 type steel in late 1990s. (Bal et al. 2008)

Figure 8 shows the yield strength distributions of S220 and S420 type steel specimens obtained from existing buildings. These distributions, obtained from fairly large sets of data, were compiled by Bal et al. (2008) from data reported in the literature. The distribution of S420 type steel was presented as pre- and post-1990 due to the knowledge of significant difference in the characteristics of S420 type steel produced before and after 1990.

It should be emphasized that the data presented in Figure 8 shows the distribution of yield strength and not the characteristic yield strength. The definition of the characteristic yield strength in TS 708 was adopted from EN 10080 as "... the lower or upper limit of the statistical tolerance interval at which there is a 90% probability ($1-\alpha=0{,}90$) that 95% ($p=0{,}95$) or 90% ($p=0{,}90$) of the values are at or above this lower limit, or are at or below this upper limit, respectively." This definition refers to 90% confidence interval and for a large number of samples ($n>1000$) corresponds to the 5%-fractile value to be compared with the required minimum. Based on the sample size and yield strength distribution of S220 type steels in Figure 8(a), the characteristic yield strength was calculated as 212 MPa, which is slightly below the code requirement. Similar calculations for the S420 type steels in Figure 8(b) produced characteristic yield strength values of 334 and 357 MPa for pre- and post-1990 production, respectively, both of which are significantly below the 420 MPa minimum required by the code.

3.2.1 *Just how low is too low?*

Quantitative assessments of concrete and steel characteristic strengths presented in the preceding section point to numerous cases of significant deficiencies compared to respective code specified minimums. These deficiencies constitute a major contributing factor to the extent of destruction and losses caused by recent major earthquakes in Turkey. The lower end region of the concrete characteristic strength distribution shown in Figure 7 especially, which obviously excludes even more extreme cases of low quality concrete shown in Figure 9, sends out serious warning signs of the devastation that may still lie ahead in case of a major earthquake near Istanbul.

A crude estimation of the proportion of substandard buildings in Turkey based solely on the material characteristics shown in Figures 7 and 8 would yield a figure well above 50% just by comparing materials characteristic strengths with code required minimums. The real challenge, however, is to estimate the proportion that is likely to suffer heavy damage or collapse due to a design earthquake. This assessment requires seismic performance evaluation and cannot be based on materials information only. Still, one cannot help but ask: "Just how low is too low when it comes to materials strength?" Is there a minimum strength below which is unacceptable even when all else conforms to the codes and specifications? From a mechanics perspective, is there a minimum concrete strength

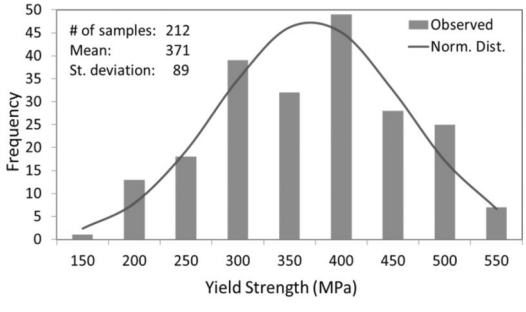

(a) S220 type smooth bars

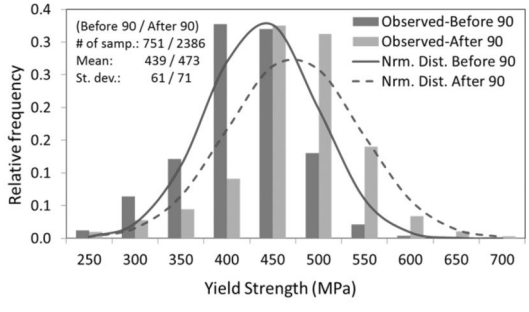

(b) S420 type deformed bars produced before and after 1990

Figure 8. Yield strength distributions of S220 and S420 type reinforcing steels used in existing buildings (reproduced from Bal et al. 2008).

below which the reinforced concrete theory does not apply due to violation of underlying assumptions such as perfect bond or ultimate concrete strain? Finally, how do durability problems such as aging of concrete and corrosion of steel reinforcement be factored in the assessment of minimum acceptable strength?

The above-posed questions do not have easy answers and the author is unaware of targeted studies in this context. It is obvious that the quality of the sample shown in Figure 9, which was taken from an existing two-story industrial building, is unacceptable, but this sample is not even represented in the distribution in Figure 7. It is conceivable that a region in the lower portion of the distribution in Figure 7 could be deemed unacceptable without any considerations beyond concrete strength, but the limit of this region should be selected rationally with proper justification.

Certain real-life occurrences and research results can perhaps be analyzed to search for guidance regarding the above presented discussion and posed questions. As one would fear based on the presented material strength distributions, there were cases of buildings that collapsed under their own weight in Turkey, caused by a combination of factors including low quality of materials. Two recent cases were the collapse of an 11-story reinforced concrete building in city of Konya in 2004 and that of a 5-story building in Istanbul in 2007. The buildings were constructed in 1997 and early 1980s, respectively. Materials investigations have shown that the average concrete strength in both buildings was approximately 9 MPa, with test results as low as 6 MPa, which can be conservatively taken as the characteristic strength. It should be noted that nearly 12% of the buildings included in Figure 7 had a concrete characteristic strength of 6 MPa or less.

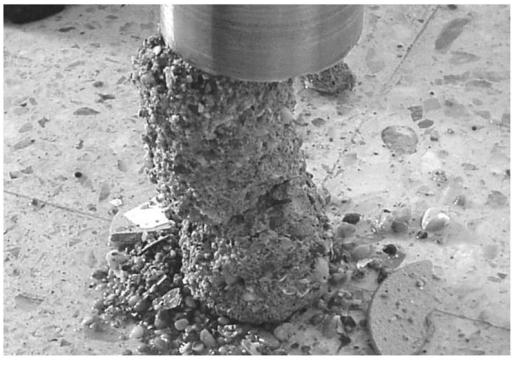

Figure 9. An extreme case of low quality concrete – a sample crumbled during coring.

A more representative guide would be the damage statistics from recent major earthquakes. Post-earthquake surveys after the 1999 Kocaeli Earthquake have revealed that approximately 12% of the occupancy units in the strongly affected regions (Kocaeli, Sakarya, Yalova and Bolu) were heavily damaged or collapsed (Gunes et al. 2006). This simply corresponds to a characteristic strength of 6 MPa or less in the distribution shown in Figure 7.

An interesting study recently completed at Istanbul Technical University (ITU) shed some light on the performance of reinforced concrete column elements with very low strength concrete (4 MPa), corroded (up to 28% section loss) smooth steel reinforcement (S220), and insufficient development length – a worst case scenario which is far too commonly encountered in Turkey (Goksu 2012, Inci et al. 2013). Figure 10a shows a column specimen subjected to accelerated corrosion and a corroded sample of steel reinforcement obtained from the column specimen is shown in Figure 10b. The backbone curves obtained from cyclic flexural testing of column specimens with corrosion up to 12% section loss are shown in Figure 10c. In the figure, transverse flexural load is normalized with respect to the calculated flexural capacity of the column after corrosion. Hence, the section loss due to corrosion is taken into account in the calculations. The objective here is not to assess the reduction in the column capacity due to corrosion, but to investigate the deviation from the calculated behavior due to the combined effects of corrosion, low concrete

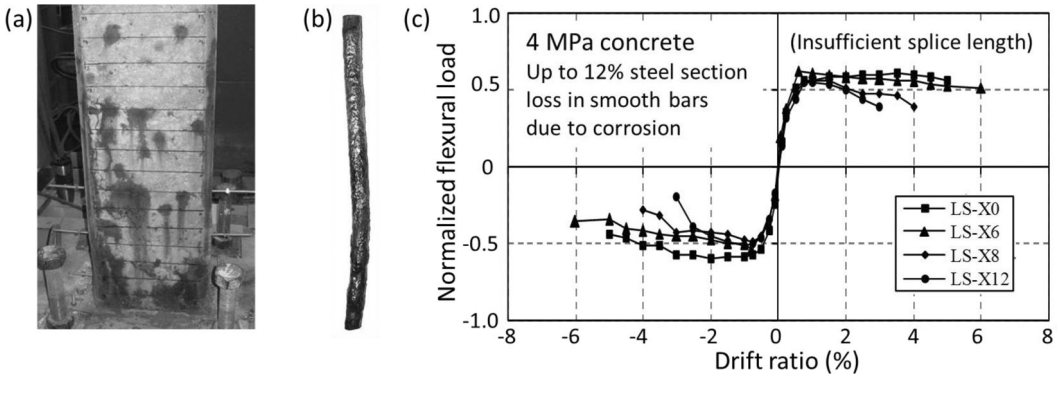

Figure 10. Reinforced concrete column subjected to accelerated corrosion (a), samples of corroded smooth (S220) and deformed (S420) steel reinforcement (b), and normalized backbone curves obtained from cyclic flexural testing of column specimens (c) (Goksu 2012, Inci et al. 2013).

strength, and insufficient development length. When the backbone curves shown in Figure 10c are compared from this perspective, it can easily be discerned that the combined effects of the said negative features reduce both the load capacity and ductility of the column specimen. Looking on the bright side, however, one could nevertheless consider it a somewhat pleasant surprise that column specimens with such serious deficiencies can still produce backbone curves that display the general characteristics of a healthy one at a reduced scale with nearly half the calculated flexural capacity and more importantly some limited degree of ductility – an essential and potentially life-saving feature from a seismic performance viewpoint.

A study of the cases presented above in three groups lead to some conflicting conclusions. In the first group, buildings made of concrete having 6 MPa characteristic strength collapsing under their own weight could suggest that a characteristic concrete strength value higher than 6 MPa should be the minimum acceptable limit with no further considerations. In the second group of cases, the proportion of heavily damaged or collapsed buildings in the hardest hit regions by a major earthquake was equivalent to a concrete characteristic strength of 6 MPa or less in a distribution obtained from the same region. Despite the shared value of characteristic strength, the type and severity of loading actions are dramatically different in these two groups of cases. A third group showed that columns made of concrete with a strength as low as 4 MPa reinforced with smooth steel bars with insufficient development length corroded to a section loss of 12% can still display certain behavioral characteristics that should not be discounted form seismic performance viewpoint.

The question posed in the heading of this section, after a not so brief discussion, essentially remains unanswered. There is no doubt that concrete characteristic strength values as low as 2 MPa in existing buildings as shown in Figure 7 seem frighteningly low and utterly unacceptable. The presented cases and discussions demonstrate, however, that it would not be properly justified to make judgment calls about safety of existing buildings without knowledge of their structural characteristics such as the number of floors, size of members, amount and detailing of reinforcement etc. Vice versa is also true since safety evaluation based only on structural characteristics without knowledge of material quality and essential properties would be incomplete and potentially wrong.

4 CONDITION ASSESSMENT AND EVALUATION OF EXISTING BUILDINGS

The preceding sections have established the nature and size of the problem and the essential components of a proper methodology. Turkey's grand challenge involves seismic safety evaluation of nearly 9 million buildings with 20 million occupancy units (Fig. 2) and retrofit or renewal of those with insufficient seismic resistance within 20 years. The proportion of reinforced concrete frame buildings, the highest risk group and hence the focus of this paper, is more than half in Turkey and more than three quarters in Istanbul (Fig. 5). More than two thirds of the older buildings are made of concrete with characteristic strength below 20 MPa, the code required minimum (Fig. 7). The characteristic yield strength of reinforcing steel is also below the respective code required minimums to various extents (Fig. 8).

Official estimates indicate that approximately one third of the nearly 20 million occupancy units have insufficient seismic resistance and need retrofitting or renewal. This estimation is in agreement with that reported by regional studies based on scenario earthquakes (Ansal et al. 2008). Actual damage observed during recent major earthquakes, however, was generally well below the estimated level except for very few near fault regions where most unfavorable effects were combined (Spence et al. 2003, Bird et al. 2004). The proportion of heavily damaged or collapsed occupancy units due to the Kocaeli Earthquake was 12% in the strongly affected regions, about 5% in the wider region subjected to moderate-to-strong ground shaking, and about 2% in all affected regions (Gunes et al. 2006). When these statistics are compared to the official estimate, the difference is equivalent to millions of buildings and billions of dollars in retrofit and renewal costs. Hence, it is vitally important that this massive undertaking incorporates reliable methodologies of condition assessment and safety evaluation so that the buildings with insufficient seismic resistance can accurately be identified.

The state of the art international documents outlining the procedures of condition assessment and structural evaluation include ASCE/SEI 41-13 (2014) and Eurocode 8-3 (EN 1998-3 2005) effective in North America and Europe, respectively. While the latter is also in effect in Turkey as an adapted standard, provisions in Chapter 7 of ABYBHY (2007), hereafter referred to as the Turkish Seismic Code (TSC), is almost exclusively used for the evaluation and strengthening of existing buildings in Turkey. Although not as comprehensive and scrutinized as its international counterparts, this chapter includes the essential components of modern seismic safety evaluation procedures including performance based evaluation.

The provisions of TSC Ch. 7 on condition assessment of existing reinforced concrete buildings are summarized in Table 2. Similar to the provisions of ASCE/SEI 41 and Eurocode 8-3, the assessment is based on three different knowledge levels as limited, intermediate and comprehensive. When calculating element capacities, the in-situ concrete and steel strength values defined in Table 2 are used without factoring with any coefficients specified in respective codes, but instead a knowledge level factor is applied

Table 2. Provisions for condition assessment of existing reinforced concrete buildings in TSC Ch. 7.

Knowledge level	Geometry	Member details	Materials
Limited	Structural system plan views produced through field work. Must be detailed enough to build a computational model and must include structural irregularities/ weaknesses and interaction with neighboring structures. Foundation system identified through test pits.	Structural drawings do not exist. Reinforcement details assumed to comply with the required minimums at the date of construction. Spot checks for verification by exposing reinforcement in 10% of columns and shear walls and 5% of beams, at least one on each floor. Nondestructive inspection of reinforcement layout in 20% of the remaining members using covermeter. Ratio of existing reinforcement to minimum required expressed as 'reinforcement realization factor' separately for beams and columns and assumed to apply to the rest of members.	At least 2 concrete core samples per floor from columns or shear walls, the lowest result obtained from compression tests used as 'in-situ concrete strength'. Reinforcing steel type determined from spot checks and 'in-situ reinforcement yield strength' assumed equal to corresponding code required minimum characteristic strength. Corrosion observed in reinforcement during spot checks marked on the plan drawings and considered in the analyses.
Intermediate	If technical drawings available, checks made for verification. Otherwise, above provisions apply. Gathered information must allow accurate calculation of building mass.	If structural drawings not available, spot checks performed on 20% of columns and 10% of beams. Otherwise above provisions apply. Reinforcement realization factors calculated only in case of mismatch between building and structural drawings, and used with a maximum value of 1 in member capacity calculations.	One concrete core sample per 400 m^2 area, minimum 3 per floor and 9 per building. Concrete strength determined as 'mean–std. deviation'. Distribution of concrete strength *can be* determined through core correlated rebound hammer tests or similar NDT methods. Reinforcement provisions same as above.
Comprehensive	Structural drawings exist. Verifications checks made and if significant deviations detected, drawings disregarded and intermediate knowledge level provisions apply.	Structural drawings exist. Above provisions apply for verification checks.	Provisions for concrete same as above except for one core sample per 200 m^2 area. For each reinforcement type identified during spot checks, a sample tested for conformance to project specifications. If conforms, above provisions apply. Otherwise, at least 3 more samples of each type tested and the lowest result used as yield strength.

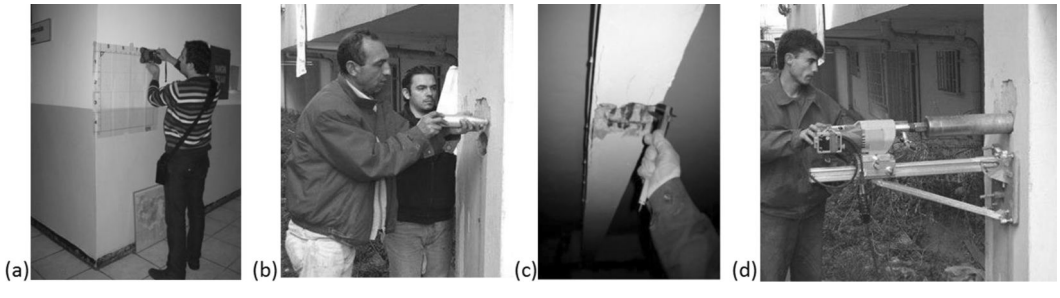

Figure 11. Methods commonly used for condition assessment of existing buildings ordered from nondestructive to destructive: (a) covermeter, (b) rebound (Schmidt) hammer, (c) spot check of reinforcement number, size and splice length, (d) concrete core sampling. (Source: Republic of Turkey Ministry of Environment and Urbanization, General Directorate of Infrastructure and Urban Transformation Services, CSB-AKDHGM).

to the calculated member capacity. This factor is specified for limited, intermediate, and comprehensive knowledge levels as 0.75, 0.90, and 1.00, respectively. Hence, for structures identified to have insufficient seismic resistance, increasing the knowledge level through additional investigations may lead to a more favorable evaluation outcome due to reduced uncertainty in capacity calculations.

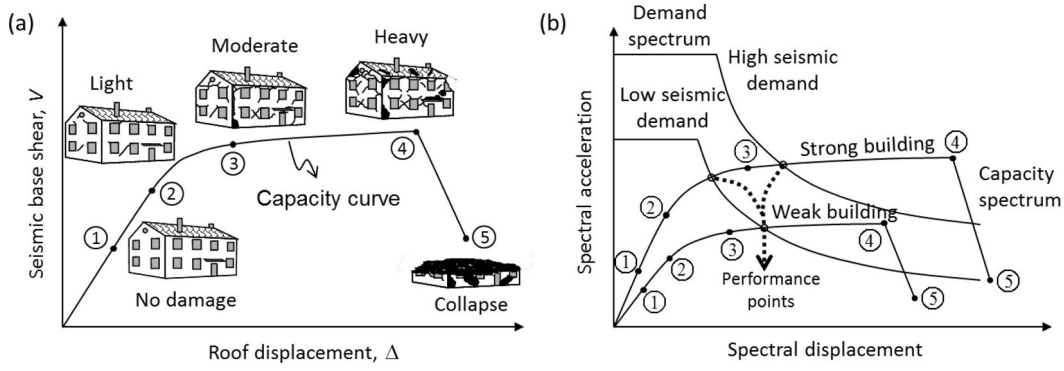

Figure 12. Building capacity curve and damage states (a), and acceleration displacement response (ADRS) representation of seismic demand and capacity spectra.

The inspection and sampling procedures mentioned in Table 2 are demonstrated in Figure 11 ordered from nondestructive to destructive methods. Use of nondestructive testing (NDT) methods in condition assessment of buildings is encouraged in all major codes but the capabilities and reliability of these methods regarding in-situ strength assessment of construction materials are not yet sufficient for them to replace destructive methods (Maierhofer et al. 2010, Buyukozturk et al. 2011). For this reason, use of NDT methods is generally allowed in conjunction with destructive methods for in-situ strength assessment so that a reliable correlation can be obtained. TS EN 13791 (2010) standard provides the procedures for use of various NDT techniques for in-situ strength assessment of concrete in conjunction with concrete core sampling as a destructive but relatively more reliable method.

The condition assessment studies summarized in Table 2 require that the gathered structural and materials information must be detailed enough to allow computational modeling of the building. Once this is achieved, structural evaluation of the building can be performed using either linear or nonlinear methods described in the TSC. Although the principles of performance based seismic evaluation are based on combined and interactive consideration of seismic demand and the structural capacity obtained from nonlinear analyses, the code allows for seismic performance evaluation of buildings based on linear methods. This is done by the help of member capacity ratios, obtained by dividing member forces calculated from equivalent lateral base shear using linear methods, by the member capacities calculated using in-situ materials strength values (see Table 2).

Seismic performance evaluation based on nonlinear methods constitutes a more proper approach to performance based evaluation since the stress redistributions among members are taken into account in the analysis. A conceptual methodology is illustrated in Figure 12. The capacity curve obtained from nonlinear static (pushover) analysis of the building is shown in Figure 12a together with the approximate damage states associated with different points on the curve. A convenient means for comparison of seismic demand with structural capacity is through the Capacity Spectrum Method in the acceleration-displacement response spectrum (ADRS) format as shown in Figure 12b (ATC 1996, 2001, Freeman 2004). A performance level is associated with the intersection of the capacity and demand curves, the so-called performance point. Figure 12b illustrates the concept for two different levels of seismic demand and structural capacity.

Seismic performance evaluation according to TSC entails calculation of the deformation demands on members based on the structure's global response and estimation of member performance levels by comparison of these demands with the member capacity curves. Estimation of seismic performance for the building is based on the individual performances of members and the proportions of members with similar performance levels in the building. The building performance levels are designated as immediate occupancy (IO), life safety (LS), and pre-collapse (PC) performance levels (Fig. 13a).

An additional concept which is not included in the TSC but is worth noting here is the probabilistic vulnerability assessment of buildings through fragility curves. The concept of seismic performance depicted in Figure 12b naturally has uncertainties attached to both seismic demand and structural capacity components as illustrated in Figure 13a. Depending on the level of these uncertainties, the location of the performance point may shift on the horizontal axis leading to different performance levels and corresponding damage states. This behavior can be used to construct the fragility curves shown in Figure 13b that show the probabilities of different damage states ranging from light to complete (collapse) based on the spectral displacement demand on the structure. This concept lends itself for use in vulnerability assessment and loss estimation for individual as well as a stock of buildings.

An advantage of the fragility curves concept is that it can be based on rigorous analytical approaches (e.g. Singhal & Kiremidjian 1996), empirical approaches

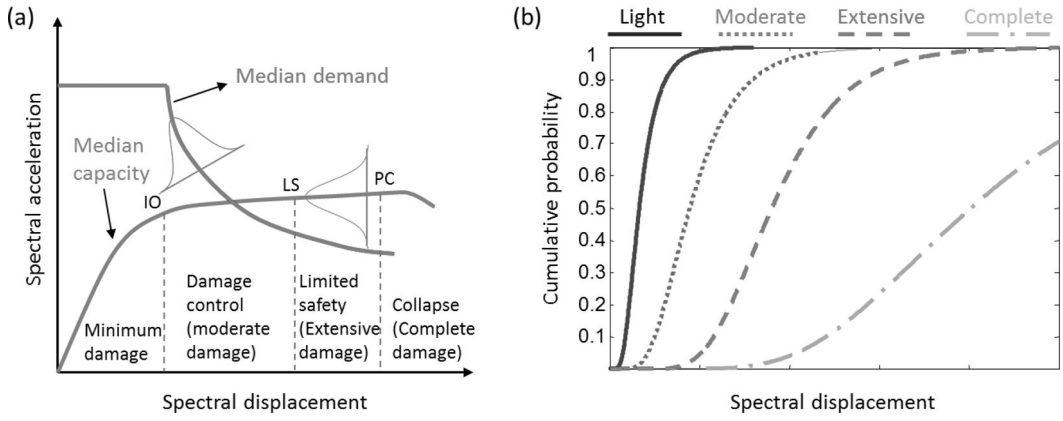

Figure 13. Uncertainties in the demand and capacity spectra (a) and sample fragility curves for different damage states.

(e.g. Rossetto & Elnashai 2003, Straub & Kiureghian 2007), hybrid approaches (e.g. Singhal & Kiremidjian 1998, Akkar et al. 2003, Erberik 2008) or just on expert opinion (ATC 1985). Curves based on empirical data can be used to obtain rough estimates of seismic damage and loss while those based on actual nonlinear analyses can provide more reliable estimates of damage and loss for individual buildings.Depending on how rationally the fragility curves are obtained, the method can provide damage estimates within various uncertainty limits.

5 RAPID ASSESSMENT AND EVALUATION

The provisions in the TSC Ch. 7 for condition assessment and seismic performance evaluation of existing buildings somewhat represents the current state of the art and has the essential elements for satisfactory evaluation of buildings. In view of Turkey's grand challenge, however, the methodology described therein presents potential problems from the viewpoint of time it takes to complete the evaluation. From a professional perspective, implementation of the methodology from beginning to end for a building takes a small team formed by an engineer and technicians in the order of a month, which can only be shortened to a certain extent. Considering that millions of buildings are to be evaluated within the urban transformation initiative, there is an urgent need for rapid condition assessment and evaluation methodologies that enable rapid surveying and preliminary evaluation of buildings primarily for prioritization for further evaluation or to a lesser extent for decisions on retrofit or renewal.

Early methodologies for rapid screening and structural evaluation of buildings include FEMA 154 (ATC 1988) and ATC-14 (ATC 1987), respectively. The former was intended to provide "a standard rapid visual screening procedure to identify, inventory, and rank buildings that are potentially seismically hazardous" (ATC 2002) while the latter presented an evaluation procedure based on equivalent lateral force procedure and allowable stress design concept using capacity over demand ratios. FEMA 178 (BSSC 1992) improved upon ATC-14 by using ultimate strength design principles in the evaluation. Later published FEMA 310 prestandard (ASCE 1998) combined the basic philosophies of FEMA 154 and FEMA 178 as well as modern performance based evaluation concepts and presented an improved 3-tier evaluation procedure. This prestandard was replaced by the ASCE 31 standard (ASCE 2003) which used the same evaluation philosophy and the tiered structure. ASCE 31 was later replaced by ASCE/SEI 41 (ASCE 2014) which combined the evaluation and retrofit processes and included performance of nonstructural elements. It is worth emphasizing that FEMA 154 and ASCE/SEI 41's first tier evaluation aimat identification and ranking of buildings that are potentially seismically at risk and to quickly identify potential deficiencies. Performance evaluation of buildings is performed using more involved and reliable methodologies.

Particularly after the 1999 Kocaeli Earthquake, there has been an increased emphasis on the development of rapid screening and evaluation methods in Turkey. Inspired by the above-mentioned standards and notable earlier studies (Hassan & Sozen 1997, Gulkan & Sozen 1999), several rapid assessment and evaluation procedures were proposed in recent years (e.g. Yakut 2004, Yakut et al. 2006, Bal et al. 2006, Sucuoglu et al. 2007). Most such methods are score-based empirical methods supported by statistical data, obtained from fairly large samples of buildings subjected to strong earthquakes, with limited or no consideration of in-situ material properties. While these methods are important and needed for screening and prioritization of existing buildings for further evaluations, all too often there is a public tendency to accept or use the results of these methods as a measure of their buildings' seismic safety. It has been shown through research studies (Ozmen, 2013) and real life events that these methods cannot be used on their own for seismic safety evaluation of individual buildings.

In order to enable rapid identification of buildings under high seismic risk, a new specification was recently developed exclusively for use within the urban transformation initiative (RYTEIE 2013). Following a brief transition period during which TSC Ch. 7 and RYTEIE were both in effect, this specification now governs the process of identification – but not performance evaluation or retrofitting – of existing buildings under seismic risk. Provisions of RYTEIE are based on those of TSC Ch. 7 with time saving simplifications. The specification also provides a score-based evaluation system for determining the regional distributions of buildings potentially under seismic risk.

Investigations for condition assessment are limited to the critical floor of buildings, defined as the lowest floor above ground or the soft story (one with a lateral stiffness considerably less than the others) if there exists one. Only two knowledge levels are defined as Limited and Comprehensive, the factors for which are specified as 0.9 and 1.0, respectively. For concrete strength, nondestructive tests are required on at least 10 columns or shear walls and minimum 5 cores are required from members yielding the lowest NDT results. The number of core samples is increased by one for each 80 m^2 of area in excess of 400 m^2. The in-situ concrete strength is calculated as 85% of the mean concrete strength obtained from compression testing of cores. Steel reinforcement types and layout is to be determined in at least 20% of columns or shear walls, 10% of which is to be performed by exposing steel reinforcement while the remaining 10% can be inspected using covermeter. In-situ yield strength of reinforcing steel is assumed as the minimum characteristic strength required by the code for the identified type of steel. If a local soil investigation is not performed, the local soil class is assumed to be Z4 which produces most unfavorable results.

Identification of seismic risk for buildings according to RYTEIE is based on linear elastic analysis using the base shear calculated from equivalent lateral force procedure. Proportion of members with demand to capacity ratios exceeding specified limits is used as the basis for seismic risk identification. As an indication of the risk level, a floor shear ratio is calculated for the critical floor calculating the total shear demand on columns and shear wall that are identified as at risk and dividing this value by the floor shear demand. This ratio can be used for ranking of evaluated buildings according to the level of seismic risk and their prioritization for further evaluation according to TSC Ch. 7.

A comparison of RYTEIE with TSC Ch. 7 reveals that the former offers some enabling tools for determining the regional distributions of potentially high risk buildings, risk identification of individual buildings based on relatively straight forward analyses, and ranking of buildings according to their approximate risk level. TSC Ch. 7 provides the next step procedure for seismic performance evaluation of identified buildings based on more rigorous analyses as a basis for retrofit or renewal decisions. When these specifications are compared from the perspective of time it takes to complete the respective assessment and evaluation procedures, however, the time savings offered by RYTEIE is not substantial. Both specifications inevitably use the essential components of condition assessment and structural evaluation such as material tests, structural information gathering, model generation, structural analysis and evaluation. Since the corresponding techniques and tools are common to the tasks in both specifications, it is unrealistic to expect drastic time savings in their implementation without improving the techniques and tools themselves.

6 WISHFUL THINKING ABOUT AN IDEAL METHODOLOGY

In view of the presented grand challenge and the methodologies currently in use, some wishful thinking may be of help towards building a vision for an improved overall methodology that is rapid, reliable, economical, efficient, tractable, and scalable. In the author's opinion, characteristics of an ideal methodology include, but are not limited to, the following:

- Adopts a probabilistic framework and a staged assessment and evaluation methodology that updates the reliability of evaluation at each stage,
- Allows rapid condition assessment and evaluation; producing the preliminary evaluation report after the first site visit, with a quantitative assessment of the associated uncertainty limits,
- Makes optimum use of technologically advanced tools that can increase the speed of assessment and evaluation,
- Information gathered or produced at each stage lends itself for use in the remaining stages,
- Allows implementation of different rapid evaluation methodologies for consideration of interested parties,
- Includes rational assessment and evaluation procedures based on science and mechanics of materials and structures, particularly in later stages of evaluation,
- Allows performance based evaluation,
- Reliability of evaluation is continuously updated as more or higher quality information becomes available,
- Building information is organized in a structure that can be stored and maintained in a central database and can be easily accessed by authorized parties,
- Includes geographical information systems (GIS) support for assessment of regional distribution and beyond,
- Through database structure and GIS support, allows instantaneous reporting of building inventory, descriptive statistics, risk and loss estimations based on statistical or performance evaluations,
- Can be used for preparedness and seismic hazard mitigation before an earthquake and for rapid damage assessment and recovery after.

A methodology that embodies all the characteristics listed above may be difficult to achieve in the short term, but it is important to note that no single list item is far-fetched in view of the current state of the art. A wise strategy may be to put emphasis on the new or improved techniques and technologies that can potentially speed up the assessment and evaluation process without significantly compromising reliability.

7 PROMISING METHODS & TECHNOLOGIES

If a time chain of events is considered in condition assessment and evaluation of existing buildings, one immediately notices that certain components of the investigations are particularly time consuming. Considering the methods of condition assessment shown in Figure 11, for instance, it is easily noticed that the results of all but concrete core tests are available at the end of the site investigations. All major current codes including those in Turkey require concrete core sampling and compression testing as the single most reliable method of in-situ concrete strength assessment. Use of nondestructive testing methods for the same purpose is allowed only when correlated with concrete core tests.

Various NDT methods that have been, or potentially can be, used for in-situ strength assessment of concrete are shown in Figure 14. The rebound hammer technique, generally called the Schmidt hammer in attribution to its inventor, is essentially a surface hardness method that can be indirectly correlated to concrete strength. This is by far the most commonly, and too often wrongly, used NDT method in Turkey and abroad. The ultrasonic pulse velocity (UPV) method makes use of the velocity of ultrasonic pulses obtained from direct (opposite faces), semi-direct (neighboring faces) and indirect (same face) arrangement of the transmitter (T) and receiver (R) transducers (Fig. 14b) to estimate concrete strength. The pull-out force method is a mechanical technique that measures the force needed to pull-out a rod embedded in concrete before or after hardening and correlates it to concrete strength. The penetration resistance technique involves driving a steel probe or pin into concrete using a powder actuated driver that delivers a known amount of energy. The measured penetration depth or the exposed length of the probe or pin is related to concrete strength. The drilling resistance method (Fig. 14e) is not yet an established method of concrete NDT but is included here for its high potential for use in strength assessment of concrete in a rapid and reliable fashion. The method simply involves estimation of concrete strength based on the ease of drilling a hole inside concrete.

TS EN 13791 provides a framework for use of the methods shown in Figure 14a-c for in-situ strength assessment of concrete in conjunction with concrete core tests. TS 13543 (2013), a recently developed umbrella standard, which is a compilation from international standards and other resources, provides an extensive list of NDT techniques applicable to reinforced concrete structures including those in Figure 14a-d with references to specific standards and resources. The drilling resistance method shown in Figure 14e is currently a topic of research and development (Pamplona et al. 2007, Felicetti 2006, 2011).

Ongoing research on nondestructive evaluation of concrete strength (e.g. within RILEM TC 249-ISC Non Destructive In Situ Strength Assessment of

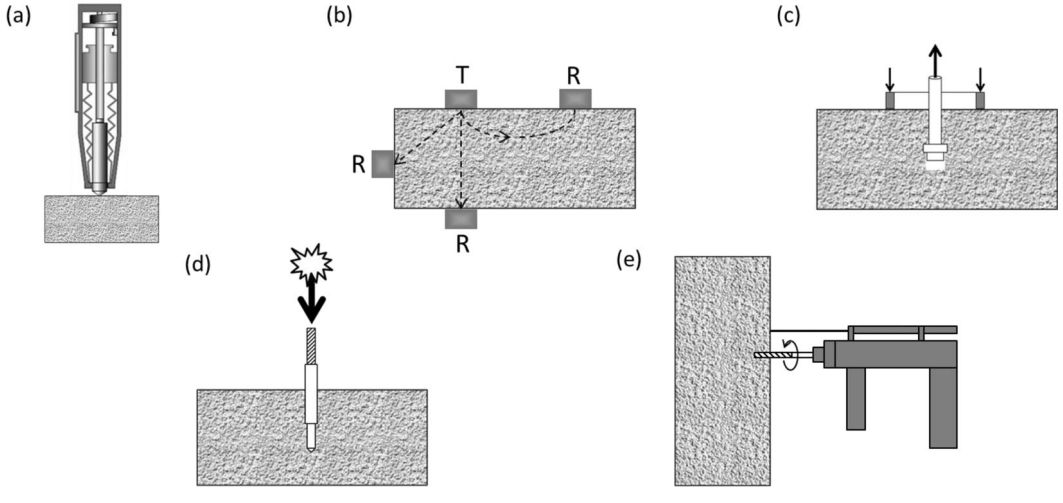

Figure 14. NDT techniques that have been or potentially can be used for in-situ strength assessment of concrete: (a) rebound (Schmidt) hammer (RH); (b) ultrasonic pulse velocity (UPV); (c) pull-out force; (d) penetration resistance; (e) drilling resistance.

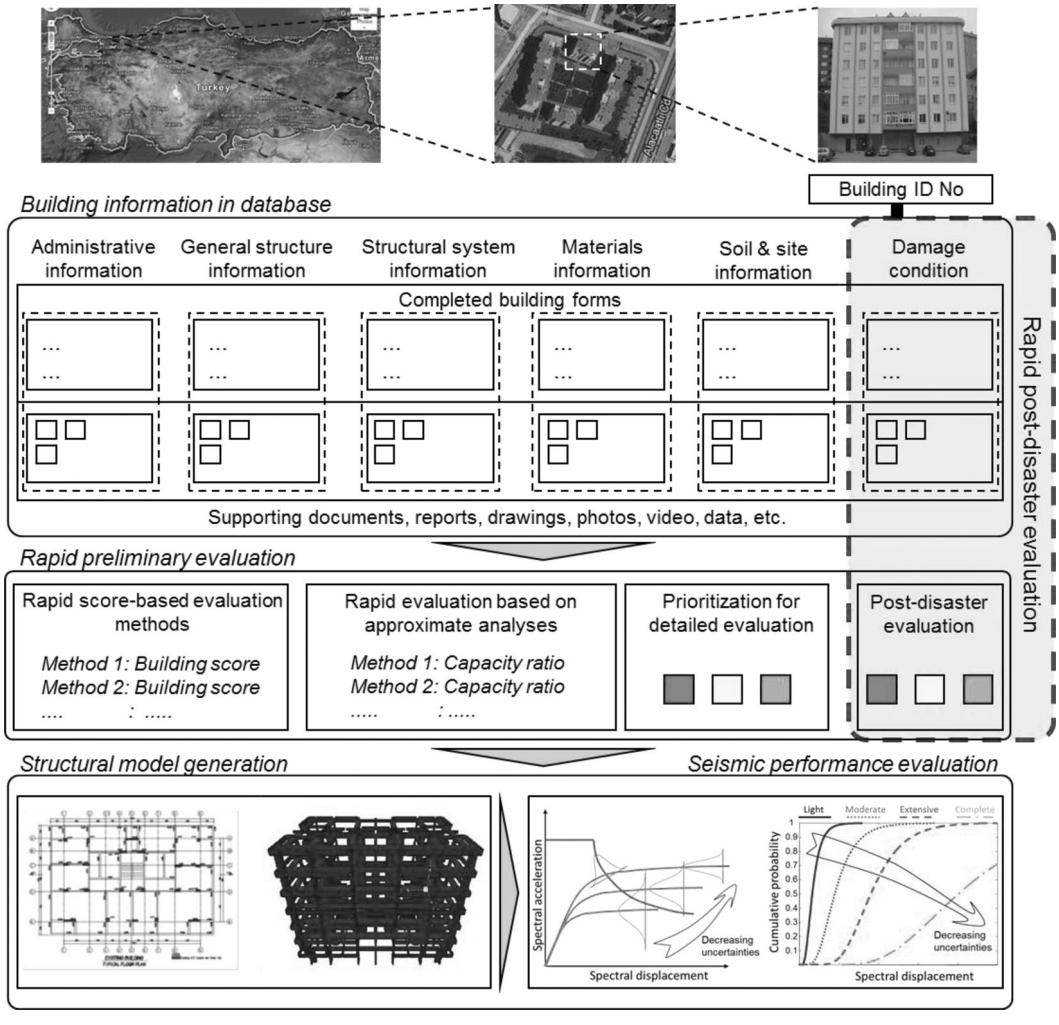

Figure 15. A possible framework methodology for condition assessment and seismic performance evaluation of existing buildings.

Concrete) is looking into ways of improving existing methods and developing new ones with particular emphasis on combined use of techniques to improve the accuracy and reliability of results (Breysse 2012a,b). Progress in this area, especially in techniques that have a mechanical component such as those in Figure 14c-e, combined with parametric and probabilistic studies investigating the sensitivity of seismic performance evaluation on the uncertainty limits of material properties, may allow replacing core tests with individual or combined NDT techniques in the near future.

Seismic performance evaluation of buildings requires linear or nonlinear structural analyses which ideally must be based on accurate knowledge of the building's structural system and member details. Gathering this information becomes particularly difficult and time-consuming when the structural drawings do not exist or do not match the existing structure, which is too often the case in Turkey. Recognizing that the worst structural model based on the actual building is better than having no model at all, a staged approach that makes use of advanced technologies can be adopted. Photogrammetry, mobile technology and augmented reality can be particularly useful for obtaining a quick structural representation of the building including the geometric dimensions of the building, the structural grid, and individual members (e.g. Kang & Wang 2013). Knowledge of the structural details can be built incrementally, starting with the findings from condition assessment investigations (see Fig. 11), making evidential deductions such as giving the structure credit for standing up and having resisted previous seismic events, and making

conservative assumptions to be updated if the determined seismic performance of the building, being unsatisfactory, warrants more reliable structural data from additional on-site investigations.

Several types of metrics can be used as an indication of seismic performance depending on the evaluation methodology. Examples of these used in Turkey and elsewhere are presented in Sections 4 & 5, ranging from structural scores obtained from preliminary surveys to performance levels obtained from pushover analysis and capacity spectrum method. One metric that appears to be applicable to all different approaches is the concept of fragility curves discussed in Section 4 (see Fig. 13). Depending on the amount and reliability of building information, the basis of fragility curves can range from expert opinion to rigorously developed analytical curves, providing a measure of performance in a similar form for all cases, but with different uncertainty limits. Seismic performance indicators in the form of fragility curves may also be a more realistic and honest representation of seismic performance from the building owners' viewpoint since the real information sought by the owner is the level of expected damage, particularly of complete damage (collapse), which always has a probability of occurrence however small it may be. It is also of interest to see how the probabilities of each damage state change with additional investigations or mitigation actions. The use of fragility curves can be further enhanced by introducing time-dependent effects of aging and deterioration, which constitutes an exciting area of future research and development (Ghosh, & Padgett 2010).

Potential improvements to the current state of the art are certainly not limited to the areas discussed above. Strategic development and implementation of improvements prioritized with respect to impact on the speed and reliability of evaluations appears to be the optimum approach. Figure 15 presents a possible framework methodology that includes GIS and database support and has pre- and post-disaster implementation potential. Elaboration on these technologies and their implementation is left to a future publication due to space restrictions.

8 CONCLUSION

Turkey's grand challenge for the next two decades is introduced with related statistical data, information on the current state of the art, and possible improvements through use of efficient techniques and new technology. It is argued that the more sensible approach to rapid evaluation of buildings is not consorting to empirical half measures but rather developing an integrated incremental methodology that favors mechanics based assessment and evaluation methods to empirical ones, expedited by use of technology and enriched by rational assessment of evaluation uncertainty. From an engineering perspective, this massive initiative represents a unique problem and presents motivation and opportunities for significant progress that may build capacity and competitiveness for Turkey and Europe.

REFERENCES

ABYBHY 2007. *Specification for Buildings to be built in Disaster Areas* (in Turkish), Ankara: Republic of Turkey, Ministry of Public Works and Settlement.

Akkar, S., Sucuoðlu, H. and Yakut, A. (2005). Displacement-based fragility functions for low- and mid-rise ordinary concrete buildings. *Earthquake Spectra*, 21(4): 901–927.

Ansal, A., Akinci, A., Cultrera, G., Erdik, M., Pessina, V., Tonuk, G., Ameri, G. 2009. Loss estimation in Istanbul based on deterministic earthquake scenarios of the Marmara Sea region (Turkey), *Soil Dynamics and Earthquake Engineering*, 29(4): 699–709.

Ansal, A., Kurtulus, A., Tonuk, G. 2010. Seismic microzonation and earthquake damage scenarios for urban areas, Soil Dynamics and Earthquake Engineering, 30(11): 1319–1328.

ASCE 1998. *Handbook for the seismic evaluation of buildings – a prestandard*, FEMA 310 Report, Washington D.C.: Federal Emergency Management Administration.

ASCE 2014. *Seismic evaluation and retrofit of existing buildings*, ASCE/SEI 41-13 Standard, Reston: American Society of Civil Engineers.

ATC 1985. Earthquake Damage Evaluation Data for California, ATC-13 Report, Redwood City, CA: Applied Technology Council.

ATC 1987. *Evaluating the seismic resistance of existing buildings*, ATC-14 Report, Redwood City: Advanced Technology Council.

ATC 1996. *Seismic evaluation and retrofit of concrete buildings*, ATC-40 Report, Redwood City: Applied Technology Council.

ATC 1998. *Rapid visual screening of buildings for potential seismic hazards: A handbook*, FEMA 154 Report, Washington D.C.: Federal Emergency Management Agency.

ATC 2002. *Rapid visual screening of buildings for potential seismic hazards: A handbook*, 2nd Ed., FEMA 154 Report, Washington D.C.: Fed. Emergency Management Agency.

ATC 2001. *Evaluation and improvement of inelastic seismic analysis procedures*, ATC-55 Report, Washington D.C.: Applied Technology Council.

Bal, ÿI.E., Tezcan, S.S., Gulay, F.G. 2006. Advanced applications of the p25 scoring method for the rapid assessment of RC buildings, *Proceedings of the 1st European Conference on Earthquake Engineering and Seismology*, 3–8 September, Paper no.: 067.

Bal, I.E., Crowley, H., Pinho, R., Gulay, F.G. 2008. Detailed assessment of structural characteristics of Turkish RC building stock for loss assessment models, *Soil dynamics and Earthquake Engineering*, 28(10–11): 914–932.

Balaban, O. 2012. The negative effects of construction boom on urban planning and environment in Turkey: unraveling the role of the public sector. *Habitat Int.*, 36: 26–35.

Bird, J.F., Bommer, J.J., Bray, J.D., Sancio, R., Spence, R.J.S. 2004. Comparing loss estimation with observed damage in a zone of ground failure: A study of the 1999 Kocaeli Earthquake in Turkey, *Bulletin of Earthquake Engineering*, 2(3): 329–360.

Bommer, J., Spence, R., Erdik, M., Tabuchi, S., Aydinoglu, N. Booth, E., del Re, D., Peterken, O. 2002. Development of an earthquake loss model for Turkish catastrophe insurance, *Journal of Seismology*, 6(3): 431–446.

Bozorgnia, Y. & Bertero, V.V. (Eds.) 2004. *Earthquake engineering: From engineering seismology to performance-based engineering*, Boca-Raton: CRC Press.

Breysse, D. (Ed.) 2012a, *Non-destructive assessment of concrete structures: Reliability and limits of single and combined techniques*, State-of-the-Art Report of the RILEM Technical Committee 207-INR, Springer, Dordrecht, The Netherlands.

Breysse, D. 2012b, Nondestructive evaluation of concrete strength: An historical review and a new perspective by combining NDT methods," *Construction and Building Materials*, 33: 139–163.

BSSC 1992. *NEHRP handbook for the seismic evaluation of existing buildings*, FEMA 178 Report, Washington D.C.: Federal Emergency Management Agency.

Buyukozturk, O. & Gunes, O 2002. Earthquake risk assessment and hazard reduction for structures: Methodologies and collaborative research needs, *NSF/TUBITAK Turkey/Taiwan Grantee Workshop*, March 24–26, Antalya, Turkey.

Buyukozturk, O. & Gunes, O. 2003. Advances in earthquake risk assessment and hazard mitigation for urban ınfrastructures with high characteristic variability, *ARI, The Bulleting of the Istanbul Technical University*, 53(2): 1–20.

Buyukozturk, O., Tasdemir, M.A., Gunes, O. and Akkaya, Y. (Eds.) 2011. *Nondestructive testing of materials and structures*, RILEM Bookseries Vol. 6, Dordrecht: Springer.

Coburn, A. & Spence, R. 2002. Earthquake protection, 2nd Ed., West Sussex: John Wiley & Sons Ltd.

Colak, N.I. 2013. Legal evaluation of the urban transformation legislation (in Turkish), *Conference on Urban Transformation and Environment*, 7 March 2013, State Council, Ankara, Turkey.

Elicin, Y. 2014. Neoliberal transformation of the Turkish city through the Urban Transformation Act, *Habitat International*, 41: 150–155.

EN 10080 2005. *Steel for the reinforcement of concrete - Weldable reinforcing steel – General*, Brussels: European Committee for Standardization.

EN 1998-3 2005. *Eurocode 8: Design of structures for earthquake resistance – Part 3: Assessment and retrofitting of buildings*, Brussels: Eur. Committee for Standardization.

Erberik, M.A. 2008. Fragility-based assessment of typical mid-rise and low-rise RC buildings in Turkey, *Engineering Structures*, 30(5): 1360–1374.

Erdik, M., Kamer, Y., Demircioglu, M., Sesetyan, K. 2012. 23 October 2011 Van (Turkey) earthquake, *Natural Hazards*, 64(1): 651–665.

Erdik, M., Aydinoglu, N., Fahjan, Y., Sesetyan, K., Demircioglu, M., Siyahi, B., Durukal, E., Ozbey, C., Biro, Y., Akman, H., Yuzugullu, O. 2003. Earthquake risk assessment for Istanbul metropolitan area, *Earthquake Engineering and Engineering Vibration*, Article ID: 1671-3664(2003)01-0001-23.

Ergunay, O. 2007. Turkey's disaster profile (in Turkish), *TMMOB Afet Sempozyumu*, Turkish Chamber of Civil Engineers, Dec. 5–7, 2007, Ankara, Turkey.

Felicetti, R. 2006. The drilling resistance test for the assessment of fire damaged concrete, *Cement & Concrete Composites*, 28: 321–329.

Felicetti, R. 2011. Assessment of fire damaged concrete via the hammer-drill pulse transmission technique, *Nondestructive testing of materials and structures*, Buyukozturk et al. (Eds), RILEM Bookseries Vol. 6, 205–212, Dordrecht: Springer.

Freeman SA. 2004. Review of the development of the capacity spectrum method. *ISET Journal of Earthquake Technology*, Paper No. 438, 41(1):1–13.

Geller, R.J. 1997. Earthquake Prediction: A Critical Review, *Geophysical Journal International*, 131(3): 425–450.

Ghosh, J. & Padgett, J.E. 2010. Aging Considerations in the Development of Time-Dependent Seismic Fragility Curves, *Journal of Structural Engineering*, 136(12): 1497–1511.

Goksu, C. 2012. *Seismic behavior of RC columns with corroded plain and deformed reinforcing bars*, Ph.D. Thesis, Istanbul Technical University, Istanbul, Turkey.

Gulkan, P. & Sozen M.A. 1999. Procedure for determining seismic vulnerability of building structures. *ACI Structural Journal*, 96(3): 336–42.

Gulkan, P. 2013. A Dispassionate View of Seismic-Hazard Assessment, *Seismological Research Letters*, 84(3): 413–416.

Gunes, B., Yakut, A., Gunes, O. 2006. Approximate Seismic Evaluation Methods for Large Building Inventories with Large Variability in Their Seismic Resistance, *Proc. 8NCEE 100th Anniversary Earthquake Conference*, April 18–22, 2006, San Fransisco, CA.

Hassan, A.F. & Sozen, M.A. 1997. Seismic vulnerability assessment of lowrise buildings in regions with infrequent earthquakes. *ACI Structural Journal*, 94(1): 31–9.

Inci, P., Goksu, C., Ilki, A., Kumbasar, N. 2013. Effects of reinforcement corrosion on the performance of RC frame buildings subjected to seismic actions, *Journal of Performance of Constructed Facilities*, 27:683–696.

Kang, S.-C. & Wang, X. (Eds.) 2013. Special issue on the applications of augmented reality in architecture, engineering, and construction, *Automation in Construction*, 33: 1–2.

Karaman, O. 2013. Urban renewal in Istanbul: Reconfigured spaces, robotic lives, *International Journal of Urban and Regional Research*, 37(2): 1468–2427.

Kidokoro, T., Okata, J., Matsumura, S., Shima, N. (Eds.) 2008. *Vulnerable cities: Realities, innovations and strategies*, Dordrecht: Springer.

Kramer, S.L. 1996, *Geotechnical Earthquake Engineering*, Upper Saddle River NJ: Prentice Hall.

Kuyucu, T. & Unsal, O. 2010. 'Urban Transformation' as state-led property transfer: An analysis of two cases of urban renewal in Istanbul, *Urban Studies*, 47(7): 1479–1499.

Maierhofer, C., Reinhardt, H.-W., Dobmann, G. (Eds.) 2010.*Nondestructive Evaluation of Concrete Structures*, 2 Vol., Cambridge: Woodhead Publishing.

Ozmen, H. B. 2013. Relation between the rapid evaluation method scores and the damage states of buildings, *Natural Hazards and Earth System Sciences*, 13(3):763–770.

Ozus, E., Turk, S.S., Dokmeci, V. 2011. Urban restructuring of Istanbul, European Planning Studies, 19(2): 331–356.

Pamplona, M., Kocher, M., Snethlage, R., Barros, L.A. 2007. Drilling resistance: overview and outlook, *Zeitschrift der Deutschen Gesellschaft fur Geowissenschaften*, 158(3): 665–676.

Parsons, T., Toda, S., Stein, R.S., Barka, A., Dietrich, J.H. 2000. Heightened odds of large earthquakes near Istanbul: An interaction-based probability calculation, *Science* 288: 661–665.

Rossetto, T. & Elnashai, A. 2003. Derivation of vulnerability functions for European-type RC structures based on observational data, *Engineering Structures*, 25(10): 1241–1263.

RYTEIE 2013. Principles for Identification of Buildings under Risk (in Turkish), Ankara: Republic of Turkey, Ministry of Public Works and Settlement.

Singhal, A. & Kiremidjian, A.S. 1996. Method for probabilistic evaluation of seismic structural damage, *Journal of Structural Engineering-ASCE*, 122(12): 1459–1467.

Singhal, A & Kiremidjian, A.S. 1998 Bayesian updating of fragilities with application to RC frames, *Journal of Structural Engineering-ASCE*, 124(8): 922–929.

Spence, R., Bommer, J., del Re, D. Bird, J., Aydinoglu, N., Tabuchi, S. 2003. Comparing loss estimation with observed damage: A study of the 1999 Kocaeli Earthquake in Turkey, *Bulleting of Earthquake Engineering*, 1(1): 83–113.

Strasser, F.O., Bommer, J.J., Þeþetyan, K., Erdik, M., Çağnan, Z., Irizarry, J., Goula, X., Lucantoni, A., Sabetta, F., Bal, I.E., Crowley, H., Lindholm, C. 2008. A comparative study of European earthquake loss estimation tools for a scenario in Istanbul, *J. of Earthquake Engineering*, 12(S2): 246–256.

Straub, D. & Kiureghian, A.D. 2008. Improved seismic fragility modeling from empirical data, *Structural Safety*, 30(4): 320–336.

Sucuoglu, H., Yazgan, U., Yakut, A. 2007. A screening procedure for seismic risk assessment in urban building stocks, 23(2): 441–458.

TS 708 2010. *Steel for the reinforcement of concrete – reinforcing steel* (in Turkish), Ankara: Turkish Standards Institute.

TS 13543 2013, *Nondestructive testing (NDT) methods applicable to Reinforced Concrete Structures* (in Turkish), Ankara: Turkish Standards Institute.

TS EN 13791 2010. *Assessment of in-situ compressive strength in structures and precast concrete components*, Ankara: Turkish Standards Institute.

TSE 2000. *Building Census 2000*, Publication No: 2471, Ankara: State Institute of Statistics.

TUIK 2011. *Population and Housing Census 2011*, Publication No: 4030, Ankara: Turkish Statistical Institute.

Uysal, U.E. 2012. An urban social movement challenging urban regeneration: The case of Sulukule, Istanbul, *Cities*, 29(1): 12–22.

Yakut, A. 2004. Preliminary seismic performance assessment procedure for existing RC buildings, Engineering Structures, 26(10): 1447–1461.

Yakut, A., Ozcebe, G., Yucemen, M.S. 2006. Seismic vulnerability assessment using regional empirical data, Earthquake Engineering and Structural Dynamics, 35(10): 1187–1202.

This page intentionally left blank

Concrete Solutions – Grantham et al. (Eds)
© 2014 Taylor & Francis Group, London, ISBN 978-1-138-02708-4

Managing post-tensioned bridges – better than before

D. Pearson-Kirk
Mouchel, Exeter, United Kingdom

ABSTRACT: Unexpected deterioration of post-tensioned concrete structures has become a matter of major concern in many countries. One effect of this deterioration, often identified after a considerable time, is that significant expenditure has to be diverted from capital works to the management of those structures. In the United Kingdom, all existing bridges of this type were to be subjected to a Post-Tensioning Special Inspection (PTSI). Reviews of reports indicated that there is insufficient information to determine with confidence the condition of over 20% of the post-tensioned bridges in the United Kingdom. This paper presents an outline of the performance of post-tensioned bridges, the need to review reports on investigations, the review processes and their findings, together with the implications for bridge owners. Post-tensioned bridge Special Inspections are not a do once and forget situation. High risk bridges need to be identified and prioritised for any necessary further investigations and remedial works.

1 INTRODUCTION

The post-tensioning method was originally invented in France by Professor Freyssinet and was used in the construction of the Veudre Bridge in 1908. The first post-tensioned segmental bridge was designed in 1939 and built in 1945 in France, over the River Marne. The use of post-tensioned construction significantly increased in Europe in the 1950s and in the United States in the 1960s and 1970s.

Figure 1. 50 year old segmental bridge. Devon, UK.

Figure 2. 50 year old segmental bridge in excellent condition.

The increasing adoption of post-tensioned construction for medium to large-span bridges clearly demonstrated the advantage it had over other options in terms of cost, buildability and aesthetic appeal. It was perhaps inevitable that such progress would be accompanied by occasional problems, and, in recent years some of the earliest bridges have exhibited evidence of serious defects, particularly corrosion of the post-tensioning systems. Post-tensioned bridges can be susceptible to the ingress of moisture, particularly at beam and deck ends, high and low sections of tendon profiles and at construction or segment joints. The complete grouting of ducts is demanding and voids can be left. This increases the risk of oxygen, moisture, salts and carbon dioxide entering the ducts and contributing to the corrosion of the tendons.

The corrosion of tendons may remain hidden until the resulting loss of strength is sufficient to promote either external evidence of the deterioration or a sudden failure. Well designed, well-constructed and well maintained post-tensioned bridges will, however, provide good service (Figures 1 and 2), even with significant increases in the number of vehicles using the bridges and increases in commercial vehicle loadings.

2 DURABILITY OF POST-TENSIONED BRIDGES

In Europe during the 1950s and the early 1960s post-tensioned concrete bridges gave satisfactory performance. The first problems with a major bridge

in the UK were found in the early 1970's when longitudinal cracks were observed in its superstructure. Upon opening the ducts they were found to contain voids and water. Cracks in the concrete had been caused by expansion of the water on freezing, but the tendons and ducts were only slightly corroded. During the 1980s, problems in the UK were identified in an increasing number of post-tensioned bridges and a significant number of bridge decks had to be replaced because of corrosion of tendons. The most serious event happened in 1985 when a single span segmental post-tensioned bridge in Wales failed without warning. Water and salts had penetrated the joints and corroded the longitudinal tendons. In 1992, a motorway bridge over the River Schelde in Belgium collapsed without warning as a result of corrosion of post-tensioned tie-down tendons. There was considerable loss of life.

In September 1992 the UK Department of Transport (DoT) announced that it would not be commissioning any new post-tensioned concrete bridges with internal grouted tendons until design and construction standards were improved. The reason for the moratorium was concern over the vulnerability of pre-stressing systems to corrosion resulting from the penetration of water and salts. At the same time the DoT announced that all existing bridges of this type would have to be systematically inspected and a similar series of inspections was initiated in France. The Highways Agency is responsible for over 1000 post-tensioned bridges in England on behalf of the UK DoT, with the Service d'Etudes Techniques des Routes at Autoroutes (SETRA) being responsible for over 3,600 post-tensioned bridges in France. These Special Inspections commenced, effectively, in the spring of 1993.

In France in the mid 1990's, particular problems were detected where grout mixes had contained superplasticisers. Some opened ducts highlighted a lack of filling and the presence of a product having the consistency of a soft wet paste. Admixtures can present an incompatibility with the cement and thereby cause instability of the grout during the set. The coexistence of the air and moisture in the paste within a duct can pose a long-term durability problem. Grout in the form of a damp, soft white paste (Figure 3) has also been found in bridges in other countries including England, Wales, Northern Ireland and the United States.

Figure 3. Voided duct with traces of soft, wet, white paste.

In a 1998 report (Poston & Wouters) on research on the "Durability of Precast Segmental Bridges" sponsored by The American Association of State Highways and Transportation Officers (AASHTO) in co-operation with the United States Federal Highway Administration (FHWA), it was noted that "... the corrosion problems with precast segmental and post-tensioned bridges in the United Kingdom were principally due to poor design choices and poor quality construction rather than a significant intrinsic susceptibility to corrosion. The study found no evidence of corrosion or other durability problems with precast segmental bridges in the United States". The last statement had to be treated with caution as visual inspection alone would not have necessarily provided any evidence of deterioration of post-tensioning systems. Investigations during 1999 and 2000 found severe corrosion and failed tendons in the Niles Channel Bridge, Mid-Bay Bridge and the Sunshine Skyway Bridge in Florida. On January 12, 2001 the FHWA issued a memorandum (U.S. DOT) stating: – "Historically the corrosion of post-tensioned bridges in the United States has not appeared to be a significant problem. That viewpoint has recently been brought into question by the discovery of failed and corroded post-tensioning tendons in the State of Florida". The memorandum stated that a nationwide notice should be issued to "alert States to the post-tensioning corrosion problems" and "to recommend the expedited inspection of their highest risk post-tensioned structures". Grouting deficiencies were subsequently found in 2001 and 2002 both in segmental and in cast-in-place post-tensioned bridges in the Central Artery/Tunnel Project being constructed in Boston, Massachusetts.

Measures were subsequently put in place to improve the key elements of design, detailing, materials, grouting and certification for installation. Agencies issued new/revised specifications, one example being Technical Report 47 "Durable post-tensioned concrete bridges" first published in 1996 with a second, updated edition, in 2002. In 1996 the UK DoT partially lifted the moratorium on the commissioning of any new post-tensioned concrete bridges with internal grouted tendons. Notwithstanding the measures detailed in TR 47, there remained the need for bridge owners/managers to be confident that they knew the condition of their existing post-tensioned bridges. Visual inspection alone had been shown not to be sufficient.

3 INVESTIGATION OF AT RISK POST-TENSIONED BRIDGES

Finding by accident that post-tensioned bridges had significant problems was clearly not acceptable. For the DoT programme of inspections referred to above, in 1993, rating equations were developed (BD 54/93 & BA 50/93) to initially rank the structures. This ensured that available resources could be targeted most cost

effectively by identifying the highest risk bridges and checking them first.

Following the priority ranking, a three phase approach was adopted for planning and carrying out investigations:-

Phase 1 – Preliminary Desk Study – to determine the fundamental design and construction details; to review previous inspection and maintenance documents for the bridge, and identify vulnerable details.

Phase 2 – Preliminary Site Inspection – to verify the design details identified in Phase 1; identify any defects; and to prepare a detailed technical plan for the Phase 3 Site Investigations.

Phase 3 – Site Investigation – to determine the condition of the bridge's post-tensioning systems; any corrosion activity and the condition of concrete and reinforcement in the vicinity of the critical locations under investigation.

Particular attention was necessary in selecting the most appropriate techniques which were required to establish the presence of voids in ducts and the condition of the grout, tendons and anchorages. In conjunction with these specific post-tensioning investigations, the surrounding structural concrete had to be tested for its durability characteristics i.e., covermeter, half-cell potential and concrete resistivity readings; and chloride ion concentrations of the cover concrete and tendon grout; cement and sulfate contents of concrete and grout; and alkali contents of concrete. The total data provided information on any current or potential deterioration of concrete, ducts, grout, tendons and reinforcement comprising the structure.

4 RESULTS OF INVESTIGATIONS

There has always been concern about the inspection of tendons in post-tensioned concrete bridges mainly because of the difficulty of detecting and quantifying any deterioration. Because of these ongoing concerns, the Highways Agency and SETRA (Godart, 2001), had initiated the obligatory checking of their post-tensioned bridges. The findings have been recorded on databases and analysed under three main headings – voids, tendon corrosion and anchorage faults. Analyses showed that overall the condition of the bridges was better than had been envisaged.

The results of investigations in England (Woodward, 2001), Northern Ireland (Pearson-Kirk and Cairns, 2007) and France (Godart, 2001) are summarised in Table 1.

Voids in themselves do not pose a problem as long as all the pre-stressing wires are covered with grout. If wires are exposed then any ingressing water and salts can present a threat to the long-term durability of a structure. The risk is related to how well voids were sealed. Moisture present in voided ducts (Figure 4) is a factor that suggests a potential for future deterioration/reduction in carrying capacity. Significant corrosion would include severe surface corrosion or pitting corrosion resulting in loss of cross-sectional area of wires or bars and fracture of wires/strands. Significant voiding (Figure 5) and corrosion of tendons has also been found in investigations in many other countries including Denmark, Germany, Italy, Poland and Japan.

Anchorage inspections have been carried out on about 60% of the bridges investigated in England. Of the anchorages inspected, 25% contained significant corrosion – severe surface corrosion or pitting corrosion with measurable loss of cross-sectional area.

Table 1. Summary of tendon investigations.

	England	France	Northern Ireland
Voids	30%	–	12%
Moisture	13%	–	10%
Significant Corrosion	10%	21%	5%
Remedial Action Needed	7%	15%	7%

Figure 4. Voided duct containing water.

Figure 5. Failed strands in ungrouted duct.

5 REVIEWING OF REPORTS ON POST-TENSIONED BRIDGES

Reviews of Phase 1, 2 and 3 reports on post-tensioned bridges have been commissioned by several agencies, including the Highways Agency, the Northern Ireland Roads Service and Transport for London (Pearson-Kirk, Pottle and Duguid, 2010). Owners need to know with confidence the condition of their post-tensioned structures and the likelihood of any deterioration progressing with time. Reviews have shown that a limited number of bridges could have long term durability problems that warranted further investigations. Having detailed any further work needed for each bridge, it was necessary to provide a priority ranking for the bridge works together with estimates of cost for carrying out those works. The further work could include additional site investigations, monitoring, protection or strengthening works.

The reviews assessed the quantity, quality and relevance of the information contained in the Phase 1, Phase 2 and Phase 3 reports for each bridge. For each report for each bridge, standard proformas were completed – the proformas comprising two distinct sections. In the first section, reference details were recorded for each item that should have been discussed and/or provided in that report, and remarks concerning particular items/deficiencies were listed. The second section of the proforma listed the actions required to address those particular items.

The Phase 1 reports often stated that construction records, including as-constructed drawings, were not available, thus any changes made during the construction period would not be known. An example of the effect of this lack of information is that any change in position of ducts may have contributed to a number of ducts "not being located" during Phase 3 intrusive investigations. The position of these ducts had to be determined. If they were substantially out of position, any assessments of load carrying capacity might need to be reviewed.

The purpose of the Phase 2 Preliminary Site Inspection was to verify construction details; to identify any areas showing signs of distress and to prepare a Technical Plan to determine the causes and consequences of any deterioration. The stated objectives for site investigation and the Technical Plans were often brief and sometimes incomplete. Duct and tendon exposures (DTEs) needed to be undertaken at certain critical sections. These should be in areas at high risk from water ingress and/or voiding in ducts, or where yield points might form in a potential collapse mechanism. Critical sections would include end support regions, midspan areas; regions over intermediate supports and locations where there were construction joints transverse to tendons and ducts. Quite often DTEs were not specified for sufficient critical locations.

End anchorage exposures (EAEs) were seldom recommended, even when anchorages were at critical locations and were readily accessible. A limited number of bridges had anchorages in the top surfaces of decks or in distinct blisters beneath a deck soffit. At those locations, EAEs should have been included in the Technical Plan.

Technical Plans often did not specify sufficient corrosion testing. This testing is an integral part of the Phase 3 Site Investigations and should be undertaken to determine the level of corrosion risk in the concrete at the DTE and EAE locations. This testing also provides base-line data should monitoring of corrosion risk be subsequently required.

In summary, the Technical Plans were sometimes considered to be incomplete and insufficient to enable an assessment to be made of the overall condition of the bridges' post-tensioning systems and of the level of corrosion risk.

The quality of the Phase 3 site investigation reports ranged from good to poor, with some of the reports being based on Technical Plans that were insufficient in extent and type of investigation specified. Any variations in the Phase 2 Technical Plan were not always fully explained. Interpretation of results ranged from extensive to very limited, with some discussion being affected by insufficient investigations having been undertaken at too few critical locations. Tendon inspections were often undertaken in 25mm diameter holes with photographs being of a variable quality. Views of ducts through 25mm diameter holes would not always facilitate an accurate assessment of the presence of voids, particularly when ducts were partially voided, and the condition of tendons.

Terminology used in certain reports was sometimes vague. Corrosion of tendons was described as moderate, moderate/severe and severe with no definitions of the descriptors. At some locations in several bridges, it was stated that certain ducts were "not located". Were ducts significantly displaced; had locations been amended during construction; or were the exposures attempted at the wrong locations? Visual inspection results were often described but sometimes defects sketches were not provided. Any future progression of defects could not then be monitored.

Recommendations for further investigations were seldom made, probably at least partially as a result of insufficient investigations having been originally specified and carried out. Very few Special Investigations (SIs) were recommended for non post-tensioned elements, but reviews demonstrated that many SIs had in fact often been recommended in other non-PTSI reports for the structures.

In summary, the reviews of reports on post-tensioned bridges often highlighted the need for further investigations in order to provide a more complete understanding of the condition of the bridges' post-tensioning systems.

6 NATIONAL AGENCIES

The Highways Agency commissioned the review of PTSI reports for 36 structures in Area 1. 11 of the

post-tensioned bridges were identified as being Priority 1 – the higher risk bridges. These bridges needed further Post-Tensioning Special Inspections, substantially as a result of defects being noted and/or insufficient investigations having been specified and carried out. These Priority 1 bridges could also require other Special Inspection(s) and/or maintenance work. Following further investigations, 3 bridges required deck replacements and 2 bridges needed remedial grouting of extensively voided ducts. Previous reports had indicated that 3 of those 5 bridges were considered to be low risk structures in good condition. The reviews also highlighted the need for further investigations not related directly to the post-tensioning investigations.

In October 2012, the Highway Agency provided a draft standard BD 54/XX "Management of Post-Tensioned Concrete Bridges" for trial use in Area 13 only. That standard provided the requirements and guidance for the management of post-tensioned concrete bridges, implementing a risk based approach to management and included advice on Special Inspections, monitoring, repairs and strengthening. EM Highway Services in Area 13 provided a spreadsheet detailing the availability of Post-Tensioning Special Inspection (PTSI) reports for the 51 structures. There were 11 structures that have not had, or for which there were no records of PTSI investigations.

The Northern Ireland Roads Service commissioned reviews of reports on the Post-Tensioning Special Inspections of 40 bridges (Pearson-Kirk & Cairns, 2007). 12 bridges were identified as being Category 1 – high priority where intrusive post-tensioning investigations were required with testing for corrosion risk. Significant problems were identified in 5 of these bridges and these subsequently required remedial works. Category 2 contained 11 bridges where testing to determine corrosion risk was required and where further intrusive investigations might be required. Category 3 contained 17 bridges where no further post-tensioning investigations were needed. The bridges in each category were given a priority ranking.

7 TRANSPORT FOR LONDON (TFL)

A number of agencies/consultants had compiled Phase 1, 2 and 3 reports on TfL's post-tensioned bridges. The inspection works revealed a range of defects and deficiencies within the bridge stock. The situation was complicated by the fact that the agencies/consultants did not adopt a uniform approach when assessing the condition of the bridges' post-tensioning systems.

In 2007, due to the number of reports, the nature and range of the problems observed on many of the structures and, because of budget constraints and the need to prioritise the implementation of remedial works, TfL commissioned a review of the PTSI reports for 42 bridges to assess the completeness of the PTSIs and the quality of reporting, as well as determining whether further deterioration in condition was likely to have occurred since the original inspections had been undertaken some 10 to 15 years earlier.

In August 2012 TfL issued a brief to EM Highway Services Limited (EM) to review the reports on 97 post-tensioned structures, which included the 42 bridges for which additional reports had become available. In addition to the PTSI reports, Principal Inspection, Special Inspection and other relevant reports were to be included in the review process. During the review process the number of structures was reduced to 91, with 58 initially being classified as High Priority for further investigations.

8 REVIEWS

The reviews undertaken for National Agencies, Transport for London, Counties and Boroughs, have assessed the quantity, quality and relevance of the information contained in the PTSI Phase 1, Phase 2 and Phase 3 reports for each bridge. Following completion of the review proformas for each of the Phase 1, 2 and 3 reports, the results of the reviews provided pertinent comments, conclusions and recommendations for any further action that might be required. The actions listed included recommended further PTSI investigations, Special Inspections, monitoring and remedial works. Most bridges were considered to need some further investigation, substantially as a result of insufficient investigation having been specified and/or carried out in the original programme.

Before any work programmes for further investigations were considered for particular structures, it was essential to liaise with Client staff to determine whether any relevant works had been carried out on those bridges subsequent to the post-tensioned investigations, and if any special access or traffic management considerations needed to be applied in planning site works.

9 PRIORITISATION OF FURTHER INVESTIGATIONS

Identification of structures at risk was carried out based on the review of the design and construction details, and previous inspection, testing and maintenance records and identified areas showing signs of the deterioration that might affect the structure's post-tensioning systems.

The prioritisation procedure developed for structures at risk was initially based on the Method of Determining Inspection Priorities from DMRB Volume 3 Section 1 Part 2 BD 54/93 "Post-Tensioned Concrete Bridges – Prioritisation of Special Inspections". In BD 54/93 six rating factors are used in an equation to calculate a Total Assessment Rating (TAR) value for each structure. The six rating factors are listed below with the value for each factor being determined from tables in BD54/93:-

Age of Bridge factor – R_a; Bridge Form factor – R_f; Vulnerable Details factor – R_d; Traffic Volume Over factor – R_v; Traffic Volume Under factor – R_u; Route Importance factor – R_i.

The Total Assessment Rating (TAR) for each structure was then calculated using the equation from BD 54/93:

$$TAR = 4R_a + 2R_f + R_d + R_v + R_u + R_i$$

TAR values ranged from 8 to 50, with the structure with the highest score being categorised as the highest priority for the Post-Tensioning Special Inspection. This prioritisation was to ensure a degree of uniformity of ranking throughout the road networks in the United Kingdom when, at that time, it was not known in which order to investigate the structures.

However, the TAR equation was not intended as a management tool for structures after post-tensioning investigations had been undertaken. This limitation meant that in order to prioritise further investigations, not only for those structures that had not had Phase 3 intrusive investigations, but also for those structures that had had Phase 3 intrusive investigations, further factors (factors P and C) needed to be introduced to the prioritisation procedure. The objective was that structures that either had not had a Phase 3 intrusive investigation; where there had been significant shortcomings in the previous investigations; where there were certain significant defects to the structure's post-tensioning system or where the structures had vertical post-tensioning elements, would be identified as being of high priority for further investigations.

Factor P 'Phase 3 Y/N' was a weighting factor whose value depended on whether or not a PTSI Phase report was available. This weighting factor was applied to the TAR value, so that TAR values were increased if a Phase 3 report was not available. If additional Phase 3 PTSI investigations had been completed or were under way, the weighting factor was 0, so the structure's ranking value became 0.

To take into consideration the results of the Phase 3 Intrusive Investigations (where they had been undertaken) and to refine the prioritisation process, a weighting factor C 'Condition' was applied to the TAR value. Factor C 'Condition' prioritised structures in order of the condition of the post-tensioning systems; whether the structures had vertical post-tensioning; the structures with a significant lack of information – these structures thus became positioned towards the top of the prioritisation ranking.

10 FINAL 'RANKING SCORE' AND PRIORITISATION

The Ranking Score was used to prioritise all structures. The highest scored structures should be investigated first. The Ranking Score was giving by equation:

$$\text{Ranking Score} = TAR \times P \times C$$

Structures were subsequently grouped into High, Medium and Low Priorities where:

- Structures were deemed as being of high priority (red) if either no Phase 3 report was available; or a Phase 3 report was significantly lacking in information; or Phase 3 results indicated significant deterioration to the post-tensioning systems; or vertically post-tensioned components were present.
- Structures deemed as medium priority (amber) had a Phase 3 report available which had concluded that there were moderate defects to the post-tensioning systems or required further investigation in order to confirm with confidence the condition of the structures' post-tensioning systems.
- Structures deemed as low priority (green/grey) were either currently having or recently had had additional PTSI investigations or had a Phase 3 report available which concluded that no or limited further PTSI works were required.

11 CASE STUDY

One group of bridges to have its PTSI reports reviewed was a viaduct with two structurally separate decks and on-slip and off-slip bridges – a total of 52 spans carrying a major route over a local road and water authority property. Each deck consisted of a constant depth post-tensioned twin cell concrete box with cantilevers, widening by increments to a four cell construction where the slip roads were accommodated. Box sections were post-tensioned longitudinally and post-tensioned transversely through crossheads which were incorporated into the deck construction at intermediate support positions. Longitudinal post-tensioning continuous deflected cables were located within the webs and straight non-continuous cables were located within the top slab in the support regions of the deck.

The reports on Phase 1, 2 and 3 of the PTSI of the structures were reviewed. The overall assessment of the post-tensioning elements was deemed to be satisfactory, although a significant number of ducts exposed had extensive voiding, or were completely voided with no grout present or serious corrosion of tendons had been noted. No exposure of longitudinal ducts and tendons within cells had been undertaken. Exposed tendon wires at the anchorages under the top slab tendons were corroded; this was considered to be as a result of previous leakage through the deck slab that had been stopped following re-waterproofing of the deck. Black rust staining of the tendons was found. Certain descriptors used were vague. The evaluation had been based on limited corrosion testing (no half-cell potential, resistivity or depth of cover surveys) and limited chemical testing, thus not providing sufficient information on the risk of possible future corrosion activity.

Principal Inspection reports were also reviewed. In the cells, the workmanship was considered to be generally poor. Timber shuttering had not been removed at

some locations throughout the structures. The shuttering to the webs inside cells at certain locations had moved and the concrete had bulged. Excess or waste concrete had not been removed from certain box cells. Leachates, water/dampness, rust staining, cracking and previous repair areas were noted within certain cells to the structure. Minor cracking and spalling were noted to several of these repairs. Leachates and a regular pattern of rust staining were noted on the vertical surfaces of the diaphragms. Water leakage from drainage pipes was noted in several cells. Corroded reinforcement present in the structure was considered to be due to insufficient concrete cover.

The review report recommended that further investigations should be undertaken at 171 locations to determine the condition of the post-tensioning elements if remedial grouting of the voided ducts has not been undertaken. Where duct and tendon exposures were to be undertaken at midspan and over the piers, more comprehensive chemical testing of the grout and concrete was needed. At selected duct and tendon exposure locations, corrosion testing was to be completed.

12 FURTHER INVESTIGATION RESULTS

The post-tensioning systems in the structures were generally found to be in good/fair condition. The ducts to the longitudinal continuous post-tensioning tendons were generally fully grouted and tendons were in good condition with no significant loss of cross-sectional area. For each structure the predominant defect was the presence of voids in ducts to the longitudinal non-continuous tendons over piers and in the cantilevers. These accounted for 15 of the 24 significant defects that were observed. At those locations no significant corrosion of the ducts was noted. Pitting corrosion of wires was recorded at three locations, with $<5\%$ loss of cross-sectional area and one wire out of five exposed was broken at another location.

13 RECOMMENDATIONS

No further investigations or monitoring were recommended with regards to the decks and post-tensioning systems of the viaduct and bridges. Maintenance actions recommended included clearing areas of pigeon droppings and nests from inside cells; clearing silt, soil and water ponding in certain spans and repairing a broken drainage pipe. It was recommended that consideration should be given to remedial grouting of voided ducts to the longitudinal non-continuous tendons if assessments were to show that extensive voiding significantly affected the load carrying capacity of the structures. If this was the case, it would be necessary to determine the extent of voiding in the ducts not yet investigated prior to possible remedial grouting of the ducts with voids.

14 CLIENTS PERSPECTIVE

The outcomes from programmes of review of Special Inspection reports on post-tensioned bridges have identified what was needed to be done in order that the condition of post-tensioned bridge stocks could be determined with confidence, particularly as it could be between 10 and 20 years since the condition of the bridges' post-tensioning systems had initially been investigated. The information to be obtained would assist in the management of the bridge stocks. Once any remedial works had been identified, then individual maintenance plans could be produced for each structure and a suitable programme of inspections, testing and monitoring carried in the future to ensure that residual life of the structures might be maximised.

15 CONCLUSIONS

The observed early deterioration of concrete bridges has been of increasing concern in many countries throughout the world because of the clear social, environmental and economical consequences. Many agencies around the world have been reporting problems with their bridges since the mid 1980's, and it has been found that there is often a problem in prioritising those structures for investigation.

Particular attention has to be made to testing and monitoring the durability of concrete structures in order that those structures may be managed in the most cost-effective manner. Staged investigations enable irregularities to be detected, causes of deterioration to be diagnosed and the solutions of problems to be determined. It is essential that the investigations be well targeted, be carried out by well trained engineering staff and that results of investigations be interpreted by experienced engineers.

Corrosion problems with post-tensioned bridges have been found not only in the United Kingdom, but also in other countries including France, Japan and the United States. Corrosion of post-tensioned tendons in grouted ducts has occurred in a small number of post-tensioned concrete bridges in the United Kingdom. The difficulty of detecting corrosion, and the absence of external evidence of deterioration in most cases, has meant that visual inspections alone have not been sufficient to determine the condition of structures' post-tensioning systems. The rare examples of failure have generally been sudden with little or no warning indications. It is considered essential that sufficient targeted investigations be carried out to each post-tensioned structure in order to obtain a reliable overview of the structures' post-tensioning systems.

Further durability problems may occur with internally grouted tendons in the future as the corrosion protection provided to-date begins to break down and moisture and salts gain access over time. Structures that show a potential for future deterioration and that are strategically important will require careful management. The condition of those structures needs to

be monitored and any necessary remedial actions identified.

Post-tensioned bridges have proven to be a robust form of construction. However, lessons learnt are that just because a previous Post-Tensioning Special Inspection has been carried out, it cannot be taken for granted that the post-tensioning system is in good condition. A regular review of the structure's condition in conjunction with a review of previous post-tensioning investigation reports is required to determine whether additional activity is needed and to determine completeness of the previous work. It is not a do once and forget about situation.

REFERENCES

BA 50/93. 1993. *Post-Tensioned Concrete Bridges, Planning, Organisation and Methods for Carrying out Special Inspections*. Department of Transport.

BD 54/93. 1993. *Post-Tensioned Concrete Bridges, Prioritisation of Special Inspections*: 14. Department of Transport.

Durable Post-Tensioned Concrete Bridges. 1996. Technical Report No. 47: 64. Concrete Society/Concrete Bridge Development Group. Crowthorne.

Durable Post-Tensioned Concrete Bridges. Second Edition. 2002. Technical Report No. 47: 70. Concrete Society/Concrete Bridge Development Group. Crowthorne.

Godart, B. 2001. Status of the Durability of Post-Tensioning Tendons in France, *Durability of Post-Tensioning Tendons Workshop*: 25–42. Ghent.

Pearson-Kirk, D. & Cairns, R.J.M. 2007. The Performance of Post-Tensioned Bridges. *International Conference: Concrete Platform 2007, Queen's University, 19–20 April*. Belfast.

Pearson-Kirk, D, Pottle, S.& Duguid, K. 2010. The Management of Post-Tensioned Bridges. *13th International Conference on Structural Faults and Repair, July.* Edinburgh.

Poston, R.W. & Wouters, T.P. 1998. *Durability of Precast Segmental Bridges*: 32. Final Report for National Co-operative Highway Research Program. Transportation Research Board, National Research Council Washington DC.

US Department of Transportation. 2001. *Memorandum on Post-Tensioning Tendon Corrosion*.Federal Highway Administration.

Woodward, R. 2001. Durability of Post-tensioned Bridges in the United Kingdom. *Durability of Post-tensioning Tendons Workshop*: 1–10. Ghent.

Patch and crack repair

This page intentionally left blank

Concrete Solutions – Grantham et al. (Eds)
© 2014 Taylor & Francis Group, London, ISBN 978-1-138-02708-4

Two-stage concrete as a repair method

H.S. Abdelgader & A.S. El-Baden
Tripoli University, Civil Engineering Department, Tripoli, Libya.

ABSTRACT: A Two-Stage Concrete (TSC) is produced by forcing a flowable cement grout mixture through the voids of a skeleton made of a compacted preplaced aggregate. From the economic and technical aspects TSC is particularly useful for construction and repair of mass concrete structures especially foundations, underwater construction, fire damage, shields around nuclear reactors, concrete dams, heritage structures, roman cement and in all kind of construction with closely spaced reinforcement. TSC differs from ordinary concrete in that it contains a higher proportion of stone aggregate and the aggregate stays in point-to-point contact as placed. Thus, the mechanical characteristics of the TSC in failure conditions are distinctly different from ordinary concrete. This paper presents the out-put results of experimental investigations conducted to evaluate the compressive, tensile strength and modulus of elasticity of TSC using grouts with different water-to-cement ratios and admixture contents. It was found that the modulus of elasticity and splitting tensile strength TSC is equivalent or higher than that of conventional concrete at the same compressive strength. Splitting tensile strength can be conservatively estimated using the American Concrete Institute (ACI) equation for conventional concrete.

1 INTRODUCTION

The preplaced aggregate concrete (PAC) or TSC gets its name from the method used for placement. Formwork is constructed and the coarse aggregate is densely placed inside the formwork. The coarse aggregate is washed and screened just prior to placement to remove all fines. Grout is then injected through the forms to provide the matrix as shown in Figure 1. Grouting is begun at the bottom of the preplaced aggregate. The grout typically consists of sand, cement, pozzolan, and an admixture. The characteristics of the grout are affected by water content, sand grading, cement, pozzolan, and the types and amounts of admixtures. For each mixture there are optimum amounts of fillers and admixtures which produce the best pumpability or consistency. Proper proportioning of the structural grout mix components is necessary to produce the required strength and durability requirements of the finished preplaced-aggregate concrete. Mixture design tests are necessary for each job. TSC has been used for the resurfacing of lock walls and dams and for the repair of tunnel linings, piers, and spillways (King 1959) It may be used advantageously on repair jobs of heritage structures, and large concrete repair jobs:

- Where placement by conventional methods is difficult (e.g., massive reinforcing steel and embedded items are present or access to the area is difficult, such as the underpinning of the toe of a dam or apron).
- When low-volume change of the repair concrete is required to avoid cracking caused by excessive tensile stresses in the overlay concrete because of drying shrinkage and restraint provided by the existing concrete.
- Where underwater placement is necessary because dewatering is difficult, expensive, or impractical and water conditions permit.

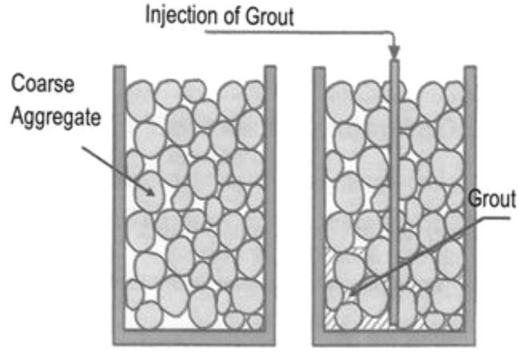

Figure 1. TSC fundamental technique.

In the last decades, TSC has been involved in many typical applications across the globe. For example, in Poland large-scale two-stage concreting was tested in two applications, namely while laying foundations for an 18 story building in Gdansk (Poland) (about 350 m^3), Figure 2, and the repair of damage to a water dam in Czchow near Cracow (Poland) (about 400 m^3) underwater concreting, on the River Dunajec. In both cases good technological and economical results were obtained (ACI-304 1997).

Figure 2. Foundation construction in 18-story building (Gdansk, Poland).

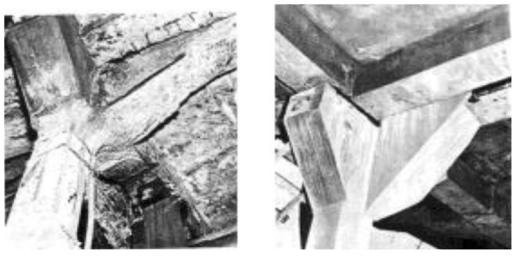

Figure 3. TSC used in column repair.

The TSC technique can be introduced in repair or strengthening of existing structures by using the jacket and collar processes. Jacketing is the process whereby a section of an existing structural member is restored to original dimensions or increased in size by encasement in new Portland cement or polymer-modified Portland cement concrete. A steel reinforcement cage is constructed around the damaged section into which shotcrete or cast-in-place concrete is placed (Abdelgader 1996). Collars are jackets, which surround only a part of a column or pier and typically are used to provide increased support to the slab or beam at the top of the column. The form for the jacket may be temporary or permanent and may consist of timber, corrugated metal, pre-cast concrete, rubber, fiberglass, or special fabric, depending on the purpose and exposure.

TSC has also been used to repair beams and columns in industrial plants as shown in Figure 3 (ACI-304 1997). The jacket form is placed around the section to be repaired, creating an annular void between the jacket and the surface of the existing member. The form should be provided with spacers to assure equal clearance between it and the existing member. A variety of materials including conventional concrete and mortar, epoxy mortar, grout, and latex modified mortar and concrete have been used as encasement materials. Techniques for filling the jacket include pumping, tremie, or two-stage concrete (Abdelgader 1996).

2 PAPER OBJECTIVES

This paper presents the output results of experimental investigations conducted to evaluate the compressive, tensile strength and modulus of elasticity of TSC using grouts with different water-to-cement ratios and admixtures content. It was found that the modulus of elasticity and splitting tensile strength of TSC is equivalent or higher than that of conventional concrete at the same compressive strength.

3 EXPERIMENTAL PROGRAM

3.1 *Materials*

The coarse aggregate used in the experiment program was sub-angular basalt. A large sample was acquired, washed, and sieved to create the gradation with a maximum size of 50 mm. The coarse aggregate had a bulk loose density 1430 kg/m^3, dry specific gravity of 2.687, absorption of 0.34%, and void ratio of 47%. Because of its low absorption and high apparent specific gravity, this basalt is considered a high quality coarse aggregate. The fine aggregate used had an absorption and specific gravity of 1.05% and 2.63 respectively. The particle size distribution of the sand was divided into three fractions: 2.0/1.0 mm (13%), 1.0/0.25 mm (67%), and 0.25/0.0 mm (20%). Its properties were checked in accordance to standards (ASTM C33 1997). The cement used throughout the research was ordinary (Type I) Portland cement, having a compressive strength of 41 MPa after 28-days of water curing and Blaine fineness of approximately 3500 cm^2/g. The cement properties conformed with standards (ASTM C150 1994). Water was used directly from the tap and was slightly colder (21°C) than room temperature. The superplasticizer used in the grout was a naphthalene-formaldehyde derivative, trade name 'SikaMent-163' and was mixed at the rate of 2% by weight of cement. The expanding agent, trade name 'Intraplast-Z' was an aluminium powder-based admixture; this was also used at the rate of 2% by weight of cement.

3.2 *Grout proportioning, specimen preparation and testing procedures*

The selection of water-cement-sand ratios is more critical in TSC because the amounts of sand and water control the pumpability and propagation of grout, therefore, an essential requirement is needed in the production of TSC (Abdelgader et al. 2008). The void content of the preplaced aggregate was 47% and the bulk density 1430 kg/m^3. Five different proportions of water to cement ratio (w/c) (0.42, 0.45, 0.50 and 0.55) were investigated with cement to sand ratios (c/s) of 1/1.5, 1/1, and 1/0.8. Grout preparation was accomplished by combining ingredients with an electric mixer for about three minutes to achieve the desired grout uniformity and consistency. Trials were made with grout to find the minimum w/c ratio at

which the preplaced aggregate could be effectively grouted. A w/c ratio of 0.45 was found to be the minimum ratio suitable for grouting; it was not possible to penetrate all voids in the aggregate skeleton with a grout at a w/c ratio of 0.42. The displacement of aggregate was less noticeable as the w/c ratio was increased; at a w/c ratio of 0.55 there was no displacement. The experimental program consisted of a series of unconfined compression tests, split tensile tests and modulus of elasticity tests on samples prepared from different grout mixtures after 28 days of curing in laboratory climate. To gain an effective comparison between results of compressive to tensile strength of concrete cylindrical specimens of size 150 × 300 mm were prepared in the same manner and tested. Grout specimens were tested in compression using standard cubes of size 100 × 100100 mm. After one day of casting all specimens were removed from their moulds and covered with moist burlap for seven days and stored in the laboratory climate. Excluding the specimens at a w/c ratio of 0.42, there were 81 concrete specimens tested. Three specimens from each one of the three grout mixtures were tested in unconfined compression, split tension and modulus of elasticity at 28 days. A separate set of 27 concrete cubes of size 300 × 300 × 300 mm were tested for compressive strength only using grout having w/c ratio of 0.45,0.5 and 0.55 and sand cement ratio of 1/1.5, 1/1 and 1/0.8. Mortar cubes were prepared and tested in unconfined compression as prescribed in standards (ASTM-C942 2010). Three cubes of each mortar were tested at 28 days using a universal hydraulic testing machine with 600 KN capacity. Unconfined compression tests on TSC cylinders were tested in accordance with standards (ASTM-C873 2010). Three specimens of each concrete were tested at 28 days using a universal hydraulic testing machine with 2200 9 KN capacity. Splitting tensile tests were also conducted on three specimens of each concrete at 28 days according to the procedures outlined in (ASTM-C496 2004). Splitting tensile tests were performed using the same machine as the mortar cubes.

4 STRENGTH INVESTIGATIONS

4.1 *Compressive strength*

Three cylinders from each concrete mix were subjected to an unconfined compression test. During the loading procedure, the vertical deformations were measured on three sides of the specimen with respect to axial force increment. On the basis of these results, stress and appropriate strain values were calculated. Some of the test results are presented in Figure 4. Compressive strength results from the cubical shape samples were presented in Table 1.

Figure 5 shows the mean and individual cylinder strengths of three specimens per w/c ratio at ages of 28 days. It can be seen that a mean compressive strength of 31.9 is attainable at 28 days with a

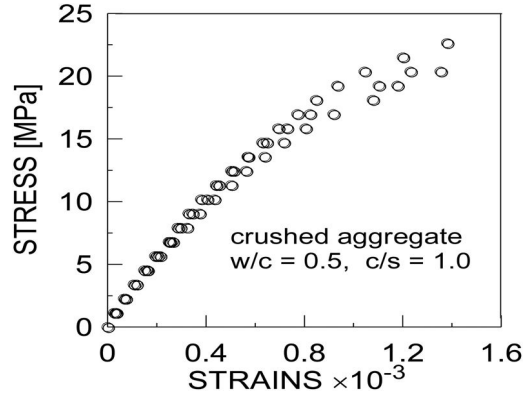

Figure 4. Stress-strain sample of results for TSC.

Table 1. Compressive strength of TSC grouts.

W/C	S/C	f'_c (MPa)
0.45	1/1.5	30.82
0.45		27.82
0.45		23.72
0.5	1/1	30.65
0.5		27.1
0.5		23.55
0.55	1/0.8	30.78
0.55		27.23
0.55		23.68

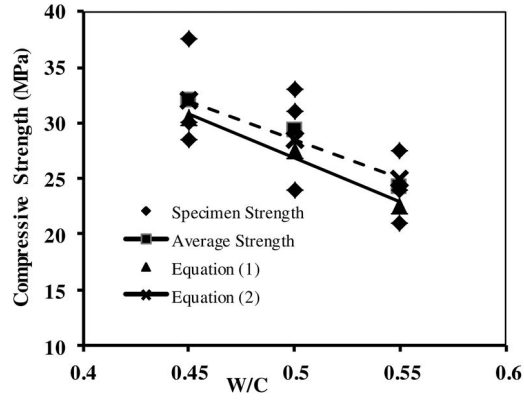

Figure 5. Compressive strength vs. water cement ratio.

w/c ratio of 0.45. Figure 5 demonstrates a strength reduction as the w/c ratio increases. Although there is some variation in strength measured per w/c ratio, the strength reduction is approximately linear. This observation is consistent with unconfined compressive strength measurements of TSC cube specimens (300 × 300 × 300 mm), in previous work for the author (Abdelgader et al. 2002) where the compressive

strength (fc′) of TSC at 28 days determined by Equation (1) as shown earlier in Table 1 as follows:

$$f_c^- = 62.08 - 71.00(w/c) + 0.52(c/s) \quad (1)$$

Equation (1) is illustrated in Figure 5 for a cement/sand (C/S) ratio of 1.0, and it can be seen that it underpredicts strength of the cylindrical specimens tested in this program. The predicted mean strength from Equation 1 is 87 to 93% of the measured mean strength. Decreasing the multiplicative factor on the w/c ratio in Equation 1 to account for cylindrical specimens yields Equation (2) as the following:

$$f_c^- = 62.08 - 68.00(w/c) + 0.52(c/s) \quad (2)$$

Only c/s = 1.0 for specimens investigated herein. Further research is required to determine the suitability of Equation 2 for a range of c/s ratios.

Another significant finding from the compressive strength data was the somewhat limited rate of strength development. This can be explained, in part, because of the fact that no fly ash or other pozzolans were incorporated in the cement grout. The observations show that, although the mechanism of stress transfer is believed to be different from conventional concrete, the mortar strength is a controlling factor in the strength of TSC. Table 2 summarizes the average compressive strength of mortar and concrete at 28 days. Firstly, it can be seen that the measured compressive strength at 28 days is sometimes high for both mortar and concrete. Secondly, the ratio of average concrete-to-mortar strengths is reasonably consistent and calculates from 0.50 to 0.51 for all mixtures at 28 days. This observation suggests that the compressive strength of two-stage concrete can be conservatively estimated as one-half of its mortar strength. If this ratio can be substantiated with more mixtures and other sources of coarse aggregate, this simple rule-of-thumb can be adopted in the design of two-stage concrete. Table 2 shows the average splitting tensile strengths of three specimens per w/c ratio at age of 28 days. The results indicate strength reduction as the w/c ratio increases. However, there appears to be little difference in strength between specimens produced with a w/c ratio of 0.45 and those produced with a w/c ratio of 0.50. This was also observed with the compressive strengths measured for the same grout mixtures. The actual values of tensile strength at w/c ratios of 0.45 and 0.50 measured from 3.1 to 3.3 MPa, which indicate satisfactory results, especially when one considers the minimum cost of concreting and that no vibration tools are used. Furthermore, excellent results can be expected even when using a high w/c ratio of 0.55, where the mean tensile strength is nearly 2.73 MPa. Test observations show that failure in splitting tension was restricted principally to the line of split and occurs through the mortar and coarse aggregate. Visual assessments of the failed specimens suggest that the percentage of failed aggregate increased in concrete with higher mortar strength (lower w/c ratio) (Abdelgader et al. 2002).

Table 2. Average compressive & tensile strength.

	Compressive Strength (fc′) (MPa)		Tensile Strength (ft) (Concrete) (MPa)
w/c	Concrete	Mortar	5
0.45	31.9	63.1	3.21
0.5	30	60.3	3.11
0.55	25.1	49.8	2.73

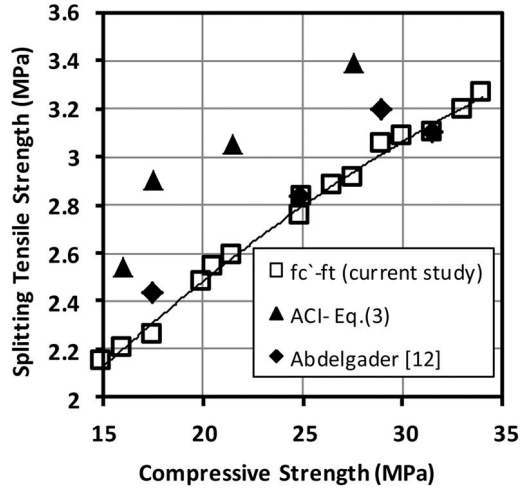

Figure 6. Compressive strength verses tensile strength for TSC.

4.2 *Compressive-tensile strength relationship*

Knowing the compressive strength (fc‘) of concrete the tensile strength (ft) of conventional concrete can be predicted by using ACI code formula as shown in Equation (3). In this investigation Equation (4) was derived from TSC data to predict the splitting tensile strengths (f′t).

$$f_t^{'} = 0.56\sqrt{f_c^{'}} \quad (3)$$

$$f_t^{'} = (0.55 - 0.56)\sqrt{f_c^{'}} \quad (4)$$

Results from Equation (4) indicated that splitting tensile strength could be well estimated using the ACI equation presented in Equation (3). Comparison between results from this investigation and another investigation conducted by the author (Abdelgader et al. 2003) showed a clear similarity as presented in Figure 6. The data from both studies show that the tensile strength of TSC is at least as high as that of conventional concrete, and in fact it can be higher depending on the selection and properties of the coarse aggregate. No causes were apparent for the relatively higher tensile strength in two-stage concrete. However, the greater mechanical interlocking among particles in

Table 3. Constants a, b, c of Equation (5).

Aggregate Type	w/c	a	b	c	Correlation Coefficient
Round	0.45	18.2	−32.5	34.0	0.9941
	0.5	1.0	−9.4	28.5	0.9978
	0.55	5.81	−22.0	32.1	0.9861

two-stage concrete could be responsible for the higher tensile strength since factors like aggregate gradation are different from conventional concrete. These observations warrant a much deeper investigation into the influence of coarse aggregate properties on two-stage concrete behavior in tension (Abdelgader et al. 2003).

4.3 *Stress-strain relationships*

The obtained results are statistically analysed to estimate equations for the compressive strain-stress relations of various two-stage concrete types. The statistical analysis is performed by use of the MINITAB program (Schaefer 2001). The Minitab Regress Package fits an equation to the experimental data by the least square method. The calculation can be divided into the following steps: assumption of the mathematical relation, estimation of the equation coefficients, testing of the assumed equation and choice of the best model. The statistical analysis of the TSC test data is performed in two successive phases. First, equations for stress-strain relations for type of coarse aggregate and different grout proportions are estimated. In this step the data consist of 27 stress-strain sets of experimental results obtained from cylinder compressive tests (Abdelgader et al. 1999 & Iwasaki et al 1985). After various trials the following simple relation for all concrete types is:

$$\hat{\sigma} = a\,\varepsilon_1^3 + b\,\varepsilon_1^2 + c\varepsilon \tag{5}$$

In the above formulae $\hat{\sigma}$ stands for the estimated concrete stresses and $\varepsilon_1 = \epsilon \times 10^3$. Where ε denotes the concrete strain. The constants a, b, and c in Equation (5) for round aggregate and each concrete type are statistically obtained and presented in Table 3 for c/s = 1/1.5 and various w/c ratios. Equation (5) gives reliable results in the strain range from 0 to 0.001. Figure 7 presents typical results of stress and strain relation for round aggregate type (Abdelgader et al. 2003).

In the second step the statistical analysis is used to obtain the TSC stress-strain relations as function of water-cement (ω = w/c) and cement-sand (ζ = c/s) ratios. After a complex analysis the functions: $a = a(\omega, \zeta)$, $b = b(\omega, \zeta)$ and $c = c(\omega, \zeta)$ in Equation (5) are assumed for round aggregate as follows:

$$\begin{aligned} a(\omega,\varsigma) &= 14.9 - 17.1\omega + 1.89\varsigma \\ b(\omega,\varsigma) &= -40.8 + 30.1\omega + 5.80\varsigma \\ c(\omega,\varsigma) &= 40.7 - 11.1\omega - 4.46\varsigma \end{aligned} \tag{6}$$

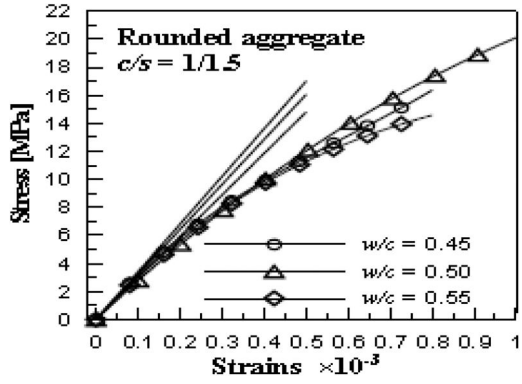

Figure 7. Graphical presentation of stress-strain results for TSC.

Table 4. Constants calculated for Equation (5).

Aggt. Type	w/c	$a(\omega, \varsigma)$	$b(\omega, \varsigma)$	$c(\omega, \varsigma)$	Correl. Coeff.
Crushed	0.45	8.47	−21.83	34.49	0.808
	0.5	7.61	−21.78	34.69	0.814
	0.55	6.76	−21.73	34.89	0.735
Round	0.45	10.8	−23.39	32.73	0.827
	0.5	8.24	−21.88	32.18	0.797
	0.55	5.68	−20.38	32.62	0.652

Some estimation results for concrete stresses according to Equation (5) by use of functions presented in equation (6) is shown in Table 4.

The test observations and the statistical analysis have proved that the linear part of the stress-strain curve in TSC may reach 85% of the ultimate cylinder strength (see Figure 7). This may result from a very good contact between the aggregate particles. In consequence the applied load is distributed mainly by the stones. During the laboratory tests it was observed that the skeleton of the two-stage concrete carried the load until the whole specimen collapsed. It was the reason why the failure of the two-stage concrete was not sudden and explosive but rather gradual. The failure specimen showed extensive lateral expansion in the form of bulging. Thus the specific stress-strain characteristics of the TSC can be explained by a dominant influence of the rigid stone skeleton. It should be pointed out that the stress-strain relations of traditional concrete result from transfer of stress through the mortar-aggregate uniform matrix. In the TSC there are no such uniform relations because the mechanical properties of TSC are mainly determined by the characteristics of the stone aggregate. Therefore, the subsequent fracture of the two-stage concrete takes place through the stone aggregate particles (Abdul 1988). In the TSC the compressive stresses in the aggregate and in the grout cannot be equal. The compressive stress is influenced by the shear stresses occurring not only in the vertical section but also in the

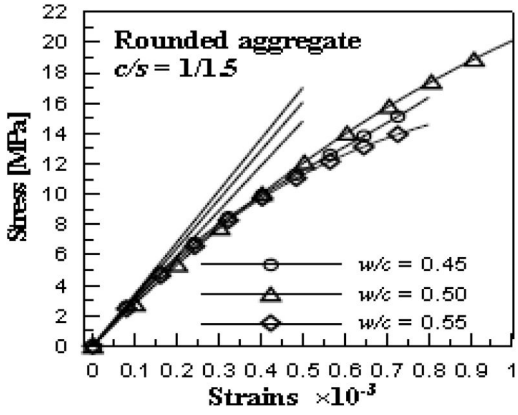

Figure 8. Tangent modulus of elasticity of TSC.

horizontal contact surfaces. The produced shear stress caused the tearing off of the aggregate grains from the grout. It was also observed that some micro cracking or interfacial cracks were randomly distributed even before the specimens were subjected to load testing. It seems that these cracks were caused by bleeding, settlements of grout, or by shrinkage stresses induced by the drying process. The cracks formed within the grout may be considered to be isolated or discontinuous.

4.4 *Modulus of elasticity*

The experimental data analysis and the statistically obtained stress-strain relations allow for formulating the relationship between the modulus of elasticity and the compressive strength of the TSC grout (fg). The compressive strength (Table 1) is calculated according to the algorithm for designing the two-stage concrete proposed by the author (Abdelgader et al. 1999):

$$\bar{f}_c = \beta_0 + \beta_1 \cdot \bar{f}_g^{\beta_2} \tag{7}$$

Where: $\bar{f}_g$ stands for compressive strength of grout [MPa], β_0, β_1 and β_2 are constants obtained from regression analysis and are given in other research by the author(Abdelgader et al 1999). The modulus of elasticity of the TSC is mainly affected by the physical properties of the coarse aggregate. The influence of the content of grout in the concrete is rather meaningless. It has been observed that the same factors that affect the compressive strength also alter the elastic modulus of the TSC. The elastic modulus is obtained from the analysis of the stress-strain curves for each type of stone aggregate and the mix proportions. The initial tangent modulus of elasticity of the TSC is found with reference to the tangent line drawn to the stress-strain curve at the starting point as presented in Figure 8.

The modulus of elasticity of TSC $E_{tsc}(\varepsilon_1)$, determined as a function of strains ε ($\varepsilon_1 = \varepsilon \cdot 10^3$), can be calculated in GPa from Equation (8) as follows:

$$E_{tsc}(\varepsilon_1) = \frac{d\hat{\sigma}}{d\varepsilon_1} = 3 \cdot a(\omega,\varsigma) \cdot \varepsilon_1^2 - 2 \cdot b(\omega,\varsigma) \cdot \varepsilon_1 + c(\omega,\varsigma) \tag{8}$$

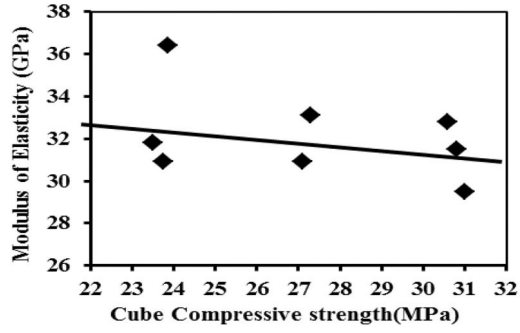

Figure 9. Modulus of elasticity verses compressive strength.

Assuming that $\varepsilon_1 = 0$ the concrete modulus E_{tsc} is estimated as:

$$E_{tsc} = c(\omega,\varsigma) \qquad \text{(GPa)} \tag{9}$$

Equation (9) indicates that function $c(\omega, \zeta)$, calculated according to Equation 6, determines the elastic modulus of the TSC. It should be mentioned that the values of the elastic modulus obtained for 30% of the cylinder ultimate strength are almost the same. In this way the initial linear feature of the strain-stress relation of the TSC has been proved. It is possible to elaborate an alternative version of the elastic modulus formulae. Making use of the regression analysis of the experimental data expressions describing the relationship between the elastic modulus and the compressive strength of the TSC the following assumption for round aggregate type can be made:

$$E_{TSC} = 28.7 + 0.08 f_c' \tag{10}$$

Where: f_c' is the cube compressive strengths. The limit value of the cube compressive strengths $\bar{f}_c$ in equation (10) is:

$$23 \text{ MPa} \le \bar{f}_c \le 32 \quad \text{MPa} \tag{11}$$

Equation (10) is graphically presented in Figure 9. It should be noticed that the obtained values of the modulus of elasticity are rather scattered. This can be explained by the random allocation of coarse aggregate in the forms. Nevertheless, Equation (10) allows for the approximate determination of the modulus of elasticity for the examined aggregate. It should be pointed out that the obtained results deviate at most ±10% from the calculated mean values.

5 CONCLUSIONS

The following conclusions can be drawn from this study:

- A grout mixture with a water-to-cement (w/c) ratio of 0.45 to 0.55 and a cement-to-sand (c/s) ratio of

1.0/1.5, 1.0/1.0 and 1.0/0.8 optimizes compressive and tensile strength of TSC. Mortar mixed with a w/c ratio below 0.42 is too viscous and does not fully penetrate the voids between coarse aggregate particles, thus creating a honeycombing effect in the hardened concrete. Even when partially bound, however, TSC provides strengths equivalent to that of fully bound concrete with mortar at a w/c ratio of 0.45.

- Compressive strength of TSC cylinders can be conservatively estimated as 50% of the mortar cube strength.
- The splitting tensile strength of TSC was found to be similar to that predicted by the ACI equation for splitting tensile strength of conventional concrete. In some cases, the measured tensile strength of TSC is in fact higher than that predicted by the ACI equation.
- The stress-strain relationships for different grout mixes (water/cement ratios and cement/sand ratios) do not show a big difference. The initial stress-strain curves can be estimated by linear relations. This may result from the stresses distributed mainly by the particles of stone aggregate (skeleton of stones). The specific way of stress transmission may also contribute to the initiation and propagation of cracks.
- The modulus of elasticity as a function of compressive strength of the TSC is elaborated. The modulus values for specific type of aggregate are described by linear constant functions. The obtained equations allow engineers to design the TSC according to the algorithm presented in (Abdelgader 1999 & Abdelgader et al. 2002).

REFERENCES

Abdelgader, H.S. 1996. Effect of quantity of sand on the compressive strength of two-stage concrete. *Magazine of Concrete Research* 48(3): 353–360.

Abdelgader, H.S. 1999. How to design concrete produced by a two-stage concreting method. *Cement and Concrete Research* 3 (29): 331–337.

Abdelgader, H.S. & Górski, J. 2002. Influence of grout proportions on modulus of elasticity of two-stage concrete. *Magazine of Concrete Research* 4(5): 251–255.

Abdul Awad, A.S. 1988. Failure mechanism of pre-packed concrete. *ASCE Structural Engineering Journal* 3(5): 727–732.

Abdelgader, H.S. & Górski, J. 2003. Stress-strain relations and modulus of elasticity of two-stage concrete. *ASCE Materials Journal* 4(2): 251–255.

Abdelgader, H.S. & Elgalhud A. A. 2008. Effect of grout proportion on strength of two-stage concrete. *Structural Concrete Journal* 3(3): 163–170.

ACI Committee (304.1 R-92). 1997. *Guide for the use of preplaced aggregate concrete for structural and mass concrete applications*: 21–24. Farmington Hills- Michigan: USA.

ASTM C230. 2001. Standard specification for flow table for use in tests of hydraulic cement. *American Society for Testing and Materials*: 129–133. Philadelphia: Pennsylvania.

ASTM C939. 2010. Standard Test Method for flow of Grout for Preplaced Aggregate Concrete (Flow Cone Method). *American Society for Testing and Materials*: 134–136 Philadelphia: Pennsylvania.

ASTM-C150. 1994. Specification for Portland cement. *American Society for Testing and Materials*. Philadelphia: Pennsylvania.

ASTM. C33. 1997. Specification for concrete aggregates. *American Society for Testing and Materials*. Philadelphia: Pennsylvania.

ASTM-C42/C42M. 2004. Standard test method for obtaining and testing drilled cores and sawed beams of concrete. *American Society for Testing and Materials*, Philadelphia: Pennsylvania.

ASTM-C496/C496M. 2004. Standard test method for splitting tensile strength of cylindrical concrete specimen. *American Society for Testing and Materials.* Philadelphia: Pennsylvania.

ASTM C642. 2006. Standard test method for density, absorption, and voids in hardened concrete. *American Society for Testing and Materials.* Philadelphia: Pennsylvania.

ASTM C942. 2010. Standard test method for compressive strength of grouts for preplaced-aggregate concrete in the laboratory. *American Society for Testing and Materials*. Philadelphia: Pennsylvania.

ASTM C873. 2010. Standard test method for compressive strength of concrete cylinders cast in place in cylinder molds. *American Society for Testing and Materials*. Philadelphia: Pennsylvania.

Iwasaki, N. 1985. Predictions of grouting process in prepacked concrete by green's function. *Proceeding of Japanese Society of Civil Engineering*: 45–50. Tokyo: Japan.

King, J.C.1959. *Handbook of heavy construction-concrete by intrusion grouting:* 211–234. New York: McGraw-Hill.

Schaefer, R.L. & Anderson, R.B. 1989. *The students edition of MINITAB statistical software adapted for education*: 5–23. New York: Addison–Weslley Company.

This page intentionally left blank

Concrete Solutions – Grantham et al. (Eds)
© 2014 Taylor & Francis Group, London, ISBN 978-1-138-02708-4

Self-healing behavior of concrete cracks

C. Baeră, H. Szilagyi & M. Păstrav
"URBAN –INCERC" National Research Institute, Cluj-Napoca Branch. Romania

A. Mircea
Civil Engineering Faculty, Technical University of Cluj-Napoca, Cluj-Napoca, Romania

ABSTRACT: Usually considered an extremely common phenomenon, not leading directly to sudden failure, cracking is the main risk factor for the general problem of concrete durability. The cracks are access paths for aggressive agents, generating reinforcement corrosion, strength reduction, spalling of the concrete cover and other damage forms. In the context of multiple new solutions for concrete manufacturing, utilization and compositions, rapidly developed in the latest years, cracking control is still difficult to ensure. An indirect possibility is "healing" cracks by inducing self-healing concrete mechanisms: further hydration of the unreacted cement determining crystallization of calcium carbonate along the crack, swelling of cement hydration products, cracks closed by small concrete particles and even mechanical properties regaining: compressive and tensile strength, dynamic modulus of elasticity. The aim of this paper is to present the effective self-healing potential of cementitious materials as a possible and accessible way for considerable deterioration rate reduction.

1 INTRODUCTION

Concrete, the most frequently used building material since its occurrence, represents a quasi-brittle composition, with good compression properties but weak points regarding tensile stress; as a consequence reinforcement is used for improvement of concrete elements under bending or tension loading, but inherent cracking will generate in time structural degradation. Crack control and crack healing (self-healing) could be possibilities for service life extension of the concrete structures by means of decreasing the deterioration rate. Implicitly, the demand for concrete civil infrastructure repair and also the need for new buildings will decrease, involving economic and ecological benefits (less pollution and less energy consumption and less CO2 emissions).

The aim of this paper is to present a realistic evaluation of self-healing capacity of cementitious materials (plain and reinforced concrete, fiber reinforced concrete FRC or High-performance fiber-reinforced cementitious composites HPFRCC). The paper includes the mechanisms that are produced within these materials in order to cure the damage, possible curing conditions or treatment and also the viability of a self-healing approach considering the gains and also the limitations of the processes, in the context of sustainable infrastructure development.

2 CONCRETE CRACKING – CAUSE AND EFFECT

Cracking represents an inherent reality regarding plain or reinforced concrete and cementitious materials in general, occurring at any point along their life interval. The cracking process can be generated by external causes (loading type and magnitude, subgrade settlement, poor design or defective execution, environmental factors like thermal contraction, freezing and thawing or thermal action and corrosion, sulphate attack (Yang et al. 2009, Homma et al. 2009) and also by internal causes, related to material itself and its dimensional, physico-chemical, mechanical heterogenic composition (Joseph et al. 2009, Buchman 1999): plastic shrinkage cracking; alkali-aggregate reaction or drying shrinkage.

In the latest decades, Delayed Ettringite Formation (DEF) was identified as an important damage phenomenon within cementitious composites: without any external sulphate contribution, several months or even years after casting of concrete elements, an internal sulphate reaction happens within the material, causing a swelling phenomenon by ettringite formation in voids, existing cracks and the contact areas between the hardened paste cement and aggregates, implicitly generating concrete deterioration (Hime 1996). A clear distinction must be performed between DEF and the external sulphate reaction (ESR), which

occurs when the sulphates penetrate via the material capillary network and produce expansion phenomena. The DEF phenomenon was identified mainly in two types of concrete: heat treated concrete and cast in place structural concrete elements. It is concluded that several cumulative parameters induce DEF: concrete composition, curing conditions and exposure conditions. (LCPC 2009).

Despite the fact that cracking and microcracking represent a common feature within cementitious materials which does not involve fatal damage in the first stages, over time it progresses negatively implying increase of crack width and implicitly decrease of internal strength and enhanced material vulnerability to external factors. As a consequence cracks can be seen as key issue for cementitious materials durability.

3 SELF – HEALING: DEVELOPMENT OF THE CONCEPT

3.1 *Definitions and terminology*

As its own name suggest, self-healing represents the material intrinsic capacity of repairing the damages occurred within its structure. Self-healing of cementitious materials happens as a complex of processes strongly related to cracking mechanisms, respectively to crack closing. The phenomenon has been noticed for quite a long time and it could explain the survival of old buildings exceeding the predicted life period without major human intervention. It is considered that the longevity of old bridges of Amsterdam may be due to the self - closing of cracks (Gosh 2009).

The particular terminology and related definitions for the general term of self - healing of Cementitious materials include (Mihashi & Nishiwaki 2012):

- SELF – CLOSING, meaning sealing of the cracks;
- SELF – HEALING, meaning restoring of the material properties;
- AUTOGENOUS HEALING, referring to self-closing/healing produced by material itself;
- AUTONOMIC HEALING representing self-closing/healing produced by engineered addition to the material;
- SELF – REPAIRING considers the concept of intelligent materials.

Over time, several definitions have been provided by researchers interested in this matter. The schematic definition (Fig. 1) introduced in 2011 by de Rooij & Schlangen (De Rooij et al. 2011) considers the action and the process type involved in the phenomenon:

In 2012 Mihashi (Mihashi & Nishiwaki 2012) performs a clear distinction (Fig. 2) between Self-healing and Self-Repairing:

3.2 *Self-healing mechanisms*

The phenomenon of self-healing of cement-based materials intrigued the scientific world, starting

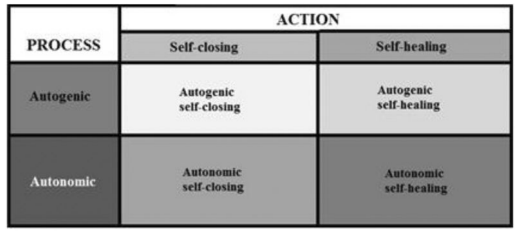

Figure 1. Definition of self-healing concrete considering the ACTION and the PROCESS (De Rooij et al. 2011).

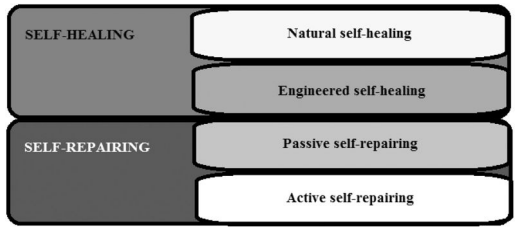

Figure 2. Definition of self-healing/repairing according to Mihashi (Mihashi & Nishiwaki 2012).

with the French Academy of Science, around 1836 (Mihashi & Nishiwaki 2012). Further on, experimental programs performed all around the world have demonstrated that cementitious materials possess a certain capacity of reducing the opening of the cracks or even to close them completely, under some specific conditions and circumstances. Calcium hydroxide conversion from hydrated cement paste into calcium carbonate was stated to be the major mechanism responsible for the natural self-sealing of the concrete cracks. Besides it, swelling and re-hydration of cement paste, crystals of calcium carbonate precipitating within the cracks together with impurities in water or small concrete spalling, represent examples of physical, mechanical or chemical interactions leading to crack closing or even restoring of material mechanical properties (Mihashi & Nishiwaki 2012).

4 SELF – HEALING: EVALUATION OF MAIN DIRECTIONS

4.1 *Autogenic self – healing*

Carola Edvardsen's experimental investigations on plain and reinforced concrete lead to some important and reliable conclusions, applicable to the entire family of cementitious composites: she certifies the fact that the main crack curing mechanism consists of calcium carbonate crystallizing inside the concrete cracks and proves that the evolution of this process is strongly related to important factors such as crack width and water pressure as curing agent; at the same time it is demonstrated that other parameters like water hardness and concrete composition are independent to the curing process. It was recorded that the first 3 to 5

days of specimen exposure to water were the most prolific regarding the $CaCO_3$ crystals precipitating in the cracks, after that the process decreases in intensity (Edvardsen 1999).

Edvardsen and other researchers (Kishi et al. 2007, Zhong & Yao 2008, Jacobsen & Sellevold, 1996) obtained autogenic self – closing and self – healing of concrete specimens (in accordance to de Rooij & Schlangen 2011 definition) but results were generally limited to 0.3 mm crack opening, which leads us to a clear limitation of the phenomenon benefits.

4.2 *Engineered self – healing*

Under these circumstances engineered self-healing of concrete developed as a particular direction of the concept, involving fibre reinforced cement-based materials. Dispersed fibres addition in concrete mix, first introduced by the American A. Berard in 1874, proved itself beneficial regarding crack width reduction and ductility improvement, by increasing the fracture energy. The new materials became popular, not only as experimental approach but also in current practice. Fibre reinforced concrete (FRC) and then High-performance fibre-reinforced cementitious composites (HPFRCC) are engineered cementitious materials which, besides superior physico-mechanical properties showed improved self-healing capacity in comparison to normal concrete, as demonstrated by worldwide experimental procedures (Hannant & Keer 1983, Yang et al. 2009, Homma et al. 2009, Mhashi et al. 2011). The global conclusion is that the fibres inside the composite matrix represent real bridges where the calcium carbonate could precipitate as a sealant over the crack.

4.3 *Engineered self healing cementitous composites*

Among the HPFRCC group, a certain type of material gained general attention: Engineered Cementitious Composites (ECC), mainly developed at the University of Michigan (USA) by Victor Li and his team (Li 2008). Its design concept, based on micromechanical principles, seeks crack control as the ultimate goal. Considering the mechanical interactions among the fibre, mortar matrix, and fibre–matrix interface and also the dimensional heterogeneities within the material (dimensions of sand grains, cement particles and admixture), resulted in two simplified criteria:

a) Strength criterion: the first crack strength must not exceed the maximum bridging stress of the fibres;
b) Energy criterion: steady-state multiple cracking must occur.

Simultaneous satisfying them generates bond strength control and implicit crack control, which leads to high tensile ductility, the strain capacity reaching 5% on uniaxial tensile stress-stress curve. Under the applied force, the specimen presents a sort of "yield point" when the first microcrack appears, meaning a metal-like behaviour. The failure of concrete as a brittle material under tension (induced as uniaxial tension or bending) is produced all at once and by the means of a central major crack that enlarges with load increasing. ECC under loading presents a strain-hardening response, characterised by multiple crack formation when increasing the force, distinct from localized crack opening. Failure happens when the peak load is reached and the fracture plane is formed by multiple cracking reunion (Li 2008).

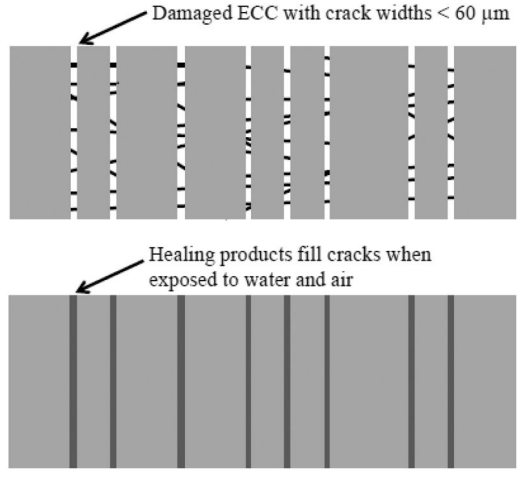

Figure 3. Self-healing of tight cracks ECC (Li & Herbert 2012).

Between the 0.01%–1% strain interval, where 0.01% corresponds to the first crack, the opening of microcracks develop from 0 to about 60 μm. The load increases and more cracks appear, none enlarging beyond the value of 60 μm); the steady-state crack width is considered to be an intrinsic material property, independent of the loading type, the geometry and size of the element or the amount of steel reinforcement inside it (Li 2008).

Besides high tensile ductility, microcracking behaviour under loading means crack control (maintaining the crack width below 60 μm) and an implicitly obvious self-healing capacity: continued hydration, pozzolanic and carbonation processes involved in natural autogenic self-healing. When curing conditions are simple, exposure of the cracked material in water and carbon dioxide (air) self-healing happens for tight cracks (Fig. 3), of maximum 100 μm or less as Li claims.

The phenomena was proved in the context of ECC materials by the means of permeability reduction (Lepech & Li 2009), also by stiffness recovery of specimens subjected to induced damaged and then placed under different curing conditions (Sahmaran & Li 2008; Yang et al. 2009; Yamamoto et al. 2010; Li & Li 2011).

The major challenge for the ECC materials is validation of their self-healing performance by the means of in-situ tests: casting of elements using ready-mix concrete, usual delivery methods, loading and curing in various exposure conditions, in the natural

environment (sometimes extreme conditions). The results obtained till now by Kishi (Kishi et al 2011) and then by Herbert (Herbert & Li 2001) seem to be promising, although the experimental programs in the matter are quite few till the present moment.

5 CONCLUSIONS

In the context of sustainable infrastructure concept based on prevention, low cost maintenance and green, ecological approach, the notion of self-healing material sounds promising and worth considering. Cracking in concrete is inevitable, so they must be closed, cured and controlled.

Among several distinct directions considered in order to achieve self-healing of cracks in cementitious materials (admixtures used in composition in order to stimulate rehydration of cement, bacteria precipitating calcite, the development of "intelligent materials" – materials containing chemical healing agent capsules, ready to break and release their content when necessary) natural, autogenic self-sealing/healing under the condition of tight crack control that ECC is offering seems for the moment the most realistic solution for substantial and quick response in this matter. It forbids the formation of cracks having widths exceeding dimensions where self-healing is possible and also their fibre content offers bridges over cracks where calcium carbonate can precipitate as a sealing agent.

Supplementary research and effective testing in real service conditions (casting, loading, curing and retesting) can validate the real potential of these new materials for extending the buildings service life and substantial reduction of maintenance costs.

REFERENCES

Buchman, J. (ed.) 1999. *Ultra high performance concrete*. Timişoara: Orizonturi Universitare.

De Rooij, M. Van Tittelboom, K. De Belie, N. & Schlangen, E. 2011. Self-Healing Phenomena in Cement-Based Materials. *Draft of State-of-the-Art report of RILEM Technical Committee*.

Edvardsen, C. 1999. Water permeability and autogenous healing of cracks in concrete. *ACI Materials journal – American Concrete Institute*, Vol. 96, No. 4: 448–454.

Ghosh, S.K. (ed.) 2009. *Self-healing materials: fundamentals, design strategies, and applications*. John Wiley & Sons.

Hannant, D.J. & Keer, J.G. 1983. Autogenous healing of thin cement based sheets. *Cement and Concrete Research*, Vol. 13, No. 3: 357–365.

Herbert, E.N. & Li, V.C. 2001. Self-healing of engineered cementitious composites in the natural environment. In: *High Performance Fiber Reinforced Cement Composites 6, Ann Arbor, MI, USA*.

Hime, W. G. 1996. Delayed ettringite formation: A concern for precast concrete?. *PCI journal,* Vol. 41 No. 4: 26–30.

Homma, D. Mihashi, H. & Nishiwaki, T. 2009. Self-healing capability of fibre reinforced cementitious composites. *Journal of Advanced Concrete Technology*, Vol. 7 No. 2: 217–228.

Jacobsen, S. & Sellevold, E.J. 1996. Self-healing of high strength concrete after deterioration by freeze/thaw. *Cement and Concrete Research*, Vol. 26, No. 1: 55–62.

Joseph, C. Lark, R. Jefferson, T. & Gardner, D. 2009. Potential application of self-healing materials in the construction industry, A report for the Institution of Civil Engineers, Cardiff University, http://www.ice.org.uk.

Kishi, T. Ahn, T.H. Hosoda, A. Suzuki, S. & Takaoka, H. 2007. Self-healing behaviour by cementitious recrystallization of cracked concrete incorporating expansive agent. In *First international conference on self-healing materials.* Springer, Dordrecht.

Kishi, T. Ahn, T.H. Morita, M. & Koide, T. 2011. Field test of self-healing concrete on the recovery of water tightness to leakage through cracks. In *3rd Int'l Conf. on Self-Healing Materials*, Bath, UK.

LCPC (Laboratoire Central des Ponts et Chaussées) – Engineering Structures 2009. *Recommendations for preventing disorders due to Delayed Ettringite Formation*, Collection Guide technique, ISSN 1151–1516.

Lepech, M.D. & Li, V.C. 2009. Water permeability in engineered cementitious composites. *Cement and Concrete Composites*, Vol. 31 No. 10: 744–753.

Li, V.C. & Herbert, E. 2012. Robust self-healing concrete for sustainable infrastructure. *Journal of Advanced Concrete Technology*, Vol. 10, No. 6, 207–218.

Li, V.C. 2008. *Engineered Cementitious Composites (ECC) Material, Structural, and Durability Performance Concrete*, Concrete Construction Engineering Handbook, Chapter 24, Ed. E. Nawy, CRC Press.

Li, M. & Li, V.C. 2011. Cracking and healing of engineered cementitious composites under chloride environment. *ACI Materials Journal*, Vol. 108 No. 3: 333–340.

Mihashi, H. Ahmed, S.F.U. & Kobayakawa, A. 2011. Corrosion of reinforcing steel in fiber reinforced cementitious composites. *Journal of Advanced Concrete Technology*, Vol. 9 No. 2: 159–167

Mihashi, H. & Nishiwaki, T. 2012. Development of engineered self-healing and self-repairing concrete-state-of-the-art report. *Journal of Advanced Concrete Technology*, Vol. 10 No.5: 170–184.

Sahmaran, M. & Li, V. C. 2008. Durability of mechanically loaded engineered cementitious composites under highly alkaline environments. *Cement and Concrete Composites*, Vol. 30: 72–81.

Yang, Y. Lepech, M. D. Yang, E.H., & Li, V.C. 2009. Autogenous healing of engineered cementitious composites under wet–dry cycles. *Cement and Concrete Research*, Vol. 39, No. 5: 382–390.

Yamamoto, A. Watanabe, K. Li, V.C. & Niwa, J. 2010. Effect of wet-dry condition on self-healing property of early-age ECC. *Proc. Japan Concrete Institute*, Vol. 32 No. 1: 251–256.

Zhong, W. & Yao, W. 2008. Influence of damage degree on self-healing of concrete. *Construction and Building Materials*, Vol. 22 No. 6: 1137–1142.

Concrete Solutions – Grantham et al. (Eds)
© 2014 Taylor & Francis Group, London, ISBN 978-1-138-02708-4

Concrete repair bond: Evaluation and factors of influence

B. Bissonnette
CRIB, Civil Engineering Department, Laval University, Quebec City, QC, Canada

L. Courard
GeMMe Building Materials, ArGEnCo Department, University of Liège, Liège, Belgium

A. Garbacz
Warsaw University of Technology, Warsaw, Poland

A.M. Vaysburd
Vaycon Consulting, Baltimore, MD, USA

K.F. von Fay
US Bureau of Reclamation, Denver, CO, USA

ABSTRACT: Repair and strengthening of existing concrete structures are among the biggest challenges civil engineers are facing today and will have to face in the years to come. Present concerns of sustainable development emphasizing repair instead of new construction will only strengthen this trend. Concerted efforts towards improving the durability of concrete repairs are still needed from scientists and engineers. One of the critical aspects of durability of concrete repairs and overlays is lasting and sufficient interfacial bond between repair material and existing concrete substrate. This paper summarizes some of the findings of a collaborative study devoted to the most significant factors influencing bond in repairs (roughness, degree of saturation and carbonation of the substrate) and its field evaluation (type of loading, device misalignment). Based on the test results collected in different test programs, guideline-type recommendations for surface preparation prior to repair were issued.

1 INTRODUCTION

In the field of civil engineering, repair and rehabilitation have drawn significant attention in the recent years. Even though engineers have been repairing deteriorated structures for many years now, the rate of unsuccessful concrete repairs remains unacceptably high. Because of the lack of knowledge gained on the influence of certain fundamental parameters, the achievement of durable repairs is reduced in some circumstances to merely a "*hit or miss*" procedure.

The aim of concrete repairs is to prolong the useful service life of an existing structure, to restore its load-carrying capacity and stiffness, and/or to strengthen its members. A prerequisite to achieve adequate composite action is lasting bond between the existing substrate and the new-cast material. In this respect, concrete surface preparation prior to repair material application is of critical importance. In fact, regardless of the repair material and application method employed, the quality of the surface preparation prior to repair will often determine whether a repair project is a success or a failure, and whether or not a repaired structure is durable.

Adhesion of a concrete repair to an existing substrate is a complex phenomenon that involves different types of bond: *chemical* bond (chemical reaction between the substrate and the repair material), *mechanical* bond (associated with the interpenetration of the repair material into the roughness and porosity of the substrate, resulting in mechanical anchorage) and *physical* bond (related to the *van der Waals* and surface tension forces (Courard, 2000). Each of these components has been studied in a number of investigations over the past 30 years, which led to significant progress in the overall understanding of the question. However, many aspects remain obscure to this day, for instance their relative importance upon bond strength development.

As part of a wider research program intended to lead to the development of performance criteria for surface preparation of concrete prior to repair, the experimental work reported herein focuses on the most influential parameters upon bond strength development. The general objective is to provide the industry with guidelines to achieve systematically strong and durable repair bond, including performance criteria

and guide specifications for surface preparation. The specific objectives were:

- to evaluate existing methods for assessment of the roughness parameters of a prepared surface;
- to establish correlation between pull-off tensile strength, shear bond strength, and surface roughness;
- to evaluate effect of load misalignment upon tensile pull-off test results;
- to evaluate the optimum moisture conditioning of a concrete substrate prior to repair; and
- to evaluate the effect of substrate carbonation upon bond strength.

2 METHODOLOGY

2.1 *Bond strength evaluation*

In different test series conducted to evaluate the effect of selected parameters upon repair bond, repaired test slabs were characterized exhaustively for bond strength using pull-off tests and, in some cases, torsional bond tests.

For the evaluation of tensile bond strength, the most widely used method is the pull-off test (e.g. ASTM C1583, EN 1542:1999). This test method consists of drilling a core through the repair material, down into the substrate, gluing a steel dolly onto the top of the core with epoxy, and using a special device to pull on the steel dolly. The tensile bond strength is equal to the maximum recorded stress when failure occurs in the interfacial zone, whereas a lower boundary value of bond strength is obtained when failure occurs elsewhere.

Under service conditions, the repair interface is in fact subjected to both tensile and shear stresses. To this day, very little data in relation with shear bond strength have been reported. Torsional shear tests have thus been carried out in this study to evaluate the bond shear response and sensitivity with respect to the tensile behavior. In this test procedure, a ring glued to the surface is twisted off using a torque housing with eccentric loading. The housing is anchored to the surface and the loading is performed with the same pulling unit as in the pull-off test procedure (different adapters).

2.2 *Influence of load misalignment*

In addition to the type of loading (tension *vs*. torsion), the influence of load misalignment upon pull-off test results was also investigated. A series of six $600 \times 400 \times 100$-mm concrete slabs was manufactured for each of three concrete mixtures (30-MPa, 40-MPa, 50-MPa). After 28 days of moist curing, the concrete slabs were prepared by sand blasting and the tensile pull-off experiments were conducted using core depths of 15 and 30 mm and coring axis inclinations of 0°, 2°, and 4°. A theoretical FEM analysis taking into account the same variables and parameters was performed in parallel.

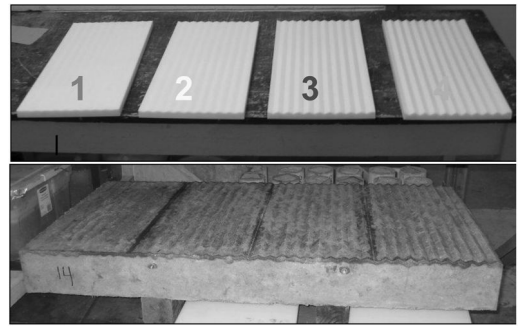

Figure 1. V-shape rippled acrylic dies and resulting profiled slab.

2.3 *Influence of surface preparation: Roughness and mechanical integrity*

In order to cover a sufficiently large spectrum in terms of roughness and, at the same time, assess the most usual surface preparation techniques, the following methods were selected for investigation: sandblasting (SaB), shotblasting (ShB), scarifying (Sc), 100-MPa handheld hydro-jetting (HJ), and 7-kg jack hammering (JH). In addition, to avoid the presence of induced damage and isolate the effect of roughness upon bond strength, an artificially profiled test slab was cast. V-shape rippled acrylic dies were installed at the bottom of the slab form to obtain wave amplitude values of 2, 4, 6 and 8 mm respectively in four adjacent areas along the specimen length, the wavelength being of 30 mm in all of them (see Fig. 1). It should be mentioned that for this artificially profiled slab, tensile bond was determined on cores tested in direct tension.

As part of the test program reported herein, two series of $625 \times 1250 \times 150$-mm concrete slabs (25-MPa and 35-MPa concrete mixtures) were manufactured. The test slabs were exposed to drying until relative dimensional stability was achieved, after what surface preparation was performed. The artificially-profiled slabs (one per slab series) were very lightly sandblasted to remove laitance.

After surface preparation, an evaluation of surface integrity and characterization of surface roughness were performed.

Surface roughness of the concrete substrates was evaluated using *Moiré*-type optical profilometry. The method has the advantage of capturing all the required information at once and storing it into a digital format, allowing a precise and quite exhaustive characterization of the surface profile. The parameter used here to describe surface roughness quantitatively is the average half-amplitude (R_a) of the profile. Complementarily, the resulting slab surface profiles were also appraised in accordance with the *Concrete Surface*

Preparation index (CSP) proposed by the *International Concrete Repair Institute* (ICRI Guideline No. 03732).

Surface integrity of the prepared test slabs was evaluated through pull-off experiments and Schmidt rebound hammer soundings. Seeking a simple and field-friendly way to assess surface integrity prior to repair, *Schmidt hammer* soundings were performed in a systematic fashion on all prepared slabs, using a template grid with regularly-spaced data points collected in the X- and Y- directions over the whole surface. Pull-off tests were performed immediately after the Schmidt soundings, in accordance with the procedure proposed by Courard and Bissonnette (2004).

2.4 *Evaluation of the substrate moisture content*

In this part of the test program, two concrete surface moisture test procedures were investigated, namely the *Initial Surface Absorption* test (ISAT) and a modified version of the *Capillary Suction* test (MCST) (Courard *et al*., 2011). The objective was to correlate the moisture condition of the concrete surface to the water penetration characteristics evaluated through these tests.

A series of test specimens was made with three ordinary Portland cement concrete mixtures (30-MPa, 40-MPa, 50-MPa). The following surface treatments were performed on subsets of specimens from each series: no treatment, sandblasting and waterjetting. The tests specimens were then submitted to eight different moisture conditioning regimens (various storage sequences in air at 50% RH, 85% RH, 100% RH, in water, and/or in an oven at 40°C) to cover the range from 30 to 100% relative humidity (RH). Following moisture content assessment (gravimetric measurements performed on companion specimens), the slabs were finally repaired (75-mm overlay) with a 45-MPa repair concrete. The repaired specimens were moist-cured for 7 days, after what they were air-dried until bond strength tests were carried out.

2.5 *Evaluation of the effect of carbonation on bond*

In this part of the project, a series of eighteen $400 \times 400 \times 100$-mm slabs were cast with a 28-MPa concrete mixture. For half of those slabs, the surface was prepared superficially for repair by sandblasting, while for the other half, a chipping hammer was used. In each group, four slabs were protected from carbonation (control), and five slabs underwent controlled carbonation in a laboratory carbonation chamber. The control slabs were protected with plastic sheet and duct tape to avoid carbonation. Slabs were undergoing carbonation for 75 days and reached a carbonation depth of greater than 3 mm. The carbonated surface of the test slabs was then overlaid with 100 mm thick, 28-MPa concrete. A total of nine pull-off bond tests were performed on each overlaid slab.

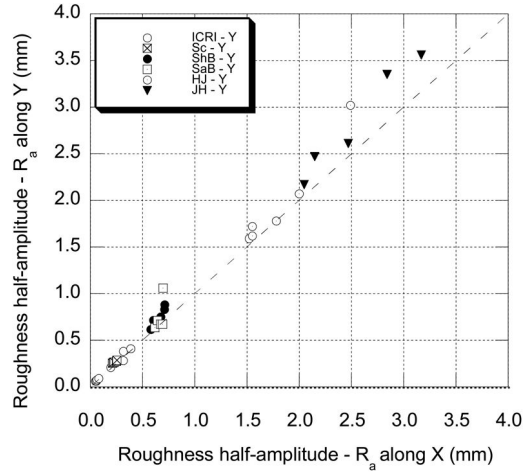

Figure 2. Results of roughness evaluation performed after surface preparation by optical profilometry on both 25- and 35-MPa substrates. (*here and elsewhere in the paper*: Sc: scarifying; ShB: shotblasting; SaB: sandblasting; HJ: hydrojetting; JH: jack hammering).

3 RESULTS AND ANALYSIS

3.1 *Influence of surface preparation*

3.1.1 *Roughness of the substrate*

The surface roughness half-amplitude values (R_a) corresponding to the various surface preparation profiles, as obtained by optical profilometry, are plotted on the graph of Figure 2. The values recorded for the ICRI CSP rubber templates are also displayed on this graph. The largest half-amplitude values (1.50–3.75 mm) were obtained with the jack hammer and hydrojetting, while the lowest values were recorded respectively for the scarified, the shotblasted and the sandblasted surfaces (<1.00 mm). It can also be observed that for all slabs and templates, surface roughness is uniform, with most data points sitting on or close to the equality line.

As shown on the graph of Figure 2, the ICRI CSP plates merely cover the roughness values recorded for scarifying, all other techniques being out of range for the experimental conditions. As convenient a tool as these templates can be, with the existing scale, their use is confined to surface treatment applications where very little material is actually removed.

It must then be emphasized that the *meso*-roughness level, which is directly related to the aggregate size distribution of the substrate concrete, is being considered here. The large waviness observed for instance on hydrojetted and jack hammered surfaces is extracted from the calculation by filtering. Nevertheless, the recorded R_a values suggest that hydrojetting and jack hammering both leave larger exposed aggregates than the other techniques.

3.1.2 *Mechanical integrity of the substrate*

The average cohesion values measured in the substrate pull-off test performed on the various types

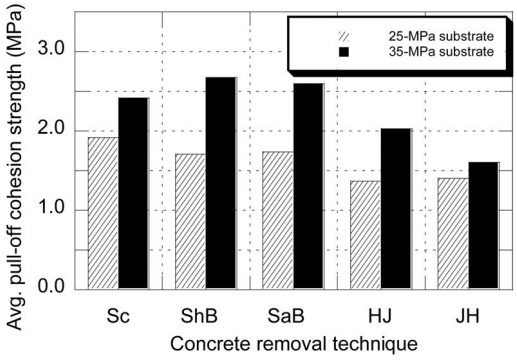

Figure 3. Results of pull-off experiments (CSA A23.2-6B modified) performed after surface preparation to evaluate the mechanical integrity of the exposed concrete surface.

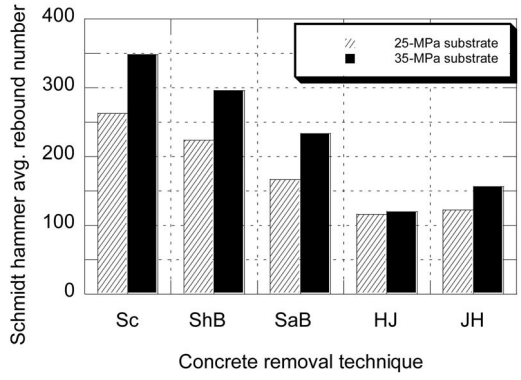

Figure 4. Results of *Schmidt hammer* (ASTM C805) soundings performed after surface preparation to evaluate the mechanical integrity of the exposed concrete surface.

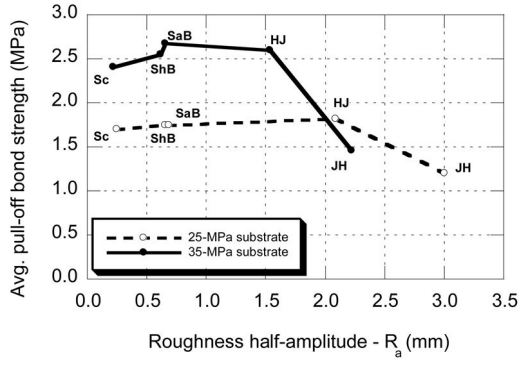

Figure 5. Results of pull-off tests (ASTM C1583) performed after repair on the slabs treated with various surface preparation techniques.

of preparation are summarized in Figure 3. Overall, the comparison of the results obtained with the 25-MPa and 35-MPa substrates respectively is consistent with the mechanical strength test results. It can further be observed that for a given substrate quality, the average cohesion values obtained with sandblasting, shotblasting and scarifying are all close from the corresponding base concrete tensile strength. These substrates were virtually left undamaged by the surface preparation operations. Actually, in most of the tests, failure occurred at the bottom of the core, far from the surface.

In comparison, the average pull-off cohesion values recorded for the jack hammered slabs are significantly lower, especially in the 35-MPa series. This is assumed to be a consequence of surface defects induced by the hammer tip, as reflected by the prevalent number of pull-off specimen failure occurrences near the surface. Such damage induced into the substrate by jack hammers and the various types of impact breakers, generally referred to as bruising, was assessed in a previous study (Bissonnette *et al*., 2006).

In the case of hydro-jetting, the lower recorded cohesion values are most likely not due to damage, as the bond strength test results subsequently show, but rather to a pull-off test bias for that given type of surface profile. Indeed, the waviness created by hydrojetting was particularly important, and although special care was taken to glue the dolly adequately and to ensure proper alignment of the testing device, it could apparently not fully compensate.

The *Schmidt hammer* soundings performed on the slabs right after surface preparation are summarized in Figure 4. As the recorded hammer rebound value is correlated to some degree to the hardness and strength of the material, it is again not surprising to see that irrespective of the surface preparation technique, the average rebound values recorded on the slabs cast with the 35-MPa concrete are systematically higher than those obtained on the 25-MPa substrates. The recorded rebound values show significant variability, as evidenced by the relatively high standard deviation numbers. This had to be expected, given the intrinsic variability of the test and the high irregularity of the tested surface. Nevertheless, the trends exhibited by the average *Schmidt hammer* results for the various investigated surface preparation techniques are somehow similar to those observed for the cohesion test results. It thus appears that except for surfaces with highly pronounced waviness, the *Schmidt hammer* can yield valuable information on the prepared substrate soundness, provided that the number and distribution of soundings are adequate.

3.1.3 *Bond strength evaluation*

The results of the various bond strength tests performed on the experimental slabs are presented in Figures 5 to 7.

Pull-off experiments

Except for the slabs prepared by jack hammering, the pull-off test results (Figure 5) are close to the corresponding substrate splitting-tensile strength values for both the 25-MPa and 35-MPa slab series($f_{st28-d} = 1.9$ and 3.2 MPa respectively). In the 25-MPa slabs, where it is particularly close, failure of the pull-off specimens

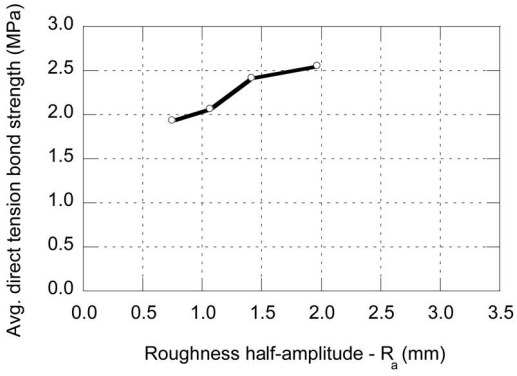

Figure 6. Results of direct tensile tests performed after repair on cores extracted from the artificially profiled 25-MPa slab.

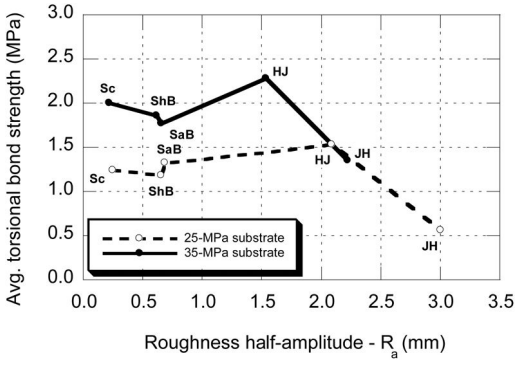

Figure 7. Results of torsional bond experiments performed after repair on the slabs treated with various surface preparation techniques.

occurred systematically in the substrate (except again for the jack hammered slabs).

On jack hammered slabs, even though lightweight hammers (7-kg) were used, the recorded pull-off strength values are significantly lower and most of the time (>90%), failure occurred in the interface area. As for the corresponding weaker superficial cohesion strength values, this has to be attributed to the presence of local defects left on the surface upon completion of the jack hammering operations.

As far as the relationship between pull-off strength and substrate roughness is concerned, it appears that pull-off values slightly increase with the value of R_a, provided that no or limited damage is induced. Where the extent of damage becomes significant, as in the case here of jack hammered slabs, the positive influence of increased roughness is completely offset by the adverse effects of bruising.

As for the pull-off test results, the direct tensile test results obtained with the artificially profiled slab (Fig. 6) show that the average bond strength in tension is increasing with the substrate roughness amplitude. It clearly suggests that in the absence of superficially induced damage, increasing the surface of contact leads to a stronger repair bond.

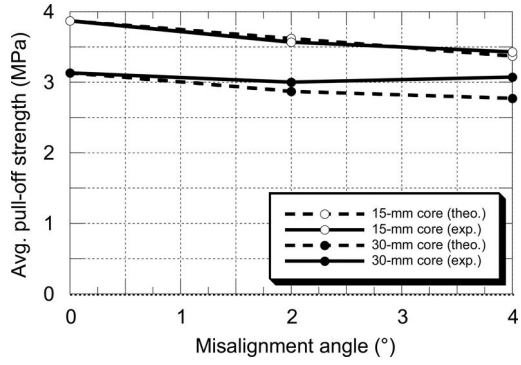

Figure 8. Comparison of predicted and experimental pull-off test results as a function of the misalignment angle.

Torsional experiments

The torsional shear bond test results are presented in Figure 7. Both in terms of magnitude and trends, they show similarity with the pull-off data. Again the substrate strength and the presence of damage are influential parameters. Contrarily to what could have been inferred, roughness does not appear to play a more important role in shear than in tension.

3.2 *Effect of loading misalignment*

The general trends observed in both numerical analysis and experiments reveal that the pull-off strength values decrease as the misalignment angle increases (see Fig. 8). The deeper coring extends into the substrate, the greater is the effect of misalignment.

Up to a certain misalignment limit angle assumed to be detectable by the average human eye (4° in the present study), load and coring misalignments were not found to yield significantly different stress fields and, for practical calculation purposes, they can be addressed in a similar manner. As for the failure mode, it can be concluded that within 4 degrees, testing misalignment does not significantly change the failure mode characteristics.

The simulation results provide a conservative, but realistic, lower bound limit for evaluation of the influence of misalignment on pull-off test results. A 2° misalignment can be expected to yield a pull-off strength reduction of 7 to 9%, respectively, for 15 and 30 mm coring depths, and the corresponding decrease resulting from a 4° misalignment reaches between 13 and 16%.

The experimental pull-off test program results are, overall, consistent with the theoretical calculations, although the observed trends are not as clear, due to the experimental variability and to the added influence of the coring depth.

From a practical standpoint, the results generated in this study indicate that pull-off test misalignment can cause the rejection of repairs with adequate bond

strength. With a number of tests sufficiently large for statistical significance, one could specify a lower acceptance pull-off strength limit in the field – with the mean acceptance value being decreased for example by 5 to 10% – to take into account the bias induced by testing misalignment. Nevertheless, in most cases, the amount of tests performed on site is quite limited and using the specified bond strength value as the field acceptance limit for quality control is conservative.

3.3 *Influence of moisture content*

Both the ISAT (permeability index) and MCST test methods yielded relatively good correlations with the concrete moisture content, especially below 80% RH.

ISAT test results were shown to be insensitive to concrete compressive strength, at least in the range of those tested. The results were influenced by the substrate surface quality, but it is difficult to conclude whether this was due to surface roughness, microcracking, or a combination of both. The relatively high variation and dispersion characterizing the ISAT test results may stem from the difficulty of performing the test on rough concrete surfaces (for instance, after hydrojetting).

The MCST test yielded clearer trends and less dispersed information than the ISAT test, as well as a better correlation with water content measurement (wet and dry weighing measurements).

Satisfactory correlation was also found between the water absorption index and the capillary absorption coefficients determined using both tests.

The influence of the substrate moisture content upon bond strength is illustrated for a polymer-modified repair mortar in Figure 9. Overall, for the repair systems considered in this task, it appears that optimum saturation levels for repair bond strength would lie somewhere between 55 to 90%.

Clearly, additional work is required to identify a methodology that could be used in field applications and, furthermore, to assess more precisely and reliably what the optimum moisture ranges are for cement-based repair materials.

3.4 *Influence of carbonation*

Experimental data on the influence of concrete substrate carbonation upon repair bond strength are presented in Figure 10 for surfaces prepared by sandblasting and jackhammering.

For substrate surfaces prepared by sandblasting, no difference in bond strength was observed between carbonated and non-carbonated concrete substrates. Conversely, for substrates prepared with a concrete breaker, a significant reduction (16%) in bond strength was found for carbonated surfaces as compared to non-carbonated surfaces. Such different effects of carbonation could be attributed to the possible micro-defects (bruising) of the surface prepared by chipping hammer. The limited number of tests performed using only one type of a repair material does not allow for

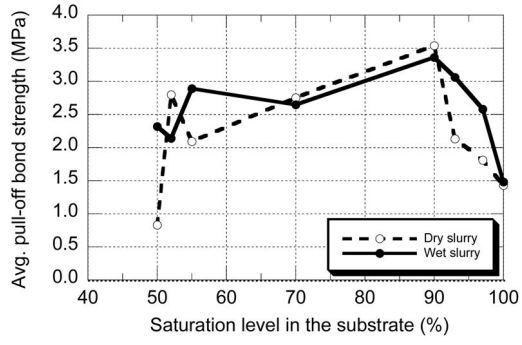

Figure 9. Pull-off test results recorded for a polymer-modified repair mortar cast over concrete substrates at various saturation levels, with dry or wet polymer-modified slurry.

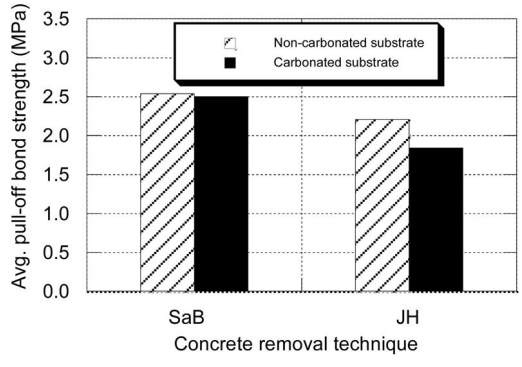

Figure 10. Pull-off test results recorded for test slabs repaired with 28-MPa concrete after different types of surface prepartion, with or without carbonation.

conclusions about the overall effect of carbonation on tensile bond strength. Different repair materials may not necessarily behave the same way in bond development to the carbonated surfaces.

It appears likely, though, that carbonation may have only a slight impact on bond strength for an otherwise sound, properly prepared concrete substrate surface.

4 CONCLUSION

The investigation has generated useful information for the evaluation and characterization of concrete surface preparation prior to repair.

The pull-off test is a convenient method for evaluating both the mechanical integrity of the concrete surface prior to repair and the repair bond strength. A reliable evaluation of these properties can be obtained, provided that a minimum number of tests are performed, with adequate equipment. The potential bias due to testing misalignment, below average naked-eye detection capability, was evaluated to reach up to approximately 15%. Yet, it can only affect the pull-off strength evaluation on the conservative side.

Bond strength of concrete repairs depends on a number of parameters. It has been shown that in the absence of substrate-induced damage, tensile bond strength increases with the substrate coarseness. Still, the most important parameter apparently remains the mechanical integrity of the substrate. In that regard, it must be stressed that the use of impacting methods such as jack hammering leaves significant damage at the surface, which can easily outweigh the benefits of an increased roughness.

Other potentially important parameters upon repair bond development are the substrate moisture conditioning and state of carbonation at the time of casting. The results obtained in the present study show that optimum moisture saturation levels for repair bond strength would lie somewhere between 55 to 90%. Carbonation may in turn have only a slight impact on bond strength for an otherwise sound, properly prepared concrete substrate surface.

Based on the results of the research program reported in this paper, a document entitled *Suggested Guide Specification for Surface Preparation of Concrete Prior to Repair* and intended for repair and overlaying with Portland cement concrete and prepackaged cement-based materials was issued by the U.S. Bureau of Reclamation (Bissonnette *et al*., 2012).

ACKNOWLEDGMENTS

This project has been financially supported by the *Concrete Research Council* of the American Concrete Institute (ACI), the Natural Sciences and Engineering Research Council of Canada (NSERC), the Québec FQRNT Research Fund, the US Bureau of Reclamation (USBR), and the industrial partners of the NSERC *Industrial Chair on Durable Repair and Optimized Maintenance of Concrete Infrastructures* at Laval University (BASF Building Systems, City of Montreal, City of Québec, Euclid, Holcim, Hydro-Québec, Kerneos, King Packaged Materials, Lafarge, Ministry of Transportation of Québec, W.R. Grace & Co.), and through Scientific Cooperation Programs of the Polish, Québec and Wallonia–Brussels governments.

REFERENCES

ASTM C39. 2005. Standard Test Method for Compressive Strength of Cylindrical Concrete Specimens, *Annual Book of ASTM Standards*, *Concrete and aggregates*, vol. 04.02, ASTM, West Conshohocken, PA, USA.

ASTM C469. 2002. Standard Test Method for Static Modulus of Elasticity and Poisson's Ratio of Concrete in Compression, *Annual Book of ASTM Standards, Concrete and aggregates*, vol. 04.02, ASTM, West Conshohocken, PA, USA.

ASTM C496. 2004. Standard Test Method for Splitting Tensile Strength of Cylindrical Concrete Specimens, *Annual Book of ASTM Standards, Concrete and aggregates*, vol. 04.02, ASTM, West Conshohocken, PA, USA.

ASTM C805. 2002. Standard Test Method for Rebound Number of Hardened Concrete, *Annual Book of ASTM Standards, Concrete and aggregates*, vol. 04.02, ASTM, West Conshohocken, PA, USA.

ASTM C1583. 2004. Standard Test Method for Tensile Strength of Concrete Surfaces and the Bond Strength or Tensile Strength of Concrete Repair and Overlay Materials by Direct Tension. Pull-off Method), *Annual Book of ASTM Standards, Concrete and aggregates*, volume 04.02, ASTM, West Conshohocken, PA, USA.

Bissonnette, B.; Courard, L. & Vaysburd, A.M. 2006. Concrete Removal Techniques –Influence on Residual Cracking and Bond Strength, *Concrete International*, **28**(12), pp. 49–55.

Bissonnette, B.; Vaysburd, A.M. & von Fay, K.F. 2012. Best Practices for Preparing Concrete Surfaces Prior to Repairs and Overlays, Report Number MERL 12–17, U.S. Bureau of Reclamation, Denver, CO, USA, 92 p.

Courard, L., 2000. Parametric Study for the Creation of the Interface between Concrete and Repair Products, *Materials and Structures*, **33**(225), pp. 65–72.

Courard, L. & Bissonnette, B.2004. Essai Dérivé de l'Essai d'Adhérence pour la Caractérisation de la Cohésion Superficielle des Supports en Béton dans les Travaux de Réparation : Analyse des Paramètres d'Essai, *Materials and Structures*, **37**(269), pp. 342–350.

Courard, L.; Lenaers, J.F.; Michel, F. & Garbacz, A. 2011. Saturation Level of the Superficial Zone of Concrete and Adhesion of Repair Systems, *Construction and Building Materials*, **25**(5), pp. 2488–2494.

CRD-C164. 1992. Standard Test Method for Direct Tensile Strength of Cylindrical Concrete or Mortar Specimens, U.S. Army Corps of Engineers (WES), Vicksburg, MS, USA.

CSA A23.2-6B. 2000. Method of Test to Determine Adhesion by Tensile Load, *CSA A23.2 Methods of Test for Concrete*, Canadian Standards Association, Rexdale, ON, Canada.

EN 1542:1999. Products and systems for the protection and repair of concrete structures – Test methods – Measurement of bond strength by pull-off, Work Item No. 00104089, European Committee for Standardization, Brussels, Belgium.

ICRI GuidelineNo. 03732. 1997. Selecting and Specifying Concrete Surface Preparation for Sealers, Coatings, and Polymer Overlays, International Concrete Repair Institute, Des Plaines, IL, USA.

This page intentionally left blank

Concrete Solutions – Grantham et al. (Eds)
© 2014 Taylor & Francis Group, London, ISBN 978-1-138-02708-4

Ureolysis and denitrification based microbial strategies for self-healing concrete

Y.C. Ersan[1,2], J.Y. Wang[1,2,3], N. Boon[2] & N. De Belie[1]
[1]*Magnel Laboratory for Concrete Research, Ghent University, Ghent, Belgium*
[2]*Laboratory of Microbial Ecology and Technology (LabMET), Ghent University, Ghent, Belgium*
[3]*The Strategic Initiative Materials (SIM) vzw, Zwijnaarde, Belgium*

ABSTRACT: Ureolysis and denitrification were examined for microbially induced calcium carbonate precipitation and concrete self-healing. In a first set of experiments, the immobilization of *Bacillus sphaericus*, an ureolytic strain, with Diatomaceous Earth (DE) and its crack healing efficiency were investigated. The ureolytic activity of DE immobilized bacteria was found to be much higher than that of non-immobilized bacteria (12–17 g/L urea degradation and 1 g/L urea degradation in 3 days, respectively) in cement slurry. Cracks with a width ranging from 0.15 to 0.17 mm in the specimens containing DE immobilized bacteria were completely healed within 40 days. The specimens having bacteria showed 70% less water absorption than the reference specimens after healing. Denitrifiers (9 unique strains) were selected from soil and exposed to dehydration stress in minimal medium. The capability of denitrifiers to re-activate after dehydration and precipitate $CaCO_3$ in a minimal medium enriched with nitrate (NO_3) and calcium (Ca^{2+}) ions were tested. A calcium carbonate ($CaCO_3$) precipitation yield of 4.8–6.7 g $CaCO_3$/g NO_3 was obtained.

Keywords: self-healing, crack, microbial $CaCO_3$ precipitation, denitrification

1 INTRODUCTION

Most bacteria can mediate the formation of calcium carbonate if given suitable conditions (Boquet et al. 1973). This biogenic carbonate precipitate has been regarded as an environmentally friendly and economical material which has a promising potential for wide engineering applications. One of the potential applications is to heal microcracks in concrete. The idea is that carbonate precipitating bacteria are added into concrete during mixing. When cracks appear, the bacteria in the crack zone will switch from dormant form to active form and then precipitate $CaCO_3$ to heal the cracks.

Bacillus sphaericus is able to precipitate calcium carbonate ($CaCO_3$) in its microenvironment by the decomposition of urea ($CO(NH_2)_2$) into ammonium (NH_4^+) and carbonate (CO_3^{2-}) ions (Dick et al. 2006). The remarkable characteristic of this strain is its high production of carbonate precipitation by the pathway of urea hydrolysis (Wang et al. 2010). This high ureolytic activity is easily controllable for practical application. However, one drawback is that, during urea hydrolysis, the by-product, ammonia, is released, which might cause environmental concerns (Karatas, 2008). Therefore, denitrification which does not produce toxic by-products and can occur under oxygen limited conditions, came into consideration as an alternative mechanism for microbially induced calcium carbonate precipitation (MICP). Denitrification processes are also mentioned to have 2 times higher carbonate yield per mole electron donor (1 mole acetate and 1.6 mole NO_3) than ureolysis (Karatas, 2008). Furthermore, supplementation of nutrients to the concrete environment is an issue for economical and durability related reasons. Since denitrification provides almost 100% utilization of electron donor, it is promising in terms of economical and practical aspects in concrete application. Denitrification has already been investigated to replace bacterial ureolysis in soil reinforcement studies because of similar issues (Karatas 2008, van Paassen et al. 2010).

Yet, concrete is a more extreme territory for bacterial growth and activity, in comparison with soil. Due to the harsh environment in the concrete, immobilization of bacterial cells before addition to concrete is preferable. DE is a natural soft siliceous sediment. It is highly porous, light in weight, and chemically stable and inert. DE has been mainly used as filtration agent and functional fillers for paints and plastics, and filling materials for concrete (Degirmenci & Yilmaz, 2009). It is also a widely used bacterial carrier (Feng et al. 1997; Yoshishige et al. 1999).

In this study, microbially induced calcium carbonate precipitate (MICP) was investigated to heal concrete cracks in-situ. The aim of this study was to use DE as a bacterial carrier to be used in the high-pH concrete environment for self-healing cracks in mortar. Initially, DE immobilized *B. sphaericus* was used for

self-healing mortar specimens: both ureolytic activity and crack healing efficiency were investigated. Afterwards, several denitrifying strains were investigated for the same application.

2 MATERIALS AND METHODS

2.1 *Bacterial strains and cultivation*

2.1.1 *Ureolytic strain*

Bacillus sphaericus LMG 22557 (Belgian coordinated collections of microorganisms, Ghent) was used in this study. It is an alkali-tolerant spore forming strain, with a high urease activity (40 mM urea hydrolyzed.OD-1.h-1), long survival time (Wang et al. 2010) and ability to produce $CaCO_3$ in a controllable way (Dick et al. 2006). *B. sphaericus* was cultivated in a sterile growth medium that consisted of yeast extract (20 g/L) and urea (20 g/L). The cultures were incubated (28°C, 100 rpm) for 24 h. The living cells were harvested by centrifugation (7000 r/min, 7 min,) and were re-suspended in sterile saline solution (NaCl, 8.5 g/L). The obtained bacterial suspension (BS, 10^9 cells/mL) was stored in a 4°C fridge for further use.

2.1.2 *Denitrifiers: isolation, characterization and selection*

The denitrifiers were isolated from soil and further characterized. Sterile M9 mediums each with a specific C-source (methanol or formate) were used. Based on the aim, M9 medium was slightly modified in different experiments. During characterization of isolated strains and investigation of dehydration capability of the strains, buffered and non-buffered M9 mediums were used, respectively. During investigation of $CaCO_3$ precipitation, non-buffered medium was enriched in terms of Ca^{2+} content (2.5 g/L) and phosphate (PO_4-P) concentration was decreased from 20 mg/L to 2 mg/L.

Following characterization and detailed comparison of 9 isolated strains (5 from methanol and 4 from formate added M9 mediums), *Diaphorobacter nitroreducens* and *Pseudomonas aeruginosa* were selected to investigate $CaCO_3$ precipitation.

The batch reactors (200 mL liquid volume, 400 mL headspace) were incubated at 28°C on a 100 rpm shaker for 5 cycles of 3 days each. At the end of each cycle, the reactors were exposed to 70°C for at least 20 minutes (pasteurization). Pasteurization is known to be the most effective method to select endospore forming bacteria from a certain environment (Logan & De Vos, 2011). After pasteurization 90% of the existing solution was replaced with the sterile fresh medium. Then headspaces of the reactors were flushed with argon (Ar) to provide anoxic conditions and the next cycle started. The cyclic operation was repeated 5 times in a row and ended up with 10 isolated strains, 9 of which were unique.

As previously mentioned, selection was focused on the isolation of denitrifiers which are able to form endospores. However, denitrifying strains which were isolated were Gram-negative, non-spore forming strains. Therefore, the resistance of isolated bacterial strains against dehydration was investigated. All the isolated strains were grown in non-buffered M9 medium. Afterwards, each strain was plated on an agar plate having identical composition with the liquid medium and specific C-source (formate or methanol specific to strains), and incubated at 28°C for 3 days. After obtaining bacterial growth, they were incubated at 37°C for 3 weeks (2 weeks for water evaporation and 1 week exposure to starvation and dehydration stress). After that, dry agars were submerged back in 50 mL of liquid medium and investigated under anoxic conditions. NO_3 reduction was monitored for 2 weeks after which the number of bacteria was determined by plate counting.

2.2 *Immobilization of B. sphaericus into/onto diatomaceous earth (DE)*

The DE used in the study had a particle size of $4\ \mu m \sim 20\ \mu m$ with large amount of pores ($0.1\ \mu m$ to $0.5\ \mu m$) on the surface. The bacterial suspension was mixed with sterile DE powders (20%, w/v); the mixture was then put on a shaker (100 rpm, 28°C) for 1h to make bacterial cells attach to the DE surface.

The ureolytic activity of the bacteria after immobilization was examined in urea media (20 g/L urea, 1 g/L yeast extract) with different pH values: pH 7.0, pH 9.0 and pH 12.5. The urea media with pH 7 and pH 9 were obtained by using a 1M NaOH solution to adjust the pH. The urea medium with pH 12.5 was obtained by adding cement powder (CEM I 52.5N, 20 g/L). As a control, the ureolytic activity of the same amount of non-immobilized cells was also investigated.

The ureolytic activity of the bacteria was indicated by the amount of urea decomposed by bacteria, which was determined by the total ammonium nitrogen tested (Ivanov et al. 2005).

2.3 *Investigation of $CaCO_3$ precipitation with denitrifiers in minimal medium*

Based on the results of section 2.1.2 *D. nitroreducens* and *P. aeruginosa* strains were further used to investigate $CaCO_3$ precipitation. The aforementioned Ca^{2+} enriched minimal M9 medium was used for growth of bacteria and further testing of precipitation. An inoculum concentration of 10^7 CFU/mL was set for every strain via correlation between colony forming units (CFU) and optical densities (at 620 nm) (data not shown) and two batches containing sterile minimal M9 medium were inoculated. Dissolved Ca^{2+} and NO_3 concentrations were analyzed. Control experiments were conducted in abiotic conditions in identical medium.

2.4 *Analytical methods*

NO_3 concentrations were measured via compact ion chromotography (IC). N_2 gas production was measured via compact gas chromatograph (GC) equipped with a thermal conductivity detector, a porabond pre-column, and a molsieve SA column.

Table 1. Composition of mortar specimens in each series.

Series	Cement (g)	Sand (g)	Water (g)	DE (g)	BS (mL)	Nutrients (g)
DE	450	1350	225	22.5	0	35
DEBS	450	1350	112.5	22.5	112.5	35

Nutrients included 1.25 g yeast extract, 11.25 g urea and 22.5 g $Ca(NO_3)_2.4H_2O$

Dissolved Ca^{2+} was measured via atomic absorption spectroscopy (AAS).

2.5 *Preparation of mortar specimens with bacterial-based self-healing agents and crack creation*

Two series of mortar specimens (40 mm × 40 mm × 160 mm) were made with a water to cement ratio of 0.5 and a sand to cement (CEM I 52.5N) ratio of 3:1. The composition is shown in Table 1. The group DE are the specimens only added with DE particles and DEBS are the ones with bacteria loaded DE particles.

Six specimens were made in each series. Reinforcement was added to the mortar specimens to control the crack width. A 10 mm mortar layer was first added into the moulds and was compacted by vibration. Subsequently, two reinforcement bars (D = 2 mm, L = 140 mm) were positioned on top of it. Afterwards, the moulds were completely filled with mortar and vibrated. All moulds were put in an air-conditioned room (20°C, 95%RH) for 24h. After demoulding, the mortar specimens were placed in the same air-conditioned room until the test age.

After 14 days, specimens were taken out of the air-conditioned room and were subjected to a three-point bending test to create cracks. Crack width was measured by a linear variable differential transformer (LVDT) which was attached at the bottom of the specimens, as described in Wang et al. (2012a). After the test, one single crack of a width around 0.15 mm to 0.17 mm was created near the center of the specimen. The cracked specimens were then immersed in water or in a deposition medium (DM, made of urea and $Ca(NO_3)_2$, 0.2M) for 40 days (n = 3).

2.6 *Evaluation of self-healing efficiency*

2.6.1 *Crack filling*

After incubation, the specimens were taken out of the immersion solution and were rinsed gently with tap water. Afterwards, they were stored at room temperature for about 3 days to let the surface dry. The crack filling in the surface dry specimens was visualized under a light microscope.

2.6.2 *Capillary water absorption*

After light microscopy analysis, the specimens were subjected to a capillary water absorption test based on RILEM 25 PEM II-6. The specimens were first dried at 40°C until the weight changes were less than 0.1% at 24 h intervals. Afterwards, they were coated with a waterproof paint at four sides adjacent to the bottom surface where the crack existed. Part of the bottom surface was also coated, except for an area of 40 mm × 20 mm around the crack. The coated specimens were weighed and immersed to a depth of 5 ± 1 mm in tap water with the bottom surface facing downwards. At regular time intervals, they were taken out from the water and weighed after wiping the surface with a wet towel (Wang et al. 2012b).

3 RESULTS AND DISCUSSION

3.1 *Ureolytic activity of DE immobilized B. sphaericus*

As shown in Figure 1, both free bacterial cells and immobilized cells showed a high ureolytic activity in neutral pH and moderate alkaline environment, in which about 95% of urea was decomposed. There was no difference in ureolytic activity between non-immobilized and immobilized bacteria. However, the amount of urea decomposed by the free bacterial cells at the pH 12.5 was greatly decreased, from 95% to less than 5%. DE immobilized bacteria kept a higher ureolytic activity than free bacterial cells: about 70% of the urea was decomposed. The values of decomposed urea measured on the 3rd day were slightly lower than the values after 1 day; this might be due to volatilization losses. It can be concluded that DE powders had a profound protective effect on the bacteria particularly in a high pH condition as can be expected in concrete. The DE particles may provide a micro-environment with reduced local pH around the bacteria (Vandamme et al. 1998).

3.2 *Self-healing effect in the specimens with DE immobilized B. sphaericus*

3.2.1 *Crack filling*

The DE specimens had very limited crack healing. Almost no precipitation was formed in the cracks for specimens immersed in water (Fig. 2(a)), while the ones immersed in DM showed a small amount of precipitation in the cracks and on the surface (Fig. 2(b)). But no cracks were completely healed. More crack healing was observed in the DEBS. Cracks in specimens immersed in water were partly healed (Fig. 2(c)); and cracks in the ones in DM were completely healed by the precipitation (Fig. 2(d)). The enhanced crack healing was due to bacterial $CaCO_3$ precipitation. It is noticed that specimens in DM had more precipitation than those in water, due to the additional supply of urea and Ca^{2+} from the DM which allows the bacteria to produce more calcium carbonate. More information can be found in Wang et al. (2012b).

3.2.2 *Capillary water absorption*

The crack healing in the specimens had a big influence on water absorption. As shown in Figure 3, the DEBS specimens with completely healed cracks after

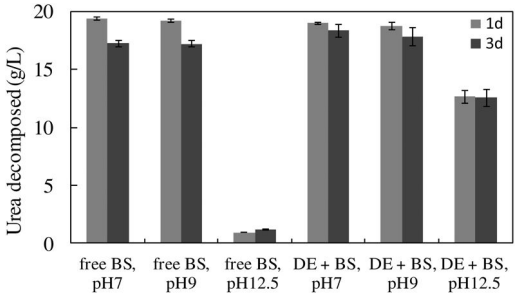

Figure 1. Ureolytic activity of DE immobilized *B. sphaericus* (DE + BS) and non-immobilized *B. sphaericus* (free BS) at different pH conditions.

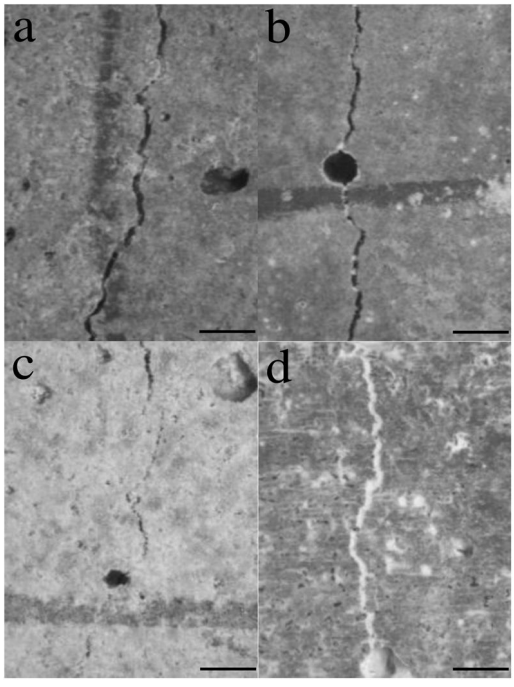

Figure 2. Crack filling in different specimens (a and b: speci-mens DE, immersed in water and in DM, respectively; c and d: specimens DEBS, immersed in water and in DM, respectively. The black bar indicates 1 mm.)

incubation in DM showed the lowest water absorption. The ones, with partly filled cracks after incubation in water, showed more water absorption, but less than the DE specimens. The water absorption for DEBS M and DEBS W was about one-third and fifty percent of that for DE W, respectively.

3.3 *Determination of denitrifier strain activity after dehydration*

As can be seen in Figure 4, after exposing the 9 isolated strains to dehydration and starvation stress for 3 weeks, most of the strains showed still remarkable activity. NO_3 reduction activity was also confirmed

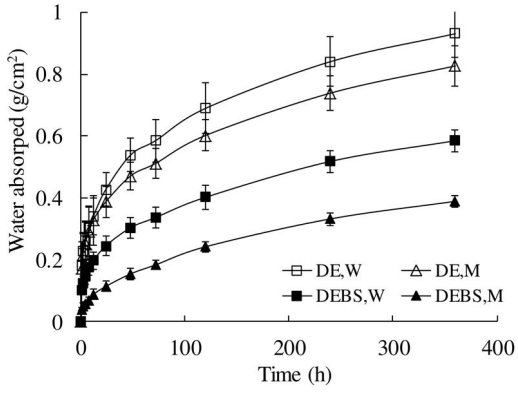

Figure 3. Capillary water absorption of the specimens after crack healing (DE, W and DE, M, DEBS, W and DEBS, M, were the specimens DE and DEBS im-mersed in water and in deposition medium, respectively; The graph is based on Wang et al. 2012b).

Table 2. Viable count results after 2 weeks of re-activation.

C-source			
Methanol		Formate	
Strain*	CFU / mL	Strain	CFU / mL
m1	9.8×10^8	f1	$<10^5$
m2	6.3×10^8	f2	3.5×10^7
m3	1.8×10^8	f3	$<10^5$
m4	2.9×10^8	f5	9.8×10^8
m5	2.7×10^8		

*m: The species cultured by using methanol as carbon source
f: The species cultured by using formate as carbon source.

with production of N_2 gas. Viability count results at the end of experiment are given in Table 2.

It was observed that all the strains isolated by using methanol as the carbon source were active. On the other hand, only two (f2 and f5) of four strains isolated by using formate as carbon source were active.

3.4 *$CaCO_3$ precipitation of denitrifiers in minimal M9 medium*

After comparing the isolated strains and checking their sensitivity to poor conditions (data not shown), *D. nitroreducens* (M5) and *P. aeruginosa* (F2) were selected for $CaCO_3$ precipitation in minimal medium.

Karatas (2008) has claimed that 0.3–2.4 g $CaCO_3$/g NO_3 could be precipitated in 3.5 to 40 days with different types of *Pseudomonas denitrificans*. Van Paassen et al. (2010) found that the rate of precipitation of *Castellaniella denitrificans* was 4.5 g $CaCO_3$/L.d in 10 days. As can be seen in Figure 5, *D. nitroreducens* (M5) reduced NO_3 partially. The precipitation yield for *D. nitroreducens* (M5) was found as ~6.7 g $CaCO_3$/g NO_3 in 18 days. On the other hand, *P. aeruginosa* (F2) consumed all NO_3. The precipitation yield for *P. aeruginosa* (F2) *was* 4.85 g $CaCO_3$/g NO_3 in 18 days.

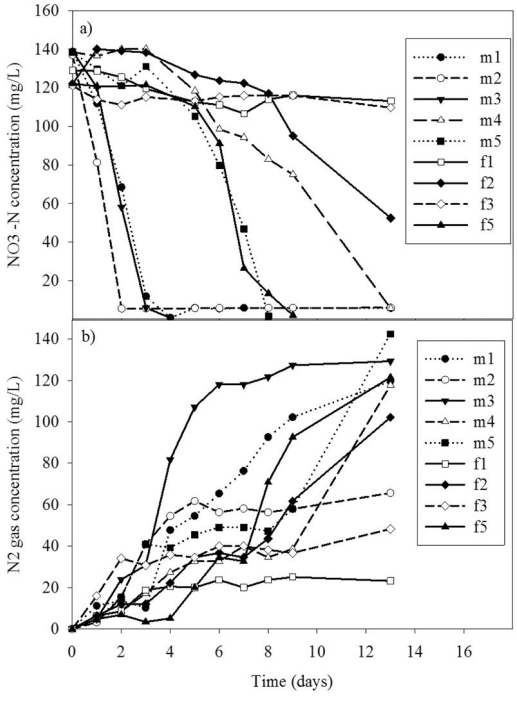

Figure 4. 2 weeks of reactivation after 3 weeks of dehydration (a: NO_3-N reduction b: N2 gas production) (m1, m2, m3, m4, m5: The species cultured by using methanol as carbon source, f1, f2, f3, f5: the species cultured by using formate as carbon source).

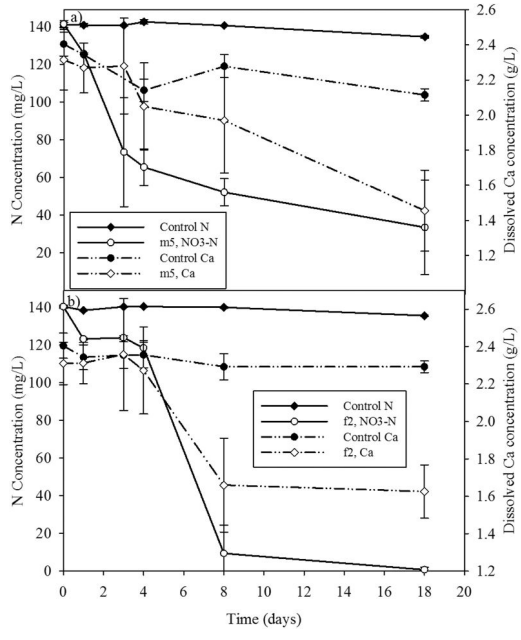

Figure 5. Nitrogen and dissolved Ca^{2+} profiles of strains during $CaCO_3$ precipitation test (a: *D. nitroreducens* (m5) b: *P. aeruginosa* (f2), Control N and Control Ca^{2+} represent abiotic conditions).

If the performances of *D. nitroreducens* (M5) and *P. aeruginosa* (F2) in dehydration/re-activation and precipitation experiments are compared, different behaviours can easily be recognized. As seen in Figure 4, for *D. nitroreducens* all NO_3 was reduced to N_2 gas while for *P. aeruginosa* some NO_3 remained and N_2 production was less.

However, in Figure 5, the NO_3 reduction performances are the other way around. This situation indicates that *D. nitroreducens* was more resistant to dehydration stress than *P. aeruginosa*, but *P. aeruginosa* could perform better than *D. nitroreducens* in presence of Ca^{2+} and limitation of PO_4-P. However, $CaCO_3$ precipitation capabilities of the strains were not affected from this difference and similar Ca^{2+} losses were observed for both strains.

4 CONCLUSIONS

Diatomaceous earth was found to have a protective effect for bacteria in a high pH cement environment. Cracks with a width of 0.15–0.17 mm in mortar specimens were partly or completely filled by the aid of DE immobilized bacteria depending on the immersion media. The more crack healing, the less water absorption. The capillary water absorption in the specimens in bacterial series was about 50% (cracks were partly filled) or 70% (cracks were completely filled) lower than in the ones without bacteria.

D. nitroreducans and *P. aeruginosa* showed remarkable potential for application in concrete by resisting 3 weeks of dehydration stress. Significant amount of $CaCO_3$ (4.85–6.7 g $CaCO_3$/g NO_3 in 18 days) precipitated in minimal medium. Further research on optimization $CaCO_3$ precipitation and in situ activity of these strains in concrete is required.

ACKNOWLEDGEMENTS

Financial support from the Research Foundation Flanders (FWO-Vlaanderen, Project No. G.0190.12) and Ghent University (a BOF grant), as well as the support of the Strategic Initiative Materials Flanders (SIM, program SHE, project SECEMIN) is gratefully acknowledged. The research leading to these results has also received funding from the European Union Seventh Framework Programme [*FP7/2007-2013*] under *grant agreement* n° 290308 (Marie Curie action SHeMat "Training Network for Self-Healing Materials: from Concepts to Market").

REFERENCES

Boquet, E., Boronat, A., Ramos-Cormenzana, A. 1973. Production of calcite (calcium carbonate) crystals by soil bacteria is a general phenomenon. *Nature,* 246: 527–529.

Degirmenci, N. & Yilmaz, A. 2009. Use of diatomite as partial replacement for Portland cement in cement mortars. *Construction and Building Materials* 23: 284–288.

Dick, J., De Windt, W., De Graef, B., Saveyn, H., Van Der Meeren, P., De Belie, N., Verstraete, W. 2006. Bio-deposition of a calcium carbonate layer on degraded limestone by *Bacillus species*. *Biodegradation* 17:357–367.

Feng, Y., Racke, K.D, Bollag, J.M. 1997. Use of immobilized bacteria to treat industrial wastewater containing a chlorinated pyridinol. *Applied Microbiology and Biotechnology* 47:73–77.

Ivanov, V.M., Figurovskaya, V.N., Barbalat, Y.A., Ershova, N.I. 2005. Chromaticity characteristics of $NH_2Hg_2I_3$ and I_2:molecular Iodine as a test form alternative to Nessler's reagent. *Journal of Analytical Chemistry* 60(7):707–710.

Karatas, I. 2008. Microbiological improvement of the physical properties of soil. PhD Thesis, Arizona State University.

Logan, N. A., De Vos, P. (Eds.), 2011. *Endospore-forming Soil Bacteria: Soil Biology* 75–77 Vol. 27, Berlin-Heidelberg: Springer-Verlag.

Van Paassen, L.A., Daza, C.M., Staal, M., Sorokin, D.Y., van der Zon, W., van Loosdrecht, M.C.M. 2010. Potential soil reinforcement by biological denitrification, *Ecological Engineering*, 168–175.

Vandamme, E.J, De Baets, S., Vanbaelen, A., Joris, K., De Wulf, P. 1998. Improved production of bacterial cellulose and its application potential. *Polymer Degradation and Stability* 59:93–99.

Wang, J.Y., Van Tittelboom, K., De Belie, N., Verstraete, W. 2010. Potential of applying bacteria to heal cracks in concrete. *Proceedings of the second international conference on sustainable construction materials and technologies,* 1807–1818, Italy, Ancona.

Wang, J.Y., Van Tittelboom, K., De Belie, N., Verstratete, W. 2012a. Use of silica gel or polyurethane immobilized bacteria for self-healing concrete, *Construction and Building Materials* 26: 532–540.

Wang, J.Y., De Belie, N., Verstratete, W. 2012b. Diatomaceous earth as a protective vehicle for bacteria applied for self-healing concrete. *Journal of Industrial Microbiology and Biotechnology* 39: 567–577.

Yoshishige, K., Koichi, S., Chihiro, I., Tadashi, C. 1999. Enhancement of the specific growth rate of *Thiobacillus ferrooxidans* by diatomaceous earth. *Journal of Bioscience and Bioengeering* 88(4):374–379.

Concrete Solutions – Grantham et al. (Eds)
© 2014 Taylor & Francis Group, London, ISBN 978-1-138-02708-4

Self-healing of dynamic concrete cracks using polymer precursors as encapsulated healing agents

J. Feiteira, E. Gruyaert & N. De Belie
Magnel Laboratory for Concrete Research, Department of Structural Engineering, Faculty of Engineering and Architecture, Ghent University, Belgium

ABSTRACT: Self-healing concrete aims at the autonomous healing of small cracks, with widths in the order of a few hundreds of micrometers. While the existing research on this topic, based on several different healing agents and mechanisms, focuses mainly on the self-healing of early age cracks, this study aims at assessing the strain capacity of polymers used as healing materials for dynamic cracks and the viability of using their respective polymer precursors as encapsulated healing agents. Loading tests were performed on cracked, healed mortar specimens, along with the acquisition of microscopic images and capillary water absorption tests. The series of tests allowed the identification of healing agents with good flowing properties that resulted in efficient bridging and sealing of cracks and determining the strain capacity of healed cracks, which was shown to be at best between 50% and 100% of its initial width.

1 INTRODUCTION

Cracking of reinforced concrete structures is unavoidable and 300 μm wide cracks are generally regarded as acceptable (CEN 2004a). However, these microcracks influence the durability of reinforced concrete structures in the long-term. Unexpected cracking can also occur due to human error during production and placing of concrete or during the lifetime of the concrete structure. It is thus expected that concrete structures undergo repair works at some point to extend their service life. Autonomous self-healing concrete could thus offer an efficient alternative to traditional repair techniques, which can represent a significant cost to the owner or be very difficult to perform due to limited accessibility.

Self-healing is a process that occurs in natural materials such as wood or skin. In concrete, it also occurs naturally (autogenous self-healing), but it is a continuous and long process only occurring in very specific conditions and for a very limited range of crack widths. To introduce an efficient self-healing capability in concrete, different self-healing technologies have been studied. These are based either on promoting autogenous self-healing, e.g. by adding fibres and superabsorbent polymers (Snoeck et al. 2012) or supplementary cementing materials (Van Tittelboom et al. 2012), or on the addition of healing agents, e.g. Calcite ($CaCO_3$) precipitating bacteria (Wang et al. 2012) or polyurethane foams (Van Tittelboom et al. 2011).

However, cracks in concrete structures are often dynamic and the rigid or semi-rigid nature of the healing agents previously studied may not be compatible with crack movements. Thus, this study uses encapsulated precursors of elastic polymers to assess their suitability as healing agents for dynamic cracks.

2 MATERIALS

2.1 *Polymer precursors*

To assure compatibility with the healing of dynamic cracks, minimum requirements were set for the selection process of commercially available products: minimum shelf life of 6 months to guarantee that the agent remains available inside the capsules for a reasonable amount of time; a maximum viscosity of approximately 500 mPas (also depending on the reaction time) to allow the agent to flow inside the crack due to capillary forces; elongation of at least 100% and good adhesion of the cured polymer to concrete.

The most relevant properties of the chosen products (sourced from their respective technical sheets) are listed in Table 1, along with their adopted designations. All of the chosen products are polyurethane-based and rely on moisture curing to form a closed-cell foam. LV and SLV exhibit limited foaming, while FOAM shows a strong foaming effect and expansive behaviour when in contact with moisture, which can aid the complete filling of the crack.

The precursors can be combined with water to improve their reaction and although there is also the possibility of using an accelerator, this was not tested in the further described experimental work.

Table 1. Properties of commercial precursors.

Precursor	Viscosity 25°C, mPas	Reaction start at 25°C, minutes	Elongation %
LV	550	65[a]	100
SLV	200	60[a]	100
FOAM	290	<1[b]	160

[a]Combined with 2% of accelerator.
[b]Combined 1:1 with water.
n/a – Not available in the technical sheet.

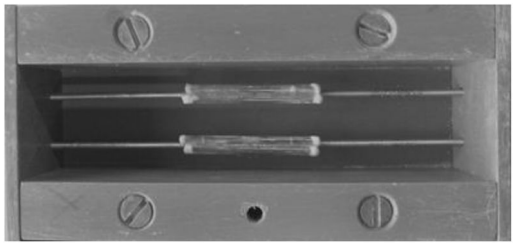

Figure 1. Mould showing the reinforcement bars and attached capsules before pouring of mortar.

3 CAPSULES

To assess their performance, polymer precursors were encapsulated in Ø3 mm glass tubes cut to a 50 mm length and sealed with Poly(methyl methacrylate) glue.

4 PROCEDURE

4.1 *Specimen preparation*

A pair of glass capsules was attached to each of two Ø3 mm threaded steel bars used as reinforcement for $40 \times 40 \times 160\,mm^3$ mortar prisms, as shown in Figure 1. For each pair of capsules, one capsule was filled with healing agent, while the other one was filled with water.

The mortar mix design consisted of cement CEM I 52.5 N, 0/4 mm sand, a cement to sand ratio of 1:3 and a water to cement ratio of 0.5. Mixing and moulding were carried out according to the procedure described in EN 196-1 and the specimens were cured in sealed conditions at 20°C for 7 days. For each series, 3 specimens were prepared.

4.2 *Cracking and mechanical loading*

The reinforced specimens were loaded in displacement-controlled 3-point bending tests in such a way that the capsules broke and a crack approximately 300 μm wide remained after unloading. After a period of 3 days, to allow the healing agent to flow and polymerize, mortar specimens with a single healed crack were tested.

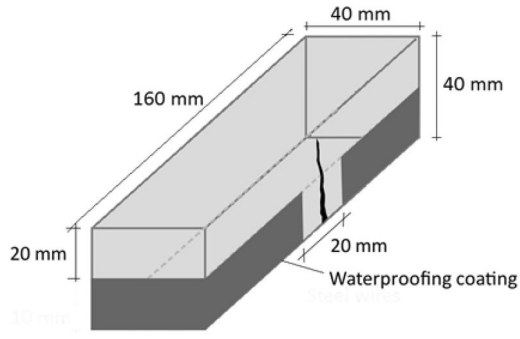

Figure 2. Specimen configuration for capillary water absorption tests.

The specimens were reloaded in different steps, so that the healed crack got increasingly larger with each step and the elastic polymer bridging the crack faces was stretched to 50%, 100% and 150% of the initial crack width. Before reloading and after each stepwise increase of crack width, images of the crack were acquired with a stereo microscope equipped with a digital camera and the specimens were subjected to a capillary water absorption test. This way, it was possible to assess the efficiency of the healing process and the strain capacity of the polymer bridging the crack.

4.3 *Capillary water absorption test*

The test procedure was based on the method described in EN 13057 and consisted of bringing the cracked face of the samples into contact with water and monitoring the mass of water uptake due to capillary absorption. Before performing the test, the specimens were partially waterproofed with liquid-applied epoxy, to maximize the influence of the crack on the total amount of water uptake. The waterproofing coating thus partially covered the side surfaces of the specimen and all of the bottom surface exposed to water, except for a section of $20 \times 40\,mm^2$ centered on the cracked section, as shown in Figure 2. The water level in the container did not exceed by more than 2 mm the bottom surface of the specimens. After the start of the water absorption test, the specimens were weighed frequently for a period of 8 h (at 15 min, 30 min, 1 h, 2 h, 4 h, 6 h, 8 h), following the removal of the excess of water on their surfaces with absorbing paper. After each absorption test, the specimens were dried in an oven at 50°C so that the amount of water absorbed during the test was lost, to within an error of 10%. Complete drying to constant mass was not performed to avoid damage to the polymers due to prolonged exposure to high temperatures. Additionally, complete drying was not considered strictly necessary, as small differences in the humidity level of the mortar matrix are expected to have a small influence on the results compared to the water uptake in the crack itself.

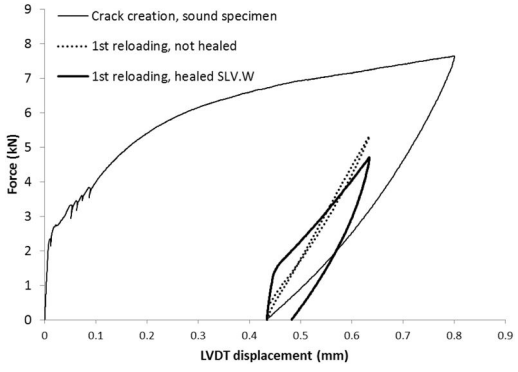

Figure 3. Stiffness regain during 1st reloading as a result of a healing action.

5 RESULTS

5.1 *Performance assessment of healing agents*

The polymer precursors listed in Table 1 were encapsulated as described in §3.1, and subjected to the performance assessment methods. The designation "W" was added after the precursor designation to indicate the use of additional water.

The first sign of a healing action appears during the first reloading cycle in the form of stiffness regain during bending. As shown in Figure 3, a specimen with a healed crack will normally exhibit higher stiffness when reloaded for the first time and compared to a cracked, not healed specimen, but still lower than the stiffness of a sound specimen. However, it should be said that a cracked specimen healed with a very flexible polymer (stiffness much lower than that of mortar) would show no significant stiffness regain even in case of a very successful healing, where the healing agent had flowed to fill the crack completely. Stiffness regain was determined as a percentage in a scale where 0% means no regain (comparable to a cracked, not healed specimen) and 100% means a strength regain leading to a full recovery of stiffness to the level of a sound specimen.

From the different series tested, only SLV.W showed stiffness regain (30%). This suggested that for all other series, either the polymers had very low stiffness or no significant crack bridging occurred, which could be due to very limited flowing of the healing agent inside the crack, premature failure of the polymer bridging the crack, or of the interface between polymer and crack wall.

Figure 4 shows microscopic images of a crack section from series SLV.W, acquired after healing and after each reloading cycle, where the healed crack width was progressively increased stepwise by 50% and 100% relative to the original crack width. It is shown that for this series, failure occurred between 50% and 100% of crack width increase, due to detachment of the polymer from the crack walls. A similar semi-quantitative assessment of strain capacity was carried out for the remaining series and the full results are presented in

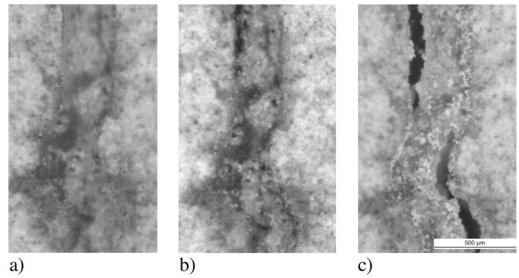

Figure 4. Section of healed $\sim$300 μm wide crack from series SLV.W: a) healed; b) after 50% width increase; c) after 100% width increase.

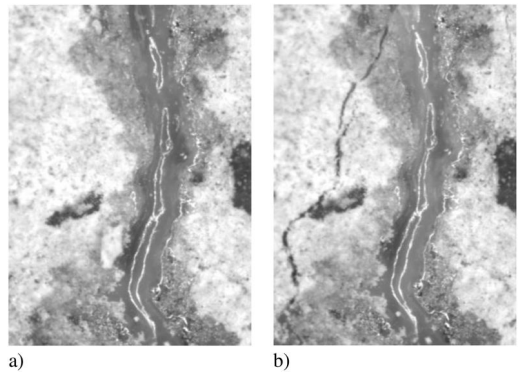

Figure 5. Section of $\sim$300 μm wide crack healed with a semi-rigid polymer: a) healed; b) after reloading.

Table 2 at the end of the section. For the series LV.W and FOAM.W, failure occurred at an elongation lower than 50%, due to detachment or failure in the polymer matrix respectively. Figure 3 shows that after unloading of the specimens in the reloading cycle, the crack returns almost to its original width. However, the little plastic deformation remaining is still enough to allow detection of failure in microscopic images of crack sections, as Figure 4 shows. As to illustrate the motivation behind this study, Figure 5 shows what happens when a cracked specimen healed with a semi-rigid (non-elastic) polymer is reloaded. It can be seen that due to the high stiffness of the polymer bridging the crack, the attempt to increase the crack width by just 50% results in a new crack in the vicinity of the healed one, probably in an area where the mortar matrix already had micro-damage due to the previous loading.

An additional way of assessing the strain capacity of the polymers bridging the cracks was through determination of capillary sorption coefficients, again after healing and after each reloading cycle. In these tests, the sorption coefficient of a specimen where efficient healing occurred (i.e. the polymer precursor successfully flowed to fill the crack completely) would be significantly lower than that of a cracked, not healed specimen and similar to that of a sound specimen. Figure 6 shows the results. In this figure, only the

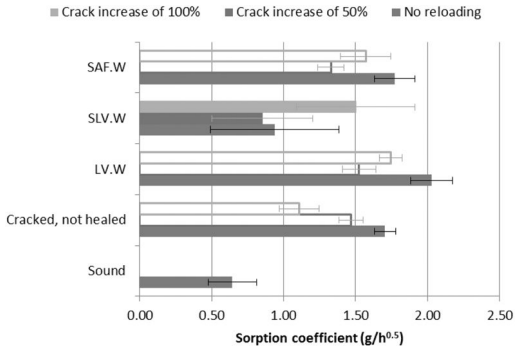

Figure 6. Capillary sorption coefficient of mortar specimens after reloading and widening of healed cracks.

columns showing relevant results are shaded. For the series already with a high sorption coefficient (same level as cracked, not healed specimens) before any reloading took place, the columns showing results after reloading are not shaded, as they are not relevant. In such a case, where there was no significant healing action and resulting sealing effect, the sorption coefficient may even decrease after reloading of the specimens, as a larger crack width increases the size of capillaries and thus reduces capillary forces. This can be clearly seen in the results of cracked, not healed specimens.

As in the loading tests that included stiffness analysis, the absorption tests also showed that only for the SLV.W series was there a significant healing action, which resulted in efficient sealing of the crack. This sealing effect remained even after the specimens were reloaded to achieve a crack width increase of 50%. After a crack width increase of 100% though, the sorption coefficient increased significantly to the level of a cracked, not healed specimen. This way, it was possible to have an additional semi-quantitative assessment of the strain capacity of this polymer, which lies between 50% and 100%, agreeing with the results from the analysis of microscopic images. For the same SLV.W series, it is also shown that the standard deviation is large. This was due to the fact that 2 out of the 3 specimens exhibited a very successful healing and sealing effect, with water absorption similar to that of a sound specimen, while the remaining specimen had a significantly higher water absorption.

For the remaining series, the results suggested that no significant sealing effect occurred, as their sorption coefficient was at the same level as that of cracked, not healed specimens, even though crack bridging was always observed at some sections of the cracks during microscopic analysis. As no significant sealing was observed before reloading and crack width increase, it was not possible to determine the strain capacity of the healed cracks for these series. The full assessment is shown in the summary of results of Table 2.

Due to very little availability of long term crack monitoring data of field concrete structures, there is no clear indication of what should be the target strain

Table 2. Summary of results of the performance assessment of healing agents.

		Strain capacity	
Series	Stiffness regain %	Microscope, %	Absorption, %
LV.W	0	[0, 50]	n/a
SLV.W	30	[50, 100]	[50, 100]
FOAM.W	0	[0, 50]	n/a

n/a – Not available, as the tests are not conclusive for the series.

capacity for healed cracks. However, a 100% elongation seems to be a reasonable performance requirement for polymers bridging dynamic cracks in the context of self-healing concrete, considering that cracks are expected to double their width in the long term due to fatigue caused by cyclic loading (ACI 2001). On the other hand, a 10% elongation has been set elsewhere as a requirement for injection products used for the repair of dynamic cracks (CEN 2004b). It is, however, reasonable to assume that in the context of crack repair, part of the crack width increase due to fatigue has already taken place.

Thus far, the performance results of the SLV precursor suggest that it may be successfully used as a healing agent for dynamic cracks in concrete. However, to confirm if its performance is adequate, better target requirements need to be established and fatigue tests will be performed in the future, where healed mortar specimens are loaded and unloaded continuously for a high number of cycles.

6 CONCLUSIONS

The series of tests designed and performed allowed assessing successfully the basic performance parameters and fitness of polymer precursors as encapsulated healing agents for dynamic cracks in self-healing concrete.

The healing agent designated SLV exhibits the best performance and the most promising fitness for the intended application, even though no clear performance requirements are available. Evidence was shown in the 30% stiffness increase of cracks healed with the SLV precursor compared to a non-healed crack, suggesting significant crack bridging, and in the low capillary water absorption through the healed crack. The latter suggested good flowing properties of the healing agent inside the crack, most probably due to its low viscosity, that resulted in efficient sealing. Microscopic images and additional capillary water absorption tests after stepwise increase of the width of healed cracks showed a strain capacity between 50% and 100%, with failure occurring at the interface between polymer and crack wall.

For the remaining precursors tested, no stiffness increase or sealing effect were observed, suggesting

limited flowing of the healing agent inside the crack. The strain capacity was limited to below 50%, either due to failure at the interface or in the polymer matrix.

ACKNOWLEDGEMENT

The research leading to these results has received funding from the European Union Seventh Framework Programme (FP7/2007-2013) under grant agreement n° 309451 (HEALCON).

REFERENCES

ACI 2001. *224R-01: Control of Cracking in Concrete Structures*. Farmington Hills: ACI.

CEN 2004a. *Eurocode 2. Design of concrete structures – Part 1-1: General rules and rules for buildings*. Belgium: Brussels.

CEN 2004b. *EN 1504-5. Products and systems for the protection and repair of concrete structures – Definitions, requirements, quality control and evaluation of conformity – Part 5: Concrete injection*. Belgium: Brussels.

Snoeck, D.; Van Tittelboom, K.; Steuperaert, S.; Dubruel, P. & De Belie, N. 2012. Self-healing cementitious materials by the combination of microfibres and superabsorbent polymers. *Journal of Intelligent Material Systems and Structures* 25(1): 13–24.

Van Tittelboom, K.; De Belie, N.; Van Loo, D. & Jacobs, P. 2011. Self-healing efficiency of cementitious materials containing tubular capsules filled with healing agent. *Cement & Concrete Composites* 33(4): 497–505.

Van Tittelboom, K.; Gruyaert, E.; Rahier, H. & De Belie, N. 2012. Influence of mix composition on the extent of autogenous crack healing by continued hydration or calcium carbonate formation. *Construction and Building Materials* 37: 349–359.

Wang, J.; Van Tittelboom, K.; De Belie, N. & Verstraete, W. 2012. Use of silica gel or polyurethane immobilized bacteria for self-healing concrete. *Construction and Building Materials* 26: 532–540.

This page intentionally left blank

Concrete Solutions – Grantham et al. (Eds)
© 2014 Taylor & Francis Group, London, ISBN 978-1-138-02708-4

Patch repair: Compatibility issues

A. Garbacz
DBME, Faculty of Civil Engineering, Warsaw University of Technology, Poland

L. Courard
GeMMe Building Materials, ArGEnCo Department, University of Liège, Belgique

B. Bissonnette
CRIB, Civil Engineering Department, Laval University, Québec (QC), Canada

W. Głodkowska
Faculty of Civil and Environmental Engineering, Koszalin University of Technology, Poland

A. Vaysburd
Vaycon Consulting, Baltimore, MD, USA

ABSTRACT: Repair of any concrete structure results in formation of complex, at least two-component repair systems. Compatibility approach is treated as a basic requirement during selection of repair material. Recently, the understanding for compatibility requirements in repair systems approach has been demonstrated in many papers. The aim of this paper is analyzing the compatibility between repair materials and the concrete substrate in the case of patch repair. The compatibility issues were discussed in the light of the various requirements which determine the mathematical space of loads, including chemical, mechanical and other physical (mainly thermal) loads. N-dimensional compatibility space is created, taking into account selected patch material control parameters. The requirements for good compatibility between repair material and concrete substrate can be formulated by using mathematical inequalities, where the variables are the material control parameters. The effects of properties of the both repair material and concrete substrate were analyzed using the computer system ANCOMP developed at Warsaw University of Technology. Usability of this approach was demonstrated using a selected case study as an example.

1 INTRODUCTION

Compatibility is considered as a basic rule for selection of materials for repair of concrete structure (Vaysburd 2006). The compatibility concept has been formulated in the early nineties (Czarnecki et al. 1992; Emmons & Vaysburd 1992). It covers four types of compatibilities (Emmons et al. 1993, Morgan 1996):

- Dimensional (E modulus, creep, shrinkage, thermal dilatation, geometry of sections),
- Permeability,
- Chemical,
- Electrochemical.

Recently, the understanding for compatibility requirements in repair systems has been demonstrated in many papers (eg. Czarnecki et al. 2000, Courard & Bissonnette 2007, Schueremans et al. 2011). So far the compatibility was in practice dealt with intuitively. This approach can be found in the new European Standard EN 1504, where the general requirement for repair was formulated as: "the achievement of the compatibility of the original concrete and reinforcement with the protection or repair products and systems and compatibility between any different products and systems, including avoiding the risk of creating conditions which may cause corrosion".

A similar requirement can be found in the ACI Concrete Repair Manual (2003): "It is also important that the repair material has mechanical properties compatible with those of the substrate concrete to ensure that the materials will act as one and no material failure will occur". Additionally some rules for selection of repair materials are formulated: "If some properties of the repair material are greatly different from those of the substrate concrete, such as the coefficient of thermal expansion, other properties should compensate for these differences for the repair to perform successfully; for example, a lower modulus of elasticity to reduce thermal stresses".

In this paper a compatibility model for patch repair is discussed. This model allows us to determine if a

Table 1. Properties of repair material and concrete substrate used in a compatibility model of patch repair.

Material property:	Repair material	Concrete substrate
Tensile strength [MPa]	f_{tp}	f_{tc}
Modulus of elasticity (in tension) [MPa]	E_{tp}	E_{tc}
Modulus of elasticity (in compression) [MPa]	E_{cp}	E_{cc}
Coeff. of thermal expansion [1/K]	α_{Tp}	α_{Tc}
Coeff. of thermal conductivity [W/mK]	λ_{Tp}	λ_{Tc}
Elongation at break [mm / mm]	ε_{tp}	–
Curing shrinkage [mm/mm]	ε_s	–
Poisson coefficient [–]	ν_p	–
Layer thickness [mm]	h_p	–
Interlayer adhesion [MPa]	$f_{Ao}^{pi/(pi+1)}$	–
Max. crack width at coating failure [mm]	w_{max}	–
Crack width [mm]	–	w_d
Crack width change [mm]	–	Δw
Adhesion to the substrate in shear [MPa]		f_{As}
Adhesion to the substrate in tensile [MPa]		f_{Ao}
Temperature gradient during service [K]		ΔT

selected repair material is able to "cooperate" well with the repaired concrete substrate in given conditions.

2 GENERAL APPROACH TO THE COMPATIBILITY SPACE MODEL

Material serviceability in construction is considered in light of the various requirements as defined by environmental service condition. These requirements determine the mathematical space of loads, including chemical, mechanical and other physical (mainly thermal) loads. N-dimensional compatibility space is created taking into account selected material control parameters.

Czarnecki et al. (1992) and Głodkowska (1994) have formulated three main compatibility models for: injection, patch repair and protective coating. Every model consists of a number of inequalities defining good compatibility requirements for selected repair systems. The material parameters proposed for evaluation of material compatibility for patch repair are presented in Table 1.

The requirements for good compatibility between repair material and concrete substrate are formulated using mathematical inequalities (see Table 2), where the variables are the material control parameters. The range of values for these parameters should be defined for the given repair type and the compatibility should be calculated over the whole domain of variability of the material control parameters. The range of material parameter values usually corresponds to that of existing repair materials. However, the compatibility space can be also determined for a "virtual" repair material, which may not exist yet. It means that the compatibility

Table 2. Compatibility requirements for patch repair.

Compatibility requirements	Remarks
$f_{tp}(t_o) \geq f_{tcm}(t_o)$ $f_{Ao}(t_o) \geq f_{tcm}(t_o)$, $f_{As}(t_o) \geq f_{tcm}(t_o)$	$f_{tcm}(t_0)$ can be exchanged by eg. EN 1504 requirements: - 2.0 MPa (R4) or 1.5 MPa (R3) for structural repair - 0.8MPa (R2) for surface repair
$f_{tp_i}(t_o) \geq f_{As}^{p_i/(p_i+1)}(t_o)$, $f_{As}^{p_i/(p_i+1)}(t_o) \geq f_{tcm}(t_o)$	For multi-layer systems
$f_{As}(t_o) \geq C$ and $f_{Ao}(t_o) \geq C$, where $C = \frac{\left(\varepsilon_{tp}(t_o)\cdot k_s - \frac{f_{tcm}(t_o)}{E_{tcm}(t_o)}\right) E_{tp}(t_o)\cdot E_{tcm}(t_o)}{E_{tp}(t_o)+E_{tcm}(t_o)}$	
$f_{As}(t_o) \geq D\cdot\Delta T$ and $f_{Ao}(t_o) \geq D\cdot\Delta T$, where $D = \frac{(\alpha_{Tp}-\alpha_{Tc})E_{tp}(t_o)\cdot E_{tcm}(t_o)}{E_{tp}(t_o)+E_{tcm}(t_o)}$	
$\frac{\lambda_{Tc}}{\lambda_{Tp}} < \frac{E_{tcm}(t_o)\cdot\alpha_{Tc}}{D}$,	For large-area repair; D as above
$\alpha_{Tp}\cdot E_{tp}(t_o) \leq 0{,}13\cdot\ln(\frac{f_{c,cube}^{G}}{2{,}44})$	For polymeric materials only
$f_{tp}(t_o) \geq \frac{\psi_p\cdot E_{cp}(t_o)\cdot\varepsilon_s(t,t_o)}{(1-\nu_p)}$, $f_{Ao}(t_o) \geq \frac{\psi_p\cdot E_{cp}(t_o)\cdot\varepsilon_s(t,t_o)}{(1-\nu_p)}$, $f_{As}(t_o) \geq \frac{\psi_p\cdot E_{cp}(t_o)\cdot\varepsilon_s(t,t_o)}{(1-\nu_p)}$, $f_{As}^{pi/(pi+1)}(t_o) \geq \frac{\psi_p\cdot E_{cp}(t_o)\cdot\varepsilon_s(t,t_o)}{(1-\nu_p)}$	ψ_p- coeff. takes into account the inelastic part of the final shrinkage strain hardening composites PC and PCC; eg. ψ_p= 0.3 for polymer mortar

approach can be also used for designing new materials that result in a repair that has a proper equilibrium among reliability, durability and economy.

When a protective coating is used the compatibility between coating and substrate as well as repaired mortar should be also evaluated. In this case, besides the requirements given in Table 2, additional requirements towards a crack-bridging ability are particularly important. The requirements for crack-bridging ability are given in the standard EN1504-2. For determination of compatibility space for protective coating the requirements presented in Table 3 were used (Głodkowska 2003).

The mathematical inequalities are formulated using simplifying assumptions so that the compatibility model is sufficiently accurate yet simple enough to use. In the case of polymer repair materials, the common simplifying assumptions include: validity of elastic behavior for repair material, lack of synergistic effects of various loads, and service conditions below

Table 3. Requirements defining crack-bridging ability (Głodkowska 2003).

Coating Type	Requirements for crack-bridging ability
High f_{tp} Low ε_{tp}, eg. epoxy coating	$\alpha \cdot [(2l_v \cdot \varepsilon_{tp}(t_o)) + (\frac{f_{tc} \cdot l_v^2}{2h_p \cdot E_{tp}(t_o)})] \geq w_d + \Delta w$ where: $l_v = \frac{f_{tp}(t_o) \cdot h_p}{f_{tc}}$ $\alpha = \frac{h_p}{w_{\max}} \cdot \frac{f_{tp}(t_o)}{E_{tp}(t_o)}$
Low f_{tp} High ε_{tp} Low E_{tp} eg. polymer –cement coating	$\alpha \cdot h_p \geq w_d + \Delta w$ α – as above

the glass transition temperature of the polymers used. The concrete substrate is assumed to be given and the proper repair system has to be selected for the given substrate and service loads.

The concept of compatibility was successfully applied in further research projects (eg. Czarnecki et al. 2004, Głodkowska 2003, Garbacz & Głodkowska 2012). Based on a large experimental program Głodkowska has proposed modifications of compatibility requirements taking into account long-term loads (Głodkowska 2011) as well as effect of coating weathering (Głodkowska & Staszewski 2007). The possibility of application of this approach for strengthening systems was showed by Garbacz et al. (2000). Recently, a basic challenge for improvement of compatibility estimation accuracy is the development of compatibility measures to take into account variability in technical properties of the both repair material and concrete substrate (Czarnecki & Runkiewicz 2005).

3 DETERMINATION OF COMPATIBILITY SPACE

The models of compatibility space of repair material and concrete substrate, presented in section 2, are mathematically described by the set of suitable N-linear and non-linear inequalities. The technical properties of polymer composites and concrete substrate are their variables. Searching of compatibility space is focused on determination of the solution of the given set of inequalities (requirements of compatibility) by successively ascribing possible values (x1, x2, …, xn) to the technical properties of repair materials and concrete substrates. The solution of the set of inequalities defines the N-dimensional compatibility space.

To determine compatibility space, suitable computer programs were developed at Koszalin University of Technology (Głodkowska 1994, Głodkowska 2003) and Warsaw University of Technology (Czarnecki et al. 1997). Currently, a new program ANCOMP for determination of compatibility space was developed (Garbacz 2013).

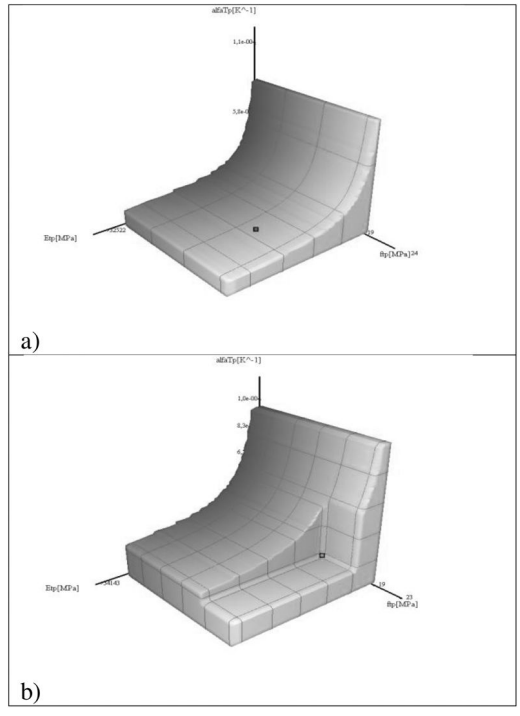

Figure 1. Examples of compatibility subspaces determined with ANCOMP program defined by elasticity modulus E_{tp}, tensile strength f_{tp} and coefficient of thermal expansion $alfa_{Tp}$: a) commercial polymer mortar with high E modulus (non-compatibility), b) commercial polymer mortar with lower E modulus (compatibility).

The Figure 1 presents the compatibility subspace determined for commercial polymer mortar used for repair of concrete substrate with characteristic compressive strength of 15 MPa. The temperature gradient during service was assumed to be 30K. The point corresponding to the mortar properties is located outside of compatibility space. The decrease of value of elasticity modulus of repair mortar causes a larger compatibility space and mortar can fulfill requirements of compatibility.

Figure 2 Shows effect of crack presence on compatibility of elastic polymer-cement protective coating (Garbacz 2013) applied on a cracked concrete substrate and non-cracked substrate (cracks will occur during service).

The compatibility requirements in the ANCOMP program can be modified very easily and can be used for analysis of compatibility issues in any multilayer system.

4 EXAMPLE OF APPLICATION OF COMPATIBILITY APROACH IN REPAIR

This section demonstrates usability of the compatibility approach in practice on the example of material

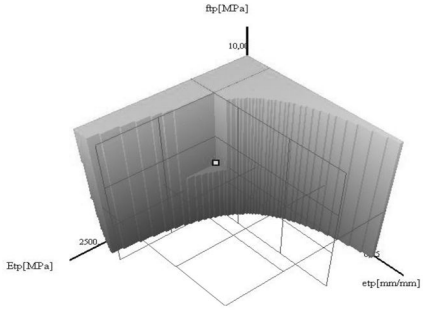

a)

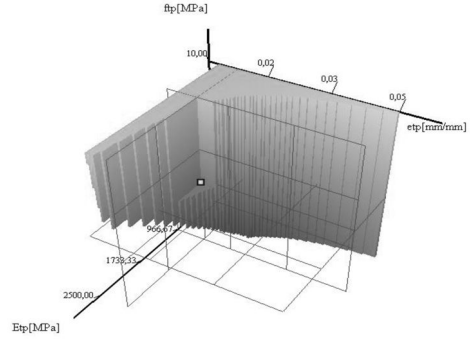

b)

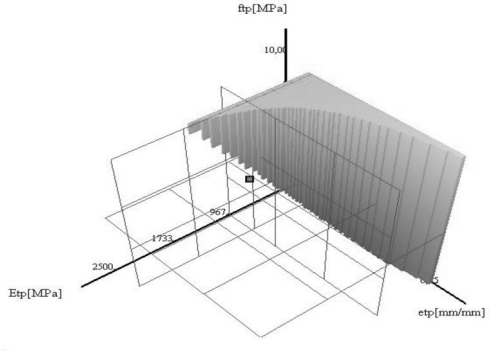

c)

Figure 2. Examples of compatibility subspaces determined with ANCOMP program defined modulus of elasticity E_{tp}, elongation at break, ε_{tp} and tensile strength f_{tp} showing effect of changes of crack width: a) $w_d = 0{,}1$ mm on cracked substrate (compatibility), b) $w_d = 0{,}1$ mm on non-cracked substrate (compatibility); c) $w_d = 0{,}2$ mm on non-cracked substrate (non-compatibility); $\Delta w = 0.03$ mm in all cases.

selection for repair and protection of reinforced concrete tanks in sewage plant (Głodkowska 2003).

Both elements were produced as monolithic members. The basic reason of the concrete structure's deterioration (Fig. 3) was technological faults: too low depth of concrete cover, improper compaction of the concrete and a lack of protection against aggressive environment.

The results of assessment, including mechanical analysis, showed that technical state of tank is

a) b)

Figure 3. General view of the damage of tank walls in: a) preliminary sedimentation tank, b) fermentation chamber.

Table 4. Selected properties of repair mortars and protective coating used for calculation of compatibility space for repaired concrete structures.

Property	Value
Concrete substrate	
f_{ctk} [MPa]	1.35
E_{ctm} [MPa]	13500
Polymer-cement mortar *)	
f_{tp} [MPa]	5.25 (4.80)
ε_{tp} [%]	0.028 (0.024)
E_{tp} [MPa]	17500 (18050)
f_{Ao} [MPa]	2.5 (2.0)
Elastic polymer-cement coating	
f_{tp} [MPa]	0.80
ε_{tp} [%]	18
E_{tp} [MPa]	500
f_{Ao} [MPa]	0.8

*) fine-grained and coarse mortar respectively.

acceptable from mechanical point of view. The performed calculations indicated that crack with maximum width of 0.2 mm can appear in the tank wall. The project of repair and anticorrosion protection of this structures was proposed using compatibility models defined by requirements presented in Tables 2 and 3.

The commercially available fine-grained and course polymer-cement mortars were selected for surface and structural repair of wall and bottom plate. To ensure the tightness of the tanks application of sprayed elastic polymer coating was proposed. Table 4 presents, determined experimentally, selected properties of concrete substrate, mortars and coating used for repair.

Calculations (Fig. 2), taking into account service conditions (concrete substrate properties, temperature gradient) indicated that selected materials should be compatible with repaired concrete substrate. After almost 25 years of service no visible deterioration is observed.

5 CONCLUSIONS

The presented results clearly demonstrate usability of the compatibility model for evaluation of requirements

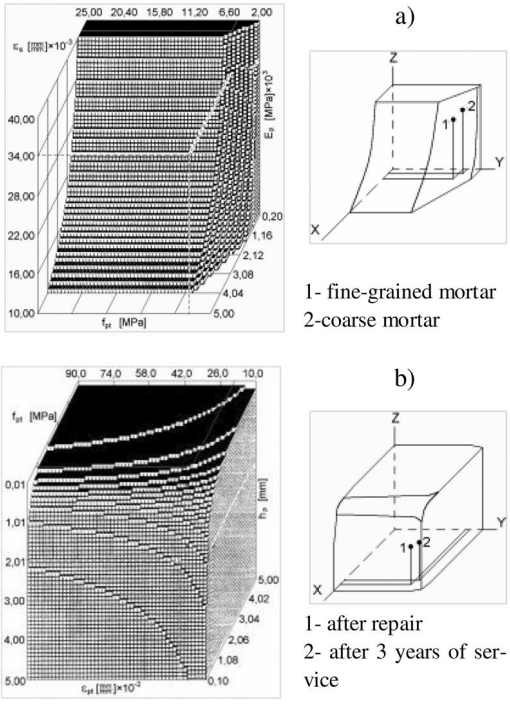

Figure 4. Compatibility subspaces for commercial materials selected for repair: a) polymer-cement mortars used for structural and surface repair of concrete tanks and the points reflecting properties of polymer-cement mortars; b) protective coating the points reflecting properties of elastic polymer-cement coating.

for a good cooperation between repair materials and concrete substrate. They also enable the prediction of behavior of the system : concrete repair material during service and an indication of the good cooperation that will not be met either at the stage of selection of repair and protective coating, or during the use of the building structure.

The usability of a compatibility approach was confirm in practice during selection of repair mortar and protective coating for protection of concrete walls in the concrete sewage tanks. After 25 years of service the mortar and coating selected on the basis of compatibility approach are in good condition and no deterioration has been observed.

The program ANCOMP, using multi-criteria models of good cooperation shown in the article, may serve as a useful tool for the design of new composites for repair and protective coatings, meet the requirements of effective and durable repair of concrete.

ACKNOWLEDGMENTS

This work has been financially supported through Scientific Cooperation Programs of the Polish, Québec and Wallonia–Brussels governments.

The ANCOMP computer program for evaluation of compatibility in multilayer systems was elaborated in the framework of the project: "*Innovative means and effective methods of improving the safety and durability of building structures and transport infrastructure in the strategy of sustainable development*"*; POIG.01.01.02-10-106/09-01 (PT2.3)*.

REFERENCES

Courard, L.; Bissonnette, B. 2007. Compatibility performance as a fundamental requirement for the repair of concrete structures with Self-Compacting Repair Mortars. Proc. of 5th International RILEM Symposium on Self-Compacting Concrete, Gent. 667–675.

Czarnecki, L., Clifton, J.R. Głodkowska, W. 1992. Problem of compatibility of polymer mortars and cement concrete system, International Colloquium Materials and Restoration, Esslingen. 964–971.

Czarnecki, L. Garbacz, A. Łukowski, P. Clifton, J. 1999. Polymer Composites for Repairing of Portland Cement Concrete: Compatibility Project, NIST Report (NISTIR 6394). United States Department of Commerce, National Institute of Standards and Technology, Gaithersburg MD, 1999.

Czarnecki, L. Głodkowska, W. Piatek, Z. 2004. Estimation of compatibility of polymer i polymer-cement composites with ordinary concrete under short-time load conditions. Archives of Civil Engineering, L(1). 133–150.

Czarnecki, L. Runkiewicz, M. 2005. On the compatibility measure in the repair systems, Proc. International Conference on Concrete Repair, Rehabilitation and Retrofitting. ICCRRR 2005 (Eds. H. Beushausen, F. Dehn and M.G. Alexander), Cape Town, South Africa. 1003–1008.

Czarnecki, L., Vaysburd, A.M., Mailvaganam, N.P., Emmons, P.H., McDonald, J.E. 2000. Repair and rehabilitation of structures – Some random thoughts, Indian Concrete Journal (74).

Emmons, P.H., McDonald, J.E., Vaysburd, A.M. 1992. Some compatibility problems in repair of concrete structures – fresh look, International Colloquium Materials Science and Restoration, Esslingen, 836–848.

Emmons, E. H., Vaysburd, A. M. and McDonald, J. E. 1993. A rational approach to durable concrete repairs. Concr. Intern., 15, (9), 40–45.

Garbacz, A. 2013. Importance of concrete substrate preparation for effective repair (in Polish), Construction Materials, 9 (493), 10–13.

Garbacz A., del Mar Lopez, M. Naaman, A. Czarnecki, L. 2000, Compatibility space model for strengthening reinforced concrete beams with CFRP laminates, Report No. UMCEE 00-07, The University of Michigan, Ann Arbor, USA.

Garbacz, A. Głodkowska, W. 2012. Compatibility of Elastic PCC Coating and Concrete Substrate, International Journal for Restoration of Buildings and Monuments, 18 (3/4) 2012, 229–238.

Głodkowska, W. 2004. Compatibility of polymer composite – cement concrete system [in Polish], W. Dissertation, Warsaw University of Technology (1994).

Głodkowska, W. 2003a, Crack resistance of protective coatings. Archives of Civil Engineering. XLIX, 1 (2003), 131–149.

Głodkowska, W. 2003b, Fundamentals and method of selection of properties of composites for the repair and protection of concrete (in Polish), Koszalin 2003.

Głodkowska, W. 2011. Forecasting crack resistance of short- and long- term loaded coatings. ACME Journal, 10 (1), 33–44.

Głodkowska, W. Staszewski, M. 2007. Weatherability of Coating Materials for Protection of Concrete. Adhesion in Interfaces of Building Materials: a Multi-scale Approach. Advances in Materials Science and Restoration (Eds. L. Czarnecki, A. Garbacz). AMSR No.2, Aedificatio Publishers, 2007.

Morgan, D. R. 1996. Compatibility of concrete repair materials and systems, Construction and Building Materials, 1, 57–67.

Schueremans, L. Cizer, Ö. Janssens, E. Serré, G. Van Balen, K. 2011. Characterization of repair mortars for the assessment of their compatibility in restoration projects: Research and practice, Construction and Building Materials, 25, 4338–4350.

Vaysburd, A. 2006. Holistic system approach to design and implementation of concrete repair, Cement & Concrete Composites, 28, 671–678.

Concrete Solutions – Grantham et al. (Eds)
© 2014 Taylor & Francis Group, London, ISBN 978-1-138-02708-4

Properties of alkali-activated fly ash/slag repair mortars

N. Ghafoori & M. Najimi
Department of Civil and Environmental Engineering and Construction, University of Nevada, Las Vegas, USA

ABSTRACT: The study presented herein evaluates fresh, strength and transport properties of alkali-activated fly ash/slag mortars, and compares their performances with those of control mixtures. To this aim, four mixtures were made including two alkali-activated and two control mortars. Alkali-activated mortars contained 50% fly ash and 50% slag as binders, with two different combinations of sodium hydroxide and sodium silicate solutions as alkaline activators. The control mixtures included a similar mixture of slag and fly ash without alkali, and a standard Portland cement mortar. The experimental program used in this study included various evaluation methodologies to determine flow, setting times, compressive strength, modulus of elasticity, absorption, void content, and chloride migration and penetration. Slump flow and setting times were tested immediately after batching. The produced samples were de-molded after one day and cured in a moist room until time of testing. Compressive strength was measured at the ages of 3, 7, 14, 21 and 28 days. Modulus of elasticity, water absorption, rapid chloride migration (RMT) and rapid chloride penetration (RCPT) tests were done on 28-day cured samples. The results of study revealed higher strength of alkali-activated mortars than those of the control mortars. Their 3-days strengths were 34 and 41 MPa, being in a suitable range for repair applications. The alkali-activated mixtures showed superior performance in RCPT, RMT, water absorption, and void content results compared to those of the control mixtures. However, their setting times were shorter than those of the control mixtures.

1 INTRODUCTION

The primary binder used to make concrete is Portland cement (PC) with an annual production of 3 billion tons (Pacheco-Torgal et al. 2012). The statistical evaluations show that in the next 40 years it will have a twofold increase reaching 6 billion tons per year (Pacheco-Torgal et al. 2012). Production of one ton of PC generates approximately 0.94 tons of CO_2 (Pacheco-Torgal et al. 2012). It is estimated that PC production accounts for nearly 7% of the world's total CO_2 emissions (Huntzinger et al. 2009, Pacheco-Torgal et al. 2012). As such, carbon dioxide gas emission as a result of cement and concrete production is becoming a global concern.

Contrary to common belief, PC concrete is not free of severe degradation problems. "In the U.S, the direct cost of corrosion in highway bridges exceeds billions of dollars per year, and indirect costs to users due to traffic delays and lost in productivity have been estimated to be ten times as much" (ACI 2001, Kirkpatrick et al. 2002, Lindquist et al. 2006). According to the latest Annual Urban Mobility Report (Schrank et al. 2012), congestion in 2011 caused urban Americans to travel 5.5 billion hours more and to purchase an extra 2.9 billion gallons of fuel for a congestion cost of $121 billion. This issue can be further recognized considering the fact that the average age of existing bridges in the U.S. is 42 years. With a design lifespan of 50 years, more than 200,000 of approximately 600,000 highway bridges are 50 years old or older. This number will double by 2030 according to the U.S. Department of Transportation National Bridge Inventory (US DOT 2013). Hence, the U.S. transportation network is expected to face several challenges due to the aging of the network components as more than one out of ten existing bridges already fall in the category of "structurally deficient," requiring major maintenance, rehabilitation, or even replacement (ASCE 2013). The problem is not limited to concrete bridges. Several problems have also been observed in concrete pavements. Concrete pavements are aging and deteriorating. They have shown varying signs of deteriorations due to age, harsh environment, excessive loading and other detrimental factors. It was reported that one third of the U.S. road system is in poor condition or worse (Van Dam et al. 2011). As such, the need for production of high performance concrete has never been more urgent.

The desire to reduce CO_2 emissions and to produce more durable concrete has given impetus to search for new binders. Several studies have been conducted in recent years to find alternative binders for PC. Although far more research is needed, several researchers suggested that alkali-activated binders may have the potential to become a sustainable replacement for cement. The discovery of alkali-rich pozzolans in ancient monuments, which have been durable over millennia, can be considered an undeniable proof of this potential (Glukhovsky 1959, Jackson

et al. 2010). This indicates that alkali-activated pozzolanic materials may prove to be a viable solution to concrete durability concerns. Alkali-activated binders are not only a more sustainable choice due in reducing PC consumption and providing adequate durability, but also they incorporate waste by-products such as slag and fly ash resulting in a reduction of waste disposal.

As alkali-activated binders are still at the early stage of development, they need further research work in order to become technically and economically viable construction materials. This study focuses on evaluation of fresh, strength and transport properties of alkali-activated fly ash/slag mortars in their comparison with those of PC mortars.

2 MATERIALS AND MIXTURE PROPORTION

The materials used in this study included Class F fly ash and slag as binders of alkali-activated mortars, Type I Portland cement as a binder for Portland cement mortar, sodium hydroxide and sodium silicate solutions as alkaline activators, fine aggregates, and distilled water. The properties of Portland cement, fly ash and slag are reported in Table 1. As can be seen, the used fly ash contained 87.2% of pozzolanic oxides (silica + alumina + iron oxide). The used slag had high amounts of calcium oxide (43.1%) and pozzolanic oxides (42.7%). The alkaline activators consisted of a 10M sodium hydroxide solution and a sodium silicate solution having Na_2O/SiO_2 of 2/1 and 55.9% water. The 10M sodium hydroxide solution was made by solving 400g of NaOH lye in enough distilled water to produce 1 liter of solution. Distilled water was used instead of tap water to avoid inclusion of the ions which may be in the tap water. The fine aggregate used in this study was natural sand having an oven-dry specific gravity of 2.76, SSD specific gravity of 2.78, apparent specific gravity of 2.82 and absorption of 0.81%. Its gradation was in the allowable range of ASTM C33.

Table 1. Properties of cement, slag and fly ash.

Properties	Cement	Slag	Fly ash
SiO_2, %	21.1	28.9	59.9
Al_2O_3, %	4.0	12.9	22.2
Fe_2O_3, %	2.0	0.9	5.2
MgO, %	2.1	4.6	–
SO_3, %	2.8	5.3	0.4
CaO, %	62.9	43.1	4.7
Na_2O Eq.,%	0.59	0.56	1.29
Loss on ignition, %	1.8	0.3	0.3
Insoluble residue, %	0.71	–	–
Blaine, cm^2/g	3406	4620	–
Density	3.15	2.87	2.31
C_3S, %	57	–	–
C_2S, %	18	–	–
C_3A, %	7	–	–

Table 2 documents mixture proportion of the studied mixtures. Alkali-activated mortars were designed by using slag-to-fly ash ratio of 1, fine aggregate-to-binder (fly ash plus slag) ratio of 2 and activator solution-to-binder ratio of 0.46. The activator solutions contained 70% sodium hydroxide and 30% sodium silicate for mixture AA30, and 50% sodium hydroxide and 50% sodium silicate for mixture AA50. The control mortars included a similar mixture of slag and fly ash without alkali (FSC), and a standard Portland cement mortar (PCC). The PCC mortar was designed according to ASTM C109 with fine aggregate-to-cement ratio of 2.75 and water-to-cement ratio of 0.485. The fly ash/slag control mortar was designed with the same ratio of fly ash to slag and water content equal to amount used in making activator solutions of mixture AA50. The water-to-binder ratio was 0.33 for this mixture. A superplasticizer was used to increase the flow of FSC to an acceptable range. The used superplasticizer wasn't compatible with the alkaline environment of alkali-activated mortars.

3 FRESH PROPERTIES

The initial and final setting times, and flow of the studied mortars were measured and the results are presented in Table 3. As can be seen, the setting times of alkali-activated mortars were significantly lower than those of the control mortars. Their setting times were averagely 90 and 95% lower than initial and final setting times of PCC mortar, respectively. While this behavior is being studied for suitable remedies, the results depict the need for compatible retarders for alkali-activated binders. The increases in percentage of sodium silicate content reduced the setting times of alkali-activated mortars. This increase, however, led to a higher flow. The flow of AA50 was almost 50% more than that of AA30. The flow of both alkali-activated

Table 2. Mixture proportions of the studied mortars (Mass ratio).

Mixture identification	Slag	Fly ash	Cement	Fine aggregates	Solution (Water or activator)	Sodium hydroxide percentage in solution, %	Sodium silicate percentage in solution, %
PC control (PCC)	0	0	1	2.75	0.485	0	0
Fly ash/slag control (FSC)	0.5	0.5	0	2	0.33	0	0
Alkali activated AA30	0.5	0.5	0	2	0.46	70	30
Alkali activated AA50	0.5	0.5	0	2	0.46	50	50

Note: Water is the solution for control mixtures, while alkali-activators were the solutions of alkali-activated binders.

mortars was lower than that of PCC and FSC mortars. Since the used superplasticizer couldn't change the flow of alkali-activated mortars, a higher level of compaction was used for mixture AA30 with the lowest flow.

4 MECHANICAL PROPERTIES

4.1 *Compressive strength*

The compressive strengths of the studied alkali-activated and control mortars were measured at the ages of 3, 7, 14, 21 and 28 days and the results are presented in Table 4. As can be seen, the alkali-activated mortars produced higher strengths than those of the control mortars. AA30 and AA50 developed 3-day compressive strengths of 34 and 41 MPa, respectively, which were sufficient for repair applications. The majority of their strength developments happened within the first 14 days. Increases in sodium silicate content led to an increase in compressive strength of alkali-activated mortars.

The 3-, 7-, 14-, 21-, and 28-day compressive strengths of AA30 were 23.4, 14.3, 20.3, 17.8 and 24.5% higher than that of PCC mortar, respectively, as shown in Table 5. When sodium silicate content increased to 50%, i.e. mixture AA50, these differences increased to 48.5, 36.2, 40.5, 33.5 and 34.8%, respectively, indicating higher strength of AA50 than that of AA30. These differences were significantly higher when alkali-activated mixtures compared with FSC mixture. The 28-day compressive strength of FSC was 29 and 26% of those of AA30 and AA50, respectively.

AA30 mortars developed 60, 75 and 87% of their 28-day strength in 3, 7 and 14 days, respectively. The use of a higher sodium silicate content increased these rates of strength developments to 67, 82 and 94% for mixture AA50, respectively. In the case of control mortars, 3-day, 7-day and 14-day compressive strengths of PCC were 61, 82 and 90% of their 28-day compressive strength. The strength development had the slowest rate for FSC. The ratios of 3-day, 7-day and 14-day compressive strengths to 28-day compressive strength of FSC mortar were 0.52, 0.69 and 0.88, respectively.

4.2 *Modulus of elasticity*

Moduli of elasticity of the studied mixtures were measured at the age of 28 days and their results are presented in Figure 1. As can be seen, the moduli of elasticity of the studied alkali-activated mortars were lower than that of PCC mortar and higher than that of FSC mortar.

The modulus of elasticity of mixture AA30 and AA50 was 9.8 and 7.5% lower than that of PCC mortar. To some extent, this difference can be attributed to the mixture proportion of PCC mortar as it had a higher amount of fine aggregate in comparison with the alkali-activated mortars.

The FSC mixture had 18.8 and 20.9% lower moduli of elasticity than AA30 and AA50, respectively.

Table 3. Fresh properties.

Mixture id.	Flow (cm)	Setting time (min)	
		Initial	Final
PCC	13.6	145	250
FSC	12.8	240	N.M[#]
AA30	7.5	14*	
AA50	12	9*	

*The initial and final setting times of AA30 and AA50 happened within almost a minute apart. [#]N.M: Not measured.

5 TRANSPORT PROPERTIES

5.1 *Water absorption*

The water absorption of AA30 and AA50 were 12 and 30% lower than that of PCC mortar, respectively, as shown in Table 5. These differences increased to 40 and 76% when compared with FSC mortar, respectively. The void content of AA30 was 1.9 and 11.6% lower than that of PCC and FSC mixtures, respectively. These reductions increased to 18.7 and 26.7%, respectively, when sodium silicate percentage increased to 50%.

ASTM C642 was used to measure density, absorption and void content of the studied mortars at the age of 28 days. The results of this test are reported in Table 6. As shown in this table, absorption and void content of alkali-activated mortars were lower than those of the control mortars. Their dry-bulk densities were almost similar to that of PCC mixture and slightly higher than that of FSC mixture. An

Table 4. Compressive strength (MPa).

Mixture id.	3 days	7 days	14 days	21 days	28 days
PCC	27.5	36.9	40.8	43.5	45.1
FSC	8.4	11.1	14.2	15.2	16.1
AA30	34.0	42.1	49.0	51.3	56.2
AA50	40.9	50.2	57.3	58.1	60.9

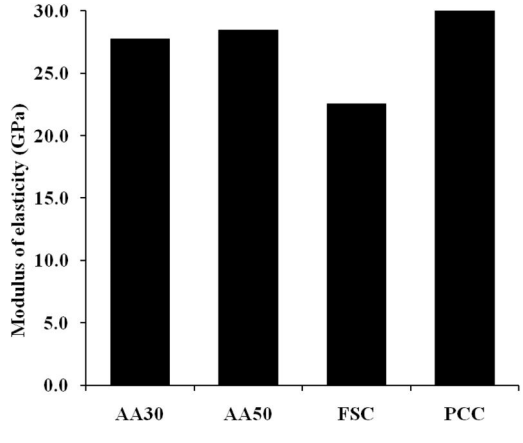

Figure 1. Results of modulus of elasticity.

Table 5. Improvements in load-dependent and transport properties of alkali-activated mortars when compared to PCC mortar (%).

Mixture id.	Compressive strength					Modulus of elasticity	Absorption	Void content	RCPT	RMT
	3 days	7 days	14 days	21 days	28 days					
AA30	23.4	14.3	20.3	17.8	24.5	−9.8	12	1.9	80	82
AA50	48.5	36.2	40.5	33.5	34.8	−7.5	30	11.6	65	77

Table 6. Results of absorption test.

Mixture id.	Water absorption, %	Void content, %	Dry-bulk density
PCC	6.3	15.5	2.18
FSC	7.9	17.2	2.12
AA30	5.6	15.2	2.17
AA50	4.5	12.6	2.19

increase in sodium silicate content from 30 to 50% led to improvements in absorption and void content of alkali-activated mortars.

While the void contents of alkali-activated mortars were lower than that of PCC mortar, their dry-bulk densities were almost similar to that of PCC mortar. Although fewer voids in alkali-activated binders resulted in a higher density, Portland cement had a higher density than that of slag and fly ash (3.15 for PC in comparison with 2.87 of slag and 2.31 of fly ash as shown in Table 1), compensating for the high void content of PCC mixture. Additionally, PCC mixture contained a higher amount of fine aggregate. The density of fine aggregate was higher than the average density of fly ash and slag, contributing to an increase in the density of PCC mixture.

The dry bulk density of alkali-activated mortars was marginally higher than that of FSC mortar by nearly 3%.

5.2 *Rapid chloride migration*

Rapid chloride migration test (RMT) was conducted on the studied mixtures at the age of 28 days and according to NT BUILD 492. In this test, a voltage of 30 V was applied on samples for 24 hrs. Afterward, the penetrated chloride depth was measured using silver nitrate sprayed on the split samples. The depths of penetrated chloride are presented in Figure 2. As can be seen, the penetration of chloride in alkali-activated mortars was considerably lower than that of PCC mortar. They were also less than that of FSC mortar. The chloride depth of AA30 and AA50 mixtures were 18 and 23% of that of PCC mortar, respectively. These ratios increased to 67 and 87% when chloride depth of AA30 and AA50 were compared with that of FSC mortar.

5.3 *Rapid chloride penetration*

Rapid chloride penetration test (RCPT) was conducted on the studied mixtures at the age of 28 days based on

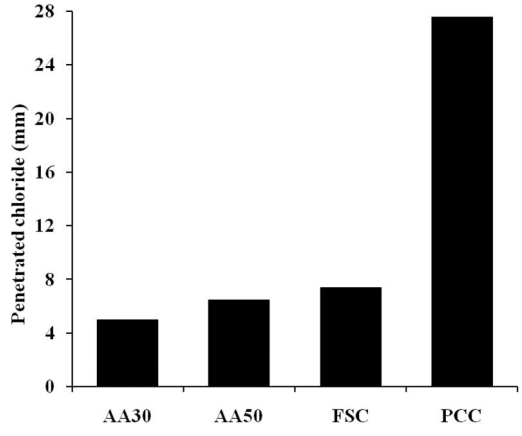

Figure 2. Results of RMT.

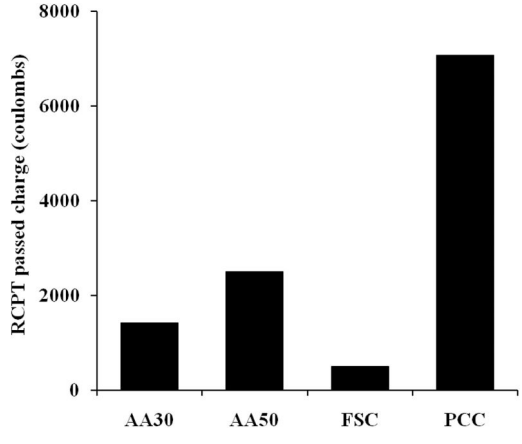

Figure 3. Results of RCPT.

ASTM C1202. The results of RCPT are presented in Figure 3. While increases in sodium silicate content increased the RCPT value, both alkali-activated mortars had lower passed charge than that of PCC mortar. The passed charges of AA30 and AA50 were 80 and 65% lower than that of PCC mortar, respectively.

The FSC mixture showed the lowest RCPT value amongst all the studied mixtures, while they had higher penetrated chloride than alkali-activated mortars (Fig. 2). This can be related to the mechanism of RCPT. This test measures not only chloride ions, but all the free ions that can move through the mortar or concrete samples. As such, alkali-activated mortars contained

more free alkaline ions which could pass through the samples, resulting in higher RCPT values.

6 CONCLUSIONS

In this study, fresh, strength and transport properties of alkali-activated fly ash/slag mortars were examined and compared with those of standard Portland cement mortar and a mixture of slag and fly ash without alkali. Based on the results of this study, the following conclusions can be drawn:

- Alkali-activated mortars had lower flow and setting times than those of the control mortars. While their flow was enough to make a suitable mortar, further research is required to find viable and economical solutions for their exceeding low setting times.
- Compressive strengths of alkali-activated mortars were higher than that of the control mortars. Their 3-day strengths were more than adequate as repair mortars.
- While strength development of fly ash/slag contained control mixture was slow due to late pozzolanic activities of fly ash, alkali activation improved the degree of reactivity of fly ash/slag mortars for their early strengths.
- Alkali-activated mortars had lower water absorption and void content than those of the control mortars. Their dry-bulk density was similar to that of the Portland cement mortar.
- The major benefits of alkali-activated mortars were observed in RCPT and RMT. Their depth of penetrated chloride and passed charge were significantly lower than those of Portland cement mortar.
- Overall, the performances of alkali-activated mortars were promising for repair applications provided their setting times can be brought up to the reasonable levels suitable for repair activities.

REFERENCES

ACI 222. 2001. Protection of metals in concrete against corrosion, ACI Committee 222, American Concrete Institute.

ASCE, 2013. ASCE Report Card, American Society of Civil Engineers, Reston, VA.

Glukhovsky, V.D. 1959. Soil Silicates. Gostroiizdat Publish, Kiev, USSR.

Huntzinger, D.N. & Eatmon, T.D. 2009. A life-cycle assessment of Portland cement manufacturing: comparing the traditional process with alternative technologies. Journal of Cleaner Production, 17, 668–675.

Jackson, M., Deocampo, D., Marra, F. & Scheetz, B. 2010. Mid-Pleistocene Pozzolanic Volcanic Ash in Ancient Roman Concretes. Geoarchaeology: An International Journal, 25, 36–74.

Kirkpatrick, T.J., Weyers, R.E., Sprinkel, M.M., & Anderson-Cook, C.M. 2002. Impact of specification changes on chloride-induced corrosion service life of bridge decks, Cem. Constr. Res. 32, 1189–1197.

Lindquist, W.D., Darwin, D., Browning, J., & Miller, G.G. 2006. Effect of cracking on chloride content in concrete bridge decks, ACI Mater. J. 103 (6), 467–473.

Pacheco-Torgal, F., Abdollahnejad, Z., Camões, A.F., Jamshidi, M. & Ding, Y. 2012. Durability of alkali-activated binders: A clear advantage over Portland cement or an unproven issue?. Construction and Building Materials, 30, 400–405.

Schrank, D., Eisele, B., & Lomax, T. 2012. Annual Urban Mobility Report, Texas A&M Transportation Institute, College Station, TX.

U.S. DOT. 2013. National Bridge Inventory, United States Department of Transportation, Federal Highway Administration, Washington, DC.

Van Dam, T., Taylor, P., Fick, G., Gress, D., VanGeem, M., & Lorenz, E. 2011. Sustainable concrete pavements: A manual of practice, Iowa Department of Transportation, Federal Highway Administration DTFH61-06-H-00011.

This page intentionally left blank

Concrete Solutions – Grantham et al. (Eds)
© 2014 Taylor & Francis Group, London, ISBN 978-1-138-02708-4

Corrosion behavior of steel bars in reinforced concrete slabs repaired by partial patching

E. Kato & Y. Kawabata
Port and Airport Research Institute, Yokosuka, Kanagawa, Japan

M. Iwanami
Tokyo Institute of Technology, Meguro, Tokyo, Japan

ABSTRACT: This study investigated the long-term behavior of macro-cell corrosion of steel bars generated in reinforced concrete slabs repaired by partial patching. Macro-cell corrosion current density in repaired test slabs was periodically measured for about 2 years. To measure the macro-cell corrosion current, segmented steel bars were embedded in the test slabs. Based on the test results, the following conclusions were obtained: 1) The steel bars in chloride-contaminated concrete near the joint acted as a macro-cell cathode in the early stage of exposure, however, a change in the electrochemical balance made the steel bars anodic; 2) The macro-cell current density at the intersection element in chloride-contaminated concrete became high, which is considered to be caused by a two-dimensional electrical current flow; and 3) Steel bars in the repair material part may tend to cause the formation of distinctive macro-cell corrosion.

1 OVERVIEW

The concrete superstructure of an open-type wharf is generally exposed to severely corrosive environmental conditions such as sea-water spray and the tidal zone. Under such conditions, there is an abundant supply of factors into the concrete, namely chloride ions, water and oxygen and embedded reinforcement bars that cause corrosion. Therefore, the concrete superstructure needs to be appropriately preserved to maintain sufficient performance throughout its service life. So repairs are a crucial part of maintenance work.

Patch repair is the most commonly used method for recovering the durability of concrete damaged by corrosion. However, if the patch repair work of chloride-contaminated concrete is not performed properly, the durability improvement does not last long because of the development of macro-cell corrosion (Nagataki et al. 1996 and 1997). The occurrence of macro-cell corrosion in reinforcing bars in patched, cracked and chloride-contaminated concrete specimens has been experimentally and computationally investigated (Maruya et al. 2007, Nanayakkara et al. 2009). However, there has been comparatively little research on the formation of macro-cell corrosion in reinforcing bars arranged in two directions.

Therefore, this study investigated the long-term behavior of macro-cell corrosion of steel bars in reinforced concrete slabs repaired by partial patching. Macro-cell corrosion current density in repaired test slabs was periodically measured for about 2 years. To measure the corrosion current, segmented steel bars were embedded in patched test slabs. Based on the test results, the time-dependent variation of macro-cell corrosion in reinforced concrete slabs repaired by partial patching is discussed.

2 EXPERIMENT

2.1 *Outline of slabs*

Figure 1 shows the test slabs repaired by partial patching. The dimensions of the slabs were $600 \times 600 \times 100$ mm. In order to investigate the macro-cell formation in the partially repaired slabs, the volume of patch repair material in each slab was varied, from 25% in Type-1/4 (one quarter) to 50% in Type-1/2 (one half) as shown in Figure 1a) and b), respectively. The chloride-contaminated concrete part was cast first and cured for 14 days before the repair material part was cast. Table 1 lists the mix proportions of the chloride-contaminated concrete. The chloride ion content in the concrete part was 4.0 kg/m^3 (1.46% of cement content) based on 54 data sets of chloride ion content at steel bars in actual concrete superstructures serviced for around 30 years. Figure 2 shows the frequency of chloride ion content in the 54 data sets. Taking into account the state of deterioration of those concrete superstructures, partial patch repair was recommended as an appropriate measure according to the Manual on Maintenance of Port and Harbour Facilities (Port and Airport Research Institute, 2007). The mix proportions and mechanical properties of the

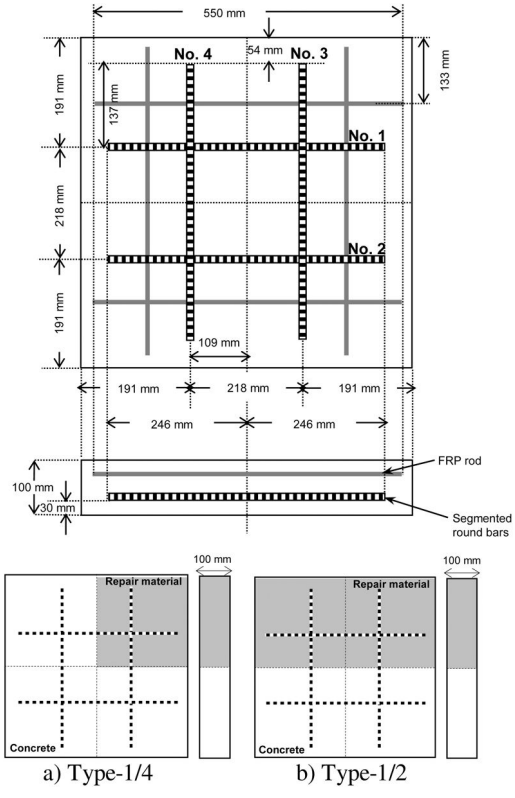

Figure 1. Test slabs repaired by partial patching.

Table 1. Mix proportions of chloride-contaminated concrete.

W/C	s/a	Unit content (kg/m^3)					AE	AEW
(%)	(%)	W	C	S	CA	Cl^-	(C%)	(C%)
55	44	150	273	822	1087	4.0	0.3	0.3

Slump = 9.0 cm, Air content = 5.3%.

Table 2. Mix proportion and mechanical properties of repair material.

Mix proportion (/m^3)	Binder powder	1919 kg
	Water	261 kg
Mechanical properties at 28 days (catalog)		
	Compressive strength	48.1 N/mm^2
	Young's modulus	2.1×10^4 N/mm^2
	Cl^- Diffusion coefficient	3.0×10^{-9} cm^2/s

patch repair materials are listed in Table 2. Slabs were cured in the wet condition for 14 days after the repair material part was cast.

In order to measure the actual macro-cell corrosion current passing through the steel bars directly, 72

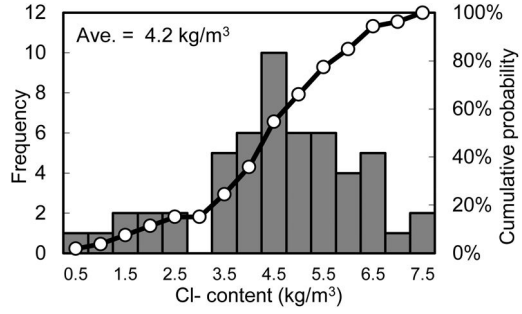

Figure 2. Frequency of chloride ion content.

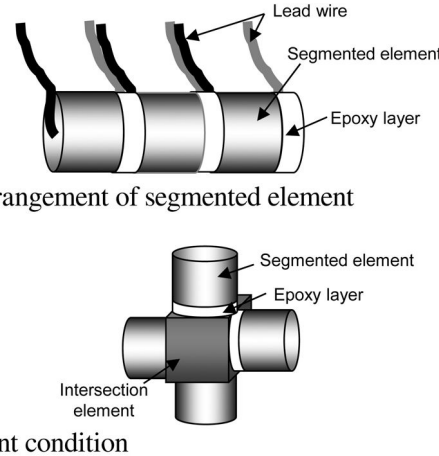

Figure 3. Details of arrangement of segmented and intersection elements.

segmented elements (round steel bar, $\phi 13 \times 20$ mm) and 4 intersection elements ($13 \times 13 \times 13$ mm) were embedded into the test slabs. The arrangement and joint condition of the segmented and intersection elements are shown in Figures 3a) and b), respectively. To make the cover depth of all segmented elements the same thickness of 30 mm, the four segmented elements were bonded to one intersection element in an intersection part. Each segmented element was electrically connected to the next segmented element with a shunt resistor by lead wires as shown in Figures 3a and 3c).

2.2 *Exposure condition*

Figure 4 shows the condition of the wet-dry cyclic exposure test in the laboratory. Repaired test slabs were

Figure 4. Exposure test in the laboratory.

exposed to the wet-dry cycle of soaking in sea water for 1 week after drying in the atmosphere for 1 week. Temperature and relative humidity were not controlled during the test. The upper sides of all slabs were always kept dry in order to prevent chloride ions from penetrating from the upper surface of the test slabs. The exposure test was continued for 22 months.

2.3 *Measurement and calculation*

During the corrosion process, ionic current flows from the cathodic part to the anodic part. By measuring the current flowing through each segmented element in the repaired test slab, the distribution of macro-cell current density in the slab can be estimated (Nagataki et al. 1996). The current density in a segmented element was calculated by the following equation, in which anodic and cathodic current densities were calculated as (−) and (+), respectively:

$$a_i = \frac{I_{i,i+1} - I_{i-1,i}}{S_i} \tag{1}$$

where a_i = macro-cell current density at segmented element i(μA/cm^2); $I_{i,i+1}$ and $I_{i-1,i}$ = macro-cell current passing through segmented elements i to $i+1$ and $i-1$ to i (μA); S_i = surface area of segmented element i (cm^2).

The currents flowing through segmented elements in the test slabs were measured every 1 or 2 weeks until 18 months exposure. Afterwards, the currents were measured after 22 months exposure.

Anodic current densities were converted to a steel mass loss w_i using Equation (2), employing Faraday's Law. In this study, a particular anodic current density $(a_i)_j$ was assumed to be constant during $[T_j - T_{j-1}]$.

$$w_i = \sum_{j=1}^{k} \frac{(a_i)_j \cdot (T_j - T_{j-1}) \cdot M_{mol}}{z \cdot F} \cdot 10^{-3} \tag{2}$$

where w_i = mass loss in segmented element i (mg/cm^2); $(a_i)_j$ = macro-cell current density at jth measurement data (μA); T_j = time from repair work at jth measurement (s); M_{mol} = molar weight of iron (55.847 g/mol); z = balance of iron (2); F = Faraday's constant (96 485 C/mol).

The total mass loss of a particular segmented element was calculated as the total sum of the mass loss of each period between measurements.

2.4 *Direct measurement of mass loss*

After 22 months exposure, no corrosion cracks or rust stains were observed on the surface of the repaired test slabs. All the segmented elements were taken out from the test slabs and the mass loss of each segmented element was directly measured as follows: at first, the epoxy layer and lead wire with solder were removed from the segmented element. Then, the segmented element was immersed in 10% diammonium hydrogen citrate solution to completely remove corrosion products. Incidentally, mass losses of eight segmented elements at the edges of a test slab could not be directly measured because they were used for fixing other segmented elements when the test slab was fabricated.

3 EXPERIMENTAL RESULTS AND DISCUSSION

3.1 *Distributions of calculated and measured mass loss*

Figures 5a) and b) show the distributions of the directly measured mass loss of segmented and intersection elements in two types of the repaired test slabs after 22 months exposure, respectively. In Type-1/4 as shown in Figure 5a), heavy mass losses were observed at the intersection element and segmented element next to the intersection in steel bar No. 2. In addition, the segmented elements in the repair material part were corroded. In Type-1/2 as shown in Figure 5b), large mass losses were observed at the intersection element in the concrete part and the segmented element at the joint. Moreover, in the repaired part, a large mass loss was observed at the segmented element near the intersection in steel bar No. 1.

Figures 6a) and b) show the distributions of the calculated mass loss of segmented elements in each test slab after 22 months exposure, respectively. The calculated mass loss reflected only the effect of macro-cell corrosion. The effects of micro-cell corrosion in a whole test slab and of macro-cell corrosion generated only within a particular segmented element were not included in the calculated results. Hence, the calculated mass losses were smaller than the directly measured mass losses. However, it can be seen that the calculated results comprehensively matched the measured results in terms of the correlation of magnitude between them. Therefore, in this study, the time-dependent variation of macro-cell current density in a particular element in the repaired test slab during the exposure period was discussed by the calculated macro-cell current density of each period.

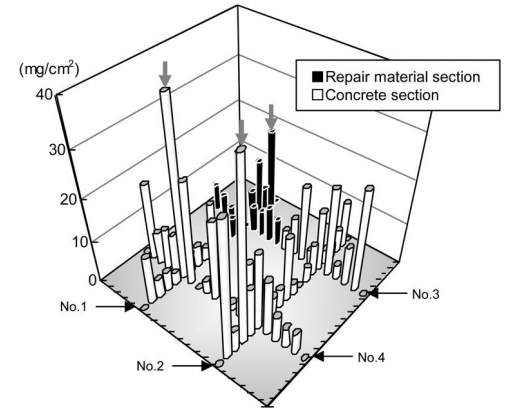

a) Type-1/4

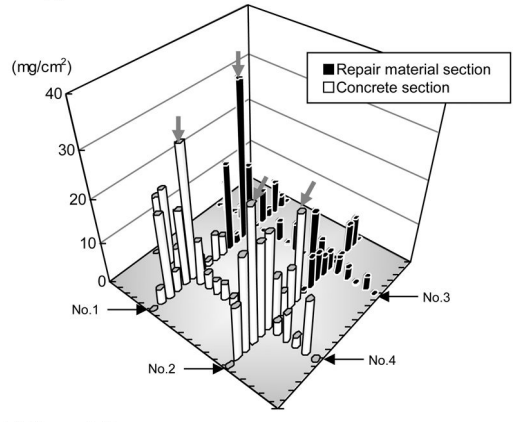

b) Type-1/2

Figure 5. Distributions of directly measured mass loss after 22 months exposure.

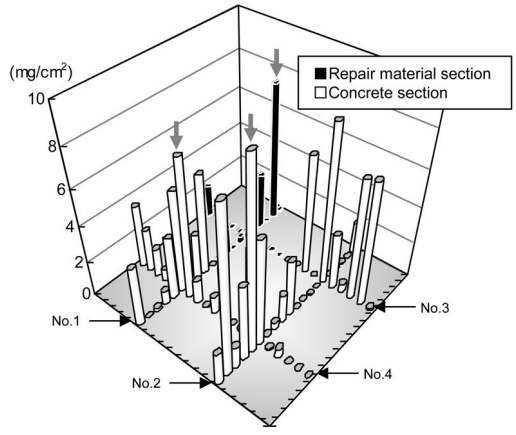

a) Type-1/4

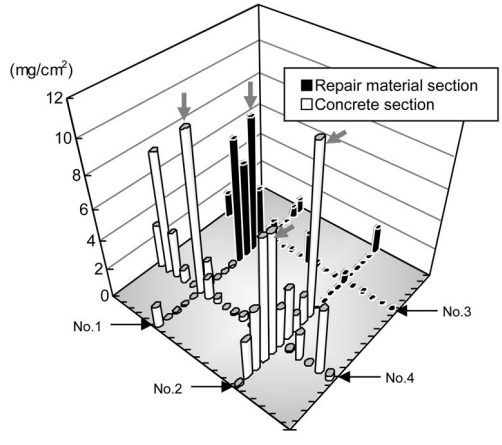

b) Type-1/2

Figure 6. Distributions of calculated mass loss after 22 months exposure.

3.2 *Variation in distribution of macro-cell current density*

From all the measured results of macro-cell current density, the anodic current densities in segmented elements were the highest in the early exposure period, and then the macro-cell current density changed with environmental temperature. Variations in distribution of the macro-cell current density of the repaired test slabs are shown in Figures 7 and 8, respectively. In both figures, Figures a), b) and c) show the distributions when the anodic current density became the highest in the early exposure period, those obtained at the minimum environmental temperature before 1 year of exposure, and those obtained at the maximum environmental temperature after 1 year of exposure. The minimum and maximum quoted environmental temperatures were 7.5°C and 31.0°C, respectively.

In the figures, the current density 0.0 μA/cm^2 is treated as 1.0 nA/cm^2 for convenience, because the vertical axis is a logarithmic scale.

3.2.1 *Type-1/4*

Figures 7a), b) and c) show the distributions of macro-cell current density in Type-1/4 at 62 days exposure (in the wet conditions), 328 days exposure (in the dry conditions), and 517 days exposure (in the wet conditions), respectively.

In Figure 7a), the current densities of all the elements in the repair material part and in steel bar No. 3 were observed in the cathodic side. The highest anodic current density was observed at the intersection element in steel bar Nos. 1 and 4. The current densities in the anodic side were observed in some segmented elements in steel bar No. 2, though they were lower than the densities at the intersection element. It was considered that most of the electrons were consumed by the anodic reaction in the intersection element in steel bar Nos. 1 and 4.

Inactivation of the corrosion reaction caused by lowering the environmental temperature was observed in Figure 7b). The elements in the anodic side were observed at a different position compared with Figure 7a). The element at the maximum anodic current density was observed in steel bar No. 4, however, the position of the element was different from that

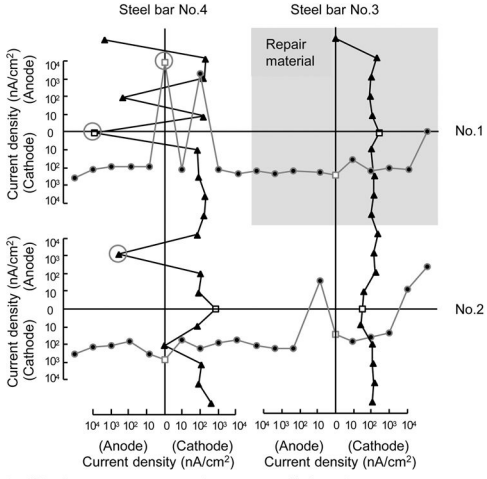

a) 62 days exposure (wet conditions)

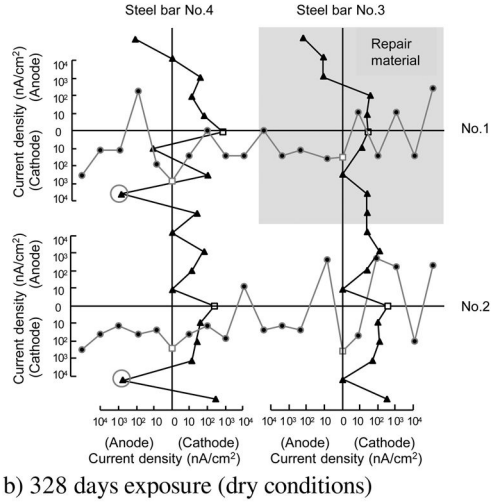

b) 328 days exposure (dry conditions)

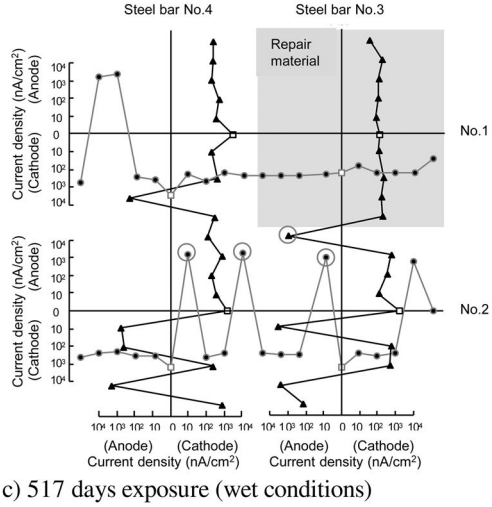

c) 517 days exposure (wet conditions)

Figure 7. Distributions of macro-cell current density in Type-1/4.

in Figure 7a). Moreover, the distribution of macro-cell current density in the repair material part varied compared with that in Figure 7a). The distinctive macro-cell corrosion may have formed only in the repair material part.

In Figure 7c), current densities of all elements in the repair material part were observed in the cathodic side. The segmented element in the concrete part at the joint of the concrete and repair material parts acted as anode (in steel bar No. 3). In steel bar No. 2, in which all the elements were in the concrete part, current densities of three segmented elements between the two intersection elements were observed in the anodic side.

3.2.2 *Type-1/2*

Figures 8a), b) and c) show the distributions of macro-cell current density in Type-1/2 at 24 days exposure (in the dry conditions), 328 days exposure (in the dry conditions), and 517 days exposure (in the wet conditions), respectively.

In Figure 8a), the current densities of almost all the segmented elements in the repair material part were observed in the cathodic side. The highest anodic current densities were observed at the intersection element in steel bar Nos. 2 and 3 and the segmented element in the concrete part near the joint of the concrete and repair material parts (in steel bar No. 4). The intersection element in steel bar Nos. 2 and 4 acted as cathode.

Inactivation of corrosion reaction caused by lowering the environmental temperature was also observed in Figure 8b). The macro-cell current distribution in the repair material part varied compared with that in Figure 8a). In addition, the segmented element at the center of steel bar No. 1 shifted to anode.

In Figure 8c), the segmented elements in the concrete part at the joint of the concrete and repair material parts acted as anode. Focusing on the intersections in the concrete part, the current density of the intersection element in steel bar Nos. 2 and 4 was observed in the anodic side and that of the other intersection element in the cathodic side. The segmented element in the center of the repair material part acted as anode, while other elements acted as cathode. The anodic current density was almost the same as the cathodic current density of the segmented element at the next side.

3.3 *Time-dependent variation of macro-cell corrosion*

From the experimental results of the variation in distribution of macro-cell current density in the test slabs repaired by partial patching, the following results were obtained: the shift in anode/cathode of elements was more frequent in the concrete part than in the repair material part. Anodic current densities of elements in the concrete part were generally higher than those in the repair material part. Though the elements in the concrete part at the joint mostly acted as a macro-cell cathode in the early stage of exposure, they became anodic at 517 days exposure.

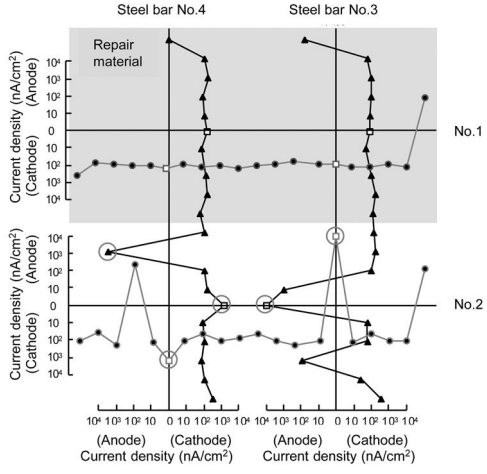

a) 24 days exposure (dry conditions)

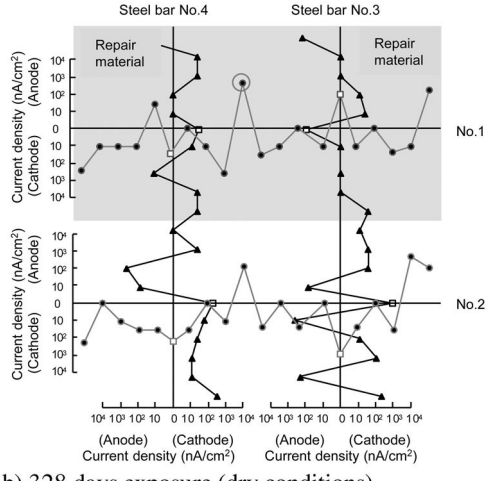

b) 328 days exposure (dry conditions)

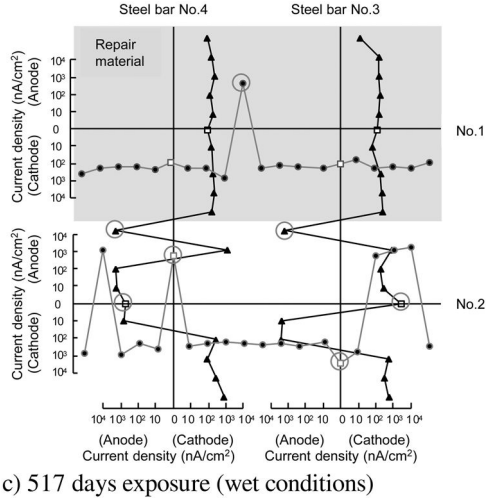

c) 517 days exposure (wet conditions)

Figure 8. Distributions of macro-cell current density in Type-1/2.

In the early stage of exposure, the elements in the concrete part near the joint acted as anode. The position of the segmented element acting as anode changed with the progress of exposure period. The change in position of the anodic element seemed to be caused by the change in electrochemical balance of all the elements in the test slab. Furthermore, it is considered that many factors may have affected the electrochemical balance, such as the dissolved oxygen concentration around the element and rust produced at the surface of the element.

The macro-cell current density of the intersection elements was almost higher than that of the segmented elements. It is considered that the corrosion current flowed into an intersection segment from two directions.

Inactivation of macro-cell corrosion reaction caused by lowering the environmental temperature was observed in the test slabs. However, the macro-cell current density distribution in the repair material part varied compared with those at other exposure periods. Hence, the distinctive macro-cell corrosion may have formed in the repair material part when the passive-film at the segmented element was destroyed. Moreover, comparing the macro-cell current densities in Types-1/4 and 1/2, it is considered that the distinctive macro-cell corrosion in the repair material formed more easily when the volume of the repair material part was larger.

4 CONCLUDING REMARKS

The time-dependent variation of the distribution of macro-cell current density was investigated to understand the long-term behavior of macro-cell corrosion formation in reinforced concrete slabs repaired by partial patching. The following conclusions were obtained from experiments on test slabs repaired by partial patching:

(1) The shift in anode/cathode of steel bars in chloride-contaminated concrete parts was more frequent than that in the repair material parts.
(2) The steel bars in chloride-contaminated concrete near the joint acted as macro-cell cathode in the early stage of exposure, however, changes in the electrochemical balance made the steel bars anodic.
(3) The macro-cell current density at the intersection in chloride-contaminated concrete became high, which is considered to be caused by a two-dimensional electrical current flow.
(4) Steel bars in the repair material part may cause the formation of distinctive macro-cell corrosion, depending on the volume of the repair part.

ACKNOWLEDGEMENT

The authors would like to extend their appreciation to Prof. Hiroshi Yokota, Hokkaido University, and Dr. Yoshikazu Akira, Toyo Construction Co. Ltd., for

their valuable suggestions regarding this research. A part of this work was supported by JSPS KAKENHI Grant Number 23360189.

REFERENCES

Maruya, T., Takeda, H., Horiguchi, K., Koyama, S. & Hsu, K-L., 2007. Simulation of steel corrosion in concrete based on the model of macro-cell corrosion circuit, Journal of Advanced Concrete Technology, 5(3), 342–362.

Nagataki, S., Otsuki, N., Moriwake, A. & Miyazato, S., 1996. The experimental study on corrosion mechanism or reinforced concrete at local repair part, Journal of Materials, Concrete Structures and Pavements, Japan Soc. Civ. Eng., 32(544), 109–119. (in Japanese)

Nagataki, S., Otsuki, N., Moriwake, A., Kamata, T. & Miyazato, S., 1997. Influence of permeability through joint on macrocell corrosion, Journal of Materials, Concrete Structures and Pavements, Japan Soc. Civ. Eng., 37(578), 31–42. (in Japanese)

Nanayakkara, O. & Kato, Y., 2009. Macro-cell corrosion in reinforcement of concrete under non-homogeneous chloride environment, Journal of Advanced Concrete Technology, 5(3), 342–362.

Port and Airport Research Institute, 2007. Manual on Maintenance and Rehabilitation of Port and Harbour Facilities, Coastal Development Institute of Technology. (in Japanese)

This page intentionally left blank

Concrete Solutions – Grantham et al. (Eds)
© 2014 Taylor & Francis Group, London, ISBN 978-1-138-02708-4

Formulation of a repair mortar based on dune sand and natural microfibers

B. Krobba, M. Bouhicha, A. Zaidi & M.F. Lakhdari
Civil Engineering Department, Structure Rehabilitation and Materials Laboratory (SREML), University of Laghouat, Algeria

ABSTRACT: This paper presents an experimental study on the development of a repair mortar based on dune sand and natural microfibers. This study permits the formulation of a simple mortar constituted of cement and dune sand and also to investigate the effect of natural microfibers added to mortars on their properties such as density, mechanical strength, shrinkage, modulus of elasticity and bonding strength. The Alfa natural microfibers (Stipa tenacissima L) used with different volume ratios were 3 to 5 mm long. The results obtained showed an enhancement in the mechanical and physical properties of mortars with natural microfibers compared to those of mortars based on the dune sand (without Alfa natural microfibers) tested in the same conditions, particularly, compressive strength, shrinkage and bonding strength.

Keywords: Natural microfibers, Dune sand, Repair mortar, Shrinkage, Mechanical strength, Modulus of elasticity, bonding strength.

1 INTRODUCTION

Construction is one of the most important and active sectors in Algeria. In recent years, considerable interest has been developed into the use of local materials in the field of building and public work to meet the huge demand of building materials. Deterioration of reinforced concrete and masonry structures such as monumental buildings, wharfs, bridges etc has occurred as in many other countries. In our country, local authorities are certainly giving a greater attention to these phenomena on either economic or sociocultural considerations.

Certainly, the rehabilitation of these structures will keep them in service and will also minimize any damage from the point of view of materials or human action (collapse, falling concrete…) in case of accidental or even environmental action. These lead us to think about new mortar, to repair these damaged structures. The developed mortar in this study was based on dune sand in very high availability especially in southern Algeria which is very low cost and natural alfa fibers. Natural fibers are a renewable resource, stronger than synthetic fibers, less costly and above all environmentally friendly. Therefore, to promote the use of cementitious building materials reinforced with vegetable fibers could be a way to achieve a more sustainable construction (Torgal, F.P & Jalali, S 2011).

These composites have considerable advantages in the building and civil engineering field where they are used to protect, repair or strengthen structures.

The literature review concluded that, in general, the incorporation of cellulose fibers significantly improves the material characteristics (ductility, mechanical strength ….), and can control the drying shrinkage cracks and plastic shrinkage (Sarigaphuti, M. et al. 1993, Ismail, M.A. 2007,Soroushian, P. & Ravanbakhsh, S. 1998, Shashi, K.S. et al. 2013, Rapoport, J.R. & Shah, S.P. 2005, Agopyana, V. et al. 2005).

Random dispersion of fibers delay cracks and limits their openings through the effects of bridging transmitted to the fracture surfaces. (Swamy, R.N, Mangat, P.S. 1975, Ardeshana, A.L. & Desai Atul, K. 2012, Kawashima, S. & S.P. Shah, S.P. 2011)

Adhesion is defined as adherence of two materials in contact or in a more colloquial way “of being stuck together”. It is not surprising that adhesion is a fundamental issue in construction engineering. The adhesion strength of repair mortar and concrete is one (if not the first) of most important technical characteristics of the repair materials. (Courard, L. & Garbacz, A. 2010, Silfwerbrand, J. & Paulsson, J. 1998, Czarnecki, L. 2008, Guangjing, X. et al. 2002).

The experimental work presented in this paper is part of the overall development program of local materials conducted by the Structure Rehabilitation and Materials Laboratory.

It is based on the following elements:

- Effect of the incorporation of Alfa vegetable fibers (Stipa tenacissima L) on physical and mechanical characteristics of mortar containing dune sand.
- Evaluation of adhesion characteristics of the repair mortar with concrete.

Table 1. Chemical composition and cement properties.

Element	%	Mineral Composition	
SiO_2	19.70	C3S	60.31
$Al2O_3$	4.52	C2S	17.41
Fe_2O_3	3.49	C3A	6.13
CaO	62.15	C4AF	11.97
MgO	1.79	Physical properties	
SO_3	2.27	Specific Density	3.04
K_2O	0.49	Specific Surface (cm^2/g)	4010
Na_2O	0.25		
Cl	0.02		
IR	1.56		
LOI	5.83		

Table 2. Characteristics of Stipa Tenacissima L fibers.

Properties	Value
Specific Density g/cm^3	0.92 – 1.10
Natural moisture content %	4.9 – 5.2
Water absorption after saturation %	180 – 220
Tensile strength MPa	103.6 – 258.4
Modulus of elasticity GPa	13.2 – 17.7
Strain at failure %	1.4 – 2.7
Hemi Cellulose %	25
Cellulose %	43.4 – 47.6
Lignin %	17. – 24.3
Extractions and others	7

2 MATERIALS AND MIX PROPORTIONS

2.1 *Materials*

The materials used in this study were Portland cement type II CEM II A 42.5, a fine silica dune sand of 0.84 fineness modulus and (0/0.5) granular size, a super plasticizer MEDAPLAST-SP40, (sulfonated polynaphthalene type) and natural microfibers of Stipa tenacissima L (so called Alfa fibres) of 3 to 5 mm length and 150 to 200 microns diameter. The chemical and physical properties of the Portland cement used are presented in Table 1 while, the main characteristics of the Stipa Tenacissima L fibers are reported in Table 2.

2.2 *Mixture*

The experimental study was carried out with a simple mortar MS (cement + sand + water), admixture mortar MA (cement + sand + water + admixture) and fiber mortar MV (cement + sand + water + admixture + fiber). Table 3 presents details of the different compositions utilized. The super-plasticizer used was 2% of the binder weight to improve the flowability of all mixtures. Eight microfiber volume ratios of 0.10, 0.20, 0.30, 0.40, 0.50, 0.75, 1.00, and 1.25% were used to prepare the mixtures MV1 to MV8, respectively.

Figure 1. Alfa fibers used in this study.

Table 3. Mixtures compositions.

Index	Cement (Kg/m^3)	Sand (Kg/m^3)	Water (Kg/m^3)	SP %	Microfibers %
MS	450	1350	315	0	0
MA	450	1350	270	2	0
MV1	450	1350	270	2	0.1
MV2	450	1350	270	2	0.2
MV3	450	1350	270	2	0.3
MV4	450	1350	270	2	0.4
MV5	450	1350	270	2	0.5
MV6	450	1350	270	2	0.75
MV7	450	1350	270	2	1
MV8	450	1350	270	2	1.25

Table 4. Mix proportions and properties of normal concrete used as substrate concrete.

Cement Kg/m^3	350
sand Kg/m^3	625
Gravel 3/8 Kg/m^3	314
Gravel 8/15 Kg/m^3	790
W/C	0.50
Slump mm	70
Density	2.300
28 days Compressive strength MPa	38
28 days Flexural Strength MPa	7

The microfibers were completely saturated with water during 24 hours.

The different types of mortars were cast in prismatic molds ($4 \times 4 \times 16\,cm^3$). The molds containing the samples were covered with plastic film, and stored in the preservation chamber.

After 24 hours, the samples were removed from the molds and stored, until the age of testing, in saturated lime water at $20 \pm 2°C$ for mechanical tests and in the environmental chamber ($T = 20°C$, $RH = 50\%$) for shrinkage tests.

The reference concrete slab specimens (Substrates) of $30 \times 30 \times 10$ cm were fabricated, according to the EN1766 standard, from a cement CPJ-CEM II/A 42.5, a crushed gravel with a maximum diameter 12.5 mm, a rolled sand (0/5) mm. Table 4 shows details of the different compositions.

In order to realize the pull off test for different types of mortars, three reference concrete slabs (substrates) were made using the mixing ratios cited in Table 4.

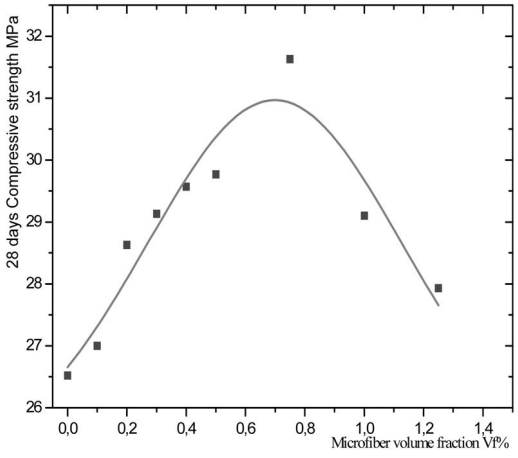

Figure 2. Relationship between fraction of microfiber and 28 day compressive strength.

The substrates have been covered with a plastic film for 24 hours after casting at a temperature of $(20 \pm 2)°C$. Then, unmolded and stored in water at $20 \pm 2°C$ for 27 days.

3 RESULTS AND DISCUSSION

3.1 *Effect of addition of microfiber on the mechanical strength*

Figure 2 shows the effect of adding fibers on the compressive strength of mortars. It can be observed that the maximum value of the compressive strength is about 31.63 MPa corresponding to the optimum value of microfiber volume ratio (V_f) of 0.75%, from which the strength decreased while maintaining a value greater than that of MS. The increase in the compressive strength is due to the addition of optimum V_f of 20% approx.

In contrast to the compressive strength, the incorporation of microfibers in the mortars led to a nearly linear increase in tensile strength as shown in Figure 3. However, the gain in strength obtained by addition of the maximum microfibers volume ($V_f = 1.25\%$) was only 16%. These two finding results are in good agreement with those published in the literature.

3.2 *Effect of addition of microfiber on the shrinkage*

The shape of curves (Figure 4) representing the shrinkage evolution as a function of the microfiber volume ratio allows us to draw the following observations:

- Almost all of the shrinkage is obtained after 2 weeks.
- The effect of an overdose of fiber although favorable at the young age (decrease of shrinkage), gives an excessive value at 28 days.
- The value of Vf = 0.75% exhibits the lowest shrinkage at 28 days, with a decrease of 13.40% compared to that of the control mortar (without fiber) as shown in Figure 5.

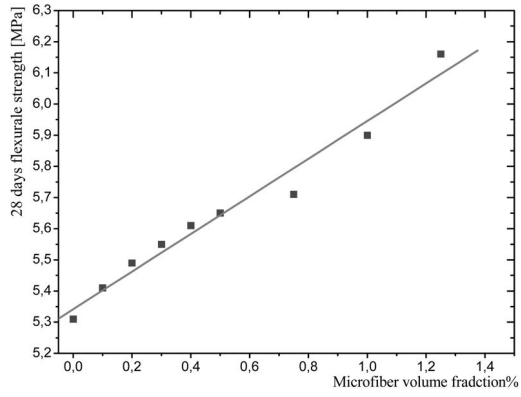

Figure 3. Relationship between volume fraction of microfibers and 28 day flexural strength.

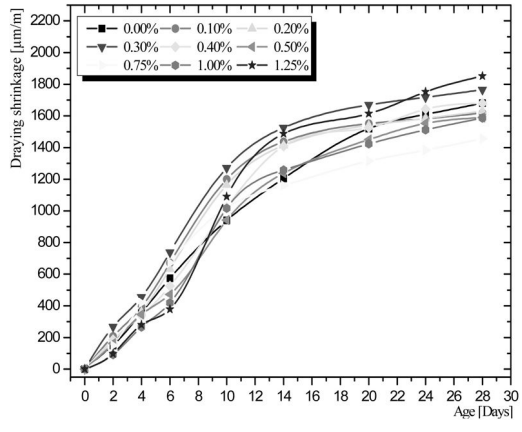

Figure 4. Variation of drying shrinkage with volume fraction of fibres at different ages.

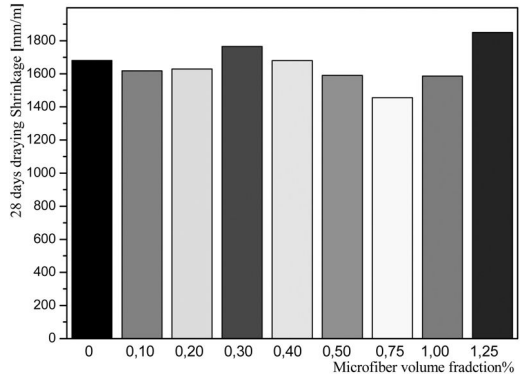

Figure 5. 28 day drying shrinkage vs. volume of microfibre.

From these results, it can be concluded that the microfiber volume ratio Vf of 0.75% seems to be an optimum value.

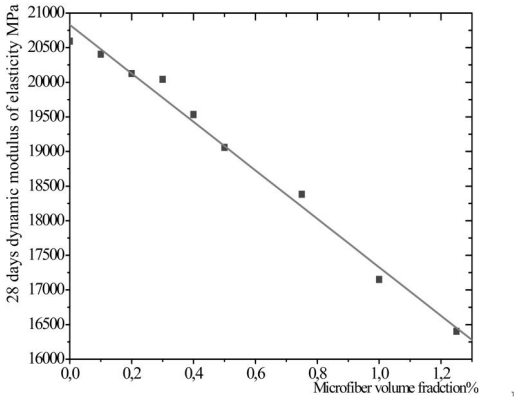

Figure 6. 28 day dynamic modulus of elasticity vs. volume fraction of fibre.

Figure 7. Pull off test.

3.3 *Effect of addition of microfibers on dynamic elasticity modulus*

The results of the evaluated dynamic elasticity modulus of mortars, presented in Figure 6 , for different values of microfiber volume show an almost linear decrease of the dynamic elasticity modulus which remains higher than that of the simple mortar MS.

The above presented results suggest that a rate of 0.75% improves the compressive strength by some 19% and reduces the shrinkage about 13%. As a consequence, this rate is considered as the optimum value expected, despite the decrease in the modulus, but it remains higher with respect to the simple mortar.

3.4 *Adhesion*

The adhesion between mortar and concrete substrate is one of the most important factors that affect the reliability and durability of the repaired concrete structures. The pull-off test as described in EN 1542-3 permits to determine the bond strength between mortar and concrete (figure 7).

The failure modes were observed: in mortar, at concrete/mortar interface, and in concrete (figure 8).

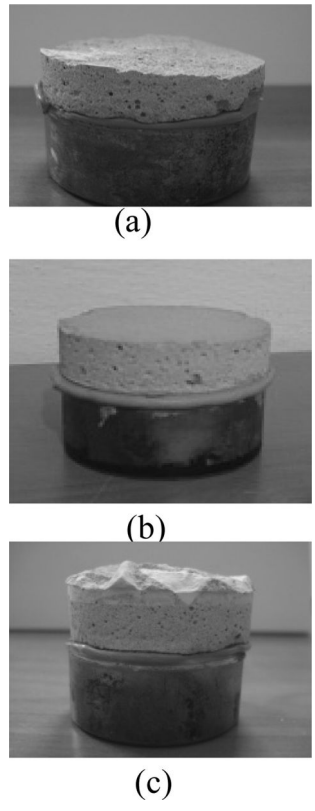

Figure 8. Failure modes: (a) In mortar (b) In interface (c) In concrete.

The bond stresses and the failure modes obtained from the different mortars tested are presented in Table 5.

The results show that the adhesion of the simple mortar (MS) with a concrete slabs is characterized by lower strengths with respect to the fiber mortar (MV) and admixture mortar (MA). These two last mortars can improve the bond strength by 15% and 13% compared to simple mortar, respectively. This gain in the bond strength obtained seems to be directly related to the rate of cracking caused by the shrinkage which is one of the factors affecting the adhesion between mortar and concrete. These results are consistent with those obtained by other researchers.

Furthermore, whatever the type of mortar, the bond strength is greater than the minimum value (1.5 MPa) required by the standard EN1504-3.

4 CONCLUSIONS

In this research, the effect of Alfa natural microfiber on bond strength, compressive strength, flexural strength and shrinkage were investigated and the results can be concluded as follow.

Table 5. Bond strengths and failure modes of mortars tested.

	Simple mortar MS		Admixture mortar MA		Fiber mortar MV	
Sample	Failure strength [MPa]	Failure mode	Failure strength [MPa]	Failure mode	Failure strength [MPa]	Failure mode
1	2.18	Interface	2.52	Concrete	2.57	Concrete
2	2.22	Concrete	2.50	Concrete	2.52	Concrete
3	2.15	Interface	2.39	Interface	2.49	Interface
4	2.13	mortar	2.41	Interface	2.50	Concrete
5	2.23	Concrete	2.47	Concrete	2.49	Concrete
Average value	**2.18**		**2.46**		**2.52**	

- The compressive strength results show that the use of 0.75% of alfa micro-fiber increases the compressive strength and the flexural strength by about 15%, and 29.83% respectively and this is due to the enhancement in mechanical bond between the cement paste and the alfa micro-fibers.
- The shrinkage results show that the use of 0.75% of alfa micro-fiber decreases the shrinkage by about 12%.
- The fiber mortar and admixture mortar can improve the bond strength by about 15.37% and 12.71% respectively compared with simple mortar. This gain in the bond strength obtained seems to be directly related to the rate of cracking caused by the shrinkage.
- The adhesion strength of different mortars developed is greater than the minimum value (1.50 MPa) provided by the standard 1504-3

REFERENCES

Agopyan a, V. & Savastano Jr.b, H. & John a, V.M. & Cincotto a, M.A. *Developments on vegetable fibre–cement based materials in São Paulo, Brazil: an overview* Cement & Concrete Composites 27 (2005) 527–536.

Ardeshana, A.L. & Desai Atul, K. *Durability of fiber reinforced concrete of marine structures.* International Journal of Engineering Research and Applications Vol. 2, Issue 4, July-August 2012, pp.215–219.

Courard,L. & Garbacz, A. *Surfology: what does it mean for polymer concrete composites?* Restor Build Monum 2010;16(4/5):291–302.

Czarnecki, L.*Adhesion-A challenge for concrete repair.* Concrete Repair, 2ND international conference on concrete repair, rehabilitation and retrofitting (ICCRRR) Cape Town, South Africa, Novembre 24–26, 2008, 935–940.

EN 1766 *Products and systems for the protection and repair of concrete structures. Test methods reference concretes for testing* 2000.

Guangjing, X. & Jinwei, L. & Gengying, L.*A way for improving interfacial transition zone between concrete substrate and repair materials.*Cement and Concrete Research 2002. 32, 1877–1881.

Ismail, M.A. *Compressive and tensile strength of natural fibre-reinforced cement base composites.* Al-Rafidain Eng 2007;15:42–51.

Kawashima, S. & S.P. Shah, S.P. *Early-age autogenous and drying shrinkage behavior of cellulose fiber-reinforced cementitious materials.* Cement & Concrete Composites 33 (2011) 201–208.

NEN-EN 1504-9. *Products and systems for the protection and repair of concrete structures – Part 9. 2008.*

NEN-EN 1504-3. *Products and systems for the protection and repair of concrete structures – Part 3; 2005*.

NEN-EN 12636. Products and systems for the protection and repair of concrete structures – test methods – determination of the adhesion concrete to concrete; 1999.

Rapoport, J.R. & Shah, S.P. *Cast-in-place cellulose fiber-reinforced cement paste, mortar, and concrete.* ACI Mater J 2005;102(5):299–306.

Sarigaphuti, M. & Shah,S.P. & Vinson,K.D. *Shrinkage cracking and durability characteristics of cellulose fiber reinforced concrete.* ACI Mater J 1993;90(4):309–318.

Shashi, K.S, & Aditya, A.K. & G.D. Ransinchung, R.N. & Praveen K. *Micro Fiber Reinforced Cement Paste and Mortar Overlays*. A Review International Journal of Pavement Research and Technology Vol.6 No.6 Nov. 2013.

Silfwerbrand, J. & Paulsson, J. *Better bonding of bridge deck overlays.* Concr Int 1998;10:56–61.

Soroushian, P. & Ravanbakhsh, S. *Control of plastic shrinkage cracking with specialty cellulose fibers.* ACI Mater J 1998;95(4):429–35.

Swamy, R.N, Mangat, P.S. *The onset of cracking and ductility of fibre concrete.* Cem Concr Res 1975;5:37–53.

Torgal, F.P. & Jalali, S. *Cementitious building materials reinforced with vegetable fibres: A review*. Construction and Building Materials 25 (2011). 575–581.

This page intentionally left blank

Concrete Solutions – Grantham et al. (Eds)
© 2014 Taylor & Francis Group, London, ISBN 978-1-138-02708-4

Alternative repair system for concrete using microencapsulated healing agents

C. Litina, A. Kanellopoulos & A. Al-Tabbaa
Engineering Department, University of Cambridge, Cambridge, UK

ABSTRACT: An intrinsic self-sustained recovery system is proposed based on the inclusion of repair agents within a concrete matrix. Three different microencapsulation protocols for the encapsulation of an acrylic-based repair material are being investigated. Polyurethane (PU), urea-formaldehyde (UF) and tetraethylorthosilicate (TEOS) based shell microcapsules were synthesised through an in situ interfacial polymerisation process. Confirmation of the encapsulation process and characterisation of structure, chemistry and thermal stabilities was performed by scanning electronic microscope (SEM), thermal analysis (TG-DTA) and FTIR spectroscopy. The results showed that PU, UF and TEOS microcapsules containing methylmethacrylate (MMA) were successfully prepared via the suggested protocols. The average microcapsule size was 0.3, 1.9 and 3.5 μm, respectively. High yields of free flowing powder were produced with all methods. Chemical and thermal characterisation infer that the produced spherical capsules satisfy the requirements for use in the proposed self-repair system.

1 INTRODUCTION

Maintaining the functionality of concrete infrastructure is recognised as a major concern in construction practices. Concrete is susceptible to numerous environmental factors which generate cracking that propagates through the material causing damage to accumulate and lead to failure (Schlangen & Joseph 2009). Therefore damage control and repair at the initial stages of crack manifestation could prove beneficial by delaying the requirements for external, often costly, patch repair works. Moreover it can address the issue of the remote location of concrete installations which prohibits manual repair of such systems.

Our research proposes a system of intrinsic self-sustained recovery/repair system based on the inclusion of the repair agents within the matrix. Thus repair is attained not through external post-damage application of appropriate repair agents but through the internal triggered release of these materials in the damaged location. The concept of creating a self-healing encapsulated system is not novel. Formative work by Dry (1994) addressed the repair of concrete structures through the embedment of a hollow glass tubing system within the cementitious matrix for the delivery of repair material. Nonetheless, the use of a brittle and bulky system would impose further limitations during the construction phase.

Therefore the use of micron-sized polymeric vessels as carriers of the repair agents within the cement matrix is suggested. These will hinder the accumulation of damage by bonding the crack surfaces and controlling the propagation of cracks. The concept of microencapsulation of self-healing agents has been widely investigated as far as polymers and polymeric composites are concerned (Blaiszik et al. 2009; Youngblood & Sottos 2008; White et al. 2001). However these concepts have been only recently expanded to the field of cementitious composites (Gilford et al. 2013; Yang et al. 2011; Pelletier et al. 2011).

Here, we report on the design and characterisation of three different types of capsules containing an acrylic-based repair agent. Polyurethane, urea-formaldehyde and organo-silicone have been considered to meet the demanding criteria required for microencapsulated systems (Brown et al. 2003; Saihi et al. 2006; Yang et al. 2011; Wang et al. 2008; Pelletier et al. 2011). Thus, they were investigated as appropriate shell materials. Methyl-methacrylate has been selected as a potential repair material due to its durability to chlorides and carbonation (Dry 2000; Van Tittelboom et al. 2011). Microcapsules were synthesised in situ through a simple one-step interfacial polymerisation process. Shell morphology, encapsulation yield, thermal stability and chemical structure were evaluated through SEM, TGA and FTIR spectroscopy.

2 MATERIALS AND METHODS

2.1 *Microcapsule materials*

The core material used in the encapsulation was methyl-methacrylate (MMA), used as received from Fisher Scientific, UK. The microcapsule wall-forming materials included urea, resorcinol, formalin (37% formaldehyde in water), polyethylene glycol (PEG

400) (Fisher Scientific, UK), ammonium chloride (ACROS Organics, UK) and tetraethoxysilane (TEOS) (Sigma-Aldrich, UK). Diphenyl methylene diisocyanate (MDI), a blend of MDI isomers, as diisocyanate monomer and dibutyl tin dilaurate (DBDL) as catalyst were obtained from Sigma-Aldrich, UK. Three different emulsifiers/stabilisers were used; poly (ethylene-alt-maleic anhydride) (EMA) (Aldrich, UK), Tween 80 and Span 85 (Sigma, UK). EMA powder was added to deionised water and mixed overnight (800 rpm) at 55°C to obtain a 2.5% (wt/vol) aqueous surfactant solution.

Solvents (toluene and cyclohexane) were purchased from Sigma-Aldrich, UK. All these products were used without further purification.

2.2 *Characterisation of microcapsules*

Thermal stability of produced microcapsules was tested using Thermo gravimetric Analysis (TGA) on a Perkin Elmer STA 6000. Small quantities of microcapsules (10–20 mg) were heated from 30 to 500°C at a rate of 10°C/min in air.

Verification of the chemical composition of the produced microcapsules was performed on a computerised Fourier Transform Infrared Spectrophotometer (FTIR, SPECTRUM 100, Perkin Elmer) in transmission mode. Spectra were collected from 600 to 4000 cm^{-1} (resolution of 4 cm^{-1}). All the output spectra were the result of the combination of 32 sequential scans for noise reduction.

Images of dried microcapsules were obtained using scanning electron microscopy (SEM, EVO LS 15, Carl Zeiss). Capsule diameter measurements and size distribution was estimated using ImageJ analysis software. Samples were prepared by dropping an aliquot (ca. 40 μl) of the particle suspension onto a SEM stub (12.5 mm diameter) and oven drying at 40°C for 30 min. The resulting powder sample was sputter coated with a thin layer of gold ($\sim$10 nm).

2.3 *Encapsulation procedure*

2.3.1 *Synthesis of PU microcapsules*

At room temperature three separate solutions were prepared. Initially, 2.5 g of Span 85 were dissolved in 90 ml of toluene (O1). A 15 ml aliquot was taken from this solution and placed into a separate beaker and set aside. 1.77 g of methylene diiosocyanate (MDI) and 0.12 g of dibutyl tin dilaurate (DBTD) were dissolved in the former aliquot (O2). 3.15 g of polyethylene glycol (PEG 400) and 6.67 g of core material were dispersed in 45 ml of deionised water (W).

Subsequently, the aqueous phase was added to the organic phase (O1) and emulsified at 3000 rpm for 5 min using an IKA T25 ULTRA TURRAX homogeniser. Finally, the solution O2 was added and stirred at 700 rpm for 10 minutes at room temperature. Then stirring was reduced to 350 rpm and the temperature was gradually raised to 63°C. The system was allowed to react for 4 hours before cooling down to ambient temperature. The formed particles were decanted, redispersed in deionised water and allowed to stabilize overnight. The formed suspension was subsequently vacuum-filtered and washed with deionised water and ethanol to remove unreacted and residual materials. Microcapsules were oven-dried for 3 hours at 40°C and kept in sealed containers prior to further analysis.

2.3.2 *Synthesis of UF microcapsules*

Microcapsules containing MMA were prepared by an in situ urea-formaldehyde microencapsulation procedure adapted from previously reported shell walls (Brown et al. 2003; Blaiszik et al. 2009).

At room temperature, 100 ml of deionised water was placed in a 600 ml beaker, along with 25 ml of 2.5% (wt/vol) EMA. Subsequently, 2.5 g urea, 0.25 g ammonium chloride and 0.25 g resorcinol were diluted in the aforementioned solution. After the addition of the wall-forming materials the pH was adjusted to 3.5 by the drop-wise addition of sodium hydroxide and hydrochloric acid. The beaker was then placed on a combined magnetic stirrer hot-plate equipped with a stir bar (40 mm diameter) and the core phase of 30 ml of MMA was dispersed in the beaker at a desired agitation rate (800 rpm) for 10 min. After 10 min, 6.33 g formalin was added and the temperature was increased from ambient to 55°C. The reaction proceeded under continuous agitation (350 rpm) at constant temperature (55°C) for 4 h. After 4 h the beaker was removed from the hot-plate and allowed to cool to ambient temperature. The microcapsule suspension was vacuum-filtered and washed several times to remove unreacted wall forming and residual core materials. Microcapsules were oven-dried for 3 hrs at 40°C and kept in sealed containers prior to further analysis.

2.3.3 *Synthesis of TEOS microcapsules*

Silica shell microcapsules were prepared via the hydrolysis and subsequent polycondensation of tetraethoxysilane (TEOS) in a surfactant stabilised water-in-oil emulsion. In order to catalyse the hydrolysis of silane, low pH is required. Hydrochloric acid was used as the acidic catalyst. 0.04 g of the core material and 0.2 g of Tween 80 were dissolved into 2.68 ml of 2M HCl solution. Subsequently, the above aqueous solution was added into 50 ml of cyclohexane solution containing 10.0 g of Span 85. After vigorous agitation at 3000 rpm for 15 min 2.5 ml of TEOS was added into the formed W/O emulsion.

The mixture was then sealed to prevent the evaporation of solvent and allowed to age under constant agitation for 24–48 hrs.

The formed suspension was subsequently vacuum-filtered and washed with deionised water and ethanol to remove unreacted and residual materials. Microcapsules were oven-dried for 3 hrs at 40°C and kept in sealed containers prior to further analysis.

Table 1. Yield and mean diameter of produced microcapsules.

Capsule Type	Microcapsule yield (%)	Mean diameter (μm)
UF_MMA	84.1	1.9 ± 1.06
PU_MMA	58.8	0.3 ± 0.12
TEOS_MMA	94.8	3.5 ± 2.6

3 RESULTS AND DISCUSSION

Three synthetic processes for the production of MMA filled microcapsules were investigated. All methods were based on the classic physicochemical technique of interfacial polycondensation, using however different reacting monomers to yield composite shells. Thus, three different types of microcapsules were produced; Poly-Urethane shell, Urea-Formaldehyde shell and Silica shell.

3.1 *Microcapsule size and distribution*

The surface and shell morphology of the developed microcapsules are shown in Figure 1. The high shear rate applied for the emulsification of the aqueous phase lead to submicron capsules. A modification of the rate of agitation would allow the synthesis of bigger particles (Blaiszik et al. 2008).

All microcapsules appeared to retain a spherical structure. SEM images of PU microcapsules revealed capsules with average diameter of 300 nm and relatively smooth and non-porous walls. They appeared individually distributed with no visible conglomeration. Conversely, UF microcapsules had mean diameter of 1.9 μm and rough shell walls. The structures showed extended conglomeration. Microcapsules prepared with silica shell had higher size distribution (mean diameter 3.5 μm). Furthermore, it was possible to observe collapsed and incomplete (highly porous) structures. This could have been due to uncompleted polycondensation of the TEOS or insufficient percentage of wall forming materials.

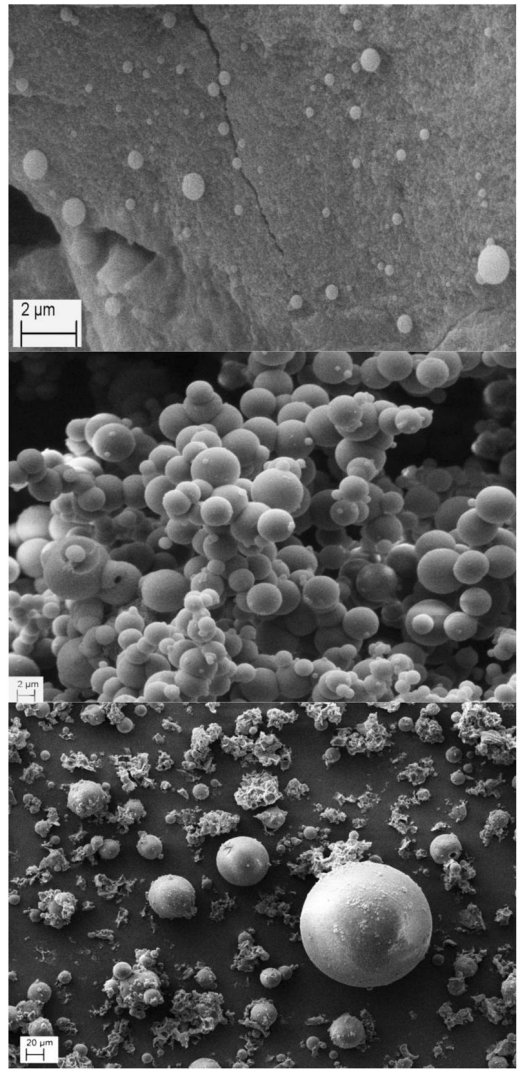

Figure 1. SEM images of produced (A) PU, (B) UF and (C) silica shell (TEOS) microcapsules.

3.2 *Yield analysis*

Microcapsule yield, shown in Table 1, was measured by the mass of capsules collected as a solid residue at the end of the experimental process compared to the mass of solids used in the encapsulation (i.e. shell wall forming materials and core). The yield appeared dependent on the wall forming materials, ranging from a low 58.8% to 94.8% for capsules prepared with MDI and SPAN 85 and TEOS correspondingly.

3.3 *Thermal analysis and stability*

In order to evaluate the chemical composition and stability of the produced microcapsules, TGA analysis of the samples was conducted. Indicative mass loss and heat flow curves of the produced PU, UF and TEOS capsules are presented in Figure 2.PU microcapsules showed three endothermic regions (Di Credico et al. 2013). The first can be located under 150°C signifying evaporation of water and residual solvents. The second between 280°C and 320°C is due to the MDI evaporation. Lastly the third is above 420°C due to the extensive decomposition of shell wall materials. Correspondingly three of the weight loss transitions are connected to the heat flow curves. It can be observed that microcapsules experienced significant weight loss at 250°C and 350°Cwhich is in good agreement with previous literature findings (Di Credico et al. 2013; Saihi et al. 2006).

Figure 2B presents thermal stability curves for UF capsules. Two distinct transitions were observed in the TGA curves following accordingly the endothermic and exothermic peaks of the heat flow (Liao et al. 2011). Two endothermic peaks are observed between 250–350°C. These could be attributed to the

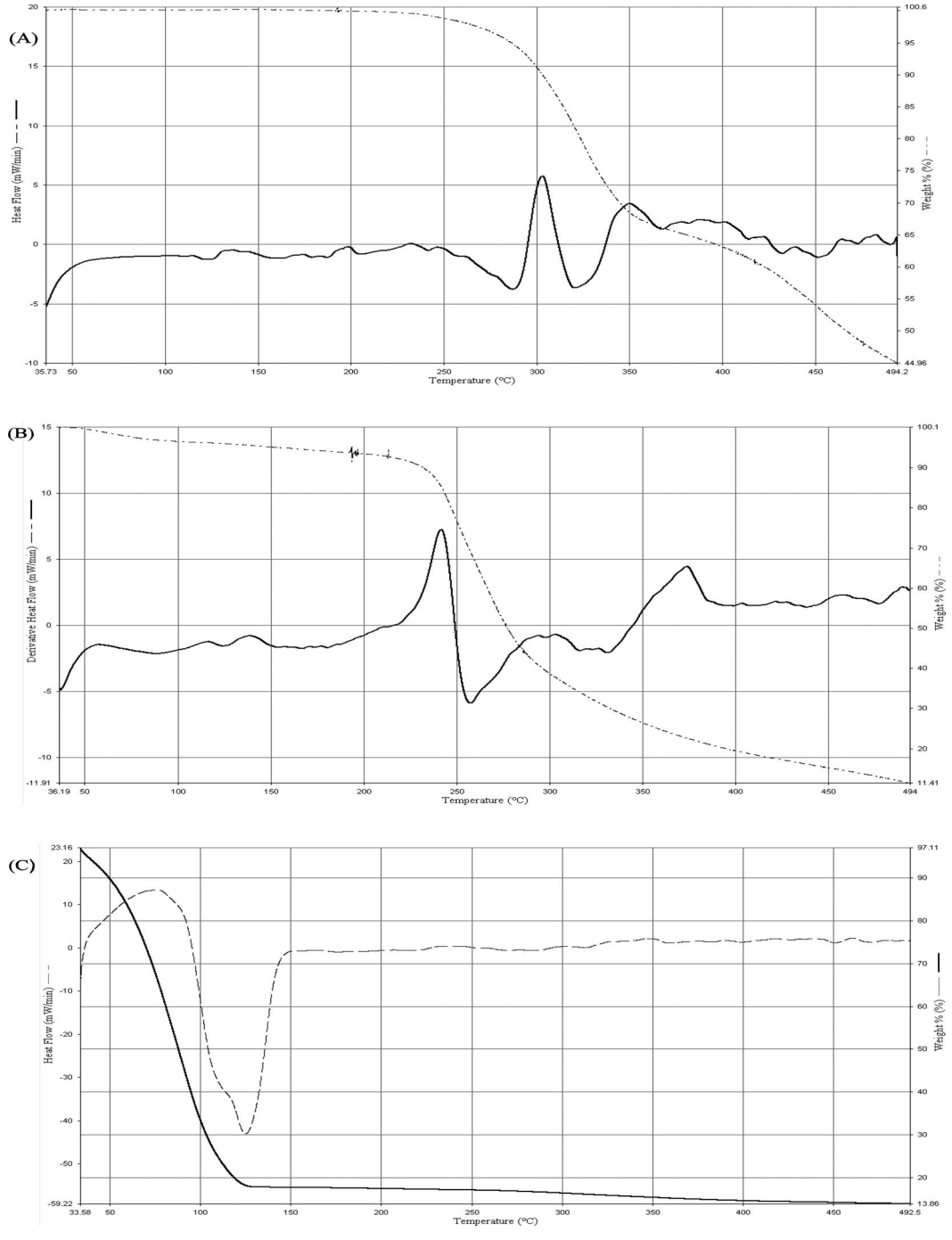

Figure 2. Mass loss and heat flow as a function of temperature of (A) PU, (B) UF and (C) silica shell (TEOs) microcapsules.

evaporation of water and free formaldehyde at lower temperatures and the decomposition of the UF shell as the temperature increases (Camino et al. 1983). The latter is accompanied by a steep weight loss. Concurrently two exothermic peaks, the first at 240°C and the second between 380–400°C manifest curing of the core material and continuous polymerisation. Further fragmentation of the residuals is evident above 450°C.

As illustrated in Figure 2C the TGA curves of TEOS microcapsules depict significant weight loss, reaching almost 80%, at 50°C followed by a mild 5% drop up to 500°C. This is correlated with the steep

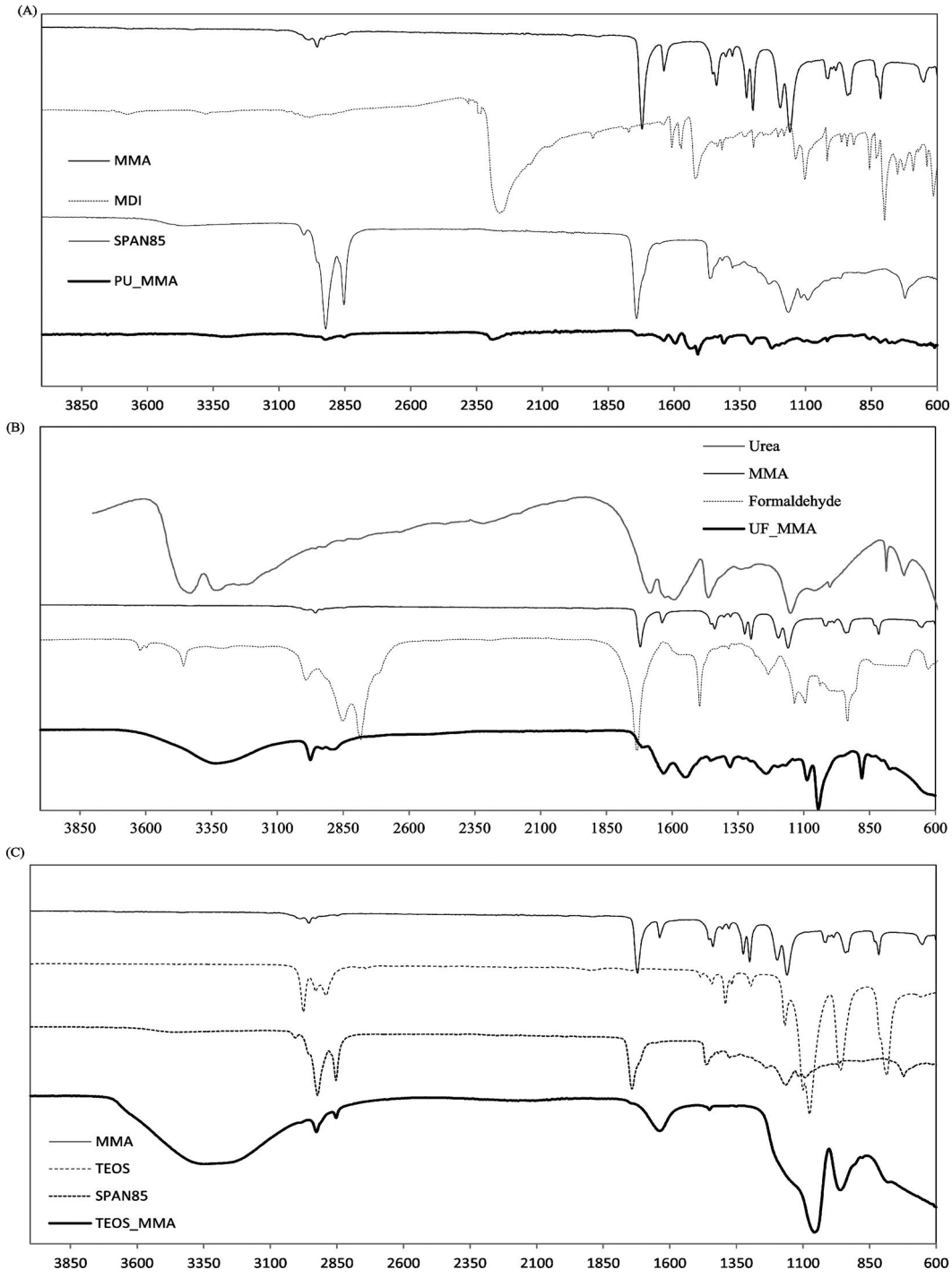

Figure 3. Transmission infrared spectra of produced microcapsules: A) PU; B) UF and C) TEOS shell.

endothermic peak between 80 and 130°C. This loss is more pronounced than relative literature findings. (Wang et al. 2008). The initial drop could be attributed to the incomplete removal of solvents and water during the drying process while the latter to the evaporation of chemically bound –OH from the silanol groups (Wang et al. 2008).

Overall PU and UF microcapsules appear more chemically stable bellow 200°C, with only small evaporation of moisture occurring between 70 and 100°C,

indicating that the suggested compositions offer good thermal viability.

3.4 *Chemical characterisation*

FTIR spectra of the synthesised microcapsules, wall-forming and core materials are presented in Figure 3. IR spectrum (Fig. 3A) suggests bands which can be assigned to groups of MDI and Span 85; C-H at 2287 cm^{-1}, aromatic group at 1594 cm^{-1}, N=C=O at 2184 and 2118 cm^{-1} for MDI; ether group at 1051 cm^{-1}, C=O at 1743 cm^{-1} for Span 85 (Saihi et al. 2006). However the intensity of the peaks has reduced compared to the pure materials which provides evidence for the reaction of these materials.

This reaction leads to the formation of carbamate groups. The FTIR spectrum of PU microcapsules shows characteristic overlapping peaks of urethane and urea at 3342 cm^{-1} (N-H stretching) and 1600 cm^{-1} (C=N stretching); C=O and C-O peaks were observed at 1743, 1637 and 1233 cm^{-1} and COO- at 1413 cm^{-1}. These indicate the presence of the NHCOO (urethane) group.

In addition we can assume the presence of MMA groups such as C-H at 2930 cm^{-1}, carbonyl stretch C=O and C-O between 1750–1700 and 1310–1000 cm^{-1} and CH_3 between 1250–800 cm^{-1}

As illustrated in Figure 3B the spectrum of UF microcapsules shows the main characteristic of urea-formaldehyde polymers. The broad adsorption centred at 3330 cm^{1} is characteristic of the stretching vibrations of amine groups. Furthermore, amide groups evident, mainly C=O, C-N and N-H deformation, at 1634, 1544 and 1243 cm^{-1} and C-H mode at 1455 and 1380 cm^{-1} confirm the presence of UF. Typical bands of MMA around 2950 cm^{-1} and 800 cm^{-1} confirm that the encapsulation was realised.

Lastly, Figure 3C shows the spectra of silica microcapsules and the corresponding shell and core materials (TEOS and MMA). Peaks at 1060 and 960 cm^{-1} can be ascribed to the vibrations of the characteristic silanol groups (Si-OH) (Karmakar et al. 2000). The same peaks appear for the pure TEOS which further infers the synthesis of silica shells. The results were also confirmed by the disappearance of the bands at 1743 cm^{-1} corresponding to the residual surfactants. Concurrently, C-H stretching at 2930 cm^{-1} and carbonyl groups C=O at 1630 cm^{-1} proved the successful encapsulation of MMA into silica microcapsules.

4 CONCLUSION

Different shell protocols for the encapsulation of a repair agent were investigated. PU, UF and TEOS microcapsules containing MMA were successfully prepared via polymerization in an O/W emulsion. Simple and versatile preparation of stable and resistant microcapsules was achieved. FTIR analysis confirms the presence of both the core and shell materials while the stability of the proposed structures is confirmed by TGA experiments. Although the size of the microcapsules lies within the range of sub microns the suggested composition appears robust for use in self-healing applications. In all cases, the yield of the process was more than satisfactory.

Investigation is under way for testing the behaviour of the capsules within a cementitious matrix.

ACKNOWLEDGEMENTS

Financial support from the Engineering and Physical Sciences Research Council (EPSRC) and the Hellenic States Scholarship Foundation for the PhD study of the first is gratefully acknowledged. Support from EPSRC for the Materials for Life project (EP/K06631/1) is also gratefully acknowledged.

REFERENCES

Blaiszik, B., Sottos, N.R. & White, S.R. 2008. Nanocapsules for self-healing materials. *Composites Science and Technology*, 68(3–4), pp. 978–986.

Blaiszik, B.J. et al. 2009. Microcapsules filled with reactive solutions for self-healing materials. *Polymer*, 50(4), pp. 990–997.

Brown, E.N. et al. 2003. In situ poly(urea-formaldehyde) microencapsulation of dicyclopentadiene. *Journal of Microencapsulation*, 20(6), pp. 719–730.

Camino, G., Operti, L. & Trossarelli, L. 1983. Mechanism of thermal degradation of urea-formaldehyde polycondensates. *Polymer Degradation and Stability*, 5(3), pp. 161–172.

Di Credico, B., Levi, M. & Turri, S. 2013. An efficient method for the output of new self-repairing materials through a reactive isocyanate encapsulation. *European Polymer Journal*, 49(9), pp. 2467–2476.

Dry, C. 2000. Three designs for the internal release of sealants, adhesives, and waterproofing chemicals into concrete to reduce permeability. *Cement and Concrete Research*, 30, pp. 1969–1977.

Gilford, J. et al. 2013. Dicyclopentadiene (DCPD) and Sodium Silicate Microencapsulation for Self-Healing of Concrete. *Journal of Materials in Civil Engineering*, p.130712025159006.

Karmakar, B., De, G. & Ganguli, D. 2000. Dense silica microspheres from organic and inorganic acid hydrolysis of TEOS. *Journal of Non-Crystalline Solids*, 272(2-3), pp. 119–126.

Liao, L. et al. 2011. Preparation and characterization of microcapsule containing epoxy resin and its self-healing performance of anticorrosion covering material. *Chinese Science Bulletin*, 56(4–5), pp. 439–443.

Pelletier, M.M. et al. 2011. *Self-healing concrete with a microencapsulated healing agent*, Kingston, USA.

Saihi, D. et al. 2006. Microencapsulation of ammonium phosphate with a polyurethane shell. Part II. Interfacial polymerization technique. *Reactive and Functional Polymers*, 66(10), pp. 1118–1125.

Schlangen, E. & Joseph, C. 2009. Self-healing Processes in Concrete. In S. K. Ghosh, ed. *Self-healing Materials Fundamentals, Design Strategies, and Applications*. WILEY-VCH Verlag GmbH & Co. KGaA, pp. 141–179.

Van Tittelboom, K. et al. 2011. Methyl methacrylate as a healing agent for self-healing cementitious materials. *Smart Materials and Structures*, 20(12), p.125016.

Wang, J.-X. et al. 2008. Direct encapsulation of water-soluble drug into silica microcapsules for sustained release applications. *Materials Research Bulletin*, 43(12), pp. 3374–3381.

White, S.R. et al. 2001. Autonomic healing of polymer composites. *Nature*, 409(6822), pp. 794–7.

Yang, Z. et al. 2011. A self-healing cementitious composite using oil core/silica gel shell microcapsules. *Cement and Concrete Composites*, 33(4), pp. 506–512.

Youngblood, J.P. & Sottos, N.R. 2008. Bioinspired Materials for Self-Cleaning and Self-Healing Self-Cleaning Surfaces?: *MRS Bulletin*, 33(August), pp. 732–741.

This page intentionally left blank

Concrete Solutions – Grantham et al. (Eds)
© 2014 Taylor & Francis Group, London, ISBN 978-1-138-02708-4

Towards cost efficient bacteria based self-healing marine concrete

D. Palin, V. Wiktor & H.M. Jonkers
Delft University of Technology, Faculty of Civil Engineering and GeoSciences, Materials & Environment Research Section, Delft, The Netherlands

ABSTRACT: Marine concrete structures are exposed to one of nature's most inhospitable environments. Bacteria based self-healing concrete is a lab proven concept, however if it is to be applied in the marine environment key challenges need to be addressed. A number of economically attractive organic carbon sources as potential bio-mineral precursor compounds and bacteria fit for the unique and challenging environment posed by marine concrete are to be investigated. Organic compounds were selected based on their cost and solubility, while mortar compatibility was assessed though their 1% weight addition to cement paste during mixing. Based on strength development at 2, 7, 28 and 56 days, magnesium acetate, saccharin sodium, gum Arabic and magnesium lactate seem promising. Bacterial strains fit for self-healing marine concrete have also been isolated. The organic compounds and isolated bacteria represent significant strides on the way towards applied bacteria based self-healing marine concrete.

1 INTRODUCTION

Marine concrete structures are exposed to one of nature's most inhospitable environments. Many physical and chemical phenomena are usually interdependent and mutually reinforcing in the deterioration of marine exposed concrete. Cracking due to physical effects increases concrete permeability paving the way for harmful chemical interactions between seawater, concrete and embedded steel reinforcement. A novel approach to self-healing is a biologically inspired technique, whereby bacteria immobilized in concrete are able to precipitate crack healing minerals, effectively sealing against the ingress of aggressive chemicals.

Concrete may appear at first to be a hostile environment for life. There are however natural analogues where bacteria thrive. Bacteria found in soda lakes are desiccation- and/or alkali-resistant, and typically spore formers. Bacterial spores are life's true survivors, highly resistant to mechanical and chemical stresses, they are able to lie dormant for prolonged periods of time until conditions are right for germination (Sagripanti and Bonifacino, 1996). In his biological approach to self-healing concrete Jonkers (2007) developed a two-component agent consisting of bacterial spores and an organic carbon source. Following spore germination the bacteria were able to metabolize the organic carbon source inducing a calcium carbonate ($CaCO_3$) crack healing precipitate. It was observed however that mineral production of an unprotected healing agent was limited. Wiktor and Jonkers (2011) later protected a healing agent in porous expended clay particles doubling the crack healing capacity as compared to controls, while providing evidence that the agent remained functional several months after casting.

Bacteria based self-healing concrete is a lab proven concept, however if it is to be applied in the marine environment, key challenges need to be addressed. Bacteria based self-healing capacity is directly related to the amount of organic carbon or food present for bacterial metabolism (Jonkers, 2007). For the technology to be cost effective, the food then should be cheap, while being readily accessible (water soluble) to the bacteria and having no adverse effect on concrete properties when included. As Jonkers (2007) pointed out, bacteria suitable for self-healing concrete should be alkali tolerant (alkaliphilic) spore formers. Add to this the harsh environment faced by marine concrete, then bacteria suitable for marine concrete applications must also be salt tolerant (halophilic) and capable of growing at low temperatures (psychrophilic). Moreover, oxygen supply in a marine concrete system may become restricted (Tuutti, 1882, Neretnieks, 1985) and so bacteria fit for application in marine concrete should be able to respire using an alternative electron acceptor with the depletion of oxygen. Many molecules may be used for bacterial respiration, however nitrate (NO_3^-) after oxygen provides the highest reduction potential and so could be added to the self-healing agent.

The objective of the current study is then to identify foods and isolate bacteria suitable for the development of a bacteria based self-healing agent for application in marine concrete.

Table 1. Selected organic compounds, including their water solubility and cost.

Organic Compound	Solubility (g/l)	Cost ($/kg)
L-rhamnose	50	1
Maltodextrin	100	0.5
Magnesium D-gluconate	50	0.7
Magnesium L-lactate	73	1
D-(+)-xylose	40	1
Gum arabic	200	1
Saccharin sodium	100	1
D-sorbitol	182	1
(+)-magnesium L-ascorbate	10	1
Magnesium-acetate	1200	0.4

Table 2. Cement, water and aggregate composition for mortar cubes.

Constituents	Amount (g/l)
Cement (CEM III/B 42.5 N LH, ENCI)	494
Water	247
Aggregate size fraction (mm):	
1–2	608
0.5–1	426
0.25–0.5	167
0.125–0.25	319

2 MATERIALS AND METHODS

2.1 *Organic bio-mineral precursor compounds*

A number of organic compounds were selected based on their water solubility and cost, for their encapsulation and inclusion in concrete as potential bio-mineral precursor compounds. Some organics however if released during mixing may have an adverse effect on concrete properties. Based on the worst-case scenario selected organic compounds were directly added at 1% of the cement weight to the cement paste during mixing. All compounds were purchased and information gained on their water solubility, from Sigma-Aldrich. Costs however are based on the lowest quote found per ton from various vendors for equivalent compounds (Table 1).

2.2 *Mortar sample preparation*

Based on its improve marine durability, blast furnace slag cement (CEM III/B 42.5 N LH, ENCI) was selected to cast mortar cubes (40 × 40 × 40 mm) with a water/cement ratio of 0.5. To the first series no organics were added, serving as a control (see Table 2 for the applied mortar mix design), while to the remaining series, selected organic compounds were added to the cement paste during mixing. Specimens were left in their moulds for 2 days before careful removal. Specimens were then placed in sealed plastic bags and kept at room temperature for 56 days curing. 5 specimens of each series were tested for their compressive strength after 2, 7, 28 and 56 days curing to investigate the effect of the compounds on material properties. Compressive strength tests were performed with a compression test machine and Cyber-Plus evolution control unit (Trevido, Italy), at a rate of 1MPa/sec.

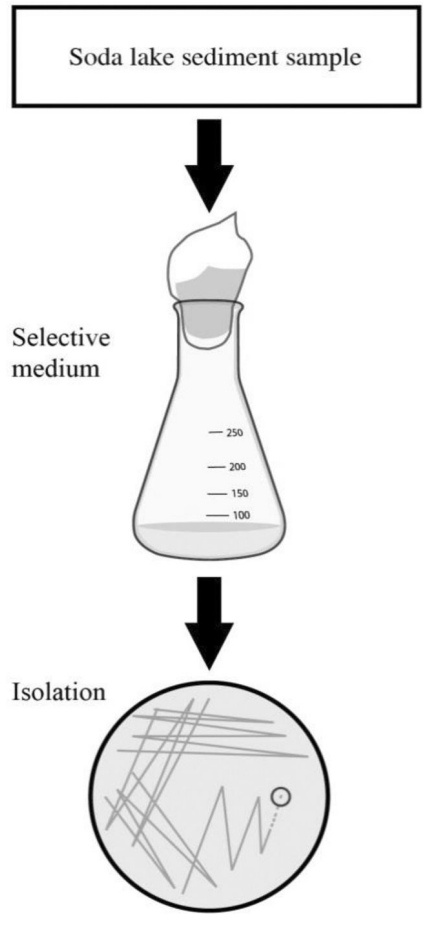

Figure 1. Flow diagram showing the enrichment and isolation process.

2.3 *Bacterial isolation*

The development of a healing agent for applied bacteria based self-healing marine concrete requires bacteria fit for purpose. For this reason an enrichment procedure (Figure 1) was undertaken on a soda lake sediment sample from Spain. Such samples may contain billions of bacteria covering a wide range of genre: the challenge then is to isolate those bacteria within the sample best suited for the intended application. Not easy and depending on the desired microorganism, this process make take months to complete. For the isolation of bacteria for self-healing marine concrete, selective pressure was placed on the sample through:

- Pasteurization (to isolate spore formers)
- Low temperature (to isolate psychrophiles) in a selective medium with;

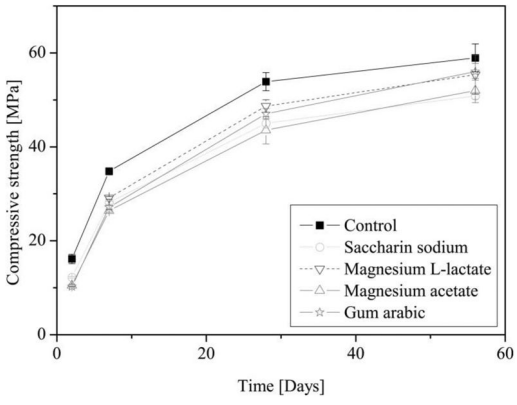

Figure 2. Compressive strength of mortar cubes after 2, 7, 28 and 56 days curing.

- High alkalinity (to isolate alkalophiles)
- Sea-water salinity (to isolate halophiles)
- Nitrate (to isolate nitrate reducers)
- Lactate and yeast (as nutrients)

Subsequent cultures were streaked onto agar plates with the same selective pressure to isolate single colonies. Isolated bacteria were re-grown in liquid media and observed after two weeks of growth through light microscopy using a Zeiss Axioplan 2, by which digital images were made through Zeiss Axiocam and Axio Vission 4.6 (Carl Zeiss, Thornwood, New York, USA)(Figure 3).

3 RESULTS

3.1 *Effect of bacterial feed on mortar specimens*

Figure 2. shows the strength development of a control and also 4 series containing 1% magnesium lactate, gum Arabic, saccharin sodium and magnesium acetates. Addition of magnesium lactate and gum

Arabic did not substantially affect mortar properties as their 28 day compressive strength was only 9.8% lower than the control. Magnesium acetate and saccharin sodium however had more of an influence on the compressive strength, being 16.4% and 19.1% lower than the control respectively. Excluded from the graph were those specimens containing magnesium L-ascorbate, D-(+)-xylose, maltodextrin, magnesium D-gluconate, L-rhamnose and D-sorbitol, as they all had a putty like consistency 2 days after casting, developing little or no late compressive strength.

3.2 *Enrichment and isolation*

The enrichment procedure was conducted on a sediment sample from a soda lake in Spain. Streaking

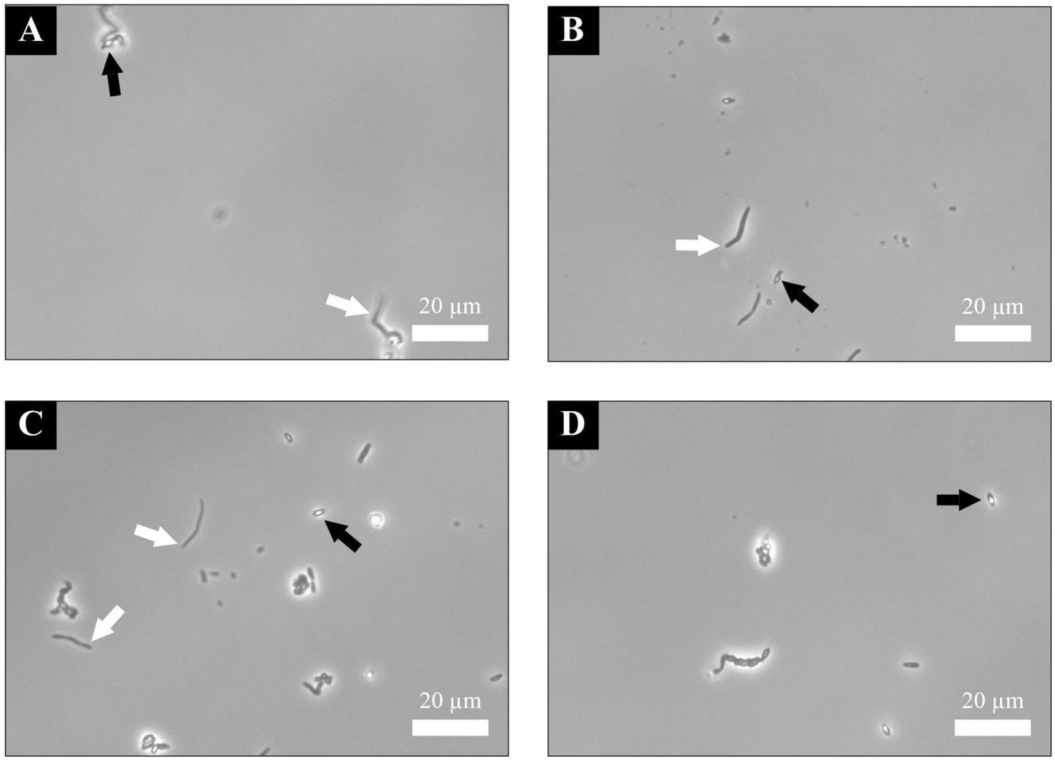

Figure 3. Light microscope images of isolated bacterial cultures, A and B representing cultures from the rose coloured colonial isolates and C and D from the beige.

of the enriched culture onto agar plates resulted in two visually distinctive colonies, the first a rose- and the second a beige- coloured colony, indicating the presence of two different bacteria cultures. The subsequent isolates were re-grown in a selective media and observed through light microscopy. The cell cultures can be observed in Figure 3 where rod shaped cells can be seen indicated by white arrows and spores indicated by black. These characteristics are indeed promising as rod shaped cells and spore production are indicative of bacteria of the *Bacillus* genus. *Bacillus* bacteria have been shown to survive the concrete casting process (Jonkers, 2007) and also improve the healing capacity of cracked concrete (Wiktor and Jonkers, 2011).

4 CONCLUSIONS

The results presented in the current paper address key needs on the road towards applied bacteria based self-healing concrete. Based on their cost, solubility and 1% to cement weight inclusion on mortar strength, four organic compounds: magnesium acetate, saccharin sodium, gum Arabic, and magnesium lactate, seem promising as bio-mineral precursor compounds. While bacteria as part of a healing agent for marine concrete applications have also been isolated. A bioassay will be conducted to assess the ability of isolated bacteria to grow on those promising organic compounds presented, allowing the design of a cost effective two-component agent for applied self-healing concrete in the marine environment. The self-healing capacity of the subsequent agent will be assessed.

ACKNOWLEDGEMENTS

We would like to thank Mitchell Geleijnse for his help with the bacterial culturing, the SHeMat network (http://www.shemat.eu/) and Marie Curie Actions for financially supporting this study.

REFERENCES

Jonkers, H.M. 2007. Self healing concrete: a biological approach. *Self Healing Materials.* Springer.

Neretnieks, I. 1985. Some Aspects on the Use of Iron Canisters for HLW. MRS Proceedings. Cambridge Univ Press.

Sagripanti, J.L. & Bonofacio A. 1996. Comparative sporicidal effects of liquid chemical agents. Appl Environmental Microbiol 62:545–551.

Tuutti, K. 1982. Corrosion of steel in concrete.

Wiktor, V. & Jonkers, H.M. 2011. Quantification of crack-healing in novel bacteria-based self-healing concrete. Cement and concrete Composites, 33, 763–770.

Concrete Solutions – Grantham et al. (Eds)
© 2014 Taylor & Francis Group, London, ISBN 978-1-138-02708-4

A proposal on repair methods for freeze-thaw damaged concrete with least re-deterioration

A. Satoh
Kumamoto University, Kumamoto, Japan

K. Shinya, K. Tashiro & K. Rokugo
Gifu University, Gifu, Japan

ABSTRACT: This study aims at presenting effective repair methods and the suitable removal depth of freeze-thaw damaged concrete before repairing, with preventing the re-deterioration after the repair. Prism specimens were exposed to pre-freeze-thaw test to give specimens freeze-thaw damage. The freeze-thaw damaged surfaces were removed with water-jet followed by patching several types of repair material on top of them. The repaired specimens were exposed to freeze-thaw test again, and after the cycles the level of freeze-thaw damage was quantified with measuring the relative dynamic modulus of elasticity. From the experiment, two important findings were revealed:Among the tested repair materials, HPFRCC and PCM have the most durable behaviour against re-deterioration. The deeper the removal depth of the freeze-thaw damaged surface with water-jet is, the less the re-deterioration of the repaired concrete becomes.

1 INTRODUCTION

One of the most dangerous types of deterioration in concrete structures is caused by freezing and thawing, because it reduces the section of the element as well as the strength of concrete. For preventing further progress of freeze-thaw damage of concrete, damaged parts are generally repaired with a certain type of patch repair method followed by removing the freeze-thaw damaged surface of the concrete. The layer of the repair is provided for preventing water from intruding into substrate concrete as well as the recovery of the section of the substrate concrete.

Though freeze-thaw damaged concrete is routinely repaired on a massive scale, patch repair work is still carried out under empirical methods with insufficient scientific basis. Especially the removal depth of the damaged substrate concrete is determined by a supervisor with an on-site-evaluation. Therefore quantitative assessment of the effective repair material for the freeze-thaw damage and the suitable removal depth of the damaged layer are required.

There are many previous studies (Kamiharako & Sugawara, 2006; Rokugo et al. 2007) which discuss effective repair methods and the suitable materials for repair, but almost all of them lead to the conclusions with observing the results from specimens with repair materials applied on non-freeze-thaw damaged substrate concrete. Only a few studies discuss the effectiveness of repair based on specimens which were repaired on the surface of freeze-thaw damaged substrate concrete. For example, Tsukinaga et al. (1994) conducted a study on the repair method with employing specimens which were repaired on the surface of a block cut from freeze-thaw damaged concrete. He discussed the efficiency of the repair method appliedon them, but this study did not discuss the suitable removal depth and the difference of the results from the different repair materials.

The authors assume that the experimental results based onspecimens with non-damaged concrete would be different from the results based on the damaged one. This study aims at clarifying the effects of several repair methods on the re-deterioration behaviour of freeze-thaw damaged of concrete. Finally, the authors propose adequate repair materials for freeze-thaw damaged concrete with the least re-deterioration as well as the suitable removal depth of the damaged substrate concrete.

2 EXPERIMENT

2.1 *Experiment protocol*

Figure 1 describes the experiment process of this study. Prismatic specimens were placed in cylindrical water containers, and exposed to freeze-thaw cycles in a temperature-controlled chamber (pre-freeze-thaw test). Freeze-thaw damaged layers were removed from the substrates to varied depths with water-jet followed by patching a type of repair material on the surface of the removed concrete. The repaired specimens were exposed to freeze-thaw cycles again (main-freeze-thaw test), and after the cycles the level of freeze-thaw

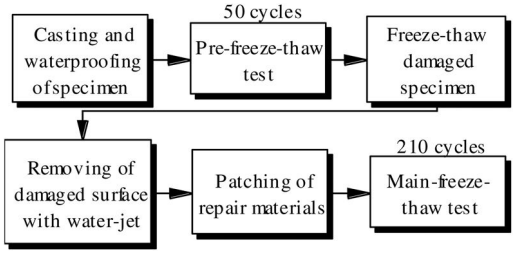

Figure 1. Flow chart of experiment protocol.

Table 1. Detail of materials for substrate concrete specimens.

Name	Detail of materials
Cement	High early strength Portland cement, Density: 3.13 g/cm^3
Fine aggregate	River sand, Density: 2.59 g/cm^3
Coarse aggregate	River gravel, Gmax 15 mm, Density: 2.61 g/cm^3
Air-entraining water reducer	Lignin sulfonate-based compound
Air-detraining agent	Polyalkylene glycol inducer

Table 2. Mix proportion of concrete.

W/C (%)	s/a (%)	Mixture composition (kg/m^3)					
		Water	Cement	Sand	Coarse aggregate	Ad[a]	Ad[b]
55	48	176	320	866	946	1.000	0.320

[a] Air-entraining water reducer
[b] Air-detraining agent

damage was quantified with measuring the relative dynamic modulus of elasticity.

2.2 *Material and mixture*

Table 1 shows the detail of material for the substrate concrete specimens. Table 2 shows mix proportion of concrete for specimens, the water-cement ratio was 0.55 and the air content of the concrete was adjusted to 2.5% after mixing using air entraining and air detraining agents.

The authors applied three different types of repair material (namely, no-shrinkage-mortar (NS), polymer cement mortar (PCM) and High Performance Fiber Reinforced Cement Composites, HPFRCC (HP)) on the surfaces of specimens after the removal of the freeze-thaw damaged layer.

NS and PCM are commercial products and the water-binder ratios of no-shrinkage-mortar and polymer cement mortar were 0.14 and 0.15 respectively. Table 3 and 4 give the details of material and mix proportions for HPFRCC respectively.

Table 3. Detail of material for HPFRCC.

Name	Detail of materials
Cement	High early strength Portland cement, Density: 3.13 g/cm^3
Fine aggregate	Silica sand, Density: 2.63 g/cm^3
Expansive additive	Ettringite and lime composite material, Density: 3.05 g/cm^3
Air-entraining highrange water reducer	Polycarboxylic acid
Thickener	Water-soluble methylcellulose
High strength polyethylene Fiber (PE)	Diameter: 12 μm, Length: 12 mm, Density: 0.98 g/cm^3, Tensile strength: 2.6 GPa, Elastic modulus: 88 GPa

Table 4. Mix proportion of HPFRCC.

W/B (%)	Mixture composition (kg/m^3)						
	Water	Cement	Sand	Ad[c]	Ad[d]	Ad[e]	Fiber
30	380	1188	395	76	37.920	1.010	12.100

[c] Expansive additive
[d] Air-entraining high-range water reducer
[e] Thickener

Table 5. Details of specimens.

Name	Damage by pre-freeze thaw test	The depth of removed surface	Repair material
NS-0	Freeze-thaw damaged	–	No shrinkmortar, NS
NS-1		Shallow	
NS-3		Normal	
NS-9		Deep	
PCM-0	Freeze-thaw damaged	–	Polymer cement mortar, PCM
PCM-1		Shallow	
PCM-3		Normal	
PCM-9		Deep	
HP-0	Freeze-thaw damaged	–	HPFRCC, HP
HP-1		Shallow	
HP-3		Normal	
HP-9		Deep	
N-NS-3	No damaged	Normal	NS
N-PCM-3		Normal	PCM
N-HP-3		Normal	HP

2.3 *Specimen*

Table 5 gives the attribute of each specimen investigated in this study. The authors prepared sixteen types of specimens which had different cases of freeze-thaw damaged concrete substrate (non-damaged case, and a case after 50 cycles), four different types of removed surfaces with water-jet (surfaces with non-removing, with shallowly removing, with normally removing and deeply removing) and three different types of repair material (NS, PCM and HP). The number of specimens was two for each case.

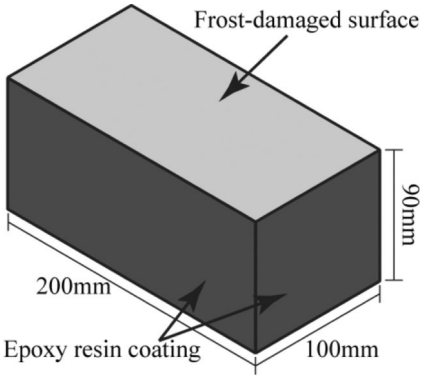

Figure 2. Specimens for pre-freeze-thaw test.

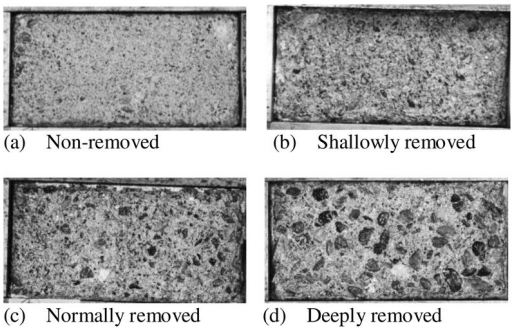

Figure 3. Damaged layer removal levels with water-jet.

Figure 2 shows the schematic illustration of the concrete prism specimens that had a section of 90 mm by 100 mm and a length of 200 mm. The original section of the specimen was 100 mm by 100 mm by 200 mm, and one surface was cut by 10 mm to make the dimension 100 mm after applying a repair material. All specimens were cast in steel moulds and removed from the moulds 24 hr. after casting and then cured in water at 20 degree centigrade for 14 days.

Five surfaces of the specimens were coated with epoxy resin leaving one surface untreated. This treatment aimed at damaging only one surface of the specimens from freezing and thawing of water permeated from the uncoated surface. Specimens coated with the epoxy resin were stored in a laboratory until the main-freeze-thaw test.

2.4 *Repair method*

The damaged specimens with pre-freeze-thaw process were repaired following the procedures described below.

The freeze-thaw damaged surfaces of specimens were removed with water-jet. Figure 3 represents four levels of the damaged layer removal. Figure 3(a) shows the non-removed surface where damaged concrete remains. Figure 3(b) shows the shallowly removed surface where many sand grains were exposed at the height of around 0.5 mm. Figure 3(c) showsthe normally removed one where the parietal region of coarse aggregate is exposedat the height ofaround 2 mm. Figure 3(d) shows the deeply removed one where the main part of coarse aggregate is exposed at the height ofaround 4 mm.

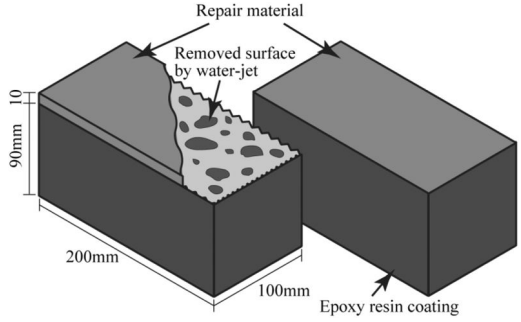

Figure 4. Specimens for main-freeze-thaw test.

After removing damaged surfaces, the water content of the specimens were curedin a thermostatic chamber at 20 degrees centigrade before repairing. Repair materials were patchedon the surface offreeze-thaw damaged concrete with a trowel. The thickness for the covering repair materials was adjusted to 10 mm, as seen in Figure 4. The sides of the layer of the repair material were coated with the epoxy resin for waterproof in fear of the detaching from the intrusion of water. Repaired specimens were cured in sealed condition with wet rags in the seal bag to prevent cracking caused by drying of repair materials. All specimens were cured in sealed condition for 14 days.

2.5 *Freeze-thaw cycling test program*

Both pre-freeze-thaw test and main-freeze-thaw test were conducted according to JIS A 1148 except for the dimensions of the test specimen (i.e., the standard dimension of the concrete specimen is 100 mm by 100 mm by 400 mm, but it is 100 mm by 100 mm by 200 mm in this study as shown in Figure 2). Two specimens were inserted in a normal rubber test container (100 mm by 100 mm by 400 mm) in a row. The temperature of the concrete specimens was controlled by a Pt sensor embedded in the center of the concrete prism. In a single cycle, the temperature of the specimens was changed from 5°C to −18°C and then changed up to 5°C, within the duration of approximately 3 to 4 hrs.

The weight change and the relative dynamic modulus of elasticity of specimens were measured periodically during the freeze-thaw testing. The relative dynamic modulus of elasticity is the ratio of the dynamic modulus of elasticity measured with Young's modulus rigidity meter after a number of freeze-thaw cycles divided by the initial modulus measured before the freeze-thaw cycles, which accords with JIS A 1148.

Equation (1) defines the relative dynamic modulus of elasticity.

$$P_n = f_n^2 / f_0^2 \times 100 \quad (1)$$

Where, P_n is the relative dynamic modulus of elasticity (%) after 'n' cycles of freeze-thaw cycling test, f_n is one dimensional resonance frequency (Hz) after 'n'cycles of freeze-thaw cycling test and f_o is one dimensional resonance frequency (Hz) before being subjected to freeze-thaw cycles.

The relative dynamic modulus of elasticity and weight were measured about every 30 freeze-thaw cycles during main-freeze-thaw test.

3 RESULT AND DISCUSSION

3.1 *Weight change*

Table 6 represents the weight change of specimens during main-freeze-thaw test, in which the data is the representative value of two specimens. In Table 6, the names of specimens are provided with the suffixes "−1 and −2" to distinguish the specimen with the same attribute. In Table 6, it is observed that all specimens' weight slightly increase until 150 cycles in main-freeze-thaw test. Absorbing water and the hydration progress of repair materials are considered to be the reasons for the slight weight increase of the specimens. However, specimens using no-shrinkage-mortar for repair material lose their weight after 150 cycles except for NS9-1. Judging from the observation of the specimen NS0-1 which has the damaged layer in substrate concrete and suffered the large weight loss, it is clear that the damaged surface has the negative effect to weight loss. Comparing the case NS0-1 with the case HP0-2 both of which have the damaged layer in substrate concrete, the weight loss for HP0-2 is not observed.

It therefore appears that the repair material and removing the damaged surface have a substantial influence on the re-deterioration.

Table 6. Change of weight during main-freeze-thaw test described in %. Plus means increase and minus means decrease.

	Number of freeze-thaw test cycles							
Name	0	30	60	90	120	150	180	210
NS0-1	0.00	0.29	0.68	1.02	1.75	0.83	−1.39	−4.56
NS1-2	0.00	0.38	0.88	1.17	1.89	0.79	−1.30	−2.48
NS3-2	0.00	0.49	0.90	1.08	1.61	1.78	1.08	0.18
NS9-1	0.00	0.09	0.34	0.59	1.02	1.27	1.54	1.87
PCM0-2	0.00	0.46	0.65	0.75	1.18	1.29	1.51	1.74
PCM1-2	0.00	0.25	0.43	0.54	1.07	1.41	1.69	2.04
PCM3-1	0.00	0.23	0.31	0.35	0.73	0.87	1.06	1.39
PCM9-1	0.00	0.32	0.47	0.55	0.97	1.15	1.36	1.66
HP0-2	0.00	0.23	0.31	0.38	0.87	1.12	1.33	1.57
HP1-1	0.00	0.35	0.58	0.65	1.18	1.40	1.55	1.84
HP3-1	0.00	0.27	0.42	0.49	0.92	1.09	1.32	1.71
HP9-1	0.00	0.18	0.24	0.27	0.66	0.84	1.03	1.37
N-NS3-2	0.00	0.16	0.30	0.56	1.05	1.30	1.54	1.92
N-PCM3-1	0.00	0.19	0.23	0.24	0.57	0.77	0.94	1.42
N-HP3-1	0.00	0.32	0.46	0.51	0.96	1.17	1.38	1.60

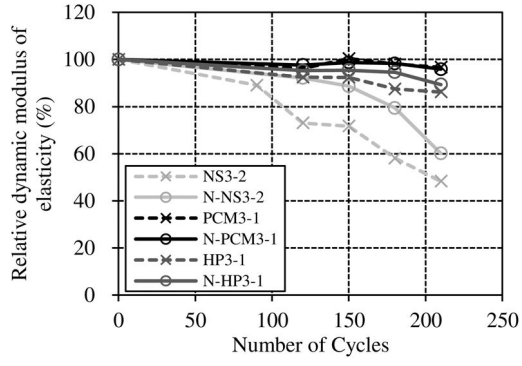

Figure 5. Influence of the freeze-thaw damage by pre-freeze-thaw-test on the relative dynamic modulus of elasticity.

3.2 *Influence of the damage of the substrate*

Figure 5 shows the relative dynamic modulus of elasticity during main-freeze-thaw test as a function of freeze-thaw cycles. There are three pairs of specimens with the same repair material but with distinct substrate concrete state (freeze-thaw damaged substrateor non-damaged substrate).

Comparing the change of the modulus between the case NS3-2 and the case N-NS3-2, the change for the case NS3-2 is larger than that of the case N-NS3-2. In the case of NS, the freeze-thaw damaged surface (the case NS3-2) has a great influence on the re-deterioration of repaired specimen by main-freeze-thaw test.

There is little difference observed in other cases (comparing PCM3-1 with N-PCM3-1, and also HP3-1 with N-HP3-1) in Figure 5. This fact demonstrates the less vulnerability from the damage of the substrate to the performance of the repair materials (PCM and HP) than NS.

Therefore, the evaluation of the repair materials and the methods for the repair work should be conducted in consideration of the above-mentioned test results. If the repair work is to be conducted on the damaged surface, the test results on the non-damaged surface may be overestimating the performance in the case of materials like NS.

3.3 *Influence of the removal of freeze-thaw damaged surface*

Figure 6(a) shows a plot of the relative dynamic modulus of elasticity of the specimens during the main-freeze-thaw test repaired with NS. In figure 6(a), it is observed that all cases of NS were re-deteriorated regardless of the removal depth of the damaged layer. All NS specimens dropped the modulus below 60% of the initial values at 210 cycles. However, the depth of removal had a slightly positive effect on the re-deterioration at 210 cycles.

Figure 6(b) shows the relative dynamic modulus of elasticity of the specimens during the main-freeze-thaw test repaired with PCM. With comparing the results of PCM with the ones of above-mentioned NS, the specimens repaired with PCM were extremely slow to re-deteriorate. For example, PCM3-1 and PCM9-1 kept 95% of the initial relative dynamic modulus of elasticity at 210 cycles. Precisely looking into the data of PCM, it is also observed that specimens which had the damaged layer deeply removed and were repaired (PCM3-1 and PCM9-1) were slow to re-deteriorate in comparison to the ones which had the damaged layer shallowly removed and were repaired (PCM0-2 and PCM1-2).

Figure 6(c) shows the relative dynamic modulus of elasticity of the specimens during the main-freeze-thaw test repaired with HP. There was little difference between the modulus of the specimens with different removal depths. Then it can be said that the removal depth of freeze-thaw damaged layer had little influence on the relative dynamic modulus of elasticity of specimens repaired with HPFRCC. All HP specimens kept more than 80% of the relative dynamic modulus of elasticity until 210 cycles, as seen in Figure 6(c). But the results at 90 cycles tell that the deeper removal depth of the damaged layer yielded a slightly improved modulus of elasticity, showing the same results as NS and PCM.

3.4 *Influence of the repair material*

Figure 7(a) represents the change of the relative dynamic modulus of elasticity of specimens with a shallowly or non-removed layer of substrate during the main-freeze-thaw test. The re-deterioration behaviour for NS0-1 was especially accelerated along with the progress of the cycles. The same tendency was observed in all other cases, but the acceleration tendency for PCM and HP was substantially slower than that for NS.

Figure 7(b) represents the change of the relative dynamic modulus of elasticity of specimens with a normally or deeply removed layer of substrate during the main-freeze-thaw test. The re-deterioration behaviour for NS9-1 was especially accelerated along with the progress of the cycles. Though the same tendency was observed in all cases in Figure 7(a), the re-deterioration tendency for PCM and HP was not an accelerated one but a steadily decreasing one in Figure 7(b).

By comparing the data of the specimens with different depths of removal in Figure 7(a) and (b), it was shown that polymer cement mortar and HPFRCC had excellent properties even if the substrate was insufficiently removed. But the insufficiently removed layer of substrate had a slightly accelerated re-deterioration tendency, which should be avoided. Then it is clear that the deeper the removed surface as,the better the performance.

The most suitable combination of the repair material and the removal depth was the one for HP9-1, which was repaired with HPFRCC on the surface of the deeply removed substrate. In this case, the ratio of the modulus of elasticity was about 100% at 180 cycles which is seen in Figure 7(b). Also PCM9-1 maintained the modulus of elasticity at 100% until 150 cycles.

The reason for the excellent performance for HPFRCC derives from the ability to develop the dispersed cracks and the impermeability of water into the material. HPFRCC was developed to be used for the ordinary repair material, and it is proved that this material has better performance than PCM which is commercially used widely in Japan. The polymer in PCM can also contribute to the waterproofing property ofthe material, which would give good performance to PCM. As PCM in this study is a pre-mixed type, the modification of the material would give the possibility of yielding better performance.

It is concluded that polymer cement mortar and HPFRCC are more effective as repair materials than no-shrinkage-mortar in this study.

4 CONCLUSIONS

The purpose of this study is to present the most effective repair methods and the most suitable removal depth of freeze-thaw damaged concrete before repair, with preventing re-deterioration after the repair. From the experiment, some important findings were revealed.

- The specimens repaired on the surface of freeze-thaw damaged substrate concrete were rapid to re-deteriorate in comparison to the specimens repaired on the surface of non-damaged substrate concrete.
- The specimens repaired on the freeze-thaw damaged layer which was removed deeply by water-jet and repaired afterwards were slow to re-deteriorate in comparison to the specimens repaired on the damaged layer which was removed shallowly.
- With comparing the re-deterioration behaviour after the repair, it is clear that polymer cement mortar and HPFRCC were more effective as repair material than no-shrinkage-mortar.

ACKNOWLEDGEMENT

The authors are grateful to Dr. S. Lim, Deros Japan, for the cooperation in the removal of the damaged layer of the substrate with water jet.

REFERENCES

Kamiharako, A. & Sugawara, T 2006. An evaluation on bond characteristics of the continuous fiber sheet under freeze-thaw environment, Proceedings of the Japan Concrete Institute, Vol. 28, No. 1: pp. 1715～1720.

Rokugo et al. 2007. Freeze-thaw resistance of HPFRCC with multiple cracks and tensile performance, Proceedings of the Japan Concrete Institute, Vol. 29, No. 1: pp. 333～338.

Tsukinaga et al. 1994. Assessment of Frost Damage of Concrete and its Repair Technique, Journal of the Society of Materials Science Vol. 43, No. 491: pp. 983～989.

This page intentionally left blank

Concrete Solutions – Grantham et al. (Eds)
© 2014 Taylor & Francis Group, London, ISBN 978-1-138-02708-4

Self-compacting repair mortars according to BS EN 1504-3

N. Strompinis
Division of Civil Engineering, University of Dundee, Dundee, Scotland, UK

K.K. Sideris, V.-Z. Douros, I. Vitsios & I. Zervos
Laboratory of Building Materials, Civil Engineering Department, University of Thrace, Xanthi, Greece

ABSTRACT: Repair mortars are the most commonly used materials in repair applications, mainly in patch repairs. At the European level their usage is covered by EN 1504-3. According to this standard, repair mortars are ranked in four different levels regarding their performance in specific tests concerning their mechanical and durability characteristics. The main target of this paper was to produce low-cost self-compacting repair mortars using combinations of common type II cement, limestone filler and ladle furnace slag. Six mortars were prepared and tested according to the procedure described in EN 1504-3. All mortars fulfilled the standards' requirements and were ranked as R2 and R3 repair mortars.

1 INTRODUCTION

Deterioration of concrete structures due to cracking and spalling of surface cover is a major problem in civil engineering. When serviceability of the deteriorated structure becomes an important issue, in comparison with the reconstruction of the concrete elements, the most cost-effective and easily achieved solution is often to use patch repair, by removing the deteriorated parts and employing a fresh repair mortar on the corresponding concrete. Self-compacting mortars (SCMs) gain increasing interest in this area due to the ease of application and mechanical advantages (Gourard et al. 2002). The highly fluid nature of SCMs brings considerable advantages when they are used in complex molding systems or sections with congested reinforcement, whilst the rapid rate of placing provides an enhanced surface finish.

The paste phase rheology of these repair mortars should possess suitable properties from the viewpoint of flowability and segregation (Wallevik, 2003, EFNARC 2005). The use of chemical admixtures i.e. superplastiscizer and viscosity modify admixtures (VMA) is inevitable to improve workability and resistance to segregation, whilst the increase in fine-grounded material content in cements modify the rheological properties of the paste, influencing self-compactibility. Therefore, the water to fines ratio and the type of chemical admixtures used is of vital importance and have to be selected carefully (Şahmaran et al. 2006).

The fresh rheological characteristics, strength and durability of repair mortars can be enhanced by the addition of supplementary powders such as limestone filler, fly ash, silica fume, slag and metakaolin. In cases where the material possesses pozzolanic properties, it can be also used as partial replacement of cement content. The selection of type and amount of inert or cementitious powders depends on the physical and chemical properties of the material i.e. particle shape, fineness, particle size distribution, surface texture and porosity, mineralogy etc, as they affect the performance of fresh and hardened paste. Ferraris et al. (2001) in a comprehensive literature survey on the effect of addition of fine grounded materials have concluded that, although there is no universally accepted agreement on the effect of the above factors due to their complex influence, the increase in fine content was generally found to increase water demand for a specific workability due to increase in the surface area. In terms of hardened properties, the incorporation of these additions has been found beneficial as they improve the microstructure of the hydrated cement paste. The reduction of pore size and interconnectivity due to the better packing which is provided, reduces significantly the diffusion coefficient of concrete and enhances its durability (Concrete Society 2011, Neville 2011).

The effectiveness of the application of SCMs in patch repairs is not only influenced by the intrinsic properties of the repair material, but also from its compatibility with the repair zone. In a repair system, compatibility refers to the combination of properties between the existing concrete substrate and the repair material that ensures the combined system is able to withstand the applied stresses and maintain its structural integrity and protective properties under certain exposure conditions over a designated service life (Tilly & Jacobs 2007). The main aspects of compatibility are dimensional and thermal stability, chemical,

electrochemical and transport properties of the parent concrete and the repair material. Dimensional stability is important because it is related with volume changes resulting from shrinkage, thermal expansion, and stresses generating form creep, that can lead to concrete cracking (Concrete Society 2009). Chemical and electrochemical properties include alkali silica reaction, attack by sulfates and chloride, and carbonation induced corrosion, whereas permeability and diffusion properties of both material and the interface between them are considered critical for a durable combined system.

Provisions for the application of these repair materials exist in individual national standards; however European Standard EN 1504: Products and systems for the protection and repair of concrete structures provides an integrated framework for the concrete repair industry throughout Europe. Part 3 of this Standard covers the use of repair mortars.

The main target of this paper was to produce low-cost self-compacting repair mortars using combinations of common type II cement, limestone filler and ladle furnace slag. Six mortars were prepared and tested according to the procedure described in BS EN 1504-3 (BSI 2005). All mortars fulfilled the standards' requirements and were ranked as R2 and R3 repair mortars.

2 MATERIALS AND METHODS

The basic properties of SCC are the filling ability, the segregation resistance and the passing ability. Rheology of the cement paste is the crucial factor in order to fulfill the above requirements. Self compactibility is strongly connected with the dosage of fine materials. All materials passing the 0.125mm sieve are considered as fine materials.

The fine materials used for the preparation of repair mortars were limestone filler and ladle furnace slag. Ladle furnace slag (LFS) is a by-product of the steel production process. In its raw state LFS is prone to expansion and spalling and spalling because of its high $Ca(OH)_2$ and MgO content. However, research has revealed that it is possible to use LFS in construction applications after weathering and grinding since then it shows weak pozzolanic and latent hydraulic properties (Anastasiou 2009). The cement used was of the type CEM II B-M 42.5R. Natural river sand was used as fine aggregate. The chemical composition of the cement and the fine materials used is presented in Table 1.

Self-compactibility of mortars was assessed by measuring the mortar flow diameter and mortar flow time (EFNARC 2005). According to previous research (Georgiadis 2010) self-compactibility and robustness is ensured when the mortar's flow diameter and flow time lay between 24–26 mm and 9–11 sec respectively. Mix design characteristics as well as the fresh properties of the produced mortars are listed in Table 2.

Table 1. Chemical composition of materials used.

Oxide composition, %	Cement	Filler	LFS
SiO_2	20.86	17.79	18.12
Al_2O_3	5.38	1.57	3.23
Fe_2O_3	2.73	1.62	–
FeO	–	–	7.77
CaO	60.88	44.24	53.88
MgO	2.31	4.04	–
SO_3	3.13	3.02	–
K_2O	1.93	–	0.03
Na_2O	–	–	0.06
TiO_2	–	0.17	0.23
P_2O_5	–	0.02	0.05
SrO	–	–	–
Cr_2O_3	–	–	0.08
ZnO	–	–	0.05
MnO	–	–	2.11
As_2O_3	–	–	0.03
V_2O_5	–	–	0.03
CoO	–	–	0.02
NiO	–	–	0.02
CuO	–	–	0.05

Table 2. Mix design and fresh properties of the tested mixtures.

	Mixes					
Materials, gr	M1	M2	M3	M4	M5	M6
Cement	875	875	875	800	800	800
LFS	130	175	220	120	200	160
Limestone Filler	295	250	205	250	250	250
Sand	2250	2250	2250	2380	2300	2340
Water	400	400	400	400	400	400
Glenium 21	25.5	25.5	26	26	18.3	19.5
Pozzolith	4	4	4	4	3	3
VMA	8.5	9.5	11	11	6	7
Agitation time, minutes	8	9.5	9	9	7.5	6.5
Slump flow, cm	26	27	26.5	27	26.5	26.5
V-funnel, sec	10.3	11	11.3	9	11.2	12

The properties measured were those required by BS EN 1504-3: 2005 i.e. the compressive strength at the age of 28 days, the elastic modulus at the same age, the capillary absorption, the unrestrained shrinkage and the carbonation resistance. Moreover the sulfate resistance and the mortars' behaviour under elevated temperatures were also assessed in order to obtain a complete view of their performance and the way they might affect the durability of the repaired structure.

3 RESULTS AND DISCUSSION

Compressive strength was measured according to BS EN 12190 (BSI 1999). Three prismatic specimens with dimensions of $40 \times 40 \times 160$ mm were prepared for

Table 3. Experimental results of all tested mixtures (for the properties indicated in BS EN 1504-3).

Property	Test method	M1	M2	M3	M4	M5	M6
Compressive strength (28 days), MPa	BS EN 12190	53.7	52.0	51.7	50.4	44.9	43.7
Elastic modulus, GPa	BS EN 13412	10.65	15.00	10.69	8.82	11.67	15.04
Capillary absorption, $kg \cdot m^{-2} \cdot h^{-0.5}$	BS EN 13057	0.281	0.209	0.194	0.151	0.251	0.249
Shrinkage[a] ($\Delta L/Lg$), %	BS EN 132617-4	0.007	0.008	0.005	0.008	0.013	0.008
Shrinkage[b] ($\Delta L/Lg$), %		0.07	0.07	0.08	0.06	0.065	0.10
Carbonation resistance/depth of carbonation, mm	BS EN 12617-4	0.08	0.50	0.08	0.93	0.78	0.85
Sulfate resistance, % of 28 days strength	ASTM C1012	94.36	96.43	96.57	81.96	95.25	94.65
Resistance to high temperatures, % of 28 days strength	–	66.21	61.32	54.84	68.91	60.12	63.72

[a]The specimens have been stored inside water baths
[b]The specimens were exposed to air

each mixture following the procedure described in BS EN 196-1 (BSI 2005). All specimens were water cured for 28 days and then tested in the laboratory's compression machine. Compressive strength of each mortar was assessed as the mean value of six specimens. The results are presented in Table 3. Mortars M1 to M4 performed compressive strength greater than 50 Mpa, while mortars M5 and M6 performed compressive strength of 44.9 and 43.7 MPa, respectively. According to the requirements of BS EN 1504-3, mixtures M1 to M4 are considered as R4 repair mortars and mixtures M5 and M6 as repair mortars of class R3.

Modulus of elasticity was determined according to BS EN 13412 (BSI 2006). For each mixture, three prismatic specimens were prepared and cured as above. At the age of 28 days the specimens were placed centrally in the compression test machine, with the strain measuring instruments attached axially. The secant modulus of elasticity was assessed as the mean value of three specimens (Table 3). Based on the requirements of EN 1504-3, mixtures M2 and M6 are characterized as class R3 repair mortars, while the rest of the mixtures belong to the classes R2 and R1, i.e. repair mortars suitable only for non-structural applications.

The capillary absorption coefficient was evaluated using the method outlined in BS EN 13057 (BSI 2002). Three cylindrical specimens with diameter of 100 mm and height of 20 mm were prepared for each mixture and water cured at 20°C for 28 days. After that age, the specimens were placed in an oven operating at 40 ± 2°C for a minimum of seven days until constant weight was achieved. Then, the specimens were placed in a flat bottomed rigid tray, resting on knife-edge supports in order to achieve a depth of water immersion of (2.0 ± 1.0)mm. Water uptake into the specimens was determined at time intervals of 12 minutes, 30 minutes, 1 hour, 2 hours, 4 hours, 8 hours and 24 hours. The absorption coefficient R was then calculated according to the formula described in EN 13057. All mixtures fulfilled the requirements of EN 1504-3 for all repair classes.

The unrestrained movement was measured according to BS EN 12616-4 (BSI 2002). In total, six prismatic specimens ($40 \times 40 \times 160$ mm) with adjusted measurement studs were prepared for each mortar. Three of them were cured in the laboratory air and the remaining was immersed in potable water at a temperature of 21 ± 2°C. Length change measurements were performed at different time intervals for a time of 56 days after demoulding (Table 3). According to Table 3, all mixtures fulfilled the requirements of EN 1504-3 for all repair classes.

Carbonation resistance was assessed according to BS EN 13295 (BSI 2004). Three prismatic specimens ($40 \times 40 \times 160$ mm) were prepared for each mixture following the procedure described in BS EN 196-1. Specimens were water cured at 21 ± 2°C till the age of 28 days. Then they were brought to even moisture content by storage in the laboratory air. After this the specimens were inserted in an accelerated carbonation chamber with a CO_2 concentration of 1%, temperature of 21 ± 2°C and relative humidity of 60 ± 10%. After 56 days in the accelerated carbonation chamber, the depth of carbonation was measured and a mean value was determined for each mixture. As Table 3 shows, all mixtures displayed carbonation depths of less than 1 mm, considerably lower than the 3 mm measured on the reference concrete specimens. Therefore, all mixtures fulfilled the requirements of BS EN1504-3 for repair classes R3 and R4.

Sulfate resistance was measured in accordance with ASTM C1202/C1012M (ASTM 2013). Three prismatic specimens with dimensions of $40 \times 40 \times 160$ mm were prepared for each mixture following the procedure described in BS EN 196-1: 2005. Specimens were immersed in a 5% Na_2SO_4 solution for a time period of six months. The sulfate resistance was assessed by calculating the ratio of the final compressive strength to the compressive strength at the age of 28 days instead of measuring the length change of the test specimens. Most mixtures retained more than 90% of their 28 days compressive strength after immersion in the aggressive solution. The only exception to this was mixture 4. In this case the residual compressive strength after 6 months of immersion was 81% of the 28 days compressive strength.

Resistance of repair mortars under elevated temperatures was tested by heating three prismatic specimens up to a temperature of 600°C. The specimens used for the fire tests were cured for the first 28 days

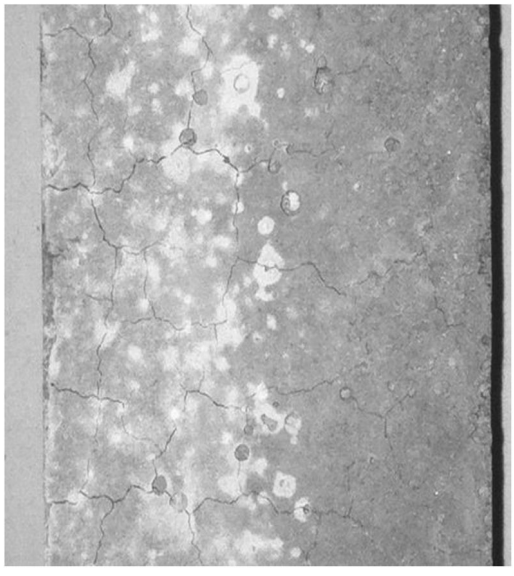

Figure 1. Crack formation in specimen after fire test.

in the curing chamber. From this age onwards they were placed in the laboratory air environment (relative humidity = 50–60% and temperature = 20 ± 2°C). At the age of 120 days, the appropriate specimens were placed in an electrical furnace with heat applied at a rate of 5°C/min until the desired temperature of 600°C was reached. In the electrical furnace the maximum temperature of 600°C was maintained for 1 hour. Specimens were then allowed to cool in the furnace and tested for compressive strength. Resistance at high temperatures was assessed as the ratio of the residual compressive strength to the one measured at the age of 28 days. All mixtures showed significant cracking after completion of the test (Fig. 1). Their residual compressive strength in all cases was between 55% and 67% of their 28 days compressive strength. Anagnostopoulos et al. (2009) observed that mixtures produced with addition of ladle furnace slag are more sensitive to elevated temperatures, and this is in agreement with the above results i.e. for mixes with the same cement content (M1 to M3 and M4 to M6), an increase in LFS content results in slightly lower residual compressive strength.

4 CONCLUSIONS

Six mortars were prepared in this study using different combinations of CEM II cement, limestone filler and ladle furnace slag and tested according to the procedure described in EN 1504-3. All mixtures fulfilled the requirements of this standard. Four of them were ranked as R2 mortars while the rest two were ranked as R3 repair mortars i.e. repair mortars suitable for structural applications. All mortars showed superior durability against different severe environments, low water permeability and satisfactory behaviour under elevated temperatures. It is therefore concluded that ladle furnace slag may be used effectively for the production of low-cost environmentally friendly self-compacting repair mortars.

REFERENCES

Anagnostopoulos, N., Sideris, K.K. & Georgiadis, A. 2009. Mechanical characteristics of self-compacting concretes with different filler materials, exposed to elevated temperatures. *Materials and Structures* 42:1393–1405.

Anastasiou, E. 2009. Utilization of steel slags and lignite fly ashes in the production of concrete for special applications. PhD thesis, Aristotle University of Thessaloniki, Thessaloniki (in Greek).

ASTM (American Institute for Testing and Material), 2013. ASTM C1202/C1012M. *Standard Test Method for Length Change of Hydraulic-Cement Mortars Exposed to a Sulfate Solution*. West Conshohocken, PA, USA: ASTM International.

BSI (British Standard Institute), 1999. BS EN 12190. Products and systems for the protection and repair of concrete structures. Test methods. Determination of compressive strength of repair mortar. London: BSI.

BSI, 2002. BS EN 12617-4. Products and systems for the protection and repair of concrete structures. Test methods. Determination of shrinkage and expansion. London: BSI.

BSI, 2002. BS EN 13057. *Products and systems for the protection and repair of concrete structures. Test methods. Determination of resistance of capillary absorption*. London: BSI.

BSI, 2004. BS EN 13295. *Products and systems for the protection and repair of concrete structures. Test methods. Determination of resistance to carbonation*. London: BSI.

BSI, 2005. BS EN 1504-3: *Products and systems for the protection and repair of concrete structures – Definitions, requirements, quality control and evaluation of conformity. Structural and non-structural repair*. London: BSI.

BSI, 2005. BS EN 196-1. *Methods of testing cement. Determination of strength*, London: BSI.

BSI, 2006. BS EN 13412. *Products and systems for the protection and repair of concrete structures. Test methods. Determination of modulus of elasticity in compression*. London: BSI.

Concrete Society, 2009. Repair of concrete structures with reference to BS EN 1504. *Technical Report No. 74*. Surrey: The concrete Society.

Concrete Society, 2011. Cementitious materials. The effect of ggbs, fly ash, silica fume and limestone on the properties of concrete. *Technical Report No. 69*. Surrey: The concrete Society.

Courard, L., Darimont, A., Willem, X., Geers, C. & Degeimbre, R. 2002. Repairing concretes with self-compacting concrete: testing methodology assessment. In: *Proceeding of the 1st North American conference on the design and use of self-consolidating concrete, Chicago, 12–13 November 2002*: 267–274.

EFNARC, 2005. *The European Guidelines for Self-Compacting Concrete*: *Specification, production and use*, www.efnarc.org

Ferraris, C.F., Obla, K.H. & Hill, R. 2001. The influence of mineral admixtures on the rheology of cement paste and concrete, *Cement and Concrete Research* 31: 245–255.

Georgiadis, A. 2010. *Design, Production and Use of self-compacting concretes for industrial application in Greece*. PhD Thesis, Democritus University of Thrace, Xanthi (in Greek).

Neville, A. M. 2011. *Properties of concrete (5th ed)*. Harlow: Prentice Hall.

Şahmaran, M., Christianto, H.A. & Yaman, İ.Ö. 2006. The effect of chemical admixtures and mineral additives on the properties of self-compacting mortars, *Cement and Concrete Composites* 28 (5): 432–440.

Tilly, G. P. & Jacobs, J. 2007. *Concrete repairs. Performance in service and current practice*. UK: IHS BRE Press.

Wallevik, O.H. 2003. Rheology – A scientific approach to develop self-compacting concrete. In O. Wallevik. & I. Nielson. (eds), *Self-compacting concrete, Proceedings of the 3rd International RILEM Symposium, Reykjavik, 17–20 August 2003*. France: Rilem Publicattions S.A.R.L.

This page intentionally left blank

Concrete Solutions – Grantham et al. (Eds)
© 2014 Taylor & Francis Group, London, ISBN 978-1-138-02708-4

Can self-repair of concrete cracks help to obtain durable concrete?

K. Van Tittelboom, M. Maes & N. De Belie
Magnel Laboratory for Concrete Research, Department of Structural Engineering, Faculty of Engineering and Architecture, Ghent University, Ghent, Belgium

ABSTRACT: Self-repair of concrete cracks is a topic which has now been studied for several years in laboratories all over the world. Different mechanisms have been developed in order to obtain autonomous crack repair; dormant bacteria are activated and precipitate calcite inside the crack, flexible polymer tendons reduce the crack width, superabsorbent polymers swell upon water ingress and block the crack etc. While the aforementioned mechanisms are all different, their ultimate goal is the same. They all aim at increasing the durability of cracked concrete structures by making their cracks impermeable for aggressive agents. In this study, it was investigated whether concrete could be made more durable through the implementation of a self-repairing function. Self-repairing properties were obtained by the use of an encapsulated polymer-based repair agent which was embedded in the matrix. Upon crack formation, the capsules break, the repair agent is released and hardens inside the crack which is in this way autonomously healed. By means of chloride diffusion tests it was proven that autonomous crack repair results in a significant lower chloride ingress compared to samples with untreated cracks.

1 INTRODUCTION

Chloride induced reinforcement corrosion is one of the main causes of the degradation of concrete structures in marine environments. If cracks appear in the concrete matrix, the penetration of chloride ions goes much faster compared to the ingress in the case of uncracked concrete. Due to this, corrosion is initiated even earlier and the service life of the structure is further vigorously decreased.

Studies have already proven that the amount of chloride ingress in cracked concrete is related to the crack width. When the crack width increases, the chloride penetration depth also increases (Audenaert et al., 2009, Djerbi et al., 2008). This effect is most distinct for crack widths between 0 and 100 μm. For larger cracks (between 100 and 200 μm) this increase becomes less clear.

Based on the aforementioned findings, it can be concluded that when cracks are closed or even partially closed, the chloride ingress will be reduced. In this study, an encapsulated repair agent was embedded in the matrix. At the moment of crack appearance the capsules break and the repair agent is released into the crack where it hardens. Compared to manual injection of repair agent into a crack, autonomous repair is less controlled and may thus be less complete. But the big advantage is that costs can be saved as regular inspection of the structure and manual crack repairs are no longer needed. In addition, as it was proven that a reduction in crack width can already largely reduce the chloride ingress, autonomous crack repair can help to reduce the risk for chloride induced reinforcement corrosion and can thus extend the service life of concrete structures.

Based on previous results (Van Tittelboom, 2010, Van Tittelboom et al., 2011), in this research it was chosen to encapsulate a polyurethane based repair agent by glass tubes. These tubes were embedded in mortar cylinders in which cracks were created by means of a crack width controlled splitting test. The influence of autonomous crack repair on the chloride ingress was investigated by means of chloride diffusion tests (Maes et al., 2013).

2 MATERIALS

2.1 *Repair agent*

In order to repair the concrete cracks, a commercial, one component polyurethane based agent, named MEYCO MP 355 1K and supplied by the BASF Chemical Company, was used. However, in this study the repair agent was used as a two component agent in order to accelerate the reaction rate. While the first component consisted of the polyurethane prepolymer, the second component consisted of a mixture of 10% accelerator and water. This repair agent was chosen as it expands during its reaction, which holds a dual advantage. The first advantage is that this expanding reaction can act as a driving force for the repair agent to flow out of the capsules. The second advantage is that the repair agent occupies a small volume during encapsulation and is able to fill a bigger crack space after reaction (up to 30 times the initial volume). In

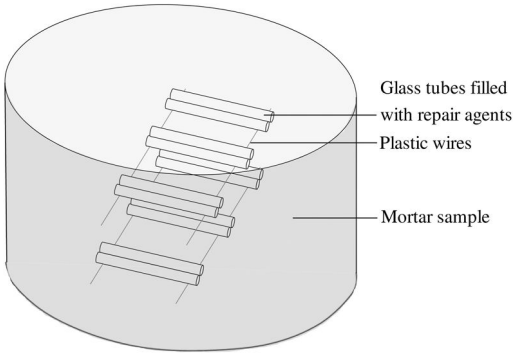

Figure 1. Position of the encapsulated repair agent inside the cylindrical mortar samples.

this way the crack can become completely filled with polyurethane foam and ingress of aggressive agents can be prevented.

2.2 *Capsules*

In order to make sure that the capsules break at the early stage of crack formation, a brittle encapsulation material is needed. Previous research (Van Tittelboom et al., 2011) demonstrated that glass tubes can serve this purpose. Here, glass tubes with an inner diameter of 3 mm and a length of 50 mm were used. The wall thickness of the capsules amounted to 175 μm.

2.3 *Mortar samples with(out) self-repairing properties*

First, glass tubes were filled with the repair agent in the following way. One end of the tubes was sealed by means of methyl methacrylate (MMA) glue. After curing, both components of the repair agent were injected in separate tubes by means of a syringe with a needle. Finally the second end of the tubes was sealed with MMA. Tubes filled with the prepolymer and the mixture of accelerator and water were positioned adjacent to each other in the sample according to the configuration shown in Figure 1. Plastic wires which went through the walls of the mould, in order to be fixed at the outer side of the mould, were used to maintain the capsules at the fixed position. One couple of wires was fixed, with an inner distance of 30 mm, at a height of 12.5 mm from the bottom of the mould while the second couple of wires was situated 37.5 mm above the bottom. Along the length of each couple of wires 3 couples of glass tubes were equally divided. They were connected to the wires by means of a droplet of MMA glue.

A mortar mixture with a water to cement ratio of 0.45 was made according to the composition shown in Table 1. First cement and water were added to the bowl of the mortar mixer. After 1 minute of mixing, the sand was added and the whole was mixed for one more minute. After a rest period of 1 minute the mixture was mixed a last time for one minute.

Table 1. Mortar composition.

Material	Amount/m^3 [kg]
Sand 0/4	1760
Cement CEM I 52.5 N	590
Water	265

Table 2. Different test series under investigation.

Code	Description
REF	Cracked, no crack repair
AUTO	Cracked, autonomous crack repair
UNCR	Uncracked

Subsequently the mortar mixture was added to the moulds. Moulds were made from poly vinyl chloride (PVC) tubes and had an inner diameter of around 100 mm and a height of about 50 mm. These PVC tubes were clamped on a wooden plate in order to prevent leakage of mortar at the bottom. While part of the moulds contained wires with adhered encapsulated repair agent, other moulds were empty to create samples which could be used as control (Table 2). Each test series consisted of 5 cylinders.

After all moulds were filled with mortar, they were vibrated on a vibrating table and they were transported to an curing room with a temperature of 20°C and a relative humidity of more than 95%. One day after casting, the samples were demoulded and stored under water until they were 21 days old.

3 METHODS

3.1 *Crack formation*

When the samples were between 21 and 28 days old, cracks were created by means of a crack width controlled splitting test. Only the UNCR series remained uncracked. To control the crack width during the splitting test, a linear variable differential transformer (LVDT, Solartron AX/0.5/S) with a measurement range of ±500 μm and an accuracy of 1 μm was attached to each side of the cylindrical specimen at middle height (Figure 2). A PVC block with a hole was glued at one half of the sample and used to clamp the LVDT. At the other half of the sample, which would later be at the other side of the crack, a metal hooked part was glued. This was used to place the tip of the LVDT against. As the crack would appear in between both attachments, the tip of the LVDT would slide out over the same distance as the width of the crack. Because the crack width may differ at both sides of the sample, an LVDT was attached at each side and the mean value was used to control the splitting test.

During the splitting test, the test machine (W+B BD 250/15) was operated by crack width

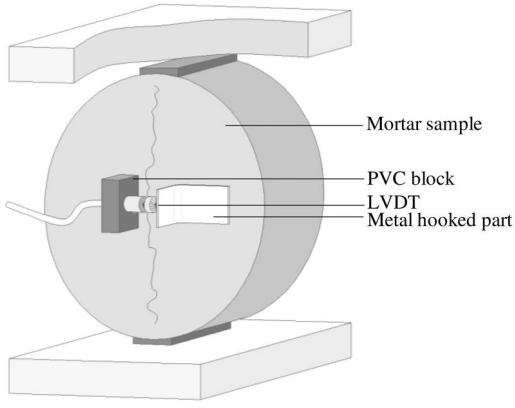

Figure 2. Performance of a crack width controlled splitting test onto a mortar cylinder.

control. The crack width was increased until 400 μm was reached. Then, specimens were unloaded resulting in a decrease in crack width. In order to make sure that the samples would not break into two parts, during loading, the circumferential area was coated with epoxy and a clamp was fixed onto the samples in the direction orthogonal to the crack.

3.2 *Crack width measurements*

As mentioned in the previous paragraph, crack widths decreased at the moment of unloading. In order to know the exact width of each crack over the whole length, crack widths were determined. At 9 positions, equally divided along the length of the crack, the crack width was measured with a stereo microscope (Leica S8APO and DFC295 camera).

3.3 *Crack repair*

Cracks of the samples containing encapsulated repair agent were autonomously healed. The embedded glass tubes broke during crack formation and both components of the repair agent were released into the crack due to capillary forces. Leakage of the polyurethane repair agent was seen at the crack faces. After several minutes, the leaked repair agent started to foam and became hard.

3.4 *Chloride diffusion*

Before the chloride diffusion test was started, all faces of the samples, except the one to be exposed to the chloride solution, were coated with epoxy. When the coating was hardened, the samples were submerged in a saturated calcium hydroxide solution for a period of 7 days. The chloride diffusion test was based on the NT Build 443 test method. The samples were placed in a closed container filled with a sodium chloride solution (165 g/l) so that only the free surface of the samples was exposed to the chloride solution. All samples were subjected to the solution for a period of 7

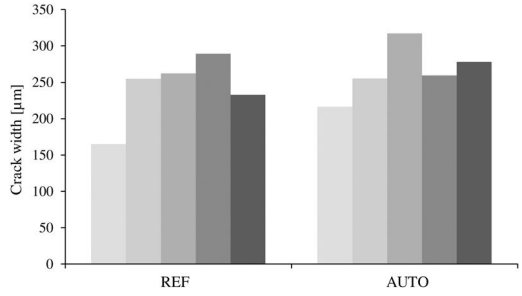

Figure 3. Measured crack width of the REF samples and the AUTO samples.

weeks. After this time span, samples were split in the direction orthogonal to the crack and the broken surfaces were sprayed with a 0.1 M silver nitrate solution to measure the chloride penetration from the white silver chloride precipitation front.

From each split sample, one half was analyzed. For each test series, the zone of the cross-section which was exposed to the chloride solution was compared to the total cross-section. Moreover, the penetration depth from the uncoated surface, exposed to the chloride solution, was measured at 18 different positions equally divided along the exposed surface. In addition, the chloride ingress, in the direction orthogonal to the crack was measured at each side of the crack on 9 positions equally divided along the crack length.

4 RESULTS

4.1 *Crack widths*

Although during crack formation the aimed crack width was set at 400 μm, it was evident that the resulting crack width was lower. For each sample, in which cracks were created, the resulting crack width is shown in Figure 3. The final crack width varied between 150 and 350 μm but did not depend on the fact whether encapsulated repair agent was present in the matrix or not.

4.2 *Chloride diffusion*

Based on the defined chloride profile the samples were classified in 4 categories as shown in Figure 4. For samples belonging to category A an equal chloride penetration was noticed. Samples belonging to category B showed some additional penetration of chlorides through the crack. For samples belonging to category C, chlorides seemed to penetrate through the whole length of the crack and even reached the opposite side of the sample. In the case samples belong to category D it was even noticed that chlorides penetrated the layer at the opposite side of the sample.

In Table 3 an overview is given of the amount of samples of each test series belonging to each of the categories. If no crack is present in the matrix (UNCR)

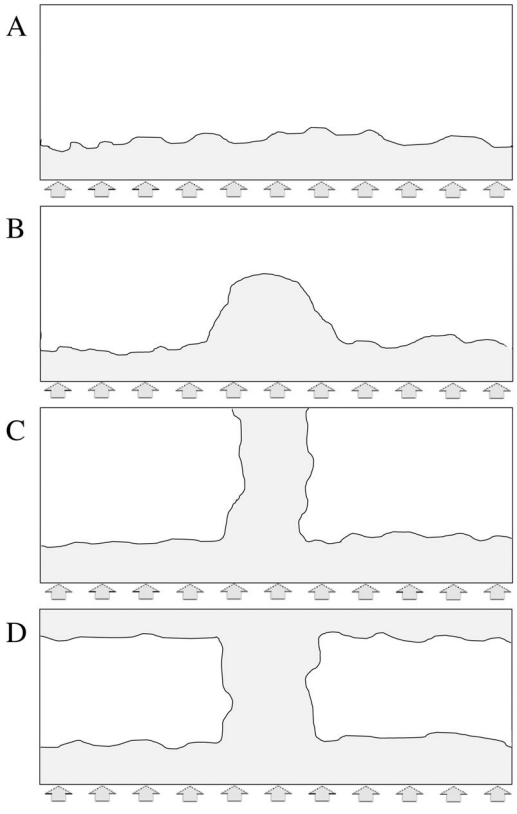

Figure 4. Measured chloride profiles: (A) Equal penetration (B) Additional penetration through crack (C) Complete penetration through crack (D) Complete penetration through crack and chlorides accumulate at opposite surface. Grey marked area corresponds to the zone where chlorides penetrated. Arrows indicate the direction of chloride ingress.

Table 3. Amount of samples belonging to each of the categories.

	REF	AUTO	UNCR
A	0%	40%	100%
B	0%	20%	0%
C	40%	40%	0%
D	60%	0%	0%

an equal chloride distribution is noticed for all samples (100% category A). This equal penetration depth generally varies around 1 cm. As soon as a crack is present in the matrix the samples shift towards the other categories. When cracks are immediately healed, due to the presence of encapsulated repair agent, still 40% of the samples shows equal chloride ingress (40% category A). For 20% of this series, no complete crack closure seemed to be obtained, resulting in the fact that some additional intrusion of chlorides was noticed around the crack. For 40% of the samples belonging to the AUTO series, chlorides were able to penetrate

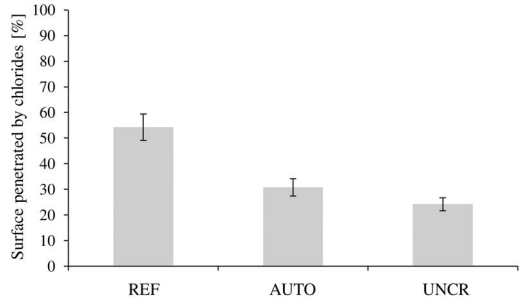

Figure 5. Surface of the split halves which was penetrated by chlorides [%].

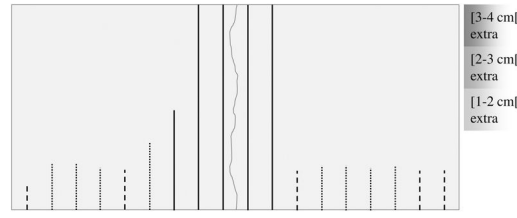

Figure 6. Schematic representation of measured chloride profile.

through the whole length of the crack and even reached the opposite side of the sample. However, for none of these samples accumulation of chlorides at the other side of the sample was noticed in contrast to the samples belonging to the REF series where 60% of the samples suffered from this phenomenon. When cracks were left untreated (REF), no samples were ranged in categories A and B. In all cases the chlorides were able to cross the whole crack length (40% category C and 60% category D).

In order to study the results in more detail, for all samples of each series, the zone of the analyzed cross-section in which chlorides penetrated was compared to the total cross-section (Figure 5). In this way a significant difference (significance level 5%) was noticed between the samples with untreated cracks (REF) and samples with treated cracks (AUTO) or uncracked samples (UNCR). For the reference samples, more than half of the analyzed cross-section showed signs of chloride ingress. This value is significantly different compared to the value of about 30% noticed for the AUTO series and 25% noted for the UNCR series. In addition, no significant difference was seen between the chloride penetration noticed for the uncracked samples and the samples of which the cracks were healed due to release of encapsulated polyurethane.

As mentioned before, the cross-sections were not only analyzed by determining the zones in which chlorides penetrated but in addition the chloride ingress from the inlet surface was measured at fixed positions. In Figure 6, a schematic representation is given of the profile measured for a cracked sample. The 5 measuring positions with least chloride ingress (indicated with a dashed lines) were used to calculate the

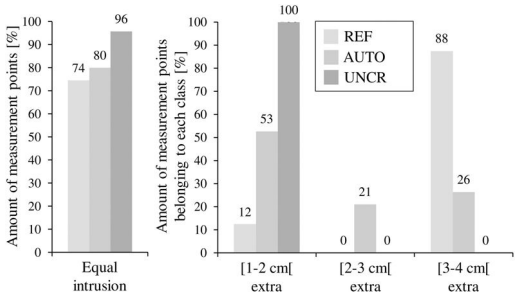

Figure 7. Chloride ingress measured at fixed positions from the inlet surface.

mean intrusion of chlorides in the mortar matrix. If the intrusion depth at other measuring points did not differ more than 1 cm from the mean value which was calculated, equal intrusion was assumed (measuring points indicated with dashed and dotted lines). The measuring positions indicated with a continuous line represent positions where additional chloride ingress was measured. Based on how far the additional ingress went, different classes were specified. While the lower classes ([1–2 cm[extra) would be less dangerous for chloride induced reinforcement corrosion, this danger becomes bigger in the case measuring points belong to one of the higher classes ([3–4 cm[extra).

The left graph of Figure 7 represents the amount of measuring points where an equal chloride intrusion was noticed. The graph at the right shows how much of the measuring points, where additional chloride intrusion was noticed, belong to each of the specified classes.

As shown in Figure 7, in the case of uncracked samples, for 96% of the measurements an equal intrusion was noticed. For the AUTO series 80% of the measuring points showed an equal intrusion and for the REF series this value only amounted to 74%. The measuring points where an equal ingress was noticed for the AUTO and REF series were located 0.5 to 1.5 cm (in horizontal direction) from the crack.

For the remaining measuring positions of these series (20% for the AUTO series and 26% for the REF series) additional chloride ingress was measured. For the AUTO series, 53%, 21%, and 26% of these measuring points belong to each of the subsequent classes.

It can be noticed that the amount of data points belonging to the worst class ([3–4 cm[extra) and signifying that the chlorides were able to penetrate through the whole thickness of the sample, was limited. For the untreated samples, however, (REF series) the amount of measuring points where additional chloride intrusion was noticed and which belonged to the worst class amounted to 88%. It can thus be seen that, although autonomous crack repair is not resulting in complete crack closure, a large improvement compared to the chloride ingress into untreated cracks is obtained.

5 CONCLUSIONS

It can be concluded that self-repairing of concrete cracks by the use of encapsulated polyurethane can help to reduce the ingress of chlorides via cracks and can thus help to make concrete structures more durable. While it was seen that the current self-repairing approach was not yet optimal as no complete crack closure was obtained, a large improvement compared to untreated cracks was already noticed. When comparing the zone covered by chlorides, a significant difference was seen between samples with untreated cracks and cracks which were autonomously healed, while no significant difference was seen between cracked samples with encapsulated repair agent and uncracked samples.

ACKNOWLEDGEMENTS

The authors would like to acknowledge Sam Vantyghem and Elke Gruyaert for their assistance in preparing and analyzing the samples. Financial support from the Research Foundation Flanders (FWO-Vlaanderen, Project No. FWO013/PDO/182) and the Agency for Innovation by Science and Technology (IWT) is gratefully acknowledged.

REFERENCES

Audenaert, K., de Schutter, G. & Marsavina, l. (2009) influence of cracks and crack width on penetration depth of chlorides in concrete. *European journal of environmental and civil engineering* 13, 561–572.

Djerbi, A., Bonnet, S., Khelidj, A. & Baroghel-Bouny, V. (2008) influence of traversing crack on chloride diffusion into concrete. *Cement and concrete research,* 38, 877–883.

Maes, M., Gruyaert, E. & Belie, N. (2013) resistance of concrete with blast-furnace slag against chlorides, investigated by comparing chloride profiles after migration and diffusion. *Materials and structures,* 46, 89–103.

Van Tittelboom, K., de Belie, N., van Loo, D. & Jacobs, P. (2011) self-healing efficiency of cementitious materials containing tubular capsules filled with healing agent. *Cement and concrete composites,* 33, 497–505.

Van Tittelboom, K., de Belie, N. (2010) self-healing concrete: suitability of different healing agents. *International journal of 3r's,* 1, 12–21.

This page intentionally left blank

Concrete Solutions – Grantham et al. (Eds)
© 2014 Taylor & Francis Group, London, ISBN 978-1-138-02708-4

Influencing factors affecting microbial metabolic processes of bio materials used for leaking repairs

I. Ujike, F. Kubo & K. Kawaai
Ehime University, Matsuyama, Japan

S. Okazaki
Port and Airport Research Institute, Yokosuka, Japan

ABSTRACT: This paper presents influencing factors on repair methods using bio grout comprising dry yeast, sucrose and calcium acetate. The investigation reveals that calcium carbonate can precipitate as crystals depending on the concentrations of those materials used in the grout and pH levels. The results suggest that the precipitates can increase even at higher concentrations than materials used, which could be attributed to the proper treatment of pH adjustment. It was found that the precipitates were large enough to seal gaps formed between concrete specimens and the effectiveness in reducing water permeability was also shown.

1 INTRODUCTION

Reinforced concrete (RC) structures have been commonly used in infrastructure facilities including bridges, tunnels and ports and airports in Japan. Among the structures, large voids on the surface of concrete exist owing to imperfections in construction or initial defects including early age shrinkage cracking and cold joints.They often lead to a decrease in durability. When it comes to RC bridges, gaps between hardened concrete members are typically formed between the slab and substrate of handrails. Leakage of rainwater through the gaps is inevitable if the water tightness of the gaps is not taken into consideration in design or construction. Thus, there is an immediate need for repair to prevent rainwater from leaking through gaps formed between concrete members.

Conventionally, polymer or epoxy impregnation methods have been used to repair cracks in cover concrete. According to practical experiences in the field application of these materials, it has been reported that they may have several issues in the application especially for leaking parts of gaps formed between concrete members. Problems include longer installation and operation periods needed and the material properties with higher viscosity, which is less practical in repairing deeper zones of cracks or gaps. In addition, they are typically comprised of cement-based materials. This is highly detrimental if the repair materials flow out into the natural environment. Therefore, it is advantageous if the materials are not based on cementitious materials but exhibit similar materials properties to concrete.

Recently, grout materials using microbial metabolic processes have been investigated (Kawasaki et al., 2006; Matsushita et al., 2010). The grout materials or bio grout are comprised of a microorganism, a nutrition source and a calcium source. When dry yeast is chosen as the microorganism, carbon dioxide produced through the metabolic processes,consuming a nutrition source such as sucrose, provides carbonate ions. The carbonate ions can react with calcium ions present in the grout, leading to precipitations of calcium carbonate depending on pH levels, as shown in Figure 1. These reactions are summarized as follows:

$$\begin{aligned} &C_{12}H_{22}O_{11} + H_2O \rightarrow 4CO_2 + 4C_2H_5OH \\ &CO_2 + H_2O \rightarrow CO_3^{2-} + 2H^+ \\ &Ca^{2+} + CO_3^{2-} \rightarrow CaCO_3 \downarrow \end{aligned} \quad (1)$$

It should be noted that the material produced through the reactions is not harmful to concrete materials because the precipitates mainly arise from calcium carbonate. Besides material properties, the bio grout is a less viscous material. This may overcome shortcomings associated with conventional repair materials as mentioned previously. Thus, it would be beneficial if materials could flow into deeper zones of the gaps formed between concrete members to improve water-tightness. However, the amount of precipitates is largely affected by the concentrations and mix proportions of materials used and the pH levels. In particular, it is crucial that the precipitates are large enough to seal the leakage parts through the gaps in the practical applications. Therefore, this study examined influencing factors contributing to larger amount

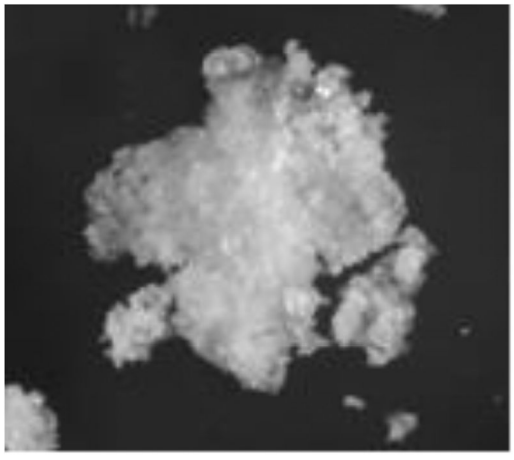

Figure 1. Crystals of calcium carbonate (×200 magnification).

of precipitates based on results of past experiments carried out by authors. Section 2.1 and 2.2 presents experimental details carried out in this study.

2 CENTRIFUGE TUBE TESTS

2.1 *Selection of basic constituents of bio grout*

Bio grout used in this study needs: 1) sources of calcium ions and 2) carbonate ions as shown in Figure 2. It is essential to control the pH levels in the grout to facilitate the precipitation of calcium carbonate. A Tris (tris hydroxymethyl aminomethane) buffer solution, which is generally used in biochemistry for a solution having an alkali buffering function, was used. The calcium source used for the bio grout was chosen based on its higher solubility and no adverse effects on concrete materials. The material should be also commercially available and cost-effective. Based on the aforementioned considerations, calcium acetate $(CH_3COO)_2Ca$ was chosen as the calcium source in this study.

In addition, carbon dioxide through the metabolism activity of the microbe or an enzyme was used as a carbonate ion source.Inorganic or organic sources of nutrients are necessary for the metabolism of the microbe. Dry yeast, which is commercially available, was used as the microbe. Sucrose ($C_{12}H_{22}O_{11}$) was chosen as a source of nutrients.

It is generally known that higher pH is a severe condition for yeast. On the other hand, microbial metabolism is less active when the pH becomes lower. According to past research, it has been reported that calcium carbonate was not produced when the pH was less than 7.5. In order to maintain the appropriate pH levels in experiments, a Tris buffer solution was mixed with hydrochloric acid which was adjustable pertaining to the pH in the solution by dilution with distilled water. The pH was specified as 9.0 in the ambient environmental condition controlled at 20°C.

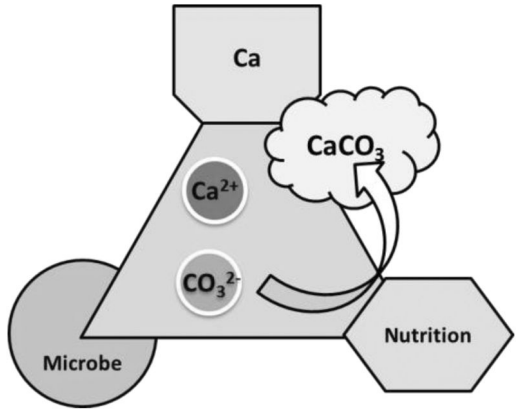

Figure 2. Basic constituents of bio grout.

Table 1. Combinations of dry yeast, sucrose and calcium acetate.

Cases	Dry yeast (g/L)	Sucrose (mol/L)	Calcium acetate (mol/L)
A1	3.0	0.10	0.05
A2			0.10
A3			0.15
A4			0.20
A5			0.25
A6			0.30
B1	4.5	0.10	0.05
B2	9.0		
B3	12.0		
C1	3.0	0.20	0.05
C2		0.30	
C3		0.40	
D1	6.0	0.20	0.10
D2	9.0	0.30	0.15
D3	12.0	0.40	0.20

With the above materials, 15 combinations of grout were formed based on the results of past research. Table 1 shows the combinations of each material tested in this study.

2.2 *Testing procedure*

In order to measure the amount of precipitates arising from the microbial metabolic processes, each mixture was prepared in a centrifuge tube. First, each material measured for the specified quantities was prepared on an evaporating dish and mixed with the Tris buffer solution in a beaker. The tube was subsequently stirred until each material was dissolved into the solution. Then, the Tris buffer solution was further added to make the solution 40 ml in total. The amount of precipitates was measured after the solution was filtered and the residue was dried in an experimental chamber controlled at 60°C. Each test was carried out using two test tubes to confirm consistency.

Based on the results of precipitates, ratios of precipitation were determined using the following formula:

$$P_{cal} = \frac{x(g)}{Q(mol/L) \times m(L) \times M(g/mol)} \times 100(\%) \quad (2)$$

Where: Pcal: ratios of precipitation (%); x: amount of precipitates of calcium carbonate (g); Q: concentration of calcium acetate (mol/L); m: amount of solution (g); and M: molar mass of calcium carbonate (100.09).

3 RESULTS AND DISCUSSION

3.1 *Results of preliminary tests*

Based on the results of past experiments carried out by Kubo et al. (2013), combinations of each material contributing to precipitates as crystals were examined using centrifuge tube examinations similar to the testing procedure specified in this study. The combinations tested were A1-A6 cases as shown in Table 1. The concentrations of calcium acetate were specified as 0.05–0.3 mol/L, which were mixed with dry yeast and sucrose with concentrations of 3.0 g/L or 0.10 mol/L respectively. Based on the results obtained, the study showed that the increase in concentrations of calcium acetate led to an increase in the amount of precipitates for the cases tested. However, crystals of calcium carbonate in the precipitates were visually confirmed only in the case of A1; others tended to form gels rather than crystals, although the amount of residue was larger than that obtained in the case of A1.

X-Ray Diffraction (XRD) analysis was also carried out for the cases of A1 and A6 in order to investigate the chemical compositions of crystals obtained in these cases. The results showed peaks at 23, 29, 36 and 39° for the case of A1, thus suggesting that the crystals were mainly comprised of calcite. Although the presence of calcite was also inferred by the test results in the case of A6, the XRD analysis registered other peaks which seemed to imply that they were formed not only by calcite but other chemicals. It should be noted that there is a need to find the best combinations contributing to larger amount of precipitates as crystals, which could be more effective in sealing leaking zones in concrete. Based on the findings, it was found that the amount of calcium ions affected the structures of crystals formed through microbial metabolic processes of the bio grout. Thus, it is necessary to adjust the concentrations of calcium acetate with concentrations of carbonate ions.

In this study, A1 case was also tested using a centrifuge tube. Figure 3–4 show the results of amounts of precipitates and changes of pH measured up to 7 days after each material was mixed in the tube. The pH was measured using commercially available pH meter.

The figures show that the amount of precipitates increased until 4 days after the mixture was added into the Tris buffer solution and reached the peak. After that, the amount of precipitates seemed not to increase until the end of measurements continued up to 7 days.

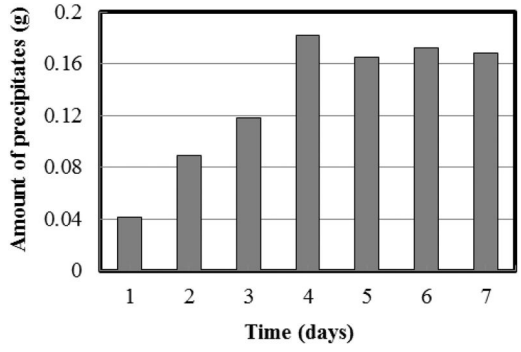

Figure 3. Amount of precipitates measured up to 7 days.

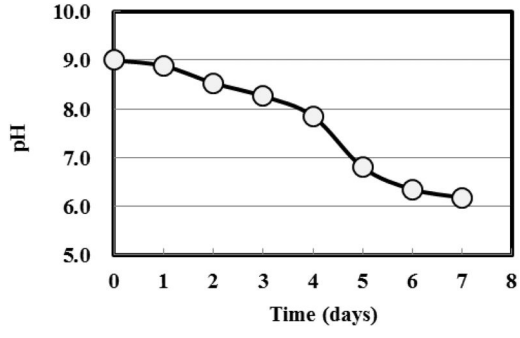

Figure 4. Changes of pH up to 7 days.

Besides the peaks confirmed on 4 days, the pH in the solution registered significantly lower values less than pH 7.0 until 5 days of the monitoring. Based on the observations made, precipitations of calcium carbonate were found to be dependent on the pH levels in the solution. The precipitation rate of calcium carbonate seems to be lower with the decrease in the pH especially below pH 7.5, which is consistent with past research results.

3.2 *Carbonate ions through microbial metabolic processes*

The presence of calcium ions as examined in Section 3.1 and carbonate ions arising from the microbial metabolic processes are essential in the precipitation of calcium carbonate. Section 3.2 reports on how concentrations of dry yeast may affect the amount of precipitates and pH levels in the solution. The mixtures investigated were B1-B3 cases as shown in Table 1. Concentrations of dry yeast were specified as 4.5, 9.0 and 12.0 g/L, which were mixed with sucrose and calcium acetate with concentrations of 0.10 or 0.05 mol/L respectively.

Figure 5–6 show results of amount of calcium carbonate precipitated and changes of the pH in the solution up to 7 days of monitoring. Figure 5 clearly showed that the precipitation of calcium carbonate were less in cases B1, B2 and B3. The lower precipitation observed in the cases of dry yeast with higher

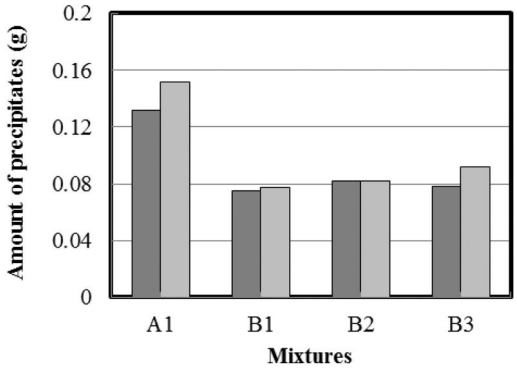

Figure 5. Amount of precipitates (A1, B1-B3 cases).

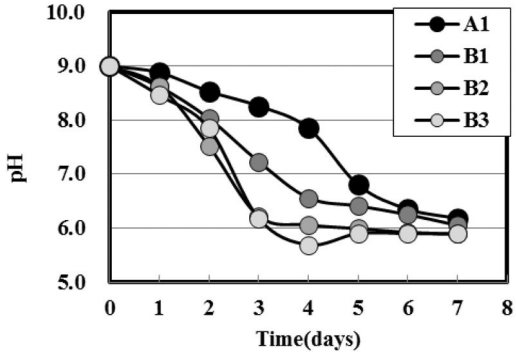

Figure 6. Changes of pH (A1, B1-B3 cases).

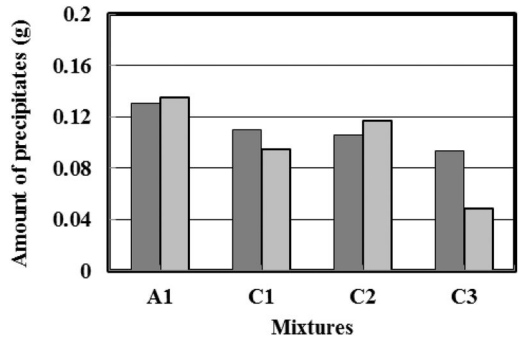

Figure 7. Amount of precipitates (C1-C3 cases).

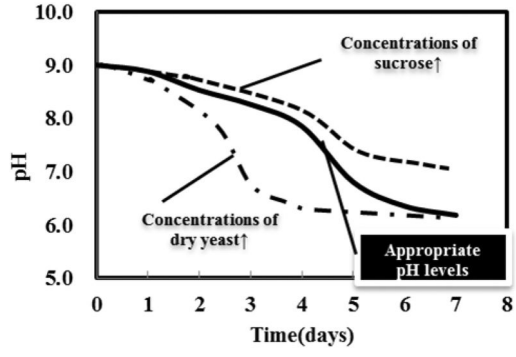

Figure 8. Changes of pH during centrifuge tube tests.

concentrations compared to that of A1 case could be attributed to rapid drops in the pH at the early stages of monitoring as shown in Figure 6. Although the pH were controlled at higher levels which were initially 9.0 through the use of Tris buffer solution, the pH decreased owing to carbonate ions arising from microbial metabolic processes of dry yeast, some of which seemed to not react with calcium ions present in the solution. Thus, the amount of dry yeast affects the rate of carbonate ions arising from its metabolic processes. It is necessary to determine the concentration of dry yeast taking into consideration the rate of calcium carbonate produced in order to maintain the appropriate pH levels at early stages of the precipitation. Section 3.3 reports on the influence of concentrations of sucrose on the precipitates.

3.3 *Concentrations of sucrose as a nutrition*

The mixtures used in centrifuge tube tests were C1-C3 cases with higher concentrations of sucrose as shown in Table 1. They were 0.2, 0.3 and 0.4 mol/L respectively. The amount of calcium carbonate precipitated was measured after 7 days of the monitoring and changes of pH were also measured after 1 and 7 days of monitoring.

Figure 7 shows the results of amount of calcium carbonate precipitated for the cases C1-C3. The results seemed to show that the amount of calcium carbonate decreased in cases C1-C3. The adverse effects of sucrose with higher concentrations on the precipitates were not completely clear; however, the pH consistently registered higher values which were about pH 7.1 for those cases after 7 days of monitoring. This highlights a distinction between A1, B1-B3 and C1-C3 cases in that the carbonate ions seemed to become smaller in the solution. Therefore, the higher concentrations of sucrose as nutrition led to uncomfortable environments for the metabolic processes of dry yeast.

Based on the results of centrifuge tube tests summarized in Section 3.1–3.3, it was found that the pH in the solution especially at the early stages of precipitation is a significant factor contributing to larger precipitates of calcium carbonate. The pH should be controlled at appropriate levels in order to sustain the precipitation of calcium carbonate.

3.4 *Changes of pH until calcium carbonate precipitates*

In the case of A1, as can be seen in Figure 8, although the pH decreased below 7.5 after 5 days of the monitoring, the amount of precipitates reached more than 80% as a ratio of precipitation calculated based on formula (2). It should be noted that calcium carbonate could form before the pH becomes lower on conditions that

the rate of carbonate ions produced meets the amount of calcium ions present.

4 DEVELOPMENT OF BIO GROUT WITH HIGHER CONCENTRATIONS OF MATERIALS USED

4.1 *General*

Section 3 examined the influencing factors on processes of microbial metabolism and the precipitates of calcium carbonate. Based on the results obtained, when concentrations of each material alone used in the bio grout increased compared to those used in the case of A1 with dry yeast (3.0 g/L, sucrose: 0.10 mol/L and calcium acetate: 0.05 mol/L), the precipitates tended to form gels or resulted in a reduction in the amount of the precipitates. These adverse effects on the processes of precipitation may be illustrated by the changes of pH, which should be taken into consideration in order to increase the precipitates of calcium carbonate as crystals. This section deals with detailed investigation on the processes of precipitation when equally increased concentrations of three materials were used for the bio grout.

4.2 *Testing procedure*

Centrifuge tube tests and monitoring of pH in the solution were carried out using mixtures D1-D3 as shown in Table 1. It should be noted that Tris buffer solution was also used to adjust the pH levels to facilitate the precipitation of calcium carbonate as crystals. Subsequently, water permeability testing was carried out to confirm the effectiveness of the bio grout proposed in this study. Hardened concrete specimens cast with a water to cement ratio of 0.4 was used with leakage parts through gaps formed between the specimens. Before the bio grout was poured into the gaps, the water permeability tests were carried out as benchmarks. The quantity of water flowing through the gap was measured at predetermined intervals as shown in Figure 9.

Then, the bio grout was poured into the gap as shown in Figure 9. It should be noted that the leakage parts were sealed with tape to prevent flowable bio grout loss. Precipitation of calcium carbonate was visually confirmed after 7 days of the monitoring, some of which were taken from the specimens and observed using a microscope. Finally, water permeability tests were carried out using the specimens which were supposed to be sealed with precipitates of calcium carbonate.

4.3 *Results of centrifuge tube tests*

Figure 10 shows the results of centrifuge tube tests using D1-D3 cases with higher concentrations of each material used. They were twice to four times those used in the case of A1 case. Based on the results

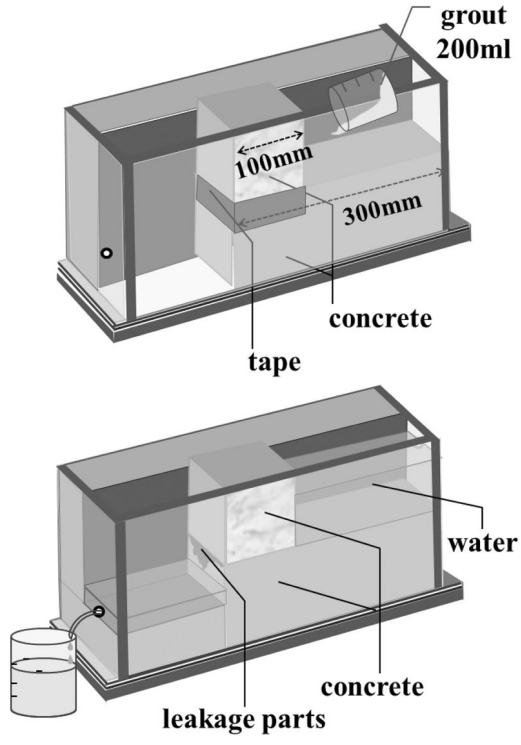

Figure 9. Water permeability tests.

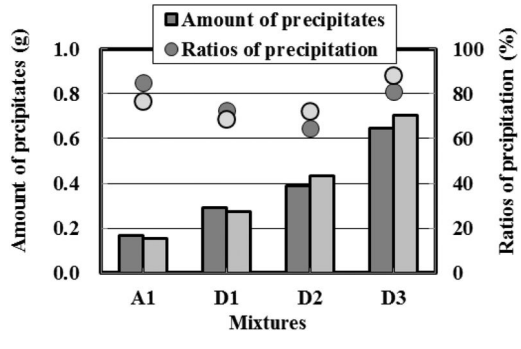

Figure 10. Results of centrifuge tube tests (D1-D3).

obtained, the precipitates especially in the case of D3 substantially increased and reached about 80% as the ratio of precipitation calculated. The increased amount of widespread precipitates immediately after the centrifuge tube test was visually confirmed as shown in Figure 11. It may be noted that the pH levels in the cases of D1-D3 significantly varied, which were not consistent with those observed in the case of A1. With the Tris buffer solution, the pH was adjusted at suitable levels in facilitating the precipitation of calcium carbonate.

The increase in the amount of precipitates was shown in Figure 12 in the case of D3 measured up to 7 days after the mixture was made. Also shown were changes of pH in the solution. As can be seen,

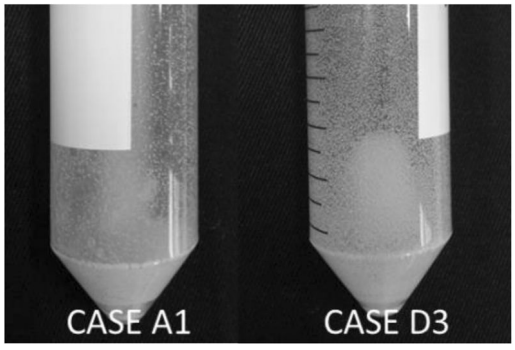

Figure 11. Comparison of precipitates (A1, D3).

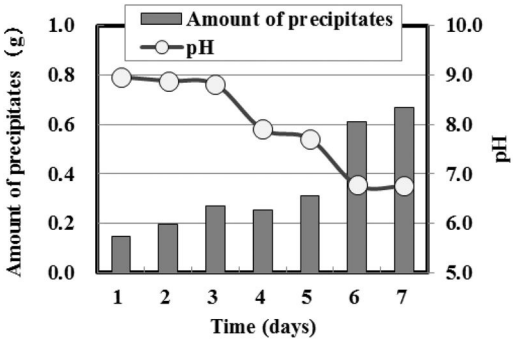

Figure 12. Results of centrifuge tube tests and changes of pH in the case of D3.

the changes of pH were observed to be consistent with those of A1 case. The precipitation of calcium carbonate significantly increased after 6 days of monitoring, which showed a distinction between A1 and D3 cases in that the mixture with higher concentrations of D3 case took longer time to precipitate. This may be attributed to the adverse effects of higher concentration of the nutrition on the propagation of the microbe. The longer time needed for the precipitation was not very practical in implementing the bio grout in the actual structures. However, appropriate treatment of bio grout with continuous wet conditions may be effective in sustaining the microbial metabolic processes and precipitation of calcium carbonate especially at leakage parts of concrete structures. Section 4.4 reports on the effectiveness of the bio grout proposed in this study when used for leakage parts formed between concrete specimens.

4.4 *Results of water permeability tests*

In this study the mixture D3 was found to be the best combination leading to the highest amount of precipitates measured. The bio grout was applied to the leakage parts formed between hardened concrete specimens. Figure13 shows the specimens used for the water permeability tests. As can be seen, it was confirmed that the gaps were sealed with precipitates

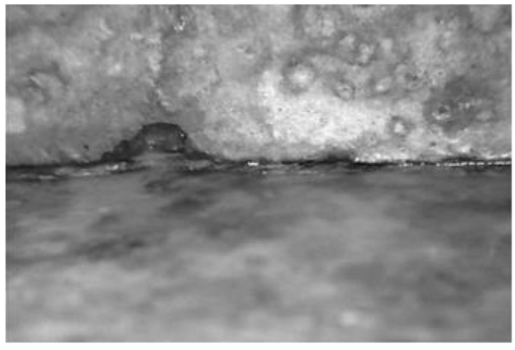

Figure 13. Visual observation of bio grout applied.

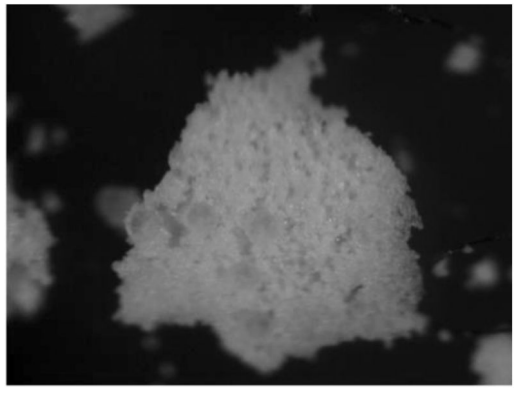

Figure 14. Precipitates (×250 magnifications).

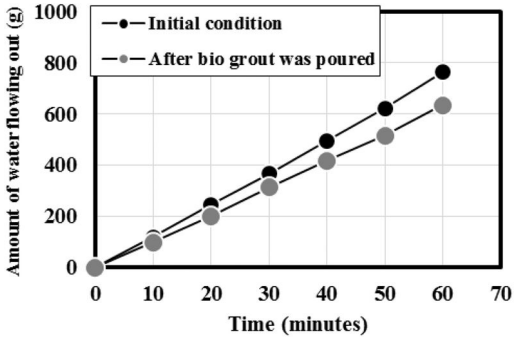

Figure 15. Results of water permeability tests.

when the bio grout was applied. The picture was taken after 7 days before the water permeability tests were carried out. The precipitates were observed to be crystals of calcium carbonate as shown in Figure 14. The effectiveness of the bio grout in repairing the leakage parts was further investigated comparing the amount of water flowing through the gaps before and after the bio grout was poured.

Figure 15 shows the results of water permeability tests carried out after the bio grout was applied to the leakage parts. Also shown was the amount of water

measured before the bio grout was applied as benchmarks. As can be seen, water flowing out through the gaps decreased and showed about 20% reduction in the amount of water when tested up to 60 minutes. The reduction observed can be attributed to the beneficial effects of the prolonged microbial metabolic processes leading to larger amount of precipitates as crystals when sustained with sufficient moisture. Although the leakage parts seemed to be partially sealed with the precipitates of calcium carbonate, the results suggest that the gaps may be fully sealed with the precipitates if the precipitates were large enough to seal the leakage parts.

5 CONCLUSIONS

In this study, the influencing factors contributing to larger amount of precipitates arising from microbial metabolic processes were investigated using centrifuge tube tests and monitoring of pH in the solution. The effectiveness of the bio grout proposed in this study was further examined using water permeability tests. Based on the results obtained, the findings were summarized as follows:

- Concentrations of dry yeast as a microbe affected the production rate of carbon dioxide through its metabolic processes. The increased concentration of dry yeast alone tended to result in a reduction in the amount of precipitates.
- The increase in the concentrations of sucrose as a nutrition alone led to a reduction in the amount of precipitates of calcium carbonate. It was found that the pH was maintained at higher levels of about 7.1 after 7 days of monitoring.
- It was found that the increase in concentrations of dry yeast, sucrose and calcium acetate is highly advantageous in increasing precipitates when the pH was adjusted at suitable levels in sustaining the precipitation of calcium carbonate.
- It is highly possible that the bio grout with higher concentrations of each material used in this study could seal fully the leakage parts formed between concrete specimens tested.

ACKNOWLEDGEMENTS

The authors express appreciation to Mr. Tomoya Yanomoto, an undergraduate student in Ehime University, for his contribution.

REFERENCES

Kawasaki, R. 2006. Fundamental Study on Novel Grout Cementing Due to Microbial Metabolism, Journal of Japan Society of Engineering Geology, Vol.47 , No.1, 2–12

Matsushita, Y., Okazaki, S., Yasuhara, H., and Ujike, I. 2010. Development of the repairing method of construction to the crack of concrete by using microbe metabolism, Proceedings of Japan Concrete Institute, Vol. 32, No. 1, 1589–1594

Kubo, F., Okazaki, S. and Ujike, I. 2013. Development of Microbial Metabolic Processes to Repair Concrete Joint Leakage,Advanced Materials Research, 845, 158

This page intentionally left blank

Concrete Solutions – Grantham et al. (Eds)
© 2014 Taylor & Francis Group, London, ISBN 978-1-138-02708-4

Field performance of bacteria-based repair system: Pilot study in a parking garage

V. Wiktor & H.M. Jonkers
Delft University of Technology, Delft, The Netherlands

ABSTRACT: This paper presents the field performance in a parking garage of the recently developed bacteria-based repair system for concrete. This liquid-based repair system aims at the sealing of cracks and decrease of the porosity due to the production of a calcium-based biomineral. The system combines advantages of both a traditional repair system for concrete (fast reacting, and short term efficiency), and bio-based methods (more sustainable, slow process, and long-term efficiency).

The bacteria-based repair system has been sprayed onto the surface of cracks and on concrete pavement. The crack-sealing efficiency and improvement of frost salt scaling were assessed by water permeability and freeze/thaw resistance tests respectively. The results were very promising as only cracks that had not been treated with the bacteria-based repair system were still heavily leaking. In addition, the freeze/thaw resistance of concrete that was treated with the bio-based repair system was higher than the untreated concrete.

1 INTRODUCTION

Concrete is the most used construction material worldwide. Indeed, even if exposed to a number of degradation processes such as carbonation or chloride ingress, concrete structures can reach a service life of more than 50 years (Emmons & Sordyl, 2006). However the presence of cracks, and the subsequent ingress of aggressive corroding substances, is a major limitation for the durability. This leads to the premature corrosion of the reinforcement and early failure of the structure. As a result, costly measures for maintenance and repair are undertaken. Nowadays a wide range of repair products, such as for instance epoxy-based fillers or silane-based water repellent, is available for concrete. However, the short term efficiency and negative impact on the environment are an issue for the repair industry.

Biodeposition, a method by which calcium carbonate (CaCO3) precipitation is induced by bacteria, has been proposed as an interesting alternative approach to protect building materials. Various pathways are involved in Microbial Induced Precipitation (MIP) process. Among them, enzymatic hydrolysis of urea in a calcium rich environment is the most commonly used system (Dhami et al. 2012). Successfully applied as a surface treatment in practice to limestone monuments, it has been considered only on a laboratory scale for cementitious material and crack repair.

Also, besides cost issues, MIP using ureolytic bacteria might generate other problems, such as environmental nitrogen loading due to the production of ammonia during the hydrolysis of urea or negative effect to the material itself due chemical reactions with ammonium salt (Dhami et al. 2012). In addition, the time required for a substantial amount of bacterially induced calcium carbonate may hold back the acceptance of MIP as an efficient repair technique by the building industry.

Bacterially mediated calcite precipitation thanks to metabolic conversion of calcium lactate instead of urea hydrolysis has been successfully applied in self-healing concrete (Wiktor & Jonkers 2010). The authors implemented this concept for the development of bio-based repair system for a real concrete structure. The novelty of such a system is to combine advantages of both a traditional repair system for concrete and bio-based methods (Wiktor & Jonkers 2011, 2012a).

In this way, a silicate-based compound, which has a composition similar to concrete, is associated with MIP without involving a urea hydrolysis pathway. Instead, the metabolic conversion of organic salts through bacterial respiration is used for MIP.

The bio-based repair system as presented in this paper is a liquid-based system which transports the bio-based agent into concrete. This paper investigates and discusses the field performance of the bacteria-based system developed in the laboratory.

2 MATERIAL AND METHODS

2.1 *Bacteria-based repair system*

The repair system consists of concrete compatible bacteria (Wiktor & Jonkers 2012b) and feed which

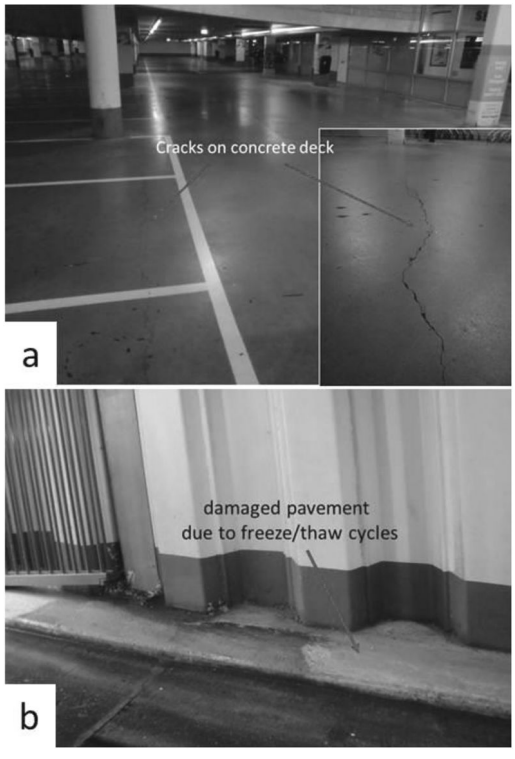

Figure 1. Test location for the application of the bacteria-based repair system. (a) cracks on the concrete deck, (b) pavement on the side of the access ramp.

produce calcite-based minerals decreasing concrete porosity. This system is composed of two solutions:

(i) Solution A – Sodium-silicate (alkaline buffer), Sodium-gluconate (Carbon source for bacteria growth), alkaliphilic bacteria.
(ii) Solution B – Calcium-nitrate (nitrate source for denitrification when O_2 is depleted and calcium for $CaCO_3$ precipitation), alkaliphilic bacteria.

The denitrification is the biological reduction of nitrogenous oxides to gaseous products during anaerobic (no oxygen) bacterial growth. This means that under the metabolic conversion of calcium nitrate, N_2 and $CaCO_3$ are produced.

The silicate-based compound, sodium silicate, ensures an alkaline pH in the system and the formation of a gel inside the crack. Although not very strong, this gel allows a rapid sealing of the crack (within a few hours) and an optimum environment for bacteria to precipitate calcium carbonate. By the time the gel becomes too weak, a substantial amount of $CaCO_3$ has been precipitated to seal the crack.

2.2 *Test location: Parking garage*

The test location was a 2 storey underground parking garage with a capacity of 300 parking places.

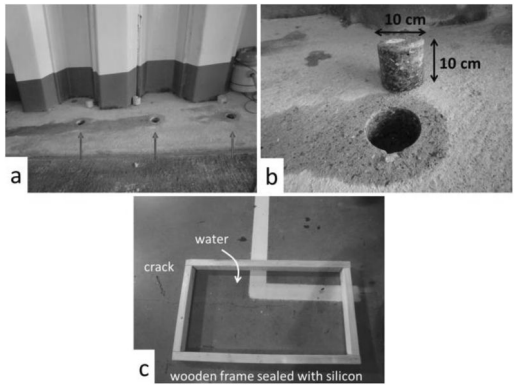

Figure 2. Evaluation of the repair system's efficiency. (a) cores drilled on the concrete pavement, (b) detail of a core, (c) water permeability testing.

The concrete deck was suffering from cracking which resulted in significant leakage of the structure (Fig. 1a). Also, the concrete pavement on each side of the access ramp was damaged due to freeze/thaw (Fig. 1b).

2.3 *Application of the bacteria-based repair system*

Part of the concrete pavement (area of 2×0.5 m) and three cracks (1–3 mm wide) of the concrete deck were impregnated with the bacteria-based repair system. Solution A and solution B were each poured in a sprayer, and manually applied at the surface of the concrete in layers until saturation of the concrete treated area.

2.4 *Evaluation of the efficiency of the repair system*

Two months after the application of the bacteria-based repair system, 6 cores were drilled (Fig. 2a-b) from two different locations on the concrete pavement: 3 from the treated area and 3 from an untreated part on the same side of the access ramp as control specimens. The resistance of the treated and untreated concrete to freeze/thaw conditions and deicing salt was then evaluated in laboratory.

The crack-sealing efficiency of the bacteria-based repair system was assessed by means of a water permeability test performed on site on 3 treated- and 3 untreated cracks (Fig. 2c).

2.4.1 *Resistance to freeze/thaw and deicing salt*

The 6 concrete cores were tested according the NPR-CEN/TS 1239-9 (Testing hardened concrete – Part 9: Freeze/thaw – scaling) and NEN-EN 13877-2 (Concrete pavement – Part 2: Functional requirements for concrete pavements). The test was performed independently by Cugla B.V. (Breda, The Netherlands). If the specimens are damaged in such a way that the mass loss is >1 kg/m^2, the test is stopped. Indeed, a mass

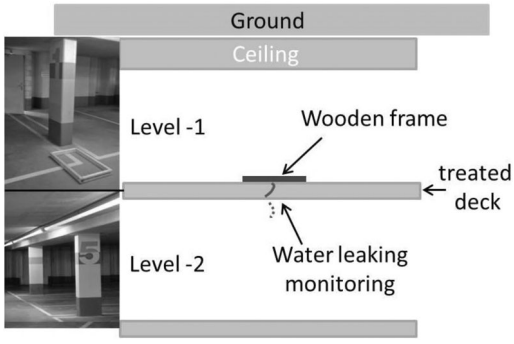

Figure 3. Schematic representation of the water permeability test performed.

loss > 1 kg/m^2 means that the concrete has a poor resistance to freeze/thaw and fits in the lowest category (FT0) according to NEN-EN 13877-2.

2.4.2 *Water permeability test*

The goal of this test was to have a rapid and practical evaluation of the crack sealing on site. For this purpose, rectangular wooden frames (1 × 0.5 m) were placed on top of the concrete deck in such a way that the crack went through the full length of the rectangle (Fig. 2c). The wooden frames were positioned on top of 3 cracks treated with the bacteria-based repair system and 3 non-treated cracks for control.

The wooden frames were sealed with silicon glue prior to pouring in 5 L of tap water. As the crack went through the whole thickness of the deck, the sealing efficiency was assessed by monitoring visually, from the other side of the deck, how much water was dripping through the crack (Fig. 3).

3 RESULTS AND DISCUSSION

3.1 *Resistance to freeze/thaw and deicing salt*

The results of the laboratory testing for scaling resistance with deicing salt are given in figure 4 and figure 5.

The test was stopped after only 7 cycles as specimens treated with the bacteria-based repair system and the control ones, both exhibited a mass loss > 1 kg/m^2. The concrete tested had a very poor resistance to freeze/thaw with de-icing salt.

However, a closer look to figure 4 and figure 5 shows that the specimens treated with the bacteria-based repair system had a significantly lower mass loss (scaling) compared to the control, 1.9 ± 0.3 kg/m^2 and 3.6 ± 1.3 kg/m^2 on average respectively.

Though treated and untreated concrete specimens falls into the lowest category (FT0) for scaling resistance, the results however suggest that the treatment with the bacteria-based system tended to improve the resistance of the concrete to freeze/thaw.

Of course, other parameters should also be taken into account while interpreting these results such as

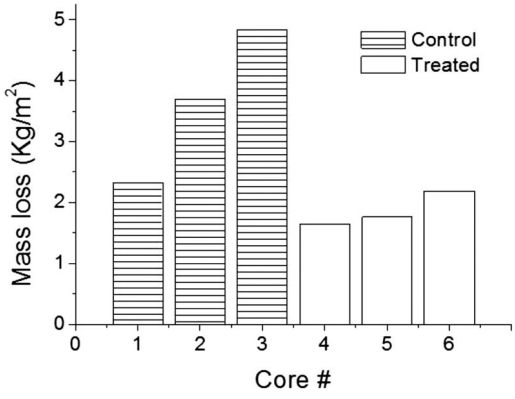

Figure 4. Scaling after 7 freeze/thaw cycles.

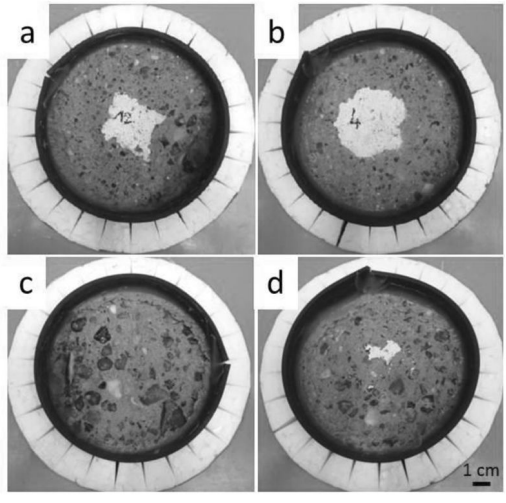

Figure 5. Observation of the control core #2 before (a) and after (c) 7 freeze/thaw cycles and treated core #5 before (b) and after (d) 7 freeze/thaw cycles.

the type of cement, mix composition or environmental factors. However, it should be noticed that very little is known about the history of this concrete. To our knowledge, the parking garage was built in 2005. The concrete has been exposed over the years to significant carbonation and freeze/thaw episodes.

Considering that the parking garage is located in the Netherlands and on a coastal area, most probably blast furnace slag cement was used.

Moreover, concretes with high slag content are known to have a lower carbonation resistance compared to Ordinary Portland Cement (OPC) which makes it more vulnerable to frost salt scaling (Copuroglu 2006). Indeed, carbonation of slag cement results not only in calcite formation as for OPC, but leads also to aragonite and vaterite formation. The combined attack of frost and chloride results in the dissolution of aragonite and vaterite and thus in microstructure coarsening (Richardson, 2006).

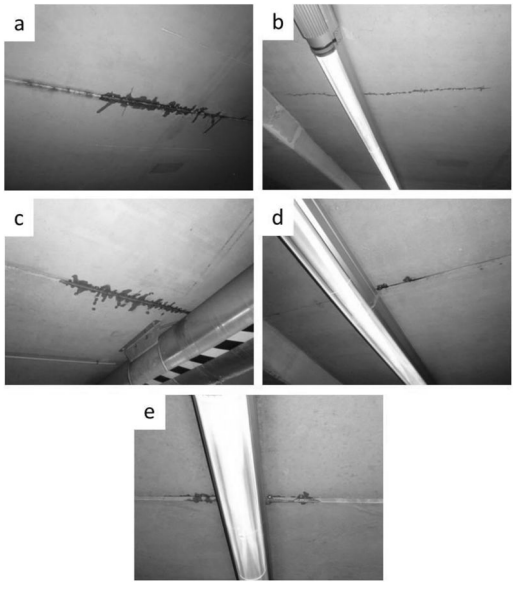

Figure 6. Observation of water leaking through the cracks during water permeability test – (a-c) control non treated cracks, (d, e) cracks treated with the bacteria-based repair system.

Therefore, based on the available information and present results, the application of the bacteria-based repair system appears as a promising approach to improve the resistance of concrete to freeze/thaw with de-icing salt. It is likely that the decrease in porosity and densification of the pore system is due to biomineral precipitation. However, further investigation on the microstructure of the concrete should be performed in order to confirm this statement.

3.2 *Water permeability test*

The crack-sealing efficiency was visually assessed on site. The results were very encouraging as the 3 control cracks were heavily leaking (Fig. 6a-c) along the full tested length while 2 cracks treated with the bacteria-based repair system exhibited only a few localized dripping spots (Fig. 6d-e). The third treated crack was not leaking at all.

4 CONCLUSION

This paper presents the field performance of the recently developed bacteria-based repair system for concrete. The system combines advantages of both a traditional repair system for concrete (fast reacting, and short term efficiency), and bio-based methods (more sustainable, slow process, and long-term efficiency).

The bacteria-based repair system has been sprayed on the surface of cracks and on a concrete slab in an underground car park. The crack-sealing efficiency and improvement of frost salt scaling were assessed by water permeability and freeze/thaw resistance tests respectively. The results were very promising as only cracks that had not been treated with the bacteria-based repair system were still heavily leaking. In addition, the freeze/thaw resistance of concrete that had been treated with the bio-based repair system was significantly higher than the untreated concrete.

These results are very encouraging for the application in practice of the bacteria-based repair system. The system is currently being optimized in order to raise its performances to complete sealing of the cracks and to develop better frost salt scaling resistance. A next step is also to assess the long term performance of the bacteria-based repair system.

ACKNOWLEDGMENTS

The authors would like to thank Cugla B.V. (Breda, The Netherlands) for testing the resistance of the concrete cores to freeze/thaw.

Financial support from Agentschap NL (IOP grant SHM012020) for this work is gratefully acknowledged.

REFERENCES

Copuroglu, O. 2006. The characterisation, improvement and modelling aspects of frost salt scaling of cement-based materials with a high slag content. PhD thesis, Delft University of Technology, Delft, The Netherlands.

Dhami, N.K., Reddy, S.M., Mukherjee, A., 2012. Biofilm and microbial applications in biomineralized concrete. In: Seto J, ed. *Advanced topics in Biomineralization*. Rijeka: In Tech, pp. 137–164.

Emmons, P.H., & Sordyl, D.J., 2006. The state of the concrete repair industry, and a vision for its future. *Concrete repair bulletin*, pp. 7–14.

Richardson D.N., 2006. Strength and durability of a 70% ground granulated blast furnace slag concrete mix. *Technical report RI99.035/RI99.035B*, University of Missouri-Rolla.

Wiktor, V. & Jonkers, H.M., 2010. Quantification of crack-healing in novel bacteria-based self-healing concrete. *Cement & Concrete Composites* (33): 763–770.

Wiktor, V. & Jonkers, H.M., 2011. Development of bacteria-based systems to increase concrete structures durability, *International Workshop on Structural Life Management of Underground Structures*, Daejon, South-Korea, pp. 51–56.

Wiktor, V. & Jonkers, H.M., 2012a. The potential of bacteria-based repair system to increase the durability of repaired concrete structures. In: Y. Guang, K. van Breugel, W. Sun and C. Miao (Editors), *Microstructural-related durability of cementitious composites*. Rilem Publication S.A.R.L, Amsterdam, pp. 169.

Wiktor, V. & Jonkers, H.M., 2012b. Application of bacteria-based repair system to damaged concrete structures, 2nd *International Workshop on Structural Life Management of Underground Structures*, Daejon, South-Korea, pp. 31–34.

Concrete Solutions – Grantham et al. (Eds)
© 2014 Taylor & Francis Group, London, ISBN 978-1-138-02708-4

Study on the preparation of polymer modified mortar and its application on the rapid repair of a ballastless track

Zhonglai Yi, Huajian Li, Yanbin Tan, Hao Jin & Yongjiang Xie
China Academy of Railway Sciences, Beijing, China

ABSTRACT: Cement emulsified asphalt mortar interlayer is regarded as a weak layer in high-speed railway slab ballastless tracks, and one which easily deteriorates during railway operation. Polymer modified mortar is suitable as a repair material for cement emulsified asphalt mortar owing to its high bond strength, low elastic modulus, good toughness and crack resistance, etc. Due to short maintenance periods allowable for high-speed railways, polymer modified mortar should also offer high early strength. The influence of ratio of polymer to cement and the type of polymer on workability performance, compressive strength, flexural strength and elastic modulus of polymer modified mortar were studied. Polymer modified mortar with similar performance to cement emulsified asphalt mortar was developed, which can be used as rapid repair material for high-speed railway ballastless track interlayers. A case study of polymer modified mortar used in the rapid repair of cement emulsified asphalt mortar interlayer of ballastless track is also introduced.

1 INTRODUCTION

Slab ballastless solutions were adopted as the main track structure for high-speed railways with speeds of 300 km/h in China, owing to their established advantages including smooth operation, high degree of standardization, good workability and low maintenance requirements (Yi et al, 2011). Slab ballastless track is mainly composed of prefabricated track slab, filling layer, concrete base or hydraulic support layer, etc. Currently, the most widely used filling layer material is emulsified asphalt cement mortar, making it one of the key materials in the slab track structure. Its main function is filling, support, force transmission and to provide appropriate elastic toughness (Hu et al, 2012). The performance of emulsified asphalt cement mortar has a direct influence on the durability of track structures, comfort of train operation and the difficulty of operation and maintenance. Emulsified asphalt cement mortar is a special kind of mortar comprising emulsified asphalt, cement, admixture agent, fine aggregate, water, antifoaming agent and aluminate powder. The special composition and application of emulsified asphalt cement mortar is dictated particularity by performance requirements (Qiu et al, 2013).

An extract of the performance index for emulsified asphalt cement mortar is shown in Table 1 (Xie et al, 2007). It can be seen that emulsified asphalt cement mortar is governed by high fluidity, appropriate mechanical properties, strict elastic modulus limit and good durability.

The emulsified asphalt cement mortar layer is the weakest part of slab ballastless track because of its special performance. It is easily deteriorated or damaged in the service of high speed railway. Engineering practice shows that emulsified asphalt cement mortar layers reveal different degrees of degradation phenomenon. Figure 1 shows a typical damage case of an emulsified asphalt cement mortar layer.

Table 1. Performance requirements of emulsified asphalt cement mortar.

Test		Requirement
Slump flow (fresh)		$\geq$ 280 mm
Slump flow (30min)		$\geq$ 280 mm
Fluidity		80 s$\sim$120 s
Air content		$\leq$ 10.0%
Expansion rate		0$\sim$2.0%
Flexural strength	1d	$\geq$ 1.0 MPa
	7d	$\geq$ 2.0 Mpa
	28d	$\geq$ 15.0 Mpa
	28d	$\geq$ 15.0 Mpa
Elastic modulus	28d	7000 MPa$\sim$ 10000 Mpa
Freeze-thaw resistance (56 times, 28d) Flaking quantity		$\leq$ 2000 g/m^2
Relative dynamic elastic modulus		$\geq$ 60%

To ensure durability and in-service safety of slab ballastless track, damage of emulsified asphalt cement mortar layer should be repaired in a timely manner. Due to short maintenance windows for ballastless track, any repair material must have high early strength. At the same time, the performance of repair material must match the performance of existing emulsified asphalt cement mortar. Polymer cement

Figure 1. Damage of emulsified asphalt cement mortar layer.

mortar has some advantages as a potential repair material, such as adjustable setting time, high bond strength, good toughness and good crack resistance. The performance of polymer modified mortar can also be matched with the emulsified asphalt cement mortar through adjustments to the mix proportions used. As such, polymer cement mortar is an ideal repair material for emulsified asphalt cement mortar layers. The influence of ratio of polymer to cement and the type of polymer on workability performance, compressive strength, flexural strength and elastic modulus of polymer modified mortar were studied as part of this research work. Polymer modified mortar with similar performance to cement emulsified asphalt mortars were developed. The intention is for these to be used as rapid repair material for high-speed railway ballastless track interlayers.

2 EXPERIMENTAL

2.1 *Materials*

(1) Cement
A rapid hardening sulphoaluminate cement according with the Chinese standard GB 20472 was used in the experimental work due to its high early strength. The chemical composition of the cement is shown in Table 2.

(2) Mineral admxiture
Fly ash and slag powders were used as mineral admixtures in the polymer modified mortar studied. The chemical composition and physical properties of these materials are shown in Table 3.

(3) Polymer
Polymer emulsion and dispersible co-polymer powder with the same chemical composition (poly(vinyl acetate)-ethylene ester) were used. The properties of polymer emulsion and dispersible copolymer powder are shown in Table 4.

(4) Sand
Quartz sand was used as the fine aggregate in the experimental work.

Table 2. Chemical composition of sulphoaluminate cement.

Component	Content (% by weight)
CaO	59.02
MgO	4.38
Fe_2O_3	2.89
Al_2O_3	5.46
Alkali content	0.81
Free CaO	0.93
Ignition loss	3.07
SO_3	2.66
Cl^-	0.016

Table 3. Chemical composition and physical properties of mineral admixtures used.

Properties	Slag powder	Fly ash
CaO (wt%)	36.71	3.38
MgO (wt%)	11.31	1.46
Alkali content (wt%)	0.36	2.18
Free CaO (wt%)	0	0.03
Ignition loss (wt%)	0.44	0.53
SO_3(wt%)	0.2	0.51
Cl^-	0.013	0.004
Density (kg/m^3)	2880	3080
Specific surface area (m^2/kg)	440	358

Table 4. Properties of polymer emulsion and dispersible co-polymer powder.

Properties	Polymer emulsion	Dispersible co-polymer powder
Appearance	White emulsion	White powder
pH value	5.8	/
Viscosity (m · Pas, 25°C)	300	/
Bulk density (kg/m^3)	/	540
Ash content (wt%)	/	11
Solids content (wt%)	54	99
Particle size (μm)	0.8	<400
Minimum film forming temperature (°C)	−10	4

(5) Chemical admixture
Polycarboxylate superplasticizer and defoaming agent were used to adjust the fluidity of the cement mortars produced.

2.2 *Mix proportions*

The mix proportions used for the experimental work are shown in Table 5. The dosage of superplasticizer and defoaming agent were determined by the fluidity of the cement mortar.

2.3 *Experiment methods*

The fluidity of polymer modified mortar was measured according to GB/T 2419 ‘Test mortar of fluidity

Table 5. Polymer modified mortar mix proportions.

Mix no.	Cement	Mineral admixture (50% Fly ash + 50% Slag)	Polymer emulsion (solid content)	Dispersible copolymer powder	Sand	Water
1#	100	80	/	/	300	75
2#	100	80	18	/	300	75
3#	100	80	36	/	300	75
4#	100	80	54	/	300	75
5#	100	80	18	18	300	75
6#	100	80	/	36	300	75

of cement mortar'. Specimens were de-moulded after curing in a standard curing room (temperature $20 \pm 2°C$, humidity $\geq 95\%$) for 7 days. Specimens were then moved to a second curing room (temperature $20 \pm 2°C$, humidity $\geq 60 \pm 5\%$) until test ages.

Flexural strength and compressive strength of polymer modified mortar were tested in accordance with the Chinese National Standard GB/T 17671 'Method of testing cements-Determination of strength'. Strength tests were conducted on $40 \times 40 \times 16$ mm test blocks.

Elastic modulus of polymer modified mortar was tested in accordance with the Chinese National Standard GB/T 50081 'Standard for test method of mechanical properties on ordinary concrete'. Elastic modulus tests were conducted on $100 \times 100 \times 300$ mm test blocks.

3 RESULTS AND DISCUSSION

3.1 *Effect of polymer emulsion on fresh mortar performance*

The effect of the ratio of polymer emulsion to cementitious materials (P/C) on fresh mortar performance is shown in Table 6. It can be seen that as the ratio of polymer emulsion to cementitious materials increased, the required superplasticizer dosage was gradually reduced to maintain a slump flow level of 300 ± 20 mm.

At the same time, the required de-foaming agent dosage gradually increased, while the air content of polymer modified mortar was maintained at $8 \pm 1\%$.

This phenomenon indicates that for polymer modified cement mortar, increasing the polymer emulsion content can significantly improve the flowability of the mortar. Polymer emulsion can provide a beneficial water-reducing and air entraining effect. Reasons for this can be explained as follows.

Firstly, the active agent on the polymer surface can disperse cement particles effectively. The active ingredient of the polymer surface can disperse the flocculation structure formed by cement hydration products. With flocculation dispersion, the free water wrapped by the flocculation structure can be released to participate in the hydration process. Thereby the polymer emulsion can improve the fluidity of cement mortar and play a water reducing effect.

Table 6. Effect of P/C ratio on fresh mortar performance.

No.	P/C ratio	Super-plasticizer	Defoaming agent	Slump flow	Air content
1#	0	1.2%	0%	290 mm	7.8%
2#	0.10	0.8%	0.02%	300 mm	8.0%
3#	0.20	0.5%	0.03%	310 mm	8.7%
4#	0.30	0.3%	0.05%	310 mm	9.0%

Secondly, the very small spherical particles (diameter 0.01–1.00 μm) in the emulsion polymer play a similar role of air entraining agent. Amounts of air can be introduced by the emulsion surfactant in the polymer emulsion. When the polymer emulsion is mixed with cement, emulsifier-coated bubbles are easily formed. Thereby, polymer emulsion can improve the air content of cement mortar and play an air entraining agent effect. Furthermore, a kind of 'ball-bearing effect' can be produced when the small polymer particles and entrained air work together (Jeongyun Do et al, 2003). As such, the fluidity of the cement mortar can be increased significantly.

3.2 *Effect of polymer emulsion on the mechanical properties of polymer modified mortar*

Polymer is clearly an important part of polymer modified cement mortar. The amount of polymer dosage has a significant impact on the properties of polymer modified cement mortar. Figures 2–3 show the effect of polymer emulsion dosage on the compressive and flexural strength of polymer modified cement mortar.

Fig. 2(a) shows that with increasing amounts of polymer emulsion, compressive strength of polymer modified cement mortar decreased. Especially in the early stages, compressive strength of the polymer modified cement mortar was very low. When the polymer dosage was 30% by weight of cementitious material, compressive strength at 2 h was only 3.8 MPa (i.e. lower than 5 MPa). This early compressive strength cannot satisfy requirements of rapid repair material. Fig. 2(b) shows that with increasing amounts of polymer emulsion, the growth rate of compressive strengths were increased. At the same time, with increasing of curing age, the growth rate of compressive strength increased significantly.

Performance trends for flexural strength in relation to amount of polymer emulsion were similar those for compressive strength, which can be seen from Fig. 3.

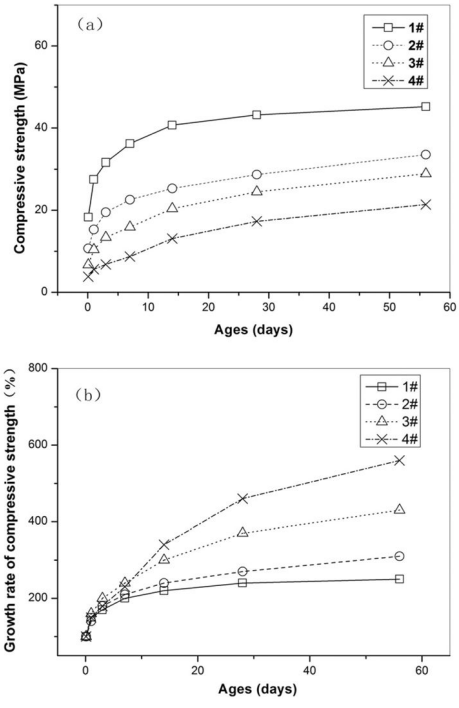

Figure 2. Effect of polymer emulsion on compressive strength of polymer modified cement mortar.

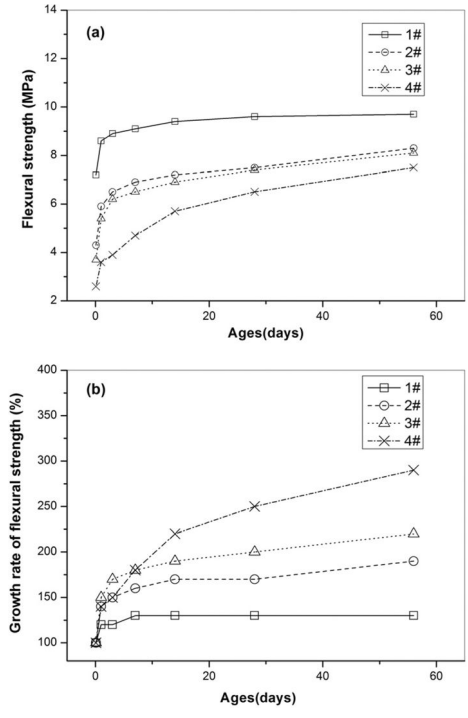

Figure 3. Effect of polymer emulsion on the flexural strength of polymer modified cement mortar.

Fig. 4 shows the effect of amount of polymer emulsion on the ratio of flexural to compressive strength. This ratio is an effectiveness index in terms of the toughness properties of cement mortar. Fig. 4 shows that with increasing amounts of polymer emulsion, the ratio of flexural strength to compressive strength gradually increased at each age. This indicates that the polymer can effectively improve the toughness of the mortar.

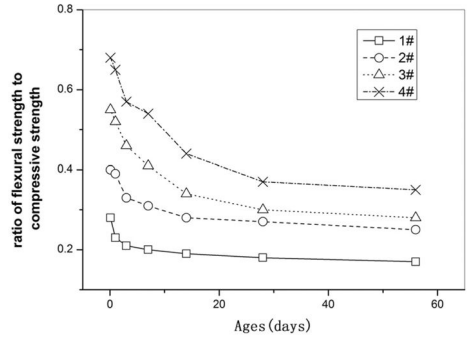

Figure 4. Effect of polymer emulsion on the ratio of flexural strength to compressive strength.

3.3 *Effect of polymer emulsion on the elastic modulus of polymer modified mortar*

Elastic modulus is an important property for mortar used for slab ballastless track filling layers. It can be seen from Table 1 that 28-day elastic modulus must be controlled at 7,000–10,000 MPa. The effect of the amount of polymer emulsion on elastic modulus of polymer modified mortar is shown in Fig. 5. It can be seen that with increasing amounts of polymer emulsion, elastic modulus values decreased. For example, when the polymer content is 10% by weight of cementitious material, the elastic modulus of polymer modified mortar at 28d is higher than 10,000 MPa. As such it cannot meet the elastic modulus requirements for slab ballastless track filling layer.

When the polymer content is 20 and 30% by weight of cementitious material, its elastic modulus of polymer modified mortar at 28d is lower than 10000 MPa, which does meet the elastic modulus requirements for the slab ballastless track filling layer.

Taking early compressive strength and elastic modulus into account together, the appropriate dosage of polymer emulsion for the polymer modified mortar is 20% by weight of cementitious material.

3.4 *Effect of polymer type on the properties of polymer modified mortar*

For polymer modified cement mortar, two types of polymer can be used; liquid polymer emulsion and dispersible co-polymer solid powder). Compared with liquid emulsion, dispersible co-polymer powder is more convenient to use and can be used to produce

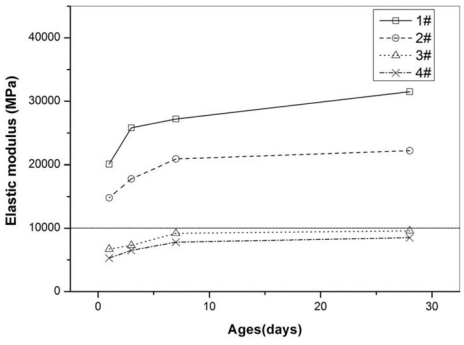

Figure 5. Effect of polymer emulsion on the elastic modulus of polymer modified mortar.

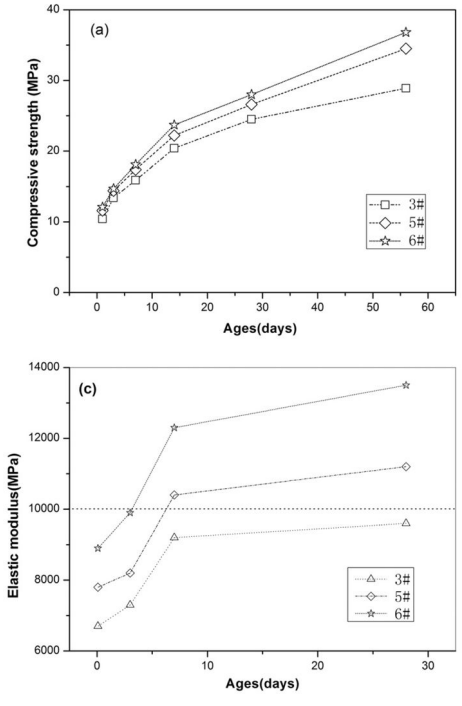

Figure 6. Effect of polymer type on the properties of polymer modified mortar.

one-component polymer modified dry mortar. Its price, however, is more expensive than emulsion.

Polymer emulsion and dispersible co-polymer powder with the same chemical composition (poly(vinyl acetate)-ethylene ester) were used to compare the effect of different polymer type on the properties of mortar. The test results are shown in Fig. 6. It can be seen that when the dosage of polymer is 20% by weight of cementitious material, the mechanical properties of the dispersible copolymer powder mortars are higher than those using polymer emulsion. Compared with the dispersible co-polymer powder, polymer emulsion increased flexibility and toughness of the mortar more directly and obviously. Equally, the elastic modulus of

Figure 7. Defect situation.

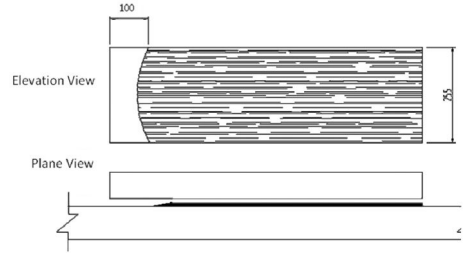

Figure 8. Defect schematic diagram.

polymer modified cement mortar can be reduced more significantly. When dispersible co-polymer powder is used in the mortar, the elastic modulus of mortar at 28d was higher than 10,000MPa, thereby not meeting the requirements for the slab ballastless track filling layers. So, considering the properties of the polymer modified mortar and the cost of materials, polymer emulsion is more suitable to produce polymer modified mortar used as repair materials for slab ballastless track filling layers.

4 FIELD APPLICATION CASE

4.1 *Defect situation*

An emulsified asphalt cement mortar filling layer of slab ballastless track was found to be deficient as shown in Fig. 7. No emulsified asphalt cement mortar filling layer at all was found from about 1 m from the edge of an operational track slab. The total non-filled area was about 0.08 m^2. The defect is described schematically in Fig. 8.

4.2 *Properties of repair materials*

Polymer modified cement mortar as developed in the paper was used as the repair materials. The properties of the polymer modified cement mortar adopted are shown in Table 7.

As can be seen in Table 7, the developed polymer modified cement mortar has high early strength, high bond strength and low shrinkage. The elastic modulus and other properties of polymer modified cement mortar are in line with properties of emulsified asphalt cement mortar. It met the rapid repair requirement for emulsified asphalt cement mortar filling layers prescribed in Table 1.

Table 7. Properties of polymer modified mortar.

Properties		Test Result
Initial setting time (min)		≥ 20
Final setting time (min)		≤ 120
Compressive strength (MPa)	1d	9.8
	7d	15.7
	28d	24.3
Elastic modulus (MPa)	1d	6600
	7d	9100
	28d	9700
Shrinkage (%)	28d	0.21
Bond strength (MPa)	7d	1.5
	28d	2.2

Figure 9. Pouring of polymer modified mortar.

Figure 10. Repair effect.

4.3 *Repair process*

The repair process for this defect was as follows:

(1) Thoroughly clean the defect area. Clean the small amount of emulsified asphalt cement mortar in the defect area. Wash the defect area and the bottom of track slab with water.
(2) Set up the formwork at the both sides of the defect area.
(3) Weigh polymer modified mortar materials and mix the mortar using a mortar mixer.
(4) Pour the mixed mortar to the defect area until the area was filled with polymer modified mortar fully (see Fig. 9).
(5) After the polymer modified mortar hardened, remove the formwork. Cut the redundant mortar.

The completed repair is shown in Fig. 10, which has now been in place for 1 year. Generally, the appearance is quite good so far.

5 CONCLUSIONS

- For polymer modified cement mortar, increasing the polymer emulsion content can significantly improve flowability of the mortar. Polymer emulsion can play a preferable water-reducing and strong air entraining effect.
- Polymer emulsion can effectively improve the toughness of cement mortar. With increasing amounts of polymer emulsion, mechanical properties of polymer modified mortar decreased gradually, but the strength growth rate and ratio of flexural strength to compressive strength gradually increased.
- Polymer emulsion can effectively decrease the elastic modulus of cement mortar. When the polymer content is higher than 20% by weight of cementitious materials, the elastic modulus at 28 days is lower than 10,000 MPa. This meets the elastic modulus requirements for slab ballastless track filling layers.
- Compared with dispersible co-polymer powder, polymer emulsion can increase the flexibility and toughness of cement mortar more directly and obviously. The elastic modulus of polymer modified cement mortar can be reduced more significantly.
- Polymer modified mortars which can be used as repair material for emulsified asphalt cement mortar filling layers were developed. It generally performed well in the field application.

ACKNOWLEDGEMENT

This work was financially supported by the National Natural Science Foundation of China (51308546) and the Key Project of China Railway Corporation (2012G008-A, 2013G 008-A-3).

REFERENCES

Hu S, Zhang Y, Wang F. 2012. Effect of temperature and pressure on the degradation of cement asphalt mortar exposed to water. *Construction and Building Materials.* 34: 570–574

Jeongyun Do, Yangseob Soh. 2003. Performance of polymer-modified self-leveling mortars with high polymer–cement ratio for floor finishing. *Cement and Concrete Research.* 33(10): 1497–1505

Qiu K, Chen H, Ye H, et al. 2013. Thermo-mechanical coupling effect on fatigue behavior of cement asphalt mortar. *International Journal of Fatigue.* 51: 116–120

Xie Y, Zhen X. Jiang C, et al. 2009. Standard for emulsified asphalt cement mortar used in CRTS II slab ballastless track for high-speed railway. Ministry of Railway of China.

Yi Z, Li H, Xie Y, et al. 2011. Degradation mechanism and repair technology of a concrete structure of a railway ballastless track. *Concrete Solutions – Proceedings of 4th International Conference, Dresden. CRC Press.* 335–340

Electrochemical repair

This page intentionally left blank

Concrete Solutions – Grantham et al. (Eds)
© 2014 Taylor & Francis Group, London, ISBN 978-1-138-02708-4

Field experience of remote monitored and controlled CP systems

C. Atkins, R. Brueckner & P. Lambert
Mott MacDonald, Spring Bank House, Altrincham, UK

M. Bennett
Halton Borough Council, Municipal Building, Widnes, Cheshire, UK

ABSTRACT: In 1993 the first of a series of Cathodic Protection (CP) systems were installed on the approach viaducts of a major UK bridge structure. Over subsequent years the structure had additional phases of repairs and CP installations. Due to the requirement to competitively tender each phase, a range of CP systems were installed between 1993 and 2013. The final phase was to replace the various power, control and monitoring systems that had been installed with a smaller number of more up to date units. As part of this process the historic operating performance of each system was employed to optimise the number and size of zones and the number of monitoring probes. In addition, a number of systems were installed but not energised until the final phase had been completed. This paper presents a review of the performance of the systems and the associated control equipment over the twenty year period.

1 INTRODUCTION

The Silver Jubilee Bridge was designed by Mott Hay and Anderson (now Mott MacDonald) and opened in 1961 (Figure 1). It is currently within the portfolio of highway structures maintained by Halton Borough Council, based in Widnes.

The bridge is a steel arch structure with a central span of 330 m and two side spans of 76 m and is the largest of its type in Europe and the largest local authority maintained bridge in the UK. The deck is reinforced concrete with a surfacing of mastic asphalt and rolled chippings. The approach viaducts to the bridge consist of reinforced concrete piers supporting four main beams, the ends of which were precast and the central spans cast insitu at the same time as the deck. The main beams were named east outer, east inner, west inner, west outer dependent on their location. The deck is waterproofed but has joints above every third pier.

The original structure was designed to carry one lane of traffic in each direction, plus a shared centre lane for overtaking. In 1977, due to the ever increasing traffic demands, the bridge was widened to form two lanes running in both directions. This necessitated the widening of the approach viaducts by increasing the number of deck beams. Where necessary the additional beams were supported off the existing piers which were widened by encapsulating the stem and crosshead. The gap contained a fibreboard material to ensure separation between the new and the old piers. Typical details are shown in Figure 2. The Runcorn Approach viaduct Piers were numbered R1 to R15 from north to south.

Figure 1. Silver Jubilee Bridge.

The Widnes approach viaduct piers were numbered N1 to N6 from north to south.

2 DEGRADATION OF THE STRUCTURES

In the UK it is common practice to waterproof bridge decks. It is often found that bridges will fail most frequently at or near the structural joints within the deck. It is at these points where movement or poor detailing can allow the ingress of water through to any structures beneath. This water is contaminated with deicing salts during the winter months, and the chlorides penetrate

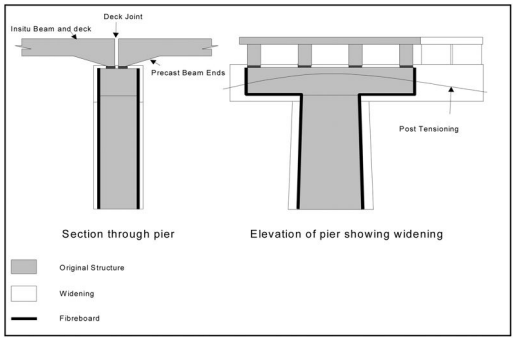

Figure 2. Typical encapsulation details.

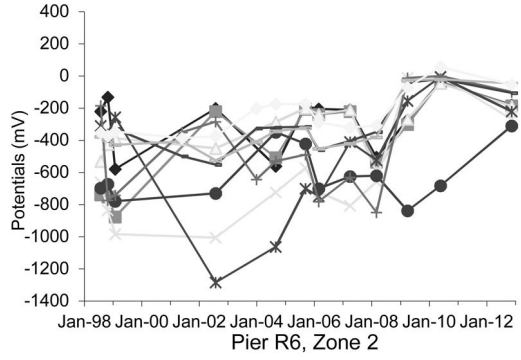

Figure 3. Instant off data.

through the joints and run over the face of the substructure below. This leads to extensive corrosion and deterioration of the concrete.

In the case of the Silver Jubilee Bridge Approach Viaducts this is exactly what had happened. Every pier that was located under a movement joint was exhibiting significant signs of degradation associated with chloride induced corrosion of the reinforcement. In addition to this, the beam ends and adjacent edges of the deck also suffered extensive chloride contamination and corrosion.

3 REPAIR STRATEGY

3It was established that the most cost effective repair strategy was to employ cathodic protection (CP). Due to the available funding it was necessary to install this over a number of phases. The repairs were prioritized to ensure the safety of the public. Holding repairs were also undertaken to remove any loose material to manage the risk of falling debris. It was felt that installing the control units in accessible areas would present a risk of vandalism and so the decision was made to install the control units at height and use remote monitoring and control for the CP. The original contract was developed with a recognition that each phase would be separately tendered, and may result in different control units being provided. It would be based on the works leaving a finish similar to the existing concrete piers, with a smooth face and appropriate features. The contract contained requirements based on the current state of the art to try and manage the risk of future compatibility. The requirements were as follows:

1. Hayes compatible modems
2. Lotus 123 and Wordperfect for data files
3. 2 No.13A sockets in each cabinet.

The standard computer operating system at the time was MS DOS, with MS Windows 3.1 just being introduced. Instant off data would be gathered daily and reviewed quarterly, depolarisations would be taken on demand, typically annually along with a hammer survey to inspect the overlays, and each unit would be able to be operated on site as well as remotely. This included a timer switch to enable on site collection of instant off data.

3.1 *Phase 1 (Piers R6/R9)*

The first contract was awarded in 1993 to repair two piers. The systems employed were mixed metal oxide coated titanium mesh in a sprayed concrete overlay each pier had 5 zones, in total there were 87 monitoring probes made up silver/silver chloride/0.5 M reference electrodes and graphite monitoring probes as the long term reliability of embedded reference electrodes in concrete was not known. The control units were supplied by Dynamics, the remote control system used MS DOS based software and the data loggers on site could store 256 kB of data. A single phone line communicated to both units.

On commissioning there was a short circuit identified between the mesh anode and steel reinforcement. This was burnt out using arc-welding equipment. A small delamination in the overlay was identified but after removing the overlay this corresponded to a bundle of cables and was judged to be the likely cause of the hollow sounding area. In general the systems and remote monitoring performed acceptably but did suffer from the millennium bug. This required a number of chips to be replaced in the data loggers.

Typical instant off data is presented in Figure 3. Generally the silver/silver chloride electrodes provided more stable instant off data, with significant changes being indicative of changes in the output current of the systems.

3.2 *Phase 2 (Widnes East Edge Beam)*

The next phase was installed in 1994. The control system employed a Corrosion Services DMS unit that operated via MS Windows. Data was stored on site and downloaded into a MS Access Database. It was a mesh and overlay system, split into 15 zones with a total of 89 monitoring probes. It was dialled in using a single phone line.

Generally this system performed well and over the years was the most reliable to obtain data from. One zone incorrectly reported current (−182 Amps) from

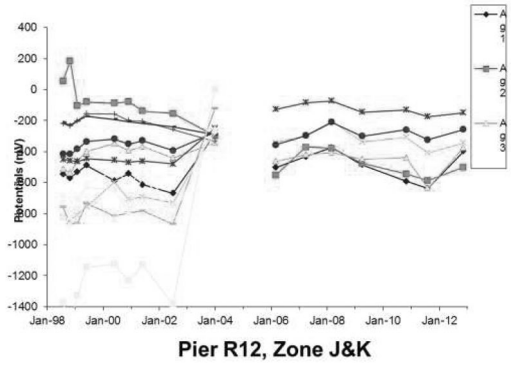

Figure 4. Pier R12 data.

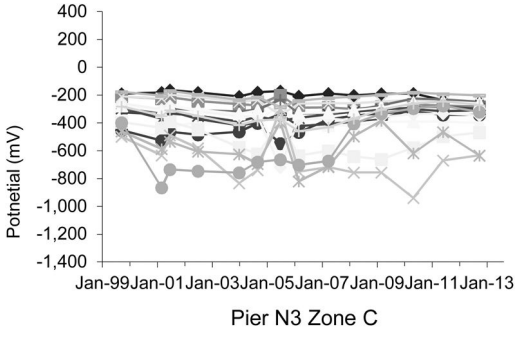

Figure 5. Pier N3 data.

a fairly early point and in the later years the database reached 72 MB in size. Whilst by modern standards this would not be considered a significant problem, the version of MS Access installed on the 1995 laptop did not perform well with files of this size. In more recent years the site storage of data also became unreliable.

3.3 *Phase 3 (Piers R3/R12)*

This phase was completed in 1995, and involved mesh and overlay to two piers. The control system used Cathtec units, which stored data on 3.5" floppy disks with a bespoke format. The systems comprised 11 zones with 94 monitoring probes. Generally these systems were reliable, although typically it would take multiple attempts to achieve a successful connection. Downloading data began to fail on one of the systems and so data collection depended on collecting screen dumps.

One of the control units suffered a small fire that was identified at an annual monitoring visit. The charred remains of a small bird were found on top of the AC feed to the cabinet. The monitoring data indicated that the steel was in a relatively benign condition. This was attributed to the prolonged application of cathodic protection. A replacement control unit from Remco was procured and installed once finance was obtained. The opportunity was taken to reduce the number of separately controlled zones and probes being monitored. This proved successful, but required the specific use of a USRobotics external modem to ensure compatibility operating via a com port. Even at the time this proved difficult to source.

3.4 *Phase 4 (Pier N3)*

This phase was completed in 1999. It comprised a mesh and wet sprayed overlay, and also incorporated discrete anodes into the beam ends. Wet sprayed overly was selected as the pier was in close proximity to a school and it was considered this would reduce the airborne dust from the works. Previous overlays were dry sprayed. The control unit was provided by Dynamics and it downloaded data to an MS Access database via a phone line. The software was installed on a laptop running MS Windows 98, and it ran extremely slowly. Shortly after the second annual delamination survey it was noted that the overlay was becoming increasingly delaminated. Investigations identified a desiccated layer at the interface between the overlay and the parent concrete, but this did not clarify whether it was an application, curing or materials problem. This was rectified by wrapping the pier in a glass fibre scrim encapsulated in a polymer modified cementitious coating. The delaminating overlay did not affect the performance of the cathodic protection system.

3.5 *Phase 5 (Pier R15)*

This phase was also completed in 1999. It comprised a mesh and dry sprayed overlay operated using a similar Cathtec system as employed on Piers R3 and R12 through a fixed phone line. It typically took a number of attempts to connect but generally performed acceptably.

3.6 *Phase 6 (Widnes West Edge Beam)*

This was completed in 2000 and comprised a mesh and dry sprayed overlay system operated via a Remco control unit over a single phone line. The Remco system was the first to require the use of a dongle.

3.7 *Phase 7 (Pier R1, 4 beams and the encapsulation of the pier installed during the widening)*

This phase was completed in 2005. Previous contracts had been procured with the contractor providing the detailed design. For this system the design was undertaken by Mott MacDonald. It was developed by looking at the systems installed previously and calculating what was actually required to achieve cathodic protection of the piers. This resulted in a significant reduction in the number of zones and monitoring probes. The varying amounts of steelwork in the beams had previously lead to up to 5 zones per beam, with multiple layers of mesh to achieve the design current density. On review of the data the operating current density was similar in all zones and so this was reduced

to a single zone per beam. The encapsulation was susceptible to ASR and contained post tensioning and so it was decided to use a galvanic system based on Galvashield CC anodes from Fosroc. Our design did not include an option to allow depolarization of the galvanic system, but the contractor supplied one, such that the anodes could be remotely disconnected. The control unit was from Electrotech CP and operated via a broadband connection provided by the contractor.

The system generally performed well but remote monitoring was significantly hampered by trying to arrange for broadband transfer from the contractor to the client. The provider selected by the contractor could not be used either by the client or Mott MacDonald. Transfer to a new provider was not a smooth process, and took over 12 months to resolve and there were compatibility issues with the control unit and the broadband provider. Ultimately Electrotech CP confirmed that monitoring could be performed without broadband and so this option was undertaken. However, in getting the broadband taken off the phone line, the entire phone line was removed in error and it took a further 6 months to re-arrange.

The only other difficulty associated with this system was due to the relays installed to allow for depolarisation of the steel. They would frequently not reconnect the galvanic anodes to the steel on completion of the depolarization.

3.8 *Phase 8 (The framework)*

Following on from the above works Halton Borough Council entered into a framework for works on the Silver Jubilee Bridge complex in April 2009. This enabled a more effective overview to be undertaken. As part of this the remaining outstanding areas requiring cathodic protection were repaired with mesh and overlay CP systems excluding power supplies, with a view to future energisation when these repairs were complete.

This comprised a further 31 zones spread over both viaducts with 4 monitoring probes per zone. In addition the cathodic protection of the bridge deck itself was completed utilizing the cassette anode system as discussed by Brueckner et al. (2011).

The installation of these systems took place over a number of years. It was expected that this would produce some incipient anode corrosion as a result of the patch repairs and this was observed for one system. In this case the CP system was energized using a 6 V battery as a temporary protection measure.

On completion of the installation works the replacement power and control system was installed utilizing CPI Duracenter units, which operate via a dedicated secure website. The existing systems were rationalised into a smaller number of 2 Amp zones, based on the actual operating current. Each Duracenter had spare channels for power to allow for the failure of future components. A networked approach was employed with a single phone line on each side of the river, such that it was no longer necessary to provide multiple phone lines for adjacent systems. The monitoring was limited to 4 probes per zone, with the additional existing probes terminated in junction boxes to allow future use. This reduced the original 68 zones down to a more manageable 15.

Commissioning in accordance with BS EN ISO 12696 suggests energizing to 20% of the design current. Since the majority of systems no longer had a formal design current requirement, they were all energised with a voltage limit of 4V and a current limit of 1 A. In the vast majority of cases this provided an acceptable level of polarization. The majority limited at 4 V rather than 1 A, but this depended on the physical size of the zones.

The default logging procedure on this control equipment was to log if values changed by more than a tolerance. The tolerances as shipped resulted in 30 MB monthly data files which took around 7 hours to download over a phone line. The tolerances were changed to log if an instant off changed by more than 50 mV, the drive voltage changed by 0.1 V, or the applied current changed by more than 0.1 A, which significantly reduced the file sizes.

4 DISCUSSION

Attempts to ensure future proofing for the remote monitoring proved to have a number of limitations due to the rapid development of computer and communication technology. As a result Mott MacDonald was relying upon a large number of increasingly elderly laptops that at some point would fail.The inclusion of daily logging of data produced files that exceeded the size that the communication software and hardware could easily manage, especially over a 20 year period. However, it did prove beneficial to have the option to enable daily logging to investigate unusual data that was occasionally captured.

Generally the silver/silver chloride electrodes were relatively stable and reliable. Approximately 5% of the installed silver/silver chloride electrodes failed. There was no evidence of this being related to age. The graphite probes,originally employed as they were considered to be less likely to fail, were more erratic and unreliable. In the later systems mixed metal oxide coated titanium probes were also used and again these proved to be unreliable.

The instant off data provided a good assessment of the performance of the system This was initially supported by undertaking 24 hour depolarisations annually, but once it had been established that protection was being reliably achieved with a given current it was considered unnecessary to carry out further depolarisations. This was beneficial as the remote systems were becoming increasing erratic, and to carry out a 24 decay would involve at least two visits.

Adjustments to the current and voltage output for all systems were rarely required after the first few years of operation.

The modems used would occasionally refuse to answer. This could often be rectified by interrupting the power supply at the main incoming feed for the systems. It is considered that simple access to be able to interrupt the power is of benefit, although in certain cases this had resulted in some systems being switched off accidentally by other parties. This was easily identified and rectified as part of the remote monitoring.

Ultimately the originally installed remote monitoring and operation systems proved less and less reliable until it started to take longer to work the remote monitoring then it did to arrange for a MEWP and carry out the monitoring and control on site.After 2000 the monitoring frequency was reduced to an annual instant off assessment and biannual depolarisations.

Where the remote monitoring no longer functioned the following procedure was adopted. Where systems did not have current interrupters installed to allow instant off data to be gathered, on potentials were used, since if the drive current and voltage had not changed significantly, it was reasonable to assume the resistivity of the concrete had not changed significantly, IR drop would therefore be similar and so on potentials provided a quick means of assessing performance that could be practically gathered.

30 minute depolarisations were used to assess the performance of the systems. This shorter depolarisation period allowed an assessment of the performance of the system without the need for multiple visits, since a significant measurable component of the 24 hour depolarisation happens within a relatively short time period. Using this technique also reduced the dependency of the performance assessment on the accurate collection of the instant off potential and enabled time to carry out any adjustments that may have been required.

The delamination surveys were discontinued as there was no significant increase in any of the previously identified areas. Such delaminations as there were did not prevent the operation of the CP systems. This is considered to be due to a hollow sounding area still retaining sufficient contact between the anode and concrete to allow the adequate passage of current.

One issue that affected the remote monitoring and control was not attributable to the systems themselves. The phone and IT system in the Mott MacDonald offices has been updated more than once over the 20 years under consideration and this has resulted in a number of issues. The translation to digital phone systems was not compatible with the majority of the monitoring, and even the use of an emulated analogue fax line did not work. This means that a dedicated true analogue line has had to be maintained.

The internal network security systems that have been introduced over the years also have effects on the ability to communicate with the latest systems, such that remote monitoring is commonly undertaken from home using a domestic broadband connection and a spare laptop.

Commissioning systems to a constant voltage with a limit on current rather than a constant current has been employed by the author on a number of structures and performed well. This has lead on most recently to the design of a CP system using a simple readily available low cost constant voltage power supply, with an LED to confirm it is operating.

5 CONCLUSIONS

This paper has presented the practical experience gained over a twenty year period of remote monitoring and control of a range of systems installed over a prolonged period on a single structure. Generally the systems have worked, although the remote side of the majority have degraded with time in parallel with advancing technology. This has resulted in a requirement to physically visit site annually. A relatively small percentage of silver/silver chloride electrodes have failed, but sufficient redundancy was included in the original installation to circumvent this. Delaminations less than $1m^2$ have not increased in size. One system that had an extensively delaminated overlay did have some remedial work applied, but the delamination did not affect the performance of the system. The actual level of intervention required rapidly reduces to a simple check that the systems are energised, and as such overly complex monitoring systems may not be required.

REFERENCES

Brueckner, R., Atkins, C., Foster, A., Merola, R., Lambert, P. Maintenance of Transport Structures using Electro-Chemical Solutions, In: Proceedings of 4th Concrete Solutions, 2011, Dresden, Germany, Taylor & Francis Group.

This page intentionally left blank

Concrete Solutions – Grantham et al. (Eds)
© 2014 Taylor & Francis Group, London, ISBN 978-1-138-02708-4

The impact of the interruption of impressed current cathodic protection on the steel/concrete interface

S. Bhuiyan, D. Law & T. Molyneux
RMIT University, Melbourne, Victoria, Australia

ABSTRACT: The corrosion of steel reinforcement in concrete structures is a global problem causing billions of dollars to be spent in repairs and maintenance to keep structures in a safe and functional state. Amongst the several techniques used to tackle this problem, Impressed Current Cathodic Protection (ICCP) has proven to be an effective method of stopping ongoing corrosion and preventing it from occurring in the future. Recent studies have shown that once passivity of steel is achieved, the applied current can be interrupted but yet be able to offer residual protection. A project is underway to study the duration of this residual effect and how it varies with the total amount of charge passed through the system. This paper reports on preliminary trial experiments which monitor a number of parameters, including, steel potential, current, pH, relative humidity and temperature at the steel/concrete interface before, during and after the application of cathodic protection.

1 INTRODUCTION

Cathodic protection is an extremely effective method of controlling corrosion of metals. Cathodic protection has historically been classed as two types: galvanic and impressed current systems, however more recently a third type – the hybrid system has been introduced (Glass, 2008). The underlying principle of all cathodic protection systems is to provide an external source of electrons sufficient to eliminate anodic reactions on the metal being protected, thereby hindering corrosion. Alternatively, the principle of cathodic protection may be viewed as the polarization of a metal using an external current source to achieve equal potentials along the metal surface, hence preventing potential gradients that cause the formation of corrosion cells. Galvanic cathodic protection works by utilizing anodes of metals less noble in the electromotive series than that of the structure/element being protected. Being more reactive, the anodes are naturally consumed in preference to the structure, releasing electrons which prevent anodic reactions at the surface of the protected metal. Impressed current cathodic protection (ICCP) on the other hand uses a DC power source to drive electrons from an anode material to the protected structure. ICCP is unique from other corrosion control measures from the point of view that it has the capability to completely stop corrosion irrespective of chloride content and that the level of protection can be adjusted as needed. It is commonly used for the protection of steel reinforcement in reinforced concrete. In order to achieve protection, the reinforcement should ideally be polarized to negative potentials such that it either lies in the zone of passivity (protection by passivity) or the zone of immunity (protection by immunity) outlined in its corresponding Pourbaix diagram (Das,1994). However this is rarely done in concrete and a potential shift of atleast 100 mV is the preferred corrosion control criterion (BS-EN 1269, 2000). Hybrid CP systems use ICCP as a temporary energizing phase to arrest corrosion and to repel chloride and regenerate passivity followed by permanent galvanic protection to sustain steel passivity.

Some past research, such as that of Page (1997)and Christodoulou et al (2010) indicated that metals cathodically polarized exhibit residual effects after interrupting the current source of an ICCP system. It was suggested that the beneficial effects of passive protection do not cease if the current is interrupted, but can rather last for several months and in some situations, give rise to the possibility of intermittent application of CP. The application of intermittent CP is an attractive technique as it would use lower current densities, thus reducing operational costs and negative side effects of ICCP such as reduction of anode efficiency, acceleration of alkali-silica reaction, bond-strength degradation and hydrogen embrittlement of prestressed steel (Aoyama et al, 2002). Studies conducted by Glass et al (2000) showed that the application of CP induced changes in the local environment of the steel/concrete interface, namely the removal of chloride and oxygen as well as the production of hydroxyl ions, which resulted in restoration of steel passivity. Intermittent CP in the form of a short-pulsated system (30min pulses every 12 hours) of varying current densities were tested and it was found that some were successful in arresting corrosion whereas others did not completely prevent corrosion but were able to reduce its rate significantly.

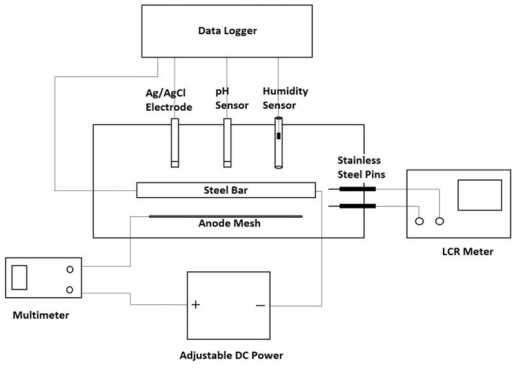

Figure 1. Schematic of specimen design.

In order to study the optimization of an intermittent CP system, it is key to examine the phenomenon of residual protection to a greater depth. It is necessary to take a closer look into the changes that occur at the steel/concrete interface during the application of CP and following its interruption. The objective of this paper is to report on the findings of preliminary testing carried out and to assess the performance of the experimental design used, prior to commencing the main experiments for the broader study, which will look into the effects of ICCP interruption specifically. The aim of these trials is to assess the monitoring techniques and the ability to polarize the steel by applying cathodic protection from the embedded anode. As such the conditioning period until corrosion will be kept to a minimum.

2 METHODOLOGY

A series of trials were used to determine the optimum test conditions to apply cathodic protection and monitor pH, resistivity, temperature, humidity, potential and corrosion rate. A schematic of the specimen design is given in figure 1.

The specimens were made from a 100% ordinary Portland (OP) cement mix with a nominal strength of 40MPa. This was chosen to simulate a standard site mix. In order to initiate corrosion, 3% NaCl by weight of cement, was added to the mix. The mix design is given in table 1.

Specimens were placed in a spray chamber to enable wet/dry cycling of the specimens to initiate corrosion. An initial wetting cycle of 1 hour in 24 hours, was adopted. A series of trials was undertaken to investigate the specimen design.

2.1 *pH Electrode*

Research has shown that application of CP promotes the formation of hydroxyl ions at the steel/concrete interface, thereby restoring the local pH to initial levels and thus steel passivity. In order to monitor the behavior of the pH change caused by application of

Table 1.

Constituent	Quantitykg/m^3
Cement	417
Water	208
Fine Aggregate	625
Coarse Aggregate (7 mm)	625
Coarse Aggregate (10 mm)	625

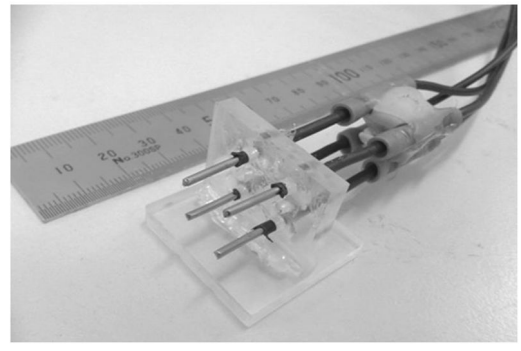

Figure 2. Resistance sensors.

CP without the use of destructive chemical analysis techniques, a double-junction pH electrode (Eutech Instruments-ECFC series) placed in close proximity of the steel bar was used for continuous monitoring. A welded-tip thermocouple was attached to the electrode before placement to measure temperature of the concrete close to the bar.The data showed that the precision of such pH electrodes in concrete was variable. In saturated steady conditions, stable pH readings were achieved, however as the concrete dried, the readings became more unstable. In order to reduce the variability, the spray cycle was modified to two 30 minute wet cycles per 24 hours to prevent drying of concrete.

2.2 *Resistance Sensors*

The aim of using resistance sensors was to observe if any change in the electrical resistance of concrete would arise from a local change in ion concentration around the bar resulting from CP application. Pairs of stainless steel pins (grade 304) were used to measure concrete resistance in a method similar to that used by McCarter et al (2005). Pins were insulated using shrink-wrap with a 10 mm tip exposed to the concrete and the other end crimped to electrical wiring that connected to a LCR meter (Isotech LCR 819). The measurements were taken using a signal with amplitude of 350 mV and a frequency of 1 kHz. All values are reported as resistance instead of resistivity since the experiment only compares readings of the same system.Two pairs of pins were placed to measure differences in resistance at different vertical distances from the steel bar; one at mid-level of the bar and the other placed 10 mm below. Figure 2 shows the setup

including the plexi-glass stand used to hold the pins in position.

2.3 *Humidity Sensor*

A commercially available relative humidity sensor (Honeywell HIH4000-01) connected to a data logger was used to monitor the change in humidity inside a cavity created in the concrete using a section of a PVC tube. After fixing the sensor inside the tube, the end exposed to the atmosphere was securely sealed, allowing humidity to equilibrate inside the cavity. Previous results showed that the accuracy of the sensor deteriorated with time. A white deposit was observed on the surface of the sensor when it was extracted after about two months of being kept continuously inside concrete. Given that the pattern of humidity is unlikely to change significantly once steady state conditions have been achieved in a controlled wet/dry cycle, it was deemed acceptable to take readings periodically at set periods, before, during and after application of CP.

2.4 *Potential and Corrosion Rate*

Steel potential readings were measured against an embedded Ag/AgCl reference electrode (Castle type LD15). Steel potentials monitored were stable during the initial trials and the methodology adopted for where B is the Stern-Geary constant, taken as 26 mV (for active corrosion) and 52 mV (for passive) and Rp is the measured polarization resistance in Ωcm^2. Corrosion rate monitoring was also undertaken using electrochemical impedance spectroscopy (EIS) however the measurements obtained were not suitable to deduce the corrosion rate as the fitting of data was not possible. the subsequent testing. The corrosion rate was monitored by the linear polarization resistance method using a corrosion- monitoring equipment (ACM Field Machine). The equipment was set to automatically compensate for the IR drop arising from the concrete cover using a 300Hz AC signal. The polarization range was set to ± 10 mV for a 30 second equilibrium period. In order to calculate the corrosion current density, the Stern-Geary equation was applied.

$$ICorr = B/\mathrm{Rp} \quad (1)$$

Instead of obtaining typical semi-circular Nyquist plots, plots of random and widely dispersed data points were obtained. This behavior is characteristic of early stages of corrosion. The LPR technique was adopted to measure corrosion for subsequent trials.

2.5 *Anode Mesh*

The initial trial adopted a current density of 20 mA/m^2 and used a platinized titanium anode ribbon. The theoretical calculation showed that an anode mesh of size 30×20 mm was sufficient. However, the data showed that no polarization of the reinforcing bar was achieved. It was speculated that the small anode size did not allow adequate current distribution along the length of the bar.

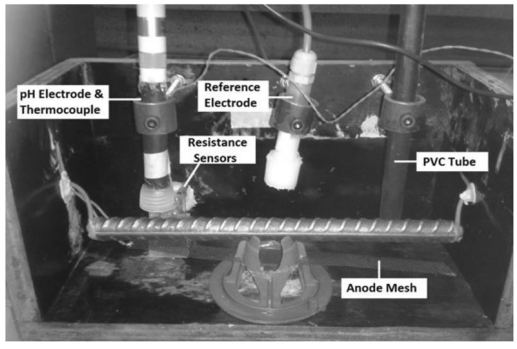

Figure 3. Final specimen design.

Two alternatives were considered. Firstly, that anodes should be spaced at regular intervals along the bar, as is normally done in practice. However, since the bar was of short length, it was decided to use a continuous piece of mesh that ran along the length of the bar. It was also decided to adopt a higher current density to ensure protection was achieved to be able to verify all the monitoring systems.

2.6 *Final Specimen design*

Following the development phase, the specimen design adopted was a 100% OP cement mix (Table 1), with dimensions $300 \times 150 \times 100$ mm with a ribbed steel bar having a diameter and length of 16 mm and 250 mm respectively. A pH electrode and a welded-tip thermocouple were installed at a distance of approximately 20–30 mm from the surface of the bar. A strip of platinized titanium ribbon with dimensions of 200×20 mm at a distance of 15 mm from the bar was used as the anode. The specimen also consisted of an Ag/AgCl reference electrode, a set of resistance sensors positioned close to the bar and a section of PVC tube used as a housing for the humidity sensor, figure 3. After de-moulding, the specimen was left to cure under atmospheric conditions and was subjected to 2 daily water spray cycles (5am and 5pm), lasting 30 minutes each. After leaving the specimen for 1 month to corrode, the CP was switched on and set at a relatively high current density of 0.65 A/m^2 for 1 week before being interrupted, to ensure passivation was achieved. Measurements of various parameters including corrosion rate were made before, during and after application of CP. Corrosion was evaluated via the steel potential and corrosion rate measurements using LPR. The CP was applied by connecting the bar to the negative terminal of the DC power source and the anode mesh to the positive terminal, with a multimeter connected in series to the circuit to measure the current. All the probes with the exception of the resistance sensors were wired to the data-logger, which was set to sample every half hour (except during depolarization period when a higher sampling rate was used).

Manual readings had to be taken from the LCR meter (connected to the resistance sensors) as a multiplexing switch control unit was not available to automatically sample the readings between sensor pairs.

3 RESULTS

3.1 *Potential*

As seen from figure 4, the potential of the steel before CP was switched on was fairly steady, ranging between −295 mV to −325 mV, indicating an intermediate risk of corrosion (ASTM C876, 1999). The spray cycles resulted in a slight increase in potentials towards more positive values, seen in figure 5. Although the humidity data shows a high internal humidity, it does not seem to indicate O_2 starvation, as potentials in the case of O_2 starvation in saturated conditions display more negative potentials, typically lower than −500 mV (Law et al, 2009). Previous research on the effect of wet/dry cycling has shown no evidence of O_2 starvation under similar conditions (Millard et al, 2001). The results show that the solution resistance and polarisation resistance vary in sync with spray cycle which implies that pores are not saturated despite high internal relative humidity and the corrosion is not being effected by O_2 starvation.

After 1 month from casting, the CP was switched on and the current adjusted till the steel potential reached just above −850 mV mark. This corresponded to a protection current density of 0.65 A/m^2, a density considered to be high for CP application. Throughout the on period of 10 days, a gradual potential shift towards more noble values is seen. From the depolarization results given in figure 6, it is seen that a depolarization of almost 300 mV in less than 10 hours was achieved.This suggests that the adoption of the anode mesh along the full length of the rebar has been successful in achieving passivation of the steel and that current densities commensurate with the 20 mA/m^2 criteria can be adopted. The potential of the bar reached approximately −170 mV in 24 hours after CP was switched off. However, the potential dropped after the next spray cycle and then stabilized around the initial corrosion potential (before CP). This suggests a very short duration of protection was sustained. The short duration of protection suggests that complete passivity was not attained as the local environment around the steel bar was not sufficiently transformed to provide a long-lasting residual effect. The aim of these trials is to establish the test conditions, ie, a suitable time for the conditioning of the specimens and whether protection can be obtained using the embedded anode and whether depolarisation can be monitored once the current has been halted. The data from this trial indicates that corrosion appears to be initiated around 20 days, though a longer period of conditioning is required to allow the corrosion to become established. The anode mesh needs to be positioned along the length of the bar to ensure protection of the bar. The corrosion can be halted and depolarisation monitored. The applied current density was significantly higher than required to achieve passivation of the samples. In the detailed experimental program of the broader study, specimens will be investigated with current densities at the 20 mA/m^2 range to simulate those applied in actual ICCP systems. In addition trials will be undertaken at higher current densities to accelerate the process. These will be in the range used in this trial, significantly higher than ICCP systems but lower than those used in desalination/re-alkalisation treatments. A correlation will be made between the charge passed in the standard and accelerated tests to determine if increase current densities can be applied to simulate the long term (10 year plus) application of ICCP, which timeframe is not feasible in laboratory trials.

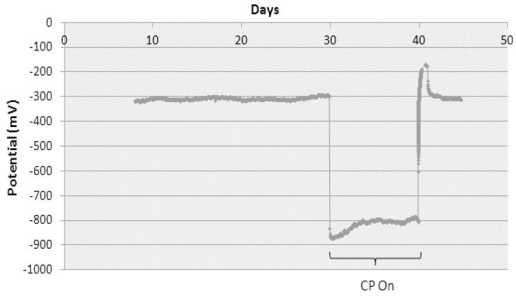

Figure 4. Variation of potential over test period.

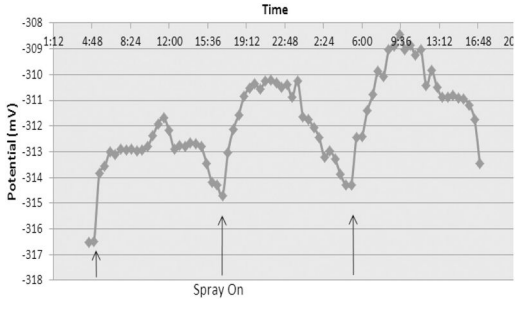

Figure 5. Effect of spray cycle on potential.

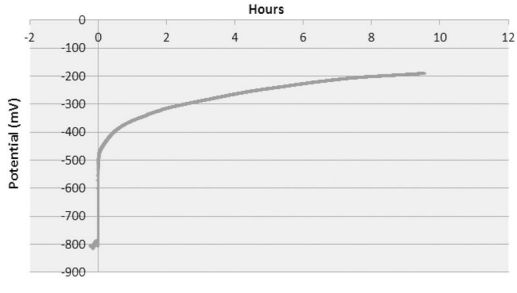

Figure 6. Depolarization curve.

3.2 *Corrosion rate*

The initial corrosion current density measured 2 days after casting shows very high values which gradually reduced over time as seen in figure 7. Intermediary readings show that fluctuations occur, often increasing and then decreasing. This unsteady behavior is often observed in literature and may be explained by a transition from a state of initial pitting corrosion to uniform corrosion (Wei et al, 2012) or more likely in this case due to the initial passivation of steel. The high initial corrosion, which decreases with time, can be attributed to the reducing area of saturated concrete (acting as the electrolyte at the steel surface) with the passage of time due to hydration reaction (Hussain, 2012). The application of CP quickly reduced the corrosion rate to virtually zero. A measurement of corrosion rate few days later confirms that corrosion had reinitiated.

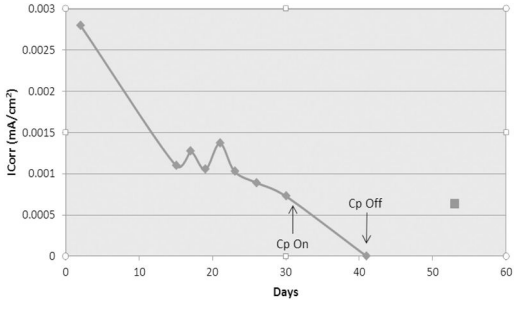

Figure 7. Evolution of corrosion rate.

3.3 *Concrete Resistance*

Figure 8a shows an increase in absolute values of the measured concrete resistance over time. The readings from the pair of steel pins positioned at mid-level of the bar is labeled as 'top' whilst that of the pins positioned 10 mm below are labeled as 'bottom'. The initial increase in resistance is expected due to progressive paste hydration and reduction of pore solution. Since it is not possible to replicate each pin exactly (pin length and spacing), it is expected that there will be some discrepancies between the two sets of results. For this reason results were normalized by taking the first readings as the denominator of each ratio, thereby eliminating unwanted effects to provide a better basis for comparison. The results of the normalized data are plotted in Figure 8b. It is observed that the normalized data are almost identical following the same trend. It was anticipated that the resistance of the top pin would be lower due to the higher concentration of ions nearer to the bar; due to production of OH^- as a result of CP, and that an overall decrease in resistance would be observed after the CP was applied, however the opposite trend is observed. The reason for the difference between the two sets of results is uncertain but may be a result of inhomogeneity of the concrete at the two locations. It is likely that the increase in resistance is a continuation of paste hydration as the concrete is still relatively 'new' and that this effect is possibly more dominant than that caused by changes in local ion concentration. Further investigation is required for a better understanding such as studying the trend over

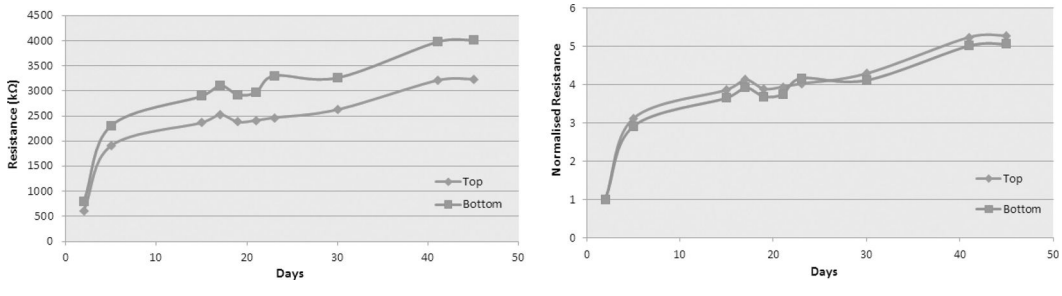

Figure 8. a) Change in absolute values of concrete resistance over time b) Change in normalized values over time.

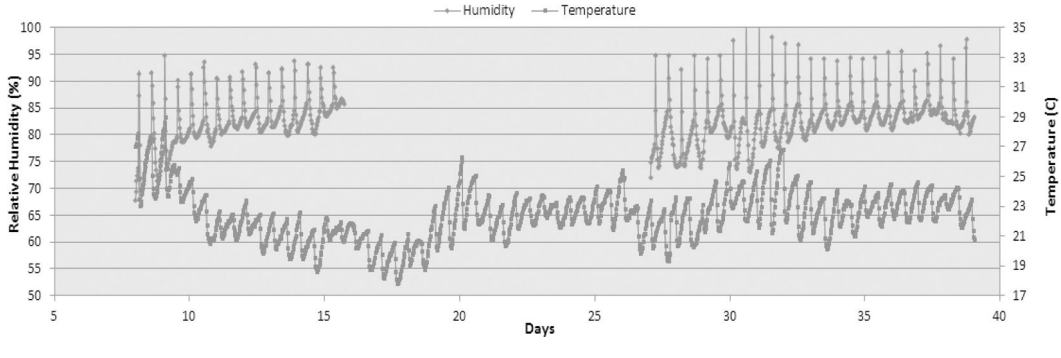

Figure 9. Change in humidity and temperature over time.

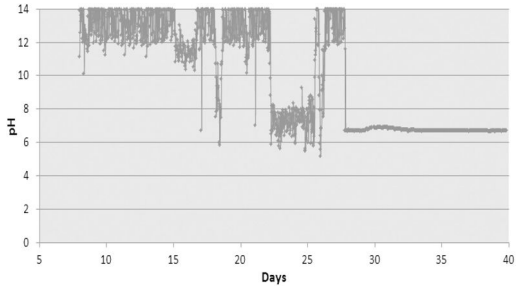

Figure 10. Change in pH with time.

a longer period of CP application and the comparison with a control specimen with no CP. During CP, readings were not possible due to the interference of the current with steel pins resulting in over-range for the LCR meter.

3.4 *Temperature and Humidity*

The results of temperature and humidity readings are both plotted in figure 9. The thermocouple cast in concrete functioned well, proving to be responsive and reliable. Due to limitation in the humidity sensor reported in section 2.3, the sensor was removed after day 15 once steady state conditions were deemed to be achieved and reinstalled at day 27 to monitor any changes during application of CP and period following. The results are as expected; during the spray cycle the temperature drops while the humidity increases. The initial temperature soon after casting is relatively high and this can be attributed to the active exothermic reaction occurring during the early stage of concrete curing. The humidity tended to increase initially (after sensor was placed) and then maintained between 80–85% on average (ignoring peak values). During the second leg of the humidity readings, peak values reached 100% which was likely caused by moisture accumulating on the sensing element, simulating a fully saturated condition.

3.5 *pH of Pore Solution*

The results from the pH electrode were by far, the most unreliable. Despite keeping the specimen under regular spray cycles to keep the concrete fairly moist, the readings were imprecise though did show an improvement in results when compared to initial trial where specimens were relatively dry. The initial readings over the first week of monitoring indicated consistently a high alkaline environment having a pH between 12 and 14, seen in figure 10. However after that the results became unpredictable, often dropping below pH 6. Towards the end, the readings stabilized at around pH 6.7 without any fluctuations, consistent with the pH of the water used in the spray cycle. It is possible that spray water had accumulated in the pores near the electrode or that the electrode had gotten damaged at this point due to deterioration. The electrode is yet to be extracted from the concrete for inspection and testing against buffer solutions. From this trial, it can be concluded that embedded pH electrodes appear unsuitable for monitoring purposes in concrete and that periodic destructive chemical techniques may have to be undertaken.

3.6 *Future work*

The results in this paper presented were used to develop a detailed experimental programme designed to investigate the effects of interrupting ICCP. An experiment is underway which will investigate the effects of duration of ICCP and current density on the residual protection. This will involve a series experiments using standard (20 mA/m^2) and accelerated (100–500 $mA/^2$) current densities and control specimens with no current applied to investigate the residual effects of ICCP on reinforcing steel. This data will be compared with site investigations being undertaken on marine structure with ICCP systems that will be suspended for a short period of time.The addition of control specimens may shed further light on the behavior encountered during this research.

4 CONCLUSIONS

As part of a trial experimental setup to monitor the effects of CP in reinforced concrete, the results from a number of tests have been reported. Upon the application of CP with a relatively high current density of 0.65 mA/m^2 for over a period of 10 days, corrosion was arrested and a polarization far over the 100 mV criteria was achieved, indicating over-protection. However, it did not take long for the potential to return to the initial corrosion potential, suggesting insufficient re-passivation was achieved.

With regards to the functionality of the sensors tested, all performed acceptably with the exception of the pH electrode which proved to be unreliable. Results from resistance sensors were inconclusive and require further testing as there did not seem to be any detectable effect caused by CP. The data also suggests that additional time should be allowed for corrosion to be fully initiated. The results of the EIS, resistance, potential and corrosion rate are indicative that corrosion was not well established before application of CP.

ACKNOWLEDGEMENTS

The authors would like to thank Castle Electrodes for generously supplying the reference electrodes for the experimental work and to thank Mr. K. Le, Mr. S. Mani and Mr. X. Gao for their assistance in the laboratory.

REFERENCES

Aoyama T.L. et al. 2002. Properties of Pre-Tensioned Prestressed Concrete Members Supplied with Cathodic

Protection for Ten Years. Repair Rejuvenation and Enhancement of Concrete: Proceedings of the International Seminar on Challenges of Concrete Construction. Duncdee, Scotland, 329–337

ASTM C876. 1999. Standard Test Method for Half-Cell Potentials of Uncoated Reinforcing Steel in Concrete

BS-EN 1269. 2000. Cathodic Protection of Steel in Concrete

Christodoulou C et al. 2010. Assessing the Long Term Benefits of Impressed Current Cathodic Protection. Corrosion Science. 52: 2671–2679

Das S.C.1994. Cathodic Protection Criteria for Steelin Concrete Some Theoretical and Practical Considerations. Proceedings of International Conference on Corrosion and Control of Steel in Concrete, Sheffield, UK.University of Sheffield.

Glass G.K. et al. 2000. Cathodic Protection Afforded by an Intermittent Current Applied to Reinforced Concrete. Corrosion Science. 43: 1111–1131

Glass G.K. et al. 2008. Hybrid Corrosion Protection of Chloride-Contaminated Concrete. Construction Materials. CM4. 163–172

Hussain R.R. 2012. Time Dependent Electrochemical Effect of Saturated Area in Capillary and Gel Pores of Concrete on the Corrosion Rate of Embedded Steel Reinforcement. International Journal of Electrochemical Science. 7:1402–1411

Law D.W. et al. 2009. Predicting Service Life of Reinforced Concrete Structures Based on Corrosion Rate Measurements. Proceedings of the International Conference on Concrete Solutions. Padova, Italy. 439–442

McCarter W.J. et al. 2005. Field Monitoring of Electrical Conductivity of Cover-Zone Concrete. Cement and Concrete Composites. 27:809–817

Millard S.G. et al. 2001. Environmenal Influences on Linear Polarisation Corrosion Rate Measurement in Reinforced Concrete. NDT&E International. 34:409–417

Page C.L. 1997. Cathodic Protection of Reinforced Concrete -Principles and Applications.Proceedings of the International Conference on 'Repair of Concrete Structures'. Svolvaer, Norway. 123–132

Wei J. et al. 2013. Corrosion Evolution of Scaled Rebar in Concrete under Dry/wet Cyclic Condition in 3.5% NaCl Solution. International Journal of Electrochemical Science. 8:2536–2550

This page intentionally left blank

Concrete Solutions – Grantham et al. (Eds)
© 2014 Taylor & Francis Group, London, ISBN 978-1-138-02708-4

Cathodic protection for the remediation of swimming pools

R. Brueckner
Mott MacDonald, Prince House, Bristol, UK

D. Wright, C. Atkins & P. Lambert
Mott MacDonald, Spring Bank House, Altrincham, UK

ABSTRACT: Reinforced concrete structures are prone to various types of deterioration of which corrosion of the reinforcement is generally the most damaging. Electrochemical techniques are well established and cost effective repair options for the prevention and reduction of corrosion in such structures. The main field of application of electro-chemical techniques, in particular Cathodic Protection (CP), is within the infrastructure section; however, other reinforced concrete structures can undergo similar deterioration processes and also benefit from its application.

Corrosion of the reinforcement generally occurs as a result of carbonation of the concrete or chloride ion attack from internal or external sources. The latter forms the major cause of deterioration in the transportation sector, largely due to the use of de-icing salts. Recreational structures, such as swimming pools, may also be affected by corrosion due to by-products of the chlorination process.

The application of CP systems for the cost-effective repair of recreational structures has become more common in recent years. Many swimming pools are generally owned and operated by or on behalf of local authorities, where achieving cost reduction has been a major driver to securing funding for refurbishment works. The main benefit of CP, that the sound but contaminated concrete can remain in place, has contributed to the interest in employing CP systems.

This paper discusses suitable CP systems for swimming pools, obstacles which may be encountered in such an environment and practical issues to obtain a durable protection system. Operation and maintenance considerations specific to such structures are also discussed.

1 INTRODUCTION

Deterioration of reinforced concrete structures is commonly associated with the infrastructure sector where bridges, viaducts, tunnels and port structures mainly suffer from degradation due to carbonation of the concrete or chloride ion attack from internal and external sources. The latter forms the major cause of deterioration in the transportation sector, largely due to the use of de-icing salts or seawater.

Structures that fall outside the well-defined maintenance regimes applied to infrastructure, such as recreational structures, can undergo the same deterioration processes and therefore also require repair and maintenance in order to provide durable and safe facilities for their users and operators.

Swimming pools are typically constructed from reinforced concrete with ducts around the perimeter that can be exposed to heavily chlorinated water. The by-products of the chlorination process can provide a significant source of external chlorides which may lead to chloride-induced corrosion of the reinforcement and deterioration of the concrete. These structures are generally owned and operated by or on behalf of local authorities which are required to identify the most cost-effective options for remediation and long-term maintenance.

2 CORROSION

The single commonest cause of serious degradation of reinforced concrete structures of any type results from the corrosion of the steel reinforcement. Concrete possesses a highly alkaline pore structure, with pH values generally in excess of 13, which is a result of the cement hydration reactions. This assists in the formation and maintenance of a protective stable passive iron oxide film on the steel surface. The protective nature of this passive film can however be compromised by two commonly encountered mechanisms, those of chloride ion attack and carbonation.

The rust or corrosion product is typically insoluble and more voluminous than the original steel. This causes tensile stresses in the concrete cover resulting in delamination of the cover zone. This, together with the associated loss in steel cross-section, can prove to be structurally sensitive.

Chloride ion attack is widely considered to be the most significant cause of concrete deterioration for transport structures subject to de-icing. When the chloride content exceeds the critical threshold, the likelihood of disruption to the passive film significantly increases causing localised areas of intense corrosion. The level at which chlorides are generally considered to represent a risk of corrosion is typically greater than 0.4% by mass of cement. Chlorides may originate from internal sources as a result of chloride containing accelerators such as calcium chloride, while inadequately washed marine dredged aggregates are another potential contributor to internal chloride levels. The major source of chloride ions for transportation structures other than maritime environments is de-icing salts. Swimming pools are usually exposed to chlorinated water which can, through various reactions, form a significant source of external chlorides in this environment (Perkins 2000). Such external sources of chloride cumulatively increase the total chloride content to beyond the critical threshold at which corrosion of embedded steel is initiated.

Carbonation induced corrosion is less dependent upon the location of atmospherically exposed structure as long as moisture in the concrete pore structure is present to initiate corrosion. The primary effect of carbonation is the reduction of alkalinity which supports the protective layer at the steel surface. The atmosphere contains a small proportion of carbon dioxide which neutralizes the alkalinity in the concrete in the presence of moisture. The rate of carbonation is largely dependent on the moisture content, with the rate decreasing where the pores are filled with water, for example, due to regular exposure to rain. However, corrosion requires moisture to proceed, so that under cycles of wetting and drying it is possible to have periods of rapid carbonation followed by periods when the steel in carbonated concrete can corrode. The highest rate of carbonation occurs on indoor elements but corrosion is less likely to initiate due to the lack of moisture. In addition, chemically bound chlorides are also released during the process of carbonation which are then free to further promote corrosion.

Once corrosion of steel in concrete has initiated and progressed, it is possible to reduce the rate of deterioration to a tolerable level through the application of electrochemical techniques. These are well established techniques for the remediation of transport structures but can also provide sustainable and cost-effective solutions for any reinforced concrete structure.

3 CORROSION PREVENTION

Corrosion can be prevented or controlled in structures by using electrochemical techniques which decrease the rate of corrosion to a tolerable level. The most commonly applied electrochemical solution is cathodic protection (CP), however, other techniques such as corrosion inhibitors, realkalisation, chloride extraction and electro-osmotic methods can be used to mitigate

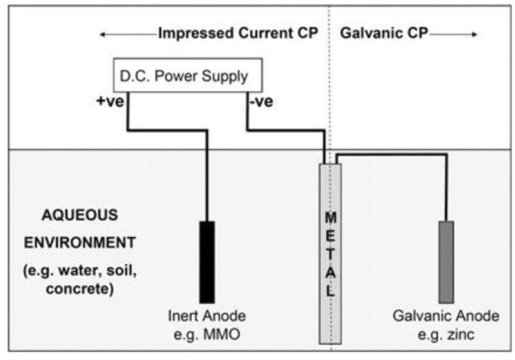

Figure 1. Schematic of Impressed and Galvanic Cathodic Protection, Lambert 2009.

the risk of ongoing corrosion in reinforced concrete structures. CP can be a particularly effective repair technique for chloride contaminated concrete where continuous exposure to external sources of chloride cannot be prevented.

On the principle that corrosion occurs due to the formation of anodic sites where metal is lost and cathodic sites which are unaffected, CP works by polarizing the reinforcement in an electrical circuit making all the steel to be protected cathodic with respect to a system of installed anodes (Chess 2013) (see Figure 1). These can be self-powered galvanic or, more commonly, inert anodes powered by a low voltage DC supply which is commonly referred to as impressed current cathodic protection (ICCP). ICCP systems generally use inert long-life electrodes such as mixed metal oxide coated titanium or titania (titanium oxide ceramic). The reinforcement is polarised using an external DC power source. Galvanic systems use less noble metal electrodes, commonly zinc, aluminium or magnesium, which corrode preferentially to the steel and thereby provide the required protection.

CP systems must be carefully designed and many different factors must be taken into account such as the aggressiveness of the environment, the area of steel to be protected, the type of anode used and the sensitivity of the concrete to other deterioration mechanisms.

A reduction of the corrosion rate to a tolerable level can also be achieved using corrosion inhibitors. These are widely used in the protection of metals in domestic, commercial and industrial applications but can also be applied on reinforced concrete elements. Vapour phase inhibitors are most successful on structures which are not already excessively damaged, are carbonated or do not have high concentrations of chloride ions. In the case of the remediation of swimming pools CP systems are considered to be the most suitable electrochemical techniques. Electrochemical chloride extraction may temporarily reduce the chloride content below the threshold but due to the constant exposure to the chlorinated water this technique will not provide a long term solution. Inhibitors may be able to provide sufficient protection but only to an experienced based lifetime of approximately 10 years which is much

Figure 2. Environment within a wet duct environment.

Figure 3. Access difficulties in dry duct crawl space.

shorter compared to at least 25 years for CP systems. Realkalisation is unlikely to be appropriate for such applications.

4 CASE STUDIES

Mott MacDonald has been approached by several local authorities in England and Scotland during recent years to inspect swimming pool structures and recommend suitable remediation strategies. Swimming pools can vary significantly in their designs, comprising wet and/or dry ducts around the pool or other systems for catching the overflow water. The accessibility may also vary from full height ducts to more confined spaces preventing routine inspections.

Wet ducts are usually constantly exposed to chlorinated water from the overflow but the surfaces can be distinguished in different exposure classes, see Figure 2. The floor, pool wall and lower section of the outer wall are fully saturated. The ceiling can be partially saturated, wet close to the overflow and surface dry towards the outer wall. The outer wall comprises sections, from bottom to top, of full saturation, i.e. below the water line, a section where capillary suction and surface evaporation takes place and a dry section towards the soffit.

Dry ducts may be located next to the wet ducts or directly next to the pool walls where an alternative overflow system has been put in place. Services, such as inlet, outlet and dosing pipes, are located in the dry ducts and as the name implies should be free from water. However, defects in the expansion joints, wet duct walls and other defects in the pipes may enable water penetration which results in exposure to chlorinated water in localised areas. The following examples will demonstrate the different types of swimming pools, their access restraints and which potential defects may be encountered.

4.1 *Case Study A*

Swimming pool A was inspected as part of a condition survey prior to the finalisation of refurbishment plans of a school pool in Scotland. The pool has a dry duct which followed the height of the pool floor and therefore access was confined through the entry point at the shallow end of the pool, see Figure 3.

Figure 4. Evidence of standing water in dry duct due to expansion joint leakage.

The interior of the duct showed minor signs of deterioration to the metallic elements due to humidity from the sump at the deep end. The water was derived from leaks in the expansion joint in the wall which also lifted tiles in the pool.

Deterioration of the concrete or major chloride contamination causing reinforcement corrosion could not be identified. Therefore the repair of the expansion joint, besides treatment or replacement of the metallic elements, was considered to be appropriate to achieve a significant life extension for the structure.

4.2 *Case Study B*

Swimming pool B was inspected by others but Mott MacDonald reviewed the findings and developed a repair and maintenance strategy to ensure the structural integrity of the pool after refurbishment of the leisure centre in the North East of England. The ducts are 1.0 to 1.3 m high and were intended to be dry but standing water was encountered. Severe deterioration was reported to have been observed on the swimming

Figure 5. Delamination of pool wall in dry duct.

pool wall, see Figure 5. Minor signs of deterioration were observed on the rear wall. The soffit showed both severe deterioration close to the pool wall and minor degradation adjacent to the outer duct wall.

Half-cell and chloride testing confirmed the observation with the highest chloride content of up to 2.9% by mass of cement in proximity to the reinforcement in the pool wall. The soffit and rear wall with signs of minor deterioration had a maximum chloride content of 0.5% by mass of cement compared to 1.8% at the soffit close to the pool wall. These observations and test results confirm the different exposure conditions which can be found in pool ducts.

Owing to the levels of chloride contamination, state of deterioration and the required design life extension of 25 years, a CP system was recommended to be the most suitable repair option. The removal of the contaminated concrete and reconstruction was not considered to be economically feasible for the local authority. Since the extent of the chloride contamination was confined to the pool wall and the adjacent soffit, the CP system could be limited to these areas.

As the ducts were classified as a confined space, a lightweight pre-fabricated bolt-on cassette CP system was selected to significantly reduce the man hours required for installation. The system consists of mixed metal oxide coated titanium (MMO Ti) ribbon anodes in a glassfibre foam filled, fibre reinforced polymer (FRP) tray which are mounted on the concrete surface using bolts. The glassfibre foam pads are impregnated with calcium nitrate to absorb moisture from the air, providing the required electrolyte, see Figure 6. The cassette system contributed positively to the health and safety considerations for the contractor in the confined space.

To further simplify the installation and to reduce the risk of corrosion, the usual 316 stainless steel bolts were replaced with polymer studs.

The system was designed to be installed at a spacing of 0.5 m centres with a cassette output of 3.5 mA per linear metre. The areas to be protected could be consolidated in one 1.75 Amp zone which was set to a 4 V driving voltage. Monitoring is carried out by four Ag/AgCl/KCl reference electrodes. Figure 7 shows the

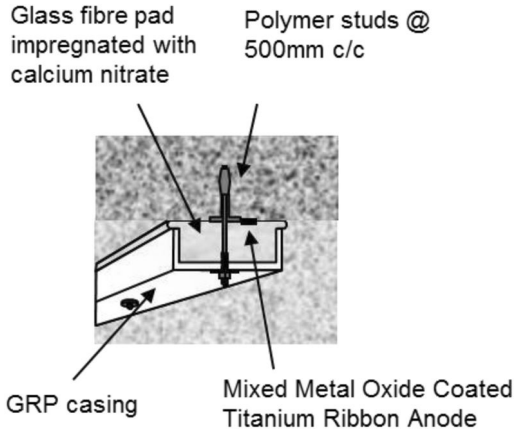

Figure 6. Schematic representation of the cassette system.

Figure 7. Cassette system installed in confined space.

confined conditions and the installed system in the duct which was energised to 20% of the design current in May 2011. Since then it has provided stable monitoring data showing satisfactory protection of the reinforcement in the chloride contaminated pool wall and soffit.

4.3 *Case Study C*

Swimming pool C is part of a leisure centre in England's West Midlands and comprises both wet and dry ducts. Mott MacDonald initially carried out a visual inspection and delamination survey and later designed a CP system once funding for the refurbishment of the centre and repair of the pool was obtained by the local authority. The visual inspection identified distinct areas of delamination on the outer wet duct walls which were partially immersed and exposed to spray from the overflow, see Figure 8. The pool wall and soffit were significantly less deteriorated as a result of constant saturation of the concrete. In contrast to these surfaces the outer wall undergoes cycles of wetting, occurring during the opening hours of the pool, and drying during periods of closure.

Figure 8. Delamination and corrosion at wet duct wall.

Figure 9. Installed cassette system.

The dry duct surrounding the wet duct was reported to have occasionally been exposed to standing water but only minor concrete deterioration was observed. Metallic fixtures in the dry duct showed signs of corrosion due to the high humidity and temperature as a result of the adjacent wet duct. An appropriate CP system, combined with the required conventional repair to the severely deteriorated outer wet duct wall, was identified to be the most appropriate repair strategy to obtain the required design life extension for the refurbished leisure centre. In addition, galvanic anodes were used to protect areas of concrete repair in the dry duct.

The CP system selected was the cassette anode system as used in Case Study B, consisting of MMO Ti ribbon anodes in a calcium nitrate impregnated glassfibre foam filled, fibre reinforced polymer (FRP) tray mounted on the concrete surface using polymer fixings. The cassettes were installed in the wet duct which is continuously exposed to running water and condensation on the majority of the surfaces. The cassettes were designed to be installed at 0.5 m centres on the pool wall, soffit and outer pool wall whereby the cassettes at the walls were partially immersed in the overflow water which is collected up to a height of 300 mm in the duct, see Figure 9.

The system was designed in three zones each of 2 Amps, reflecting the different environments in the duct, i.e. continuously wet pool wall due to the overflow, the soffit which experiences significant condensation and the outer wall which undergoes cycles of wetting and drying. The system was energised to 500 mA and the driving voltage set to 4 V in May 2011.

Monitoring is carried out by four Ag/AgCl/KCl reference electrodes in each zone and a satisfactory potential shift was observed during commissioning. During the following regular monitoring exercises, less satisfactory depolarisation data were obtained indicating insufficient polarisation for the pool and duct wall. This was investigated and found to be a result of the cassettes being partially immersed in the water 'dumping' a proportion of the current in this zone of low resistivity. The reference electrodes in the wet duct wall are located above the water level and the zone of capillary suction but tests showed that sufficient polarisation can be achieved when the resistivity around the references electrodes is decreased. Based on these observations it was concluded that the wet duct wall is sufficiently protected. The soffit zone, which is exposed to more even conditions of constant condensation, showed satisfactory depolarisation results after 12 months but the current output reduced from 500 mA to 225 mA after 24 months requiring an increase of the driving voltage to 6 V.

The lower levels of polarisation observed on the pool wall after 24 months was identified to be a result of displacement of the glassfibre pads providing the contact between anode and concrete surface. The cassettes were originally developed to protect jetties and harbours which are exposed to tidal and wave actions; however, at the pool wall they are exposed to a constant one-directional flow of water. The manufacturer has not experienced such degradation and reported that the long term performance of the system installed on harbours and jetties has been satisfactory to date. In areas of worst deterioration it was observed that the cassettes were not installed as tight to the wall, allowing water to pass between the pads and the concrete surface.

In addition, the grade of polymer used for the studs was found to be sensitive to the acid generation at the anodes which loosened some cassettes. The acid generation also discoloured the PVC outer sheath of the cables but the used XLPE/PVC and XLPE cables are acid resistant. As access to and into the 2 metre high duct was relatively easy, the cassettes were refixed in one day by drilling out the old studs and using polypropylene cladding panel fixings with more appropriate chemical resistance.

5 CONCLUSIONS

Swimming pools can suffer from severe deterioration of the reinforced concrete elements of the dry and wet ducts whereby the wet ducts are at the highest risk. However, undetected or ignored water ingress

in dry ducts may result in the same level of deterioration. The deterioration may be observed during routine inspections and other maintenance work if the ducts are easily accessible. The more difficult to access ducts are more likely to be dry ducts and therefore less vulnerable due such damage, although leakage, for example through faulty expansion joints, may still result in severe deterioration to the structure.

The exposure conditions within a duct, in particular a wet duct, can vary significantly. The pool wall which is usually exposed to the water overflow is generally fully saturated. The duct wall may be exposed to cycles of wetting due to spray from the overflow during opening hours and drying during the periods of closure. This can result in a significant increase in the chloride content in these sections of the walls. In addition to the different exposure conditions of the two walls, both are partially immersed in water resulting in capillary suction and evaporation in the duct wall. The soffit is usually moist due to condensation but the level of saturation may be expected to increase towards the overflow opening. These different exposure conditions cause significantly varying levels of deterioration.

The application of a CP system in addition to conventional concrete repair can be a cost-effective solution for a significant lifetime extension of swimming pools. Furthermore it can provide vital cost savings during refurbishment works for the owners of the pools, often local authorities, as chloride contaminated concrete can be kept in place, reducing the need for extensive reconstruction and associated lengthy closures and loss of facilities.

The CP system designed for the two pools as described above was considered to be the simplest to install, significantly reducing the man hours spent in the confined spaces of the ducts. Discreet anodes can be difficult to install and could cause damage to the pool structure if drilled too deep. Mesh and overlay systems may cause significant health and safety risks to the contractor during the application of the overlay and further reduce the already limited work space.

The different exposure conditions in the wet ducts can result in difficulties in achieving the required polarisation. Current may be 'dumped' in low resistivity zones, i.e. where the anodes are immersed in water. This can lead to misinterpretation of the monitoring results if the reference electrodes are located in areas with higher resistivity and therefore needs to be taken into account during the design and operation stages.

In addition to the above points it is essential that the cassettes are installed as tightly as possible at the pool wall to avoid the glassfibre pads being exposed to regular one-directional water flow resulting in wash-out of the material. The cassette mounting bolts must be resistant to acid generation at the anodes. Polypropylene fixings are considered to be sufficiently robust and easy to install.

REFERENCES

Chess, P. 2013. Design of a Cathodic Protection System for Exposed Reinforced Concrete Structures. Cathodic Protection of Steel in Concrete and Masonry, Second Edition. Spon Press: pp 109–128.

Lambert, P. 2009. Sustainability of Metals and Alloys in Construction. Sustainability of Construction Materials. Woodhead Publishing: pp 148–170.

Perkins, P.H. 2000. Factors Affecting the Durability of Reinforced Concrete and Cement-based Materials used in the Construction of Swimming Pools. Swimming Pools – Design and Construction, Fourth Edition. Spon Press: pp 48–60.

Concrete Solutions – Grantham et al. (Eds)
© 2014 Taylor & Francis Group, London, ISBN 978-1-138-02708-4

Site performance of galvanic anodes in concrete repairs

C. Christodoulou
AECOM Europe, Birmingham, UK

C.I. Goodier & S.A. Austin
Loughborough University, School of Civil and Building Engineering, Loughborough, UK

ABSTRACT: Galvanic anodes can be used to limit the extent of concrete replacement and extend the service life of patch repairs to reinforced concrete (RC) structures. They respond to changes in environmental conditions and this attribute has been employed to extend their use.

Traditionally, galvanic anodes are installed within the repair area itself. Although simple to install, this has certain limitations however, due primarily to the resistivity of the repair material. A recent alternative has been to install galvanic anodes in pre-drilled cavities in the parent concrete around the perimeter of the patch repair.

This paper reviews and compares the performance of discrete galvanic anodes installed both within the repair area and parent concrete in full-scale RC structures. Results indicate that galvanic anodes installed within the parent concrete had a more profound effect on the polarisation of the steel around the perimeter of the patch repair. This provides the empirical basis for alternative designs incorporating galvanic anodes that will enable increased corrosion protection to the steel reinforcement around the patch repair, which is generally considered to be at the highest risk.

1 INTRODUCTION

Patch repairs of deteriorating concrete is a common approach to rehabilitate defective concrete structures. Bridge Advice Note 35 (DMRB 1990) suggests that areas which show chloride concentrations greater than 0.3% by weight of cement and half-cell potential measurements higher than −350 mV should be removed. Concrete replacement to this extent on chloride-contaminated structures can be very onerous and expensive (Christodoulou 2008).

Galvanic anodes have been used to limit the extent of concrete replacement and extend the service life of patch repairs to RC structures (NACE 2005, Concrete Society 2011, Christodoulou et al. 2011). They are based on the principle that different metals produce different potentials (Broomfield 2007). Therefore, particular metals can be used which will corrode sacrificially to protect the steel reinforcement and offer a protective effect. Their main advantage over other electrochemical treatments is the lack of need for a power supply and associated complex wiring installations. In addition, performance monitoring is straight forward and does not involve complex electronics. However, it is acknowledged that they have a lower protective current output and as a result might be ineffective in concrete with high corrosion rates (Christodoulou et al. 2009).

Galvanic anodes respond to changes in the environmental conditions that they are exposed to (John and Cottis 2003, NACE 2005, Christodoulou et al. 2009). Such an effect will be more dominant in parent concrete that has a residual level of chloride contamination as opposed to non-contaminated repair concrete or mortar and this has been employed to extend the use of galvanic anodes (Holmes et al. 2011, Glass et al. 2012).

The work presented here examined the performance of discrete galvanic anodes installed both within the parent concrete around the perimeter of the repair and also within the patch repair area itself. Early results of this work have also been reported previously (Christodoulou et al. 2011).

2 METHODOLOGY

This section describes the full-scale RC structure that received patch repairs with galvanic anodes both within the patch repair itself and in the parent concrete around the patch repair, the properties of the galvanic anodes and the testing arrangement.

2.1 *Structure*

A multi-storey car park (MSCP) in the UK suffering from chloride-induced corrosion was selected for this work (Figure 1). The structure was built in the early 1970s with one-way spanning concrete ribbed type deck arrangement.

Intrusive investigations were undertaken in 1997, 1999 and 2008 to determine the extent of chloride

Figure 1. General condition of the MSCP's soffit indicating leaching, dynamic cracking and deterioration of the concrete elements.

contamination whilst also assessing the probability of corrosion activity with potential mapping. The decks and soffits, especially adjacent to the expansion joints, appeared to have high levels of chloride concentration at the depth of reinforcement; hence according to Bridge Advice Note 35 (DMRB 1990) there was a significantly high risk of corrosion. By 2008, there were locations where the chloride levels were up to 2.9% by weight of cement at a depth of 30 to 55 mm, where the reinforcement was located.

The profile of the chloride levels over a period of approximately 11 years suggested that chlorides were brought to the unprotected surface of the decks by cars and had penetrated the concrete surface. In addition, de-icing salt had been routinely spread on the roof decks to prevent ponding water from freezing.

2.2 *Galvanic anodes*

The design for the structural repairs involved removing only physically deteriorated concrete by jack hammer. The breakouts extended beyond the back of the reinforcement to minimum additional depth equal to the aggregate size of the repair mortar plus 3 mm. The steel was cleaned by means of rotary steel wire brushes (Christodoulou et al. 2013).

The nature of commercial contracts and their risk allocation typically require that a contractor uses specialist repair materials conforming to a standard. For the restoration of the concrete profile a class R3 structural repair mortar in accordance to BS EN 1504-3 was applied (Concrete Society 2009, BSI 2005). The repair materials was a Portland cement based flowable, polymer modified, shrinkage compensated micro-concrete, which is poured and trowel finished.

Anodes type A, were installed in pre-drilled holes of 25 mm diameter and 45 mm long in the parent concrete, as close as practically possible to the edge of the patch and then filled with proprietary backfill (Figure 2). A titanium wire integrated with the galvanic anodes made a connection to the steel reinforcement within the repair area. Their installation spacing was 250 mm centres.

Table 1. Summary of anode types, installation location and properties.

Anode type	Installation location	Properties
A	Parent concrete	Cylindrically shaped, diameter 20 mm, length 40 mm, 65 grams of zinc, coated with activator
B	Patch repair	Circularly shaped, diameter 65 mm, thickness 30 mm, 60 grams of zinc, encapsulated in activator

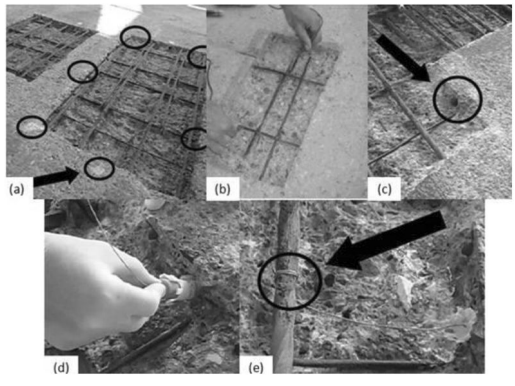

Figure 2. Galvanic anode type A installation procedure, (a) repair area following breakout and with location of anode installation marked out, (b) testing for reinforcement continuity, (c) pre-drilled holes for anode installation, (d) installation of galvanic anode and (e) connection of galvanic anode to the steel reinforcement and anode hole following filling with the proprietary backfill (Christodoulou et al. 2014).

Anodes type B were installed within the patch repair on the side of the exposed reinforcement, as closely as possible to the edge of the repair. A steel wire integrated with the galvanic anodes made a connection to the steel reinforcement. The anodes were also encapsulated in a proprietary embedment mortar to provide a conductive path to the substrate (Figure 3). Their installation spacing was 250 mm centres.

2.3 *Testing regime*

Measuring steel potentials against the potential of a standard reference electrode (i.e. absolute potentials) is a well established non-destructive monitoring technique (Elsener 2001, Elsener 2003, Concrete Society 2004, ASTM 2009). An alternative to this, are electrode to electrode potentials (i.e. relative potentials) which provide information on the electric field in concrete and as such locating areas of actively corroding

Figure 3. Galvanic anode type B installation procedure, (left) anode tied to the reinforcement as close as practically possible to the edge of the repair and (right) galvanic anode encapsulated in proprietary embedment mortar.

steel by considering spatial variation of potentials (Elsener 2003, Glass et al. 2010).

Potential maps were obtained on a 50 mm square grid using a portable Ag/AgCl/0.5 M KCl reference electrode and a high impedance multi-meter. The size of each grid varied in accordance to the size of the repair but in general it extended up to 700 mm in the parent concrete when measured from the edge of the repair. All the potential values herein are reported relative to the most positive value obtained at the time of the measurement.

3 RESULTS

The following sections provide a summary of the results for anode types A and B.

3.1 *Anode Type A*

The typical polarisation effect afforded by anodes type A at a distance away from the edge of the patch repair between 110 and 215 days following installation is shown in Figure 4. It can be observed that the anodes affected the potentials to a distance of approximately 600 mm from the edge of the repair even after 215 days. The time dependant trends observed can be attributed to changes in the weather conditions.

Figure 5 demonstrates the results of potential mapping around the perimeter of a patch repair with anode type A over a period of 195 days. It can be observed that the anodic points identified in the mapping, coincided at all times with the location of the galvanic anodes (anodic points have been circled). It can be observed that the potentials never rose higher than the imaginary lines connecting the anodic spots, suggesting that there are no other anodic spots between the galvanic anodes.

These results were typical and re-occurring findings through all the patch repairs on this MSCP for the polarisation effect afforded by galvanic anodes type A to steel in parent concrete at a distance from the edge of the patch repair. Readings past 215 days could unfortunately not be obtained, as thereafter the slabs received a surface applied waterproofing coating.

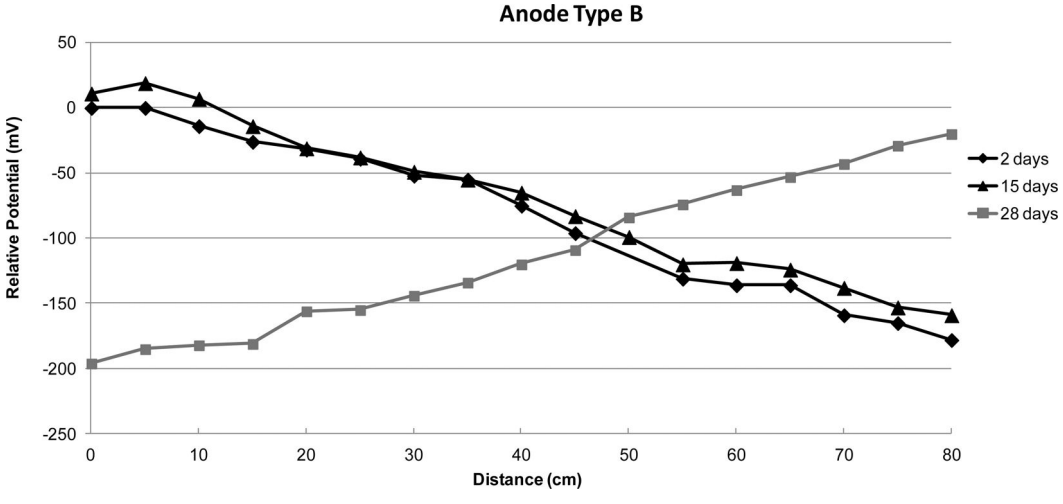

Figure 4. Polarisation effect afforded by anodes type A at a distance from the edge of a patch repair over a period of 215 days.

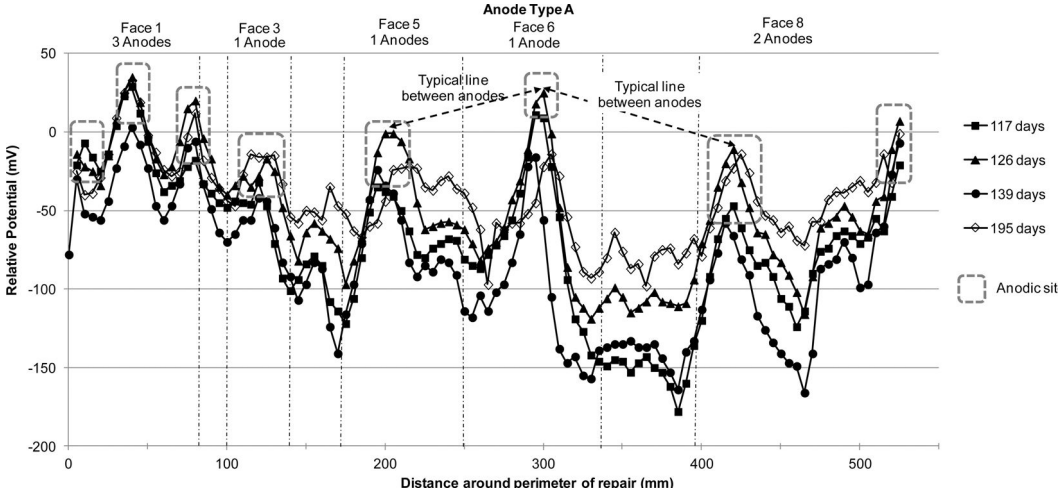

Figure 5. Potential mapping around a patch repair location with anodes type A over a period of 195 days.

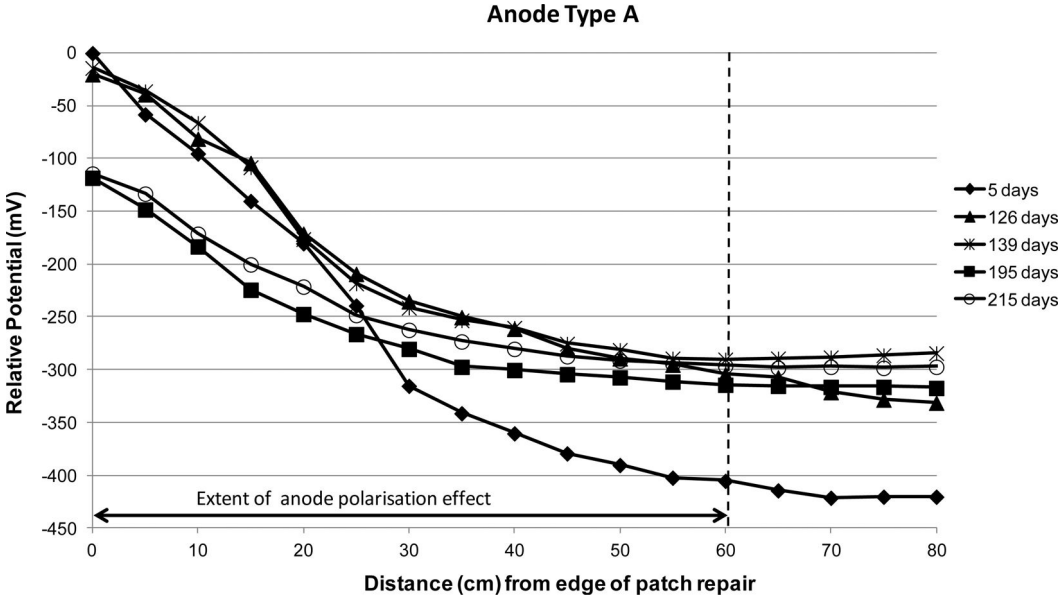

Figure 6. Polarisation effect afforded by anodes type B at a distance from the edge of a patch repair over a period of 28 days.

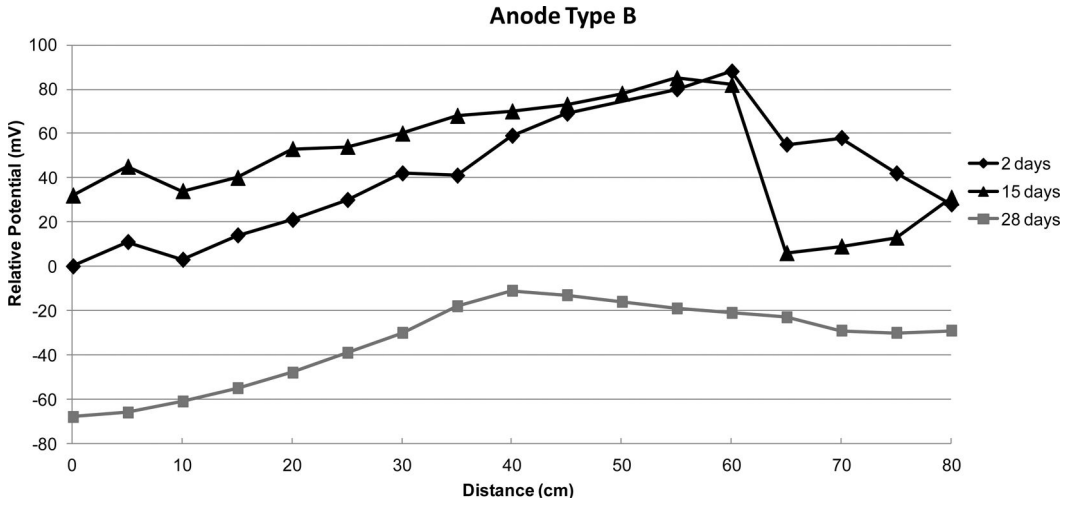

Figure 7. Polarisation effect afforded by anodes type B at a distance from the edge of a patch repair over a period of 28 days.

3.2 *Anode Type B*

The typical polarisation effect afforded by anodes type B at a distance away from the edge of the patch repair over a period of 28 days following installation is shown in Figure 6. It can be observed that there was a polarisation effect almost over the entire measurement length of 800mm over the first 15 days. However, at 28 days it was observed that the effect was entirely lost and no polarisation was afforded to the steel in the parent concrete adjacent to the repair.

In a similar repair with type B anodes, potential mapping over a period of 28 days demonstrated that the anodes provided no polarisation effect at all to the reinforcement in the parent concrete adjacent to the patch repair (Figure 7). Unlike the previous repair, this behaviour was experienced from day 2 and throughout the testing. The above, are typical and re-occurring findings for the polarisation effect afforded by galvanic anodes type B to steel in parent concrete at a distance from the edge of the patch repair. Readings over 28 days could not be obtained, as thereafter the local concrete patch repairs received a surface applied waterproofing coating.

4 DISCUSSION

This study investigated the performance of two different types of galvanic anodes installed both in the parent concrete and the patch repair material itself. Monitoring was performed by close-interval relative potential mapping around the perimeter of the repairs to verify that the anodes were still active, and at staged distances away from the repairs to assess the polarisation effect afforded by the anodes to the steel in the parent concrete.

The monitoring data indicated a variance in the performance between anode types A and B. Galvanic anodes type A, installed in the parent concrete around the repair, demonstrated polarisation effects of up to 600 mm away from the patch repair itself over a period of 215 days. However galvanic anodes type B, embedded within the patch repair itself, demonstrated limited polarisation effects and in cases none at all over a period of 28 days. Similar observations have also been made by Dugarte and Sagues (2007).

These above observations suggest that the choice of repair material may have an influence in the performance of galvanic anodes. In this particular case, the repair material was a structural repair mortar class R3 in accordance to BS EN 1507 (British Standards Institution 2005). As such, consideration should be given in the compatibility between galvanic anodes and repair material. It is considered appropriate that materials conforming to the requirements of BS EN 1507 (BSI 2005) are used at all times for concrete repairs and the installation of galvanic anodes is amended to suit. An opposite approach, would result in the use of non-conforming repair materials and increase the risk for failure of the concrete repair.

Traditionally, half-cell potential mapping in the UK is undertaken based on a 500 mm grid and for rapid corrosion assessment spacing up to 1.2 m is occasionally employed (ASTM 2009). Undertaking relative potential mapping at a small grid (50 mm), as in the case of this study, has the advantage of collecting time-dependent spatial variation information regarding the condition of the reinforcement. This is particularly suited to galvanic systems which are often installed without any monitoring facility (including a connection to the steel reinforcement).

A new criterion to that of 100 mV depolarisation (BSI 2012), may be adopted for assessing the performance of galvanic anode systems by means of potential mapping to obtain spatial variations. Potential mapping around the perimeter of a patch repair with galvanic anodes installed in the parent concrete, should demonstrate that the anodes afford a dominant

(i.e. be dominant over any effect of a steel anode) influence on the steel potentials away from the area of the patch repair that is at least equal to half the spacing between anodes. This alternative performance criterion is also in line with the work of Holmes et al. (2011).

5 CONCLUSIONS

The results of this work lead to the following conclusions:

- Galvanic anodes type A, installed in pre-drilled cavities formed in the parent concrete exposed within an area of patch repair, can provide substantially higher levels of polarisation to the steel reinforcement in the parent concrete outside the repair compared to galvanic anodes embedded directly within the patch repair itself (type B). Type A, had a dominant effect on potentials within the concrete to a distance of approximately 600 mm from the edge of the patch repair over a period of 215 days, type B the latter had no influence after 28 days.
- A repair material that conforms to standards for structural repairs such as BS EN 1504 (BSI 2005) can significantly affect the performance of galvanic anodes type B (within the patch repair), whereas it had no effect on the performance of galvanic anodes type A.
- Close-interval potential mapping (50 mm spacing) is an effective technique to assess the performance of galvanic anodes. It has the additional advantage that localised active corrosion spots can also be detected if present.
- An alternative criterion, to that of 100 mV depolarisation, is proposed for assessing the performance of galvanic anodes: the anodes should afford a dominant (i.e. be dominant over any effect of a steel anode) influence on the steel potentials away from the area of patch repair that is at least equal to half the spacing between anodes.

REFERENCES

American Society for Testing and Materials, 2009. ASTM C 876 – 2009, Standard Test Method for Corrosion Potentials of Uncoated Reinforcing Steel in Concrete, West Conshohocken, Pennsylvania, USA.

British Standards Institution, BS EN ISO 12696:2012, Cathodic protection of steel in concrete, London: BSI, 2012.

British Standards Institution, BS EN 1504:2005 Products and Systems for the Protection and Repair of Concrete Structures – Definitions, Requirements, Quality Control and Evaluation of Conformity – Part 3: Structural and Non Structural Repair, BSI, London, 2005.

Broomfield J.P., Corrosion of Steel in Concrete: Understanding, Investigation and Repair, second ed., Taylor and Francis, UK, 2007.

Christodoulou C., Electrochemical treatments of corroded reinforcement in concrete. IN: Alexander, M. et al. (eds.) Concrete Repair, Rehabilitation and Retrofitting II – Proceedings of the 2nd International Conference on Concrete Repair, Rehabilitation and Retrofitting, ICCRRR-2, 24–26 November 2008, Cape Town, South Africa, pp. 297–298, ISBN 978-0-415-46850-3

Christodoulou, C., Glass, G., Webb, J. 2009. Corrosion management of concrete structures, The Structural Engineer, Volume 87, 23/24, December 2009.

Christodoulou C., Glass G., Webb J., Austin S.A. Goodier C.I., A new approach for the patch repair of car parks using galvanic anodes, Concrete Solutions 2011: Grantham, M., Mechtcherine, V. and Schneck, U. (eds). Concrete Solutions 2011: Proceedings of the 4th nternational Conference on Concrete Repair 2011. London: CRC Press, ISBN 978-0-203-13468-9.

Christodoulou C., Goodier C.I., Austin S.A, Webb J., Glass G., Diagnosing the cause of incipient anodes in repaired reinforced concrete structures, Corrosion Science, 69 (2013), pp. 123–129 DOI information: 10.1016/j.corsci.2012.11.032

Christodoulou C, Goodier C, Austin S, Webb J, Glass G, A new arrangement of galvanic anodes for the repair of reinforced concrete structures, Construction and Building Materials, 50 (2014), pp. 300–307, DOI information: 10.1016/j.conbuildmat.2013.09.062

Concrete Society 2004, Technical Report 60, Electrochemical tests for reinforcement corrosion, Surrey, UK.

Concrete Society 2009, Repair of concrete structures with reference to BS EN 1504, Technical Report 69, Surrey, UK.

Concrete Society 2011, Technical Report 73, Cathodic Protection of Steel in Concrete, Surrey, UK.

Design Manual for Road and Bridges, Volume 3, Section 3, Part BA 35/1990 Inspection and Repair of Concrete Highway Structures, Departmental Standard, UK.

Dugarte M., Sagüés A.A., Galvanic point anodes for extending the service life of patched areas upon reinforced concrete bridge members, Contract No. BD544-09, Final Report to Florida Department of Transportation, Tampa, Florida, USA, September 2009.

Elsener B. 2001. Half-cell potential mapping to assess repair work on RC structures, Construction and Building Materials, 15, 133–139.

Elsener B. 2003, Half cell potential measurements–potential mapping on reinforced concrete structures, RILEM TC 154-EMC: electrochemical techniques for measuring metallic corrosion, Mater. Struct. 36, pp. 461–471.

Glass G., Christodoulou C., Holmes S.P., 2012, Protection of steel in concrete using galvanic and hybrid electrochemical treatments, IN: Alexander, M.G. et al. (eds.), Concrete Repair, Rehabilitation and Retrofitting III – Proceedings of the 3rd International Conference on Concrete Repair, Rehabilitation and Retrofitting, ICCRRR 2012, pp. 523–526, ISBN 978-0-415-89952-9.

Glass G.K., Davison N., Roberts A.C. 2010, Monitoring Method, UK Patent GB 2449039 B.

John G., Cottis B., Laboratory Testing and Computer Modelling of the Performance of Sacrificial Anodes for use in Reinforced Concrete Structures, Paper number 03302, Corrosion 2003, NACE International, Houston, USA.

Holmes S.P., Wilcox G.D., Robins P.J., Glass G.K., Roberts A.C., Responsive behaviour of galvanic anodes in concrete and the basis for its utilisation, Corrosion Science, 53 (2011), pp. 3450–3454.

NACE International Publication 01105, Item No. 24224, Sacrificial Cathodic protection of Reinforced Concrete Elements — A State-of-the-Art Report, Houston, USA, March 2005.

Concrete Solutions – Grantham et al. (Eds)
© 2014 Taylor & Francis Group, London, ISBN 978-1-138-02708-4

Anode performance: The use of ballasted mixed metal oxide coated titanium anodes in impressed current systems installed within historic steel frame masonry clad structures

Paul Chess
CP International, Denmark

Gina Crevello
Echem Consultants LLC, New York, USA

Paul Noyce
Axieom LLC, New York, USA

ABSTRACT: Corrosion damage in historic steel frame structures has a great physical and financial impact on the performance and treatment of the building façade. Minor cracking and displacement of masonry can eventually lead to spalling and loss of stones and, as seen in rare instances, the loss of life if large masonry units become dislodge and fall from great heights due to corroding steel supports.

Cathodic Protection is a corrosion mitigation technique, which minimizes stripping of the masonry while simultaneously protecting the steel from corroding. The core philosophy for the use of Impressed Current Cathodic Protection (ICCP) in historic buildings is to protect cultural heritage from the ravages of corrosion and the designer's scope is meant to follow conservation guidelines. This approach anticipates that no additional harm will be incurred by a building upon or after installation of a system. For this reason, the appropriate anode must be utilized within the parameters of the structure.

It is critical that electrochemical reactions be minimized at the surface of the masonry. The reaction can have dire consequences on historic masonry, not only deteriorating the mortar, but dissolving limestone or cast stone in the correct circumstances. The designers' role is to recommend the best anode system for the subject building.

The use of ballast anodes within these circumstances have led to better overall performance of ICCP Systems in Historic Steel Frame Structures. The paper will look at two case studies where different ballast anodes types were installed within historic steel frame structures, and discuss the benefits of the Ballast resistors.

1 BALLAST ANODE DESIGN

1.1 *History*

In 1985 in Denmark Impressed Current Cathodic Protection (ICCP) was starting to be used in limited areas for the protection of steel in concrete. It was apparent that the challenging aspect of the ICCP installation was the anode. The anode is the part of the ICCP system where the electrical current is introduced into the structure. At this time, most of the anode types were surface applied to the concrete. Anode types include conductive coatings and coated titanium meshes which were sprayed with gunite to encapsulate the anode.

Neither of these anodes was suitable for the particular problem of chloride induced corrosion exhibited in Denmark and the Nordic countries. Since the 1960s communal housing has been favoured with large apartment buildings being built for social housing. These apartments have a covered entrance on one side and an open balcony on the other side. The balconies are used as a fire escape. In a Danish winter, snow is common and deicing salts have been routinely applied to keep the balconies clear of ice and snow. By the 1980s there was clear evidence that the steel reinforcement in these balconies was actively corroding and the only cost effective method of preventing further damage was to employ the use of ICCP. The balconies were painted, so to apply a surface anode the coating would have to be removed and then a subsequent coating applied over the anode.

An obvious answer was to drill holes and install anodes within these holes. Experiments began to determine whether this was practical and which materials were required to do so effectively. The starting point for the primary anode was platinised titanium. This is where platinum metal is electroplated onto a titanium substrate. Titanium was chosen as a substrate as below a certain voltage its oxide film prevents it passing current. Effectively all the current output passes through the platinum which has a very low dissolution rate.

The next challenge was how to couple the anode to the original concrete. The obvious first choice was a repair mortar. This would hydraulically set and link the primary anode to the structure. The platinized titanium anodes were laboratory and field trial tested. The mortar was found to suffer acid damage at the high currents densities (800 mA per m^2 of anode surface area). These anodes were capable of passing high current at reasonable voltages in chloride contaminated concrete. Thus, graphite, which is an acid resistant material, ionically conductive, and available as a powder, was tested. It was found that there was zero loss of the graphite with the passage of the current. This was not a surprise as graphite anodes had been successfully used on many conventional ICCP installations and it was known that at high acidity the weight loss of graphite reduces. As it was difficult to dry pack a hole with the graphite, a stabilized graphite emulsion was made. The graphite paste was then put in 350 ml cartridges and dispensed with a skeleton gun.

1.2 *Anode field trials*

Through anode trials, it quickly became apparent that current distribution and output of the anodes varied significantly. The trials were installed at the precast beams supporting the balconies. Individual anodes were measured using a zero resistance ammeter across a small resistor (typically 1 ohm). While all anodes were all at the same distance to the reinforcement, output was very uneven. The outputs of the anodes varied significantly along the beam.

The reason for this appeared to be the penetration of the chloride ions into the concrete through shrinkage cracks. Because this was not a broad front, the resistance of the concrete electrolyte varied significantly. In an attempt to minimize this variation, higher value resistors were substituted for the small resistor and the outputs rechecked. It was found that by using resistors of 256 ohms or 512 ohms the current could be moderated in the low resistance pathways so a relatively even current spread could be obtained.

For these simple structures all monitoring was undertaken with an external half-cell where 'on' 'instant off' and 4 hours off were recorded on a grid of 500 mm centers. This showed the depolarization of the steel over a 4 hour period and allowed an optimization of the spacing of the anodes to provide adequate current with a minimum quantity of anodes.

Based on the success of the trials, the ballast arrangement anodes were produced in commercial quantities. They were exported to various countries with particular corrosion problems such as Australia and Japan.

As the system was used on an ever more diverse series of structures improvements were made:

- The platinum coating was substituted for a mixed metal oxide (MMO) coating. There were two reasons for this. Firstly electroplating platinum involved a lot of very hazardous chemicals so it became less popular whereas the MMO coating was spray applied and then baked. The MMO coating could also withstand changes in potential more easily.
- The graphite base was improved to give greater frost resistance
- The resistor was moved from a box which supplied each individual anode into the anode body itself. This meant the larger chains of anodes became economic with better aesthetics
- The couplant was changed from a graphite base to a cement base which hydraulically set. This meant that the anode current density had to be reduced so a new perforated tubular structure was substituted for the rod.
- The anode top was redesigned so that it could pierce the coated titanium feeder wire improving reliability and speed of installation
- A range of resistances are offered to allow customization of the current spread profiles of different anodes.

2 MARSHALL FIELD'S FLAGSHIP STORE

2.1 *History*

The Marshall Field's Flagship Store, located on South State Street, is probably the most important store in downtown Chicago and a cornerstone of the city.

Figure 1. Marshall Field's Flagship Store Terra Cotta Columns at the 11th and 12th floor. Authors Photograph.

Marshall Field's is one of the world's first department stores and has an international reputation for quality. The building was designed by Daniel Burnham, a renowned Chicago architect and city planner responsible for the plan of the 1893 World's Columbian Exposition. This neo-classical building is a tribute to the prominence and wealth of Chicago at the end of the 19th Century. Marshall Field spared no luxury during the construction of his flagship store. It was the first building ever to have a Tiffany Favrile glass mosaic ceiling.

The first building was erected in 1893, with further additions beginning in 1907. As the company expanded, the structure grew through the 1920s to its current configuration.

The importance of the Marshall Field's building is demonstrated by the fact that Selfridge's Department Store on Oxford Street, London (recognized as the UK's first true steel framed building) which also now has ICCP, was a copy of the Marshall Field's Store and designed by Burnham. Marshall Field's Flagship Store is the first American historic building to have an Impressed Current Cathodic Protection system installed.

2.2 *Original construction*

The Marshall Field's Department Store is comprised of a semi-rigid structural steel skeleton frame encased in granite up to the third floor and white glazed terracotta to the remaining ten stories.

The form of construction is typical of the period with the terracotta bonded to the steel frame with a mortar or brick in-fill. The white terracotta blocks are individually tied back to the infill material using ¼ inch (6 mm) square section anchor bars approximately 6 inches in length. The anchors are located in preformed holes in the terracotta blocks at the corner of each block.

The eleventh and twelfth floors of the building are recessed approximately 6 feet (180 cm) from the main facade, expressing the structural- steel building columns. The terra-cotta facades on the northeast quadrant of the building have 23 two-story-tall, fluted terra-cotta-clad columns, which are partially engaged into the wall behind. The terra-cotta cladding at these columns was observed to be extensively cracked and spalled. Years of water infiltration had caused corrosion of the underlying steel columns and lateral anchors (Kelley 2013).

The expansive forces generated by the corrosion process were causing deterioration of the terracotta units in the form of cracking and spalling, representing on-going maintenance and safety issues for the building owner.

2.3 *Feasibility trial*

The authors were commissioned by Wiss Janney Elstner Associates, Inc. (WJE) on behalf of the Target Corporation to conduct the ICCP feasibility trial of the fluted terracotta columns spanning the 11th and 12th floor of the North Wabash building constructed circa 1914. The aim of the feasibility trial was to examine the possibility of installing the ICCP system which would prevent continued corrosion of embedded structural steel stanchions and associated steel/iron masonry anchors. In the trials, the following critical issues were addressed:

- Method of construction and presence of voids in the in-fill masonry
- Corrosion rates for the steelwork
- pH and chloride levels of the infill mortar in contact with the steel frame
- Conductivity of the masonry
- Level of continuity in the steel frame and associated masonry anchors
- Anode Current Distribution
- Level of difficulty in establishing electrical continuity with electrically discontinuous metal components
- Ease of polarizing the steel with a Cathodic current indicating the suitability of ICCP techniques
- Ability to train local masonry workforce in the application of ICCP

Owing to the success of the trial, it was concluded that an ICCP system could be developed as a terracotta conservation technique. The application of the ICCP would control corrosion and allow in-situ stabilization of deteriorated terracotta. In addition to the conservation benefits of this approach, the costs were significantly lower – saving approximately 50% in comparison to repairs involving widespread terracotta removal and replacement.

2.4 *ICCP design*

Owing to the success of the feasibility investigations, commercial viability and conservation benefits, the authors were commissioned to design a full scale ICCP system to protect the fluted columns between at the 11th and 12th floors. In addition, supervision of both local masonry and electrical contractors was to be provided.

The design consisted of small ½″ (12.5 mm) diameter × 4″ (10 cm) long inert ballast anode electrodes installed into the 3/8″ (ca. 10 mm) mortar joints. The anode was encapsulated with the graphite paste. These anodes were interconnected by a small 16AWG insulated titanium wire buried in the mortar. A monitoring sensor was installed in each column and individual connections to each of the terracotta anchors were made to ensure their protection by the ICCP system.

The monitoring system and anodes were wired back to an intelligent power supply allowing the engineers a presentation of the data in real time CAD layouts on the embedded computer screen on the Main Control Unit. The system utilized touch screen computer technology allowing the user to access and understand

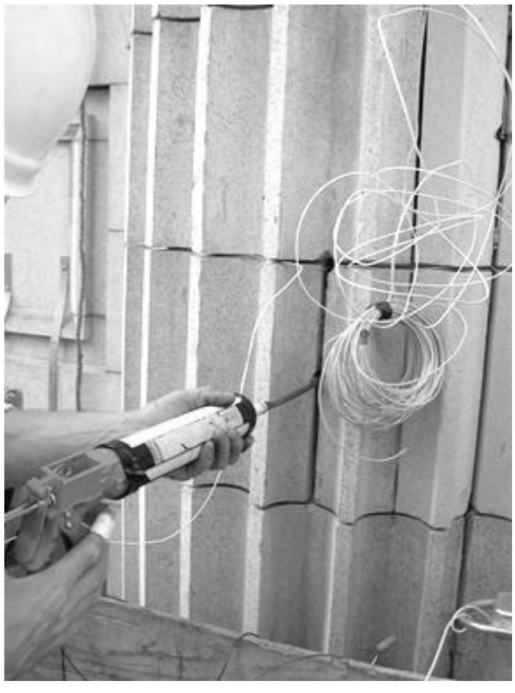

Figure 2. Anode Installation at a Pilaster Column. Author's Photograph.

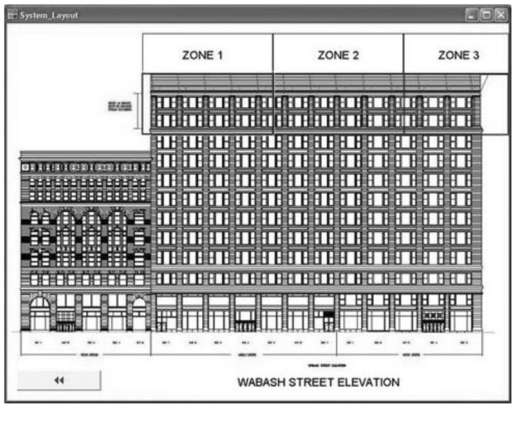

Figure 3. Screen Shot of Main Control Unit and Monitoring System.

the ICCP system layout simply by touching menus and drawings/images on the PC screen.

2.5 *Monitoring*

The most recent inspection in December 2010 was carried out to determine if the system was still operating within design limits as no physical inspection had been carried out since 2007.

The Main Control Unit (MCU) is placed on the 13th floor and the system is designed with remote access via a modem and dedicated phone line which is currently out of service.

The MCU was accessed, power was evident and the system was operational. Manual measurements of voltages were taken with a standard Fluke multimeter as all zones were receiving current. Reference cells readings were taken and verified against the main control unit display. All of these readings were accurate and within a few millivolts of the MCU.

All of this information reflected that the system was running and affording some level of protection to the embedded steel in each zone.To establish overall operation of the system a four hour depolarization test was setup to establish depolarization values. Prior to starting this test the following operational levels of each zone were recorded as follows:

- Zone 1 – 3 V 25 mA (7% Operating Criteria)
- Zone 2 – 6.28 V 34 mA (8% Operating Criteria)
- Zone 3 – 6.74 V 270 mA (47% Operating Criteria)
- Zone 4 – 4.16 V 200 mA (29% Operating Criteria)

Table 1 shows a summary of the instant off and decay values from the depolarization test carried out. NOTE: All Potentials are with respect to Ag/AgCl reference electrodes:

Table 1. Marshal Field's ICCP Polarization Decay.

Reference	Instant Off (mV)	Polarization Decay (mV)
Zone 1		
R1Z1	−569	329
R2Z1	−632	400
R3Z1	−720	479
R4Z1	−654	422
R5Z1	−587	352
Zone 2		
R1Z2	−612	311
R2Z2	−584	315
R3Z2	−496	258
R4Z2	−308	7
R5Z2	−280	10
Zone 3		
R1Z3	−259	9
R2Z3	−160	15
R3Z3	−192	22
R4Z3	−274	55
Zone 4		
R1Z4	−379	23
R2Z4	−363	3
R3Z4	−482	349
R4Z4	−625	483
R5Z4	−574	438
R6Z4	−563	437
R7Z4	−412	191
R8Z4	−297	101
R9Z4	−586	434
R10Z4	−469	331

In summary after the system had been commissioned in August 2004 with little to no maintenance and as of December 2010 all zones were operating within acceptable levels in accordance with international standards. The following was concluded from the inspection:

- No Anode Zone had voltage limited (8 V).
- All reference electrodes were functioning
- In the majority of cases 100 mV criteria was met.
- All Power supplies were operational.

2.6 *Summary*

Our conclusion of the system was that the ballast anode system had performed extremely well and was providing adequate levels of cathodic protection to this iconic structure.

In addition with the design of the ballast anode multiple pilaster columns were able to be installed to the same power source reducing overall power supply cost. This makes the overall system cost lower without affecting performance.

By using the ballast anode approach the concern for long term anode durability is reduced as excessive current dumping will not exist. This is particularly important when dealing with historic building where the materials are of historical significance, and can be adversely affected by acidification. The ballast anode is critical in controlling this reaction

3 CALHOUN COLLEGE

3.1 *History*

Calhoun College, Yale University is a dormitory for the students of the Yale University. Yale College was transformed, beginning in the early 1930s, by the establishment of residential colleges. Taking medieval English universities such as Oxford and Cambridge as its model the campus looks strikingly familiar to the traditional Universities. Modeling the buildings in the popular collegiate gothic style of the early 20th century, each college is extremely detailed and ornate.

Each building surrounds a courtyard and occupies up to a full city block, and each has its own dining hall, library, seminar rooms, recreation lounges, and other facilities.

Calhoun College was one such building constructed during this building campaign of the 1930s, and dates to 1931 through 1933.

3.2 *Original construction*

The building is between three and seven stories in height with towers at the southeast and northwest corners. The building has a total of eight elevations with the internal courtyard,. The construction is typical steel frame construction, with brick masonry infill and various cladding materials. Limestone, sandstone

Figure 4. Construction of Calhoun College. Ca. 1931.

and granite clad the exterior walls while the courtyard primarily utilizes brick as a cladding material.

The embedded structural steel is coated in red oxide shot coat which was a factory applied coating. The lead oxide coatings are a common method to inhibit corrosion during transportation to aconstruction site and during construction. Once embedded in mortar, which is a highly alkaline environment, the lead oxide coatings are ineffective in protecting the steel against corrosion. The steel beams and columns were partially covered with a bituminous asphalt flashing at critical locations throughout the structure.

3.3 *Conditions found*

During the initial investigation it was found that a number of areas, primarily the gables and higher level spandrel beams and columns were suffering severely from the effects of corrosion. The steel within these areas are typically the first to exhibit the signs of corrosion based on location, exposure to the elements, and water infiltration from the roof level.

The root cause of the corrosion was found to be caused by carbonation. The existence of a carbonated front allowed the steel frame to corrode in the presence of oxygen and moisture exist. Although corrosion caused by carbonation is not usually as structurally damaging as chloride induced corrosion, it can have a major impact to the cost of restoration due to the damage imparted upon the masonry. Areas exhibiting the highest corrosion on the building had caused the displacement of the masonry in areas of up to ½ inch (12 mm) at gable ends, and up to 1″ (25 mm) in locations of previous repairs and subsequent macrocell corrosion. The amount of cracking and displacement was directly attributable to and in relation to the amount of accumulated corrosion scale.

Corrosion was also evident in other areas of the building as exhibited by opening of the mortar joints in areas of recent repointing and hairline cracking of the masonry. In these areas, the small cracks had allowed oxygen and moisture to enter the system, fueling the corrosion process.

Figure 5. Gable end where parallels cracking coincides with the embedded steel beam flanges.

3.4 *Condition assessment*

The Corrosion Rate and Corrosion Potentials carried out allowed the engineers to confirm that;

- Corrosion was present
- Corrosion was active, and
- Corrosion was causing distress to the masonry.

In the original report to the client (Leavitt, 2008) it was concluded that ICCP would provide a long term solution for the corrosion issues (Crevello and Noyce, 2007). The report also identified that corrosion would continue to cause distress to the masonry with expected damage within 5–20 years in the majority of the areas tested. The electrochemical testing showed there was corrosion occurring on the structure with high steel potentials and corrosion rates. Temperature and humidity monitoring also showed an environment conducive to corrosion activity.

As part of the assessment, the structures' corrosion condition was divided into four (4) stages of corrosion related deterioration, as example, activity versus damage. The lower floors of Calhoun College fall into the early portions of Stage 3, while the upper levels, parapets, copings, and balconies, fall in the later portions of Stage 3. It can be seen in Fig. 8 that corrosion damage begins to act exponentially in the later portions of Stage 3 and Stage 4. By Stage 4, the damage to the masonry cladding require removal to clean and treat the steel rather than the option of electrochemical repair.

The construction details of the building demonstrated it was a prime candidate for ICCP. Limit anode choices were possible due to the complex nature of the varying materials, the vast differences of steel sizes within the same anode zones, and the distribution of the steel elements that were designated for ICCP.

Figure 6. Gable end detail. Note corrosion scale within web and cracking stemming from flange.

Table 2. Deterioration Models.

	Time to Reach Cracking Years	Time to Reach 1/8″ Section Loss
Location 1	3.91	5.25
Location 2	5.95	7.99
Location 3	26.10	35.06
Location 4	14.98	20.13
Location 5	17.21	23.13
Location 6	11.08	14.89

3.5 *ICCP Trial and Design*

Prior to design it is always necessary to carry out an ICCP feasibility trial to historic buildings. This allows the engineers to validate if the system is going to be capable of providing long term corrosion mitigation. At Calhoun this trial was carried out at three different locations allowing the engineers to determine anode location, current density and installation procedures in different cladding materials. Each of the following materials: Granite, Sandstone, and Brick were tested for suitability, feasibility, and efficacy. Each location had a trial size of approximately 6 linear feet (180 cm), this equated to 12–15 feet (3.6–4.5 m) of joint removal and replacement.

Work for the trial began on March 10, 2008 and was completed by March 15, 2008. All areas tested were deemed feasible for ICCP subject to the use of a ballast anode. The ballast anode enabled the designers to have larger areas of anodes without affecting current distribution. It was found within the trial that the varying conditions provided different challenges most of all the varying resistivities of the different masonry which were in the same potential anode zone.

With the MMO ballast anode design the power supply requirements could be minimized and larger areas grouped together would form the basis of the design.

The final design for Calhoun ended up at thirty five (35) zones with 140 Ag/AgCl reference electrodes

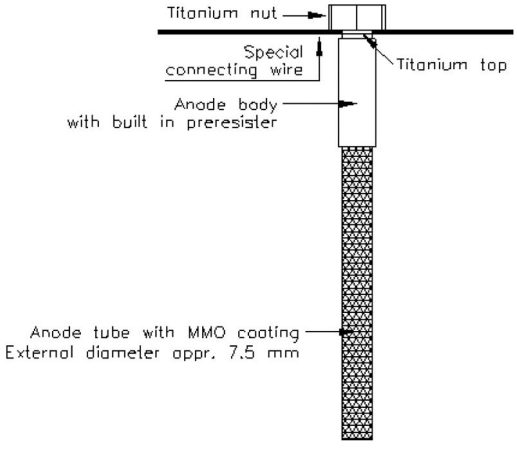

Figure 7. Anode Design.

Table 3. Anode performance.

Anode 30 Day Performance	Output per Anode mA
Maximum	0.405
Minimum	0.040
Average	0.306
Standard Deviation	0.117

for monitoring current distribution and performance around the building. This was a significantly lower quantity of power supplies due to the use of the ballast anode.

Four thousand one hundred and sixty one (4,161) MMO anodes were finally installed around the building protecting over 6,000 linear feet (1.8 km) of steel.

3.6 *Monitoring*

The system was energized in December 2009 and the following table shows typical anode performance at startup of the system.

The above data indicated that the maximum current density on the anode surface was 57.3 mA/m^2 almost half of the operating current density (108 mA/m^2) for a 40 year life conventional concrete. The average current density was 43.3 mA/m^2.

During the most recent monitoring visit in May 2013 the anode voltages and operating current densities remained stable after almost 3 ½ years in service. All anode zones met the 100 mV criteria and the system was operating within the design parameters.

The anode outputs had been reduced from startup as follows:

Although the maximum anode current density had not changed there had been a reduction in the overall average current density which had dropped to 24.8 mA/m^2.

Table 4. Anode Performance 3 ½ years in service.

Anode 3 ½ Year Performance	Output per Anode mA
Maximum	0.405
Minimum	0.006
Average	0.175
Standard Deviation	0.121

Figure 8. Anode Layout, Zone 2. College Street Elevation.

Figure 7 shows a typical anode layout for one zone at the main entrance of the building. All major steel members with less than 10 inches (25 cm) masonry cover were protected with ICCP at the top two floors of the entire building. Critical ancillary steel was also treated. As can be noted within the photograph below, the construction, cladding, stone assemblies and steel configuration were complex.

3.7 *Summary*

The ballast anode design has performed remarkably well considering all of the variations of masonry, levels of corrosion, and internal wall conditions at this historic building.

When challenged with such complexity the ballast anode allows the design to operate without issues deriving from current distribution. This ensures that all areas required to receive cathodic protection are adequately protected.

It can be seen after almost 3 ½ years in service that the anode performs very consistently to that of the original graphite based anode design.

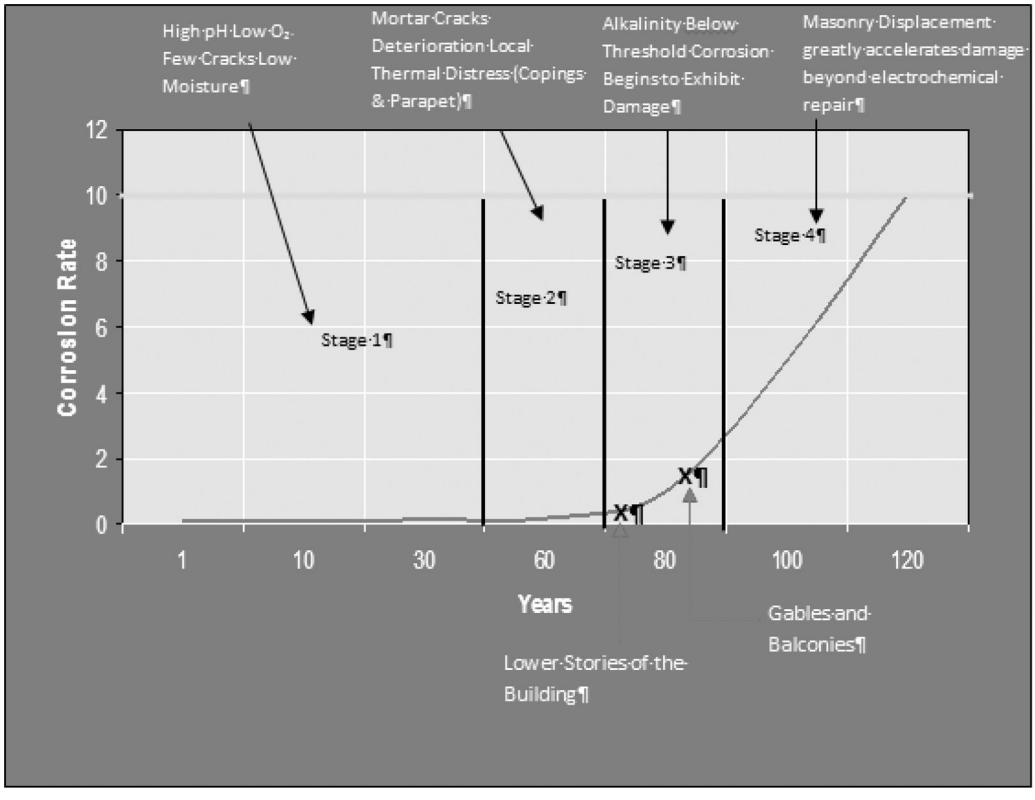

Figure 9. Calhoun College–Corrosion map.

4 CONCLUSIONS

In conclusion, it has been determined that finite control of current density is desired in many applications for ICCP. For historic masonry clad buildings, this level of control for current output an even current distribution must be maintained. Where finite control is not available, there may be a risk not only to the mortar, but the historic masonry itself.

The ballast anode design which was developed to minimize uncontrolled current output has been successfully utilized on numerous historic buildings. Case studies dating back 10 years have provided consistent data on the performance and use of the anode. In the two case studies examined, both systems were functioning well below the design current density and providing protection to the embedded steel.

With this finite control, the designer can utilize the anodes with confidence that the historic steel frame will be protected, further limiting damage to the masonry from corrosion, and that there will be no adverse effects to the mortar or masonry itself from acidification.

REFERENCES

Crevello, G. and P. Noyce. "Corrosion Evaluation for Residential Hall at Yale. Professional Report." Electro Tech CP. November 2007.

Crevello, G. and P. Noyce. 2007. "Corrosion Evaluation for Residential Hall at Yale. Professional Report." Electro Tech CP.

Crevello G. and P. Noyce. 2008. Trial Data collected in March 2008.

Kelley, Stephen. 2013. The Potential for Application of Cathodic Protection in Masonry-Clad, Steel-Frame Buildings. *APT Bulletin*. Vol. 43. No. 4: pp. 36–37.

Leavitt, J.K. 2008. Embedded Steel Condition Assessment, Residential Hall, Yale University." Professional Report Issued to Client.

Pridmore, J. 2002. *Marshall Field's*. Rohnert Park California: Pomegranite.

Concrete Solutions – Grantham et al. (Eds)
© 2014 Taylor & Francis Group, London, ISBN 978-1-138-02708-4

Cathodic protection of steel in concrete – experiences on parking garages in Germany

Hernani Esteves, Sebastian Mayer & Ronny Stöcklein
Ed. Züblin AG, Stuttgart, Germany

ABSTRACT: In the last 12 years, ICCP on concrete structures became a steadily growing market in Germany, in particular in the private sector for car parks. Many of these structures are at least 25 years old, a great number of them with little or without any maintenance at all. Consequently, leaking joints and defective surface protection systems lead to permanent water penetration into the concrete. During winter time, the water brought in by frequent traffic is loaded with de-icing salt which very often results in severe corrosion on floors, column and wall bases and joints. Within the last 4 years, Züblin has executed more than 20 repairs on car parks applying ICCP. When the construction works were finalized, all ICCP systems were switched on and since then protect the structures from any further corrosion damage. Maintenance according to EN 12696 is secured by Züblin's service contracts, tailor-made for each project.

1 INTRODUCTION

Companies dealing with concrete repair in Germany today are confronted with high expectations of clients and engineers with regard to quality and speed, the same to durability and sustainability. Last but not least, repair work shall be low in costs. With Rili-SIB there is a German guideline for repair work on concrete with a clear bundle of concepts given to engineers and executives how repair has to be executed. Rili-SIB is in line with EN 1504, but describes the principles of repair more deeply and near practise. In the latest version of Rili-SIB, a major focus is set on durability of repair solutions.

One technique in Rili-SIB is described as principle "K" (K stands for cathodic protection, called CP) presenting repair of reinforced concrete with cathodic protection. In Europe, CP on concrete is specified with reference to the standard EN 12696: 2012–05. In recent years, CP became more and more attractive as a speedy, smart and – in many cases – economically attractive solution when it comes to repair work on concrete structures suffering from corrosion-initiated damages.

This paper presents several projects in which CP was chosen to be the best way to face the problem of corrosion on weakening concrete structures. Even though we do not focus on formal demands in this paper too much, it is necessary to mention that all products involved in CP such as mortar, spray concrete, sensors, anodes etc. must be tested by independent institutes specialised in CP. For instance, on cement based mortars to embed titanium anodes, the electrolyte resistivity in certain conditions, the current distribution, the alkaline buffer capacity and other parameters have to be detected and evaluated. Moreover, all single products must be set up in a laboratory CP demonstration to prove the performance in a full-scale system set-up. All this ends in a system report by the institute mentioned above, stating the product to be suitable for CP or not, if necessary with certain restrictions for individual cases.

According to Rili-SIB today, all CP installations in Germany must pass a so called "Zustimmung im Einzelfall" (Individual case by case agreement) of the federal state in which the project is located. Normally, the agreement is given if all requirements mentioned above are fulfilled and proven.

2 RESULTS AND EXPERIENCES

2.1 *Multi-story parking "Am Ludwigsplatz" in DARMSTADT*

The multi-story parking "Am Ludwigsplatz" in Darmstadt is a car park with eight floors in the city centre of Darmstadt, a 150,000 citizen town in the Southwest area of Germany. The parking is half-split with four floors an each side, vertically offset by half a story, which makes 8 floors in total. The floors are connected by separate access and exit ramps. The ICCP system protects an area of more than 7,500 square metres, covering all floors, wall and column bases and some selected beams and horizontal members. Some of the columns contain pre-stressed elements. Due to the special demands to pre-stressed steel in

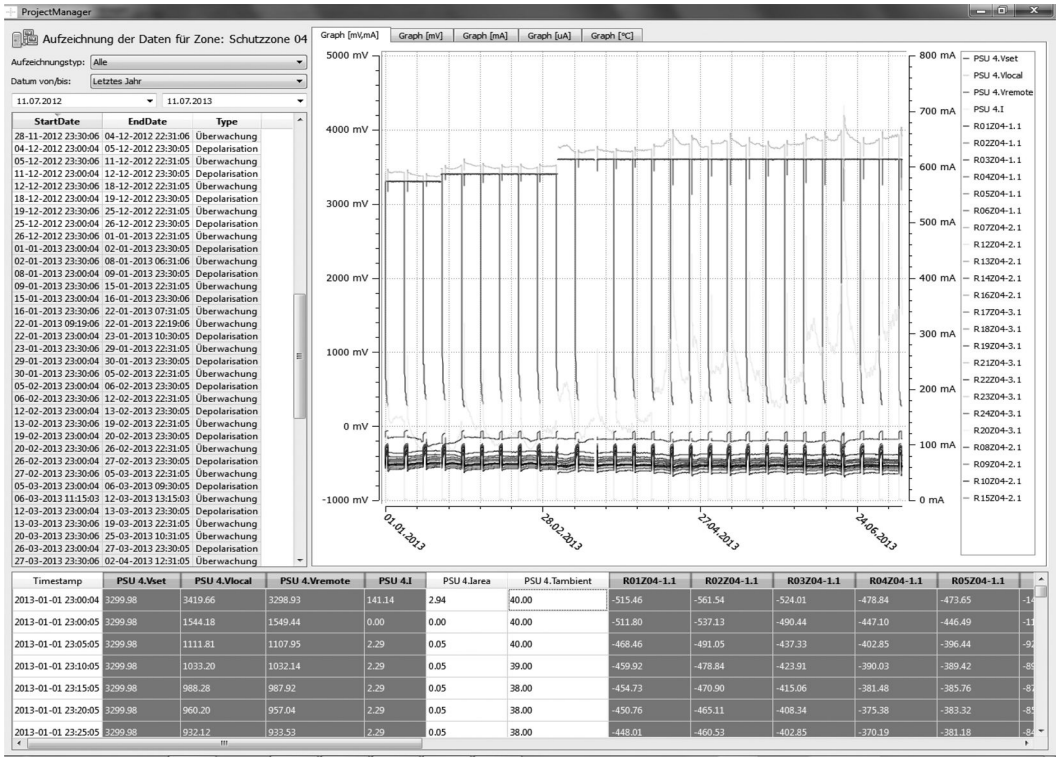

StartDate	EndDate	Type
28-11-2012 23:30:06	04-12-2012 22:31:06	Überwachung
04-12-2012 23:00:04	05-12-2012 23:30:05	Depolarisation
05-12-2012 23:30:06	11-12-2012 22:31:05	Überwachung
11-12-2012 23:00:04	12-12-2012 23:30:05	Depolarisation
12-12-2012 23:30:06	18-12-2012 22:31:05	Überwachung
18-12-2012 23:00:04	19-12-2012 23:30:05	Depolarisation
19-12-2012 23:30:06	25-12-2012 22:31:05	Überwachung
25-12-2012 23:00:04	26-12-2012 23:30:05	Depolarisation
26-12-2012 23:30:06	01-01-2013 22:31:05	Überwachung
01-01-2013 23:00:04	02-01-2013 23:30:05	Depolarisation
02-01-2013 23:30:06	08-01-2013 06:31:06	Überwachung
08-01-2013 23:00:04	09-01-2013 23:30:05	Depolarisation
09-01-2013 23:30:06	15-01-2013 22:31:05	Überwachung
15-01-2013 23:00:04	16-01-2013 23:30:06	Depolarisation
16-01-2013 23:30:06	22-01-2013 07:31:05	Überwachung
22-01-2013 09:19:06	22-01-2013 22:19:06	Überwachung
22-01-2013 23:00:04	23-01-2013 10:30:05	Depolarisation
23-01-2013 23:30:06	29-01-2013 22:31:05	Überwachung
29-01-2013 23:00:04	30-01-2013 23:30:05	Depolarisation
30-01-2013 23:30:06	05-02-2013 22:31:05	Überwachung
05-02-2013 23:00:04	06-02-2013 23:30:05	Depolarisation
06-02-2013 23:30:06	12-02-2013 22:31:05	Überwachung
12-02-2013 23:00:04	13-02-2013 23:30:05	Depolarisation
13-02-2013 23:30:06	19-02-2013 22:31:05	Überwachung
19-02-2013 23:00:04	20-02-2013 23:30:05	Depolarisation
20-02-2013 23:30:06	26-02-2013 22:31:05	Überwachung
26-02-2013 23:00:04	27-02-2013 23:30:05	Depolarisation
27-02-2013 23:30:06	05-03-2013 22:31:05	Überwachung
05-03-2013 23:00:04	06-03-2013 09:30:05	Depolarisation
06-03-2013 11:15:03	12-03-2013 13:15:03	Überwachung
12-03-2013 23:00:04	13-03-2013 23:30:05	Depolarisation
13-03-2013 23:30:06	19-03-2013 22:31:05	Überwachung
20-03-2013 23:30:06	25-03-2013 10:31:05	Überwachung
26-03-2013 23:00:04	27-03-2013 23:30:05	Depolarisation
27-03-2013 23:30:06	02-04-2013 12:31:05	Überwachung

Timestamp	PSU 4.Vset	PSU 4.Vlocal	PSU 4.Vremote	PSU 4.I	PSU 4.Iarea	PSU 4.Tambient	R01Z04-1.1	R02Z04-1.1	R03Z04-1.1	R04Z04-1.1	R05Z04-1.1
2013-01-01 23:00:04	3299.98	3419.66	3298.93	141.14	2.94	40.00	-515.46	-561.54	-524.01	-478.84	-473.65
2013-01-01 23:00:05	3299.98	1544.18	1549.44	0.00	0.00	40.00	-511.80	-537.13	-490.44	-447.10	-446.49
2013-01-01 23:05:05	3299.98	1111.81	1107.95	2.29	0.05	40.00	-468.46	-491.05	-437.33	-402.85	-396.44
2013-01-01 23:10:05	3299.98	1033.20	1032.14	2.29	0.05	39.00	-459.92	-478.84	-423.91	-390.03	-389.42
2013-01-01 23:15:05	3299.98	988.28	987.92	2.29	0.05	38.00	-454.73	-470.90	-415.06	-381.48	-385.76
2013-01-01 23:20:05	3299.98	960.20	957.04	2.29	0.05	38.00	-450.76	-465.11	-408.34	-375.38	-383.32
2013-01-01 23:25:05	3299.98	932.12	933.53	2.29	0.05	38.00	-448.01	-460.53	-402.85	-370.19	-381.18

Figure 1. Monitoring mask parking Darmstadt, zone 04.

a cathodic protection installation[1], all columns containing pre-stressed steel where gathered in one protection zone, named zone number four. In Darmstadt, only solid manganese-dioxide electrodes (Mn/MnO_2) where used for permanent monitoring due to the stabile and robust characteristics of that type of electrode. Since the potential of a Mn/MnO_2 electrode vs. NHE is 180 mV more positive than Ag/AgCl/ 0.5 M KCl vs. NHE, the system alarm for minimum instant-off potential of each electrode in protection zone four was set to −1,080 mV.

In June 2011, the ICCP system was started-up and since then kept in constant operation mode. For almost two years, approximately 200 permanent reference electrodes, managed with a digital data system, are the basis to evaluate system performance and effectiveness of the ICCP.

At the same time, the data management system comes with a remote control function that enables the engineer to change settings and update project information by wire.

[1] The instant-off potential of pre-stressed steel in concrete shall never be <−900 mV vs. Ag/AgCl/0.5 M KCl according to EN 12696: 2012–05, chapter 8.6, in order to avoid hydrogen evolution and steel embrittlement.

2.2 *Underground parking "Amerikahaus" in BIELEFELD*

The underground parking "Amerikahaus" is a two story garage constructed in 1996 and consists of two separate parking units. One unit is the so called northern part with an area of 5.000 sqm each story. Further, there is a southern unit named "Neumarkt" which makes another 3.300 sqm each story.

Due to the detected degree of damage and deterioration, only the northern part of the parking was equipped with a cathodic protection system on the floor and the wall sockets in the first subfloor. The repair works came along with general concrete repair and a new coating system. Beyond this, one part of the former parking area was separated in order to become a new archive for documents of literature.

For the planning and layout of the cathodic protection system, not only the structural parameters like the level of reinforcement in different structure elements, relative humidity, concrete quality and damage form a platform to start from. Also the future use (and change of use) is an essential factor when setting up a system. As there were specific requirements for protection against fire in the future archive, all cabling, cable channels and cable boxes had to be executed to a fire safe standard.

Finally, the cathodic protection system in the underground parking Amerikahaus came with seven zones

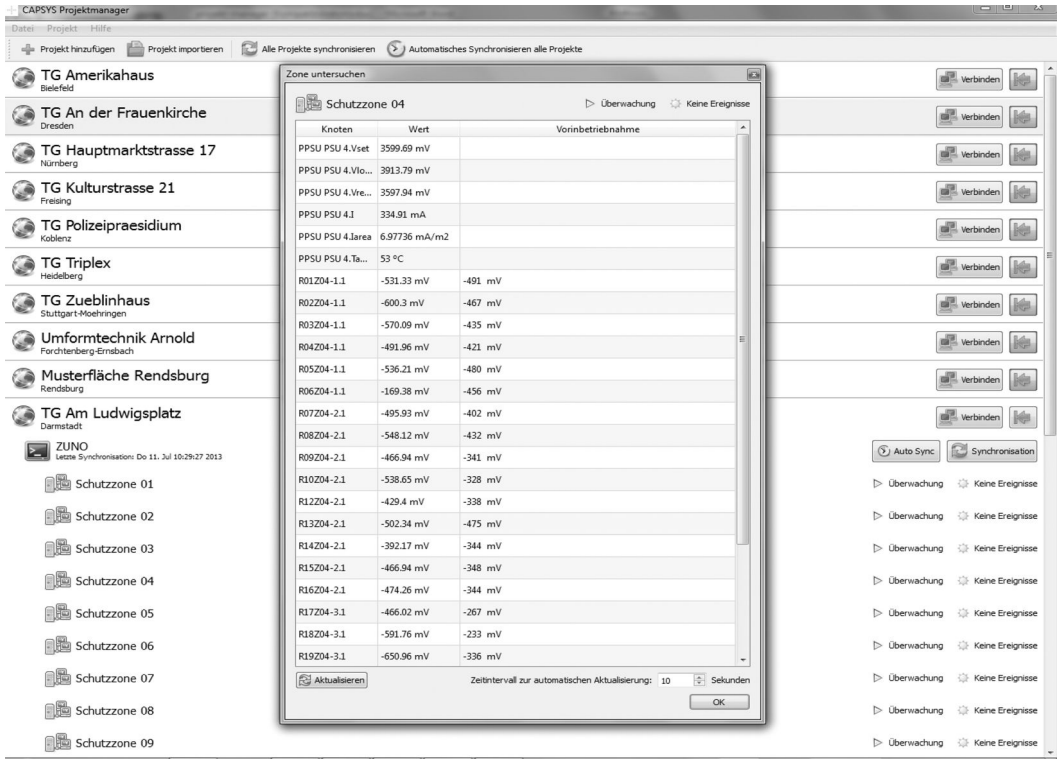

Figure 2. Live data parking Darmstadt, zone 04.

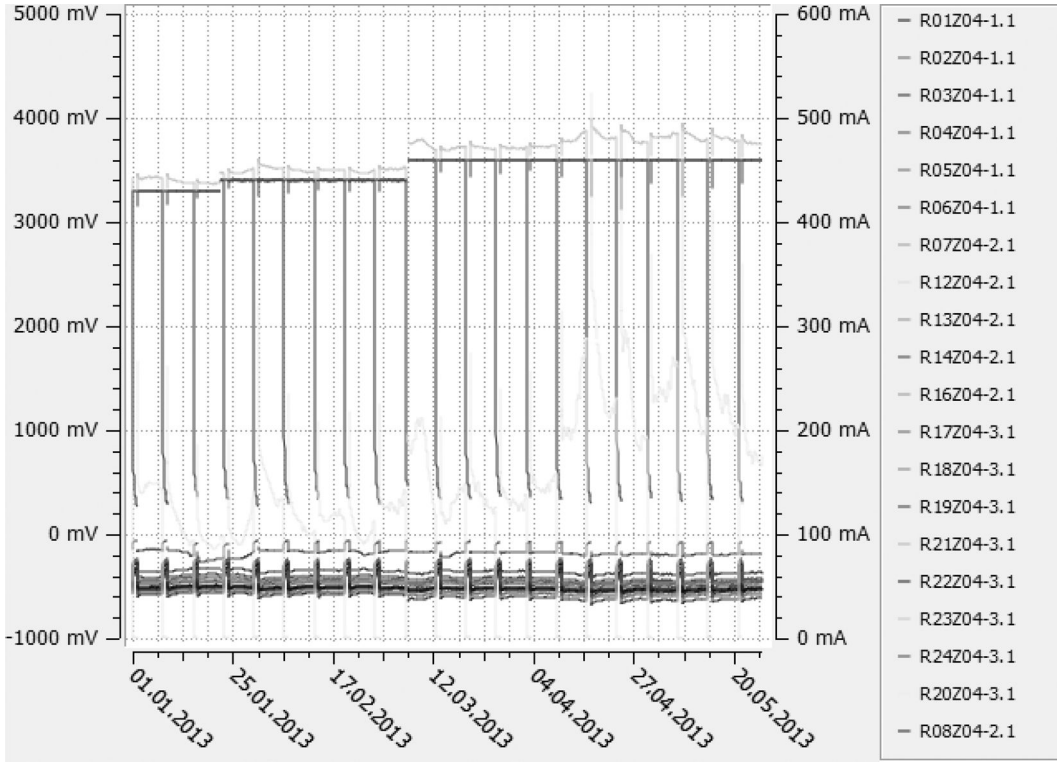

Figure 3. Data of parking Darmstadt, zone 04, five month period.

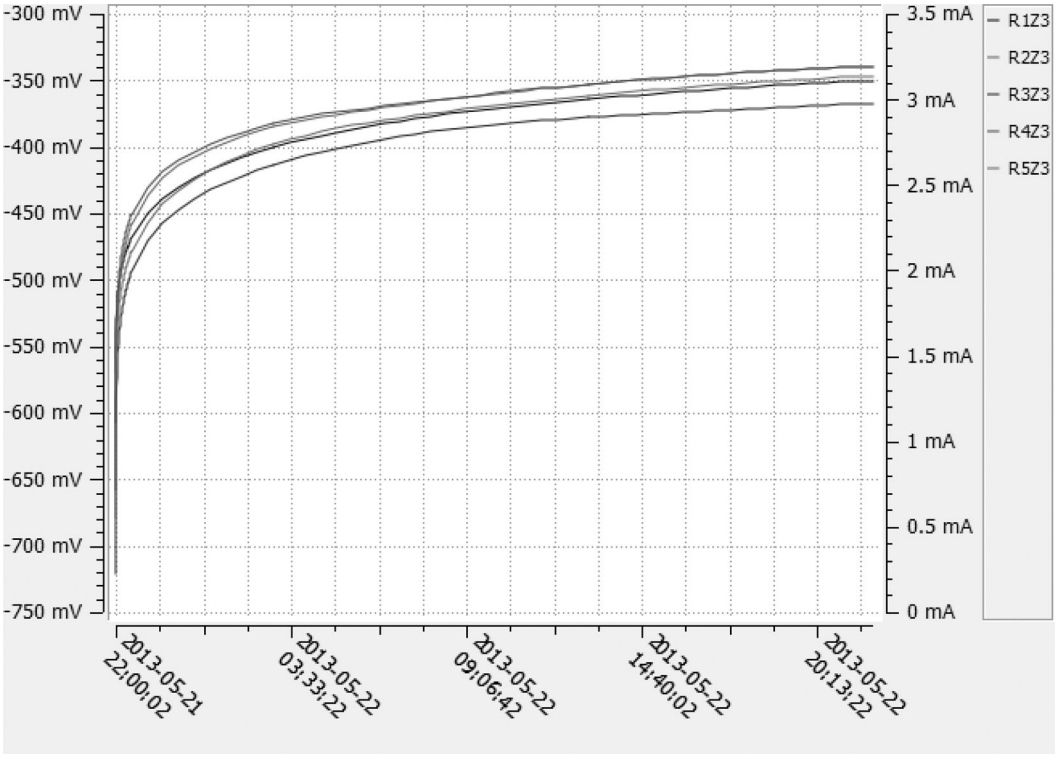

Figure 4. 24 h depolarisation zone 03 (floor).

on the floor and three zones on the wall sockets up to 50 cm above floor level. The design of all zones was based on MMO coated titanium ribbon mesh anodes. For the floor, polymer cement concrete (PCC) was used as an overlay to cast in the anode on top of the existing slab. On the wall sockets, the anode and cabling was covered with a layer of spray polymer cement concrete (SPCC). Both the PCC and SPCC must fulfil specific requirements according to EN 12696 for cementitious overlay on ICCP.

As there were different densities of reinforcement in the slab in areas above columns and the fields in between, the ribbon mesh anodes were placed with closer distances above the columns and greater spacing in the fields. That way, different current capacities were available even in one and the same zone. According to the specifications, the target was to create a system capable of supplying 20 mA/m^2 of steel in the parking area and 15 mA/m^2 of steel in the future archive facilities.

In May 2011, the ICCP system was switched on and has been constantly operating since that time; monitored and controlled by telephone landline.

2.3 *Underground parking "An der Frauenkirche" in DRESDEN*

The two-story underground parking "An der Frauenkirche" is located in the city centre of Dresden, just below the market square and only a two minutes walk away from the tourist attraction Frauenkirche, a church with cupola and tower which was destroyed in the Second World War and reassembled using 3D-computer modelling.

During pre-investigations undertaken in 2009, the engineers in charge detected that there was no seal on top of the top slab of the parking garage. In the consequence, there was a constant water penetration from the paved market square through the soil down to the top side of the cover of the garage. Moreover, de-icing salt washed into the soil lead to drastically increased chloride contents in the upper part of the top slab's cross section.

Based on the global condition of the underground parking, the engineers in charge suggested ICCP to be applied on the floors of the first and second story, on the ramps as well as on the ceiling of the first story. On the floors, ICCP was set up with a MMO coated titanium mesh. At the ramps, tubular anode rods were installed form the underside of the ramps. The same type of anode was chosen to set up cathodic protection for the chloride contaminated cover of the garage.

One highlight of the ICCP at the ceiling was a specially tailored rod which only provides current to the upper cross section of the top slab since corrosion is likely on the top side due to penetrating water and salt. In a standard situation, the market square would have been closed and the cover of the garage would have been covered with a sealer. With ICCP, no repair works were undertaken on top – instead of working

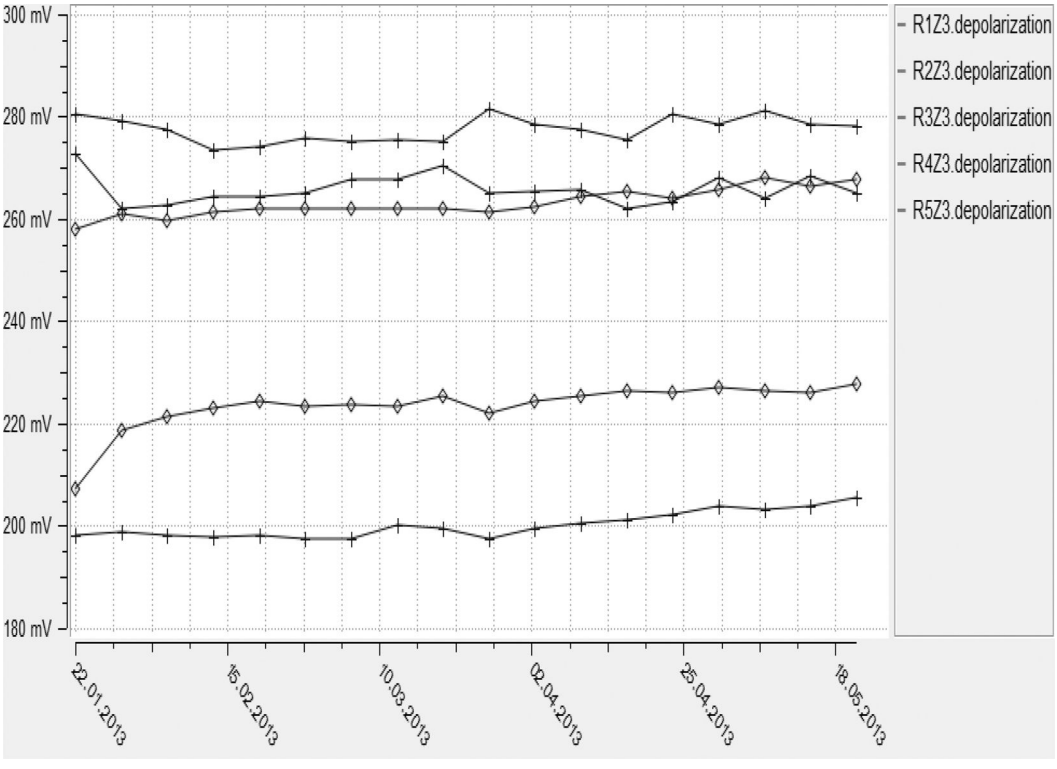

Figure 5. 24 h depolarisation trend line zone 03 (floor).

on the market square, the anode rods were mounted in drill holes from the underside. Since May 2010, when the system was energized, an effective technology for corrosion protection has been operating successfully, steadily track-recorded by data monitoring, with remote control and system performance tests according to EN 12696.

2.4 *Underground parking "Am Hauptmarkt" in NUREMBERG*

The underground parking "Am Hauptmarkt" in Nuremberg belongs to a five story building just above the garage, a building located in the inner city centre of the Bavarian metropolis Nuremberg.

The parking comprises 4 levels which are all linked together by ramps, traffic spinning up and down in a circle around the inner core. The two ground floors 3 and 4 are set on different levels with half a story in height difference. Floor level 2 is just above level 4, level 1 above level 3. Both entry and exit of cars to and from the parking are possible by a straight ramp.

ICCP was realized with five zones. Zone 1 consists of floor 1 and floor 3, zone 2 of floor 2 und floor 4. All wall sockets in the garage made of reinforced concrete are collected in zone 3. In zone 4, all circular column sockets in the garage are gathered. Finally, as one highlight of the system, zone 5 is a stripe of floor on level 1 und 2 which is designed stronger with the target to protect both the upper and lower reinforcement layer in the slab. In order to monitor the ICCP in that section and to evaluate the effectiveness both on top and on the bottom of the slab, reference electrodes were installed both on top and at the bottom.

After 20 months of service it is clear that the system works effectively; even in zone 5 full protection can be registered both on the upper and lower reinforcement layer according to the protection criteria of EN 12696.

3 SERVICE AND MAINTENANCE

As soon as a CP system is started up and put into operation mode, it runs permanently for the lifetime it is designed for (standard 30 years). All relevant system data like DC driving voltage, current output, potentials and temperature are logged. Logging frequency and limitations with alerts can be set in the system mask, as well as time and date for automatic depolarisation measurements.

In order to assure that the system works properly, it is important that specialists control the data and adjust the system if necessary. For that reason, today's standard is remote access to all CP systems, either by telephone line, internet or UMTS connection. Data

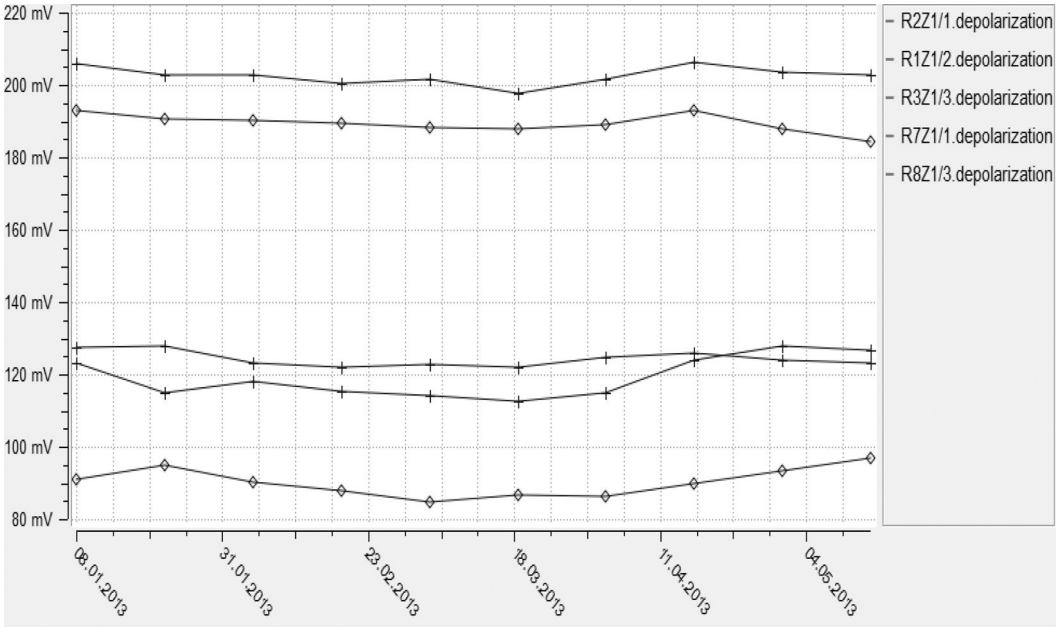

Figure 6. 24 h depolarisation trend line zone 01.

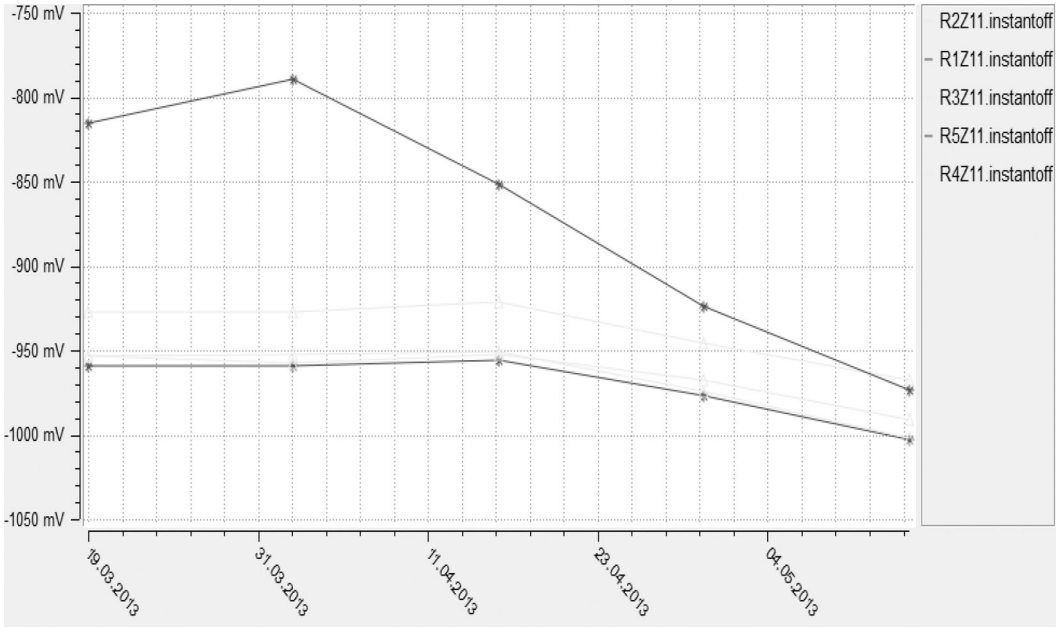

Figure 7. Instant-off potential trend line zone 11.

can be downloaded by wire at any time and adjustments at the system can be made from a central office by the engineer. In EN 12696, there is a clear demand on clients to make sure service and maintenance on a CP system is given for the entire lifetime. Even more, an annual system report must state the condition and effectiveness of a system and record what measures are undertaken during service. For this report, a visual inspection on site must be executed. Clients are more and more used to CP service contracts and accept related costs as normal when they finally make a decision for a CP installation.

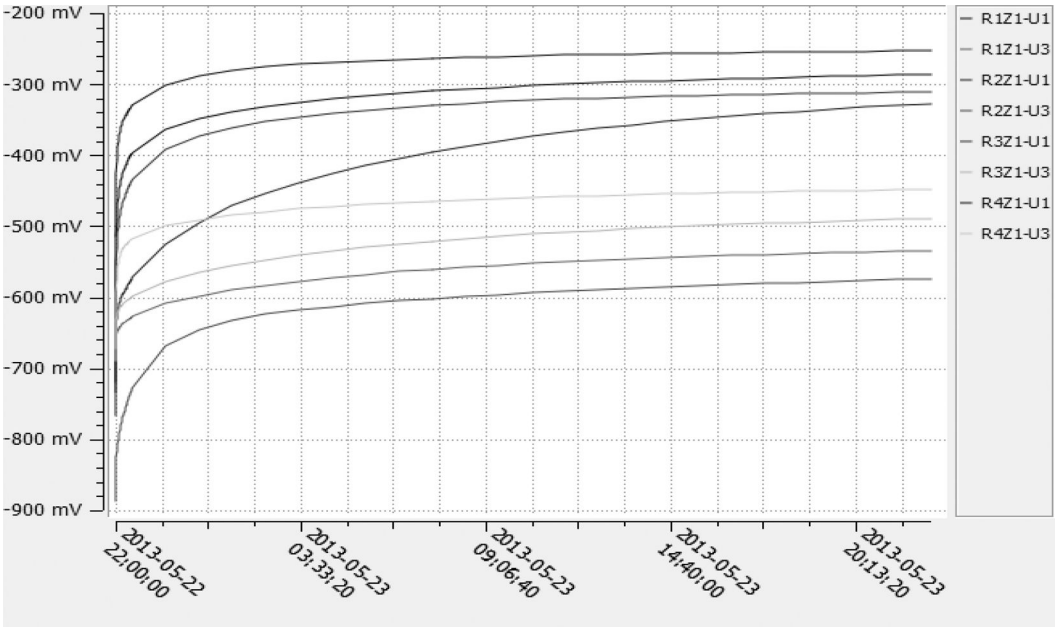

Figure 8. 24 h depolarisation zone 01.

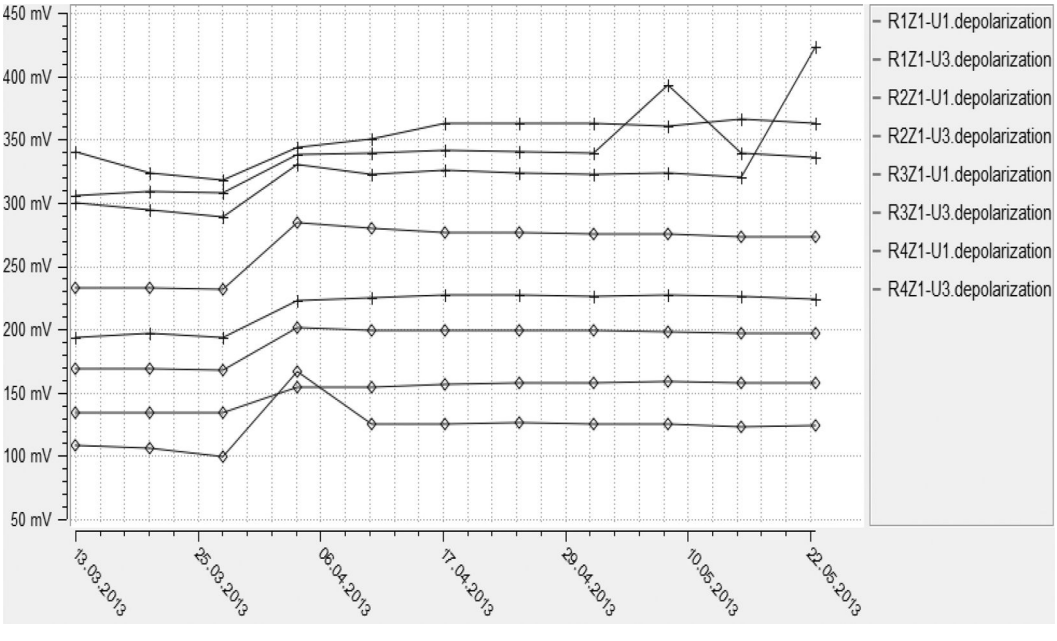

Figure 9. 24 h depolarisation trend line zone 01.

In future, IT and communication technologies will give a wide range of possibilities for remote monitoring and CP operation. The continuous record of data gives a clear picture of the structure's condition which is – with an effectively working CP system – a real add-value factor over time for any client.

REFERENCES

DIN EN ISO 12696:2012–05 Cathodic protection of steel in concrete, 2012.

Deutscher Ausschuss für Stahlbeton: Empfehlung des Deutschen Ausschusses für Stahlbeton (DAfStb) zu den

erforderlichen Nachweisen der Bauprodukte für den kathodischen Korrosionsschutz (KKS) im Betonbau, 2009-06-05.

Institut für Bauforschung (IBAC), Technische Hochschule Aachen: Gutachterliche Stellungnahme zum Anwendungsbereich des SPCC Betonersatzsystems SikaCem Gunit 212 S als Reparaturmörtel und Anodeneinbettmörtel für Titanmischoxidanoden beim KKS von Stahlbeton, 2008-08-11.

Institut für Bauforschung (IBAC), Technische Hochschule Aachen: Untersuchungen zur Eignung von StoCrete TG 114 als Reparatur- und Einbettungsmörtel für Titan-Mischoxid-Anoden für den KKS von Stahlbeton, 2009-06-29.

Institut für Bauforschung (IBAC), Technische Hochschule Aachen: Untersuchungen an StoCrete TS 100 zur Bestimmung von Eingangsparametern für die numerische Simulation, 2009-02-20.

Ingenieurbüro Raupach Bruns Wolff, Hr. Dipl.-Ing. Bruns: Gutachterliche Stellungnahme zum Einsatz des KKS anstelle einer Abdichtung an der Deckenplatte der TG "An der Frauenkirche" in Dresden, 2009-08-06.

Ingenieurgesellschaft Prof. Dauberschmidt & Vestner mbH: Stellungnahme, Systemprüfbericht 2012 KKS-Anlage PH Am Ludwigsplatz in Darmstadt, 2012-03-12.

Ed. Züblin AG Direktion Stuttgart, Bereich Bauwerkserhaltung: Technical documentation capsys® system, 2013-06.

STRABAG SE: Corrosion monitoring and cathodic protection with capsys®, Research, Development, Innovation, Edition Projects 2010/2011.

Concrete Solutions – Grantham et al. (Eds)
© 2014 Taylor & Francis Group, London, ISBN 978-1-138-02708-4

Issues using potential decay techniques to assess a cathodic protection system of steel in concrete caused by macrocell corrosion

R. Giorgini
CorrPRE Engineering BV, Reeuwijk, The Netherlands

ABSTRACT: An experiment was undertaken to simulate steel in concrete macrocell corrosion and to measure the macrocell corrosion rates under dry and wet circumstances and its affect on potential decay (depolarisation) readings when using a CP-system. Two steel in concrete specimens were prepared: one specimen with passive bars and the second specimen with active bars and coupled together. The experiment conducted simulated a situation in which passive bars are surrounded in close vicinity by active bars which are polarised by a galvanic anode. It was performed to understand the effect of current distribution on depolarisation readings. Results indicated clearly a change of current direction coming from the active bars in a wet environment when the anode's current supply was switched-off when starting the instant-off measurement readings. Depending on the humidity and surface area of the active bars in relation to the passive surface area it should be clear that the amount of current produced by the active bars will have noticeable influence on the potential decay (depolarisation) readings.

1 INTRODUCTION

Cathodic Protection has been used for many years to inhibit corrosion of reinforced concrete. One of the main challenges when designing a CP-system specifically for reinforced concrete is to understand the parameters affecting the performance and the working area which is also called the anode's "throwing power" and can be studied by analysing polarisation and depolarisation potentials of the structure in a predefined zone around the anode. This paper describes an experiment which was performed to clear up some dubious depolarisation issues resulting from a previous experiment in which newly developed anodes were tested. The purpose of this experiment was to give a better understanding of these phenomena by simulating a situation in which active and passive bars are combined in concrete specimen.

2 EXPERIMENT PROCEDURES

An experiment was conducted to simulate a situation in which active bars are surrounded in close vicinity by passive bars which are polarized by an anode to understand the effect on current distribution and depolarization readings. The anode chosen was a sacrificial zinc surface applied anode which was a zinc sheet with pre-applied ion-conductive adhesive as can be seen in Figure 2. The main reason to use such an anode system was its simplicity, ease of application and having no physical and mechanical impact on the concrete samples, avoiding any electric field irregularities or electric field concentrations which might have affected the potential decay measurements.

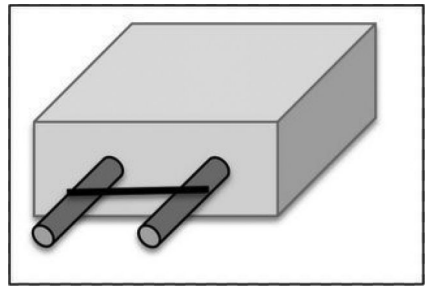

Figure 1. Concrete samples.

Two concrete samples as shown in Figure 1 were prepared with the following composition: Portland cement 300 kg/m^3, 0–15 mm mixed aggregates, superplasticizer 1,17 ltr/100 kg cement, water cement ratio of 0.6, and only sample 2 with mixed in calcium chloride ($CaCl_2$) with a 3% Cl^- ion m/m cement weight. The dimensions of the concrete samples were: (L × W × H) 10 × 10 × 4 cm. Each of the samples contained 2 bars with a diameter of 10 mm and a total steel surface area of 25 cm^2. The zinc sheet had a total surface area of 100 cm^2.

3 RESULTS

The system was connected and the data was logged for every 10 minutes for a total of 44 hrs. Figure 5 shows

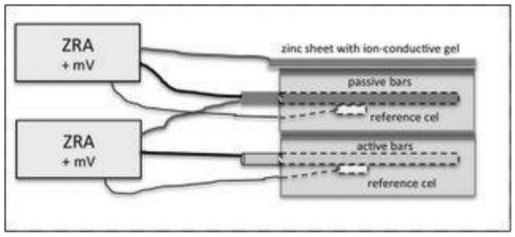

Figure 2. Experimental set-up.

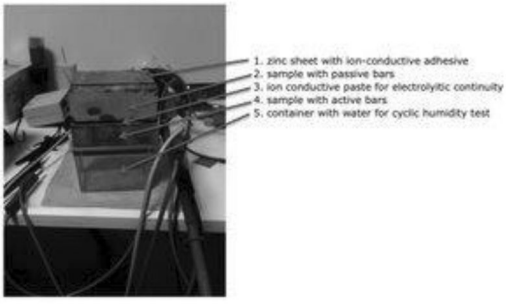

Figure 3. Picture of the experimental set-up.

Figure 4. Lab set-up with two ZRAs measuring the current distribution and direction.

that the current measured between the samples and the zinc anode is called A_1, which is an imposed current by the zinc anode. A positive current sign means an electron flow from the zinc anode to the samples. A negative current sign means an opposite direction of electron flow. A_2 is the current flow between sample 1 and sample 2. A positive current sign means an electron flow from sample 1 to sample 2. A negative current sign means an opposite direction of electron flow.

3.1 *Step 1 (open circuit macrocell condition)*

For the first 10 minutes, the potentials of both samples were logged. Both samples were not electrically connected neither was the anode. Both samples were

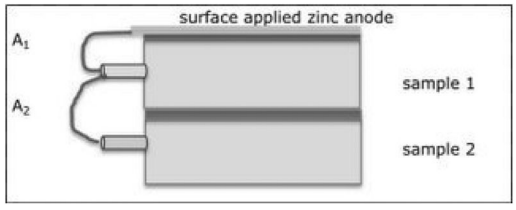

Figure 5. Sample 1 has passive bars, and sample 2 has active bars.

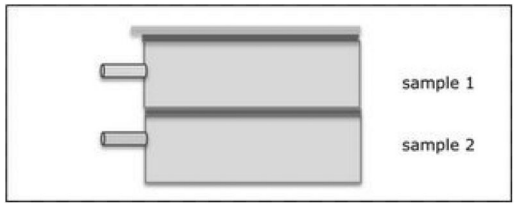

Figure 6. Sketch of the samples.

Table 1. Potentials and currents measured during step 1.

Sample 1				Sample 2	
hrs	min	CSE mV	A_1 uA	CSE mV	A_2 uA
0	0	165	0	−490	0
	10	168	0	−487	0

Table 2. Potentials and currents measured during step 2.

Sample 1			Sample 2		
min	CSE mV	A_1 uA	CSE mV	A_2 uA	
10	168	0	−487	0	Bars connected
20	−123	0	−481	−51	
30	−173	0	−491	−52	
40	−179	0	−493	−48	
50	−177	0	−490	−49	

also kept in an environment with 65% RH and 20°C. Figure 6 shows a sketch of the situation including Table 1 and Figure 7 showing the potentials and current measured.

3.2 *Step 2 (closed circuit macrocell condition without anode current)*

The next step involved a closed circuit between sample 1 and sample 2. In this condition the electron flow A_2 measured was caused by the macrocell condition. Both potentials and current were measured till the values stabilised. The results are shown in Table 2 and presented graphically in Figure 9 and 10.

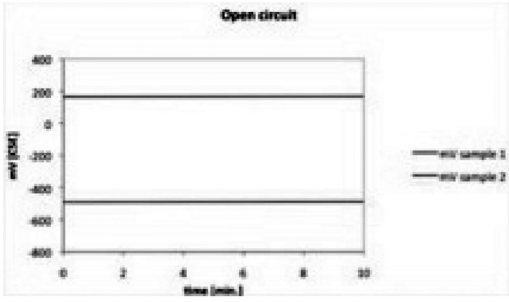

Figure 7. The results from Table 1 presented graphically.

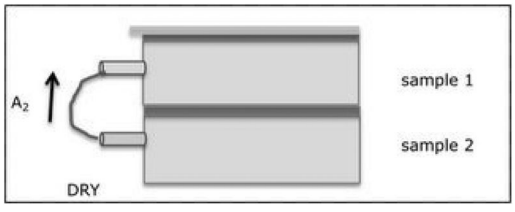

Figure 8. Electron flow of the macrocell condition.

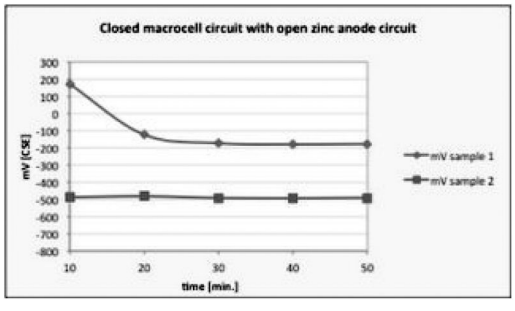

Figure 9. The potentials [mV] from Table 2 presented graphically.

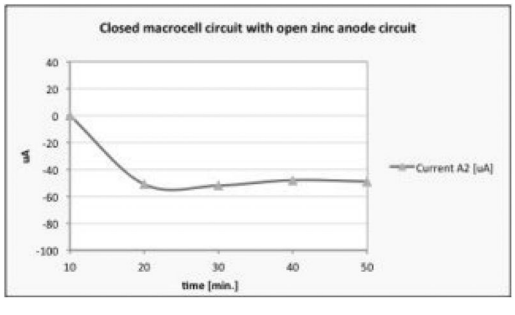

Figure 10. The current [μA] from Table 2 presented graphically.

3.3 *Step 3 (closed circuit macrocell condition with anode current)*

Step 3 involved a closed circuit between sample 1, sample 2 and the anode. In this condition an electron flow A_1 and A_2 were measured as shown in Figure 1.

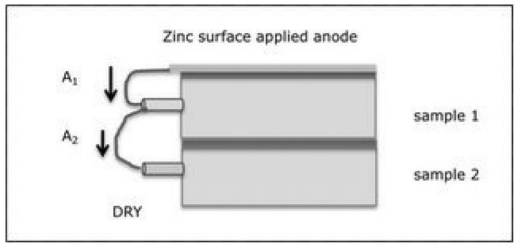

Figure 11. A_1 and A_2 show the electron flow measured.

Table 3. Potentials and currents measured during step 3.

Sample 1				Sample 2		
hrs	min	CSE mV	A_1 uA	CSE mV	A_2 uA	
	50	−177	0	−490	−49	Anode conn.
1	60	−437	114	−495	35	
	70	−545	111	−517	36	
	80	−572	108	−520	34	
	90	−536	105	−518	31	
	100	−585	101	−519	33	
	110	−527	95	−519	35	
2	120	−531	91	−517	31	
3	180	−571	73	−520	27	

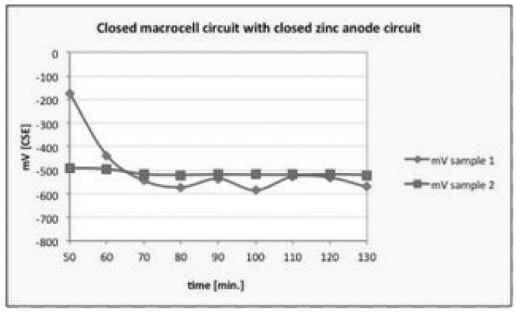

Figure 12. The potentials [mV] from Table 3 presented graphically.

The zinc anode was able to supply not only an electron flow to sample 1 but also to sample 2 (A_2). Both samples were dry. The results can be found Table 3 and presented graphically in Figure 12 and 13.

3.4 *Step 4 (closed circuit macrocell condition with anode current)*

Step 4 involved similar situation as step 3 a closed circuit between sample 1, sample 2 and the zinc anode. However the sample with the active bars was affected by high humidity. The sample was put on top of a container filled with water as shown in Figure 14. Immediately the humidity started to penetrate the sample with active bars as can be seen in Table 4 and presented graphically in Figure 15 and 16.

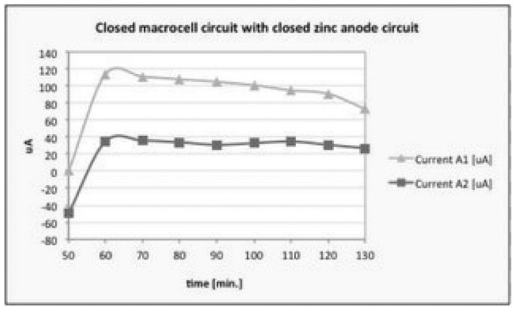

Figure 13. The currents [μA] from Table 3 presented graphically.

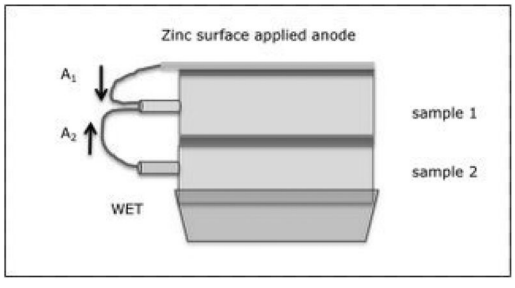

Figure 14. Sample 2 placed on top of a water container.

Table 4. Potentials and currents measured during step 4.

Sample 1				Sample 2		
hrs	min	CSE mV	A_1 uA	CSE mV	A_2 uA	
3	180	−571	73	−520	27	Sample
4	240	−580	67	−522	21	wetted
5	300	−590	63	−521	18	
6	360	−564	59	−522	13	
7	420	−593	57	−521	6	
8	480	−626	57	−521	1	
9	540	−554	55	−522	−4	
10	600	−602	56	−522	−9	
11	660	−619	55	−522	−12	
12	720	−547	54	−520	−15	
13	780	−619	53	−520	−17	
14	840	−606	55	−519	−18	
15	900	−554	55	−521	−16	

3.5 *Step 5 (closed circuit macrocell condition with anode current)*

Figure 17 shows step 5 which is actually the same situation as described step 3. In this situation the sample with the active bars has been taken from the container with water and slowly got back to a dry environment. The results are found in Table 5 and presented graphically in Figure 18 and 19.

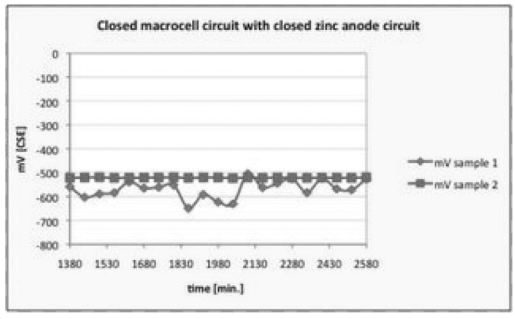

Figure 15. The potentials [mV] from Table 4 presented graphically.

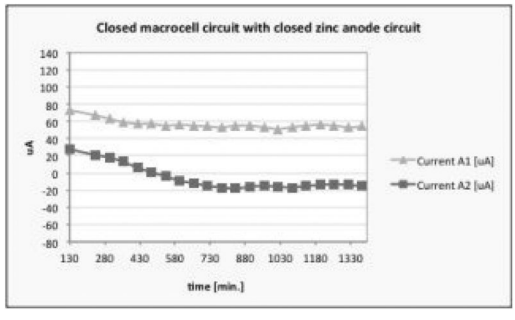

Figure 16. The currents [μA] from Table 4 presented graphically.

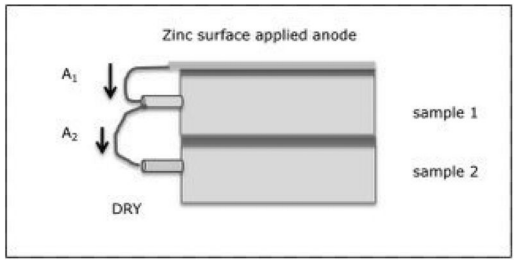

Figure 17. Situation turned as in Figure 11 in Step 3.

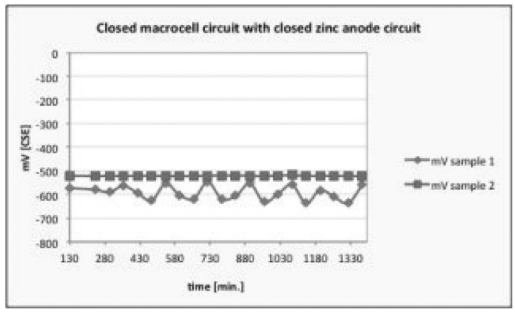

Figure 18. The potentials [mV] from Table 4 presented graphically.

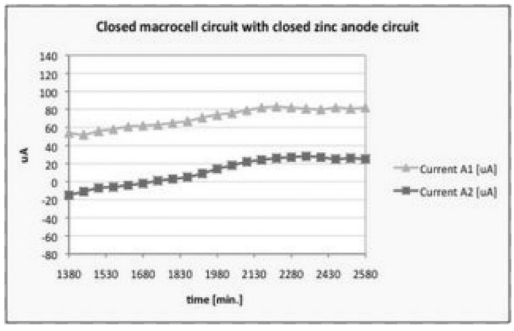

Figure 19. The currents [μA] from Table 4 presented graphically.

4 DISCUSSION

Unfortunately there is a lack of discussions about design criteria to get reliable monitoring readings of CP-systems for steel in concrete. Specifically, for galvanic anodes, the position of reference cell in relation to the anode can be critical when judging whether a system is working or not. On the other hand surrounding circumstances which sometimes are not well judged can have quite an impact on the values measured and undervaluate the performance. This is what happened during previous experiments in getting better understanding of the throwing power, current densities and overall performance of newly developed discrete sacrificial anodes to see whether they complied with the ISO12696 criteria.

This original experiment was based on a total of four concrete slabs each with dimension 100 × 100 × 15 cm of which two slabs were contaminated with chlorides. One slab was used to simulate a concrete slab with traditional repairwork. This particular slab was heavily contaminated with chlorides and the top of this slab (appr. 10 cm) was replaced by a traditional mineral repair mortar. These slabs contained reference cells on strategic locations to get depolarisation readings at different distances from the anodes. The depolarisation readings were quite disappointing and not in agreement with the current readings of the anodes which were impressive, specifically in the region with active corroding bars due to the low polarisation resistance of the active corroding bars. Similar effects were also noticed in previous studies (Bertolini et al.) in which single anodes were analysed for their performance and "throwing power" immediately after switching off the current during instant-off readings.

After having studied and analysed the results of the original experiment as described above, there were already assumptions indicating that the readings were possibly affected by the actively corroding bars in close vicinity of the reference electrodes. Similar situations may occur in case where, per unit surface area, too few anodes with too low anode surface area are used in combination with active bars in wet zones. This will lead also to situations resulting in insufficient polarisation capacity of the anodes simply because they follow the mixed potential theory. The mixed potential theory indicates very clearly that sacrificial anodes need a minimum required surface area in proportion to the steel surface area to gain sufficient steel polarisation (Giorgini & Papworth), (Kelly & Scully).

Therefore it was decided to conduct a new experiment to simulate a situation in which passive bars are surrounded in close vicinity by active bars in combination with a CP-system to understand the current distribution and its effect on depolarisation readings. When considering the current densities and potentials presented in the data it is helpful to consider the overall potential as the sum of several electrochemical processes called overpotentials or polarisations, which are:

η_{act} = *activation polarisation*
(also called charge transfer polarisation or charge transfer overpotential)
to overcome the charge transfer resistance (R_{ct})

η_{conc} = *concentration polarisation*
to overcome diffusional resistance due to mass transport limitations (R_D), and

η_{Ω} = *ohmic polarisation*
to overcome ohmic risistance also called solution or electrolytic resistance R_S (Cherry).

Activation polarisation is actually the potential required to trigger the reaction at the surface and keep it running. It can be described by the Tafel Equation (1):

$$\eta_{act} = -\beta_c \ln x (i_c / i_{corr}) \quad (1)$$

η_{act} = *activation polarisation*
β_c = *Tafel coefficient*
i_c = *cathodic current density*
i_{corr} = *corrosion current density*

Concentration polarisation occurs during the depletion of charge-carriers at the electrode surface.The mass transport of these charge-carriers could become rate controlling. It can be described in Equation (2):

$$\eta_{conc} = R_D \text{ x } (T/n) \text{ x } F \ln(1 - [i_c / i_{corr}]) \quad (2)$$

η_{conc} = *concentration polarisation*
R_D = *mass transport limitations*
T = *absolute temperature*
F = *Faraday constant*
n = *number of electrons involved*
i_c = *cathodic current density*
i_{corr} = *corrosion current density*

Ohmic polarisation is actually the potential gradient caused by solution or electrolyte resistance. Ohmic overpotential is described by Ohm's law and is often called Ohmic drop as presented in Equation (3):

$$\eta_{\Omega} = I \text{ x } R_{\Omega} \quad (3)$$

η_{Ω} = *ohmic polarisation*
I = *current*
R_{Ω} = *also R_S, ohmic drop*

The total overpotential (η_{total}) gives Equation (4):

$$\eta_{total} = (\eta_{act} + \eta_{conc}) + \eta_{\Omega}$$

$$= [-\beta_c \times \ln(i_c / i_{corr}) + (R_D \times T/n \times F) \times \ln(1 - [i_c / i_{corr}])] + I \times R_{\Omega} \quad (4)$$

to overcome:

$$R_{tot} = [R_{ct} + R_D] + R_S$$

of which

$$[R_{ct} + R_D] = R_p$$

makes Equation (5) :

$$R_{tot} = R_p + R_S \quad (5)$$

Each individual parameter can be derived from the polarisation curves shown in figures 23–26 which illustrate steps 2, 3 and 4. To understand these individual parameters within a corrosion process, it may help to visualise the elements of the circuit as electrical components to simulate the corrosion process. The most common equivalent circuit used in electrochemistry is called the Randle's circuit as shown in Figure 20. Additional to all individual resistances there is also a capacitive element C_{dl} due to the double layer present at the electrode/solution interface which acts like a capacitor.

We will not go into detail how to determine each of these individual parameters because the goal of this experiment is to visualise that part of overpotential which is caused by the macrocell corrosion current.

When studying the results caused by macrocell corrosion it becomes obvious that the polarisation values are strongly affected by the macrocell corrosion currents. This means that it affects equally the depolarisation or potential decay readings. Figure 21 shows the overall curve of all 5 steps together and clearly shows the effect on polarisation due to macro corrosion currents.

When zooming in on the first 180 minutes it is even possible to quantify the exact amount of polarisation caused by the macrocell corrosion current. It can be clearly seen in Figure 22 the strong effects of these macrocell corrosion currents and hence the error of depolarisation or potential decay readings during monitoring if these currents are not excluded.

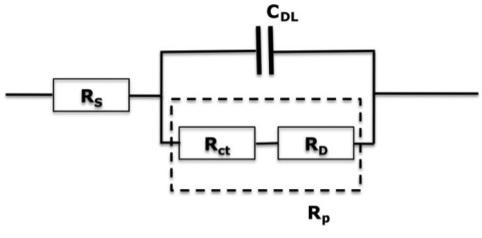

Figure 20. Randles circuit.

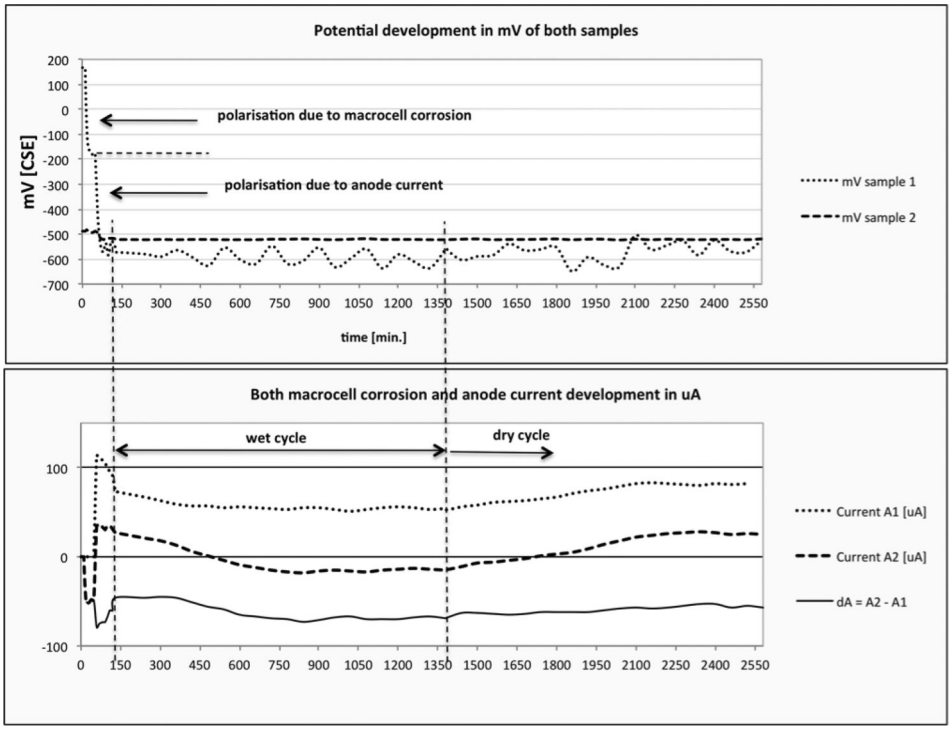

Figure 21. The currents [μA] and potentials [mV] from all steps presented graphically.

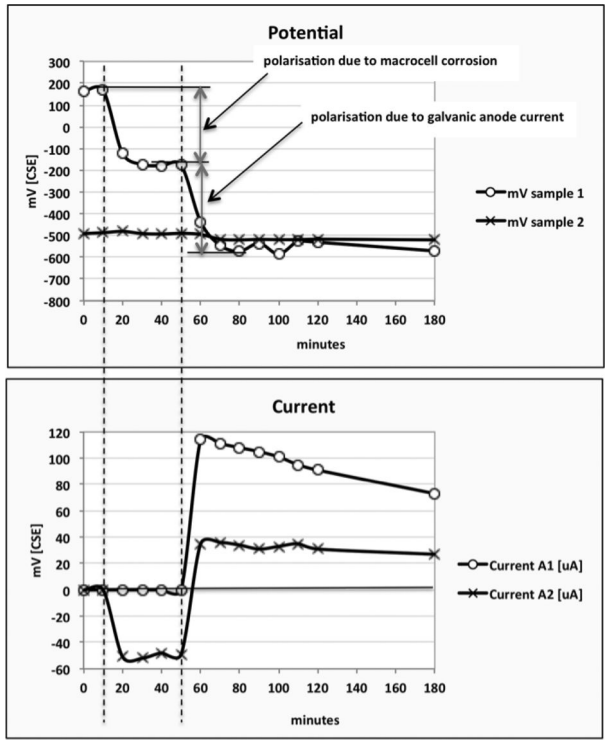

Figure 22. The currents [μA] and potentials [mV] from all steps presented graphically.

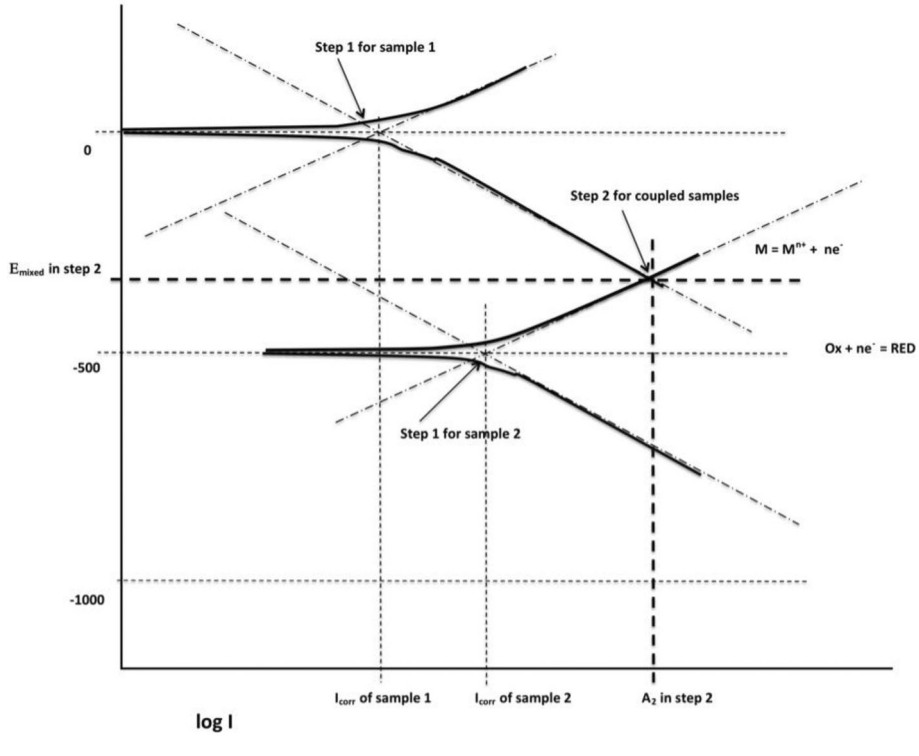

Figure 23. Schematic Evans diagram and polarisation curves illustrating step 2.

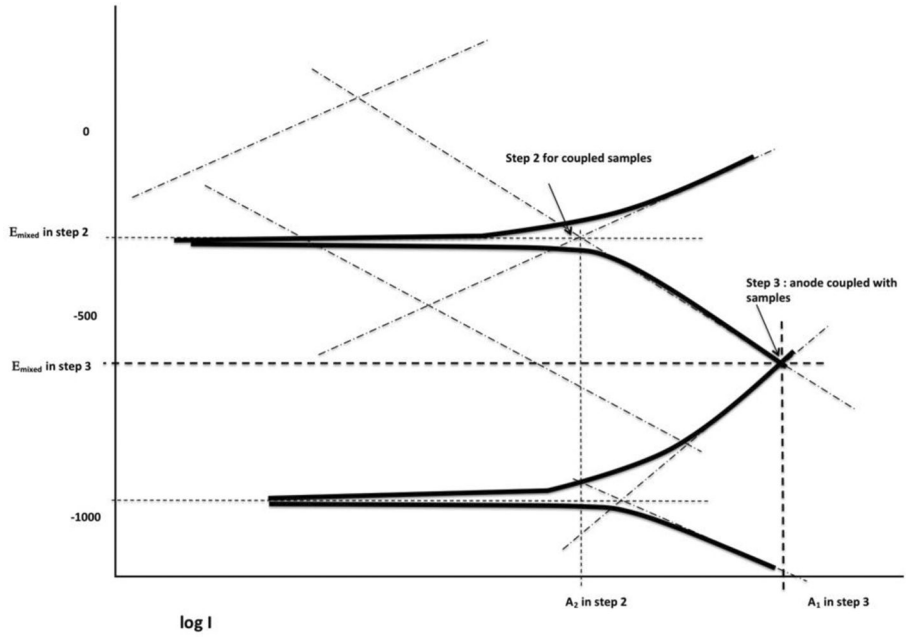

Figure 24. Schematic Evans diagram and polarisation curves illustrating step 3.

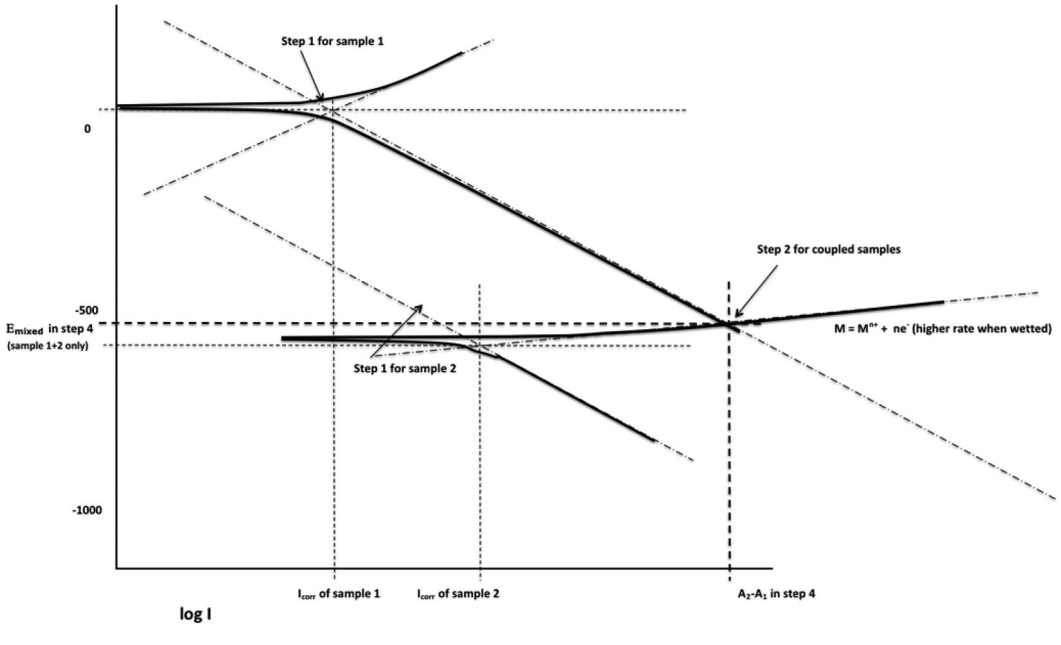

Figure 25. Schematic Evans diagram and polarisation curves of the two concrete samples coupled illustrating step 4, assuming the anode would not participate in the coupling.

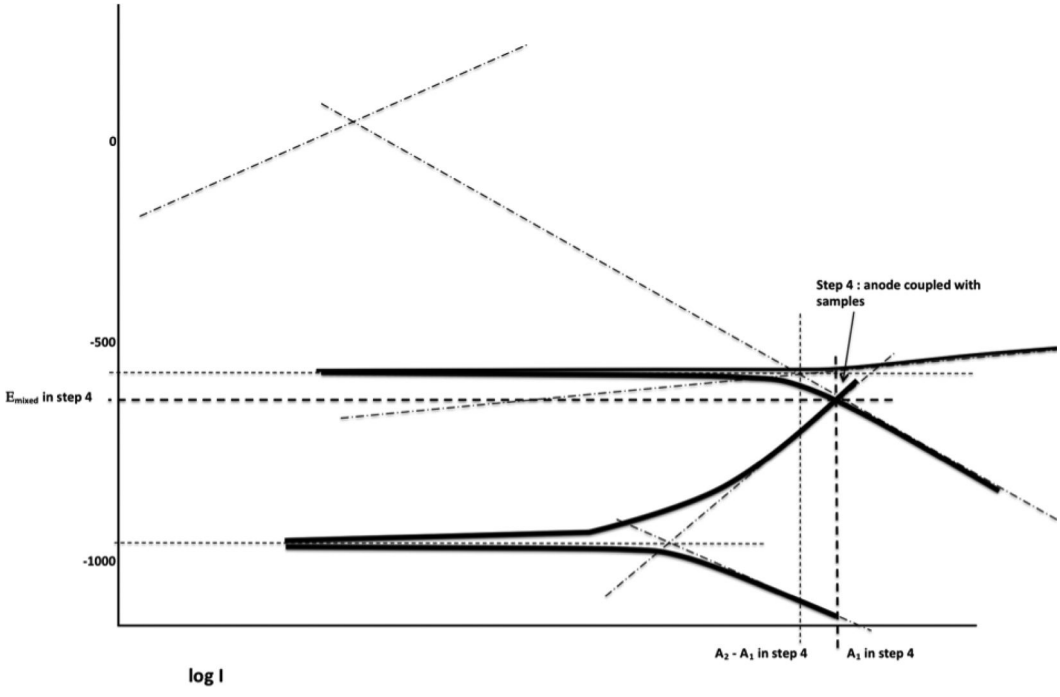

Figure 26. Schematic Evans diagram and polarisation curves illustrating step 4.

5 CONCLUSIONS

This experiment showed very clearly the effect of macrocell corrosion on steel polarisation in concrete samples.

It also showed that the combination of passive and active bars in close vicinty produce such an amount of corrosion current to be able to give strong polarisation effects and hence erroneous depolarisation readings.

It is therefore strongly recommended that CP-designers consider these effects in their CP-system designs to avoid errors in their readings and hence misinterpretations.

REFERENCES

Bertolini, L. Protection of reinforced concrete piles in marine structures with sacrificial anodes.

Cherry, B.W. The Journal of Corosion Science and Engineering. Volume 9, Paper 6. February 2006. How instant is instant.

Giorgini. R. &Papworth, F. 2011. Galvanic cathodic protection system complying with code based protection criteria.

Kelly, R.G. & Scully, J.R. 2003. Electrochemical techniques in corrosion science and engineering.

This page intentionally left blank

Concrete Solutions – Grantham et al. (Eds)
© 2014 Taylor & Francis Group, London, ISBN 978-1-138-02708-4

Numerical simulation of the current and potential distribution of surface applied CP-anode systems

C. Helm & M. Raupach
Institute of Building Materials Research, RWTH Aachen University, Aachen, Germany

ABSTRACT: Cathodic Protection (CP) is a common repair method for reinforced concrete structures affected by chloride induced macro cell corrosion. The current and potential distribution and thereby the effectiveness of the CP system is influenced by many parameters such as rebar content, concrete cover thickness or concrete resistivity. Furthermore the design (laminar or discrete) and the material of the CP anode (MMO, carbon based conductive coating) affect its polarisation behaviour and hence the performance of the CP system. Within this work a numerical model is introduced. It is capable of predicting the current and potential distribution within the concrete structure as well as on the anode system itself. The influence of several impact factors on the current and potential distribution will be pointed out by means of parametric studies. Possible future applications as a design tool for the layout of CP systems will be presented.

1 GENERAL

1.1 *Introduction*

Cathodic protection (CP) is a common repair method for reinforced concrete (RC) structures affected by chloride induced macro cell corrosion. It's effectiveness has been proven by numerous scientific research projects as well as case studies. However, not all knowledge from these studies has expanded into practice. The line of action in the design and maintenance of today's CP systems applied on reinforced concrete structures is still governed by empirical calculations and criteria. This paper presents methods and examples for the application of numerical simulations of the current and potential distribution within reinforced concrete members during CP in order to demonstrate possible future applications in practice.

1.2 *Theoretical background*

The anode chosen for a CP system has a major impact on its performance, durability and cost effectiveness. In theory two different types of CP systems exist, galvanic and impressed current systems. Today, impressed current systems can be considered state of the art. This is due to their controllability, higher driving voltages and durability. In some cases, such as protection of beams, columns or joints, discrete anodes are used, but the most common application today is the protection of laminar structures, such as deck surfaces. For these structures, three anode types are generally used. These are mesh or ribbon mesh anodes made from mixed metal oxide coated titanium (MMO) or carbon based conductive coatings. Both types require the establishment of protection zones and current requirements [Bennett et al., 1993]. The methods used for this process are mainly based on empirical data and practical experience as well as cost effectiveness. Only the ohmic drop within the anode material itself is taken into account.

Numerical modeling can be used as a tool for layout of CP systems. Earlier work [Bruns & Raupach, 2008; Helm et al., 2010; Helm et al., 2011] dealt mainly with the modeling of MMO based CP systems. For these systems, the ohmic drop within the material itself can be neglected. The model presented in this paper is accounting for geometry of concrete, rebar and anode distribution, the concrete resistivity, the polarisation behaviour of all electrodes (active/passive rebar, CP-anode) as well as the ohmic drop within the anode material. Therefore it is capable of reproducing also conductive coatings serving as CP anodes. Hence, the focus of the investigations described below is set on this type of anodes.

To generate feasible results, the quality of the input parameters is fundamental. The respective experimental procedures are described in the following chapter.

2 EXPERIMENTAL

2.1 *Polarisation testing*

To assess the polarisation properties of the CP anode, potentiodynamic measurements were conducted. The specimen setup is given in Figure 1.

The counter electrode was made from MMO mesh instead of rebar in order to achieve a homogeneous

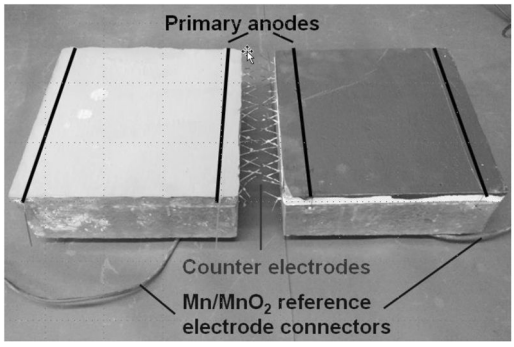

Figure 1. Specimen for the determination of the polarisation properties of conductive coatings.

Table 1. Concrete mix.

Parameter	Value	Unit
Binder	OPC	[–]
Binder content	275	[kg/m^3]
w/b-ratio	0.65	[–]
Chloride content	3	[M.-%/b]

electrical field. The coating served as the working electrode. The measurements were done versus a cast in Mn/MnO_2 reference electrode. A feed rate of 0.0333 mV/s was used. Within this study the polarisation behavior of a commercially available conductive coating on an OPC concrete was assessed. The specimen was stored and tested at 20°C/80% RH. The concrete mix was chosen to reflect a typical on site concrete, found in an aged structure affected by chloride induced macro cell corrosion and is given in table 1.

The test was conducted up to a current density of 20 mA/m^2 with respect to the concrete surface. After each run, an instant-off measurement was conducted in order to determine the ohmic drop, which was then eliminated calculatively from each reading. The dimensions of the specimens were 25 × 25 × 9 cm.

2.2 *Fitting of polarisation curves*

To integrate the measured polarisation behavior of the electrodes into the numerical model, an analytical description is needed. The numerical model presented below contains two different electrode types, the conductive coating (CP anode) and active rebar. For both types the Butler-Volmer Equation (1) was used to fit the respective polarisation curves.

$$i = \frac{i_0 \cdot \left[\exp\left(\frac{2.3 \cdot \eta}{b_a}\right) - \exp\left(\frac{-2.3 \cdot \eta}{b_c}\right) \right]}{1 + \frac{i_0}{i_{\lim,ox}} \cdot \exp\left(\frac{2.3 \cdot \eta}{b_a}\right) - \frac{i_0}{i_{\lim,red}} \exp\left(\frac{-2.3 \cdot \eta}{b_c}\right)} \quad (1)$$

Table 2. Fit parameters for conductive coating and active rebar.

Parameter	conductive coating	active rebar	unit
i_0	0.0017	0.0055	[A/m^2]
E	−0.2	−0.526	[V]
b_a	0.34	0.15	[V/dec]
b_c	0.04	0.265	[V/dec]
$i_{lim,ox}$	0.045	1.0	[A/m^2]
$i_{lim,red}$	−1.2	−1.0	[A/m^2]

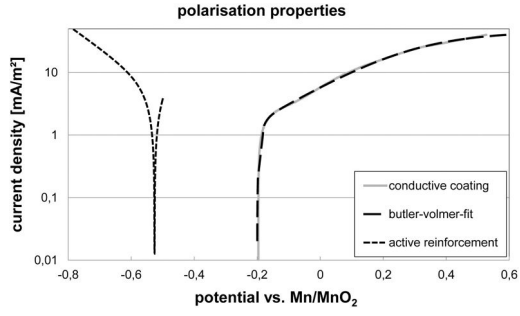

Figure 2. Input data.

Where I = current density on steel surface; i_0 = exchange current density; η = over potential ($E - E_0$); E = potential; E_0 = free corrosion potential; b_a = anodic tafel slope; b_c = cathodic tafel slope; $i_{lim,ox}$ = limiting current density of the anodic reaction and $i_{lim,red}$ = limiting current density of the cathodic reaction.

The fit parameters were chosen to approximate the readings as far as possible within the expected potential range during the application of CP. This may lead to a suboptimal fitting of other regions as well as parameters outside the theoretical limits. The parameters chosen for the model below are given in table 2. A visualization of the measured data as well as the respective fit functions are given in Figure 2. The input data for the active rebar were determined the same as in section 2.1 on a macro cell specimen with the same concrete mix.

3 NUMERICAL MODELLING

3.1 *General*

Any arrangement of electrically connected anodes and cathodes inside an electrolyte will result in the formation of certain potentials on the electrode surfaces. This causes the formation of a spatial variable electrical field inside the electrolyte. The resulting current densities of the anodic and cathodic reactions can then be assessed by use of the following boundary conditions [Brem, 2004].

The potential distribution inside the concrete can be described by Laplace's equation (2), assuming that the electrolyte is homogeneous:

$$\nabla^2 U = 0 \tag{2}$$

The current flow in any direction results in:

$$I_{xj} = \sigma \cdot \nabla E \tag{3}$$

The total current density for any part of the electrode surfaces can be calculated via Ohm's law:

$$I_s = \sigma \cdot \frac{\partial E}{\partial n} \tag{4}$$

Where $E =$ Potential; $\nabla^2 =$ Laplace-operator; $I_{xj} =$ Current flow in direction xj; $\nabla =$ Nabla-operator; $I_s =$ Total current density; with:

$$\sigma = \frac{1}{\rho} \tag{5}$$

Where $\rho =$ Resistivity. The vector normal to the potential gradient has to be zero at all isolating surfaces:

$$\frac{\partial E}{\partial n} = 0 \tag{6}$$

Due to electro neutrality the sum of all currents inside the system has to be zero as well:

$$\int_F i dA = \int_{F_a} i_a dA + \int_{F_c} i_c dA = 0 \tag{7}$$

The current density is a function of the electrode potential and can be described by a polarisation curve for each electrode:

$$i_a = f_a(E_a) \tag{8}$$

$$i_c = f_c(E_c) \tag{9}$$

Where $i_a =$ Current density of the anodic reaction; $i_c =$ Current density of the cathodic reaction; $E_a =$ Anodic potential; $E_c =$ Cathodic potential; $f_a =$ Anodic polarisation curve; $f_c =$ Cathodic polarisation curve. The equations above allow an analytical calculation of Laplace's equation for any given set of linear polarisation curves. In case of non-linear polarisation behaviour numerical methods have to be applied [Helm et al., 2010].

3.2 *Geometry and input data*

The geometrical arrangement of the numerical model used in this study is given in Figure 3. It represents a conductive coating anode system on a deck surface. The spacing of the rebar is 15 cm in order to represent a reinforcing mesh sheet. The length of the model

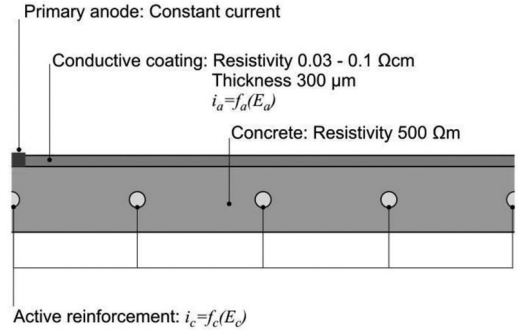

Figure 3. Geometrical arrangement of the numerical model.

is 75 cm, which is half the size of a regular spacing of primary anodes, in order to use symmetry. A rebar diameter of 10 mm and a concrete cover thickness of 20 mm were chosen. For the concrete a bulk resistivity was assumed. The thickness and resistivity of the coating resistivity were taken from manufacturer's data. The initial protection current density was set to 10 mA/m^2 with respect to the concrete surface. The standard concrete resistivity was 500 Ωm.

I_c and I_a in this case are represented by formulations of Equation 1, using the respective parameters from table 2. Using this model, parametric studies can be conducted in order to assess the influence of each input parameter on the current and potential distribution and therefore on the performance of the CP system.

3.3 *Parametric study*

Within the parametric study, several input parameters were varied, starting from the standard case described above. It can be distinguished between parameters that are given by the structure, such as concrete resistivity, concrete cover or diameter of rebar and those directly related to the layout of the CP system. This could be e.g. protection current or primary anode spacing. Within this study, concrete resistivity, concrete cover and the protection current have been varied. The results of the parametric study are presented below.

4 RESULTS

4.1 *Concrete resistivity*

In Figure 4, the influence of different concrete resistivities on the current distribution on the anode surface is given. The rebar is located at distances of 0, 0.15, 0.30, 0.45, 0.60 and 0.75 m. Figure 5 presents the lowest polarisation achieved on each rebar surface.

It can be seen, that an increase of the concrete resistivity causes a more and more heterogeneous current distribution. The general decrease of current observed from left to right is caused by the sheet resistance of the CP anode. The heterogeneity is caused by a constriction of equipotential lines over the rebar. The concrete

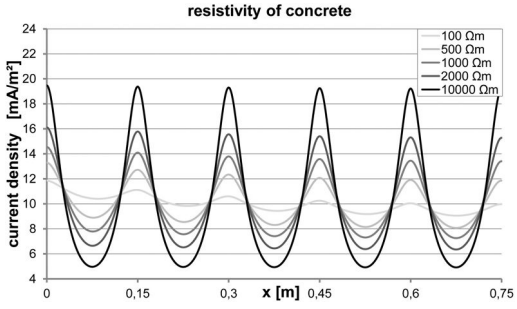

Figure 4. Impact of concrete resistivity on the current distribution on the surface of the CP anode.

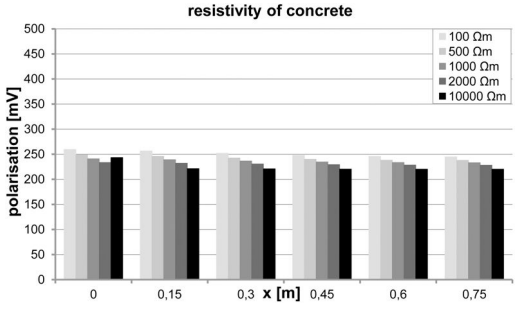

Figure 5. Impact of concrete resistivity on the polarisation of the rebar.

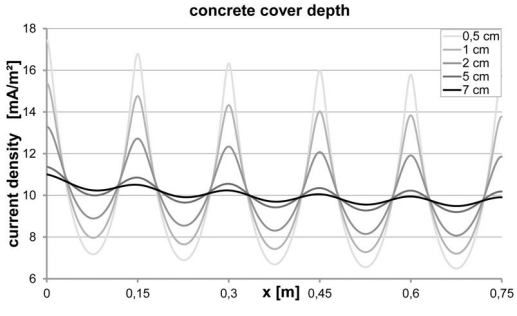

Figure 6. Impact of concrete cover depth on the current distribution on the surface of the CP anode.

resistance becomes predominant and exceeds polarisation resistances by far. The impact on the achieved polarisation on the rebar surface is small. The slight decrease can be stated to the fact that with increasing concrete resistivity less current reaches the back of the rebar. Nevertheless, it is obvious that high concrete resistivities may cause a harmful overpolarisation of the CP anode.

4.2 *Concrete cover depth*

In Figure 6, the influence of different concrete cover depth on the current distribution on the anode surface is given. Figure 7 presents the lowest polarisation achieved on each rebar surface. The concrete cover depth was varied from the initial value of 20 mm.

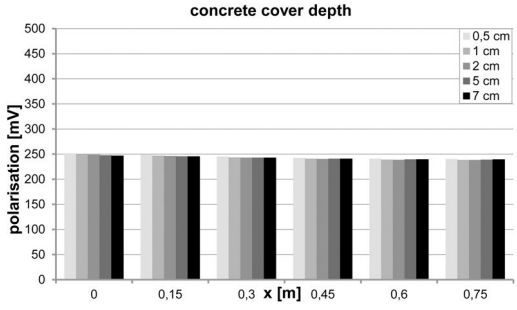

Figure 7. Impact of concrete cover depth on the polarisation of the rebar.

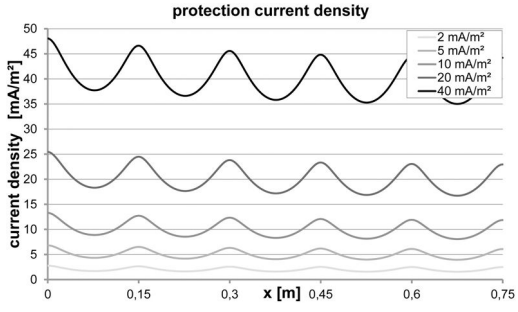

Figure 8. Impact of protection current density on the current distribution on the surface of the CP anode.

It can be seen, that a reduction of concrete cover depths has a similar effect on the current and potential distribution as an increase of concrete resistivity. In this case the effect is of geometrical nature. The distance of the CP-anode surface towards the rebar becomes heterogeneous with a reduction of cover depth. Therefore the impact of concrete resistance exceeds those of polarisation resistances even for the reasonable concrete resistivity of 500 Ωm. Again there is hardly any effect on the polarisation of the rebar, but the risk of durability issues regarding the CP anode is increased.

4.3 *Protection current density*

In Figure 8, the influence of different protection currents on the current distribution on the anode surface is given. Figure 9 again presents the lowest polarisation achieved on each rebar surface. The protection current density was varied from the initial value of 10 mA/m^2 with respect to the concrete surface.

The results indicate how numerical modeling can be used as a design tool for the layout of CP systems. In this case the results show that a protection current density of less than 5 mA/m^2 would be sufficient for the given geometry. It is also possible to predict the maximum anode current densities for any given mean value, in order to verify the compliance with manufacturer's product specifications.

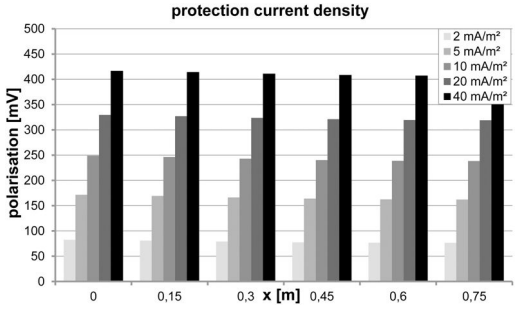

Figure 9. Impact of protection current density on the polarisation of the rebar.

5 CONCLUSIONS AND OUTLOOK

5.1 *Conclusions*

Numerical calculations have been applied in order to predict current and potential distribution during the CP of reinforced concrete. For this study a carbon based conductive coating served as CP anode. The calculations showed reasonable results. The following conclusions can be derived from these results.

- The characteristics of carbon based conductive coatings serving as CP anodes, especially the finite sheet resistance, can be imaged by the model
- Increasing concrete resistivities lead to a more and more heterogeneous current distribution along the CP anode
- This heterogeneity is not detectable by monitoring the compliance with the 100 mV decay criterion
- Low concrete cover depths again cause heterogeneous, high concrete covers more and more homogeneous current distributions
- Numerical calculations can be used to predict protection currents before installation of the CP system and therefore allow for a choice of the optimal components operation parameters

5.2 *Outlook*

Current activity deals with the modeling of more complex geometries as well as 3-dimensional models. The latter is very important because a crossing rebar causes local maxima of the rebar surface and should therefore result in maxima of anode current densities as well. These crossings in some cases might form the design case and cannot be accounted for in 2d.

Furthermore the models results need to be linked to realistic durability relevant current and potential limits which might differ from those given by the manufacturers.

ACKNOWLEDGMENTS

The authors would like to thank the German Research Foundation (DFG) and German Federation of Industrial Research Associations (AiF) for the funding of this research.

REFERENCES

Bennett et al., 1993. Cathodic Protection of Concrete Bridges: A Manual of Practice. Contract, 100, 102D

Brem, 2004. Numerische Modellierung der Korrosion in Stahlbetonbauten. Anwendung der Boundary Element Methode. Zürich: Eidgenössische Technische Hochschule Zürich, 2004.- Diss.ETH Nr. 15567

Bruns & Raupach, 2008. CP of the Rear Reinforcement in RC-Structures – Numerical Modeling of the Current Distribution. London [u.a]: CRP Press Taylor & Francis Group, 2009. – In: *Proceedings of the 2nd International Conference on Concrete Repair, Rehabilitation and Retrofitting (ICCRRR), Cape Town, South Africa, November 24–26, 2008*, (Alexander, M.G.; et al., (Eds.)), [CD] S. 813–819, [Hbk] S. 301–302 ISBN 978-0-415-45850-3

Helm et al., 2010. Numerical Evalutation of Chloride Migration Caused by Cathodic Protection of RC-Structures. Moscow: Congress Center of World Trade Center, 2010. – In: *From the Earth Depths to Space Heights, EUROCORR 2010, Moscow, 13–17 September 2010*, 16 pages ISBN 978-5-317-03383-5

Helm et al., 2011. Time Dependency of Current and Potential Distribution During the Cathodic Protection of RC Structures. Stockholm: Swerea KIMAB, 2011. – In: *Developing Solutions for the Global Challenge, EUROCORR 2011, Stockholm, 4–8 September 2011*, 11 pages.

This page intentionally left blank

Concrete Solutions – Grantham et al. (Eds)
© 2014 Taylor & Francis Group, London, ISBN 978-1-138-02708-4

A novel assessment of the electrochemical lithium impregnation treatment used to mitigate alkali-silica reaction in concrete

J. Lizarazo-Marriaga, J. Lozano, J. Silva & L. Fonseca
Universidad Nacional de Colombia, Bogotá, Colombia

G. Hermida
SIKA Colombia, Bogotá, Colombia

P. Claisse
Coventry University, Coventry, UK

ABSTRACT: Lithium compounds are used to prevent alkali–silica reaction (ASR) in concrete. If lithium is mixed in wet concrete, the swelling effects of ASR are mitigated. Electrochemical lithium impregnation techniques have been also used successfully on a number of older structures. This paper evaluates the electrochemical penetration and ASR performance of lithium in hardened concrete. Reactive Colombian aggregate and commercial cement were used to prepare mortar mixes and lithium nitrate performance was evaluated using the accelerated ASTM C1260 Mortar-Bar Method. Two penetration methods were used to introduce lithium into concrete. First, concrete was mixed with lithium in the mix water and expansion was measured using ASTM C1260. Second, lithium ions were migrated into ASTM 1260 mortar bars using an electric field.

A novel experimental method was developed for electrochemical treatment and assessment of the mortar bars. Samples were cast in ASTM C490 molds used in determining the length change of mortar bars ($25 \times 25 \times 250$ mm). Stainless steel electrodes were used in the migration cells, which were filled using 0.3 M KOH + 0.1M NaOH in the cathode reservoir and 30% $LiNO_3$ in the anode reservoir. Voltages of 15 and 20 Volts were applied for 4 days. After electrochemical treatment, samples were tested to ASTM C1260. Compressive strength tests were carried out to determine the effects of lithium. Results indicate that lithium significantly mitigates the reactivity of aggregate and the ionic lithium migration seems to be more effective than initial mixing.

Keywords: alkali–silica reaction (ASR), electrochemical lithium impregnation, lithium migration.

1 INTRODUCTION

The alkali-silica reaction (ASR) is one of concrete's many pathologies that need special care when it is involved, or potentially involved, in the construction of a concrete structure. This reaction takes place when alkali ions, such as Na^+ and K^+ react with a specific type of reactive silica compounds present in the concrete aggregates, forming a gel that absorbs water and increases its volume causing an increase of pressure inside the concrete (Page, 2007). The result on the large scale of this microscopic reaction is cracking of the hardened concrete, causing severe damage to the structure.

Therefore, many studies have been conducted in order to understand and analyze the occurrence of this phenomena and, even more importantly, ways to prevent and mitigate ASR.

One successful way to partially prevent ASR occurrence is by adding lithium salts to the concrete (McCoy, 1951). This admixture may slow down the reaction when applied on fresh concrete and it can also work when applied to hardened concrete via an electrochemical process (Wang, 2012, Thomas, 2004).

The adding of lithium as an admixture is a way of preventing the reaction from happening, or, at least, making it occur at a lower rate (Folliard, 2002). Giving the hardened concrete an electrochemical treatment is a way of controlling the ongoing ASR. This treatment can be carried out because of the concrete's structure, in which the pores can be used for ion migration. For this to happen, two electrodes must be placed on the concrete so that lithium ions may be forced into the concrete thought its pores by the electrical field that is applied. Adapting Electrochemical Chloride Extraction technology, a method was implemented to electrochemically drive lithium ions into the concrete.

Although several reports on experimental electrochemical lithium impregnation on real structures (i.e., bridge decks) have been published (Thomas, 2004) (Folliard, 2002), real tests are expensive and limited. This paper shows research to investigate small scale

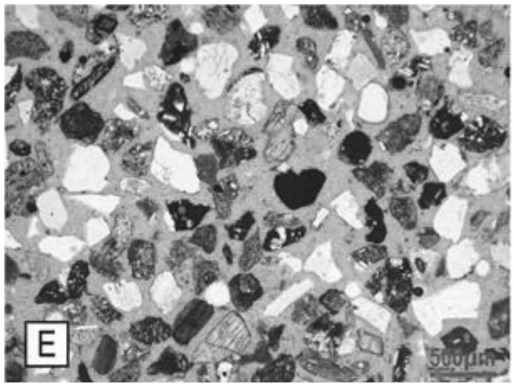

Figure 1. Sand particles (#100).

laboratory experiments, which can also be effective. In this work the electrochemical penetration and ASR performance of lithium nitrate in hardened concrete has been assessed. For this, a reactive Colombian aggregate and high alkali cement were used to prepare mortar mixes and two methods of impregnation were investigated. Concrete was mixed with lithium in the mix water and lithium ions were migrated into ASTM 1260 mortar bars using an electric field. After the treatment, expansion was measured using ASTM C1260.

2 EXPERIMENTAL PROCEDURES

2.1 *Materials*

A reactive Colombian aggregate from a quarry located in the southern Pacific area of the country was used. It was crushed and prepared in order to obtain the grading requirements of ASTM C1206.

The aggregate was mainly particles from igneous origins, such as basaltic andesite and volcanic tuffs, with porphyritic texture, characterized by considerably large crystals of plagioclase, pyroxenes, micas upon others, floating on a microcrystal (holocrystalline), volcanic glass (holohyaline) or mixed (hypocrystalline) matrix, with partially or totally devitrified sectors, with some amorphous silica content.

Based on thin section microscopical analysis, the internal composition of the constituents was determined and it was found that some aggregates presented specific characteristics that could make them potentially reactive or harmful. This was the case for the basaltic andesite with holohyaline or hypocrystalline texture, with tuffs, cherts, quartzite and polycrystalline quartz, representing a 70% of the sample. Figure 1 shows a thin section of the aggregate used.

Commercial blended limestone cement was used. Results for the alkali oxides determined by XRF were 0.11% for Na_2O and 0.7% for K_2O. The total equivalent alkali contribution of the cement ($Na_2O + 0.658K_2O$) was 0.57 percent. A commercial lithium based admixture was used, which was a solution containing 30 percent lithium nitrate ($LiNO_3$).

2.2 *Mix design*

Two different kinds of mortar mixes were prepared according to the ASTM 1260 mortar-bar method (1 inch by 1 inch by 11.25 inches – 25 mm × 25 mm × 29 mm approx.). The proportion used was 1 part of cement to 2.25 parts of dry graded aggregate by mass. The water to binder ratio was set equal to 0.47 by mass. A group of standard mixes was cast without the ASR inhibitor and another group of mixes was cast mixing with the ASR inhibitor.

The dosage recommended by the admixture's supplier corresponds to the standard dosage reported by McCoy and Caldwell's (McCoy, 1951), where the molar ratio of lithium to alkali metals ([Li]/[Na + K]) is equal to or greater than 0.74. The amount of ASR inhibitor depends on the alkali content of the cement used, in which 4.6 litres should be used for every kilogram of total alkali expressed as sodium equivalent. In order to keep the water to binder ratio constant, the free water content was adjusted (0.85 liters of water were subtracted for each litre of ASR inhibitor used).

2.3 *Experiments*

ASR was investigated by measuring the expansion of mortar bars according to the accelerated ASTM C1260 Method, in which samples are subjected to high temperatures and high NaOH concentrations. After casting, mortar bars were stored at laboratory temperature for 1 day and then demoulded and immersed in tap water at 80°C (176°F) for 1 day. After the second day, mortar bars were removed from water and the zero length reading was taken as a reference. Mortar bars were then immersed in a 1 N NaOH solution at 80°C (176°F), and length change was monitored several times per week.

A total of four different groups of samples were tested: a reference without ASR inhibitor, a sample in which the ASR Inhibitor was mixed together with the raw materials, and two samples in which lithium ions were migrated electrochemically after mortar hardening through the application of an electric field at different voltages.

A novel experimental setup was developed for electrochemical treatment and assessment of the mortar bars. The cell consisted of two reservoirs, each containing stainless steel electrodes and electrolyte. The mortar bars (cast in standard ASTM C490 molds) were located between the two reservoirs and an electrical field was applied between the metallic electrodes. For these tests, the catholyte consisted of a solution of 0.3M KOH + 0.1M NaOH, saturated with $Ca(OH)_2$. The anolyte consisted of the ASR inhibitor (30% lithium nitrate solution). Voltages of 15 and 20 Volts were applied for 4 days. After that treatment, samples were tested conventionally according to the ASTM C1260 standard. For each experiment, three replicates were used and the results correspond to the average of those. Table 1 shows a summary of bar expansion tests carried out.

Table 1. Summary of expansion tests.

Sample	Mixing raw materials	Curing (ASTM 1260 – after demolding)	Impregnation treatment (after curing)	Bar expansion measurement (after impregnation)
Ref (reference)	Cement + Reactive aggregate	Hot curing (80°C) during 24 hours	None	Measurement during 26 days in ASTM C1260 conditions
LM (lithium mixed)	Cement + Reactive aggregate + 30% lithium nitrate	Hot curing (80°C) during 24 hours	None	Measurement during 26 days in ASTM C1260 conditions
ET1 (Electrochemical treatment 1)	Cement + Reactive aggregate	Hot curing (80°C) during 24 hours	Electrochemical impregnation 15 V – 4 days	Measurement during 26 days in ASTM C1260 conditions
ET2 (Electrochemical treatment 1)	Cement + Reactive aggregate	Hot curing (80°C) during 24 hours	Electrochemical impregnation 20 V – 4 days	Measurement during 26 days in ASTM C1260 conditions

The compressive strength was measured at early (1 or 2 days) and later ages (38 days) to determine the influence of lithium on the mechanical properties of mortar. Normal and hot curing (ASTM 1260) conditions were investigated. For this, a hydraulic testing machine was used in accordance with ASTM C109: "Compressive Strength of Hydraulic Cement Mortars" (ASTM-C109). Three cubic specimens of 2 inches (50 mm) of width were tested on a compression machine for each mix.

3 RESULTS AND DISCUSSIONS

Results for expansion are shown in figure 3. They confirm that the aggregate was potentially reactive as was indicated by the petrographic analysis. For all samples, the expansion was greater than 0.10% after 14 days in the alkaline solution. Length change measurements were taken beyond 14 days in order to understand the expansion at later ages.

For all lithium treatments a decrease in the expansion was observed; however, electrochemical tests were more effective than initial lithium mixing. At 28 days the reference (REF) showed an expansion near to 0.8%, the lithium mixed (LM) showed an expansion near to 0.5%, the electrochemical treatment 1 (ET1) near to 0.45%, and the electrochemical treatment 2 (ET2) near to 0.35%. This represents a reduction of the expansion of 37.5%, 44%, and 56%, respectively compared with the REF. Although the expansion decrease was significant for all treatments, none was sufficient to mitigate the reaction to the limit in the ASTM standard (0.20%). Despite the use of the additive, the expansion obtained was still relatively high.

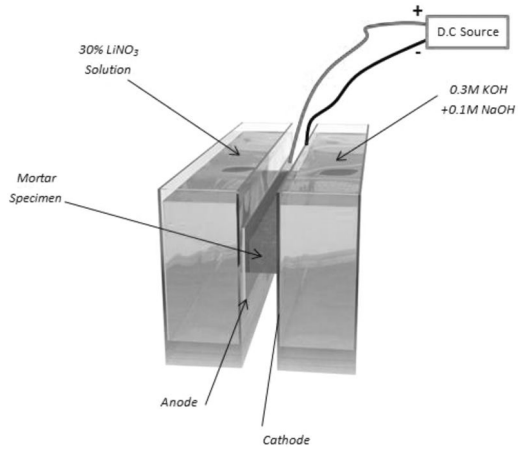

Figure 2. Setup of the electrochemical impregnation treatment developed.

The application of lithium electrochemical treatments in comparison with the direct mixing have shown a significant improvement in controlling the expansion in a concrete affected by ASR. The efficacy of the electrochemical migration treatment seems to be directly related to the voltage applied, with the higher voltage of 20 V proving to be more effective. However for practical applications the voltage could not be too high because of the joule effect and the corresponding rise in temperature. During all experiments, it was noted that the specimen temperature did not rise above 35°C. Figure 4 shows the appearance of mortar bars after experiments. Significant deterioration of samples is apparent after the ASTM C1260 tests. As was expected, the pattern of damage found was in accordance with the expansion measurements. Major cracks were found in the reference samples; however, the cracking decreased when the treatment was applied.

Although for the lithium mixed samples there was a high density of cracks, they were much smaller than those of the reference.

Based on these results, a hypothesis to explain this phenomena is that the electrochemical treatment is more effective than lithium salts mixed into the concrete because during mixing, lithium is partially adsorbed chemically by cement compounds and just a fraction remains within the pore solution to produce an ASR inhibitor effect. In contrast, during electrochemical migration almost all the lithium remains in the pore solution, where an increment in the electrical field gives more penetration into the sample.

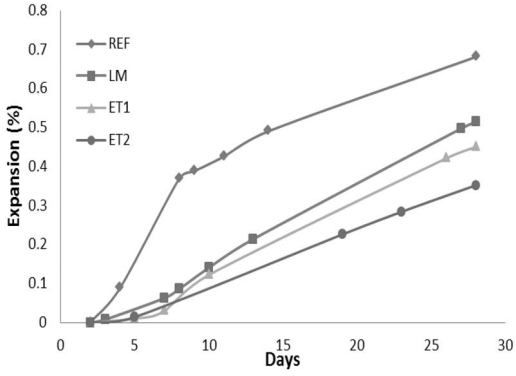

Figure 3. Length change measurements (ASTM C1260).

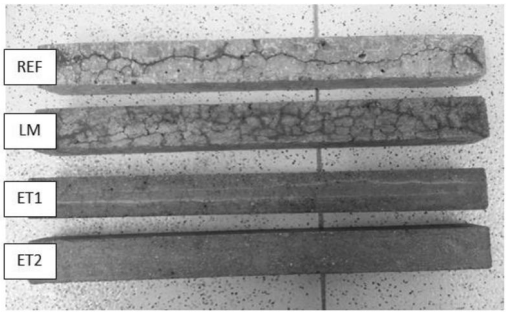

Figure 4. Mortar bar's appearance after experiments.

There will also be significant direct benefits from using the electrical system. The lithium will be a positive ion and will go into the sample but the nitrate (which is not needed to suppress the reaction) will not. Similarly a main beneficial effect of the electromigration will be the removal of the free alkali ions (sodium and potassium) in the pore solution. The potassium ions at the cathode are positive and will not penetrate the sample.

If lithium admixtures are to be used in new concrete structures, it will be necessary to know their effect on the compressive strength. For this, cubes under standard wet curing were tested at 1, 7 and 38 days. In the same way, samples cured using 80°C for 1 day and standard wet curing for the remainder, were tested at 2 and 38 days. Figure 5 shows the results of compressive strength for all samples. It can be seen in the figure that regardless of the method of curing, lithium produces an increase of mortar strength for all ages. For normal curing the increase due to the lithium was around 20% and for hot curing the increase due to the lithium admixture was around 25%.

The main purpose of the 1 day hot curing was to accelerate the hydration of cement as can be seen in Figure 5. However, for accelerated samples, the final strength was always lower than samples cured under standard conditions.

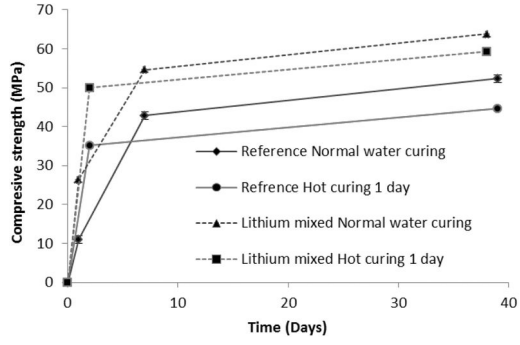

Figure 5. Compressive strength of samples under hot and normal curing.

4 CONCLUSIONS

- Lithium nitrate may be applied effectively to concrete using an electro-migration technique in order to reduce the effects of ASR.
- Results of comparative tests on mortar bars show that this method is more effective than adding lithium nitrate to the original mix. Moreover, as voltage (also current) increases, the linear expansion of the mortar bars decreases. However, precautions should be taken due to the Joule effect when high voltages (>20 V) are applied.
- It is postulated that the increased effectiveness of the electro-migration technique may also be caused by removal of alkali ions.
- However, in the present work, neither method was able to inhibit ASR sufficiently to meet ASTM standards for non-reactive aggregates.
- The addition of lithium nitrate to mortar increases the concrete strength both in normal and hot water curing by at least 20% in the dosages used.

REFERENCES

Folliard, K. J. et al. (2002) "Guidelines for the use of lithium to mitigate or prevent ASR". Federal Highways Administration McCoy W. & Caldwell A. G. (1951) "New approach to inhibiting alkali-aggregate expansion". Journal of the American Concrete Institute, Vol 22, pp 693–706.

Page, C. L. & Page, M. M. (2007) Durability of concrete and cement composites, Abington, England, Woodhead Publishing in materials.

Thomas, M. D. A. & Stokes, D. (2004) Lithium impregnation of ASR-affected concrete: preliminary studies. Proceedings of the 12th International Conference on Alkali-Aggregate Reaction in Concrete. Beijing, China, World Publishing Corporation.

Wang, W. C. et al. (2012) "Effective ASR inhibiting length and applied electrical field under accelerated lithium migration technique". Journal of Marine Science and Technology.

Whitmore, D. & Abbot, S. (2000) "Use of an applied electric field to drive lithium ions into alkali-silica reactive structures". Proc. 11th ICAAR. Quebec City, Canada.

Concrete Solutions – Grantham et al. (Eds)
© 2014 Taylor & Francis Group, London, ISBN 978-1-138-02708-4

Experience and recent innovations in cathodic protection of steel in concrete

R.B. Polder
TNO Technical Sciences/Structural Reliability, Delft, The Netherlands
Delft University of Technology, Civil Engineering and Geosciences, Delft, The Netherlands

W.H.A. Peelen
TNO Technical Sciences/Structural Reliability, Delft, The Netherlands

ABSTRACT: This paper reviews 25 years of experience with cathodic protection of steel in concrete in The Netherlands. Three phases have passed from the late 1980s until present: pioneering, development and maturity. In the first period CP was mainly applied to precast elements corroding due to mixed in chlorides. The parties involved worked together to draw up a Technical Guideline. In the second period, application to bridges was developed, including post-tensioned structures, which was then innovative. Furthermore, galvanic anode systems were introduced. In the third period, CP became a fully accepted method of securing safety and serviceability. The annual number of projects increases considerably and increased competition has reduced prices. Renewed collaboration led to a database that allowed analysis of various aspects of CP system working life; and to new developments in modelling. Major successes and lessons learned will be presented. Technical and non-technical developments are highlighted and some recent findings on long term behaviour are discussed.

1 INTRODUCTION

Corrosion of reinforcing steel in concrete structures may occur, either due to penetration of chloride ions from de-icing salts or sea water spray or due to chloride ions having been mixed in as a set accelerator (Bertolini et al. 2013). Other causes of corrosion are carbonation of concrete, which is only relevant for concrete of poor quality or structures with low cover depths; or stray currents, which are limited to cases where concrete is subjected to strong direct current interference, mainly DC powered railways. Reinforcement corrosion causes concrete cracking, spalling of the cover and steel diameter reduction, eventually resulting in loss of safety. Conventional repair involves heavy, labour intensive and costly work. Competition pressure works against the required quality and quantity levels (cleaning of reinforcement, removal of contaminated concrete). Consequently, conventional repair is short lived in many cases. Corrosion reappears quickly and structures need to be repaired again after a relatively short time, further increasing their life-cycle cost. In a European study it was found that repairs had a short life in practice of ten years on average (Tilly & Jacobs 2007) and a Dutch review of repair projects presented a similar result (Visser & Zon 2012). A completely different situation exists for cathodic protection (CP) as a corrosion protection method. Cathodic protection of reinforcing steel has been applied to concrete structures with corrosion damage in Europe for over 25 years and slightly longer in the US (Broomfield 2006, Grefstad 2005, Nerland et al. 2007, Polder 1998, Wenk & Oberhänsli 2007, Tinnea & Cryer 2008). A recent study reports positive results on long term performance of CP systems in UK motorway structures (Christodoulou et al. 2010). This paper presents experience with CP of concrete in The Netherlands with reference to developments abroad.

Cathodic protection of steel in concrete works by supplying a small direct current from an external electrode, called the anode, through the concrete to the reinforcing steel. This current polarises the steel into the negative direction, suppressing corrosion reactions and forcing (beneficial) cathodic reactions (Pedeferri 1996). The principle layout and the main components for a CP system with a conductive coating on the concrete surface are shown in Figure 1.

2 PIONEERING PHASE 1987–1995

In the 1970s corrosion of steel in concrete developed on a large scale in the US. Early experiments with CP by Stratfull (1974) showed the effectiveness of the principle; subsequently, applications started. In the mid-1980s American technology was introduced in Europe. The first CP system in The Netherlands was installed in 1986/7 on a cycle lane of a bridge, the Stadium Viaduct in Rotterdam (Polder 1998). The anode was made up of carbon filled polymer cables with a copper wire core. This marked the start of the pioneering period of CP in The Netherlands.

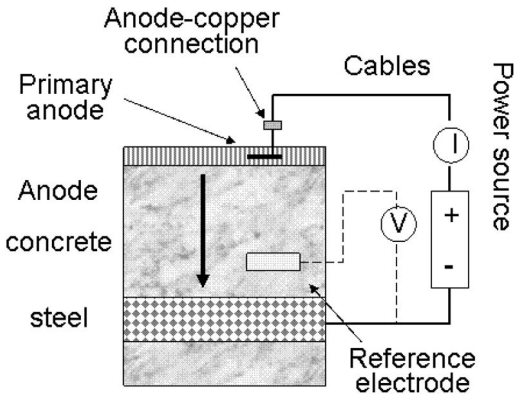

Figure 1. CP system principle layout and main components.

Subsequently, a few projects were made with this anode. Next, activated titanium anodes were introduced and used in a precast concrete façade with penetrated chloride due to proximity of the coast. Titanium strips were placed in holes drilled longitudinally in 2500 precast cantilever beams with mixed in chloride in two apartment buildings in Tilburg in 1990; two more such projects were made in Groningen in 1997 and 1998. It appeared that repair of precast concrete with mixed in chloride was a major problem area in the country that was not solved effectively by conventional repair: after such repairs corrosion and concrete cracking reappeared within a few years in many cases. On the other hand, CP proved to be effective and durable. Carbon based conductive coatings were introduced as anode material and were applied to several buildings. For long term performance of some of these early systems, see section 5. Considering that uniform current distribution was important and would be mainly determined by the electrical resistivity of the concrete, it was felt that the resistivity of materials used for repairs associated with CP should be similar to that of the parent concrete. This notion was adopted by the European Standard on CP of concrete (CEN 2000). CP companies and knowledge institutes worked together to draw up a CUR Recommendation published in 1996 (CUR 1996). It addressed curative application to reinforced concrete and had the character of a guideline including technical considerations and limiting values. In this period, a total of 16 structures had been provided with CP, mainly buildings with mixed in chloride, either with activated titanium anode strips in boreholes or with conductive coatings on the concrete surface.

3 DEVELOPMENTAL PHASE 1996–2004

In the next phase, application of CP to bridges and other infrastructure was developed. In one project, drilled in titanium strip anodes were foreseen in a thick wall of a basement of a bridge where corrosion induced delamination of the cover was widespread. However, reinforcing bars were not positioned at regular intervals as expected and many additional holes had to be drilled to avoid short circuiting between anode strips and reinforcing bars. In this case, steel continuity was largely absent, such that all rebars had to be connected. To avoid this, the preliminary investigation should have looked more carefully for presence or absence of continuity. It also appeared impossible to install a regular maintenance contract between the managing organisation and the CP company.

In another bridge, corrosion had developed in the edge beam of a bridge deck above the abutments adjacent to leaking joints. The complication was that the deck was post-tensioned and concern existed for overprotection, causing hydrogen evolution and possibly hydrogen embrittlement of the prestressing steel. The problem was solved following a consultation with Pietro Pedeferri, who made clear that monitoring the potential of the prestressing steel ducts and maintaining it above a safe value would exclude hydrogen evolution (Pedeferri 1996). This approach and the safe value were later adopted in the European Standard EN 12696, that was published in 2000 (CEN 2000). In addition to allowing CP of prestressed concrete, it also included preventive application, Cathodic Prevention, which had been introduced by Pedeferri (1996). The Standard had a performance based approach (rather than being a technical guideline). In this period galvanic anodes were introduced for CP in concrete, based on the sacrificial action of zinc. Zinc sheet with an ion conductive adhesive was applied to both buildings and bridges. In this period, a total of 79 structures were provided with CP, comprised of buildings with mixed in or penetrated chloride, bridges and parking structures exposed to de-icing salts and swimming pools. In some cases a single structure comprised more than one CP system, e.g. one on the facades and one on a basement floor.

4 MATURITY PHASE 2005-PRESENT

In this period, CP has become a well-accepted method for long term protection of concrete structures with corrosion damage. Involved companies, although relatively small and with economic ups and downs, joined in sponsoring a collective research project by TNO. It included setting up a database of CP systems in the country and further developing numerical modelling of CP (as follow up to previous work in collaboration with Politecnico Milano and in EU project ARCHES). These items will briefly be related here.

Up until 2010, a total of 150 concrete structures in The Netherlands had CP installed, comprised of 105 buildings (apartment blocks, offices, parking and industrial buildings) and 45 bridges and other infrastructure, with a total of 85,000 square meters of protected concrete surface (Polder et al. 2013). A diagram of the number of structures per year that had a CP system installed is shown in Figure 2. These numbers

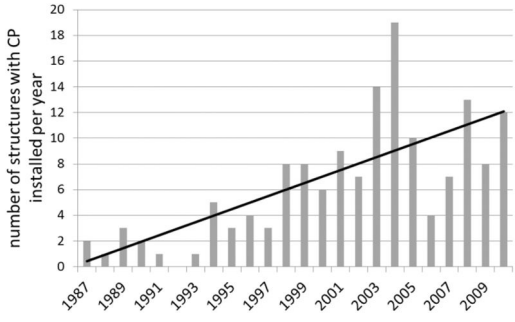

Figure 2. Number of concrete structures with CP systems installed in The Netherlands per year (bars) and trend line.

do not include 65,000 m^2 of ground floor elements with mixed in chloride provided with CP.

Out of 150 CP systems, 65 had conductive coating anodes, 50 activated titanium and 35 galvanic anodes. For 105 systems, good documentation was provided, usually by the company that installed it and carried out maintenance. 50 documented cases had been operating for ten years or more and 55 cases for less than ten years. The remaining 45 cases were not documented and/or not monitored.

The survey and subsequent analysis showed a mixed picture of some weak details and an overall low rate of system degradation (Polder et al. 2013). Weak details included accelerated corrosion of poorly insulated anode-copper connections; and some degradation of primary anodes in coating anode systems, in particular in older ones (see Figure 1). It seems that primary anodes should be made of truly inert materials, e.g. noble metals like platinum; less resistant materials may degrade over the years. Companies had improved most of these weak points, as was borne out by later systems. Very low numbers of overall anode degradation were found. However, local degradation of conductive coatings due to water leakage from overlying parts was an important cause of the need for (some cases of) maintenance. In particular conductive coating anodes on buildings with relatively sheltered facades may last as long as 15 to 20 years; for an example see section 5. Activated titanium systems perform well over at least 20 years in documented cases; working lives of 25 and more years seem very well possible. This experience is in agreement with a recent study on long term performance of CP systems on motorway structures (Christodoulou et al. 2010), which showed that conductive coating anodes may work for a very long time, also in infrastructural works.

Numerical modelling of CP can be attractive in the design phase for minimising anode material while guaranteeing good protection where needed including in depth (throwing power). Such models are a combination of finite element modelling of the steel and concrete geometry and electrochemical input parameters for steel, concrete and anode. First attempts were based on numerical modelling of corrosion (Redaelli et al. 2006) and showed a reasonable agreement with practical cases for preventive effects in a 2-dimensional scheme (Polder et al. 2009). Recent work allows full 3-dimensional modelling of sizeable volumes (up to 1 m^3). However, further work is needed on time dependent effects, although their influence may be rather small beyond a few days or weeks (Polder et al. 2011). Importantly, the polarisation of prestressing steel can be predicted, which facilitates safe application to prestressed structures.

5 LONG TERM PERFORMANCE OF SELECTED CASES

Two cases are reported here. One concerns seven identical apartment buildings dating from the late 1950s with corrosion due to mixed in chloride and partial carbonation. Between 1993 and 1999, the gallery slabs and frames were provided with CP by applying a conductive coating anode and a cosmetic top coat; more information is provided in (Polder 1998). In 2013, the operation and performance of the CP systems was addressed. It appeared that all had been operated at a constant voltage of about 2.0 Volts. Current densities were low (below 1 mA/m2 of concrete surface) and depolarisation was systematically below 100 mV, the minimum value required by the Standard (CEN 2000). Nevertheless, visual signs of corrosion or concrete damage were largely absent. Primary anodes had deteriorated to some extent. In 2014 the need for replacement of primary anodes will be investigated. This case shows that despite some degradation of primary anodes and a generally low current density, causing depolarisation being below the standard's performance criterion, CP is able to provide long term protection of steel and concrete. This should not be taken as proof that less than 100 mV depolarisation should be accepted in general, however.

The second case concerns two apartment buildings each with 528 precast cantilever beams supporting gallery and balcony slabs, with mixed in chloride at levels approximately between 0.4 and 1% of chloride ion by mass of cement. Several beams had developed corrosion and related damage; some were heavily cracked and these were replaced. CP was applied to the remaining beams in 1997 and 1998 by drilling in activated titanium strips in boreholes parallel to the main beam axis, and filling the hole with cementitious grout. These two systems were evaluated in 2013. They operated at a constant voltage of about 2.0 V and the current density running varied between approximately 0.4 and 1.2 mA/m^2 of steel surface area. Depolarisation was between 145 and 240 mV in 24 hours, except one incident in one of the buildings, when it was about 50 mV, possibly due to measuring errors and/or malfunctioning of the data logger. Visual inspection in 2013 revealed the absence of signs of corrosion, except in one beam that may have been disconnected from the system. This example shows that an activated titanium CP system may work well for nearly 20 years at

relatively low current density, including complying to the depolarisation criterion.

6 CHANGING EXTERNAL CONDITIONS

The good experience with CP of concrete structures has been well known to a small group of scientists, engineers and companies involved in CP of concrete. It is becoming of much wider interest for the construction industry, however, as a consequence of the aging of concrete infrastructure. Aging in many cases means degradation in the form of reinforcement corrosion, in particular due to penetration of de-icing salts. From a survey of concrete motorway bridges in The Netherlands it has been found that at an age of 40 years about 5% of these bridges have developed (chloride induced) corrosion related concrete damage, and 50% has such damage after 70 years of service (Gaal 2004, Polder et al. 2012). The majority of Dutch concrete bridges were built between 1960 and 1980. Combining with data on repair life mentioned above (Tilly & Jacobs 2007, Visser & Zon 2012) and assuming a total number of all concrete bridges in the country of 40,000 (i.e. ten times the c. 4000 motorway bridges), further analysis has predicted the amount of bridges with corrosion damage (Polder et al. 2012). For a repair life of ten years, the analysis shows that in 2012 about 500 bridges need repair; in 2024 some 1000 bridges need repair and in 2040 about 2100. A significant (and increasing) number of these repairs involve repair of old repairs! These repairs would involve considerable costs and significant effects on traffic flow. Using CP with an assumed but not unrealistic mean life of 25 years, these numbers would reduce to roughly half. Consequently, large sums of money and societal impact can be saved by applying CP instead of conventional repair.

On another level, a significant development is that organisations responsible for infrastructure tend to employ fewer and fewer technical experts. Risk and responsibility for maintaining infrastructure are more and more transferred to contracting companies, who traditionally have a focus on new construction. Contractors thus are facing responsibility for long-term maintenance of road networks including existing structures, for periods between 20 and 50 years. This poses challenges and opportunities: general contractors are usually not very experienced in concrete repair; yet, a method like CP with a proven track record may very well fit in their business philosophy. Moreover, CP monitoring provides unequivocal data of good performance (absence of corrosion); which usually is the criterion for evaluation of such contracts.

Recently some owners of concrete infrastructure have realized the possibility of corrosion and the expensive consequences. Thus, they have decided to incorporate CP into their asset management schemes for relevant cases. Two are briefly mentioned here.

In 2012 and 2013, CP has been installed on c. 30 motorway bridges on a total of 1300 (precast, post-tensioned) beam heads at risk from corrosion due to joint leakage. Monitoring and maintenance are organised in a 20 year contract. More information will be provided in a paper by Hondel et al. 2014

After having to repair and protect a number of older structures with corrosion induced damage due to leaking joints, the Province of Groningen now has decided on a pro-active policy. In the half-joints of a number of new bridges they have installed cathodic prevention (CPre). As shown by Pedeferri in the 1990s, a low current suffices to prevent corrosion, which allows economical systems to be installed with simple monitoring (Pedeferri 1996). In each of the abutments and in the end beams of the deck, titanium strip anodes precast in cementitious mortar are embedded, to provide preventive current to the reinforcement. Potentials of post-tensioning anchorages and ducts will be monitored. These systems will be commissioned early 2014, so at the moment of writing this paper no data is available.

7 CONCLUSIONS

The experience of the last 25 years or so worldwide has shown that CP is a reliable and dependable method to halt corrosion of reinforcement in concrete structures. This paper focuses on experience in The Netherlands. Three phases can be distinguished: pioneering, development and maturity. In the pioneering phase, CP application to precast elements with corrosion damage due to mixed-in chlorides was developed. Dozens of such structures have been kept safe and serviceable over more than a decade thanks to CP. In the development period, applications were widened to bridges and other structures. In the maturity phase, confidence has grown and smaller projects can now be installed more cost effectively. Lessons have been learned from previous projects, resulting in improved materials and details. Degradation was mainly limited to primary anodes suffering corrosion of insufficiently resistant materials and to accelerated corrosion of anode-copper connections due to poor insulation. Degradation of conductive coating anodes was found to be mild, even over up to 20 years and is significant only under exposure to water leakage. Critical design issues can be addressed by numerical modelling, including minimum anode material use and maximum throwing power, while prestressing steel polarisation can be predicted and kept to a safe level. Overall confidence has grown with both CP companies and owners. Unit prices have decreased due to increased (long term) confidence and improved techniques. At the same time, prices for proper conventional repairs have increased. Based on the market in The Netherlands CP prices for protection of infrastructural works are competitive. CP systems work for a very long time and their good performance is systematically shown by measurements. It is expected that the market for CP of concrete will increase considerably in the next few years up to a decade, in particular in infrastructure.

ACKNOWLEDGEMENTS

The input of members of the Dutch Knowledge Centre for CP of concrete (www.kb-kenniscentrum.nl) is appreciated. The permission to publish case information obtained from Housing Company "Christelijke Woningstichting Patrimonium" Groningen is gratefully acknowledged.

REFERENCES

Bertolini, L., Elsener, B., Pedeferri, P., Redaelli, E., Polder, R.B. 2013. Corrosion of Steel in Concrete: Prevention, Diagnosis, Repair, 2nd Edition, Wiley-VCH Verlag GmbH & Co. KGaA, Weinheim, ISBN 3-527-33146-8, p. 414.

Broomfield, J.P. 2006. Corrosion of Steel in Concrete, Understanding, Investigation and Repair, 2nd Edition, Taylor and Francis, ISBN 978-0-415-33404-4, pp. 296.

CEN 2000. Cathodic protection of steel in concrete. EN 12696.

Christodoulou, C., Glass, G.K., Webb, J., Austin, S., Goodier, C. 2010. Assessing the long term benefits of impressed current cathodic protection. Corrosion Science vol. 52, p 2671–2697.

CUR 1996. Aanbeveling 45 Kathodische bescherming van wapening in betonconstructies, Cathodic protection of reinforcement in concrete structures, in Dutch, CUR, Gouda.

Gaal, G.C.M. 2004. Prediction of Deterioration of concrete bridges, Ph.D. thesis, Delft University Press, Delft, Netherlands.

Grefstad, K. 2005.Cathodic protection applied on Norwegian concrete bridges. Experience and recommendations. Eurocorr05, Lisboa.

Hondel, H. van den, et al. 2014. Maintaining and monitoring durable cathodic protection systems applied on concrete bridges with prestressed steel, Concrete Solutions, Belfast.

Nerland O.C.N., Eri, J., Grefstad, K.A., Vennesland, Ø. 2007.18 years of Cathodic Protection of Reinforced Concrete Structures in Norway – facts and figures from 162 installations. Eurocorr07, Freiburg.

Pedeferri, P. 1996.Cathodic Protection and Cathodic Prevention, Construction and Building Materials, vol. 10, n. 5, p. 391–402.

Polder, R.B. 1998. Cathodic protection of reinforced concrete structures in The Netherlands–experience and developments. HERON vol. 43, n. 1, p. 3–14.

Polder, R.B., Peelen, W.H.A., Lollini, F., Redaelli, E., Bertolini, L. 2009.Numerical design for Cathodic Protection systems for concrete, Materials and Corrosion, vol. 60 n. 2, p. 130–136.

Polder, R.B., Peelen, W.H.A., Stoop, B., Neeft, E., 2011.Early stage beneficial effects of cathodic protection in concrete structures, Materials and Corrosion, vol. 62, n. 2, p. 105–110.

Polder, R.B., Peelen, W.H.A., Courage, W. 2012. Non-traditional assessment and maintenance methods for aging concrete structures – Technical and non-technical issues, Materials and Corrosion, vol. 63, n.12, p. 1147–1153.

Polder, R.B., Leegwater, G., Worm, D., Courage, W. 2014. Service life and life cycle cost modelling of Cathodic Protection systems for Concrete Structures, Cement and Concrete Composites, vol. 47, p. 69–74.

Redaelli, E., Bertolini, L., Peelen, W.H.A., Polder, R.B. 2006. FEM-models for the propagation of chloride induced reinforcement corrosion, Materials and Corrosion, vol. 57 n. 8, p. 628–635.

Stratfull, R. F. 1974.Cathodic protection of a bridge deck, Materials Performance, vol. 13, n. 4, p. 24.

Tilly, G.P., Jacobs, J. 2007. Concrete repairs – performance in service and current practice, Bracknell: IHS BRE Press.

Tinnea, J.S,.Cryer, C.B. 2008. Corrosion control of Pacific coast reinforced concrete structures: A Summary of 25 years experience. In: 1st International Conference on Heritage and Construction in Coastal and Marine Environment MEDACHS08, Portugal.

Visser, J.H.M., Zon, Q. van 2012. Performance and service life of repairs of concrete structures in The Netherlands, International Conference on Concrete Repair, Rehabilitation and Retrofitting III, Alexander et al. (eds.), Taylor & Francis, London, ISBN 978-0-415-89952-9.

Wenk, F., Oberhänsli, D. 2007. Long-term experience with cathodic protection of reinforced concrete structures, Eurocorr07, Freiburg.

This page intentionally left blank

Concrete Solutions – Grantham et al. (Eds)
© 2014 Taylor & Francis Group, London, ISBN 978-1-138-02708-4

Durability aspects of electrochemical realkalisation treatment

E. Redaelli & L. Bertolini
Politecnico di Milano, Department Chemistry, Materials and Chemical Engineering "G. Natta", Milan, Italy

ABSTRACT: Electrochemical Realkalisation (ER) is a technique used for the repair of concrete suffering carbonation-induced corrosion of steel reinforcement. It aims at restoring high levels of pH through the application of a temporary cathodic current to steel, and subsequent production of alkalinity at the steel surface; a further mechanism of realkalisation relies on the ingress of an alkaline solution in the concrete through the surface in contact with the anode. ER does not require the replacement of carbonated concrete, if it is not damaged, and so it can be advantageous compared to conventional repair, that usually requires the removal of large amounts of mechanically sound concrete. Although ER was introduced in the 1980s and has been used since then for the repair of carbonated structures, there are still some aspects connected with its application that need further investigation. This paper presents the results of an experimental research aimed at investigating the durability of ER, considering both the realkalisation of carbonated mortar and the protection of reinforcement from corrosion.

1 INTRODUCTION

Electrochemical realkalisation (ER) is a repair method for reinforced concrete structures suffering carbonation-induced corrosion (Polder & van den Hondel 1992, Mietz 1998, Bertolini et al. 2013). It aims at restoring high values of pH in concrete through the application of a temporary cathodic current to the reinforcement, that produces alkalinity at the steel surface, combined with the penetration of an alkaline solution (usually sodium carbonate) from the concrete surface. Similarly to other electrochemical techniques, ER does not require the replacement of carbonated concrete, allowing to minimise the removal of sound concrete, which is a laborious and usually undesired operation. Moreover, being a temporary technique it leaves the surface unchanged allowing its application on complex shapes or when the colour and texture of the surface should be preserved. For this reason, it is often considered suitable for fair-faced concrete elements, statues and artifacts with historical, architectural or cultural value (De Jonge 1997).

Although ER has been used as a repair method for carbonated concrete structures for decades, several aspects connected with its application are not fully clear yet. One of these aspects is related to the durability of the effects of the treatment over time, both in terms of keeping in time the alkalinity of concrete and the protection of steel from corrosion.

Literature contributions on the short-term effects of ER are relatively numerous, for instance in terms of the role of several parameters (as concrete composition and circulated charge) on concrete realkalisation and on corrosion conditions of steel reinforcement (Mietz 1995, Redaelli & Bertolini 2011, Tong et al. 2012, Yeih & Chang 2005). Conversely, contributions regarding the long-term effects are few. This note presents the results of experimental research on the long-term behaviour of concrete specimens subject to the treatment. The evolution of concrete realkalisation and corrosion conditions of steel was monitored on mortar specimens subjected to ER treatment and compared to reference carbonated and alkaline specimens.

2 METHODOLOGY

2.1 *Materials*

A mortar (named *A*) was prepared with a portland limestone cement type CEM II/A-LL 42.5R and water/cement ratio of 0.65 (Table 1). Siliceous sand aggregate was used with rounded shape and maximum size of 4 mm. Mortar *A* was used to prepare both plain (i.e. non-reinforced) and reinforced specimens.

Reinforced specimens contained an ordinary carbon steel bar with diameter of 10 mm, that was obtained by cutting segments with length of 160 mm from a ribbed bar. Bars were drilled on one side for

Table 1. Composition of mortar *A* ($w/c = 0.65$).

Constituent	dosage kg/m^3
Cement CEM II/A-LL 42.5R	377
Water	245
Sand	1620

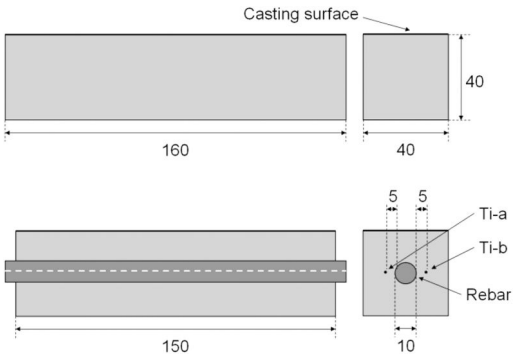

Figure 1. Geometry of plain mortar specimens (*top*) and reinforced mortar specimens (*bottom*). Dimensions in mm.

electrical connection, then they were sandblasted and kept in desiccator until casting of specimens.

2.2 *Specimens*

A total number of 39 specimens were prepared: plain specimens were indicated as A-01 to A-15 and reinforced specimens as A-16 to A-39.

Mortar specimens had dimensions of 40 mm × 40 mm × 160 mm and were used to measure the compressive strength of mortar, to perform absorption tests of the alkaline solution of sodium carbonate (Na_2CO_3 1M) used as anolyte in ER tests and to characterise the resistance to carbonation of the mortar before and after absorption. Reinforced specimens had dimensions of 40 mm × 40 mm × 150 mm and were used to study the corrosion behaviour of steel in alkaline, carbonated and realkalised mortar exposed to an environment with 95% RH and 20°C. Geometric details are shown in Figure 1.

Each reinforced specimen contained two embedded reference electrodes made with a wire of activated titanium (MMO, mixed metal oxide) that were used to monitor the steel potential and to allow electrochemical measurements. The electrodes were placed parallel to the steel bar at a distance of 5 mm, as indicated in Figure 1, and were indicated as Ti-a and Ti-b. They had the same length of the rebar, but they were isolated so that only a short section (with length of 10 mm), in the middle of the specimen, was in contact with mortar.

All the specimens were de-moulded the day after casting and then wet cured at 98% RH and 20°C for 7 days (except specimens used for compression test that were wet cured for 28 days).

2.3 *Experimental tests*

The mechanical properties of mortar *A* were characterised by measuring the compressive strength after 28 days of wet curing on two specimens. The average value of compressive strength was 29.5 MPa.

The rest of the specimens, which were wet cured for 7 days, were allowed to dry in the laboratory for 7 days and coated with epoxy on mortar or steel bar, if necessary. They were used for different types of tests that will be described in the following.

The resistance to carbonation of initially alkaline mortar was evaluated in accelerated conditions (2% CO_2) and in natural conditions (external environment, sheltered from the rain). The specimens were sealed with epoxy on all sides except one and, after an overall period of 28 days from casting, they were exposed to the carbonation environments. Carbonation depth was evaluated by means of phenolphthalein test (§2.3.1) after various exposure times.

Plain and reinforced specimens that needed to be completely carbonated for the following tests were put in a chamber with 65% RH and 2% CO_2. Two plain specimens were used as sacrificial specimens to check the complete carbonation: when they were completely carbonated (and this occurred after about 40 days), also the rest of the specimens was considered to be carbonated, without any further destructive test. Then, four carbonated plain specimens were used to measure the penetration of alkaline solution of sodium carbonate in the absence of applied current (§2.3.2) and then to measure the resistance to carbonation after the penetration of the alkaline solution, either in accelerated conditions with 2% CO_2 or in natural external conditions. Before exposure to the carbonation environment they were coated on all sides except one. Carbonated reinforced specimens were partly subjected to electrochemical realkalisation treatment (§2.3.4) and partly used as reference to monitor the corrosion conditions of steel in carbonated mortar (§2.3.3). Finally, one reinforced specimen was used for tests of absorption of sodium carbonate, without applied current (§2.3.2).

Alkaline specimens, both plain and reinforced, were used for comparison tests. During carbonation of the previous specimens they were kept in a sealed container to prevent carbonation until the beginning of the tests. Plain specimens were used to measure the penetration of alkaline solution of sodium carbonate in alkaline mortar in the absence of applied current (§2.3.2) and then to accelerated carbonation. Reinforced specimens were subjected to electrochemical realkalisation treatment with duration of 21 days to determine its effects on passive steel embedded in alkaline concrete (§2.3.4). Some specimens were used as reference to monitor the corrosion conditions of steel in alkaline mortar (§2.3.3).

Selected reinforced specimens (realkalised and reference) were used for anodic potentiostatic tests (§2.3.5).

In the following, details of experimental procedures are described. The realkalisation tests, either by absorption of alkaline solution or application of cathodic current, were performed in parallel; before and after realkalisation tests, all specimens were conditioned at 95% RH.

2.3.1 *Measurement of carbonation/realkalisation*

pH indicators were used to detect the advancement of carbonation or realkalisation. Phenolphthalein

Figure 2. View of specimens during absorption test with alkaline solution of Na_2CO_3 1M.

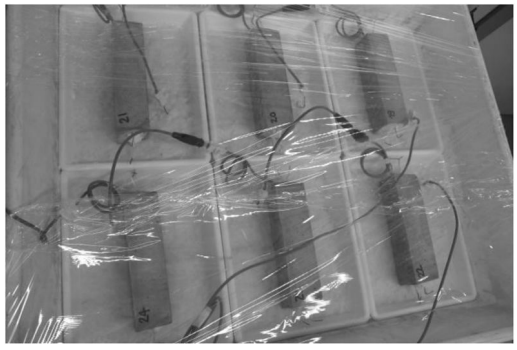

Figure 3. View of specimens during ER test.

indicator (that has a pH transition around 9) and a universal indicator based on thymolphthalein (that has a range of colours as a function of pH, in particular it turns dark blue for pH higher than 12) were sprayed on the freshly broken or cut surface of mortar, and the colour distribution on the surface was observed.

2.3.2 *Absorption tests with alkaline solution*

Tests of absorption of alkaline solution, without any applied current, were carried out on carbonated and alkaline specimens and, in addition, on one carbonated reinforced specimen. The specimens were placed over a layer of cellulose pulp soaked with a solution of Na_2CO_3 1M for 21 days (Fig. 2). The mass of each specimen was measured daily; in addition, after 7, 14 and 21 days some specimens were broken and fracture surfaces were sprayed with phenolphthalein and commercial pH indicators to determine the alkalinity of the mortar.

2.3.3 *Monitoring of corrosion conditions of steel*

Steel potential was measured versus the internal reference electrode Ti-a, that was calibrated versus an external reference electrode (silver/silver chloride, SSC, placed on the cast surface). Corrosion rate was measured with linear polarization technique, by applying a potential of ±10 mV with respect to the free corrosion potential and measuring the circulating current after 30 s.

2.3.4 *Application of ER treatment*

Electrochemical realkalisation treatment was applied with a cathodic current density of 0.5 A/m^2 referred to steel surface. This relatively low value was selected to highlight realkalisation fronts over the mortar thickness of 15 mm. Treatment durations of 7 (ER 7d), 14 (ER 14d) and 21 (ER 21d) days were considered, that correspond to circulated charge densities of 84, 168 and 252 A·h/m^2, respectively. Each specimen was placed over a layer of cellulose pulp soaked with a solution of Na_2CO_3 1M containing an activated titanium mesh as anode (Fig. 3). The cast surface of each specimen was placed laterally, so that Ti-b was at the bottom (close to the anode) and Ti-a was at the top. During the treatment the applied current, feeding voltage and steel potential were monitored with on-off techniques. After interruption of the treatment, some specimens were cut to measure realkalisation.

2.3.5 *Anodic potentiostatic test*

Anodic potentiostatic tests were carried out by applying a potential of +150 mV/SSC to steel reinforcement and measuring the circulating current for a period of 24 h. Potentiostatic tests were carried out on reference specimens and on specimens subject to ER either immediately after the end of the treatment (i.e. about a week after the interruption of the current) or several months later, to investigate the evolution of corrosion conditions of steel.

3 RESULTS AND DISCUSSION

3.1 *Evolution of realkalisation*

The comparison between realkalisation due to simple absorption of alkaline solution of sodium carbonate (evaluated on plain specimens) and realkalisation due to applied current (evaluated on reinforced specimens) was previously discussed in Bertolini et al. (2012), and is shortly summarised here. Figure 4 shows an example of the alkalinity profiles of initially carbonated mortar after 7, 14 and 21 days of absorption of alkaline solution. All specimens showed a high penetration of solution close to the cast surface, that led to an irregular penetration front. This result can be attributed to the higher porosity of mortar in this area compared to the rest of the specimen due to bleeding phenomena (during casting of the specimens this surface was oriented upwards). Hence, the amount of realkalisation was evaluated as the fraction of the surface area with pH higher than 9: average values of 38.7% (7 days), 47.7% (14 days) and 55.9% (21 days) were obtained (Table 2). These results indicate that the realkalisation of a relatively porous mortar with *w*/*c* ratio of 0.65 by the simple contact with the alkaline solution of sodium carbonate does not exceed a depth of few tens of millimetres.

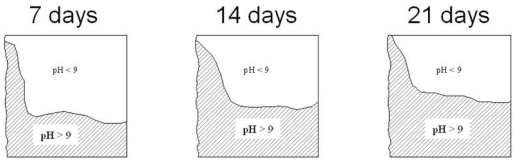

Figure 4. Evolution of mortar realkalisation on an initially carbonated specimen subject to absorption of alkaline solution of Na_2CO_3 1M. Penetration of solution through bottom side; left side (irregular) represents cast surface.

Table 2. Average amount of realkalised area evaluated on plain specimens subject to absorption of alkaline solution of sodium carbonate and reinforced specimens subject to *ER* treatment.

	7 days	14 days	21 days
Absorption			
pH > 9	38.7%	47.7%	55.9%
ER treatment			
pH > 9	54.6%	72.1%	95.6%
pH > 12	9.3%	16.2%	21.8%
9 < pH < 12	45.4%	55.9%	74.7%

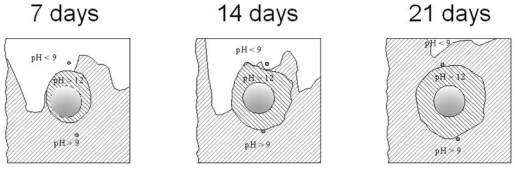

Figure 5. Evolution of mortar realkalisation on an initially carbonated reinforced specimen subject to ER treatment. Anodic system at the bottom side; left side (irregular) represents cast surface.

Figure 5 shows an example of the evolution of realkalisation of an initially carbonated specimen subject to ER treatment. Overlapping results obtained with phenolphthalein and commercial indicator allowed to distinguish areas with pH lower than 9, between 9 and 12, and higher than 12. Average values of the percentage of realkalised surface are reported in Table 2. The realkalised area with pH higher than 9 is considerably higher compared to results from simple absorption tests: 54.6% after 7 days, 72.1% after 14 days and 96.5% after 21 days. Even neglecting the areas with pH higher than 12 (that are certainly due to the cathodic reaction, since the pH of the alkaline solution is around 10.5) and considering only areas with pH between 9 and 12 (that can be attributed to the penetration of the alkaline solution), values of 45.4% (7 days), 55.9% (14 days) and 74.7% (21 days) are obtained, which are higher than those obtained in simple absorption. This suggests that the applied cathodic current contributes to the realkalisation process not only through the cathodic reaction at the steel surface, but also through the promotion of the ingress of the alkaline solution.

Table 3. Average depth of carbonation measured with phenolphthalein tests on plain specimens before and after absorption of the alkaline solution of sodium carbonate (slash separates replicate values).

	Carbonation depth mm
Initially alkaline mortar	
Accel. (2% CO_2), 28 days	13/17
Natural (ext. sheltered), 28 days	0/0
Natural (ext. sheltered), 1 year	6/7
Natural (ext. sheltered), 4.7 year	10/12
After penetration of sodium carbonate	
Accel. (2% CO_2), 28 days	0/3
Accel. (2% CO_2), 28 days*	0/0
Natural (ext. sheltered), 28 days	0/1
Natural (ext. sheltered), 3.7 year	>23**

*Alkaline specimens that were not carbonated before absorption of alkaline solution.
**Depth of realkalisation at the end of absorption treatment.

3.2 *Resistance to re-carbonation*

Results shown in the previous section indicate that at the end of the realkalisation treatment both plain and reinforced specimens underwent penetration of the alkaline solution of sodium carbonate and a front of realkalised mortar of at least 15 mm was detected.

The resistance to carbonation of the specimens after realkalisation was evaluated on plain specimens, both in accelerated and natural conditions, and it was compared with that initially measured on alkaline specimens. Results are shown in Table 3.

After 28 days of exposure to 2% CO_2, initially alkaline mortar showed a depth of penetration of 15 mm. After realkalisation, mortar in the same exposure condition showed a negligible depth of carbonation (1.5 mm). Alkaline specimens that were subjected to absorption of the alkaline solution also showed a negligible carbonation depth.

In natural conditions of carbonation, initially alkaline mortar showed depth of carbonation of 6–7 mm after 1 year and 10–12 mm after almost five years. Realkalised mortar showed an almost completely carbonated surface after about four years of exposure, in spite of the alleged buffer effect of the solution of sodium carbonate. It seems that in this case the alkalinity reached through penetration of alkaline solution was more ephemeral compared to that of a sound, non-carbonated mortar. Hence, a discrepancy emerged between results of accelerated tests, that indicate a beneficial effect of the alkaline solution in delaying re-carbonation, and results of long-term tests in natural conditions, that seem to suggest that this effect may vanish on the long term in terms of contribution to protection from future carbonation.

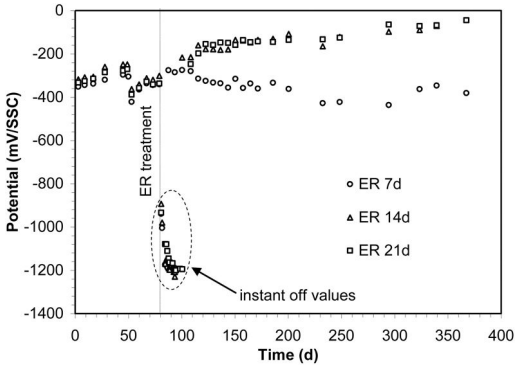

Figure 6. Free corrosion potential of steel of carbonated specimens subjected to ER treatment with various durations, during exposure to 95% RH.

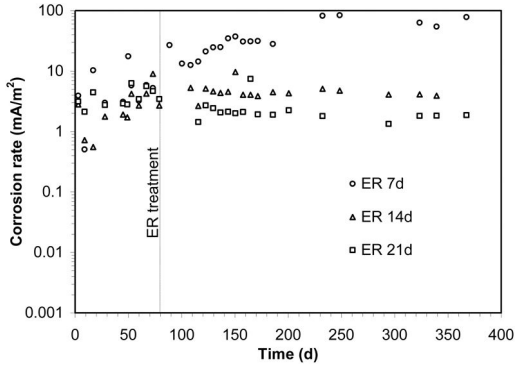

Figure 7. Corrosion rate of steel of carbonated specimens subjected to ER treatment with various durations, during exposure to 95% RH.

3.3 *Corrosion conditions of steel*

The effectiveness of the electrochemical realkalisation treatment in stopping reinforcement corrosion was investigated by monitoring the corrosion conditions of steel in realkalised specimens and comparing with reference specimens, in a wet environment where the propagation of corrosion on active steel is promoted.

Figure 6 shows an example of the trends of potential on specimens subject to ER treatment with different durations (instant off values of potential measured during the treatment are also reported). Before the treatment potential values were between −200 and −400 mV/SSC for all the specimens; these values are representative of active corrosion in carbonated concrete in moist conditions. After the treatment, no substantial changes in potential occurred for the specimens treated for 7 days, while a significant increase in potential was observed on specimens treated for 14 and 21 days. The increase of the free corrosion potential after the application of the treatment is often taken as indication of steel repassivation. Figure 7 shows the trends of corrosion rate measured with the

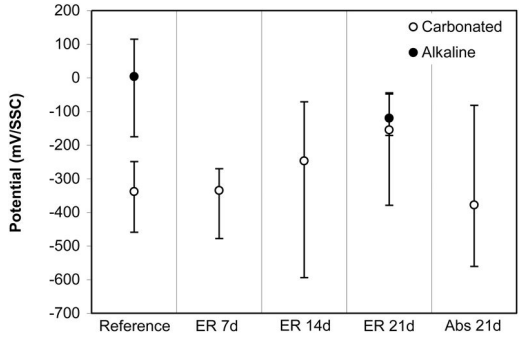

Figure 8. Free corrosion potential of steel during exposure to 95% RH on reference specimens and realkalised specimens.

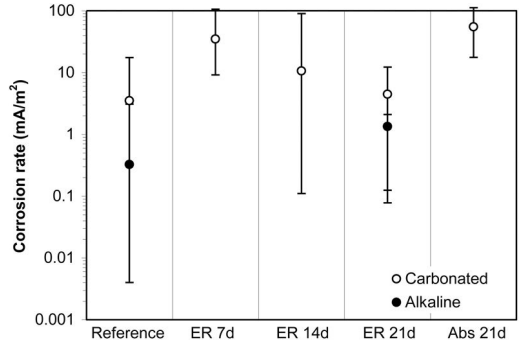

Figure 9. Corrosion rate of steel during exposure to 95% RH on reference specimens and realkalised specimens.

linear polarisation technique on the same specimens. The corrosion rate decreased with increasing treatment duration from values higher than 10 mA/m^2 (much higher than those measured on the same specimen before the treatment) to values of about 2 mA/m^2.

Figures 8–9 summarise the free corrosion potential and corrosion rate for all the conditions considered. In initially carbonated specimens a progressive increase in potential by increasing the treatment duration was observed. However, values measured after 21 days of treatment were still lower compared to passive steel in alkaline concrete. This occurred even for the alkaline specimen that was subjected to the ER treatment for 21 days. For the corrosion rate a similar trend with the treatment duration was observed, since the corrosion rate decreased by increasing the treatment duration, however the values were higher compared not only to passive steel, but also to active steel in carbonated concrete. This apparent detrimental effect of the treatment is in contrast with the expected beneficial effects of an applied cathodic current.

This aspect was further investigated through potentiostatic anodic tests: Figure 10 shows examples of current densities measured during application of a potential of +150 mV/SSC to steel for 24 h. At this potential, if the steel is passive and in contact with

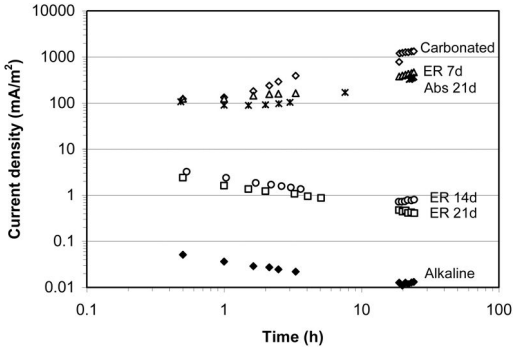

Figure 10. Anodic current density measured on steel during 24 h of polarisation at +150 mV/SSC on reference specimens and realkalised specimens.

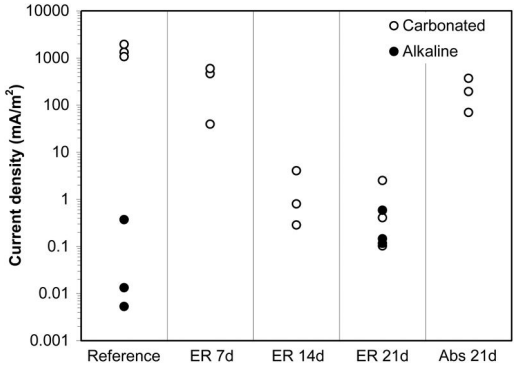

Figure 11. Anodic current density measured on steel after 24 h of polarisation at +150 mV/SSC on reference specimens and realkalised specimens.

alkaline concrete, the circulating anodic current density would be roughly the passivity current density, i.e. a negligible value, as it was obtained for the alkaline reference specimens that showed values of current density always lower than 0.1 mA/m^2. In carbonated concrete the current density was very high, around 100–1000 mA/m^2: such values are representative of active steel. Realkalised specimens showed two distinct behaviours: those with treatment duration of 7 days or with simple absorption of alkaline solution showed values of anodic current density of 100 mA/m^2 or higher, whilst those with treatment duration of 14 or 21 days showed values around 1 mA/m^2, much lower than the previous ones although still higher than passive steel.

Results of potentiostatic anodic tests are summarised in Figure 11 that shows the final value of anodic current density measured after 24 h (multiple values refer to tests repeated at several times on the same specimen). The anodic current density on specimens subjected to ER treatment was progressively decreasing with the treatment duration and it was always lower compared to carbonated reference condition. Considering the anodic current density measured during potentiostatic tests as a measure of the anodic activity of steel, these results are more consistent with the expected progressive beneficial effect of the applied cathodic current in terms of protection of steel from corrosion. Conversely, corrosion rate measured with the linear polarization resistance technique may not be reliable, as it was reported by several authors (Kubo et al. 2008, González et al. 2007). However, comparing results shown in Figure 11 with the realkalisation pattern obtained with pH indicators, it is evident that the detection of a realkalised layer around the steel cannot guarantee by itself the achievement of protection from corrosion, since the corrosion activity of steel can still be relatively high. As a matter of fact, the corrosion activity of steel after 7 days of ER treatment was comparable to that in carbonated concrete, although a layer with pH higher than 12 was detected around the steel bar (Fig. 5).

Finally, Figures 10–11 also suggest that it is unlikely that mortar realkalisation due to the simple absorption of alkaline solution can fully protect steel from corrosion, as indicated by the high corrosion activity of steel highlighted by potentiostatic tests on the reinforced specimen subject to absorption test (Figs. 10–11).

4 CONCLUSIONS

The cathodic current applied during ER treatment contributes to the realkalisation process not only through the production of alkalinity at steel surface but also through the promotion of the ingress of the alkaline solution of sodium carbonate.

The ingress of the alkaline solution by itself, through a mechanism of simple absorption, seems unsuitable to provide a durable protection neither in relation to future carbonation of mortar, nor in relation to the protection of steel from corrosion.

The effectiveness of ER treatment cannot be assessed only through pH analyses, since the detection of areas with high pH close to steel surface may not be representative of protection conditions for steel. However, even the measurement of electrochemical parameters can be misleading; in particular, high values of corrosion rate can be detected after treatment. Although it is unlikely that a treatment with short duration may have a detrimental effect on steel, an incomplete protection may result in a high corrosion activity, comparable to that in reference carbonated condition.

REFERENCES

Bertolini, L., Elsener, B., Pedeferri, P., Redaelli E. & Polder R. 2013. *Corrosion of steel in concrete. Prevention, diagnosis, repair. 2nd edition*. Weinheim: Wiley-VCH.

Bertolini, L., Lupica Spagnolo, S. & Redaelli, E. 2012. Electrochemical realkalization as a conservation technique for reinforced concrete. *International Journal of Architectural Heritage* 6(2): 214–227.

De Jonge, W. 1997. Concrete repair and material authenticity: electrochemical preservation techniques. *APT Bulletin* 28(4): 51–57.

González, J.A., Miranda, J.M., Otero, E. & Feliu, S. 2007. Effect of electrochemically reactive rust layers on the corrosion of steel in a $Ca(OH)_2$ solution. *Corrosion Science* 49(2): 436–448.

Kubo, J., Sawada, S., Page, C.L. & Page, M.M. 2008. Electrochemical inhibitor injection for control of reinforcement corrosion in carbonated concrete. *Materials and Corrosion* 59(2): 107–114.

Mietz, J. 1995. Electrochemical realkalisation for rehabilitation of reinforced concrete structures. *Materials and Corrosion* 46(9): 527–533.

Mietz, J. (ed.) 1998. *Electrochemical rehabilitation methods for reinforced concrete structures. A state of the art report*. London: The Institute of Materials.

Polder, R.B. & van den Hondel, H.J. 1992. Electrochemical realkalisation and chloride removal of concrete. State of the art, laboratory and field experience. In: *RILEM Int. Conf. on Rehabilitation of Concrete Structures, Melbourne, August-September 1992*.

Redaelli, E. & Bertolini, L. 2011. Electrochemical repair techniques in carbonated concrete. Part I: electrochemical realkalisation. *Journal of Applied Electrochemistry* 41(7): 817–827.

Tong, Y.Y., Bouteiller, V., Marie-Victoire, E. & Joiret, S. 2012. Efficiency investigations of electrochemical realkalisation treatment applied to carbonated reinforced concrete – Part 1: Sacrificial anode process. *Cement and Concrete Research* 42(1): 84–94.

Yeih, W. & Chang, J.J. 2005. A study on the efficiency of electrochemical realkalisation of carbonated concrete. *Construction and Building Materials* 19(7): 516–524.

This page intentionally left blank

Concrete Solutions – Grantham et al. (Eds)
© 2014 Taylor & Francis Group, London, ISBN 978-1-138-02708-4

Maintenance and repair of steel reinforced concrete structures by simultaneous galvanic corrosion protection and chloride extraction

W. Schwarz & F. Müllner
CAS Composite Anode Systems GmbH, Wien, Austria

A. van den Hondel
Cathodic Protection Supplies b.v., Capelle aan den Ijssel, The Netherlands

ABSTRACT: A novel galvanic zinc anode system, composed of a zinc mesh embedded into a proprietary binder that solidifies into a solid matrix with ion exchange properties, was developed by CAS. The solid matrix of the embedded zinc anode system (EZA) is based on a tecto-alumosilicate-binder containing additives that prevent passivation of the zinc anode, assure high and durable galvanic activity of the zinc anode and high and durable adhesion towards the concrete overlay.

The efficiency of the galvanic corrosion protection (GCP) of the steel reinforcement with a novel embedded zinc anode (EZA) is evaluated on four types of civil structures – abutment of a road bridge in the Styrian Alps in Austria, concrete abutments of a steel bridge and support-beams for the bearings of four viaducts in the Netherlands and a parking deck in Switzerland.

The efficiency of the GCP was monitored with embedded reference cells, concrete resistivity – and macro cell sensors. Data collected over a period of more than 6 years show that the EZA protects the steel reinforcement efficiently and reliably. Based on these data, estimation of expected service time is discussed. Data indicate an efficient migration of chloride ions towards the anode and their chemical immobilization in the binder matrix.

1 INTRODUCTION

Galvanic corrosion protection of steel in concrete is based on the formation of a galvanic element if a metal less noble than cast iron steel, in direct contact with the concrete overlay, is electrically connected to the steel rebars. The reinforcing steel is protected from corrosion as long as sufficient galvanic current flows between the galvanic anode and the steel reinforcement. Most commonly, zinc is used as the sacrificial anode material. The galvanic element formed corresponds to a conventional zinc/air battery that is becoming popular again as an alternative source of energy.

Galvanic corrosion protection was first employed to protect a bridge deck in Illinois in 1977 within the cooperative highway research program, with mixed results (Kepler et al. 2000). A problem with the initially applied sacrificial anodes was that their protection current decreases with time, and they eventually become passive, so most systems had a relatively short useful life (Virmani & Clemena 1998).

In the 1990's, sacrificial anode systems based on sprayed zinc anodes, zinc foil glued to the concrete surface (zinc hydrogel system), zinc mesh pile jackets around bridge columns filled with sea water were starting to be evaluated and used for the protection of bridge structures (Virmani & Clemena 1998, Kessler et al. 2002, Szabo & Bakos 2006, Bullard et al. 2009). To a limited extent, zinc anodes embedded into the concrete overlay, are used to protect the steel reinforcement especially accompanying concrete repair.

The efficiency of galvanic corrosion protection depends on the lasting activity of the zinc anode. Deposition and agglomeration of the anodic products like zinc hydroxide and zinc hydroxychlorides or contact with calcium hydroxide in the pore solution may passivate the zinc anode surface. Service time of the zinc anode may be limited by self corrosion that increases with the activation of the zinc anode and may reach up to 70% of the zinc consumed during operation.

Sprayed zinc anodes require sufficient humidity and high chloride contents to operate satisfactorily (Bäßler et al. 2006). Experience showed that most failures of galvanic systems occurred due to the failure of the adhesion of the anode to the concrete overlay and due to passivation of the anode exposed to frequent wet dry cycles or due to loss of alkalinity of the embedding mortar. Zinc-Hydrogel anodes are especially sensitive to exposure to high humidity with subsequent delamination.

A novel galvanic zinc anode system, composed of a zinc mesh embedded into a proprietary binder that solidifies into a solid matrix based on a

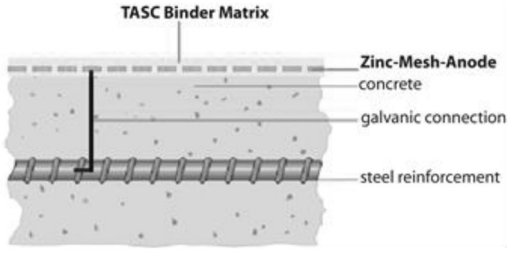

Figure 1. Embedded galvanic zinc anode (EZA): zinc mesh embedded into the EZA binder matrix.

tecto-alumosilicate-binder containing additives that prevent passivation of the zinc anode, assure high and durable galvanic activity of the zinc anode and high and durable adhesion towards the concrete overlay.

The efficiency of the galvanic corrosion protection (GCP) of the steel reinforcement with a novel embedded zinc anode (EZA) is evaluated on four types of civil structures – a road bridge in the Styrian Alps in Austria, concrete abutments of a steel bridge, support-beams for the bearings of a road bridge in the Netherlands and a parking deck in Saas Fee in Switzerland.

2 DESCRIPTION OF THE SYSTEM

The galvanic EZA system is composed of a zinc mesh embedded into the proprietary solid electrolyte (figure 1). The TASC binder matrix is formed by the hardening of the hydraulic binder containing tecto-alumosilicate-cement. The TASC binder matrix function as a solid electrolyte, that ascertains an optimum electrolytic contact between the zinc anode and the concrete overlay, it prevents the self passivation of the zinc anode and therefore assures an optimum and reliable protection of steel reinforcement endangered by, or already damaged by chloride induced corrosion.

The EZA is placed on the surface of the concrete member in which the steel reinforcement is to be protected from corrosion: The concrete surface has to be prepared with the standard procedures for placing coatings on concrete surface (preferably grit blasting, high-pressure (400 bar) water jetting, etc.). Adhesion strength after 24 hours is in the range of 0.6–1.0 MPa, after 7 days >2 MPa and after 28 days about 2.5–3.0 MPa at ambient temperatures of 20–25°C and depending on substrate strength.

The efficiency of corrosion protection of the steel reinforcement by the EZA may be evaluated according to the procedure described in EN 12696 – the 24 h depolarisation criterion and/or by macro cell current measurements (Schwarz & Tritthart 2009). To monitor the efficiency of the installed EZA systems, reference cells, macro-cell-, concrete resistivity, temperature and humidity sensors were installed and monitored with an automated monitoring system.

Figure 2. County road bridge "Alplgrabenbrücke" in the Styrian Alps on the county road B72.

3 FIELD INSTALLATIONS

3.1 *Alpine Road Bridge*

For the evaluation of the efficiency and durability of the EZA system, a road bridge in an alpine region of Styria (Austria) was chosen (figure 2) for the following reasons:

The bridge is located in the Styrian Alps in an altitude of 1000 m above sea level. The climate in that region is characterized by rapid wetting and drying cycles with large temperature differences in the summer including temperature changes crossing the thaw point and by frequent frost-thaw cycles with high exposure to deicing salt during winter.

3.1.1 *Description of Bridge Condition*

The bridge structure showed visible concrete damages – cracks, spalling and corrosion – near the abutment "Birkfeld". Water and saltwater during wintertime penetrated the bridge deck through cracks due to the bridge deck bumping against the abutment. Chloride contents of 4.0–5.6 wt. %/cement weight down to a depth of 2 cm were measured in the areas that were frequently wetted. In the less frequently wetted areas, the chloride content was in the range from 0.5–0.9 wt. %/cement weight, carbonation depth was ≥4 cm at a concrete cover of 20–40 mm.

Therefore one has to assume high corrosion activity of the steel reinforcement of the concrete members with the risk of significant loss of cross section of the steel reinforcement in the future.

3.1.2 *Installation of the EZA – System*

The EZA system for the galvanic corrosion protection (GCP) of the steel reinforcement in the concrete members of the county road bridge "Alplgrabenbrücke" was installed in September 2007. The EZA system was put into operation on 1 November 2007. Operational and performance data were presented at the ICCRRR [8]. The data proved that the steel reinforcement is reliably protected from corrosion by the EZA system. The owner of the bridge – the Styrian department of bridge construction and repair – decided during the general bridge repair, executed from 21 June until 21

Figure 3. View on the EZA installed on the abutment of the Alplgrabenbridge.

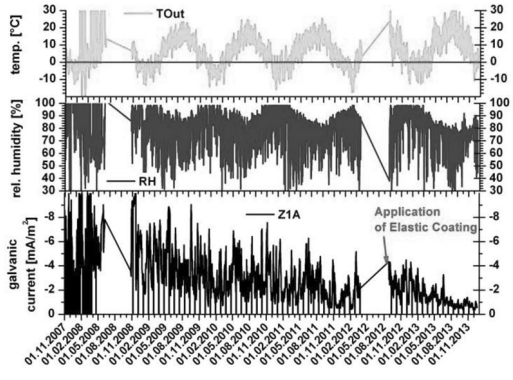

Figure 4. Galvanic Current of the EZA-System in comparison with the ambient relative humidity (RH) and temperature (Tout). Data from 1 November 2007 till 19 December 2013.

August 2012, to take over the EZA on the abutment. To assure frost thaw salt resistance and to increase performance, especially with respect to the galvanic chloride extraction, the EZA was coated with an elastic acrylic coating. In an area of about one m^2, the EZA was renewed by embedding a zinc mesh into the EZA binder on top of the existing EZA (figure 3).

3.1.3 *Data of Operation of the EZA – system*

The operating data of the EZA-system over a period of more than six years (1 November 2007 – 19 December 2013) were evaluated and analyzed with respect to stability, performance and durability (Figure 4):

The course of the galvanic current of the EZA-system show that the initially high galvanic currents decreased during the first three months continuously and stabilized after about 2 years.

The galvanic current decreased at dry ambient air (RH <50%) and temperatures below freezing but increased immediately if humidity levels and/or temperature increased again to the values previously measured at the corresponding humidity and/or temperature levels. Furthermore, the numerous wet/dry and freeze/thaw cycles did not affect the long-term performance of the EZA-system. The galvanic zinc anode protects the steel reinforcement reliably and durable from corrosion.

The efficiency of the corrosion protection of the GCP systems was verified by depolarization

Figure 5. De Meernbrugg steel bridge in Utrecht.

measurements according to EN 12696 (Schwarz et al. 2011, Schwarz et al. 2012). The EZA system is fully functional after seven years of operation enduring seven alpine winters.

Drilled cores showed that in areas where the EZA was soaked with de-icing salt solution from the inside through cracks across the bridge deck, the compound between the EZA mortar and the concrete remained fully intact. The galvanic corrosion protection was therefore guaranteed in all areas in which the EZA anode is installed. From the charge passed during the operation of the system and based on samples of the zinc mesh drawn from various areas, a service time of about 15 years is estimated.

3.2 *De Meernbrug Steel Bridge*

The De Meernbrug Steel Bridge over the Amsterdam-Rijn canal (figure 5) project in Utrecht, The Netherlands, was realized 2010.

Reinforcement corrosion was initiated due to high levels of penetrated chloride readily available from de-icing salts from the overlying road. Over 1% mass of chloride by mass of cement was present at the rebar level in the damaged areas. Undamaged concrete showed high levels of chloride as well, but were slightly lower as in the damaged areas. During repair works a decision was made to change traditional repair work to cathodic protection.

The three main reasons were: reduction of direct costs due to the fact that traditional repair conforming to EN1504-standards would mean excessive removal of chloride contaminated concrete while cathodic protection would mean limited repair of delaminated and disintegrated spots; reduction of risks for future development of concrete damage on the none repaired locations and reduction of over-all execution time of the work being done. For the protection, some minor surface repairs were performed, after which a zinc mesh with a total amount of 4 kg zinc per m^2 of concrete surface was applied on a total of 200 m^2 concrete surface. The EZA system as applied was finalized with an aesthetic coating system based on the Sika Decadex system (figure 6).

Figure 6. De Meerenbrugg steel bridge with EZA installed on the concrete abutment.

Figure 7. EZA installed on the beams supporting the bearings of the Hubertus viaduct in The Hague.

This is a typical installation of an "install and forget" system as there is no need for a power supply on this remote site and no need for extensive monitoring and control as the system is always "on". Both issues were demands made by the department responsible for the future maintenance of the bridge. As inspected in 2013 the system's performance is up to the industry's standards. Expected service time is 25–30 years.

3.3 *'Hubertusviaduct' in Den Haag*

This 2008 project in The Hague was initiated by the municipality. During damage assessment of a large fly-over junction 'Hubertusviaduct,' with 4 abutment walls, there was a chloride induced reinforcement corrosion problem in the concrete just beneath the expansion joints. During the repair works, all expansion joints were replaced with new, water-tight rubber joints. The concrete damage was re-paired and the abutment was cathodically protected.

In total 90 m^2 were covered with zinc mesh with a total of 2 kg per m^2 of concrete (figure 7 & 8). Considering the low reinforcement density, a lifetime of over 10 years is expected. A total area of 90 m^2 of concrete was protected on 4 different locations, divided into 5 separate zones.

Each zone was installed with a decay-probe (activated titanium Ti*) and a reference-electrode (manganese dioxide MnO_2-type). All connections within a zone to the reinforcement, the zinc-anode, the decay-probe and the reference-electrode were made in a connection box. The entire surface was coated with the Decadex coating system.

Table 1. Verification of the effectiveness of the GCP by the EZA by 24 h depolarisation measurements according to ISO EN 12 696. Potential values in mV, measured on beams shown in figure 7.

Date of meas.	Ref. Cell Type	On-potential	Instant-off	4 h off	24 h off	24 h Depol.
30 June 2011	MnO_2	−547	−457	−386	−288	169
	Ti*	−366	−278	−183	−91	187
30 July 2013	MnO_2	−551	−499	−404	−245	254
	Ti*	−356	−314	−237	−70	244

Figure 8. EZA installed on the beams supporting the bearings of the Hubertus viaduct in The Hague.

Table 2. Verification of the effectiveness of the GCP by the EZA by 24 h depolarisation measurements according to ISO EN 12 696. Potential values in mV, measured on beams shown in figure 8.

Date of meas.	Ref. Cell Type	On-potential	Instant-off	4 h off	24 h off	24 h Depol.
30 July 2013	MnO_2	−559	−507	−466	−327	**180**
	Ti*	−288	−245	−194	−115	**130**

Already after a few years, the joints had started to leak again and the EZA was exposed to deicing salt solution during wintertime. The EZA has outlasted six winters, four of them were harsh. Performance has been above expectation in the first 6 years. The system is capable of withstanding water load, deicing salts, proves to be frost-thaw salt resistant and shows no signs of aging.

3.4 *'Parking Deck in Saas Fee*

The parking garage in Saas Fee is designed to take in all cars of tourists and inhabitants of Saas Fee – the village of Saas Fee is free of fuel powered vehicles. The parking deck was erected 1979/80 and extended

Figure 9. Central parking deck in Saas Fee, Switzerland.

Figure 10. EZA-installation in one parking booth.

with a new section 1980/81, offering 2900 parking lots (figure 9).

The concrete overlay of the decks are impregnated with chlorides ranging from 0.5–3.0 wt.%/wt% cement near the loose steel reinforcement. The decks are reinforced with unbonded post-tensioned tendons. Conventional techniques would require the removal of with chloride contaminated concrete, coating of the steel reinforcement and refurbishment with repair mortar or concrete. This procedure would be highly delicate with regard to the unbonded tendons in the parking deck – damage to these tendons has to be avoided under any circumstances.

With regard to the pre-stressed tendons and the risk of CP induced hydrogen embrittlement, galvanic corrosion protection offers a safe and reliable remediation technique. In July 2011, on a parking booth, the EZA system was installed on 30 m^2 concrete surface (figure 10).

The EZA system has been coated with a tough elastic, static crack-bridging waterproofing and wearing surface layer of broadcast total solid epoxy Sikafloor-390, covered by a high abrasion resistant sealcoat of total solid epoxy Sikafloor-354.

The EZA is in operation since August 2011, exposed to the harsh alpine conditions 1880 m above sea level. Data show that it is protecting the steel reinforcement reliably and safely with 0-maintenance expenditures.

4 SERVICE TIME EXPECTATIONS & GALVANIC CHLORIDE EXTRACTION

The maximum expected service time of galvanic systems is usually calculated according to Faradays law from the measured galvanic current integrated over time. The current is usually measured over a relatively large area. Currents may vary strongly locally depending on the humidity, chloride content and on the density of the reinforcement in the concrete overlay. From zinc-mesh samples drawn in August 2012 from the EZA installed on the Alplgraben bridge it is estimated that currents vary by a factor of up to 2,2. Highest current consumption and therefore zinc consumption will occur at areas of high chloride content, high humidity and high density of reinforcement – areas in which corrosion protection is most required. From an mean galvanic current of 3,6 mA/m^2 one would expect a service time of 36 years. Considering the local variation of current densities one may estimate the service time of the EZA of 16 years. Therefore, the service time of the EZA, containing 2 kg Zinc/m^2, is estimated to be about 15 years.

An important aspect with regard to the service time of zinc based galvanic anodes and the durability of corrosion protection of steel in concrete is the "galvanic chloride extraction". Migration leads to an accumulation of anions, especially of chloride ions, at the anode and a depletion of chlorides near the steel rebar surface. Migration is counterbalanced by diffusion. Once the rate of diffusion of chloride ions accumulated at the anode into the concrete cover is equal to the rate of migration towards the anode then no net movement of chloride ions and therefore no further chloride ex-traction will occur. Differing from all other anode systems used for CP or for chloride extraction, chloride ions are chemically immobilized near the zinc anode by reacting with anodically formed zinc hydroxide as zinc-hydroxychlorides – zinc-hydroxychlorides are nearly insoluble in water (Clever et al. 1992). This "one-way" transport of chlorides towards the galvanic zinc anode results in an efficient chloride extraction of chlorides from the concrete cover and subsequentely, leads to the repassivation of the steel reinforcement confirmed by rest potential and macro-cell current measurements. It was proven to be highly efficient in the AS-EZA system in laboratory and pilot trials and is currently evaluated in EZA field installations. One may expect that chloride is efficiently removed from the concrete cover at the end of the service time of the EZA provided that the EZA is coated with an elastic membrane impermeable to liquid water.

5 CONCLUSIONS

The performance of the novel EZA galvanic corrosion protection system, consisting of a zinc mesh embedded into a proprietary non-cementitious binder matrix was evaluated on the abutments of three different civil structures – an alpine road bridge in Austria, a steel bridge in Utrecht, NL and a viaduct in The Hague, NL and on the pavement of a parking deck. Measurements according to ISO EN12696 and with macro cell sensors over a period of up to nearly 6 years show that the EZA system has protected the steel reinforcement of the concrete members reliably from corrosion.

Coating of the EZA with an elastic membrane reduces the influence of ambient humidity and temperature significantly and assures frost-thaw salt resistance. Calculated from the galvanic currents integrated over time and from zinc mesh samples drawn from an EZA field installation, service time of the EZA containing 2 kg zinc/m^2 is estimated to be about 15 years. Results indicate that within the expected service time, galvanic chloride extraction and immobilization in the EZA will be efficient enough to prevent renewed corrosion of the steel after the end of service time.

ACKNOWLEDGEMENTS

The authors gratefully acknowledge the support of the Styrian Road authority that made this project possible.

The authors would like to express their thanks to Katarzyna Komorowska and Rafat Kubik of the Wroclav Research Centre EIT+ for the great care with which ESEM/SEM micrographs and EDX analysis were recorded and analyzed. The results will be presented at the conference.

REFERENCES

Bäßler R., Burkert A., Eichler G., and Mietz J., Integrated Protection System for Chloride Deteriorated Concrete Structures, in M.G. Grantham, R. Jaubertie, C. Lanos, (Eds.), *Concrete Solutions, Proceedings of the Second International Conference on Concrete Repair*, St. Malo, France, 27–29 June 2006: 220–234. Garston Watford: BRE Press

Bullard S.J., Cramer S. and Covino, B., *Final Report – Effectiveness of Cathodic Protection,* SPR 345. Report No. FHWA-OR-RD-09-18, National Energy Technology Laboratory, Oregon, 2009

Clever H.L., Derrick M. E., and Johnson S.A., *The Solubility of Some Sparingly Soluble Salts of Zinc and Cadmium in Water and in Aqueous Electrolyte Solutions*, J. Phys. Chem. Ref. Data 21, 1992, pp 941–999

Kepler J.L., Darwin, D. and Locke JR. C.E., Evaluation of Corrosion Protection Methods for Reinforced Concrete Highway Structures, *Structural Engineering and Engineering Materials SM Report No. 58*, University of Kansas Center for Research Inc., Lawrence, Kansas, May 2000

Kessler R.J., Powers R.G., and Lasa I.R., Un update on the long-term use of cathodic protection of marine structures, *Corrosion 2002*, paper 02254, NACE International

Schwarz W., Müllner F., Van den Hondel A., Galvanic corrosion protection of steel in concrete with a zinc mesh anode embedded into a solid electrolyte (EZA), *Concrete Solutions, Eds. Grantham M., Mechtcherine V, Schneck U. Dresden*, CRC Press, London 2011, pp 163–176

Schwarz W., Müllner F., Van den Hondel, A., Galvanic corrosion protection of steel in concrete with a zinc mesh anode embedded into a solid electrolyte (EZA): Operational Data and Service Time Expectations, *Concrete Repair, Rehabilitation and Retrofitting III,* Eds. Beushausen M.G., Dehn F., Moyo P., CRC Press 2012, pp 357–358

Schwarz W., Tritthart J., *Effect of Cathodic Protection (CP) on Macro Cell Currents: A Viable Method to Monitor and Control the Efficiency of CP?*, Materials and Corrosion, 2009, 60, 138–147

Szabo S., Bakos I., Cathodic Protection with Sacrificial Anodes, *Corrosion Reviews* 24: 2006, pp 231–280

Virmani Y. P., Clemena G.G., Corrosion Protection–*Concrete Bridges Report No. FHWA-RD-98-088*, Federal Highway Administration, Washington, D.C., 1998

Concrete Solutions – Grantham et al. (Eds)
© 2014 Taylor & Francis Group, London, ISBN 978-1-138-02708-4

Extending residual service life of steel reinforced structures by the use of galvanic anodes

G. Sergi & A.M.G. Seneviratne
Vector Corrosion Technologies Ltd., West Midlands, UK

ABSTRACT: Corrosion of steel reinforcement, usually caused from chloride contamination, leads to cracking and spalling of the cover concrete. If patch repairs are carried out, they can often lead to the transfer of corrosion sites beyond the perimeter of the repairs owing to a phenomenon known as incipient anode formation. The use of galvanic anodes within the patch repairs has been successful over the last 14.5 years in avoiding this phenomenon. Furthermore, galvanic anodes used in a grid configuration have also been shown to control reinforcement corrosion. In both cases the use of galvanic anodes had significantly extended the residual service life of the steel reinforced concrete component or structure.

Study of monitored site results and complementary laboratory investigations have increased the understanding of the performance of galvanic anodes in concrete resulting in the development of better performing units. This has widened the scope for the application of galvanic anodes for remediation against corrosion initiation or for controlling corrosion by its initial arrest followed by prevention of further corrosion.

This paper, first, gives examples of achieving enhanced steel reinforced concrete durability by the use of galvanic anodes, presenting and analysing results of discrete anode systems in patch repairs as well as in global corrosion control. Secondly, it presents new studies indicating how corrosion can be stopped over relatively short periods and, with subsequent use of galvanic anodes at relatively low current densities, enable planned effective residual service life extension of structural components.

1 INTRODUCTION

Chloride induced corrosion of steel reinforcement in concrete construction is a major worldwide problem. Chlorides can be introduced into the concrete via de-icing salts or seawater, or, in certain cases, as contaminants or additives in the initial concrete mix. This leads to localized breakdown of the normally passive steel reinforcement in the form of pitting corrosion. The most common repair option is to apply a patch repair where cracked or spalled concrete is removed, the steel is cleaned locally and a fresh repair mortar or concrete is applied. Unless all chloride-contaminated concrete around the patch is removed, however, the repair process can lead to the formation of incipient anodes, new corrosion sites just outside the repaired area driven by the very cathodic steel within the patch (Sergi, G & Page, C.L. 1999, Page, C.L. & Sergi, G. 2000). Further repairs are thus necessary within relatively short timescales. Often, the whole repair process needs to be repeated several times over the residual service life of the structure.

This problem has practically been eradicated as placement of discrete galvanic anodes around the perimeter of patch repairs is controlling incipient anode formation and avoids corrosion initiation over several years (Sergi, G. et al. 2008, Sergi, G. 2011). The oldest site trial in which such anodes were used has been in operation for 14.5 years and, as will be discussed later, is showing no signs of failure. The anodes are continuing to produce sufficient galvanic current to avoid corrosion initiation in the vicinity, a phenomenon termed cathodic or corrosion prevention (Bertolini. L., et al. 1993, Pedeferri, P. 1996).

Similar galvanic anodes have been used in either a grid configuration or as elongated chains parallel to the main steel reinforcement to control low level steel corrosion in yet undamaged reinforced concrete elements which were shown to be at risk of corrosion or where incipient anode formation was considered to be a risk. This application is known as corrosion control whereby no new corrosion sites can be initiated and corrosion at any existing sites is gradually reduced. These have also shown consistently good performance (Sergi, G. 2010).

The continuous monitoring of a number of sites and further laboratory investigation has enabled a better understanding of the performance and capability of galvanic anodes leading to a widening of the utilisation and scope in a variety of applications.

The paper summarises the results of some key trials and illustrates how anodes can be best utilised in the future.

Photo 1. Leicester Bridgeabutments with monitored area indicated.

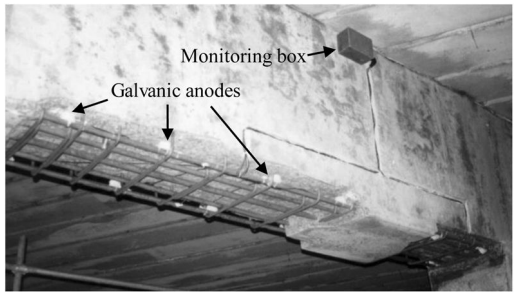

Photo 2. Monitored area prior to application of repair showing position of 12 galvanic anodes and monitoring box of Repair-1.

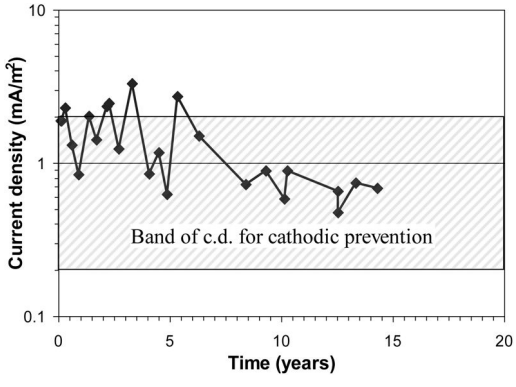

Figure 1. Mean current density with time delivered by the galvanic anodes in Repair-1.

2 SITE TRIALS

2.1 *Corrosion Prevention in Patch Repair*

The longest running trial of galvanic anodes (Repair-1) was set up as part of an overall repair programme of a bridge in Leicester in 1999 (Photo 1).

The concrete area, which had suffered from corrosion of the reinforcement and spalling, was found to contain between 0.9% and 2.2% chloride at the depth of the reinforcement. All the spalled and damaged concrete was removed to about 100 mm behind the bars and until clean uncorroded steel was exposed. Specially adapted galvanic anodes, which ensured that connection to the steel was via a cable to the junction box, were installed around the periphery of the patch at approximately 600 mm centres (Photo 2). The whole area, which was 1.6 m long and 0.89 m wide, was then repaired using a commercially available patch repair material.

The junction box allowed connection and disconnection of each individual anode to the steel reinforcement which enabled monitoring of each individual anode current output. Potential maps were performed whilst the anodes were connected and either 4 hours or 24 hours after disconnection, allowing pseudo-depolarisation and depolarised potentials to be determined.

The current output during the 14.5 years as mean current density over the patch area and up to 300 mm outside the patch in shown in Figure 1. It is still within the 0.2 to 2 mA/m^2 range suggested in BS EN 12696 for cathodic prevention.

The concrete, both within and outside the patch repair, remains in a very good condition with no signs of cracking. The determined depolarisation varied between 10 mV and 95 mV with a mean of around 40 mV. A degree of depolarisation is still achieved up to 300 mm outside the patch repair. The depolarised potential, the potential 24 hours after disconnection of the anodes, has gradually risen from an initial value more negative than −300 mV vs. saturated copper/copper sulphate to between −100 and −200 mV indicating improved passivation of the steel surface with time.

By removing and analysing two anodes in an adjacent repair after 10 years of exposure, it was possible to determine an actual reduction in the mass of the zinc metal in the anodes and compare it to that determined by the total charge delivered by the anodes, as calculated by Faraday's Law, which allowed an estimate in the efficiency of the anodes. This was found to be around 85%. Taking the efficiency into account it was then possible to estimate the weight loss of all the anodes within the monitored area from the current output (Figure 2). This shows a mean consumption of around 45% in 14.5 years indicating that theoretically the anodes on this site have at least a 30 year life.

A newer area, Repair-2, was set up on a column of the same bridge, this time using second generation improved anodes of two nominal current outputs, one (×2) having double the surface area of the other (×1). These were set up within the patch, as shown in Figure 2, at a spacing of 300–400 mm.

Chloride levels at 7 locations outside the existing patch repairs were found to be 1.5–2.7% by weight of cement but were insignificant within the existing patch

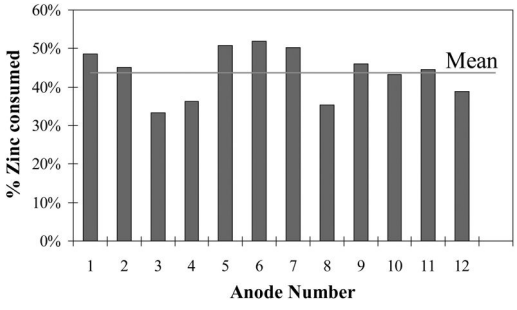

Figure 2. Anode consumption over the 14.5 year period.

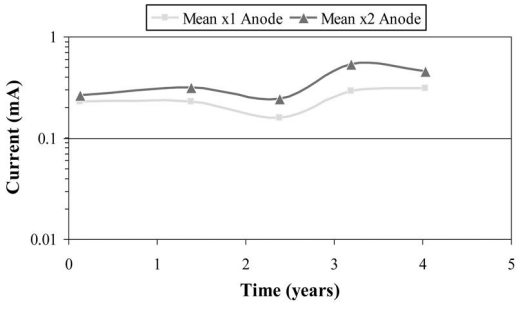

Figure 4. Mean current output of individual anodes in Repair-2.

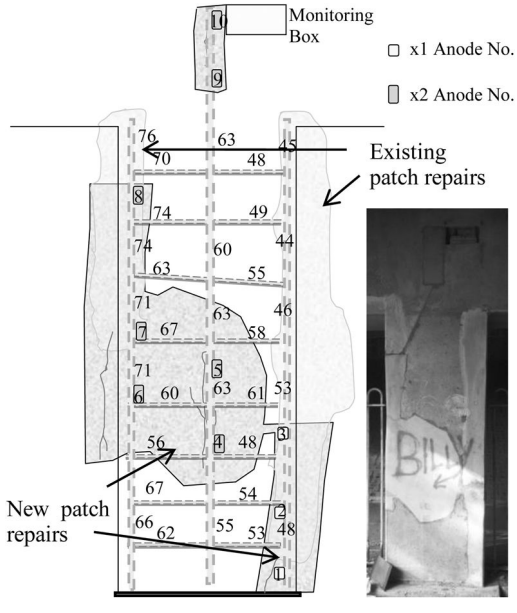

Figure 3. Repair-2 showing existing and new patch repairs, position of anodes, steel cover depth (mm) and location of cracks.

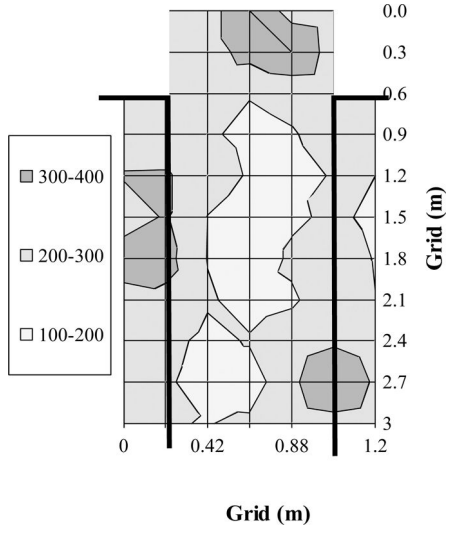

Figure 5. Depolarisation for Repair-2 recorded 24 hours after disconnection of the anodes at 4 years depicted as a contour map.

repairs. The high chloride concentrations had caused corrosion of the reinforcement which led to cracking of the concrete (Fig. 3).

The monitoring was set up as in Repair-1 allowing measurement of the same parameters. Figure 4 indicates the variation of the mean current output of the two sets of anodes, Set-2 (×2), with double the surface area of zinc, delivering more but not always double the current of Set-1 (×1). This translates to a mean current density over the whole column face of around 2–4 mA/m^2.

The mean depolarisation potential as measured 24 hours after disconnection of the anodes, both within and outside the repaired area, was shown to be considerably larger than that recorded for Repair-1. Even though the values were not compensated for ir drop, they still appear as impressive at levels of 200–250 mV, particularly outside the repairs as the anodes are all embedded within the repairs. As an example, the latest recorded depolarisation at Year-4 is depicted in Figure 5 as a contour map.

The Butler-Volmer equation (eq. 1) was used to estimate the corrosion current of the steel reinforcement at roughly annual periods.

$$i_{corr} = \frac{i_{appl}}{\exp\left(\frac{2.3\eta}{\beta a}\right) - \exp\left(\frac{-2.3\eta}{\beta c}\right)} \quad (1)$$

Where, i_{corr} = corrosion current density, i_{appl} = applied current, i.e. current density, η = potential shift, i.e. depolarisation potential, βa = Anodic Tafel Constant (assumed as 120 mV), βc = Cathodic Tafel Constant (assumed as 60 mV).

The corrosion rate was calculated to be 0.02–0.04 mA/m^2, a value much lower than the threshold

Photo 3. Placing of cylindrical anodes in a grid configuration.

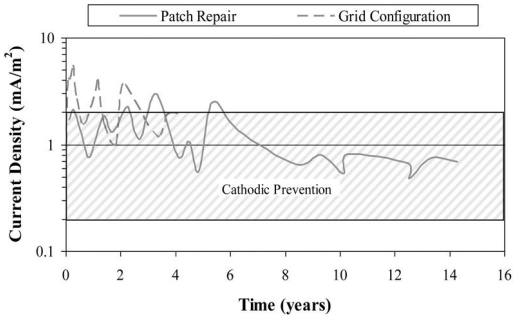

Figure 6. Current density of anodes arranged in a grid configuration compared to the current density in Repair-1.

of 1–2 mA/m^2 assumed to be the limit for acceptable corrosion. This indicates very passive conditions. In comparison, the corrosion current of the steel in Repair-1 ranged in the region of 0.06–2 mA/m^2.

2.2 *Global Corrosion Control*

Two very good but different types of application that have been utilised to control corrosion of the steel reinforcement more globally are presented. The first made use of cylindrical discrete anodes installed in drilled holes in a grid configuration (Photo 3). These were connected together in chains of up to 9 anodes and connected to the steel via a junction box which enabled monitoring of the current.

The current output is shown in Figure 6. Compared to the Leicester trial in a patch repair it is thus far overall higher, the distribution of the current reflecting the larger surface area of the units.

The second example where anodes were utilised in a global way is when long 'rods' were embedded in fresh concrete along the main steel reinforcing bars in order to optimise current delivery (Photo 4). The abutment, requiring both repair and strengthening, had been contaminated with chloride which had caused destructive corrosion of the steel reinforcement. Removal of the

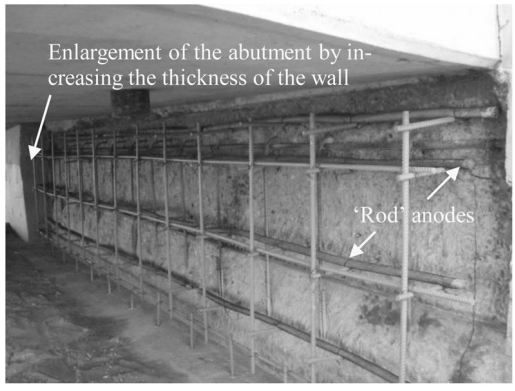

Photo 4. Long 'rod' anodes positioned at strategic locations for optimum current delivery to the existing steel reinforcement during enlargement of the abutment.

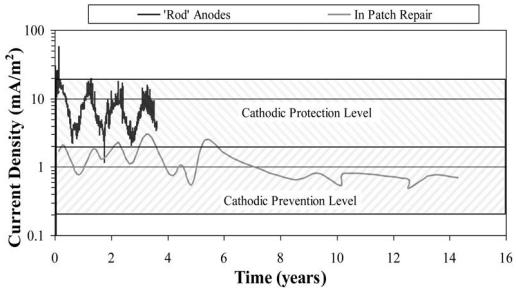

Figure 7. Current density of 'Rod' anodes compared to the current density in the Repair-1.

cover concrete was undertaken and new steel reinforcement positioned ahead of the surface to enable casting of a further thickness of concrete, as required for the upgrade of the bridge. The concern was that chlorides were likely to exist in the concrete beyond the original cover depth leading to renewed corrosion of the existing steel.

The better performance of these types of anode is illustrated in Figure 7. Compared to the Patch repair anodes, these essentially delivered an order of magnitude higher current densities to the steel, levels which are comfortably within the range 2–20 mA/m^2 normally achieved in impressed current cathodic protection systems. Depolarised potentials were constantly higher that 100 mV, sometimes higher than 200 mV indicating that cathodic protection was achieved as defined by BS EN 12696.

3 UNDERSTANDING STEEL POLARISATION

3.1 *Background*

In common with other steel polarisation techniques, anodes placed in a grid configuration polarise the steel reinforcement cathodically and prevent corrosion for considerable periods. Over time, many other

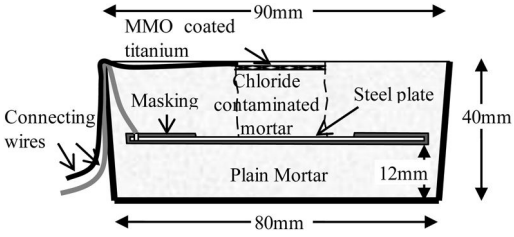

Figure 8. Specimens used for electrochemical treatment of corroded steel embedded in mortar.

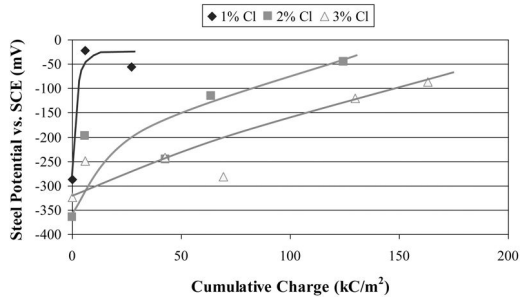

Figure 9. Mean steel depolarised potential after each consecutive passage of charge as a function of increased cumulative charge.

benefits are gained which aid the protection of the steel against corrosion. For example, the essentially cathodic steel repels aggressive chlorides away from the steel concrete interface. Other beneficial effects are the prolonged realkalisation of the steel from the cathodic reaction.

$$\tfrac{1}{2}\,O_2 + H_2O + 2e^- \rightarrow 2OH^- \qquad (2)$$

That, together with the migration of the alkali cations Na^+, K^+ & Ca^{++} to the steel owing to the driving voltage between the sacrificial anode and steel enhance the alkali concentration around the steel and both reinstate and improve its protective passive film. There is also some evidence that solid alkali rich phases deposit within defects and pores at the steel concrete interface, improving the physical barrier against chloride migration (Glass, G.K. & Reddy, B. 2002).

3.2 *Laboratory evidence*

Some evidence of these benefits were seen in controlled laboratory tests. The specimens employed are depicted in Figure 8. The main features were a mild steel plate masked with beeswax in such a way as to expose only a central circular area of around 8 cm^2 of the steel and a counter electrode made of mixed metal oxide coated titanium mesh, both embedded within a Portland cement mortar. The mortar was cast in two stages, a small cylindrical opening allowing a mortar dosed with 0, 1, 2 or 3% chloride by weight of cement to be cast in contact with most of the exposed steel, apart from the edges in order to avoid crevice corrosion. Three sets of specimens were cast in duplicate. Sets 1 and 2 were produced with a water/cement (w/c) ratio of 0.5 and Set-3 with 0.4 w/c.

All the specimens were exposed in a high (>90%) humidity environment to encourage corrosion. Once corrosion was confirmed both by the potential of the steel (around −300 mV or less) and by the galvanic current between the MMO coated titanium mesh and the steel (10 mA/m^2 or more by steel area), a cathodic charge was applied to the steel plate of the specimens. In Set-1 the charge was applied in short periods at an average current density of 30 mA/m^2, each time allowing the steel to depolarise. The process was repeated until the depolarised potential of each specimen indicated passivity. Figure 9 details the results

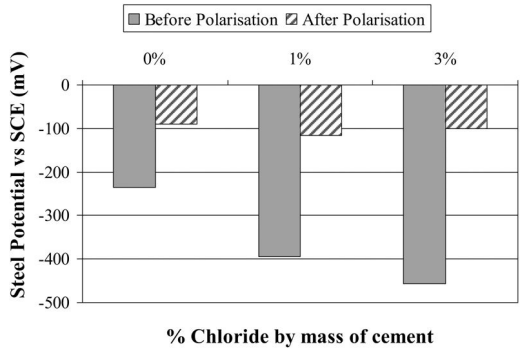

Figure 10. Potential of steel before and after passage of a charge of 150 kC/m^2 in 0.4 w/c mortar specimens dosed with 0, 1% and 3% chloride by weight of cement.

and shows that corrosion of the steel was essentially stopped for all chloride concentrations but it required a higher charge as the chloride level increased.

Sets 2 and 3 were similarly allowed to corrode as indicated by the same criteria. They were then charged at a constant current density of 40 mA/m^2 until a charge of just short of 150 kC/m^2 of steel area was passed in each case. Some specimens were left uncharged and were used as controls. In all cases, the charge was sufficient to stop corrosion (see for example Fig. 10). An interesting observation was the fact that the potentials of all specimens, including those not dosed with chloride, had reached very passive levels of potential of around −100 mV after polarisation.

Control specimens dosed with chloride continued to corrode throughout, as indicated in Figure 11, as opposed to those polarised, which had all achieved passivity.

This effect of reducing and eventually stopping corrosion was seen with the use of galvanic anodes in a steel reinforced concrete slab dosed with 2%Cl^- by weight of cement (Sergi, G. et al. 2011). Anodes placed in three rows of three at a spacing of around 300 mm in a 1 m × 1 m × 0.25 m slab were shown to reduce

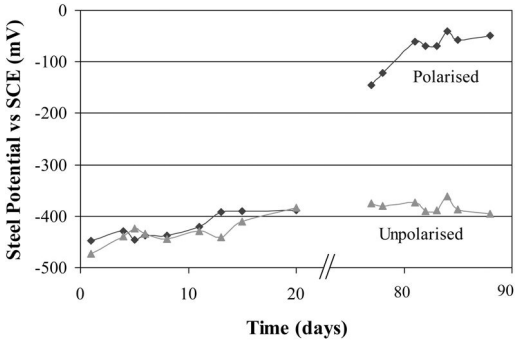

Figure 11. Potential of steel exposed to 3% chloride by weight of cement in 0.5 w/c mortar showing pre- and post-polarisation potentials compared to control unpolarised sample.

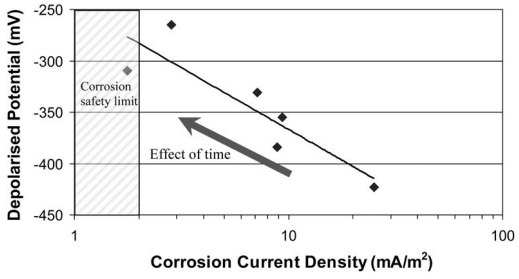

Figure 12. Effect of time on the corrosion current density and the potential of the steel during polarisation by galvanic anodes.

the corrosion current density of the steel to approximately insignificant levels over a period of about 7 months. The mean current density to the steel produced by the anodes was 8.3 mA/m^2 and a total charge of 140 kC/m^2 was delivered over the period. The modification of the corrosion current density and steel potential is depicted in Figure 12. From a corrosion potential of −425 mV vs SCE and a corrosion current density of 26 mA/m^2 indicating high corrosion of the reinforcement, this level of charge achieved at least an order of magnitude reduction in the corrosion current density. For established passivation of the steel it is likely to have required a further charge at this current density, possibly in excess of 200 kC/m^2. Comparing this to the effect of the charge at the higher current density of 30 mA/m^2 (Fig. 9), it appears that a higher current density requires a lower total charge to achieve the same polarising effect.

The inference of the above-mentioned observations is that a two stage process could be designed to achieve long-term protection of steel reinforcement. Furthermore, galvanic anodes are capable of delivering the required current density to achieve the necessary initial arrest of steel corrosion. For a two-stage process, a galvanic anode is required to produce a high enough current output over the required period to deliver the charge required to stop corrosion and passivate the steel. Beyond the passivation, a low current density, 0.2–2 mA/m^2, is then sufficient to maintain the steel in a passive condition and prevent corrosion initiation (cathodic prevention). This lower level of current density will work the same way as the anode-set in Repair-1 ensuring low consumption of the zinc metal and prolonged life.

The work is continuing with the objective of establishing the best combination of early high current density and subsequent constant current density. A better understanding of the beneficially improved properties of the steel/concrete interface following polarization is also being sought.

4 CONCLUSIONS

The conclusions can be summarised as follows:

- Galvanic anodes used to mitigate steel reinforcement corrosion around the perimeter of a patch repair in a bridge have been producing sufficient current over a period of nearly 15 years without any sign of corrosion. They have sufficient zinc still available to continue to protect the steel for a total of up to 30 years.
- Similar anodes positioned in a grid configuration or as a part of long continuous lines of anode set parallel to the main steel reinforcement are also performing well and, owing to improved design, were shown to be capable of delivering currents compatible with impressed current cathodic protection systems. Galvanic systems of this type are low cost and simple to monitor and have flexibility of use.
- It has been shown that cathodic charge applied to steel in concrete can arrest corrosion. The level of charge is dependent on the level of chloride contamination and on the applied current density.
- A two stage process can be designed, first, to deliver a sufficiently high current density to arrest steel corrosion and, secondly, to maintain a lower current density to maintain the steel passivity. This is being further investigated. In particular, better understanding of the possible enhancement of properties of the steel/concrete interface by electrochemical polarisation of the steel is sought.

REFERENCES

Bertolini, L. Bolzoni, F. Cigada, A. Pastore, T. & Pedeferri, P. 1993. Cathodic protection of new and old reinforced concrete structures, *Corros. Sci.* 35: 1633–1639

Glass, G.K. & Reddy, B. 2002. The influence of the steel concrete interface on the risk of chloride induced corrosion, In R. Weydert (ed.), *COST 521: Corrosion of steel in reinforced concrete structures – Final Reports of Single Projects*, Luxembourg University of Applied Sciences: 227–232

Page, C. L. & Sergi, G. Feb. 2000. Developments in cathodic protection applied to reinforced concrete. *J, Mat. in Civil*

Eng., Sp. Issue, Durability of Construction Materials: 8–15

Pedeferri, P. 1996. Cathodic protection and cathodic prevention, *Construction and Building Materials* 10(5): 391–402

Sergi, G. & Page, C. L. 1999. Sacrificial anodes for cathodic protection of reinforcing steel around patch repairs applied to chloride-contaminated concrete, *Proc. Eurocorr '99, European Corrosion Congress*, Aachen, Germany.

Sergi, G., Simpson, D. & Potter, J. 2008. Long-term performance and versatility of zinc sacrificial anodes for control of reinforcement corrosion. *Proc. Eurocorr 2008, European Corrosion Congress,* Edinburgh.

Sergi, G. 2010. Extension of residual service life by galvanic cathodic protection, In K van Breugel, G. Ye & Y. Yuan (eds), *Service Life Design for Infrastructure,. Proc., 2nd Int. Symp., Vol. 2,* RILEM Publications SARL: 613–621

Sergi, G. 2011. Ten-year results of galvanic sacrificial anodes in steel reinforced concrete. *Materials and Corrosion* 62(2): 98–104

Sergi, G. Simpson, D. & Ball, J.C. Nov 2011. Galvanic Anodes for Steel Reinforced Concrete Structures, *Proc. 18th Int. Corrosion Congress*, Perth, Australia, Paper 393

This page intentionally left blank

Concrete Solutions – Grantham et al. (Eds)
© 2014 Taylor & Francis Group, London, ISBN 978-1-138-02708-4

Study on lithium migration for electrochemical treatment of concrete affected by alkali-silica reaction

L.M.S. Souza & O. Çopuroğlu
TU Delft, Faculty of Civil Engineering and Geosciences/Materials and Environment, Delft, The Netherlands

R.B. Polder
TU Delft, Faculty of Civil Engineering and Geosciences/Materials and Environment, Delft, The Netherlands
TNO Technical Sciences/Structural Reliability, Delft, The Netherlands

ABSTRACT: Alkali-silica reaction (ASR) is one of the major durability problems in concrete and affects many structures worldwide. Nevertheless, currently, there are no definite treatments to stop it once it has started. Lithium is known to have beneficial effects on ASR. Indeed, the use of lithium-based admixtures has been acknowledged as a preventive method for over 50 years. Nevertheless, in existing structures, this is no longer possible: lithium ions need to be driven into the concrete and ionic migration is the most effective transport method. Although several studies have been conducted on the use of migration to transport lithium ions into concrete, so far, there is no agreement on the conclusions. It is still necessary to fully understand lithium migration into concrete before developing a possible treatment against ASR. This study aims to investigate lithium migration through experimental testing and modelling.

1 INTRODUCTION

Alkali-silica reaction (ASR) is a deterioration mechanism where hydroxyl and alkali (potassium and sodium) ions interact with reactive siliceous components in the aggregate, forming a gel. This gel is hygroscopic and, as it absorbs humidity from the surrounding pore solution, it swells, building internal tensions. This might lead to deleterious expansion and cracking of the concrete element. Whereas there are plenty preventive methods available against ASR, once the reaction has already taken place, currently, there are no definitive methods to fight against it.

Lithium ions are known to form a non-expansive gel (Feng et al. 2010), when added in the possibly reactive mixture. In fact, the use of lithium-based admixtures has been acknowledged as a preventive method against ASR in new concrete structures for more than 50 years (McCoy & Cadwell, 1951). In hardened concrete, however, the incorporation of lithium ions in the fresh mixture is no longer possible. In this case, ions need to be driven into the cementitious matrix. Amongst ionic transport techniques, such as simple diffusion or vacuum impregnation, migration is the most effective method (Thomas et al. 2007, Santos Silva et al. 2008).

The application of an electric field to transport lithium ions into ASR affected concrete has been investigated by several authors since the 90s (e.g. Page 1995, Whitmore & Abbot 2000, Thomas & Stokes 2004, Santos Silva et al. 2008, Pacheco & Polder 2010, Bentivegna et al. 2011, Liu et al. 2011, Ueda et al. 2013). However, there is no consensus on whether lithium migration is an effective treatment against ASR deleterious expansion. Indeed, full understanding of the principles of lithium migration and its effect on ASR affected concrete is still needed. The present paper brings preliminary results on the investigation on lithium migration through experimental testing and a numerical model is proposed.

2 EXPERIMENTAL

2.1 *Materials and specimen preparation*

Mortar specimens were cast in cylindrical moulds (diameter of 98 mm and height of 50 mm) with water to cement ratio of 0.5 and sand to cement proportion of 3:1, according to EN 196 1:2005. They were cured in a fog room during 36 days. Portland cement type CEM I 42.5 N, standard sand with D_{max} of 2.00 mm (according to EN 196 1:2005) and deionized water were used.

2.2 *Experimental procedure*

A two-chamber lithium migration test was performed in a set-up as described by ASTM 1202 – Standard

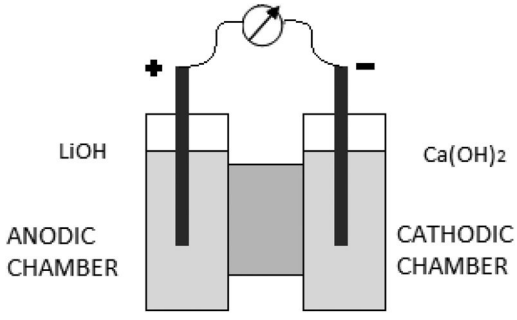

Figure 1. Diagram of the experimental set-up.

Test Method for Electrical Indication of Concretes Ability to Resist Chloride Ion Penetration, shown in Figure 1. In that type of set-up, the specimen is positioned between two chambers with electrolytes, each with a stainless steel electrode. As an electric potential is applied between the electrodes, cations move towards the cathode while anions are attracted towards the anode.

The anolyte was a saturated LiOH solution (4.9 M) while the catholyte was a saturated $Ca(OH)_2$ solution (0.02 M). Two specimens (replicates) were tested under 40 V during a week. Catholyte temperature and passing current were continuously monitored. Electrical resistance of the cell was measured four times during the experiment with a multimeter at 120 Hz, in resistance mode. Resistivity can be calculated by Equation 1 below:

$$\rho = R^* A/L \quad (1)$$

where R = the electrical resistance (Ω); A = specimen surface area (m^2); L = specimen thickness (m).

The pH was also measured four times. For cathodic solutions, a pH-electrode was used. In the anodic solutions, on the other hand, due to high alkalinity (pH above 13), pH test strips were used. Electrolyte samples were collected three times during the experiment and were analysed by Inductively Coupled Plasma (ICP), in order to obtain the concentration of sodium, potassium and lithium and calcium (the latter only in anolyte).

2.3 *Experimental results*

Figure 2a shows the current density that passed through the specimens. In the first couple of hours, the current density rapidly increased, which was also noted by other authors (Pacheco & Polder, 2010; Liu et al. 2011). Maximum current was reached in less than 24 hours and, after that, it decreased until the third day, when it stabilized until the end of the test. Catholyte temperatures during the experiment are shown in Figure 2b. The rise of temperature in all cells influenced the resistivity values, as it will be further discussed. The average of the total charge that passed through the specimens, obtained by the integration of the current plots, was 93442 C, with 10.9% of variation. As no connection issues were detected, further experiments might be necessary to explain this deviation.

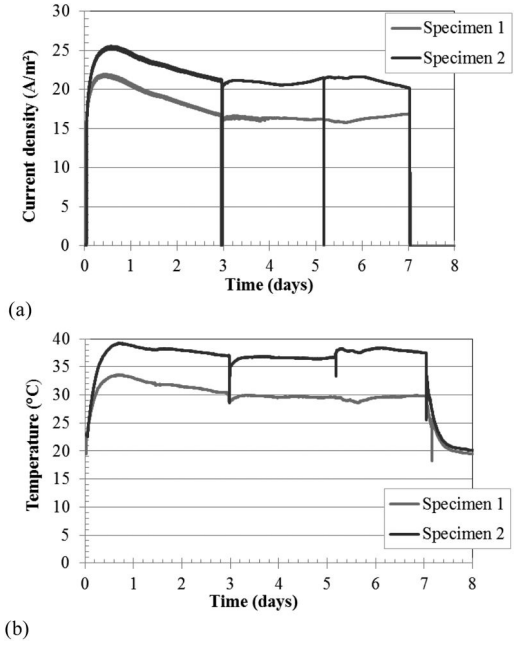

Figure 2. Current density (a) and temperature (b) plots.

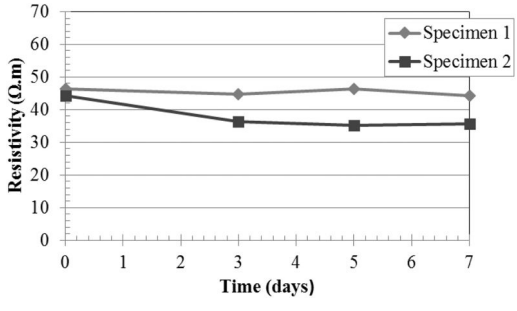

Figure 3. Electrical resistivity.

Figure 3 shows the cell electrical resistivity values during the experiment. The average initial resistivity was 45.30 (±1.58) Ω.m. Comparing Figure 3 and Figure 2(b), it is possible to notice that resistivity and temperature variations are related: higher temperatures led to lower resistivity values and vice versa. These findings are different from what was reported by Pacheco & Polder (2010), where increasing resistivity was noted until the end of the experiment.

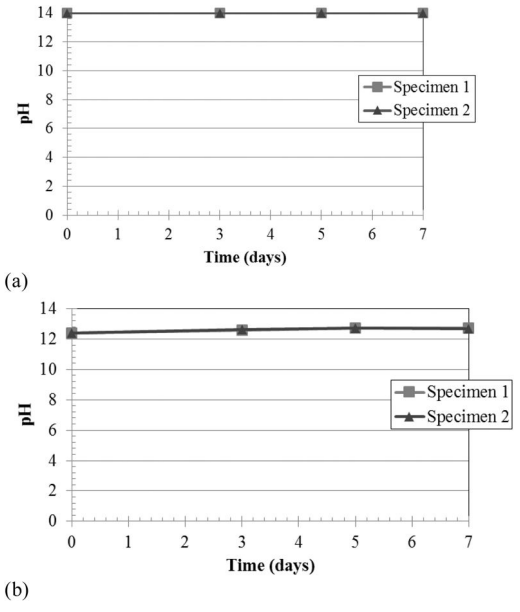

Figure 4. pH of catholyte (a) and anolyte (b).

Variations in pH in catholyte and anolyte are related to the cathodic and anodic reactions, respectively shown in Equations 2 and 3 below:

$$2H_2O + 2e^- \rightarrow 2OH^- + H_2 \quad (2)$$

$$2OH^- \rightarrow H_2O + \frac{1}{2}O_2 + 2e^- \quad (3)$$

The progress of pH during the experiment can be seen in Figure 4. The catholyte in both cells presented a fairly stable pH value around 12, with slight increase during the experiment. On the other hand, the high initial pH of the anolyte resulted in a solution of high buffer capacity. Therefore, the pH remained constant at 14 until the end of the test.

The variations in chemical composition in the anolytes and catholytes are shown in Figures 5 and 6, respectively. As it can be seen in Figure 5, sodium, potassium and calcium ions were transported to the anolyte through diffusion. In fact, both specimens exhibited close behaviour regarding the concentration of potassium and sodium in the anolyte, apart from the measurements on the third day. This difference is probably due to experimental error. Nevertheless, for the rest of the test, both specimens followed similar trend. As for the concentration of calcium in the anolyte, even though there were divergences between specimens, the values fluctuate around a trend. The concentration of lithium in the anolyte, however, was expected to decrease, as ions would enter the specimen (Fig. 5d). At the moment, there is no explanation for the increase in concentration and further investigation is needed. In Figure 6a-b, it is possible to observe the transport of potassium and sodium ions into the catholytes. As expected, the concentrations are much higher than those in the anolyte, evidence that, indeed, migration is the most relevant transport mechanism in this test. Finally, the concentrations of lithium in the catholyte can be observed in Figure 6c.

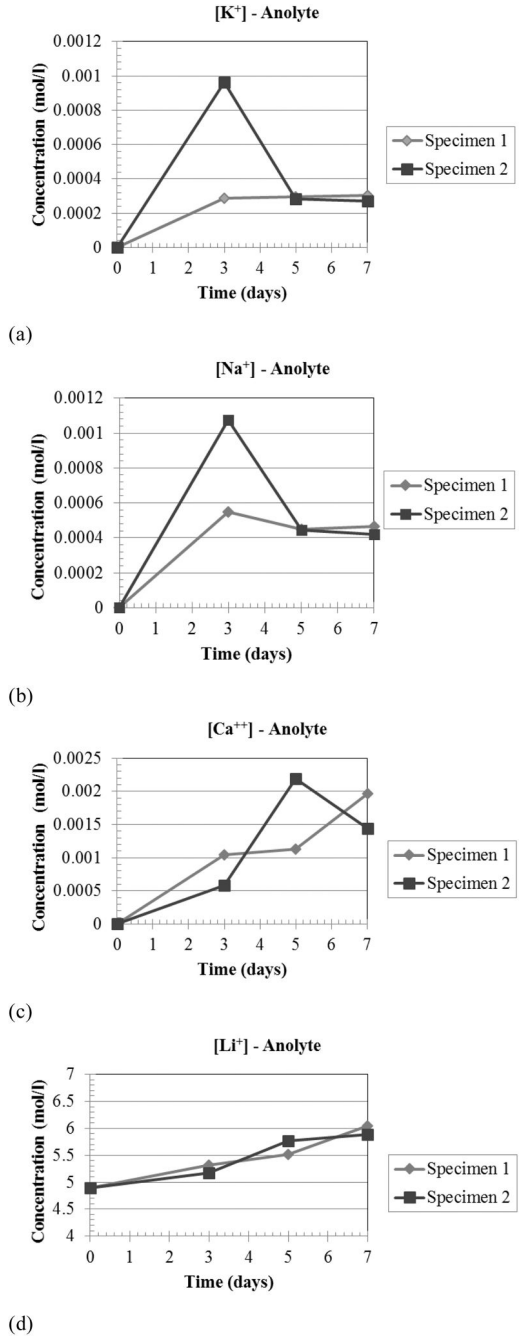

Figure 5. Concentration of potassium (a), sodium (b), calcium (c) and lithium (d) ions in the anolyte.

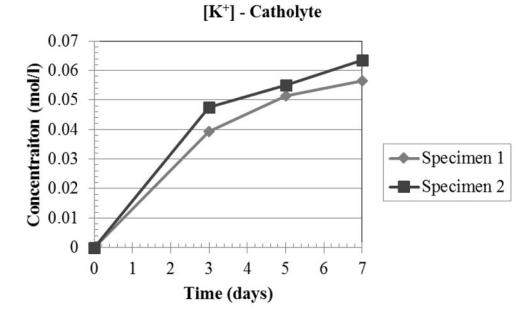

(a)

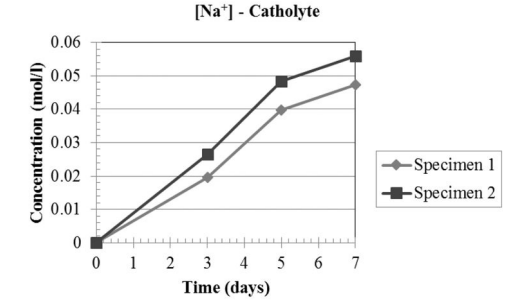

(b)

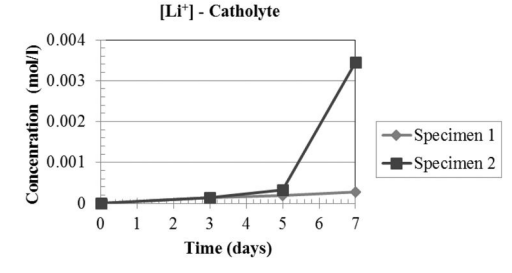

(c)

Figure 6. Concentration of potassium (a), sodium (b) and lithium (c) ions in catholyte.

3 MODEL

3.1 *Mathematical model*

The movement of charged particles in a solution under an electric field can be described by the version of Nernst-Plank equation presented by Equation 4 for ionic transport by convection, diffusion and migration. Besides the mass balance, electroneutrality is assumed and described by Equation 5. The conservation of electric charge is stated by Equation 6 (Newman & Thomas-Alyea, 2012):

$$\frac{\partial c_i}{\partial t} = -\nabla \cdot (c_i \mathbf{u}) + \nabla \cdot (D_i \nabla c_i + u_{m,i} c_i \nabla \phi) + \mathbf{R}_\mathbf{i} \quad (4)$$

$$\sum z_i c_i = 0 \quad (5)$$

Table 1. Ionic mobilities in water solution at 25°C (Moore, 1972; Bertolini et al., 2013).

Cation (+)	Ionic mobility $m^2/s.V$	Anion (−)	Ionic mobility $m^2/s.V$
H^+	36.30×10^{-8}	OH^-	20.52×10^{-8}
K^+	7.62×10^{-8}	SO_4^{2-}	8.27×10^{-8}
Li^+	4.01×10^{-8}	Cl^-	7.91×10^{-8}
Na^+	5.19×10^{-8}	NO_3^-	7.40×10^{-8}
Ca^{++}	5.95×10^{-8}	HCO_3^-	4.61×10^{-8}

$$\nabla \cdot \mathbf{i} = F \sum_{i=1}^{n} z_i \mathbf{R}_\mathbf{i} \quad (6)$$

where c_i = concentration of species i (in mol/m^3); D_i = diffusion coefficient of species i (in m^2/s); $\mathbf{u}$ = velocity of the solvent (in m/s); $u_{m,i}$ = ionic mobility (in m^2/s.V); ϕ = electric potential (in V); $\mathbf{R}_i$ = reaction term (in mol/m^3.s); $\mathbf{i}$ = current density vector (A/m^2).

Ionic mobility is a property related to the size of the ion, including its adherent water molecules, and it is defined as the velocity of the ion in an electric field of unit strength. Ionic mobility values of some ions can be found in Table 1.

The diffusion coefficient of an ion, which describes the movement due to a concentration gradient, is related to the ionic mobility by the Nernst-Einstein equation in Equation 7 (Newman & Thomas-Alyea, 2012):

$$D_i = RT * \frac{u_{m,i}}{z_i F} \quad (7)$$

where R = gas constant (in J/K.mol); T = absolute temperature (in K); u_i = the ionic mobility (in m^2/s.V); z_i = ion valence; F = Faraday's constant (96490 C/mol).

Equations 3–5 describe the movement of ions in a solution. In a porous medium, however, transport is affected by porosity, saturation degree, tortuosity and constrictivity. The factor that takes into account these properties is the effective transport coefficient (Paz-García, 2012), described in Equation 8 below:

$$K^* = \frac{p\theta}{\tau_C} \quad (8)$$

where p = porosity; θ = saturation degree; τ_c = tortuosity-constrictivity factor.

Therefore, in a porous material, ionic transport is described by Equation 9 below:

$$\frac{\partial c_i}{\partial t} = -\nabla \cdot (c_i \mathbf{u}) + \nabla \cdot (K^* D_i \nabla c_i + K^* u_{m,i} c_i \nabla \phi) + \mathbf{R}_\mathbf{i} \quad (9)$$

where c_i = concentration of species i (in mol/m^3); D_i = diffusion coefficient of species i (in m^2/s);

Table 2. Pore solution concentration of a CEM I mortar after 28 days of curing (Bertolini et al., 2013).

Ion	Concentration (mmol/l)
OH^-	391
K^+	288
Na^+	90
Ca^{++}	< 1

$\mathbf{u}$ = velocity of the solvent (in m/s); $u_{m,i}$ = ionic mobility (in m^2/s.V); ϕ = electric potential (in V); $\mathbf{R}_i$ = reaction term (in mol/m^3.s); K^* = effective transport coefficient.

3.2 *Numerical implementation*

A 1-D model was implemented using the Nernst-Planck mode in COMSOL Multiphysics. Three domains were considered: anolyte, (from 0 to 0.04 m) specimen (from 0.04 m to 0.09 m) and catholyte (from 0.09 m to 0.13 m). Equation 3 was used in the domains of the electrolytes whereas Equation 7 described the transport in the specimen. Transport by convection was not considered relevant when compared to diffusion and migration. Therefore, the velocity of the solvent was considered null in all domains.

In the specimen, for concentration of most important ions in the pore solution, values correspondent to similar mortar were taken from Bertolini et al. (2013), as shown in Table 2.

As the specimens were considered to be saturated, the saturation degree was one while the estimated porosity was 20%. The tortuosity-constrivicty factor was estimated by the ratio between the theoretical resistivity (calculated considering the capillary pores as cylindrical tubes) and the measured resistivy and it was considered to be 68.

According to Equations 2–3, OH^- ions are consumed in the anolyte and produced in the catholyte. The reaction rate of OH^- in the electrolytes was estimated by the experimental value of total charge that passed through the specimen and it was equal to -6.9×10^{-6} mol/m^3.s in the anolyte and 6.9×10^{-6} mol/m^3.s in the catholyte. In the specimen, the reaction rate was considered to be null.

3.3 *Modelling results*

Figure 7 shows the model results for the current density that passed through the specimen. They are in agreement with the experimental results (Fig. 2a). In fact, the model result exhibited similar behavior – rapid initial increase of current, slower decrease until a somewhat constant plateau.

In Figures 8–12, it is possible to observe the concentration fronts, in time, of sodium, potassium, calcium, hydroxyl and lithium ions. As expected, sodium, potassium and calcium ions were attracted to the cathode, leaving most of pore solution of the specimen with null concentration by the end of the experiment. It is worth noting that there is an accumulation of those ions at the region of the cathode and this might be important in the

Table 3. Comparison between experimental and model results for final ion concentration in anolyte and catholyte.

	Anolyte		Catholyte	
	Experiment	Model	Experiment	Model
Ion	(mol/l)	(mol/l)	(mol/l)	(mol/l)
Na^+	4.2×10^{-4}	5.7×10^{-3}	5.6×10^{-2}	1.3×10^{-1}
K^+	2.7×10^{-4}	1.4×10^{-2}	6.4×10^{-2}	3.7×10^{-1}
Ca^{++}	1.4×10^{-3}	4.2×10^{-4}		
Li^+	5.9	3.9	3.4×10^{-3}	1.1×10^{-1}

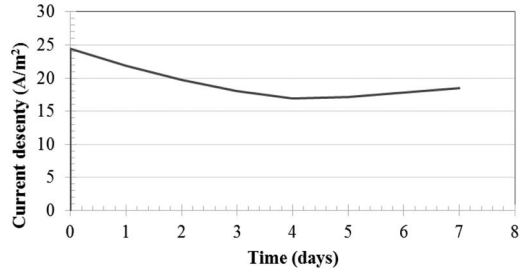

Figure 7. Model result for current density in the specimen.

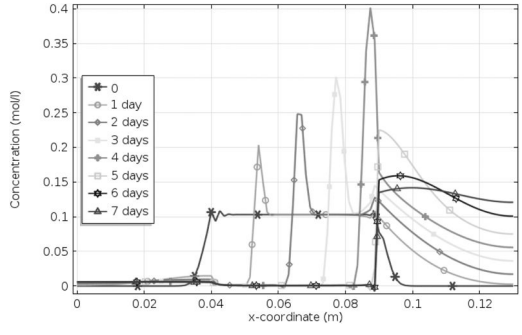

Figure 8. Model result for sodium concentration.

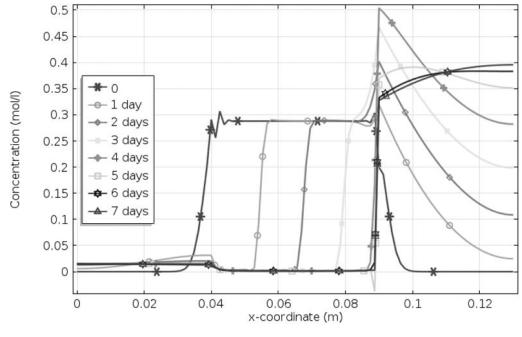

Figure 9. Model result for potassium concentration.

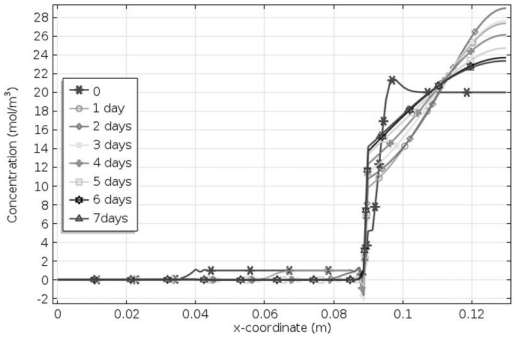

Figure 10. Model result for calcium concentration.

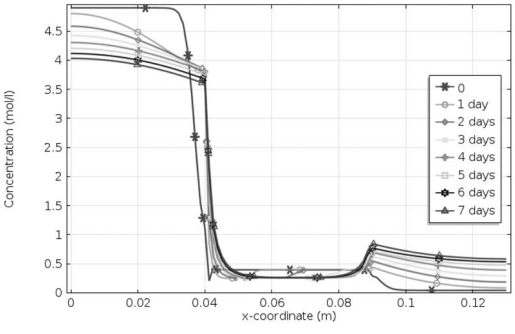

Figure 11. Model result for hydroxyl ions concentration.

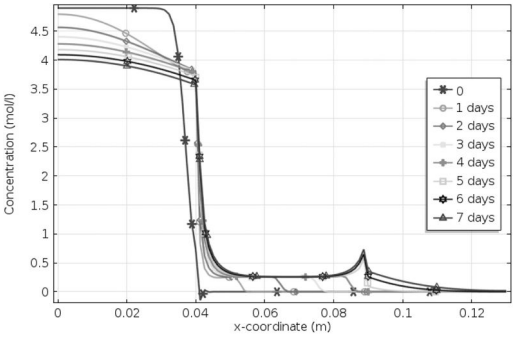

Figure 12. Model result for lithium concentration.

case where a reinforcement bar is used as the cathode. Even though hydroxyl ions are attracted by the anode, as they are consumed by the anodic reaction, there is a decay on the concentration. In Figure 12, lithium front concentration can be observed. Although it is possible to drive lithium ions through the specimen, the model suggests that there is a limit concentration inside of the specimen – once that concentration in the pore solution is reached, lithium ions accumulate in the cathodic area. In order to confirm this behaviour, it is necessary to check the experimental concentration profiles of the specimens and further analysis is needed.

Even though the overall behaviour of the model concentration results was according to theory, when comparing to the experimental results obtained so far, there are divergences. Table 3 brings the comparison between the experimental and model final concentrations in catholyte and anolyte. The concentration of sodium and potassium in both electrolytes and lithium in the catholyte was overestimated by the model, while calcium in the anolyte was underestimated. The experimental final concentration of lithium in the anolyte, as mentioned before, was not expected. One possibility is that there were sampling errors during the experiment. It could be argued that the values for the initial pore solution concentrations did not reflect the reality. However, if that was the case, the model results for the current density would not have agreed with the experimental values, as ions are the charge carriers. Nevertheless, further investigation is still needed.

4 CONCLUSIONS

According to the results of this study, the numerical modelling of lithium migration is possible and it brings more information on the transport mechanism. However there are still divergences between experimental and model results.

This study is a work in progress. Other experiments (e.g. obtaining lithium profiles in the specimens) and future developments in the model (e.g improving the calculation of reaction rates) are still needed in order to better understand the differences between model and experimental results and, finally, obtain the required further understanding of the mechanism behind lithium migration.

ACKNOWLEDGMENT

Financial support by the Dutch Technology Foundation (STW) for the project 10971: “Modelling, non-destructive testing and Li-based remediation of deleterious Alkali-Silica Reaction in concrete structures” is gratefully acknowledged.

REFERENCES

Bertolini, L.; Elsener, B.; Pedeferri, P.; Redaelli, E. & Polder, R.B., 2013. *Corrosion of Steel in Concrete: Prevention, Diagnosis, Repair*. Weinheim: Wiley-VCH.

Bentivegna, A.F.; Giannini, E.R.& Folliard, K.J. 2012. Use of electrochemical migration to mitigate alkali-silica reaction in large scale concrete structures. In. Michael Grahtham, Viktor Mechtcherine & Ulrich Schneck (eds) *Concrete Solutions; Proc. 4th Intern. Conf. of Concrete Repair, Dresden, Germany, September 2011.* London: Taylor & Francis Group.

Feng, X.; Thomas, M.D.A.; Bremmer, T.W.; Folliard, K.J. & Fournier, B. 2010. New Observations on the Mechanism of Lithium Nitrate Against Alkali Silica Reaction. *Cement and Concrete Research* 40(1): 94–101.

Liu, C.-C.; Wang, W.-C. & Lee, C. 2011. Behavior of cations in mortar under accelerated lithium migration technique controlled by a constant voltage. *Journal of Marine Science and Technology* 19 (1): 26–34.

McCoy, E.J. & Caldwell, A.G. 1951. New approach to inhibiting alkali-aggregate expansion. *Journal of the American Concrete Institute* 22: 693–706.

Moore, W.J. 1972. *Physical Chemistry*. London: Longman.

Newman, J. & Thomas-Alyea, K.E. 2012. *Electrochemical Systems.* E-book. Wiley.

Pacheco Farias, J. & Polder, R.B. Preliminary study of electrochemical lithium migration into cementitious mortar. 2010. In Klaas van Breugel, Guang Ye & Yong Yuan (eds) *Proceedings 2nd International symposium on service life design for* infrastructure, Delft, October 2010. Bagneux: RILEM publications.

Page, C. L. & Yu, S. W. 1995. Potential effects of electrochemical desalination of concrete on alkali-silica reaction. *Magazine of Concrete Research* 47 (170): 23–31.

Paz-García, J.M. 2012. *Physicochemical and Numerical Modeling of Electrokinetics in Inhomogeneous Matrices. PhD Thesis, November 2012.* Lyngby: Technical University op Denmark.

Santos Silva, A.; Salta, M.; Melo Jorge, M.E.; Rodrigues, M.P. & Cristino, A.F. 2008. Research on the suppression expansion due to ASR. Effect of coatings and lithium nitrate. In Broekmans, M.A.T.M. & Wigum, B.J. (eds) *Proceedings 13th International Conference on Alkali-Aggregate Reaction in Concrete (ICAAR), June 2008, Trondheim*.

Thomas, M.D.A.; Fournier, B.; Folliard, K.J.; Ideker, J.H. & Resendez Y. 2007. *The use of lithium to prevent or mitigate alkali-silica reaction in concrete pavements and structures. Report from Federal Highway Administration FHWA-HRT-06-133*, Washington D.C: U.S. Department of Transportation.

Thomas, M.D.A. & Stokes, D.B. 2004. Lithium impregnation of ASR-affected concrete: preliminary studies. In Mingshu Tang & Min Deng (eds), *Proceedings 12th International Conference on Alkali-Aggregate Reaction in Concrete (ICAAR), Beijing, October 2004, 659–667*. Beijing: Beijing World Publishing Corporation.

Ueda, T.; Baba, Y. & Nanasawa, A. 2013. Penetration of lithium into ASR-affected concrete due to electro-osmosis of lithium carbonate solution. *Construction and Building Material* 39: 113–118.

Whitmore, D. & Abbot, S. 2. 2000. Use of an applied electric field to drive lithium ions into alkali-silica reactive structures. In M. A. Bérubé, Benoît Fournier & Benoit Durand (eds) *Proceedings 11th International Conference on Alkali-Aggregate Reaction in Concrete (ICAAR), Quebec City, June 2000, 1089–1098*. Sainte-Foy : Centre de Recherche Interuniversitaire sur le Béton (CRIB)

This page intentionally left blank

Concrete Solutions – Grantham et al. (Eds)
© 2014 Taylor & Francis Group, London, ISBN 978-1-138-02708-4

Evaluation of electrochemical repair effects using near-infrared spectroscopic technique

T. Ueda & Y. Hamada
The University of Tokushima, Tokushima, Japan

M. Kohri
Fujita, Tokushima, Japan

A. Nanasawa
Denki Kagaku Kogyo Kabushiki Kaisha, Niigata, Japan

ABSTRACT: Electrochemical repair methods are becoming popular for reinforced concrete (RC) structures deteriorated by chloride attack or carbonation. However, it is difficult to check the repair effects of such electrochemical methods on site. So, a simple method without chemical analysis to judge the repair effect on site is needed. As such, a near-infrared spectroscopic technique has been assessed recently since this technique can detect chloride contents in concrete without chemical analysis. Results obtained in this study showed that near-infrared spectroscopy has the potential to be a useful tool for evaluating repair effects, including the advantage of enhanced alkalinity due to applying electric current.

1 INTRODUCTION

Electrochemical repair methods are becoming popular as the repair methods for RC structures deteriorated by chloride attack or carbonation (Page 2002, Hondel & Polder 1992). However, it is difficult to check the repair effects of such electrochemical methods on site because the appearance of the structure doesn't change by applying electric current. In order to grasp the electrochemical repair effect, chemical analysis for measuring distributions of ions in concrete or long-term measurement of half-cell potential of steel in concrete are necessary. So, a simple method without chemical analysis to judge the repair effect on site has been demanded. A near-infrared spectroscopic (NIRS) technique has been assessed recently since this method can rapidly detect the chloride content in concrete without chemical analysis (Kanada et al. 2005, Kohri et al. 2007, Furukawa et al. 2008). The outline of NIRS application to a concrete structure is shown in Figure 1. Moreover, recent research has suggested that NIRS could detect variations of alkalinity in concrete (Ueda et al. 2012a). As such, there is a possibility that NIRS would be a useful tool for evaluating electrochemical repair effects considering the enhancement of alkalinity due to applying electric current.

In this study, electrochemical chloride removal (desalination) was conducted with reinforced concrete specimens containing pre-mixed chlorides. Absorbed spectrum data by NIRS were measured with the specimens after the electrochemical treatment. As an index

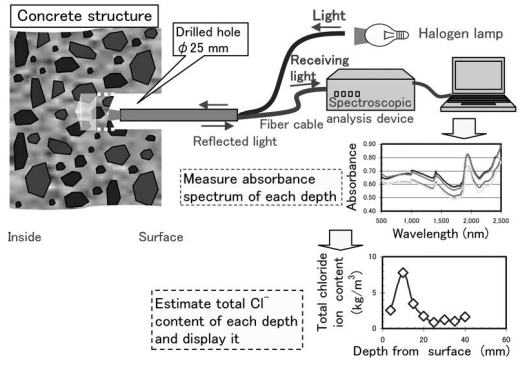

Figure 1. Outline of application of NIRS to concrete structure.

for confirming the repair effect, the molar ratio of chloride ions to hydroxide ions (Cl^-/OH^- molar ratio) was evaluated both by chemical analysis and NIRS method. This index was chosen because it could express not only reduction of the chloride content but also the enhancement of alkalinity after applying electrochemical repair methods.

2 EXPERIMENTAL PROGRAM

2.1 *Preparation of specimens*

Mix proportions of concrete adopted in this study are shown in Table 1. Ordinary Portland

Table 1. Mix proportions of concrete.

W/C	s/a	Gmax	Unit content (kg/m^3)						
(%)	(%)	(mm)	C	W	S	G	NaCl	WRA	AEA
45	48	15	366	165	805	888	13.2	0.9	0.02
55	48	15	324	178	805	888	13.2	0.9	0.02

Where WRA and AEA stand for water reducing agent and air entraining agent respectively.

Table 2. Fresh properties and compressive strength of concrete.

W/C (%)	Slump (cm)	Air content (%)	Compressive strength at the age of 28 days (iN/mm^2)
45	6.0	5.0	39.5
55	7.0	5.0	31.0

cement (density: 3.16 g/cm^3, specific surface area: 3280 cm^2/g) and crushed aggregates (density of fine aggregate: 2.56 g/cm^3, density of coarse aggregate: 2.55 g/cm^3) were used. Water to cement ratio (W/C) of concrete was 0.45 or 0.55 and the amount of premixed Cl^- was 8.0 kg/m^3, simulating a severe condition of chloride induced steel corrosion (Ueda & Miyagawa 2010). Cl^- ions were premixed in the concrete as NaCl dissolved in water. Fresh properties and compressive strength of the concrete are shown in Table 2. From this table it can be seen that there is no remarkable difference of slump and air content between the two mixtures of concrete. However, compressive strength of the 0.45 W/C concrete was 1.3 times greater than the case of 0.55 W/C.

Specimens prepared in this study were reinforced concrete prisms (100 × 100 × 200 mm) with a deformed steel bar D13 SD295A in the center of the square section. After membrane curing for 28 days in a room with a controlled temperature of 20°C, five concrete surfaces of the each specimen were coated with epoxy resin and one surface remained uncoated for permitting passage of electric current.

2.2 *Electrochemical treatment*

After the coating, each specimen was immersed in an electrolyte liquid in a plastic container and direct electric current was supplied between rectangular shaped titanium mesh as the anode and the steel bar in concrete as the cathode. A current density of 1.0 A/m^2 exposed to the concrete area was adopted. The treatment period was 8 weeks. The electrolyte liquid was 0.1 mol/lLi_3BO_3 solution. The experimental factors described above were used referring the conventional conditions of desalination applied in Japan (JSCE 2001). The electrolyte liquid was selected for its ability to retain its alkalinity during the treatment without chlorine gas production. The temperature of the electrolyte liquid was 20 or 40°C. These temperature levels were controlled using rod-type heaters immersed in the electrolyte liquid. The list of specimens prepared in this study is shown in Table 3.

Table 3. List of specimens.

W/C	Temperature during treatment (°C)	Current density (A/m^2)	Name
0.45	20	0.0	45-N
		1.0	45-LD
	40	1.0	45-HD
0.55	20	0.0	55-N
		1.0	55-LD
	40	1.0	55-HD

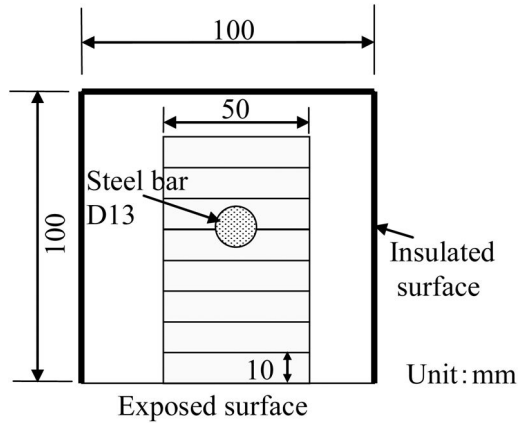

Figure 2. Cutting of a specimen for chemical analysis.

2.3 *Tests after treatment*

After the treatment, eight concrete plates were cut out from the central part of each specimen using a concrete cutter as shown in Figure 2. Distribution of Cl^- content in the specimen was obtained by measurement of average Cl^- content in each concrete plate. Total Cl^- content and water-soluble Cl^- content of each plate were measured by the method following 'JIS A1154 Method of test for chloride ion content in hardened concrete'. The Na^+ and K^+ contents were measured by means of atomic absorption spectrometry using a crushed fine powder sample from each concrete plated is solved by HNO_3 solution.

The adopted device used for measuring the absorbance spectrum was a portable near-infrared ray spectrum analysis device, the Field Spec Pro FR, made by ASD Company. The scanning range was a broad wavelength of 350–2500 nm at a high speed using sampling intervals of 1.4 and 2 nm. This device was able to display a series of data corresponding to the continuous wavelength in real time. The integrated contact-probe with source and receiving light shown in Figure 3 was used for the measurement of the absorbance spectrum of the drilled powder samples filled in a stainless cell.

Figure 3. Outline of the integrated contact probe.

It was able to measure the mean value within a diameter of 20 mm. The absorbance data of the powder samples were obtained by following the procedures below.

1) Reflected light strength Is(λ) of a standard white board was measured for calibration.
2) Reflected light strength I(λ) of the sample was measured.
3) Absorbance A(λ) was calculated by equation (1) using reflectivity R(λ) from equation (2).

$$A(\lambda) = \log[\, 1/R(\lambda)] \quad (1)$$

$$R(\lambda) = I(\lambda) / Is(\lambda) \quad (2)$$

The drilled powder samples for NIRS measurement were gathered from different depths in 10 mm increments from the exposed surface to 40 mm depth for each specimen.

Distributions of Cl^-/OH^- molar ratio in concrete were evaluated by using drilled powder samples gathered for NIRS measurement. Concentration of Cl^- was calculated by water-soluble Cl^- content and concentration of OH^- was measured by neutralization titration using 0.01 mol/lHCl after the stirring of sample solution (30 g distilled water was added to 0.3 g powder sample) for 24 hours.

3 DISTRIBUTION OF IONS IN CONCRETE

3.1 *Distribution of Cl^- in concrete*

Distributions of Cl^- content in the concrete specimens immediately after completing electrochemical treatment are shown in Figure 4. Distributions of (water-soluble Cl^-)/(total Cl^-) ratio in concrete after the treatment are shown in Figure 5. The location of a steel bar in a concrete specimen is also shown in this figure. From Figure 4 it is evident that Cl^- content is reduced by the application of the treatment from a premixed

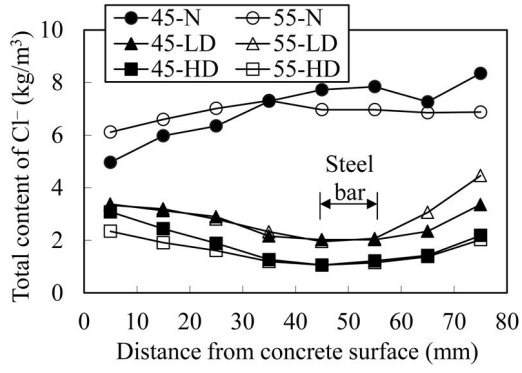

Figure 4. Distributions of total Cl^- content in concrete after treatment.

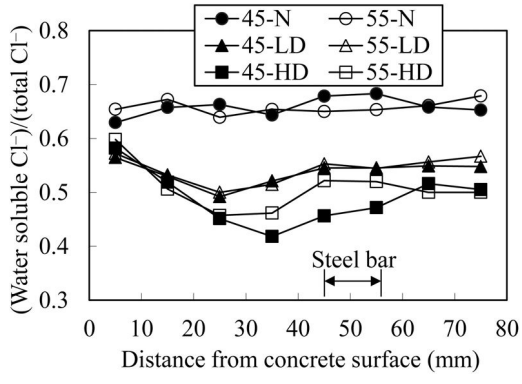

Figure 5. Distributions of (water-soluble Cl^-)/(total Cl^-) ratio in concrete after treatment.

Cl^- content of 8.0 kg/m^3 or from the Cl^- content of the non-treated specimens, 45-N and 55-N. Here, it can be seen that significant removal is apparent around the steel bar. Moreover, the rise of electrolyte temperature causes greater removal of Cl^-. Such a tendency is in agreement with results previously published by the authors (Ueda et al. 2012b).

Regardless of concrete W/C, the remaining Cl^- after desalination at a temperature of 20°C is about 2.0 kg/m^3 around the steel bar, while it is about 1.2 kg/m^3 after desalination at a temperature of 40°C. The required Cl^- content level after desalination is generally less than the critical Cl^- content for initiation of steel corrosion which is defined as 1.2 kg/m^3 in Japan (JSCE 2007). From this viewpoint, controlling temperature may be useful in order to satisfy the required standard for electrochemical treatment.

Furthermore, Figure 5 shows that in the non-treated cases, data of water-soluble Cl^-/total Cl^- ratio in concrete distribute around 0.65 while in the treated cases, values of the ratio become lower. At higher temperatures (40°C), electrolytes exhibited lower values of the ratio than at lower temperatures (20°C). Water-soluble Cl^- can be assumed to be nearly the same as free Cl^- in pore solution. Although desalination can extract Cl^- ions on the basis of the electrophoresis

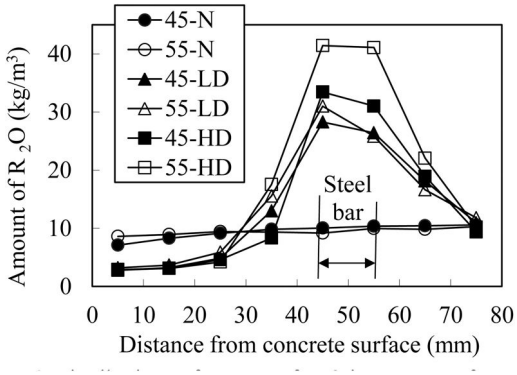

Figure 6. Distributions of amount of R_2O in concrete after treatment.

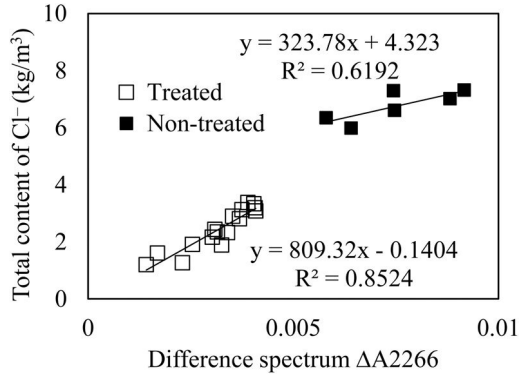

Figure 7. Correlation between difference spectrum ΔA2266 and total content of Cl^-.

principle, water-soluble Cl^-/total Cl^- ratio in concrete wouldn't become zero since a new equilibrium state of Cl^- in concrete pore solution would be formed rapidly after the treatment. However, this result indicated that the rise in temperature of electrolyte could enhance the protection effect against steel corrosion due to the reduction of free Cl^- concentration in pore solution.

3.2 *Distribution of cations in concrete*

Distributions of amount of R_2O in the concrete specimens immediately after desalination are shown in Figure 6. Amount of R_2O was calculated by the following equation using measured contents of Na^+ and K^+.

$$R_2O=Na_2O+0.658\ K_2O \quad (3)$$

Cations in concrete, like Na^+ or K^+, accumulate around the steel bar due to electrochemical migration as a result of carrying out desalination. Such an accumulation could cause degradation of the bond strength of the steel and accelerate ASR while it could contribute to the formation of a high alkalinity around the steel bar in concrete with the generation of OH^- due to the cathodic reaction during the treatment. From Figure 6, it can be seen that a rise of electrolyte temperature accelerates accumulation of R_2O like the case of Cl^-. However, the effect of temperature on R_2O accumulation is smaller than that of Cl^-.

4 EVALUATION OF REPAIR EFFECT BY USING NIRS METHOD

4.1 *Evaluation of total Cl^- content in concrete*

Correlation between the difference spectrum ΔA2266 and total content of Cl^- both are measured by using drilled powder is shown in Figure 7. According to past research, fixed Cl^- content in concrete like Friedel's salt has a high correlation with difference spectrum ΔA2266 which is the peak height of absorbance spectrum at the wavelength of 2266 nm obtained by means of NIRS method. Then, if the content proportion of free Cl^- and fixed Cl^- in concrete is constant, the correlation between the difference spectrum ΔA2266 and total content of Cl^- must be high. As methods to evaluate total Cl^- content in concrete, a method using difference spectrum ΔA2266 directly and a method of multiple regression analysis has been proposed (Kohri et al. 2010).

In this study, the simple method using difference spectrum ΔA2266 was adopted.

According to Figure 7, the correlation shows different linear relationships in the cases of treated specimens and non-treated specimens. The reason why such difference occurred is considered that the proportion of free Cl^- content to total Cl^- content was decreased by applying desalination as shown in Figure 5. As a result, if total Cl^- content is evaluated by using difference spectrum ΔA2266 without using multiple regression analysis, a calibration curve of total Cl^- content especially in the electrochemically treated concrete should be prepared.

4.2 *Evalation of Cl^-/OH^- molar ratio*

Distributions of Cl^-/OH^- molar ratio in concrete measured using drilled powder gathered from each 10 mm depth from exposed surface to 40 mm depth after the treatment are shown in Figure 8. Here, Cl^- concentration (mol/l) in pore solution was estimated using water-soluble Cl^- content referring the results of past research (Tanaka et al. 2007). OH^- concentration in pore solution was estimated by the way described in 2.3.

As shown in Figure 8, the values of Cl^-/OH^- molar ratio decrease due to the application of the electrochemical treatment compared with the cases of non-treated specimens. Especially, at the 35 mm depth point, the nearest place to the steel bar, the values of Cl^-/OH^- molar ratio in all treated specimens was less than 0.6, which is considered the threshold for initiation of steel corrosion (Hausmann 1967). As shown in Figure 4, in the case of treatment with 20°C electrolyte, the remaining total Cl^- was about 2 kg/m^3. However, it can be said that even in such

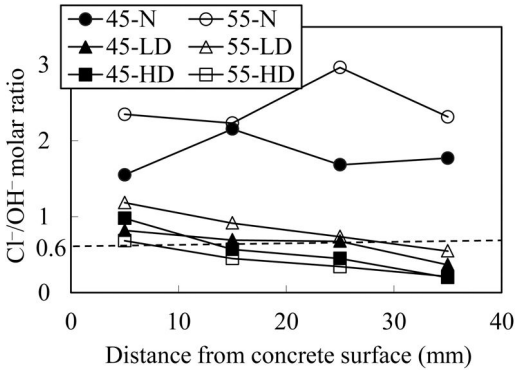

Figure 8. Distributions of Cl^-/OH^- molar ratio in concrete after treatment.

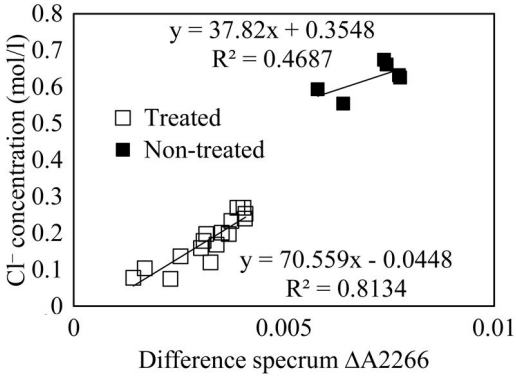

Figure 9. Correlation between difference spectrum ΔA2266 and Cl^- concentration.

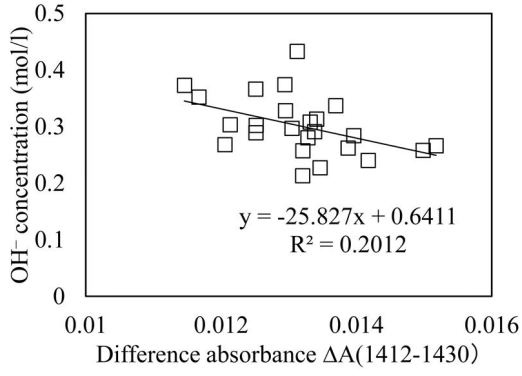

Figure 10. Correlation between difference absorbance ΔA(1412-1430) and OH^- concentration.

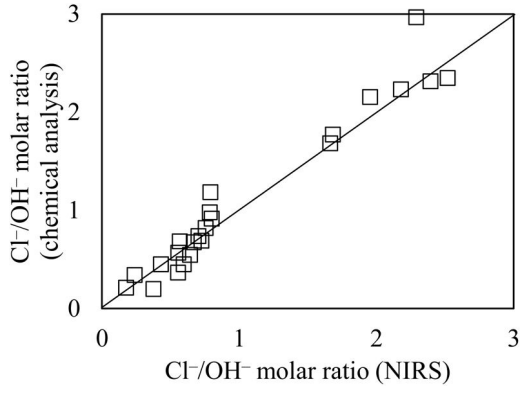

Figure 11. Correlation between data of Cl^-/OH^- molar ratio by NIRS and those by chemical analysis.

cases, Cl^-/OH^- molar ratio could be less than 0.6 considering the enhancement of OH^- concentration due to applying electrochemical treatment.

Correlation between the difference spectrum ΔA2266 and Cl^- concentration in pore solution is shown in Figure 9. Correlation between the difference absorbance ΔA(1412-1430) and OH^- concentration in pore solution is shown in Figure 10. According to the authors' past research (Ueda et. al. 2012), OH^- concentration originated from $Ca(OH)_2$ as the hydration products of cement in concrete is correlates well with the difference absorbance ΔA(1412-1430) which is the difference of the absorbance at the wavelength of 1412 nm and that of 1430 nm.

From Figure 9, it can be said that the Cl^- concentration in the pore solution could be estimated by using the difference spectrum ΔA2266 because of the linear relationship between them, although the tendency is different between the case with the treatment and without treatment, as shown in Figure 7. On the other hand, from Figure 8, the correlation between difference absorbance ΔA(1412-1430) and OH^- concentration becomes relatively low. The reason for this is considered that OH^- ions in this case may be mainly supplied by the cathodic reaction with the electrochemical treatment rather than by $Ca(OH)_2$ as the hydration products in concrete. Then, the accuracy of the detection of OH^- ions may be decreased. This point is a future problem to be solved and absorbance peaks of other wavelengths should be also investigated.

Correlation between data of Cl^-/OH^- molar ratio evaluated by NIRS method and those by chemical analysis is shown in Figure 11. It can be seen that there is relatively high correlation between them although a little scattering is observed because of the low accuracy of the estimation of OH^- concentration as mentioned above. The possibility to evaluate Cl^-/OH^- molar ratio in concrete after the electrochemical treatment by using NIRS method is shown by this result.

5 CONCLUSIONS

Results obtained from this research are summarized as follows:

- The chloride removal efficiency with the treatment using the electrolyte of 20°C was lower than the case of 40°C and remaining Cl^- around the steel bar after

treatment was about 2 kg/m^3. However, Cl^-/OH^- molar ratio after the treatment was less than 0.6, including the case of 20°C.

- When Cl^- content in concrete is evaluated by using difference spectrum $\Delta A2266$ without using multiple regression analysis, a calibration curve of Cl^- content especially in the electrochemically treated concrete should be prepared.
- Although the accuracy of the estimation of OH^- concentration was relatively low, the possibility to evaluate Cl^-/OH^- molar ratio in concrete after the electrochemical treatment by using NIRS method was confirmed.

REFERENCES

Furukawa, T., Ueda, T., Kohri, M. & Nanasawa, A. 2008. Evaluation of Friedel's salt content in mortar using near-infrared spectroscopic technique. *Proc. of the Fifth International Conference on Advanced Materials Development and Performance*.

Hausmann, D. A. 1967. Steel Corrosion in Concrete: How Does It Occur?, *Materials Protection*, 6(11): 19–23.

Hondel, A. J. & Polder, R. B. 1992. Electrochemical Realkalisation and Chloride Removal of Concrete. *Construction Repair*: 19–24.

Japan Society of Civil Engineers. 2001. Recommendation for design and construction of electrochemical corrosion control method. *Concrete Library of JSCE* 107.

Japan Society of Civil Engineers. 2007. Standard specifications for concrete structures – 2007, Maintenance.

Kanada, H., Ishikawa, Y. & Uomoto, T. 2005. Utilization of near-infrared spectral imaging system for inspection of concrete structures. *New Technologies for Urban Safety of Mega Cities in Asia*.

Kohri, M., Ueda, T. & Mizuguchi, H. 2007. Application of a near-infrared spectroscopic technique to estimate the chloride ion content in mortar deteriorated by chloride attack and carbonation. *Proc. of the MDCMS* 2:374–379.

Kohri, M., Ueda, T. & Mizuguchi, H. 2010. Estimation of chloride ion content in cement paste or mortar using near-infrared spectroscopic technique. *Journal of Advanced Concrete Technology*, 8(1):15–25.

Page, C. L. 2002. Application of electrochemical techniques for maintenance of corroding reinforced concrete structures. *Proc. the 1st fib Congress*: 147–158.

Tanaka, S., Ueda, T, Kagawa, T. & Nanasawa, A. 2007. Monitoring of steel corrosion in fly ash concrete. *Proc. of the Japan Concrete Institute*, 29(1), 1371–1376.

Ueda T. & Miyagawa T. 2010. Deterioration of Concrete Structures and Some Relevant Issues. *Corrosion Engineering*, 59: 111–116.

Ueda, T., Matsuda, S, Yamamoto, T. & Tsukagoshi, M. 2012a. Influence of fly ash and carbonation on a NIRS spectrum of ASR affected concrete. *Proc. of the Japan Concrete Institute*, 34(1), 1816–1821.

Ueda, T., Wakitani, K. & Nanasawa A. 2012b. Influence of electrolyte temperature on efficiency of electrochemical chloride removal from concrete. *Electrochimica Acta*, 86, 23–27.

Strengthening materials and techniques/Repair with composites

This page intentionally left blank

Concrete Solutions – Grantham et al. (Eds)
© 2014 Taylor & Francis Group, London, ISBN 978-1-138-02708-4

State-of-the-art review on FRP strengthened concrete columns

K. Abdelrahman & R. El-Hacha
University of Calgary, Calgary, Canada

ABSTRACT: The use of Fibre Reinforced Polymer (FRP) sheets to confine concrete columns is an attractive technique due to the significant enhancement associated with the strength and ductility of the concrete. A comprehensive understanding of the mechanisms, characteristics and parameters involved with FRP confined concrete is essential in order to optimize the design and research process. This paper includes a review of aspects and concepts that have been lightly addressed in the current literature. A brief review about the confinement mechanics and the stress-strain characteristics of FRP confined concrete is provided. This paper also includes an insight into the failure mechanics, confinement models, cost and ductility effectiveness of FRP confined concrete columns. A review of new instrumentation technique using photogrammetric concepts to measure strain across the surface of FRP confined concrete is also discussed.

1 INTRODUCTION

Deterioration of concrete structures is a challenging area of research that requires immediate and effective solutions. Numerous strengthening techniques adopted over the years include concrete and steel jacketing. However, the materials involved with these strengthening techniques suffer similar deterioration effects to the parent concrete structure. Thus, materials such as Fiber Reinforced Polymers (FRP) became attractive to researchers due to the numerous benefits they provide. The advantages of FRP materials are that they do not corrode and have high strength-to-weight ratios.

Experimental, analytical, and numerical research conducted on FRP confined columns highlights the significant enhancement in the strength and ductility of the concrete (Nanni & Bradford 1995, Karbhari & Gao 1997, Mirmiran & Shahawy 1997, Toutanji 1999, Toutanji & Deng 2002, Thermou & Pantazopoulou 2007a and 2007b, Abdelrahman & El-Hacha 2012a and 2012b and 2012c, El-Hacha & Mashrik 2012, Thermou et al. 2014).

Several factors of FRP confined concrete columns were also investigated such as the environmental exposure effects (Karbhari & Eckel 1994, Mirmiran et al. 1998, El-Hacha et al. 1999, Shahawy et al. 2000, Karbhari et al. 2000, Karbhari 2002, Masia et al. 2004, Thériault et al. 2004, El-Hacha et al. 2005 and 2006, Green et al. 2006, Jiang & Teng 2006, Silvia & Rodrigues 2006, Belarbi & Bae 2007, El-Hacha et al. 2010), and size and slenderness effects (Issa et al. 2009, Smith et al. 2010, Abdelrahman 2011, Abdelrahman & El-Hacha 2012d, El-Hacha & Abdelrahman 2013).

In order to progress with this area of research, it is important to comprehend and evaluate the current research undertaken. Thus, the main objective of this paper is to review certain critical topics related to FRP confined concrete columns such as the confinement mechanism, failure mechanism, confinement models, and shed light on certain areas such as the cost and ductility effectiveness studies and photogrammetric measuring techniques that enhance the quality of the research and provide deep understanding of the topic.

The topics presented in this paper were carefully selected to cover a variety of grounds related to FRP confined concrete columns ranging from experimental, technical and analytical. The confinement mechanism and the stress-strain characteristics of FRP confined concrete were introduced to serve as a basis to the forthcoming topics. Then, the fracture mechanics concepts were integrated to the failure mechanism of concrete and FRP in order to investigate the failure mode associated with FRP confined concrete columns. Some of the commonly referenced confined models and design codes/guidelines were discussed. In addition, topics that have received only small coverage in previous articles such as the cost and ductility studies and photogrammetric techniques are also presented.

2 CONFINEMENT OF FRP WRAPPED CONCRETE COLUMNS

2.1 *Confinement mechanism*

In most cases, the confinement mechanism applied by the FRP sheets is passive in nature, which means that the FRP sheets become activated only when the concrete experiences significant transverse expansion at loads approaching the unconfined concrete compressive strength. The confinement mechanism is directly related to the loading stages of the concrete columns.

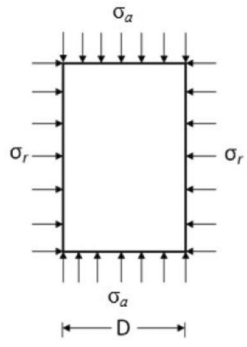

Figure 1. Tri-axial stress of concrete.

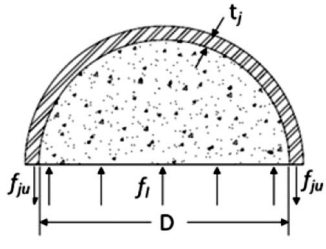

Figure 2. Circular cross-section of FRP confined concrete.

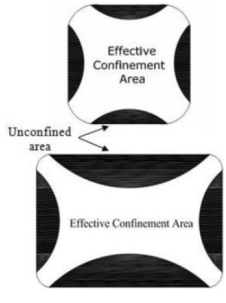

Figure 3. Effective confinement area of non-circular section.

At lower compressive loads, concrete is known to behave elastically and the transverse (hoop) strain is linearly related to the longitudinal strain by the Poisson's ratio. At this stage, the concrete dilation is not sufficient to trigger the activation mechanism of the FRP sheet. As the load progresses, micro-cracks begin to coalesce forming macro-cracks that increase the transverse strain of the concrete. The FRP sheets are then activated by resisting the concrete expansion through a confinement pressure forcing the concrete to be in a tri-axial state of stress (Fig. 1). It is well established that concrete under a tri-axial state of stress has higher strength and ductility than concrete subjected to uniaxial compression (Richart et al. 1928).

2.2 *Lateral confinement pressure*

The lateral confinement pressure is one of the most critical parameters, which is directly related to the strength and ductility enhancement of the concrete.

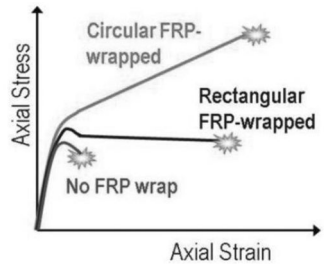

Figure 4. Typical axial stress-strain curves for unconfined and FRP confined concrete columns.

The lateral confinement pressure depends on certain factors such as: (1) geometry of the FRP sheets, (2) mechanical properties of the FRP sheets, and (3) cross-sectional area of the confined concrete.

The shape of the confined cross-section is a very critical component that affects the lateral confining pressure. In circular columns, the FRP sheets are assumed to provide a uniform lateral confinement pressure around the perimeter of the column (Fig. 2). In this case, the FRP sheets are activated along the entire perimeter of the circular section resulting in significant enhancement to the strength and ductility of the concrete. However, square and rectangular columns tend to develop stress concentrations at the corners (Fig. 3). These stress concentrations reduce the effectiveness of the lateral confining pressure and affects the axial stress-strain behaviour of the FRP wrapped concrete column (Fig. 4). The use of mechanical anchors and rounding the corners are some techniques implemented to increase the effective confinement area and reduce the stress concentrations.

3 STRESS STRAIN BEHAVIOUR OF FRP CONFINED CONCRETE COLUMNS

Various stress-strain behaviours were reported in the literature database resulting from extensive experimental testing of FRP confined concrete columns. In general, the stress-strain behaviour can be characterized into three cases (Case A, B and C). In all of these cases, the stress-strain behaviour of FRP confined concrete is normally divided into two portions. The first portion of the stress-strain curve up to the point f'_{co} presents the stress-strain curve of the unconfined concrete (Fig. 5). However, after this point, the stress-strain curve is bilinear and the behaviour varies depending on the level of confinement applied to the concrete.

If the concrete is well-confined, the second portion of the stress-strain curve consists of an ascending bi-modular shape as shown in Case A (Fig. 5a). In this case, both the maximum compressive strength and the ultimate strain are reached at the same point significantly increasing the strength and ductility of the concrete. For other cases of FRP confined concrete, the maximum confined concrete compressive strength f'_{cc}

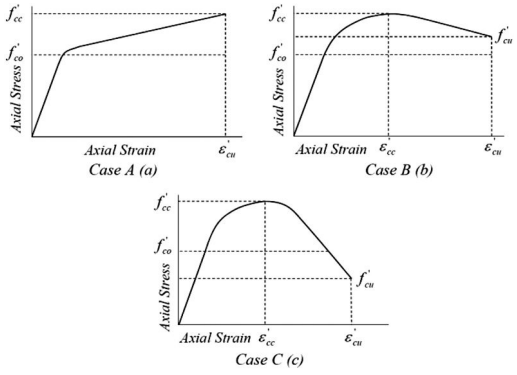

Figure 5. Classification of stress-strain curves.

might not be equal to the ultimate concrete compressive strength f'_{cu} corresponding to the ultimate concrete strain. Although for Case B (Fig. 5b), the second portion of the curve is a descending bi-modular curve, the ultimate strength f'_{cu} is still greater than the unconfined concrete compressive strength f'_{co}. This means that the FRP confinement is sufficient to lead to an enhancement in the strength and ductility of the concrete. For Case C (Fig. 5c), the second branch of the curve is also a descending bi-modular curve, but f'_{cu} is below f'_{co} forming a post-peak descending curve, where the compressive strength of the concrete is reached before the FRP rupture (Lam & Teng 2003).

4 FAILURE MODE

Understanding the failure mode of any material requires investigating the visual failure experimentally and the science involved theoretically. With regards to the FRP confined concrete columns, there is a consensus of opinion in the literature database about the visual failure form. Generally, at the failure load, the FRP sheets fracture and the already crushed concrete shatters catastrophically. However, there are several theories suggested about the science involved in the fracture behavior of FRP confined concrete columns. According to these theories, the crushing of concrete plays a significant role in the failure mechanism of the FRP sheets. Thus, in this section, the failure mechanism of concrete is first presented, followed with the discussion of several theories involving the failure of the FRP sheets.

4.1 *Failure mechanism of the concrete*

Experimental investigation of concrete columns subjected to uni-axial compression loading showed significant hoop strain variation across the surface of the column. This variation could be attributed to the dispersion of aggregates within the concrete, the formation of cracks, and the heterogeneous nature of the concrete. The most significant factor leading to localized failure of the FRP sheets is initiated through

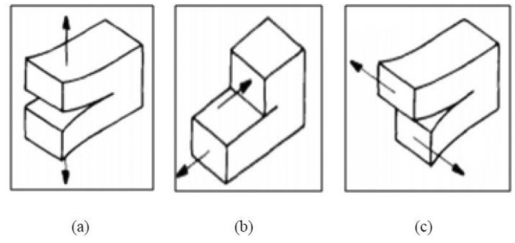

Figure 6. Fracture modes (a) Mode I, opening; (b) Mode II, in-plane shear; and Mode III, out of plane shear.

the formation of cracks within the concrete. These cracks then develop high stress concentrations at localized points leading to the failure of the FRP sheets.

In order to grasp a complete understanding on the behaviour of FRP confined concrete columns, the investigation of the concrete failure mechanism is necessary. Thus, in this section, a brief discussion of the crack formulation and the failure pattern of the concrete are presented.

The main theory related the facture mechanism of concrete is believed to be initiated due to pre-existing geometrical flaws such as voids, pores, fissures and cracks that pre-exists in the concrete material. Based on fracture mechanics, in order for a flaw to initiate and propagate there must be sufficient energy and stress applied. A well-defined definition of the energy and the stress criterion is defined to aid the understanding of the crack propagation behaviour. The energy criterion is defined as the energy released by a unit increment in the crack surface area that must be at least as much as the energy required for that increment. The stress criterion is defined as the local tensile stress developed around a flaw that must be large enough to overcome the local cohesive strength of the material. Thus, depending on the state of the applied stress, the geometry of the flaw, and the material properties, the crack propagation and initiation can be governed by the energy criterion or the stress criterion or both (Wang & Shrive 1999). Under compression load, similar voids in the concrete may have similar stress concentrations, which can result to the initiation of the cracks at various void locations.

The fracture mechanics theory specify three types of displacement modes, Mode I (opening), Mode II (in-plane shear), and Mode III (out of plane shear) as shown in Figure 6 (Anderson 2001). Concrete subjected to uni-axial compression develops multiple visible cracks (Fig. 7) that propagate parallel to the direction of the applied loading. These visible cracks can only be developed through a separation mechanism as Mode I displacement. Accordingly, this implies that even through the applied loading is compressive in nature; the cracks are formed due to tensile stresses.

4.2 *Failure theory of the FRP sheets*

The primary cause of failure of the FRP sheets has been a controversial matter to researchers over the past

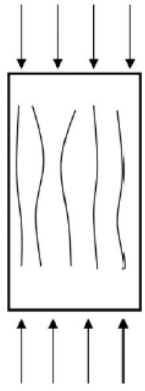

Figure 7. Vertical compression cracks of plain concrete.

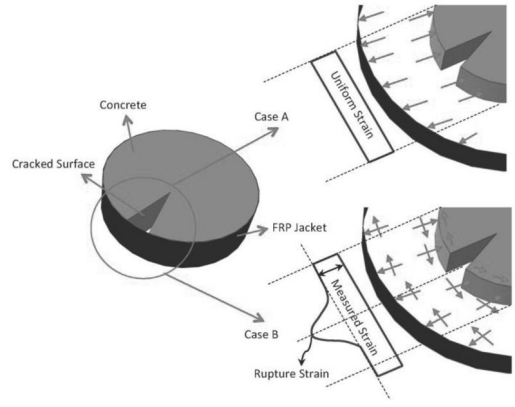

Figure 8. Schematic representation of: Case A: uniform strain failure and Case B: localized strain failure.

years. According to the current literature, many of the FRP confined concrete columns are argued to fail prematurely at a lower hoop strain than the ultimate tensile strain of the FRP sheet. There are mainly two primarily suggested theories to the premature failure of the FRP sheet.

The first theory states that the premature failure of the FRP sheets can occur due to the following factors: the bond performance between the FRP laminate and the concrete, the degree of the fibre alignment, the curvature of the FRP sheets, indirect loading of the FRP sheets creating a state of multi-axial stress, size effects and the presence of voids on the concrete surface. The second theory states that the premature failure of the FRP sheets can occur due to significant hoop strain variation in the form of localized failure points on the FRP sheets (Scholefield 2004, Pessiki et al. 2001).

4.3 *Failure mechanism of the FRP sheets*

Once cracks are formed on the surface of the concrete, it is important to recognize their interaction with the FRP sheets. Cracks developing on the concrete surface produce high stress concentrations that are much higher in magnitude than the average confinement pressure applied by the FRP sheets. Thus, the development of a crack leads to mainly two possible scenarios to the failure of the FRP sheets.

The first possible scenario is to develop a uniform hoop strain in the FRP sheet around the perimeter of the circular concrete cross-section (Fig. 8a). This uniformity in the strain is developed when the FRP sheets are not bonded to the concrete resulting in an interface that is frictionless. In this case, there is no transmission of the shear force across the interface between the FRP sheet and the concrete.

In the second case where the FRP sheets are bonded to the concrete surface, transmission of forces occurs. The possible failure scenario in this case is when the cracks developed in the concrete surface produce localized regions of high strain in the FRP sheets (Fig. 8b). These localized regions experiencing high strains tend to deform altering the uniform hoop strain distribution of the FRP sheets around the perimeter of the circular concrete columns. If the strains measured using conventional strain gauges were not mounted at exact locations corresponding to regions of high strain concentration, the measured strains at rupture will be lower than the actual FRP rupture strain (Pessiki et al. 2001). This is where a photogrammetric technique becomes beneficial to capture strains at any location across the surface of the concrete. A more detailed discussion on the use of the photogrammetric technique is presented in later sections of this paper.

5 CONFINEMENT MODELS

The confinement models available in the literature and design codes/guidelines are mainly categorized into two types: analysis oriented and design oriented models (Lam & Teng 2004). Analysis oriented models are developed from incremental numerical procedure that results in sophisticated models difficult to be practically implemented by designers. On the other hand, design oriented modes are developed empirically usually through best fitting techniques of the experimental data. These types of models are most commonly available in the literature due to the simplicity involved with developing and implementing the confinement model.

Some of the most commonly used design codes/guidelines to predict the ultimate strength of FRP confined concrete columns are: the American Concrete Institute (ACI Committee 440.2R. 2008), the Canadian Highway Bridge Design Code (CAN/CSA-S6-06. 2010) and the Design and Construction of Building Components with FRP (CAN/CSA-S806. 2012). In addition, there are several confinement models available in the literature to predict the stress-strain characteristics of FRP confined concrete columns. Some of the most commonly used models were developed by Samaan et al. (1998), Spoelstra & Monti (1999), Wu et al. (2003), Youssef et al. (2007), Fahmy & Wu (2010), and Abdelrahman & El-Hacha

(2013b). All of the above mentioned confinement models are categorized as design-oriented equations that are usually presented in the following form:

$$f'_{cu} = \alpha\, f'_{co} + k_l\, f_l^{\beta} \quad (1)$$

The ultimate FRP confined concrete compressive strength (f'_{cu}) is usually a function of the unconfined concrete compressive strength (f'_{co}), the maximum confinement pressure (f_l), and the confinement parameters (α, β, and k_l). The unconfined concrete strength can be determined based on a 28-day compressive strength or can be a predetermined design value. The maximum confinement pressure is also dependent on known parameters, which are the FRP type, the number of FRP layers, and the cross-section shape of the column. For a circular column, the maximum confinement pressure can be determined using the following equation:

$$f_l = \frac{2\, n\, t_f\, f_{fu}}{D_g} \quad (2)$$

where n = number of FRP layers; t_f = thickness of the FRP layer; f_{fu} = design FRP ultimate tensile strength; and D_g = external diameter of the circular section.

The confinement parameters of FRP confined concrete are determined empirically from experimental data. The parameter α is the multiplication factor to the unconfined concrete strength. Certain confinement models such as the FRP Building Code S806-12 apply this factor as a safety measure due to discrepancies in the unconfined concrete strength. The second parameter k_l is defined as the confinement effectiveness coefficient. This coefficient can be described as a function of the maximum confinement pressure or considered as an empirical value. The third parameter β describes the behaviour between the maximum confinement pressure and the confined concrete strength. A value of one assumes a linear relation, whereas a value different from 1 refers to a nonlinear relationship. The confinement parameters of the abovementioned confinement models for the circular sections are summarized in Table 1.

It is important to note that the nature of the empirical models currently available in the literature rely on best-fit techniques of the experimental data. Thus, calibration of the confinement models currently developed is either based on experimental results from a particular type of FRP sheet, or a combination of varying FRP sheets. This signifies that the current models are not suitable for extension to predict the behaviour of concrete columns wrapped with the newly developed sfrp sheets. A recent study conducted by abdelrahman (2013b) showed that the current design codes/guidelines experimentally calibrated against CFRP, GFRP, and AFRP sheet, fail to predict the ultimate strength of SFRP confined concrete with a percentage error of up to 36%. This implies that there is a need to develop a unified confinement model that incorporates the behaviour of the SFRP confined concrete column, in addition to the commonly used fibres (CFRP, GFRP, and AFRP).

Table 1. Summary of the confinement models.

Model	α	β	k_l
Samaan et al. (1998)	1	0.7	6
Spoelstra & Monti (1999)	0.2	0.5	3
Wu et al. (2003)	1	1	3
Youssef et al. (2007)	1	1.25	2.25
ACI Committee 440.2R-08	1	1	3.135
Bridge Code S6-06 S6-06 (2010)	1	1	2
Fahmy & Wu (2010)	1	1	$4.5f_l^{-0.3}, f'_{co} \leq$ 40MPa $3.75f_l^{-0.3}, f'_{co} >$ 40MPa
FRP Building Code S806 (2012)	0.85	1	$6.7f_l^{-0.17}$
Abdelrahman & El-Hacha (2013)	1.35	1	2.7

6 COST AND DUCTILITY EFFECTIVENESS

A common area that is lightly addressed in the current literature is the cost and ductility effectiveness of the FRP confined concrete columns. Thus, this section will shed some light onto the definitions of the cost and ductility effectiveness parameters, and how these parameters can significantly alter the analysis and understanding of the test data.

The cost effectiveness parameter is defined through a strength efficiency scale, SE_{ff}, which is determined as the percentage increase in strength of the FRP confined concrete specimens, with respect to the unwrapped specimens, over the total cost involved with the construction and the FRP confinement of the concrete columns (Eqn. 3). The second parameter to evaluate the effectiveness of the FRP sheet is ductility effectiveness parameter that is defined through a ductility effectiveness scale, DE_{ff}. The ductility effectiveness is determined as the percentage increase in the ductility of the FRP wrapped columns, with respect to the unwrapped columns, over the total cost associated with the construction and the FRP confinement of the concrete column (Eqn. 4).

$$SE_{ff} = \frac{\%\ Increase\ in\ the\ strength\ of\ FRP\ confined\ column}{Total\ Cost\ of\ FRP\ confined\ column} \quad (3)$$

$$DE_{ff} = \frac{\%\ Increase\ in\ the\ ductility\ of\ FRP\ confined\ column}{Total\ Cost\ of\ FRP\ confined\ column} \quad (4)$$

Few researchers analyzed the cost and ductility effectiveness of concrete columns confined with Carbon FRP (CFRP) and Steel FRP (SFRP) sheets (Mashrik 2011, and Abdelrahman & El-Hacha 2013a). In these studies, a typical research procedure includes similar concrete columns strengthened using CFRP

or SFRP sheets. An assumption is generally made about the cost of the concrete, reinforcing steel, epoxy, and transportation costs to be equivalent for all the columns. Thus, these costs are ignored from the cost and ductility effectiveness analyses. The only varying parameters are the material costs and the labour costs.

The results presented in the above-mentioned studies highlight the importance of cost considerations, while determining the overall efficiency of the composite FRP strengthened concrete column. The strength and ductility enhancement of FRP confined concrete columns can be tremendous. However, when the cost criterion is considered, the overall beneficial value of the strengthening system can be significantly reduced or negligible in certain cases. Thus, the underlying concept of the cost and ductility analysis aids in achieving an optimum and effective design of FRP confined concrete columns.

7 DIGITAL IMAGE CORRELATION (DIC) TECHNIQUE

Over the years, researchers have investigated several techniques to measure strains across the surface of the concrete, in order to avoid the numerous limitations associated with the use of the conventional strain gauges. Once mounted onto the surface of the concrete, these gauges can only measure the strains at localized points, specifically at the location that the strain gauge is installed. These limited discrete points are insufficient to capture completely the nature of the strain variation. In addition, there is a high probability that the location of the strain gauge does not correspond to the location of the maximum strain. This problem can be avoided by installing significant amount of strain gauges at various locations across the concrete surface. However, this solution is time-consuming and impractical. Another drawback associated with conventional strain gauges lies in the bond-contact application with the concrete surface. During experimental testing, the concrete suffers from significant cracking that cause the strain gauge to de-bond or become damaged.

Recently, a photogrammetric technique termed Digital Image Correlation (DIC) technique has been developed to capture strains across the surface of the concrete. This DIC is based on a Matlab module that works by defining particular sets of regions that are traced along subsequent images. The output is displacements in the image-space (coordinates in terms of pixels in the image) that can be converted into strains. Further technical information concerning the DIC can be found in White & Take (2002) and White et al. (2003).

Various researchers have validated the DIC method (Fitzwilliam 2006, Bisby & Take 2009, Abdelrahman 2011, Abdelrahman & El-Hacha 2011, Barrington et al. 2011, Bisby & Stratford 2011, Islam et al. 2011). The validation process usually involves comparison of strain data from conventional strain gauges at the corresponding location with the virtual gauge readings

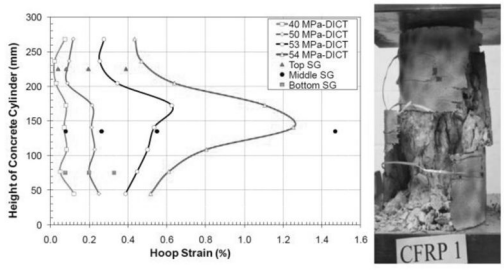

Figure 9. DIC analysis of CFRP wrapped concrete cylinder and its corresponding failure mode (Abdelrahman 2011).

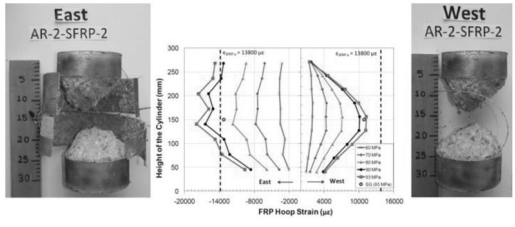

Figure 10. DIC analysis of SFRP wrapped concrete cylinder and its corresponding failure mode (Abdelrahman 2011).

from DIC. These studies showed that at similar elevations, the strain captured from DIC showed good agreement with strain readings from the strain gauge (Figs 9–10). Thus, the application of this technique to measure strain provides greater insight into the nature of the strain variation across the surface of the concrete, as well as capturing the maximum strain (Figs 9–10).

Experimental evidence from DIC analysis showed that axial and hoop strains vary significantly along the height and circumference of the concrete columns. The strain variation also depends on the size of the column. For short columns, the frictional effects from the loading platens alter the hoop strain distribution forming a bell-shaped curve with the maximum strain achieved at the mid-height region (Figs 9–10). However, as the height of the columns is increased, the regions affected by the friction induced from the loading plates decreases. Regions outside the frictional zones have a random strain distribution.

8 CONCLUSIONS AND FUTURE WORK

This paper has presented a review on critical aspects concerning the behaviour of FRP confined concrete columns. It complements the existing knowledge of the current literature and also discusses areas such as the cost and ductility effectiveness and photogrammetric techniques that have received only minimum coverage.

Several gaps were identified during the investigation of the current literature database on FRP confined concrete columns. The primary concern is associated

with the empirically developed confinement models. These models are solely useful to predict stress-strain characteristics only within the experimental data-range used to develop the model. In addition, certain models are calibrated against a particular FRP type, and produce significant errors once extended for use to predict concrete columns wrapped with a different type of FRP sheet. Thus, a critical need for a unified model to predict the ultimate strength and strain of Carbon/Steel/Glass/ Aramid FRP confined concrete is essential.

The most common analysis technique adopted in the literature focuses on comparisons of strengths and ductility. However, the overall global behaviour can be significantly altered through cost and ductility effectiveness analysis. Adopting this type of analysis in future research and design consideration can lead to optimum and effective solutions to FRP confined concrete columns.

REFERENCES

Abdelrahman, K. 2011. Effectiveness of steel-fibre reinforced polymer for confining circular concrete columns, *MSc Thesis*: Department of Civil Engineering, University of Calgary, Calgary, Canada.

Abdelrahman, K. & El-Hacha, R. 2011. Validation of digital image correlation technique on CFRP and SFRP wrapped cylinders subjected to freeze-thaw environmental exposure; *Proc. of the 4th International Conference on Durability and Sustainability of Fiber Reinforced Composites for Construction and Rehabilitation (CDCC-4), Quebec City, Canada, 20–22 July 2011*.

Abdelrahman, K. & El-Hacha, R. 2012a. Behavior of circular concrete cylinders wrapped with CFRP and SFRP sheets; *Proc. of the 6th International Conference on Advanced Composite Materials in Bridges and Structures (ACMBS), Kingston, Canada, 22–25 May 2012*.

Abdelrahman, K. & El-Hacha, R. 2012b. Behaviour of large-scale concrete columns wrapped with CFRP and SFRP sheets. *Journal of Composites for Construction ASCE* 16(4): 430–439.

Abdelrahman, K. & El-Hacha, R. 2012c. Ductility study of the slenderness effects on SFRP wrapped concrete columns; *Proc. of the 3rd International Structural Specialty Conference (CSCE-2012), Edmonton, Canada, 6–9 June 2012*.

Abdelrahman, K. & El-Hacha, R. 2012d. Stress-strain behaviour and size effects of axially loaded circular concrete specimens confined with CFRP and SFRP sheets; *Proc. of the Conference of FRP Composites in Civil Engineering (CICE), Rome, Italy, 13–15 June 2012*.

Abdelrahman, K. & El-Hacha, R. 2013a. Cost and ductility effectiveness of concrete columns wrapped with CFRP and SFRP sheets; *Proc. of the 2nd Conference on Smart Monitoring Assessment and Rehabilitation of Civil Structures (SMAR 2013), Istanbul, Turkey, 9–11 September 2013.*

Abdelrahman, K. & El-Hacha, R. 2013b. Strength prediction of SFRP confined concrete columns; *Proc. of the 11th International symposium on fiber reinforced polymers for reinforced concrete solutions (FRPRCS-11), Guimaraes, Portugal, 26–28 June 2013.*

ACI Committee 440. 2008. Guide for the design and construction of externally bonded FRP systems for strengthening concrete structures. *ACI 440.2R-08.*

Anderson, TL. 2000. *Fracture Mechanics; Fundamentals and Applications* Florida: CRC Press.

Barrington, J., Dickson, D., Bisby, L. & Stratford, T. 2011. Strain development and hoop strain efficiency in FRP confined square columns. *American Concrete Institute ACI* 255: 1–20.

Belarbi, A. & Bae, SW. 2007. An experimental study on the effect of environmental exposure and corrosion on RC columns with FRP composite jackets. *Composites: Part B Engineering* 38(5–6): 223–232.

Bisby, L. & Take, W. 2009. Strain localization in FRP confined concrete: new insights. *Structural Building* 162(5): 301–309.

Bisby, L. & Stratford, T. 2010. The ultimate condition of FRP confined concrete columns: new experimental observations & insight; *Proc. of the 5th International Conference on FRP composites in Civil Engineering (CICE-2010), Beijing, China, 27–29 September 2010.*

Canadian Standards Association. 2010. Canadian Highway Bridge Design Code. *CAN/CSA S6-06 (2010),* Ontario, Canada.

Canadian Standards Association. 2012. Design and Construction of Building Components with Fiber Reinforced Bridge Design Code. *CAN/CSA S806-12,* Ontario, Canada.

El-Hacha, R., Green, M. & Wight, G. 1999. CFRP wrapped concrete cylinders in severe environmental conditions and exhibition on extending the life of bridges; *Civil + Building Structures Conference, London, England, 13–15 July 1999.*

El-Hacha, R., Callery, K., Green, MF. & Archibald, J. 2005. Assessment of FRP wrapped and hybrid polyurethane/polyrea coated reinforced concrete columns under field exposure conditions; *Proc. of, the 4th Middle East Symposium on Structural Composites for Infrastructure Application (MESC-4), Alexandria, Egypt, 20–23 May 2005.*

El-Hacha, R., Callery, K., Green, MF. & Archibald, J. 2006. Environmental effects on the behaviour of FRP wrapped and hybrid polyurethane/polyuria coated concrete cylinders: laboratory evaluation; *Proc. of the International Conference on Civil Engineering Infrastructure Systems (CEIS-2006), Beirut, Lebanon, 12–14 June 2006.*

El-Hacha, R., Green, M. & Wight, G. 2010. Effect of severe environmental exposures on CFRP wrapped concrete columns. *Journal of Composites for Construction ASCE* 13(2): 83–93.

El-Hacha, R. & Mashrik, M. 2012. Effect of SFRP confinement on circular and square concrete columns. *Engineering Structures* 36: 397–393.

El-Hacha, R. & Abdelrahman, K. 2013. Slenderness effects of circular specimens confined with SFRP sheets. *Composites Part B: Engineering* 44(1): 152–166.

Fahmy, M. & Wu, Z. 2010. Evaluating and proposing models of circular concrete columns confined with different FRP composites. *Composites Part B: Engineering* 41: 199–213.

Fitzwilliam, JM. 2006. Fibre-reinforced polymer wraps for slender eccentrically loaded reinforced concrete columns, *MSc Thesis*: Department of Civil Engineering, Queen's University, Kingston, Ontario, Canada.

Green, MF., Bisby, LA., Fam, AZ. & Kodur, VKR. 2006. FRP confined concrete columns: Behaviour under extreme conditions. *Cement and Concrete Composites* 28(10): 928–937.

Islam, MM., Choudhury, MSI., Abdulla, M. & Amin, AFMS. 2011. Confinement effect of fiber reinforced polymer wraps in circular and square concrete columns; *Proc. of the 4th Annual Paper Meeting and the 1st Civil Engineering Congress, Dhaka, Bangladesh, 22–24 December 2011*.

ISIS Educational Module 4. 2006. An Introduction to FRP-strengthening of concrete structures; *The Canadian Network of Centers of Excellence on Intelligent Sensing for Innovative Structures (ISIS Canada), University of Manitoba, Winnipeg, Canada, March 2006*.

Issa, MA., Alrousan, RZ. & Issa, M. 2009. Experimental and parametric study of circular short columns confined with CFRP sheets. *Journal of Composites for Construction ASCE* 13(2): 135–147.

Jiang, T. & Teng, JG. 2006. Strengthening of short RC columns with FRP jackets; *Proc. of the 3rd International Conference on FRP composites in Civil Engineering (CICE-2006), Miami, Florida, USA, 13–15 December 2006*.

Karbhari, V. & Eckel II, DA. 1994. Effect of cold regions climate on composite jacketed concrete columns. *Journal of Cold Region Engineering ASCE* 8(3): 73–86.

Karbhari, V. & Goa, Y. 1997. Composited jacketed concrete under uniaxial compression-verification of simple design equations. *Journal of Materials in Civil Engineering ASCE* 9(4): 185–193.

Karbhari, V., Rivera, J. & Duta, PK. 2000. Effect of short-term freeze-thaw cycling on composite confined concrete. *Journal of Composites for Construction ASCE* 4(4): 191–197.

Karbhari, V. 2002. Response of fiber reinforced polymer confined concrete exposed to freeze and freeze-thaw environmental exposure. *Journal of Composites for Construction ASCE* 6(1): 343–355.

Lam, L. & Teng, J. 2003. Design-oriented stress-strain model for FRP-confined concrete. *Construction and Building Materials* 17(6–7): 471–489.

Lam, L. & Teng, J. 2004. Ultimate condition of fiber reinforced polymer-confined concrete. *Journal of Composite for Construction ASCE* 8(6): 539–548.

Mashrik, MA. 2011. Performance evaluation of circular and square columns wrapped with CFRP and SFRP sheets. *MSc Thesis* Department of Civil Engineering, University of Calgary, Calgary, Canada.

Masia, M., Gale, T. & Shrive, N. 2004. Size effects in axially loaded square-section concrete prisms strengthened using carbon fibre reinforced polymer wrapping. *Canadian Journal of Civil Engineering* 31(1): 1–13.

Mirmiran, A. & Shahwy, M. 1997. Behavior of concrete columns confined by fiber composites. *Journal of Structural Engineering ASCE* 123(5): 583–590.

Mirmiran, A., Shahwy, M., Samaan, M., El Echary, H., Mastrapa, J. & Pico, O. 1998. Effect of column parameters on FRP-confined concrete. *Journal of Composites for Construction ASCE* 2(4): 175–185.

Nanni, A. & Bradford, N. 1995. FRP jacketed concrete under uniaxial compression. *Construction and Building Materials* 9(2): 115–124.

Pessiki, S., Harries, K., Kestner, J., Sause, R. & Ricles, J. 2001. Axial behaviour of reinforced concrete columns confined with FRP jackets. *Journal of Composites for Construction ASCE* 5(4): 237–245.

Richart, F.E., Brandtzaeg, A. & Brown, R.L. 1928. A study of the failure concrete under combined compressive stresses. *Bulletin No. 186*, Engineering Experimental Station, University of Illinois, Urbana, USA: 26(12).

Samaan, M., Mirmiran, A. & Shahawy, M. 1998. Model of concrete confined by fiber composites. *Journal of Structural Engineering ASCE* 124(9): 1025–1031.

Scholefield, BWJ. 2003. The strengthening of reinforced concrete columns with various methods, *MSc Thesis*: Department of Civil Engineering, University of Calgary, Calgary, Canada.

Shahawy, M., Mirmiran, A. & Beitelman, T. 2000. Test and modeling of carbon-wrapped concrete columns. *Composites: Part B* 31(6–7): 471–480.

Silva, MAG. & Rodrigues, CC. 2006. Size and relative stiffness effects on compressive failure of concrete columns wrapped with glass FRP. *Journal of Material Engineering ASCE* 18(3): 334–342.

Smith, ST., Kim, SJ. & Zhang, H. 2010. Behaviour and effectiveness of FRP wraps in the confinement of large concrete cylinders. *Journal of Composites for Construction ASCE* 14(5): 573–582.

Spoelstra, M. & Monti, G. 1999. FRP-confined concrete model. *Journal of Composites for Construction ASCE* 3(3): 143–150.

Thériault, M. & Neale, K. 2004. Fiber-reinforced polymer-confined circular concrete columns: Investigation of size and slenderness effects. *Journal of Composites for Construction ASCE* 8(4): 323–331.

Thermou, GE. & Pantazopoulou, SJ. 2007a. Metallic fabric jackets: an innovative method for seismic retrofitting of substandard RC prismatic members. *Structural Concrete* 8(1): 35–46.

Thermou, GE. & Pantazopoulou, SJ. 2007b. Seismic retrofit of square reinforced concrete columns using composite jacketing; *Proc. of the 8th International Symposium on Fiber Reinforced Polymer Reinforcement for Concrete Structures Patras, Greece, 16–18 July 2007.*

Thermou, GE., Katakalos, K. & Manos, G. 2014. Concrete confinement with steel-reinforced grout jackets. *Materials and Structures* DOI 10.1617/s11527-013-0239-6.

Toutanji, H. 1999. Stress-strain characteristics of concrete columns externally confined with advanced fiber composite sheets. *ACI Materials Journal* 96(3): 394–404.

Toutanji, H. & Deng, Y. 2002. Strength and ductility performance of concrete columns confined with AFRP composite sheets. *Composites: Part B Engineering* 33(4): 251–261.

Youssef, M., Feng, M. & Mosallam, A. 2007. Stress-strain model for concrete confined by FRP composites. *Comosites Part B: Engineering* 38: 614–628.

Wang, EZ. & Shrive, NG. 1999. A 3-D ellipsoidal flaw model for brittle fracture in compression. *Internal Journal of Solids and Structures* 36(27): 4089–4109.

White, D. & Take, W. 2002. Particle Image Velocimetry (PIV) software for use in Geotechnical testing. *CUED/D-Soils/TR322*: 1–14.

White, D., Take, W. & Bolton, M. 2003. Soil deformation measurement using Particle Image Velocity (PIV) and Photogrammetry. *Géotechnique* 57(7): 619–682.

Wu, G., Lu, ZT. & Wu, ZS. 2003. Stress-strain relationship for FRP confined concrete cylinders; *Proc. of the 6th International Symposium on Fiber Reinforced Polymer Reinforcement for Concrete Structures (FRPRCS-6), Singapore, 8–10 July 2003*.

Concrete Solutions – Grantham et al. (Eds)
© 2014 Taylor & Francis Group, London, ISBN 978-1-138-02708-4

Strengthening of concrete ground floors in industrial halls – a case study

G. Dmochowski & P. Berkowski
Wrocław University of Technology, Wrocław, Poland

ABSTRACT: Concrete ground floors in industrial buildings are a very important part of their construction and also represent a significant cost in the construction of these buildings. They are designed very sparingly and their execution is difficult and requires the right equipment and experienced staff. However, damage of industrial floors is frequent and in case of changes in use it is almost always necessary to strengthen them, either locally or over a larger area. The paper presents an example of spatial analysis of strengthening methods of a thin concrete floor in a high-bay warehouse. The possibility of strengthening the floor or spreading the loads acting on it using different kinds of steel grids or an additional concrete slab was analyzed. From the conducted analyses it can be shown that in the case of large point loads the only effective way to reinforce the floor is by thickening it using an additional RC slab. Some methodology of an examination of damaged floors, determination of their capacity and methods of strengthening is also presented.

1 INTRODUCTION

Floor surfaces are one of the most important and most intensively exploited elements of industrial facilities. They carry most of the useful loads which are encountered in industrial halls. Because of this specificity, there have been many studies carried out which include the theoretical basics (e.g. Alani et al. 2013, Ślusarek 2007), and also detailed recommendations regarding the design process of durable industrial floors (ACI 302.1R-96 1996, Technical report No. 34 2003).

The cost of executing a floor constitutes a significant part of the cost of the whole investment. On average, the cost of executing an industrial floor in Poland ranges from 15 to 20 euro/m^2, which constitutes 15 to 20% of the total cost of the investment when the average cost of a hall construction is equal to 100 euro/m^2.

Despite such a significant contribution, both in the cost and in the process of using the whole investment, the process of designing floors, however, is often very limited and only involves determining the thickness of the floor and its loads. The whole design process usually shifts to a contractor of the floor, who in turn is mainly interested in designing and executing as cheaply as possible. In addition, the investor, who orders a bay warehouse, in many cases, is not quite able to specify what actual load the floor will be carrying. Not without significance, regarding the correct execution of a floor, is the fact that it is a large surface object which requires a properly prepared subsoil in order to function appropriately. This hampers the correct execution of the element on the entire and sometimes very wide surface area, and also the control of this execution, which is commonly carried out discreetly and only on certain points of the floor surface.

Figure 1. Cracks in an industrial floor.

Therefore, sometimes at the time of execution, new floors do not have any reserve of bearing capacity, and they even are not able, in an adequate way, to transfer their predicted useful loads. Overloaded floors undergo damage and require repair.

Usually cracks are forming, often very extensive, but sometimes there is also a mutual displacement of floor elements, especially in the area of expansion joints. In practice, there are no floors on which cracks do not arise during operation. Examples of such damage are presented in Fig. 1 and Fig. 2. An equally frequent issue is the need to strengthen a floor due to

Figure 2. Cracks in an industrial floor.

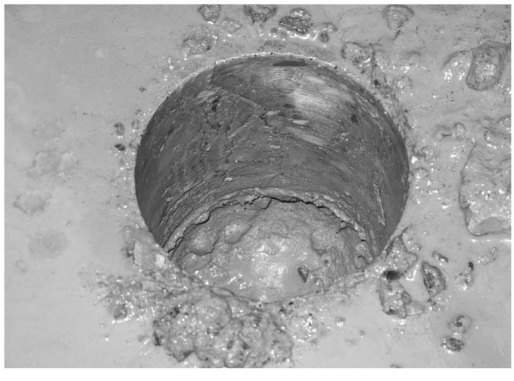

Figure 3. Drill hole in a floor.

changes in how a bay warehouse is used or because of locally designed extra loads, such as additional shelves or devices.

2 DETERMINATION OF THE LOAD BEARING CAPACITY OF AN EXISTING FLOOR

Before designing the strengthening of a floor, it is necessary to recognize its construction and determine the load bearing capacity of the subsoil under the floor. There is often a lack of executive floor documentation and reports of acceptance tests. It can also occur that such documentation is not entirely coherent with the actual execution. Therefore, it is necessary to always perform adequate research in order to define the parameters needed to calculate the floor. Drilling through a floor is usually carried out, as shown in Fig. 3 and Fig. 4, in which the thickness of the floor is defined and from the collected cores and test samples are prepared. Next, using the collected samples, the concrete class of the floor is determined with a compression testing machine.

The degree of compaction of the subsoil in the drilled holes is determined with the use of a manual probe. Based on the fracture of a sample, the degree

Figure 4. Core from a drill hole.

of the floor reinforcement can also be indicatively determined. A floor foundation is often stabilized with cement and therefore there is a need to use a mechanical drilling rig in order to carry out tests. Because of the fact that they are spot tests, it is beneficial to extend the scope of research with the use of non-destructive methods. In addition to sclerometric testing, ultrasonic tomography testing (Hoegh et al. 2012, Hoła & Schabowicz 2010, Rens et al. 2000, Schabowicz 2013) is particularly useful and due to this the profile of the floor, its thickness and also the reinforcement distribution (Fig. 5) can be determined.

3 THE DESIGN OF CONCRETE FLOOR STRENGTHENING

The design of floor strengthening is often limited to a recommendation of crack bonding and/or a reduction of the floor loads and in extreme cases the execution of a completely new floor. In such cases, simplified calculations are carried out with the use of the empirical formulas of Westergard and Heteneyi (Bentur & Mindess 2007, Knapton 2003, Soutsos et al. 2012) and the general theory of plates resting on a Winkler elastic foundation (Dempsey et al. 1990). Sometimes, however, it is necessary to thoroughly check the load bearing capacity of a plate due to a concentrated load, or strengthen the existing plate for such loads, e.g. for high storage racks or additional devices such as manipulators or jacks. Such devices not only cause vertical impacts (Fig. 6) but also horizontal impacts which are practically impossible to take into account in traditional calculations.

In such cases, detailed calculations with the aid of a computer should be carried out. There are two computational examples of a floor located in an industrial high-bay warehouse presented below.

The existing floor was made of fibro concrete (Glinicki 2002) with a thickness of 12 cm and C20/C25 concrete with an addition of steel fibers equal to 20.0 kg/m^3 and polypropylene fibers equal to 0.6 kg/m^3. The assumed and required deformation modulus of the subsoil, according to the authors of

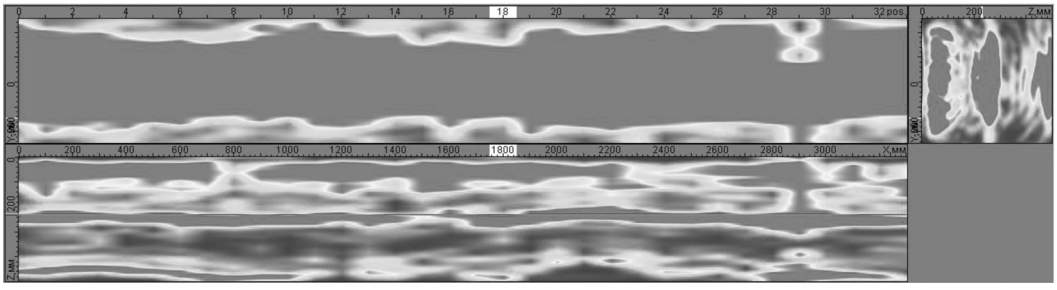

Figure 5. Display of reinforcement distribution – ultrasonic tomography study (Schabowicz 2010).

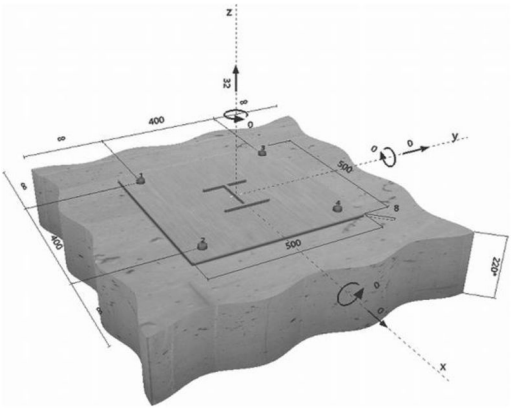

Figure 6. Scheme of concentrated loads of a floor.

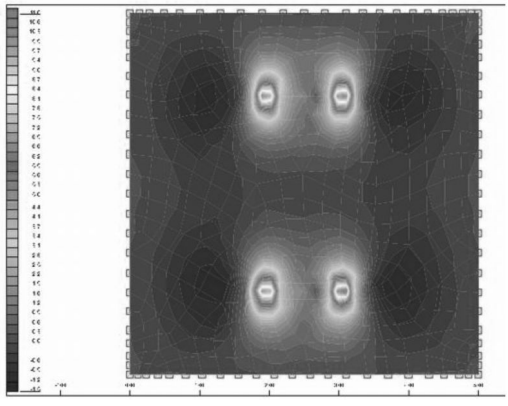

Figure 7. Mx-x moment distribution – steel grid.

the floor project, should be equal to $E_2 \geq 90.0$ MPa and $E_2/E_1 \geq 2.5$ MPa. Under the floor, a sliding layer made of polyethylene foil and a concrete foundation made of C8/C10 concrete with a thickness of 10 cm should be executed. Based on the drilling carried out and research which was described above, the compatibility of the design assumptions to the actual floor construction have been confirmed. Owing to a lack of detailed data about the type of steel fibers which were used in the floor, the equivalent tensile strength of fiber concrete of the floor was determined according to Glinicki (2002) and was equal to $f_{ez} = 1.9$ MPa. The maximum permissible bending moment in the floor was calculated to be equal to $M_{max} = 1900 \cdot 0.12^2/6 = 4.56$ kNm. According to the obtained data, high storage racks were meant to be placed on the floor with a maximum load equal to $P = 60$ kN applied to the middle leg stand of the rack and a maximum load equal to $P = 30$ kN applied to the outer leg stand. The dimensions of one of the rack leg supports were equal to 7.6×7.6 cm.

The preliminary calculations showed that the existing floor did not have an adequate load bearing capacity in order to transfer such concentrated loads. Therefore, strengthening of the existing floor with a steel grid made of profiles or a reinforced concrete slab resting on the existing floor was assumed. Strengthening elements could not be connected to the existing floor permanently, as it was assumed that they should be possible to remove.

3.1 *Strengthening of the floor with a steel grid*

The existing thin reinforced concrete floor with a thickness of 12.0 cm and strengthened with the use of a steel grid made of HEA160, HEA180 or HEA240 profiles, which are placed directly on the floor, were spatially modeled. It was assumed that the designed grid which distributes concentrated loads cannot be permanently attached to the floor. The example results of calculations (bending moment map) are shown in Figures 7 and 8.

For the grid made of HEA160, HEA180 and HEA 240 profiles, the obtained stresses in the existing floor were still too large and exceeded the permissible values for the existing floor.

The designed grid was too flimsy to appropriately distribute concentrated loads. The increase of the profile height also did not give satisfactory results in the form of increased and rapid drops of stresses in the floor.

3.2 *Strengthening of the floor with the use of a reinforced concrete slab*

Based on calculations carried out for the floor loaded with a steel grid, it can be seen that strengthening reinforced concrete floors for concentrated loads using

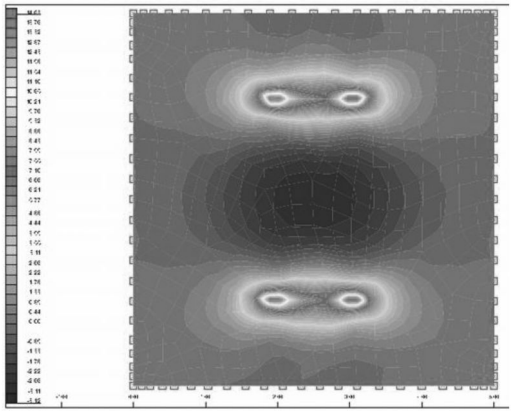

Figure 8. My-y moment distribution – steel grid.

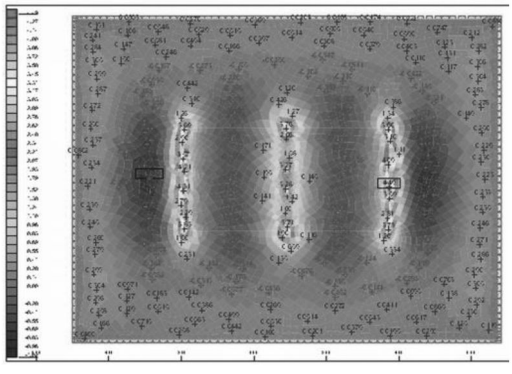

Figure 9. Mx-x moment distribution – concrete slab.

such a solution is inefficient and uneconomical. Therefore, it was decided that the existing floor would be strengthened with an additional reinforced concrete slab. Strengthening of the floor with a reinforced concrete slab was spatially modeled. The slab was assumed to be made of C20/C25 concrete and rests on the existing floor. It was also assumed that the new slab cannot be connected to the floor in order for it to be possible to remove in the future. So, the new slab is separated from the floor with a sliding layer made of two layers of PVC film.

Calculations were carried out for different thicknesses of the slab ranging from 14 to 24 cm, with 2 cm increments. However, only for a 24 cm thick slab, stresses in the existing floor were lower than permissible values. Example results of calculations (bending moment map) are presented in Figures 9 and 10.

4 CONCLUSIONS

The execution of floors in industrial halls should be preceded by a careful and thoughtful executive project which takes into account projected loads and a reserve of load bearing capacity due to possible changes in using the bay warehouse. Preparation of a strengthening or floor repair project requires the execution of many destructive, semi-destructive and non-destructive tests (Sadowski 2013, Schabowicz 2013, Schabowicz & Hoła 2012), and with the use of which, the basic parameters of the subsoil under the floor, and also the floor can be specified. According to the authors of this paper, the strengthening of concrete floors for concentrated loads with the use of steel grids is inefficient and uneconomical and an overlay slab appears to be a more efficient solution.

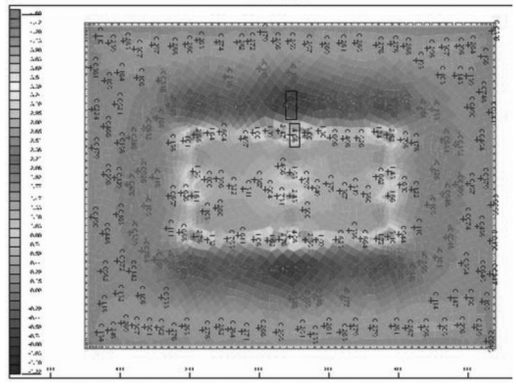

Figure 10. My-y moment distribution – concrete slab.

REFERENCES

ACI 302.1R-96. 1996. *Guide for concrete floor and slab design*. ACI Committee report.

Alani, A.M., Rizutto, J. & Beckett, D. 2013. Structural behaviour and deformation patterns in loaded plain concrete ground supported slabs. *Structural Concrete. J. of the fib* 14(4). DOI: 10.1002/suco.201300043.

Bentur, A. & Mindess, S. 2007. *Fibre reinforced cementitious composites*. Modern concrete technology series. Milton: Taylor & Francis.

Dempsey, J.P., Zhao, Z.G., Minnetyan, L. & Li., H. 1990. Plane contact of an elastic layer supported by Winkler foundation. *J. of Applied Mechanics* 57(4): 974–980.

Glinicki, M.A. 2002. Evaluation and design of fibre reinforced concrete using the equivalent flexural strength. *Drogi i Mosty* (3): 5–36 (in Polish).

Hoegh, K., Khazanovich, L. & Yu, H.T. 2011. Ultrasonic tomography for evaluation of concrete pavements. *Transportation Research Record: Journal of the Transportation Research Board*, Vol. 2232/2011 Geomaterials 2011: 85–94.

Hoła, J. & Schabowicz, K. 2010. State-of-the-art non-destructive methods for diagnostic testing of building structures – anticipated development trends. *Archives of Civil and Mechanical Engineering*, 10(3): 5–18.

Knapton, J. 2003. *Ground bearing concrete slabs*. London: Thomas Telford Publishing.

Rens, K., Transue, D. & Schuller, M. 2000. Acoustic tomographic imaging of concrete infrastructure. *Journal of Infrastructure Systems*, 6(1): 15–23.

Sadowski, Ł. 2013. Non-destructive evaluation of the pull-off adhesion of concrete floor layers using rbf neural network. *J. of Civil Engineering and Management* 19(4): 550–560.

Schabowicz, K. 2010. *Non-destructive testing of ground floor in an industrial floor.* Report SPR 12/2010. Building Engineering Institute (in Polish).

Schabowicz, K. 2013. Methodology for non-destructive identification of thickness of unilaterally accessible concrete elements by means of state-of-art acoustic techniques. *J. of Civil Engineering and Management* 19(3): 325–334.

Schabowicz, K. 2014. Ultrasonic tomography – The latest nondestructive technique for testing concrete members – Description, test methodology, application example. *Archives of Civil and Mechanical Engineering* 14(2): 295–303.

Schabowicz, K. & Hoła, J. 2012. Nondestructive elastic-wave tests of foundation slab in office building. *Materials Transactions*, 53(2): 296–302.

Soutsos, M.N., Le, T.T. & Lampropoulos, A.P. 2012. Flexural performance of fibre reinforced concrete made with steel and synthetic fibres. *Construction and Building Materials* (36): 704–710.

Ślusarek, J. 2007. Selected problems of industrial concrete ground floor design. *Electronic J. of Polish Agricultural Universities*. 10(3).

Technical report No. 34. 2003. *Concrete industrial ground floors – A guide to design and construction*. Concrete Society.

This page intentionally left blank

Concrete Solutions – Grantham et al. (Eds)
© 2014 Taylor & Francis Group, London, ISBN 978-1-138-02708-4

Experimental evaluation of RC beams defected in both concrete strength and steel reinforcement and retrofitted by fiber reinforced polymers

T. M. Elrakib
Housing and Building National Research Center, Cairo, Egypt

ABSTRACT: Insufficient reinforcement lap-splice is one of the defects, which negatively affect the structural behaviour of reinforced concrete beams. Experimental investigation was carried out to study the efficiency of transverse FRP sheets on enhancing the structural behaviour of RC beams that had defected lap splice zones with normal and low concrete strength. Eight RC rectangular beams were tested in positive bending, four of them were strengthened by transverse FRP wraps in the defected lap splice region and the other four beams were kept unstrengthened and considered as control specimens. The main parameters were concrete compressive strength, type of FRP sheets and the retrofitting length as a percentage of the defected lap splice length. The cracking behaviour, failure modes, load-deflection relationships and the strains in longitudinal steel were investigated. It was concluded that the transverse FRP confining system provided a new mechanism whereby most bars over the spliced region could be used more effectively in the stress transfer between steel and concrete leading to a more ductile failure mode combined with a noticeable increase in the ultimate load.

1 INTRODUCTION

Previous experimental researches reported in the literature have shown that there are mainly two effective methods for enhancing bond strength in the lap splice regions of beams. Harjli (2001) showed that the use of steel fibers in the concrete matrix increased both the tensile strength and toughness of normal strength concrete resulting in higher bond strength and leading to a considerable improvement in ductility. Research conducted by Najjar (2002) showed that the use of transverse reinforcement in the form of hoop stirrups could cause higher bond strength levels and more ductile bond behaviour leading to adequate bond strength with a relative shorter lap splice length. On the other hand, FRP composites have been used widely for repairing of deteriorated RC elements and they are also used to strengthen existing structures against shear and flexural failures. FRP-laminated composites present significant advantages such as high-strength/weight ratio, lightweight, ease of handling and application and faster construction rates Ashour (2004) and Baha (2005). However, a limited number of studies were conducted to investigate strengthening RC beams defected in the lap splice zone with FRP sheets. Hamed (2004) experimentally and analytically studied the effect of confinement provided by FRP on bond strength of tension lap splices anchored in high strength concrete beams. Although the strengthened beams showed a more ductile response in comparison with the control beams, the final mode of failure was splitting of the concrete cover. Reinforced concrete beams with defects in both their compressive strength and steel reinforcement lap splice length are currently faced in a considerable number of structures constructed under inadequate quality control procedures. This study evaluates the efficiency of FRP sheets as an alternative and efficient tool to enhance the bond strength of defected lap splice reinforced concrete beams.

2 TEST PROGRAM

The experimental test program involved eight RC beams $150 \times 300 \times 200$ mm designated as B1 to B8. Control beams B1 and B2 had full lap splice length according to ECP (2007). Beams B3 and B4 had a shortage in the lap splice length. Beams B5 to B8 were retrofitted with U-shaped FRP sheets with different schemes in the defected lap splice region.

Table 1 and Figure 1 show the details of the tested beams. The modulus of elasticity, tensile strength and thickness of the CFRP sheets used were 240 GPa, 3900 MPa and 0.11 mm respectively while they were 65 GPa, 1700 MPa and 0.135 mm for the GFRP sheets.

3 TEST RESULTS AND ANALYSIS

3.1 *Mode of failure and load-deflection behaviour*

The test beams were loaded to failure and the observed behavior in terms of cracking, modes of failure and load-deflection response were recorded. Generally, for all the control beams (B1 to B4) two major flexural

Table 1. Details of the tested beams.

Beam no.	F_{cu} N/mm^2	Lap splice length L_s, mm	FRP configuration	Retrofitting length, mm
B1	35	750		----
B2	19	960		----
B3	35	0.4x750= 300		----
B4	19	0.4x960= 380		----
B5	35	300		100%L_s=300
B6	19	380		100%L_s=380
B7	19	380		100%L_s= 380
B8	19	380		200%L_s=760

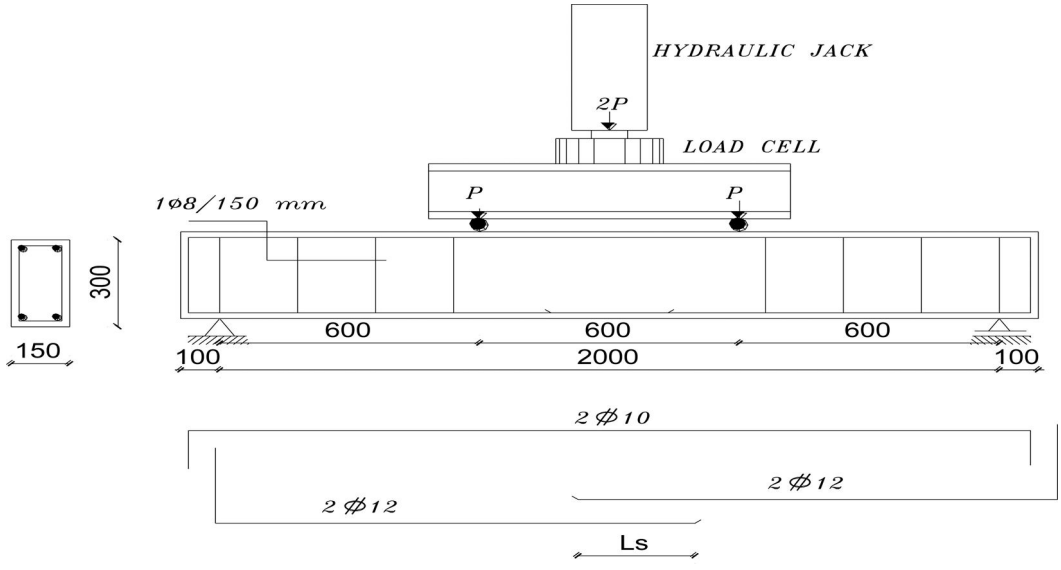

Figure 1. Test setup and reinforcement details of tested beams, mm.

cracks initially appeared at the critical sections adjacent to the end of the lap splice zone and extended vertically by the increase of load up to failure. In addition to the two major cracks minor diagonal tension cracks appeared. For the control beams B1 and B2 failure occurred by yielding of tension reinforcement followed by splitting the concrete cover within the lap splice zone. In beams B3, B4 with inadequate lap splice length, failure occurred suddenly and was accompanied by a loud sound after the formation of longitudinal splitting cracks in the bottom cover of the tension side.

The failure of beams B3 and B4 could be classified as a pronounced sudden and brittle mode of failure. Beams B5, B6, and B7 with transverse FRP sheets showed a noticeable enhancement in the overall structure behavior as they exhibited a more ductile failure mode. For those beams, two major vertical cracks appeared at the two ends of the splice zone followed by noticeable signs of longitudinal splitting cracks in the bottom and side concrete cover within the splice region. The clamping force developed by the FRP sheets delayed the propagation of the longitudinal splitting cracks and forced the beams to carry additional load. After reaching the peak load, the load dropped gradually with increasing deflection. Beam B8 with FRP sheet cover of 200% of the defected splice zone showed a similar mode of failure.

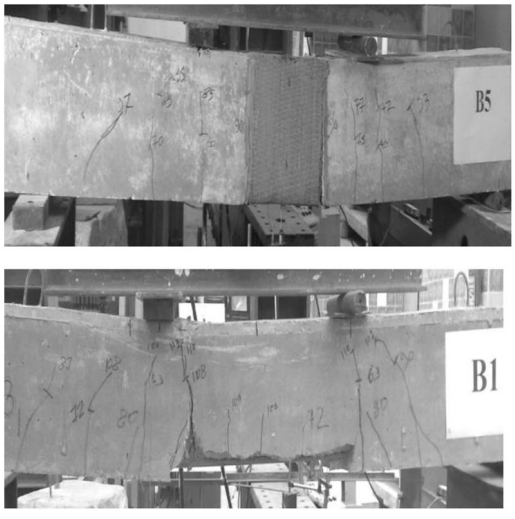

Figure 2. Mode of Failure of Beams B1 and B5.

The appearance of some of the tested beams after testing is shown in Figure 2. Ultimate load P_u, deflection at failure Δ_f, defection at yield Δ_u, steel strain at ultimate load ε_u are shown in Table 2. On the other hand, the applied load was plotted against the vertical deflection measured at midspan for all tested beams as shown in Figures 3 (a,b). For beams B1, B3 and B5, a noticeable increase in the ultimate load and deflection of the strengthened beam B5 compared with the control beam B3 was found. The load deflection relationships for beams B2, B4 and B6, led to the same observations.

3.2 *Stiffness, ductility and strains in longitudinal steel reinforcement*

The stiffness of each beam was evaluated as the slope of the linear ascending part of the load deflection curve and is presented in Table 2. It can be noticed that the unstrengthened control beams (B3, B4) had relatively lower stiffness compared with those with full lap splice length (B1 and B2). Meanwhile, beams with U-shaped CFRP sheets (B5, B6 and B8) had approximately the same stiffness compared with unstrengthened control beams (B3, B4) indicating that the use of transverse FRP sheets did not affect the flexural stiffness of the strengthened beams.

On the other hand, many authors adopted the displacement ductility index, μ_Δ, to evaluate the ductility level of RC beams, Ashour (2004) and Baha (2005).

$$\mu_\Delta = \Delta_f / \Delta_y \quad (1)$$

Where Δ_f = Deflection at 80% of the ultimate load on the descending branch of the load-deflection curve, Δ_y = Deflection at yield load was calculated from the load-deflection curve as the corresponding displacement of the intersection of the secant stiffness at a load value of 80% of the ultimate lateral load and

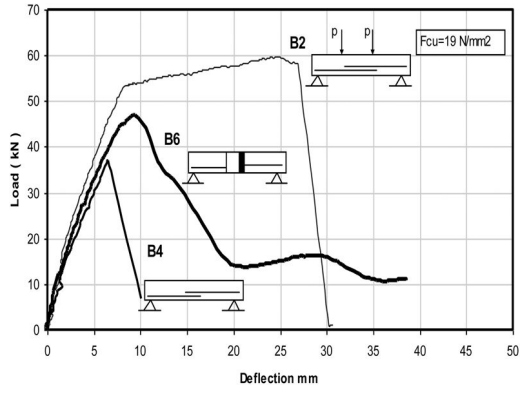

Figure 3a. Load deflection relationship for beams B2, B4.

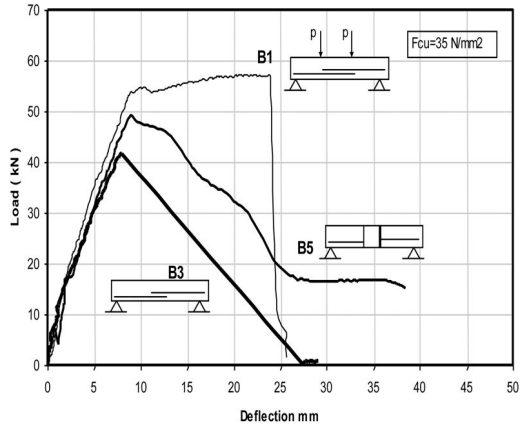

Figure 3b. Load deflection relationship for beams B1, B3, and B5.

the tangent at the ultimate load. Regarding Table 2, beams with U-shaped FRP sheets had a meaningful increase in the ductility indexes compared with B3 and B4. Also, it was noted that the longitudinal steel strain values for all tested beams, except for B3, are much higher than the yield strain $\varepsilon_y = 2000$ indicating that the longitudinal reinforcing steel of these beams reached the hardening range leading to ductile behavior. As shown in Table 2, the difference in the steel strain values between the control specimen B1 and the strengthened one B5 was quite small and the strain of both recorded about 5000 ($\times 10^{-6}$). The maximum strain of B3 hardly reached 1993 indicating that using FRP wraps allowed steel bars along the splice zone to participate more effectively in the stress transfer within the lap splice zone.

4 EFFECT OF KEY PARAMETERS

4.1 *Effect of type of FRP*

Figure 4 and Table 2 show that the ultimate load of B6 and B7 was 27% and 22% higher than that of the

Table 2. Experimental results of the tested beams.

Beam	Ultimate load, P_u(kN)	Δ_f mm	Δ_y mm	Steel strain at ultimate load, $\varepsilon_u \times 10^{-6}$	Stiffness N/mm	Ductility ratio $\mu_\Delta = \Delta_f/\Delta_y$
B1	57.00	24.4	8.56	5100	6670	2.85
B2	59.00	26.5	8.69	4000	6700	3.05
B3	41.60	12.5	7.14	1993	6100	1.75
B4	37.05	8.5	6.58	2712	5900	1.29
B5	49.10	18.3	7.46	4334	5800	2.45
B6	47.05	13.6	6.32	3370	6000	2.15
B7	45.15	14.3	6.36	–	5400	2.25
B8	59.50	23.5	8.55	4200	6300	2.75

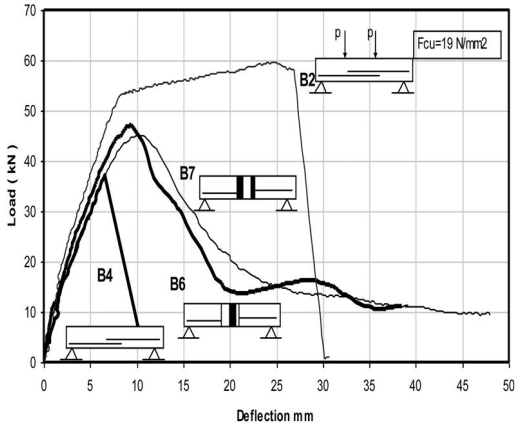

Figure 4. Load deflection relationship for beams B2, B4, B6, and B7.

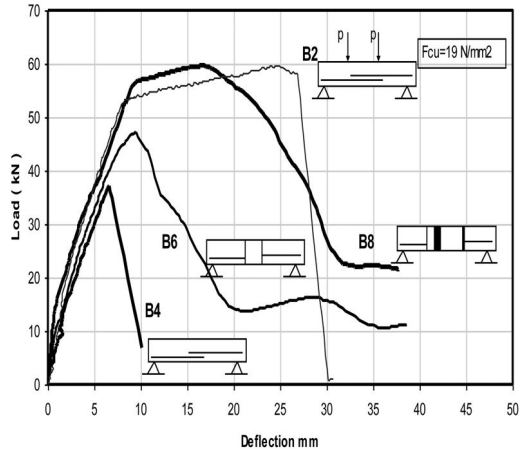

Figure 5. Load deflection relationship for beams B2, B4, B6 and B8.

control beam B4 and lower than the ultimate load of control beam B2 by 20% and 23% respectively.

The displacement ductility indexes of B6 and B7 increased by 66.66% and 74.42% respectively compared with that of the defected beam B4. The overall structural behaviour of beams B6 and B7 showed that the type of FRP sheets, glass or carbon, confining the splice zone had no significant effect on load-deflection behaviour or mode of failure.

4.2 *Effect of length of the strengthened zone*

Figure 5 presents the load deflection relation for B6 with a strengthened zone equal to 100% of lap splice length and B8 with strengthened length equal to 200% of the same lap splice length. The ultimate loads of the strengthened beams B6 and B8 were higher than that of the defected beam B4 by 27% and 60% respectably. In addition, the ultimate load of beam B6 was lower than that of the control beam B2 by 20%, whereas the ultimate load of the strengthened beam B8 was almost identical to the ultimate load of the control beam B2.

Table 2 shows that the ultimate load and ductility index of beam B8 were higher than that of beam B6 by 26% and 27% respectively. The pronounced improved behaviour of beam B8 in comparison with beam B6 indicate that the negative effect of the defected splice zone on the beam behaviour practically extends beyond the lap splice area and the extension of the U-shape FRP wraps is practically required to restore the structural behaviour of the defected beam.

4.3 *Effect of concrete compressive strength*

Figure 6-a shows the load deflection relation of beams B1, B2, B3, and B4. Beams B1 and B2 represent the control beams which had reinforcement lap splice lengths according to the provisions of the Egyptian code while, beams B3 and B4 represent the defected beams which had 40% of the lap splice lengths assigned for beams B1 and B2, respectively.

In addition, Figure 6-b shows the load deflection of the retrofitted beams B5 and B6 in comparison with the control beams B1 and B2. Although the compressive strength of beam B2 (19 MPa) was lower than that of B1 (35 MPa) by 45.70%, the ultimate load was slightly higher than that of beam B1 by 3.50% in clear contradiction with the expected behaviour.

The previous behaviour could be attributed to two reasons; firstly, the lap splice length of beam B2, which was 960 mm, was longer than the distance between the

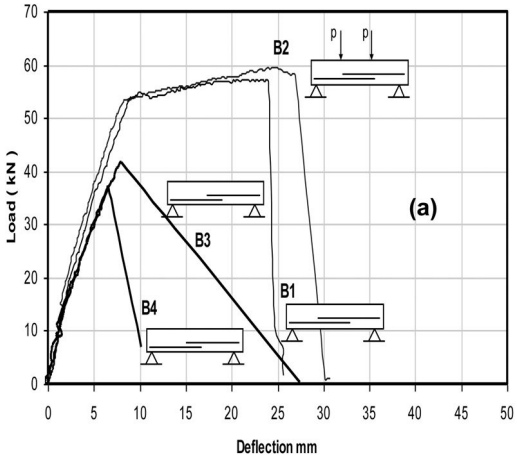

Figure 6a. Load deflection relationship for beams B1, B2, B3, and B4.

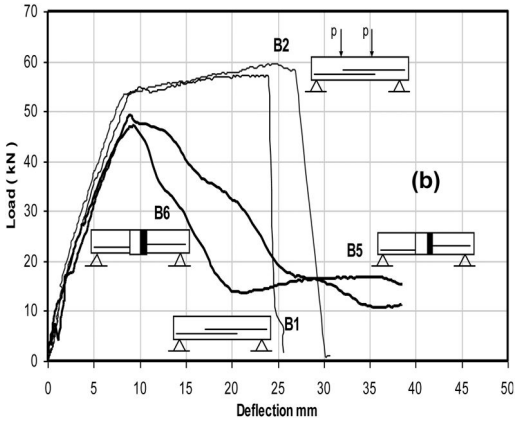

Figure 6b. Load deflection relationship for beams B1, B2, B5, and B6.

two-point load (600 mm) and consequently the beam actually contained four longitudinal steel bars at the constant moment region. Secondly, the concrete compressive strength has a minor effect on the ultimate strength of the flexural members. The load deflection responses of the defected beams B3 and B4 were approximately similar. However, beam B4 was more negatively affected by the shortage of lap splice length regarding the ultimate load and ductility. Reducing the concrete compressive strength by 45.70% for beam B4 in comparison with B3 resulted in reduction of ultimate load and ductility by 10.90% and 26.30% respectively, which could lead to the conclusion that the Egyptian Code equation of calculating lap splice length is conservative for low quality concrete. The load deflection relations of the retrofitted beams B5 and B6 shown in Figure 6-b support the previous conclusion. As shown in Figure 6-b, the retrofitted beams B5 and B6 had almost the same behaviour although the ductility of beam B6 was slightly lower than that of beam B5 by 12%.

5 CONCLUSIONS

Based on the presented experimental test results, the following conclusions could be drawn:

- Wrapping the insufficient lap splice length zone of reinforced concrete beams having either normal or low concrete strength by FRP is highly effective in enhancing both the ultimate load and the mode of failure. A ductile mode of failure instead of brittle mode was observed for all wrapped beams. In addition, the load deflection flexural stiffness was almost the same for all the tested beams.
- None of the FRP U-shaped strengthened beams experienced debonding or separation of the sheet at the end of the U-shape and based on the results of the tested beams, no special anchorage system is needed for bonding the FRP sheets on the concrete faces.
- Wrapping the beams in the lap-splice zone by GFRP showed a comparable structural performance in comparison with those beams wrapped by CFRP. In both cases, the mode of failure changed from brittle mode to ductile and the enhancement in ultimate load and ductility were approximately the same. In addition, increasing the FRP strengthening length beyond the defected lap splice length zone completely restored the beam performance including ultimate load and ductility.

REFERENCES

Ashour, A. F., El-Refaie, S. A. & Garrity, S. W. "Flexural strengthening of RC Continues Beams using CFRP Laminates", *Cement and Concrete Composites Journal*, Vol. 26, Mars 2004, pp. 765–775.

Baha, T., Khafaga, M., "Strengthening of Continuous RC Beams Using CFRP Laminates", *The 7th International Conference on Multi-Purpose High Rise Towers and Tall Buildings*, Dec. 2005, Dubai, UAE.

ECP203, "*Egyptian Code of the Design and Construction of Reinforced Concrete Structures*", Housing and Building National Research Center, 2007, Egypt.

Hamed, B., Soudki, K., Harajli, M. & Rteil, A., "Experimental and Analytical Evaluation of Bond Strength of Reinforcement in Fiber-Reinforced Polymer-Wrapped High Strength Concrete Beams", *ACI Structural Journal*, Vol. 101, No. 6, July 2004, pp. 747–754.

Harajli, M., Hamed, B. & Jumaa, G., "Effect of Fiber Reinforcement on Bond Strength of Tension Lap Splice in HSC", *ACI Structural Journal*, Vol. 98, No. 5, Nov.2001, pp. 638–647.

Najjar, S. & Hamad, B., "Evaluation of the Role of Transverse Reinforcement in Confining Tension Lap Splices in HSC", *Materials and Structures Journal*, Vol. 35, 2002, pp. 219–228.

This page intentionally left blank

Concrete Solutions – Grantham et al. (Eds)
© 2014 Taylor & Francis Group, London, ISBN 978-1-138-02708-4

Flexural strengthening of reinforced concrete beams with prestressed externally bonded CFRP sheets

M. Hadiseraji & R. El-Hacha
University of Calgary, Calgary, Alberta, Canada

ABSTRACT: Strengthening reinforced concrete (RC) members with Externally Bonded (EB) Carbon Fibre Reinforced Polymer (CFRP) sheets has shown promising results and gained general acceptance among civil engineers worldwide. However, the use of non-prestressed CFRP sheets for flexural strengthening is not an efficient way of exploiting the full strength of the CFRP material. By prestressing the CFRP sheet, the material can be used more efficiently for strengthening purposes and not only increases the flexural carrying capacity of the RC members, but also improves the serviceability by delaying the onset of cracking, reducing cracking extent, decreasing deflections, as well increasing yielding of the strengthened members. Four RC beams were tested, two of which were strengthened with the CFRP sheet post-tensioned to 33% and 41% of the CFRP's ultimate tensile strain, one beam strengthened with non-prestressed CFRP sheet, and one un-strengthened control beam for comparison purposes. For prestressing the CFRP sheets, an innovative anchorage system was developed using Shape Memory Alloy (SMA) bars that acted as actuators and eliminated the use of hydraulic jacks. The flexural behaviour of the prestressed beams under static four-point bending was investigated and compared to the beam strengthened with non-prestressed CFRP sheet as well as to the un-strengthened control beam.

1 INTRODUCTION

The strengthening and repair of Reinforced Concrete (RC) members either for changing the use of the structure (increasing the service load) or restoring the initial strength of deteriorated concrete members is becoming a common trend. Strengthening RC members with Near-Surface Mounted (NSM) or Externally Bonded (EB) Fibre Reinforced Polymer (FRP) materials is known to be one of the most reliable and effective methods of increasing the load carrying capacity of the RC members. In addition, strengthening of RC beams with prestressed FRP materials has many advantages over non-prestressed FRPs. This specialized application of FRP materials combines the benefits of non-prestressed bonded FRPs with the advantages of external prestressing (El-Hacha et al. 2009). This application of FRPs can be also used to restore prestress to a system that has a loss of internal prestressing due to rupture of prestressing tendons (El-Hacha et al. 2009). Prestressing also helps to exploit the full capacity of the high-strength FRP materials. In the application of prestressed FRP material for flexural strengthening of RC beams, the anchorage/prestressing system plays a major role in determining the efficiency of the strengthening system in terms of labour and time costs. Many researchers have made special efforts in recent years to develop practical, simple and cost-effective anchorage systems to apply prestressing force to FRP material. The currently developed anchorage systems for prestressing EB FRP material can be classified into two major groups: indirect and direct prestressing systems (El-Hacha et al. 2005). An external reaction frame is used to induce the desired prestressing force to the FRPs in the indirect prestressing system. In the direct prestressing system, the FRP is prestressed against the beam itself, and there is no need for any external reaction frame. Triantafillou & Deskovic (1991), Garden & Hollaway (1998), Meier et al. (2001) and Yu et al. (2006) developed systems to indirectly prestress EB FRP material, while Wight (1998), El-Hacha (2000) and Neubauer et al. (2007) developed direct prestressing system for strengthening RC beams with EB FRP material. A state-of-the-art paper has been published recently by El-Hacha and Soudki (2013) that summarizes research on prestressed NSM FRP for flexural strengthening of RC beams along with a comprehensive review of the techniques and anchorage systems developed to prestress the NSM FRP. In the current study, an innovative direct anchorage system was developed to prestress EB CFRP sheets using Shape Memory Alloy (SMA) bars as actuators. The use of SMA actuators eliminated the need for a hydraulic jack for applying prestressing force to the CFRP material and simplified the prestressing procedure compared to other existing anchorage/prestressing systems.

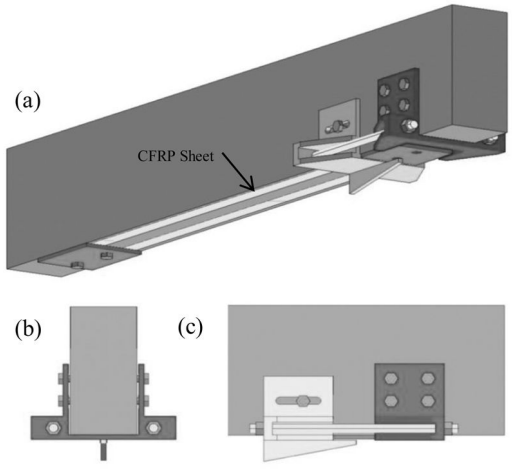

Figure 1. EB technique end steel anchors (blue plates) along with temporary anchorage system components: (a) isometric view, (b) elevation, (c) side-view.

2 EXPERIMENTAL PROGRAM

2.1 *Testing matrix*

Four 2-meter long RC beams with a centre-to-centre span length (between the supports) of 1.8 m were cast and tested under four-point bending until failure. The beams had a typical rectangular cross-section of 150 mm × 305 mm (width × height) and were reinforced with 2–15 M, 2–10 M and 10 M @150 mm spacing as bottom, top and shear reinforcement, respectively. Three beams were strengthened with two layers of EB CFRP sheets. The CFRP sheets were prestressed to 33% and 41% of their ultimate tensile strength in beams B-EB-33% and B-EB-41%, respectively; while, one beam was strengthened with non-prestressed EB CFRP sheets (B-EB-00). In addition, one un-strengthened control beam (B-00) was also tested for comparison purposes.

2.2 *Material properties*

The beams were cast using normal density cast-in-place concrete with a 28-day compressive strength of 40 MPa. The concrete mix cement to fine aggregate to coarse aggregate weight proportions were 1.00 to 3.05 to 3.93. A water to binder ratio of 0.4 was used in the mixture. The cement and fly ash contents were 250 kg/m^3 and 111 kg/m^3, respectively. The specified yield strength and modulus of elasticity of the longitudinal bottom reinforcement used for fabrication of beams were 458 MPa and 172 GPa, respectively. The transverse and top reinforcement of the beams had a yield strength and modulus of elasticity of 610 MPa and 183 GPa, respectively. SikaWrap® Hex 230C CFRP sheet, manufactured by Sika Canada Inc., was used as strengthening material in the strengthened beams. The ultimate strength, modulus of elasticity, and ply thickness of the CFRP laminate (with Sikadur® 330 epoxy adhesive) were reported to be 894 MPa, 64 GPa, and 0.381 mm, respectively (Sika Canada, 2009a). Sikadur® 330 epoxy adhesive was used to bond the prestressed or non-prestressed EB CFRP sheets to the tension soffit of the beams. The adhesive's yield strength and modulus of elasticity were 30 MPa and 3.8 GPa, respectively (Sika Canada, 2009b).

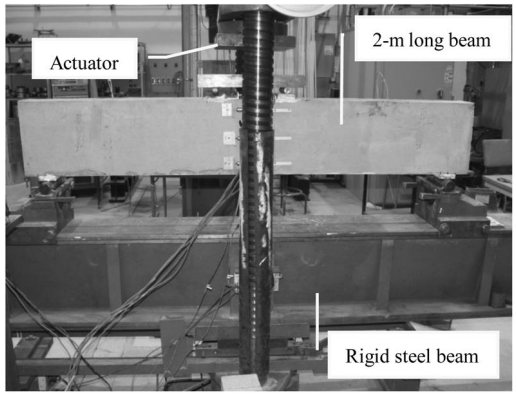

Figure 2. Test set-up.

2.3 *Anchorage/prestressing system*

In order to prestress the CFRP sheets in beams B-EB-33% and B-EB-41%, an innovative anchorage system was developed using prestrained SMA actuators. Figure 1 demonstrates the prestressing system mounted on the beam along with the end CFRP sheet steel plates. The prestressing force was applied to the CFRP sheets by activating the prestrained SMA bars through heating them above their activation temperature.

2.4 *Test setup*

All the beams were tested under four-point flexural loading until failure. The beams were supported on roller and hinge supports at the ends. The load was applied at a consistent rate of 2 kN/min to the beams. The load was transferred to the beam through a thick steel plate attached to the actuator. Then, the load was spread between two points, 300 mm apart, using two 1-inch diameter steel rollers sitting on a 75 × 150 × 12 mm steel plate. Figure 2 shows the test set-up for control beam (B-00).

2.5 *Test results*

2.5.1 *Load-deflection and moment curvature*

Figures 3 and 4 demonstrate the load-deflection and moment-curvature curves for the tested beams, respectively. The curvature at mid-span is calculated based on the strain of the bottom steel and top concrete fibre. As shown in these figures, the behaviour of all beams was linear until the first flexural crack occurred at mid-span, causing a sudden slight increase in deflection and steel strain under

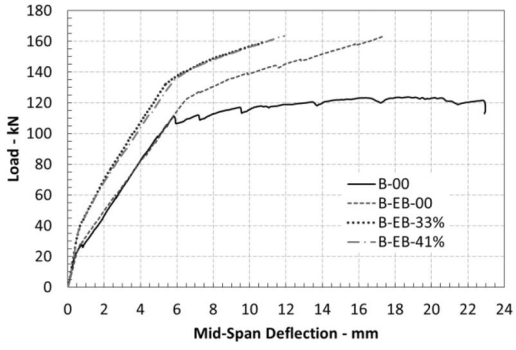

Figure 3. Load – mid-span deflection curves.

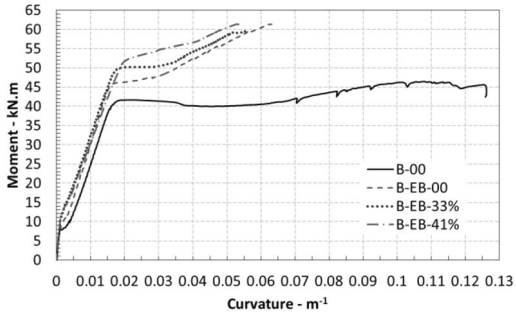

Figure 4. Moment-curvature curves.

constant load. The cracking loads were 19, 22.4, 26 and 31 kN for beams B-00, B-EB-00, B-EB -33% and B-EB-41%, respectively. These cracking loads correspond to a mid-span deflection of 0.35 mm, 0.5 mm, 0.4 mm, and 0.47 mm, respectively.

Yielding of the bottom steel caused the beam to deflect at a faster pace. The bottom steel strain value at the onset of yielding was $\sim$2600 $\mu\varepsilon$. The bottom steel started to yield at a load of 104 kN for beam B-00, whereas the yielding load was 114, 127 and 125 kN for beams B-EB-00, B-EB-33% and B-EB-41%, respectively. These yielding loads correspond to a deflection of 5.97, 5.1, 0.4, and 5.24 mm for beams B-EB-00, B-EB-33%, and B-EB-41%, respectively.

The control beam (B-00) failed by concrete crushing, while all other beams failed by rupture of the CFRP sheets. The ultimate load for all beams was defined as the load at which concrete crushed or CFRP sheet ruptured. For the control beam, concrete crushing at top fibre was observed at a strain of 4400 $\mu\varepsilon$. The CFRP rupture occurred at strains of 12000, 8800 and 9700 $\mu\varepsilon$ for beams B-EB-00, B-EB-33% and B-EB-41%, respectively. It should be mentioned that these strain values do not include the initial strain in the sheets due to prestressing (3594 and 4626 $\mu\varepsilon$ for beams B-EB-33% and B-EB-41%).

The test was stopped after failure of the beams, whether by concrete crushing or by the CFRP sheet rupture, as it was impossible to maintain the load

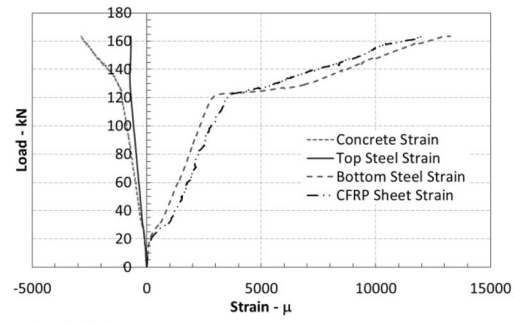

(a) B-EB-00

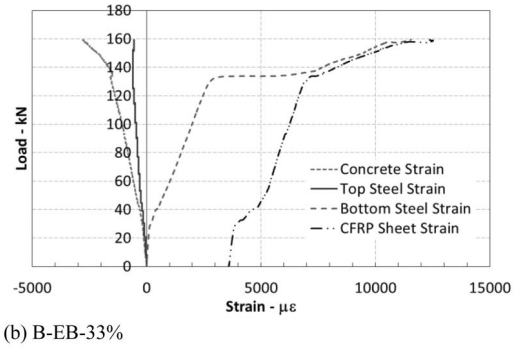

(b) B-EB-33%

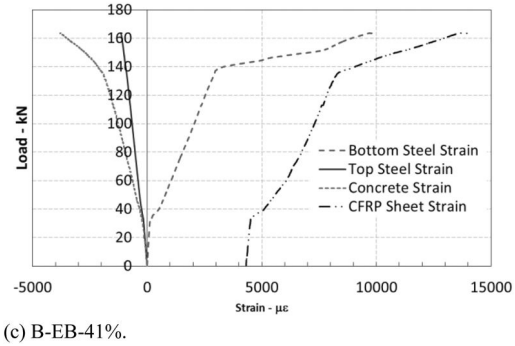

(c) B-EB-41%.

Figure 5. Load-Strain Curves.

on the beams (load-control test). The ultimate loads for beams B-00, B-EB-00, B-EB-33% and B-EB-41% were 124, 163.5, 159, and 163 kN, respectively.

2.5.2 *Load-strain curves*

Concrete, bottom steel, top steel and CFRP strip strain variation at mid-span is presented in Figure 5 with respect to the applied load for beams B-EB-00, B-EB-33% and B-EB-41%. Initial strains in the CFRP sheet due to prestressing are included in these graphs. Ignoring the initial strain in the CFRP sheet, strain values in the sheet was slightly higher than the bottom steel strain up to the yielding load, where the steel strain started to increase dramatically. The CFRP strain was lower

than the bottom steel strain for the portion of the graphs between yielding and ultimate load for all beams.

2.5.3 *Strain distribution*

The strain distributions at mid-span cross-section are presented in Figure 6 for the strengthened beams. Average values of strain at mid-span are used for top concrete fibre, bottom steel and CFRP sheet to develop these graphs. It is noted that the strain value in the CFRP sheet at the ultimate stage was lower than the corresponding bottom steel strain value for all strengthened beams (strain lag), causing non-linear strain distribution along the depth of cross-section at ultimate load. The lower strain value in the CFRP sheet could be attributed to the localized debonding at concrete–epoxy interface causing the bottom steel strain value to increase dramatically while the force in the CFRP sheet was locally released. The lower strain value in the CFRP sheet can also be attributed to the plastic deformation of the bonding agent layer causing the additional stress to be carried by the steel reinforcement rather than the CFRP sheet.

3 DISCUSSION AND COMPARISON

3.1 *Comparing B-EB-41% to B-00*

Strengthening the beam with prestressed CFRP sheets considerably reduced the extent of flexural cracks at ultimate load. Flexural test results showed that the cracking, yielding and ultimate loads of the strengthened beam (B-EB-41%) were increased by 63%, 20% and 31%, respectively in comparison with the unstrengthened beam (B-00). Besides, the beam deflection at ultimate load was reduced by 48%, proving that prestressing successfully improved serviceability of the beam. The CFRP sheet has a very brittle behaviour and behaves linearly under tension until failure. This caused the ductility index (ratio of the deflection at ultimate over deflection at yield) of beam B-EB-41% to decrease by 49%, compared to the control beam (4.3 versus 2.2 for B-00 and B-EB-41%, respectively). Besides, the amount of energy absorbed (the area under load-deflection curve) by the beam before failure showed 26% decreases (1899 versus 1389 kN.mm for B-00 and B-EB-41%, respectively). The decrease in the energy absorbed is attributed to both brittle behaviour of the CFRP sheet and its relatively low modulus of elasticity (∼86 GPa).

3.2 *Comparing B-EB-41% to B-EB-00*

Strengthening the beam with prestressed CFRP sheet instead of non-prestressed strengthening material not only increased the flexural capacity of the beam, but also improved the serviceability. For beam B-EB-41% the deflection at cracking, yielding and ultimate load decreased by 6%, 12%, and 32% respectively. The prestressing did not affect the flexural capacity of the beam at ultimate as both beams failed by rupture of

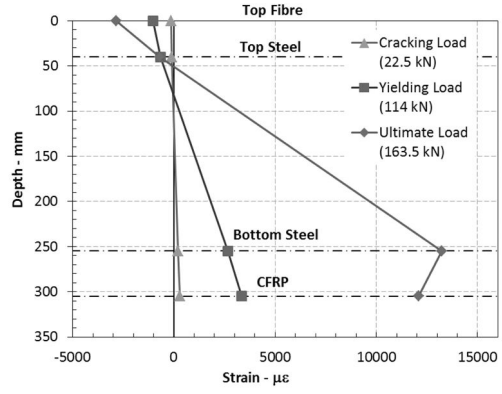

(a) B-EB-00

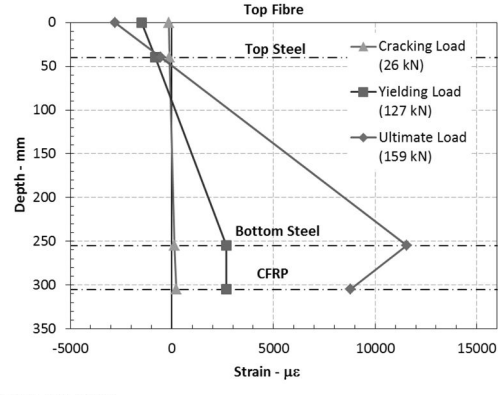

(b) B-EB-33%

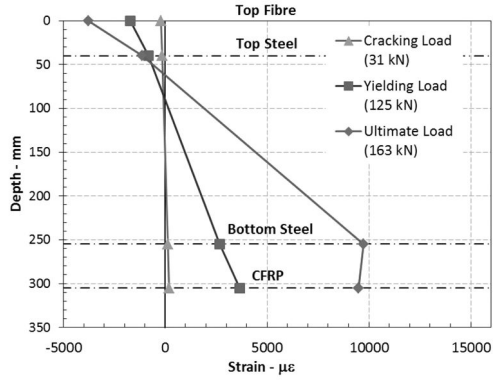

(c) B-EB-41%

Figure 6. Load – mid-span deflection curves.

the CFRP sheet. The prestressing decreased the ductility index (μ) and the energy absorption capability of the beam ($E_{absorbed} = 2026$ and 1389 kN.mm, and $\mu = 2.9$ and 2.2 for B-EB-00 and B-EB-41%, respectively). Post-tensioning the CFRP sheets decreased the available strain for elongation in the CFRP material

before rupture and hence caused the decrease in ductility index (μ) and in the amount of absorbed energy ($E_{absorbed}$).

4 CONCLUSIONS

The flexural test results showed that strengthening RC members with prestressed EB CFRP sheet is a reliable method for improving the serviceability and increasing flexural capacity of these structural members. Using a non-ductile material (e.g. CFRP sheet) as strengthening material, however, has some disadvantages. Strengthening RC beams with CFRP sheets, as a brittle material, reduces the ductility of the member. Furthermore, increasing the prestress level can lead to further decrease in the ductility index.

ACKNOWLEDGEMENT

The authors would like to acknowledge SIKA Canada for donating the CFRP sheets and epoxy adhesives, the technical staff at University of Calgary for their assistance: Mr. Terry Quinn, Mr. Don Anson, Mr. Mirsad Berbic, Mr. Dan Tilleman and Mr. Dan Larson. The authors also wish to acknowledge and the University of Calgary for sponsoring the project.

REFERENCES

El-Hacha, R. 2000. Prestressed CFRP sheets for strengthening concrete beams at room and low temperatures. *Ph.D. thesis, Queen's Universisty*, Kingston, Ontario, Canada. 551.

El-Hacha, R., Green, M.F., & Wight, R.G. 2005. Prestressed CFRP sheets strengthening technique: development from research laboratory to field application. *Proceeding, 3rd International Conference: Construction Materials: Performance, Innovations and Structural Implications (CONMAT2005)*. Vancouver, BC, Canada. (CD-Rom 10 p.)

El-Hacha, R., Green, M.F. & Wight, R.G. 2009. strengthening concrete structures with prestressed FRP systems. *Proceeding, 4th International Conference on Construction Materials: Performance, Innovations and Structural Implications (CONMAT 2009)*, August 24-26 . Nagoya, Japan, 593–602.

El-Hacha, R., & Soudki, K., 2013. Prestressed Near-Surface Mounted fibre reinforced polymer reinforcement for concrete structures — a review, Canadian Journal for Civil Engineering, Vol. 40, September, 1127–1139.

Garden, H.N., & Hollaway, L.C. 1998. An experimental study of the influence of plate end anchorage carbon fibre composite plates used to strengthen reinforced concrete beams. *ELSEVIER: Composite Structures 42*, 175–188.

Meier, U., Stlocklin, I., & Terrasi, G.P. 2001. Making better use of the strength of advanced materials in structural engineering. *Proceedings, International Conference on FRP Composites in Civil Engineering (CICE)*, Vol. 1, Hong Kong, China, December 12–15, 2001, 41–48.

Neubauer, U., Berg, W. V., & Onken, P. 2007. Structural strengthening with a new system of prestressed CFRP strips. *Proceeding, 8th International Symposium on Fiber Reinforced Polymer Reinforcement for Concrete Structures (FRPRCS-08)*. July 16–18, Patras, Greece: University of Patras. 10.

Sika Canada. 2009a. Product Data Sheet: Carbon Fibre Fabric for Structural Strengthening System. Montreal, Canada: Sika Canada Inc.

Sika Canada. 2009b. Product Data Sheet: Impregnation Resin for Fabric Reinforcement. Montreal, Canada: Sika Canada Inc.

Triantaflllou, T. C., & Deskovic, N. 1991. Innovative prestressing with FRP sheets: mechanics of short-term behavior. *ASCE: Journal of Engineering Mechanics*, Vol. 117, Issue 7. July, 1652–1672.

Wight, G., Green, M.F., & Erki, M.-A. 2001. prestressed FRP sheets for poststrengthening reinforced concrete beams. *ASCE: Journal of Composites for Construction*, Vol. 5, Issue 4, November, 214–220.

Yu, P., Silva, P.F., & Nanni, A. 2006. Flexural performance of RC beams strengthened with prestressed CFRP sheets. Report. Center for Infrastructure and Engineering Studies, University of Missouri-Rolla, 9.

This page intentionally left blank

Concrete Solutions – Grantham et al. (Eds)
© 2014 Taylor & Francis Group, London, ISBN 978-1-138-02708-4

Experimental study concerning the material behavior of CFRP confined plain and reinforced concrete

K. Holschemacher & S. Käseberg
HTWK Leipzig, University of Applied Sciences, Faculty of Civil Engineering, Leipzig, Germany

ABSTRACT: It is well known that confinement introduced by CFRP (Carbon Fiber Reinforced Polymer) jackets highly increases the ultimate compressive strength and ductility of concrete. Various experimental research programs have been proposed to express the increase in strength and strain by the use of CFRP jackets, but, in the majority of cases, the additional effects of reinforcing elements, like ties or spirals, have not been analyzed very well. This paper provides the investigations on wrapped short concrete columns with and without ties and spirals. In an extensive research program the volumetric ratio of the CFRP jacket and the ratio of transverse reinforcement were varied. Thereby, columns with different geometrical shape, different CFRP thickness, and with different transverse reinforcement elements were produced. Executed deflection controlled compression tests provided investigations concerning the structural behavior of the test specimens. The main results of these tests will be explained. A solution is proposed to take the confinement action of the external CFRP material and of the internal transverse reinforcement into account.

1 INTRODUCTION

1.1 *Confinement pressure provided by ties or FRP confinement*

Confinement is generally applied to members in compression with the goal to increase their strength and ductility. Besides conventional transverse tie reinforcing steel also advanced FRP (Fiber Reinforced Polymers) materials have recently recognized as favorable confinement devices. FRP consists of strengthening fibers (for example carbon fibers) in a resin system. The FRP confinement appears by orienting the fibers transverse to the longitudinal axis of the concrete member. Through FRP strengthening by confinement, concrete's lateral expansion is efficiently restricted in cases of imposed axial compressive deformation; therefore, the elastic FRP resisting response generates an ever increasing lateral compressive stress state on concrete, leading to structural upgrade of the member core to provide sufficient deformability. If concrete cylinders are of interest, the confining pressure σ_l (also denoted as f_l) can be found from Equation 1 (fib 2001).

$$\sigma_l = \frac{1}{2}\rho_j \cdot \sigma_j = \frac{1}{2}\rho_j \cdot E_j \cdot \varepsilon_j \quad \text{with} \quad \rho_j = \frac{4 \cdot t_j}{D} \tag{1}$$

where ρ_j = volumetric ratio of FRP jacket, σ_j = stress in FRP jacket, E_j = modulus of composite material, ε_j = circumferential strain in FRP jacket (max $f_l \rightarrow \varepsilon_j = \varepsilon_{ju}$ = ultimate strain of FRP jacket), t_j = FRP thickness, and D = diameter concrete cylinder.

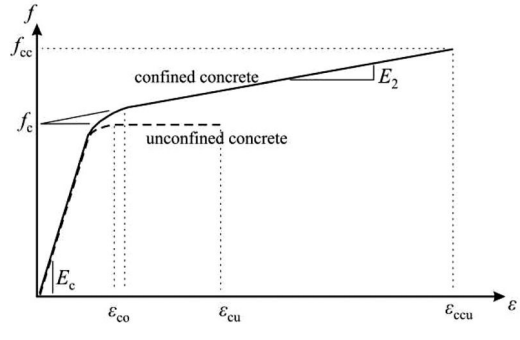

Figure 1. Stress-strain model for CFRP confined concrete by Lam and Teng (2003).

1.2 *Stress-strain models of CFRP confined concrete*

In the past, various experimental research programs had been carried out by other researchers to express the increase in strength and strain by the use of CFRP (Carbon Fiber Reinforced Polymer) jackets.

Some of them were adopted by design recommendations. Examples are the stress-strain model by Lam & Teng (2003) in ACI 440.2R-08 (2008) or the model by Spoelstra & Monti (1999) in technical report by the fib (2001). The stress-strain model by Lam and Teng is illustrated in Figure 1. The maximum confined concrete compressive strength f_{cc} can be calculated with the following equations by Lam and Teng (Equation 2) or by Spoelstra and Monti (Equation 3). Thereby, f_{c0} is the unconfined concrete strength and

k explains the impact of confinement pressure onto axial stress.

$$f_{cc} = f_{c0} + k \cdot f_l = f_{c0} + 3.3 \cdot f_l \tag{2}$$

$$f_{cc} = f_{c0}\left(0.2 + 3\sqrt{\frac{f_l}{f_{c0}}}\right) \tag{3}$$

The ultimate strain ε_{ccu} of the confined concrete member can be calculated if using Equation 4 by Lam and Teng or Equation 5 by Spoelstra and Monti.

$$\varepsilon_{ccu} = \varepsilon_{c0} \cdot \left(1.75 + 12 \cdot \frac{f_l}{f_{c0}} \cdot \left(\frac{\varepsilon_{ju}}{\varepsilon_{c0}}\right)^{0.45}\right) \tag{4}$$

$$\varepsilon_{ccu} = \varepsilon_{c0} \cdot \left(2 + 1.25 \cdot \frac{E_c}{f_{c0}} \cdot \varepsilon_{ju} \sqrt{\frac{f_l}{f_{c0}}}\right) \tag{5}$$

where ε_{c0} = unconfined concrete strain at peak stress and E_c = initial tangent modulus of elasticity of concrete.

Finally, like shown in Figure 1, the second modulus E_2 of the confined concrete can be determined. With the presented models and equations only the contribution of the CFRP jacket is explained. It is only possible to calculate confined plain concrete, but the presented equations are not suitable for reinforced concrete. The contribution of the internal transverse steel reinforcement and other effects, like, for example, the instability of the longitudinal steel reinforcement, can not be taken into account.

2 EXPERIMENTAL INVESTIGATIONS

2.1 *Emphases of research*

In the majority of cases, the additional effects of reinforcing elements, like ties or spirals, are not analyzed very well. It results of the limited experimental evidence on the area of FRP confinement of real-size RC columns. Additionally, these limits have not allowed the appropriate implementation of key effects in current models. Hence, the goals of the research work presented in this paper are the production and test of circular columns with different diameters (from 15 up to 30 cm), different steel ties and steel spirals, and with CFRP jackets of different thickness and material properties.

2.2 *Experimental program*

In an extensive research program the volumetric ratio of the CFRP jacket ρ_j as well as the ratio of transverse reinforcement ρ_{st}, which are mainly accountable for effective confining pressure, were varied. Columns with different geometrical shape, different strength, different CFRP thickness, and with different transverse reinforcement elements (steel ties and spirals)

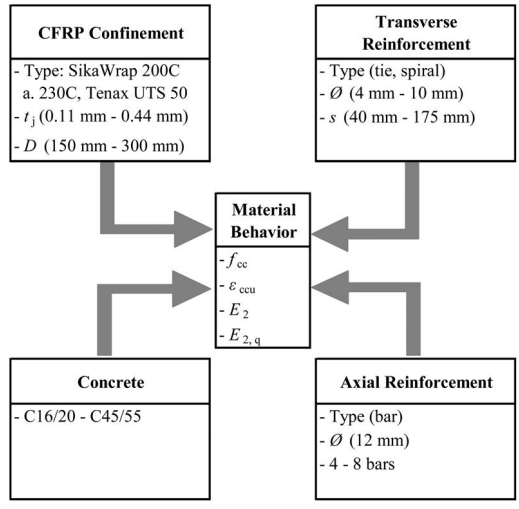

Figure 2. Variation of material properties.

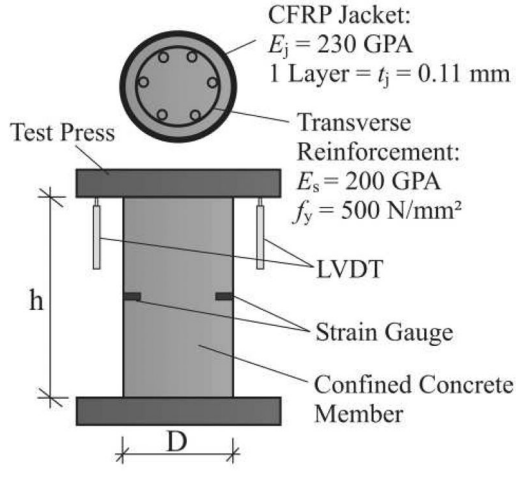

Figure 3. Test setup.

were produced and tested. During the tests, two different measurement systems were used. In all the specimens, beside the strain gauges on the FRP jacket (at midheight), two LVDT's were fixed at two opposite sides of each specimen in order to measure the axial shortening.

Figure 2 presents the experimental setup. Figure 3 explains typical stress-strain curves in longitudinal and transverse directions derived from the compression tests.

In Figure 3 the stress-strain curves of specimens with a diameter of 150 mm, which where confined with one up to three layers of CFRP, are shown. The stress-strain behavior (longitudinal and transverse) of the CFRP confined specimens was bilinear in general, and consisted of the three phase behavior reported in Figure 1. The second modulus E_2 could be observed in the longitudinal (E_2) as well as in the transverse ($E_{2,q}$)

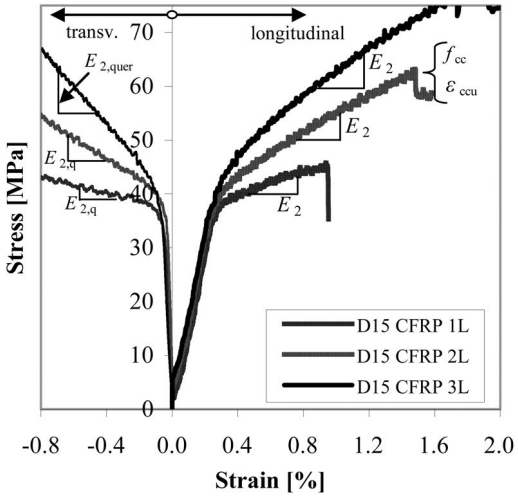

Figure 4. Typical stress-strain curves.

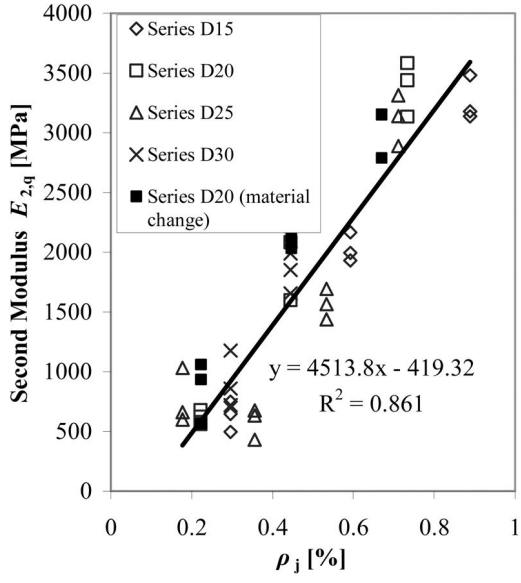

Figure 5. Second modulus $E_{2,q}$ as a function of ρ_j.

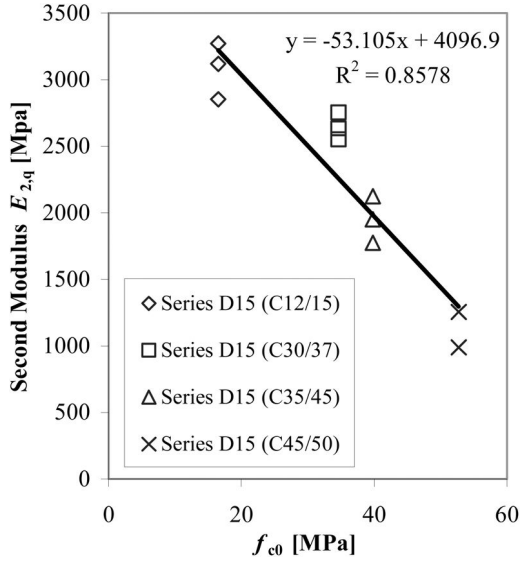

Figure 6. Second modulus $E_{2,q}$as a function of f_{c0}.

direction (cf. Figure 3). The failure of CFRP confined plain or steel reinforced specimens was 'explosive' due to the sudden and noisy fracture of CFRP sheets at ultimate strength f_{cc} and strain ε_{ccu}. Furthermore, Figure 3 also explains the interrelationship between the second modulus and the volumetric ratio of the CFRP jacket. More layers of CFRP produce higher volumetric ratios, and this circumstance results in higher second modulus and in higher ultimate states of strength and strain. These connections were used for the discussion of the compression tests in the next sections.

3 RESULTS AND DISCUSSION

3.1 *CFRP confined plain concrete*

This section explains the results on confined plain concrete. Columns with different geometrical shape and different CFRP thickness were produced to vary the CFRP thickness t_j and the diameter of the column D. Both are responsible for the volumetric ratio of the CFRP jacket. The left diagram of Figure 4 describes the second modulus $E_{2,q}$ (transverse) as a function of the volumetric ratio of the CFRP jacket. It clearly can be seen that there is a big influence of the volumetric ratio on the second modulus. It is possible to find a regression curve for mathematical interpretation. Thereby, the volumetric ratio is able to take account of potential size effects.

The regression curves of small (D15), medium (D20 and D25), and large specimens (D30) are almost the same. These results permit the conclusion that there is no size effect on the material behavior of confined specimens. Figure 5 explains the big dependency of $E_{2,q}$ on the unconfined concrete strength f_{c0}. In this case, only f_{c0} was changed. The column diameter (150 mm) and the properties of the deployed CFRP system remained unchanged.

Because of this, the proposal of Xiao & Wu (2003) was used to involve the unconfined strength into analysis. If the confined modulus E_{jl} is deployed in relation to f_{c0}, very good regressions can be found to explain E_2 and $E_{2,q}$.

$$E_{jl} = \frac{1}{2}\rho_j \cdot E_j \tag{6}$$

An example is shown in Figure 6. Herein, $E_{2,q}$ is described as a function of the ratio between E_{jl} and f_{c0}. The very high coefficient of determination clearly confirms the proposal of Xiao and Wu.

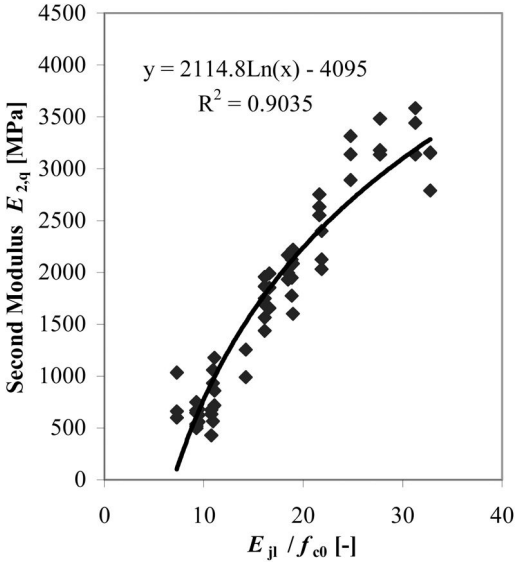

Figure 7. Second modulus $E_{2,q}$ as function of E_{j1}/f_{c0}.

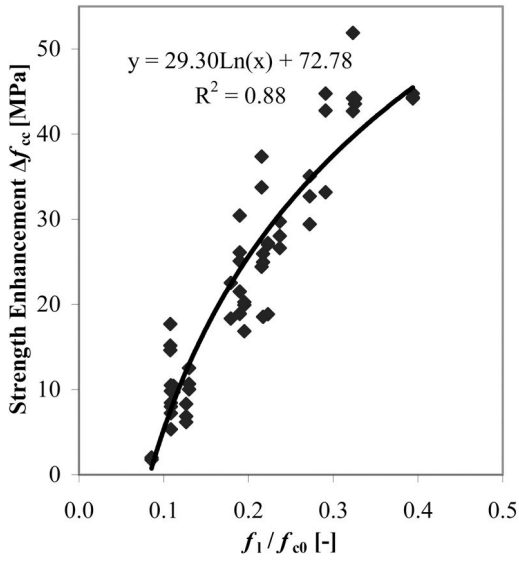

Figure 8. Strength enhancement Δf_{cc} as function of the ratio between f_l and f_{c0}.

Furthermore, by adding the ultimate strain ε_{ju} of the CFRP material it is possible to find proper regressions to calculate the ultimate stress f_{cc} and the ultimate strain ε_{ccu} of a confined concrete column (cf. Equation 1). Figure 7 provides an example. Herein, the strength enhancement Δf_{cc} is now described as a function of the ratio between f_l and f_{c0}. The strong coefficient of determination of the regression curve indicates the reliability of the ratio between confinement pressure and unconfined concrete strength to predict the load bearing capacity of a CFRP confined concrete member.

It appears not sufficient to work with a fixed value to describe the factor k in Equation 2, as supposed by Lam & Teng (2003). Accordingly, it becomes urgent to take into account the relation between CFRP confinement system and concrete properties.

3.2 *CFRP confined reinforced concrete*

This section describes the results on confined reinforced concrete. Thereby, the effect of a dual confinement (consisting of transverse steel reinforcement and CFRP confinement) was the point of interest. Dual confinement strongly increases the load bearing capacity in general. In doing so, it is possible to summarize the shares of the confinement pressures of CFRP and steel confinement.

$$f_{l(\mathrm{FRP,\,steel})} = \frac{1}{2}\rho_{\mathrm{j}} \cdot E_{\mathrm{j}} \cdot \varepsilon_{\mathrm{ju}} + \frac{1}{2}\rho_{\mathrm{st}} \cdot f_y \cdot k_{\mathrm{e}} \qquad (7)$$

where ρ_{st} = transverse steel volumetric ratio, f_y = yield stress, and k_e = coefficient of lateral and vertical efficiency of transverse steel reinforcement.

In the diagrams of Figure 8 and 9, the strength enhancement as well as the ultimate strain reached for

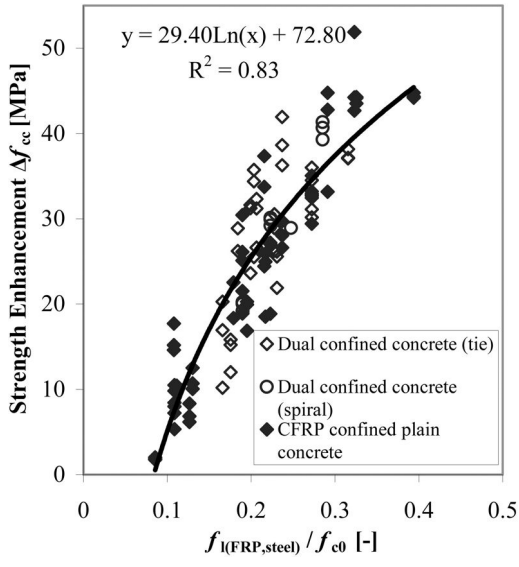

Figure 9. Strength enhancement Δf_{cc} as function of $f_{l(\mathrm{FRP,steel})}/f_{c0}$.

the confined plain concrete columns and of the reinforced ones are shown as functions of the ratio between $f_{l(\mathrm{FRP,steel})}$ and f_{c0}. Again, it is possible to find common regression curves for mathematical interpretation.

Concerning the material behavior of reinforced specimens in the axial direction, an analogy is obvious, where continuous decrease of specimens' axial rigidity occurs. However, this transition zone is more prolonged and smooth than plain FRP confined specimens showed.

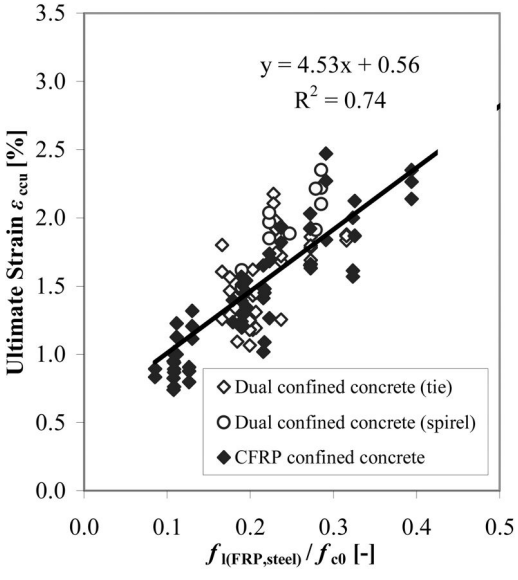

Figure 10. Ultimate strain ε_{ccu} as functions of $f_{l(FRP,steel)}/f_{c0}$.

Figure 10 describes the differences in the material behavior with a comparison between a CFRP confined concrete specimen and a column dual confined by spiral and CFRP jacket.

In this case, a CFRP confined (2 layers) specimen with a diameter of 300 mm and a spiral ($Ø = 10$ mm, $s = 55$ mm) is compared with a specimen of the same diameter and confinement but without reinforcement.

As explained in Equation 7, it is assumed that for the case of steel transverse reinforcement a constant confining pressure can be expected when the steel is yielding and the stress-strain relationships of steel-confined concrete gradually decrease after the yielding of the steel. The following second modulus is similar to the E_2 observed in confined plain concrete. The reason is that a further strength enhancement only depends on the CFRP action now. Likewise, Figure 10 reveals that the strain development in the CFRP jacket and transverse reinforcement is different. After leaving the elastic range of the concrete material, the obtained strain of the deployed transverse reinforcement increased slowly compared to the strain determined in the CFRP jacket. An important fact, if it is considered that different material models (Hu et al. 2012, Eid & Paultre 2008) assume that $\varepsilon_j = \varepsilon_{st}$.

3.3 *Influence of longitudinal reinforcement*

It is well known that at the rupture of FRP the hoop strain reached in the jacket ε_{ju} is generally considerably smaller than the ultimate tensile strain found from flat coupon tensile tests ε_{FRP}. Because of this reason, Lam & Teng (2003) established an FRP efficiency factor k_ε.

$$\varepsilon_{ju} = k_\varepsilon \cdot \varepsilon_{FRP} \tag{8}$$

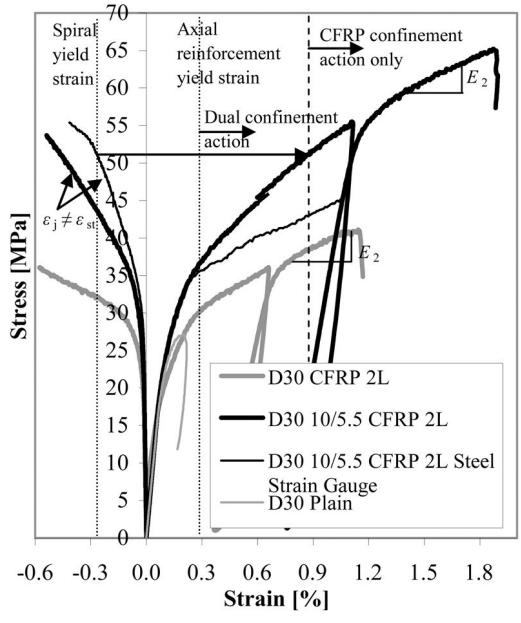

Figure 11. Comparison between a confined concrete specimen (D30 CFRP 2L) and a reinforced concrete specimen (D30 10/5.5 CFRP 2L).

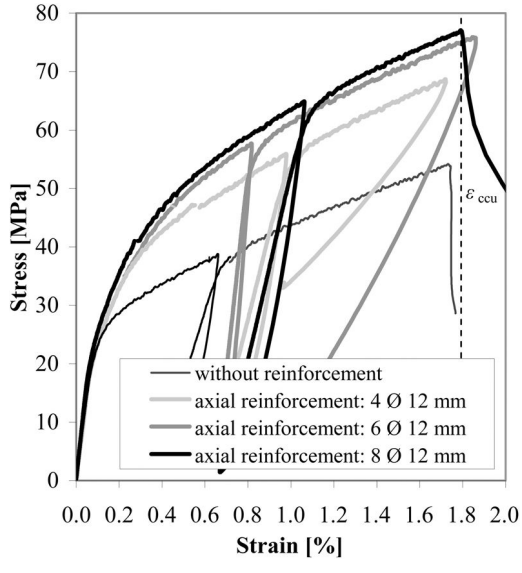

Figure 12. Comparison between confined reinforced concrete specimens with a different amount of longitudinal bars.

Their own experimental program revealed a k_ε of approximate 0.7 for SikaWrap 200C and 230C fibers. For Tenax UTS 50 fibers the reached k_ε was around 0.5.

Furthermore, some research groups (Pellegrino & Modena 2010) propose that the longitudinal reinforcement has an impact on k_ε. This is due to the fact that external FRP confinement in columns provides

additional restraining for vertical steel bars, postponing buckling especially when steel stirrups are poorly stepped. Pellegrino and Modena propose that this results in further strain concentrations, mainly near the location of the vertical steel bars, and causes a further decrease of k_ε.

Their own investigations with CFRP confined reinforced specimens did not confirm this assumption. The longitudinal reinforcement remained without impact. Evidence can be given with Figure 11. Therein, CFRP confined specimens with a diameter of 200 mm and the same tie configuration ($\varnothing = 6$ mm, $s = 100$ mm) but with different amount of longitudinal bars ($\varnothing = 12$ mm) are compared. Thereby, the number of bars differed between 4 and 8.

It is obvious that in all cases nearly the same maximum axial strain ε_{ccu} was reached. A strong impact of the longitudinal reinforcement on ε_{ju} should influence the confinement pressure f_l. Hence, this should reduce ε_{ccu}, but such a behavior could not be observed. The reduction factor k_ε remains the same whether longitudinal reinforcement is deployed or not.

4 CONCLUSION

The FRP confinement can significantly increase the strength and ductility of concrete and reinforced concrete. The present study confirms the bilinear stress-strain model by Lam and Teng for confined plain and reinforced concrete. The proposal of Xiao and Wu to work with the ratio between confinement modulus E_{jl} and unconfined concrete strength f_{c0} also could be confirmed. The dual confinement effect of steel and CFRP confinement resulted as the total of transverse steel reinforcement and the CFRP jacket. Thereby, it is possible to find regression curves in order to explain mathematically the influence of the confinement pressure, which is provided by CFRP and steel confinement, on the stress-strain behavior of wrapped concrete.

REFERENCES

American Concrete Institute (ACI) 2008. *Guide for the Design and Construction of Externally Bonded FRP Systems for Strengthening Concrete Structures*. Farmington Hills: 2008.

Eid, R. & Paultre, P. 2008. Analytical Model for FRP-Confined Circular Reinforced Concrete Columns. *Journal of Composites for Construction* 12 (5): 541–552.

Federation internationale du béton (fib) 2001. *Technical report: Design and use of externally bonded fibre reinforced polymer reinforcement for reinforced concrete structures*. Lausanne: International Federation for Structural Concrete.

Hu, H., Seracino, R., Chen, H. & Feng, P. 2012. Constitutive Model for FRP-and-Steel-Confined circular Concrete Columns in Compression. *Proceedings of the 5th International Conference on FRP Composites in Civil Engineering (CICE 2012)*, Rome, Italy, 13–15 June 2012.

Lam, L. & Teng, J.-G. 2003, Design-oriented Stress–Strain Model for FRP-confined Concrete in Rectangular Columns. *Journal of Reinforced Plastics and Composites* 22 (13): 1149–1186.

Pellegrino, C. & Modena, C. 2010. Analytical Model for FRP Confinement of Concrete Columns with and without Internal Steel Reinforcement. *Journal of Composites for Construction* 14 (6): 693–705.

Spoelstra, M. R. & Monti, G. 1999. FRP-Confined Concrete Model. *Journal of Composites for Construction* 3 (3): 143–150.

Xiao, Y. & Wu, H. 2003. Compressive Behavior of Concrete Confined by Various Types of FRP Composite Jackets. *Journal of Reinforced Plastics and Composites* 22 (13): 1187–1201.

Concrete Solutions – Grantham et al. (Eds)
© 2014 Taylor & Francis Group, London, ISBN 978-1-138-02708-4

Proposal of a material model for FRP confined, circular, short concrete columns with and without internal reinforcement

S. Kaeseberg & K. Holschemacher
HTWK Leipzig, University of Applied Sciences, Faculty of Civil Engineering, Leipzig, Germany

ABSTRACT: In the past, various experimental research programs were carried out by other researchers to express the increase in concrete strength and strain by the use of CFRP (Carbon Fiber Reinforced Polymers) jackets. In the majority of cases, the additional effects of reinforcing elements, like ties or spirals, are not analyzed very well. By deploying our own data base, which provides a lot of results concerning the ultimate strength and strain as well as the stress strain behavior of CFRP confined plain and reinforced concrete, it was able to find regression curves in order to explain mathematically the influence of the unconfined concrete strength and of the confinement pressure, which is provided by the CFRP confinement and the transverse reinforcement. Further data bases, which are available in literature, confirmed the own proposals. It was possible to find proper common regression curves despite the fact that different testing machines, test setups, and raw materials (for concrete and CFRP confinement) were deployed. As a result, the paper will present a common empirical model for predicting the compressive axial behavior of CFRP confined, short concrete columns with and without reinforcement.

1 INTRODUCTION

1.1 *Confinement in general*

Normal transverse reinforcement, like steel ties, specified in design codes for beams and columns aims at the three main functions to prevent buckling of longitudinal bars, to avoid shear failure, and to confine the concrete core. This paper addresses only the confinement functions. Confinement is generally applied to members in compression with the goal to increase their strength and ductility. Thereby, the effective confining pressure f_{ls} caused by conventional spiral or tie reinforcing steel can be calculated with Equation 1 (fib 2001).

$$f_{ls} = \frac{1}{2}\rho_{st} \cdot f_y \cdot k_e \qquad \text{with} \quad \rho_{st} = \frac{4 \cdot A_{st}}{s \cdot d_s} \tag{1}$$

where ρ_{st} = transverse steel volumetric ratio, f_y = yield stress, A_{st} = cross-section of transverse steel, s = spacing of hoops (spirals), d_s = diameter of transverse reinforcement, and k_e = confinement effectiveness coefficient.

Besides conventional transverse tie reinforcing steel also advanced FRP (Fiber Reinforced Polymers) materials have recently been recognized as favorable confinement devices. These materials can provide a maximum confinement pressure at the moment of reaching the rupture strain of the reinforcing fibers.

$$f_l = \frac{2 \cdot t_j \cdot E_j \cdot \varepsilon_{ju}}{D} \tag{2}$$

where f_l = confinement pressure, E_j = modulus of composite material, ε_{ju} = ultimate strain of FRP, t_j = FRP thickness, and D = diameter specimen.

1.2 *Impact of confinement pressure*

Today, there are a lot of material models concerning the relation between confinement pressure provided by CFRP jacket and/or transverse reinforcement and the bearing capacity f_{cc} and corresponding maximum strain ε_{ccu} of a confined column. The typical compressive strength equation is given as follows.

$$f_{cc} = f_{c0} + f_{c0} \cdot k \cdot \frac{f_l}{f_{c0}} \tag{3}$$

where k = confinement effectiveness coefficient.

In the majority of cases, the additional effects of reinforcing elements, like ties or spirals, are not analyzed very well. It results from the limited experimental evidence on the area of FRP confinement of real-size RC columns. Additionally, these limits have not allowed the appropriate implementation of key effects in the current models.

By deploying our own data base, which provides a lot of results concerning the ultimate strength and strain as well as the stress strain behavior of CFRP confined plain and reinforced concrete, we were able to find regression curves in order to explain mathematically the influence of the unconfined concrete strength f_{c0} and of the confinement pressure, which is provided by the CFRP confinement and

the transverse reinforcement. This experimental program is detailed and explained within this conference proceeding (Holschmeacher & Käseberg 2014).

Concerning f_{cc} the following Equation can be given.

$$f_{cc} = f_{c0} + 30 \cdot \ln\left(\frac{f_{l(FRP,steel)}}{f_{c0}}\right) + 73 \quad (4)$$

$$f_{l(FRP,steel)} = \frac{2 \cdot t_j \cdot E_j \cdot \varepsilon_{ju}}{D} + \frac{1}{2}\rho_{st} \cdot f_y \cdot k_e \quad (5)$$

Equation 6 describes the relation between $f_{l(FRP,steel)}$ and ε_{ccu}.

$$\varepsilon_{ccu} = \varepsilon_{c2} \cdot 5.5 + 0.045 \cdot \frac{f_{l(FRP,steel)}}{f_{c0}} \quad (6)$$

These equations confirm that it is possible to summarize the shares of the confinement pressures of CFRP and steel confinement. In a further step our own data base was compared with experimental results internationally released. For better understanding, the next section distinguishes in comparison of data concerning confined plain concrete and comparison with respect to confined reinforced concrete.

2 COMPARISON WITH EXPERIMENTAL RESULTS OF OTHER RESEARCH GROUPS

2.1 *Test series consisting of confined plain concrete*

Our own results (Holschmeacher & Käseberg 2014) for CFRP confined plain concrete were compared with the test results of Xiao & Wu (2003), Lee et al. (2004), Eid et al. (2009), and Lam & Teng (2004). Because of this procedure, we were able to significantly enlarge our own data base. Figures 1–2 include two samples. Figure 1 describes the obtained results for the strength enhancement Δf_{cc} of confined plain concrete columns as functions of the ratio between f_l and f_{c0}. The second sample in Figure 2 describes the ultimate strain ε_{ccu} as function of f_l/f_{c0}.

Both diagrams prove a very good agreement between the different test series. It is possible to find proper common regression curves despite the fact that different testing machines, test setups, and raw materials (for concrete and CFRP confinement) were deployed. In both cases, the obtained regression curves correspond with the Equations 4 and 6 with only minor difference.

2.2 *Test series consisting of confined reinforced concrete*

This section compares our own results for confined reinforced concrete with the test results of Lee et al. (2004), Eid et al. (2009), Ilki et al. (2008), and Matthys et al. (2005). These references offered sufficient data concerning deployed CFRP system and

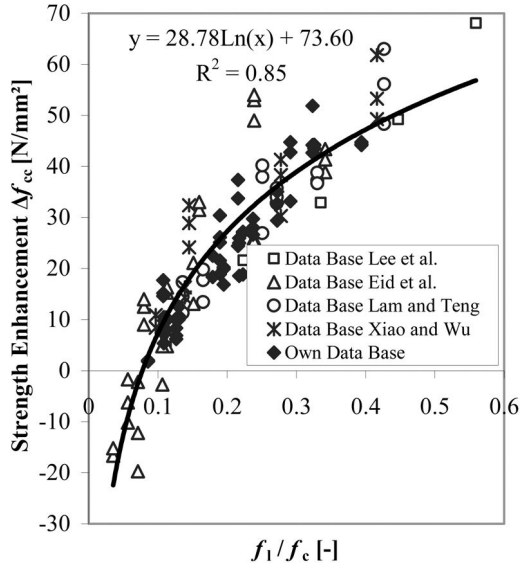

Figure 1. Strength enhancement Δf_{cc} as function of the ratio between f_l and f_{c0}.

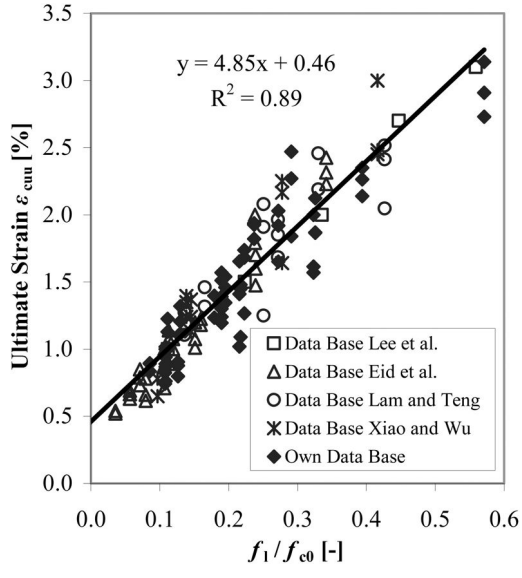

Figure 2. Ultimate strain ε_{ccu} as function of the ratio between f_l and f_{c0}.

transverse reinforcement as well as information with respect to reached f_{cc} and ε_{ccu}. Hence, a sum of our own experimental experience and the results of other research groups was aspired to obtain proper regression curves to predict f_{cc} and ε_{ccu}. Figures 3–4 provide two samples. Both describe the dependency of Δf_{cc} and ε_{ccu} on the ratio between total confinement pressure $f_{l(FRP,steel)}$ and unconfined concrete strength f_{c0}. In both cases, it is possible to find very good and common regression curves for mathematical interpretation.

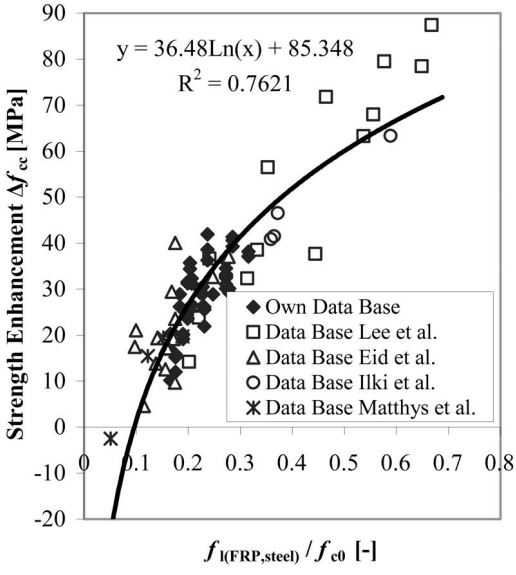

Figure 3. Strength enhancement Δf_{cc} as function of the ratio between $f_{l(FRP,steel)}$ and f_{c0}.

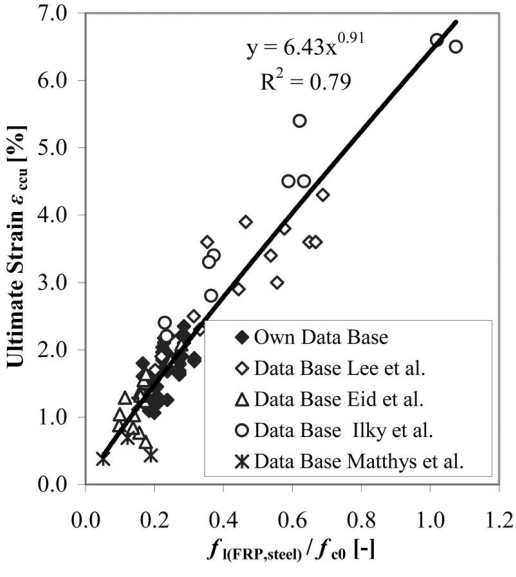

Figure 4. Ultimate strain ε_{ccu} as function of the ratio between $f_{l(FRP,steel)}$ and f_{c0}.

Thereby, the area of tested ratios $f_{l(FRP,steel)}/f_{c0}$ covered by our own results can be enlarged in regions up to $f_{l(FRP,steel)}/f_{c0} = 1.0$. This means that the confinement pressure exceeds the unconfined concrete strength. A consolidated view on the diagrams of Figures 3–4 confirms that deploying the ratio between confinement pressure and unconfined concrete strength is a very good proposal to explain the material behavior of confined concrete.

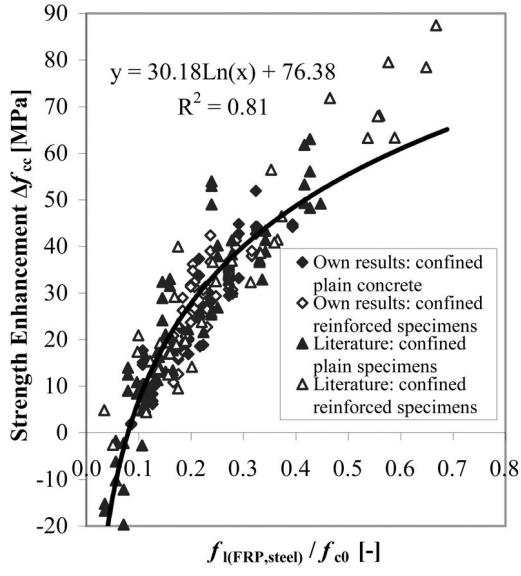

Figure 5. Strength enhancement Δf_{cc} as function of the ratio between $f_{l(FRP,steel)}$ and f_{c0}.

2.3 *Common regression curves for confined plain and reinforced concrete*

In a last step, all results concerning f_{cc} and ε_{ccu}, for CFRP confined plain concrete specimens as well as CFRP confined reinforced concrete specimens, are described in one regression analysis. This is possible if the portion for the transverse reinforcement in Equation 5 is zeroed for specimens without transverse reinforcement.

In Figures 4–5 the results are presented. A very good accordance is obvious if the total confinement pressure is deployed for regression analysis.

We are able to propose common equations for predicting f_{cc} and ε_{ccu}.

$$f_{cc} = f_{c0} + 30 \cdot \ln\left(\frac{f_{l(FRP,steel)}}{f_{c0}}\right) + 75 \tag{7}$$

$$\varepsilon_{cc} = \varepsilon_{c2} \cdot 1.75 + 0.0575 \cdot \frac{f_{l(FRP,steel)}}{f_{c0}} \tag{8}$$

where: ε_{c2} = unconfined concrete strain at peak stress.

3 STRESS-STRAIN MODEL

3.1 *Stress-strain curve*

For a complete stress-strain model the Lam and Teng (Lam & Teng 2003) stress-strain curve is adopted.

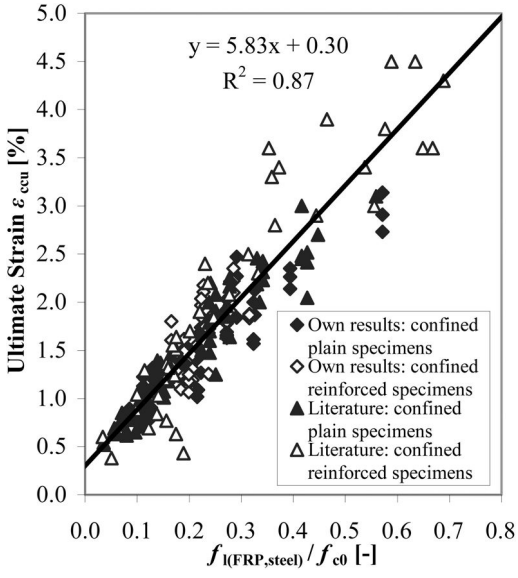

Figure 6. Ultimate strain ε_{ccu} as function of the ratio between $f_{l(FRP,steel)}$ and f_{c0}.

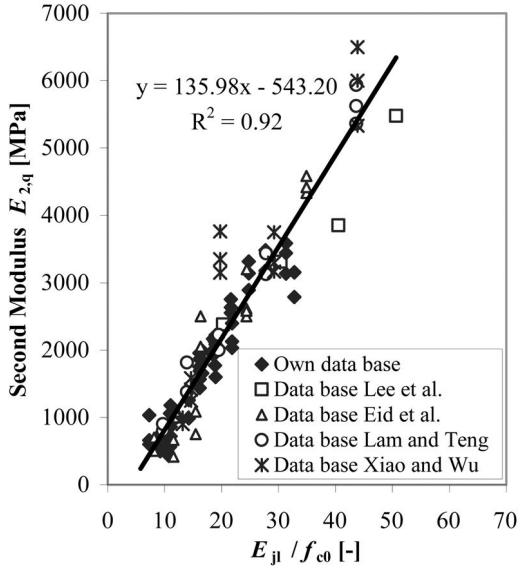

Figure 7. Second modulus $E_{2,q}$ as function of E_{jl}/f_{c0}.

This curve consists of a parabolic first portion and a straight-line second portion.

$$\sigma_c = \begin{cases} E_c \cdot \varepsilon_c - \dfrac{(E_c - E_2)^2}{4 \cdot f_c^*} \cdot \varepsilon_c^2 & (0 \le \varepsilon_c \le \varepsilon_t) \\ f_c^* + E_2 \cdot \varepsilon_c & (\varepsilon_t \le \varepsilon_c \le \varepsilon_{cc}) \end{cases} \quad (9)$$

$$f_c^* = f_{cc} - E_2 \cdot \varepsilon_{ccu} \quad (10)$$

$$\varepsilon_t = \frac{2 \cdot f_c^*}{E_c - E_2} \quad (11)$$

The compressive strength as well as the ultimate strain can be calculated with Equations 7–8. The so called second slope E_2, which describes the linear second portion in Equation 9, is explained in the next section.

3.2 *Calculation of second slope E_2*

Our own wn analysis with respect to E_2 indicated that E_2 mainly depends on the volumetric ratio of the CFRP jacket and the unconfined concrete strength. Due to this fact, the proposal of Xiao & Wu (2003) was considered to involve the unconfined strength into analysis. If the confined modulus E_{jl} is deployed in relation to f_{c0}, very good regressions can be found to explain E_2 and $E_{2,q}$.

$$E_{jl} = \frac{1}{2} \rho_j \cdot E_j \quad (12)$$

$E_{2,q}$ describes the linear second portion in transverse stress-strain response. In this case, a simple linear function is sufficient to explain the relation between $E_{2,q}$ and E_{jl}/f_{c0}.

Again, it was able to find a common regression curve for our own results and experiments found in the literature. The analysis is given in Figure 7. The following Equation is proposed.

$$E_{2,q} = 136 \cdot \frac{E_{jl}}{f_{c0}} - 540 \quad (13)$$

In a last step, it became urgent to take axial-transverse strain response into consideration. Again, the proposal of Xiao & Wu (2003) was deployed to work with the ratio between E_{jl} and f_{c0} to find a regression curve to predict the secant Poisson's ratio ν'_{cc}. As the axial strain increases, the ratio between the transverse strain and axial strain increased, indicating the acceleration of the dilation of the concrete.

In Figure 8, our own experimental results and the results of other research groups (with respect to ν'_{cc}) are presented. It is obvious that there is a strong impact of E_{jl}/f_c on ν'_{cc}. It is possible to give a proper equation to predict the secant Poisson's ratio.

$$\nu'_{cc} = 7 \cdot \left(\frac{E_{jl}}{f_{c0}} \right)^{0,7} \quad (14)$$

Hence, the requested second slope E_2 can be calculated with Equation 15.

$$E_2 = E_{2,q} \cdot \nu'_{cc} \quad (15)$$

This procedure enables the calculation of all values necessary to work with Equation 9.

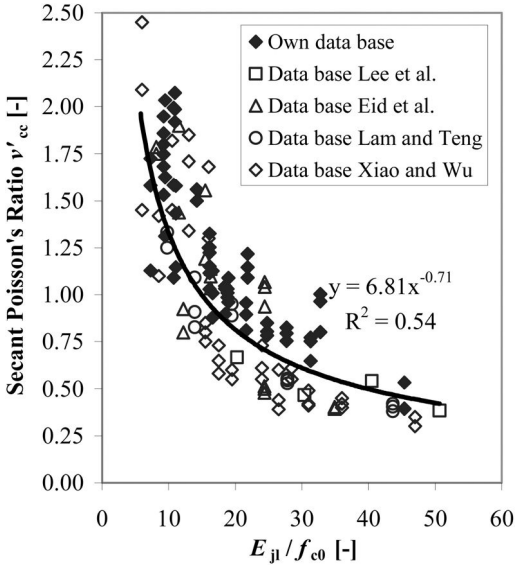

Figure 8. Secant Poisson's ratio as function of E_{jl}/f_{c0}.

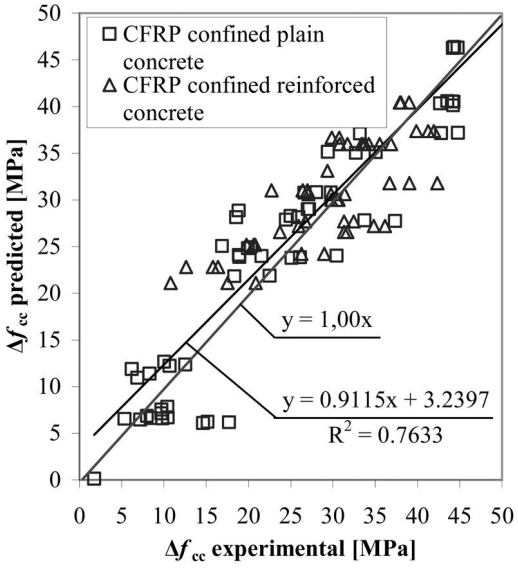

Figure 9. Comparison of predicted and experimental obtained strength enhancement Δf_{cc}.

3.3 *Comparison between proposed model and test data*

This section provides a comparison between results for f_{cc} and ε_{ccu} predicted with Equations 7–8 and our own experimental data base. In Figure 9 the calculated results for f_{cc} are presented as a function of the experimental values. Furthermore, Figure 10 shows an assessment of the accuracy of calculated results concerning ε_{ccu}. It can be observed that the new proposal shows a good performance for the prediction of both peak stress and ultimate strain. The predictive

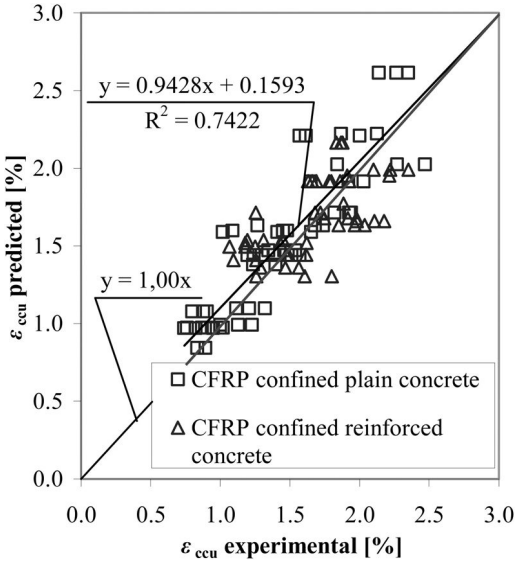

Figure 10. Comparison of predicted and experimental obtained ultimate strain ε_{ccu}.

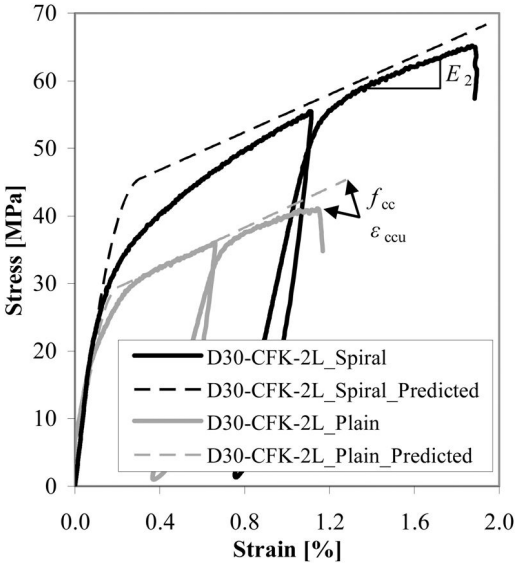

Figure 11. Comparison of predicted stress strain curves and curves obtained by own experiments.

equations for the ultimate strength and strain show a satisfactory correlation with the experiments. In both cases, the shown regression curves are close to the perfect line, with only minor difference in slope.

Figure 11 provides comparisons between analytical stress-strain curves received by the proposed model and some experimental curves obtained by own experiments with short columns ($D = 300$ mm) with and without spiral reinforcement ($Ø = 10$ mm, $s = 55$ mm). In both cases, the same CFRP system ($t_j = 0,22$ mm; $E_j = 230$ GPA) was deployed.

Again, a satisfactory correlation between predicted and measured stress-strain curves can be noticed. The calculated values for f_{cc} and ε_{ccu} are sufficient, too, with only minor overestimation. Moreover, the comparison between the two specimens reveals the strong impact of the spiral reinforcement concerning f_{cc} and ε_{ccu}. This is strong evidence that it is urgent to take all confinement elements (CFRP confinement as well as transverse reinforcement) into consideration.

4 CONCLUSIONS

CFRP confinement can significantly increase the strength and ductility of concrete and reinforced concrete. This paper presents a common empirical model for predicting the compressive axial behavior of FRP confined, short concrete columns with and without steel tie reinforcement. For the processing of this model, our own experimental results and a wide data base of different research groups were deployed. We were able to develop sufficient equations for predicting the load bearing capacity and corresponding ultimate strain of such a building element. Both values mainly depend on the ratio between confinement pressure and unconfined concrete strength. Furthermore, a proposal for calculation of the second slope enables the prediction of proper stress-strain curves. For a complete stress strain-model, the Lam and Teng stress-strain curve, which consists of a parabolic first portion and a straight-line second portion, was adopted.

REFERENCES

American Concrete Institute (ACI) 2008. *Guide for the Design and Construction of Externally Bonded FRP Systems for Strengthening Concrete Structures*. Farmington Hills: 2008.

Eid, R., Roy, N. & Paultre, P. 2009. Normal- and High-Strength Concrete Circular Elements Wrapped with FRP Composites. *Journal of Composites for Construction* 13 (2): 113–124.

Federation internationale du béton (fib) 2001. *Technical report: Design and use of externally bonded fibre reinforced polymer reinforcement for reinforced concrete structures*. Lausanne: International Federation for Structural Concrete.

Holschemacher, K. & Käseberg, S. 2014. Experimental study concerning the material behavior of CFRP confined plain and reinforced concrete. *Proceedings 5th International Conference on Concrete Repair (Concrete Solutions)*, Belfast, Northern Ireland UK, 01–03 September 2014.

Ilki, A., Peker, O., Karamuk, E., Demir, C. & Kumbasar, N. 2008. *Journal of Materials in Civil Engineering* 20 (2): 169–188.

Lam, L. & Teng, J.-G. 2004, Ultimate Condition of Fiber Reinforced Polymer-Confined Concrete. *Journal of Composites for Construction* 8 (6): 539–548.

Lee, J.-Y., Oh, Y.-J. Park, J.-S. & Mansour, M. Y. 2004. Behaviors of Concrete Coulmns confined with both Spiral and Fiber Composites. *Proceedings 13th World Conference on Earthquake Engineering (13 WCEE)*, Vancouver, Canada, 01–06 August 2004.

Matthys, S., Toutanji, H., Audenaert, K. & Taerwe, L. 2005. Axial Load Behavior of Large-Scale Columns Confined with Fiber-Reinforced Polymer Composites. *ACI Structural Journal* 102 (2): 258–267.

Xiao, Y. & Wu, H. 2003. Compressive Behavior of Concrete Confined by Various Types of FRP Composite Jackets. *Journal of Reinforced Plastics and Composites* 22 (13): 1187–1201.

Concrete Solutions – Grantham et al. (Eds)
© 2014 Taylor & Francis Group, London, ISBN 978-1-138-02708-4

Behaviour of ferrocement jacketed cylindrical concrete specimens under compression

A.B.M.A. Kaish, M. Jamil, S.N. Raman & M.F.M. Zain
Sustainable Construction Materials and Building Systems (SUCOMBS) Research Group, Faculty of Engineering & Built Environment, Universiti Kebangsaan Malaysia, Bangi, Selangor, Malaysia

ABSTRACT: An experimental investigation analyzing the behaviour of ferrocement-confined cylindrical concrete specimens under axial compression is presented. A total of 12 cylindrical concrete specimens of three different sizes (150100 and 75 mm diameters) were tested. Each type of specimens were jacketed with ferrocement having single layer of welded wire mesh. The present experimental study is also intended to investigate the size effect of concrete specimens on the confinement action of ferrocement jackets. Test results show that additional confinement by means of a ferrocement jacket can enhance the strength and deflection capabilities of cylindrical concrete specimens. It was also found that the confinement action is more effective in case of smaller cylindrical concrete specimens.

1 INTRODUCTION

Repair and strengthening of concrete structures is becoming a more and more important part of construction work all over the world. Strengthening of reinforced concrete (RC) structures is required when they are used in a different manner than previously planned. It is also demanded due to the upgrading of seismic code provisions. Structures with deterioration and structures of insufficient seismic capacity make these works more significant. New strengthening techniques of concrete structures have been suggested in recent years. A variety of materials and methods have been and are being tried to increase the strength and ductility of existing unsafe or deteriorated concrete structures. The strengthening materials and techniques applied should be effective and at the same time be of reasonable cost; cost effectiveness is the main concern for developing countries like Bangladesh and Malaysia.

Ferrocement, which was invented in the 19th century, is an extensively used building material in both developed and developing countries due to its ease of fabrication (Naaman, 2000). Ferrocement, as defined by ACI 549.1R-93, is a form of RC using closely spaced multiple layers of mesh and/or small-diameter rods completely infiltrated with, or encapsulated, in mortar (American Concrete Institute Committee 549, 1993). The most common type of reinforcement used for such application is steel mesh. It could be one of the promising materials for repairing/strengthening the structural elements due to its improved structural properties like tensile and flexural strength, toughness, fracture, crack control and good ductility (Kumar & Rao, 2006).

RC columns are important structural elements designed to support vertical loads of frame structure buildings. RC columns require lateral confinement for enhanced performance against axial loads. Insufficient lateral confinement may lead to failure of RC columns. The insufficient lateral confinement could be minimised by providing an auxiliary external confinement. Many researchers have recommended the use of ferrocement jacketing as a potential confinement material for concrete columns. Sandowich & Grabowski, (1981) have studied the behaviour of circular composite columns made of ferrocement pipes filled with concrete under axial and eccentric loading. Balaguru (1988) has tested wire mesh composite plain concrete cylinders under axial compressive loading. In this work wire mesh was placed on the inner circumference of cylindrical moulds, and then concrete poured into the mould. Singh & Kaushik (1989) studied the effectiveness of ferrocement confinement for repairing concrete columns. They tested both circular and square short concrete columns under axial compression after confining with external ferrocement jackets. Walliudin & Raffeeqi (1994) studied the order of casting of ferrocement for confining plain concrete. The methods of confinement studied were: (i) mesh layer cast integrally, (ii) mesh layers in precast shell, and (iii) wrapped mesh layer on precast core. Mourad (2006) investigated the behaviour of plain concrete, externally confined with welded wire mesh. He studied the effect of different methods of wire mesh attached around concrete specimens. Kondraivendhan & Pradhan (2009) have investigated the behaviour of ferrocement confined cylindrical concrete specimen of different grade. Xiong et al. (2011) investigated the strength and ductility of plain concrete encased

with ferrocement including skeletal steel bars under uni-axial compression.

A preliminary investigation has been carried out by Kaish et al. (2012) to improve the square ferrocement jacketing in order to strengthen square RC columns. They have proposed some improved square ferrocement jacketing. The performance of those improved square ferrocement jacketed square RC columns under concentric compressive load was verified later by Kaish et al. (2013). Kaish et al. (2011, 2012) also investigated the behaviour of ferrocement encased square RC columns under small eccentric load. Ho et al. (2013) proposed a method of strengthening circular columns using high-performance ferrocement (HPF) and achieved very good performance of strengthened columns.

As demonstrated in the available literature, ferrocement is a proven material for providing auxiliary external confinement of RC column. However, the available research on ferrocement as a confinement material is not much like research carried out on other strengthening materials and techniques. Although ferrocement is an established material, there is still a big gap in scientific knowledge to use this material as a repair/strengthening material. Unknown is the size effect of concrete specimens on the confinement action of ferrocement jackets. This gives the necessity to investigate the effect of ferrocement jacketing for concrete columns.

This research is intended to further the understanding of the confinement mechanism of ferrocement (made of welded wire mesh) jacketing for low strength circular concrete members. The study is also projected to investigate the size effect of the specimens on the confinement effectiveness of ferrocement jackets.

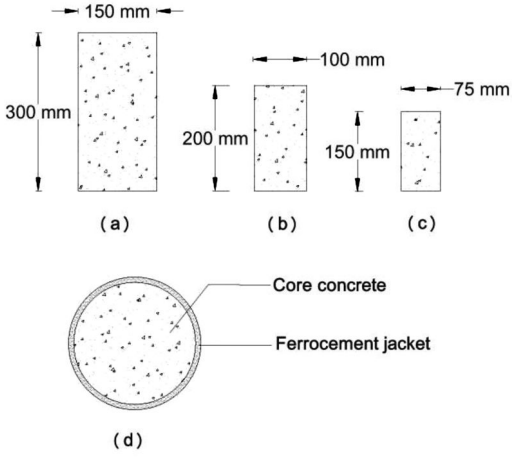

Figure 1. Details of benchmark and jacketed specimens.

Table 1. Specimen details.

Specimens	Designation	Size of Specimens (mm) Height	Diameter	Type of jacket
Small	SS-NJ	150	75	Non-jacketed
	SS-J	150	75	Jacketed*
Medium	MS-NJ	200	100	Non-jacketed
	MS-J	200	100	Jacketed*
Large	LS-NJ	300	150	Non-jacketed
	LS-J	300	150	Jacketed*

*Single layer wire mesh ferrocement jacket of 12.5 mm thickness.

2 EXPERIMENTAL PROGRAM

The experimental study carried out composed of testing twelve cylindrical concrete specimens of different sizes. The height of cylindrical concrete specimens studied in this research were 300, 200 and 150 mm for cylinders of diameter 150, 100 and 75 mm respectively. Four concrete specimens were prepared for each size, two of which were taken as benchmark (denoted as NJ) specimens and two jacketed with ferrocement. The thickness of the ferrocement jacket was 12.5 mm for all jacketed specimens. The ferrocement jacket consisted of a single layer welded wire mesh encapsulated with rich mix cement mortar. The details of the benchmark and jacketed specimens are shown in Figure 1. The numbers and designation details are given in Table 1.

2.1 *Materials*

All materials used in this study were sourced locally. The cement used was of strength class 32.5 N CEM-II conforming to EN 197. A 12 mm downgrade crushed stone was used as coarse aggregate. The specific gravity and water absorption capacity of the coarse aggregate were 2.62 and 1.05% respectively. Coarse river sand was used as fine aggregate. The specific gravity and water absorption capacity of sand were 2.58 and 0.95% respectively. The same sand was used in preparing mortar for ferrocement and conformed to ACI 549.1R-93. The specification of sand used for ferrocement mortar is given in Table 2. Normal tap water supplied in the concrete laboratory of Universiti Kebangsaan Malaysia was used in making concrete and mortar for ferrocement. The welded wire mesh of

Table 2. Specification of sand for ferrocement mortar (ACI 549.1R-93).

Sieve size, U.S. standard square mesh	Percent passing by weight	Percent passing by weight used in this study
No. 8 (2.36 mm)	80–100	95
No. 16 (1.18 mm)	50–85	70
No. 30 (0.60 mm)	25–60	50
No. 50 (0.30 mm)	10–30	20
No. 100 (0.15 mm)	2–10	5

12.5 mm square opening was used as reinforcement for ferrocement jacket. The diameter of wires in the mesh was 0.85 mm.

2.2 *Mix design*

A concrete mix was designed to obtain a compressive strength of 20 MPa at 28 days. The design amounts of materials in the mix were 400 kg/m^3 cement, 1026 kg/m^3 coarse aggregate, 624 kg/m^3 fine aggregate and 180 kg/m^3 free water.

The mortar mix proportion was 1:2 by weight of cement and sand respectively. The water to cement ratio was taken as 0.5 for mixing the mortar. The compressive strength of mortar was 31.5 MPa after 28 days of curing.

2.3 *Preparation of concrete specimens*

Cylindrical steel moulds of required sizes were used for casting the concrete specimens. All moulds were oiled first and then placed on the vibration table before concrete casting. After that, concrete was prepared and placed into the moulds. The casting of concrete was done in three layers. Low speed table vibration for 1 min was used after pouring each layer of concrete for proper compaction of concrete into the moulds. All twelve specimens were cast from the same batch of concrete mix to maintain the same strength of concrete. After casting, all specimens were covered with plastic sheets. All specimens were de-molded after 24 hours and placed under water in a tank for proper curing. Benchmark specimens were cured for another 27 days. However, the core concrete for jacketed specimens was only cured for 13 days after de-molding.

2.4 *Ferrocement jacketing*

Ferrocement jacketing of concrete specimens were undertaken after 14 days of concrete casting. After curing, the specimens were taken out of the water tank and left to stand for 2 hours to achieve a surface dried condition. After achieving this, six horizontal strain gauges were placed at two opposite sides of the specimens to get the strain on the concrete surface. The strain gauges were placed at three different levels (mid-height and 25 mm from the top and bottom faces of concrete specimens). Ferrocement jackets were then applied around the surface of cylindrical concrete specimens. The wire mesh was wrapped first and then the mortar was applied by plastering the concrete specimens. All specimens were jacketed with ferrocement from the same batch of mortar mix. A gap of 10 mm was kept in between the concrete cross-sectional surface and the ferrocement jacket at both the top and bottom. This gap was kept to avoid the direct compressive load on the ferrocement jacket. The newly jacketed specimens were cured in air for 24 hours to get a hard ferrocement jacket. Afterward, the specimens were placed under water to finish 28 days of curing from the date of concrete casting. A representative specimen after jacketing is shown in Figure 2.

Figure 2. Specimen after ferrocement jacketing.

2.5 *Test setup and instrumentation*

Specimens were placed vertically on the floor of a 10,000kN capacity universal testing machine and tested under monotonically increasing compressive load. The load was recorded by a load cell placed at the top of the specimen. Two LVDTs of 100 mm gauge length were placed vertically in two opposite sides of the specimen in order to measure vertical deflections. Six LVDTs of 50 mm gauge length were installed horizontally in two opposite directions at three different levels (mid-height and 25 mm away from the top and bottom surface of the specimens). All LVDTs and pre-installed strain gauges were connected to the Data Logger to get the reading before the test. The test was carried out under displacement control with a strain rate of 0.5 mm/min. Figure 3 presents the specimen under the compression testing machine before carrying out the test.

3 RESULTS AND DISCUSSIONS

The experimental data for each specimen was collected from a data acquisition system and analysed. Table 3 shows the average ultimate load and the average ultimate axial stress of specimens. Table 4 shows the ultimate axial and lateral deflections of the tested specimens. The axial displacement was obtained from the average reading of two LVDTs placed vertically.

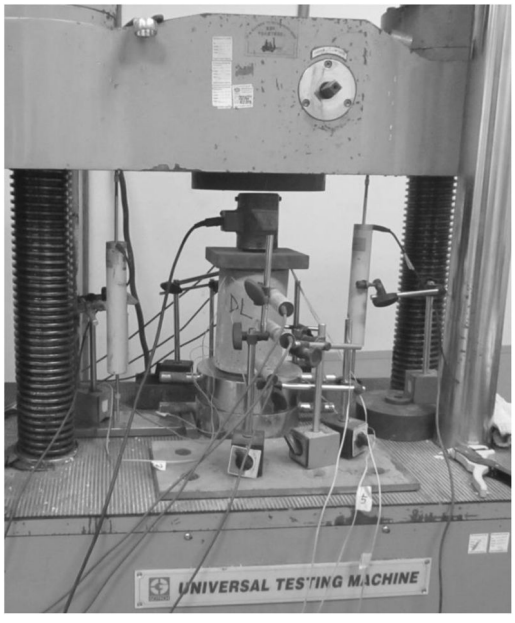

Figure 3. Test setup and instrumentation.

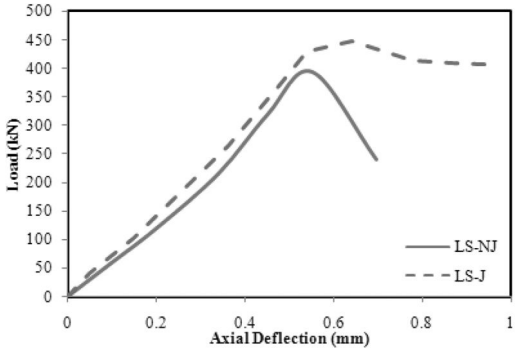

Figure 4. Typical load-deflection curves of LS specimens.

Figures 3, 4 and 5 present the load-deflection curves of LS, MS and SS specimens respectively.

3.1 *Ultimate load capacity*

It can be observed from Table 3 that the ultimate load carrying capacity of jacketed specimens is higher than the benchmark specimens for all three sizes. The load capacities of jacketed specimens are 1.13, 1.17 and 1.18 times of the benchmark specimens for type LS, MS and SS specimens respectively. The high load capacity of jacketed specimens is due to the confinement effect of ferrocement jacket. As the ferrocement jacket did not reach to the end of the specimens, the loading area was the same for both the non-jacketed and jacketed specimens. Therefore, the ultimate axial stress was also increased in jacketed specimens as

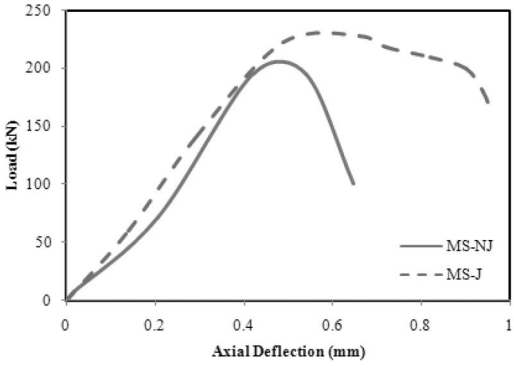

Figure 5. Typical load-deflection curves of MS specimens.

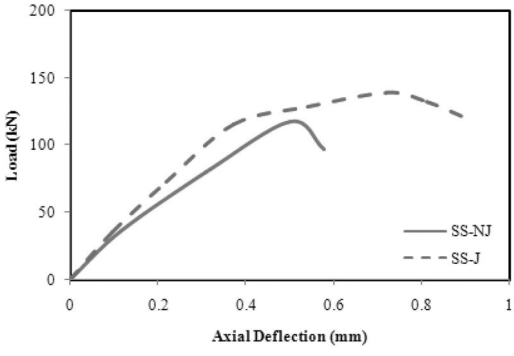

Figure 6. Typical load-deflection curves of SS specimens.

Table 3. Ultimate loads and ultimate axial stress.

Specimens	Ultimate load (kN)	Relative to NJ	Ultimate axial stress (MPa)
SS-NJ	117.80	–	26.66
SS-J	139.34	1.18	31.54
MS-NJ	195.25	–	24.86
MS-J	228.12	1.17	29.05
LS-NJ	394.58	–	22.33
LS-J	447.74	1.13	25.34

given in Table 3. It should be noted that the increment in load carrying capacity and the ultimate axial stress is higher in the smaller size specimen.

3.2 *Ultimate deflection capacity*

It can be observed from Table 4 that the ultimate axial deflection capacity of jacketed specimens is higher than the non-jacketed concrete specimens. The relative increments in ultimate axial deflection of jacketed specimens are 16, 57 and 44% of the benchmark specimens for type LS, MS and SS specimens respectively. These increments in ultimate lateral deflections are 25, 27 and 31%. The higher deflection capacity is due to the ductile nature of ferrocement jacket which allows the specimens to bulge slowly under higher load.

Table 4. Ultimate deflections.

Specimens	Axial deflection at ultimate load		Lateral deflection at ultimate load	
	Measured (mm)	Relative to NJ	Measured (mm)	Relative to NJ
SS-NJ	0.5	–	0.13	–
SS-J	0.72	1.44	0.17	1.31
MS-NJ	0.42	–	0.15	–
MS-J	0.66	1.57	0.19	1.27
LS-NJ	0.55	–	0.12	–
LS-J	0.64	1.16	0.15	1.25

Figure 7. Typical failure mode of jacketed specimen.

3.3 *Failure mode of jacketed specimens*

The failure of ferrocement jacketed specimens was initiated by hairline cracks in the mortar of the ferrocement jackets throughout the height of the specimens. The crack width increased with increase of axial load. The failure of jacketed specimens was mainly due to the failure of wire mesh throughout the height of the specimens. Figure 6 presents a representative tested ferrocement jacketed specimen.

4 CONCLUSION

Based on the test results of this study, the following conclusion can be drawn:

1. Ferrocement jackets can enhance the load carrying capacity of concrete specimens.
2. Load carrying capacity is more enhanced in smaller size specimens, which in this study was 18% of non-jacketed specimen.
3. Lateral bulging capacity is also enhanced to about 25 to 31% due to the presence of the external ferrocement jacket.
4. The failure pattern indicates that the confinement effect of ferrocement jacket is effective throughout the height of the specimens.

ACKNOWLEDGEMENT

The authors acknowledge the Ministry of Education of Malaysia for providing the necessary funding required for research through the ERGS Grant Scheme (ERGS/1/2011/TK/UKM/02/10). In addition, the first author would also like to extend his gratitude to UKM for the financial support provided through the Research University Zamalah Scholarship.

REFERENCES

ACI 549.1R-93 1993. *Guide for design, construction & repair of ferrocement*. Michigan: American Concrete Institute.

Balaguru, P. 1988. Use of ferrocement for confinement of concrete. *Proceedings of the third International Conference on Ferrocement, Roorkee, India, 1988*. 296–305.

Ho, I.F. Lam, E.S. Wu, B. Wang, Y.2013. Monotonic Behavior of Reinforced Concrete Columns Confined with High-Performance Ferrocement. *Journal of Structural Engineering* 139(4): 574–583.

Kaish, A.B.M.A. Wahed, M.A. Alam, M.R. 2011. Behaviour of Ferrocement encased square reinforced concrete column under eccentric loading. *International Conference on Structural Engineering, Construction and Management, CDROM, Kandy, Sri Lanka, 15–17 December 2011*.

Kaish, A.B.M.A. Alam, M.R. Jamil, M. Zain, M.F.M. Wahed, M.A. 2012. Improved ferrocement jacketing for restrengthening of square RC short column. *Construction and Building Materials* 36(11): 228–237.

Kaish, A.B.M.A. Alam, M.R. Jamil, M. Wahed, M.A. 2012. Ferrocement jacketing for restrengthening of square reinforced concrete column under concentric compressive load. *Procedia Engineering* 54: 720–728.

Kondraivendhan,B. Pradhan, B. 2009. Effect of ferrocement confinement on behavior of concrete, *Construction and Building Materials* 23: 1218–1222.

Kumar, R. Rao, C.B.K. 2006. Constitutive behavior of high-performance ferrocement under axial compression. *Magazine of Concrete Research* 58(10):647–656.

Mourad, S.E.M. 2006. *Performance of Plain Concrete Specimens Externally Confined with Welded Wire Fabric*. Research Report, College of Engineering Research Center, King Saud University, Saudi Arabia.

Naaman, A. E. 2000. *Ferrocement and laminated cementitious composites*. Ann Arbor, Michigan:Techno press 3000.

Sandowich, M. & Grabowski, J. 1981. The properties of composite columns made of ferrocement pipes filled with concrete tested in axial and eccentric compression. *International Symposium on Ferrocement, Bergamo, Italy, 1981*. 1/93–1/99.

Singh, K.K. & Kaushik, S.K. 1988. Ferrocement composite columns. *Proceedings of the third International Conference on Ferrocement, Roorkee, India, 1988*. 216–225.

Walliuidin, A.M. & Rafeeqi, S.F.A.1994. Study of behaviour of plain concrete confined with ferrocement. *Journal of Ferrocement* 24(2): 139–145.

Xiong, G.J. Wu, X.Y. Li, F.F. Yan, Z. 2011. Load carrying capacity and ductility of circular concrete columns confined by ferrocement including steel bars, *Construction and Building Materials* 25: 2263–2268.

Concrete Solutions – Grantham et al. (Eds)
© 2014 Taylor & Francis Group, London, ISBN 978-1-138-02708-4

Strains in CFRP – strengthened reinforced concrete beams

M. Kaminski & E. Kusa
Institute of Building Engineering, Wroclaw University of Technology, Wroclaw, Poland

ABSTRACT: Today novel composites, such as CFRP (Carbon Fibre Reinforced Polymer) strips, are increasingly often used instead of steel plate to strengthen reinforced concrete structures. CFRP is a quite new material and the properties, strains and rheological behavior of structural materials is significant.

The studies focusing on strains in CFRP-strengthened concrete beams. This papers presents the results of tests aimed at determining the deformations of reinforced concrete beams strengthened with carbon fibre strips bonded into grooves which were cut in the concrete, in comparison with those of an unstrengthened RC beam. The test results have confirmed the beneficial effect of the CFRP materials on the strains in reinforced concrete elements subjected to sustained and momentary loads.

1 INTRODUCTION

When damaged, e.g. as a result of rebar corrosion, existing civil engineering structures need strengthening. Also when a structure's permissible load or its static diagram is to be changed it to may become necessary to strengthen the structure. Until recent years the most popular way of strengthening reinforced concrete beams has been to stick flat bars or steel plates on them. The method is highly effective, nevertheless it has some drawbacks which can be overcome through the use of composite materials. As opposed to steel, CFRP materials do not corrode and are lighter and easier to apply.

Owing to their higher flexibility, long lengths of CFRP materials, which can be rolled to reduce the space occupied by them (this cannot be done in the case of steel flats and strips), can be more easily transported. There is no limit as regards the producible length of such a material, whereas this limitation exists in the case of steel materials. Because of all the differences mentioned above, design engineers increasingly often prefer FRP materials over steel, for strengthening purposes. The world research carried out to date (Meier et al. 1992; Steiner 1996; Yost et al. 2007 and Al-Mahmoud et al. 2009) has shown that strengthening effected by sticking composite materials onto the tensioned zone of RC beams results in reducing the length and width of cracks. Moreover, it increases the stiffness and strength of the member strengthened in this way. The effectiveness of such strengthening depends on the primary steel reinforcement ratio, the number of layers of the composite reinforcement and their stiffness as well as on the distance between the composite material end and the support of the beam. The first recommendations concerning the principles of designing structural elements strengthened with FRP materials were developed by such organizations as: ACI Committee 440 (2000), ISIS Canada (2001), Fib Bulletin 14 (2001), The Concrete Society (2004) and JBDPA-Japan (1999).

There are also numerous publications on other structural reinforced concrete members, such as columns (Trapko et al. 2012) or even masonry (Kwiecień 2012).

Similar research but on long term loading of reinforced concrete beams strengthened with steel fibres were conducted by Kaminski (2008).

2 SURVEY OF LITERATURE ON RHEOLOGICAL INVESTIGATIONS OF CFRP MATERIALS

The investigations of the rheological properties of CFRP materials to date can be divided into: tests of the carbon fibre composites themselves, tests of the resins used to bond CFRP materials to the base, tests of the bond between the composite and another material and tests of entire structural members strengthened with CFRP composites.

During tests carried out on CFRP specimens by Ascione et al. (2008) negligibly small strains were observed in the first stage of creep. The specimens were CFRP strips of different width, characterized by a high elastic modulus and a high carbon fibre content in the matrix. The tests were being carried out at a constant temperature of 20°C for over a year. All the specimens were subjected to a time-invariable tensile force applied as a counterweight to a system of pulleys. From the study the authors concluded that the materials would limit the strains caused by the creep of the elements strengthened with them.

In their work Ferrier et al. (2010) presented the results of creep tests carried out on four different polymer resins used together with composite strips, subjected to sustained loads at a temperature of 20–60°C for 115 days. Each of the tested polymer resins was characterized by a different glass transition temperature. It was found that the ambient temperature had an influence on the stresses in the tested elements while the resin glass transition temperature had an influence on the strains induced by creep at the same ambient temperature. The test results suggested that polymer resins can be safely used only at an ambient temperature at least 15°C lower than the glass transition temperature of the resin polymer.

Meshgin et al. (2009) focused on the effect of time elapsed between CFRP strip application to a specimen and the instant of force application. Specimens for which application-loading time ranged from 1 to 7 days were tested in constant temperature-humidity conditions. It was found that the final creep strain would decrease as the above time increased.

Also whole structural members strengthened with CFRP materials and subjected to sustained load began to be tested. Pelvris et al. (1994) tested reinforced concrete beams strengthened with FRP strips of different width. It was found that the larger the surface area of the composite material, the smaller the deflections caused by creep. Also Chami et al. (2009) tested RC beams strengthened with CFRP strips and subjected to a sustained force. The beams had the same outside dimensions and the cross-sectional area of the strips and that of the compressed reinforcement were constant, whereas the cross-sectional area of the tension reinforcement would vary. A negligible effect of the CFRP strips on deflections under light sustained loads and a barely perceptible effect of the strips on deflections under heavy sustained loads were observed.

Interesting tests were carried out by Muller et al. (2007). Five beams, some of which were strengthened before and some after cracking, were tested. Unfortunately, the beams were very small ($80 \times 125 \times 1250$ mm). Therefore it would be worthwhile to repeat the experiment on full-scale elements.

Attempts have also been made to describe sustained load induced deflections of RC beams strengthened with FRP materials, by means of mathematical models. Mari et al. (2012) analyzing the up-to-date test results reported by other researchers used mathematical models to describe deflections.

So far, papers on the rheological properties of reinforced concrete elements strengthened with FRP composites have been rare. In many cases, the tests were carried out on small elements and so their results may have been influenced by the scale effect. Moreover, only a few papers deal with carbon fibres on RC beams under bending and even fewer cover problems relating to the near-surface-mounting (NSM) of CFRP strips. Although this method is more difficult and more labour-intensive, by using it one can better protect the composite material against fire or elevated temperature.

Therefore the authors decided to carry out tests on full-scale RC beams strengthened using the NSM method. In addition, the tested elements were strengthened not only before loading, as it has been the case in most of the tests reported so far, but also already cracked elements were strengthened. In this way the state which actually occurs in existing structures could be re-created.

3 TEST PLAN

The aim of the tests was to compare the behaviour of beams, strengthened respectively before and after cracking, under sustained loads with that of an unstrengthened reference beam. Moreover the tests were to add to the knowledge of the rheological properties of reinforced concrete beams strengthened with CFRP materials. The tests were carried out in the Accredited Research Laboratory of the Institute of Building Engineering at Wrocław University of Technology. Three elements: beam Bo – without strengthening and beams Bw and Bwz with CFRP reinforcement glued into previously cut grooves (the NMS method) were tested. Beam Bw was strengthened before cracking, whereas beam Bwz prior to strengthening was subjected to loading and at a crack with of 0.1 mm (under a constant load) it was strengthened. Subsequently, after 24 hours the load acting on all the beams was increased to a constant value amounting to 50% of the design load-bearing capacity of the unreinforced beam. Under this load the elements were tested for 315 days. The results would be read off over the period of 3 weeks since loading. Then the reading rate would be decreased to one reading per week. After 150 days the reading rate was reduced to one reading per two weeks.

4 DESCRIPTION OF MATERIALS USED

The 150 mm × 150 mm × 150 mm cubic specimens and the cylindrical specimens, 113 mm in diameter and 350 mm high, were used to determine the compression strength of the concrete. The cylindrical specimens were also used to determine Young's modulus. Concrete cubic specimens obtained compression strength 37 MPa while cylindrical specimens obtained 32 MPa. The modulus of elasticity was defined for concrete as 30 GPa.

Based on experimental results with steel bars of nominal diameter 12 mm gave: tensile strength of 636 MPa; elasticity modulus of 190 GPa and steel bars of nominal diameter 6 mm gave: tensile strength of 500 MPa; elasticity modulus of 187 GPa. The beam reinforcement (top and bottom) was made from ϕ12 mm ribbed bars and ϕ6 smooth stirrups, as shown in Figure 1.

100 mm × 1.4 mm CFRP (MC-DUR CFK 160/2400) strips made by MC-Bauchemie were used for

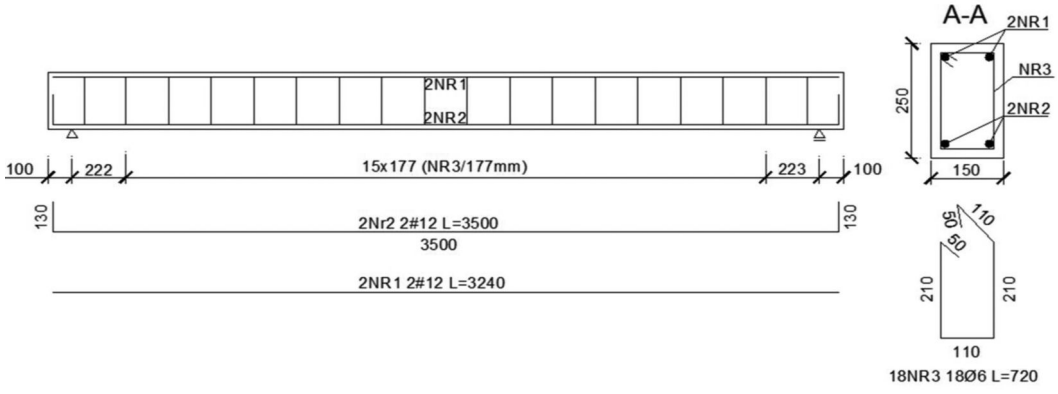

Figure 1. Schematic of beam reinforcement.

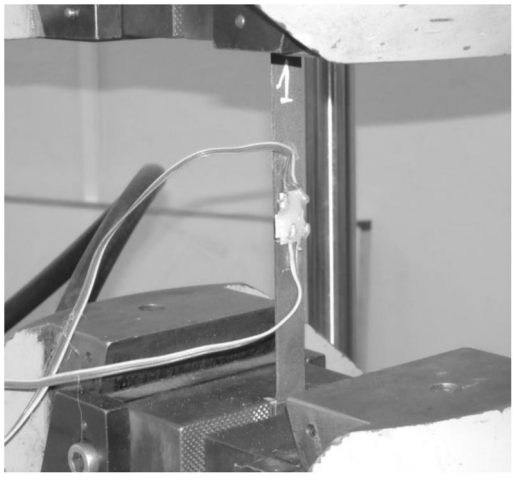

Figure 2. CFRP specimen before test.

Figure 3. CFRP specimen after failure.

strengthening. Young's modulus (177 GPa) and tensile strength (2.34 GPa) were determined for the strips.

15 mm × 1.4 mm × 250 mm specimens were made from the strips. 15 mm × 5 mm × 50 mm aluminium plates were glued to the ends of the specimens in order to prevent them from slipping in the strength tester jaws (Figs 2–3).

Two-component resin MC- Bauchemie MC-DUR 1280 was used to bond the strip with the concrete.

5 TEST RIG

Beam Bo was placed on a separate test rig while beams Bw and Bwz were installed on a shared double test rig (Fig. 4). All the beams on the test rigs were under a plastic tent reducing the influence of the external environment, as shown in Figure 5.

Each of the beams was a freely supported beam with a span of 3100 mm, loaded with two concentrated forces located at a distance of 2000 mm from each other (Fig. 6).

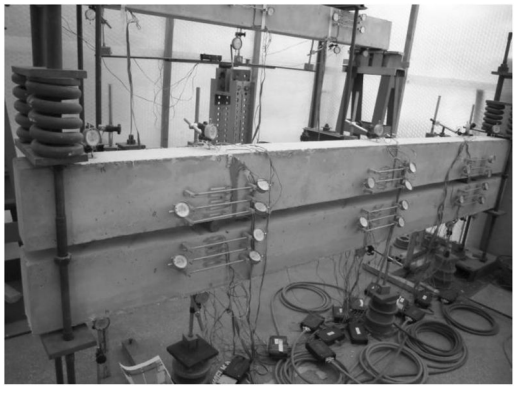

Figure 4. Double test rig for beams Bw and Bwz.

An air conditioner and an air humidifier kept the temperature at about 20°C and the humidity at 60%. The tent was set up in the laboratory. The beam load was applied by means of jacks and force gauges.

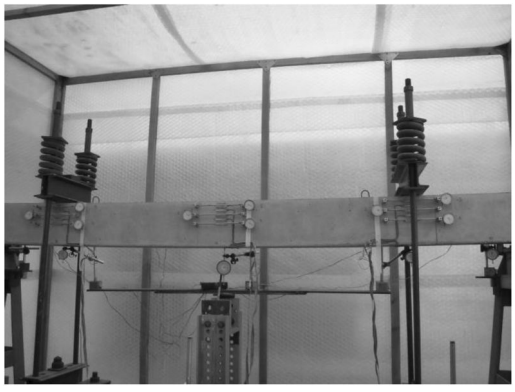

Figure 5. Test rig for beam Bo under tent.

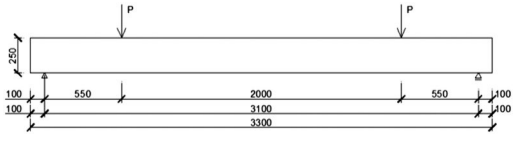

Figure 6. Static diagram of beams.

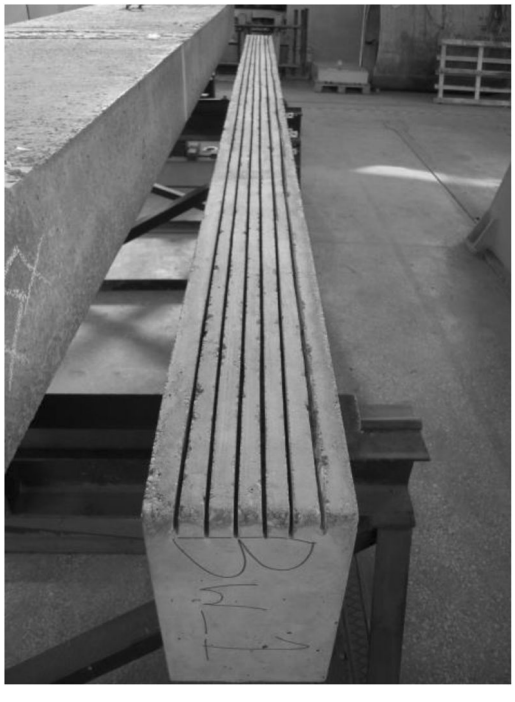

Figure 7. Beam with cut grooves.

One type of CFRP strip strengthening, i.e. bonding strip lengths into the beam (NSM), was used in the tests. Six grooves, 6 mm wide and 20 mm deep, were cut in the beam (Fig. 7) and CFRP strips were glued into them. The cross-sectional area of the bonded-in

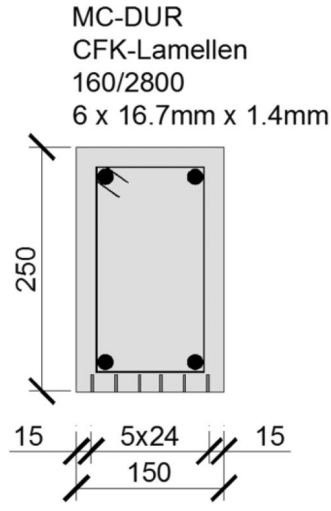

Figure 8. Cross sections of strengthened beams.

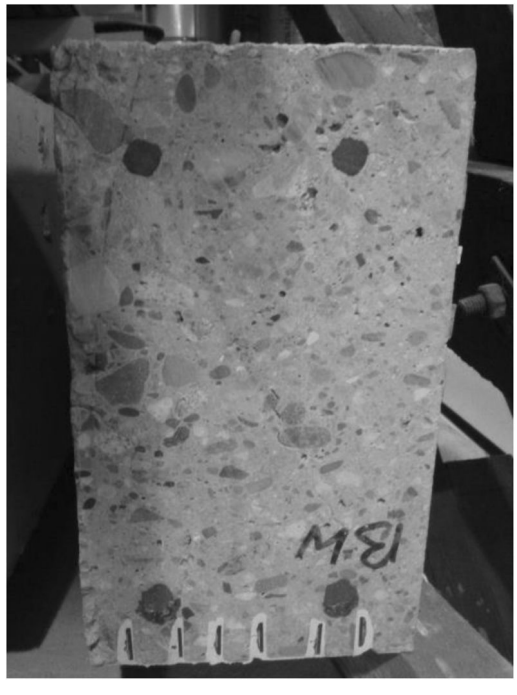

Figure 9. Photo of cross sections of strengthened beams.

strip material amounted to 140 mm^2 and it was divided equally among the individual strips. The cross section of the strengthened beams is shown in Figure 8 and Figure 9.

6 TEST EQUIPMENT

Before the beams were subjected to loading, paper electrical resistance strain gauges were stuck onto

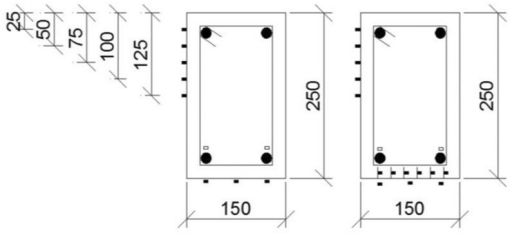

Figure 10. Arrangement of strain gauges.

them. Each of the beams had two strain gauges RL 120/20 on the tension reinforcement under the forces and in the middle of the span. In addition, 3 strain gauges RL 300/50 were also located under the load points and at midspan. Such strain gauges were also located on the side of the concrete cross section under the forces and at midspan, as shown in Figure 10.

Additional strain gauges RL 120/20 were stuck to the CFRP strips (one gauge per strip) under the forces and at midspan. Moreover, there were dial gauges under the forces and at a distance of 100 mm from the supports.

Three dial gauges with a basis of 1 mm were placed on the side surface of each of the beams. In addition, compensating strain gauges were introduced to eliminate the influence of temperature variation on the read off strains. The compensating strain gauges were created separately on the steel specimen, the concrete specimen and the CFRP strip. All the strain gauges and sensors were in the same tent and were exposed to the same impact of variations in temperature and humidity as the tested reinforced concrete elements. Readings from the strain gauges were taken using the Hottinger Baldwin Messtechnik SPIDER-8.

7 APPLICATION OF COMPOSITE MATERIALS

Prior to strengthening one should first properly prepare the surface to be strengthened. Each place on which a CFRP strip was to be stuck was cleaned of dust and loose pieces and then degreased with acetone. Compressed air was used to remove any loose material from the grooves. Also the strips were cleaned of dust and degreased before they were stuck on.

MC-DUR 1280 is a two-component adhesive based on epoxy resin. The base to hardener ratio was 4:1. After the base itself was mixed, a proper amount of hardener was added and the whole was mixed slowly for 3 minutes. The components of the adhesive were mixed at a temperature of 20°C, which, according to the manufacturer, gives about 40 minutes for the use of the adhesive after mixing.

First, adhesive was carefully placed in the grooves by means of a spatula and subsequently, CFRP strips were smeared with adhesive on both sides and pressed into the cuts along the whole length of the beam (Fig. 11).

Figure 11. Placing adhesive into grooves cut in beam Bwz.

Figure 12. Finished beam with glued-in CFRP strips.

The excess adhesive which flowed out was used to mask the grooves (Fig. 12).

8 TEST RESULTS

The width of cracks was recorded in the course of the test. The width of the cracks amounted to: less than 0.1 mm, 0.1 mm and 0.5 mm in respectively beam Bw, Bwz, and beam Bo. Figure 13 shows a diagram of deflection in the span under sustained load for all the three beams. It is apparent that beam Bo (without

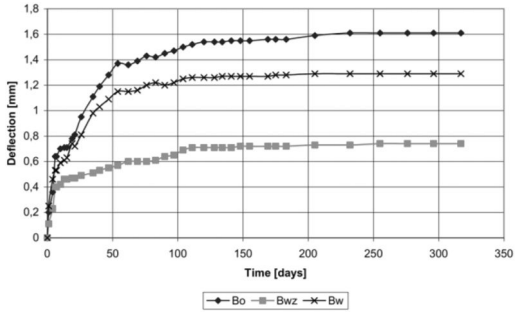

Figure 13. Diagram of rheological deflections at midspan.

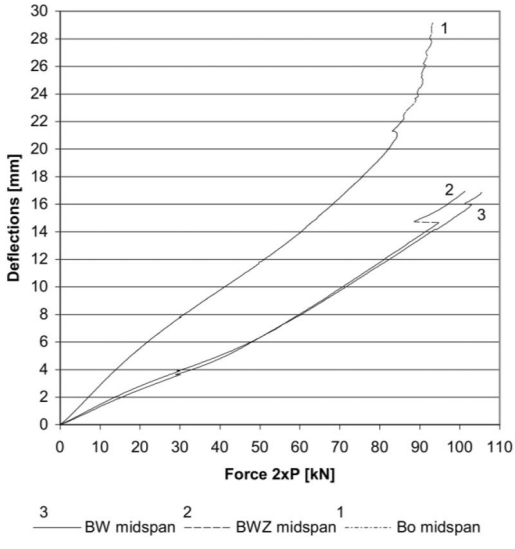

Figure 14. Diagram of immediate deflections at midspan.

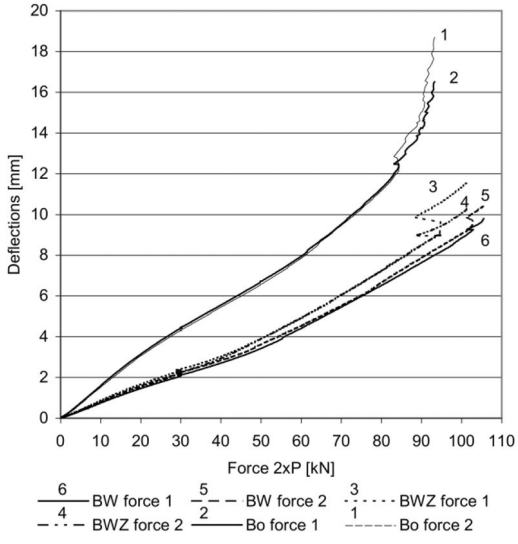

Figure 15. Diagram of immediate deflections at load point.

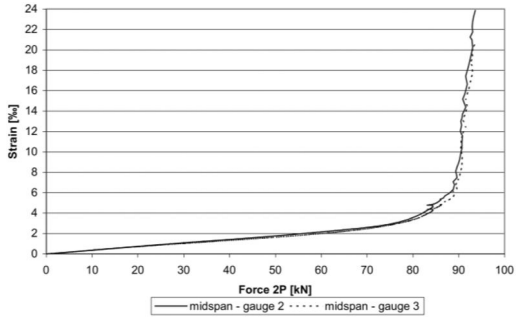

Figure 16. Diagram of midspan immediate strains in tension reinforcement steel for beam Bo.

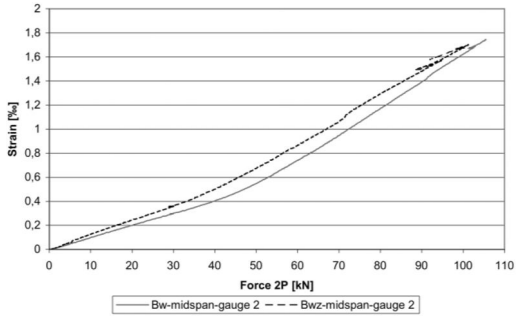

Figure 17. Diagram of midspan immediate strains in tension reinforcement steel for beams Bw and Bwz.

strengthening) deflects much more in comparison with beams Bw and Bwz. The deflections of beam Bw are larger than those of beam Bwz. However, beam Bw, being the lower beam on the double test rig, was loaded with a moment 1 kNm greater than that applied to beams Bo and Bwz. The deflections were measured in the middle of the span.

After 315 days, the immediate deflections of all the three beams, both at midspan (Fig. 14) and under the load points (Fig. 15), were examined. It is apparent from the two diagrams that the immediate deflections in the case of unstrengthened beam Bo were much greater than for the strengthened beams. The immediate deflections of beams Bw and Bwz were comparable.

A difference in strains between beam Bo and strengthened beams Bw and Bwz was also visible in figures 16 and 17 which show midspan immediate strains in tension reinforcement steel. For beam Bo loaded with a force greater than 90kN steel yielding was observed, whereas in beams Bw and Bwz the steel yield amounted to about 1.4‰.

The same situation can be seen in figures 18 and 19 which show strains at the force application

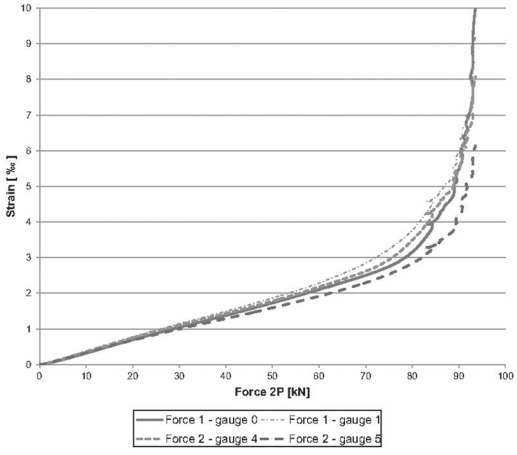

Figure 18. Diagram of immediate strains in tension reinforcement steel for beam Bo in force application point.

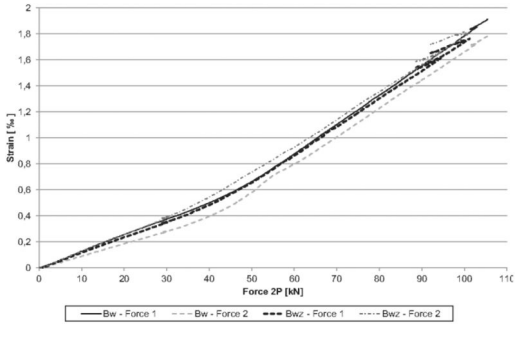

Figure 19. Diagram of immediate strains in tension reinforcement steel for beams Bw and Bwz in force application point.

point. Beams Bw and Bwz have much smaller strains compared to the beam Bo.

9 CONCLUSIONS

On the basis of the course of the tests and their results the authors have drawn the following conclusions:

- the strengthening of the reinforced concrete beams with the CFRP materials results in a considerable increase in the stiffness of the former,
- the increase in the stiffness of the tested elements results in a reduction in their deflections and immediate load strains,
- also the rheological deflections are reduced for the strengthened beams,
- the CFRP materials contribute to a decrease in the width and propagation of cracks,
- the fact whether the CFRP materials are applied before or after the element cracks has a slight bearing on the resulting strains and deflections.

ACKNOWLEDGEMENTS

The authors would like to thank the BETARD company in Długołęka for providing the concrete elements and also thank MC-Bauchemie for the supplied materials.

REFERENCES

ACI Committee 440. 2000. Guide for the Design and Construction of Externally Bonded FRP Systems for Strengthening Concrete Structures. ACI 440.2R-02.

Al-Mahmaud, F.; Castel, A.; Francois, R. & Tourneur, C. 2009. Strengthening of RC members with near-surface mounted CFRP rods. *Composite Structures* 91(2): p. 63–70.

Ascione, F.; Berardi, V.P.; Feo, L. & Giordano, A. 2008. An experimental study on the long-term behaviour of CFRP pultruded laminates suitable to concrete structures rehabilitation. *Composites: Part B* 39(2008): 1147–50.

Chami, G.A.; Thériault, M. & Neale, K.W. 2009. Creep behaviour of CFRP-strengthened reinforced concrete beams. *Construction and Building Materials* 23(4): p. 1640–52.

Ferrier, E.; Michel, L.; Jurkiewiez, B. & Hamelin P. 2011. Creep behaviour of adhesives used for external FRP strengthening of RC structures. *Construction and Building Materials* 25(2).

ISIS Canada. 2001. Design Manuals Parts 1–4. Intelligent Sensing for Innovative Structures.

JBDPA-Japan. 1999. Seismic Retrofitting Design and Construction Guidelines for Existing Reinforced Concrete (RC) Buildings with FRP Materials. Japan Building Disasters Prevention Association.

Kaminski, M. & Bywalski, C. 2008. Influence of creep deformations on value of long term deflections of steel fibre-reinforced concrete beams, *Proceedings of the 8th International Conference on Creep, Shrinkage and Durability of Concrete and Concrete Structures, 30 September–2 October 2008*, Ise-Shima, Japan, Edited by Tanabe et al., vol. 1: p. 729–734.

Kwiecień, A. 2012. Stiff and flexible adhesives bonding CFRP to masonry substrates-Investigated in pull-off test and Single-Lap test. *Archives of Civil and Mechanical Engineering* 12(2) p. 228–239.

Marí, A.R.; Oller E.; Bairán J.M. & Duarte N. 2012. Simplified method for the calculation of long-term deflections in FRP-strengthened reinforced concrete beams. *Composites: Part B* (2012): in press.

Meier, U.; Deuring, M.; Meier, H. & Schwegler, G. 1992. Strengthening of Structures with CFRP Laminates: Research and Applications in Switzerland. Advanced composite materials in bridges and structures, *Canadian Society of Civil Engineers*: p. 243–251.

Meshgin, P.; Choi, K-K. & Reda Taha, M.M. 2009. Experimental and analytical investigations of creep of epoxy adhesive at the concrete-FRP interfaces. *International Journal of Adhesion & Adhesives* 29(2009): p. 56–66.

Muller, M.; Toussaint, E.; Destrebecq, J.F. & Grédiac, M. 2007. Investigation into the time-dependent behaviour of reinforced concrete specimens strengthened with externally bonded CFRP-plates. *Composites: Part B* 38(2007): p. 417–28.

Pelvris, N. & Triantafillou, T.C. 1994. Time-dependent behaviour of RC members strengthened with FRP laminates. J *Struct Eng, ASCE* 120(3): p. 1016–42.

Ramana, V.P.V.; Kant, T.; Morton, S.E.; Dutta, P.K.,;Mukherjee, A. & Desai, Y.M. 2000. Behaviour of CFRPC strengthened reinforced concrete beams with varying degrees of strengthening. *Composites: Part B* 31: p. 461–70.

Steiner, W. 1996. Strengthening of Structures with CFRP Strips. *Advanced Composite Materials and Structures* p.407–417.

The Concrete Society. 2004. Design guidance for strengthening concrete structures using fibre composite materials. Camberley: The Concrete Society.

Trapko T. & Musiał, M. 2011. The effectiveness of CFRP materials strengthening of eccentrically compressed reinforced concrete columns. *Archives of Civil and Mechanical Engineering* 11(1): p. 249–262.

Trapko, T. & Trapko, W. 2012. Load-bearing capacity of compressed concrete elements subjected to repeated load strengthened with CFRP materials. *Journal of Civil Engineering and Management* 18(4): p. 590–599.

Yost, J.R.; Gross, S.P.; Dinehart, D.W. & Mildenberg, J.J. 2007. Flexural behaviour of concrete beams strengthened with near-surface-mounted CFRP strips. *ACI structural journal* 104(4): p. 430–437.

Concrete Solutions – Grantham et al. (Eds)
© 2014 Taylor & Francis Group, London, ISBN 978-1-138-02708-4

Rehabilitation of concrete beams pre-failed in shear using near-surface-mounted composite strips

T.A. El-Maaddawy
United Arab Emirates University, Al Ain, United Arab Emirates Housing & Building National Research Center, Giza, Egypt

ABSTRACT: The viability of using post-installed near-surface-mounted carbon fiber reinforced polymer (NSM-CFRP) composite strips to restore and upgrade the shear capacity of reinforced concrete beams pre-failed in shear is examined in this paper. The study comprised testing of 12 specimens. Test parameters included the amount of internal steel stirrups, angle of inclination of the post-installed NSM-CFRP composite strips, and presence of shear-damage prior to retrofitting. The shear-damaged beams were first tested to failure, retrofitted, then retested to failure for a second time. Test results demonstrated that rehabilitation of RC beams pre-failed in shear with the NSM-CFRP composite strips fully restored the beam shear strength. The shear capacity of the pre-failed beams after retrofitting was even higher than the original shear strength recorded in the first shear test to failure. The strengthening effectiveness decreased with an increase in the amount of internal steel stirrups. The inclined NSM-CFRP composite strips were more effective in improving the shear capacity than the vertical strips. The validity of an analytical approach published in the literature to predict the NSM-CFRP shear resistance has been demonstrated by comparing its predictions with the experimental results.

1 INTRODUCTION

Reinforced concrete (RC) beams are vulnerable to fail in shear due to overloading, accidental impact damage, or under extreme events such as an earthquake. In such cases, immediate measures shall be undertaken to repair and strengthen the damaged beams thus restoring the shear capacity. The complete replacement option is very costly, time and labor consuming. It would also result in safety hazards and large financial losses.

The near-surface-mounted (NSM) composite system is a promising technique for shear strengthening of deficient RC structural components (De Lorenzis & Teng 2007). In this system composite reinforcement, in the form of rods or strips, is installed into grooves precut on the concrete surface and held in place using an epoxy adhesive. The composite reinforcement in the NSM system is protected from acts of vandalism and weathering (Islam 2009, El-Hacha & Wagner 2009, Dias & Barros 2011).

Experimental studies on shear strengthening with the NSM composite system are relatively few. In the absence of internal steel stirrups, the NSM composite system can result in up to a two-fold increase in the shear resistance (De Lorenzis & Nanni 2001, Nanni et al. 2004, Barros & Dias 2006). The NSM technique is less effective for concrete beams with internal steel stirrups. In the presence of a limited amount of internal steel stirrups and properly detailed NSM composite reinforcement, appreciable shear strength gain in the range of 22% to 80% can be achieved (De Lorenzis & Nanni 2001, Dias & Barros 2008, Rizzo & De Lorenzis 2009, Cisneros et al. 2012, Dias & Barros 2012). For RC beams with a significant amount of internal steel stirrups strengthened with NSM composite reinforcement, a negligible shear strength gain of 4% was achieved (Chaallal et al. 2011). Decreasing the spacing between the NSM composite reinforcement or changing their angle of inclination from 90° to 45° or 60° tended to increase the shear strength gain but for beams with a very closely spaced NSM composite reinforcement, the relative proximity of the composite strips could result in a premature detachment of the side concrete covers of the beam's lateral faces (Barros & Dias 2006, Dias & Barros 2008, El-Maaddawy & Chekfeh 2013). In such cases, the use of closely spaced vertical or inclined NSM composite reinforcement may not benefit the shear capacity but could even result detrimental (Dias & Barros 2008, Rizzo & De Lorenzis 2009).

The viability of the NSM composite system to upgrade and restore the shear capacity of RC beams pre-failed in shear has received little attention in the literature. Practical applications would involve rehabilitation of shear-damaged RC beams. In most of previous studies, the amount of internal shear reinforcement was kept constant. Further research is then needed to genuinely understand the interaction between the failure mechanism, amount of internal

Table 1. Test matrix.

Group	Stirrups spacing	Shear damage	Inclination of CFRP	Specimen
[A]	120 mm	No damage	–	S1-ND-NR
			90°	S1-ND-R90
			45°	S1-ND-R45
		Pre-failed	–	S1-D2-NR*
			90°	S1-D2-R90
			45°	S1-D2-R45
[B]	75 mm	No damage	–	S2-ND-NR
			90°	S2-ND-R90
			45°	S2-ND-R45
		Pre-failed	–	S2-D2-NR*
			90°	S2-D2-R90
			45°	S2-D2-R45

*These two specimens were subjected to repeated cycles of loading-unloading till complete collapse without retrofitting.

steel stirrups, and angle of inclination of the NSM composite reinforcement.

This paper aims at evaluating the viability of using post-installed near-surface-mounted carbon fiber reinforced polymer (NSM-CFRP) composite strips to restore and upgrade the shear capacity of RC beams with different amounts of internal steel stirrups and pre-failed in shear. The contribution of the NSM-CFRP strips to the shear resistance of undamaged and pre-failed concrete beams is determined experimentally and compared to predictions of an analytical procedure published in the literature.

2 EXPERIMENTAL PROGRAM

2.1 *Test matrix*

The experimental program is summarized in Table 1. A total of 12 specimens were tested. The specimens were grouped into two main series; [A] and [B] based on the spacing between the internal stirrups. Specimens of groups [A] and [B] included 6 mm diameter closed double-legged stirrups with a center-to-center spacing of either 120 mm or 75 mm that corresponded to $0.6d$ and $0.375d$, respectively, where d = effective depth of the tensile steel reinforcement. Prior to restoration, the beams were either undamaged or pre-failed in shear. Each group included two specimens without NSM-CFRP shear reinforcement to act as benchmarks. The NSM-CFRP shear reinforcement in the retrofitted specimens was aligned at a center-to-center longitudinal spacing of $s_f = 120$ mm with an angle of inclination of either 90° or 45° with respect to the longitudinal axis of the beam.

2.2 *Materials*

The cylinder concrete compressive strength was, on average, 30 MPa with a corresponding standard deviation of 1.4 MPa. The longitudinal steel reinforcement was deformed bars with a nominal yield strength

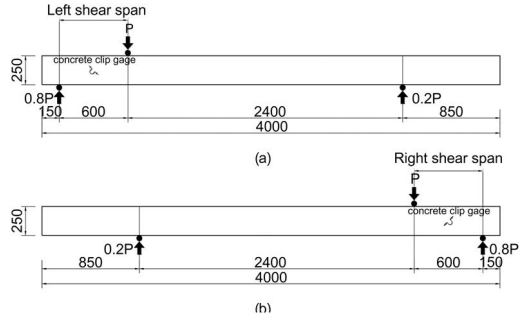

Figure 1. Loading regime. (a) test of the left shear span (first specimen). (b) test of the right shear span (second specimen).

of 520 MPa. The shear reinforcement in the test region was plain bars with measured yield strength of 345 MPa. A typical CFRP strip used in the NSM reinforcement has a cross section of 2.5×15 mm, tensile modulus of 165 GPa, tensile strength of 3100 MPa, and an ultimate elongation of 1.9%. An epoxy-based adhesive with a typical tensile modulus of 4.5 GPa, tensile strength of 25 MPa, and an ultimate elongation of 1% was used for bonding the CFRP strips to the concrete.

2.3 *Test specimens and procedure*

The test specimen had a rectangular cross section of 125×250 mm and effective depth of $d = 200$ mm. The specimens were heavily reinforced in flexure to ensure that they would fail in shear. The loading regime adopted in this study allowed two specimens to be tested on each beam as shown in Figure 1. The left shear span (first specimen) was first tested keeping the right end zone overhung and unstressed as shown in Figure 1a. The right shear span (second specimen) was then tested keeping the left end zone, already tested previously, overhung and unstressed as shown in Figure 1b.

Each beam had a total length of 4000 mm. The specimens were tested under three-point bending with an effective span of 3000 mm and a short shear span (test region) of 600 mm. This rendered a shear span to effective depth ratio of $a/d = 3$. The load was applied incrementally by means of a hydraulic jack until failure. The deflection under the load point was monitored using a linear variable displacement transducer (LVDT). Electrical resistance strain gages (SG) were bonded to the surface of the internal stirrups and external NSM-CFRP shear reinforcement. A concrete clip gage, with a gage length of 100 mm, inclined at 45° was mounted on the concrete surface at the mid-point of the shear span to measure the diagonal deformation across cracks.

2.4 *Retrofitting methodology*

The preexisting cracks in the pre-failed beams were chased out in a V-shape to a depth of approximately

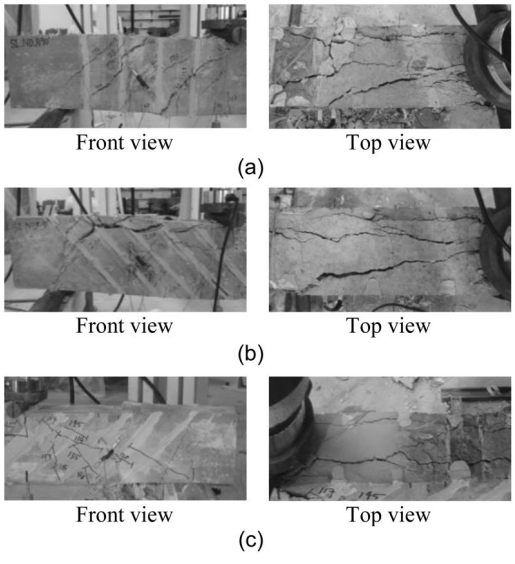

Figure 2. Failure mode of sample retrofitted specimens. (a) non-damaged specimen S1-ND-R90. (b) non-damaged specimen S2-ND-R45. (c) pre-failed specimen S1-D2-R45.

13 mm, surface-filled with epoxy adhesive, and struck off flush with the concrete surface. Grooves, each having a width of 10 mm and a depth of 20 mm, were cut on both beam's lateral faces at desired location using a slitting machine. The grooves were cleaned of dust using an electrical dust blower then partially filled with the epoxy adhesive. The CFRP strips were then inserted into the grooves and lightly pressed until the adhesive flowed around the strips. The surface was then cleaned and leveled using a trowel.

3 EXPERIMENTAL RESULTS

3.1 *Failure mode*

The non-retrofitted specimens exhibited a classical "diagonal-tension" shear mode of failure. The specimens retrofitted with the vertical NSM-CFRP strips failed by formation of diagonal shear cracks in the shear span crossing the NSM-CFRP strips followed by separation of the side concrete covers of the specimen's lateral faces which rendered two longitudinal cracks at the top and bottom surfaces of the specimen. Photos of sample retrofitted specimens after testing are shown in Figure 2.

In some specimens, vertical cracks developed at the adhesive-concrete interface connecting the inclined cracks in between the NSM-CFRP strips. The specimens retrofitted with the inclined NSM-CFRP strips initially experienced inclined shear cracks in-between the NSM-CFRP strips. As the load progressed, the developed cracks could not cross the inclined NSM-CFRP strips, and hence they tended to find a different pathway thus inducing peeling-off of the top concrete cover in-between the NSM-CFRP strips. This occurred

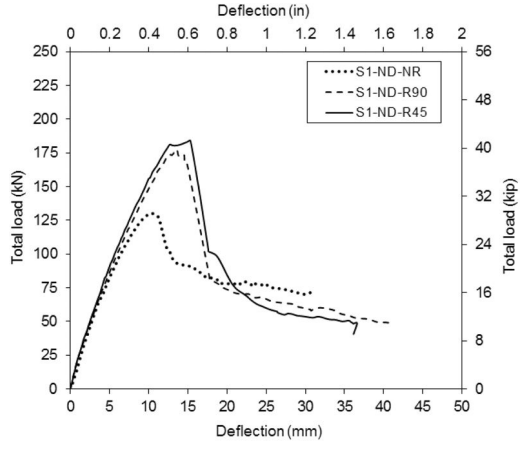

Figure 3. Load-deflection response of non-damaged specimens of group [A], 120 mm stirrup spacing.

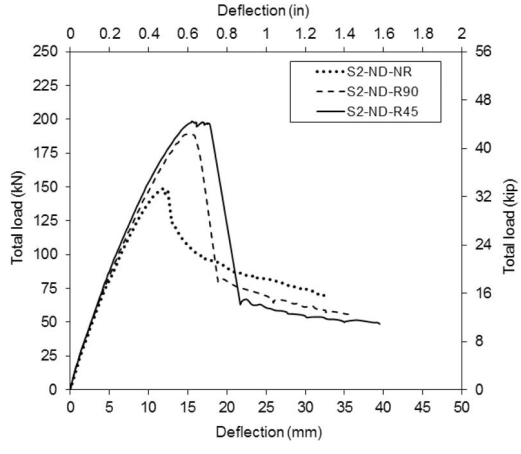

Figure 4. Load-deflection response of non-damaged specimens of group [B], 75 mm stirrup spacing.

simultaneously with detachment of the side concrete covers of the specimen's lateral faces. The retrofitted specimens that were pre-failed prior to retrofitting experienced a failure mode similar to that of their counterparts that were not shear-damaged prior to restoration. Nevertheless, for the pre-damaged specimens with the inclined NSM-CFRP strips, separation of the side concrete covers took place solely without peeling-off of the top concrete cover.

3.2 *Load-deflection response*

The load-deflection curves of the specimens of groups [A] and [B] that were not shear-damaged prior to retrofitting are depicted in Figures 3 and 4, respectively.

All specimens exhibited a quasi-linear deflection response untill peak load. The specimens with the inclined NSM-CFRP reinforcement were slightly

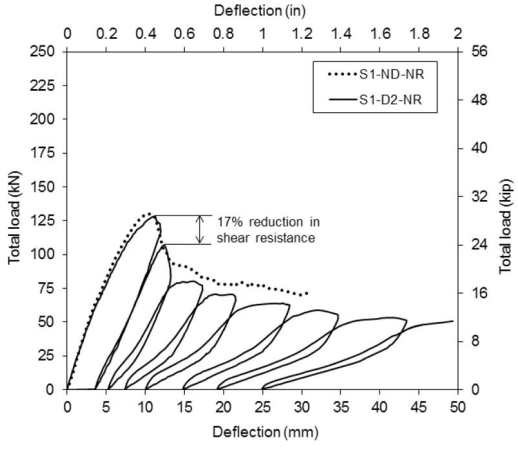

Figure 5. Load-deflection response of the unstrengthened specimens of group [A].

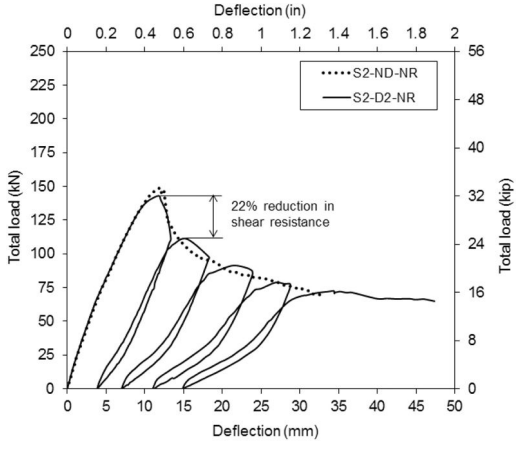

Figure 6. Load-deflection response of unstrengthened specimens of group [B].

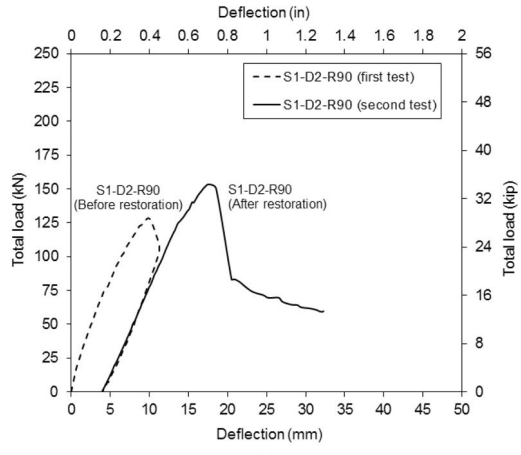

(a)

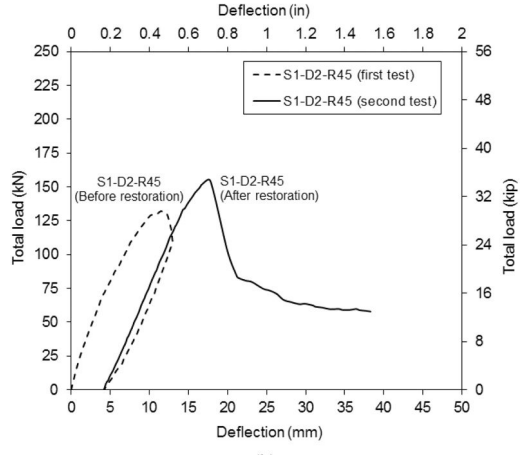

(b)

Figure 7. Load-deflection response of the pre-failed specimens of group [A]. (a) S1-D2-R90. (b) S1-D2-R45.

stiffer than their counterparts with the vertical NSM-CFRP strips. The NSM-CFRP shear strengthening significantly increased the shear resistance. The inclined NSM-CFRP strips were more effective in improving the shear response than the vertical strips. The shear strength gain was inversely proportional to the amount of the internal steel stirrups. Decreasing the spacing between the internal steel stirrups from 120 mm to 75 mm reduced the shear strength gain from 36 to 27%, respectively for the specimens with the vertical NSM-CFRP strips, and from 41% to 34%, respectively for the specimens with the inclined NSM-CFRP strips.

The load-deflection responses of the unstrengthened specimens of groups [A] and [B] are plotted in Figures 5 and 6, respectively. The envelopes of the load-deflection response of specimens S1-D2-NR and S2-D2-NR under repeated cycles of loading-unloading coincided with the response of the control specimens S1-ND-NR and S2-ND-NR, respectively that were tested to failure under monotonically increasing static loading. The residual shear strengths of specimens S1-D2-NR and S2-D2-NR after one cycle of loading to failure-unloading were 78 and 83% of their original shear strengths, respectively.

The load-deflection curves of the pre-failed specimens of groups [A] and [B] are depicted in Figures 7 and 8, respectively. One cycle of loading to failure-unloading resulted in a permanent deflection of approximately 3.8 mm which shifted the load-deflection curves of the specimens after retrofitting.

The shear resistance of the pre-failed specimens significantly improved after retrofitting. The shear resistances of the retrofitted specimens of groups [A] and [B] with the higher and closer spacing of internal steel stirrups were, on average, 20 and 9% higher than their original shear strengths recorded in the first shear test to failure, respectively. This indicates that the NSM-CFRP strips were less effective in improving the shear resistance of the pre-failed specimens with the higher amount of internal steel stirrups.

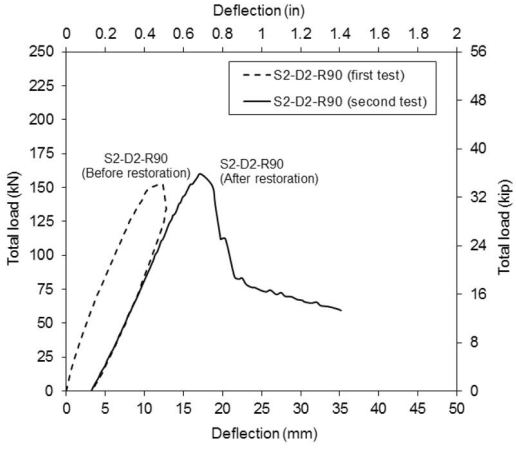

(a)

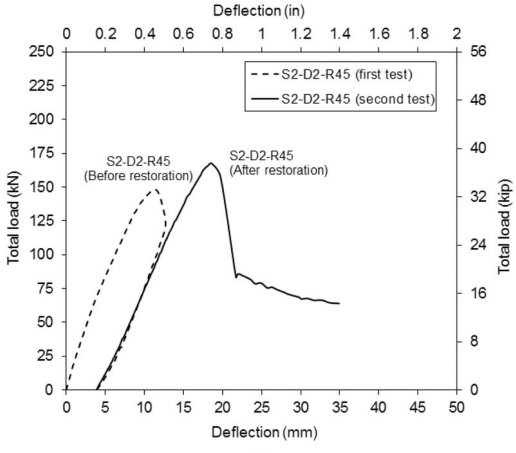

(b)

Figure 8. Load-deflection response of the pre-failed specimens of group [B]. (a) S2-D2-R90. (b) S2-D2-R45.

The inclined NSM-CFRP strips were, generally, more effective than the vertical strips in upgrading the shear resistance of the pre-failed specimens.

3.3 *Diagonal displacement across cracks*

Typical load versus diagonal tensile displacement curves are depicted in Figure 9. The curve of the non-retrofitted specimen featured three phases. In the first phase, no diagonal displacements were recorded till initiation of the shear cracks. Following cracking, the diagonal tensile displacement started to increase at almost a constant rate up to a diagonal tensile displacement across cracks of approximately 0.5 mm. In the third stage, the specimen exhibited a plastic response. The NSM-CFRP shear strengthening significantly reduced the rate of increase of the diagonal displacement across cracks. The specimen S1-ND-R45 with the inclined NSM-CFRP strips experienced lower diagonal displacements across cracks relative to those exhibited by the specimen S1-ND-R90 with the vertical NSM-CFRP strips.

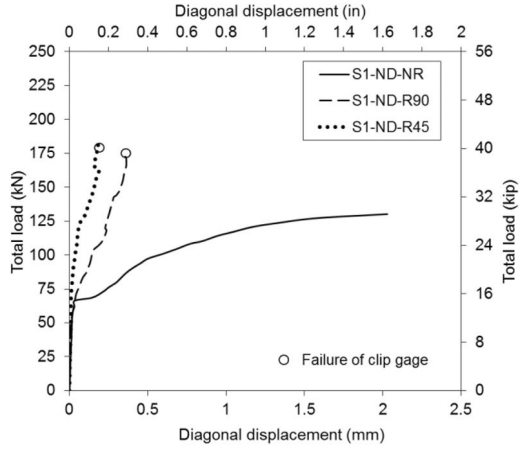

Figure 9. Typical load-diagonal displacement response.

3.4 *Stirrups strain response*

The effect of strengthening on the maximum stirrups strain measured in the undamaged specimens is depicted in Figure 10. The stirrups started to contribute to the shear resistance after crack initiation. The rate of increase of the stirrups strain in the post-cracking stage was a maximum for specimen S1-ND-NR with the higher spacing of stirrups and no NSM-CFRP shear reinforcement whereas it was a minimum for specimen S2-ND-R45 with the closer spacing of stirrups and inclined NSM-CFRP shear reinforcement. The specimens with the closer spacing of internal steel stirrups, typically, exhibited lower strains than those of their counterparts with the higher spacing of stirrups. The NSM-CFRP reinforcement reduced the strains in the internal steel stirrups, delayed their yielding and hence increased the shear capacity. The specimens S1-ND-R90 and S2-ND-R90 with the vertical NSM-CFRP strips exhibited almost a plastic response after yielding of stirrups. The specimen S2-ND-R45 was over-reinforced for shear and hence yielding of stirrups occurred when the specimen reached its peak load.

3.5 *CFRP strain response*

The effect of initial shear damage on the CFRP strain response is demonstrated in Figure 11. The specimens that were not damaged prior to retrofitting featured a tri-linear CFRP strain response. In the first stage, the NSM-CFRP strips remained unstrained until initiation of the shear cracks at about 75 kN. In the post-cracking stage, the CFRP strains increased almost at a constant rate up to yielding of the stirrups at approximately 125 kN. In the third stage, the CFRP strain further increased but at a higher rate. The specimens S2-D2-R90 and S2-D2-R45 featured a quasi-linear CFRP strain response till the peak load. The specimens

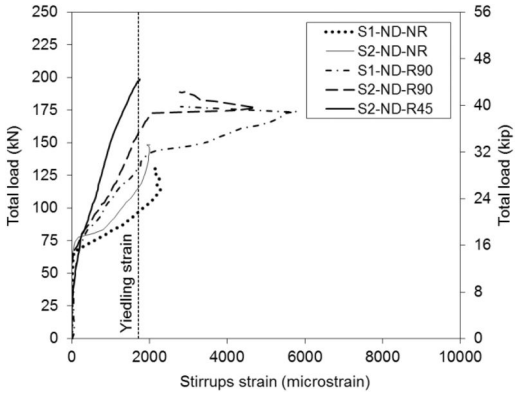

Figure 10. Stirrups strain response.

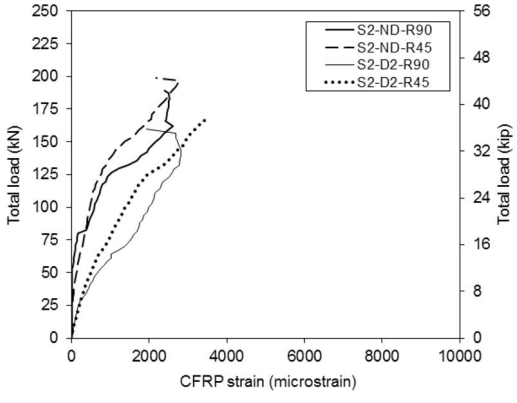

Figure 11. CFRP strain response.

with the inclined CFRP strips tended to exhibit lower CFRP strains than those of the specimens with the vertical strips. Since the CFRP strains were measured in the longitudinal direction of the CFRP strips, the vertical component of the CFRP strains in the specimens S2-ND-R45 and S2-D2-R45 would be even lower. The rate of increase of the CFRP strains in specimens S2-D2-R90 and S2-D2-R45, that were pre-failed prior to retrofitting, was significantly higher than that of specimens S2-ND-R90 and S2-ND-R45, respectively. This can be ascribed to the severe concrete damage that occurred in the first shear test to failure, which reduced the contribution of the concrete to the shear resistance and hence overstrained the NSM-CFRP strips.

4 ANALYTICAL PROCEDURE

The nominal shear resistance provided by the NSM-CFRP composite system is the vertical projection of the maximum tensile stresses in the NSM-CFRP strips intercepted by a 45° shear crack, which can be calculated by the analytical approach proposed by Nanni et al. (2004).

$$V_{fn} = 4(a_f + b_f)\tau_b \Sigma_i L_i \sin\alpha \quad (1)$$

where V_{fn} = contribution of the NSM-CFRP strips to the shear capacity predicted analytically; a_f = thickness of the NSM-CFRP strip; b_f = width of the NSM-CFRP strip; τ_b = average bond stress of a NSM-CFRP strip; L_i = effective length of a NSM-CFRP strip crossed by a 45° shear crack; and α = angle of inclination of the NSM-CFRP strips. The effective length of the NSM-CFRP strip, L_i, is calculated as follows.

$$L_i = \begin{cases} \dfrac{s_f}{\cos\alpha + \sin\alpha}\, i \quad \le l_{\max}, & i = 1.....\dfrac{N}{2} \\ l_{net} - \dfrac{s_f}{\cos\alpha + \sin\alpha}\, i \quad \le l_{\max}, & i = \dfrac{N}{2} + 1....N \end{cases} \quad (2)$$

$$l_{net} = l_b - \frac{2c}{\sin\alpha} \quad (3)$$

$$N = \frac{(l_b \sin\alpha - 2c)(1 + \cot\alpha)}{s_f} \quad (4)$$

where s_f = spacing between the NSM-CFRP strips; l_{net} = net length of a NSM-CFRP strip; N = number of NSM-CFRP strips intercepted by a 45° diagonal shear crack; l_{max} = length of a NSM-CFRP strip needed to maintain the concrete shear integrity; l_b = actual length of a vertical NSM-CFRP strip; and c = concrete cover to the center of the tensile steel reinforcement.

The terms N and $N/2$ in Equation 2 are rounded off to the smallest integer number. The first limitations in this equation takes into account the bond as the controlling failure mechanism since it represents the minimum effective length for a CFRP strip intercepted by a 45° diagonal shear crack as function of the CFRP strip location. The second limitation, $l_{\max}$, takes into account the shear integrity of concrete by limiting the strain in the CFRP strip to a maximum value of ε_{eff}. For a rectangular CFRP strip, $l_{\max}$ is given by the following equation:

$$l_{\max} = \frac{\varepsilon_{eff}}{2} \frac{a_f b_f}{a_f + b_f} \frac{E_f}{\tau_b} \quad (5)$$

where E_f = tensile modulus of the NSM-CFRP strips and ε_{eff} = effective CFRP strain needed to maintain the shear integrity of the concrete.

For a CFRP strip embedded in a groove size at least 3 times the strip width using an epoxy-based resin, a nominal value of $\tau_b = 16$ MPa can be employed based on experimental data published in the literature (Barros & Dias 2006, Dias & Barros 2008). For the specimens of the present study, the effective CFRP strains, ε_{eff}, measured in the undamaged and pre-failed specimens were on average, 2750 and 2500 microstrain, respectively. These values have been employed in the analytical procedure. A comparison between the experimental and analytical CFRP shear resistances; $V_{f,exp}$ and V_{fn}, respectively, is given in Table 2.

From this table, it can be seen that the analytical procedure gives a reasonable prediction for the CFRP

Table 2. Analytical and experimental results.

Specimen	Experimental $V_{f,exp}$ (kN)	Analytical V_{fn} (kN)	Ratio ($V_{fn}/V_{f,exp}$)
S1-ND-R90	37.8	34	0.90
S1-ND-R45	42.9	48	1.12
S1-D2-R90	37.5	31	0.83
S1-D2-R45	38.4	44	1.15
S2-ND-R90	32.6	34	1.04
S2-ND-R45	40.2	48	1.19
S2-D2-R90	39.1	31	0.79
S2-D2-R45	45.0	44	0.98

shear resistance. The ratio of the predicted to experimental CFRP shear resistance was in the range of 0.79 to 1.19 with an average of 1.0 and a standard deviation of 0.15. It is recommend to adopt a strength reduction factor of 0.75 in order to obtain conservative predictions for the contribution of the NSM-CFRP strips to the shear resistance for both undamaged and pre-failed RC beams.

5 CONCLUSIONS

The presence of shear damage in test specimens prior to retrofitting did not reduce the shear strength gain attributable to the post-installed NSM-CFRP reinforcement. The NSM-CFRP composite system fully restored the shear capacity of the specimens pre-failed in shear. The shear strength of the pre-failed specimens after retrofitting was higher than their original shear strength recorded in the first shear test to failure. The gain in shear resistance caused by the NSM-CFRP strips decreased with an increase in the amount of internal steel stirrups. The NSM-CFRP strips inclined at 45° were more effective than the vertical strips in improving the shear response. The analytical approach by Nanni et al. (2004) gave reasonable predictions for the nominal contribution of the NSM-CFRP strips to the shear resistance. Maximum CFRP strains of 2750 and 2500 microstrain along with a strength reduction factor of 0.75 should be adopted in order to obtain conservative predictions for the contribution of the NSM-CFRP strips to shear strengths of undamaged and pre-failed beams, respectively.

ACKNOWLEDGMENTS

The author would like to express his gratitude to the UAEU for financing this project under the seed grant no. 21N146.

REFERENCES

Barros, O. & Dias, S. (2006). Near Surface Mounted CFRP Laminates for Shear Strengthening of Concrete Beams. *Cement and Concrete Composites* 28(3): 276–292.

Chaallal, O., Mofidi, A., Benmokrane, B., and Neale, K. W. (2011). Embedded Through-Section FRP Rod Method for Shear Strengthening of RC Beams: Performance and Comparison with Existing Techniques. *Journal of Composites for Construction* 15(3): 60–68.

Cisneros, D., Arteaga, A., De Diego, A., Alzate, A. (2012). Experimental Study on NSM FRP Shear Retrofitting of RC Beams. *Proc. 6th Intern. Conference on FRP Composites in Civil Engineering (CICE-2012)*, *Rome, 13–15 June 2012*, Italy.

De Lorenzis, L. & Teng, J. (2007). Near-Surface Mounted FRP Reinforcement: An Emerging Technique For Strengthening Structures. *Composites Part B: Engineering* 38(2): 119–143.

De Lorenzis, L. & Nanni, A. (2001). Shear Strengthening of Reinforced Concrete Beams with Near-Surface Mounted Fiber-Reinforced Polymer Rods. *ACI Structural Journal* 98(1): 60–68.

Dias, S. & Barros, J. (2011). Shear Strengthening of RC T-Section Beams with Low Strength Concrete Using NSM CFRP Laminates. *Cement and Concrete Composites* 33(2): 334–345.

Dias, S. & Barros, J. (2008). Shear Strengthening of T Cross Section Reinforced Concrete Beams by Near-Surface Mounted Technique. *Journal of Composites for Construction* 12(3): 300–311.

Dias, S. & Barros, J. (2012). Performance of Pre-Cracked RC Beams Shear Strengthened with NSM CFRP Laminates," *Proc. 6th Intern. Conference on FRP Composites in Civil Engineering (CICE-2012)*, *Rome, 13–15 June 2012*, Italy.

El-Hacha, R. & Wagner, M. (2009). Shear Strengthening of Reinforced Concrete Beams using Near-Surface Mounted CFRP Strips. *Proc. 9th Intern. Symp. on Fiber-Reinforced Polymer Reinforcement for Concrete Structures (FRPRCS-9)*, *13–15 July 2009,* Sydney, Australia.

El-Maaddawy, T. & Chekfeh, Y. (2013). Long-Term Performance of Corrosion-Damaged Reinforced Concrete Beams. *ACI Structural Journal* 110(5): 779–790.

Islam, A. (2009). Effective Methods of Using CFRP Bars in Shear Strengthening of Concrete Girders. *Engineering Structures* 31(3): 709–714.

Nanni, A., Di Ludovico, M., and Parretti, R. (2004). Shear Strengthening of a PC Bridge Girder with NSM CFRP Rectangular Bars. *Advances in Structural Engineering* 7(4): 97–109.

Rizzo, A. & De Lorenzis, L. (2009). Behavior and Capacity of RC Beams Strengthened in Shear with NSM FRP Reinforcement. *Construction and Building Materials* 23(4): 1555–1567.

This page intentionally left blank

Concrete Solutions – Grantham et al. (Eds)
© 2014 Taylor & Francis Group, London, ISBN 978-1-138-02708-4

Flexural strengthening for R.C. beams using CFRP sheets with different bonding schemes

Alaa M. Morsy, Karim M. Helmy, Nabil H. El-Ashkar & Mohamed Nada
Construction & Building Department College of Engineering & Technology, Arab Academy for Science, Technology, and Maritime Transport, Egypt

ABSTRACT: An experimental program was performed through this research to assess the flexural strengthening capacity of reinforced concrete beams strengthened using CFRP sheets with variable end anchorage systems to enhance the bond between CFRP sheets and concrete, as well as examining the effect of the number of CFRP layers. Four point bending tests were performed on eight R.C. beams, a control beam without strengthening, two beams strengthened with one and three layers of CFRP and bonded using only epoxy, three beams strengthened with one layer of CFRP sheets using three different end anchorage systems, and two beams strengthened with three layers of CFRP sheets using end anchorage systems. The specimens strengthened with the one layer of CFRP sheets and variable end anchorage systems showed a slight improvement in the flexure capacity ranging from 9% to17%, compared with the control beam while for the three layers showed 50% improvement compared with the control beam. On the other hand, the proposed end anchorage systems had a more significant effect compared to the conventional bonding with epoxy especially in the case of strengthening with three layers. The bottom reinforcement and the CFRP sheets showed a close load – strain behaviour, which indicates perfect bonding between the concrete substrate and the FRP sheets.

Keywords: FRP, flexural, strengthening, beams, anchorage, ductility, bond

1 INTRODUCTION

Strengthening Reinforced Concrete (RC) structures with Fiber Reinforced Polymers (FRP) has been studied and successfully implemented in field applications since the early 1990's. In addition to the superior properties of FRP, such as high strength to weight ratios and corrosion resistance, strengthening RC structures with FRP in most cases is easier and requires less labor and time than conventional strengthening techniques. FRP has been used in strengthening RC columns and beams both in flexure and in shear (Kortynia et al. 2008 and Alaa et al. 2012).

Strengthening with externally bonded Fiber Reinforced Polymer (FRP) fabric has been shown to be applicable to many kinds of structures. It is well known that reinforced concrete beams strengthened with externally bonded fiber-reinforced polymer (FRP) to the tension face can exhibit ultimate flexural strength greater than their original flexural strength. However, these FRP strengthened beams could lose some of their ductility due to the brittleness of FRP. In these studies RC beams were strengthened with (CFRP) plates.Researchers concluded that the flexural strength of reinforced concrete beams could be significantly increased by externally bonded CFRP or FRP plated to their tension surface (Saadatmanesh et al. 1997 & M. Arduini et al. 1997). However, they indicated in their experimental research that the ductility of reinforced concrete beams using externally bonded FRP was reduced, and the extent of reduction in ductility depended upon the change of stiffness of strengthened beam as compared to the stiffness original beams (Thomsen et al. 2004 & Maghsoudi et al. 2006).

Externally bonded fiber reinforced polymers systems are successful in strengthening reinforced concrete structures. It is often said that end anchorage (Kortynia, R et al. 2008), is needed to delay or prevent de-bonding, which is the main cause of failure of such systems (Arduini et al. 2004, Brena et al. 2003, Grace et al. 200 and Garden et al. 1998). De-bonding is also sudden in nature; therefore, the ductility of the externally bonded element is reduced (Lamanna et al. 2004).

2 PROBLEM STATEMENT

Strengthening of R.C. beams with FRP sheets depends mainly on the bond strength between FRP and the concrete substrate: the adhesive layer between the concrete and FRP sheets present problems for the behavior of the strengthened flexural member causing de-bonding of FRP, so the main challenge facing designers is delaying or eliminating debonding allowing maximum utilization of the strength of FRP sheets or plates.

3 RESEARCH SIGNIFICANCE

This research presents an experimental investigation undertaken to study the effect of applying end anchorage systems to RC beams strengthened using FRP sheets. A four point loading tests was performed on eight RC beams. Special attention was given to the enhancement in flexural load carrying capacity, ductility of strengthened beams, and effect of number of layers of FRP sheets with the end anchorage system.

4 EXPERIMENTAL PROGRAM

4.1 *Specimen details*

A total of 8 specimens were constructed in this study to assess the effects of test variables on the flexure strengthening capacity of RC beams strengthened with FRP sheets, using different strengthening techniques. All specimens had a 150 × 300 mm cross section and a total length of 2400 mm as shown in Figure 1. The length of FRP sheets was 80% of the effective span of 1600 mm length and 100 mm wide. Stirrups having a diameter of 8 mm were placed at 75 mm intervals through the entire beam except for the middle 800 mm, where the spacing was 100 mm as shown in Figure 1. The specimen was designed to be weak in flexural with a top and a bottom reinforcement of two 16 mm diameter bars.

Four point loading was applied to specimens up to failure as shown in Figure 1. One beam was used as control without strengthening, while two other specimens were used as control for FRP strengthening without end anchorage with one and three FRP layers. The five other specimens had three different end anchorage systems and variable number of FRP sheets.

4.2 *Testing parameters and specimen preparation*

The test parameters were the number FRP layers (one and three layers) and the end anchorage systems applied on the ending point of sheets (three different techniques), as shown in Table 1. Figure 2 shows the beam designation for all tested specimens. Specimen B00 was the control beam for comparison purposes, while beam B10 & B30 were considered the control beams for strengthening of beams using one layer and three layers of FRP sheets, without end anchorage.

Preparation of the concrete substrate and application of CFRP materials were carried out in accordance with the guidelines that were provided by the sheet's manufacturer. The surfaces of all beams were ground using a mechanical metallic brush to remove any cement laitance, loose and friable material to achieve a profiled open textured surface and ensure strong bond between the concrete and CFRP sheets. The prepared concrete surface was coated with a layer of epoxy using a short nap roller, placing the fabric in the required direction onto the layer of epoxy. Carefully working the fabric into the epoxy with a plastic impregnation roller parallel to the fiber direction until the epoxy was

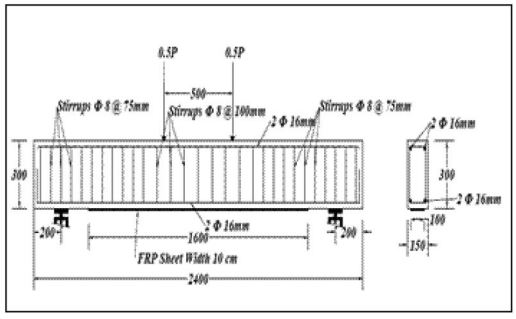

Figure 1. Specimen dimensions and reinforcement (all dimensions in mm).

Table 1. Specimen strengthening schemes.

Beam No.	Strengthening system	Number of layers
B00	No strengthening	—
B10	No end anchorage	One
B11	Strengthened with one layer of CFRP sheets embedded through vertical gap	One
B12	Strengthened with one layer of CFRP sheets wrapped around horizontal drilled bar	One
B13	Strengthened with one layer of CFRP sheets wrapped around two vertical drilled bolts	One
B30	No end anchorage	Three
B31	Strengthened with 3 layers of CFRP sheets embedded through vertical gap	Three
B32	Strengthened with 3 layers of CFRP sheets wrapped around horizontal drilled bar	Three

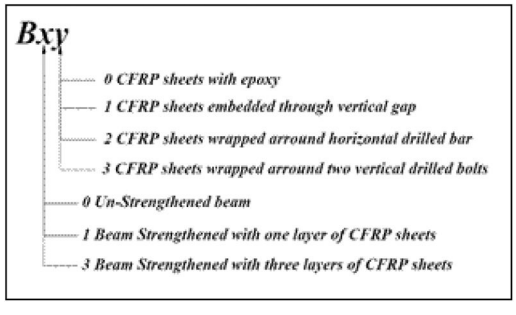

Figure 2. Specimen designations.

squeezed out between and through the fiber strands and distributed evenly over the whole fabric surface, avoiding excessive force when laminating to prevent folding or creasing of the fabric.

Wherever a second layer was required, the first sheet was coated with another layer of epoxy and excessive epoxy was removed. The second layer of CFRP sheets was then applied in the same manner mentioned

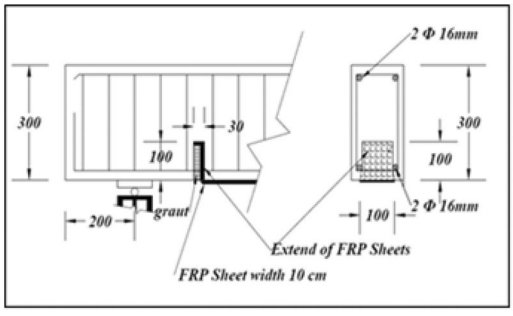

Figure 3a. Beams strengthened with CFRP sheets embedded through vertical gap.

Figure 3b. Beams before grouting the beam.

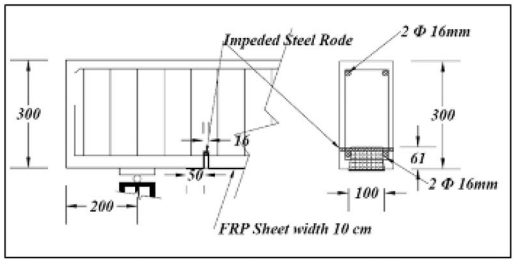

Figure 4a. Beam strengthened with CFRP sheets wrapped on horizontal drilled bar (all dimensions in mm).

above. The application of additional layers was within 60 minutes of the previous layer.

For beams B11 & B31 the sheets were anchored by drilling a hole between reinforcement bars to a depth of 100 mm, then the sheets were applied followed by grouting the concrete holes, as shown in Figure 3a, 3b.

For B12 & B32 strengthened by the second proposed end anchorage system, a groove was made between the main reinforcement to a depth of 5 cm in the vertical direction, and a hole was drilled in the horizontal direction passing through the vertical groove above the bottom reinforcement. Sheets were applied through the groove and a steel rod was embedded through the hole so that the sheets were laid on the embedded steel bar, as shown in Figure 4a, 4b.

Beam B13 was strengthened by the third end anchorage system, two 16 mm diameter holes were drilled at the beam ending was drilled to a depth of 10 cm, the sheets was applied around steel rivets which

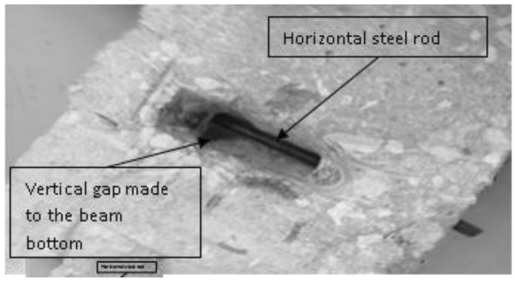

Figure 4b. Real picture showing the beam with the horizontal steel rode before applying the FRP sheets and epoxy application

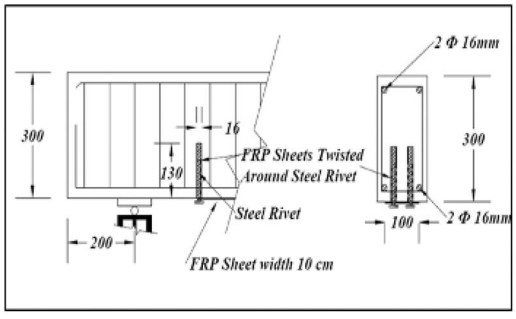

Figure 5. Beam strengthened with CFRP sheets wrapped on two vertical drilled bolts.

Table 2. Properties of used materials.

Material	Dimension, mm	Tensile strength, MPa	Modulus of elasticity E, GPa
Steel	diameter = 16	360	200
	diameter = 8	240	200
CFRP Sheets	0.131 mm based on fiber content	3450	230
Epoxy resin	–	30	3.8

were embedded into the drilled holes filled with epoxy as shown in Figure 5.

4.3 *Materials*

Concrete with an average cubes characteristic compressive strength of 35±2 MPa was used for the casting of the tested beams. High tensile steel of grade 360/520 was used for upper and lower reinforcement and mild steel of grade 240/350 for stirrups. The carbon fiber sheets used in this investigation were unidirectional CFRP sheets weighting 230 gm/m^2 (Sika wrap hex C230). These CFRP sheets were used for all strengthened beams. The sheets were glued using the manufacturer recommended epoxy resin (Sikadur 330). The properties of the used materials are given in Table 2.

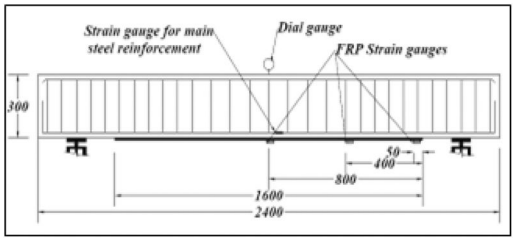

Figure 6. Strain gauges and dial gauges position.

4.4 *Test set up and Instrumentation*

The beams were tested using a load control MAGNUS testing machine. The loads were applied at intervals and recorded, along with the dial gauge and strain gauge readings, using a digital strain indicator. Application of the loads and the recording process continued until complete failure of the beam occurred.

The beams were instrumented to measure applied load, deflection and strain in the steel reinforcement & FRP strain during testing as shown in Figure 6. The deflection of the beam was measured by dial gauges placed at top mid span of the specimen. The strains in reinforcing bars and externally bonded CFRP sheets placed in five different locations were monitored during testing using 120 ohm electrical resistance strain gauges. Two strain gauges were placed at mid span of the bottom reinforcement. While for the CFRP sheets, strain gauges placed at mid span of the FRP sheet, 400 mm from mid span. The data was manually collected. The location of cracks and their propagation were clearly marked.

5 TEST RESULTS & DISCUSSION

5.1 *Specimen behaviour and failure mode*

The failure mode of each test specimen was determined by referring to the initiation and growth of the cracks and values of strain attached to the CFRP sheets and main tensile steel bars. The modes of failure for the test specimen are shown in Table 3.

Cracks for all beams specimens were tracked as the load was applied and the first crack load values were recorded.

The first cracks were identified visually and were also based on the average of the tensile steel strain reading at the centre of the beam characterised by sudden increase in the steel reinforcement strains. The first crack loads (P_{cr}) for all specimen are shown in Table 3. Also the yielding load was identified according to the train value in the bottom reinforcement measured with strain gauges, and accordingly the yielding point deformation was obtained as shown in Table 3. Finally the failure load and deformation was measured according to beam failure as shown in Table 3.

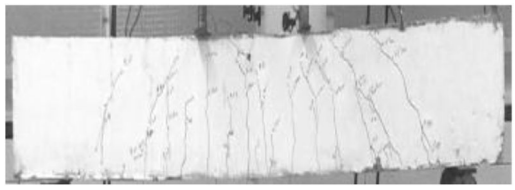

Figure 7. Failure mode of beam B00.

Figure 8. Failure mode for beam B10.

5.2 *Crack pattern and failures modes*

5.2.1 *Control specimen (B00) "without strengthening"*

For the control specimen, the first visible crack appeared at a load of about 30 kN and was flexural at the mid span of the beam, the cracks extended from the bottom of the beam and started to spread to the top of the beam along the whole span of the beam. Shear cracks started to appear at 60 kN. As loading progressed the cracks widened as seen in Figure 7. The specimen failed at a load of 82 kN. Failure started with steel yielding followed by failure in concrete in compression.

5.2.2 *Specimen (B10) flexural strengthened with CFRP sheets and bonded with epoxy*

The first visible crack appeared at a load of 30 kN at the mid-span of the beam. As loading progressed cracks widened then shear cracks started to appear at 50 kN. Finally failure was caused by fracture of the FRP Sheets at the mid span of the beam at a load of 90 kN as shown in Figure 8, followed by concrete failure in compression.

5.2.3 *Specimen (B11, B12& B13) flexural strengthened with CFRP sheets and bonded with the proposed end anchorage system*

The first visible crack appeared at loads of 30, 20 and 40 kN for beams B11, B12, and B13 respectively. Crack patterns started with flexure cracks followed by the appearance of shear cracks and close to the failure of the beams, localized de-bonding of the FRP sheets started to take place followed by fracture of the FRP sheets at the mid span for B11 and B12. However, beam B13 failed by fracture of FRP sheets at the end of the FRP sheet connection with the end anchorage system. The beams failed in a sudden manner at a load of 90,

Table 3. Test results

Beam no.	Cracking Point		Yielding Point		Ultimate point		% Increase In Load	Mode Of Failure
	$P_{cr,}$ kN	Δ_{cr}, mm	P_y kN	Δ_y mm	P_{ult} kN	$\Delta_{ult.}$ mm		
B00	25	1.62	82	8.22	84	22.25	–	Failed in Flexure
B10	30	4.67	–	–	90	14.12	7.14%	FRP fracture
B11	30	3.37	–	–	92	16.02	9.5%	FRP fracture
B12	20	2.93	–	–	100	16.12	19.05%	FRP fracture
B13	40	3.44	–	–	98	21.13	16.67%	FRP fracture at anchorage end
B30	30	2.4	100	12.19	110	30.72	30.9%	De-bonding FRP sheets
B31	30	3.4	95	11.34	125	24.12	48.8%	Fracture of FRP at end anchorage
B32	30	2.26	94	10.23	125	22.09	49%	Fracture of FRP at end anchorage

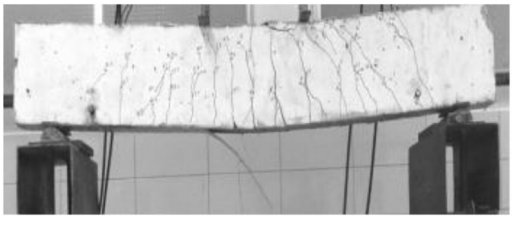

Figure 9. Failure mode of beam B12

Figure 10. Failure mode for beam B30.

100 and 98 kN for beam B11, B12 and B13. Figure 9 shows the beam B12 at failure.

5.2.4 *Specimen (B30) flexural strengthened with CFRP sheets and bonded with epoxy*

The first visible crack appeared at a load of 30 kN at the mid-span of the beam. As loading progressed cracks widened then shear cracks started to appear at 70 kN. The beam failed by de-bonding of the FRP sheets from the concrete surface at load of 110 kN as shown in figure 10. It was noticed that a thin layer of concrete was attached to the FRP sheet after failure, which indicated that the bonding epoxy worked well till the transverse shear stress exceeded its allowable stresses.

5.2.5 *Specimen (B31 & B32) flexural strengthened with CFRP sheets*

The first visible crack appeared at a load of 30 kN at the mid-span of the beam for both beams. As loading progressed, cracks widened then shear cracks started

Figure 11. Mode of failure of beam 32.

to appear at 60 and 50 kN for beams B31 and B32. Both beams failed at a load of 125 kN. Both beams had a similar failure of de-bonding of FRP sheets, followed by a sudden fracture of the sheets at the areas of the anchorage of the sheets, followed by the failure of the beam in compression, as shown in the figure 11.

5.3 *Load-deflection and load-strain relationships*

Figure 12, shows the load deflection curve of beam strengthened with one layer of FRP sheets, compared with un-strengthened beam.

The end anchorage system improved the load carrying capacity for beams B11, B12 and B13 by 9.5%, 19.1% and 16.7%. However this did not provide much improvement compared with the beam without end anchorage. The end anchorage systems provided a slight increase in the load carrying capacity over beam B10.

Figure 13, Shows the load deflection curves for the beams strengthened with three layers of FRP sheets and the control beam. The beams strengthened using the end anchorage systems (B31 & B32) showed an improvement in the beam carrying capacity by 50% reaching 125 kN as compared to the control beam's failure load of 84 kN, and a 14% improvement as compared to the beam strengthened with three layers of FRP sheets without end anchorage. The beam's stiffness increased for B31 & B32 compared to beam B00, while it was almost the same stiffness as beam B30.

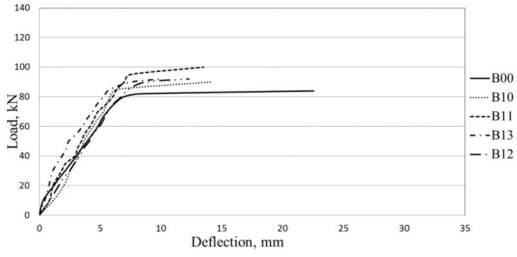

Figure 12. Load deflection curve for beams strengthened with one FRP sheet layer.

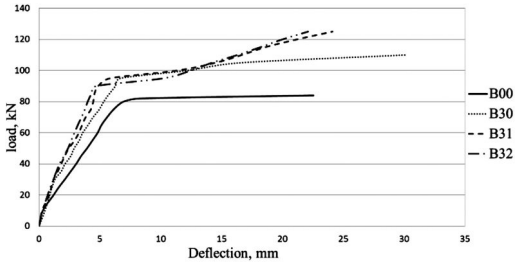

Figure 13. Load deflection curve for beams strengthened by three layers.

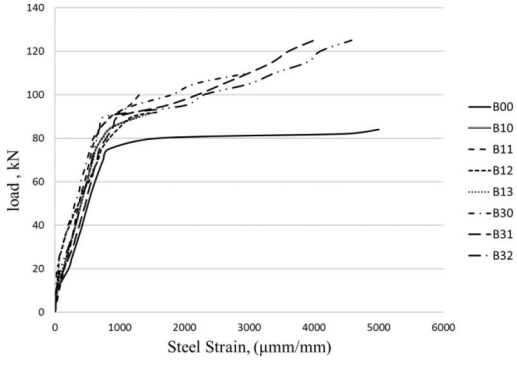

Figure 14. Strain load curve for bottom steel reinforcement.

Figure 14, Shows the load-strain curves for bottom steel reinforcement. All beams had the same reinforcement ratio but variable number of FRP sheets and end anchorage system schemes. All beams had almost the same stiffness prior to the yielding of the steel reinforcement but they had different failure strains. Beam B00 had the highest strain among all the tested beams. Beams (B11, B12, B13) all failed initially before steel yielding, however all beams strengthened with three layers of CFRP sheets and beam B10 reached yielding point.

It was clearly shown for all beams that there was a significant decrease in beam stiffness at the bottom steel reinforcement strain at about 700–800 μmm/mm due to crack propagation at that strain level.

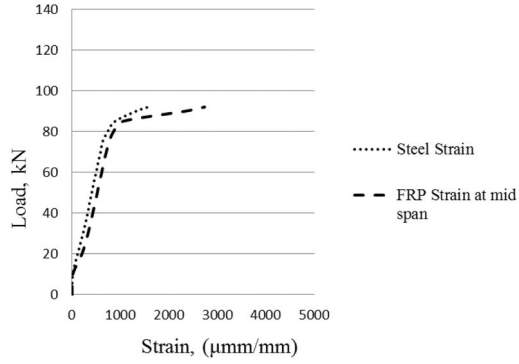

Figure 15. Strain load curves mid steel and FRP, B13.

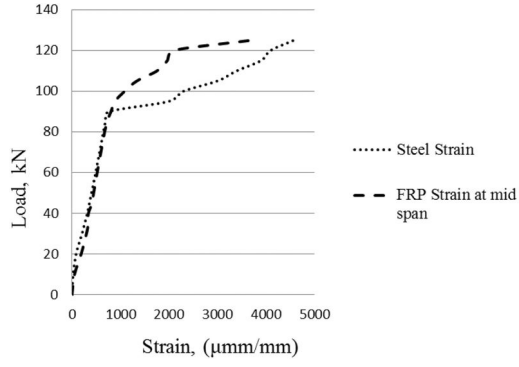

Figure 16. Strain load curve mid steel and FRP, B32.

5.4 *Strain compatibility*

FRP sheet strain and lower reinforcement strain were recorded for all specimens as shown in figure 15 and 16 for beams B13 and B32. It was clearly shown that both curves for FRP sheets and steel reinforcement coincided in trend and value which indicated full bond between FRP sheets and the concrete surface.

6 DUCTILITY

A ductile material is one that can undergo significant strain while resisting load. When applied to RC members, the term ductility implies the ability to sustain significant inelastic deformation prior to collapse. As the evolving technology of using bonded CFRP for strengthening RC beams has attracted much attention in recent years and because concrete behaves like a brittle material, understanding the effects of such strengthening techniques on the ductility of RC beams is critical. (Maghsoudi et al. 2006, Hashemi et al, 2008 and Thomsen et al. 2004).

Ductility has been measured by a ratio called the ductility index, which is obtained based on deflection (μ_d) and curvature (μ_ϕ) computation. Deflection (μ_d) defined by mid span deflection at ultimate load divided

Table 4. Ductility index.

Beam No.	Deflection μ_d
B00	2.71
B10	1
B11	1
B12	1
B13	1
B30	2.47
B31	2.13
B32	2.16

by mid span deflection at the point where the steel yields that will be performed through this research.

$$\mu_d = \Delta_u / \Delta_y \quad (1)$$

Where:

Δ_u = deflection at failure point
Δ_y = deflection at yielding point

This ductility index 'μ' is assumed to provide a reasonable basis for consistent evaluation of material behavior and can represent the ability of RC beams to undergo large deformation while maintaining their load resisting capacity or a significant portion of it. It simply represents the ability of the material to absorb and dissipate energy by post elastic deformation. The normalization of this index gives a good basis for comparative purposes between various specimens with different strengths. The higher the ductility index the better the performance. The deflection ductility index is used in this research. Table 4, shows the deflection ductility index for all beams.

Table 4 shows the ductility index for all beams. For all beams strengthened with one layer of CFRP sheets reinforcement steel did not yield, therefore the ductility index has a value of one, as Δ_y will have a similar value as Δ_u.

On the other hands beams strengthened with three layers of FRP sheets have a lower ductility index than the control beam. Beams strengthened with three layers showed a small decrease in the ductility index, compared to the control beam. Additionally the anchored beams had slightly less ductility than the unanchored beam, however the decrease in ductility was very small.

7 CONCLUSION

Based on the study reported:

1. Beams strengthened using one and three layers of FRP increased the load carrying capacity with 7% and 30% compared with the un-strengthened beam.
2. There was no significant effect for beams strengthened with an end anchorage system compared with beams strengthened with FRP without end anchorage in the case of using one layer of FRP sheets, due to fracture of the FRP sheets.
3. Beams strengthened with three FRP layers with a different end anchorage system had almost the same load carrying capacity with a 14% increase compared with a beam strengthened with three layers of FRP without end anchorage system and a 50% increase compared with un-strengthened beam.
4. Beams strengthened with three layers of FRP sheet either with or without an end anchorage system showed a full FRP sheet de-bonding prior to failure, and final failure was fracture of the FRP sheet in end anchorage connection.
5. There was a full compatibility between strain in FRP and strain in the lower steel, which indicates that the FRP sheet was bonded effectively to the concrete surface.
6. All beams strengthened with FRP showed a decrease in ductility index compared to an un-strengthened beam. In the case of a beam strengthened with one layer of CFRP, the lower reinforcement did not reach yielding point at failure, while in the case of three layered FRP samples, there was a slight decrease in ductility.

REFERENCES

Arduini M., Di Tommaso, A. and Nanni, A. July-Aug 1997. Brittle failure in FRP plate and sheet bonded beams. *ACI Struct. J.*, vol. 94, no. 4, pp. 363–370.

Kortynia, R.; Abdel Baky, H.; Neale, K.W.; and Ebead, U.A. 2008. Flexural Strengthening of RC beams with externally Bonded CFRP systems: test results and 3D nonlinear FE Analysis. Journal of composites for construction, ASCE, V. 12, No. 2, pp. 190–201.

Arduini, M.; Nanni, A.; and Romagnolo, M. Mar–Apr 2004. Performance of One Way Reinforced concrete slabs with externally Bonded Fiber-Reinforced Polymers Strengthening. ACI Structural Journal, Vol. 101, No. 2.

Brena, S. F.; Bramblett, R. M.; Woood, S. L.; and Kreger, M. E. Feb. 2003. Increasing Flexural Capacity of Reinforced Concrete Beams Using Carbon Fiber Reinforced Polymer Composite. ACI Structural Journal, V. 100, No. 1, pp. 36–45.

Grace, N. F.; Abdel-Sayed, G.; and Ragheb, W.F. 2002. Strengthening of concrete beams Using Innovative Ductile Fiber Reinforced Polymer Fabric. ACI Structural Journal, V. 99, No. 5 Sep.–Oct., pp. 692–700.

Garden, H. N., and Hollaway, L.C. 1998. An Experimental Study of the Influnce of Plate End Anchorage of Carbon Fiber Composite Plate Used to Strengthen Reinforced Concrete Beams. Composite Structure, V. 42, pp. 175–188.

Hashemi, H., Maghsoudi, A.A. and Rahgozar, R. 2008. Flexural Ductility of Reinforced HSC Beams Strengthened with CFRP Sheets. Structural Engineering and Mechanic.

Lamanna, A. J.; Bank, L.C.; and Scott, D. W. 2004. Flexural Strengthening of RC beams by Mechanically Attaching FRP Strips. Journal of Composites for Construction, ASCE, V. 8, No. 3, pp. 203–210.

Maghsoudi, A.A. and Akbarzadeh, H. 2006. Flexural Ductility of HSC Members. Structural Engineering and Mechanics, 24 (2).

Morsy, A. and El Mahmoud, T. 2012. Bonding techniques for flexural strengthening of R.C. beams using CFRP laminates. Ain Shams Engineering Journal.

Saadatmanesh H., and. Ehasani. M.R Nov 1997. RC beams strengthened with FRP plates-experimental study. *ASCE J. Struct. Eng.*, vol. 117, no. 11, pp. 3417–3433.

Thomsen, H.H.; Spacone, E.; Limkatanyu, S. and Camata, G. 2004. Failure Mode Analysis of Reinforced Concrete Beams Strengthened in Flexure with Externally Bonded Fibre-Reinforced Polymers. Journal of Composites for Construction, 8, 123–131.

Concrete Solutions – Grantham et al. (Eds)
© 2014 Taylor & Francis Group, London, ISBN 978-1-138-02708-4

Nonlinear finite element modeling of reinforced concrete beams in shear – strengthened with near surface mounted laminates

Alaa M. Morsy, Nabil H. El-Ashkar & Ihab S. Mattar
Construction & Building Engineering Department, College of Engineering & Technology, Arab Academy for Science, Technology, and Maritime Transport, Egypt

ABSTRACT: This research aims towards modeling the behavior of RC beams shear-strengthened with FRP using the FE method. The modeling process is carried out using the FE software package ABAQUS CAE 6.11-3 after examining the available material models in the software package suited for preparing the analysis model. Experimental data for specimens failing in shear has been available where an analysis model for each specimen has been prepared based upon loading conditions, material properties and boundary conditions. For the purpose of model verification, the results obtained from the modeling procedure have been compared with the experimental results. The available data was mainly load-deflection curves at mid-span, failure load, strain as well as cracking pattern, where a slight variation of results has been noticed upon comparison. Finally a parametric study has been carried out so as to study the effect of various parameters included in the strengthening process on the beam behavior.

Keywords: FRP, NSM, strengthening, shear, verification, parametric study, ABAQUS

1 INTRODUCTION

Long term behavior of reinforced concrete structures has been one aspect of civil engineering continuously under study for various purposes: either repair or maintenance. Various factors such as creep, shrinkage as well as other factors which may be environment induced such as corrosion may cause cracking, reduce the structure's load carrying capacity resulting in failure of the structure system to function properly and may lead to system failure. Accordingly developing new techniques regarding repair and maintenance of reinforced concrete structures has become one necessity which cannot be ignored. From such prospect various techniques for strengthening reinforced concrete structures have been developed in order to prolong the service duration of existing structures as well as preventing their deterioration.

One of the most commonly used methods to strengthen existing reinforced concrete structures is the use of FRP through various methods including externally bonded sheets, near surface mounted rods or internally embedded reinforcement. Known for their high strength, lightweight as well as being corrosion resistant and highly versatile, FRP represents a highly reliable structural material despite being linear elastic with high initial material cost. Therefore, many experimental procedures have been carried out in order to study the behavior of FRP strengthened concrete structures so as to further understand their behavior in order to allow a wider field of application. However, the lack of accurate modeling procedures due to the large number of variables included in the model arising from the composite action caused by the interaction between FRP and concrete causes a drawback in predicting the behavior of such structures. Accordingly throughout this research, modeling of FRP strengthened beams using the finite element method shall be illustrated.

Throughout this research, modeling of FRP shear-strengthened reinforced concrete beams will be carried out for the purpose of predicting the future behavior of elements with similar performance. The process is to be carried out through the study of the behavior of a number of beams, modeling them using the finite element method. The modeling results are to be compared with the experimental data obtained from the modeled beams where such data includes load-deflection curves at mid-span, failure load, strain as well as cracking pattern for each specimen. The ABAQUS CAE 6.11-3 finite element package will be used for the modeling process.

2 RESEARCH SIGNIFICANCE

Since use of fibre composites for flexural and shear strengthening for R.C. beams is relatively new, theoretical work in this area is limited to models originally developed for R.C. beams. Applying such models to fibre-bonded concrete may result in strength

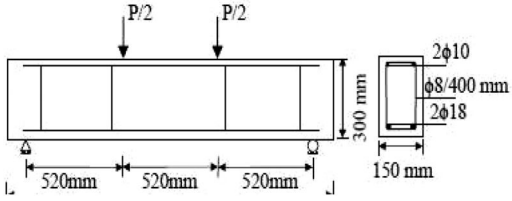

Figure 1. Geometry, arrangement of reinforcement and load for beam tested by [1].

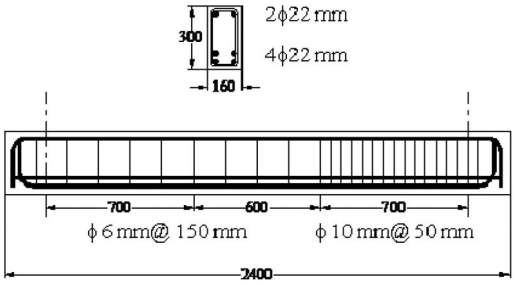

Figure 2a. Geometry, arrangement of reinforcement and load for control specimen (Morsy et al, 2011).

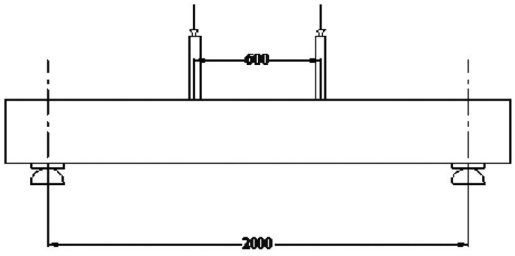

Figure 2b. Boundary conditions for control speciment (Morsy et al, 2011).

overestimation and unsafe design. The absence of reliable models may lead to either avoiding the use of advanced composites, or to incorporate high "factors of safety," making composite construction less economical. A need exists to apply the FE method in order to model R.C beams shear-strengthened with FRP for the purpose of predicting the behavior of similar elements.

3 EXPERIMENTAL DATA

The experimental data is obtained from (Obaidat, 2007) and (Morsy et al, 2011). Test setup and specimen details are shown in Fig. 1 and Fig. 2a, 2b.

Strengthening schemes are shown in Table 1 and material properties are given in Table 2 and Table 3.

Table 1. Strengthening schemes for specimens examined by (Morsy et al, 2011).

Specimen	Strengthening technique	Strengthening Material	Material Dimensions	Spacing
CB	None	–	–	–
NSM*	Near surface mounted strips	CFRP	1.2* 15 mm strips	75 mm

*Strengthening is only in the weak side along 700 mm span.

Table 2. Material properties for control specimen examined by (Obaidat, 2007).

Material	Property	Value
Steel	Yield Stress	507 MPa
	Modulus of elasticity	210000 MPa
	Poisson ratio*	0.3
	Density*	7.85 kg/m^3
Concrete	Characteristic Strength	30 MPa
	Density	2.5 kg/m^3
	Poisson ratio*	0.2
	Fracture Energy**	0.122 Nmm/mm^2
	Modulus of elasticity**	26365 MPa
	Tensile Strength**	2.445 MPa

*Assumed values as the values for density and Poisson ratio were not specified in the original procedure.
**Material Properties obtained from material models discussed throughout the analytical procedure.

4 MATERIAL MODELS

4.1 *Concrete*

The Stress-Strain curve for concrete under compression is obtained based upon an experimentally verified numerical model (Hsu and Hsu 1994). The model obtains the stress-strain curve under uni-axial compression up to 0.3 characteristic strength (f_{cu}) in the descending portion based upon the maximum compression strength f_{cu}. Such a model is also characterized as by having a linear Stress-Strain relationship in accordance with Hook's Law till $0.5f_{cu}$. The stress strain relation-ship based on the numerical model is shown in Fig. 3. Equations (1–4) emphasize the use of the model to obtain the stress-strain curve of concrete

$$\sigma_c = \left[\frac{(\eta*\beta)*(\varepsilon_c/\varepsilon_i)}{(\eta*\beta)-1+(\varepsilon_c/\varepsilon_i)^{(\eta*\beta)}}\right] * \sigma_{cu} \quad (1)$$

$$\beta = \frac{1}{1-[\sigma_{co}/(\varepsilon_o * E_o)]} \quad (2)$$

$$\varepsilon_o = (8.9 * 10^{-5} * \sigma_{cu}) + 2.114 * 10^{-3} \quad (3)$$

$$E_o = (1.2431 * 10^2 * \sigma_{cu}) + (3.28312 * 10^3) \quad (4)$$

where:

Table 3. Material properties for control specimen examined by (Morsy et al, 2011).

Material	Property	Value
General	Modulus of	210000 MPa
Reinforcement	Elasticity	0.3
Properties	Poisson ratio*	7850 kg/m^3
	Density*	
High Tensile Steel		
22 mm bars	Yield Stress	360 MPa
10 mm bars	Yield Stress	360 MPa
Ordinary Mild Steel		
6 mm bars	Yield Stress	240 MPa
	Characteristic	20 MPa
	Strength	2500 kg/m^3
	Density*	0.2
	Poisson ratio*	0.0898 mm/mm^2
Concrete	Fracture Energy**	25122 MPa
	Modulus of elasticity**	1.898 MPa
	Tensile Strength**	
FRP	Modulus of	165000 MPa
	Elasticity	1.6 kg/m^3
	Density, t/mm^3	0.3
	Poisson ratio	

*Assumed values as the values for density and Poisson ratio were not specified in the original procedure.
**Material Properties obtained from material models discussed throughout the analytical procedure.

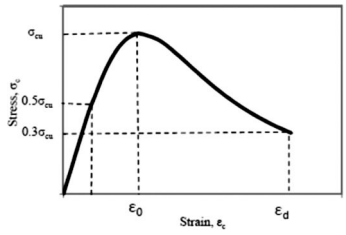

Figure 3. Compressive stress-strain relationship for concrete (Hsu and Hsu 1994).

β: A material parameter which depends on shape of stress-strain diagram
ε_o: Strain at peak stress
E_o: Initial tangential modulus (Kip/in^2)
ε_d: Strain at $0.3f_{cu}$ in the descending portion and is iteratively calculated using equation (1) at $s_c = 0.8^* s_{cu}$
s_c: Compressive strength (Kip/in^2)
s_{cu}: Ultimate compressive strength (Kip/in^2)

(1 MPa = 0.145037743 Kip/in^2)

n: Material parameter which depends on s_{cu}

$0 < s_{cu} < 62$ MPa → n = 1
62 MPa ≤ s_{cu} <76 MPa → n = 2
76 MPa≤ s_{cu} <90 MPa → n = 3
90 MPa≤ s_{cu} → n = 5

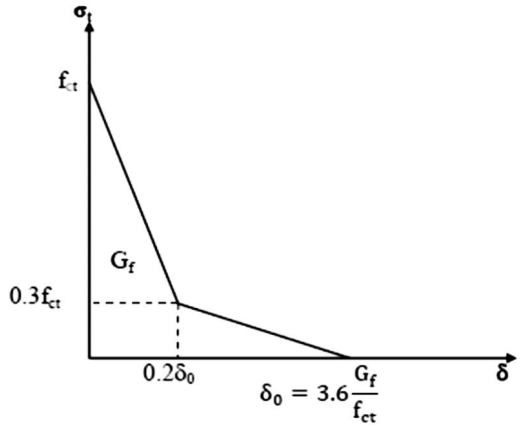

Figure 4. Softening curve for concrete under uni-axial tension (Hillerborg, 1985).

In order to represent the softening behavior of concrete under tension model (Hillerborg, 1985) is used as shown in Fig. 4. Concrete assume a linear elastic behavior till maximum tensile stress (f_{ct}) after which tensile softening follows the curve in Fig. 4.

Values for f_{ct} (in MPa) can be obtained by referring to (CEB-FIP, 1993) where upper, lower bounds as well as mean value are specified as by the equations (5–7)

$$f_{ctk,min} = 0.95 * (0.1 * f_{ck})^{2/3} \quad (5)$$

$$f_{ctk,m} = 1.4 * (0.1 * f_{ck})^{2/3} \quad (6)$$

$$f_{ctk,max} = 1.85 * (0.1 * f_{ck})^{2/3} \quad (7)$$

where:
f_{ck}: Concrete compressive strength (MPa)
$f_{ctk,min}$: Minimum value for tensile strength (MPa)
$f_{ctk,m}$: Mean value for tensile strength (MPa)
$f_{ctk,max}$: Maximum value for tensile strength (MPa)
$\delta°$: Crack opening displacement (mm)
G_f: Fracture energy (Nmm/mm^2), energy required to propagate a tensile crack of unit surface area projected in a plane parallel to the crack direction.

Values for G_f (Nmm/mm^2) can be obtained by referring to (CEB-FIP, 1993) by using equation 8, where the resulting deviations in value of G_f are up to ±30%

$$G_f = G_{fo} * (0.1 * f_{ck})^{0.7} \quad (8)$$

where:
f_{ck}: Concrete compressive strength (MPa)
G_{fo}: Base value for fracture energy (Nmm/mm^2) and depends on maximum aggregate size as shown in Table 4.

4.2 *Reinforcement*

Reinforcement is considered elastic-perfectly plastic behavior identical in tension and compression as shown in Fig. 5.

Table 4. Base values for fracture energy (CEB-FIP, 1993).

d_{max} (mm)	G_{fo} (Nmm/mm^2)
8	0.025
16	0.030
32	0.058

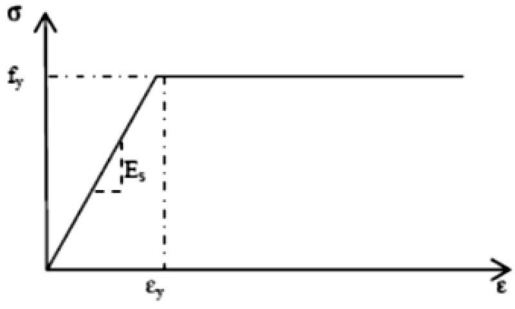

Figure 5. Stress–strain behavior for reinforcement.

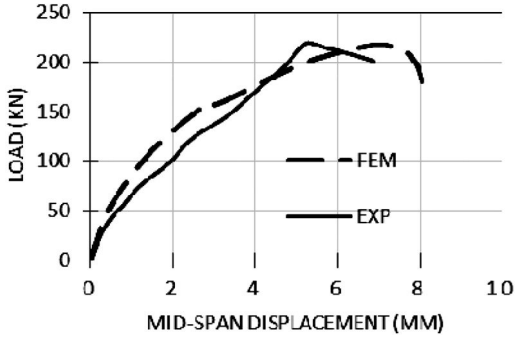

Figure 6. Load–displacement curve for control specimen examined by (Obaidat, 2007).

4.3 *FRP*

FRP is modelled as a linear elastic isotropic material till failure. Although FRP is an orthotropic material since the composite is mainly stressed in the fibre direction, the modulus in the fibre direction is more important.

5 FINITE ELEMENT MODEL

Simulation for R.C. is done with C3D4 mesh elements. Also it should be noticed that concrete is modeled using the concrete damaged plasticity model. Reinforcement steel is modeled as wire elements of mesh element type T3D2 where the interaction between R.C. and reinforcement is done using the embedded element constraint. FRP is modeled using same mesh element type as that used for R.C. Regarding numerical analysis, three-dimensional nonlinear analysis has been carried out using Newton's method.

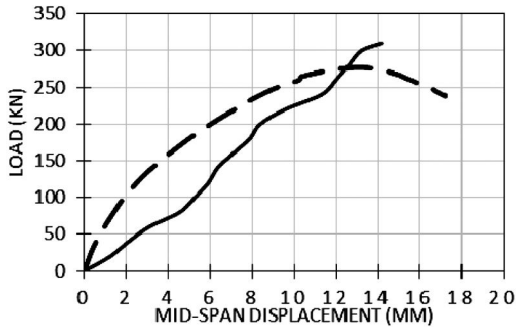

Figure 7. Load–displacement curve for control specimen CB.

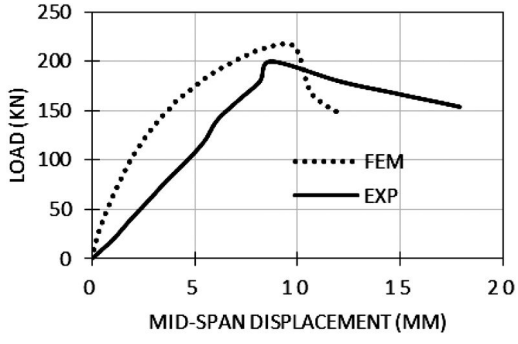

Figure 8. Load–displacement curve for specimen NSM.

6 COMPARISON OF PREDICTIONS AND EXPERIMENTAL RESULTS

6.1 *Load displacement curves*

Load–displacement curves for control specimen (Obaidat, 2007) obtained from experimental procedure as well as FEM are shown in Fig. 6. There is good agreement between FEM and experimental results. FEM results predict a stiffer behavior for the beam, however, variation of load carrying capacity is slight. Experiments indicate a load carrying capacity of 220 kN while FEM predicts a load carrying capacity of 218 kN making a 1% variation.

Regarding specimens CB and NSM (Morsy et al, 2011), it is noticed that all load-displacement curves obtained from FEM shown in Fig. 7, 8 predict a stiffer behavior for the beams which may be due to excessive free body motion during performance of the experimental procedure. Regarding the load carrying capacity it is noticed that the results are in agreement, where the variation in load carrying capacity is about ±6%.

6.2 *Load strain curves*

Load–strain curves for specimens CB and NSM (Morsy et al, 2011), are shown in fig. 9, 10 and 11. FEM predictions are in good agreement with experimental procedure which indicates that the model

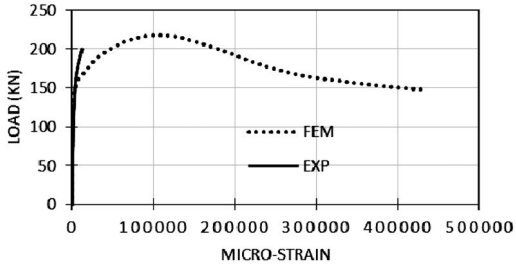

Figure 9. Load–strain curve for concrete for control specimen CB examined by (Morsy et al, 2011).

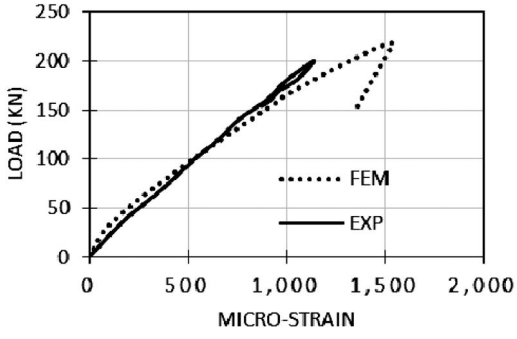

Figure 10. Load–strain curve for lower reinforcement mid-span control specimen CB.

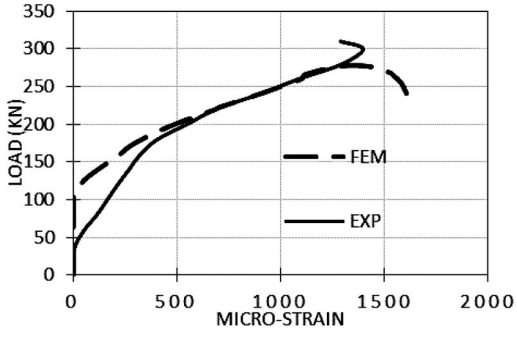

Figure 11. Load–strain curve for second stirrup after the support for specimen NSM.

can capture the behavior of the structural element accurately.

6.3 *Cracking pattern*

The concrete damaged plasticity model in ABAQUS does not have a notation for cracks, however, it is assumed that cracking initiates at the points where the maximum principal plastic strain is positive (Lubliner et al., 1989). The direction of the vector normal to the crack plane is assumed to be parallel to the direction of the maximum principal plastic strain [7]. Cracking patterns as well as direction of the vector normal to the cracking plane are in shown in Fig. 13, 15, 16, and 17. Upon Comparing FEM to cracking patterns obtained

Figure 12. Shear failure for control specimen examined by (Obaidat, 2007).

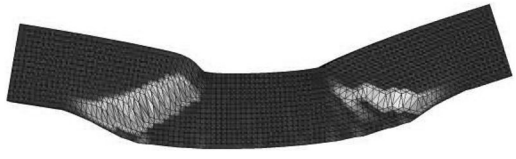

Figure 13. Cracking pattern obtained from FEM for control specimen examined by (Obaidat, 2007).

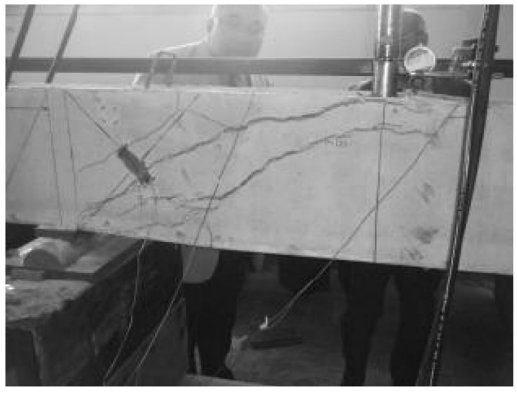

Figure 14. Shear failure for control specimen CB (Morsy et al, 2011).

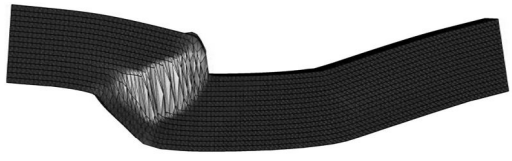

Figure 15. Cracking pattern obtained from FEM for control specimen (CB).

from experimental results shown in Fig. 12, 14. It is noted that the FEM cracking pattern is in good agreement with experimental results which indicates that the FEM can capture the fracture mechanism.

6.4 *Stress distribution*

Stress distribution for specimens (Morsy et al, 2011). is shown in Figs. 18 and 19. Upon comparing stress

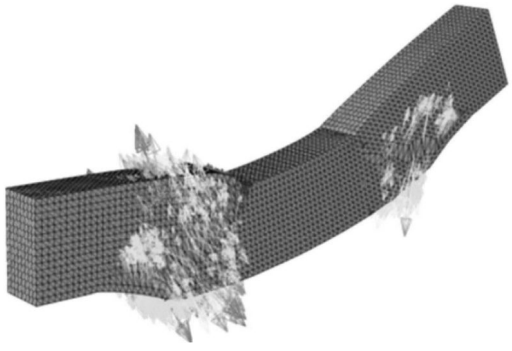

Figure 16. Direction of the vector normal to the cracking plane obtained from FEM for control specimen examined by (Obaidat, 2007).

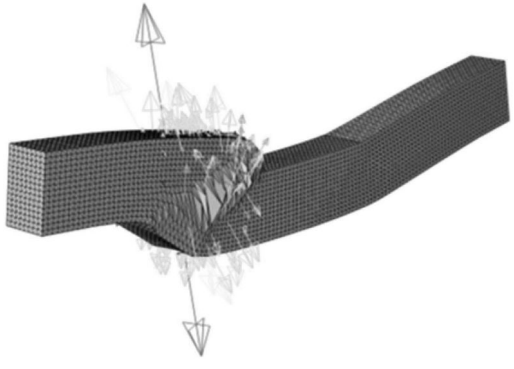

Figure 17. Direction of the vector normal to the cracking plane obtained from FEM for control specimen CB.

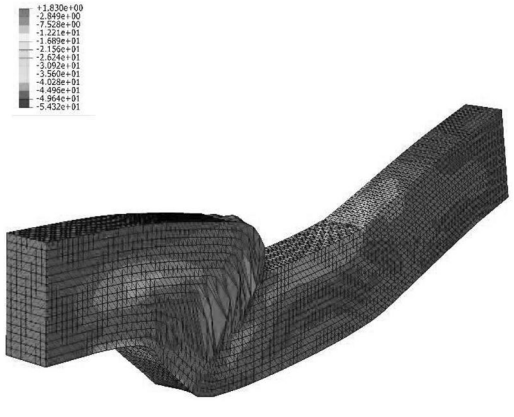

Figure 18. Stress distribution obtained from FEM for control specimen CB.

distribution diagram for Control beam CB (Morsy et al, 2011). and strengthened specimen NSM (Morsy et al, 2011). a variation in stress distribution in the non-strengthened region is noted which indicates that FRP strengthening has a global effect on the structural element and is not local to the strengthened region.

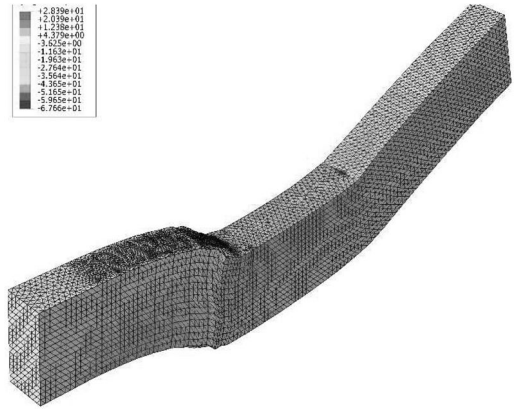

Figure 19. Stress distribution from FEM for specimen NSM.

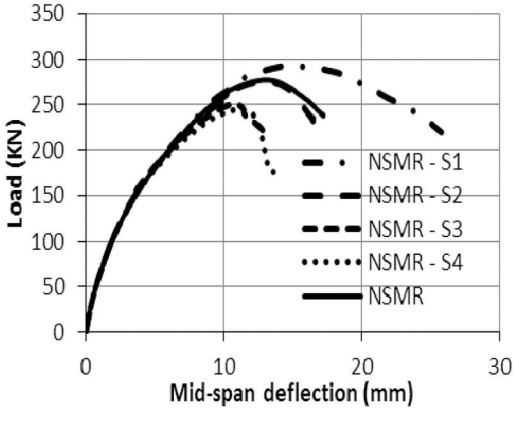

Figure 20. Load-displacement curve for specimen NSM upon varying laminae spacing.

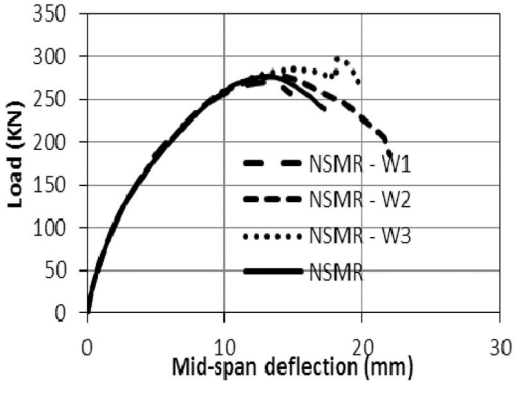

Figure 21. Load-displacement curve for specimen NSM upon varying laminate Width

7 PARAMETRIC STUDY

In order to study the effect of various strengthening parameters on the beam behavior, a parametric study is carried out on specimens studied by (Morsy

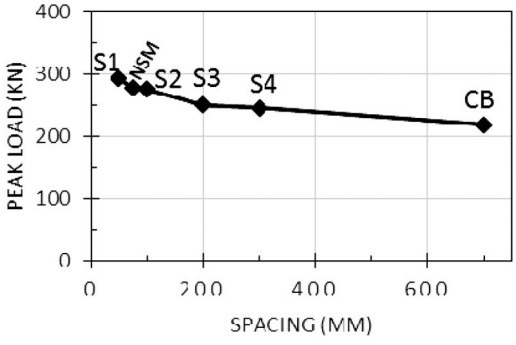

Figure 22. Relation between peak load and spacing for specimen NSM (Morsy et al. 2011).

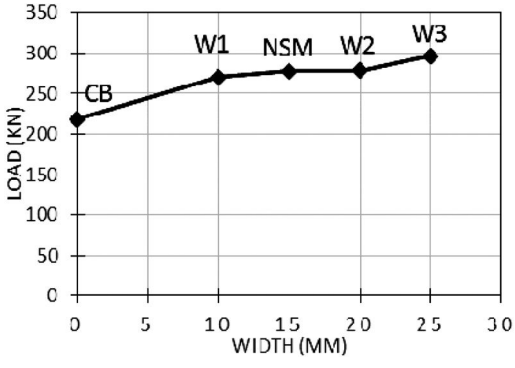

Figure 23. Relation between peak load and laminate width for specimen NSM (Morsy et al. 2011).

et al, 2011). Actual experimental results were not available for such specimens. Specimens NSM-S1, NSM-S2, NSM-S3 and NSM-S4 are modelled with spacing 50 mm, 100 mm, 200 mm and 300 mm respectively. Specimens NSM-W1, NSM-W2 and NSM-W3 are modelled with laminate width 10 mm, 20 mm and 25 mm respectively. Parameters under study were mainly dimensions and spacing of FRP strengthening elements. Results for the parametric study are shown in Fig. 20, 21, 22, 23. It is shown that dimensions and spacing of strengthening material had a noticeable effect. Increased load carrying capacity and increased ductility is noticed upon increasing FRP dimensions and also upon decreasing spacing and vice versa.

8 CONCLUSION

A Finite element modelling process is carried out on a number of specimens using the FE software package ABAQUS-CAE 6.11 where the behavior of such specimens has been experimentally examined. Finally a parametric study is carried out to study effect of various strengthening parameters on the element behavior. Upon examining the FEM results the following conclusions are drawn:

1. Upon comparing the load-displacement curve, load-strain curve as well as the cracking pattern obtained from FEM with those obtained from experimental procedure only a slight deviation is noticed which indicates that the FEM model can properly capture the fracture mechanism.
2. Upon comparing the stress distribution for strengthened specimen NSM (Morsy et al. 2011). and unstrengthened specimen CB (Morsy et al, 2011). a variation in the stress distribution in the unstrengthened region is noticed which indicates that the strengthening process has a global effect and is not local to the strengthened region.
3. The parametric study carried out to study the effect of laminate spacing as well as laminate width on beam behavior indicate an increase ductility and increased load carrying capacity upon decreasing laminate spacing and vice versa. Also increasing laminate width is accompanied by increased load carrying capacity and increased ductility and vice versa.

ACKNOWLEDGEMENTS

The authors would like to thank Eng. Matin Shayan-Mehr (MS Structural Engineering-Takestan), Eng. Mohammad Naisipour (MS Structural Engineering – Iran University of Science and Technology) and Eng. Markus Lengauer for providing assistance in data analysis. The authors would also like to acknowledge the assistance of Prof.Nabil Ibrahim Fawzy Mohareb (M.Phil./PhD – University of Liver pool – School Of Architecture,UK) for providing valuable material throughout the research process.

REFERENCES

Dassault Systèmes Simulia Corp. ABAQUS Theory manual, User manual, Analysis manual and Example Manual, Version 6.11. Providence, RI; 02909–2499.numerical simulation of various engineering applications.

Gorinevsky, D., Boyd, S., Stein, G. Optimization-based tuning of Beton, C. E.-I. (1993), CEB-FIP Model Code 1990 (CEB-FIP MC90), Bulletin D'Information, No. 215, Lausanne.

Hillerborg, A.1985. The theoretical basis of a method to determine the fracture energy G_f of concrete. Materials and Structures, RILEM 50-FMC, 108, pp. 291–296.

Hsu, L.S., & Hsu, C.-T.T. (1994). Complete stress-strain behavior of high-strength concrete under compression. Magazine of Concrete Research, 46(169), 301–312.

Lubliner J, Oliver J, Oller S, Onate E. 1989.A plastic-damage model for concrete. Int J Solids Struct, 15:299–329.

Morsy, A., et al. 2011. "A Comparative Study for Shear Strengthening Techniques of Reinforced Concrete Beams Using FRP". Fourth international conference on concrete repair with cooperation by technical university Dresden. Germany.

Obaidat, Y. 2007. "Retrofitting of reinforced concrete beams using composite laminates," Master Thesis, Jordan University of Science and Technology.

This page intentionally left blank

Concrete Solutions – Grantham et al. (Eds)
© 2014 Taylor & Francis Group, London, ISBN 978-1-138-02708-4

Ductility of FRP reinforced RC structures: A critical review of definition and expressions

F. Oudah & R. El-Hacha
University of Calgary, Calgary, Alberta, Canada

ABSTRACT: The use of Fibre Reinforced Polymer (FRP) reinforcement has been increasing world-wide due to its superior behavior in terms of its light weight and its corrosion resistant nature. The FRP materials are used widely in strengthening applications of bridges using either Externally Bonded (EB) sheets/plates or using the Near Surface Mounted (NSM) technique. The ductility performance of the RC structures reinforced using FRP reinforcement is very important in evaluating the suitability of using FRP as an internal or strengthening material. In this research, a critical review about the definition of the ductility in the context of FRP reinforced structures is conducted. The different ductility models that are available in the literature are also examined with emphasis on their applicability in determining the ductility of fatigued beams. Finally, the ductility performance of RC beams strengthened using NSM Carbon FRP reinforcement prestressed to several prestressing levels is evaluated. Eight beams were fatigued before testing them monotonically to failure and eight beams were tested without being subjected to fatigue loading. It was found that the ductility was enhanced by the application of the fatigue loading and a No Fatigue Effect on Ductility (NFED) prestress strain was defined as the prestress strain at which there is no difference in the ductility between the fatigued and the un-fatigued beams. The NFED prestress strain ranges between 1.05% to 1.41% which means that the ductility of the fatigued beams is enhanced for most of the practical prestress strains.

1 INTRODUCTION

The ductility of Reinforced Concrete (RC) structures is considered to be one of the most important aspects in the ultimate state design and in the capacity seismic design philosophies. It is defined as the ability of the structure to sustain the load for adequate amount of deformation without collapse (ISIS Canada Design Manual, 2008). The basic definitions of ductility in terms of curvature ductility and displacement ductility indices was adopted and used to quantify the deformation capacity of RC structures. However, with the increasing use of Fiber Reinforced Polymer (FRP) reinforcement as an internal reinforcement or as an external strengthening reinforcement, a re-visit is required to evaluate the adequacy of using the conventional ductility expressions in determining the ductility capacity of FRP reinforced and strengthened concrete structures.

The FRP material is increasing used as a strengthening material in bridge applications and, therefore, the effect of fatigue loading on the ductility capacity of the concrete girders needs to be studied. The movement of the vehicles on RC bridges induces fluctuating stresses in the RC girders strengthened using FRP reinforcement. The repeated nature of these stresses leads to deterioration of the structure in terms of increased cracking associated with altering the behavior of the structure in the long run. One of the important issues to be considered when analyzing the effect of fatigue loading on the girders is the effect of fatigue loading on the ductility capacity of the structure.

In this research, a critical review is conducted on the available ductility indices in order to determine their adequacy in quantifying the ductility behavior of RC structures reinforced or strengthened using the FRP material. The effect of the loading history (fatigued or un-fatigued) is also taken into account in this study. Finally, a ductility evaluation is conducted on RC beams strengthened using prestressed and non-prestressed NSM CFRP reinforcement.

2 DUCTILITY: CRITICAL REVIEW

What is ductility? For the first glance this question seems to be easy to answer. However, lots of misconception is found in the literature with regard to the definition of ductility. The term ductility was first introduced in the design of steel structures. It was defined as the ability of the structure to sustain the load without collapse for a certain amount of deformation. Here, the word deformation may refer to curvature, rotation, or displacement. Steel experiences plastic deformation when the load and the deformation exceed the yielding point. The increase in the deformation beyond the yielding point directly implies that the energy dissipation is increased due to the plastic

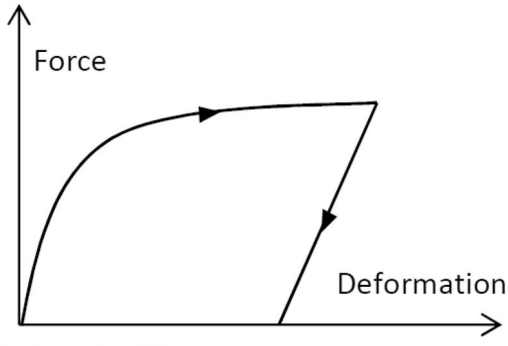

(a) Conventional RC structure

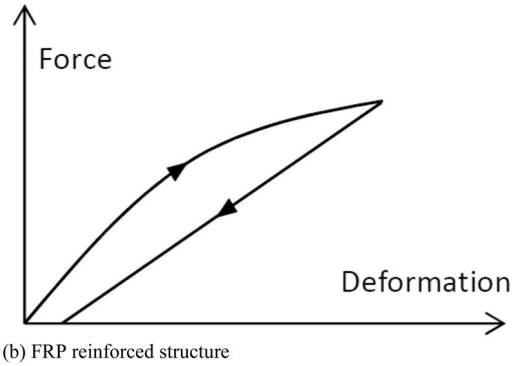

(b) FRP reinforced structure

Figure 1. Force-deformation relationships.

phenomenon observed in steel. Therefore, the energy dissipation ability is implicitly included in the ductility definition stated earlier. This fact is crucial in understanding the ductility and how to implement it in the design of RC structures. The force-deformation behavior of conventional RC structure and a concrete structure reinforced using FRP is illustrated in Figure 1. Observing the unloading branch indicates that for the same deformation, the energy dissipated (area under the force-deformation curve) in the RC structure is higher than that in the FRP reinforced structure. Therefore, large deformations do not imply high energy dissipation for the FRP reinforced RC structures. Thus, the conventional definition of ductility is no longer valid for the design of FRP reinforced structures and that ductility expressions should take into account the energy dissipation capacity in order to better represent ductility.

There are three cardinal points observed in the force-deflection relationship in concrete structures reinforced using the conventional steel; cracking, yielding, and ultimate. The two critical ones are the yielding and the ultimate points due to the fact that the difference in the deformation between those two points is the largest compared to the difference between the cracking and the yielding points. Therefore, the conventional ductility models that are used to define the ductility of concrete structures reinforced using the conventional steel are based on the yielding and the ultimate points and can be expressed in terms of the curvature ductility index, μ_c:

$$\mu_c = \frac{\psi_u}{\psi_y} \tag{1}$$

where $\psi_u =$ curvature at the ultimate moment and $\psi_y =$ curvature at the yielding moment.

Also, it can be expressed in terms of the displacement ductility index, μ_d:

$$\mu_d = \frac{\Delta_u}{\Delta_y} \tag{2}$$

where $\Delta_u =$ displacement at the ultimate moment and $\Delta_y =$ displacement at the yielding moment.

Also, it can be expressed in terms of the rotation ductility index, μ_r:

$$\mu_r = \frac{\theta_u}{\theta_y} \tag{3}$$

where $\theta_u =$ rotation at the ultimate moment and $\theta_y =$ rotation at the yielding moment.

Knowing that FRP RC structures do not exhibit yielding due to the elastic nature of the FRP material, another method of characterizing the deformation capacity is needed. In an attempt to overcome the difference in the behavior between steel reinforced and FRP reinforced structures in terms of force-deformation behavior, Abdelrahman et al. (1995) proposed a new concept called the deformability index. This new concept relies on the two cardinal points experienced by the FRP RC structures which are; the cracking point and the ultimate point. However, it does not rely directly on the load and deformation at the cracking point. Instead, it extrapolates the behavior at the un-cracked stage to calculate the displacement at the ultimate stage. Thus, it relies on the difference in the behavior between the cracked and the un-cracked states of the structures. The index is expressed as follows:

$$\mu_a = \frac{\Delta_u}{\Delta_I} \tag{4}$$

where $\Delta_I =$ equivalent deflection at the ultimate load based on the un-cracked section properties.

It is should be noted that the name of this concept '*deformability*' is used in order to avoid the confusion with the concept of 'ductility' since the former one does not take into account the energy dissipation capacity of the structure unlike the latter one which takes it into account implicitly.

Several other researchers used the deformability concept to develop new expressions that quantify the deformation ability of FRP RC structures. The deformability index by Mufti et al. (1996), μ_M,

adopted by the CSA (2004), takes into account the curvature and the moment values at the service limit (at concrete top fiber strain of 0.001) and at the ultimate condition. The deformability index is expressed as follows:

$$\mu_m = \left(\frac{\psi_u}{\psi_{0.001}}\right) \times \left(\frac{M_u}{M_{0.001}}\right) \quad (5)$$

where $\psi_{0.001}$ = curvature at the service limit state, M_u = moment at ultimate, and $M_{0.001}$ = moment at the service limit state.

Zou (2003) proposed a modified version of the Mufti et al. (1996) expression in order to make it easier and more practical to determine. The deformability index, μ_z, is expressed as follows:

$$\mu_z = \left(\frac{\Delta_u}{\Delta_c}\right) \times \left(\frac{M_u}{M_c}\right) \quad (6)$$

where Δ_c = displacement at the cracking moment.

Another trend of characterizing the deformation capacity of FRP RC structures is based on relating the energy dissipation to the deformability of the structure. Naaman & Jeong (1995) proposed a ductility index that is based on the relation between deformability and energy dissipation in order to define the ductility of the structure. It is also noted that this expression has been used extensively in characterizing the ductility ability of FRP RC structures and it was also recommended by design guidelines (ISIS Canada Design Manual, 2008). However, a critical review reveals that the basic assumptions used in the development of this index are not suitable for the behavior of FRP RC structures. It assumes that the structure behaves in an elastic-perfectly plastic manner and that the elastic energy stored in the system is equivalent to that stored in steel RC structures. Therefore, the authors of this paper highly question the validity of using this expression, μ_N, in quantifying the ductility capacity of FRP RC structures.

$$\mu_N = \left(\frac{E_{tot}}{2\,E_{els}}\right) + 0.5 \quad (7)$$

The slope of the unloading branch, S, is calculated as follows:

$$S = \frac{P_c S_1 + (P_y - P_c) S_2}{P_y} \quad (8)$$

where E_{tot} = total energy stored in the system, E_{els} = elastic energy stored in the system, P_c = cracking load, P_y = yielding load, S_1 = slope of the un-cracked load-deflection curve, and S_2 = slope of the load-deflection curve between P_c and P_y.

Knowing that prestressing the FRP reinforcement in FRP strengthened RC beams increases the post-yielding stiffness, the inaccuracy in the calculating the ductility using the expression by Naaman & Jeong (1995) increases since it assumes an elastic-perfectly plastic behavior. Therefore, it is important to include the cracking point and the post-yielding stiffness in defining the ductility of prestressed structures since they are enhanced.

The need to have a ductility expression that relates between the deformability and the energy dissipation capacities accurately, accounts for the history of the applied load, and accounts for the application of prestressing had driven the motivation for Oudah & El-Hacha (2012a) to develop a general ductility expression, $\mu_{o,}$. The ductility expression can be used for steel RC structure, FRP RC structure, or FRP strengthened RC structure. It can also be used for prestressed or non-prestressed structures. Moreover, it can be used for fatigued or un-fatigued structures.

$$\mu_o = \mu_d \times \beta \quad (9)$$

in which, the compatibility factor, β, for the un-fatigued beams and the slope of the unloading branch, S, are calculated as follows:

$$\beta = \frac{S\,\Delta_y (P_y(\Delta_u - \Delta_c) + P_u(\Delta_u - \Delta_y) + P_c \Delta_y)}{P_u^2 \Delta_u} \quad (10)$$

$$S = \frac{P_y - P_c}{\Delta_y - \Delta_c} \quad (11)$$

The compatibility factor, β, for the fatigued beams and the slope of the unloading branch, S, are calculated as follows:

$$\beta = \frac{S\,\Delta_y (P_y \Delta_u + P_u(\Delta_u - \Delta_y))}{P_u^2 \Delta_u} \quad (12)$$

$$S = \frac{P_y}{\Delta_y} \quad (13)$$

where P_u = ultimate load and Δ_c = displacement at cracking.

The ductility index, μ_o, was developed originally for RC structures strengthened using FRP reinforcement and for steel RC structures. However, it can be used for the case of concrete structures reinforced internally using FRP material with slight modifications. In this case, Equation 12 can be used for both fatigued and un-fatigued beams and P_y would refer to the global yielding (since there is no steel reinforcement in this case). The global yielding can be defined as the point at which the curve changes stiffness due to the nonlinearity experienced by the extreme concrete fiber subjected to compression forces.

3 DUCTILITY EVALUATION

The ductility of FRP strengthened RC beams is evaluated in this section. As stated earlier, fatigue loading

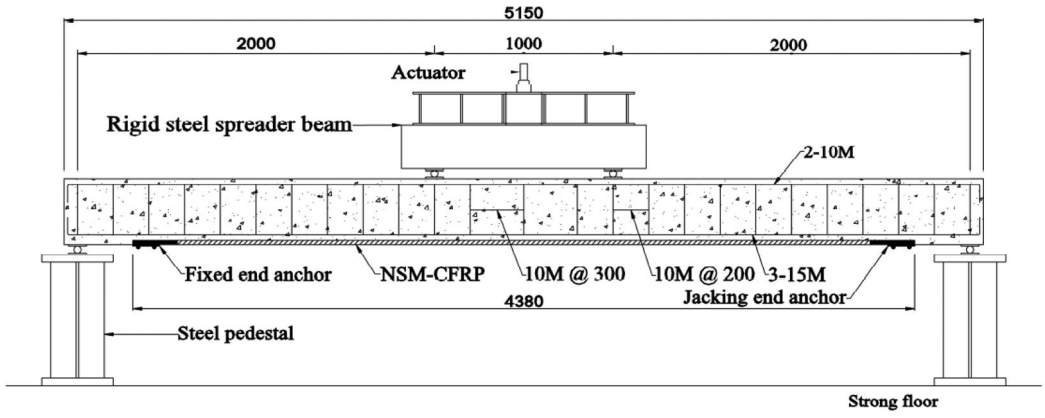

(a) Beam dimensions

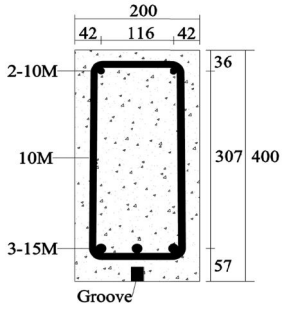

(b) Cross-section

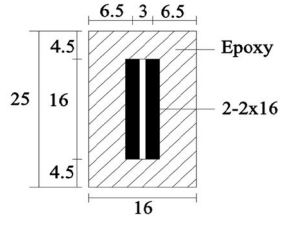

(c) Groove-strips

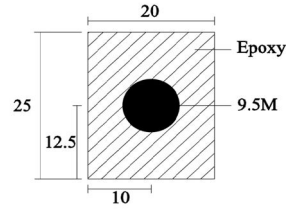

(d) Groove -rod

Figure 2. Beam details (dimensions are in mm).

may alter the properties of the RC section depending on several factors such as; the stress range in the reinforcement, the number of cycles, the frequency of the applied loading, etc. The damage in the RC beam is manifest in the increased deflection and the increased cracking. In this study, the ductility performance of RC beams strengthened with prestressed and non-prestressed CFRP reinforcement is evaluated. A total of 16 beams grouped into two groups are considered in this research. Nine beams were fatigued and nine beams were not fatigued.

In each group there are four beams strengthened using CFRP rods and four beams strengthened using CFRP strips. Three of the strengthened beams in each group were prestressed to 20%, 40%, and 60%.

3.1 *Fatigue regime*

The fatigued beams were subjected to 3 million cycles at a 2 Hz testing frequency. The maximum and the minimum loads were chosen such that to induce a stress range of 125 MPa in the tension steel reinforcement (CSA, 2004) with a maximum stress of 70% of the yield stress in the first cycle.

3.2 *Beam details*

The beams details are shown in Figure 2. The 168 beams had the same specified material strength. The specified 28 days concrete compressive strength is 40 MPa. The specified yield stress of the 10M and the 15M steel reinforcements is 440 MPa.

The mechanical properties of the CFRP strips as specified by the manufacturer are 2108 MPa tensile strength, 124 GPa modulus of elasticity, and 1.7% ultimate strain (Hughes Brothers, 2010a). The mechanical properties of the CFRP rods as specified by the manufacturer are 2068 MPa tensile strength, 124 GPa modulus of elasticity, and 1.6% ultimate strain (Hughes Brothers, 2010b). It is noted that the mechanical properties specified by the manufacturer represent the guaranteed properties (mean minus two standard deviations). The prestressed beams were prestressed using an innovative prestressing system developed by Gaafar (2007). The system is composed of permanent and temporary parts that are used to prestress the beam against itself.

Two types of epoxies were used; Sikadure® 30 that was used to fill the concrete groove and to bond the CFRP reinforcement to the concrete (Sika, 2010a) and

Sikadure® 330 that was used to bond the CFRP reinforcement to the steel anchors at both ends of the CFRP reinforcement (Sika, 2010b). The detailed description of the prestressing system, prestressing materials, testing procedures, and testing results are included in the following references: (El-Hacha & Gaafar, 2011; Oudah & El-Hacha, 2012b,c).

3.3 *Ductility analysis*

It is noted that not all of the available ductility and deformability models can be used to calculate the ductility of the fatigued beams. Fatigue loading causes the beams to be cracked, therefore, ductility and deformability indices that depend on the cracking load such as the μ_a index (Eq. 4) and the μ_z index (Eq. 6) cannot be used. Furthermore, it was determined not to include the μ_r index (Eq. 3) since it depends on determining the plastic hinge length which depends on empirical expressions. It was also found that the μ_M index (Eq. 5) provide low correlation coefficients for the best fit lines (0.14 and 0.23 for the un-fatigued and the fatigued beams, respectively). Therefore, the scatter nature of the data makes it difficult to deduct firm conclusions about the ductility performance, and hence, it was excluded from this study. Only the following expressions were used to examine the ductility performance of the un-fatigued and the fatigued beams; μ_c (Eq. 1), μ_d (Eq. 2), μ_N (Eq. 7), and μ_o (Eq. 8)

The results of the ductility analysis are included in Figure 3 and Figure 4 for the un-fatigued and the fatigued beams, respectively. The ductility indices are plotted against the prestress strains of the beams. It is noted that no distinction is made with regard to the type of the CFRP reinforcement (strips versus rod) due to the fact that the ductility performance was found not to depend on the geometry of the CFRP reinforcement. As can be seen in Figures 3 and 4, the ductility indices of the fatigued beams are higher than those of the un-fatigued beams for all the indices. All the indices are based on the relative deformation and/or the energy released/dissipated between the ultimate state and the yielding state. Knowing that the concrete is fully cracked under the neutral axis (i.e. there is no tension stiffening) for the case of the fatigued beams leads to the bilinear load-deformation relationship of the fatigued beams. This simply means that for identical beams, the yielding point in the fatigued beams is reached earlier than that in the un-fatigued beams which in turn means that the ductility indices increase in the case of the fatigued beams.

The best fit lines of all the trends of the four indices are linear and expressed as follows:

$$\mu = a \times \varepsilon + b \tag{14}$$

where a = slope of the best fit line, ε = strain, and b = constant.

The values of the a and b values along with the correlation coefficients (R^2) of the un-fatigued and

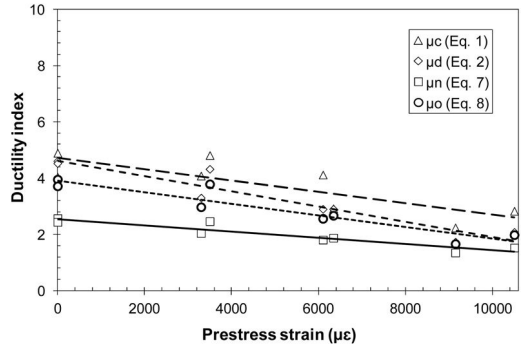

Figure 3. Ductility trends for the un-fatigue beams.

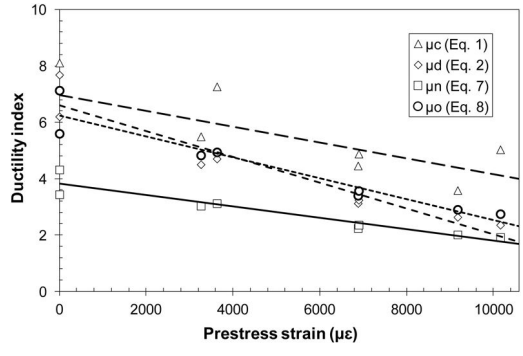

Figure 4. Ductility trends for the fatigue beams.

the fatigued beams are included in Table 1. The lowest correlation coefficient is for the μ_c index while the other indices experience considerably high correlation coefficient. The μ_c index depends on the curvature behavior that is calculated using the strain values obtained from the strain gauges mounted on the longitudinal steel reinforcement while the other indices are based on the displacement values of the beams. The strain in the longitudinal steel is not uniform when the concrete is cracked, and hence, the value of the strain in the steel reinforcement depends on the location of the strain gauge (mounted on the steel at the crack location or between the cracks). This explains the low correlation coefficients of the trends obtained using the μ_c index. The slope of all the trends increased with the application of the fatigue loading. The slopes of ductility indices of the μ_c, μ_d, μ_n, and μ_o indices increased by 38%, 70%, 84%, and 81%, respectively, due to the application of the fatigue loading. The μ_d, μ_n, and μ_o indices experience high percentage increase as compared with the μ_c index. The percentage increase by the μ_c index can be explained in light of the scatter nature of the strains in the steel reinforcement explained earlier. It is also noted that the slopes of the ductility indices of the fatigued beams are limited by the nature of the fatigue loading and can be only viewed in the context of testing regime adopted in this study which is mainly concerned with the steady-state

Table 1. Constants obtained from the ductility analysis.

	Un-fatigued			Fatigued		
Index	a	b	R^2	a	b	R^2
μ_c	-2.03×10^{-4}	4.72	0.66	-2.80×10^{-4}	6.96	0.55
μ_d	-2.69×10^{-4}	4.60	0.90	4.58×10^{-4}	6.59	0.91
μ_n	-1.09×10^{-4}	2.54	0.87	-2.01×10^{-4}	3.81	0.90
μ_o	-2.05×10^{-4}	3.91	0.87	-3.71×10^{-4}	6.25	0.91

fatigue behavior of the strengthened beams (stabilized state).

The increase in the slope of the ductility trends with the application of the fatigue loading points out to an important observation which is the point at which the ductility trends of the fatigued and the un-fatigued beams intersect. This point represent the prestress strain at which the application of the fatigue loading does not have an effect on the ductility performance of the fatigued beams. Thus, it is called the No Fatigue Effect on Ductility (NFED) prestress strain. The NFED prestress strain can be used in design codes and guidelines as a measure of the ductility performance of the fatigued beams. In this study, the NFED was found to be 1.05%, 1.38%, and 1.41% using the μ_d, μ_n, and μ_o indices, respectively, while the μ_c index failed to predict the NFED prestress strain. It is observed that the NFED prestress strains obtained using the ductility indices are significantly high and do not represent practical values for prestress applications. This means that the ductility is enhanced for most of the prestress applications. It is, therefore, recommended to achieve a flat ductility trend for the fatigued beams in order to ensure the enhancement of the ductility performance of the fatigued beams. Further research is needed to identify all the factors that contribute to the ductility performance of the fatigued beams in order to ensure the achievement of flat ductility trends. The effect of the strengthening technique on the NFED prestress strain values also needs to be examined.

4 CONCLUSIONS

The ductility definition and the applicability of the different ductility and deformability indices in quantifying the deformation capacity of FRP strengthened beams were evaluated in this paper. The ductility of RC beams strengthened using prestressed and non-prestressed NSM CFRP reinforcement and subjected to fatigue and static loading was evaluated. It was found that the application of fatigue loading enhances the ductility of the strengthened beams calculated using the curvature, displacement, Naaman and Jeong, and Oudah and El-Hacha ductility indices. Also, a prestress strain called the No Fatigued Effect on Ductility (NFED) was defined as the prestress strain at which the application of fatigue loading does not alter the ductility performance of the fatigued beam. The NFED prestress strain was found to range between 1.05% to 1.41% depending on the ductility index that is used to calculate it. Therefore, it is concluded that the ductility is enhanced with the application of the fatigue loading for most of the practical prestress strains.

ACKNOWLEDGMENT

The authors would like to express their gratitude to Lafarge Canada for providing the concrete, Hughes Brothers for donating the CFRP rods and strips, Sika Canada for providing the epoxy, and the technical staff at University of Calgary for their assistance in the laboratory. The authors are also grateful for the financial support towards this research provided by the Canadian Networks of Centers of Excellence on Intelligent Sensing for Innovative Structures (ISIS Canada), the Natural Sciences and Engineering Research Council of Canada (NSERC), and the University of Calgary.

REFERENCES

Abdelrahman, A.A. 1995. Serviceability of concrete beams prestressed by fibre reinforced plastic tendons. *Ph.D. thesis, University of Manitoba*, Winnipeg, MB, Canada, 331.

Canadian Standards Association (CSA). 2006. *Canadian highway bridge design code (CHBDC). CSA S6-06*, Toronto.

El-Hacha, R. & Gaafar, M. 2011. Flexural strengthening of reinforced concrete beams using prestressed near-surface mounted CFRP bars. *PCIJournal* 54(4), 134–151.

Gaafar, M.A. 2007. Strengthening reinforced concrete beams with prestressed near surface mounted fibre reinforced polymers. *M.Sc. thesis, University of Calgary*, Calgary, AB, Canada, 205.

Hughes Brothers. 2010a. Aslan 500 CFRP tape, product data sheet, Aslan 500 CFRP tape for near surface mount (NSM) structural strengthening (flexure & shear) of existing concrete, masonry or wood members. http://aslanfrp.com/Aslan500/aslan500-pg1.html

Hughes Brothers. 2010b. Aslan 200 CFRP rebar, product data sheet, Aslan 200 CFRP rebar for near surface mount (NSM) structural strengthening (flexure & shear) of existing concrete, masonry or wood members. http://aslanfrp.com/Aslan200/aslan200cfrpbar.html

ISIS Canada Design Manual No.3. 2008. Prestressing concrete structures with fibre-reinforced polymers. *The Canadian Networks of Centers of Excellence on Intelligent Sensing for Innovative Structures*, University of Manitoba, Winnipeg, Manitoba, Canada.

Mufti, A.A., Newhook, J.P. & Tadros, G. 1996. Deformability versus ductility in concrete beams with FRP reinforcement. *Proceeding, 2nd Advanced Composite Materials in Bridges and Structures (ACMBS-II)*, Montreal, QC, 189–199.

Naaman, A.E. & Jeong, S.M. 1995. Structural ductility of concrete beams prestressed with FRP tendons. *Proceeding, 2nd International Symposium on Fiber Reinforced Polymer Reinforcement for Reinforced Concrete Structures (FRPRCS-2)*, Ghent, Belgium, 379–386.

Oudah, F. & El-Hacha, R. 2012. A new ductility model of reinforced concrete beams strengthened using fiber reinforced polymer reinforcement. *Composites Part: B* 43(8), 3338–3347.

Oudah, F. & El-Hacha, R. 2012. Fatigue behavior of RC beams strengthened with prestressed NSM CFRP rods. *Composite Structures* 94(4), 1333–1342.

Oudah, F. & El-Hacha, R. 2012. Performance of RC beams strengthened using prestressed NSM-CFRP strips subjected to fatigue loading. *Journal of Composites for Construction* 16(3), 300–307.

Sika. 2010a. "Sikadure® 30", product data sheet, high modulus, high strength, structural epoxy paste adhesive for use with sika CarboDur reinforcement [Internet]. 06.2010/v1. <http://can.sika.com/content/canada/main/en/solutions_products/document_download/Structural_Strengthening.html>.

Sika. 2010b. "Sikadure® 330", product data sheet, impregnation resin for fabric reinforcement [Internet]. 06.2010/v1. <http://can.sika.com/content/canada/main/en/

Zou, P.X.W. 2003. Flexural behavior and deformability of fiber reinforced polymer prestressed concrete beams. *Journal of Composites for Construction* 7(4), 275–284.

This page intentionally left blank

Concrete Solutions – Grantham et al. (Eds)
© 2014 Taylor & Francis Group, London, ISBN 978-1-138-02708-4

Cracking in polymer concrete pipes-comparison of exact events in a pipe jacking project and numerical 3D modeling analyses

K. Pakiman
Tehran Micro Tunneling Project, Kayson Inc., Iran

A. Jenabi & Payam Soltan Sanjari
Water & Wastewater Division, Kayson Inc., Iran

Babak Mohammadi
Tehran Micro Tunneling Project, Kayson Inc., Iran

ABSTRACT: In this paper, the performance of a slurry micro-tunneling machine used for the Tehran Sewage network plan which is under construction, is presented. The total project route is 3855 meters. Total numbers of manholes are 30 which are constructed after which the pipe jacking is completed. Polymer concrete pipes with 1400 mm, 1600 mm and 1800 mm diameters are used at this project which 56% completed until the paper is being prepared. A Brief description of the project including the Herrenknecht micro-tunneling machine and shaft and pipes are presented. Geology condition and water table are briefly described.

In addition, some obstacles encountered during execution of the Tehran pipe jacking project are described. One of the biggest obstacles was the location of the site (at the center of capital) that put this project in the category of urban projects. The second obstacle consisted of the pipe jacking operation through an unstable river bed and loose soil and some other problems with the special geology of the site. Three operation methods during project were considered:

1. Using FRP
2. Using bolts around the crack
3. Using one designed structure to connect to pipes in rear and front of cracked pipe known as the Steel Jacket method

For each method an exact model in ANSYS software was built and analyzed to compare and choose the best way for controlling the cracking. We used exact jacking forces during performance of the pipe line and put these forces into each model to study variations of crack during pipe jacking. This paper includes useful information about cracking in concrete polymer pipes and comparison of exact result with numerical 3D modeling is included.

1 INTRODUCTION

Nowadays with the aid of progressive science and technology, some new technologically developing methods are utilized in order to construct infrastructures for new megacities all around the world. With these advanced methods, machine technologies take the place of manpower so it allows an efficient construction of megacities. The Pipe jacking method as one of the increasingly using methods provides the following advantages:

- Least disturbance and obstacle in cities so less traffic jam.
- Avoids infrastructure damage due to least soil disturbance.
- Crossing under highly important roads, highways, rivers and canals.
- Less total cost
- Higher construction rate and safety increase.
- Environmental advantages

In this study some problems and obstacles during pipe jacking operation in Tehran will be reviewed and the solution strategies will be explained in the following.

2 PROJECT SPECIFICATION REVIEW

2.1 *Project overview*

Tehran's comprehensive sewage network plan is being operated in recent years in almost all areas of the city. Two operating projects by Kayson Inc. are located in the northeast and west parts of the city.

The project includes operation of main transmission swage lines by the pipe jacking method. Diameters of pipes in the northeast part of project are 1400, 1600 and 1800 mm with the length of 551, 2170 and 1175 meters respectively. The pipe diameters in the western project are 1600 and 1800 mm and length of 4200 and 600 respectively. In the followings some problems during pipe jacking operation in the northeast project is reviewed.

3 PIPE JACKING METHOD INTRODUCTION

Pipe jacking is a technique for implementation of underground pipelines, ducts and culverts. Powerful hydraulic jacks are used to push specially designed pipes through the ground behind a shield when machine excavation takes the place of the hand shield.

Pipe jacking is started after installation of jack in the driving shaft, setting direction and leveling them before construction of trust wall. Also directional guidance systems are set in the shaft with survey team continuous inspections and after connecting all slurry, water, hydraulic and electronic connections, machine is ready to use. Operator can control excavation and machine-soil pressure from control cabin. Pipes are transferred into the driving shaft one after another and jack system pushes them into the ground until the cutter heads arrives at the receive shaft.

Based on the ground geology, a large variety of different instruments can be mounted on the machine cutter head. The direction of the machine is controlled by one laser that points on one target inside machine. To take out the cuttings, water from storage tank is sent by connection pump to the machine's cutter head and after mixing with the cuttings it comes out through a slurry line. The slurry line comes to a separation plant which separates water from soil. After separating cuttings from water, the separation system sends water back to a storage tank to complete the circulation. To set the direction of the jack and distribute the jacking force, the thrust wall is constructed.

Based on the field geology explained in the previous section, presence of giant boulders and disturbed soil Fabric during pipe jacking operation seem inevitable. So in this project we encountered very dense rock layers each causing respective challenges in operation. Moreover, the friction between ground and pipes increased due to a sudden increase in ground stiffness as well as higher pipe- ground involvement while driving reached the rock layer. High jack pressure on one hand and intense soil- pipe friction on other hand led to repeated crack occurrences in polymer concrete pipes. Accordingly, the crack occurrence in the pipe requires more relevant researches in the field to find practical solutions. The pipe jacking operation method is described in fig. 1.

3.1 *Equipment*

The type of cutter head was selected by taking both geological test results and manufacturer instruction and guidance into the consideration. Finally two devices were selected. First The AC 1600 mm machine with mixed cutter head along with upsize extension kit to 1800 mm and second the TC 1200 mm machine with rock cutter head along with upsize extension kit to 1400 mm. figures 2 and 3 show the device's cutter head.

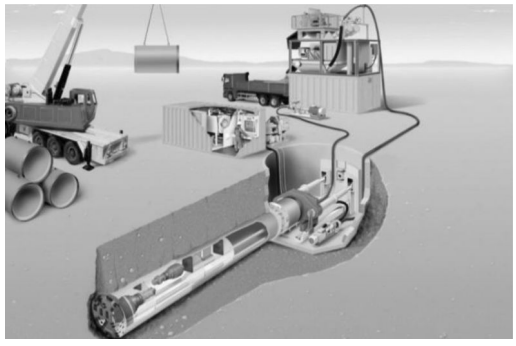

Figure 1. Pipe jacking method.

Figure 2. 1800 mm set.

Figure 3(a). 1400 mm set.

Figure 3(b). 1400 mm set.

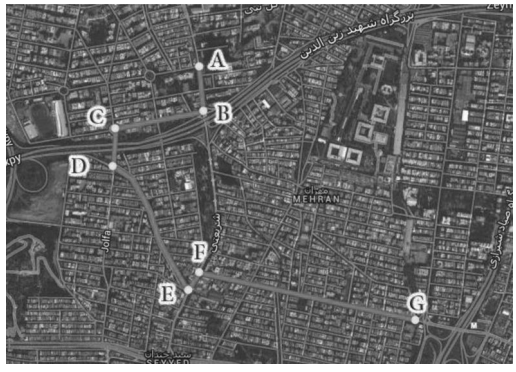

Figure 4. Project geology zone.

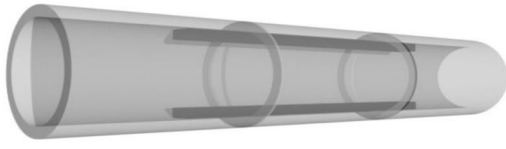

Figure 5. Steel jacket in damaged pipe.

3.2 *Geology condition*

From the geological point of view, site is located on very dense alluvium layers with a wide range of rock lenses sorted from silt stone to giant boulders. Moreover, Tehran is located on quaternary rheology. Tehran alluvium has been merged from the sedimentation of two large rivers which led to the existence of huge boulders and anisotropic sediments of soil layers. The congestion of boulders causes many obstacles like cutter head blocking, high pressure of jack, blocking in feed and slurry line by crushed piece of boulders, high friction between pipes and ground that causes cracking and fracture in pipes. To take the geological importance of the project into the consideration, geotechnical investigations were done at the first phase of the project. Table 1 shows the geotechnical properties of the soil. Figure 4 also shows the project geology zone.

3.3 *Crack control methods*

The geology was the main cause of crack occurrence in pipes. Two types of crack in pipes include:

1–Surface cracks

2–Deep cracks

High jack pressure and intense rock-pipe friction are the main causes of deep cracks. In this case, the pipe is not functional and useable anymore and must be removed eventually. To achieve this, either all parts of the damaged pipe must be demolished and removed or bypass (transmit) the horizontal pushing load from the previous pipe to the next one by installation of a steel frame in the place of the damaged pipe.

This structure is called a "Steel Jacket" and is joined to the pipe by bolt and nut by taking special considerations. Figure 5 describes the schematic steel jacket procedure. The operation method and acquiring the bearing capacity (including two pipes and steel structure) have been obtained in the field and were compared to the ANSYS software results.

But as for surface cracks, if the pipe cracks near the driving shaft, the pipe can be removed and replaced with a new one. Otherwise, the crack must be controlled and operation is continued until it arrives at the reception shaft. This attitude to a large extent benefits the project economically and eventually saves operation time.

Among a variety of available methods, two methods were proposed by the technical department of the project:

1–Utilizing FRP sheets in order to increase the bearing capacity of the cracked pipe (figures 6a & b)

2–Utilizing plate & bolt around the crack in order to prevent progress of the crack in the pipe. According to

Table 1. Geotechnical properties of project.

Line	Bulk Density ton/m^3	Cohesion Kg/cm^2	Friction Angle	E-Gpa	Rock Comp. Strength (Mpa)	Rock Tensile Strength (Mpa)
A-B	1.95–2.12	0.15	39	100–120	200	19
	1.89–2.06	0.25	36	50–75	200	19
B-C	1.97–2.13	0.21	38	100–120	200	19
C-D	1.94–2.11	0.23	37	100–120	200	19
E-D	1.92–2.09	0.2	37	35–50	200	19
G-F	1.85–1.95	0.1	45	100–120	200	19

Figure 6(a). Installation of FRP in pipe.

Figure 6(b). Installation of FRP in pipe.

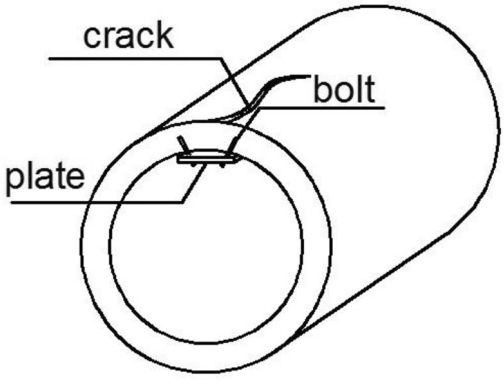

Figure 7. Bolts and plat.

fig. 7, the system is capable of covering the damaged area so increasing the pipe serviceability.

Both proposed methods were surveyed in practice and the results were analyzed by the ANSYS software to find the advantages and disadvantages of the each method.

To use each method, it was necessary to model and analyze both the cracked zone and the enforced element in ANSYS software and select the best method

Figure 8(a). Sample test in the laboratory.

Figure 8(b). Test in laboratory.

for any condition. However, before any analyzing it is necessary to calibrate the program to gain accurate and precise data.

4 CALIBRATION

Several samples were removed by coring from the available pipes and were tested in the laboratory to control the software results accuracy. The sample test results are shown in Figures 8a and 8b. Fortunately, the software test results coincided exactly to the laboratory test results. The sample coring in a selected pipe is shown in figure 10.

Figure 9. Coring from the pipe.

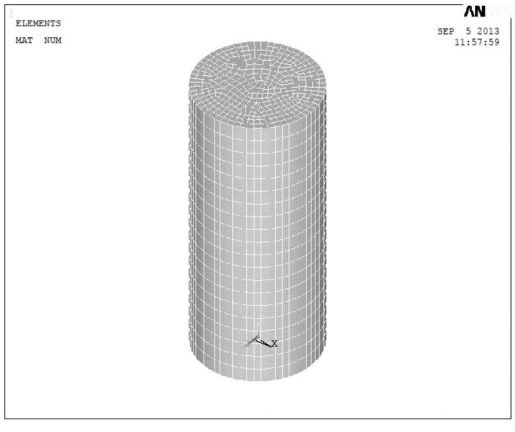

Figure 10. Cylinder model in ANSYS.

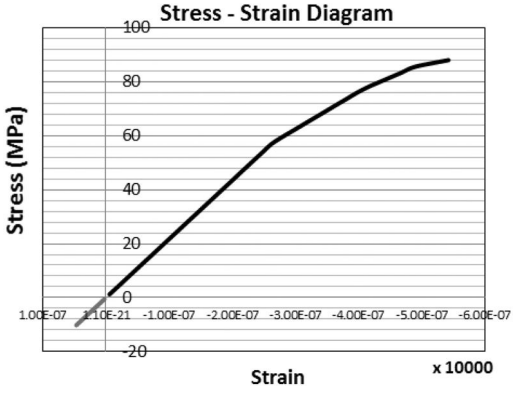

Figure 11. Result from ANSYS.

In addition, we created a 3D model of an exact cylinder in ANSYS software and exerted the same loading and boundary condition to obtain the result. (Fig. 10).

It is clear from figure number 11 and 12 that the lab results and 3D modeling results were the same and we could get accurate data from our 3D modeling analyses in ANSYS software.

5 SOFTWARE MODELING

The ANSYS software was used to analyze the models. The following requirements must be met to simulate the real test conditions according to figure 13.

1 Loading conditions
2 Support conditions
3 GRP modeling and pipe connections
4 Crack modeling
5 Steel jacket modeling
6 FRP modeling
7 Bolts, Nuts and Plates modeling

5.1 *Loading conditions*

In the software modeling, it is necessary to apply the load from the jack in the shaft to simulate the real condition correctly. So loading has been considered as applied pressure on the area of initial pipe. This applied pressure increased linearly to the ultimate value tolerated by the real model.

5.2 *Support conditions*

The pipe is in a direct contact to the surrounding ground. So the pipe-ground interaction dominates the modeling process. The support conditions at the beginning and at the end of the pipe line (the location of the pipe- jack connection) doesn't provide displacement of the pipe perpendicular to the pipe jacking operation. On the other hand, although it allows the horizontal displacement of pipes in the direction of the line, it is closed at both beginning of the line due to close connection with the ground and at the end of the line due to connection with the jack. The whole explained conditions were considered in the software modeling.

5.3 *GRP modeling and pipes connection*

The joint section of the pipe consists of two special parts as shown in figure. 14 and most important part of this connection is called GRP (Glass fiber Reinforced Plastic). The pipe GRP prevents the displacement of the second pipe in which is connected. So the GRP at the joint zone allows the directional pipe displacement and prevents the vertical displacements of the pipe. Moreover, the Contact element in the software was used to simulate the transmission of the contact loading from one pipe to another.

5.4 *Crack modeling*

One damaged pipe was selected for modeling of crack. The crack was located on the top of one pipe during the pipe jacking operation and led to ceasing operation due to further investigations. To survey a close model in reality, the crack in the software model was at the place where it existed in the real pipe. (50 cm long and 1 mm wide) meshing and element dimensions were considered smaller near the crack to increase accuracy. Figures 15a and 15b present the crack in the real pipe and its model in the software respectively.

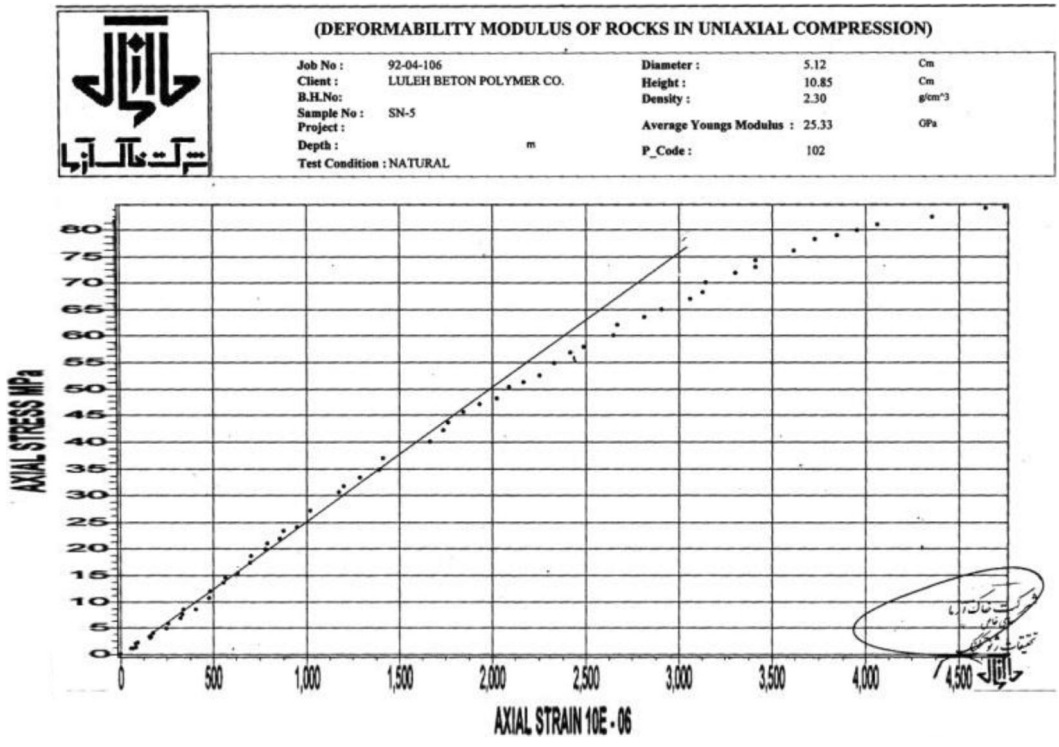

Figure 12. Result from laboratory test.

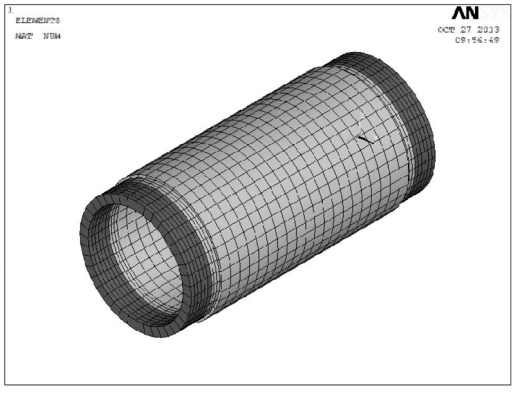

Figure 13. Pipe model in ANSYS.

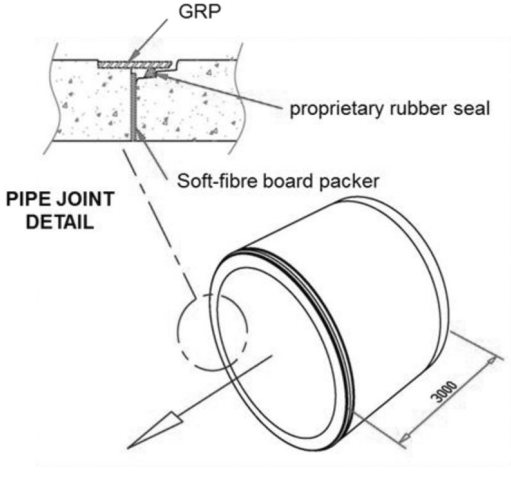

Figure 14. Pipe joint detail with GRP.

5.5 *Steel jacket modeling*

The steel beam was connected to the pipe by bolts and the system was utilized to model the steel jacket. As the connection joints for this structure are similar to the plate and bolt connection, the bolt and plate joints were used exactly for our modeling. The section's specifications are as follows:

1 IPE for four beams
2 24 bolts of number 20
3 Two rings with 4 cm thickness and 30 cm width.

5.6 *FRP modeling*

A Shell 181 element was used to model the FRP sheets. The property of the FRP materials was considered with orthotropic properties according to the Table 2 to model two FRP layers with angles of 0 & 90 degrees in the preferred zones. It also should be noted that the nodes of both elements in the FRP sheets and polymer concrete connection joints have been merged.

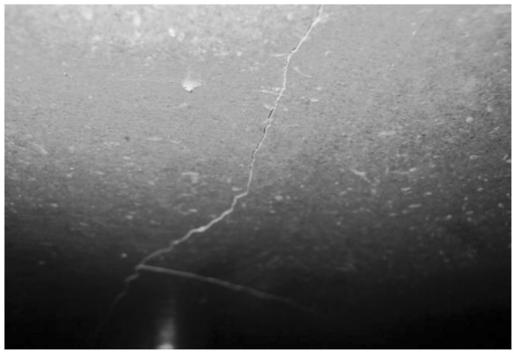

Figure 15(a). Crack in pipe.

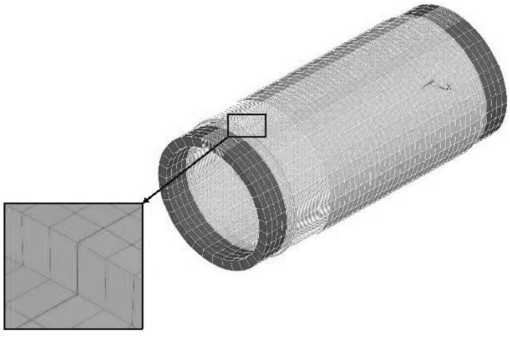

Figure 15(b). Crack model in ANSYS.

5.7 *Plate & bolt modeling*

The solid 185 model was used for plate and bolt modeling. The material behavior is elastic and the contact element in the concrete-bolt connection joint has been used in order to model the pressure transmission from pipe to the bolt and vice versa.

5.8 *Analysis of cracked pipe*

At the first analysis the modeled cracked pipe was loaded under the jack pressure to the maximum determined bearing capacity (tolerable loading capacity) of the pipe. The stress distribution in figures 16a and 16b clearly shows the maximum stress in the pipe joints. It can be concluded from the test result shown in figure. 16 that the ultimate loading capacity of the cracked pipe is about 3770 tons which is almost 26% less than the value for the original pipe.(5055 tons)

6 ANALYSIS OF CRACKS

6.1 *Analysis of surface crack in pipe using FRP*

In this model the FRP sheets are settled on the crack zones. (Fig. 18 and 19) This covering system was simulated in the ANSYS software to investigate the maximum bearing capacity of system. Results are shown in table 2. It can be understood from the

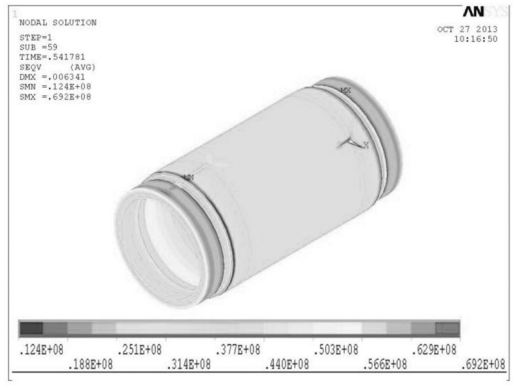

Figure 16(a). Stress in pipe with crack.

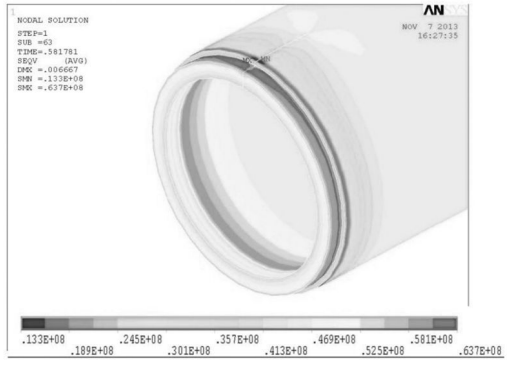

Figure 16(b). Stress in pipe with crack.

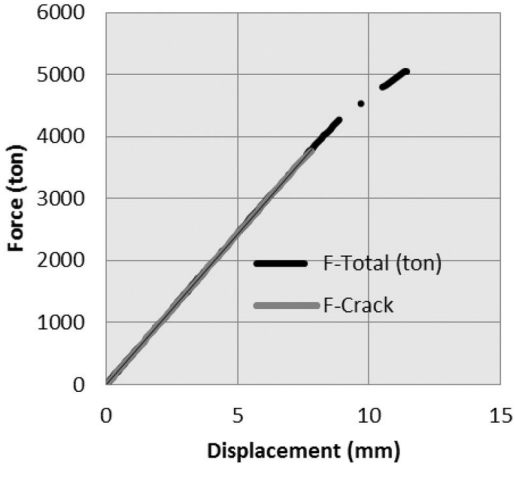

Figure 17. Comparison between load capacity of pipe without crack and with crack.

table that the ultimate bearing capacity of the FRP model is about 4823 tons. So the FRP model increases the system's bearing capacity by 28% compared to the cracked pipe only. (3770 tons) This reveals the

Table 2. Material properties of FRP.

Elastic Modulus (MPa)	Major Poisson	Tensile strength (MPa)	Shear Modulus (MPa)
Ex = 62,000	ν xy = 62,000	958	Gxy = 62,000
Ey = 62,000	ν xz = 62,000		Gxx = 62,000
Ez = 62,000	ν yz = 62,000		Gyz = 62,000

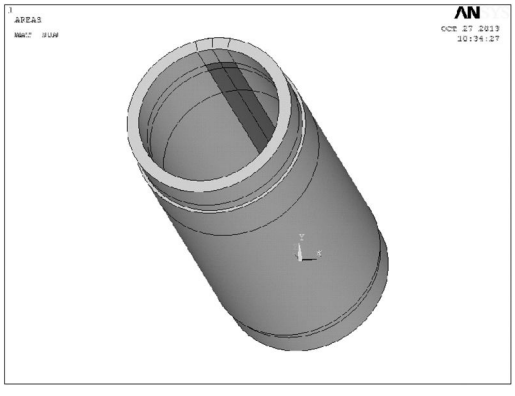

Figure 18. FRP model in pipe.

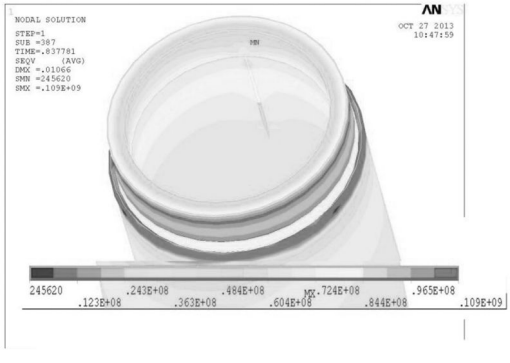

Figure 19. Stress distribution in cracked pipe with FRP.

advantages of using FRP sheets to control the damaged pipe serviceability.

6.2 *Analysis of surface crack in pipe using bolt & plate*

The stress distribution and bolt and plate model in the software are shown in figures 21 and 22. The pipe deflection model during pipe jacking operation is also shown in fig. 23. The ANSYS model was also used to investigate the bolt and plate reinforcement efficiency. As can be seen from fig. 24. The system's maximum bearing capacity is approximately 4980 tons which shows a dramatic 32% increase compared to the cracked pipe itself.

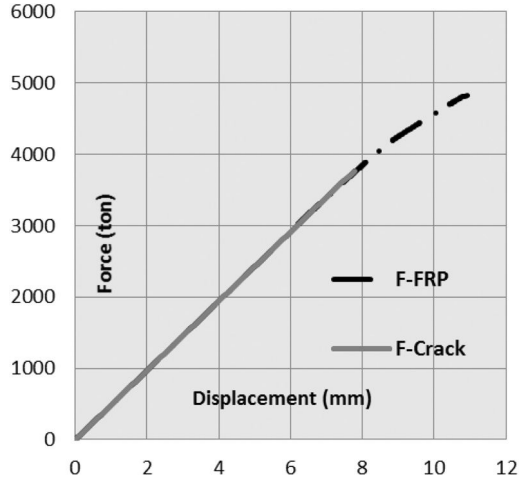

Figure 20. Comparison between load capacity with FRP and without FRP.

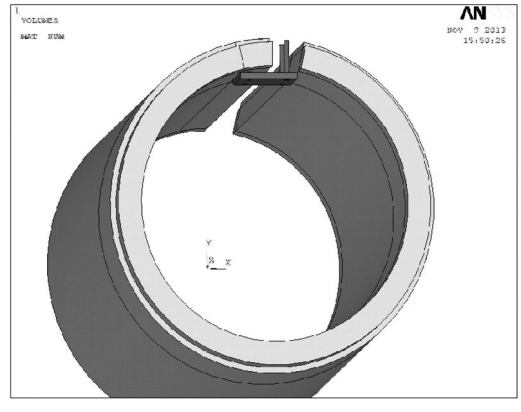

Figure 21(a). Bolt and plate model.

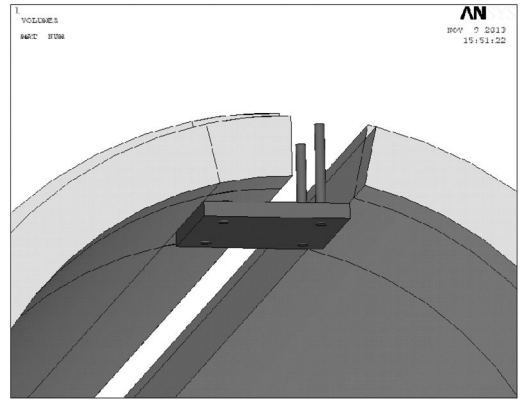

Figure 21(b). Bolt and plate model.

6.3 *Analysis of deep cracked pipe and steel jacket application*

As previously mentioned, when a deep crack occurs in a pipe, it is possible to transfer the pressure from the

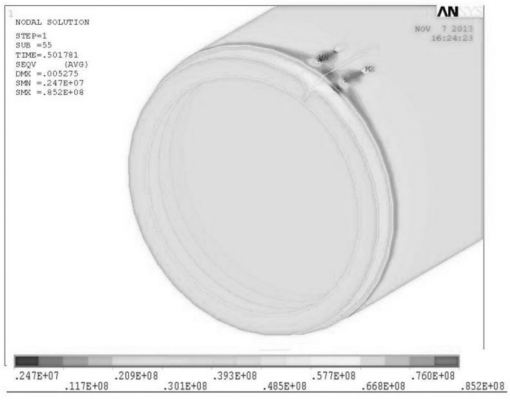

Figure 22. Stress in bolt and plate model.

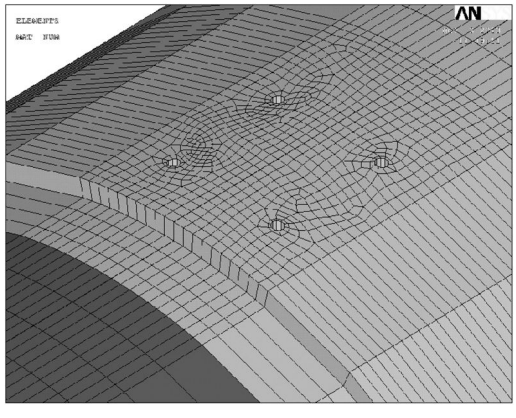

Figure 23. Deflection around the bolts.

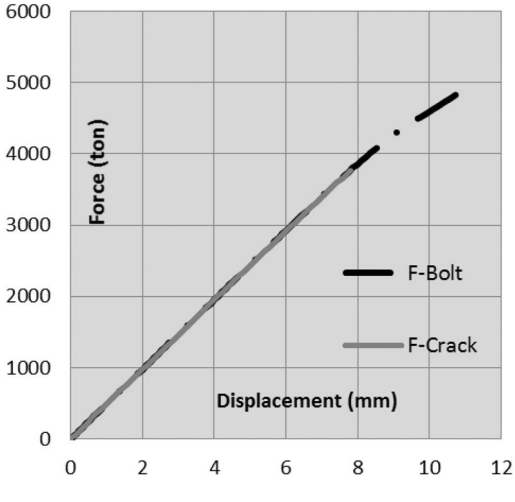

Figure 24. Comparison between load capacity of pipe with bolt and plate model and without bolt.

back pipes to the front ones using a particular structure and omit applying load to the cracked pipe. In addition, the ANSYS model was created to analyze the model as well as finding the maximum bearing capacity of

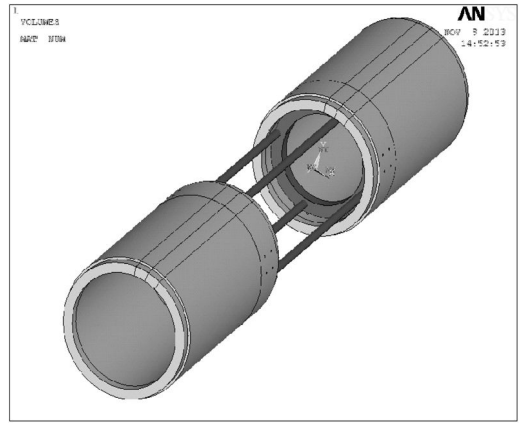

Figure 25(a). Steel jacket model.

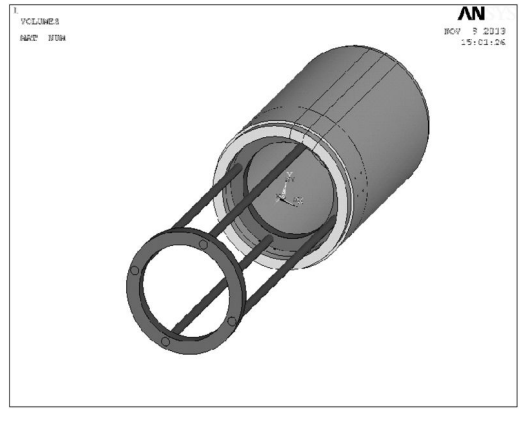

Figure 25(b). Steel jacket model.

system. Figures 25a and 25b presents the schematic detail of the steel jacket model. Additionally, figures 25 and 26 provide the stress distribution around bolts in the steel jacket method.

According to fig. 28 the maximum bearing capacity of system is 614 tons. The 84% capacity loss is because of load transmission of the jack by only 12 bolts from the pipe to the steel structure which causes the high local tension in bolts zone and local fracture.

7 CONCLUSIONS

From result of all methods we can summarize the data in one table below:

- From the table it is clear that with observing cracks in pipes during pipe jacking operations, the loading capacity of the pipe is decreased by some 25%.
- Both methods of FRP and BOLT methods are suitable and increase the bearing capacity of the system nearly back to that of the uncracked pipe.
- From the performance point of view the FRP method is very simple compared to the BOLT

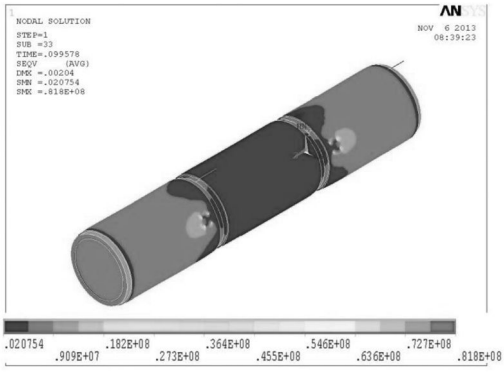

Figure 26. Stress distribution in three connected pipes (steel jacket model).

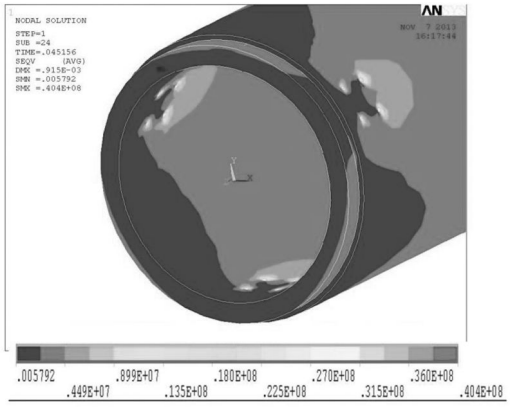

Figure 27(a). Stress around bolts.

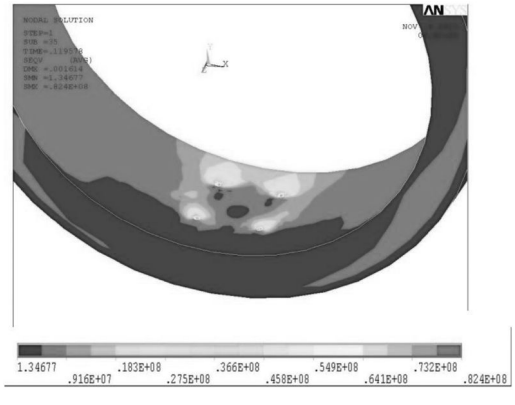

Figure 27(b). Stress around bolts.

method. Additionally, in the BOLT method it is required to select the location of bolts carefully and any mistake in drilling holes can affect the loading capacity.

- The FRP method is performed faster than any other methods so it reduces repair operation time by choosing this method.

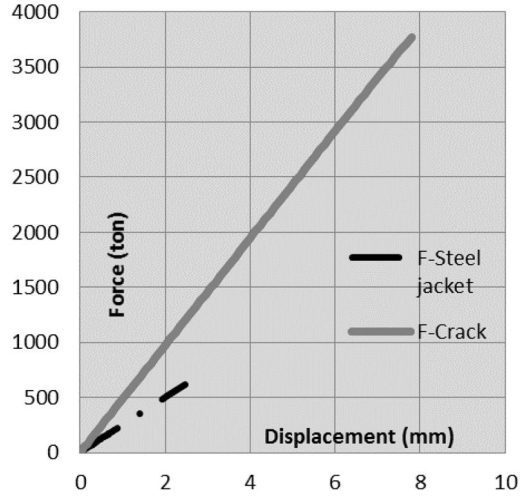

Figure 28. Comparison between load capacity of pipe with steel jacket and without steel jacket.

Table 3. Comparison of all models result.

Method type	Strength from analysis (Ton)	Load Capacity Reduction %	Allowable Jack Load (Ton)
Pipe without crack	5055		754
Pipe with crack	3770	25	562
FRP-method	4823	5	719
Bolt-method	4981	1	743
Steel jacket Method	614	84	123

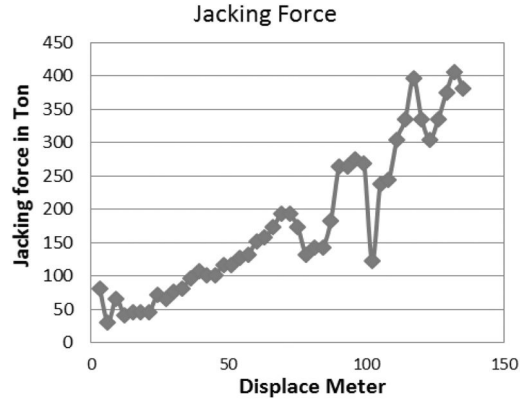

Figure 29. Jacking force during pipe jacking.

- Although the ultimate loading capacity of the BOLT method is higher than the FRP method, it is proposed to use FRP because of easier and faster performance.
- The Steel Jacket method is not suitable in the case of cracked pipes, but in some situations, if faced with big and deep cracks or the pipe is fracturing, this method can be used with control of the jacking

Figure 30(a). Steel jacket method.

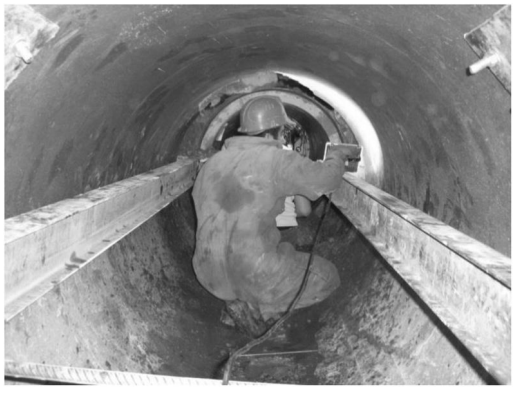

Figure 30(b). Steel jacket method.

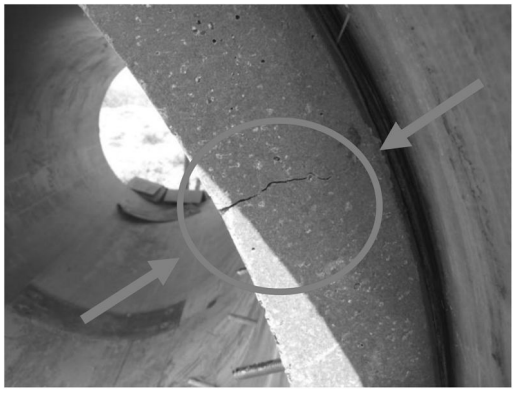

Figure 31. Deep crack in concrete polymer pipe.

load up to 123 tons for continuing and completing the line.

- In our project, after observing cracks in pipes we control and monitor jack load carefully. in Fig 29 can be seen one of our jacking loads during pipe jacking. In this drive we had one crack in the pipe when at 65 meters into the tunnel. After observing the crack we checked the jack force and if the jacking force had risen to 500 tons we would have had to choose either the FRP or BOLT method for increasing loading capacity but fortunately we had a maximum 420 tons of load and we finished the line successfully without any consideration.

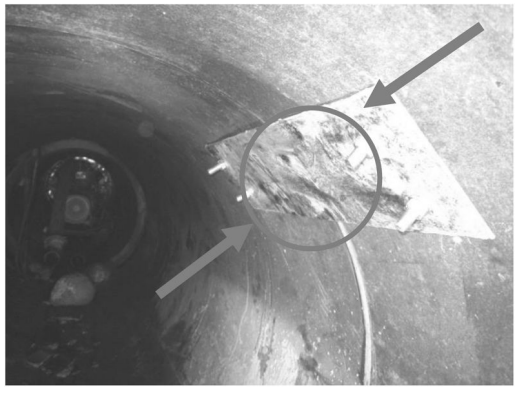

Figure 32. Bolt and plate method.

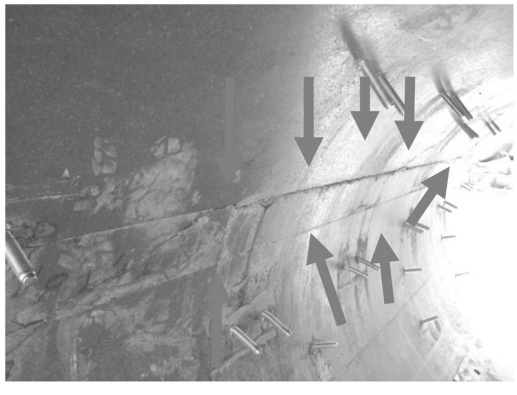

Figure 33. Control of crack by bolt and plate method.

For future research we propose to:

1. Survey the effect of crack size in each model
2. Analyze the effect of bolt size and position around the crack
3. Analyze the steel jacket with more bolts or other designed structures

In our project we used steel jackets with different structures for transferring broken pipes to shaft.

During our project we used the BOLT and FRP method many times and chose each method based on the ANSYS result. In all cases we completed each one successfully by using suitable methods that indicated our modeling result was correct.

REFERENCES

-*Technical documentation*, Concrete Polymer Pipe Company, Iran

-Kachlakev, D.and Miller, T.*Finite element modeling of reinforced concrete structure strengthened with FRP laminates*, Oregon Department of Transportation, 2001
-Merkle, D.Schrader, B&Thomes, M*Hydraulics, basic level,* Festo Didactic GmbH & Co. KG, 73770 Denkendorf/Germany, 2003
-DIN 54815-2, *Pipe made of filled polyester resin molding materials, 1998*
-ACI 224R-01, *Control of cracking in concrete structures*
-ACI 546.3R-06, *Guide for the selection of materials for the re-pair of concrete*
-ACI 546R-04, *Concrete repair guide*
-ACI 548.1R-09, *Guide for the use of polymers in concrete*
-ASTM D 6783, *Standard specification for polymer concrete pipe*
-*Herrenknecht AG manual*, AVN1200TC
-*Herrenknecht AG manual*, AVN1600AC
-(Fig 8(a)), http://www.structural.net (accessed May 2014)
-(Fig 8(b)), http://www.quakewrap.com (accessed May 2014)

Concrete Solutions – Grantham et al. (Eds)
© 2014 Taylor & Francis Group, London, ISBN 978-1-138-02708-4

Effect of thermal cycling on the behaviour of CFRP-to-concrete joints

D. Petkova, T. Donchev & A. Jawad
Kingston University London, London, UK

ABSTRACT: Deterioration of infrastructure is one of the most pressing concerns facing today's civil engineering community. As a result, new rehabilitation techniques, such as the external bonding of fibre-reinforced polymer (FRP) are being developed. In cold regions, repaired beams for bridges and exterior parking structures will be exposed to temperature extremes. This could lead to a detrimental effect on the performance of the strengthened systems, especially when combined with increased humidity due to rain and snowfall. The effect of freeze-thaw cycles could reduce the capacity of the elements if the thermal actions contribute to the development of cracks and could results in the premature failure of the samples.

The purpose of this paper is to present an investigation on the behaviour of FRP to concrete joints and the effect of thermal cycles of elevated and low temperatures.. The experimental investigation was conducted using a single lap shear configuration test of the samples where two types of reinforcement were prepared. Only uniaxial carbon FRP laminates were considered. The specimens were subjected to temperatures between +45°C and −15°C for 28, 56, and 84 cycles. The duration of the exposure was 4 h at the elevated and low temperatures after which the specimens were tested to destruction. The developments of strain along the bonded length were measured and the failure mode indicated. The result of the experiment was analyzed followed by an evaluation of the effect of thermal cycle on bond between fibre-reinforced polymer (FRP) and concrete.

1 INTRODUCTION

FRP strengthened beams would be exposed to harsh weather conditions during their service life. In cold regions, bridges and exterior parking structures will be subjected to daily temperature extremes which could lead to freeze-thaw cycles in the presence of water, and seasonal variations between low temperatures and elevated temperatures.

The presented experimental investigation was conducted using a single lap shear configuration test. Only uniaxial carbon FRP (CFRP) laminates were considered. The specimens were exposed to cycles from −15 °C to +45 °C for 28, 56, and 84 cycles consisting of four hours of exposure to the elevated and low temperatures after which the specimens were tested to failure. The strain changes along the bonded length were measured and the failure mode indicated. The result of the experiment was analyzed followed by an evaluation of the effect of thermal cycle on bond between the FRP and concrete.

2 BACKGROUND

Material behaviour could be affected by the presence of water and freeze-thaw cycles. Such treatment would influence the properties and result in a more vulnerable structure. Furthermore, freeze–thaw cycles and thermal impact may reduce the stiffness of the FRP composite and induce thermal stresses due to the different thermal expansion coefficients of the constituents. Similar impact could be expected in structural members strengthened with FRP at extreme service temperatures where the FRP-to-substrate bond has to be considered (Nardone, et al. 2011).

The research conducted on the use of FRPs when exposed to cold climates is relatively limited. Thermal incompatibility and polymer embrittlement are two main areas of interest when the behaviour of FRP products subjected to freeze-thaw exposures is concerned (Kong et al. 2000). The different coefficient of thermal expansion of the fibres and the polymer matrix could result in thermal incompatibility. The epoxy resins used as adhesives and coatings in FRPs have coefficients of thermal expansion in the range of 45 to 65×10^{-6}/°C while the fibres show negligible expansion (12×10^{-6}/°C for concrete). Thus the developed tensile stress in the matrix could make it vulnerable to micro cracking. The magnitude of these cracks may grow with the exposure to thermal cycling, causing cracks to propagate in the resin matrix, and finally leading to strength degradation or failure (Oldershaw, 2008).

Strengthened samples of concrete substrate and the FRP plates rely on a good bond and their properties could be affected by freeze and thaw cycles and changes in temperature (ACI-440, 2007). Though the high quality of the resin matrix would minimize the appearance of air voids, factors such as poor surface

preparation and moisture presence can lead to the entrapment of air between the FRP and the concrete surface. Once water is able to penetrate into these voids and freeze, a lensing effect will occur and the voids will expand with subsequent freezing and thawing cycles (ACI-440, 2007).

An experimental study was conducted by Green et al. (2000) which evaluated the freeze-thaw resistance of 22 small-scale concrete beams strengthened with either CFRP or GFRP sheets after 200 cycles of freeze and thaw. These results indicate that for both types of FRP, thermal cycling did not consistently affect the strength or the mode of failure. Additionally, it was found that the measured strains were below those specified by the manufacturer.

In a study by Oldershaw (2008), forty eight small scale FRP strengthened concrete beams were tested and the beams were exposed to 100 freeze-thaw cycles. According to the study, CFRP and GFRP strengthened beams were found to lose strength of 21% and 27% respectively. The failure mode of the specimens was also affected by the cycles. Another type of CFRP was applied for strengthening small scale beams and subjecting the systems to 300 freeze thaw cycles (Soudki et al. 2007). The test was carried out with pre-cracking of the beams and discovered that the application of load prior to bonding the CFRP to the soffit of the beams resulted in more noticeable effects from the freeze thaw cycling with a 40% drop in strength.

Silva and Biscaia (2008) tested the bond strength of rectangular concrete slabs strengthened with GFRP and CFRP strips and found a reduction up to 31% decrease in strength at 10000 h of temperature cycles to −10°C and +10°C. In another study Silva et al. (2013) presented results of CFRP samples subjected to hygrothermal cycles and salt fog cycles and the GFRP beams subjected to salt fog cycles, dry/wet cycles in salt water, freeze/thaw cycles and total immersion in water. The externally bonded CFRP samples were found to be more susceptible to the variations of relative humidity than salt fog cycles. GFRP samples exhibited greatest reduction of maximum load under freeze- thaw cycles followed by the treatment using salt fog.

Colombi et al. (2010) tested 6 concrete prismatic samples strengthened with CFRP plates and wraps after the concrete samples had been subjected to 100 and 200 of freeze- thaw cycles from −18°C to +4°C. The results were compared with unconditioned samples and the freeze and thaw cycles were found to have little effect on the debonding force.

3 EXPERIMENTAL SET-UP

Twenty four samples with dimensions 100 mm by 100 mm by 500 mm and twenty four cubes of strength class C30/37 were prepared and tested in this study. Two types of reinforcement (single bar reinforcement and cage reinforcement) were used and the samples were divided in two groups of 12 (Figure 1). After

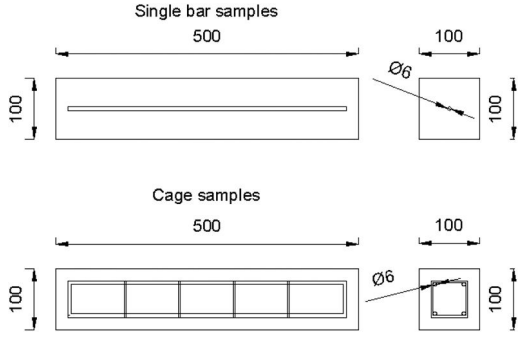

Figure 1. Reinforcement of the samples.

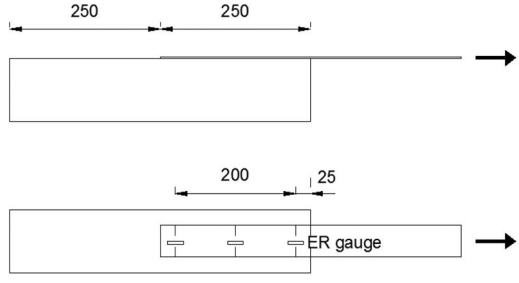

Figure 2. Experimental set-up and strain gauges.

samples were cured for 28 days and strengthened using 2 part epoxy structural adhesive (Weber) and 50 mm wide CFRP plates with characteristic tensile strength 2850 MPa they were submerged in water for 24 h. They were then wrapped with plastic foil before being placed in an environmental chamber and exposed to freeze-thaw cycles. The samples were divided into groups: control (group 1), 28 days (group 2), 56 days (group 3) and 84 days (group 4) cycle.

After the samples were taken out of the environmental chamber they were tested in single shear lap configuration. Electrical resistance strain gauges were placed on the CFRP surface, near the loaded end and the relative displacements along the length of the CFRP were measured during the test (Figure 2).

4 EXPERIMENTAL RESULTS

The samples were tested in a single shear lap configuration after 0, 28, 56, and 84 cycles to −15°C to +45°C. The failure of the samples was due to the formation of a crack in the concrete prism at the end of the CFRP plate due to the applied load after which a brittle delamination occurred between the CFRP and the concrete.

Figure 3 presents the average ultimate load for the two types of samples and the effect of freeze-thaw on their ultimate capacity. Both single bar and cage reinforcement groups exhibited a similar trend of ultimate load reduction with an increase in the number of cycles. For single bar samples, the average ultimate

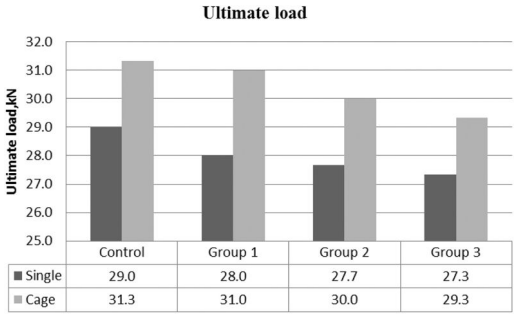

Figure 3. Average ultimate load for single bar and cage reinforced samples.

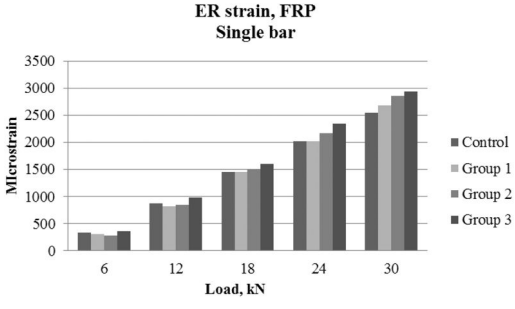

Figure 4. ER strain gauge readings measured on the CFRP plate for single bar reinforced samples.

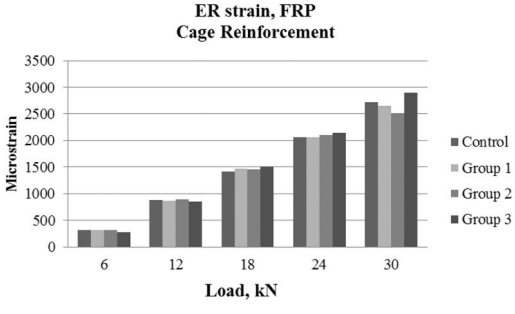

Figure 5. ER strain gauge readings measured on the CFRP plate for cage reinforced samples.

load dropped from 29 kN of the control group to 27.3 kN for the group subjected to 84 cycles of freeze and thaw. The cage reinforced samples failed at higher loads with a load of 31.3 kN for the control beam and 29.3 kN after 84 cycles of freeze and thaw.

The effect of freeze and thaw on the deformability of the samples is shown in figure 4 and 5. There is a steady increase in the deformations for the different levels of loading with a clearer trend at loads between 18kN and 24 kN.

Single bar samples exhibited increased deformability with the control group developing strains at 18 kN of average 2000 microstrain to 2300 microstrain after 84 cycles of freeze and thaw. The trend remained up to 30 kN as the control group registered strain about 2500 microstrain up to 2900 microstrain after 84 cycles (figure 4). The deformability of the cage reinforcement samples also increased with the number of cycles. The proximity of the cage to the strengthened surface reduced the effect on the deformations as the range between control and group 3 was significantly smaller. At 18 kN the strain ranged from 1400 to 1500 microstrain whereas at 30 kN the effect of the cycles was more pronounced with microstrain of 2700 for the control group and 2900 microstrain for the group subject to 84 cycles.

5 ANALYSIS OF RESULTS

Figure 6 presents the reduction in the capacity of the single bar and cage reinforced concrete samples with increase in freeze-thaw cycles. After 86 cycles the ultimate load for both single bar and cage reinforcement samples is about 94% of the capacity of the control group. Such a reduction corresponds with the findings of other studies where freeze and thaw cycles could lead to reduction greater than 20%.

Single bar samples showed greater reduction in capacity after 28 days of freeze/thaw capacity compared with cage reinforced specimens. For groups 3 and 4 corresponding to 56 and 84 cycles the rate of reduction is similar.

6 CONCLUSIONS

On basis of the analysis conducted, the following conclusions could be drawn:

- The ultimate capacity of cage reinforced specimens was higher up to the first 28 cycles.
- Failure of single bar samples occurred at lower levels of loading due to the greater depth of the concrete cover.
- The mode of failure for all groups was not affected by the number of cycles, initiating in the concrete prism.
- Percentage of reduction of the failure load for single bar samples and for cage reinforcement was about 6%.
- The strain development could be affected by the number of cycles with a greater number of cycles marking the greater strains as well for bigger concrete cover.

ACKNOWLEDGEMENTS

The authors would like to express their gratitude to Mr Sean Downey and Mr Mario Todino for their technical support.

REFERENCES

ACI 440.2007. *Report on fiber-reinforced polymer (FRP) reinforcement for concrete structures*. ACI Committee 440.XR-07. Michigan. U.S.A.

Colombi, Pierluigi, Fava, Giulia & Poggi, Carlo. 2010. Bond strength of CFRP–concrete elements under freeze–thaw cycles. *Composite Structures* 92: 973–983

Cromwell, J.R, Harries K.A., & Shahrooz, B.M. 2011. Environmental durability of externally bonded FRP materials intended for repair of concrete structures, *Construction and Building Materials* 25: 2528–2539

Green, M.F., Bisby, L. A., Beaudoin, Y & Labossiere, P. 2000. Effect of freeze-thaw cycles on the bond durability between fibre reinforced polymer plate reinforcement and concrete. *Canadian Journal of Civil Engineering* 27: 949–959

Kong, A., Fam, A.Z., and Green, M.F. 2005. Freeze-thaw behavior of FRP-confined concrete under sustained load. In: *7th International Symposium on Fiber-Reinforced (FRP) Polymer Reinforcement for Concrete Structures* issue 230, vol. 1

Nardone, Fabio Ludovico, Marco Di De Caso y Basalo, Francisco J., Prota Andrea Nanni, Antonio. 2012. Tensile behavior of epoxy based FRP composites under extreme service conditions, *Composites: Part B* 43: 1468–1474

Oldershaw, Brant. 2011. *Combined effects of freeze-thaw and sustained loads on reinforced concrete beams strengthened with FRPs*, Master's thesis, Queen's University, Kingston, Ontario, Canada

Silva, Manuel A.G. & Biscaia, Hugo. 2008. Degradation of bond between FRP and RC beams. *Composite Structures* 85: 164–174

Silva, Manuel A.G., Biscaia, Hugo C. & Marreiros, Rui. 2013. Bond–slip on CFRP/GFRP-to-concrete joints subjected to moisture, salt fog and temperature cycles, *Composites: Part B*55: 374–385

Soudki, K, El-Salakawy, E. and Craig, B. 2007. Behaviour of CFRP strengthened reinforced concrete beams in corrosive environment. *Journal of composites for construction* May/June: 291–298

Concrete Solutions – Grantham et al. (Eds)
© 2014 Taylor & Francis Group, London, ISBN 978-1-138-02708-4

Retrofitting of RC panels subjected to blast effects using elastomeric polymer coatings

S.N. Raman & M. Jamil
Department of Architecture, Universiti Kebangsaan Malaysia, UKM Bangi, Selangor, Malaysia

T. Ngo & P. Mendis
Department of Infrastructure Engineering, The University of Melbourne, Victoria, Australia

T. Pham
Department of Civil and Industrial Construction, University of Civil Engineering, Hanoi, Vietnam

ABSTRACT: This paper presents the findings from the experimental programme and Finite Element (FE) analysis performed to study the behaviour of polyurea coated RC panels subjected to blast effects. The overall findings of the research, including detailed experimental findings of three of the tested panels (one un-retrofitted and two polyurea coated panels), and the subsequent FE analysis performed to simulate the blast trials, are discussed in this paper. All 3 panels had dimensions of 1700 (L) × 1000 (W) × 60 (T) mm. Among the retrofitted panels, one panel was subjected to a 4 mm polyurea coating on the non-blast facing face, whereas the other was coated with a 4 mm polyurea coating on both faces. All the panels were subjected to blast loads resulting from the detonation of 1.0 kg Ammonite charge placed at a 1.0 m stand-off. Identical panels were then modelled and analysed using the explicit solver of the non-linear FE code, LS-DYNA. The results from both experimental programme and FE analysis suggest that while the polymer coating technique does enhance the resistance of the RC panels to the applied blast load, a higher level of protection is provided when the protective coating is applied on the blast facing face of the structure.

1 INTRODUCTION

Reinforced concrete (RC) has been the most widely used structural system across the globe and the situation is envisaged to continue in the next decades. However, it cannot be overlooked that RC system also comes with its own limitations where it may undergo deterioration and face reduction in its structural capacity over time. This can be due to various factors such as increased load intensity, weathering effects, the change of function of the building, material deterioration, etc. This gives rise to the need for structural retrofitting and strengthening works to be undertaken on these structures to ensure that their capacity meets the needs of the design.

Over the last few decades, various external factors such as increase in terrorist activities, accidental explosions and proliferation of weapons have resulted in a new type of challenge to RC structures. These events result in the structure being exposed to extreme impulsive loadings, where most RC structures in the civilian domain are not designed and constructed for. In view of this scenario, structural and material engineers are seeking novel and cost effective protective solutions to mitigate the destruction that may be caused by such extreme loading events. One approach to increase the resistance of structures to blast load is by increasing their mass and ductility. This can be accomplished by using additional concrete and reinforcement, or by using external reinforcing techniques (such as carbon or glass fibre reinforced composites, or by using steel plates). However, the feasibility of external strengthening applications is usually restricted by limitations in the material's technical capacity and the requirement for higher resources in installing them.

In recent years, elastomeric polymers (such as polyurea) are finding relevance for strengthening and retrofitting applications of structures being subjected to blast, ballistic and impact loadings. Polyurea is an elastomeric polymer derived from the rapid reaction of an isocyanate component and a polyamine. The technique of using polyurea for structural retrofitting capitalises on the high strain capacity of the polymer, the composite action between the polymer and the structural material, as well as on the ability of the polymer layer to buffer the debris and fragments resulting from the blast event from propelling.

This technique was explored for the first time by Knox et al. (2000) where they investigated feasibility of using the polyurea coating technique on masonry and lightweight steel structures subjected to blast loading. The positive findings from this initial experiment

resulted in various researcher investigating the suitability of this innovative approach on masonry structures (Baylot et al. 2005, Davidson et al. 2004a, 2005), on steel structures and plates (Ackland et al 2013, Amini et al. 2010a,b, Chen et al. 2008) and on composite structures and systems (Bahei-El-Din & Dvorak 2007a, b, Tekalur et al. 2008, Grujicic et al. 2010, LeBlanc et al. 2013). Most recently, the applicability of this technique has also been investigated on and resulted in positive outcome on aluminium-polyurea composite plates under impact loading (Mohotti et al. 2013, 2014).

It can be observed that while this technique has been widely explored on various other structural systems, its feasibility on concrete structures is yet to be investigated in detail. This research endeavour was initiated to address this knowledge gap, by investigating the applicability of the polyurea coating technique to retrofit RC structures subjected to blast loads. Several RC panels, both un-retrofitted and polyurea retrofitted (with various coating thickness and location configurations) were tested under real blast loads. This paper reports the findings of the experimental investigation and finite element (FE) analysis on three of the tested panels

2 RESEARCH METHODOLOGY

The following sections provide the description on the methodology adopted in the experimental programme and FE analysis of this research.

2.1 *Experimental programme*

The comprehensive experimental blast trial programme for this study was undertaken in Vietnam in two stages, designated as Vietnam Trial 1 and Vietnam Trial 2, respectively. Several RC panels, both un-retrofitted and polyurea coated (with various coating thickness and location configurations) were tested experimentally during these trials. The 3 panels that will be discussed in this paper were tested during Vietnam Trial 2.

2.1.1 *Configuration of specimens*

All three panels were identical, with dimensions of 1700 (L) × 1000 (W) × 60 (T) mm, and were modified scaled models of an existing precast panel. Normal-strength concrete of 43 MPa strength were used in constructing the panels, and were reinforced in both longitudinal and transverse directions with one layer of 5 mm bars at 100 mm spacings, placed at the mid thickness of the specimen (Fig. 1). The nominal yield stress of the reinforcement was 500 MPa.

Of the 3 panels, one was an un-retrofitted control panel (designated as UR2), whereas the remaining two (PUB4 and PUTB4) were applied with polyurea coatings. The polyurea coatings were applied by using a spray-on procedure. Specimen PUB4 was subjected to a 4 mm polyurea coating on the bottom (non-blast

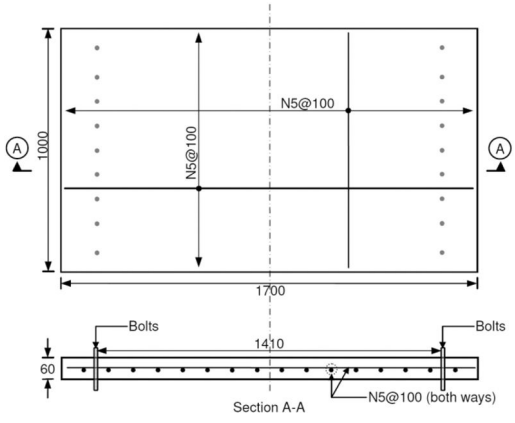

Figure 1. Geometry (in mm) and reinforcement details of the specimens (Raman et al., 2012).

Figure 2. Specimen fixing assemblage.

facing) face, whereas PUTB4 was coated on both its faces with 4 mm polyurea.

2.1.2 *Specimen fixing assemblage and instrumentations*

A special test bunker was constructed for the experimental programme using 100 MPa high-strength concrete. The overall dimensions of the bunker was 1900 (L) × 1000 (W) × 1780 (H) mm, with 200 mm thick RC wall and base. The wall and base of the bunker was reinforced with 10 mm reinforcement bars.

The test specimens were mounted onto the bunker using angled cleat and bolt connections. As shown in Figure 2, nine M20 bolts (vertical bolts) were used to connect the shorter span of the panel to a 100 × 100 × 10 mm steel cleat, while another nine M20 bolts (horizontal bolts) were used to attach first steel cleat to a second 150 × 70 × 10 mm cleat. This assemblage was then secured to the test bunker using three M22 bolts (Fig. 2).

The instrumentation utilised during the blast trials was mainly to measure the displacement of the panels and the crack formations. A custom designed mechanical displacement measurement system was

used to measure the displacement of the panels at their central mid-span. This system comprised of one threaded steel rod, one cubic clay block, and four hollow rectangular tubes, and was designed to capture the maximum downward, maximum upward and residual displacement of the test specimens. The measurement consistency of the system was calibrated with a LVDT during Vietnam Trial 1 (Pham, 2010).

Prior to the blast trials, 50 mm meshes were drawn on each of the panel to facilitate in the in-situ evaluation of the crack patterns and dimensions. The post-blast crack widths on the test specimens were measured with a EL35-2505 type crack detection pocket microscope.

2.1.3 *Application of blast load*

Ammonite type explosive material was used to impart the blast pressure onto the test specimens. All the panels tested during Vietnam Trial 2 were subjected to the detonation of 1.0 kg Ammonite charge with a stand-off distance of 1.0 m, where each panels were tested separately.

The TNT equivalency ratio for the Ammonite charge was established to be 1.0, based on comprehensive analysis of the findings on blast pressure parameters measured in Vietnam Trial 1 and Vietnam Trial 2. The detailed description on the comprehensive analysis undertaken to determine this value is available in Raman (2011).

2.2 *Finite Element (FE) analysis*

The identical RC panels were subsequently modelled and analysed by using the explicit solver of the non-linear FE code, LS-DYNA (2009).

2.2.1 *Elements and constitutive models*

Four main structural components were involved in the modelling exercise of the present study, namely concrete, steel reinforcement, the polyurea coatings and the support system. Existing material constitutive models available in the LS-DYNA library were adopted to simulate the behaviour of these four components. However, in order to simulate the behaviour of the materials more accurately, several spreadsheets were developed to compute the mechanical properties of the materials based on existing analytical equations developed by various researchers.

The concrete elements were modelled using eight-noded solid elements, by adopting two material models available in LS-DYNA, namely Mat_Concrete_ Damage_Rel3 (MAT_72R3) and Mat_Winfrith_Concrete (MAT_084). MAT_72R3 was identified based on comprehensive literature review and preliminary analysis, as the most suitable to simulate the behaviour of concrete material under extreme dynamic loadings more realistically and with sufficient accuracy. A significant part of the analysis in the present study was performed using this material card for concrete. Meanwhile, MAT_084 was used mainly to simulate crack formation on the RC panels.

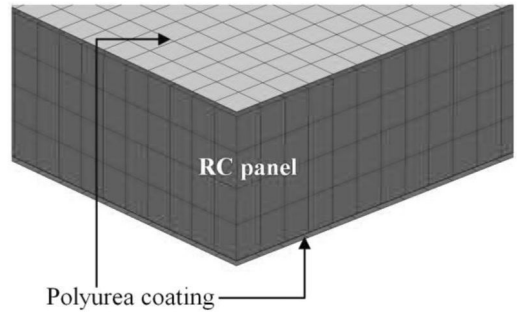

Figure 3. A section of the FE model of panel PUTB4 with the polyurea coatings.

The steel reinforcement (for RC panels modelled with MAT_72R3) was modelled as three-noded Hughes-Liu beam elements using Mat_ Piecewise_Linear_Plasticity (MAT_024). The high strain rate parameters for yield and ultimate stress of reinforcement as proposed by Malvar (1998) were incorporated into the material card. Meanwhile, for the RC panels modelled with MAT_084, the reinforcements were modelled by adopting the smeared approach using Mat Winfrith Concrete Reinforcement (MAT_085) in conjunction with MAT_084.

As for the support system of the RC panels, all the bolts were modelled as 3-noded Hughes-Liu beam elements using Mat_Plastic_Kinematic (MAT_003) material card, while the steel cleats and plates were modelled as 8-noded solid elements by using the same material card. The vertical section of the cleat was not included in the FE model.

The polyurea coatings were modelled using four-noded Belytschko-Tsay shell elements. Three material models were selected in the analysis to simulate the behaviour of the coatings, namely Mat_ Strain_Rate_Dependent_Plasticity (MAT_019), Mat_Piecewise_Linear_Plasticity (MAT_024) and Mat_Plasticity_Polymer (MAT_089). The comprehensive high strain rate parameters of the polyurea material, as discussed in Raman et al. (2013), were incorporated into material cards appropriately. Figure 3 illustrates a section of the FE model of retrofitted panel PUTB4 with the mesh of the polyurea coatings.

2.2.2 *Characteristics of polyurea sample at high strain rates*

One of the most important processes in ensuring that accurate simulations are obtained in the FE modelling exercise, is to incorporate the high strain rate parameters of the polyurea sample used in this study into the material cards. The high strain rate characteristics in tension of the polyurea sample used in this study have been investigated and discussed comprehensively in Raman et al. (2013). To summarise the findings of the high strain rate characteristics of the polyurea sample, Table 1 below presents its mechanical properties at quasi-static condition whereas Figure 4 presents

Table 1. Physical and quasi-static properties of polyurea (Raman et al., 2013).

Properties	Values
Density, ρ	950 kg/m^3
Modulus of elasticity, E	49.5 MPa
Tangent modulus, E_{tan}	1.9 MPa
Yield stress, σ_Y	5.5 MPa
Proportional (stress) limit, σ_{pl}	5.2 MPa
Stress at fracture, σ_f	10.7 MPa
Strain at fracture, ε_f	2.98

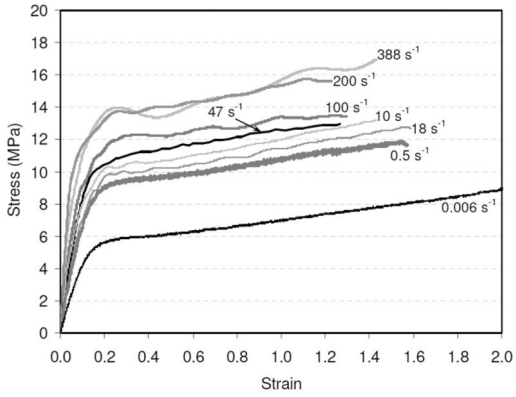

Figure 4. The engineering stress–strain curves of polyurea at various increasing strain rates (Raman et al., 2013).

the engineering stress-strain curves of the sample at various increasing strain rates.

2.2.3 *Contact options and boundary conditions*

The reinforcement was modelled as perfectly bonded with the concrete elements. On the other hand, the interface between the concrete panel and the steel cleat was defined using the Contact_Automatic_Surface_To_Surface algorithm (LS-DYNA, 2009). These two elements were only tied at the location (nodes) where the bolts were tied to the steel sections (Fig. 5). Meanwhile, the experimental findings (Section 3.2) have indicated that the polyurea coatings were bonded well with the concrete surface in all the retrofitted panels. To idealise this interaction, the contact surface of these two materials was modelled as perfectly bonded using the Contact_Tied_Surface_To_Surface algorithm, by defining two surface segments (LS-DYNA, 2009).

The support boundary conditions of the panel were idealised in the FE model by applying translational fixity to the two edge nodes located closest to the vertical section of the cleat (Fig. 5). Upon validating the findings from the FE analysis of panel UR2 with the experimental results (Fig. 8), the panel was optimised further by considering the boundary conditions and symmetrical planes of the panel. A quarter model of the RC panel was subsequently developed

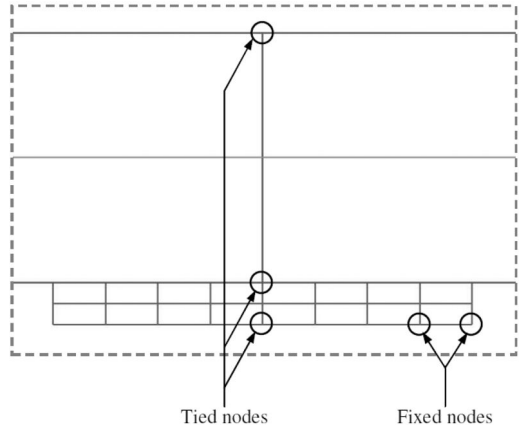

Figure 5. Support boundary conditions of the panels.

with the similar mesh fidelity, element formulation, and boundary conditions as the full model.

2.2.4 *Application of blast load*

The blast pressure application was automated in the FE analysis by using the LOAD_BLAST_ ENHANCED keyword (LS-DYNA, 2009), and the blast pressure was applied on the top surface of the panels.

3 RESULTS AND DISCUSSIONS

3.1 *Blast pressure and impulse*

As stated previously, all the panels tested during the blast trials were subjected to blast load resulting from the detonation 1.0 kg Ammonite charge with a stand-off distance of 1.0 m. Figure 6 presents the time history of reflected pressure and reflected impulse at angle of incidence, $\alpha = 0$, as computed from the CONWEP code (Hyde, 1992) with a TNT equivalence ratio of 1.0. The peak reflected pressures and the corresponding reflected impulse as computed from CONWEP were 4265 kPa and 559 kPa.ms, respectively.

3.2 *Experimental findings*

The centre-point of the detonation was located 1.0 m vertically from the panels. Upon the execution of the detonation, all the panels deflected downwards, then followed by an upward deflection and then finally settling to a permanent (downward in all cases) deflection. These displacements were recorded at the central mid-span of the panels using the mechanical displacement measurement system custom designed for these blast trials. The summary of maximum downward, upward and permanent displacements are summarised in Table 2.

From the results shown in Table 2, it can be observed that the application of polyurea coating on the bottom (non-blast facing) face (in PUB4) resulted in

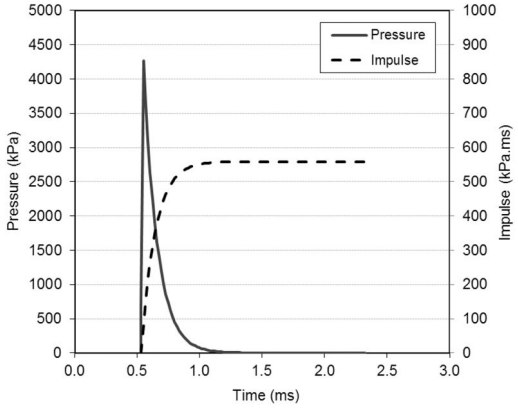

Figure 6. Time history of reflected pressure and impulse at angle of incidence of zero.

Table 2. Summary of maximum displacements of the test panels.

	Recorded Displacements		
Specimen ID	Maximum downward (mm)	Maximum upward (mm)	Permanent (Downward)
UR2	37.3	7.9	19.2
PUB4	33.3	9.4	14.3
PUTB4	22.5	5.0	7.7

a marginal reduction (11 %) in the maximum displacement recorded at the mid-span of the panel. On the other hand, the recorded mid-span displacement on panel PUTB4, which was sandwiched with 4 mm polyurea on both its faces, was almost 40 % lower than the maximum displacement recorded in the control panel. Based on these findings, it can be deduced that the placement of the coating on the blast facing face of the panel is more effective in reducing the maximum displacement of the panel.

The post-blast crack formation on the panels was measured using a EL35-2505 type crack detection pocket microscope. Table 3 summarises the details of the main crack formation recorded on the top and bottom faces of the un-retrofitted and polyurea coated specimens. It should be noted that only the measurement of the main crack (maximum width) formation on each panel is shown in Table 3. The comprehensive findings of all the crack formations on both surfaces of all panels are provided in Raman (2011).

From the results, it can be observed that the width of cracks were considerably decreased with the application of the protective coatings on the retrofitted panels. Another noteworthy finding observed was that there was no crack formation on the top surface of panel PUTB4. The main distinction between specimen PUTB4 and the other retrofitted panel was the presence of a polyurea layer on the blast-facing face of the

Table 3. Summarised details of crack profiles and formations on the specimens.

Specimen ID	Maximum average crack width (mm)	Crack length/ span (mm/mm)	Distance from centreline (north edge) (mm)
	Top surface		
UR2	1.65	1000/1000	45
PUB4	0.30	1000/1000	48
PUTB4	Nil	Nil	Nil
	Bottom surface		
UR2	1.19	1000/1000	−15
PUB4	0.31	1000/1000	−30
PUTB4	0.36	1000/1000	−255

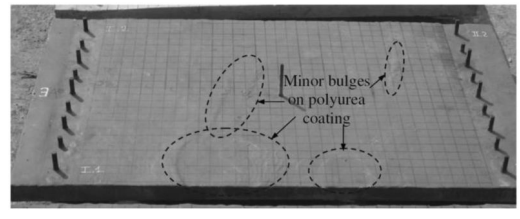

Figure 7. The appearance of the coating on the bottom surface of panel PUB4 (Raman et al., 2012).

panel. It is obvious that this layer played a major role in reducing the level of damage sustained by the structure as the blast pressure would need to pass through this layer prior to impacting the panel.

In both the retrofitted panels, the polyurea coating were generally undamaged after the blast event. The coatings were well bonded with the concrete surface and they had to be scrapped off from the surface on the concrete. The only type of minor damage observed were minor bulges at some locations of the coating layer, as shown in Figure 7 for the PUB4 panel.

3.3 *Finite Element (FE) analysis*

The explicit solver of the non-linear FE code, LS-DYNA (2009) was used to validate the findings of the experimental study. Extensive amounts of trial-and-error preliminary analysis were performed prior to arriving at a "final working" model to simulate the response of the un-retrofitted panel. As described previously, at the beginning, the FE model of the panel was developed as a full panel, prior to optimising it to a quarter model by observing its planes of symmetry. Figure 8 presents the mid-span displacement–time histories of the full FE model and the quarter FE model of the model developed with MAT_72R3. Meanwhile, Figure 9 illustrates the prediction of crack formation larger than 0.02 mm on the top and bottom face of panel UR2. It can be observed that this material model was able to reasonably predict the formation of flexural cracks on both the top and bottom surfaces of the panel.

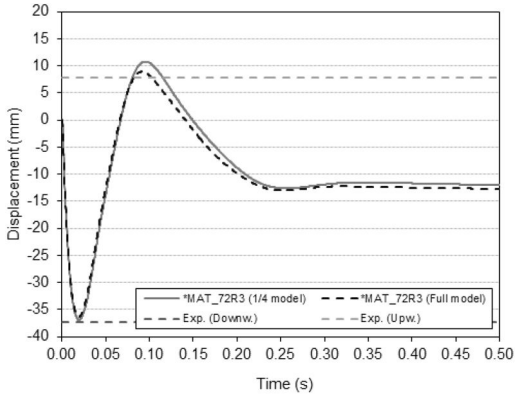

Figure 8. Comparison of mid-span displacement-time histories of the FE model of specimen UR2 (MAT_72R3) with the displacements recorded in the blast trial.

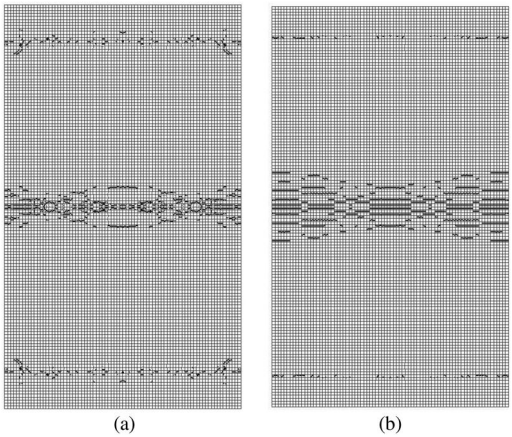

Figure 9. Simulated crack patterns on panel UR2 [Dimensions: 1700 (L) × 1000 (W) × 60 (T) mm] modelled with MAT_084, on the: (a) top surface, and (b) bottom surface.

As discussed previously, the polyurea material in this study was modelled using three different material models available in the LS-DYNA library, namely Mat_Strain_Rate_Dependent_Plasticity (MAT_019), Mat _ Piecewise _ Linear _ Plasticity (MAT _ 024) and Mat_ Plasticity_Polymer (MAT_089). MAT_019 allows for the implementation of comprehensive strain rate effects of the material by specifying individual curves for yield stress versus effective strain rate, and Young's modulus versus effective strain rate. MAT_024 on the other hand allows users to specify a series of true stress versus effective plastic strain curves at various strain rates. However, this material model only allows for a constant Young's modulus.

Meanwhile, MAT_089 is an elasto-plastic constitutive model that is suitable to simulate the response of polymeric materials, which can change their ductile state at the quasi-static regime to be more leathery-like and then brittle as the strain rates are amplified

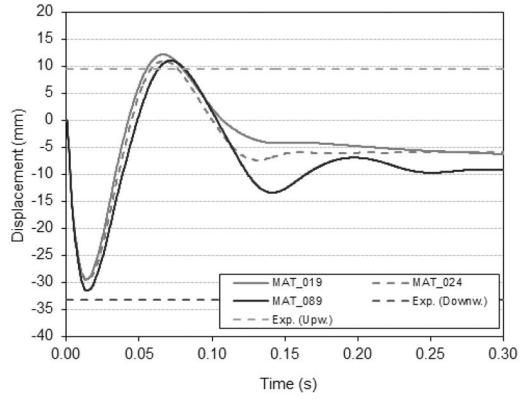

Figure 10. Mid-span displacement-time histories of the FE model of specimen PUB4.

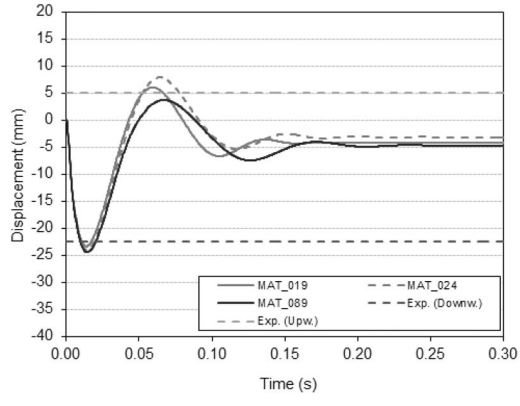

Figure 11. Mid-span displacement–time histories of the FE model of specimen PUTB4.

(Davidson et al., 2004b; LS-DYNA, 2009). This material card allows for the comprehensive implementation of strain rate effects, where the stress–strain curves of the material were defined by using total true stress–strain curves.

Figure 10 presents the mid-span displacement–time histories of the FE model of specimen PUB4. In comparing these curves, though they seem to be similar in the initial stages, they start to diverge minimally after attaining the maximum displacement, and further after the rebound. It can be observed that MAT_089 stands out among these material models, as it was able to predict the response of the panel, including its permanent displacement with significant accuracy.

A similar deduction can be made for the FE simulation of panel PUTB4 (Fig. 11), where MAT_089 provided the closest representation of the maximum downward, rebound and permanent displacement of the panel. The next closest prediction was provided by MAT_019. The main limitation of the other material models is their inability to capture the stiffening effect of polyurea at higher strain rates. The enhanced Young's modulus in polyurea at higher strain rates marginally reduces the disparity between the stiffness

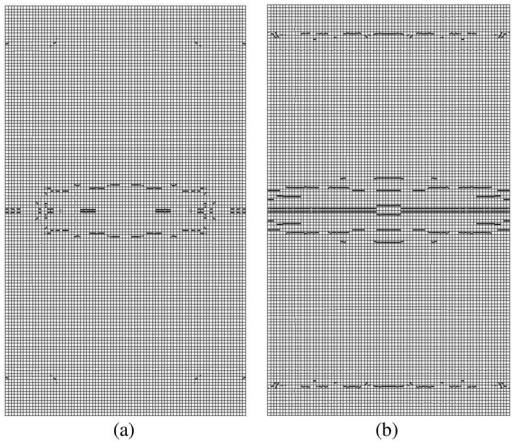

(a) (b)

Figure 12. Simulated crack patterns on panel PUTB4 [Dimensions: 1700 (L) × 1000 (W) × 60 (T) mm] as modelled with MAT_084 for concrete and MAT_089 for polyurea, on the: (a) top surface, and (b) bottom surface.

of the materials, though the Young's modulus of concrete is still significantly higher than polyurea. This contributes towards more accurate prediction of the panel's response when MAT_089 is used, compared to the other material models.

The simulation of crack formation on the top and bottom faces of panel PUTB4 as modelled with MAT_084 for concrete and MAT_089 for polyurea is illustrated in Figure 12. Although the experimental results indicated no crack formation on the top surface of the panel, minimal (hairline) crack formations were still observable in the FE model. The cracks predicted on the bottom surface matched reasonably well in comparison with the experimental observation.

One of the main advantages of using elastomeric polymers such as polyurea for retrofitting application of concrete structures under blast effects is the ability of the coating layer in shielding the concrete debris and fragments propelled during the blast. This is made possible by the high elongation capacity of the polyurea coating and its ability in holding the structure without collapsing.

4 CONCLUSIONS

This study was undertaken to evaluate the potential of using an elastomeric polymer (i.e. polyurea) to develop an innovative structural retrofitting scheme to enhance the resistance of RC structural elements to blast effects. This paper presented the findings from the experimental investigation and FE analysis performed as part of this research to analyse the behaviour of polyurea coated RC panels under blast effects.

The following conclusions can be drawn based on the findings of this study:

1. The polyurea coating contributed positively in terms of reducing the deflection of the panels.
2. The application of the polyurea coating also contributed significantly in reducing the post-blast crack formation on the retrofitted panels.
3. The findings of the FE analysis compared reasonably well with the findings of the experimental programme.
4. Mat_Plasticity_Polymer (MAT_089) indicated to be the most suitable to model the properties and behaviour of polyurea, by considering the comprehensive strain rate parameters of the material.
5. The results from both experimental FE analysis suggest that while the polymer coating technique does enhance the resistance of the RC panels to the applied blast load, a higher level of protection is provided when the protective coating is applied on the blast-facing face of the structure.

ACKNOWLEDGEMENT

The authors duly acknowledge the contribution of Ministry of Education, Malaysia in providing the necessary funding for this research and supporting this publication through the FRGS Grant Scheme (FRGS/1/2012/TK03/UKM/03/1).

REFERENCES

Ackland, K., Anderson, C. & Ngo, T.D. 2013. Deformation of polyurea-coated steel plates under localised blast loading. *International Journal of Impact Engineering* 51: 13–22.

Amini, M.R., Isaacs, J.B. & Nemat-Nasser, S. 2010a. Experimental investigation of response of monolithic and bilayer plates to impulsive loads. *International Journal of Impact Engineering* 37(1): 82–89.

Amini, M.R., Simon, J. & Nemat-Nasser, S. 2010b. Numerical modeling of effect of polyurea on response of steel plates to impulsive loads in direct pressure-pulse experiments. *Mechanics of Materials* 42(6): 615–627.

Bahei-El-Din, Y.A. & Dvorak, G.J. 2007a. Wave propagation and dispersion in sandwich plates subjected to blast loads. *Mechanics of Advanced Materials and Structures* 14(6): 465 – 475.

Bahei-El-Din, Y.A. & Dvorak, G.J. 2007b. Behavior of sandwich plates reinforced with polyurethane/polyurea interlayers under blast loads. *Journal of Sandwich Structures and Materials* 9(3): 261–281.

Baylot, J.T., Bullock, B., Slawson, T.R. & Woodson, S.C. 2005. Blast response of lightly attached concrete masonry unit walls. *Journal of Structural Engineering* 131(8): pp. 1186–1193.

Chen, C., Linzell, D.G., Alpman, E. & Long, L.N. 2008. Effectiveness of advanced coating systems for mitigating blast effects on steel components.. *Proc. 10*th *International Conference on Structures under Shock and Impact*. Algarve, Portugal, 14–16 May 2008.

Davidson, J.S., Porter, J.R., Dinan, R.J., Hammons, M.I. & Connell, J.D. 2004a. Explosive testing of polymer retrofit masonry walls. Journal of Performance of Constructed Facilities 18(2): 100–106.

Davidson, J.S., Sudame, S. & Dinan, R.J. 2004b. Development of computational models and input sensitivity study of polymer reinforced concrete masonry walls subjected

to blast. (Report No. AFRL-ML-TY-TR-2006-4522): Air Force Research Laboratory, Tyndall AFB, FL, USA.

Davidson, J.S., Fisher, J.W., Hammons, M.I., Porter, J.R. & Dinan, R.J. 2005. Failure mechanisms of polymer-reinforced concrete masonry walls subjected to blast. *Journal of Structural Engineering* 131(8): 1194–1205.

Grujicic, M., Bell, W.C., Pandurangan, B. & He, T. Blast-wave impact-mitigation capability of polyurea when used as helmet suspension-pad material. *Materials & Design* 31(9): 4050–65.

Hyde, D.W. 1992. CONWEP. *Conventional Weapons Effects Program*: US Army Engineer Waterways Experiment Station, Vicksburg, MS.

Knox, K.J., Hammons, M.I., Lewis, T.T. & Porter, J.R. 2000. Polymer materials for structural retrofit. (Report). Florida: Force Protection Branch, Air Expeditionary Forces Technology Division, Air Force Research Laboratory, Tyndall AFB.

LeBlanc, J., Gardner, N. & Shukla, A. 2013. Effect of polyurea coatings on the response of curved E-glass/vinyl ester composite panels to underwater explosive loading. *Composites Part B: Engineering* 44(1): 565–574.

LS-DYNA. 2009. *LS-DYNA Keyword User's Manual, Version 971 / Release 4*. Livermore, California, US: Livermore Software Technology Corporation (LSTC).

Mohotti, D., Ngo, T., Mendis, P. & Raman, S.N. 2013. Polyurea coated composite aluminium plates subjected to high velocity projectile impact. *Materials & Design* 52: 1–16.

Mohotti, D., Ngo, T., Raman, S.N, Ali, M. & Mendis, P. 2014. Plastic deformation of polyurea coated composite aluminium plates subjected to low velocity impact. *Materials & Design* 56: 696–713.

Pham, T.T. 2010. Behaviour of reinforced concrete panels and their fixing assemblies subject to blast loading. *PhD Thesis.* Department of Civil and Environmental Engineering, The University of Melbourne, Australia.

Raman, S.N. 2011. Polymeric coatings for enhanced protection of reinforced concrete structures from the effects of blast. *PhD Thesis*. Department of Civil and Environmental Engineering, The University of Melbourne, Australia.

Raman, S.N., Pham, T., Ngo, T. & Mendis, P. 2012. Experimental investigation on the behaviour of RC panels retrofitted with polymer coatings under blast effects. *Proc. 2nd International Conference on Sustainable Built Environment*: 14 pgs. Kandy, Sri Lanka, 14–16 December 2012.

Raman, S.N., Ngo, T., Lu, J. & Mendis, P. 2013. Experimental investigation on the tensile behavior of polyurea at high strain rates. *Materials & Design* 50: 124–129.

Tekalur, S.A., Shukla, A. & Shivakumar, K. 2008. Blast resistance of polyurea based layered composite materials. Composite Structures 84(3): 271–281.

Concrete Solutions – Grantham et al. (Eds)
© 2014 Taylor & Francis Group, London, ISBN 978-1-138-02708-4

Modeling of continuous composite girders partially reinforced with CFRP

A. Sharif & M. Samaaneh
King Fahd University of Petroleum and Minerals, Dhahran, Saudi Arabia

ABSTRACT: The loss of composite action at the negative moment region for continuous composite girders reduces its strength and stiffness. This paper presents numerical evaluation of maintaining the composite action of continuous composite girders by bonding Carbon Fiber Reinforced Polymer (CFRP) sheet to the top of concrete slab at the negative moment region. Finite element modeling is used to evaluate the performance of the continuous composite girder with CFRP up to failure. The ultimate strength of the girder is evaluated analytically using plastic analysis approach. The analytical results confirmed the strength and stiffness improvement by bonding CFRP to the top of concrete slab at the negative moment region. The girder strength is directly proportional to CFRP thickness. Premature failure of CFRP sheet delamination occurred when its length is cut short of the inflection points within the negative moment region. Analytical solution conservatively estimated the ultimate capacity of the girder.

1 INTRODUCTION

The continuous composite steel-concrete girders composed of cast in place concrete slab and steel girders are widely used in bridges and buildings. The concrete slab at the negative moment region is ignored and the steel girders either act alone or compositely with the slab reinforcement. Such loss of the composite action at the negative moment region for continuous composite girders reduces its strength and stiffness. Basu et al (1987) partially prestressed a concrete slab at the negative moment region to maintain the composite action. Chen et al (2009) used external prestressing for continuous composite girder to overcome loss of composite action at the negative moment region. Both studies have resulted in strength and stiffness improvement of the continuous composite girder. The recent development of carbon fiber reinforced polymer (CFRP) sheet offered an attractive solution for strengthening structures. Several researchers have used CFRP to improve strength of concrete and steel structures.

This paper numerically evaluates the effect of bonding CFRP sheet to the top of concrete slab at the negative moment region for continuous composite girders. Finite element modeling is done for a two span continuous composite girder using the commercial software ANSYS. The modeled girder without CFRP is verified with the experimental values tested by Chen et al (2009). However, experimental values of continuous composite girder with CFRP are not yet available. The thickness and length of CFRP are varied to evaluate their effect of the girder behavior. Plastic analysis of the continuous composite girder with CFRP is used to evaluate to evaluate the ultimate capacity of the girder.

2 MODELED GIRDER

The two span continuous composite girder tested by Chen et al (2009) is used for modeling. The girder dimensions and loading are shown in figure 1. The steel section dimensions given in table 1 are selected to eliminate local buckling, lateral torsional buckling and effect of concentrated load. The bonding of CFRP sheet to the top of concrete slab at the negative moment region is shown in figure 2 and its properties given in table 2. CFRP used is a unidirectional mid strength carbon fibers bonded to concrete slab by epoxy adhesive with properties given in table 3. The stress-strain diagrams for concrete, steel, and CFRP are shown in figures 3 to 5. Thickness and length variation of CFRP are given in table 4. The smallest thickness used represents the lowest commercial available thickness.

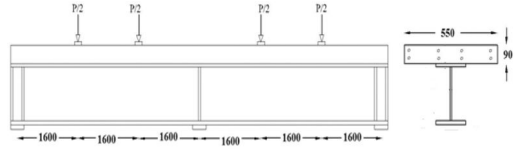

Figure 1. Dimension of modeled two span continuous composite girder.

Table 1. Steel section properties.

Top flange thickness	Bottom flange thickness	Flanges width	Web thickness	Web depth
10 mm	14 mm	120 mm	6 mm	255 mm

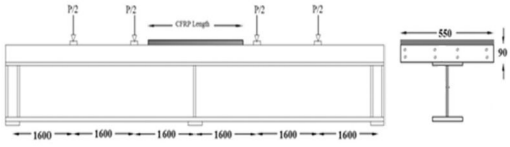

Figure 2. CFRP bonded to top of concrete slab at negative moment region.

Table 2. Properties of CFRP.

Epoxy Property	Value
Fiber Orientation	0°
Fiber density	1.8 gm/cm^3
Tensile strength	3800 N/mm^2
Tensile modulus	63 KN/mm^2
Elongation at break	1.64%

Table 3. Properties of epoxy adhesive.

Epoxy Property	Value
Tensile strength	30 N/mm^2
Shear strength	22 N/mm^2
Flexural modulus	3800 N/mm^2
Tensile modulus	4500 N/mm^2
Elongation at break	0.9%

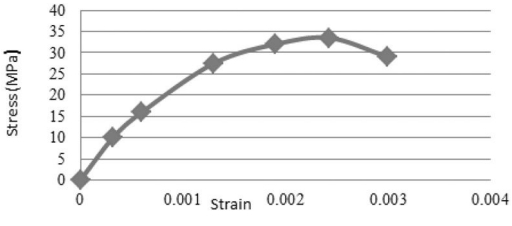

Figure 3. Stress-strain diagram of concrete.

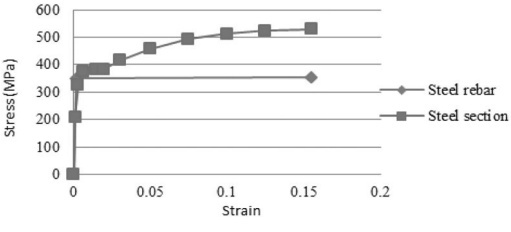

Figure 4. Stress-strain diagram of steel.

The length of 2360 mm is extended up to the inflection points. CFRP sheet are cut shorter and longer with respect to the inflection points as 1560 mm and 3150 mm respectively.

3 FINITE ELEMENT MODELING

A non-linear finite element model is developed using the commercial software ANSYS. The concrete slab and steel section are considered fully composite in the model. The steel section is modeled using three dimensional eight nodes element SOLID45 capable of simulating plasticity and large strain. The steel reinforcement is modeled using unidirectional element LINK8 capable of simulating plasticity and large deflection. The concrete slab is modeled using eight nodes element SOLID65 capable of cracking in tension and crushing in compression. CFRP and adhesive material are modeled using eight nodes element SOLID46 capable of modeling different material layers.

The steel is modeled as a nonlinear isotropic material. The concrete in compression is described with initial linear-elastic up to 30% of its compressive strength, after which it is represented as a nonlinear isotropic material using William and Warnke model to define its failure. The concrete in tension is initially linear elastic followed by a softening approach after occurrence of cracking. An overview of the assembled and meshed model is depicted in figure 6.

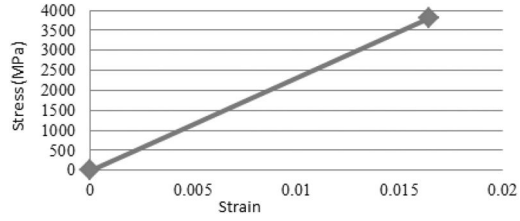

Figure 5. Stress-strain diagram of CFRP.

Table 4. Lengths and thicknesses of CFRP for modeled girders.

Girder	CFRP thickness (mm)	CFRP length (mm)
GR	–	–
G1	0.15	2360
G2	0.25	2360
G3	0.5	2360
G4	1.00	2360
G5	3.00	2360
G6	0.25	3150
G7	0.25	1560

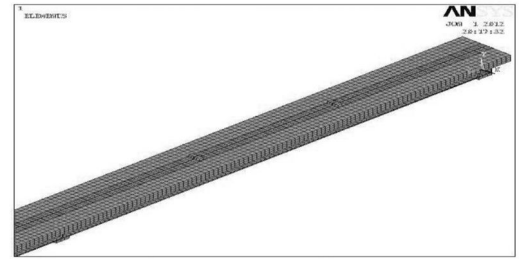

Figure 6. Overview of the assembled and meshed model.

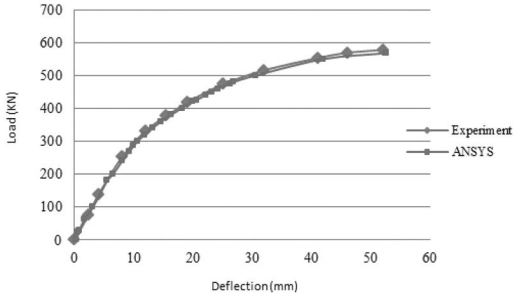

Figure 7. Load vs. deflection at mid-span.

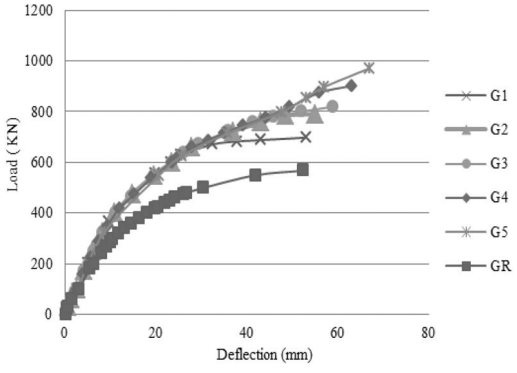

Figure 8. Load vs. deflection at mid-span for different thicknesses.

4 NUMERICAL RESULTS

4.1 *Verification of the model*

The finite element results for girder GR without CFRP is validated against the experimental results measured by Chen et al (2009). The experimental and numerical values for the load versus mid-span deflection are shown in figure 7. The numerical results are in a very good agreement with the experimental ones. The numerical results for girders with CFRP could not be verified since no experimental results are yet available.

4.2 *Thickness of CFRP*

The numerical results for girders with different CFRP thicknesses are compared with girder GR as shown in figure 8. The effect of bonding CFRP to top of concrete slab has improved strength and stiffness of girders G1 to G5 as compared to GR. The strength improvement of the girders is directly proportional to CFRP thickness.

The stress and strain distributions over the interior support for the full plastic stress of steel section and ultimate capacity of girder G1 are shown in figures 9 and 10 respectively. CFRP stress at ultimate capacity of girder G1 is only 11.3% of CFRP ultimate stress. Incremental increase of CFRP stress between the full plastic stress of steel section and the ultimate capacity of the girder are given in table 5. Such incremental increase of CFRP stress is small and not affected

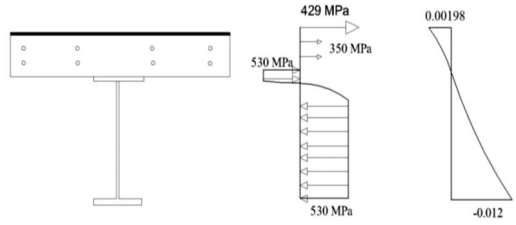

Figure 9. Stress and strain distribution over the interior support at full plastic stress.

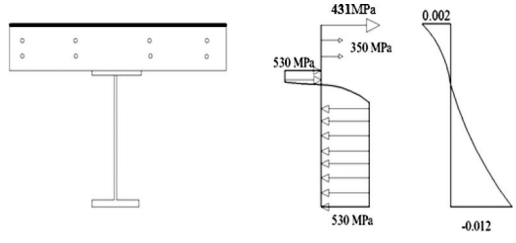

Figure 10. Stress and strain distributions over the interior support at ultimate load.

Table 5. Incremental increase of CFRP stress (MPa).

	Level of Loading				
Girder	G1	G2	G3	G4	G5
Full Plastic stress of steel section	429	408	297	249	206
Ultimate capacity of girder	431	410	300	255	217
Incremental increase of CFRP stress	2	2	3	6	11

Table 6. Ratio of section capacity at negative to positive moment regions.

Girder	G1	G2	G3	G4	G5
α	0.75	0.76	0.78	0.8	0.85

by thickness variation. It can be concluded that the first plastic hinge formed over the interior support is defined by reaching full plastic stress distribution of the steel section. The ratio α of section capacity (plastic moment) at the negative moment region to that at the positive moment region is not greatly affected by CFRP thickness variation as given in table 6.

4.3 *Length of CFRP*

CFRP length taken up to and beyond the inflection points of the negative moment region has no effect on

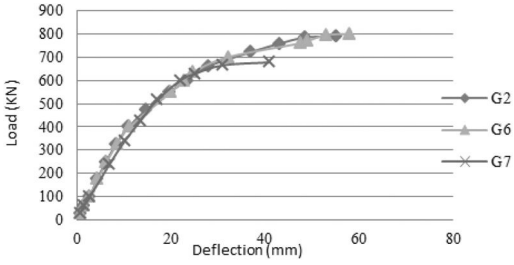

Figure 11. Effect of CFRP length.

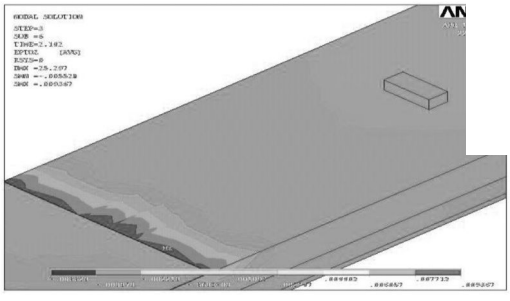

Figure 12. Exceeding maximum tensile stress of adhesive material.

the girder strength as shown for girder G2 and G6 in figure 11. However for length cut short of the inflection points within the negative moment region leads to premature failure as shown in figure 11 for girder G7. The shear and tensile stresses of the adhesive material at both ends of CFRP sheet are exceeded as shown in figure 12 leading to its separation from concrete slab and consequently loss of composite action.

5 PLASTIC ANALYSIS

The ultimate capacity of the continuous composite girder with CFRP bonded to top of concrete slab at negative moment region is evaluated based on plastic analysis approach.

5.1 *Assumptions*

- Full composite action between CFRP sheet – concrete slab and concrete slab-steel section.
- Steel behaves as elastic-plastic material.
- Concrete under tension is neglected.
- Concrete compression strain is limited to 0.003.
- Geometrical instabilities of steel section are eliminated to ensure sufficient rotation over the interior support to develop the girder failure mechanism.
- The ultimate moment over the interior support (i.e. first plastic hinge) is assumed constant till the formation of the second plastic hinge at the positive moment region. This assumption is confirmed by the numerical results indicating negligible incremental increase of CFRP stress.

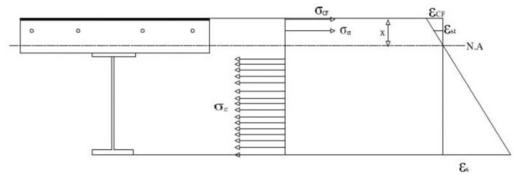

Figure 13. Stress and strain distributions at ultimate moment. Virtual work method.

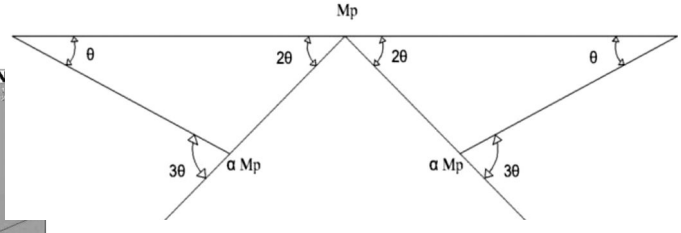

Figure 14a. First possible failure mechanism.

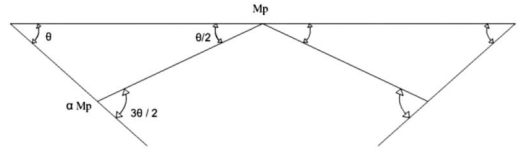

Figure 14b. Second possible failure mechanism.

5.2 *Section ultimate moment capacity*

At the positive moment region, the ultimate moment of the section is evaluated based on stress equilibrium and strain compatibility which are well documented in literature [10]. At the negative moment region, the stress and strain distributions at ultimate moment are shown in figure 13. The section moment capacity is evaluated through iterative process since both CFRP strain and neutral axis (N.A) location are unknown. CFRP strain is first assumed and the N.A location is varied to satisfy equilibrium. The assumed CFRP strain should be selected to insure yielding of top flange of steel section and concrete should be limited to crushing strain.

The collapse mechanism of the girder is evaluated by virtual work method. The two possible failure mechanisms are shown in figures 14.a and 14.b The internal work and external work due to virtual rotation θ for the controlling failure mechanism shown in figure 14.b are:

$$\text{Internal work} = (3\alpha+1)(\text{Mp}\ \theta/2) \quad (1)$$

$$\text{External work} = \text{PL}\ (\theta/2) \quad (2)$$

Mp is the ultimate moment capacity at the interior support and α is the ratio of ultimate moment at negative and positive moment region.

Equating equations 5.1 and 5.2 to evaluate the ultimate load, then:

$$\text{P} = (2+6\alpha)\ \text{Mp/L} \quad (3)$$

The ultimate load P from the plastic analysis of girder G1 is 530 KN as compared to numerical results of 698 KN. The conservative result of the plastic analysis is due to the assumption made by neglecting the strain hardening of the steel section and tensile strength of concrete.

6 CONCLUSION

The three dimensional finite element model demonstrated that bonding of CFRP sheet to top of concrete slab at the negative moment region improved the continuous composite girder strength and stiffness. CFRP thickness is directly proportional to strength and ductility of the girder. Length of CFRP should be extended beyond the inflection points to eliminate premature failure. Plastic analysis conservatively estimated the collapse load.

ACKNOWLEDGEMENT

The authors appreciate the support of this work provided by King Fahd University of Petroleum and Minerals.

REFERENCES

Ansys Release, "12.1, ANSYS," Inc., PA, 2010.

Basu, P. K. Sharif, A. M. and Ahmed N. U., "Partially Prestressed Continuous Composite Beams. I," Journal of Structural Engineering, vol. 113, pp. 1909–1925, 1987.

Chen, S. Wang X., and Jia Y., "A comparative study of continuous steel-concrete composite beams prestressed with external tendons: Experimental investigation," Journal of Constructional Steel Research, vol. 65, pp. 1480–1489, 2009.

Galal K.,. ElDin H. M. S, and Tirca L., "Flexural Performance of Steel Girders Retrofitted Using CFRP Materials," Journal of Composites for Construction, vol. 1, p. 212, 2011.

Khudeira S., "Strengthening of Deteriorated Concrete Bridge Girders Using an External Posttensioning System," Practice Periodical on Structural Design and Construction, vol. 15, p. 242, 2010.

Liu X., Silva P., and Nanni A., "Rehabilitation of steel bridge members with FRP composite materials," strain, vol. 11, p. 13, 2001.

Miller T. C., Chajes M. J., Mertz D. R., and. Hastings J. N, "Strengthening of a steel bridge girder using CFRP plates," Journal of bridge engineering, vol. 6, p. 514, 2001.

Salmon C. G., "Steel Structures: Design And Behavior Author: Charles G. Salmon, John E. Johnson, Faris A. Malhas, Publisher," 2008.

Tavakkolizadeh M., "Strengthening of steel-concrete composite girders using carbon fiber reinforced polymers sheets," Journal of Structural Engineering-ASCE, vol. 129, 2003.

Wolanski A. J., "Flexural behavior of reinforced and prestressed concrete beams using finite element analysis," Faculty of the Graduate School, Marquette University, 2004.

This page intentionally left blank

Concrete Solutions – Grantham et al. (Eds)
© 2014 Taylor & Francis Group, London, ISBN 978-1-138-02708-4

Experimental study on shear strengthening of R.C. beams using FRP repair techniques

M.S. Tughar
Department of Civil Engineering, Faculty of Engineering, Al Mergeb University, Libya

ABSTRACT: This paper presents results of an extensive experimental investigation of strengthening of reinforced concrete beams pre-damaged in shear using fiber reinforced polymer repair techniques.Typically carbon or glass fiber sheets externally bonded to the bottom and sides of RC beams were used for the shear strengthening of RC beams. Another technique, previously studied by the author, is to strengthen RC beams in shear by drilling holes through the depth of the beams and then embedding FRP rods in these holes. In this paper a comparison of these two techniques in strengthening and repairing RC beams is presented. Six beams were tested; a control beam without strengthening, two beams strengthened using externally bonded CFRP (Carbon Fiber Reinforced Polymer) sheets and two beams strengthened using embedded CFRP rods. For each technique, one specimen was preloaded beyond the formation of the first crack before strengthening, while the other was not preloaded in order to study the effects of preloading. The last specimen was the control specimen which was retrofitted after being loaded to failure in shear then retested again after repair. Research findings have shown the use of FRP sheets for strengthening damaged reinforced concrete beams is an efficient technique that can maintain structural integrity and enhance the behavior of such beams.

1 INTRODUCTION

Generally, reinforced concrete beams fail in either flexural or shear failure mode. In the case of flexural failure mode, the beam gives enough warning in the form of cracks and large deflection. However, brittle shear failure mode takes place in the case of beams having little amount of shear reinforcement. For this reason, codes of practice recommend that reinforced concrete beams should have enough shear reinforcement in order to ensure the occurrence of ductile flexural failure rather than a brittle shear failure (Morsy, 2012, Tughar, 2013 & Others). Existing reinforced concrete R.C structures may require strengthening for a variety of reasons. For example, it is often desirable to increase the loading to which a structure is subjected, as when a bridge must carry increased traffic or when a building must be used for purposes other than those for which it was originally designed. It may also be necessary to strengthen old RC structures as a result of new code requirements or because of structural damage due to environmental stresses.

Repairing and strengthening of reinforcement concrete beams to increase their strength against shear forces is a common task in construction society. Traditional methods are mainly used such as strengthening the concrete beams and repair to increase the resistance to shear forces. This can be a major problem in local conditions as a result of increasing loads due to changing the use of such buildings, poor design or weather conditions and a tough environment which can decrease building resistance. However, the use of traditional methods for beam strengthening like increasing reinforcement or section enlargement, have the disadvantages of high cost and increased beam section.

Practically, repairing or strengthening such beams by adding internal shear reinforcement is very difficult. It was found, however, that such strengthening may be easily achieved externally by bonding either steel plates or fiber reinforced polymers (FRP) to the beam surface using suitable epoxy resins. Experimental investigations reported and cited elsewhere in the paper indicated a basic difference in the mode of failure for externally strengthened beams than that in the case of beams having internal stirrups. In the case of beams reinforced with internal stirrups, the shape and position of those stirrups placed inside the concrete ensure sufficient anchorage, thus failure is controlled by the tensile strength of stirrups. However, in contrast, in the case of externally strengthened beams, the failure is always controlled by the loss of anchorage in the form of de-bonding of strengthening materials (Morsy, 2012). Different materials were used through previous experimental studies for the external strengthening and retrofitting of RC beams deficient in shear. These materials were bonded to the external surface of the beam using suitable epoxies. These studies included the application of either traditional steel plates or fiber

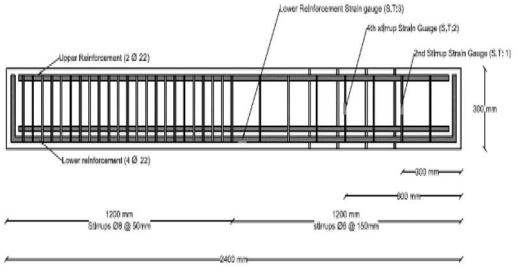

Figure 1. Reinforcement details of the tested RC beams.

composites (Tughar, 2013). Different types of fiber composites were used such as glass fiber and carbon fiber.

2 EXPERIMENTAL WORK

In this study, six RC beam specimens were tested. The specimens included three repaired beams; two strengthened beams and one control beam without strengthening. All specimens had a cross section of 160 mm × 300 mm, and a total length of 2.40 meters. The specimens were designed to fail in shear at one side (The weak side). For flexure reinforcement four 22 mm deformed bars arranged in two layers were used as bottom reinforcement with 3.16% reinforcement ratio, while two 22 mm deformed bars were used as top reinforcement. The bottom and top reinforcement used deformed bars with a steel grade of 360/520. The shear reinforcement for the strong side consisted of 10 mm closed-type stirrups spaced at 50 mm, while the shear reinforcement for the weak side consisted of 6 mm bars with a spacing of 150 mm. Figure 1 shows the reinforcement details of the beams.

In this research two different techniques for repairing or strengthening RC beams against shear were used. The first technique used Internally Embedded Reinforcement (I.E.R.). In this technique 12 mm CFRP bars were embedded in circular holes drilled through the depth of the beams. All the bars had a spacing of 150 mm. Figures 2, 3 show the preparation work for the repaired specimens using I.E.R. technique.

In the second technique, CFRP sheets were externally used to repair or strengthen the beams in shear. The CFRP sheets were externally bonded (E.B.) to the sides and bottom of the beam forming a U shaped wrap around three sides of the beam. A single layer of 60 mm wide sheets with a spacing of 150 mm was used to strengthen these specimens. Figure 4 shows the strengthening of EB specimen. The configuration of the specimens was chosen so all specimens would have an equal amount of material.

For each technique, one specimen was preloaded beyond the formation of the first crack before strengthening while the other was not preloaded in order to study the effects of preloading. The last specimen was the control specimen which was retrofitted after being

Figure 2. Drilling of holes for specimen IER.

Figure 3. Installing of reinforcement in specimen IER.

Figure 4. Strengthening of specimen EB.

loaded to failure in shear then retested again after it was repaired using the I.E.R. technique.

The preloaded specimens were given the designation “R”, while the specimens that were strengthened without preloading were given the designation “S”. These designations are followed by designations E.B. or I.E.R. indicating the technique used for strengthening. The numbers following indicate the load level prior to strengthening. Table 1 provides a summary of the details of the specimens used in this program.

Table 1. Specimen details.

Specimen	Type of Strengthening /Repair	Loading before repair	Dimensions of material	Spacing
Control	—	—	None	—
R-I.E.R. -100%	Internally embedded reinforcement	100% P_f *	12 mm Bars	150 mm
R-I.E.R. -70%	Internally embedded reinforcement	70% P_f *	12 mm Bars	150 mm
R-E.B -70%	Externally Bonded Sheets	70% P_f *	60 mm wide sheets (One layer)	150 mm
S-I.E.R.	Internally embedded reinforcement	0.0	12 mm Bars	150 mm
S-E.B	Externally Bonded Sheets	0.0	60 mm wide sheets (One layer)	150 mm

*P_f : Failure Load

2.1 *Material properties*

The concrete strength for all specimens was 30 MPa based on testing 100 mm cubes, except specimen R-I.E.R-70%, which had a concrete strength of 20 MPa.

The steel bars used for the flexure reinforcement and the stirrups on the strong side had a nominal yield strength of 360 MPa, while the bars used for reinforcing the weak side had a nominal yield strength of 240 MPa. The sheets were supplied by Sika under the commercial name (Sikawrap Hex-230C). The thickness of the CFRP sheets was 0.13 mm. The tensile strength and modulus of elasticity of CFRP sheets were 3.5 and 230 GPa, respectively as provided by the product data sheet. Two-component epoxy adhesive (Sikadur 330), supplied by the same company, was mixed according to the proportions recommended by the manufacturer to bond the CFRP sheets to the target surfaces of the tested beams. 12 mm V-Rod CFRP bars manufactured by Pultral Inc. were used for IER specimen, Sikadur 31 CF epoxy adhesive was used for fixing the internally rods inside the holes. The cracks in the control beam was patched after testing to failure using cementitious materials as shown in Figure 5. Afterwards the beam was repaired using the I.E.R technique, and then retested.

2.2 *Test set up and instrumentation*

All specimens were tested under four point bending. The span of the beams was 2.0 m and the distance between the loads was 0.6 m. The shear span for both sides was 0.7 m which is larger than 2.5 times the depth of the beam to avoid the effects of arching action. Three dial gauges were used to measure the deflection at mid-span, and both loading points. As train gauge was

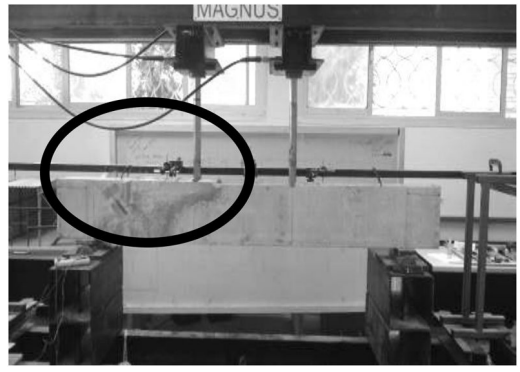

Figure 5. Repaired specimen.

mounted on the second stirrups after the support at the weak side. Long strain gauges were also mounted on the concrete surface at a 45° angle. In addition strain gauges were also mounted on the second sheet and second bar after the support for specimens EB and IER respectively. Loading was applied manually through a hydraulic pump to two hydraulic jacks at increments of 10 kN, at which time readings from the dial gauges and strains were manually recorded. Figure 6 shows the loading set-up for tested beams & tested specimen.

3 TEST RESULTS

All specimens failed in shear and all of the strengthened beams failed due to debonding. Since the specimens had different concrete strengths, and the beams were lightly reinforced in shear at the weak side, the main factor contributing to the shear strength of the beam will be the concrete strength. The Load Level is calculated from Equation 1 to for the purpose of comparing the specimens' failure load according to the specimens' concrete strength "f_{cu}" values explained in the experimental program (Tughar, 2013 & et al). The Equations are percentage ratios of the actual load on a beam to the fcu value of the same beam divided by the ratio of the failure load on the control beam to the control beam value.

$$Failure\ load\ level = \left(\frac{P_{if}/f_{cui}}{P_{cf}/f_{cuc}}\right) * 100 \quad (1)$$

Where:
P_{if}: Failure load on selected beam
f_{cui}: Characteristic compressive strength of concrete after 28 day of selected beam
P_{cf}: Failure load of control beam and
f_{cuc}: Characteristic compressive strength of concrete after 28 day of control beam.

Table 2 presents a summary of the test results (loads are for one jack only). The following sections provide a description of the specimens' behavior during testing.

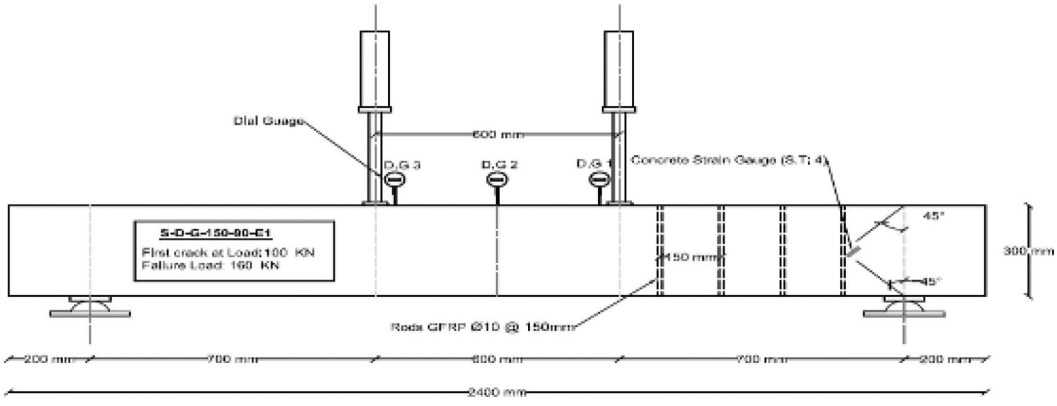

Figure 6. Test set up and instrumentation.

Table 2. Failure load level.

Specimen	Cracking Load* (kN)	Failure Load* (kN)	Load Level (%)	Deflection at max. load (mm)
Control	70	100	100	10
R-I.E.R. -100%	–	80	80	6.4
R-I.E.R. -70%	70	80	120	6.4
R-E.B.R. -70%	84	130	130	10.4
S-I.E.R.	70	138	138	12
S-E.B.R.	78	130	130	14

*Loads are for one jack only

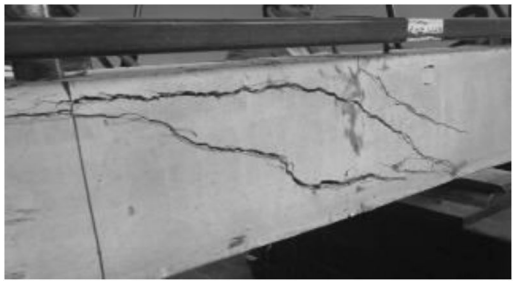

Figure 7. Crack patterns of control specimen.

3.1 *Control specimen*

For the control specimen, the first visible crack appeared at a load of about 70 kN. The crack extended from the point of loading to the support in the weak side. As loading progressed, the crack widened, and another major crack appeared in addition to several minor ones as seen in Figure 7. The specimen failed at a load of 100 kN (for one jack only). Although the failure was brittle it was less sudden than in the case of all other specimens.

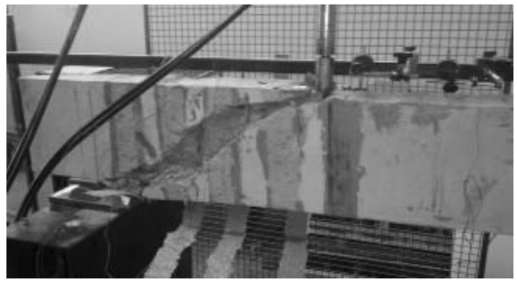

Figure 8. Crack patterns of specimen S-EBR.

3.2 *Strengthened specimen using externally bonded reinforcement (S-E.B.R)*

The first visible crack appeared at a load of 78 kN between the sheets. As loading progressed, cracks widened then the specimen finally failed in a brittle manner at a load of 130 kN after debonding started at the second sheet after the support. Then with further loading, the failure occurred progressively one sheet at a time.

Post failure examination of the specimen showed a similar crack pattern to the control specimen as seen in Figure 8. It was noticed that the bonding failure took place in the concrete thin layer adjacent to the sheet, not in the epoxy adhesive.

3.3 *Strengthened specimen using internally embedded reinforcement (S-I.E.R)*

For the internally embedded reinforcement specimen, the first visible crack appeared at a load of 70 kN at the loading point at a steeper angle than the case of the control specimen and even when compared with the specimen strengthened with externally bonded sheets. This can be related to the crack arresting action of the embedded bars which altered the cracking pattern compared to the control specimen. Several other cracks appeared and widened as the loading progressed, although at steeper angle as seen in Figure 9. Failure occurred suddenly at a load of 138 kN due

Figure 9. Crack patterns of specimen S-IER.

Figure 10. Debonded CFRP bar.

to the de-bonding at the thin layer of concrete adhered to the CFRP bars. Some de-bonding occurred between the inner core of the CFRP bars and the outer coating of the bar as shown in figure 10. This can represent a weak point for the FRP bars as this outer coating is added to the bar to enhance its bonding properties with the surrounding concrete specimen.

This specimen was then reloaded until failure. The first visible crack was noticed at a load level around 84% of the maximum load of the control specimen which is significantly higher than first cracking load (70%). This can be due to the repairing action with the cementitious material that hardened the concrete. Then the failure took place at load level of 130% of the maximum load of the control specimen when the sheets started to fail in de-bonding mode with the concrete. This made the failure takes place in a more sudden and brittle fashion than the control R.C beam specimen. This show that the EB repairing technique is a promising technique to be used in repairing RC beams cracked or damaged in shear.

3.4 *Repaired specimen after 70% preloading using internally embedded reinforcement (R-I.E.R.-70%)*

For the RC beam specimen (R-IER-70%) which was loaded to the first visible crack (around 70% of the failure load of the control specimen) then unloaded and repaired using the IER technique, when reloaded, the first visible crack appeared at load level about 70% of the maximum load of the control beam. After the first crack took place, several cracks had spread from the subjected load on the repaired side to the support. As loading progressed, the cracks widened until failure occurred at load level 120% of the maximum load of the control beam. This result shows that the IER

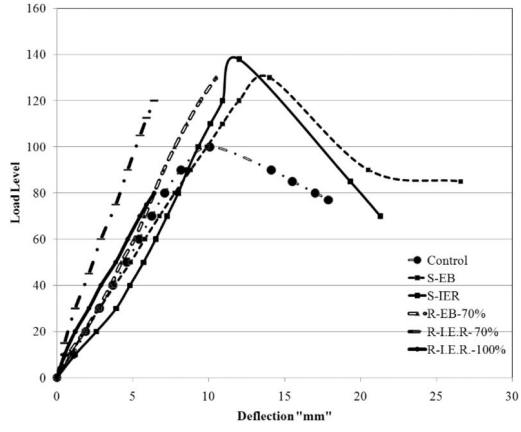

Figure 11. Deflection behavior of the different beams.

technique is an efficient and effective technique that can be used for repairing RC beam specimens cracked in shear.

3.5 *Repaired specimen after failure (R-I.E.R.-100%)*

After the failure of the control specimen, the loading was continued beyond the failure (maximum) load decreasing till about 70% of the maximum load which caused a lot of damage to the beam itself and more than one major visible crack could be noticed very easily by visual inspection. After unloading, and since the beam suffered from intensive damage, repair works to this beam were conducted included using cementitious material as shown in Figure 5. Afterwards the failed control beam was repaired using the I.E.R method. The control beam was reinforced with four CFRP rods150 mm apart located starting at 35 cm from the edge of the weak side in the beam. After retrofitting, beams were reloaded to failure. The specimen showed a more brittle failure than the control specimen but it only reached an 80% level of the control beam maximum load. This may be due to the extensive damage that took place during the first loading.

3.6 *Deflection behavior*

Figure 11 shows the mid-span deflection behavior of all specimens. From this figure it can be concluded that the load-deflection behavior of all repaired beams don't have a post peak behavior and all fail in a brittle manner while all the strengthened beams and the control beam failed in a more ductile fashion and showed a post peak or post failure behavior, this may be due to the fact that the strengthened beams act as single composite unit from the beginning of the loading till failure. Consequently, the load is distributed between the concrete, stirrups, and the strengthening FRP bars or sheets leading to a behavior of a more ductile fashion. On the other hand, when repairing a cracked beam, most of the load is transferred directly to

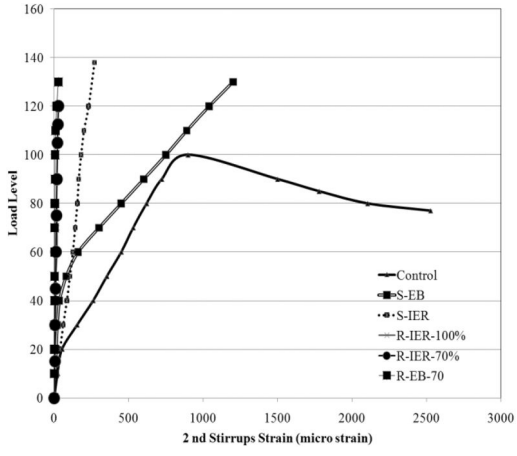

Figure 12. Second stirrups strain behavior.

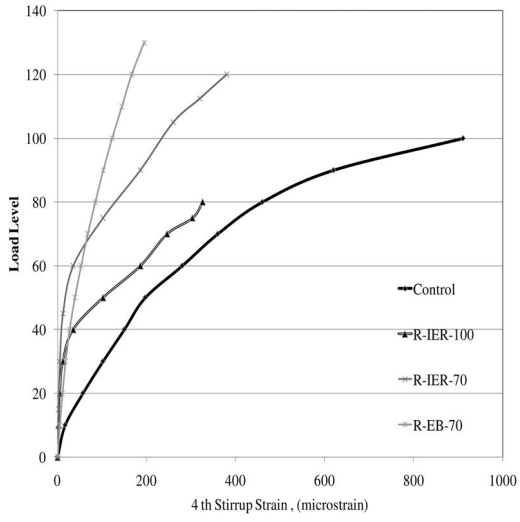

Figure 13. Fourth stirrups strain behavior.

the strengthening FRP sheet, or bars leading to sudden failure due to de-bonding between FRP and concrete.

Also it can be shown that a slight increase in stiffness of all repaired beams is noticed when compared with the control beam or the strengthened beams. This might be due to the major role played by the strengthened FRP bars or sheets in carrying the load in the pre-cracking stage which had a bigger role in the slight increase of stiffness.

3.7 *Strain in steel stirrups*

Figure 12 shows the load versus strain in the second stirrup after the support for the control beam, compared with the strain behavior of the second stirrups for all strengthened beams and the repaired beams. It is clearly shown that all the repaired beams exerted lower strain than the strengthened beams or the control beam. Based on this fact, it can be concluded that the stirrups in the repaired beam carried lower load than the stirrups in both control or strengthened beams. This may be due to the same conclusion drawn from the deflection behavior that the FRP carried most of the load in the repaired beams leading to a much lower load in the stirrups. Also it can be related to that the repaired beams are retrofitted after cracking and while unloaded to zero level. Therefore when reloading takes place, most of the load is picked up by the new repaired materials (FRP rods or sheets) leaving the stirrups with lower levels of loads. This can explain the more brittle nature of the failure pattern for the repaired beams as when failure takes place due to the de-bonding of the FRP from the concrete, there is no other part to pick up the load.

Figure 13 shows the load vs. strain in the fourth stirrup after the support. By comparing the strain behavior of the second stirrup with the fourth stirrup, it can be found that the strain in the fourth stirrups in all beams is much higher than the second stirrups in repaired beam, this may be related to the position of the strain gauge that meet the crack propagation.

4 DISCUSSION OF RESULTS

4.1 *Effect of pre-loading level for the repaired beams*

Comparing the repaired beams (R-I.E.R.-70%) and (R-I.E.R. – 100) pre-damaged under two different pre-loading levels 70% and 100% of the failure load respectively, it was found that the repairing technique using I.E.R. is an effective technique for repairing beams especially if the beams are repaired after the appearance of the first visible crack (which corresponds in this research to 70% from the failure load). Also it is noticed that when repairing beams just after first crack formation (loading up to 70% of the ultimate load) exceeds the control beam (without strengthening) by 20% strength gain.

On the other hand, when repairing the control specimen after being fully damaged and after continuing damage till the dropped load reached around 70% of its ultimate load, it was seen that the beam could not sustain a load more than 80% of its original ultimate load before loading (at the first loading). This shows the importance of the quick actions for making the repair decision for the cracked beams not to wait until great damage has taken place.

4.2 *Comments on strengthening versus methods of repair*

Generally, by comparing the results of all specimens, it can be seen that repaired and strengthened specimens using both techniques (IER and EB) showed almost comparable results. Also, these beams showed almost the same mode of failure which is de-bonding in the epoxy layer which attached the CFRP to the concrete substrate.

Generally, it was noticed that the RC beam specimens repaired using both techniques (IER and EB) gained a slight increase in the stiffness compared with the strengthened specimens and even the control specimens. On the other hand, the strengthened RC beam specimens showed a more ductile fashion of failure than the repaired specimens based on the post peak behavior of the strengthened specimens which showed a gradual decrease in load. Conversely, the repaired RC beam specimens suffered a more sudden failure and sudden drop in the load after the peak load.

Also, comparing the IER repairing technique with the EB one, it can be seen that both techniques showed similar failure loads and also almost the same mode of failure. This indicates that both techniques are valid and appropriate for using as a promising repair technique especially since both techniques showed 20–30% higher failure load than the control RC beam specimen. Also their results were nearly comparable with strengthened RC beam specimens.

5 FINAL COMMENTS

Preliminary results from this on-going study has led to the following concluding points &comments :

- Repairing the beams for shear using both internally embedded reinforcement and externally bonded methods is an effective technique for repairing pre-damaged RC beams in shear.
- When using the IER technique, it is recommended to start the repairing action at minimum damage to the RC beams to gain the best strengthening for the beams.
- The strengthened RC beam specimens failed in a more ductile fashion and showed a superior post peak or post failure behavior than the repaired RC beam specimens.
- Using the internally embedded strengthening technique can provide almost the same effect as the externally bonded technique.
- This study demonstrates the efficiency of the techniques for maintaining the structural integrity and to enhance the behavior of such concrete beams incorporating these strengthening materials.

REFERENCES

Case Studies of Rehabilitation, Repair, Retrofitting, and Strengthening of Structures. Structural Engineering Documents, 12. *IABSE Publications,* Zurich, pp. 180, (2010).

Chaallal O., M. J. Nollet, and D. Perraton, , Shear Strengthening of RC Beams by Externally Bonded Side CFRP Strips", *Journal of Composite for Construction, ASCE,* 2 (2), pp. 111–113 (1998).

Li A., J. Assih, and Y. Delmas., Shear Strengthening of RC Beams with Externally Bonded CFRP Sheets , *Journal of Structural Engineering, ASCE,* 127 (4), pp. 374–380 (2001).

Morsy, A., N. El Ashkar , K. Helmi. A Comparative Study for Shear Strengthening Techniques of Reinforced Concrete Beams Using FRP, *Proc. Of 4th International Conference Concrete Solutions*, Germany, pp. 278–294 , 25th. – 29th. Sept., (2011).

Nabil H. E, Morsy A., Morsy M., and Karim M. Helmi. FRP Repair of RC-Beams Predamged in Shear, *Proc. Of 14th. International Conference on Structural Faults & Repair-2012*, Edinburgh, UK, pp. 72, (2012).

Norris T., H. Saadatmanesh, and M. R. Ehsani. Shear and Flexural Strengthening of RC Beams with Carbon Fiber Sheets, *Journal of Structural Engineering, ASCE,* 123 (7), pp. 903–911 (1997).

Sharif, A., G. J. Al-Sulaimani, I. A. Basunbul, M. H. Baluch, and M. Husain. Strengthening of Shear damaged RC Beams by External Bonding of Steel Plates, *Magazine of Concrete Research,* 47 (173), pp. 329–334 (1994).

Spadea G., R. N. Swamy, F. Bencardino. Strength and Ductility of RC Beams Repaired with Bonded CFRP Laminates, *Journal, of Bridge Engineering, ASCE,* 6 (5), (2001).

Swamy N. R., P. Mukhopadhyaya, and C. J. Lynsdale. Strengthening for Shear of RC Beams by External Plate Bonding, *The Structural Engineer,* 77 (12), pp. 19–30 (1999).

Tughar S. M., Fiber Reinforced Polymer Repair Techniques for Reinforced Concrete Beams Pre-Damaged in Shear, *Proc. Of The International Congress on Materials & Structural Stability, CMSS2013,* Rabat, Morocco, pp. 139, 27th. – 30th. Nov. 2013. Tughar S. M., Experimental Study on Shear Capacity of RC T-Beams strengthened by CFR Plastic, *Proc. Of 14th. International Conference on Structural Faults & Repair-2012,* 3*rd*. –5th. July, Edinburgh, U.K., pp. 69, (2012).

Tughar S. M., Experimental Investigation on Strengthening of Concrete Using Basalt Fibres, *Proc. Of 7th. International Conference on Structural and Geotechnical Engineering*, Alexandria, Egypt, pp. MT 1–2, (2010).

This page intentionally left blank

Concrete Solutions – Grantham et al. (Eds)
© 2014 Taylor & Francis Group, London, ISBN 978-1-138-02708-4

Response of 4 × 4 bays, 15 storey RC building frames with and without external steel bracings and internal steel bracings

A.S.V. Venkatesh & B.M.R. Apoorva
Department of Civil Engineering, PESIT, Bangalore, Karnataka, India

C.G. Narayana
Head Department of Civil Engineering, SJCIT, Chickaballapur, Karnataka, India

ABSTRACT: Many existing Reinforced Concrete (RC) buildings need retrofit to overcome deficiencies to resist seismic loads. The use of steel bracing systems for strengthening or retrofitting seismically inadequate reinforced concrete frames is a viable solution for enhancing earthquake resistance. The present study is concerned with the structural response of a 4 × 4 bays, 15 storeys RC building on incorporating steel bracings externally or internally and masonry infill as diagonal strut at the center of the middle frame of the building up to 10 stories as Lateral Load Resisting System (LLRS). The models analyzed consist of one basic moment resisting RC frame (bare frame) with square column of size 900 × 900 mm and others include the same bare frame, but provided with External Steel Bracing at the centre of the middle frame of the building, Internal steel bracing at the centre of the building and masonry infill at the centre frame of the building as LLRS. The detail investigations are carried out in zone V of seismic zones of India, considering primary loads (dead, live and seismic loads) and their combinations. The results obtained from the linear static analysis are thoroughly investigated for maximum values of joint displacements, support reactions, beam forces and truss forces. The results indicate better resistance to lateral loads in the presence of masonry infill provided at centre frame of the building up to 10 stories.

Keywords: earthquake loads, external steel bracings, internal steel bracings, masonry infill, linear static analysis, RC frame.

1 INTRODUCTION

Existing structures need to be evaluated and strengthened based on evaluation criteria before an earthquake. Earthquake damage depends on many parameters, including intensity, duration and frequency content of ground motion, geologic and soil condition, quality of construction, etc.

Earthquakes are one of the great damaging natural hazards. In the last three decades, the study of the variation effect on the seismic response of civil structures advanced significantly. They can cause large loss of life and property and disrupts essential services such as water supply, sewerage systems, communication and power, transport etc. They not only destroy villages, towns and cities but the aftermath leads to destabilization of the economic and social structure of the nation.

On the basis of the mode of deformation of the Lateral Load Resisting Systems of tall buildings when subjected to lateral loading, they may be distinguished as Frames, Tubular systems, Infill, Shear walls and Steel bracings

Masonry Infill and shear walls are commonly used to increase the in-plane shear resistance of RC-framed buildings subjected to earthquake loading. Steel bracing in RC frames has recently been shown to be a suitable alternative to shear walls. Different bracing methods fall into two categories, namely External Bracing and Internal bracing. In the external bracing method, existing buildings are retrofitted by attaching a local or global steel bracing system to the exterior frames. In the internal bracing method, the buildings are retrofitted by positioning a bracing system inside the individual bays of the RC frames.

2 THE PRESENT INVESTIGATION

It is observed that for commercial purpose and depending upon the local guidelines 15 storey buildings are common in practice. Thus, the present investigation concernes with a detailed 3D study of the results of an analysis of a fifteen storey Moment Resisting Frame having four bays along X and four bays along Z, provided with External Steel Bracing or Internal Steel Bracing or masonry infill (idealized as a diagonal compressive strut), as Lateral Load Resisting Systems (LLRS), in comparison with identical Moment Resisting Bare Frame (without any special LLRS features) subjected to gravity load, seismic load and their combinations. The study is hoped to be helpful

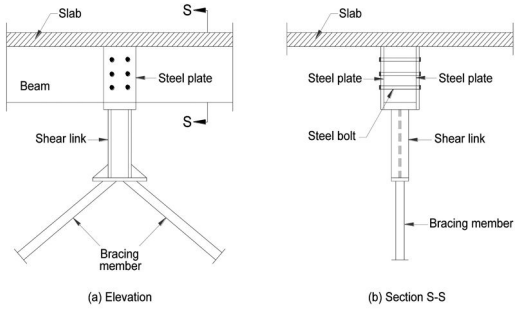

Figure 1. Connection details of a vertical link.

during retrofitting of such structures which are initially designed only for gravity loads and found unsafe for seismic loads and any combination of loads.

3 DETAILS OF THE PROBLEM CHOSEN

3.1 *Method of analysis*

Earthquake response analysis corresponds to stimulate the behavior of a structure subjected to earthquake ground motion by the means of a mathematical model of the structure. A 3D model has independent displacements at each node and thus can stimulate the behavior of a structure.

The present study undertaken deals with Linear Static Method of Analysis or Equivalent Static Method of analysis of 3D frames that can be used for regular structure with limited height.

3.2 *Modeling of the structure*

For the present 3D study, the STAAD.Pro software package is used.

3.3 *Connection details*

- The external steel bracings are connected at the junction with the beams, column and ground as carried out by S.V.Venkatesh et al.
- In case of internal steel bracings, the connection at the beam centre is realized through a vertical steel shear link as shown in Figure 1 and proposed by Ghobarah A. The formula for calculating the length of a cantilever link is as given in Eqs. (1)

$$e_{crit} = \frac{2b_f t_f}{t_w} \quad (1)$$

Where, b_f and t_f are the width and thickness of the flange and t_w is the web thickness of a wide flange section link. This arrangement is considered as the concrete beams are incapable of performing as a ductile link for the steel bracing system that is inserted in the frame bays. In the present work, steel bracing section considered is ISMB250, whose section properties are $b_f = 125$ mm, $t_f = 12.5$ mm and $t_w = 6.9$ mm. Therefore, $e_{crit} = 450$ mm $= 0.45$ m.

- The masonry infill is considered as a diagonal strut as per FEMA 273.

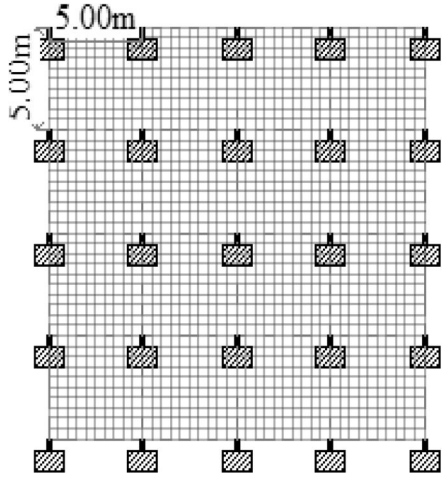

Figure 2a. Plan at plinth level for bare frame.

3.4 *Bare frame*

The plan consists of four bays in both X and Z directions of span 5.0 m as shown in figure 2.a. The typical fifteen storey building has each storey height of 3.0 m along Y direction as shown in figure 2.b. (BF).

- *Beam cross-sections*
  Plinth beam size:
  P1 (Along both directions): 300 mm × 300 mm
  Floor beam size:
  B1 (Along both directions): 300 mm × 500 mm
- *Column size:*
  Square column: 900 mm × 900 mm
- *Slab Thickness*: 175 mm
- *Masonry Wall thickness*: 230 mm
- *Steel Section*: ISMB250

3.5 *Frames with special features of LLRS*

- Basic 3D frame as in 3.4, with External Steel Bracings at middle frame of the building up to 10 storeys as shown in Figures 3.a., 3.b. (10ESBM).
- Basic 3D frame as in 3.4, with Internal Steel Bracings at middle frame of the building up to 10 storeys as shown in Figure 4.a., 4.b. (10ISBM).
- Basic 3D frame as in 3.4, with masonry infill at the centre frame of the building up to 10 storeys as shown in Figure 5.a., 5.b. (10MDSM).

3.6 *Seismic zones*

Zone V, the very severe seismic zone of India as per IS code, was considered in the analysis, with a zone factor (Z) of 0.36.

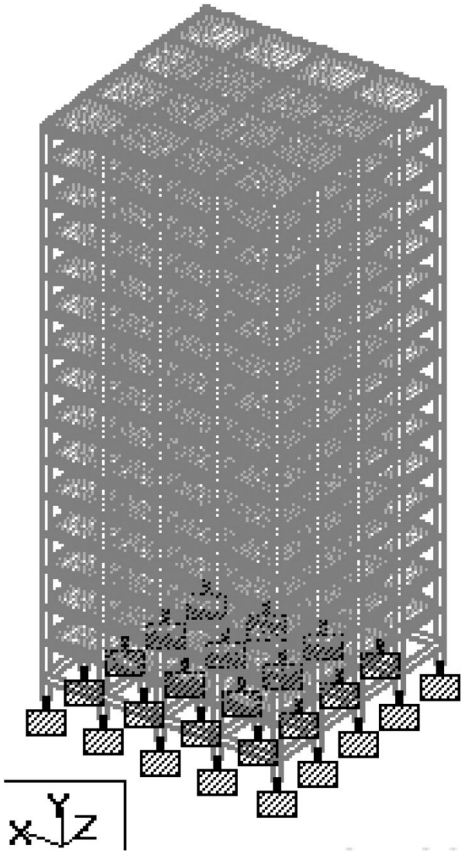

Figure 2b. Elevation for bare frame.

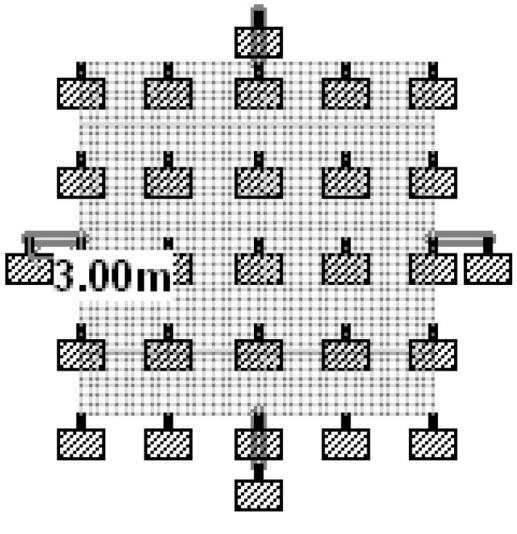

Figure 3a. Plan at plinth level for 10ESBM.

3.7 *Types of primary loads and load combinations*

The structural systems are subjected to 3 types of Primary Load Cases as stipulated by the Indian Standard

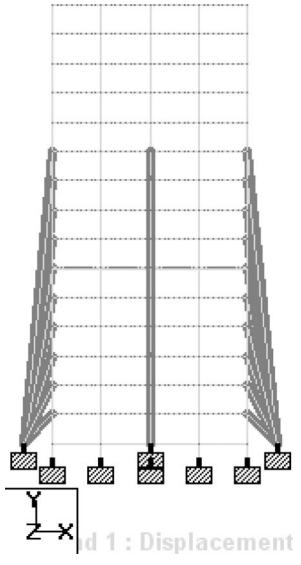

Figure 3b. Elevation for 10ESBM.

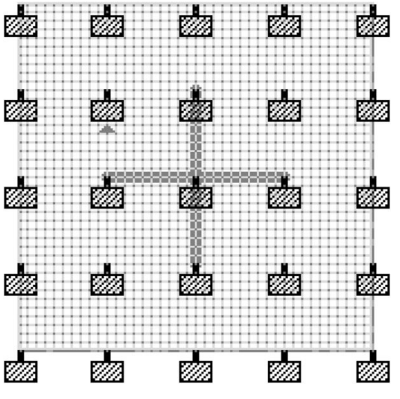

Figure 4a. Plan at plinth level for 10ISBM.

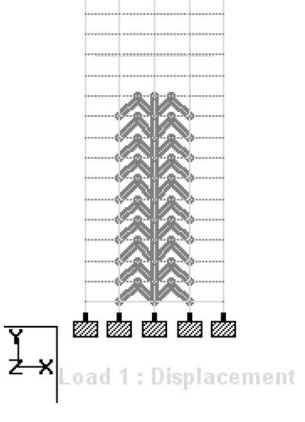

Figure 4b. Elevation for 10ISBM.

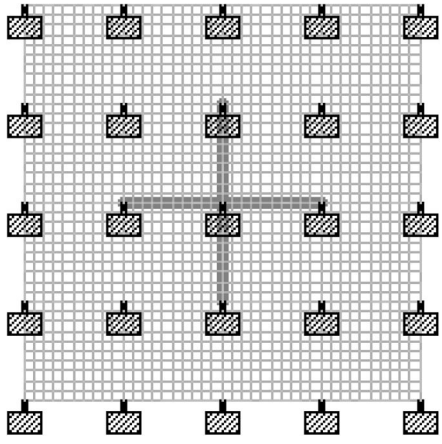

Figure 5a. Plan at plinth level for 10MDSM.

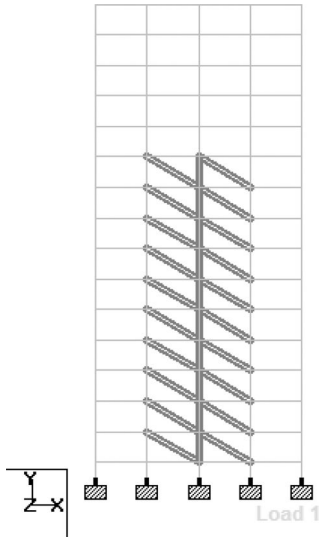

Figure 5b. Elevation for 10MDSM.

Code of Practice for Structural safety of Buildings, loading standards IS 875-1987 (Part I). These are:

1. Dead Load case (Vertical or Gravity load), denoted as "DL"
2. Live Load case (Vertical or Gravity load), denoted as "LL"
3. Seismic Load in X-direction (Lateral or Earthquake load), denoted as "ELx"
4. Seismic Load in Z-direction (Lateral or Earthquake load), denoted as "ELz"

The structural systems were subjected to 13 types of Load Combinations as per provisions of IS 1893 (Part 1): 2002, Clause 6.3.1 they are:-

5. 1.5(DL + LL)
6. 1.2(DL + LL + ELx)
7. 1.2(DL + LL − ELx)
8. 1.2(DL + LL + ELz)
9. 1.2(DL + LL − ELz)
10. 1.5(DL + ELx)
11. 1.5(DL − ELx)
12. 1.5(DL + ELz)
13. 1.5(DL − ELz)
14. (0.9DL + 1.5ELx)
15. (0.9DL − 1.5ELx)
16. (0.9DL + 1.5ELz)
17. (0.9DL − 1.5ELz)

Table 1. Lateral loads at each storey level for 15 storey's building in zone V kN.

	X-Axis	
Floor	End frame	Mid frame
1	0.63	0.93
2	2.51	3.72
3	5.65	8.37
4	10.05	14.88
5	15.70	23.26
6	22.60	33.49
7	30.77	45.58
8	40.18	59.53
9	50.86	75.35
10	62.79	93.02
11	75.97	112.56
12	90.42	133.95
13	106.11	157.21
14	123.07	182.33
15	104.79	158.62

The gravity loads (dead and live load) on the frame have been calculated based on the provisions of the Indian Standard Code of Practice for Structural safety of Buildings, loading standards IS 875 (Part I & Part II): 1987. The dead load consists of the self-weight of structural elements and wall load.

The live load considered is as adopted for medium office, hospital or hostel building (i.e., 4 kN/m^2). The equilibrium static method of analysis is adopted for the calculation of the lateral load at each floor level as per IS: 1893 (part I): 2002 and are given in Table 1.

3.8 *Physical properties considered for present analysis*

- Density of the brick walls = 18.85 kN/m^3
- 'E' for reinforced concrete = 2.24 × 10^7 kN/m^2
- Density of concrete = 25 kN/m^3
- 'E' for brick wall = 4.2 × 10^6 kN/m^2

4 RESULTS AND DISCUSSION

The results obtained by "Equivalent Static Lateral force Method" of analysis for all models are the storey drift, joint displacements (X and Z directions), support reactions, beam end forces (axial force, shear force, and bending moment) and truss forces. Of these, the important results relevant to the structural member under consideration, are taken for discussion. The

Table 2. 15 Storey building – zone V, maximum storey drift along both x & z direction.

Height	BF	10ESBM	10ISBM	10MDSM
1.5	0	0	0	0
0	0.19	0.08	0.26	0.13
3	1.51	0.84	1.91	0.96
6	3.69	2.22	4.20	2.23
9	6.41	4.10	6.64	3.76
12	9.46	6.39	9.03	5.43
15	12.70	8.95	11.33	7.16
18	16.01	11.68	13.59	8.92
21	19.30	14.50	15.83	10.69
24	22.49	17.32	18.10	12.44
27	25.52	20.06	20.41	14.17
30	28.34	22.66	22.72	15.93
33	30.89	25.06	24.94	17.74
36	33.16	27.19	26.97	19.49
39	35.13	29.05	28.76	21.08
42	36.80	30.63	30.31	22.48
45	38.25	31.99	31.66	23.71

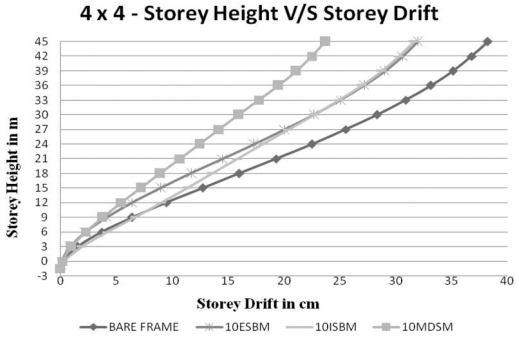

Figure 6a. Storey height V/S storey drift.

results are presented in Tables 2 to 6 and Figures 6 to 14, which represent the maximum values of forces obtained, among the 3 primary load cases and 13 load combinations considered. Since the frame considered is symmetrical, the results along only one horizontal direction are represented.

4.1 *Maximum storey drift in frames (Max.X)*

From Table 2. and Figure 6.a. it is observed that the maximum joint displacement at each level increases as the height of the building or storey increases and the maximum displacements in X-direction occur at the top storey. So, only the top storey displacements in X direction are taken for further discussions. It is seen that the displacement (δx) at each level are maximum for bare frame and all the LLRS considered reduce the displacement. The minimum displacement at each storey in the case of frames with masonry infill are at the central frame.

From Table 3. And Figure 6.b. it is observed that the displacement reduces due to the introduction of LLRS.

Table 3. 15 Storey building – zone V, maximum joint displacement.

Max. X in mm

Frame type	Node	L/C	X-Trans
BF	373	11	382.81
10ESBM	373	10	320.22
10ISBM	60	10	320.35
10MDSM	373	14	237.30

Max. Y in mm

Frame type	Node	L/C	Y-Trans
BF	22989	5	−20.89
10ESBM	22584	5	−20.85
10ISBM	22989	5	−20.68
10MDSM	22989	5	−20.94

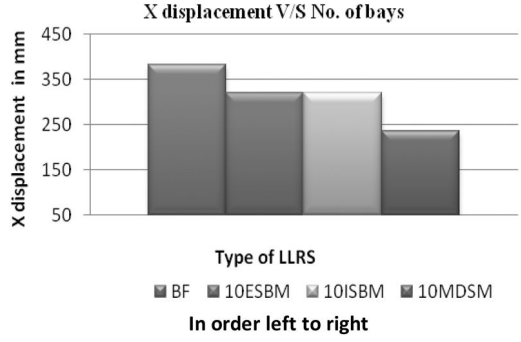

Figure 6b. X displacement V/S type of LLRS.

The efficiency of LLRS graded in its decreasing order based on δx value is as follows 10MDSM,10ESBM, 10ISBM and Bare frame.

4.2 *Maximum support reactions (Fx, Fy, Fz, Mx, My and Mz)*

The results obtained from the analysis corresponding to Maximum support reactions, namely forces in X and Y directions (Fx, Fy) and bending moments in Z directions (number of bays in both X & Z directions are same hence only Fx, Fy and Mz are considered, My not being considered since the values are negligible), among all the 3 load cases (seismic and non seismic) and 13 load combinations considered, maximum values are presented in Table 4 and Figure 6 to 8, which are bar charts indicating the support reaction values versus type of LLRS.

- The maximum support reaction Fx and moment Mz occurs when the seismic load combination is applied.
- The Maximum Support reaction Fy occurs when the non-seismic load case 5 i.e 1.5(DL + LL) is applied in the case of the frames with steel bracing.

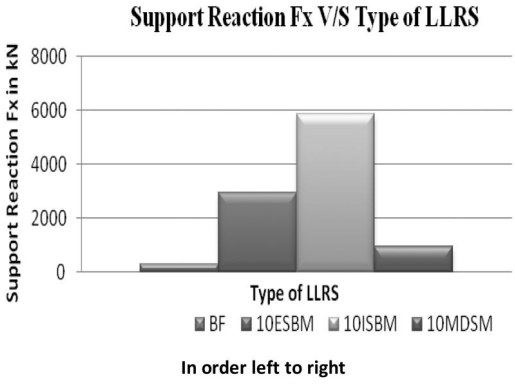

Figure 7. Support reaction Fx V/S type of LLRS.

Table 4. 15 Storey building – zone V, maximum support reactions.

Max. Fx in kN			
Frame type	Node	L/C	Fx
BF	206	11	−306.85
10ESBM	25267	11	−2945.00
10ISBM	5	11	5856.00
10MDSM	223	10	−952.44
Max. Fy in kN			
Frame type	Node	L/C	Fy
BF	5	11	10062.00
10ESBM	206	5	10053.48
10ISBM	206	5	10312.00
10MDSM	223	10	16112.60
Max. Mz in Kn-m			
Frame type	Node	L/C	Mz
BF	206	14	2180.68
10ESBM	393	11	1127.49
10ISBM	206	15	3422.52
10MDSM	223	10	2175.69

- The greatest value for Fx & Mz of all maximum support reactions occurs in the case the of frames with internal steel bracings upto 10 stories.
- The maximum support reaction Fx increases by 860%, which occurs at the new support. The maximum support reaction Fy remains constant and the maximum support bending Mz reduces by 48% with the addition of External Steel Bracings.
- The maximum support reaction Fx increases by 2134%, the maximum support reaction Fy reduces by 25% and maximum support bending moment Mz increases by 109% with the addition of Internal Steel Bracings.

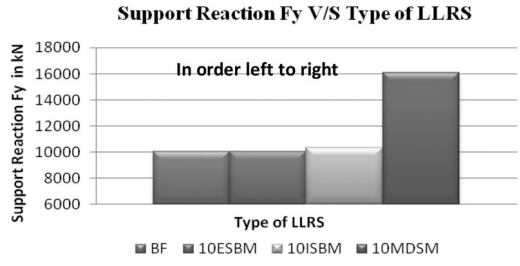

Figure 8. Support reaction Fy V/S type of LLRS.

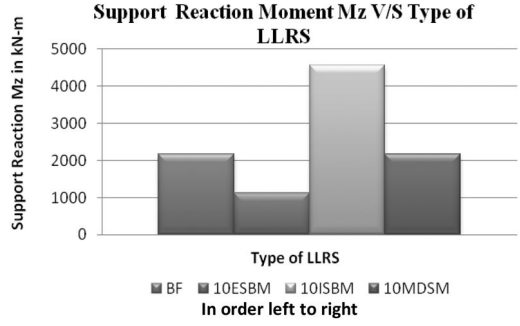

Figure 9. Support reaction moment Mz V/S type of LLRS.

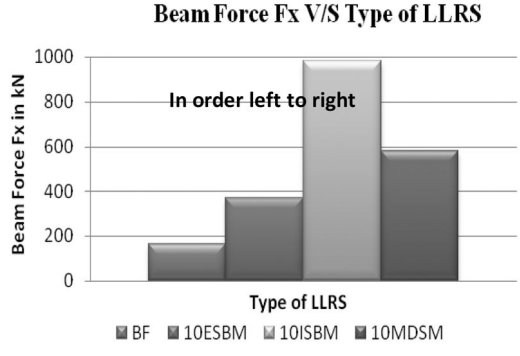

Figure 10. Beam force Fx V/S type of LLRS.

- The maximum support reaction Fx increases by 210%, the maximum support reaction Fy increases by 60% and maximum support bending moment Mz remains constant.

4.3 *Maximum beam forces (Fx, Fy Fz, Mx, My and Mz)*

The results obtained from the analysis corresponding to the maximum beam forces like axial force Fx, shear force Fy and bending moment Mz among all the load cases and load combinations considered are presented in Table 5. The graphical representation of the maximum beam forces versus type of LLRS is presented in Figure 10. to Figure 12.

- The maximum beam force Fx, Fy and the maximum beam moment Mz occurs in seismic load combination.

Table 5. 15 Storey building – zone V maximum beam forces.

Max. Fx			
Frame type	Node	L/c	Fx
BF	101	12	162.59
10ESBM	241	10	370.106
10ISBM	1	12	984.01
10MDSM	1102	12	−578.10
Max. Fy			
Frame type	Node	L/c	Fy
BF	229	11	289.84
10ESBM	247	10	276.61
10ISBM	178	11	241.53
10MDSM	1019	12	217.83
Max. Mz			
Frame type	Node	L/c	Mz
BF	297	11	428.609
10ESBM	247	13	423.37
10ISBM	379	10	334.908
10MDSM	1744	12	310.90

- The least value of the maximum beam forces Fy and Mz occurs in case of frames with MDS.
- When beam forces developed in the frames with ESB are compared with ISB the maximum beam axial force Fx, and bending moment Mz decreases whereas beam shear force Fy increases.
- The maximum beam forces Fx increases by 128%, the maximum beam forces Fy reduces by 5% and the maximum beam bending Mz reduces by 1% with the addition of External Steel Bracings.
- The maximum beam forces Fx increases by 506%, the maximum beam forces Fy reduces by 17% and the maximum beam bending moment Mz reduces by 22% with the addition of Internal Steel Bracings.
- The maximum Beam Forces Fx increases by 256%, the maximum beam forces Fy reduces by 25% and the maximum beam bending moment Mz reduces by 27% with the addition of masonry infill. An increased value of the beam forces indicates that beams also require local retrofitting.

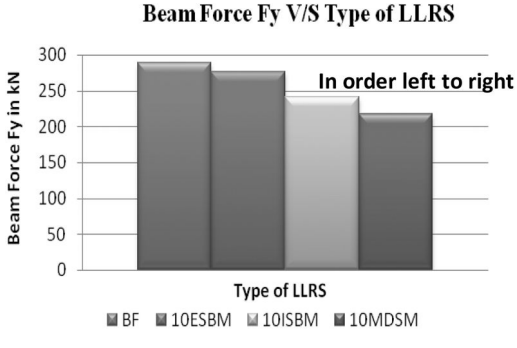

Figure 11. Beam force Fy V/S type of LLRS.

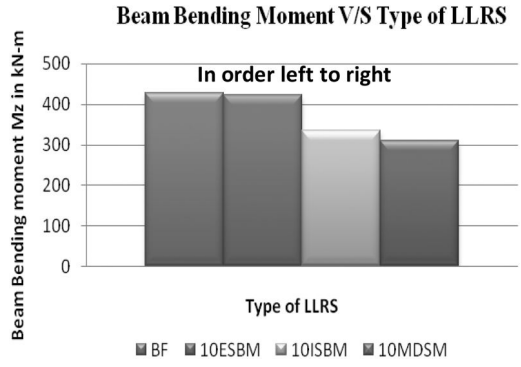

Figure 12. Beam bending moment Mz V/S type of LLRS.

Table 6. 15 Storey building – zone V maximum beam forces.

Max. Axial force in kN			
Frame type	Node	L/c	Axial force
10ESBM	36632	12	1341.77
10ISBM	36739	13	1695.95
10MDSM	36628	10	2071.18
Max. Axial Stress in N/mm^2			
Frame type	Node	L/c	Axial Stress
10ESBM	36642	12	282.47
10ISBM	37099	13	357.42
10MDSM	36669	10	8.70

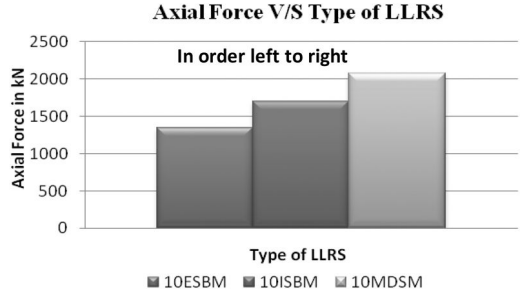

Figure 13. Axial force V/S type of LLRS.

4.4 *Maximum truss forces*

The Truss forces considered are the maximum Axial Force and Axial Stress in the Strut obtained from the analysis corresponding to maximum among all the load cases and load combinations considered and are presented in Table 6. Figure 13 and 14 shows the axial

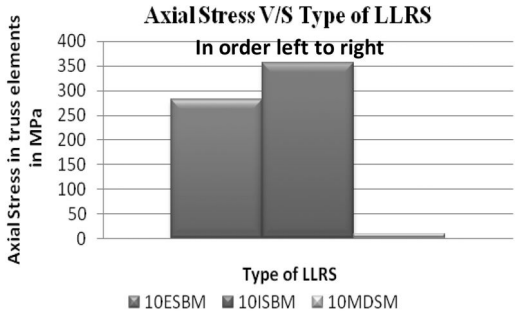

Figure 14. Axial stress V/S type of LLRS.

force and axial stress for Frames with masonry infill, Frames with External steel bracings and frames with Internal Steel Bracings.

Maximum Axial Force and maximum Axial Stress occurs for the seismic load case. Axial Force for Frame with Internal Steel Bracings are less compared to the Frames with External steel bracings and frames with masonry infill.

5 CONCLUSIONS

Based on the limited study carried out the following conclusions are drawn.

- Generally, the critical load combination occurs when the seismic loads are considered (except along global Y). Hence, it is important and necessary to consider seismic loads in analysis of the structural systems.
- It is seen that the displacement (δx) at each storey level are maximum for bare frame and all the LLRS considered effectively reduce the displacement. The minimum displacement at each storey level are obsereved in the case of the frames with Masonry Diagonal Strut.
- Provision of ESB, ISB and MDS effectively reduce large joint displacements found in bare frame by 16, 16 and 38 % respectively.
- Compared to the Bare Frame, support reaction moment is reduced only in case of frames with External Steel Bracing, where as all other support reaction parameters increases.
- Compared to the Bare Frame Beam shear force, Beam bending moment is reduced in all the llrs, where as axial force increses in all the LLrs considered, which requires attention during retrofitting.
- Axial Force for Frames with Internal Steel Bracings are less compared to the Frames with External steel bracings.
- Of all the LLRS considered performance of Masonry Infill (MDS) is superior to other LLRS in resisting seismic loads.

6 LIMITATIONS

- It is assumed that a proper connection between existing structure and LLRS provided exists.
- The study is carried out assuming that the loads applied are within the elastic range (Service Loads). Hence the results may not be valid when loads applied are such that the material is no longer elastic.
- It is assumed that all the LLRS considered are in full contact with the frames and there is no separation between them.
- In the present study frames and lateral load resisting systems considered are symmetric in geometry.

REFERENCES

Ghobarah. A, Abou Elfath. H, (2001), "Rehabilitation of a reinforced concrete frame using eccentric steel bracing", Engineering structures 23 (2001) pp. 745–755.

IS: 1893 (Part – 1) – 2002 – Code of Practice for Criteria for Earthquake Resistant Design of Structures, Part 1: General Provisions and Buildings, Bureau of Indian Stds., New Delhi.

IS: 875 – 1987 – Code of Practice for Design Loads (other than Earthquake) for Buildings and Structures, Part 1: Dead Loads, Part 2: Imposed Loads, Part 5: Special Loads and Load Combinations, Bureau of Indian Stds., New Delhi.

NEHRP guidelines for the seismic rehabilitation of building, FEMA 273/October 1997.

Venkatesh S.V, Dr. Sharada Bai H., Divya S.P, "Behaviour Of 3-Dimensional Building Frames with Steel Bracings as Lateral Load Resisting Systems Subjected to Seismic Load", Thrust areas in Engineering (NCTAE 2012).

Venkatesh S.V, Dr. Sharada Bai H., Divya S.P, "Seismic Analysis of 3D Building Frame with Masonry Infill and Steel Bracings as Lateral Load Resisting Systems". Engineering and Technological Innovations, July 13 -2012.

Venkatesh S.V, Dr. Sharada Bai H., Divya S.P, " Response of a 3-Dimensional 2 X 3 Bays Ten Storey RC Frame with Steel Bracings as Lateral Load Resisting Systems Subjected To Seismic Load", International journal of scientific & Engineering rearch (2013), volume 4, issue 5, pp. 139–142.

Venkatesh S.V. Dr. Sharada Bai H and R. Rajeshwari, "Effect of shear wall and steel bracing as lateral load resisting system on a ten storey building" The Fourth International Conference on Structural Engineering, Mechanics and Computation (SEMC 2010), University of cape Town, South Africa.

Surface protection methods and materials

This page intentionally left blank

Concrete Solutions – Grantham et al. (Eds)
© 2014 Taylor & Francis Group, London, ISBN 978-1-138-02708-4

Performance of silane impregnants for the protection of reinforced concrete

C. Christodoulou
AECOM Europe, Colmore Plaza, Birmingham, UK

H. Tiplady
Atkins, Chadwick House, Warrington, UK

C.I. Goodier & S.A. Austin
Loughborough University, School of Civil and Building Engineering, Loughborough, UK

ABSTRACT: Silanes can act as hydrophobic pore liners for Reinforced Concrete (RC) structures. They can significantly reduce the depth of chloride penetration, a major cause of steel reinforcement corrosion. There is little published information however, on their long-term performance. For this study, 32 concrete cores were extracted from eight full-scale RC bridge supporting cross-beams which had been treated with silane 20 years ago. Their rate of water absorption by capillarity was measured and compared with 16 control cores extracted from four non-silane treated RC cross-beams constructed at the same time. Results show that these silanes provide a residual protective effect against water even after 20 years of service.

The performance of silane impregnations on concrete incorporating blended cements, and the effects of different formwork, ages of concrete and curing conditions prior to impregnation were also investigated. Concrete specimens were cast with CEM III/A (Portland cement with 50% ground granulated blast furnace slag) cement. The performance of the silane impregnation was assessed by the rate of water absorption due to capillary action. The results indicate that improvements in performance were identified within the sample groups of lower w/c ratios, steel finishes, outside curing and double coatings of silane treatment.

The findings from both research programmes indicate that silane impregnations can provide a significant reduction to the water absorption characteristics of both site retrieved and laboratory cast concrete samples. It was observed that performance was reduced with increasing the age of the silane impregnation service life. In addition, silane impregnations applied at specimens with plywood or tampered finish demonstrated a greater reduction on water absorption than specimens with a steel finish.

1 INTRODUCTION

Concrete is a naturally porous material. The size and distribution of pores in concrete varies and depends on the constituent materials, quality of compaction, the materials used in the mix design, the water-to-cement ratio, the degree of hydration, and curing (Concrete Society 2008). Some of these pores will be interconnected to form a network of pore space that can be penetrated by water, gas or ions.

The relevant transport mechanisms for the ingress of water, gases and ions are (Kropp and Hilsdorf 1995):

- diffusion of free molecules or ions due to a concentration difference;
- permeation of gases or liquids through water saturated specimens due to hydraulic pressure difference; and
- capillary suction of liquids due to surface tension acting in capillaries.

Whilst, these mechanisms act together under natural environmental exposure conditions for atmospherically exposed concrete, capillary suction tends to be the dominant mechanism (Concrete Society 2008, Kropp and Hilsdorf 1995, Ungricht 2004). Ions such as chlorides are transported into the concrete pore system by being dissolved into water, which can subsequently cause corrosion of the steel reinforcement and ultimately spalling of the surrounding concrete cover.

Surface impregnations, such as silanes, are used in various forms in the construction industry to prevent water ingress into concrete structures. Evidence from numerous studies and field applications illustrate that the application of a silane impregnation significantly reduces chloride ingress and therefore corrosion risk of the reinforcement (Basheer et al. 1997, Vries and Polder 1997, Medeiros and Helene 2008, Calder and McKenzie 2008 Polder and de Vries 2001).

However, there is little or no knowledge regarding their long term performance. The research undertaken by Schueremans et al. (2007) is one of the few studies which investigated their long-term effects on a quay-wall in a port. They showed that the silane was still present after 12 years of exposure in a marine

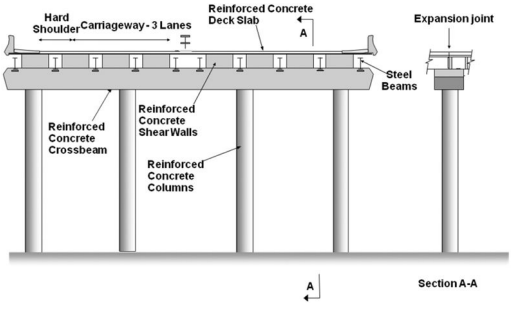

Figure 1. Typical sub-structure arrangement of the UK's Midland Links Motorway Viaducts (MLMV) (Christodoulou et al. 2013).

environment and had a residual protective effect on the concrete.

The objective of this study was to address the gap in knowledge with regards to the long-term performance of silane impregnations by undertaking testing of full-scale RC structures and comparing them with data from laboratory cast specimens. Early results of this work have also been reported (Christodoulou et al. 2012, Christodoulou et al. 2013).

2 METHODOLOGY

This section presents an overview of the structures from which specimens were extracted, the laboratory programme and the testing procedures.

2.1 *Site specimens*

Figure 1 illustrates a typical sub-structure arrangement of the motorway bridge supporting cross-beams that were examined during this study. Silanes have been applied to a total of 135 similar cross-beams across the UK's Midland Link Motorway Viaducts (MLMV). Of these, 93 cross-beams were located in the viaduct that was chosen for these investigations.

The cross-beams were constructed between 1968 and 1970, although the exact date is not known. Due to the age of the cross-beams, there were no historical records available providing information on concrete mix design such as maximum aggregate size.

Twelve cross-beams were selected, of which eight had previously received a silane treatment 20 years following their construction, whereas the remaining four had not, hence were acting as control specimens (Table 1). The chemical composition of the silane treatment was isobutyl trimethoxy silane. No historical records exist detailing the exact surface preparation procedures, application rates or weather conditions at the time of the application, important factors that can affect silane performance.

Four cores (diameter and length of 80mm) were extracted from the top surface of each cross-beam, which represents the most critical area for water ingress. This residual risk can be attributed to the simply supported articulation arrangement with expansion joints above every cross-beam that were known to be susceptible to water leakage. After coring, each core hole was carefully repaired with a shrink-resistance compensating repair mortar.

Table 1. Age of cross-beams based on an average construction date of 1969 and age of silane treatment at testing (Christodoulou et al. 2013b).

Cross-beam Reference	Year of silane application	Age of cross-beam at silane application (years)	Age of silane at testing (years)	Age of cross-beam at testing (years)
A1	1991	23	20	43
B1	1993	25	18	
B2	1993			
B3	1993			
B4	1993			
B5	1993			
B6	1993			
C1	1999	31	12	
D1	Control	–	–	
D2	cross-			
D3	beams			
D4	(No silane)			

2.2 *Laboratory specimens*

Laboratory specimens were cast to investigate the influence of different surface finishes, water-to-cement ratios (w/c) and cement replacements on the performance of silane impregnations. A CIIIA mix design was used with a 50% total content of ground granulated blast furnace slag (GGBS) and w/c ratios of 0.3, 0.35 and 0.4. Furthermore, plywood, steel and hand trowel finishes were also investigated.

Four beams were therefore cast for each mix design with plywood panels inserted between the $1075 \times 100 \times 100$ mm moulds in order to create the different surface finishes. The concrete was mixed for approximately 2 minutes in a rotary mixer before placing into the moulds and vibrating on a vibration table for between 3–4 minutes to ensure good compaction and the removal of any air voids.

From each beam, 12 cores (60 mm diameter and 50 mm length) were extracted for each type of surface finish examined (Figure 2). The silane impregnation was brush applied at different time intervals in order to also investigate the effect between their performance and age of concrete. In total, 3 different ages were examined, 7 days (single application), 28 days (single application), and 7 & 28 days (double application) (Table 2).

The silane impregnation applied was a proprietary water based alkyl alkoxysilane with 20% solid content by weight.

2.3 *Testing*

Concrete in contact with a salt solution will become contaminated with chlorides primarily due to capillary

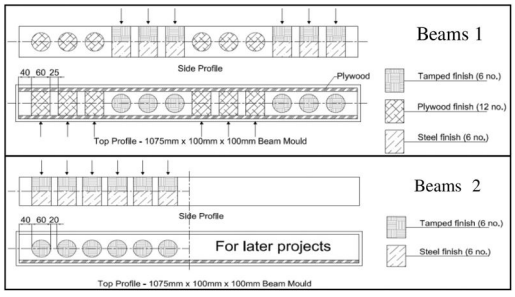

Figure 2. Beam coring layout.

Table 2. Summary of specimens including finish and silane application.

Type of Finish	Details of Specimens
Tamped Finish:	3 cores with silane applied at 7 days
Total of 12 cores.	3 cores with silane applied at 28 days
	3 cores with silane applied at 7 and 28 days
	3 control cores
Steel Finish:	3 cores with silane applied at 7 days
Total of 12 cores.	3 cores with silane applied at 28 days
	3 cores with silane applied at 7 and 28 days
	3 control cores
Plywood Finish:	3 cores with silane applied at 7 days
Total of 12 cores.	3 cores with silane applied at 28 days
	3 cores with silane applied at 7 and 28 days
	3 control cores

absorption rather than diffusion alone. Absorbed chlorides can continue to penetrate by diffusion but at a significantly lower movement rate (Christodoulou et al. 2013). Thus, measuring the rate of absorption (or sorptivity) can provide useful information on the condition of silane treatments. The procedure outlined by BS EN 13057 (British Standards Institution 2002) was employed.

The rate of water absorption can be expressed by equation (1) (Kropp and Hilsdorf 1995). Sorptivity is the uni-axial one-dimensional capillary absorption and can be expressed by equation (2) (British Standards Institution 2002, Kropp and Hilsdorf 1995).

$$\text{Rate of water absorption} = \frac{W_w}{(A_c\sqrt{t})}\ kg/m^2/h^{0.5} \quad (1)$$

$$\text{Sorptivity} = \frac{V_w}{(A_c\sqrt{t})}\ \ m/h^{0.5} \quad (2)$$

where W_w (grams) is the weight gained by the specimen, A_c (mm^2) the surface area of the specimen in contact with the water, t (seconds) the time of exposure and V_w (mm^3) the volume of water absorbed.

Measurement of water sorptivity can also be related to the rate of chloride absorption (Medeiros and Helene 2009, Austin and Al-Kindy 2000).

3 RESULTS

The results section is divided in two parts, one for results relating to site specimens and the other for the laboratory specimens.

3.1 *Site specimens*

The average cumulative water uptake for each cross-beam's group of specimens over a period of 4 hours of capillary absorption testing is provided in Figure 3. From this, the rate of absorption can therefore be calculated.

It can be observed that specimens from all cross-beams initially had a high rate of water absorption over the first 15 minutes of testing (0.08 hours or 0.29 $hours^{0.5}$). After this time, for the silane treated cross-beams, in most cases the rate of water absorption was significantly reduced or almost eliminated, indicating steady state conditions. For the control cross-beams, in most cases, the rate of water absorption was reduced but never eliminated.

As such, three distinct rates of water absorption may be derived, i.e. initial between zero and 15 mins, secondary between 15 mins and 4 h and overall average. It can be observed that control cross-beams D2, D3 and D4 exhibited high rates of water absorption for the initial, secondary and average rates of water absorption. Although all control structures (D1, D2, D3 and D4) initially performed better than silane treated cross-beam B6, the later quickly reached near steady state conditions whereas control cross-beams continued their water absorption.

Cross-beam C1, with the youngest silane treatment at 12 years at time of testing, had a relatively high initial rate of water absorption but quickly reached steady state conditions with overall a very low total cumulative water uptake. Cross-beam B5, with the silane treatment at 18 years at time of testing, was one of the best performing based on initial, secondary and average rates of water absorption and reached near steady state conditions after 15 minutes of testing.

3.2 *Laboratory specimens*

Figure 4 illustrates the cumulative water absorption of laboratory specimens with w/c 0.4. It can be observed that in all cases, the rate of water absorption of control samples was higher than those of silane treated. This was particularly evident for the specimens with a steel finish. By examining the performance of the control specimens, it can also be observed that the plywood finish resulted in lower rates of water absorption, with the steel finish resulting in the highest.

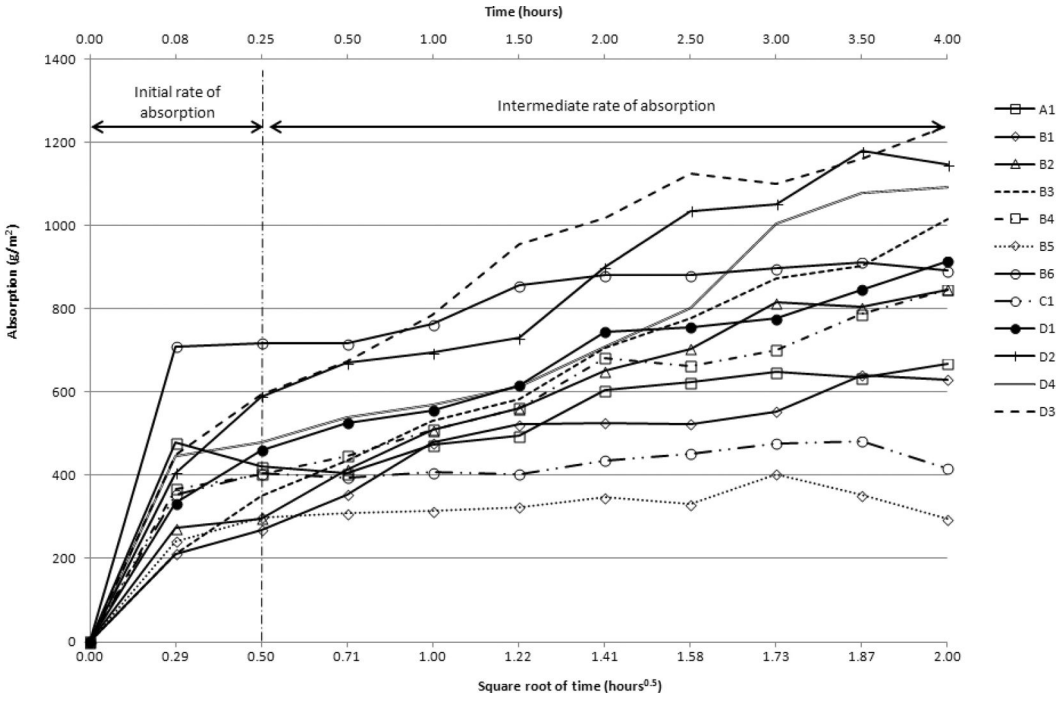

Figure 3. Average cumulative absorption for each cross-beam's group of specimens over 4 hours of capillary absorption testing.

In addition, in all but one cases it was observed that a double application of a silane impregnation offered significantly lowered rates of water absorption. This was not the case for the steel finish, where a double silane application had identical performance to a silane impregnation applied at 7 days.

Figure 5 illustrates the cumulative water absorption of laboratory specimens with w/c 0.35. Again the rate of water absorption of the control samples was in all cases, higher than those of silane treated. However, with this lower w/c ratio there were not significant performance differences in the rate of water absorption for the control specimens with different surface finishes. Interestingly, in this occasion, specimens with a steel finish performed slightly better than plywood and tampered finish.

Again in all but one case it was observed that a double application of a silane impregnation offered significantly lower rates of water absorption. This was not the case for the plywood finish, where a double silane application resulted in a worse performance than a single application at 7 and 28 days

Figure 6 illustrates the cumulative water absorption of laboratory specimens with w/c 0.3. The rate of water absorption of the control samples was in all cases, higher than those of silane treated. In a similar manner to specimens with a w/c 0.35, a steel finish resulted in lower rates of water absorption for the control specimens.

Interestingly, in all but one case a double application of silane impregnation was generally similar to one application at 28 days. Only in the case of a steel finish, there was a significant reduction by a double application of a silane impregnation. Furthermore, it was also observed that a silane impregnation was significantly more effective with a steel finish.

4 DISCUSSION

The results suggest that the specimens extracted from silane treated RC structures exhibited a residual protective effect even after 20 years of service life. In particular, specimens from cross-beam C1 – which had had the most recent application – outperformed all specimens except those from cross-beam B5. Possible reasons for the difference in performance between specimens of silane treated cross-beams include time dependant effects such as weathering, surface preparation, application rates, environmental conditions at the time of application and differences in the quality of the concrete (Christodoulou et al. 2013). Unfortunately, no historical records exist providing these details.

The cumulative water absorption of these extracted specimens (Figure 3) was found to have a fluctuating rate throughout the duration of the test. This is not uncommon, especially when dealing with specimens extracted from full-scale structures (Calder and McKenzie 2008). This variance may be partly explained by changes in the micro-structure of the specimens as water progress from the cover zone

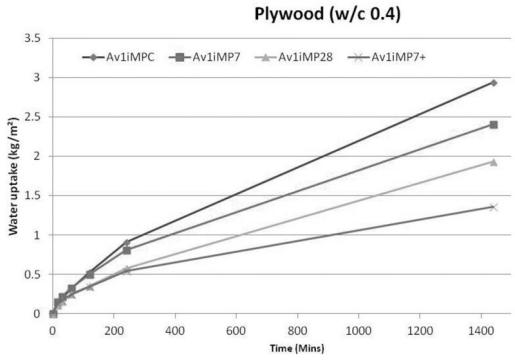

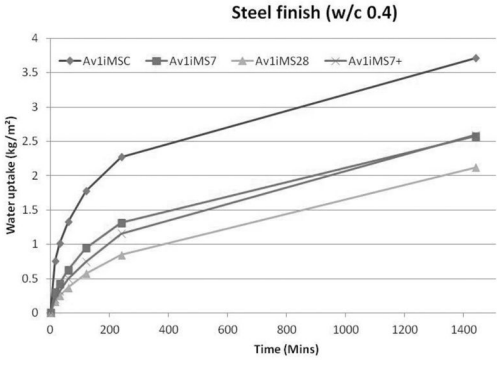

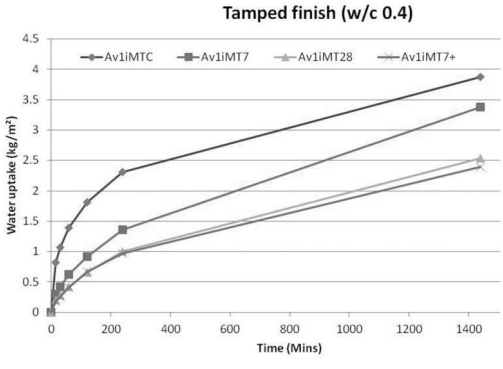

Figure 4. Cumulative absorption for laboratory cured specimens with a w/c 0.4 and different surface finishes (Av1iMTC denotes control specimens, Av1iMT7 denotes silane applied at 7 days, Av1iMT28 denotes silane applied at 28 days and Av1iMT7+ denotes silane applied at 7 and 28 days).

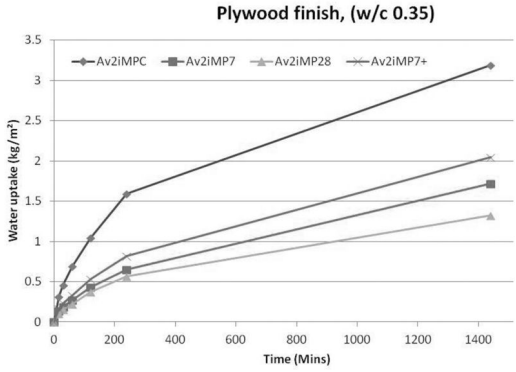

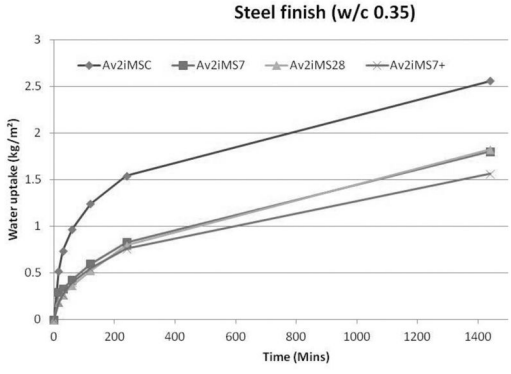

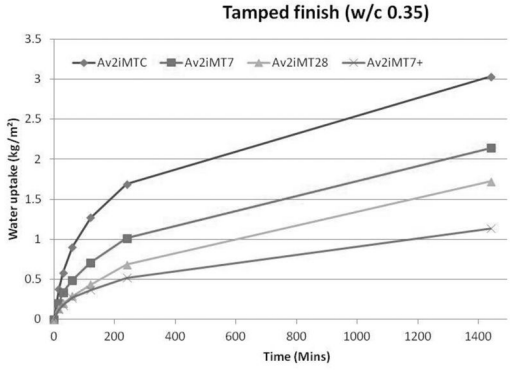

Figure 5. Cumulative absorption for laboratory cured specimens with a w/c 0.35 and different surface finishes (Av1iMTC denotes control specimens, Av1iMT7 denotes silane applied at 7 days, Av1iMT28 denotes silane applied at 28 days and Av1iMT7+ denotes silane applied at 7 and 28 days).

(where concrete may be more porous and exhibit surface cracking) towards the core of the specimens. The thickness of this cover zone is affected by quality control on-site and curing conditions. The specimens for this study were extracted from the top of the RC cross-beams an area where concrete is predisposed to bleeding and segregation which can give rise to inconsistencies of the cover zone.

The rate of water absorption of the laboratory-cast control specimens for the 3 different w/c ratios with a plywood finish remained fairly constant. This suggests that a plywood finish allows even hydration at the cover zone area despite varying w/c ratios. In contrast, there was a significant reduction in the rate of water absorption for the steel and tampered finishes when the w/c ratio was reduced. In particular, at a w/c ratio of 0.3, the steel and tampered finish specimens had a lower absorption that plywood. This reinforces the view that the w/c ratio will have a significant effect, particularly for steel and tampered finishes.

In most cases, the application of a silane impregnation at a concrete age of 7 days, provides a lesser

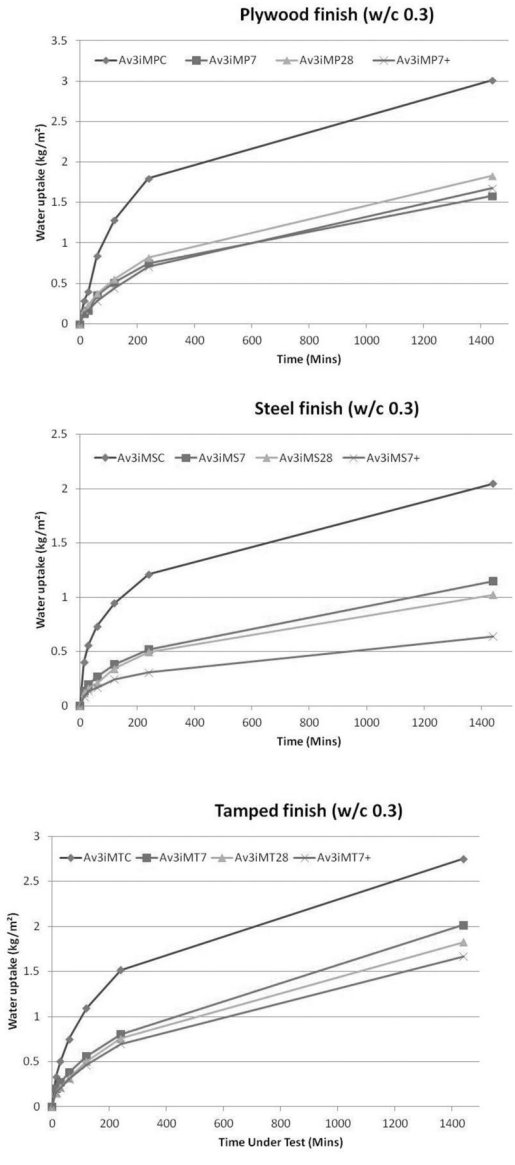

Figure 6. Cumulative absorption for laboratory cured specimens with a w/c 0.30 and different surface finishes (Av1iMTC denotes control specimens, Av1iMT7 denotes silane applied at 7 days, Av1iMT28 denotes silane applied at 28 days and Av1iMT7+ denotes silane applied at 7 and 28 days).

reduction in the rate of water absorption than applications at 28 days. The main exception related to specimens with a steel finish where there was hardly any difference between 7 and 28 days. This reinforces the view, that it is generally preferable to allow at least 28 days of concrete hydration before the application of a silane impregnation.

Furthermore, in all but one case, a double application of silane impregnation at a concrete age of 7 days and again at 28 days again resulted in the highest reduction of rates of water absorption, as would be expected. In practice, this may not always be possible as silane impregnations are primarily applied retrospectively. Nevertheless, a double application can provide improved water absorption characteristics and could be taken under consideration depending upon cost.

Overall, silane impregnations should be considered when determining the corrosion management strategy of a RC structure. Treatments as old as 20 years can still be present and offer a residual protective effect. This is in line with work by Polder and de Vries (2001), Schueremans et al. (2007) and Rodum and Lindland (2012). Their presence and effectiveness over time can be evaluated by extracting cores and testing them in the laboratory by capillary absorption testing.

5 CONCLUSIONS

Overall, very little published empirical evidence is available on the durability of silane treatments and their long-term (i.e. 10 years plus) residual protection. Such a gap in knowledge is undesirable given the number, variety and scale of infrastructure treated with hydrophobic treatments such as silanes. From the results of this study, based upon specimens from full-scale RC structures and laboratory cast, the following can be concluded:

- All the treated cross-beams demonstrated that the silane impregnation still provides a residual hydrophobic effect, even with the oldest application from 20 years ago.
- In all but one cross-beam, the most recent silane treated specimens outperformed the older silane treated specimens, suggesting a relationship between degradation of the silane impregnation and duration of environmental exposure.
- Application of silane impregnations after at least 28 days of hardening will result in reduced rates of water absorption as opposed to applications at 7 days only.
- A double application of silane impregnation is usually beneficial and can further reduce the rate of water absorption. This effect was more pronounced at higher w/c ratios.
- A plywood finish allows for more even hydration and as a result similar rates of water absorption at varying w/c ratios (0.3, 0.35 and 0.4). This suggests that a plywood finish may be preferable for full-scale construction as it provides consistency between casting.
- Steel finishes resulted in greater variations in the rate of water absorption depending on the w/c ratio, especially at values of 0.4. It is postulated that as the w/c ratio increases, the hydration of concrete may not be even causing variations in the microstructure of the cover zone. This should be taken into consideration when casting large concrete segments with steel formwork.

- Silane impregnations were most effective as the w/c ratio was reduced. This suggests, that the specimens may not have been fully hydrated resulting in a more porous micro-structure allowing greater penetration by the silane impregnation. In particular, the greatest reduction of water absorption was afforded to specimens with a steel finish and a w/c ratio of 0.35.

REFERENCES

Austin S.A. and Al-Kindy A.A. 2000, Air permeability versus sorptivity: effects of field curing on cover concrete after one year of field exposure, Mag Concr Res; 52:17–24.

Basheer P.A.M., Basheer L., Cleland D.J., Long A.E. 1997, Surface treatments for concrete: assessment methods and reported performance, Const. Build Mat; 11:413–429.

British Standards Institution, BS EN 13057:2002, Products and systems for the protection and repair of concrete structures – Test methods – Determination of resistance of capillary absorption, London: BSI; 2002.

Calder A. and McKenzie M. 2008, Performance of impregnants. Published Project Report 362. Transportation Research Laboratory.

Christodoulou C., Goodier C., Austin S., Glass G. Webb J. 2012, Assessing the long-term durability of silanes on reinforced concrete structures, 1st International Congress on Durability of Concrete, Trondheim, Norway; ISBN 978-82-8208-031-6. https://dspace.lboro.ac.uk/2134/10925.

Christodoulou C, Goodier C, Austin S, Webb J, Glass G 2013, Long-term performance of surface impregnation of reinforced concrete structures with silane, Construction and Building Materials, 48, pp. 708–716 DOI information: 10.1016/j.conbuildmat.2013.07.038, https://dspace.lboro.ac.uk/2134/13023.

Concrete Society 2008, Technical Report 31, Permeability testing of site concrete. Surrey, UK.

Kropp J., Hilsdorf H.K. 1995, RILEM Report 12, Performance criteria for concrete durability, Taylor and Francis, Oxford, UK.

Medeiros M.H.F. Helene P. 2008, Efficacy of surface hydrophobic agents in reducing water and chloride ion penetration in concrete, Mater Struct; 41:59–71.

Medeiros M.H.F. Helene P. 2009, Surface treatment of reinforced concrete in marine environment: Influence on chloride diffusion coefficient and capillary water absorption, Const. Build Mat; 23:1476–1484.

Polder R.B. de Vries H. 2001, Prevention of reinforcement corrosion by hydrophobic treatment of concrete, Heron; 46:227–238.

Rodum E. and Lindland J. 2012, Effect of different surface treatment products after 10 yrs. of field exposure, IN: Proceedings of the 1st International Congress on Durability of Concrete, Trondheim, Norway, ISBN 978-82-8208-031-6.

Schueremans L., Gemert D.V. Giessler S. 2007, Chloride penetration in RC-structures in marine environment-Long term assessment of a preventative hydrophobic treatment, Const. Build Mat; 21:1238–1249.

Ungricht H. 2004, Wasserhaushalt und Chlorideintrag in Beton – Einfulls der Exposition und der Betonzusammensetzung, Ph. D. Thesis (In German), Universities of Zurich and Basel.

Vries J., Polder R.B. 1997, Hydrophobic treatment of concrete, Const. Build Mat; 11:259–265.

This page intentionally left blank

Concrete Solutions – Grantham et al. (Eds)
© 2014 Taylor & Francis Group, London, ISBN 978-1-138-02708-4

Effect of silicate-based surface penetrant on concrete durability

Y. Kato & N. Someya
Department of Civil Engineering, Faculty of Science and Technology, Tokyo University of Science, Japan

ABSTRACT: This paper presents an experimental study examining the effect of silicate-based surface penetrants on the concrete durability made with OPC or OPC with fly ash. The durability was evaluated by the accelerated carbonation test and the water absorption test. To assist the hydration reaction of the penetrants, calcium hydroxide was utilized in the case of high water-binder ratio. Silicate-based penetrants were applied to the water-cement ratio 0.55 specimens and improved the concrete durability against carbonation. And it could be seen that the application was more effective at 14 days for OPC specimens but more effective for FA at 7 days. In the case of high water-binder ratio, it could not be seen the effect of the penetrants clearly even though the application of calcium hydroxide was utilized. And the improvement depth of concrete was around 0.4 to 2 mm depending on the concrete quality and the kind of penetrants.

1 INTRODUCTION

When the performance of a concrete structure is less than the required performance due to aging and deterioration, the performance needs to be restored through measures such as repair or reinforcement. Surface penetrants can improve the durability of concrete and delay the degradation of the structure. In addition, when applying penetrants at an early age for preventive maintenance, the progress of deterioration can be reduced from the beginning (JSCE 2005). Silicate-based surface penetrants are one type of surface protection construction methods, and their application to the concrete surface can improve the durability of the concrete. The application of silicate-based surface penetrants has several benefits such as ease of maintenance and the ability to visually check the surface after application.

The main ingredient of silicate-based surface penetrants reacts with calcium hydroxide and produces a C-S-H gel like cement hydration product. Examples of the chemical reaction are as follows (JSCE 2012).

Sodium silicates type:

$$Na_2O \cdot SiO_2 + xCa(OH)_2 + yH_2O \rightarrow xCaO \cdot SiO_2 \cdot zH_2O + 2NaOH + (x + y - z - 1)H_2O$$

Lithium silicates type:

$$Li_2O \cdot SiO_2 + xCa(OH)_2 + yH_2O \rightarrow xCaO \cdot SiO_2 \cdot zH_2O + 2LiOH + (x + y - z - 1)H_2O$$

In the past studies, it was found that the effect of silicate-based surface penetrants varies depending on the quality of the early-age concrete (Hazehara, et al. 2010), and it was also shown that the penetrants could improve the durability of concrete containing microcracks and protect against carbonation. However, it is believed that the state of the concrete such as water content, degree of hydration, etc., to which the penetrant will be applied is important, and the effect of application on the mass transport properties of concrete is unclear.

This paper presents an experimental study examining the effect of penetrants which were applied to early-age specimens.

2 EXPERIMENTAL PROGRAMS

2.1 *Procedure*

The flow for the experiments is shown in Figure 1. For N-55 and FA-55, to understand the effect of application timing on the durability, penetrants were applied to specimens aged 7 and 14 days, after which the specimens were placed in a controlled environment (20°C, R.H. 60%) for 4 weeks. And the effectiveness of penetrants was evaluated by the water absorption test and the accelerated carbonation test.

The effectiveness of an additive (calcium hydroxide) for assisting the reaction of surface penetrants was examined in the cases of NA-60 and FA-60, because the amount of calcium hydroxide produced by the cement hydration may be a little. And the effectiveness of penetrants was evaluated by the accelerated carbonation test.

2.2 *Material and specimens*

Table 1 describes the two types of silicate-based surface penetrants and the calcium hydroxide additive.

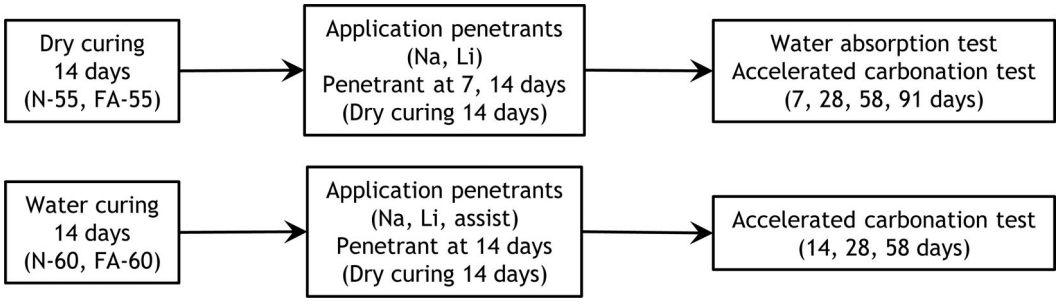

Figure 1. Flow of testing procedure.

Table 1. Description of the penetrants and the assisting additive.

Code	Ingredient	Application quantity (g/m^2)
Na	Sodium silicates	120
Li	Lithium silicates	120
Assist	Calcium hydroxide	120

Table 2. Concrete mix proportions.

			(kg/m^3)					
Code	W/C (%)	s/a (%)	W	C	F	S	G	AE (%)*
N-55	55	45	175	318	–	804	1016	0.002%
FA-55	55	46	175	318	107	698	1001	0.05%
N-60	60	45	175	292	–	804	1025	0.006%
FA-70	70	52	175	248	44	923	888	0.013%

*AE dosage = binder weight %

The application method was carried out depending on the penetrant quality. Concrete was made with ordinary portland cement (C, density: 3.15 g/cm^3, Blaine fineness: 3440 cm^2/g) or ordinary portland cement with fly ash (F, density: 2.28 g/cm^3, Blaine fineness: 3920 cm^2/g, JIS A 6201 II grade ash). The fine aggregate was river sand (S, density: 2.61 g/cm^3, fineness modulus: 2.91) while the coarse aggregate was crushed sandstone with G_{max} of 20 mm (G, density: 2.73 g/cm^3, fineness modulus: 6.61).

The concrete mix proportions are shown in Table 2. The dosage of air entrained agent (AE) was decided to obtain the following fresh properties. The slump of fresh concrete was 10 ± 2.5 cm and the air content was 4.5 ± 1.5 %. The water-binder ratio (W/(C + F)) of FA-55 and FA-70 was 0.41 and 0.60 respectively.

The water absorption test was carried out on an area of 150 × 150 × 150 mm, and the carbonation rate test carried out on an area of 150 × 150 × 200 mm. Specimens were given a surface treatment to limit the number of mass transport surfaces. Table 3 shows the number of application sides and measurement area of the specimens, and an illustration of the specimens is shown in Figure 2.

Table 3. Details of specimen measurement areas.

Item	Measurement area (mm)	Application surface
Water absorption test	150 × 150 × 150	2 opposing surfaces
Carbonation test	150 × 150 × 200	2 opposing surfaces

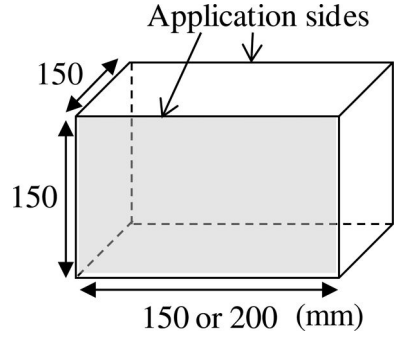

Figure 2. Illustration of test specimens showing application surfaces.

2.3 *Test methods*

2.3.1 *Water absorption test*

The water absorption test for N-55 and FA-55 was carried out according to JSCE-K 572-2012. The specimen was removed from the testing container seven days after the start of the test and the mass was measured (W_{ai}) after removing the surface water. Using this value the water absorption rate (W_a) was calculated using Equation 1. The reported absorption rate is the mean of three values.

$$W_a = \frac{W_{ai} - W_{a0}}{W_{a0}} \times 100 \quad (1)$$

where W_a = absorption rate (%); W_{a0} = mass before the examination (g) ; and W_{ai} = mass at the time of the measurement (g).

2.3.2 *Carbonation test*

The accelerated carbonation test was carried out according to JSCE-K 572-2012. The examination

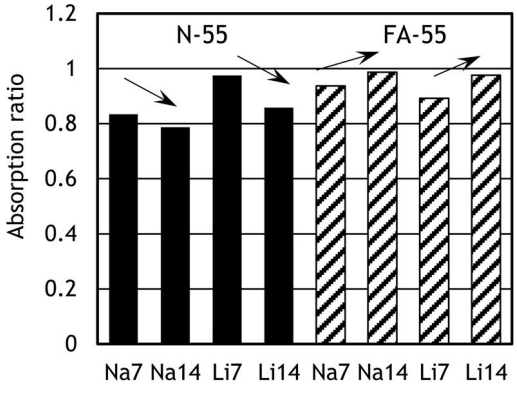

Figure 3. Water absorption ratio (N-55, FA-55).

condition used a temperature of 20°C, R.H. 60%, 5% CO_2 density, and the carbonation depth was measured after 7, 28, 56, and 91 days for N-55 and FA-55, and after 14, 28, and 56 days for N-60 and FA-70. The carbonation depth was measured by applying phenolphthalein on the fracture surface, and the reported value was calculated as the mean of six data points, which were measured twice per specimen (the depth from two opposing sides).

3 RESULT AND DISCUSSION

3.1 *Water absorption test*

The results showed that the timing of the penetrant application at 7 days and 14 days affected the water absorption ratio (calculated as the ratio of the test result to the water absorption rate in the case that no penetrant was applied) as shown in Figure 3.

N-55 experienced improved durability against water absorption, and the absorption ratio was lower when the penetrants were applied at 14 days than at 7 days.

FA-55 specimens experienced improved the durability against water absorption, and the absorption ratio was lower when the penetrants were applied at 7 days than at 14 days. And the FA55 shows a marginal improvement, especially at 14 days.

The effectiveness of the penetrants in the case of OPC is higher than that of FA. It may be due to the amount of calcium hydroxide in concrete.

3.2 *Carbonation test*

The progress of carbonation depth is shown in Figures 4 and 5. And the carbonation ratio which was calculated as the ratio of the case applying a penetrant to the case with no penetrant is shown in Figures 6 and 7 in order to understand the effectiveness of the penetrants clearly.

From Figure 7, it can be understood that the resistance against carbonation of concrete was not improved. In the cases of N-60 and FA-70, the amount

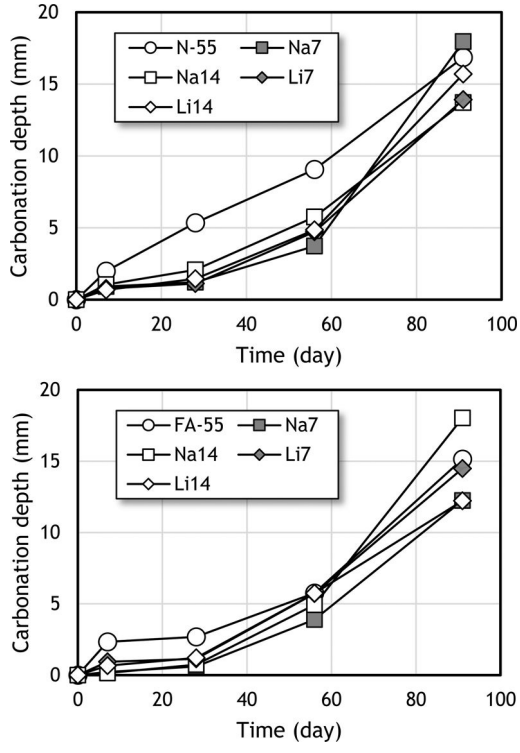

Figure 4. Carbonation depth (top: N-55, bottom: FA-55).

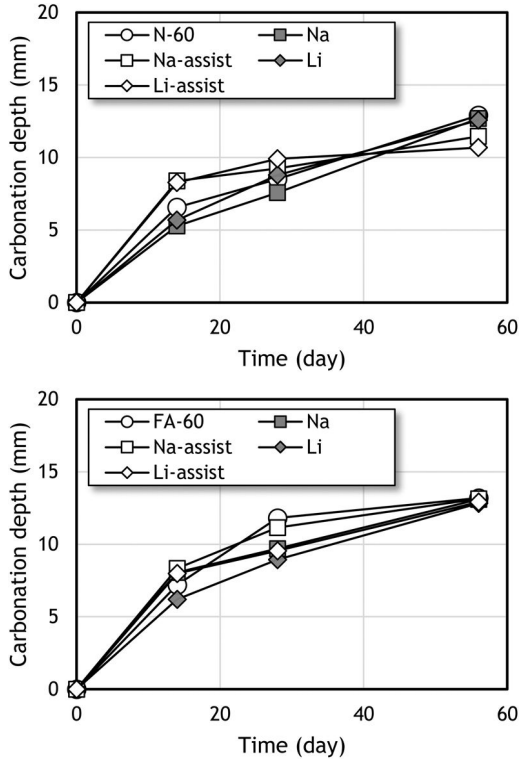

Figure 5. Carbonation depth (top: N-60, bottom: FA-70).

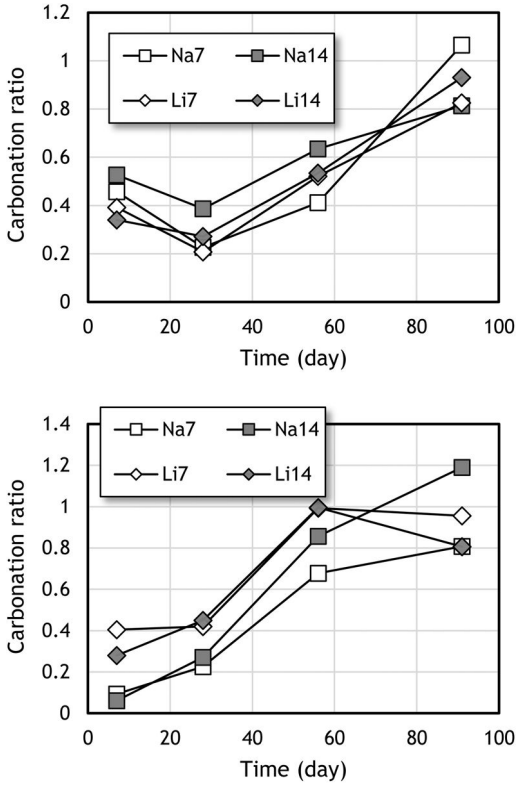

Figure 6. Carbonation ratio (top: N-55, bottom: FA-55).

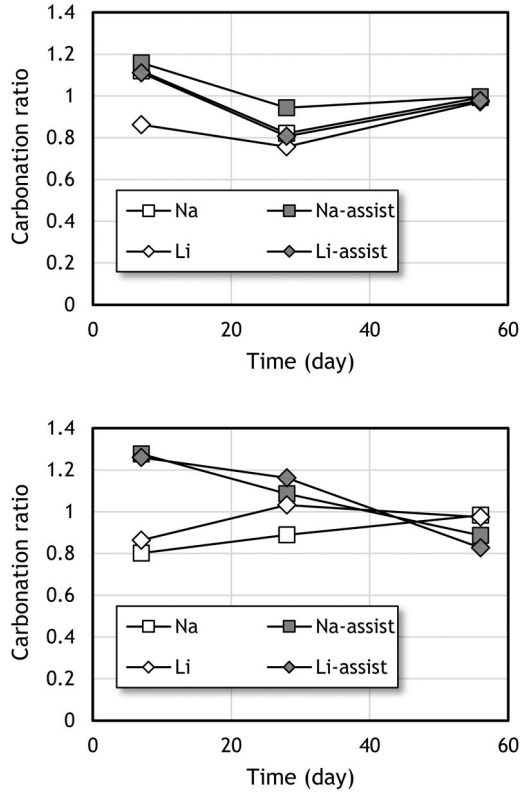

Figure 7. Carbonation ratio (top: N-60, bottom: FA-70).

of calcium hydroxide is less than that of N-55 and FA-55. So, the reactive amount of the penetrants in these cases (N-60 and FA-70) is also a little even though the additive for assisting the reaction was added.

From Figure 6, it is thought that N-55 and FA-55 specimens with penetrants had improved the resistance against carbonation due to an improvement in concrete surface quality. In the case of FA-55, the carbonation ratio closes to 1.0, which means the effectiveness of the penetrants was gone, at around 56 days, although it can be seen that the effectiveness may continue at least at around same time in the case of N-55. In the FA specimens, the amount of calcium hydroxide may be less due to the pozzolanic reaction of FA, and thus the carbonation ratio of FA specimens with the silicate-based surface penetrant at 56 days was higher than that of OPC specimens.

The progress of carbonation depth of concrete when the penetrants is applied can be expressed by Equation 3 (see Figure 8).

$$\begin{aligned} y &= \alpha_p \sqrt{t} && y \le z \\ y &= z + \alpha_c \left(\sqrt{t} - z/\alpha_p \right) && y > z \end{aligned} \tag{3}$$

where y = carbonation depth (mm); t = time (day); α_p = carbonation rate for penetrant application (mm/day$^{0.5}$); z = improvement depth by penetrants

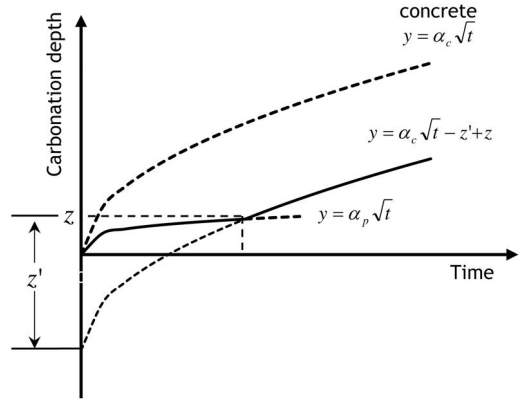

Figure 8. Image of carbonation progress.

(mm); and α_c = carbonation rate for no penetrant application (mm/day$^{0.5}$).

The improvement depth of concrete by the penetrants (z) can be calculated by using Equation 3. Then, the carbonation rate for penetrant application was obtained using the measured data until 28 days.

The calculation result of the improvement depth is shown in Table 4. The calculation could not be carried out for N-60 and FA-70 because the carbonation depth already exceeded the improvement depth. The results

Table 4. Improvement depth calculation result.

Code	N-55 (mm)	FA-55
Na7	1.5	0.48
Na14	1.9	0.42
Li7	1.1	0.76
Li14	1.4	0.71

showed that the improvement depth became around 1 to 2 mm for N-55 and around 0.4 to 0.8 mm for FA-55. In the case of the sodium-type silicate application, the difference between concrete types appears to be large, whereas for lithium-type silicate the penetration depth is around the same for the two concrete types. In the previous studies, the penetration depth was reported to be around 20 mm from the surface (Sakamoto, et al. 2011). Therefore, the affected depth found in this experiment was lower than that in previous studies.

4 CONCLUSIONS

The effect of the application of silicate-based surface penetrants on the mass transport properties of concrete was experimentally examined. The results are summarized as follows.

1) When comparing OPC specimens with FA specimens, it could be seen that the application was more effective at 14 days for OPC specimens but more effective for FA at 7 days. And the FA55 showed a marginal improvement, especially at 14 days.
2) Silicate-based surface penetrants were applied to the water-cement ratio 0.55 specimens and improved resistance against carbonation. In the case of high water-binder ratio, the effect of the penetrants could not be seen clearly even though the application of calcium hydroxide was utilized.
3) The improvement depth of concrete in the case of water-binder ratio = 0.55 was around 0.4 to 2 mm depending on the concrete quality and the kind of penetrants.

ACKNOWLEDGMENT

A part of this work was supported by KAKENHI (23360189).

REFERENCES

Hazehara H., Takewaka K., Yamaguchi T. and Sirosawa N. 2010. Fundamental study on performance and difference of various surface improvement material. *Proceeding of the Japan Concrete Institute*. 32(1): 1619–1624. (in Japanese)

Japan Society of Civil Engineers (JSCE). 2005. *Recommendation for Concrete Repair and Surface Protection of Concrete Structures*. Concrete Library 119. (in Japanese)

Japan Society of Civil Engineers (JSCE). 2012. *RGuideline on Design and Application Methods of Silicate-based Surface Penetrants used for Concrete Structures*. Concrete Library 137. (in Japanese)

Sakamoto S., Takewaka K., Yamaguchi T. and Hazehara H. 2011. Effects of surface improvement material on chloride panetration and neutralization. *Proceeding of the Japan Concrete Institute*. 33(1): 1625–1630. (in Japanese)

This page intentionally left blank

Concrete Solutions – Grantham et al. (Eds)
© 2014 Taylor & Francis Group, London, ISBN 978-1-138-02708-4

Hybrid surface protection repair system using UHP-SHCC for concrete structures – from design to application

M. Kunieda
Department of Civil Engineering, Gifu University, Gifu, Japan

ABSTRACT: Surface protection repair is one of the effective methods to recover the durability performance of deteriorated concrete structures due to penetration of corrosive substances such as chloride ions, water, CO_2 and so forth. Re-deterioration such as cracking, delamination and swelling of repair material itself has, however, been reported. This paper introduces a hybrid surface protection repair system that has the function of both a patching repair and a surface coating. The system comprises an Ultra High Performance-Strain Hardening Cementitious Composite (UHP-SHCC) having a dense matrix applied by a spraying technique. It can also contribute to reduce the construction process compared to an ordinary surface coating repair. This paper also represents an example of a trial site application.

1 INTRODUCTION

Surface protection repair is one of the effective methods to recover the durability performance of deteriorated concrete structures due to penetration of corrosive substances such as chloride ions, water, CO_2 and so forth. In ordinary repair for concrete structures with rebar corrosion, patch repair to recover the cross section of concrete and surface coating by polymers have been applied. Figure 1 shows a retaining wall with alkali silica reaction (ASR), and re-deterioration such as cracking, delamination and swelling have been observed on the surface coating material. In addition, it requires many construction processes and time. There is also a technical issue on ordinary surface coating repair. In general, the coating consists of several layers, such as a main layer and top coating, and it involves longer repair time.

Figure 1. Example of re-deteriorated repair system.

Ultra High Performance-Strain Hardening Cementitious Composites (UHP-SHCC) have been developed for repair of concrete structures (Kunieda 2009, 2010, 2011). UHP-SCC is a cement based repair material that exhibits high strength with multiple fine cracking phenomena and high resistance against penetration of corrosive substances. And also, not only a casting but also a spraying technique has been developed for repair applications.

This paper introduces this hybrid surface protection repair system (hybrid system) that has the function of both a patch repair and surface coating, and presents an example of a trial site application.

2 CONCEDPTUAL IDEA AND ADVANTAGES OF HYBRID SURFACE PROTECTION REPAIR

One of the advantages of the hybrid system is to provide high protective performance by the UHP-SHCC having a dense cement based matrix.

As shown in Table 1, the UHP-SHCC consists of low heat Portland cement, silica fume, expansive additive, quartz sand and high strength polyethylene (PE) short fibers. To obtain high strength and high protective performance, the water to binder ratio is 0.22. Fiber addition reduces cracking due to drying and autogenous shrinkage, in addition to material ductility. The length and diameter of the fiber is 6 mm and 12 micron, respectively. The volume fraction of the fiber is 1.5%. As tabulated in Table 2, compressive strength and tensile strength at the age of 28 days are over 80 Ma and 8 MPa, respectively, and compressive strength at the age of 91 days is over 110 MPa. Tensile strain capacity is over 2.0%, and crack width at that time is less

Table 1. Mix proportions of the UHP-SHCC.

W/B	Water	Cement	Silica fume	Expansive add.	Sand	Supeplasticizer	AE agent	Fiber
0.22	342	1344	207	39	165	12.2	0.41	23.8

Table 2. Mechanical properties of the UHP-SHCC.

Age	Compressive strength (MPa)	Tensile strength (MPa)	Strain at tensile strength (%)
28 days	84	8.7	2.5
91 days	113	8.9	2.1

Table 3. Properties of resistance against penetration of corrosive substances.

	UHP-SHCC	Ordinary concrete (W/C = 0.56)
Effective diffusion coef. (cm^2/year)	0.05	2.4
Air permeability coef. by Torrent (10^{-16} m^2)	0.005	5.4
Water permeability (ml/day)	0.03	8.2

Table 4. Advantages of hybrid system with the UHP-SHCC.

(1) Impermeable material	The UHP-SHCC has a dense matrix, and higher resistance against penetration of corrosive substances. After cracking, multiple fine cracks contribute to prevent sudden reduction of durability performance.
(2) Jointless protective layer	A Jointless protective layer is required in durable repair. Construction in situ (spraying technique) is adopted, to give a protection layer without joints.
(3) Thickness of protection layer helps monitoring	Thickness of protection layer is about 10 mm. The thickness is helpful to detect penetration depth of chloride ion though drilling technique. This contributes to reliable maintenance.
(4) Simplified construction process	Many construction processes in ordinary patch repair and surface coating repair can be simplified such as primer.
(5) High tensile strength	High tensile strength – can be used on a load bearing member.

than 0.05 mm with multiple cracking. This cracking phenomenon can prevent a significant reduction of durability after cracking.

Material ductility due to short fibers can impart higher resistance against spalling of cover concrete by corrosion to structures after the repair.

The UHP-SHCC without (before) a crack has resistance against penetration of substances such as chloride ions, water, oxygen and so forth, as shown in Table 3. A hybrid system using the UHP-SHCC can reduce the thickness of cover concrete.

Advantages of the hybrid system are tabulated in Table 4. Since a jointless layer system is required for durable repair, a precast system is not suitable because of durability of joint itself. A spraying technique in situ is adopted in the hybrid system.

The hybrid system uses a thickness of about 10mm, whereas in ordinary surface coating repair using epoxy resin, the thickness is only micron level. Sudden deterioration such as cracking, delamination, swelling is observed because of thinness of the layer. In the developed repair, about 10 mm thickness is useful to detect penetration depth of chloride ion or depth of carbonation by means of drilling technique. If the depth can be monitored, re-deterioration can be controlled, and reliability of the system will be increased.

In ordinary patching repair and surface coating repair, there are many construction processes. These increase the construction period and decrease service to society because of, for example, traffic jams. Therefore, the construction process should be decreased as far as possible. The hybrid system has two functions: recovery of cross-section of a member and making a protective layer, rather than both an ordinary patching repair and surface coating repair.

Finally, the UHP-SHCC has high tensile capacity, and the repaired layer is also a strengthening layer. The contribution of the material to mechanical performance should be considered in design.

3 APPLICATIONS TO AN RC WALL IN A BRIDGE

3.1 *Outline*

The target of application was an RC wall in bridge. The height of the wall was about 1 m. As shown in Fig. 2, corrosion of rebar and spalling of cover concrete

were observed. The dominant deterioration mechanism was carbonation. The sound areas in the figure were also undoubtedly corroded or would be potentially corroded in the near future. In this study, three kinds of repair method were applied for comparison; one was the hybrid system, the second one was an ordinary patch repair system using polymer cement mortar (Acrylic resin type) and the last one was both patch repair and surface coating repair (Epoxy resin type). As shown in Fig. 3, the area of construction was 15 m^2 for each system.

Figure 2. Deteriorated RC wall in bridge.

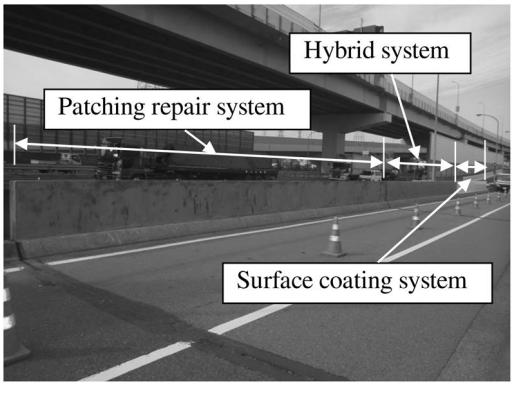

Figure 3. Overview of construction site and each applied system.

3.2 *Procedures for repair applications*

Table 5 shows the procedures for the three kinds repair applications including the hybrid system.

In the first stage, removal of carbonated and cracked concrete was carried out up to the depth of rebar, and anti-corrosion agent was painted on the rebar. Note that these processes were common in all series.

Because the patch repair process in the hybrid system using the UHP-SHCC is similar to an ordinary patch repair system using PCM with spraying technique, the total period required for construction was 10 hours. On the other hand, surface coating system with patching repair and surface coating repair involves preparation of substance, painting of main and top coats, in addition to the patch repair process, each process also requires curing time. Eventually, surface coating system involves 2 days totally for complete. Moisture on the substrate should be controlled severely.

Eventually, the construction period for the hybrid system was dramatically squeezed, and duration of regulation of traffic could also be reduced, compared to a surface coating system.

4 CONCLUSIONS

This paper described the concept of hybrid surface protection repair system and its application. There

Table 5. Procedures for applied repair systems.

System	Procedures
(1) Hybrid system (the UHP-SHCC) (10 hours for 15 m^2)	• Spraying of the UHP-SHCC (Thickness: ordinary surface level + 10 mm) • Troweling
(2) Patching repair system (10 hours for 15 m^2)	• Primer • Spraying of Polymer Cement Mortar (Thickness: ordinary surface level + 15 mm) • Troweling
(3) Surface coating system (2 days for 15 m^2)	<Patching repair> • Primer • Spraying of Polymer Cement Mortar (Thickness: ordinary surface level) • Troweling <Surface coating repair> • Preparation of substance (Epoxy primer) • Substrate putty (Epoxy resin) • Main coat (Epoxy resin) • Top coat (Fluorocarbon)

*Preparation of substrate including concrete removal and anti-rust preparation were carried out in all process

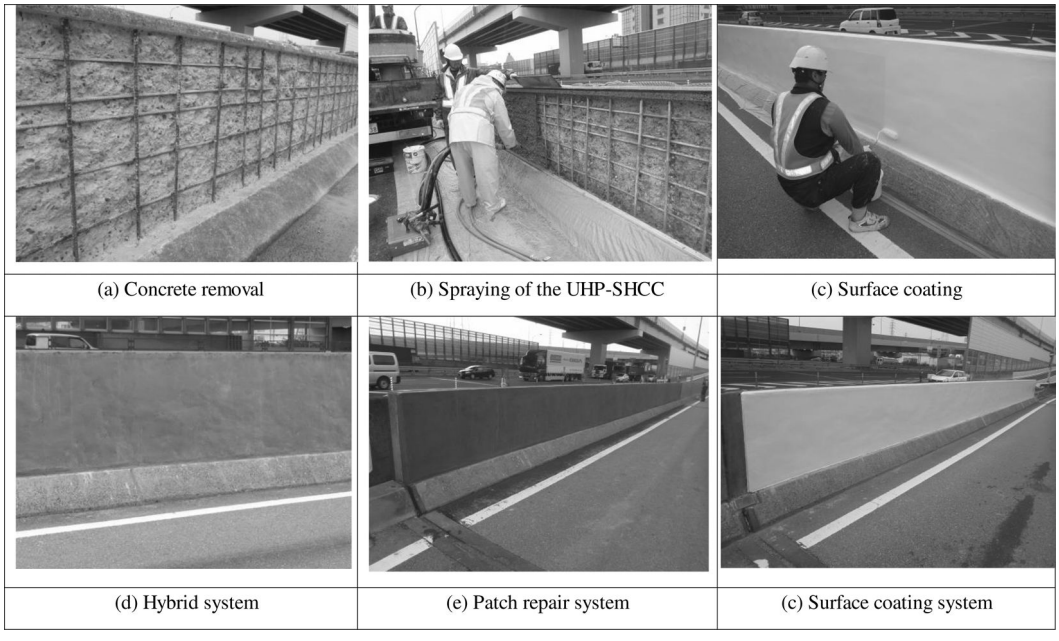

Figure 4. Photo of each construction process.

are many advantages of the system from construction phase to maintenance phase. A monitoring of the repaired RC wall has been started, and the results will be presented in a later paper.

REFERENCES

Kunieda, M., Ueda, N. and Nakamura, H. 2009. Ultra High Performance Strain Hardening Cementitious Composites (UHP-SHCC) for repair applications, *Proc. of 4th International Conference on Construction Materials*, pp. 313–318.

Kunieda, M., Hussein, M., Ueda, N. and Nakamura, H. 2010. Enhancement of crack distribution of UHP-SHCC under axial tension using steel reinforcement, *Journal of Advanced Concrete Technology*, 8(1), 49–57.

Kunieda, M., Umeda, Y., Ueda, N. and Nakamura, H. 2011. Rapid jacketing technique by using UHP-SHCC for damaged RC column under seismic loading. In Parra-Montesinos, G. J., Reinhardt, H. W. and Naaman, A. E. (eds.), *High Performance Fiber Reinforced Cement Composites 6*, pp. 429–436.

Concrete Solutions – Grantham et al. (Eds)
© 2014 Taylor & Francis Group, London, ISBN 978-1-138-02708-4

The impact of curing compounds on the leaching from concrete

D.W. Law & S. Setunge
RMIT University, Melbourne, Victoria, Australia

ABSTRACT: When concrete structures are constructed in water they can potentially have a detrimental effect on the surrounding environment by causing the pH in the water to rise. This rise in pH can harm both animal and plant life. One method of trying to control this leaching is to apply a curing compound to the concrete prior to exposure to water. This paper presents the results of a research project that investigated four different generic curing compounds to determine their effect of rate of leaching and the peak pH produced. Tests were conducted in slow flowing water, analogous to systems where impacts have been observed. A range of curing compounds, together with a control specimen, was investigated. The results showed that while all the curing compounds demonstrated a reduction in leaching only one compound actually reduced the peak pH to a level below which any impact on the flora and fauna may occur.

1 INTRODUCTION

Concrete is the most widely used construction material today with an estimated ten billion tons produced world-wide each year. A significant quantity of this concrete is used in the construction of structures which are built in water, such as bridge supports, piers and culverts. Construction in water can cause environmental concerns including the release of ions, such as aluminum, calcium, magnesium, sodium, potassium and zinc, into the surrounding water and can increase the pH in the water, due to leaching from the concrete.

When freshwater becomes highly alkaline it can become toxic to fish. For example a change from pH 7 to pH 8 will result in ammonia becoming ten times more toxic to fish. In the open sea and flowing river systems the released hydroxyl ions are rapidly diffused and diluted. However, in small, slow flowing streams, this may not be the case, with possible adverse impacts on local aquatic species.

To date the majority of previous research has focused on the long term leaching from concrete, particularly with regard to the containment of waste materials and the leaching of metal ions rather then monitoring the pH directly. Research has shown that in long term exposure, the alkali metals, Na^+ and K^+ are removed first. This is followed by the dissolution of the Portlandite and finally leaching of Ca^{2+} from the C-S-H gel.

Kamali (2008) showed that the water to cement ratio is particularly important as the greater the ratio the more water there is available in the concrete to aid the leaching process. The volume to surface area ratio has also been shown to affect the rate of leaching since the surface area will affect the specific solid/liquid exchange surface.

In long term tests, Alonso (2006) reported an initial rise in pH when conventional concretes, as well as high and ultrahigh performance concretes, were exposed to water, though these specimens were cured in limewater for 28 days before exposure. Research by Setunge (2009) on concrete exposed at one day showed that the pH of stagnant water rose to approximately 11.5 and then fell to a steady state of approximately 9, similar results were observed by Law.

Research by Sagüés (1997) in a small volume of water showed that as Ca^{2+} is leached out of the concrete, the pH of the water rose until a terminal pH was reached. While Law and Evans (2013) reported a similar trend for Ordinary Portland (OP) cement, Fly Ash (FA) and Blast Furnace Slag (BS). Jain observed that leaching of Ca^{2+} was reduced by the use of blended cements, compared to ordinary Portland cement.

At present a number of Authorities in Australia (Tasmanian Department of Primary Industries, Parks, Water and Environment, RTA New South Wales), and worldwide, have best practice guidelines that suggests any cast-in-place concrete should be isolated from the waterway for at least 48 hours to allow the pH to neutralise. However, recent collaborative research at RMIT has suggested that little reduction in the degree of leaching and rise in pH is observed even after 7 days gap prior to exposure. A potential method to control this initial rise in concrete would be to apply a curing compound to the concrete to reduce/halt the leaching from the concrete. This paper reports the results of a research project that investigated four different generic curing compounds to determine their effect of rate of leaching and the peak pH produced.

Table 1. Curing compound: Type and designation.

Type	Designation
Wax Based Emulsion	WBE
Water Borne Hydrocarbon Resin	WBHR
Water Borne Acrylic Emulsion	WBAE
Water Based Acrylic Curing Compound	WBACC

Table 2. Mix design.

Constituent	Quantity (kg/m^3)
OP cement	350
Aggregate 10 mm	570
Aggregate 7 mm	570
Aggregate sand	589
Water	158

2 EXPERIMENTAL

A total of four commercially available curing compounds were selected for testing, Table 1. These were selected to cover a range of curing compounds available. Curing compounds identified as potentially harmful to the environment were discounted.

The coatings were applied in accordance with the manufacturer's specifications on to a standard OP concrete. The specimen size was $0.1 \times 0.1 \times 0.2$ m (giving a Surface Area:Volume ratio of 50. The concrete used was a standard OP concrete with a nominal 28 day compressive strength of 45 MPa. The mix specification is given in Table 2.

In addition to the four curing compounds a control specimen with no coating was also cast from the same mix and monitored for pH verses time.

Specimens were demoulded at 24 hours and placed in the leaching tank with a constant rate of flowing water. A number of test methods have been used by previous researchers to investigate leaching of monolithic materials under flow conditions and have shown the validity of using flowing water tests.

The leaching tank was designed with a 201 cm internal diameter, Figure 1. The base was attached to the cylinder by silicone cement and the lid was sealed with a foam ring and held down by bolts attached to a ring around the tube just below the lid. The inlet pipe was terminated close to the bottom of the tank to ensure full circulation within the tank allowing the water to come into contact with the specimen. The pipe had an internal diameter of 17 mm and a neck on the end to initiate a swirling effect around the tank. The height of the tank was 325 mm. A pH probe was placed at the end of the outlet pipe where the leaching discharged.

The water volume in the tank was 6.3 litres. The flow rate was 5 ml/s. Tap water was used in the experiments to provide a constant flow of water. The specimen was immersed in the middle of the tank allowing circular flow of water around the specimen. The pH was measured using a Thermo scientific Alpha pH 500 pH transmitter and data were stored using an automated data collection unit. The pH was monitored until it returned to the initial pH of the water.

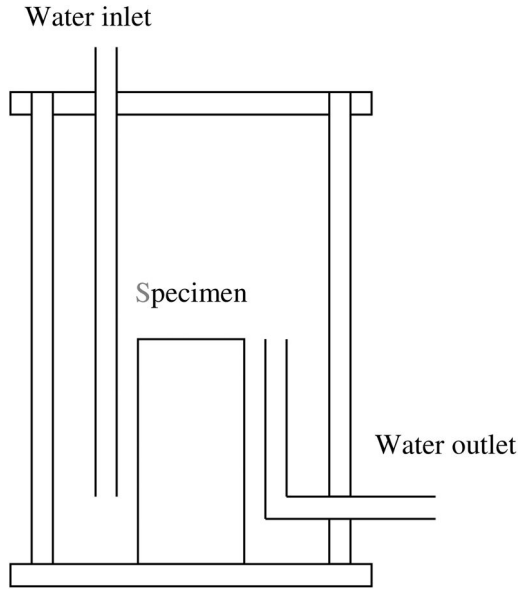

Figure 1. Leaching tank.

Table 3. Peak pH and time to peak pH.

Specimen	Peak pH	Time to peak (min)
WBE	9.10	70.5
WBHR	9.05	135.5
WBAE	7.43	59.5
WBACC	9.29	54.0
Control	9.81	60.5

3 RESULTS

Duplicate specimens were tested and the average reported for each compound together with the control. The pH versus time was recorded and the peak pH and time to pH are given in Table 3.

The results for the WBE, WBHR, WBACC and the control all show similar trends. The data show a rapid increase in pH followed by a gradual decrease back to the initial pH of the water. This is a similar profile to that found by other authors. The plots of time vs pH are given in Figures 2–5.

The highest pH was observed with the control giving a peak pH of 9.81. The WBE, WBHR and WBACC did show a slight reduction in peak pH, with values of 9.10, 9.05 and 9.29 respectively. These values are again consistent with those observed by other authors. While these curing compounds achieved a slight reduction, the pH's measured are still in excess of values that

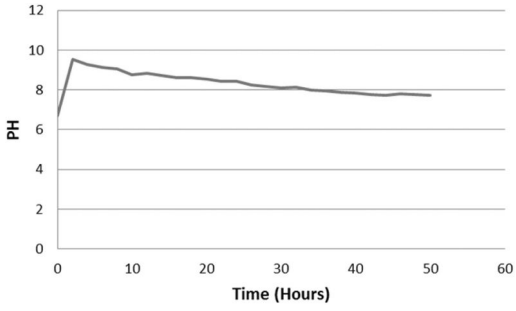

Figure 2. pH vs. time, control.

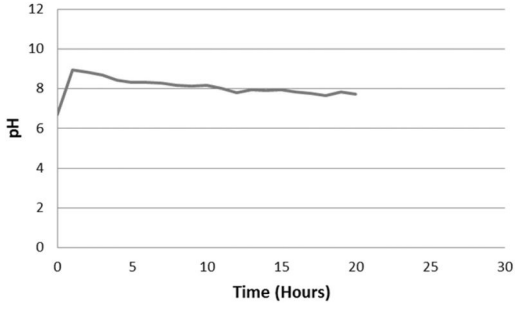

Figure 3. pH vs. time, WBE.

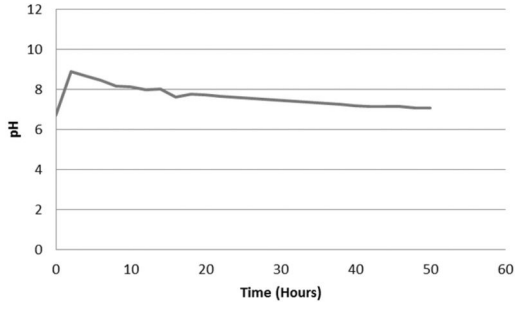

Figure 4. pH vs. time, WBHR.

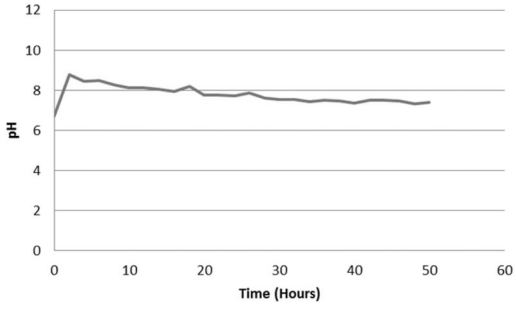

Figure 5. pH vs. time, WBACC.

would be expected to have a harmful effect on the aquatic flora and fauna exposed to the leachate.

The time to the peak pH was also similar for the WBE, WBACC and the control, all being in the region of 50–60 minutes. The WBHR did double the time

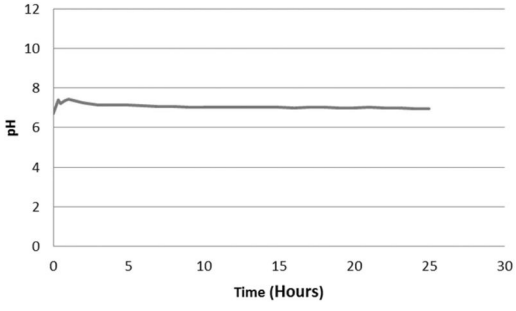

Figure 6. pH vs. time, WBAE.

Table 4. Cumulative hydroxyl ion concentration.

Specimen	Peak pH	Cumulative [OH^-] (moles)
WBE	9.10	0.0120
WBHR	9.05	0.0136
WBAE	7.43	0.0005
WBACC	9.29	0.0149
Control	9.81	0.0743

passed until the peak pH was reached but had little effect on the peak pH achieved. The other common factor was that all of the specimens with curing compounds applied showed a much sharper peak pH peak with a rapid fall in pH following the peak compared to the control concrete.

The WBAE, Figure 6, however, produced a significant reduction in the peak pH, 7.43 though had no impact on the time to the peak. The overall shape of the plot remained the same as for the other specimens.

In addition to the peak pH and the time to the peak the total number of hydroxyl ions leached was determined, Table 4.

The cumulative data indicates that while the WBE, WBHR and WBACC only give a minimal reduction in the peak pH they reduce the total quantity of hydroxyl ions leached by 80–85%. The WBACC has an even greater impact reducing the concentration of hydroxyl ions by 99%.

4 DISCUSSION

All of the tests show an initial sharp rise in pH followed by a slow decline in pH back to the initial pH of the water. The observations can be explained by the hydration process. In the long term leaching from concrete, the more soluble Na^+ and K^+ are leached first, followed by dissolution of the Portlandite, $Ca(OH)_2$, before finally the C-S-H gel. However, when concrete is immediately exposed to the water the hydration reaction is still ongoing. In OP concrete the cement undergoes hydration on addition of the mix water to form CSH gel and $Ca(OH)_2$. As for the long term

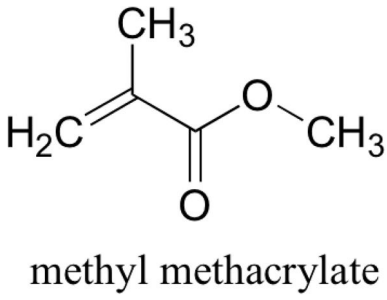

Figure 7. Structure of the methyl methacrylate monomer.

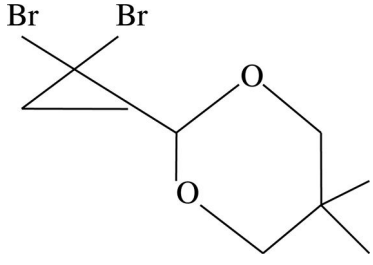

Figure 8. Structure of the WBHR monomer.

leaching it is anticipated that the more soluble Na^+ and K^+ are again leached first, followed by the $Ca(OH)_2$ which is produced by the hydration reaction. The peak pH and cumulative number of moles of hydroxyl ions leached will be dependent upon the quantity Na^+ and K^+ available from the cement used and to a larger degree on the amount of $Ca(OH)_2$ produced during the hydration reaction.

The results show that all the specimens with curing compounds gave a significant reduction in the total quantity of hydroxyl ions leached from the concrete. However, the most effective curing compound used was the water borne acrylic emulsion, with the other three systems all giving similar results. The WBAE contains about 10% methyl methacrylate in emulsion. Methyl methacrylate is an organic compound with formula $CH_2{=}C(CH_3)COOCH_3$, Figure 7.

The WBHR is composed of 30–60% polymer resin made from a 9 carbon monomer, using 10–30% light aliphatic naphtha as a solvent. The chemical structure of the monomer is given in Figure 8.

The WBACC is a liquid acrylic emulsion membrane curing compound containing 40% solids and the WBE is a wax based emulsion containing <10–*30% wax/emulsifier, and 10–30% wax.

The curing compounds form a film or membrane around the concrete to retain water and prevent drying out of the concrete. It has previously been reported that the wax based emulsions give a higher water retention efficiency than either the hydrocarbon resins or acrylic based compounds, Figure 9.

The results indicate that the water retention efficiency is not the dominant factor in the leaching from the concrete. Indeed given that both the WBAE and the

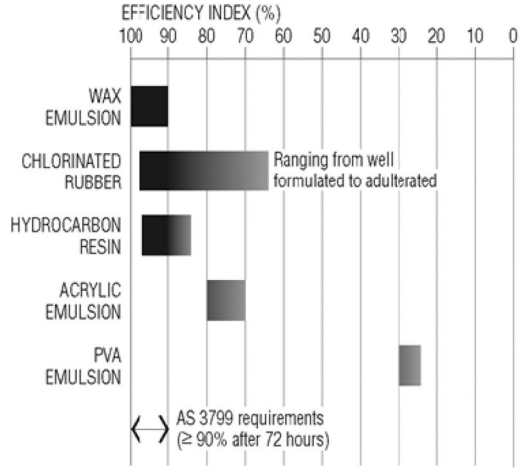

Figure 9. Water retention efficiency index.

WBACC are acrylic based it is hypothesized that it is the specific active ingredient, i.e. the methyl methacrylate that is the primary factor in the WBAE compound that is causing the reduction in the leaching of the hydroxyl ions from the concrete. This may be due to the methacrylate reacting with the cementitious material to prevent the leaching of the hydroxyl ions from the $Ca(OH)_2$ formed during the hydration process, or alternatively by providing a stronger barrier/film to prevent the hydroxyl ions from diffusing out of the concrete. That the cumulative and peak pH are both reduced, coupled with the observation that none of the other compounds give any reduction in the peak pH and a lesser reduction in the cumulative concentration of hydroxyl ions leached, suggests that it is more likely that it is a chemical reaction with the methacrylate that is impacting on the leaching process.

This is supported by the increase in curing time, but not in peak or cumulative pH, for the WBHR compound. This would suggest that the barrier/film produced by the curing compounds can delay the leaching process but has a minimal impact on the process itself.

5 CONCLUSIONS

Leaching from freshly cast concrete can lead to an increase in pH to above 9.0. This increase in pH can be detrimental to the health of flora and fauna.

The application of a wax based emulsion, a water borne hydrocarbon resin and a water borne acrylic curing compound to freshly cast concrete gave a small reduction in peak pH, but the peak value observed was still above pH 9.

The application of a water borne hydrocarbon resin curing compound was able to delay the time to the peak pH.

The wax based emulsion, water borne hydrocarbon resin and water borne acrylic curing compounds

reduced the cumulative quantity of hydroxyl ions leached by 80%.

The water borne acrylic emulsion curing compound was able to reduce the peak pH to less than 7.5 and to reduce the cumulative hydroxyl ion concentration by up to 99%.

It is hypothesized that it is the methyl methacrylate present in the water borne acrylic emulsion which is the dominant factor in reducing the peak and cumulative pH due to leaching.

REFERENCES

Alabaster, J.S., and R. Lloyd. "Water Quality Criteria for Freshwater Fish." In *European Inland Fisheries Advisory Commission Report*, 1980.

Alonso, C., M. Castellote, I. Llorente, and C. Andrade. "Ground Water Leaching Resistance of High and Ultra High Performance Concrete's in Relation to the Testing Convection Regime." *Cement and Concrete Research* 32 (2006): 1283–594.

Andac, M., and F. P. Glasser. "Long-Term Leaching Mechanisms of Portland Cement-Stabilized Municipal Solid Waste Fly Ash in Carbonated Water." *Cement and Cement and Concrete Research* 29, no. 8 (1999): 179–86.

C&CA. "Curing of Concrete." edited by Cement and Concrete Aggregates. Australia, 2006.

Clifford, N., J. French, and J. Hardisty. *Turbulence – Perspectives on Flow and Sediment Transport*. New York: John Wiley & Sons Ltd, 1993.

Geankoplis, C *Transport Processes and Separation Process Principles*. Professional Technical Reference Prentice Hall, 2003.

Jain, J., and N. Neithalath. "Analysis of Calcium Leaching Behaviour of Plain and Modified Cement Pastes in Pure Water." *Cement and Concrete Research* 31 (2009): 176–85.

Kamali, S., M. Moranville, and S. Leclerqc. "Material and Environmental Parameter Effects on the Leaching of Cement Pastes: Experiments and Modelling." *Cement and Concrete Research* 38 (2008): 575–85.

Law, D. W., and J. Evans. "The Effect of Leaching on the Ph of Water." *ACI Materials Journal* 110, no. 3 (2013): 291–96.

Law, D. W., S. Setunge, R. Adamson, and L. Dutton. "Effect of Leaching from Freshly Cast Concrete on Ph." *Magazine of Concrete research* 65, no. 15 (2013): 889–97.

Meyer, C. "The Greening of the Concrete Industry." *Cement and Concrete Composites* 31 (2009): 601–05.

Neville, A. M. *Properties of Concrete*. Prentice Hall, 2012. 5th Edition.

Sagues, A. A., E. I. Moreno, and C. Andrade. "Evolution of Ph During the in-Situ Leaching in Small Concrete Cavities." *Cement and Concrete Research* 27, no. 11 (1997): 1747–59.

Setunge, S., N. Nguyen, B. Alexandar, and L. Dutton. "Leaching of Alkali from Concrete in Contact with Waterways." *Water Air Soil Pollution Focus* 9 (2009): 381–91.

van der Sloot, HA "Comparison of Characteristic Leaching Behaviour of Cements Using Standard (En 196-1) Cement Mortar and an Assessment of Their Long Tern Environmental Behaviour in Construction Products During Service Life and Recycling." *Cement and Cement and Concrete Research* 30 (2000): 1079–96.

This page intentionally left blank

Concrete Solutions – Grantham et al. (Eds)
© 2014 Taylor & Francis Group, London, ISBN 978-1-138-02708-4

Determination of chloride ion diffusion coefficient in outer layer of concrete with silicate-type surface penetrant

S. Miyazato & D. Kuroiwa
Kanazawa Institute of Technology, Ishikawa, Japan

ABSTRACT: Surface penetrants are often employed as part of preventive maintenance procedures for concrete structures. Guidelines for the use of surface penetrants state that chloride ingress into the reformed surface parts is different from that into the deeper, nonreformed parts; to ensure durability after repair, the design of the structure should consider the chloride ion diffusion coefficients of both the parts. However, there is no established method to determine the diffusion coefficient of the reformed part.

This paper proposes a method for determining the apparent chloride ion diffusion coefficient in outer concrete layers reformed by silicate-type surface penetrants. The extent of surface penetration was investigated on the basis of the Vickers hardness distribution inside the concrete. Subsequently, a concrete specimen to which a surface penetrant was applied was exposed to a chloride environment, and the chloride ion concentration distribution in the concrete was measured. Simultaneously, the chloride ion distribution was measured for a concrete specimen without the penetrant treatment, and the two specimens were compared. To determine the diffusion coefficient of the penetrated part, a comparison was made by considering the equivalent cover depth. Such measurements imply that a segmented thickness with a low diffusion coefficient (conferred by the surface penetrant) can be replaced with a cover depth of normal concrete. The results showed that the penetration depths of the surface penetrants were 3–7 mm, and the apparent chloride ion diffusion coefficient was 0.4–0.6 cm^2/year.

The applicability of the results was demonstrated by gauging the effect of the surface penetrant in delaying the onset of corrosion by using the apparent chloride ion diffusion coefficients calculated in the study. The results confirmed that the use of surface penetrants delays the initial stages of corrosion by up to a maximum of 18 years.

1 INTRODUCTION

Design methods for concrete structures have changed from specification-based to performance-based; this transition applies not only to the design of new structures but also to the repair of existing structures. Accordingly, guidelines for performance-based structural design describe procedures for their durability after the repair. However, these guidelines do not provide methods to measure input data for repair work, such as the chloride ion diffusion coefficient; the upgrade after the repair cannot be quantitatively evaluated.

The maintenance of concrete structures has shifted to taking preventative measures from taking corrective measures; treatment by surface penetrants is one such method, which prevents the penetration of salt water into the structure. This technique allows simple inspection by visual observation after its application because of its transparency.

Two main types of surface penetrants exist: silane-type and silicate-type. Silane-type surface penetrants confer a water-repellent layer to the concrete surface, which is described in EN 1504-2 as "hydrophobic impregnation (H)". The design guideline was published in 2005 by Japan Society of Civil Engineers (JSCE). Conversely, silicate-type surface penetrants form an extremely dense protective outer concrete layer via the formation of a C-S-H gel, which is described in EN 1504-2 as "impregnation (I)." The design guideline was finally published in 2012 by JSCE.

When surface penetrants are applied, the chloride ion diffusion coefficient in the reformed part becomes different from the nonreformed part. However, methods to identify the reasons for this phenomenon have not yet been established; the penetration of the chloride ion into concrete applied with surface penetrants cannot be predicted quantitatively.

This paper proposes a method to estimate the chloride ion ingress when silicate-type surface penetrants are applied to concrete in preventative maintenance; a method to determine the apparent chloride ion diffusion coefficient in the reformed parts of the structure is reported. To demonstrate the practical application of such methods, the influence of surface penetrant application in delaying the onset of corrosion was examined.

2 FLOWCHART FOR DETERMINING DIFFUSION COEFFICIENT

When part of an outer concrete layer is reformed by surface penetrants, the penetration of chloride ions through the layer is prevented. The cover depth is increased, and therefore, an extra amount of non-reformed concrete guarantees the same effect as shown in Figure 1. This thickness is known as the equivalent cover depth (JSCE, 2005).

Additionally, the part reformed by silicate-type surface penetrants is very dense. As a result, the hardness of the reformed part increases; in this study, the distribution of the Vickers hardness values in the concrete outer layer are useful as an index to distinguish between the reformed and nonreformed parts.

A flowchart to determinate the apparent chloride ion diffusion coefficient in the reformed part of the structure is shown in Table 1 and Figure 2. The left

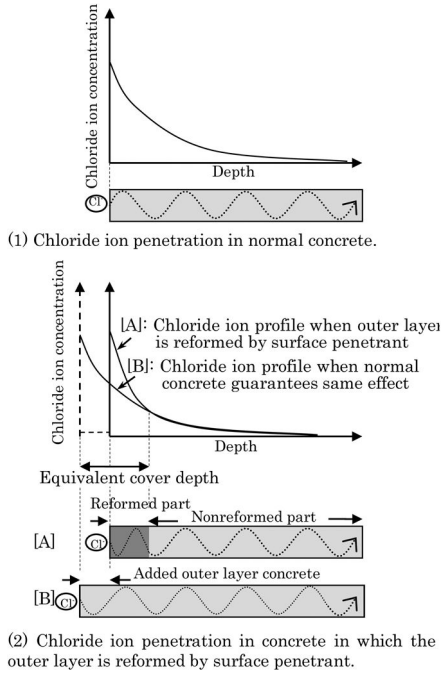

Figure 1. Equivalent cover depth.

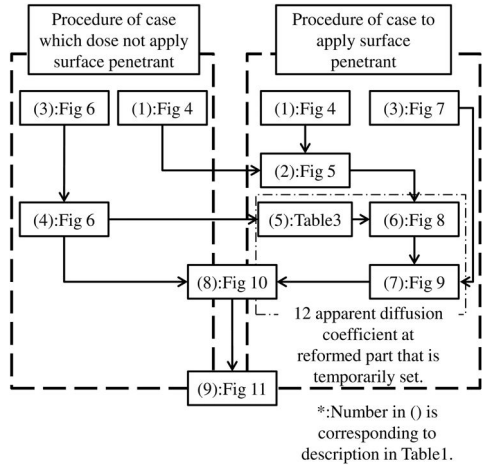

Figure 2. Flowchart to determine apparent chloride ion diffusion coefficient.

Table 1. Step to determination of apparent chloride ion diffusion coefficient.

Step	Operation
(1)	Vickers hardness at the concrete outer layer part in both cases is measured.
(2)	Area of hardness of the specimen where the penetrant is applied is found to be larger than that of specimens with no penetrant application; this is identified as the reformed depth, i.e., the side nearer to the surface than the reformed depth becomes the reformed part, while the further side becomes the nonreformed part.
(3)	Concrete powder from the outer layer part is collected using a drill. Chloride ion concentration is determined as a function of depth by the analysis set out in JSCE-G 573.
(4)	The apparent diffusion coefficient in the nonreformed part is identified by analysis under Fick's laws of diffusion, as shown in equation (1): $$C(x,t) = C_0\left(1 - erf\frac{x}{2\sqrt{D \cdot t}}\right) \quad (1)$$ $C(x,t)$: chloride ion concentration at depth x (cm) and time t (years) (kg/m^3) C_0: chloride ion concentration at the concrete surface (kg/m^3) D: apparent chloride ion diffusion coefficien (cm^2/year) erf: error function
(5)	The apparent diffusion coefficient in the reformed part is temporarily set at 12 levels in the range 1%–50% of the apparent diffusion coefficient at the nonreformed part.
(6)	The equivalent cover depth is converted, while the ratio of the apparent diffusion coefficients at the reformed and nonreformed parts is considered. This equivalent cover depth is added as an outer layer of concrete.
(7)	The chloride ion concentration measured in the penetrant-applied specimen is redistributed so that it is plotted over the plus direction in the x-axis, including the added outer layers of concrete.
(8)	Twelve values of the apparent diffusion coefficients set in step (5) are compared with the value of the apparent diffusion coefficient for the nonapplied specimen obtained in step (4). The value that most closely accords with the value in step (4) is chosen.
(9)	This value is identified as the apparent diffusion coefficient in the reformed part.

section of Figure 1 shows the procedure for the case which does not apply a surface penetrant, while the right section shows the procedure in cases where a penetrant is applied.

In this study, it is assumed that the apparent diffusion coefficient in the reformed part is constant in the area shallower than the reformed depth, according to the guidelines in "Recommendation for concrete repair and surface protection of concrete structures" (JSCE 2005).

3 EXPERIMENTAL PROCEDURES

3.1 *Specimen preparation*

The specimen configuration is shown in Figure 3. The water cement ratio of the concrete was 55%. Four sides were coated with epoxy resin after curing underwater for 28 days, whereupon four types of silicate-type surface penetrant shown in Table 2 were applied to the top surface. After the surface penetrant material was applied to the specimen, it was cured in wet air for 14 days, and in dry air for 14 subsequent days.

The influence of the main component in the silicate-type surface penetrant on the apparent diffusion coefficient in the reformed part was not compared, as this was beyond the scope of the study.

3.2 *Accelerated exposure method*

One cycle of the exposure consisted of immersion in salt water (30°C, 3.0% NaCl (aq.)) for 12 hours, followed by treatment with dry air (30°C, RH70 %) for 72 hours. The process was repeated 75 times.

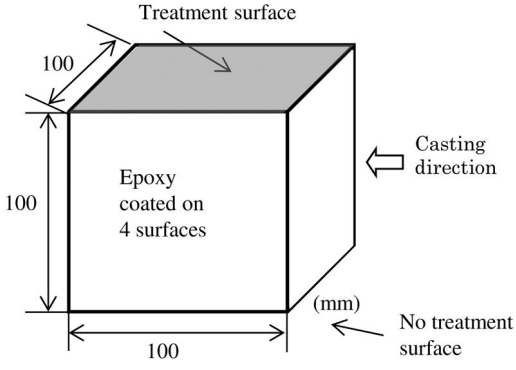

Figure 3. Specimen configuration.

Table 2. Varieties of silicate-type surface penetrant.

Case	Main ion in surface penetrant	Molar ratio $[SiO_2]/[R_2O]$	All dry solid content ratio (%)
No	–	–	–
A	Li	3.37	23.20
B	Na	3.32	21.80
C	K	3.70	23.56
D	Na + K Na:K = 1:1	3.51	22.73

3.3 *Measurement procedures*

The Vickers hardness was measured in accordance with JIS Z 2244. The test force was 0.098 N, and the retention time was 30 seconds. Ten sets of measurements were carried out at each point.

The chloride ion concentration was measured in accordance with JSCE-G 573; the density of the concrete was measured, followed by the collection of concrete powder from the specimen every 10 mm down from the surface using a drill. The sample (1 g) was dissolved in hot water (10 mL) at 50°C for 24 hours and the chloride ion concentration was measured, obtaining the soluble chloride ion concentration per unit concrete volume. Thereafter, total chloride ion concentrations were converted as shown in equation (2) (Goto, 2010).

$$y = 1.09x + 0.23 \quad (2)$$

y : total chloride ion concentration (kg/m^3)
x : soluble chloride ion concentration (kg/m^3)

4 RESULTS

4.1 *Vickers hardness*

Figure 4 shows, as an example, the relationship between the depth from the surface and the Vickers hardness of specimen studied in case C. The figure identifies that the reformed depth of case C is 3 mm. The identified reformed depth in each case is shown in Figure 5.

4.2 *Determination example of apparent chloride ion diffusion coefficient*

The procedure for determining the apparent chloride ion diffusion coefficient is explained using the

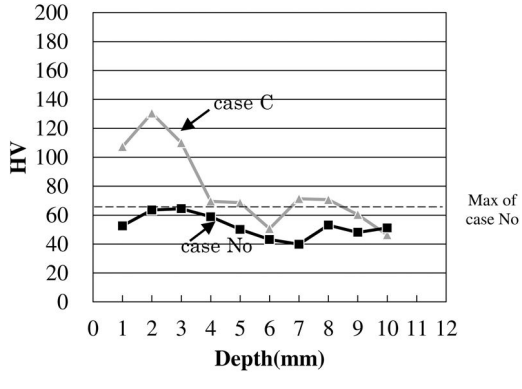

Figure 4. Vickers hardness distribution in case C.

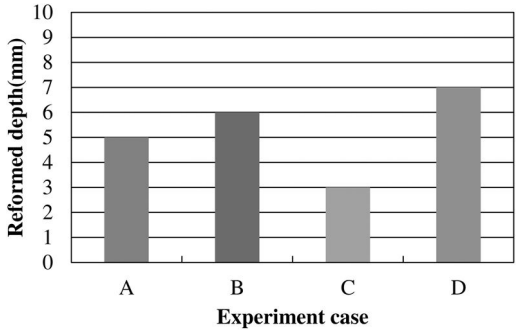

Figure 5. Identified reformed depth.

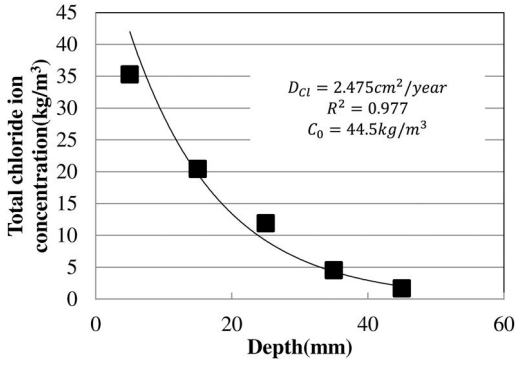

Figure 6. Distribution of measured total chloride ion concentration in case No.

experimental results obtained from case C as an example.

Figure 6 shows the distribution of total chloride ion concentration in case No (where "No" denotes non-treated concrete). The apparent diffusion coefficient in the nonreformed part was analyzed using Fick's laws of diffusion. As a result, the apparent chloride ion diffusion coefficient was calculated as 2.475 cm^2/year.

Figure 7 presents the total chloride ion concentration distribution in case C. From the reformed depth shown in Figure 5, the reformed and nonreformed parts were distinguished, with a boundary at a depth of 3 mm.

Figure 8 shows the total chloride ion concentration distribution after converting into the equivalent cover depth using equation (3):

$$C_i = C_s \times \frac{\sqrt{D_c}}{\sqrt{D_s}} \quad (3)$$

C_i : equivalent cover depth (mm) C_s : reformed depth (mm) D_s'F apparent chloride ion diffusion coefficient

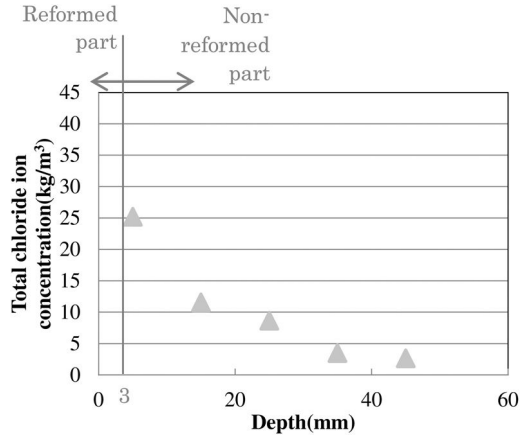

Figure 7. Distribution of measured total chloride ion concentration in case C.

Table 3. Temporarily set apparent chloride ion diffusion coefficients in reformed part of specimen in case C.

Percentage against no-reformed part (%)	Apparent chloride ion diffusion coefficient at reformed part (cm^2/year)	Shown in Fig 8 and Fig 9
1	0.025	–
4	0.100	(1)
8	0.200	–
12	0.300	(2)
16	0.400	–
18	0.450	(3)
20	0.500	–
24	0.600	(3)
28	0.700	–
32	0.800	(5)
40	1.000	(6)
50	1.230	–

in the reformed part (cm^2/year) D_c'F apparent chloride ion diffusion coefficient in the nonreformed part (cm^2/year)

The penetration of the chloride ion is prevented by the surface penetrant in the reformed part. Therefore the cover depth equivalent to this effect can be added outward from the concrete surface. The diffusion coefficient of 12 levels in the reformed part (shown in Table 3) was set temporarily. Six of these levels are introduced in Figures 8 and 9. For example, Figure 8 (1) shows the case where the diffusion coefficient was set at 0.100 cm^2/year. As shown in equation (4), the equivalent cover depth was estimated to be 15 mm:

$$15 = 3 \times \frac{\sqrt{2.475}}{\sqrt{0.100}} \quad (4)$$

It was therefore estimated that the reformed depth of 3 mm became the normal concrete depth of 15 mm,

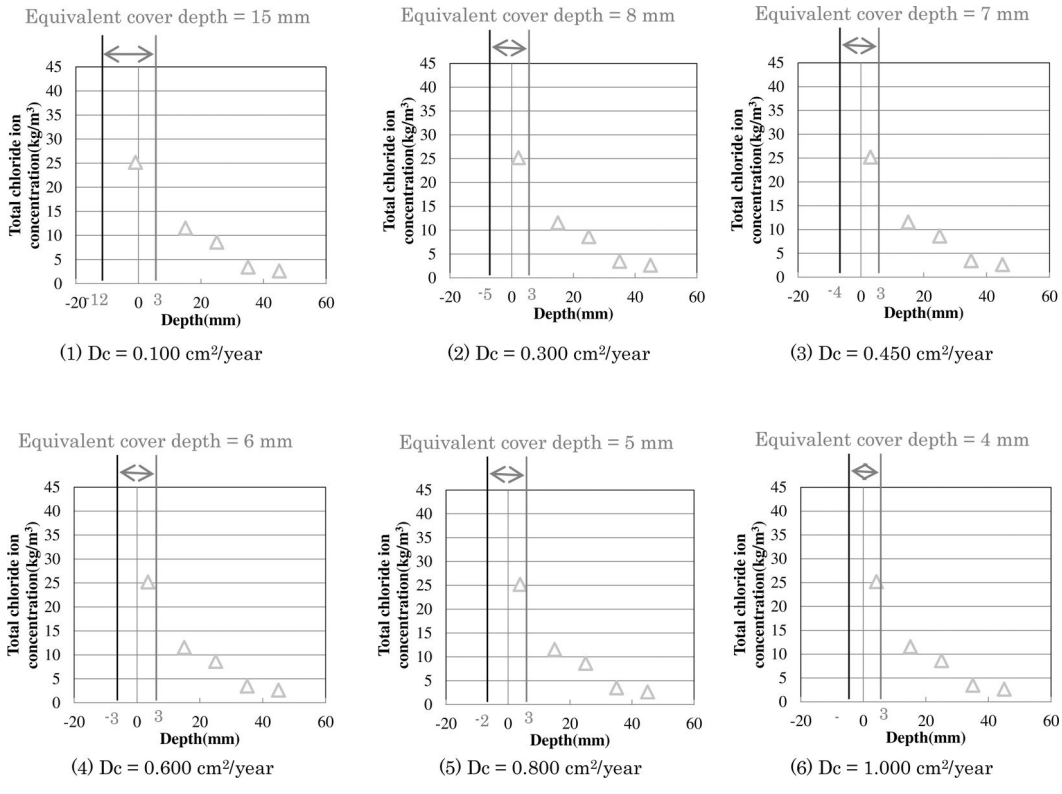

Figure 8. Distribution of measured total chloride ion concentration in case C.

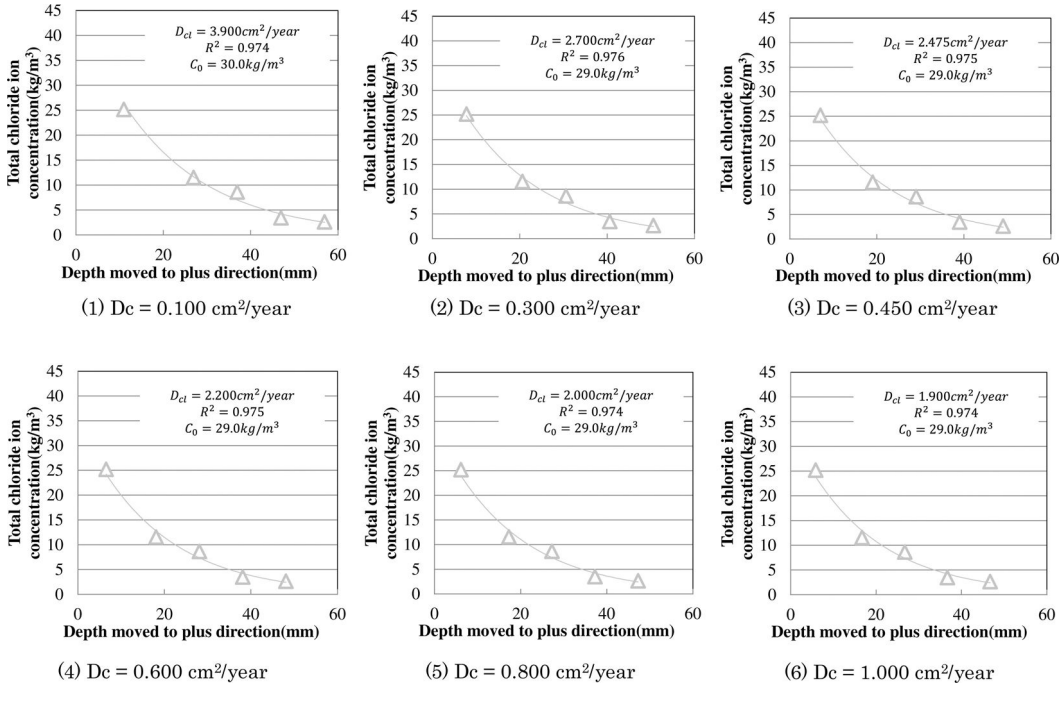

Figure 9. Distribution of chloride ion concentration moved in plus direction.

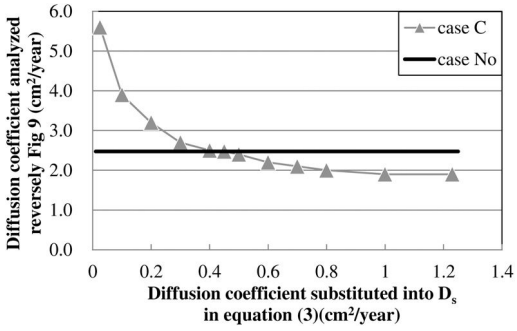

Figure 10. Comparison between temporarily set apparent chloride ion diffusion coefficient in reformed part of case C and case No.

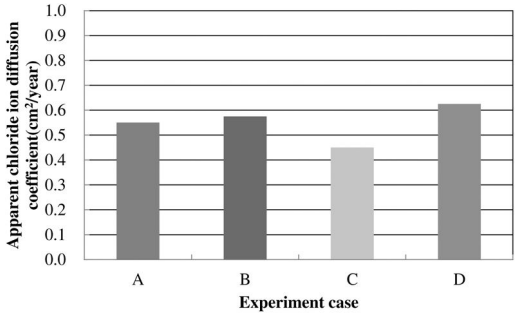

Figure 11. Apparent chloride ion diffusion coefficient in reformed part of all experimental specimens.

i.e., a 12-mm-thick (15 mm–3 mm) concrete layer was coated outward from the surface.

After considering the equivalent cover depth, concrete surfaces increased in the minus direction (where "minus direction" denotes $x < 0$). In Figure 9, the chloride ion concentration distribution moved in the plus direction (where "plus direction" denotes $x > 0$) in order to cancel the concrete in the minus area on the x axis. For example, the profile of the chloride ion concentration distribution shown in Figure 9 (1) was moved to plus 12 mm compared to the x axis shown in Figure 8 (1).

The most suitable value among the temporary set of apparent diffusion coefficients at the reformed part was then assessed; the chloride ion concentration distribution as a function of equivalent cover depth (shown in Figure 9) was analyzed by Fick's laws of diffusion and the apparent diffusion coefficient was calculated. The result is shown on the x axis of Figure 10; the values for all 12 levels are shown in Table 3, including the results shown in Figures 8 and 9. The figure shows that when the apparent diffusion coefficient (as a function of the equivalent cover depth) becomes 0.45 cm^2/year, it is equal to that of case No; this value was the apparent diffusion coefficient in the reformed part of specimen C.

Table 4. Conditions in trial calculations.

Interval from coastline (m)	Surface chloride ion concentration (kg/m^3)
0	13.0
100	4.5
250	3.0
500	2.0
1000	1.5

Table 5. Converted cover depth.

Case	Converted cover depth (mm)
A	56
B	57
C	54
D	57

4.3 *Determination for all experimental cases*

Figure 11 shows the apparent diffusion coefficient results in the reformed part of the specimen for all cases studied.

5 TRIAL CALCULATION OF DELAY OF CORROSION ONSET

5.1 *Trial calculation conditions*

Corrosion occurrence times were calculated assuming silicate-type surface penetrants were applied immediately after notional construction using the conditions shown in Table 4. The cover depth was set to 50 mm. The condition of the concrete was the same as in Section 3. The period before the total chloride ion concentration around the steel bar reached 1.2 kg/m^3 (JSCE, 2008) was estimated using the reformed depth identified in Figure 5 and the apparent diffusion coefficient determined in Figure 11.

5.2 *Calculation procedure*

The apparent diffusion coefficients shown in Figure 11 were substituted into equation (3), and the equivalent cover depths were calculated. Table 5 shows the converted cover depth for all cases. These converted cover depths and the apparent diffusion coefficients in the nonreformed part were substituted into Fick's laws of diffusion. As a result, the year in which the total chloride ion concentration around the steel bar reached the threshold value was calculated.

5.3 *Calculation result and evaluation*

Figures 12–16 show the trial calculation results.

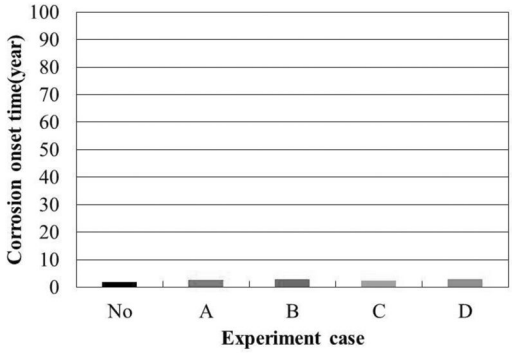

Figure 12. Trial calculation result for structures located on a coastline.

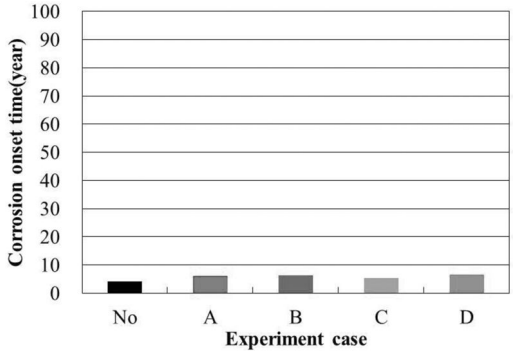

Figure 13. Trial calculation results for structures located 100 m from a coastline.

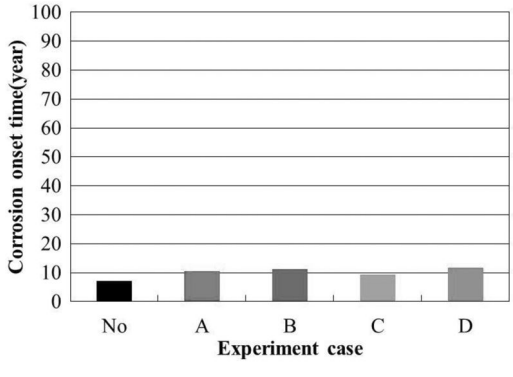

Figure 14. Trial calculation results for structures located 250 m from a coastline.

According to Figures 12–14, prominent effects cannot be experimentally confirmed under these conditions, even if a silicate-type surface penetrant is applied to structures located at 0 m, 100 m and 250 m from a coastline.

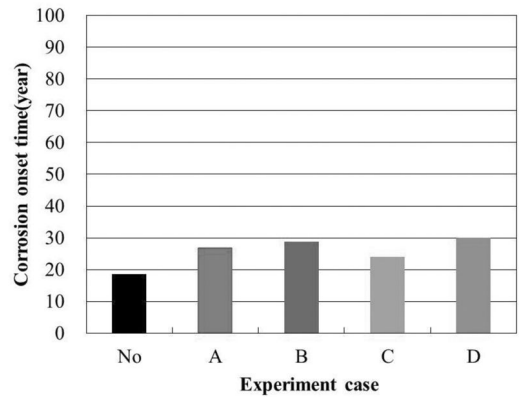

Figure 15. Trial calculation results for structures located 500 m from a coastline.

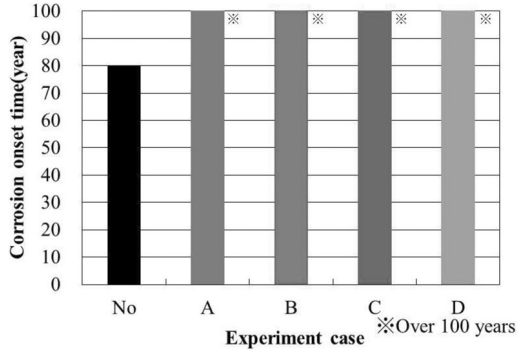

Figure 16. Trial calculation results for structures located 500 m from a coastline.

According to Figure 15, it is confirmed that when silicate-type surface penetrants are applied, the corrosion onset time is delayed by 9–18 years for structures located 500 m from a coastline, i.e., the steel bar will potentially not corrode for 28–37 years.

According to Figure 16, it is suggested that the steel bar may not corrode for 80 years in structures located 1,000 m from a coastline even with a cover depth of 50 mm in cases of no applied penetrant. It can be seen from these results that it is not necessary to apply silicate-type surface penetrants in preventive maintenance procedures at such distances.

6 CONCLUSION

The following conclusions are drawn from the results obtained in this study:

1) A method to determine the apparent chloride ion diffusion coefficient in the outer layer of concrete

reformed by silicate-type surface penetrants was devised.

2) When silicate-type surface penetrants were applied to concrete with a 55% water cement ratio, the reformed depths were 3–7 mm. It was determined that the apparent chloride ion diffusion coefficients in the reformed parts were 0.45–0.63 cm^2/year. Here, the diffusion coefficient in the nonreformed part was 2.48 cm^2/year.
3) If a structure was located 500 m from the coastline, with a concrete water cement ratio of 55% and a cover depth of 50 mm, the application of the silicate-type surface penetrant potentially delays the onset of corrosion by 9–18 years.

REFERENCES

Goto, T. Kondo, H. & Nojima, S. (2010) Development of the rapid measuring method of total chloride ion content in hardened concrete, Proceedings of the Japan Concrete Institute, Vol. 32, No. 1, pp. 785–790

Japan Society of Civil Engineers (2005) Recommendation for concrete repair and surface protection of concrete structures, Concrete Library 119

Japan Society of Civil Engineers (2012) Guideline on design and application methods of silicate-based surface penetrant used for concrete structures, Concrete Library 137

Japan Society of Civil Engineers, Standard (2008) specifications for concrete structures – 2007

Concrete Solutions – Grantham et al. (Eds)
© 2014 Taylor & Francis Group, London, ISBN 978-1-138-02708-4

Performance of concretes with surface treatment based on silicate solutions (liquid glass)

S. Monosi & M.L. Ruello
Università Politecnica delle Marche, Ancona, Italy

ABSTRACT: Concrete, one of the most widespread building materials, may be affected by many chemical and physical deterioration processes as a consequence of the penetration of aggressive substances. The improvement of concrete durability is a subject of great interest to researchers and the use of surface treatments, aimed at making hydrophobized mortars and concretes, is becoming a quite common practice.

The study presented in this paper examines the effectiveness of some inorganic products based on alkali silicates as hydrophobic agents; it also tries to connect the chemical and physical characteristics of the silicates to the results obtained in concretes with different characteristics and quality, in terms of resistance to capillary absorption and drying for hydrophobic impregnation. It was found that the water repellent effect is dependent on the intrinsic porosity (amount and size of pores) of the cement matrix; in particular it is more evident when the porosity is lower. However, when the test is carried out with water under pressure, the opposite happens. The humidity loss by evaporation is maintained at about the same rate regardless of the type of conglomerate. The results obtained with several silicates do not show significant differences; furthermore one aspect improves when another worsens. The results don't seem ascribable to the chemical composition of the silicates used, maybe to their fluidity that means different depths of impregnation, reduction of the open porosity and/or formation of surface film.

1 INTRODUCTION

Concrete is a porous material and the porosity significantly affects permeability and durability; concrete, when exposed to the environment, can be penetrated by aggressive agents.

Water is the main vehicle for the penetration of aggressive ions from sea or industrial areas. Water is a vehicle for the penetration of water soluble gases such as CO_2 and SO_2 which cause the reduction of concrete alkalinity. Moreover water is a necessary ingredient for every destructive chemical reaction and when the temperature decreases, ice crystals provoke damage by means of freezing/thawing cycles.

The volume of capillary pores and consequently the permeability can be reduced by reducing water-cement ratio. However the cover zone usually remains of poor quality because of insufficient wet curing (Pigino B. et al. 2012). In older structures, the durability aspect is often neglected during the construction, including the lack of knowledge of the mechanisms of degradation and their causes (Basheer PAM et al. 1997, Dai J-G et al. 2010).

This has led the industry to choose water-cement ratios that are too high; also the low thickness of the concrete cover has helped to exacerbate the situation and repair work to older structures has become of considerable urgency.

To make the concrete cover less permeable and to increase the durability of the concrete structures, it is possible to treat the surfaces with protective impregnation (La Rosa Thompson J et al. 1997). Various surface coatings are used to prevent the degradation of concrete structures. Most of them are constituted by organic coatings that use volatile organic compounds that are unwelcome for the operators and for the environment (Barbucci A et al 1997). Some inorganic coatings that exhibit similar composition to the cement, were then taken into account (Moon HY et al. 2007). This study intends to assess the effectiveness of commercial inorganic coatings usually used as concrete surface treatment.

2 MATERIALS

Four different types of hydrophobic agents, all based on alkali silicates, easily available on the market, were selected.

Table 1 shows the characteristic of the products in terms of chemical composition, dry solids content and fluidity, expressed as flow time of 120 ml of solution through a laboratory funnel (walls angle = 60°, stem length = 60 mm, Inner diameter of the stem = 2.5 mm).

Table 1. Characteristics of the four hydrophobic products.

	Si %	Na %	K %	Solid %	Fluidity sec
NS1	57.6	40.9	1.5	9	135
NS2	55.2	44.4	0.4	14	145
NS3	60.4	39.4	0.1	8	134
KS	48.3	3.3	48.3	16	308

Table 2. Composition of the two different concretes used in the study.

Type	C045	C065
Cement (kg/m^3)	395	260
Water (kg/m^3)	143	143
Sand (kg/m^3)	1415	1145
Gravel (kg/m^3)	355	760
Superpl.(kg/m^3)	3.2	1.5
w/c	0.45	0.65

Following is some information taken from the data sheets of the four products.

NS1 is presented as a "waterproofing and protective" agent able to penetrate into the porosity and micro-cracks and make the surface impermeable to water.

According to its data sheet, **NS2** is a product characterized by a high capacity to penetrate the cementitious material forming a protective barrier.

NS3 is described as a waterproofing agent which counteracts concrete deterioration through the formation of a permanent protective barrier that hinders the penetration of aggressive materials.

KS is defined as a natural consolidating agent fit for breathable plasters and screeds.

The products were applied on specimens made with two different concretes whose characteristics are shown in Table 2. The cement used was a CEM II A-LL 42.5R (limestone-portland blended cement according to EN 197-1). A mixed sand (natural and crushed) with $D_{max} = 8$ mm and a natural gravel with $D_{max} = 15$ mm were used as aggregate. Different dosages of the same poly-carboxylate superplasticizer were used in the two concretes, in order to obtain the same workability (slump 8–10 **c**m).

3 EXPERIMENTAL PROGRAM

3.1 *Drying for hydrophobic impregnation (EN 13579)*

The test of "drying for hydrophobic impregnation" consists in comparing the drying speed of cubic specimens, treated and not treated with the hydrophobic agent, manufactured with the same concrete mix. The ratio between the drying speed in treated specimens and that in plain ones is called the "coefficient of drying speed", and is indicated as "DRC".

In the present study, the test was carried out on 24 cubic specimens (side 100mm), 12 for each type of mixture. After 28 days of curing under water the cubes were wiped on the surface with absorbent paper and weighed. Two specimens of each type were oven dried at T = 105°C to measure the water absorption. All the other specimens were initially conditioned in a cabinet at 21°C with RH = 60 ± 10% for a week. Then, eight specimens of each type of concrete were treated on the surface with the four different solutions of silicates (two specimens for each product), following the instructions of the manufacturer and the specifications contained in the above mentioned standard. Before and after treatment, the specimens were weighed to know the amount of product applied. The remaining four samples (2 for each concrete) were tested without treatment, to provide a comparison with those treated.

According to the standard specifications, the drying test started immediately after the conditioning period for the plain samples, while for those which had been treated it started 48 h later.

The test consists in keeping the treated specimens, in a chamber conditioned at 30°C and 40% R.H. for 48 hours. The specimens are weighed before being placed in the chamber, after the first 24 hours of testing (d_1) and at the end of the test (d_2); the drying speed (D_t) is then calculated through equation (1):

$$D_t=(d_1-d_2)/24*0.06 \text{ expressed in g/(m}^2\text{hr)} \quad (1)$$

In the case of untreated specimens, the test requires the recording of the weight after 6 hours (d_1) and then after a further 18 hours (d_2) of storage in the chamber at 30°C and 40% R.H. The drying speed (D_u) is, then, defined by equation (2):

$$D_u=(d_1-d_2)/18*0.06 \text{ expressed in g/(m}^2\text{hr)} \quad (2)$$

Finally, the drying speed coefficient "DRC" is calculated as the ratio between the rate of drying of the treated specimens and that of the untreated specimens: $DRC = D_t/D_u$.

3.2 *Resistance to capillary absorption (UNI EN 13057)*

The test consists of evaluating the water absorption by capillarity by measuring the weight increase of specimens kept with the bottom face in contact with water.

In the present study, the test was carried out on 10 specimens (100 × 100 × 25 mm) for each type of mix.

After 28 days of curing, the specimens were oven dried at 40°C, up to constant mass. Afterwards, 8 specimens for each mix were treated with the solutions of silicates (two specimens for each product), while the remaining two were kept untreated and used as reference.

Six consecutive measurements of weight were performed for each specimen, at intervals specified by the standard and commensurate with the rate of absorption. After the first two hours, in addition to the weight, the extent of capillary rise was recorded by means of detecting the position of the damp front.

In this test, the water absorption per unit area "**i**" is, finally, calculated, for each increment of time (expressed as $hr^{0.5}$), dividing the mass of water absorbed (expressed in Kg) by the area of the face in contact with it (expressed in m^2). The curves which interpolate the above data, are plotted as a function of the square root of time, allow the determination of the absorption coefficient "**S**" ($kg/m^2\ hr^{0.5}$) defined as the gradient of the first linear portion of the graph, and the saturation time "$\mathbf{t_c}$", if any, which corresponds to the abscissa of the point where the curve changes slope. Depending on the type of curve obtained, the standard indicates the methods for obtaining these values.

3.3 *Depth of penetration of water under pressure (EN 12390-8)*

This test is performed to evaluate the resistance provided by concrete to water penetration under pressure. In this study, the test was performed on cubic specimens (150 × 150 × 150 mm) cured for 28 days under water and then maintained for an additional 7 days in the laboratory at 21 ± 2°C and 60 ± 10%. R.H. The specimens subjected to treatment with silicates, had been cured after the treatment, for about 30 days in controlled environmental conditions (T = 21 ± 2°C and RH = 60 ± 10%).

According to the standard specifications, the test has a duration of three days during which one face of the specimen is subjected to contact with water at a constant pressure of 500 kPa. At the end of the test, the specimens are broken perpendicular to the face on which the water under pressure was applied and the maximum depth of water penetration is measured.

3.4 *SEM observation*

Samples taken from the surface of the treated specimens (only for the concrete with w /c = 0.65) were observed by a scanning electron microscope in order to detect any significant difference in the mechanism of hydrophobization of the various products. EDAX analysis were also carried out.

4 RESULTS AND DISCUSSIONS

4.1 *Compressive strength*

As expected, the two concrete mixes exhibited very different performances in terms of compressive strength. The mix C065 exhibited compressive strength of 34 MPa at 28 days while for the mix C045 the compressive strength was as high as 54 MPa. This is a consequence of the different w/c adopted in order to verify the behavior of the hydrophobic products in concrete with very different characteristics and porosity. Figure 1 shows the results of compressive strength obtained between 1 and 28 days of curing.

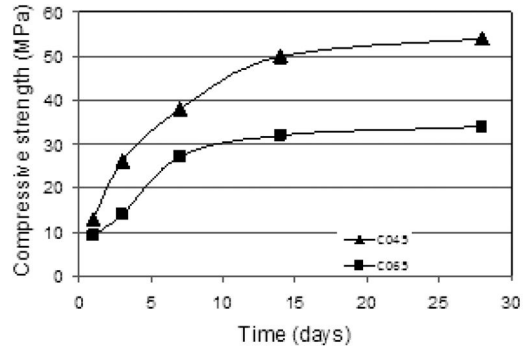

Figure 1. Compressive strength of the concretes.

Table 3. Drying speed (D) and drying speed coefficient (DRC) of the conglomerates.

	D(g/m^2*h)		DRC%	
Type	C045	C065	C045	C065
NS1	3.854	1.424	49.54	51.26
NS2	4.431	1.632	57.32	58.75
KS	4.167	1.549	53.91	55.76
NS3	5	1.493	64.68	53.74
Plain	7.73	2.778	100	100

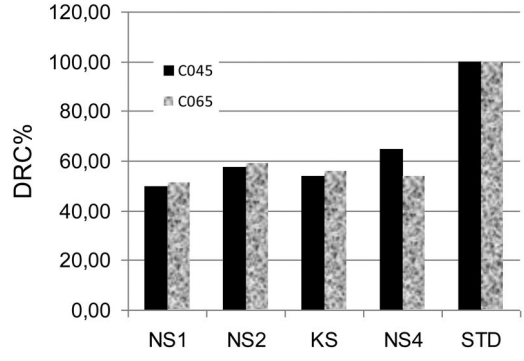

Figure 2. Drying speed coefficient (DRC) of the conglomerates.

4.2 *Drying for hydrophobic impregnation*

Table 3 and Figure 2 show the results obtained in the test of drying for hydrophobic impregnation in terms of DRC (%).

For all four products tested, DRC was much less than 100%, with values between 50% and 65%. This means that, contrary to what is reported in some

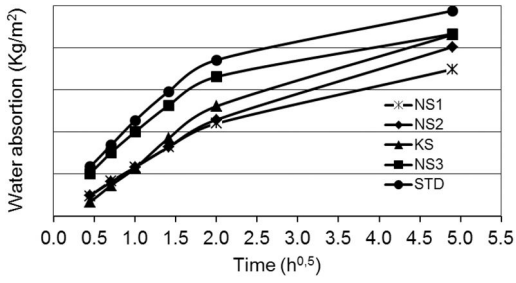

Figure 3. Capillary absorption curves of the conglomerates C065, plain and treated.

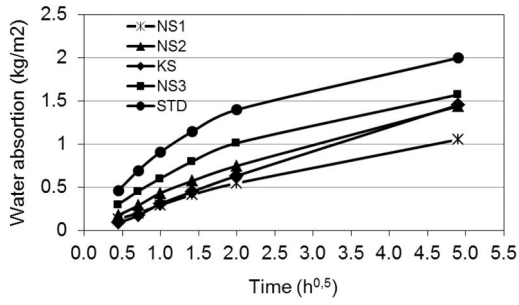

Figure 4. Comparison between the different curves of the conglomerates C045.

Table 4. Saturation time (t_c) and absorption coefficient (S) of the conglomerates C065.

C065	t_c(h)	S(Kg/m^{2*}h^{0,5})
NS1	2.89	0.595
NS2	3.24	0.594
NS3	2.50	0.8327
KS	2.76	0.7813
Plain	2.25	0.9266

Table 5. Saturation time (t_c) and absorption coefficient (S) of the conglomerates C045.

C045	t_c(h)	S(Kg/m^{2*}h^{0,5})
NS1	–	0.2066
NS2	–	0.283
NS3	2.50	0.5094
KS	—-	0.3066
Plain	1.99	0.698

data sheet, all the products significantly reduced the transpirability of the concrete.

Except for the product NS3, the reduction of transpirability seems not to depend on the porosity of concrete.

4.3 *Resistance to capillary absorption*

Figure 3 compares the capillary absorption curves of the samples prepared with mix C065, untreated or treated with the four products.

All the curves show a change in slope and a slowing down in the final section; then they fall in the case of complete saturation of the specimen at the end of the test.

The saturation time (t_c) and the absorption coefficient (S) derived from the analysis of the curves are given in Table 4.

The time of saturation of the concretes having higher w/c, were all less than 3 and a half hours: the shortest time was recorded, as expected, in the specimen without surface treatment, while the treated samples showed slightly longer saturation times. The absorption coefficient was the highest for the reference concrete while it was lower in the treated samples. In each case, three of the silicates used showed very similar behavior while the NS3 product was, without doubt, the least effective.

In the case of concretes with lower porosity (w/c = 0.45) complete saturation of the specimen occurred only in the untreated specimen and in the case of treatment with the NS3 product.

In the specimens treated with the other silicates, the curve was non-linear and it was not possible to identify a clear change of slope that could be interpreted as point of saturation. In these cases, the coefficient S was calculated as the gradient of the line starting from the origin and intercepting the curve at the last reading.

Again, the product NS3 appears the least effective of the four tested. The values obtained from the curves are shown in Table 5.

4.4 *Resistance to water penetration under pressure*

In the test of penetration of water under pressure all specimens with w/c = 0.45 suffered a penetration of less than 20 mm, with slight differences between the plain concrete and those treated with silicates.

Probably, the concretes characterized by a good degree of impermeability not appear to benefit from surface treatment, except for the case of the product NS3 that, instead, had the worst performance in the test of capillary absorption.

In the case of concretes with higher porosity (higher w/c), the difference between the untreated specimens and those treated was well evident. In all cases, in fact, there was a net reduction in the penetration depth as a result of the surface treatment. The silicate solution NS3 was still the most effective in reducing the penetration of water under pressure.

4.5 *SEM observation*

The SEM observations show that the various solutions of silicates have a different ability to penetrate inside the concrete according to their viscosity.

Table 6. Penetration depth of water under pressure of the conglomerates C065.

Type	C045 *Max depth (mm)*	C065 *Max depth (mm)*
NS1	19	24
NS2	18	20
NS3	11	17
KS	20	28
Plain	19	43

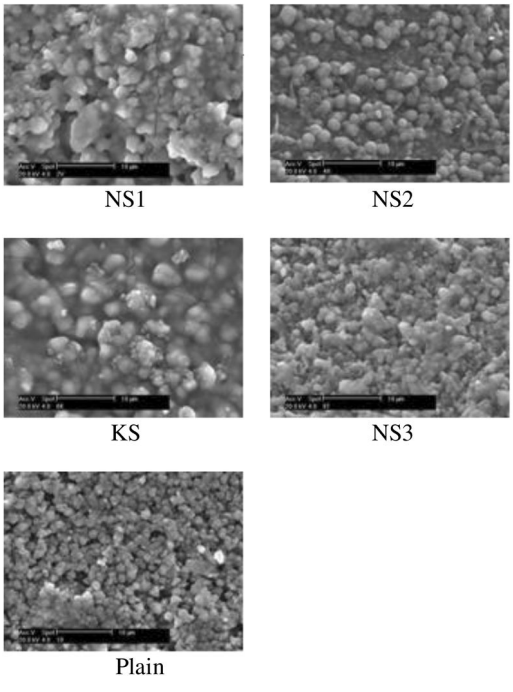

Figure 5. SEM images of the five concrete specimens (plain and treated).

In particular, the product KS, more viscous than the others, showed a lower capacity of penetration into the concrete, and a tendency to form a surface film. On the contrary, the NS3 product was the one that showed the greater depth of penetration.

Considering the results obtained in terms of capillary absorption and penetration of water under pressure, it could, therefore, be assumed that the products that penetrate less in the concrete and form a surface film are more effective in reducing the absorption by capillarity while those in able to penetrate deeper into the pores are more effective in reducing the penetration of water under pressure.

5 CONCLUSIONS

The surface treatment with silicates significantly reduced the transpirability of the concrete and its drying speed. The effect was substantially independent of the capillary porosity of the concrete, that is, of its w/c.

The capillary absorption was modified by the treatment both in terms of rate of absorption and of time of saturation. The speed was halved in concrete with a lower w/c and significantly reduced (at least in two cases) in the concretes with higher w/c .

The products characterized by lower penetration ability inside the concrete, accompanied by a tendency to the formation of a surface film showed a better effectiveness in terms of reduction of capillary absorption while the product (NS3) that is most penetrated inside the pores showed the worst performance.

On the contrary, the same products characterized by the tendency to form a surface film without penetrating inside the pores were the worst in reducing the penetration of water under pressure while the one (NS3) characterized by the best penetration ability provided, in this test, the best results.

REFERENCES

Barbucci A, Delucchi M, Cerisola G "Organic coatings for concrete protection: liquid water and water vapour permeabilities", Progress in Organic Coatings, 1997, 30, 293–297.

Basheer P.A.M., Basheer L, Cleland DJ, Long AE "Surface treatments for concrete: assessment methods and reported performance". Construction and Building Materials 1997;11(7–8):413–29.

Dai J-G, Akira Y, Wittmann FH, Yokota H, Zhang P "Water repellent surface impregnation for extension of service life of reinforced concrete structures in marine environments: the role of cracks" Cement and Concrete Composites 2010, 32, 101–9.

La Rosa Thompson J, Silsbee MR, Gill PM, Scheetz BE "Characterization of silicate sealers on concrete" Cement and Cocrete Research, 1997, 27, 1561–7.

Moon HY, Dong GS, Doo SC "Evaluation of the durability of mortar and concrete applied with inorganic coating material and surface treatment system", Construction and Building Materials, 2007, 21, 362–369.

Pigino B, Leemann A, Franzoni E, Lura P "Ethyl silicate for surface treatment of concrete – Part II: Characteristics and performance" Cement & Concrete Composites 2012, 34, 313–321.

UNI EN 12390-8 "Testing hardened concrete-Depth of penetration of water under pressure", 2002.

UNI EN 13057 "Products and systems for the protection and repair of concrete structures", 2003.

UNI EN 13579 "Products and systems for the protection and repair of concrete structures", 2003.

This page intentionally left blank

Concrete Solutions – Grantham et al. (Eds)
© 2014 Taylor & Francis Group, London, ISBN 978-1-138-02708-4

Design of a cementitious coating system for corrosion protection: Phase 1 binder materials selection

G. Nery, H. Hüsken & H.-C. Kühne
BAM Federal Institute for Materials Research and Testing, Berlin, Germany

ABSTRACT: This paper presents the first results of an ongoing research project on the development of a cementitious thin layer coating system with high resistance against chloride penetration and carbonation. It is intended to display the decision process used for selecting raw materials as well as the conclusions based on test results and theoretical deliberations. In this phase, only the influence of the binder materials was analyzed concerning mechanical properties. The system should enhance the durability of new and old concrete structures exposed to aggressive environments,be based on market available materials and fulfill the requirements of the German guideline for concrete repair (Rili-SIB).

1 INTRODUCTION

1.1 *Durability of concrete structures*

One of today's biggest challenges for civil engineers is to produce concrete structures that can resist a long period of time exposed to aggressive environment without intervention. The most common problem that can afflict a concrete structure is corrosion of the reinforcement and the two key ways for that to happen are the ingress of chloride ions and the carbonation of the concrete (Rincón et al. 2006, Basheer et al. 1996).

Concrete structures in dense urban or industrial areas are more exposed to carbon dioxide and are more likely to suffer from carbonation. Other unfavorable situations for concrete structures are marine environments and regular contact with de-icing salts, in these cases the structures are especially affected by the ingress of chloride ions (Papadakis 2000). To prevent these attacks, specific regulations and standards demand high quality for the concrete used in these cases (Basheer et al. 2001). However, despite these policies, old and new concrete structures exposed to these aggressive environments are being affected by reinforcement corrosion and demand repair. Sýkora et al. (2013) highlighted in their paper the huge number of structures affected by the problem in Europe. Cramer et al. (2002) reported the same in North America.

Usually, the rehabilitation of concrete structures attacked by corrosion of the reinforcement is expensive, time consuming and effortful. The protection of the concrete against chloride ingress and carbonation can extend the periods between interventions or even avoid them, saving time, money and natural resources. Because of that, a lot of research has been done on the subject and there are many ways proven to be effective in making a concrete less susceptible to carbonation and to chloride attack. However, it takes a long time for the knowledge produced in the laboratory to reach the market in form of a product and produce real benefit for society.

One common and effective way to protect concrete from carbonation and chloride ingress is realized by surface coating (Batis et al. 2003, Al-Zahrani et al. 2003, Medeiros & Helene 2009, Almusallam et al. 2003). Beushausen & Burmeister (2013) tested different coating systems and verified that all of them protect the concrete from carbonation. Malheiro et al. (2011) concluded in their experiment that even a porous mortar coating can have a protective effect on the concrete substrate regarding chloride ion ingress.

The present paper describes the first steps of an on going research project on the development of a cementitious coating system for concrete protection against carbonation and chloride ions ingress. The development should apply the knowledge produced in the last decade regarding carbonation and chloride ingress resistance and utilize Ultra High Performance Concrete (UHPC) principles and market available materials. It needs also to be based on field applicable methods.

1.2 *Chloride ions ingress and carbonation*

The steel embedded in concrete is protected from corrosion by a passive oxide film formed by the typical high alkalinity found in concrete. With carbonation of the concrete or the ingress of chloride ions, this film can be broken down allowing corrosion to happen (Seneviratne et al. 2000 & Wang et al. 2014).

It is well known that the speed of carbonation and chloride ingress into concrete is also related to porosity, permeability, cracks and some chemical characteristics of the concrete. Therefore, a dense micro

structure of the concrete matrix enhances considerably the capacity to withstand these attacks.

UHPC is known by the extremely dense structure and high resistance against carbonation and chloride ingress (Scheydt et al. 2008). Taking that in consideration, a cementitious coating system developed based on UHPC principles would have a good protective effect and extend the service life of the concrete structure.

1.3 *Supplementary Cementitious Materials (SCM)*

A vast number of research projects in the past years have aimed at analyzing the influence of different SCM's on the performance of concrete. Pozzolanic materials showed advantageous results like the reduction of costs and permeability, and the increase of chemical resistance of the concrete. Because of that, they are now recognized as important materials for a durable concrete (Habert et al. 2008, Siddique & Klaus 2009 and Otieno et al. 2014).

Pozzolanic materials are rich in reactive SiO_2 and Al_2O_3. These compounds react with $Ca(OH)_2$ forming C-S-H gel. This pozzolanic reaction takes place after the hydration of the Portland cement and is much slower. The SCMs contribution is specially related to their effect on the pore structure by micro-filler effect, increased C-S-H content, wall effect and pore blocking. The combination of these effects refines the pore structure and reduces the permeability.

Güneyisi et al. (2012) analyzed the effects of micro silica and metakaolin in concrete and concluded that for all the concentrations tested, the compressive strength was higher and the shrinkage and crack widths were lower. Gleize et al. (2007) also concluded in their study that metakaolin reduces the autogenous shrinkage of cement pastes at late ages. Valipour et al. (2013) tested different concentrations of micro silica and metakaolin and found a positive effect for both materials, improving electrical resistivity, compressive strength, gas permeability, sorptivity, water absorption and chloride diffusion. Nath & Sarker (2011) concluded that fly ash in concrete decreases drying shrinkage, reduces sorptivity and enhances chloride resistance.

Despite the recognized performance of blast furnace slag for the improvement of concrete properties, it wasn't considered as a suitable SCM in this study because of the salt scaling problem. A review on this subject can be found on the work of Valenza II & Scherer (2007a and 2007b).

A good overview on the effects of using SCM on concrete for chloride resistance can be found in the work of Shi et al. (2012).

2 MATERIALS AND METHODS

2.1 *Cements*

For the selection of the cement, six commercially available cements were tested being: 2 ordinary Portland cements (OPC) (1 and 2), 2 cements with high sulfate resistant (3 and 4) and 1 ultra fine cement with high sulfate resistance (5) as shown in Table 1. They were tested regarding compressive and flexural strength (DIN EN 196-1), consistence and free shrinkage.

Table 1. Cements.

Number	Type (DIN EN 197-1)
1	CEM I 52.5N
2	CEM I 52.5R
3	CEM III/A 52.5N-HS/NA
4	CEM I 42.5R-HS/NA
5	CEM I 52.5R-HS/NA

Table 2. Pozzolanic materials composition.

Chemical compound	MS [%]	MK [%]	FA [%]
SiO_2	96.01	52.39	51.32
Al_2O_3	0.38	43.79	26.30
Fe_2O_3	0.21	1.11	5.78
TiO_2	<0.01	0.52	5.37
CaO	0.42	0.12	3.29
MgO	0.54	0.06	1.36
Na_2O	0.31	0.11	1.14
K_2O	0.88	0.91	4.18
SO_3	0.27	0.15	0.78
Others	0.97	0.82	0.47

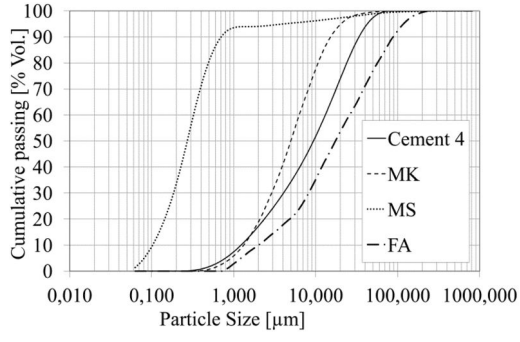

Figure 1. Particle size distribution of the cement and SCMs.

2.2 *Supplementary cementitious materials*

For the SCM tests, micro silica (MS), metakaolin (MK) and fly ash (FA) were chosen to be part of the research as they have a well known benefit on the durability properties of concrete. From the products available in the market, one of each type was chosen accordingly with the availability and some characteristics as particle size distribution (PSD), chemical composition and price. Table 2 shows the chemical composition of the selected materials measured according to DIN EN 196-2. The PSDs of the SCMs were determined by laser diffraction and are presented in Figure 1 together with one of the cements.

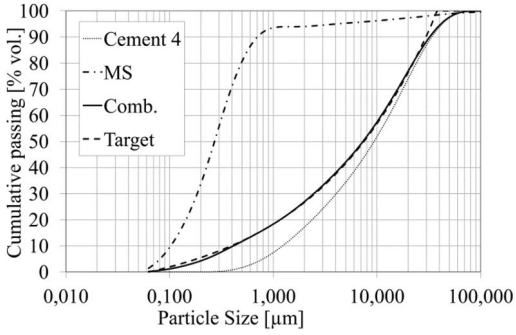

Figure 2. PSD optimization by modified Adreasen & Andersen equation.

Table 3. Binder mixes used in the SCM tests.

Name	Cement [g]	MK [g]	MS [g]	FA [g]
Ref.	450	0	0	0
MS2.5	438.75	0	11.25	0
MS5	427.5	0	22.5	0
MS12.7	392.85	0	57.15	0
MK4	432	18	0	0
MK7.5	416.25	33.75	0	0
MK15	382.5	67.5	0	0
FA4	432	0	0	18
FA12	396	0	0	54
FA24	342	0	0	108

The tests with the SCMs were carried out using CEM I 42.5R-HS/NA (cement 4). The mixes were tested in exactly the same way as the cement mixes. The sand and water/powder ratio (w/p = 0.5) were maintained and part of the cement was substituted by the SCM (mass) in three different proportions. The proportions were defined by optimum quantities found in the literature and a PSD optimization of the powders using the modified Adreasen & Andersen equation (Eq. 1) as described by Hüsken & Brouwers (2008). Figure 2 shows an example of the PSD optimization. The target PSD was calculated and the proportion between cement and SCM was optimized to produce a combined PSD that is the closest possible distribution related to the target function.

Table 3 presents the mix proportions of the powders in the tested mortars. The sand and water were kept constant at 1350 and 225 g, respectively.

$$P(D) = \frac{D^q - D_{min}^q}{D_{max}^q - D_{min}^q} \quad \forall D \in [D_{min}, D_{max}] \qquad (1)$$

whereby D represents the size of the sieve used for analyzing the solid ingredients. D_{min} and D_{max} are accounting for the minimum and maximum particle size in the mix and the distribution modulus q influences the ratio between coarse and fine particles.

The MS12.7 and FA4 were PSD optimized quantities. For the MK the optimized quantity calculated was 7.98% of cement by mass and it overlaps the literature optimum quantity range. Because of that a 4% mix was used to include a low MK quantity mix in the study as well.

2.3 *Aggregates*

At this point of the research, the aggregates were not on focus and CEN-Standard sand as recommended by DIN EN 196-1 was used to simplify the tests.

2.4 *Tests procedure*

The cement and SCM were pre-mixed in dry state and the sequence of mix used was the one recommended by DIN EN 196-1. All the mortars were mixed in a standard mortar mixer that complied with the requirements of DIN EN 196-1. The samples were kept immersed in water in a climate room at a temperature of 23°C ± 1 until the date of the test.

The mechanical properties were tested according to DIN EN 196-1 for 1, 3, 7 and 28 days. Consistence was measured by means of the flow table test following the procedure of DIN EN 1015-3.For the free shrinkage measurements,the samples were stored in a climate chamber with relative humidity of 50% ±5 at a temperature of 23°C ± 1 (standard climate DIN 50014-23/50-2), following the procedures of the standard DIN 52450. The measurements were done up to 91days.

3 RESULTS AND DISCUSSION

3.1 *Cement*

For the selection of the cement, the most important characteristic considered was the shrinkage of the standard mortar followed by its consistence. A small shrinkage result will contribute to fewer cracks in the coating system and enhance the protective effect for the concrete. The consistence was considered as an indicator of the water demand of the mortar. With lower water demand it is possible to achieve the desired consistence with less water generating a denser microstructure of the mortar (less capillary pores). This will also be beneficial in the optimization phase when less plasticizer will be needed or a lower w/b can be used.

Figure 3 shows the results for shrinkage and it is possible to see the good performance of cements 4 and 5, having less than 1 mm/m after 91 days. Cement 1 passed this value before 21 days. It is also possible to notice that all sulfate resistant cements presented lower shrinkage in relation to the normal ones. This is due to the low C_3A and C_4AF content and is in agreement with the conclusions of Holt (2005) and Yodsudjai & Wang (2013).

In Figure 4, the results of consistence measured by flow table test are shown and the cement 5 showed the

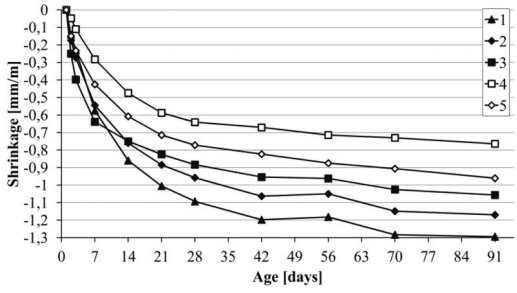

Figure 3. Shrinkage of the tested cements (DIN 52450).

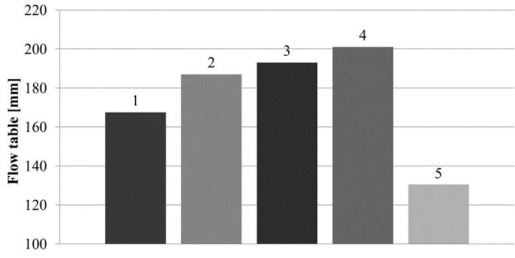

Figure 4. Consistence of the standard mortar with the tested cements (DIN EN 1015-3).

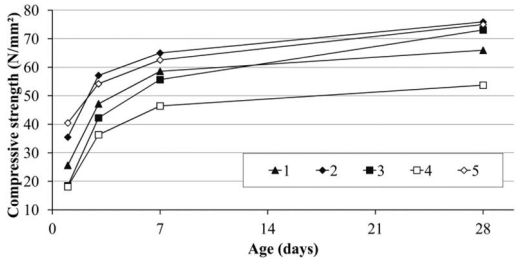

Figure 5. Compressive strength of the tested cements (DIN EN 196-1).

lowest value. This was already expected as cement 5 is an ultrafine cement and the higher specific surface area demands more water to be covered. Cement 4 showed the highest spread flow and, therewith, the best workability.

The results of the compressive and flexural strength tests are shown in Figure 5 and Figure 6, respectively. Cement 4 presented the lowest results in both cases. This is normal as it is a CEM I 42.5R while the other cements fulfill the requirements of the strength class 52.5. In this case, cement 4 is still the better choice as SCMs will be incorporated in the mix design, water/cement ratio will be reduced by means of plasticizers and the PSD of the mix will be optimized. With all the changes mentioned, the mechanical properties will be enhanced. The mechanical characteristics of the coating system should be in line with the hardened

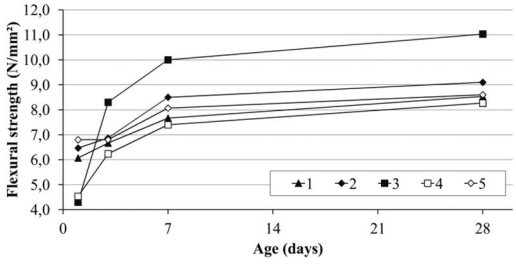

Figure 6. Flexural strength of the tested cements (DIN EN 196-1).

Table 4. SCM test results.

Mortar	Flow table [mm]	Comp. Str. 28d [N/mm^2]	Flex. Str. 28d [N/mm^2]
Ref.	201.0	53.7	8.3
MS2.5	185.5	53.9	8.1
MS5	176.0	60.8	8.4
MS12.7	145.5	68.2	8.7
MK4	185.5	57.9	7.7
MK7.5	171.5	60.0	8.1
MK15	147.5	61.5	8.7
FA4	202.0	51.4	7.6
FA12	211.0	50.9	7.3
FA24	222.5	43.3	6.9

old concrete and they should not have excessively different mechanical or thermal properties.

Cement 4 showed the best performance in both of the main tests and acceptable performance on the mechanical tests. Strunge & Deuse (2008) listed this type of cement as cement for high strength concrete with extended durability. They also give examples of structures made with concrete using this cement that have good performance in aggressive environments. Therefore, cement 4 was selected as the cement for the coating system and all the tests described subsequently were performed using cement 4.

3.2 *SCM*

All experimental results are condensed in Table 4, followed by comments and graphs.

The SCM consistence test (Figure 7) shows linear behavior of the flow table results and the quantity of SCM with r^2 higher than 0.99. The FA was the only SCM with a positive influence on the flow table results. That is explained by its low specific surface area and coarser grain size compared with cement 4.

When the PSDs of the SCMs (Figure 1) and the flow table results (Figure 7) are compared, it is clear that the grain size (fineness) of the SCM influences the consistence of the mortar for the same water quantity. It is also noticeable that the PSD optimization applied to the powders did not influence these results.

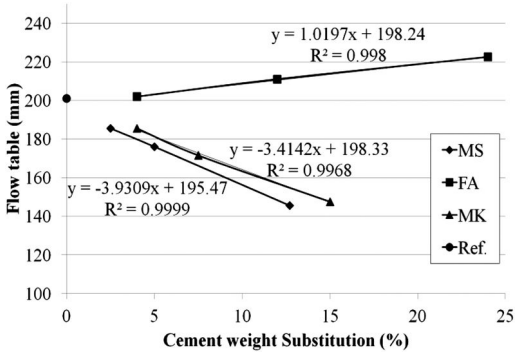

Figure 7. Consistence of the reference mortar with different additions and proportions (DIN EN 1015-3).

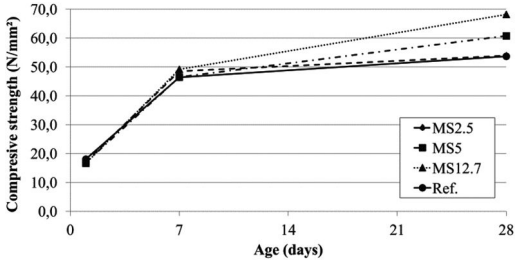

Figure 8. Compressive strength of the mortars with different MS concentrations (DIN EN 196-1).

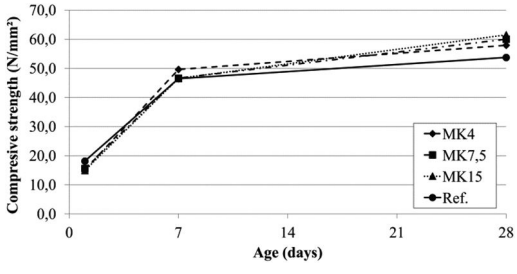

Figure 9. Compressive strength of the mortars with different MK concentrations (DIN EN 196-1).

The compressive and flexural strength results are presented in Figure 8 and Figure 13 separated by SCM type and test. The results of the reference mix (Ref.) were obtained using the standard mortar and pure cement 4.

Regarding the compressive strength (Figure 8 and Figure 10), the increase in the SCM quantity influenced the 28 days value differently.

In the analyzed range, the mortar showed an increase in compressive strength with the increase of MS. The 2.5% substitution did not affect the results compared to the reference mix, the 5% substitution provoked a 13.2% increase and the maximum

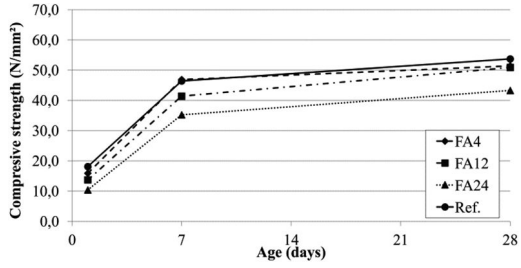

Figure 10. Compressive strength of the mortar with different FA concentrations (DIN EN 196-1).

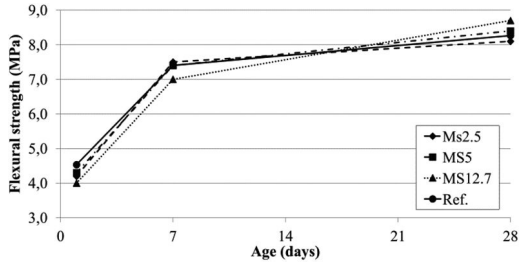

Figure 11. Flexural strength of the mortars with different MS concentrations (DIN EN 196-1).

increase was 27% obtained at 12.7% cement substitution by mass.

The increase of MK showed an increase of compressive strength as well, but did not present considerable differences at 28 days. The three different quantities enhanced the compressive strength by 7.8, 11.7 and 14.5%, respectively. Although, considering the speed of pozzolanic reaction, it is possible that MK mortars would present better results at a later age. Both MS and MK presented the same influence in the concrete compressive strength as those tested by Valipour et al. (2013).

FA shows a decrease of compressive strength with an increase in FA quantity. For the tested range, all the mortars with FA presented a decrease in compressive strength. The decrease ranged from 4.3 to 19.4%. The same behavior was observed in the study of Kayali & Ahmed (2013) for concrete after 1 year.

The SCM additions showed less improvement in the flexural strength than in the compressive strength (Figure 11 and Figure 13). For the MS, the MS2.5 and MS5 showed almost no difference from the reference mix and the MS12.7 showed less than 5% improvement. The MK showed similar results and only the MK15 had a positive influence related to the reference mix – similar to MS12.7. As with the compressive strength, all the FA mortars showed a decrease in flexural strength. The FA 4, FA12 and FA24 had results 8.4%, 12% and 16.9% lower than the reference mix. The decrease in strength caused by the addition of FA was also confirmed by Kayali & Ahmed (2013).

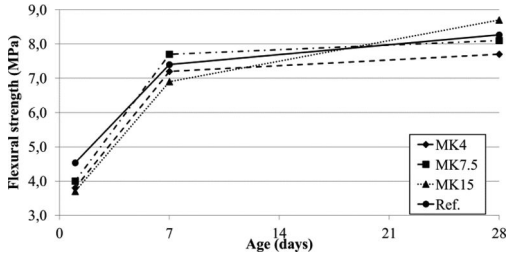

Figure 12. Flexural strength of the mortars with different MK concentrations (DIN EN 196-1).

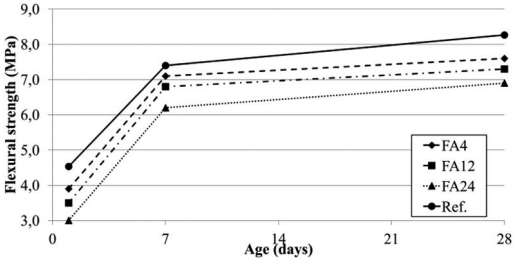

Figure 13. Flexural strength of the mortars with different FA concentrations (DIN EN 196-1).

4 CONCLUSION

From the results of the test program and comparison with literature results it is possible to conclude that:

- The behavior of the tested market available products match most of the conclusions of laboratory research.
- From the 5 cements evaluated, the CEM I 42.5R-HS/NA (cement 4) showed the best performance regarding the vital characteristics of the coating system and will be used.
- The tested FA does not enhance compressive and flexural strength. Furthermore, contradictory statements regarding the effect of FA use in mortar have been found in the literature. Also, the high variability of characteristics that FA can present demands a frequent correction of the mix proportions, which is undesirable. As a result, FA was excluded from the next steps of the research.
- MS and MK showed good results. The results are in agreement with other researchers conclusions.Therefore, MS and MK will be tested in different arrangements in future development of the coating system.
- Ternary blends using cement, MS and MK will be analyzed as well as the interaction between the powders with different plasticizers.
- The PSD optimization applied to the powders did not enhance the mortar characteristics significantly.

REFERENCES

Almusallam, A.A.; Khan, F.M.; Dulaijan, S.U. & Al-Amoudi, O.S.D. 2003. Effectiveness of surface coatings in improving concrete durability. *Cement & Concrete Composites* 25 (4-5):473–481.

Al-Zahrani, M.M.; Maslehuddin, M.; Al-Dulaijan, S.U. & Ibrahim, M. 2003. Mechanical properties and durability characteristics of polymer-and cement-based repair materials. *Cement & Concrete Composites* 25:527–537.

Basheer, L.; Kropp, J. & Cleland, D.J. 2001. Assessment of the durability of concrete from its permeation properties:a review. *Construction and Building Materials* 15(2–3): 93–103.

Basheer, P.A.M.; Chidiac, S.E. & Long, A.E. 1996. Predictive models for deterioration of concrete structures. *Construction and Building Materials* 1(10):27–37.

Batis, G.; Pantazopoulou, P. & Routoulas, A. 2003. Corrosion protection investigation of reinforcement by inorganic coating in the presence of alkanolamine-based inhibitor. *Cement & Concrete Composites* 25:371–377.

Beushausen, H & Burmaister, N. 2013. The use of surface coatings to increase the service life of reinforced concrete structures for durability class XC. *Materials and Structures*. (DOI 10.1617/s11527-013-0229-8).

Cramer, S.D.; Covino, B.S.; Bullard, S.J.; Holcomb, G.R., Russel, J.H.; Nelson, F.J.; Laylor, H.M & Soltesz, S.M. 2002. Corrosion prevention and remediation strategies for reinforced concrete coastal bridges. *Cement & Concrete Composites* 24:101–117.

Gleize, P.J.P.; Cyr, M. and Escadeillas, G. 2007. Effects of metakaolin on autogenous shrinkage of cement pastes. *Cement & Concrete Composites* 29(2):80–87.

Güneyisi, E.; Gesoglu, M.; Karaoglu, S. & Mermerdas, K. 2012. Strength, permeability and shrinkage cracking of silica fume and metakaolin concretes. *Construction & Building Materials* 34:120–130.

Habert, G.; Choupay, N; Montel, J.M.; Guillaume, D. & Escadeillas, G. 2008. Effects of the secondary minerals of the pozzolans on their Pozzolanic activity.*Cement and Concrete Research* 38(7):963–975.

Holt, E. 2005. Contribution of mixture design to chemical and autogenous shrinkage of concrete at early ages. *Cement & Concrete Research* 35(3):464–472.

Hüsken, G. & Brouwers, H.J.H. 2008. A new mix design concept for earth-moist concrete: A theoretical and experimental study. *Cement & Concrete Research* 38: 1246–1259.

Kayali, O. & Ahmed, M.S. 2013. Assessment of high volume replacement fly ash concrete – Concept of performance index. *Construction & Building Materials* 39(ISCCM 2011):71–76.

Malheiro, R.; Meira, G.; Lima, M. & Perazzo, N. 2011. Influence of mortar rendering on chloride penetration into concrete structures. *Cement & Concrete Composites* 33:233–239.

Medeiros, M.H.F. & Helene, P. 2009. Surface treatment of reinforced concrete in marine environment: Influence on chloride diffusion coefficient and capillary water absorption. *Construction and Building Materials* 23:1476–1484.

Nath, P. & Sarker, P. 2011. Effect of fly ash on the durability properties of high strength concrete. *Procedia Engineering* 14:1149–1156.

Otieno, M; Beushausen, H & Alexander, M. Effect of chemical composition of slag on chloride penetration resistance of concrete. *Cement and Concrete Composites* 46:56–64.

Papadakis, V. G. 2000. Effect of supplementary cementing materials on concrete resistance gainst carbonation

and chloride ingress. *Cement & Concrete Research* 30 (2):291–299.

Rincón, O. T. et al. 2006. Durability of concrete structures: DURACON, an iberoamerican project. Preliminary results. *Building and Environment* 41: 952–962.

Scheydt, J.C.; Müller, H.S. & Herold, G. 2008. Long term behaviour of ultra high performance concrete under attack of chlorides and aggressive waters. *Proceedings of the Second International Symposium on Ultra High Performance Concrete*. Kassel, Germany.

Seneviratne, A.M.G.; Sergi, G. & Page, C.L. 2000. Performance characteristics of surface coatings applied to concrete for control of reinforcement corrosion. *Construction and Building Materials* 14:55–59.

Shi, X.; Xie, N.; Fortune, K. & Gong, J. 2012. Durability of steel reinforced concrete in chloride environments: an overview. *Construction and Buildings Materials* 30: 125–138.

Siddique, R. & Klaus, J. 2009. Influence of metakaolin on the properties of mortar and concrete: A review. *Applied Clay Science* 43(3–4):392–400.

Strunge, J & Thomas, D. 2008. Special cements for ultra high performance concrete.*Proceedings of the Second International Symposium on Ultra High Performance Concrete*. Kassel, Germany.

Sýcora, M.; Holický, M & Marková, J. 2013. Verification of existing reinforced concrete bridges using the semi-probabilistic approach. *Engineering Structures* 56:1419–1426.

Valenza II, J.J.; Scherer, G.W. 2007a. A review of salt scaling: I. Phenomenology. *Cement and Concrete Research* 37:1007–1021.

Valenza II, J.J.; Scherer, G.W. 2007b. A review of salt scaling: II. Mechanisms. *Cement and Concrete Research* 37:1022–1034.

Valipour, M.; Pargar, F.;Shekarchi, M. & Khani, S. 2013. Comparing a natural pozzolan, zeolite, to metakaolin and silica fume in terms of their effect on the durability characteristics of concrete: A laboratory study. *Construction & Buildings Materials* 41:879–888.

Wang, Z.; Zeng, Q.; Wang, L.; Yao, Y & Li, K. 2014. Corrosion of rebar in concrete under cyclic freeze-thaw chloride salt action. *Construction and Building Materials* 53:40–47.

Yodsudjai, W & Wang, K. 2013. Chemical shrinkage behavior of pastes made with different types of cements. *Construction & Buildings Materials* 40:854–862.

This page intentionally left blank

Concrete Solutions – Grantham et al. (Eds)
© 2014 Taylor & Francis Group, London, ISBN 978-1-138-02708-4

Microstructural and permeability changes due to accelerated Ca leaching in ammonium nitrate solution

Quoc Tri Phung
Belgian Nuclear Research Centre, Belgium
Magnel Laboratory for Concrete Research, Ghent University, Belgium

Norbert Maes & Diederik Jacques
Institute for Environment, Health, and Safety, Belgian Nuclear Research Centre (SCK · CEN), Belgium

Geert De Schutter
Magnel Laboratory for Concrete Research, Ghent University, Belgium

Guang Ye
Microlab, Delft University of Technology, Delft, The Netherlands

ABSTRACT: Although Ca leaching in cement-based materials is an extremely slow process, this process is relevant for long-term assessments of the evolution of concrete used in radioactive waste disposal systems. In the present work, an ammonium nitrate solution of 6 mol/l was used to accelerate the leaching kinetics of cement paste. The change of sample mass over time was monitored by weighing, whereas the amount of calcium ion leached out during the test was followed by ion chromatography. A variety of post-analysis techniques like XRD, MIP and BET were used to characterize the microstructural changes and portlandite content, while the degraded front was determined by phenolphthalein spraying. The effect of accelerated leaching on transport properties was studied by measuring changes in water permeability. Results showed that (i) the porosity of the leached samples increased significantly, (ii) the critical pore size was shifted to larger radius and (iii) the BET specific surface area of the leached sample was also significantly increased. These changes resulted in a one to two order increase in water permeability depending on the immersed time.

1 INTRODUCTION

Leaching is a process of extracting ions from solid compounds by dissolving when contacting with an aqueous phase. In cement based-materials, leaching of calcium, also called decalcification, is of utmost importance because of the high calcium (Ca) content in cement compared to other potentially leachable ions (Fe^{2+}, Al^{3+}, Mg^{2+}, etc.) and the high solubility of the aqueous Ca-controlling phase portlandite. Ca leaching is one of the most serious degradation processes in concrete and reinforced concrete structures in the long-term (nuclear waste disposal system) or in hydro structures (dam, bridge, water tank) but it has only been studied since the 1980s despite the long history of concrete. The reason is that leaching of concrete is an extremely slow process under normal conditions (few mm leaching front in a hundred years (Yokozeki et al. 2004)). However, the lifetime of civil concrete structures is normally under one hundred years and that is too short to see the effects of leaching degradation.

Considering the slow degradation process but the need to study long-term durability of concrete, accelerated testing is a relevant approach to better understand the leaching phenomenon and the coinciding alteration of microstructure and transport properties. Acceleration is also a good way to verify prediction models. A variety of accelerated methods have been proposed such as applying an electrical field (Saito and Deguchi 2000), using deionized water (Haga et al. 2005; Jain and Neithalath 2009), using low pH solutions (Bertron, Duchesne, and Escadeillas 2005; De Windt and Devillers 2010); applying flow-through conditions (Butcher et al. 2012) or using high concentration ammonium nitrate (NH_4NO_3) solution (Carde, Escadeillas, and François 1997; Chen, Thomas, and Jennings 2006). Among them, using an ammonium nitrate solution to accelerate the leaching kinetics is one of the most popular methods because it results in faster degradation compared to other methods under diffusive-transport conditions and has the same end-products. The mechanism of acceleration is not only the low pH of NH_4NO_3 solution but also an increase in the solubility of the leachable phases in cementitious matrix induced by NH_4NO_3. When diffusing into cement-based materials, NH_4NO_3 reacts

with most of main phases in cement paste according to following reactions:

With **portlandite**: $Ca(OH)_2 + 2NH_4NO_3 \rightarrow \mathbf{Ca(NO_3)_2} + 2NH_{3(aq)} + 2H_2O$ (1)

With **Calcium silica hydrates (C-S-H)**:

$C_xS_yH_z + 2NH_4NO_3 \rightarrow C_{x\text{-}1}S_yH_{z\text{-}1} + \mathbf{Ca(NO_3)_2} + 2NH_{3(aq)} + 2H_2O$

$C_{x\text{-}1}S_{y\text{-}1}H_{z\text{-}1} + 2(x\text{-}1)NH_4NO_3 \rightarrow (y\text{-}1)SiO_2 + (x\text{-}1)\mathbf{Ca(NO_3)_2} + 2(x\text{-}1)NH_{3(aq)} + (z{+}x\text{-}2)H_2O$ (2)

With **Ettringite (AFt)**: $2C_6A\dot{S}_3H_{32} + 24NH_4NO_3 \rightarrow 3CaSO_4 + 9\mathbf{Ca(NO_3)_2} + Al_2(SO_4)_3 + 2Al(NO_3)_3 + 24NH_{3(aq)} + 76H_2O$ (3)

With **Monosulfoaluminate (AFm)**: $4C_4A\dot{S}H_{12} + 48NH_4NO_3 \rightarrow CaSO_4 + 15\mathbf{Ca(NO_3)_2} + Al_2(SO_4)_3 + 6Al(NO_3)_3 + 48NH_{3(aq)} + 72H_2O$ (4)

Calcium nitrate is a very soluble salt. Therefore, the concentration of Ca ion in pore solution is much higher than a portlandite-controlled system. Furthermore, aqueous NH_3 converts to gaseous NH_3 which escapes from the system hence it drives the reactions (1) to (4) to the right side. It helps to prevent the equilibrium of the system which stops the leaching acceleration.

Many studies predict the degraded depth of leached materials and characterize its mechanical behavior (de Larrard et al. 2012; Nguyen et al. 2007). But there are only a few studies that discuss the modification of the microstructure after leaching (Yang et al. 2012; Poyet et al. 2012) and the effects of leaching on transport properties (Perlot, Verdier, and Carcasses 2006; Gallé, Peycelon, and Bescop 2004). This study aims at strengthening and bridging the relationship between leaching degradation of cement paste (by means of an accelerated method using a strongly aggressive environment (NH_4NO_3)); and permeability change; and microstructural modification.

2 ACCELERATED CALCIUM LEACHING

2.1 *Materials*

Experiments were performed on cement paste with a water/cement ratio of 0.425. Type I ordinary Portland cement (CEM I 52.5 N) was used. This cement has Blaine specific surface area of 435 m^2/kg and density of 3100 kg/m^3. Table 1 gives a summary of the chemical composition.

Ammonium nitrate, NH_4NO_3, solution 6 M was used to accelerate the leaching process.

2.2 *Experimental procedure and test setup*

Cement paste was poured in a cylindrical PVC tube with inner diameter of 97.5 mm. The sample was then rotated during 24 hours to prevent segregation (Phung et al. 2013). Afterwards, the sample was cured in a sealed condition in a temperature controlled room ($22 \pm 2°C$) for 27 days. The 28-day-cured cement paste was sawn into 25 mm thick slices. In order to study one dimensional leaching, the PVC cover in the axial direction remained on the cement paste slice. Additionally, epoxy resin was poured to fill the gap (if available) between PVC cover and cement paste as shown in Fig. 1. In such a way radial leaching is prevented.

Table 1. Chemical composition and some properties of the cement CEM I 52.5 N (from manufacturing fact sheet).

Determinant	Percent	Determinant	Percent
CaO	63.0%	Chromium(VI)	$<2.10^{-4}$%
SiO_2	20.0%	Cl-	0.06%
Fe_2O_3	3.0%	Na_2O eq.	0.85%
Al_2O_3	5.0%	Loss on ignition	1.60%
Sulphate SO_3	2.9%	Insoluble residue	0.50%

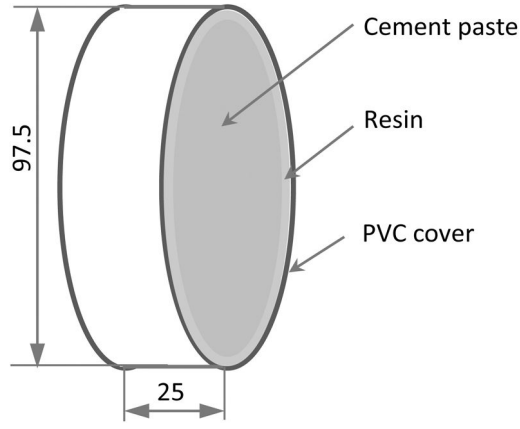

Figure 1. Preparation of cement paste slice for accelerated leaching in ammonium nitrate 6 mol/l solution.

The cement slices were saturated in saturated lime solution in order to avoid initial leaching. An effective saturation procedure by using vacuum chamber can be found in (Phung et al. 2013). The saturated cement slices were immersed in ammonium nitrate solution chambers with a capacity of 1.2 l of solution. The ratio between NH_4NO_3 solution over the contact surface area of the sample was 8 cm^3/cm^2. Such a factor was chosen to ensure that the pH of solution was always lower than 9.25. When higher pH is reached, the solution needs to be changed to maintain leaching acceleration (Heukamp, Ulm, and Germaine 2001). The renewal of solution is avoided because the solution is used for quantitative analysis of the leached Ca amounts.

A picture of the test setup is given in Fig. 2. Nitrogen was bubbled through the system to prevent carbonation during leaching and to remove the formed NH_3 gas

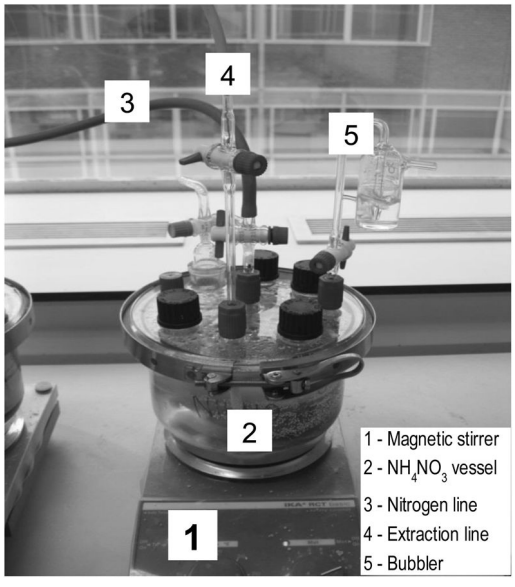

Figure 2. Accelerated leaching setup using NH_4NO_3 solution.

via the bubbler (water lock). The solution was homogenized by a magnetic stirrer. There was an extraction line to extract solution for further analysis and follow up the pH of solution. The setup had 3 NH_4NO_3 chambers which allowed simultaneously running three experiments. Reference samples were prepared from the same batch of cement paste and under the same conditions except for immersing in ammonium nitrate solution.

3 CHARACTERIZATION OF LEACHED MATERIALS

3.1 *Degraded depth, total leached Ca amount and mass loss*

The leaching tests were stopped after 7, 14, 21 and 28 days to examine different leaching grades. The leached samples were cut into hemispherical parts and sprayed by a phenolphthalein solution to determine the leached depth (RILEM 1988). Sawing the sample can have an effect that the degraded depth can be smeared out due to cross contamination by dust. Alternatively, a freshly exposed surface can be prepared by axially breaking the sample using a hammer. It should be noted that the phenolphthalein indicator only roughly quantifies the leached zone because it detects only the zone with a pH lower than approximately 9.

In order to quantify the amount of calcium leached out from the sample, the surrounding solution was extracted every seven days up to the end of the experiment. The Ca^{2+} ion concentration was determined by ion chromatography (IC). Prior to the measurement, the solution was filtered through a 0.45 μm syringe filter, and then diluted with milli-Q water to a (1:1000) solution. The IC analysis was performed by using a Dionex CS12A column and a 20 mM MSA isocratic elution. Detection was performed by a Dionex EC50 electro conductivity detector.

In addition, the mass of samples before and after leaching were determined under saturated condition by a precise balance. This is a direct method to quantify the mass loss due to leaching.

3.2 *Microstructure and portlandite content modifications*

The changes in microstructure of the leached samples were examined via mercury intrusion porosimetry (MIP) and nitrogen gas adsorption (BET) methods, while X-ray diffraction (XRD) was applied to qualitatively study portlandite content modification. The measurements were performed on both reference and degraded samples.

Dried samples were required for these techniques. In order to minimize the influence of the drying process on microstructure of the samples, freeze drying was chosen to prepare samples for MIP and nitrogen adsorption measurements. Freeze drying can efficiently prevent micro cracks generated due to the direct transformation of water crystals to gaseous phase without passing the liquid state which can avoid capillary stress generation (Gallé 2001). This method also gives a dried sample in a quite fast period. Samples were directly immersed in liquid nitrogen until the escape of gas bubbles stopped. Subsequently, the samples were transferred to a vacuum chamber where vacuum was applied under 10^{-2} mbar for 24 hours. For XRD measurements, cement powder was drilled and kept in small sealed containers to prevent air carbonation.

MIP experiments were performed on PASCAL 140/440 porosimeter in which the pressure of mercury is continuously increased up to a maximum pressure of 200 MPa. Nitrogen adsorption measurements were done on a TriStar II 3020 surface area analyzer. XRD measurements of samples were done using a Philips X'Pert Pro Diffractometer. The samples were scanned over the 2θ range of 5–70° using Cu-Kα radiation. All measurements were conducted on leached samples after 28 day exposure in NH_4NO_3 solution. For reference samples, the measurements were performed at the same ages of leached samples (but not immersed in NH_4NO_3 solution).

4 CHANGES IN TRANSPORT PROPERTIES

After finishing the leaching tests, the samples were stored in water in attendance of the water permeability measurements. This was to prevent drying of the samples and migration of calcium nitro-aluminate (a reaction product of calcium nitrate and hydrated aluminates) to the dry surface which can generate micro cracks (Carde, Escadeillas, and François 1997). Prior to permeability measurements, the samples were embedded in polycarbonate rings by a resin under

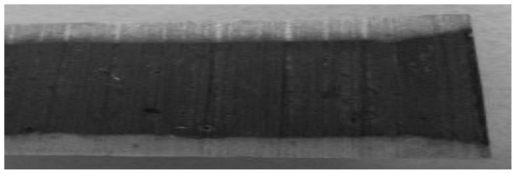

Figure 3. Determination of leached depth by phenolphthalein spraying after 7 days of leaching.

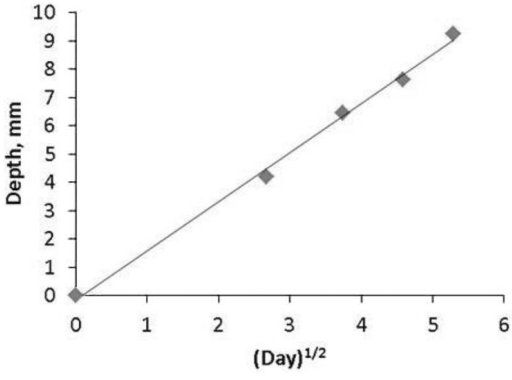

Figure 4. Leached depth vs. immersed time of cement paste with w/c = 0.425 in 6 mol/l NH_4NO_3.

an atmosphere of 100% relative humidity. Permeability was determined using a controlled constant flow method as described in (Phung et al. 2013). Permeability measurements were performed on reference and leached samples after different immersed time in ammonium nitrate solution: 1, 2 and 8 weeks, to see the effects of degradation degree on permeability. Due to the significant decrease in strength of leached samples, the maximum water pressure applied on leached samples was limited to 5 bar to prevent mechanically induced cracking and shrinkage of the pore system under compression. On the other hand, a pressure around 10 bar can be applied on reference samples to reduce the testing time (see (Phung et al. 2013)).

5 RESULTS AND DISCUSSION

5.1 *Degraded depth*

Fig. 3 shows a sample with typical leached depth determined by phenolphthalein. The degraded zone (lowered pH) is grey while the intact zone will make the phenolphthalein become pink due to its high pH.

Fig. 4 shows that the degraded depth increases linearly with the square root of time. This is one of the indicators which illustrates that leaching in ammonium nitrate solution is still a diffusion controlled phenomenon. A rate of 1.73 mm/day$^{1/2}$ for the decalcification front propagation was found which is quite similar to result reported in (Gallé, Peycelon, and

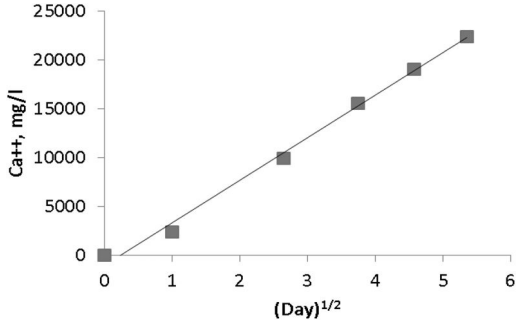

Figure 5. Calcium ion concentration in leaching solution (6 mol/l NH_4NO_3) vs. immersed time.

Bescop 2004) despite the specimens with a slight difference in w/c ratio (0.425 in this study compared to 0.45 in the reference).

5.2 *Amount of leached calcium and related mass loss*

Fig. 5 presents the concentration of calcium in the surrounding solution which is linearly related to the amount of calcium leached out from cement paste (initial concentration ~ 0) as shown in eq. (5). Again, a linear relation of leached amount over square root of time is shown. It is possible to calculate the decrease of sample weight from IC results by making the following assumptions: (i) mass loss due to the leaching of other ions (K^+, Na^+, Mg^{++}) is negligible; (ii) the decalcification of C-S-H is not a direct process, but forms portlandite which is then leached out from the cement matrix (Jain and Neithalath 2009).

The amount of portlandite leached out is calculated from Ca ion concentration in surrounding solution as follows:

$$CH = [Ca]V_a \frac{M_{CH}}{M_{Ca}} \tag{5}$$

where CH = portlandite content, g; $[Ca]$ = Ca ion concentration determined by IC, g/l; V_a = volume of NH_4NO_3 solution, l; M_{CH} = molar mass of $Ca(OH)_2$, 74 *g/mol*; and M_{Ca} = molar mass of Ca, 40 *g/mol*. The change in porosity due to portlandite dissolution is simply expressed as:

$$\Delta\phi = \frac{CH/M_{CH} V_{CH}}{V_s} 100\% \tag{6}$$

where V_{CH} = molar volume of $Ca(OH)_2$, 0.033 *l/mol* and V_s = sample volume, l. It is assumed that leaching of portlandite will create capillary pores which are completely filled by water, while the C-S-H decalcification will release gel pores which is hardly

accessible by water under normal condition. Therefore, the decrease of sample mass can be derived as follows:

$$\Delta m = \frac{CH - CH/M_{CH} V_{CH} \rho_w}{M_s} 100\% \quad (7)$$

where Δm = percentage of mass loss, %, M_s = sample mass, g and ρ_w = density of water, $1000\, g/l$. Fig. 6 shows a comparison of the mass loss during leaching based on directly measuring the weight change of samples and ion chromatography method. It can be seen that both methods agree quite well. The mass of samples also linearly decreases over the square root of immersed time.

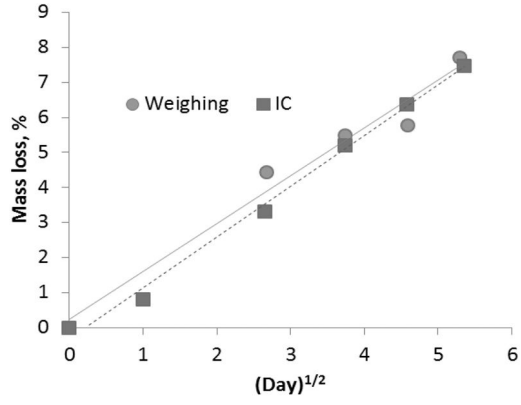

Figure 6. Mass loss of sample during leaching determined by ion chromatography and weighing methods.

5.3 *MIP and nitrogen gas adsorption results*

As mentioned above, pressure of the porosimeter is increased up to 200 MPa during the MIP intrusion process. However, mercury could not intrude into the leached sample when pressure reached 143 MPa, while for the reference sample the intruded volume continued increasing until the maximum pressure is reached as shown in Fig. 7. Mercury cannot penetrate into a sample when there are no pores remaining or the remaining pore radii are too narrow. There are two possibilities which can explain this phenomenon: (i) the leached sample is compressed and all pores are clogged at a pressure of 144 MPa or (ii) there is no gel porosity because the C-S-H phase is completely dissolved. However, BET results are in contradiction with the latter possibility (shown later). The complete dissolution of portlandite and partial decalcification of C-S-H can induce a strong loss of elasticity. As a result, the ductility of leached material will be higher. The deformation at failure of leached samples can increase with a factor of 5 in tension and 2 in uniaxial compression (Heukamp, Ulm, and Germaine 2005). Obviously, during the mercury intrusion process, the sample is under isotropic compression. Therefore, the deformation must be higher than that reported in (Heukamp, Ulm, and Germaine 2005). In this study, the sample was checked after finishing the MIP test to make sure that it was not broken during the test. No broken sample was seen.

The porosimeter interprets sample compression as the occurrence of pores. Thus, in order to account for the deformation of sample, the measurement needs to be corrected by subtracting the volume of sample compression as follows:

$$v_c = v_i - \left(\frac{1}{\rho_b} - \frac{1}{\rho_a} \right) \quad (8)$$

where v_c = specific compression volume, cm^3/g; v_i = specific intruded volume, cm^3/g; ρ_b = bulk density, g/cm^3; and ρ_a = apparent density which is

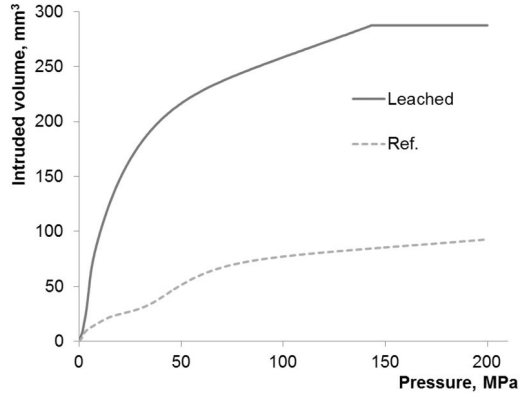

Figure 7. MIP intrusion curves of reference and 28-day leached samples.

defined as unit weight of sample at the end of the filling process, g/cm^3:

$$\rho_a = \frac{m_s}{V_b - V_i^{cor}} \quad (9)$$

where m_s = sample mass, g; V_b = sample volume (including pores), cm^3; V_i^{cor} = corrected intruded volume, cm^3 and can be calculated as follows:

$$V_i^{cor} = (v_i - v_c) m_s \quad (10)$$

Fig. 8 presents the intrusion curves of a leached sample before and after correcting for the compression effect. It can be seen that the pore volume is compressed by 33%. Such a quite high value cannot be disregarded. The pore size distribution (PSD) obtained by MIP of the reference and leached samples is shown in Fig. 9. It clearly shows that the critical pore size which is the most frequently occurring pore size in interconnected pores shifts to larger size after leaching. Furthermore, the leached sample shows a bimodal

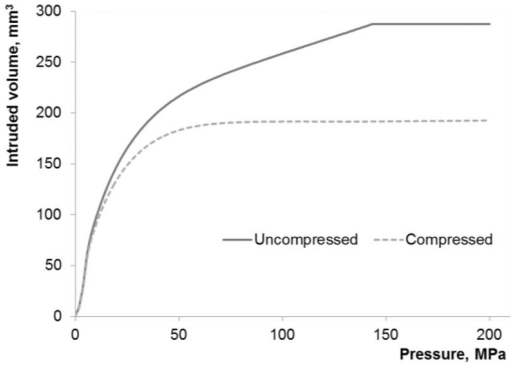

Figure 8. Compression corrected MIP in-and extrusion curves of the leached sample.

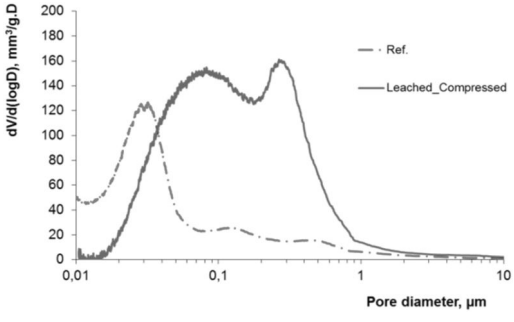

Figure 9. MIP pore size distribution of 28-day leached sample shifts to higher pore sizes compared to reference sample.

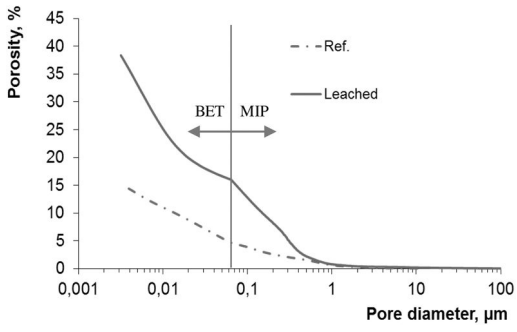

Figure 10. Increase of porosity due to leaching after 28-day immersion in 6 mol/l NH_4NO_3.

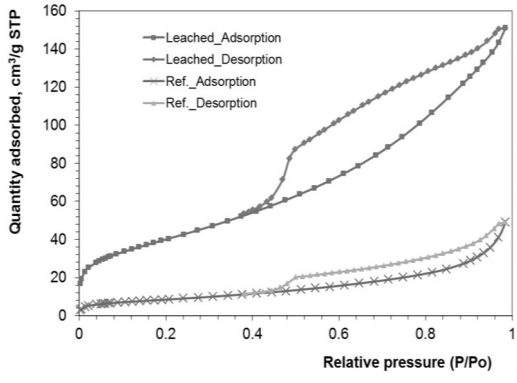

Figure 11. Adsorption isotherms of reference and 28-day leached samples.

distribution compared to the unimodal distribution of the reference sample. The larger critical pore size of leached samples results in higher transport properties of cement-based materials.

Even with compression correction, the MIP corrected results cannot be considered as the real pore structure of the tested sample because the pore volume of the sample is always bigger than the mercury intruded volume due to pore volume compression under pressure. The difference is larger when the pressure increases. In the context of this study, at a pressure of approximately 25 MPa (corresponding to a pore diameter of 0.06 μm), the corrected and uncorrected curves start diverging more and more. For this reason, combining MIP and gas adsorption measurements will give a better understanding of the pore structure of cementitious materials, especially for leached paste. The MIP gives reasonable results for pore sizes larger than 0.06 μm while BET provides information on the smaller pores. In this way, pore structure information is obtained in a broad pore size range without the complicating compression effect.

Fig. 10 shows the increase in porosity of the leached sample compared to the reference samples as determined from the combination of MIP and BET methods. In the range of 3 nm–100 μm, the porosity of the leached sample hugely increases up to 38% compared to 15% for the reference sample. Such a large porosity increase is not only due to the decalcification of portlandite but also the (partial) C-S-H system because the maximum change in porosity obtained by completely dissolving portlandite is about 12.8% (Phung et al. 2014 (submitted)).

Fig. 11 shows a comparison of nitrogen adsorption isotherms of leached and reference samples. The shape and size of the desorption hysteresis loop of the leached sample is characteristic for large ink-bottle shaped pores whereas the pore system is rather slit-shaped or plate-like in the reference sample (Gregg and Sing 1982). Such a plate-like pore system corresponds to C-S-H gel which consists of very thin sheets (Powers and Brownyard 1948). The alteration towards ink-bottle shaped pores illustrates that part of the C-S-H is dissolved after leaching. The surface areas determined by the BET method of reference and leached samples were 31.6 and 153.6 m^2/g, respectively. There was a significant increase in specific surface area of leached material. Such a large increase is not only attributed to the dissolution of portlandite but also probably the dissolution of C-S-H. The gel pores of C-S-H which have higher specific surface

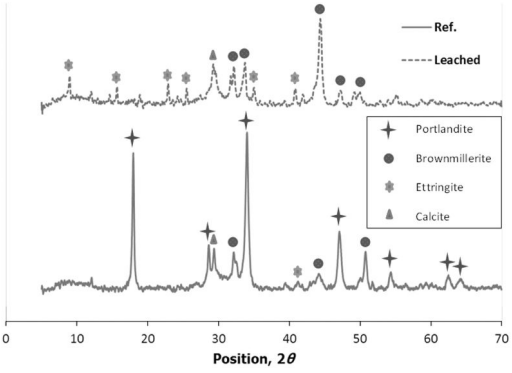

Figure 12. XRD patterns of reference and 28-day leached samples.

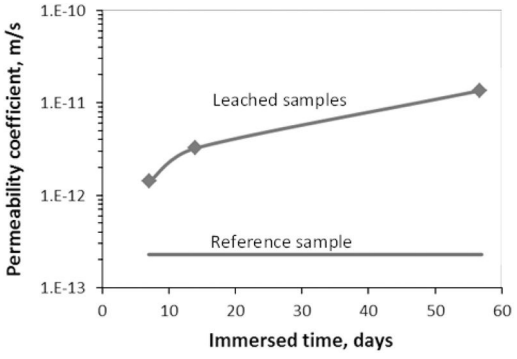

Figure 13. Change in permeability of leached sample due to leaching in 6 mol/l NH_4NO_3 as a function of immersed time; permeability of reference sample is determined at the same age of 8-week leached sample.

area compared to micro/meso pores are more easily accessible by nitrogen after leaching.

5.4 *XRD results*

Fig. 12 presents the XRD patterns for leached and reference samples. Note that leached sample is only taken from the leached zone (pH < 9). It is clearly observable that the portlandite is completely dissolved in the leached sample. There are two strong peaks at $2\theta = 17.9$ and 34.2° for the reference sample which totally disappeared in the leached sample. Except for C-S-H which is impossible to detect (amorphous phase), the most visible phases in the XRD pattern of the leached sample are ettringite and brownmillerite (C_4AF) which indicates that they are hardly degraded by NH_4NO_3 solution.

5.5 *Permeability change*

Permeability is significantly increased after leaching as shown in Fig. 13. After one week of NH_4NO_3 immersion, the permeability coefficient increased 6 times, from 2.3×10^{-13} to 1.4×10^{-12} m/s. It continued increasing up to 3.2×10^{-12} m/s and 1.4×10^{-11} m/s after 2 weeks and 8 weeks NH_4NO_3 immersion, respectively. It is worth mentioning that the decalcification of the sample was not uniform with depth (e.g. total degradation depth in terms of the phenolphthalein indicator was smaller than half of the sample thickness, Fig. 4) and thus, the permeability represents a composite permeability. It is not surprising that permeability increases when the degraded depth proceeds further. However, it seems that permeability of the zone with pH larger than 9 also increases. Otherwise it is unlikely that the composite permeability increases so fast – 6 times after 7 day immersion – because the composite permeability is still dominated by the permeability of "non-invasion" zone. Therefore, the authors assume that there exists a relatively thick transition zone over which permeability is increased to a value somewhere between that of the degraded zone and the reference sample. However, further analyses (SEM, QXRD at different depth within a sample) on leached samples are needed to confirm this assumption and quantify the depth of the transition zone.

The increase of permeability of degraded material can be explained due to the larger amount of capillary pores (Figs. 9 and 10) which is the result of portlandite dissolution. In general, mass transport properties are mainly affected by capillary and large pores (Perlot, Verdier, and Carcasses 2006). However, calcium leaching is a process in which Ca ion is leached out from the system, and as a result the created pathways can increase the connectivity at all gel, micro and meso pore levels. Thus the authors suggest that the dissolution of C-S-H contributes to the change in permeability during accelerated leaching. As shown in the study of (Agostini et al. 2007), when the sample has been completely degraded (complete decalcification of portlandite), then if it is immersed for 8 days further in NH_4NO_3 solution, the intrinsic permeability slightly increases from 1.7×10^{-16} to 2.3×10^{-16} m^2. This is to say that further degradation of C-S-H (and probably other less leachable phases) can increase the permeability.

6 CONCLUSIONS

In the present work, an ammonium nitrate solution of 6 M was used to accelerate the decalcification kinetics of hardened cement paste samples and examine the changes in microstructure and permeability of leached materials. A variety of techniques including IC, XRD, MIP and BET were used to characterize the microstructural changes, while the degraded front was determined by phenolphthalein spraying. The effect of accelerated leaching on transport behavior was studied by measuring changes in the water permeability.

Results show that NH_4NO_3 solution is an aggressive agent which can be used to accelerate leaching

kinetics while still keeping the "nature" of leaching in terms of transport mechanisms. In this way, we can imitate long-term naturally degraded cementitious materials. The square-root-time law of degradation is applicable under accelerated condition indicating diffusive transport conditions. Portlandite is completely degraded in the leached zone while C-S-H is probably partially dissolved. A combination of MIP – nitrogen adsorption analysis is needed to obtain useful information on the pore size distribution changes because the compression effect (due to higher ductility of leached cement paste) is avoided. The accelerated leaching significantly alters the microstructure of the cement paste to a material with a higher specific surface area, increased total porosity and a shift to larger pore sizes. Those changes lead to a significant, one to two orders of magnitude, increase in water permeability depending on degradation state.

ACKNOWLEDGEMENTS

This work is supported by a grant from Belgium Nuclear Research Centre (SCK · CEN). The authors are thankful to M. Honty and W. Verwimp at SCK · CEN for their help in XRD and BET measurements.

REFERENCES

Agostini, F., Z. Lafhaj, F. Skoczylas, and H. Loodsveldt. 2007. Experimental study of accelerated leaching on hollow cylinders of mortar. *Cement and Concrete Research* 37 (1):71–78.

Bertron, A., J. Duchesne, and G. Escadeillas. 2005. Accelerated tests of hardened cement pastes alteration by organic acids: analysis of the pH effect. *Cement and Concrete Research* 35 (1):155–166.

Butcher, E. J., J. Borwick, N. Collier, and S. J. Williams. 2012. Long term leachate evolution during flow-through leaching of a vault backfill (NRVB). *Mineralogical Magazine* 76 (8):3023–3031.

Carde, C., G. Escadeillas, and A. H. François. 1997. Use of ammonium nitrate solution to simulate and accelerate the leaching of cement pastes due to deionized water. *Magazine of Concrete Research* 49 (181):295–301.

Chen, J. J., J. J. Thomas, and H. A. Jennings. 2006. Decalcification shrinkage of cement paste. *Cement and Concrete Research* 36 (5):801–809.

de Larrard, Thomas, Stéphane Poyet, Magalie Pierre, et al. 2012. Modelling the influence of temperature on accelerated leaching in ammonium nitrate. *European Journal of Environmental and Civil Engineering* 16 (3-4):322–335.

De Windt, L., and P. Devillers. 2010. Modeling the degradation of Portland cement pastes by biogenic organic acids. *Cement and Concrete Research* 40 (8):1165–1174.

Gallé, C. 2001. Effect of drying on cement-based materials pore structure as identified by mercury intrusion porosimetry: A comparative study between oven-, vacuum-, and freeze-drying. *Cement and Concrete Research* 31 (10):1467–1477.

Gallé, C., H. Peycelon, and P. Le Bescop. 2004. Effect of an accelerated chemical degradation on water permeability and pore structure of cementbased materials. *Advances in Cement Research* 16 (3):105–114.

Gregg, S. J., and K. S. W. Sing. 1982. *Adsorption, Surface Area and Porosity*. 2nd ed. London: Academic Press.

Haga, K., S. Sutou, M. Hironaga, S. Tanaka, and S. Nagasaki. 2005. Effects of porosity on leaching of Ca from hardened ordinary Portland cement paste. *Cement and Concrete Research* 35 (9):1764–1775.

Heukamp, F. H., F. J. Ulm, and J. T. Germaine. 2001. Mechanical properties of calcium-leached cement pastes: Triaxial stress states and the influence of the pore pressures. *Cement and Concrete Research* 31 (5):767–774.

Heukamp, F., F. Ulm, and J. Germaine. 2005. Does Calcium Leaching Increase Ductility of Cementitious Materials? Evidence from Direct Tensile Tests. *Journal of Materials in Civil Engineering* 17 (3):307–312.

Jain, Jitendra, and Narayanan Neithalath. 2009. Analysis of calcium leaching behavior of plain and modified cement pastes in pure water. *Cement and Concrete Composites* 31 (3):176–185.

Nguyen, V. H., H. Colina, J. M. Torrenti, C. Boulay, and B. Nedjar. 2007. Chemo-mechanical coupling behaviour of leached concrete: Part I: Experimental results. *Nuclear Engineering and Design* 237 (20–21):2083–2089.

Perlot, C., J. Verdier, and M. Carcasses. 2006. Influence of cement type on transport properties and chemical degradation: Application to nuclear waste storage. *Materials and Structures* 39 (5):511–523.

Phung, Quoc Tri, Norbert Maes, Geert De Schutter, Diederik Jacques, and Guang Ye. 2013. Determination of water permeability of cementitious materials using a controlled constant flow method. *Construction and Building Materials* 47 (0):1488–1496.

Phung, Quoc Tri, Norbert Maes, Diederik Jacques, Geert De Schutter, and Guang Ye. 2014 (submitted). Decalcification of cement paste in NH_4NO_3 solution: Microstructural alterations and its influence on the transport properties. Paper read at 10th fib International PhD Symposium in Civil Engineering, at Québec, Canada.

Powers, T.C., and T.L. Brownyard. 1948. *Studies of the physical properties of hardened portland cement paste*: Research Bulletin 22, Portland Cement Association.

Poyet, Stéphane, Patrick Le Bescop, Magalie Pierre, Laure Chomat, and Cécile Blanc. 2012. Accelerated leaching of cementitious materials using ammonium nitrate (6M): influence of test conditions. *European Journal of Environmental and Civil Engineering* 16 (3–4):336–351.

RILEM. 1988. CPC-18 Measurement of hardened concrete carbonation depth. *Materials and Structures* 21 (6): 453–455.

Saito, H., and A. Deguchi. 2000. Leaching tests on different mortars using accelerated electrochemical method. *Cement and Concrete Research* 30 (11):1815–1825.

Yang, Hu, Linhua Jiang, Yan Zhang, Qi Pu, and Yi Xu. 2012. Predicting the calcium leaching behavior of cement pastes in aggressive environments. *Construction and Building Materials* 29 (0):88–96.

Yokozeki, K., K. Watanabe, N. Sakata, and N. Otsuki. 2004. Modeling of leaching from cementitious materials used in underground environment. *Applied Clay Science* 26 (1–4):293–308.

Concrete Solutions – Grantham et al. (Eds)
© 2014 Taylor & Francis Group, London, ISBN 978-1-138-02708-4

Efficiency of materials used for repair measures of concrete structures exposed to chlorides

A. Rahimi, T. Reschke & A. Westendarp
Federal Waterways Engineering and Research Institute (BAW), Karlsruhe, Germany

C. Gehlen
Centre for Building Materials (cbm), Technische Universität München, Munich, Germany

ABSTRACT: This paper deals with the performance of cement-based repair materials with respect to their chloride penetration resistance. Results of current laboratory investigations are presented, comparing the development of the chloride diffusion resistance of several PCC (Polymer modified Cement Concrete) and SPCC (Sprayed Polymer modified Cement Concrete) materials over time. The results of the laboratory tests Rapid Chloride Migration (RCM) and unidirectional diffusion are used to develop a methodology for assessing the performance of repair materials with respect to their chloride penetration resistance.

1 INTRODUCTION

In saline exposure conditions such as marine environments, chloride-induced corrosion is the main problem with respect to the durability of reinforced concrete structures. Reinforcement corrosion is initiated when chloride ions penetrate into concrete and reach a threshold at the surface of the rebar which disrupts the passive layer protecting the rebar.

A traditional and feasible repair measure is the application of cement-based repair mortars or concretes to repassivate the rebars. Depending on the depth of chloride penetration and the chloride concentration in the structural element, the concrete cover is removed either partially or completely, as are deeper areas behind the reinforcement if necessary, and replaced with repair material. The repairs can cover large areas or be limited to selected points.

The repaired areas have to meet requirements concerning loadbearing capacity, durability and adhesion to the existing concrete. For assessing the durability concerning chloride-induced corrosion the time- and depth-dependent chloride concentration in the repaired layer can be estimated by means of mathematical models in the same way as for concrete components (cf. section 2). For this purpose, however, the relevant characteristic values of the materials are first to be ascertained.

Cement-based repair materials are usually polymer-modified mixes, the composition of which is generally not disclosed by the manufacturers. The long-term behaviour of these relatively recently developed materials has not yet been investigated. The unknown composition on the one hand and the lack of experience concerning the effect of the polymers on the chloride penetration resistance and, above all on their long-term behaviour on the other make it more difficult to estimate the performance of such repair materials.

This paper presents and discusses the results of current laboratory investigations into the chloride penetration resistance of six different repair materials. Observations from Rapid Chloride Migration (RCM) tests and unidirectional diffusion tests, which are both performed in the laboratory, are used to develop a methodology for assessing the performance of repair materials with respect to their chloride penetration resistance. The composition of the materials and its influence on the results of the laboratory tests are not taken into account here.

2 MODELLING THE CHLORIDE PENETRATION IN CONCRETE

Mathematical models are used to estimate the initiation period of the corrosion by calculating the penetration of chlorides into concrete as a function of time and depth. A widely used formula is based on Fick's second law of diffusion, as diffusion is the most active mechanism in chloride transport in concrete. Equation (1) constitutes the mathematical description of chloride penetration in uncracked concrete used in "*fib* Model Code for service life design" *fib* bulletin 34 (2006), "*fib* Model Code for concrete structures" *fib* MC (2010) and ISO 16204 (2012).

$$C(x,t) = C_0 + (C_{S,0} - C_0) \cdot \left[1 - \operatorname{erf} \frac{x}{2 \cdot \sqrt{D_{app}(t) \cdot t}} \right] \qquad (1)$$

where C_0 is the initial chloride content (wt.-%/c), $C_{S,0}$ is the chloride content at the surface (wt.-%/c), erf stands for error function, x is the depth with a corresponding content of chlorides $C(x,t)$ (mm), t is the time (years) and $D_{app}(t)$ is the apparent chloride diffusion coefficient at time t (m^2/s).

It can be concluded that the rate at which chlorides penetrate concrete is governed by the diffusivity of the concrete (material) and the concentration of the chloride load (environment).

Two common approaches are used to determine $D_{app}(t)$:

Approach A: in this approach, used in *fib* bulletin 34 (2006), *fib* MC (2010) and ISO 16204 (2012), $D_{app}(t)$ is determined by means of equation (2).

$$D_{app}(t) = D_{app}(t_0) \cdot \left(\frac{t_0}{t}\right)^{\alpha} \quad (2)$$

where $D_{app}(t_0)$ is the apparent chloride diffusion coefficient at a reference time t_0 (s) deriving by means of an inverse analysis from measured chloride profiles (see figure 3 in section 4) from existing structures or laboratory diffusion tests, α is the ageing exponent giving the decrease over time of the apparent chloride diffusion coefficient (–).

The ageing exponent is both material- and exposure-dependent and cannot be determined by laboratory tests alone. In order to determine the ageing exponent, D_{app} values in at least two different points in time are required. However, for a realistic determination of the ageing exponent, the long-term behaviour of D_{app} for existing structures has to be considered.

The higher the ageing exponent is, the more and faster D_{app} decreases in time, i.e. it is more favourable for concrete durability. In *fib* MC (2010) and ISO 16204 (2012) expected values of 0.2 to 0.8 are given for the ageing exponent, depending on the type of binder and the micro environmental conditions.

Approach B: in this approach, used in *fib* bulletin 34 (2006) and *fib* MC (2010), $D_{app}(t)$ is determined by means of equation (3).

$$D_{app}(t) = k_e \cdot D_{RCM(t_0)} \cdot \left(\frac{t_0}{t}\right)^{\alpha} \quad (3)$$

where $D_{RCM}(t_0)$ is the chloride migration coefficient at the reference point of time (m^2/s), t_0 is the reference point of time (s), α is the ageing exponent (–) and k_e is the environmental variable (–) and is determined by means of equation (4).

$$k_e = \exp\left(b_e\left(\frac{1}{T_{ref}} - \frac{1}{T_{real}}\right)\right) \quad (4)$$

where b_e is the temperature coefficient (K), T_{ref} is the reference temperature (for laboratory tests) (K) and T_{real} is the temperature of the structural element or the ambient air (K).

$D_{RCM}(t_0)$ is simply determined by the rapid chloride migration (RCM) test method (NT Build 492 1999, BAW Code of Practice MCL 2012) and substitutes in this approach the parameter $D_{app}(t_0)$ which is to be determined by means of costly diffusion tests or analysing the chloride profiles from existing structures.

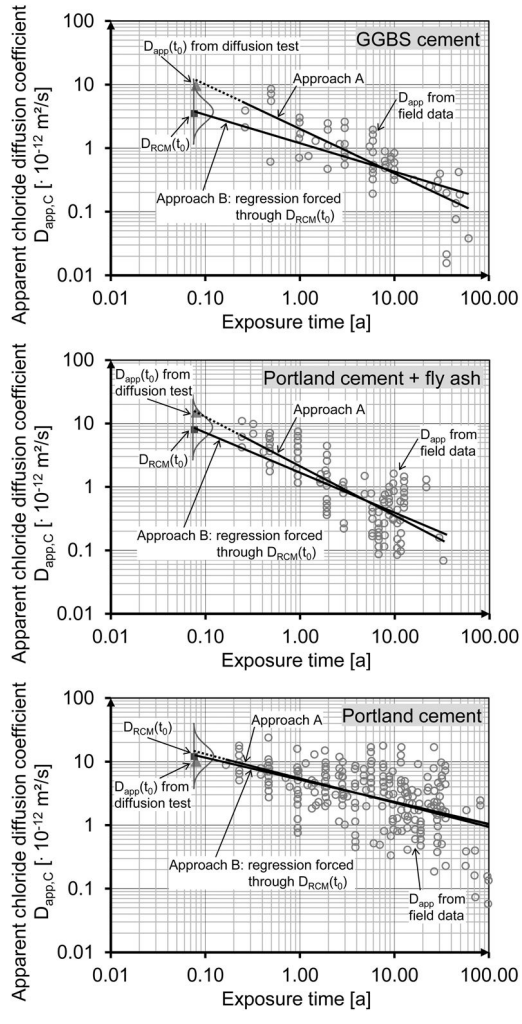

Figure 1. Development of the apparent chloride diffusion coefficient D_{app} over time for concrete with GGBS cement (top), Portland cement with fly ash (middle) and Portland cement (bottom) from Gehlen (2000). Approach A: regression analysis on D_{app} from field data. Approach B: regression analysis on D_{app} from field data and forced through the chloride migration coefficient $D_{RCM}(t_0)$ from laboratory RCM test. Triangular points: $D_{app}(t_0)$ from own diffusion tests.

The ageing exponent α used in approach B is derived by considering the $D_{RCM}(t_0)$. This results often in a lower ageing exponent compared to approach A since D_{RCM} of most concretes is lower than D_{app} at early ages (see below and figure 1).

Although the ageing exponent is dependent on the exposure conditions, binders have characteristic

Table 1. Ageing exponents calculated in Gehlen (2000).

Type of binder	Ageing exponent α [–][3]	
	Approach B[1]	Approach A[2]
CEM III/B	βD (**0.45** / 0.20 / 0.0 / 1.0)	0.70
CEM I + FA	βD (**0.60** / 0.15 / 0.0 / 1.0)	0.78
CEM I	βD (**0.30** / 0.12 / 0.0 / 1.0)	0.38

[1] βD: Beta Distribution (mean value/standard deviation/ lower boundary/upper boundary)
[2] Mean values
[3] [–] means no unit

ageing exponents. The ageing exponents of concretes with the three main types of binder Portland cement (CEM I), Portland fly ash cement (CEM I + FA ($f \geq 0.20 \cdot c$)) and ground-granulated blast-furnace slag cement (CEM III/B) have been quantified statistically in Gehlen (2000). For this purpose, published chloride profiling data ($D_{app}(t)$) of existing concrete structures (field data) with each binder type ($0.40 \leq w/c \leq 0.60$) exposed in conditions submerged / splash / tidal were collected and plotted vs. exposure time. A first regression analysis was performed giving the ageing exponent via considering only the field data (approach A). In a further step, new concrete mixes with the same binder type and of comparable quality were tested in the laboratory by the RCM method at a reference age of $t_0 = 28\,d$. The spread of the RCM test results at the age t_0 was determined; the mean value was added into the diagram of published results. The previously calculated regression line was forced (boundary) through the data of new concretes (RCM results). This regression line introduces the new ageing exponent (approach B) which is lower than the first one.

This procedure is depicted in figure 1 for concretes with the three main types of binder mentioned above. It can clearly be seen that the difference between the regression lines for the GGBS cement-concretes is higher than for the other two cases. For Portland cement-concretes the lines are almost superposed. The regression lines meet in all three cases in a time of about 10 years.

Table 1 shows the ageing exponents thus calculated in Gehlen (2000). Since the field data used for Portland cement-concretes are very scattered, being on the safe side, an ageing exponent of 0.30 is assumed which is lightly lower than the calculated value of ca. 0.35 by the regression analysis (approach B).

Results of current unidirectional diffusion (inversion) tests (t = 28 d exposure after 28 d curing) on comparable concretes are added into the diagrams in figure 1 (triangular points). These match very well to the regression lines, which means that they can be used as $D_{app}(t_0)$ in order to apply the approach A for calculating the $D_{app}(t)$.

In figure 1 it can be seen that after the regression lines meet (ca. 10 years) the $D_{app}(t)$ derived by approach A is lower (more favourable) than the ones by approach B. In section 6.2 it will be illustrated by means of a reliability analysis, how far this difference affects the prediction of the service life.

The introduced model is applied for probabilistic service life design of concrete structures. The model and the input parameters are described in detail in *fib* bulletin 34 (2006) and Gehlen (2000).

3 LABORATORY INVESTIGATIONS

3.1 *Materials and specimen preparation*

Six different commercially available repair materials were selected for the investigations. They are hydraulically hardening, polymer-modified cement mixes, four of which were dry sprayed concretes (SPCC: Sprayed Polymer Cement Concrete) and two were pre-mixed dry mortars (PCC: Polymer Cement Concrete). The SPCC materials contained aggregates with a maximum particle size between 4 mm and 8 mm, while the PCC materials had a maximum particle size of 2 mm. No further information on the raw materials or the composition of the repair materials was available; such information is not disclosed by the manufacturers.

After adding water in accordance with the manufacturer's instructions, the repair materials were used to make slabs with the dimensions $300 \times 300 \times 80\,mm^3$. The dimensions of the specimens for the determination of the chloride migration coefficients of repair materials were selected in accordance with the BAW Code of Practice MCL "Resistance of Concrete to Chloride Penetration" (2012). After preparation, the slabs were left in the moulds for a day and protected against drying out. After removal from the moulds and depending on which test was being performed, the specimens were either immersed in water for 6 days at 20°C and subsequently stored at 20°C/65% RH (tests on hardened concrete, e.g. compressive strength) or immersed in water at 20°C until testing (RCM and diffusion tests). In the case of the SPCC materials, large slabs ($1000 \times 1000 \times 80\,mm^3$) were first made using the dry-spraying method. Smaller slabs with the dimensions $300 \times 300 \times 80\,mm^3$ were then cut out of the large slabs (at an age of 7 days).

Table 1 shows the material characteristics bulk density, compressive strength and porosity of the prepared slabs. The specimens required for these tests were taken from the slabs. The density and compressive strength were determined using drill cores with a diameter of 50 mm and a length of 50 mm at an age of 28 d. To determine the porosity, discs with a diameter of 100 mm and a thickness of 30 mm were prepared and immersed in water at a pressure of 150 bars for 24 h (based on Bunke 1991).

The density and porosity of the specimens determined in the tests are comparable with those of common normal-weight concretes. The materials exhibit compressive strength classes between C30/37 and C50/60.

3.2 *Test methods*

Rapid Chloride Migration tests (RCM) and unidirectional diffusion tests (exposure method: inversion) were used in the laboratory investigations.

The RCM tests were performed in accordance with the BAW Code of Practice MCL "Resistance of Concrete to Chloride Penetration" (2012). The MCL is a German code published by the Federal Waterways Engineering and Research Institute (BAW). The RCM test performed as specified in the MCL is very similar to the RCM test method according to NT Build 492 (1999). The main difference between the two tests is the test voltage and the resulting test duration. While the specimens are subjected to a voltage of 30 V during the RCM test according to the MCL, the test voltage used in the RCM test according to NT Build 492 ranges from 10 V to 60 V (depending on the current measured initially). The chloride migration coefficients D_{RCM} determined as specified in the MCL are generally lower than those determined according to NT Build 492 (e.g. Gulikers 2011). This is probably due to the rise in the temperature of the specimens owing to the high voltages used in the test according to NT Build 492 which accelerates the migration of ions (Joule effect).

Table 2. Investigated repair materials.

Repair Material [–]	Density [kg/m^3]	Compressive Strength [N/mm^2]	Porosity (150 bar) [% of vol.]
SPCC 1	2280	65.2	15.0
SPCC 2	2220	70.5	16.5
SPCC 3	2210	62.8	18.6
SPCC 4	2170	46.4	20.7
PCC I	2080	68.9	25.2
PCC II	2220	55.0	14.5

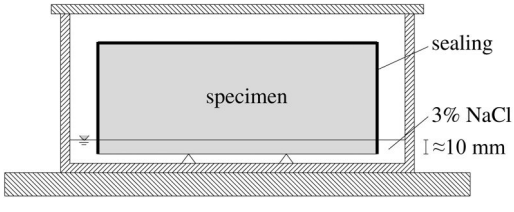

Figure 2. Diffusion test setup (inversion).

Table 3. Laboratory tests and specimens.

Test	Specimen	Time [d]
Density	ϕ/L: 50/50 mm	28
compressive Strength		28
Porosity	ϕ/ L: 100/30 mm	28
RCM	ϕ/L: 100/50 mm	28, 56, 90, 180, 365
Diffusion	200 × 200 × 80 mm^3	28, 90, 180, 365 *

* Time from beginning the diffusion test at specimen's age of 28 d

The RCM tests were performed on the specimens at the ages of around 28 d, 56 d, 90 d, 180 d and 365 d. The specimens were kept immersed in water until testing (cf. section 2.1).

The electrolyte resistance of the specimens was also determined in the RCM tests. This was done by means of the Two Electrode Method (TEM) directly before the specimens were installed in the RCM measuring cells.

The unidirectional diffusion tests were based on CEN/TS 12390-11 (2010). As exposure method "inversion" was chosen. A slab of each repair material was removed from the water bath at an age of 28 d. With the exception of the surface to be tested, five surfaces were sealed by coating them with epoxy resin. The slabs were stored at 20°C/65% RH for one day to allow the resin to dry. During that time, the surface to be tested was covered with a damp mat to reduce water loss. The sealed slabs were then stored under water in plastic containers with lids for 24 h prior to immersion in a 3% NaCl solution in order to minimise the uptake of chloride due to absorption. The slabs were placed on spacers with a height of around 5 mm. The containers were filled with the NaCl solution up to around 10 mm above the bottom of the slabs. The solution was occasionally topped up during the storage period to maintain it at a constant level.

The slabs were first cut down to 200 × 200 mm^2 to enable them to be placed in the containers. The test setup is shown in figure 2.

Samples of concrete dust were taken by drilling at depth intervals of 5 mm at three points on each slab at the specified times of around 28 d, 90 d, 180 d and 365 d after the beginning of the storage period. The overall chloride content of the dust samples was determined photometrically and by chemical analysis.

The laboratory tests and specimens prepared from the base slabs (300 × 300 × 80 mm^2) are shown in table 3.

4 RESULTS

The chloride profiles determined up to a depth of 30 mm in the diffusion tests are shown in figure 4. The apparent chloride diffusion coefficients D_{app} were calculated from the chloride profiles and by performing a regression analysis. To do so, the relationship shown in equation (1) was fitted into the chloride depth profile obtained in the diffusion tests by minimising the squared errors. The output parameters of the regression are the surface chloride concentration $C_{S,0}$ and D_{app}. Figure 3 shows the chloride profile and the value of D_{app} thus determined for SPCC 2 in the diffusion test after 90 d by way of an example.

The diagrams in figure 5 show the values of the chloride migration coefficient D_{RCM}, apparent chloride diffusion coefficient D_{app} and specific electrolyte resistance ρ over time, evaluated on the basis of the results of the RCM and diffusion tests. The graphs for

D_{RCM} and D_{app} were plotted by logarithmic scaling of the two axes (log-log).

The results for the development of the measured material parameters over time and their correlations as well as the assessment of the chloride penetration resistance of the repair materials under investigation are discussed below.

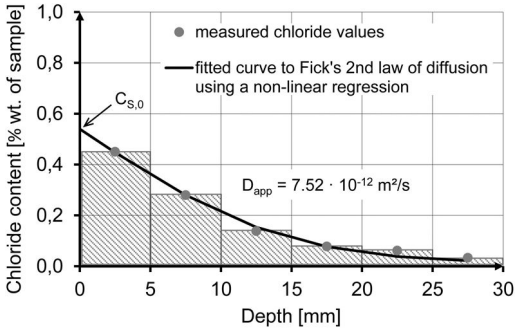

Figure 3. Appraisal the apparent chloride diffusion coefficient by regression analysis (SPCC 2 after 90 d diffusion test).

5 DISCUSSION

5.1 *Chloride profiles*

The chloride profiles determined after inversion of the specimens in a 3% NaCl solution for 28, 90, 180 and 365 days in the diffusion tests showed a continuous increase in the chloride content of the specimens (figure 4). The depth-dependent development of the chloride content can be modelled very well with the error function solution of Fick's second law of diffusion (equation 1) for all specimens (e.g. SPCC 2 after 90 d, cf. figure 2) with the exception of SPCC 4. The SPCC 4 specimen had a far higher chloride concentration at lower depths than the other specimens. The two PCC specimens had the lowest chloride contents,

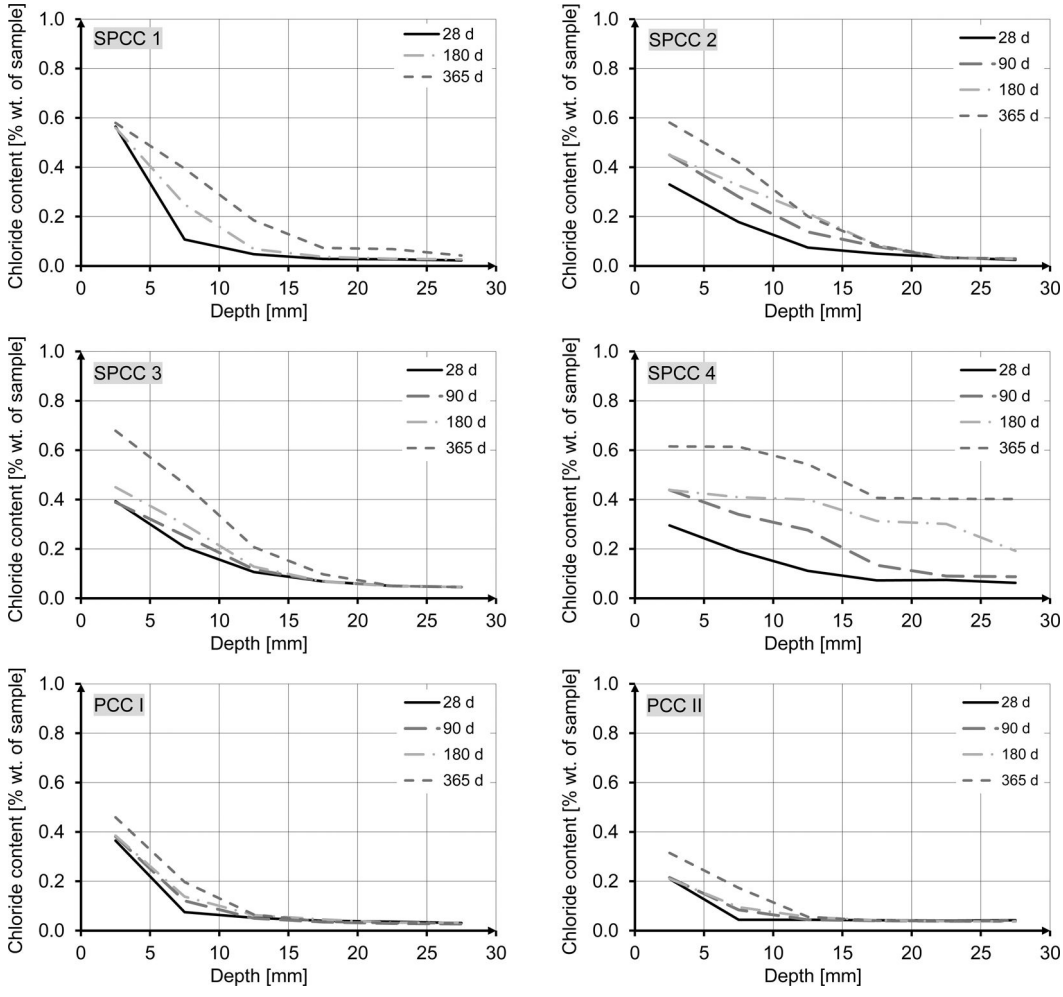

Figure 4. Chloride profiles derived from the specimens in diffusion tests.

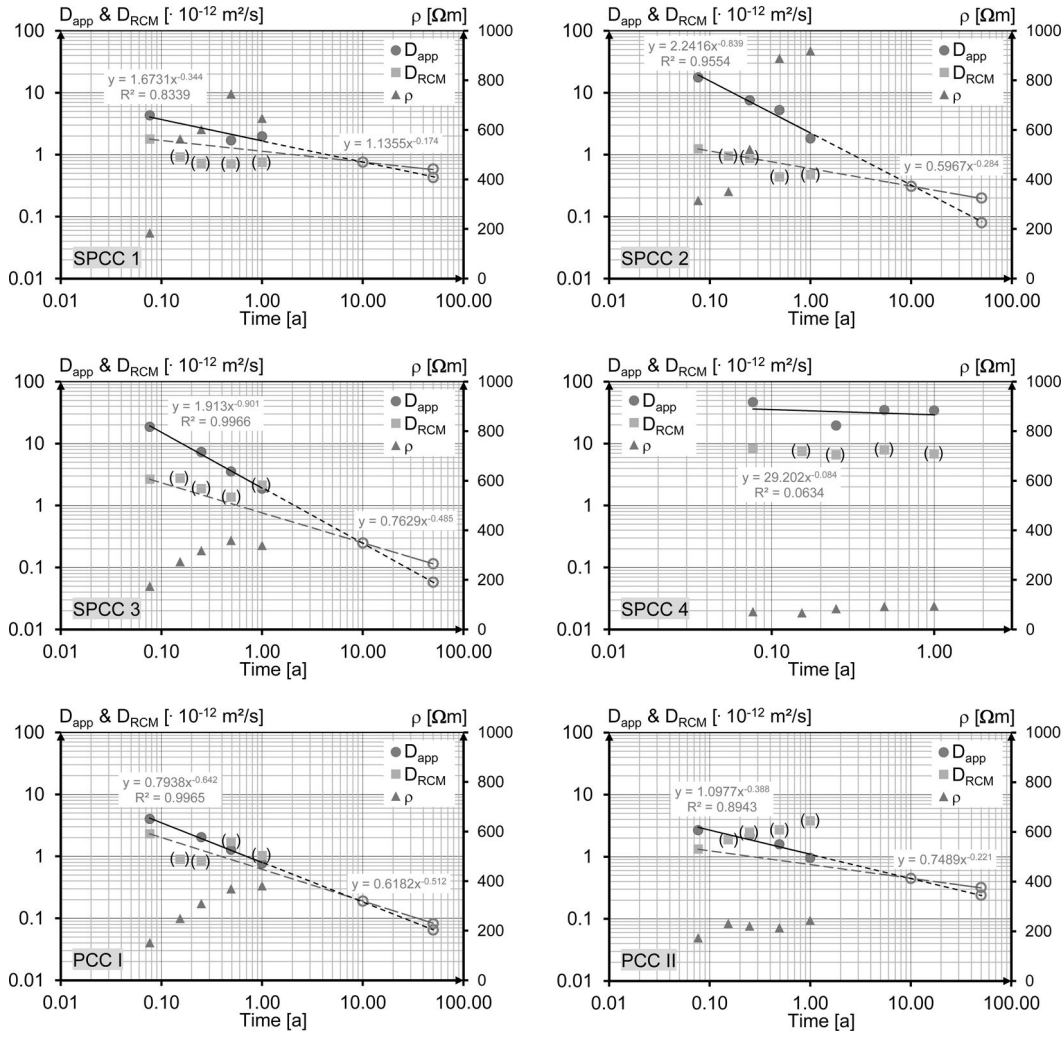

Figure 5. Development of the parameters over time.

while the chloride contents for the SPCC 1, 2 and 3 specimens were similar.

The chloride contents determined on the surface of the specimens (down to a depth of 5 mm) developed differently over time. While the surface chloride concentration in the SPCC 2, 3 and 4 specimens increased over time, it was either constant or increased only slightly for the SPCC 1 specimen and the two PCC specimens. However, it must be noted that the surface chloride concentration is subject to relatively large inaccuracies. Possible causes of this are variations in the chloride content on the surface of the specimens if they are removed from the solution for a relatively long period of time or the build-up of salt crystals on the surface of the specimens.

The initial chloride content of the specimens was measured and varied between 0.01 and 0.03% wt. of sample.

5.2 *Development of apparent chloride diffusion coefficient D_{app} over time*

A reduction in the apparent chloride diffusion coefficient D_{app} over time can be expected owing to the continuing hydration of the binder, which increases the density of the microstructure. This tendency can be seen in all specimens (cf. figure 5) but varies a great deal. The development of D_{app} over time is shown in the log-log diagrams in figure 5 by means of a regression line. The regression function (power: $y = a \cdot x^b$) and the coefficient of determination (R^2) are also given. The exponent of the regression function (b) corresponds in this case to the ageing exponent α in equation (2) (approach A). However, it was explained in section 2 that the ageing exponent is dependent both on the material and the environment and is derived by assessing the chloride profiles obtained in the structural investigations. The ageing exponent calculated

in the diffusion tests under continuous chloride exposure is only material-dependent and is used, in the first instance, to assess and compare the repair materials under investigation. Detailed considerations on this are carried out in section 6.1.

Here too, the behaviour of the SPCC 4 specimen differs from that of the other specimens. An ageing exponent could not be determined for this specimen (the coefficient of determination was too low: $R^2 = 0.06$, cf. figure 5). Ageing exponents between 0.34 (SPCC 1) and 0.90 (SPCC 3) with coefficients of determination between $R^2 = 0.83$ (SPCC 1) and $R^2 \sim 1.0$ (SPCC 3 and PCC I) were calculated for the other specimens. It should be considered that the gradual adjustment of the chloride content at the surface of the specimen to a constant value affects the thus calculated ageing exponent opportunely. The high ageing exponents calculated for SPCC 2 and SPCC 3 (0.83 and 0.90 respectively) were to some extent due to this effect.

5.3 *Chloride migration coefficient D_{RCM}*

With the exception of SPCC 4, the values of D_{RCM} obtained in the RCM test at an age of 28 d ($t_0 = 28$ d) were far lower (more favourable) than for Portland cement concretes (approx. 9–25 m^2/s depending on the w/c, Gehlen 2000) and in some cases lower than for GGBS cement concretes (approx. 1–4 m^2/s depending on the w/c ratio, Gehlen 2000).

The RCM test is usually conducted on early age specimens ($28\ d \leq t_0 \leq 56$ d) and the parameter $D_{RCM}(t_0)$ is used for the modelling the chloride transport as explained in section 2 (approach B). Commonly there is no need to apply the RCM test at later ages additionally, but in this work the development of D_{RCM} over time was considered as an attempt to find out more about the investigated repair materials. Therefore the points in figure 5 are put in brackets with the exception of $D_{RCM}(t_0 = 28\ d)$.

As observed for the parameter D_{app}, a reduction in the chloride migration coefficient D_{RCM} over time owing to the increase in the density of the microstructure as a result of the continuing hydration of the binder can be expected. However, it can be seen in the graphs in figure 5 that this tendency is far less pronounced than for D_{app} and that D_{RCM} even increases continuously for PCC II.

In the literature, it is mostly assumed that there will be a reduction in D_{RCM} over time in concretes. Lay (2006) observed the development of D_{RCM} over time for concretes made with different types of binder (CEM I, CEM II/A-LL, CEM II-B/T, CEM II/B-S, CEM I + FA, CEM III/A and CEM III/B) over a period of around two years. A clear and pronounced reduction in D_{RCM} over time was identified for concretes containing fly ash, followed by CEM III concretes. This reduction was considerably less for concretes made with Portland cement (CEM I) and CEM II/A-LL. The development of D_{RCM} over time was formulated mathematically in Lay (2006).

Data from several sources in the literature demonstrate that the behaviour of CEM I concretes is inconsistent as regards the development of D_{RCM} over time (e.g. Yu et al. 2013, Maage et al. 1996, Tang 1996). According to these sources, D_{RCM} usually increases after decreasing initially. This effect was observed for higher w/c ratios in particular. An increase in D_{RCM} after curing (immersion in water) for around 180 days was observed for three Portland cement concretes with w/c ratios of 0.4, 0.5 and 0.6 respectively in Yu et al. (2013). After more detailed investigations, the authors surmised that the increase in D_{RCM} may be caused by a transformation from low density CSH phases to high density CSH phases at more advanced concrete ages, resulting in a shift in the pore size distribution towards the coarser range (Yu et al. 2013). Further investigations are needed to explain this phenomenon.

The accelerated test method RCM test was developed in order to avoid the long test periods involved in the diffusion test. The RCM test has proven useful for evaluating concretes as the test period is short, the method is easy to use, not susceptible to error and has a sufficiently high degree of precision. A great deal of the data in the literature indicates that there is a good correlation between D_{RCM} and D_{app} for concrete at an early age (Gehlen 2000, Gehlen & Ludwig 1999, Frederikson et al. 1996, Tang et al. 2010). This applies to Portland cement concretes in particular. However, a comparison between the values of D_{RCM} and D_{app} determined for the repair materials under investigation clearly shows that, with only a few exceptions, the D_{RCM} values are lower than the D_{app} values (cf. figure 5). The difference is considerable for the SPCC materials while the D_{RCM} and D_{app} values of the two PCC materials are similar in magnitude. It should be considered that the regarding time in RCM test is the curing time (specimen age) and in diffusion test it is the exposure period.

5.4 *Specific electrolyte resistance ρ*

The specific electrolyte resistance ρ [Ωm] is determined from the electrolyte resistance [Ω] measured by the Two Electrode Method (TEM), taking account of the dimensions of the specimens (factor: cross-sectional area [m^2] / height [m]).

The specific electrolyte resistances ρ thus obtained tended to increase over time (cf. figure 5). This trend and the values of ρ were different for all six materials. A more or less constant value, which was extremely low compared with other materials, was obtained for SPCC 4 at each testing time. A low value of ρ, which increased slightly over time, was also obtained for PCC II.

The results showed a relatively good correlation between ρ and D_{RCM}, both in magnitude and development over time (cf. figure 6). A good functional relationship between ρ and D_{RCM} was also observed for concretes by several authors (e.g. Gehlen & Ludwig 1999, Bamforth 1997). The specific electrolyte resistance ρ is usually measured in the RCM tests by way

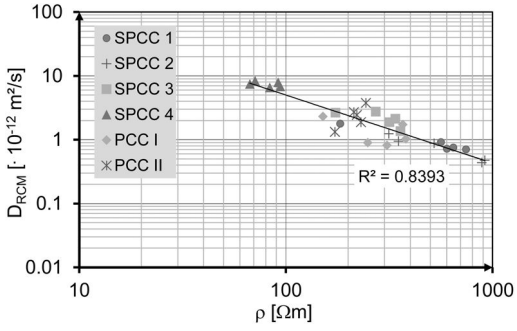

Figure 6. Correlation between D_{RCM} and ρ.

of an additional check and is determined by means of the Two Electrode Method (TEM) as this test is straightforward and involves little effort.

6 ASSESSMENT OF THE EFFICIENCY OF REPAIR MATERIALS

It is very important to be able to evaluate the performance of repair materials correctly by conducting the appropriate investigations and by means of an appropriate methodology as the necessary experience with such materials is lacking, both in the laboratory and in practice, and the manufacturers do not disclose the composition of the materials.

In this section, the efficiency of the investigated repair materials is assessed (i) by comparing the parameters derived from the laboratory investigations and (ii) by means of reliability analysis used for predicting the service life.

The repair material SPCC 4 had a different behaviour than the other materials under investigation and its chloride resistance was deficient comparatively, as already observed, hence it is not included in the following executions.

6.1 *Assessing by comparing the derived parameters from the laboratory investigations*

As explained in section 2, the material resistance is taken into account by means of two parameters, $D_{app}(t_0)$ or $D_{RCM}(t_0)$ (approach A and B respectively) and the ageing exponent α, when modelling the time- and depth-dependent chloride penetration into the concrete. The calculated ageing exponents according to approach A (cf. section 2) are already discussed in section 5.2. In order to derive the ageing exponent according to approach B, the following procedure is undertaken. The D_{app} at the time of 10 years is determined by extending the regression line of the data from the diffusion test. The exponent of the line through the two points $D_{RCM}(t_0 = 28d)$ and $D_{app}(t = 10a)$ is taken as the ageing exponent according to approach B. The $D_{app}(t = 10a)$ is applied here in analogy with the concrete samples in figure 1, wherein the regression lines of approaches A and B meet at a time of about 10 years. The calculated ageing exponents according to approach B are considerably lower than the ones according to approach A (from 0.17 for SPCC 1 to 0.51 for PC I).

Table 4. Comparison of the investigated repair materials by means of the derived parameters.

Parameter	Order: best → worst
$D_{RCM}(t_0)$ [m^2/s]	SPCC 2 ≈ PCC II, SPCC 1, PCC I, SPCC 3
$D_{app}(t_0)$ [m^2/s]	PCC II, PCC I ≈ SPCC 1, SPCC 2 ≈ SPCC 3
$D_{app,A}(50a)$[1)] [m^2/s]	SPCC 3, PCC I, SPCC 2, PCC II, SPCC 1
$D_{app,B}(50a)$[1)] [m^2/s]	PCC I, SPCC 3, SPCC 2, PCC II, SPCC 1
$C_{cum}^{2)}$ [wt.-%/mm^2]	PCC II, PCC I, SPCC 1, SPCC 2, SPCC 3

[1)]Predicted D_{app} after 50 years' exposure according to approach A and B respectively
[2)]Cumulative chloride content in the first 30 mm of specimens after 1 year diffusion test (cf. figure 7)

The six repair materials under investigation are assessed in table 4 as a function of the parameters $D_{RCM}(t_0)$ and $D_{app}(t_0)$ determined in the RCM and diffusion tests as well as the predicted parameter $D_{app}(50a)$ according to both approaches A and B.

The values determined for parameters $D_{app}(t_0)$ and $D_{RCM}(t_0)$ lead to different assessments of the materials. The difference in ageing exponent of the materials leads to a different evaluation regarding the predicted $D_{app}(50a)$. The calculated $D_{app}(50a)$ according to both approaches provide almost the same evaluation, which approve the materials PCC 3 and PCC I as the best choices.

A further parameter in table 4 is the cumulative chloride content C_{cum} in the first 30 mm depth of the specimens after inversion of the specimens in a 3% NaCl solution for a period of one year during the diffusion tests. The assessment of the materials in accordance with this parameter is the same as for $D_{app}(t_0)$. The development of C_{cum} over time is shown in figure 7.

6.2 *Assessing with respect to reliability-based service life*

The previous analyses (section 6.1) regarding the efficiency of the repair materials were deterministic considerations. In fact, the parameters regarding material resistance as well as action are uncertain quantities. They are therefore to be introduced as random variables. A probabilistic analysis can be conducted by contrasting these variables in a limit state function in order to assess a reliability-based service life of structures.

In this context, reliability analyses were done based on the probabilistic service life design concept in *fib*

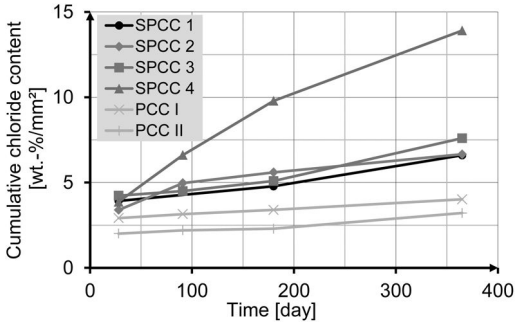

Figure 7. Development of cumulative chloride content in the first 30 mm depth of specimens over time (up to 365 d).

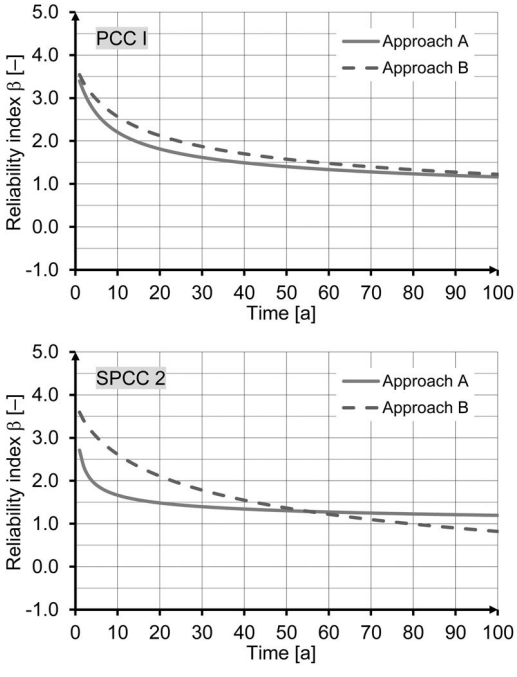

Figure 8. Development of reliability index over time for an exemplary structural element made of PCC I (top) and SPCC 2 (bottom) in a defined exposure condition.

bulletin 34 (2006). The derived parameters from the laboratory investigations ($D_{app}(t_0)$, $D_{RCM}(t_0)$, α) were converted to stochastic variables which demonstrate along with freely chosen construction parameters (cover thickness) the material resistances; as action an arbitrary environmental load was chosen.

Figure 8 shows, by way of an example, the development of the reliability index over time calculated for the Materials PCC I and SPCC 2 with the derived parameters according to both approaches A and B. In the case of PCC I, which has relatively similar regression lines according to approach A and B (cf. figure 5), the curves run close to each other. The curves meet at a time of 100 years and before that the curve of approach A lies under the one of approach B which means that approach A would lead to more conservative estimation (on the safe side). By contrast to PCC I, the reliability indices for SPCC 2 are in both magnitude and development significantly different, which matches to its considerable different regression lines (cf. figure 5). In the case of SPCC 2 the curve of approach B starts with higher values than the one of approach A and met it after about 55 years. The curve of approach A exhibits a very slow gradient after about 20 years which is consistent to the high ageing exponent of 0.84. Considering the service life of structures within the first 55 years, which is a plausible expected service life, the approach A would be again on the safe side.

SPCC 3, which also has a high ageing exponent according to approach A (0.90), exhibits a similar behaviour of reliability run as SPCC 2. The reliability runs of SPCC 1 and PCC II are similar. The curves of approaches A and B run close to each other and meet after around 25 years in case of SPCC 1 and 10 years in case of PCC II.

Table 5 shows the assessment of the repaired materials under investigation by means of the thus conducted reliability analyses. The parameters β_A(50a) and β_B(50a) lead to an almost identical assessment which is the same evaluation of the investigated materials like the parameter $D_{app}(50a)$ according to both approaches A and B in table 4.

Considering a realistic service life of repaired structural elements of less than 50 years, estimating the service life with the approach A would be on the safe side. For a final evaluation the results of further investigations remain to be seen.

Table 5. Reliability-based assessment of the investigated repair materials.

Parameter[1)]	Order: best → worst
β_A(50a) [–]	PCC I ≈ SPCC 3, SPCC 2 ≈ PCC II, SPCC 1
β_B(50a) [–]	PCC I, SPCC 3 ≈ SPCC 2, PCC II, SPCC 1

[1)] Predicted reliability index after 50 years exposure ; analysis by means of parameters derived according to approach A and approach B respectively

7 CONCLUSION AND OUTLOOK

To sum up, the results of the laboratory tests conducted on the six selected repair materials enable the following conclusions to be drawn:

- With the exception of SPCC 4, it was possible to model the depth-dependent development of the chloride content in diffusion tests very well with the error function solution of Fick's second law of diffusion for all materials.

- The materials (with the exception of SPCC 4) had, all in all, a very good chloride penetration resistance compared with conventional concretes.
- The chloride migration coefficients D_{RCM} determined in RCM tests were far below the apparent chloride diffusion coefficients D_{app} determined in diffusion tests.

Two approaches are introduced and compared for assessing the performance of repair materials with respect to their chloride penetration resistance.

The laboratory investigations are being performed over a period of at least two years and the next tests are scheduled to take place in 1.5 years' and 2 years' time. The next step is to investigate the constituents and composition of the materials to enable the results to be understood. For a final evaluation the results of further investigations remain to be seen.

Repair materials need to be investigated under actual conditions in practice, not only in the laboratory, in order for their performance to be assessed. Exposure tests with large specimens comprising different repair materials have been conducted since 1991 (23 years) (Rößler et al. 2009). The first results were obtained by performing tests after 3 and 6 years' exposure (Rößler et al. 2009) as well as after 21 years' exposure (Rahimi et al. 2014).

REFERENCES

Bamforth, P.B. 1997. Corrosion of Reinforcement in Concrete Caused by Wetting and Drying Cycles in Chloride – Containing Environments. Middlesex: Taywood Engineering Ltd, 1997. – BSI Supported Project PBB/BM 1746.

BAW Code of Practice MCL "Resistance of Concrete to Chloride Penetration" 2012.

Bunke, N. 1991. Prüfung von Beton – Empfehlungen und Hinweise als Ergänzung zu DIN 1048. Berlin: Beuth.

CEN/TS 12390-11 (2010). Testing hardened concrete – Part 11: Determination of the chloride resistance of concrete, unidirectional diffusion.

fib bulletin 34 (2006). Model Code for Service Life Design, prepared by *fib* Task Group 5.6.

fib MC (2010). Model Code for concrete structures.

Frederikson J.M., Sørensen H.E., Andersen A., Klinhoffer O. 1996. The Effect of Water/Cement Ration on Chloride Transport into Concrete – Immersion, Migration and Resistivity Tests. Copenhagen, Danish Road Directorate, Report No 54 1996.

Gehlen C., Ludwig H.M. 1999. Compliance Testing for Probabilistic Design Purposes. Brussels: European Union – Brite EuRam, 1999. – Contract BRPR-CT95-0132, Project BE95-1347, Document BE95-1347/R8.

Gehlen C. 2000. Probability-based service life design of reinforced concrete structures – Reliability studies for prevention of reinforcement corrosion. DAfStb Heft 510, Berlin, Beuth, 2000.

Gulikers J. 2011. Analysis and evaluation of a European Round Robin Test on Rapid Chloride Migration. Report of Rijkswaterstaat Ministerie van Verkeer en Waterstaat, Utrecht.

ISO 16204:2012. Durability – Service life design of concrete structures.

Lay S., Schießl P. 2006. Dauerhaftigkeitsbemessung von Stahlbetonkonstruktionen. Forschungsbericht AiF/DBV-Nr. 12525/225, Technical University München (in German).

Maage M., Helland S., Poulsen E., Vennesland Ø., Carlsen J.E. 1996. Service Life Prediction of Existing Concrete Structures Exposed to Marine Environment. ACI MATERIALS JOURNAL. November-December 1996.

NT Build 492 (1999). Nordtest method: Concrete, Mortar and Cement-Based Repair Materials: Chloride Migration Coefficient from Non-Steady-State Migration Experiments.

Rahimi A., Gehlen C., Reschke T., Westendarp A. 2014. Approaches for Modelling the Residual Service Life of Marine Concrete Structures. International Journal of Corrosion. Volume 2014, Article ID 432472.

Rößler G., Westendarp A., Dauberschmidt C., Meng B., Pierkes R., Schwamborn B., Wiens U. 2009. Instandsetzung von Meerwasserbauten, ibac-Forschungsbericht F647, (in German).

Tang L. 1996. Chloride transport in concrete – measurement and prediction. Ph.D. thesis, Chalmers University of Technology, Gothenburg, Denmark.

Tang L. Utgenannt P., Lindvall A., Boubitsas D. 2010. Validation of models and test methods for assessment of durability of concrete structures in road environment. Uppdragsrapport No. P802606, Lund, Sweden.

Yu Z., Ye G., Hunger M., Noort v. R. 2013. Disscussion of the evolution of the chloride coefficient of Portland cement concrete tested by rapid chloride migration (RCM) test at long-term curing periods up to 5 years. Proceedings of international conference Concrete under Sever Conditions – Environment and Loading (CONSEC13), September 2013, Nanjing, China.

Concrete Solutions – Grantham et al. (Eds)
© 2014 Taylor & Francis Group, London, ISBN 978-1-138-02708-4

Fundamental research on the carbonation control effect by coating materials

M. Sugiyama
Hokkai Gakuen University, Sapporo, Japan

ABSTRACT: Carbonation of concrete is an important factor which influences the durability of a building structure. This research applied three kinds of coating materials to the surface of concrete specimens and examined the carbonation performance. The three kinds of coating materials were a silicate system surface impregnation material, a silicone system surface impregnation material, and a polymer cement.

The materials are marketed in Japan and used for concrete treatment. The main ingredients of the polymer cement product are cement powder and an acrylic resin. As a result, the covering material of polymer cement had the largest carbonation control performance.

1 INTRODUCTION

When considering degradation of reinforced concrete structures in the architecture field, carbonation is an important examination matter. Carbonation is a phenomenon in which the alkaline nature of concrete is lost with carbon dioxide in the atmosphere. This research observed the performance of three kinds of surface protection materials. The purpose of this research is to find out the coating material with the largest durability for basic housing concretes. The experiment was carried out with concrete test specimens on which were coated three kinds of surface protection materials. The three kinds of coating materials were a silicate system surface impregnation material, a silicone emulsion system surface impregnation material, and polymer cement. The main ingredients of the polymer cement product were cement powder and an acrylic resin. These test specimens compared the carbonation inhibition effect. This paper reports these test results.

2 TEST PLAN AND METHOD

2.1 *Experimental design*

Table 1 shows the planning of the experiment and Figure 1 shows the outline of the experiments. The surface protection material used for the test is shown in Table 2.

Accelerated carbonation was carried out on the test specimens which coated three kinds of surface protection material. A test plan is shown in Table 1. The test specimens were $100 \times 100 \times 400$ mm.

The silicate system surface penetration material penetrates the surface and reacts with unreacted cement constituents by crystallization, and aims at the interception effect of degradation factors, such as water and carbon dioxide. The silicone system works as a surface osmosis material and forms a water absorption prevention layer in the surface. The polymer cement system covering material aimed at the interception effect of the degradation factor by covering the surface.

Table 1. Planning of experiment.

Mark.	Type of surface protection material.	Acceleration carbonation test. Duration of test.	Shape of a test specimens.
1	With no treatment.	4 weeks, 8 weeks, 12 weeks, 25 weeks.	Three 10*10*40-cm rectangular parallelepipeds.
2	Silicate system.	4 weeks, 8 weeks, 12 weeks, 25 weeks.	Three 10*10*40-cm rectangular parallelepipeds.
3	Silicone system.	4 weeks, 8 weeks, 12 weeks, 25 weeks.	Three 10*10*40-cm rectangular parallelepipeds.
4	Polymer cement system.	4 weeks, 8 weeks, 12 weeks, 25 weeks.	Three 10*10*40-cm rectangular parallelepipeds.

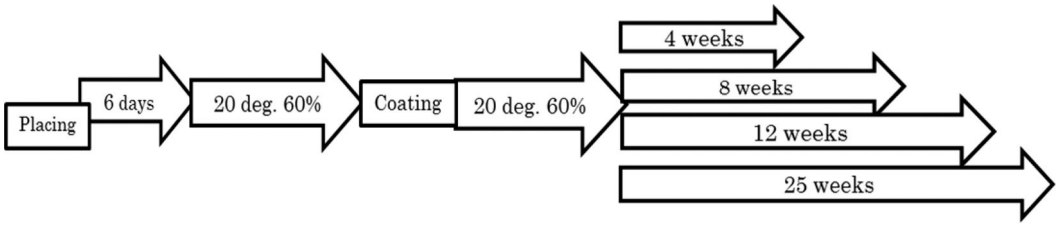

Figure 1. Outline of experiments.

Table 2. Summary of the surface protection materials.

Mark Type	2 Silicate system.	3 Silicone oil emulsion system.	4 Polymer cement system.
Main components	Silicate sodium. Water glass system.	Silicone system compound.	The mixture of cement powder and a water-soluble acrylic resin.
Coating.	The first amount of recommendation is coated (0.15 kg/m^2 of diluted solutions). + Curing by water spraying. + The second amount of recommendation is coated (0.15 kg/m^2 of diluted solutions). + Curing by water spraying.	The first amount of recommendation is coated (0.3–0.4 kg/m^2 of diluted solutions). + Dry curing. + The second amount of recommendation is coated (0.3–0.4 kg/m2 of diluted solutions.).	The 1st lower coating material (0.9 kg/m^2) is coated. + Dry curing. + The 2nd glazing material (0.3 kg/m^2) is coated.

Table 3. Mix proportion (kg/m^3).

W/C	Cement	Water	Sand 1	Sand 2	Gravel	Admixture
55%	302	166	419	421	1009	0.755

Table 4. Quality of fresh concrete.

Slump	Air	Temperature of placing concrete	Density.
16.5 (cm)	3.6 (%)	26 (degree)	2317 (kg/m^3)

2.2 *Concrete test specimens*

The samples were removed from the form on the day following casting. After doing underwater curing for six days, the samples were air-dried for three weeks. The conditions of air were the temperature of 20°, and 60% humidity.

The concrete of the test specimens used W/C 55%, a strength of 24 MPa, and a slump of 16.5 cm, with ordinary portland cement which is typically well used for housing basic concrete.

A proportioning table is shown in Table 3. The test results of the fresh concrete are shown in Table 4.

2.3 *Acceleration carbonation test method*

The acceleration carbonation test method followed the measuring method of the carbonation depth of the concrete of JIS A 1153. The removal of the concrete test specimens was carried out after 1 day and then cured underwater (for six days), and in air (three weeks). The coated surface protection material was applied to the test specimens and acceleration carbonation testing was started after curing for two weeks (six weeks of material ages). Carbonation depth was measured by slicing the test specimens put in in the test tub, spraying with phenolphthalein liquid on the surface, and measuring the carbonation depth.

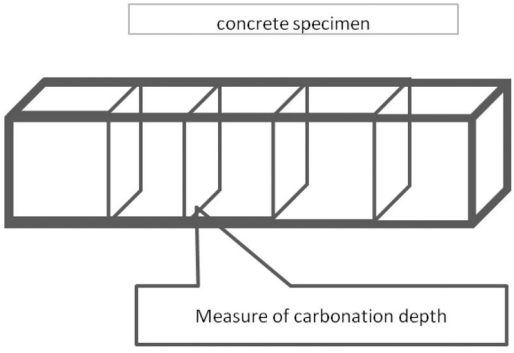

Figure 2-1. Accelerated carbonation test specimen.

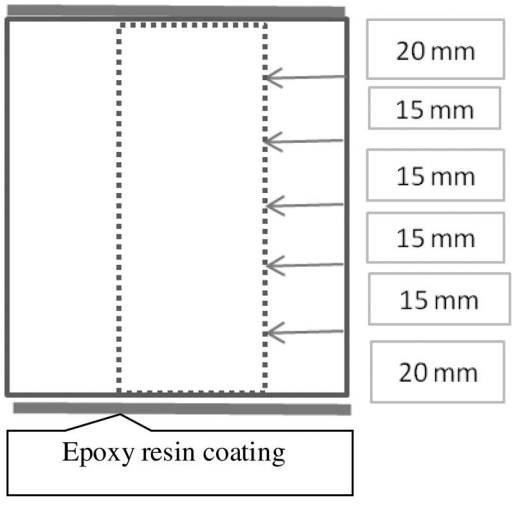

Figure 2-2. Location of carbonation depth specimens.

After this, the test specimens was split for every predetermined accelerated carbonation period, and measured similarly. In addition, the inside of the accelerated carbonation test tub was set at the temperature of 20°, 60% of relative humidity, and 5% of carbon dioxide levels. The outline of the test specimens is shown in Fig. 2.

The accelerated carbonation test results for the experiment are shown in Fig. 3.

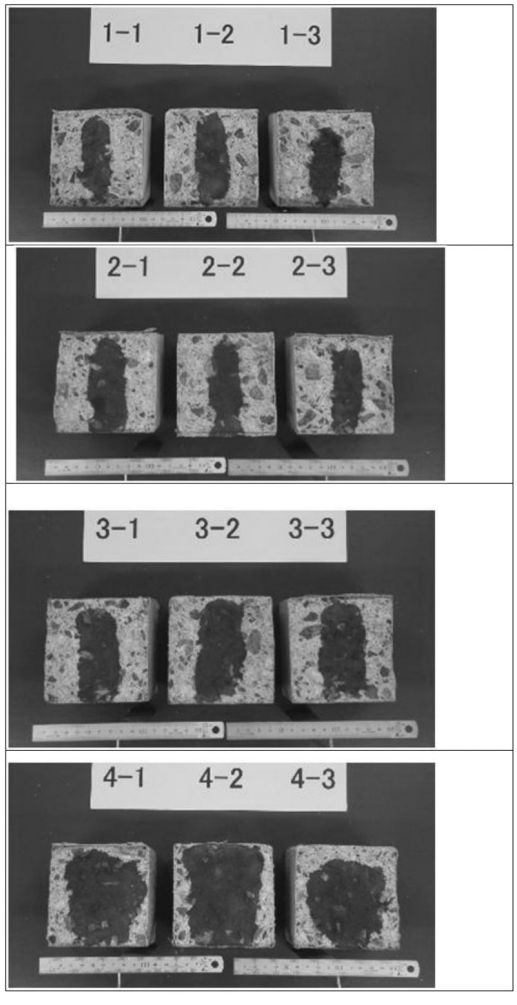

Figure 3. Result of accelerated carbonation test, 25 weeks.

3 RESULTS AND DISCUSSION

On the basis of an unprocessed test specimens, the carbonation inhibition effect by each protective layer was considered. The results are shown graphically in Figure 4 and in a table as Table 5.

The silicate system (No 2) had the smallest effect on carbonation inhibition and carbonated almost to the same depth as the control (98%) by 4 weeks.

The Silicone system (No. 3) showed surface penetration material of about 80% of carbonation compared with no treating. (From 70% to 86% between 4 and 25 weeks)

The protective layer with the highest (largest effect) carbonation inhibition was the polymer cement system surface covering material (No. 3). This showed a carbonation depth varying from 15% to 48% of the control, between 4 and 25 weeks.

4 CONCLUSIONS

The following can be concluded as a result of this test.

- The surface protection material with the highest effect of carbonation inhibition was the polymer cement system surface covering material.
- The surface osmosis material with the next highest carbonation control effect was the silicone system.
- The surface penetration material with the smallest effect of carbonation inhibition was the silicate system surface osmosis material.

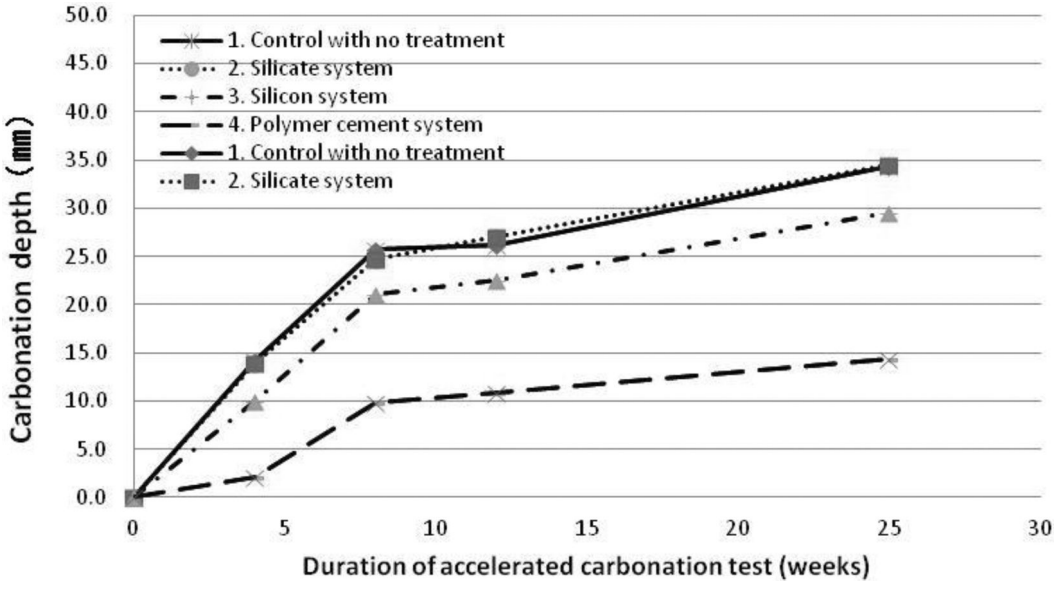

Figure 4. Accelerated carbonation test results.

Table 5. Accelerated carbonation depth test values (averages).

Duration of accelerated carbonation test (weeks)	0	4	8	12	25
Carbonation depth					
1. control with no treatment	0.0	14.2	25.8	26.2	34.3
2. Silcate system	0.0	13.9	24.8	27.0	34.5
3. Silicone system	0.0	10.0	21.1	22.6	29.5
4. Polymer cement system	0.0	2.1	9.8	10.9	14.3
Carbonation ratio					
1. control with no treatment	0	100	100	100	100
2. Silcate system	0	98	96	103	101
3. Silicone system	0	70	85	84	86
4. Polymer cement system	0	15	43	52	48

REFERENCES

Sugiyama M (2012) Fundamental research on the freezing thawing resistance of the concrete which delay-added the drying shrinkage reducing agent. Proceedings of the 2nd International Conference on Microstructure Related Durability of Cementitious Composites, Amsterdam 11–13 April 2012, TU-Delft

Sugiyama M (2012) Fundamental research on the freezing thawing resistance of the concrete which delay-added the drying shrinkage reducing agent. Proceedings of the 10th International Conference on Superplasticizers and Other Chemical Admixtures, Prague 28-31 October 2012, CANMET/ACI, ISBN 978-0-9916737-2-8

Sugiyama M (2008) Freeze-thaw Test Results of Porous Concrete with Crushed Scallop Shell Material Added. Proceedings of the STRUCTURAL FAULTS + REPAIR-2008, Edinburgh 10–12 Juner 2008

Concrete Solutions – Grantham et al. (Eds)
© 2014 Taylor & Francis Group, London, ISBN 978-1-138-02708-4

Development and use of flowable calcium aluminate mortars in sewer environments

C.J. Weale & D.P. Ferguson
GHD Pty Ltd, Melbourne, Australia

ABSTRACT: A recent trend of using calcium aluminate mortars in the rehabilitation of waste water structures is partly based on its high resistance in this aggressive environment. Additionally, its rapid strength development is of benefit for remediation works where construction is restricted to a short time window, based on cyclic wastewater flow. This paper describes the development and initial testing of a flowable calcium aluminate mortar and discusses its use in the form and pour style structural remediation of a deteriorated trunk sewer structures.

1 INTRODUCTION

1.1 *Outline*

The need for precise tolerance control in the rehabilitation of a reinforced concrete wall within a trunk sewer drop structure led to the development of a flowable calcium aluminate based repair mortar. This paper reviews the factors that influenced the selection of the calcium aluminate based repair mortar and reports on the field trials and performance of the final product.

1.2 *Structure background*

The East Drop Structure (EDS) is a 26 m deep, 8 m diameter cast insitu reinforced concrete manhole structure that forms part of Melbourne's trunk sewer system. The original general arrangement is shown in Figure 2. The incoming 2.1 m diameter sewer discharged into a rectangular trough structure. At low flows, the sewage dropped through two cast iron pipes cast into the trough base to the plunge pool below, and at higher wet weather flows spilt over the sloped ogee crest shaped weirs along the trough walls. A penstock gate at mezzanine slab level closes flow from the incoming sewer, with flow being re-directed via two weirs each side of the incoming sewer through twin bypass conduit structures to the lower plunge pool chamber. The outgoing sewer tunnel passes on grade under the Yarra River.

1.3 *Structure rehabilitation*

The manhole structure underwent major structural rehabilitation to remedy significant concrete degradation to the original Trough drop channel, access slabs and lower shaft walls arising from hydrogen sulphide induced acid attack. The full project details are provided in Weale (2013).

The degraded concrete mezzanine slab and Trough structure had lost of the order of 100 to 200 mm of structural concrete and were found unsafe and were demolished. An options study determined the preferred rehabilitation method was to install an alternative weir hydraulic structure, intended to reduce the energy of incoming sewage that was to free flow into the plunge pool, and to provide a durable, low maintenance facility for an additional 20 years' service.

The new weir design comprised a stainless steel toothed plate that was to be bolted to the concrete shaft wall under the remaining nib of Trough concrete. The plate had the additional function of providing structural integrity to the concrete shaft wall supporting the penstock gate frame. A cross section of the plate arrangement is show in Figure 3. The shaft wall concrete, that the plate was to be fixed to, was similarly degraded as other concrete surfaces in the manhole, and the weir plate design allowed for reinstatement of approximately 100 mm of acid damaged concrete. Figure 1 shows the bypass wall under the penstock gate after hydro-demolition of acidified concrete.

Figure 1. Bypass wall under penstock gate after hydro-demolition of acid damaged concrete and prior to initial remedial work.

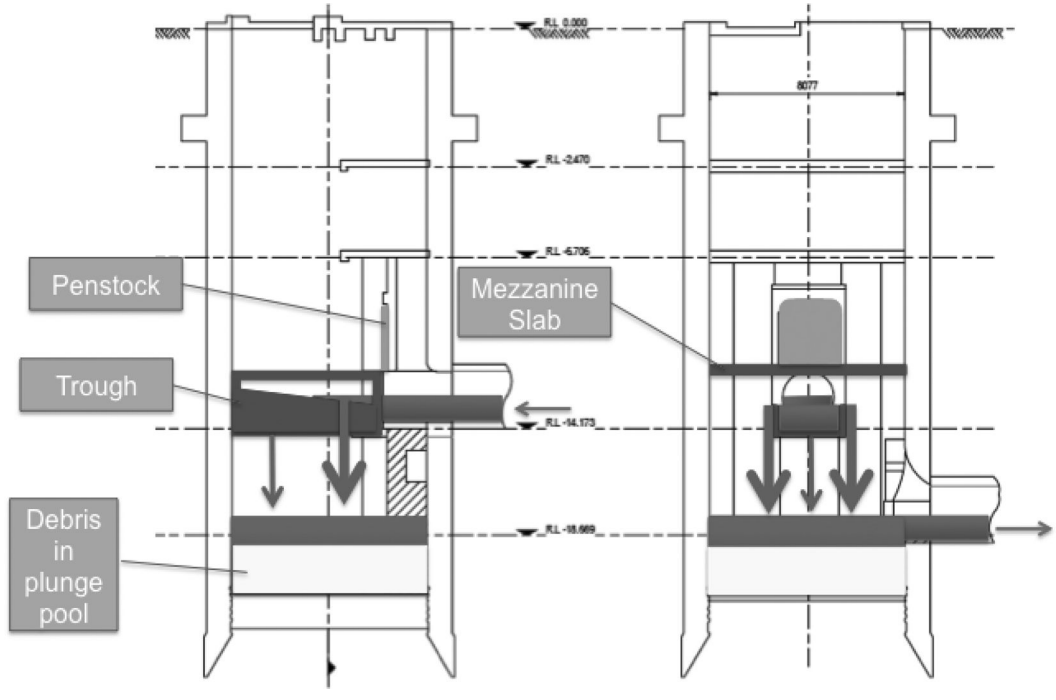

Figure 2. Original drop structure layout and operation.

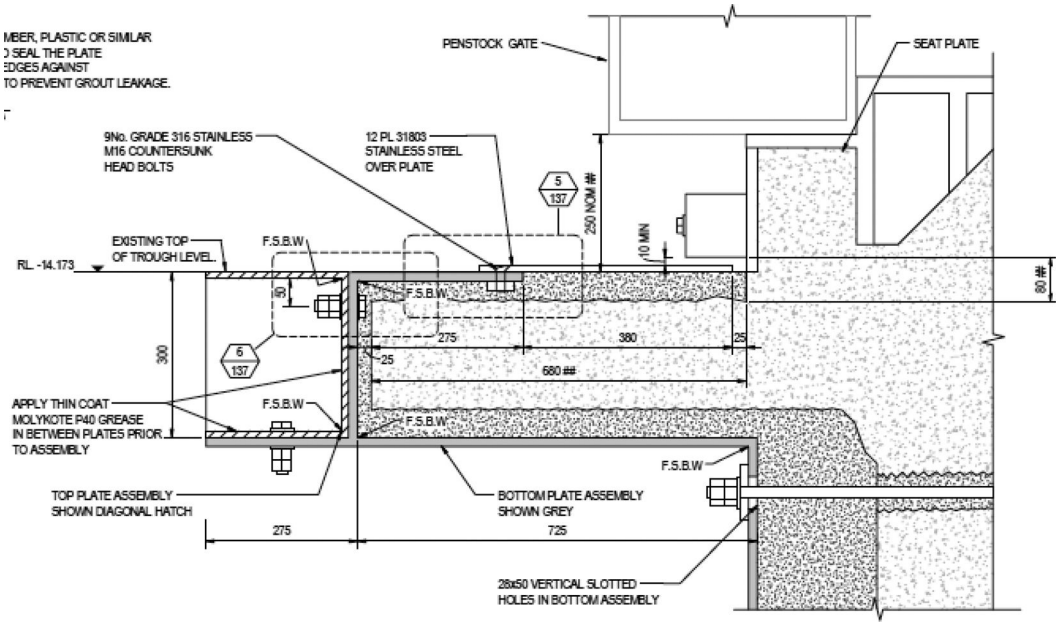

Figure 3. Cross section of initial weir plate design, installed to the concrete shaft wall and stabilising the penstock grate frame.

During initial repairs to the shaft wall, located under the new weir, significant thinning of the shaft wall was identified, in particular at the location of the internal bypass conduits, and the wall was found structurally unsafe for peak wet weather load conditions. This section of wall therefore required initial and permanent strengthening works before the weir plate could be installed.

2 CALCIUM ALUMINATE CONCRETE

2.1 *General properties of CAC concrete*

The mechanism of the oxidation of hydrogen sulphide gas to sulphuric acid by aerobic bacteria (thiobacille) in the moist atmospheric parts of sewer structures is well known (Pomeroy & Boon 1976).

Calcium aluminate cement (CAC) is hydraulic cement with favourable properties for use in wastewater environments.

CAC based concrete hardens rapidly, with compressive strength gain typically of the order 25 MPa after 6 hours, and in some cases 100 MPa after 24 hours (Kerneos, 2013).

CAC based repair concretes typically achieve high early strength through minimizing the w/c ratio by use of high amounts of superplasticiser, and a set accelerator (such as lithium carbonate) to initiate early hardening. Such concretes can have properties similar to a self-compacting concrete, but may lose workability quickly. Maintaining the balance between flowability and strength properties can be difficult as water content is considered critical for calcium aluminate cements; a maximum of 0.4 w/c ratio is necessary to ensure that the minimum strength after conversion will be sufficient for the application (Scrivener et al. 1999).

CAC concrete undergoes a conversion process, whereby the initial hydration products form a more stable microcrystalline structure, with increased porosity of the matrix and a consequent reduction in strength of the order 30 to 50%. The strength reduction can occur within days or years, depending on the peak exothermic temperature, w/c ratio, mix constituents and environmental exposure conditions (Barborak 2010).

CAC concretes have several useful properties: high inherent abrasion resistance - hence its use for repairs to structures damaged by high hydraulic abrasion, such as dam spillways; low residual moisture within days of casting, with use in flooring applications; high early heat of hydration with use in low temperature concreting; and high temperature and thermal shock resistance, with applications in fire protection and high temperature industrial processing.

2.2 *CAC acid resistance in sewers*

Whilst all cementitious materials are susceptible to acid attack because they are basic in nature, CAC is naturally much more resistant to acid attack in sewer environments than Portland cement. This is partly because CAC has a much greater acid neutralization capacity than Portland cement (Espinosa 1996), and the alumina hydrate is stable to pH of 3.5 to 4 (Scrivener et al. 1999) compared to the calcium silica hydrate (CSH) phases of cement paste which lose all strength at $pH < 9$ (Baston et al. 2012). CAC concretes can also be formulated with the aggregate fraction being entirely comprised of synthetic aggregate manufactured from calcium aluminate clinker (100% calcium aluminate). The chemical and mechanical properties of such concretes are significantly enhanced, with effectively approximately a threefold increase in acid neutralisation capacity compared to a CAC cement with non-calcium aluminate aggregate.

CAC concrete also has high inherent biogenic acid resistance, as solubilized aluminium inhibits the growth of the aerobic bacteria (thiobacille), which converts H_2S to sulphuric acid (Geoffroy 2008).

The high inherent resistance of concrete containing CAC binder and aggregate has led to its use as a reinstatement/protective layer without other protective coatings, such as epoxy coatings, in sewer environments.

2.3 *Field use of CAC materials*

There are many historical examples of CAC mortar use in the rehabilitation or construction of sewers. Predominantly, CAC materials have been used as a protective coating treatment in large diameter sewer or manhole rehabilitation in the form wet- and dry-spray concrete (Kurtovich & Lawson 2008).

CAC repair mortars were used to repair concrete wastewater treatment plant channels and tank structures in New Zealand. Repairs were typically of the order 20 to 60 mm of concrete reinstatement. CAC was selected because of ease of application in an operational plant, with wet substrates, rapid setting time enabling early return or service and cost effectiveness (Bruce & Freitag 2005).

CAC based sewer re-lining material has typically been wet or dry spray applied to a thickness of the order 25 mm. If greater depth of concrete cross section reinstatement has been required, this has been achieved using a Portland cement based sprayed concrete or mortar, primarily to reduce costs. Dry sprayed CAC mortar up to 75 mm thick was used to reline the 1.5 m diameter Western Interceptor sewer in Auckland at areas of sewer pipe that had exposed reinforcement (Barker & Lawson 2003).

CAC mortar was also used to line a new steel rising main trunk sewer, with a nominal liner thickness of 16 mm and maximum crack width specified of 0.3 mm (Egan et al. 2005).

CAC concrete is suitable for use in environments with damp surfaces and/or high humidity.

Inspections of sewer manholes relined using CAC mortars after 5 to 10 years' service has found the CAC mortar to be in excellent condition (Kurtovich and Lawson 2008).

3 SHAFT WALL REHABILITATION

3.1 *General project constraints*

The EDS has high daily sewage flows up to 6 m^3/s peak wet weather flow, and only short-term (6 to 8 hours) temporary interruption of flow using a penstock gate, with temporary storage in the upstream sewer system. Works in the lower part of the manhole required closing

Figure 4. Plate weir in operation during rehabilitation works.

of the penstock gate. A full bypass system was not feasible due to the high flows, sewer depth, operational issues and physical constraints.

On closing the flow, the sewage would back up in the incoming sewer tunnel to the level of the bypass weirs, then pass via the conduits directly into the chamber under the trough, creating significant splash. Temporary sealing of the conduit outlet managed this. However, the plunge pool contained flowing sewage during the bypass. On opening the penstock gate, the rehabilitation works below the incoming sewer were subject to full flow conditions. An impression of the strong sewage flow can be gained from Figure 4, taken after installation of the new weir.

It was not possible to install temporary work platform in the plunge pool, as this would risk quickly blocking the sewer from rapid build-up of rags. The temporary work platform was therefore suspended on structural steelwork fixed to brackets in the walls. The sewage level in the manhole controlled the minimum level of the platform. A crane was used to lower the platform, materials and personnel to the work area.

The observed high rate of concrete deterioration confirmed that the EDS environment was highly corrosive. During the works, typical H_2S levels were recorded as 180-225 ppm. Whilst a planned air filtration system was expected to significantly reduce H_2S levels, the concrete repair works needed to have high resistance to H_2S attack.

The normal high risks of working under confined space conditions in a major deep trunk sewer meant that remedial works that minimized working time and enhanced safety were preferred.

3.2 *Concrete repair requirements*

The wall structural strengthening arrangement is shown in Figure 5.

The concrete repair material needed to meet the following requirements:

- Set and develop high early strength (20 MPa within 2 hours) to enable resistance to significant hydraulic abrasion from resumed flow, and so prevent early wash-out/weakening of the material

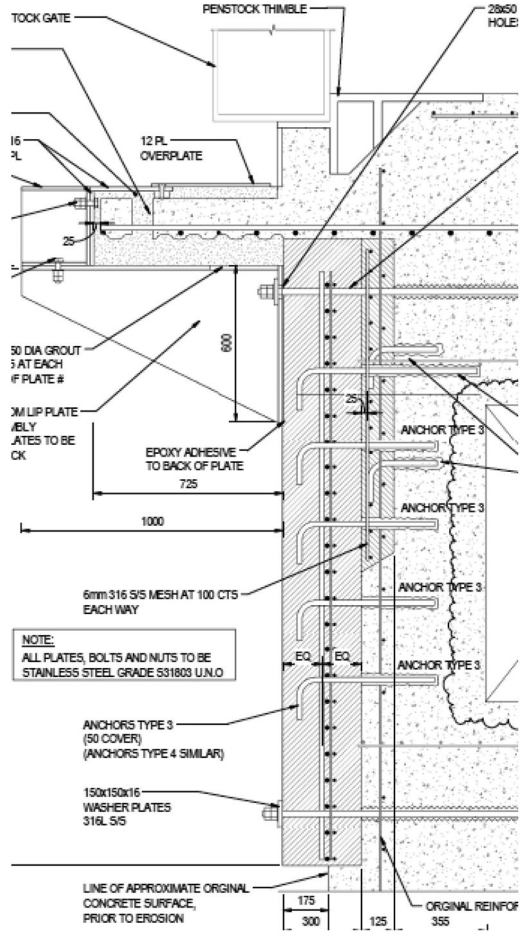

Figure 5. Cross-section of bypass wall strengthening design.

- High inherent resistance to H_2S attack so that additional protective coatings that were not required
- Service life of 20 years without need for maintenance, due to significant difficulty of future access on completion of the works
- Cost effective rehabilitation
- Compressive strength (after conversion) of 32 MPa
- Maximum crack width 0.2 mm
- The reinstated wall was specified to have a finish to AS 3610 Class 2 Quality, except that it was to achieve a flatness tolerance of 3 mm, with maximum gradual deviation of 1 mm/m, in order to achieve even load transfer at the weir plate-wall interface

3.3 *The case for calcium aluminate cement*

CAC concrete was identified as the preferred material with the potential to meet the fast setting, high early age strength and high abrasion resistance, and high inherent resistance to biogenic acidification requirements of the EDS rehabilitation.

Although significantly more expensive than Portland cement based repair mortars and grouts, cost was not a major factor for this difficult and critical project.

As noted in Section 2, CAC mortars had a successful track record of rehabilitating degraded concrete in sewer systems. The design assumed a 40% strength reduction would occur due to conversion of the hydrated CAC.

3.4 *Constructability issues*

The initial bypass wall strengthening works were undertaken using a proprietary dry spray CAC mortar at thickness of the order 50 to 100 mm.

Following additional investigations into the extent of wall degradation, it was determined that the wall reinstatement needed to be an additional 300 mm thick, and to extend as close to the low water level as practicable, nominally 2.3 m high.

The Contractor determined that it was unlikely under the difficult site conditions to achieve the required flatness tolerance using a sprayed material, and that a form and pour method would be required. However, it was also impractical to install a waterproof formwork at the low level required by the design. A compromise was agreed, with the lower wall section to be reinstated using dry spray CAC and the upper, more critical section reinstated using form and pour.

4 DEVELOPMENT OF A FLOWABLE CAC MORTAR

4.1 *Available products*

Whilst proprietary CAC wet and dry spray mortars and CAC binder and aggregates were readily available from suppliers such as Kerneos, a castable/flowable CAC product was not available in Australia.

One identified product was the spray applied calcium aluminate mortar such as SewperCoat® (a Kerneos product), which had been increasingly used in New Zealand and Australia in sewer and manhole rehabilitation.

SewperCoat® is a 100% calcium aluminate product manufactured from a combination of calcium aluminate cement and aggregates, and is designed to be either wet- or dry- sprayed. It is a low-alumina aluminium cement containing typically 39–44% Al_2O_3 and 9–15% Fe_2O_3 by weight. It can achieve fast setting times and very high early strength ($>$20 MPa at 6 hours, $>$40 Mpa at 24 hours) (Parchem 2013), which meant it was a suitable product for the wall rehabilitation, however as described above, it was considered that spray-applied concrete would not successfully achieve the construction tolerances required.

Flowable micro-concretes, such as Renderoc LA55, were first developed for projects such as the UK Midland Links elevated motorway crosshead soffit rehabilitation. This type of flowable, self compacting material would allow the precision grouting which the bypass wall rehabilitation and weir plate required. However, Renderoc LA55 only achieves 5 MPa compressive strength at 24 hours, and has low inherent acid resistance, making it unsuitable for this application.

No commercially available products that combined the required properties were identified.

4.2 *Laboratory development*

The Contractor made an approach to Parchem Construction Supplies to develop a suitable flowable CAC material. Parchem, through its association with Kerneos in Australia and Fosroc in the United Kingdom, combined technical knowledge of flowable micro-concretes with the calcium aluminate technology in laboratory development of a suitable product.

Laboratory trials were undertaken to modify the properties of SewperCoat® so that it could be successfully poured in laboratory conditions. To maintain the favourable corrosion resistance properties of the product, the amount of calcium aluminate aggregate and cement in the product could not be altered. As such, one of the key difficulties in this early stage was achieving a fluid consistency with only minimal changes in the product ingredients possible. The maximum aggregate size in the spray applied SewperCoat® products was small enough that a flowable product was considered possible. Favourable flow properties were achieved through the modification of the admixtures.

4.3 *Field trials*

Once a suitable mixture was successfully trialed under laboratory conditions, field trials were undertaken. Calcium aluminate cements and aggregates are very sensitive to very small changes to the additional admixtures that are used and when the material is placed in large volumes it can react differently from the laboratory environment. This makes larger scale field trials very important to ensure the product can be used successfully.

4.3.1 *Stage 1*

Field trials were undertaken on site using the same plant to be used in the construction. A leak proof test panel formwork with dimensions of 1600 mm high $\times$ 600 mm wide by 200 mm deep was constructed for the trial, as shown in Figure 6. The dimensions were selected prior to finalisation of the bypass wall strengthening design works and were intended to reflect the probable dimensions of the wall repair. The 100% calcium aluminate material was supplied in 20 kg bags and clean water accurately measured for each bag. For the trial, water content was specified as $\pm$100 mL per bag of material.

The first trial was abandoned after six hours, with the material not setting. At over 26 hours to initial set, the first trial was considered unsuccessful. It was identified that the mix was over plasticized, retarding the set. Other properties of the mix were considered to

Figure 6. Flowable CAC site trial.

Table 1. Compressive strength results – field trial 2.

	Compressive Strength MPa			Average MPa
Cast cylinders*				
6 hours	41.0	40.5	40.0	40.5
24 hours	59.0	53.0	56.0	56.0
7 days	67.5	67.0	67.5	67.3
Concrete Cores**				
24 hours	49.5	60.5	53.5	54.5
7 days	51.5	61.0	52.0	54.8

*Compressive strength tested to AS 1012.9
**Compressive strength tested to AS 1012.14

achieve the product aims and further laboratory trials were undertaken to refine the mixture further.

4.3.2 *Stage 2*

Following the first site trial, the formulation was adjusted to account for the slow set. The modified product set quickly (less than 3 hours) and the second trial was considered a success.

As part of the trials two sets of compressive strength data were taken using cast cylinders and cores diamond drilled from the trial pour. Table 1 contains the compressive strength test results obtained from these samples.

The field trials achieved compressive strength values which significantly exceeded the final technical data sheet for the >20 MPa at 6 hours, >35 MPa at 24 hours. These values were considered acceptable for the project. The lower average strength and lack of additional strength development for the core samples suggests a degree of strength conversion occurred during the casting process.

The final Flowable SewperCoat® product typically contained 40–43% Al_2O_3 and 10–14% Fe_2O_3 by weight, representing a tightening of the manufacturing formula for this specialty product from the previously available wet- and dry- spray product. (Parchem 2013).

Figure 7. Bypass wall under the penstock strengthened using grade 316 stainless steel bars and dry spray (lower section) and flowable (upper section) calcium aluminate concrete, location of the pour break after pump malfunction.

Table 2. Compressive strength results – construction.

	Compressive Strength MPa			Average MPa
1st Pour Cast cylinders*				
24 hours	51.5	49.5	48.5	50
7 days	67.0	69.5	71.5	69
2nd Pour Cast cylinders*				
24 hours	56.5	51.5	54.0	54
7 days	76.0	78.5	79.0	78

*Compressive strength tested to AS 1012.9

5 CONSTRUCTION

5.1 *Casting issue*

A rare fracture failure of the worm pump, and lack of a back up machine, during casting of the upper section led to flash setting of the flowable SewperCoat® product. In order to avoid a cold joint, the formwork was stripped off and the concrete scabbled to provide a good key for the second pour, refer to Figure 7. Whilst this caused a delay and additional costs, the quality of the completed concrete reinstatement was not affected. The completed wall had nil cracking or other defects, and the weir plate was successfully installed, refer to Figure 8.

Compressive strength data for cast cylinders cast indicated the average 24 hour strength was in line with the trial data, and the 7 day strength was higher, at 69 and 78 MPa.

5.2 *Grouting voids around installed plate weir*

The weir plate design included using a Portland cement based high strength, low shrinkage grout to fill the voids inside the plate assembly and encapsulate the remaining trough concrete. The design assumed that the top plates would provide adequate protection to

Figure 8. Installed stainless steel toothed plate weir as replacement for original trough structure.

the grout during setting, as only a 25 mm gap under the penstock gate remained. In practice, this grout was partly washed out by the resumed sewer flow, and was subsequently successfully reinstated using the flowable calcium aluminate concrete. This confirmed that the calcium aluminate concrete was the correct choice of material for the shaft wall concrete reinstatement.

6 CONCLUSIONS

The rehabilitation works in the East Drop Structure required innovation in materials selection to enable practical reinstatement of structural concrete under challenging physical and safety conditions. The material needed to be highly fluid, self-compacting, set quickly and gain strength rapidly in order to withstand high hydraulic abrasion, and provide long-term corrosion resistance to hydrogen sulphide biogenic acidic attack. A flowable type of 100% calcium aluminate concrete was developed specifically to meet these challenges.

ACKNOWLEDGEMENTS

The authors thank Melbourne Water Corporation and GHD for permission to publish this paper, and acknowledge the assistance of both (Andrew Dickinson (Parchem Construction Supplies) and Andrew Martin (Kerneos).

Parchem Construction Supplies is an authorized user of the SewperCoat® brand through a licence from Kerneos.

The opinions expressed in this paper are the authors own.

REFERENCES

Barborak, R. Calcium Aluminate Cement Concrete (Class CAC Concrete) TxDOT Special Specification SS-4491 Tip Sheet, 2010

Barker, R. & Lawson, M. Repairing a large diameter interceptor using an innovative bypass technique and high performance calcium aluminate concrete. *NZ Waste and Water Association, Environz 03*, Auckland, September 2003

Baston, G. M. N. et al. 2012. Calcium silicate hydrate (C-S-H) gel dissolution and pH buffering in a cementitious near field. *Mineralogical Magazine* 76(8): 3045–3053

Bruce, S.M. & Freitag, S.A. Concrete durability in wastewater reticulation and treatment facilities and its sensitivity to small changes in exposure conditions, *Corrosion & Prevention*, Brisbane, November, 2005, Paper 023

Egan, D. et al. The use of calcium aluminate cement for corrosion control in a sewer pumping main. *Corrosion & Prevention*, Brisbane, 20–23 November 2005, Paper 021

Espinosa, B. at al. Acid attack of hydraulic cement-bound materials: corrosion kinetics and neutralization capacity. *13th International Corrosion Conference, Melbourne, November 1996*, Paper 445

Geoffroy, V.A. et al. 2008. Evaluation of aluminium sensitivity on a biodegrading bacteria acidithiobacillus thiooxidans: definition of a specific growth medium. In Fentiman CH, Mangabhai RJ and Scrivener KL. (ed.), *Calcium Aluminate Cements: Proceedings of the Centenary Conference, Avignon, 30 June–2 July 2008*. IHS BRE Press.

Kerneos Australia Technical Literature, Ciment Fondu, Fondag High Performance Pre-mixed Concrete

Kurtovich, M. & Lawson, M. The repair of live wastewater facilities using calcium aluminate mortars. *Corrosion & Prevention, Wellington, 16–19 November 2008,* Paper 078

Scrivener, K.L. et al. 1999. High-performance concretes from calcium aluminate cements. *Cement and Concrete Research* 29: 1215–1223

Parchem technical literature, SewperCoat® product range

Pomeroy, R. D. & Boon A.G. *The problem of hydrogen sulphide in sewers. 1976. Westminster:* John Taylor & Sons

Weale, C. J. 2013. East Drop Structure Assessment and Rehabilitation, *Corrosion and Materials*, June 2013

This page intentionally left blank

Concrete Solutions – Grantham et al. (Eds)
© 2014 Taylor & Francis Group, London, ISBN 978-1-138-02708-4

The application of modified hydrotalcites as chloride scavengers and inhibitor release agents in cement mortars

Z. Yang
Materials innovation institute (M2i), Delft, The Netherlands
Materials and Environment, Faculty of Civil Engineering and Geosciences, Delft, The Netherlands

H. Fischer
TNO Materials Performance, Eindhoven, The Netherlands

R. Polder
Materials and Environment, Faculty of Civil Engineering and Geosciences, Delft, The Netherlands
TNO Structural Reliability, Delft, The Netherlands

ABSTRACT: Owing to the unique molecular structure and high ion exchange capacity, hydrotalcites are believed to have a potential to be modified and tailor-made as an active component of concrete. In this paper, two types of modified hydrotalcites (MHT-pAB and MHT-NO_2) were incorporated into cement mortars with two dosage levels (replacing 5% and 10% cement by mass) and a constant water-to-(cement + MHT) ratio of 0.50. A designated testing programme including strength test, porosity test, and rapid chloride migration and diffusion test were employed to investigate the effect of modified hydrotalcites on chloride penetration in cement mortar. The results reported in this study showed the incorporation of MHT-pAB at 5% dosage in mortar specimens produced a notably improved chloride diffusion resistance with little or no influence on the development of mechanical strength.

1 INTRODUCTION

An essential feature in the long term durability of a reinforced concrete structure is the protection of the steel reinforcement. Under normal conditions, steel in concrete is protected from corrosion by a passive layer that is formed due to the high alkalinity of the concrete pore solution. However, the passive layer can be destroyed and corrosion subsequently initiated by certain aggressive species at the steel surface which may penetrate through the concrete cover (Bertolini et al. 2013). Among the aggressive species, chloride is the most detrimental culprit and has been recognized as one of the major factors affecting the service life of reinforced concrete structures (Polder et al. 2002, Yang et al. 2009). As proposed by Tuutti (Tuutti 1982), the development of corrosion in reinforced concrete consists of two different stages. The first stage (i.e., initiation phase) is related to the penetration of the critical chloride concentration up to the surface of reinforcement; the second stage (i.e., propagation phase) is related to reinforcement corrosion and concrete cover cracking and spalling, and is associated with severe damage. Therefore, the best corrosion prevention strategy may accordingly need to include two aspects: 1) to improve the chloride binding capacity of the concrete or other inherent properties slowing down chloride transport in concrete which subsequently would result in a delayed corrosion initiation of the reinforcing steel; 2) to slow down the corrosion propagation after corrosion has initiated. Most traditionally available corrosion prevention approaches such as coatings on reinforcing steel, concrete surface sealer, stainless steel reinforcement and cathodic protection (Cigna et al. 2002, Elsener et al, 2010, Elsener 2001, Pedeferri 1996) focus on one of the aspects and less attention has accordingly been paid to the other. A promising option is using modified hydrotalcites as an alternative approach against chloride ingress into concrete (Yang et al. 2013a, Yang et al. 2014). Hydrotalcite is one representative of a large mineral group of Layered Double Hydroxides (LDHs), in general formula $[M^{II}_{1-x}M^{III}_{x}(OH)_2]^{x+}[(A^{n-}_{x/n})]^{x-}\cdot mH_2O$, where M^{II} and M^{III} are di- and trivalent metals respectively and A^{n-} is an exchangeable interlayer anion with valence n. The x value is in the range of 0.22–0.33. A schematic of their structure and more detailed information related to modified hydrotalcite's (MHTs') molecular structure and chemical composition can be found elsewhere (Yang et al. 2013b). Due to the unique characteristic of the molecular structure and high anionic exchange capacity, hydrotalcite is believed to have a potential to be modified or tailor-made as an active component of concrete.

Hydrotalcite has been found in hydrated slag cements, which are known to bind more chloride ions than pure Portland cements (Dhir et al.1996, Arya and Xu 1995, Glass and Buenfeld 2000).More recently, Kayali et al. (Kayali et al. 2012) demonstrated the remarkable role of hydrotalcite in chloride binding and corrosion protection in concretes with ground granulated blast furnace slag. Preliminary studies (Yang et al. 2013a, Yang et al. 2014) conducted in chloride-containing alkaline solution have shown that ion exchange indeed occurred between chlorides and intercalated inhibitors in MHT's structure in addition to the inhibiting effect on the corrosion of steel conferred by the simultaneously released inhibitors. A distinctive feature of MHTs relative to the other corrosion prevention approaches is their dual function working mechanism: capturing aggressive chlorides and simultaneously releasing inhibitive interlayer anions to protect the reinforcing steel from corrosion (Yang et al. 2013b). As such the effects of modified hydrotalcites were set to be investigated on both plain and reinforced mortars with a focus on their interaction with chloride ions in plain mortar and in reinforced mortar focusing on their inhibition influence by the released inhibitors on corrosion of the reinforcing steel. In this paper, research is reported focusing on the effect of modified hydrotalcites on chloride penetration in plain cement mortars.

2 EXPERIMENTAL

2.1 *Materials*

A European specification CEMI 42.5N Portland cement in accordance with EN 197-1(EN 197-1 2011),CEN-Standard sand (particle size: 0-2 mm) conforming to EN 196-1(EN 196-1 2005) and deionized water were used. Two types of MHTs denoted as Mg(2)Al-pAB and Mg(2)Al-NO_2(with "2" in parentheses showing that the atomic ratio of Mg/Al is 2:1).were used in this study. They were synthesized by the modification of Mg(2)Al-CO_3 with sodium p-aminobenzoate (-pAB) and sodium nitrite (-NO_2) respectively through a calcination-rehydration procedure (Yang et al. 2013a). NaOH, $NaNO_2$ and p-aminobenzoic acid were obtained from Sigma-Aldrich. The hydrotalcite (Mg(2)Al-CO_3) used in this study was a commercially available product PURAL® MG 63 HT provided by Sasol Germany GmbH.

2.2 *Sample preparation*

The mortar samples were prepared with a constant water-to-binder (cement+MHT, in this case MHT is counted as one of the binders) mass ratio of 0.50, a constant (cement+MHT) content, a constant sand-to-binder mass ratio of 3 and a MHT-to-cement mass ratio of 0%, 5%, 10%, respectively. For both the reference (without MHT admixed) and mortar specimens admixed with MHTs, three specimens were prepared to ensure statistical reliability of test results. For the specimens admixed with MHTs, the MHT powder was mixed first with dry cement in a mixer, and then sand was added and stirred thoroughly at a low speed for 30 s. Afterwards, deionized water was added into the mixture and stirred for about 90 s (low speed for 30 s and high speed for 60 s) to achieve good workability. After mixing, the fresh mixtures were cast in the specific moulds (prisms, cylinders) and were carefully compacted on a vibrating table to minimize the amount of entrapped air. All the specimens were demoulded after curing under room temperature (RT) and local lab environment for 24 h. Afterwards, they were moved to a fog room at 23 ± 2°C and over 95% relative humidity and continually cured for 2, 6 or 27 additional days before subjecting to any assigned testing.

2.3 *Testing methods*

2.3.1 *Mechanical test*

The mechanical properties especially the compressive and flexural strength were investigated at curing ages of 3, 7 and 28 days by a standard three-point bending test using 40 mm × 40 mm × 160 mm mortar prisms. The test was carried out in accordance with EN 196-1. The flexural strength was measured by applying the load vertically to the mortar prisms at the rate of (50±10) N/s by a MACBEN (Servo plus evolution) materials testing equipment. The samples used for measuring the compressive strength were 40 mm cubes sawn from the prism halves from the flexural strength test and the compression load was applied at the rate of (2400 ± 200) N/s. At least three replicates were performed for both of the tests.

2.3.2 *Mercury intrusion porosimetry*

The Mercury Intrusion Porosimetry (MIP) method was used to determine the porosity of mortar specimens admixed with/without MHTs by a "Micrometritics Poresizer 9500" mercury intrusion porosimeter. The porosity measurement was carried out in two stages. The first stage was at low pressure: from 0 to 0.0036 MPa. The second stage was at high pressure running from 0.0036 to 210 MPa and followed by an extrusion running from 210 to 0.14 MPa. The MIP samples were taken from the intact parts of the mortar samples after the mechanical test in order to facilitate a possibly better link with the results from the mechanical test. The samples were first crushed by hammer into small pieces with dimensions of 1–2 cm^3. Then these pieces were immerged in liquid nitrogen for about 3 minutes to stop the hydration and stored in a vacuum freeze-dryer at −28°C for more than two months until a stable mass loss of 0.01%/day was reached before conducting the test. The quick freezing and drying process at low temperatures allowed the remaining liquid solution to transform into ice microcrystals and be removed by sublimation without significant damage to the microstructure.

2.3.3 *Rapid Chloride Migration (RCM) test*

The RCM tested was conducted following the procedures described in Nordtest method NT Build 492(NT

Build 492 1999) to determine the chloride migration coefficient of the mortar. After curing for 28 days, the 100 mm x 85 mm mortar cylinders were taken out from the fog room. Two slices of 15 mm and 20 mm were cut respectively from top and bottom of the specimen and consequently a 100 mm × 50 mortar slice was obtained as test specimen. The newly cut top surface was the one exposed to the chloride solution. The applied voltage was selected based on the initial current flowing through the test specimen at a voltage of 30V. The higher is this initial current, the lower is the applied voltage. In this study, voltages of 20V and 15V were selected respectively for the reference and mortar specimens admixed with MHTs based on the obtained initial current. The test duration in these cases was always 24 h.

2.3.4 *Natural diffusion test*

The natural diffusion test was performed in accordance with Nordtest method NT Build 443(NT Build 443 1995) on two mortar samples. At the ages of 28 days, the 100 mm × 85 mm mortar cylinders were taken out from the fog room. A 15 mm mortar slice was cut from top of the sample and consequently a 100 mm x 70 mm mortar slice was obtained as the test specimen. The surface that was newly cut was the one exposed to the chloride solution. After being fully saturated with $Ca(OH)_2$ solution, all the faces of the test specimens except the newly exposed one were dried at room temperature to a stable white-dry condition and then given a thick epoxy coating in order to allow the chloride to penetrate through the specimen in one direction driven by the concentration gradient. When the coating had hardened, the test specimen was fully saturated again with $Ca(OH)_2$. Afterwards, the mortar specimens were immersed in a plastic bucket filled with the 16.5% NaCl solution. The ratio between the exposed area and the volume of NaCl solution was kept constant at 3 cylinders in 6*l*. The plastic buckets were covered tightly by the lid and stored in laboratory condition for a total of 68 days. This solution was used for 35 days and then replaced by a new 16.5% NaCl solution. The plastic bucket was shaken once every week during the test period. After the exposure a total chloride profile was obtained.

2.3.5 *Chloride profiles*

After being immersed in 16.5% NaCl solution for 68 days, the mortar specimens were taken out and washed by tap water. After wiping off excess water from the surface, a profile grinder was used to obtain mortar powders by precision grinding at 2 mm depth increments in layers parallel to the exposed surface up to a depth of 25 mm for determination of the chloride profile. The grinding was performed within a diameter approximately 25 mm less than the full diameter of the mortar cylinders to avoid the risk of edge effects and potential disturbance from the epoxy coating. The mortar powders that were collected were then dried in an oven at 105°C for 24 h. The chloride profile consisted of two analyses, the extraction of total chloride and the determination of the binder content (i.e., MHT + cement, in this case). The chloride extraction was carried out following a similar procedure described in EN 14629(EN 14629 2007). Typically, 2 g of dry powder was weighed into a 250 ml beaker in which 30 ml deionized water and 10 ml 5M nitric acid was added subsequently. The mixture was shaken manually for 30 s following by heating until boiling and boiled for about 4 min under continual magnetic stirring. After cooling down, the mixture was vacuum filtered using a Buchner filter with a medium grade filter paper. The residue both in the beaker and on the filter paper was rinsed several times with deionized water to ensure all the chlorides had been collected. The filtrates along with the rinse water were then transferred from the filter flask into a volumetric flask. The solution in the volumetric flask was filled up with deionized water to 100 ml and 5 ml solution was pipetted into a clean plastic cup in which 45 ml deionized water was added for dilution to give a pH value of the solution between 1–2. The chloride content in the diluted solution was analyzed photometrically by a Spectroquant® NOVA 60 photometer with a chloride test kit. On the other hand, the solid residue left on the filter paper was dried in an oven at 105°C for 24 h.The cement content was then calculated by subtracting the weight of insoluble substances from the initial weight of the oven-dried mortar powder and correcting for hydrated water assuming 18% of the acid soluble cementitious mass was hydration water in addition to subtraction of 5% and 10% MHTs from the total acid soluble mass.

3 RESULTS AND DISCUSSION

3.1 *The effect of MHTs on mechanical properties*

Strength is an important engineering parameter to check the quality of concrete in its hardened state. According to EN-197, the standard compressive strength of a CEMI 42.5N cement at 28 days is at least 42.5 MPa and hence this could be considered as a lower limit to check the quality of cementitious mixtures made from this type of cement. In addition, concrete with low porosity usually has high strength and high resistance to the penetration of aggressive ions, such as chlorides. Therefore, some researchers link strength and diffusion coefficient data to the porosity of the concrete in order to globally assess the effect of a certain material on penetration of chloride. In this study, the effect of the partial replacement by MHTs of cement on the development of compressive strength and flexural strength was studied. The results of the compressive strength and flexural strength test are shown respectively in figures 1& 2, where each value is averaged from the results of three individual tests. As shown from these figures, comparing to the reference specimens (i.e., Ref.), the incorporation of MHTs results in observable but relatively small strength reductions at all test ages. However, all of the compressive strength values at 28 days are higher than 42.5 Mpa, the limit value in EN-197 for such cement.

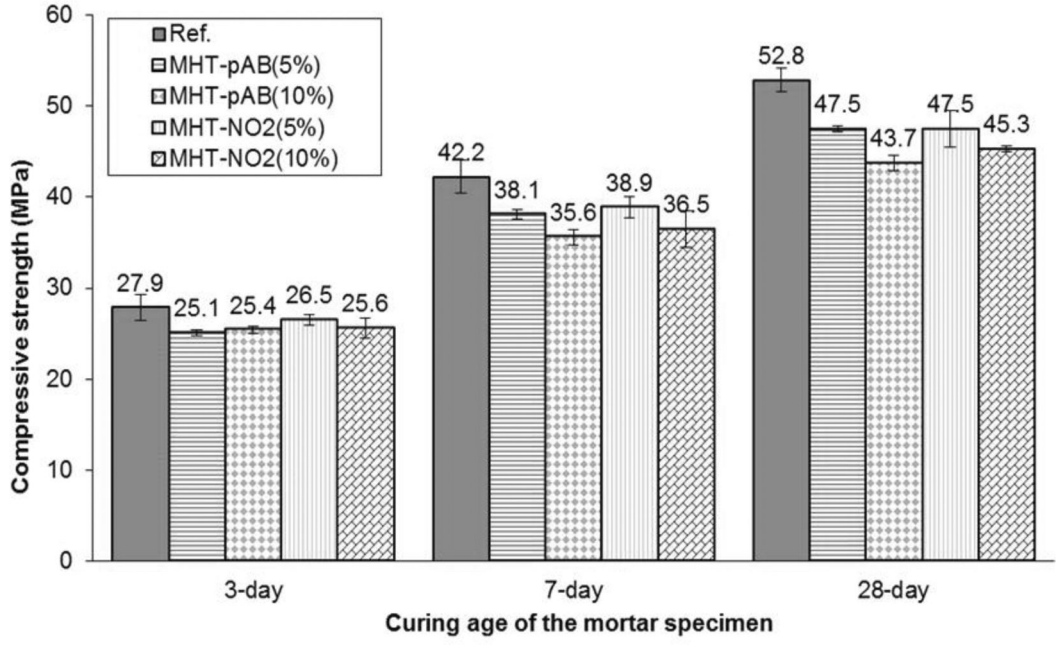

Figure 1. Compressive strength of the mortar specimens with/without MHTs. The bars are in order left to right as presented in the key.

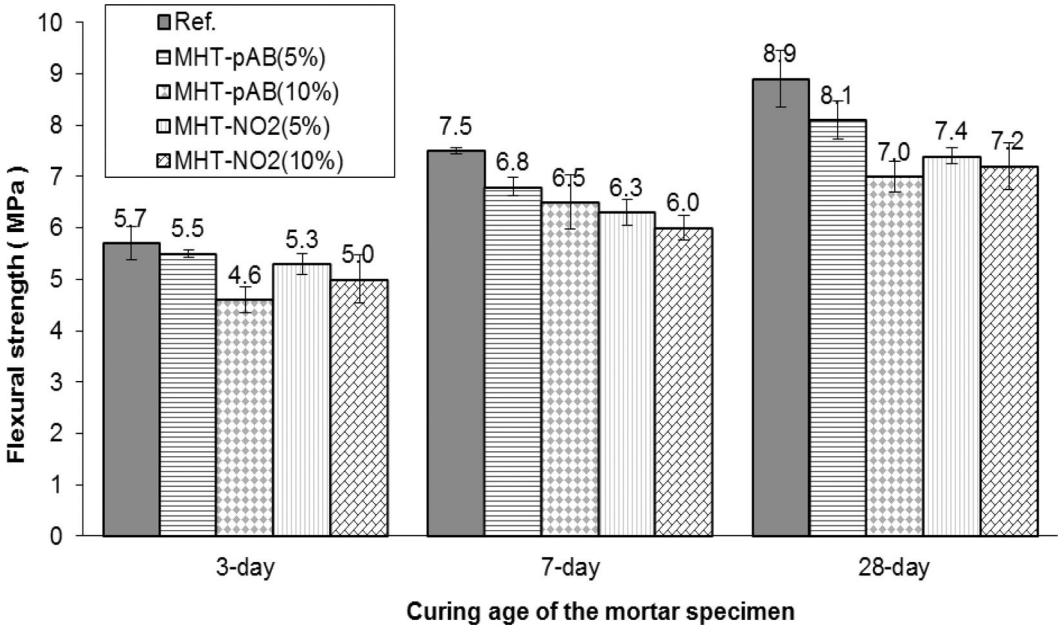

Figure 2. Flexural strength of the mortar specimens with/without MHTs. The bars are again in order left to right.

Therefore, one may conclude that no to minor negative effect on the strength development would result from the incorporation of MHTs in the cement mortar. Among the samples admixed with MHTs, the use of MHT-pAB at 5% dosage performed the best in general. Additionally, likely due to the lower porosity (see figure 3 and following discussion), the mortar samples admixed with the two types of MHTs at 5% dosage presented higher compressive and flexural strength values than those at 10% dosages at the three test ages.

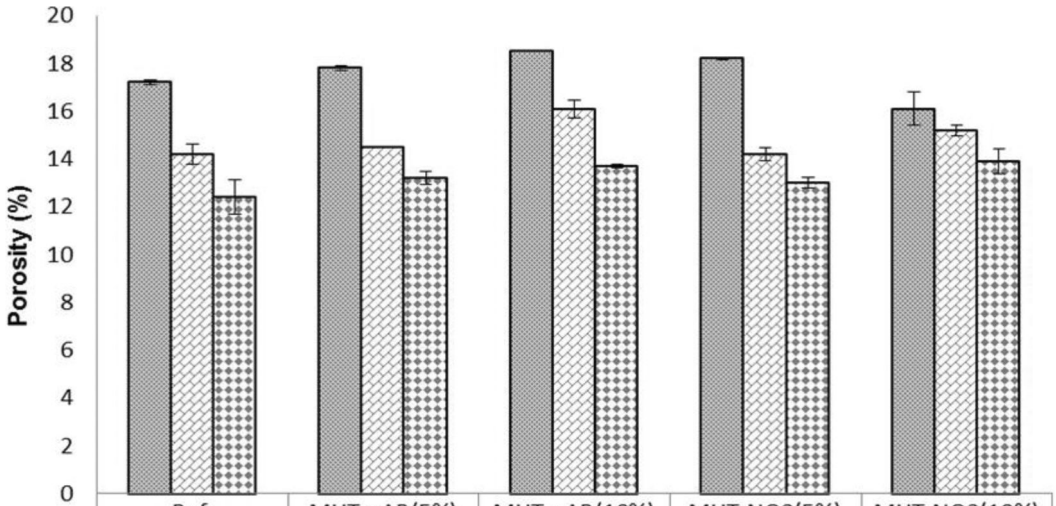

	Ref.	MHT-pAB(5%)	MHT-pAB(10%)	MHT-NO2(5%)	MHT-NO2(10%)
3d	17.2	17.8	18.5	18.2	16.1
7d	14.2	14.5	16.1	14.2	15.2
28d	12.4	13.2	13.7	13.0	13.9

Figure 3. Porosity of the mortar specimens with/without MHTs by MIP.

3.2 *The effect of MHTs on porosity*

The MIP test has been performed on mortar samples at curing ages of 3, 7 and 28 days. The Washburn equation as shown below is used to calculate the diameter of pores intruded by mercury at each pressure step.

$$D = -\frac{4\gamma\cos\theta}{P} \quad (1)$$

where D is the pore diameter (m), γ is the surface tension of mercury (N/m), θ is the contact angle between mercury and the solid materials and P is the applied pressure (Pa). The MIP test procedure includes intrusion and extrusion. The surface tension value used here is 0.485 (N/m) and the contact angle of is 132° based on reported studies for cementitious material (Cook et al. 1991). According to the Washburn equation, the pore size ranging from 350μm to 0.007μm can be detected. Figure 3 shows the total porosity of all the test mortar specimens in which each value is the average of two parallel measurements. As can be seen from Figure 3, relative to the Ref. specimen, the total porosity of the mortar has been increased in all the three test ages due to the incorporation of the MHTs in both of the two different dosage levels (5% and 10%) with the exception of MHT-NO_2(10%) whose porosity at 3 days, however, presented a relatively lower value. The increased porosity indicates the incorporation of the two types of MHTs has made the mortar a little more porous which in turn may increase the risk for chloride ion penetrating through the mortar matrix without considering the chloride binding behavior. As also seen from Figure 1 & 2, the increased porosity has indeed led to some loss of the strength although minor. In addition, when the results from the strength and porosity test are linked together, it is found that the development of the strength and porosity of the mortar admixed with MHTs followed the same trend with the curing time (i.e., strength increased and porosity decreased as hydration proceed) as those of reference specimens which might indicate the incorporation of MHTs has no or little influence on the cement hydration process. Furthermore, one has to be realized that differences in water-cement ratio between the specimens caused by the partial replacement of cement by MHTs could be also responsible for certain parts of strength loss and changed porosity.

3.3 *The effect of MHTs on chloride penetration*

3.3.1 *RCM test*

Once the tests were finished, all specimens were split axially into two pieces and sprayed with 0.1 M silver nitrate ($AgNO_3$) solution immediately onto the freshly split mortar pieces to visualize the penetration depth of chloride. The average penetration depth of chloride was recorded accordingly. The non-steady-state migration coefficient (D_{RCM}) was then calculated by the following equation proposed by NT Build 492.

$$D_{RCM} = \frac{0.0239(273+T)L}{(U-2)t}\left(x_d - 0.0238\sqrt{\frac{(273+T)Lx_d}{U-2}}\right) \quad (2)$$

where D_{RCM} is the non-steady-state migration coefficient, $\times 10^{-12}$ m^2/s; X_d is the average of the chloride penetration depths, mm; T is average of the initial and final temperatures in anolyte solution °C; U is the

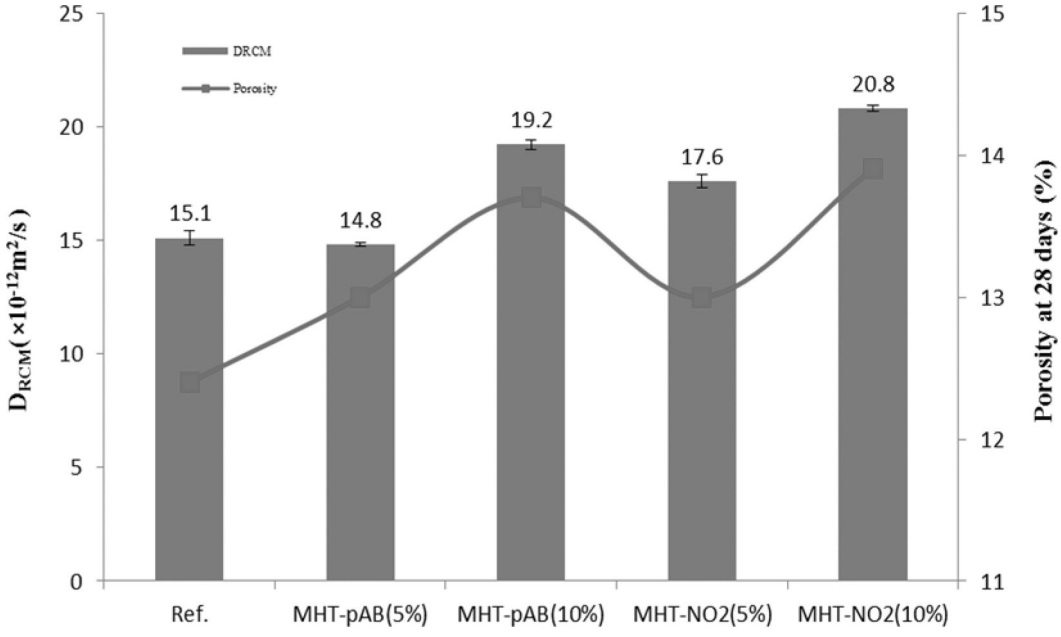

Figure 4. Chloride diffusion coefficient obtained from RCM test (bars and numbers) and porosity at 28 days obtained from MIP test (squares and line).

applied voltage V; L is the thickness of the specimen, mm;t is the test duration, h.

The chloride migration coefficient determined by the RCM test has been widely used as one of the important parameters for resistance of cementitious materials to chloride penetration. Figure 4 shows the RCM test results averaged from three test specimens combined with the porosity results from MIP test at a curing age of 28 days. As can be seen from Figure 4, mortar specimen of MHT-pAB(5%) presented the lowest RCM coefficient (D_{RCM}) among all specimens that were tested and on the other hand, when compared with the Ref. specimens presented a relatively higher porosity. Considering the factor that mortar specimens with higher porosity would normally give a higher value of D_{RCM} if no active chloride binding was considered, the co-occurrence of lower D_{RCM} and higher porosity of mortar specimen admixed with MHT-pAB (5%) may be attributed to an active chloride binding behavior due to the incorporation of MHT. The active chloride binding behavior in the MHT-pAB (5%) specimens could be traced back to the high anionic exchange capacity of MHTs which makes exchange of the interlayer ions by the intruded chlorides easily achieved as the following Equation 3 shows (Yang et al. 2013b).

$$\text{MHT-}Inh + Cl^- \rightarrow \text{MHT-Cl} + Inh^- \quad (3)$$

where -*Inh* represents the interlayer ions in the molecular structure of MHT (i.e., –pAB and $–NO_2$ anions in these cases). For the other MHT samples, the higher porosity may dominate the chloride migration process by the externally imposed electrical field although the ion exchange reactions might have occurred as well.

Figure 4. Chloride diffusion coefficient obtained from RCM test (bars and numbers) and porosity at 28 days obtained from MIP test (squares and line)

3.3.2 *Natural diffusion test*

The transport of chloride into concrete is usually described by Fick's second law (Equation 4) for unidirectional diffusion into a semi-infinite homogeneous medium. Fick's second law counts for a non-steady-state condition under which the flow of ions is not constant and the ion concentration changes with time. However, the diffusion coefficient is assumed to be constant.

$$\frac{\partial c}{\partial t} = D\frac{\partial^2 c}{\partial x^2} \quad (4)$$

In this condition, the mathematical solution to this problem is the error function,:

$$C(x,t) = C_s - (C_s - C_i)\cdot erf\left(\frac{x}{\sqrt{4D_e \cdot t}}\right) \quad (5)$$

where c (x,t) is the chloride concentration at depth x and time t (mass%), C_i the initial chloride concentration (mass%), C_s the chloride concentration at the surface (mass%), D_e then on-steady-state diffusion coefficient also known as the effective chloride transport coefficient (m^2/s), x the distance from the surface until the middle of the considered layer (m) and t the exposure time (s).

After finishing the natural diffusion test, the values for surface total chloride concentration (C_s) and effective chloride transport coefficient (D_e) are determined

by fitting the error function equation to the measured chloride concentration by applying a nonlinear regression analysis in accordance with the least squares method. The measured chloride profiles in which total chloride concentration has been averaged from two test specimens as well as the best fitting curves are shown in Figure 5. Considering the accuracy, the first point of the profile determined from the sawn face (i.e., 1 mm distance from the exposed surface) was omitted in the regression analysis. The fitted results of C_s and D_e are given in Table 1 accordingly. It should be pointed out that since D_e is coupled with C_s in the curve-fitting, the value of D_e alone may not reflect the actual resistance of the mortar or concrete to the chloride penetration although C_s is often used as one of the major parameters to estimate the chloride binding capacity of cementitious materials. Therefore, the synergy of C_s and D_s should be taken into account in order to better facilitate the interpretation and comparison of the results.

Table 1. Surface total chloride concentration and effective chloride transport coefficient obtained by fitting the error function equation to the measured chloride profiles.

Sample ID	C_s (mass% of cement)	$D_e(\times 10^{-12}$ m^2/s)
Ref.	4.7	8.6
MHT-pAB(5%)	6.0	4.8
MHT-pAB(10%)	6.3	15.5
MHT-NO_2(5%)	5.3	11.3
MHT-NO_2(10%)	5.5	19.5

As can be observed from Figure 5, All the MHTs specimens except for MHT-pAB(5%) showed higher total chloride concentrations in the profiles of all the layers than those of reference specimen indicating relatively weak resistance to chloride penetration. For MHT-pAB(5%), the total chloride concentrations were higher over the first 6 mm depth, while beyond 6 mm they were lower than those of the reference mortar indicating a stronger resistance to chloride penetration. On the other hand, as can be seen from table 1, when comparing to the reference specimen, all the MHT specimens exhibited higher C_s values indicating active chloride binding activity occurred due to the incorporation of MHT. This could be further validated by the higher D_e values (excepted for MHT-pAB(5%) specimen) and also higher porosity (see Figure 3) of MHT specimens relative to the reference specimens since higher D_e values and higher porosity should usually give a lower C_s value without considering the binding behavior. For those mortar specimens with incorporated MHTs, the total chloride concentration increased with the increasing dosages for both of the two types of MHTs, most likely due to the higher porosity of those specimens admixed with higher dosages of MHTs. Obviously, the higher porosity had dominated the chloride transport process when higher dosages

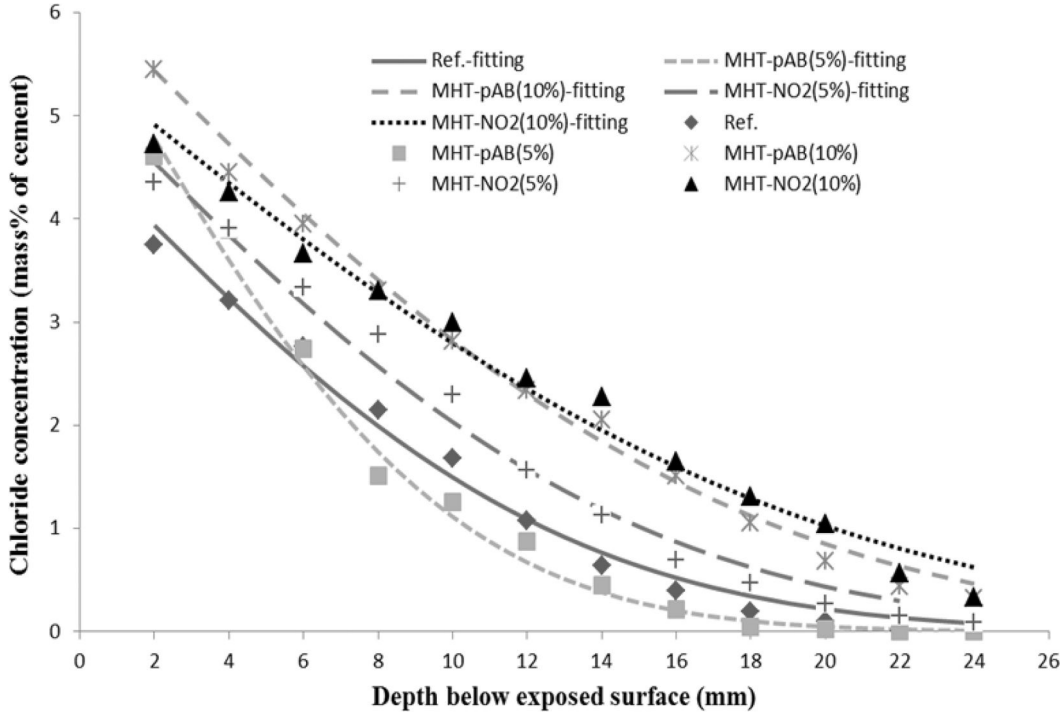

Figure 5. Chloride profiles after 68 days exposure to a 16.5% NaCl solution and the curves by fitting the error function equation to the measured data.

of MHTs were incorporated in spite of any possible chloride exchange or binding behavior that may proceed during the test. Mortar admixed with MHT-pAB presented higher C_s values and lower D_e values at the two respective dosage levels than mortar admixed with MHT-NO_2. In addition, considering the relatively small differences between the porosity of MHT-pAB and MHT-NO_2 specimens at 28 days, this may indicate that MHT-pAB had a higher chloride exchange capacity than MHT-NO_2. Nevertheless, the combined information from Figure 5 and Table 1 confirms the higher chloride binding capacity of the mortar due to the incorporation of MHTs, hence in MHT specimens more chlorides are bound at the surface compared to reference specimens. Specially, MHT-pAB(5%) possesses a notably improved chloride diffusion resistance compared to all the other test specimens indicated by the relatively higher C_s and lower D_e values.

4 CONCLUSION

In this paper, two types of modified hydrotalcites (denoted as MHT-pAB and MHT-NO_2) were incorporated into cement mortars with two dosage levels (replacing cement at 5% and 10% by mass).The mortar samples were prepared with a constant water-to-(cement+MHT) mass ratio of 0.50 and a constant sand-to-(cement+MHT) mass ratio of 3. The mortar properties such as compressive and flexural strength, total porosity, and rapid chloride migration and diffusion coefficients were investigated to shed light on a global picture of the effect of the two types of MHTs on chloride penetration in cement mortars and to study the potential correlation between these properties. The strength and porosity tests revealed that no or minor negative influence on the strength development would result from the incorporation of MHTs in the cement mortar although the porosity to a certain degree was increased when comparing to the reference specimens. In addition to that, it is worth noting that differences in water-cement ratio between mortar specimens caused by the partial replacement of cement by MHTs could also be responsible for some of the strength loss and changed porosity. Considering the fact that mortar with higher porosity would exhibit a higher D_{RCM} if no chloride binding was considered, the co-occurrence of lower D_{RCM} and higher porosity of mortar admixed with MHT-pAB(5%) therefore suggested an active chloride binding behavior that exists in its matrix.

Furthermore, the relatively higher Cs and lower De values from natural diffusion test indicated that MHT-pAB(5%) specimen possessed a notably improved chloride diffusion resistance hence in MHT specimens more chlorides were bound at the surface compared to reference specimens. Nonetheless, the active chloride binding behavior and the improved chloride diffusion resistance of the mortar specimens incorporated with MHT, especially for MHT-pAB(5%) specimen, further validated that the MHT could be a promising alternative for chloride scavenging within the concrete cover when an appropriate mixing dosage is adopted, which would subsequently results in slower chloride transport, thus delaying initiating the corrosion of the reinforcing steel. Using such materials could result in a longer expected service life of reinforced concrete structures.

ACKNOWLEDGEMENTS

The research was carried out under project number M81.609337 in the framework of the Research Program of the Materials innovation institute (M2i) (www.m2i.nl).Sasol Germany GmbH is acknowledged for the gift of hydrotalcite that was used in this research.

REFERENCES

Arya, C., Xu, Y. 1995. Effect of cement type on chloride binding and corrosion of steel in concrete. *Cem. Conc. Res*. 25(4), p.893–902.

Bertolini, L., Elsener, B., Pedeferri, P., Redaelli, E., Polder, R. 2013. *Corrosion of Steel in Concrete: Prevention, Diagnosis, Repair.* Weinheim: Wiley-VCH.

Cigna, R., Andrade, C., Nürnberger, U., Polder, R. Weydert R. and E. Seitz (Eds.) 2002. *COST 521: Final Report. Luxembourg*.

Cook, R.A., Hover, K.C. 1991. Experiments on the contact angle between mercury and hardened cement paste. *Cem. Concr. Res.* 21(6), p.1165–1175.

Dhir, R.K., El-Mohr, M. A. K. and Dyer, T.D. 1996. Chloride binding in GGBS concrete. *Cem. Conc. Res.* 26(12), p.1767–1773.

Elsener, B. 2001. Corrosion Inhibitors for Steel in Concrete-State of the Art Report. *EFC Publication No. 35*, London: IOM Communications.

Elsener, B., Addari, D., Coray, S. and Rossi, A. 2010. Stainless Steel Reinforcing Bars-Reason for Their High Pitting Corrosion Resistance. *Mater. Corros.* 61, p.1–9.

EN 14629, 2007. Products and systems for the protection and repair of concrete structures-Test methods-determination of chloride content in hardened concrete.*European standard*.

EN 196-1. 2005. Methods for testing cement-Part 1: Determination of strength, *European standard.*

EN 197-1. 2011. Cement-Part 1: Composition, specification and conformity criteria for common cements. *European standard.*

Glass, G. K. and Buenfeld, N. R. 2000. The influence of chloride binding on the chloride induced corrosion risk in reinforced concrete. *Corros. Sci.* 42(2), p.329–344.

Kayali, O., Khan, M.S.H, Ahmed, M.S. 2012. The role of hydrotalcite in chloride binding and corrosion protection in concretes with ground granulated blast furnace slag. *Cem. Concr. Compos.* 34(8), p.936–945.

NT Build 443,1995. Concrete hardened:accelerated chloride penetration.*NordTest*, Espoo.

NT Build 492, 1999. Concrete, mortar and cement-based repair materials: chloride migration coefficient from non-steady-state migration experiments. *NordTest*, Espoo.

Pedeferri, P. 1996. Cathodic Protection and Cathodic Prevention. *Constr. Bldg. Mater*.10(5), p. 391–402.

Polder, R., Peelen, W.H.A. 2002. Characterisation of chloride transport and reinforcement corrosion in concrete under cyclic wetting and drying by electrical resistivity. *Cem. Concr. Compos.* 24(5), p.427–435.

Tuutti, K. 1982. *Corrosion of steel in concrete*. Stockholm: Swedish foundation for concrete research (CBI).

Yang, Z., Fischer, H., Cerezo, J., Mol, J.M.C., Polder, R. 2013a. Aminobenzoate modified Mg-Al hy-drotalcites as a novel smart additive of reinforced concrete for anticorrosion applications. *Constr. Bldg. Mater*. 47, p.1436–1443.

Yang, Z., Fischer, H., Polder, R. 2013b. Modified hydrotalcites as a new emerging class of smart additive of reinforced concrete for anti-corrosion applications: a literature review. *Mater. Corros.* 64, p.1066–1074.

Yang, Z., Fischer, H., Polder, R. 2014. Synthesis and Characterisation of Modified Hydrotalcites and Their Ion Exchange Characteristics in Chloride-rich Simulated Concrete Pore Solution. *Cem. Concr. Compos*, 47, p.87–93.

Yang, Z., Shi, X., Creighton, A. T. and Peterson, M. M. 2009. Effect of Styrene-Butadiene Rubber Latex on the Chloride Permeability and Microstructure of Portland Cement Mortars. *Constr. Bldg. Mater* 23(6), p.2283–2290.

This page intentionally left blank

Repair of fire damage

This page intentionally left blank

Concrete Solutions – Grantham et al. (Eds)
© 2014 Taylor & Francis Group, London, ISBN 978-1-138-02708-4

Effects of Micromist fire extinguishing on the residual strength of heated and cooled concrete

T. Donchev, S. Dembele, D. Petkova & A. Lawrence
Kingston University London, UK

ABSTRACT: The proposed publication is based on experimental investigation which allows estimating the level of damage of concrete due to the usage of Micromist. The Micromist equipment is existing equipment in Kingston University. Forty eight cubic samples of same type of concrete were casted. They were divided in three groups according to the method of cooling in heated conditions – cooled in air at room temperature, cooled in tap water and cooled via Micromist treatment. The temperatures of heating are 100, 200, 300, 400 and 500°C. The residual strength of the samples is investigated using destructive and non-destructive (rebound hammer) methods.

The positive outcome indicates additional benefits of Micromist technology. The obtained results are analysed and corresponding conclusions offered in aspect of a generally smaller reduction of the residual strength of the concrete in comparison with other methods.

1 INTRODUCTION

The exposure to fire and high temperatures is without a doubt one of the most destructive processes that a concrete structure can be subjected to (Kowalski, 2007). As the use of concrete in construction continues to increase it has become necessary to develop measures in place to minimize the destructive effects on the concrete, including considerations of both aspects of fire as heating and cooling process. The effects of raised temperatures on the mechanical properties of concrete have been investigated and analysed in many works since the 1940's (Peng et al, 2008). Despite this fact there are a limited number of publications expressing the extent of the effects cooling regimes have on similar characteristics. This study will investigate the effects of high temperatures on the residual strength of concrete and analyse the effects of Micromist cooling technology on the residual strength of concrete in comparison with existing methods.

2 BACKGROUND

Concrete has been the leading construction material for nearly a century with 2 billion tonnes produced globally each year (Chan et al, 2000). As urbanization increases, these statistics are expected to increase with figures projected to reach 4 times this amount by 2050 (Tam et al, 2003). Recent findings on the subject of the safety of buildings has enforced the need to include fire protection within design (Yu et al, 2009) and shed light upon previous methods for active fire protection such as the use of sprinkler systems and inert gases. Given the advantages aslack of damage to the environment and high efficiency, advanced water mist fire extinguishing technology has a good chance to become a preferred alternative to previously popular halon agents (Kizilkanat et al, 2013).

Investigations such as those carried out by Kowalski (2007) have looked into the effects of cooling on the residual properties of heated concrete. It was observed that the degradation of the properties of concrete at high temperatures takes place due to stresses that the concrete was subjected to during rapid heating or to high thermal gradients from rapid cooling thereafter. It was concluded that the most negative influence of rapid cooling on the strength of the concrete was noticed at temperatures of around 330°C and by 550°C the decrease in strength was less dependent on the method of cooling.

In facilities where the usage of large amounts of water could prove hazardous or extremely damaging such as museums and libraries, a newer and potentially superior method is being investigated. Micromist is the term used to describe ultra-fine nano sized particles of water less than 10 microns in size.

The Micromist device expels large proportions of fine water droplet mists with a distinctive rapid discharge producing properties superior to conventional water mists systems (Luo et al, 2000). From the experiments looking into the effects and rate of cooling, it is clear that methods such as quenching cause an action of thermal shock to concrete previously under elevated temperatures. Compared with natural cooling, thermal shock induced by quenching and other methods caused a significant reduction in terms of the compressive strength of concrete (Karakoc, 2013). Due to the minimized amount of water being rapidly forced on to the concrete it is reasonable to expect that the concrete

Figure 1. Sample cubes inside the Carbolite oven.

could have lesser reduction of the residual strength after its application.

In order to investigate the difference in the effects that cooling methods have on concrete properties, a comparative experiment is needed. In response to this idea this paper investigates the effects of Micromist fire extinguishing on the durability of concrete structures through the analysis of the residual compressive strength of concrete. Samples were tested after being heated to temperatures between 100°C and 500°C and cooled by one of three methods; quenching (water tank), Micromist spaying and air cooling.

3 EXPERIMENTAL STUDY

The experimental aspect of the study consisted of four main stages: production of the concrete samples, heating the samples, cooling using three different regimes and destructive and non-destructive testing.

3.1 *Production of the concrete samples*

Ordinary Portland cement PC 52,5n in accordance with BS EN197-1 CEM 1 was combined with Thames valley coarse aggregates, maximum size 20 mm and fine aggregate 5-0 mm. For the purpose of the study 48 cubes were cast (45 test samples and 3 control samples). The cubes were 100 × 100 × 100 mm, concrete class C50. The concrete mix design consisted of 60.9 kg cement, 29.25 l water, 86.70 kg sand (fine aggregate) and 175.80 kg Thames Valley aggregate (coarse aggregate).Once the cubes were cast they were cured for 28 days at 22°C and 95% humidity of the air in the curing room. On the 28th day all groups of samples were taken out of the curingroom to be heated.

3.2 *High temperature heating*

Five temperatures were chosen to help identify changes in concrete strength at a range of different degrees of heating. Groups of 9 samples were carefully placed in the carbolite oven (figure 1). The cubes were stacked with spacing between them to allow air flow to ensure uniform heating. The samples were heated to temperatures of 100°C, 200°C, 300°C, 400°C and 500°C correspondingly. The cubes were continuously heated at each level until the temperature at the centre of a dummy cube with an internal thermocouple reached the specified temperature indicating uniform heating. The cubes were then held in the furnace at this temperature for 60 minutes to ensure enough time for processes in the concrete due to high temperature to be fully developed. The samples were then removed from the oven and cooled.

Figure 2. Micromist device in operation.

3.3 *Cooling regimes*

Each group of nine cubes was divided further into three smaller groups for cooling. Three cubes were exposed to air cooling, three to Micromist cooling (5 min) and three samples placed in a water tank (5 min) at approximately 20°C. A slower cooling process was then implemented to allow the samples to reach room temperature through air cooling. The Micromist device was set with water heated up to 180°C and saturation pressure of 10 Bars inside the reservoir. The saturated water was then released at ambient pressure, generating small droplets through flash atomisation. Figure 2 shows the Micromist device during operation.

3.4 *Sample testing for estimation of compressive strength*

The samples were then subjected to destructive and non-destructive tests to determine the effect of cooling on compressive strength and compare the results from the two tests. Samples were first tested using a

Table 1. Average compressive strength (MPa).

Heated Temperature	Average Compressive strength (N/mm^2)		
	Air cooling	Water tank	Micro-mist
20°C	50.17	50.17	50.17
100°C	45.50	44.63	43.02
200°C	44.39	39.49	46.23
300°C	41.32	35.28	45.28
400°C	34.77	30.09	33.12
500°C	18.26	16.67	20.88

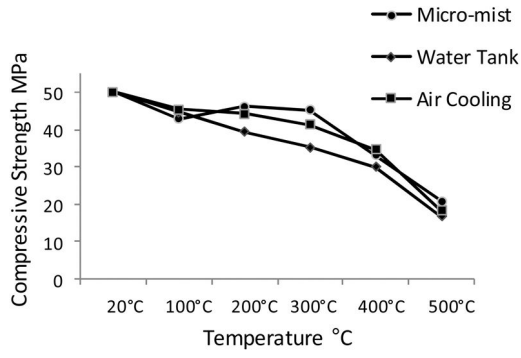

Figure 3. The reduction of compressive strength of samples based on destructive testing.

Schmidt hammer, 10 horizontal readings were taken and averaged. A compressive test machine was then used to load the samples with increasing force until failure determining the compressive strength of the sample in accordance with BS EN 12390-3:2009.

4 EXPERIMENTAL RESULTS

The results of the destructive compressive strength tests are presented in table 1.

Between 200°C and 300°C a larger distinction in residual strengths between cooling methods can be made. The samples heated to these temperatures show a clear difference in the compressive strength retained after heating and cooling depending on the method of cooling (Figure 4). For 200°C and 300°C the highest residual strength is observed for samples cooled by Micromist which combines the beneficial exposure to vapour for the hydration of the concrete and the reduced thermal shock compared to the water cooling.

Whilst the cubes cooled using air and Micromist continued to preserve their compressive strength, the data for the cubes cooled in a water tank depicted a gradual decline in compressive strength up to 400°C. This indicates that cooling by quenching had further effects on residual strength of concrete at stronger medium temperatures than the other methods used.

Despite having shown variations between them in the amount of residual strength at temperatures up to 400°C, those variations are gradually reduced and the strength of the samples of all three cooling methods fell concurrently to similar figures at 500°C.

From the graph in Figure 3 can be seen that by 400°C and 500°C the damages undergone by the concrete samples due to the extent of heating further outweigh the damage caused by the use of different cooling methods. Throughout the heating process damage to the surface of the concrete became increasingly visible as the temperature increased. Samples heated to both 400°C and 500°C began exhibiting signs of degradation, such as intensive cracking.

When the figures obtained for the reduction in strength for samples heated to 500°C and cooled in a water tank are compared against the control samples a 67% reduction in compressive strength was

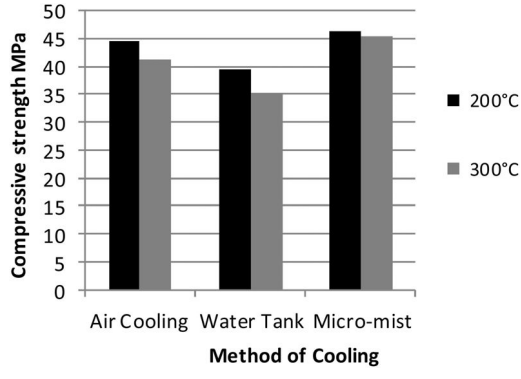

Figure 4. Compressive strength for 200°C and 300°C.

recorded. Despite a significant reduction in compressive strength of the Micromist samples they retained nearly 10% more strength than those who were cooled by quenching. The overall reduction in strength observed for samples cooled by air is 63% however the smallest reduction can be seen from the results of the samples cooled using Micromist as the sample tested at 500°C fell by 58%.

5 CONCLUSIONS

When concrete is subjected to raised temperatures it is natural for a decline in compressive strength to appear, however the methods used subsequently to cool the concrete can also prove to have a significant effect. From the three methods of cooling, water cooling (quenching) appears to have the strongest negative effect on residual strength of the concrete. This reduction is evident in the destructive testing results as the sample which underwent heating to 500°C suffered the highest loss in strength than that of any other sample in the experiment. The similarity of the results obtained for samples heated to higher temperatures (above 300°C) could be explained by the severe effect of the high temperatures on the residual strength of the

concrete, which is diminishing the effects of different types of cooling.

- The experimental study showed that the Micromist cooling resulted in better strength of the concrete than air and water cooling. The summary of the results and analysis indicate following main conclusions:
- For the temperatures below 100°C and above 400°C the method of cooling has relatively small effect on the residual strength of the concrete
- Cooling with Micromist produced smaller reductions of compressive strength in comparison with water cooling for all temperatures above 100°C
- For the temperatures of 200°C and 300°C Micromist results are better than air cooling

REFERENCES

Chan, S., Luo, X. and Sun, W. (2000). Effect of high temperature and cooling regimes on the compressive strength and pore properties of high performance concrete. *Construction and building materials*, 14 (5), *pp. 261–266*.

Karakoc, M. B. (2013). Effect of cooling regimes on compressive strength of concrete with lightweight aggregate exposed to high temperature. *Construction and building materials, 41 pp. 21–25.*

Kizilkanat, A. B., Yuzer, N. and Kabay, N. (2013). Thermophysical properties of concrete exposed to high temperature. *Construction and building materials, 45 pp. 157–161*.

Kowalski, R. (2007). The effects of the cooling rate on the residual properties of heated-up concrete. *Structural concrete*, *8 (1), pp. 11–15.*

Luo, X., Sun, W. and Chan, S. (2000). Effect of heating and cooling regimes on residual strength and microstructure of normal strength and high-performance concrete. *Cement and concrete research, 30 (3), pp. 379–383.*

Peng, G., Bian, S., Guo, Z., Zhao, J., Peng, X. and Jiang, Y. (2008). Effect of thermal shock due to rapid cooling on residual mechanical properties of fibre concrete exposed to high temperatures. *Construction and building materials*, *22 (5), pp. 948–955.*

Tam, V., O'Connell, M., Pedersen, G. and Renwick, P. (2003). Testing of the micromist device: an active soft barrier for explosion control. *Journal of loss prevention in the process industries*, *16 (1), pp. 81–88.*

Yu, M., Yang, K., Jia, H., Lu, C. and Lu, L. (2009). Coal combustion restrained by ultra-fine water mist in confined space. *Mining science and technology (china), 19 (5), pp. 574–579*.

Concrete Solutions – Grantham et al. (Eds)
© 2014 Taylor & Francis Group, London, ISBN 978-1-138-02708-4

Fire damage evaluation and repairs for reinforced concrete turbine table top foundation, Durango, Mexico

A. Garduno & F. Ballhausen
Comision Federal de Electricidad, Mexico D.F., Mexico

ABSTRACT: On May 2011, a fire occurred on one of the two units of a fossil turbine power plant, located in the State of Durango, Mexico. The fire lasted for almost 2 hours before it was extinguished by firefighters. Temperatures exceeded 800°C. During the investigations for establishing the causes of the fire, the evaluation of the reinforced concrete table top foundation of the turbine was also conducted. The damage must be known in order to propose demolition or rehabilitation. This paper presents the studies that were done for evaluating the table top foundation, which included visual inspection, pulse velocity measurement, concrete powder and core sampling, laboratory testing to verify mechanical properties (compressive strength and elastic modulus), determination of pH and X-ray fluorescence analysis. Thermal analysis of the concrete beam more exposed to the heat of the fire was also done. Results of the evaluation and analysis helped to establish the rehabilitation procedures, which are in process, and are discussed is this paper.

1 INTRODUCTION

On May 2011 a fire occurred on one of the two units of a fossil turbine power plant located in the state of Durango, Mexico. The fire lasted for almost 2 hours before it was extinguished by firefighters. Temperatures exceeded 800°C, because of oil deposits from the seal system located close to the steam/turbine generator, which ended completely damaged.

During the investigations for establishing the causes of the fire, the evaluation of the concrete table top foundation of the turbine was also conducted. The severity and extension of damages had to be known in order to propose total or partial demolition of the reinforced concrete structures and their rehabilitation. The main concern was to define if the tabletop would be able to receive the generator after its rehabilitation.

This paper presents the studies that were done for evaluating the reinforced concrete table top foundation, and include, visual inspection, pulse velocity measuring, concrete powder and core sampling, laboratory testing to verify mechanical properties (compressive strength and elastic modulus), determination of pH and X-ray fluorescence analysis. Control samples from non-exposed to fire areas were also tested. Thermal analysis of the concrete beam which was closely exposed to the heat of the fire of the tabletop foundation was done.

Finally, the extent of the damage was established and the procedures for repair were proposed. Rehabilitation of the concrete table top foundation is almost finished, and it is programmed that the repaired turbine generator will be installed by March 2014.

2 DESCRIPTION OF THE STRUCTURES

The power plant has two units of 160 MW each. It started operation by 1990. The foundation of the turbo generators consists on reinforced concrete table tops. Figure 1 presents a general scheme.

Representative section for the beams was 3.6×2.5 m and for columns was 2.0×2.6 m. Compressive strength of concrete for construction of the table top foundation was 25 MPa. Alluvial aggregates were used, with a maximum size of 38 mm. Reinforcement concrete cover was about 7 cm.

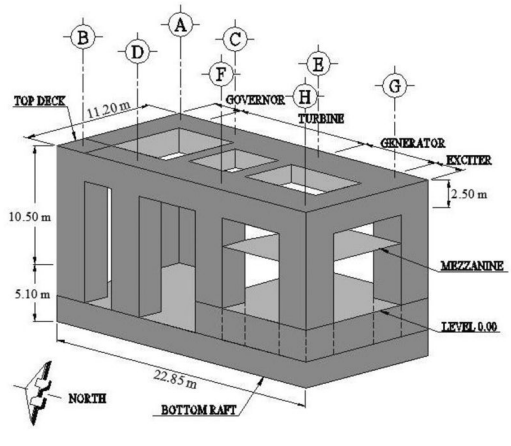

Figure 1. Scheme of the turbine table top foundation.

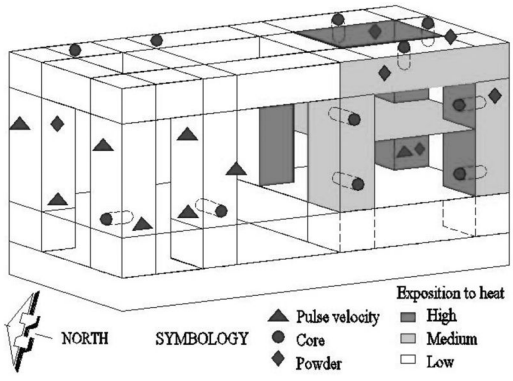

Figure 2. Testing and sampling places, and heat exposition zoning.

3 EVALUATION OF CONCRETE TABLE TOP FOUNDATION

The site works for the evaluation began in late May and were finished by June 2011. At that time, it was difficult to access all the structures because the remains of the fire were not removed; most of the concrete was blackened (smoked) on its surface. The evaluation was focused on the columns and beams exposed to highest heat. Sampling was complicated with secondary structures in the way and with precarious temporary supports. Figure 2 presents a scheme indicating the general location for sampling and testing. Control samples from non-exposed to heat areas were also considered.

3.1 *Visual inspection*

It was possible to know that during the fire temperature exceeded 800°C by looking at the fire debris, for example, some of the support structures and valves systems had bronze parts that were melted; bronze melting temperature is about 900°C [Technical Report No. 68]. The location of the oil deposit on a mezzanine below the turbine top deck, helped to identify which elements were more exposed to heat, as indicated in figure 2.

The table top foundation showed good quality concrete: homogeneity, no pores, nor segregation, no rebar steel corrosion stains were found. Cracking was observed in some surfaces, cracking along longitudinal reinforcement on beams was associated with steel rebar expansion due to the high temperature exposure (Fig. 3).

Concrete coloration was observed on site, and afterwards, on cores, to look for changes from the original concrete. It was expected that concrete on the surface would have a color from reddish to grey [ASTM C856, Technical Report No. 54]. This was not so noticeable, but some examples were found and the change in coloration occurred on less than 5 cm from the surface. Figure 4 shows color changes on a core.

Figure 3. Crack generated by reinforcement expansion.

Figure 4. Change in color on concrete core.

While core drilling it was also noted if concrete was sound enough to extract the core. In most cases, drilling in the exposed to heat columns and beams was not possible until a depth 10 to 15 cm was surpassed and weak material was removed.

3.2 *Non destructive tests*

Representative structures and locations to test with ultrasonic pulse velocity technique [ASTM C597] were chosen to compare, qualitatively, density and homogeneity of concrete inside the structures and to evaluate possible the possible effects of high temperature exposure, as well as to calculate the dynamic modulus of elasticity. Direct measurements were done on columns, at 2 heights (Fig. 5), but it was not possible on beams because of accessibility limitations.

Table 1 shows representative results. They have considerable variations, but it can be seen that concrete exposed to heat presented average lower velocities than unexposed concrete, which was as expected due to the damage (microcracking) [Technical Report 68, Mena-Ferrer]. Pulse velocities measured on cores showed the same tendency, higher velocities on sound samples, as will be mentioned later.

3.3 *Core and concrete powder sampling*

Concrete coring was done on representative beams and columns up to depths of 40 to 70 cm (Fig. 6). This

Figure 5. Direct pulse velocity measurement in column.

Table 1. Representative results of ultrasonic pulse velocity measurements on columns.

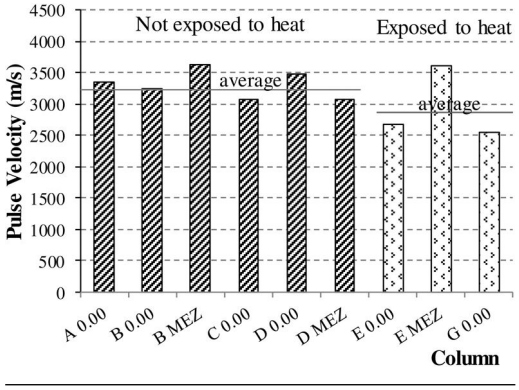

Figure 6. Core drilling on beam.

allowed us to verify concrete soundness below the surface of the structures and to obtain information about the concrete such as change in color, particle size distribution, which was adequate, as well as mechanical properties when tested in laboratory. Core holes were refilled with grout.

Table 2. Results of pulse velocity and density on cores at different depths.

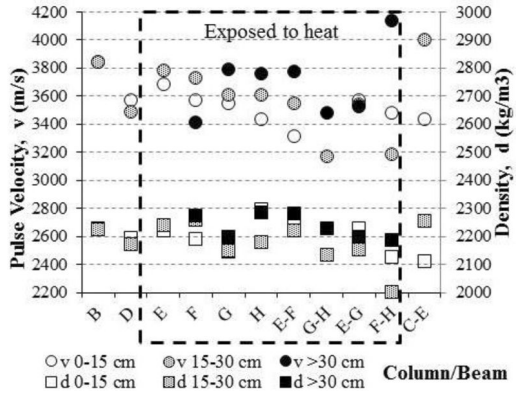

Samples of concrete powder were extracted with an electric drill at several depths, 0–5 cm, 5–10 cm, 10–15 cm and 15–20 cm depth.

3.4 *Laboratory testing*

Concrete cores were segmented into smaller samples representative of different depths, and pulse velocity, density, compressive strength and modulus of elasticity, were determined, tested in accordance with ASTM C597, C642, C42 and C469.

Densities and pulse velocity results were not clear indicators of damage or weakness on the surface. This was attributed to the core drilling process: if concrete was weak, the sampler had to go deeper. Core densities were representative of normal weight concrete [Neville, 1995], and there was not a noticeable difference from exposed cores to control ones. Control samples (not exposed to heat) presented slightly higher average pulse velocities. Results are presented in Table 2, related to depth.

Compressive strength and elasticity modulus results were, in general, higher on deeper cores; there was not much difference between control samples and cores exposed to high temperature, as shown in Table 3. The lowest compressive strength results may be associated with cracking at the steel reinforcement vicinity.

Powder samples were analyzed to determine pH variations in accordance with ASTM D1293. X-ray fluorescence techniques were also applied to concrete powder to determine calcium oxide content CaO at different depths: over 500°C calcium hydroxide $Ca(OH)_2$ goes to CaO; and over 700°C hydrated silicate calcium $CaSiO_3$ goes to $CaO + SiO_2$ [ASTM C-856, Di Maio]. Table 4 shows average results for different depths, from surface to 20 cm depth. Results of both parameters do not show a differentiation related to the depth up to the rebars, and behind reinforcement.

Table 3. Results of compressive strength and modulus of elasticity on cores at different depths.

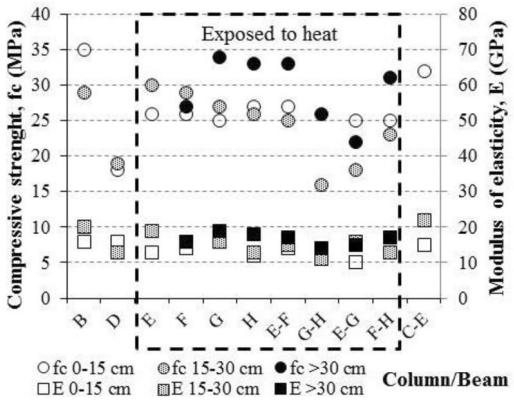

Table 4. Average pH and Calcium Oxide content at several depths.

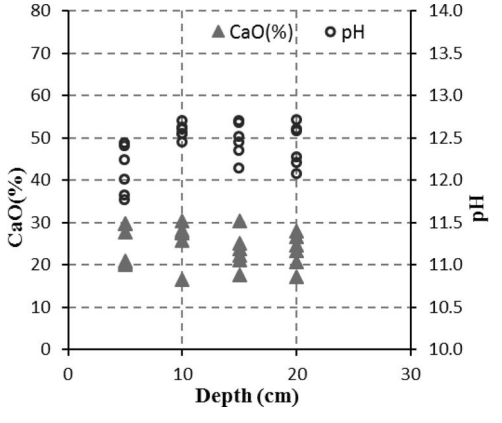

4 THERMAL ANALYSIS

Finite element thermal analysis for the beam more exposed to heat was done using the Geostudio 2007 program. The main objective was to establish the depth up to which a harmful temperature for concrete was acting during the fire, and to infer the extension of its effect on steel reinforcement and on concrete. No metallic embedded elements were considered. Thermal parameters used for the analysis are typical for these materials and are presented in Table 5.

The function of the change on temperature used for the analysis is shown in Figure 7. It considers temperature rise during the fire, taking into account that oil deposits acted as fuel, and the fire duration [Vidaud].

According to this analysis, the maximum temperature reached at the first reinforcement layer (7 cm depth) was about 500°C, and at the second layer (13 cm depth) was 200°C. Reinforcement was never subjected to 600°C, considered the limit for permanent damage on steel reinforcement [Technical Report No. 68, Mena-Ferrer]. Figure 8 presents maximum temperatures estimated in the inside of the beam.

This analysis also showed that any plate on the concrete surface could have reached 900°C, and thus, permanent damages.

From this analysis it could be verified that the maximum depth affected by heat, in zones without bolting, plates or embedded elements, was 15 to 20 cm at most.

Table 5. Thermal properties used for the analysis.

Material	Thermal conductivity (kJ/h/m/°C)	Specific volume change capacity (kJ/m^3/°C)
Concrete	10	2400
Steel	180	7500

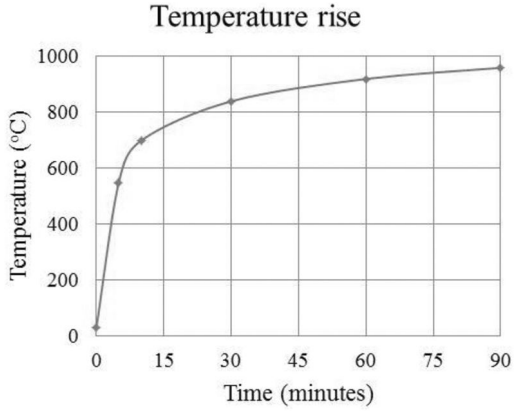

Figure 7. Temperature rise during the fire.

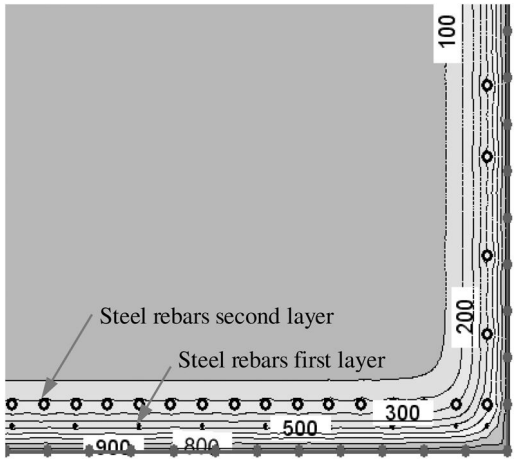

Figure 8. Temperatures (°C) in the inside of the beam (bottom corner) by thermal analysis.

5 INTERPRETATION OF RESULTS

With the inspection data, results of NDT, laboratory tests, and thermal analysis the conditions of the concrete columns and beams that were exposed to high temperatures were established.

Results of estimated temperatures by thermal analysis are congruent with the results of pH and CaO content, which did not show relevant changes because temperatures in the inside were not high enough to produce them. This is also congruent with the observed soundness: weak concrete could be found up to 15 cm. This is attributed to the low thermal conductivity of concrete and the duration of the heat exposure [Potha-Raju].

Comparing compressive strength and modulus of elasticity results from control samples and samples from the exposed columns and beams, it is difficult to see a differentiation; which is congruent with the limitation for drilling cores, if concrete is not sound enough cores cannot be extracted, so results are representative of not damaged concrete.

6 REPAIR PROCEDURES

Damage on the table top foundation was zoned by element (beam or column) and by face orientation (North, South, East, West), and repairs were proposed accordingly. Half of the columns and beams, northern elements of the table top, did not present damage. Critical zones required removing weak concrete and replacing it, with good care on the bond with the sound concrete. Table 6 shows a summary of treatments including depths of concrete to remove. In no case was it necessary to replace steel reinforcement.

Removal of weak concrete was done using hand held equipment, such as electrically powered demolition hammers. Concrete was removed up to 30 mm behind the steel reinforcement to assure that rebars would be surrounded by the repair concrete. While breaking out concrete, areas close to the turbine generator anchorage were identified as weak, and a thorough demolition was done as preparation for new anchors (Fig. 9).

Repair procedures included an adequate design for the wooden formwork and the propping, due to the dimension of the structural elements and the fluidity of the concrete (Fig. 10).

Characteristics of the concrete for repair included self-consolidating concrete; compressive strength at 28 days (minimum 35 MPa), maximum size aggregates of 9.5 mm. The mixture had to be fluid enough to be able to pass through the form and reinforcement, and internal vibrating was not required. Curing was done with a membrane.

Repairs of columns were supposed to be done prior to the beams. But demolition of weak concrete was done for all the structures, and the beams stayed unreinforced for several months. The stability and safety of the foundation, considering that status of the structures was checked and it proved that the beams were sturdy enough to work as unreinforced structures.

A very important issue was the bond between the original concrete and the repair one. The substrate preparation consisted of cleaning the surface with pressure water jetting, but it was not possible to apply

Table 6. Required repair for columns and beams.

	Repair zoning			
Element	North	South	East	West
Columns				
A	sound	sound	sound	sound
B	sound	sound	sound	sound
C	sound	sound	sound	sound
D	sound	sound	sound	sound
E	surface	10	surface	10
F	surface	10	10	10
G	10	surface	surface	10
H	15	15	15	15
	North	South	Upper	Lower
Beam				
A-B	sound	sound	sound	sound
C-D	sound	sound	sound	sound
E-F	surface	surface	surface	surface
G-H	15	15	15	surface
	East	West	Upper	Lower
A-C	sound	sound	sound	sound
B-D	sound	sound	sound	sound
C-E	surface	surface	surface	surface
D-F	surface	surface	surface	surface
E-G	15	15	15	surface
F-H	15	15	15	surface

sound: (not damaged) removing stains
surface: cleaning and local repairs
10 or 15: depth in *cm* to be removed and restored with self-consolidating concrete

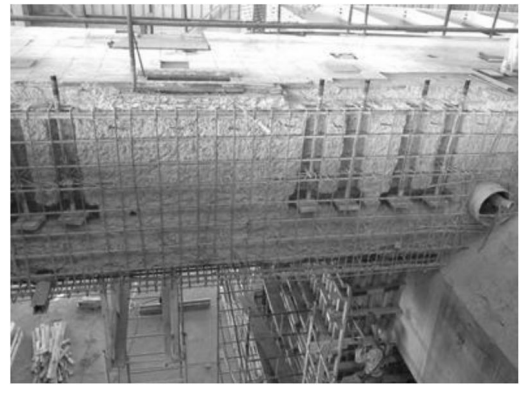

Figure 9. Beam after removing weak concrete. Notice the detailed area around anchorage.

Figure 10. Forming on column, propping, and view of a repaired column.

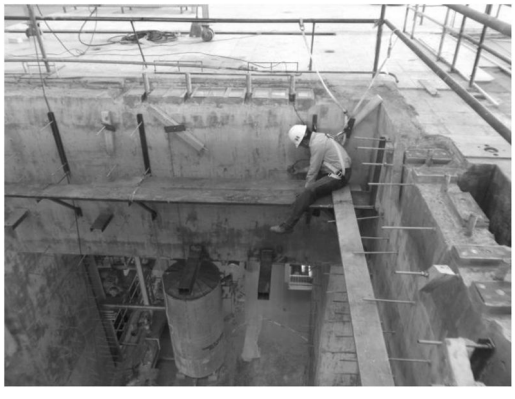

Figure 11. Direct pulse velocity measurement on repaired beam.

a bonding product. After repairs were finished, cores were drilled and it could be seen that the bond was adequate. It was not possible to test direct tensile to verify the bond because cores broke in the old concrete area while drilling, due to the size of the core (76 mm) in relation to the size of the aggregate of the old concrete and because it was rounded alluvial aggregate instead of crushed.

NDT was also helpful for quality control. In this case, pulse velocity was intended to verify homogeneity of concrete and to identify if there was a joint between old and new concrete. Velocities proved continuity and similar velocities to the ones measured on columns not exposed to heat were found. Figure 11 shows pulse velocity measurements on a repaired beam.

7 CONCLUSIONS

During the inspection of the turbine table top foundation it became apparent that some structures suffered damage during the fire. The extent of damage could be established with the information from NDT as well as laboratory results and thermal analysis. Northern columns and beams, in the area of the governor, did not present damage at all. In the other structural elements, damage was basically on the concrete cover, so repair was possible. Damage was not deeper due to the short duration of the fire and temperature exposure.

Results of pulse velocity were useful to rapidly compare concrete elements not exposed to heat against concrete elements exposed to heat. But in order to establish the depth of weak concrete to be removed, it was necessary to have information at different depths. Calcium oxide content is a good indicator of temperatures reached inside the concrete, and in this case, it showed that temperatures were not so harmful. Results obtained from cores, such as compressive strength and density, can be indicators of good quality concrete, but due to the drilling process they cannot be representative of affected concrete. Thermal analysis proved to be an accurate way of knowing if steel reinforcement suffered permanent damage.

At the time of writing, the repairs were almost finished, and during concrete removal it could be verified that the extent of damage defined was very close to the damage found. The bond of the repair concrete to the original one was a key factor to ensure that the table top foundation would work properly when the turbine is reinstalled.

NDT, pulse velocity measurements, are very useful in the diagnosis stage, but can also be helpful during repair, as part of quality control. They were applied as a way to verify the bond between old and new concrete, by checking if there was a joint.

REFERENCES

ASTM C42. 2010. *Standard Test Method for Obtaining and Testing Drilled Cores and Sawed Beams of Concrete*. American Society of Testing and Materials, West Conshohocken, PA.

ASTM C469. 2010. *Standard Test Method for Static Modulus of Elasticity and Poisson's Ratio of Concrete in Compression*. American Society of Testing and Materials, West Conshohocken, PA.

ASTM C597. 2009. *Standard Test Method for Pulse Velocity through Concrete*. American Society of Testing and Materials, West Conshohocken, PA.

ASTM C642. 2006. *Standard Test Method for Density, Absorption, and Voids in Hardened Concrete*. American Society of Testing and Materials, West Conshohocken, PA.

ASTM C856. 2002. *Standard Practice for Petrographic Examination of Hardened Concrete*. American Society of Testing and Materials, West Conshohocken, PA.

ASTM D1293. 2012. *Standard Test Method for pH of Water*. American Society of Testing and Materials, West Conshohocken, PA.

Di Maio, A., et al., 1999, Anales SAM, *Hormigones expuestos a altas temperaturas: Evaluación de la permeabilidad y otras propiedades físicas*.

Mena-Ferrer, M. 1994. *Manual de Tecnología del Concreto sección 3*, Limusa Noriega Editores, CFE México.

Neville, A.M. 1995. *Properties of concrete 4th edition.* Publ. Longman.

Portha-Raju, M., et al., 2008.Concrete for fire Engineering, *Theoretical assessment of flexural strength of heated reinforced concrete beams.* Proceedings of the International Congress, Concrete: Construction Sustainable Option, Scotland UK, July 2008. HIS BRE Press.

Technical Report No. 54, *Diagnosis of Deterioration in Concrete Structures*, The Concrete Society, 2000.

Technical Report No. 68, *Assessment, Design and Repair of Fire-damaged Concrete Structures*, The Concrete Society, 2008.

Vidaud, E., 2011, La acción del fuego sobre las estructuras de concreto, *Construcción y Tecnología del Concreto*, IMCYC, Julio 2011, México.

This page intentionally left blank

Concrete Solutions – Grantham et al. (Eds)
© 2014 Taylor & Francis Group, London, ISBN 978-1-138-02708-4

Evaluation and repair of fire damage to the concrete structures of a high-rise building

Chuanming Zhai & Yufei Guo
C+E Center for Engineering Research Test and Appraisal, Beijing, China

Yu Lou
China Electronics Engineering Design Institute, Beijing, China

Yan Lu
School of Civil Engineering, Tianjin University, Tianjin, China

ABSTRACT: Structural fire design and fire prevention management face new challenges as more high-rise buildings are constructed. The evaluation of fire damage to such structures can help formulate efficient structural fire design and fire prevention management. The procedure for evaluating fire damage to concrete structures was discussed using a burnt high-rise building as an example. Such procedures included an emergency investigation of the fire site, an estimation of fire temperature, the initial division of floors and areas based on the visual damage they showed and the inspection of burnt structural members. The concrete structures were evaluated according to the degree of fire damage they received as well as their characteristics. Lastly, rehabilitation. measures for the concrete structures were proposed based on fire damage grades.

1 INTRODUCTION

Numerous high-rise buildings were constructed in China during the past decade as a result of the rapid development of the economy of the country. A number of these structures even became landmarks in several large and medium-sized cities. These buildings developed higher chances of catching fire because of their complex structural designs and large space utilization. Moreover, the scale, damage, and economic loss caused by fires in high-rise buildings are more serious than those observed in ordinary buildings. For example, the 9/11 attacks on the North and South Towers of the World Trade Center in the United States (which both had more than 100 floors) caused huge explosions and fires which led to the meltdown and collapse of the two buildings. This event resulted in a significant number of casualties, tremendous property losses, and adverse social impact.

Several research institutions abroad have studied fire resistance of building structures over the past years. These studies mainly focused on the development process of fires in buildings, the structural behavior of elements in fires, structural fire design methods, and evaluating fire damage to structures (Fan & Lv 1999; Li G. et al. 2008). A number of corresponding standards and codes were published along with these studies (GB 50016:2012; ASCE 29-05:2007; EN 1992-1-2:2004). Several Chinese researchers also made remarkable achievements in designing fire-resistant structures. Among them are Li (Li G. et al. 2006), who summarized the calculation methods for fire-resistant designs of steel and steel–concrete composite structures; and Han (Han et al. 2012), who systematically introduced the principles for fire-resistant designs of steel–concrete composite structures in terms of fire-resistant performance, design methods, and protection measures. The level of structural fire protection has significantly improved in recent years because of the rapid development of computer simulation technologies and the gradual advancement of structural fire design methods.

However, the current theoretical system for inspecting and evaluating fire damage in building structures remains imperfect. An explicit standard for selecting an evaluation index and for developing an evaluation system for structural damage caused by fires is still not available despite the recent advancements in fire damage inspection techniques and methods. Most existing evaluation methods are qualitative instead of quantitative (Li M., 2005). A number of newly developed mathematical models have been recently adopted to establish an evaluation system for fire damage to concrete structures. Li (Li M. et al. 2008) proposed a comprehensive evaluation model for fire damage to high-concrete structures based on fuzzy

mathematics, which considered strength loss, durability damage, spalling degree, and crack width as evaluation indicators. Fang (Fang et al. 2010) established a fire damage evaluation model for concrete structures using the projection pursuit evaluation method and a genetic algorithm, with evaluation indicators based on the model proposed by Li (Li M. et al. 2008). Wang (Wang et al. 2008) considered strength loss, antipermeability loss, spalling degree, and crack width as evaluation indicators; in addition, Wang established the matter element evaluation model for burnt concrete structures. Although the aforementioned studies contribute to the development of an evaluation theory for burnt concrete structures, such quantitative methods exhibit several disadvantages, which are described as follows. First, the fixed values of the evaluation indexes for the entire structure are difficult to determine. Second, the weight of the evaluation indexes and the classification criteria for structural damage grades are influenced by human factors. Therefore, qualitative and empirical methods are primarily used in the actual evaluation of structural damage, and quantitative calculation methods serve as supplements. The evaluation of fire damage to concrete structures of a high-rise building presented in this paper can serve as a guide in inspecting burnt concrete structures.

2 OVERVIEW OF THE HIGH-RISE BUILDING AND THE FIRE INCIDENT

A high-rise building, constructed in 2004, is located in the Beijing central business district. The building is 159.68 m high, and its architectural area is 103,648 m^2. It has 30 floors and 2 additional underground floors. The building (Figure 1) consists of a main building and a skirt building. The main building uses a frame shear wall system composed of a huge steel-support cross-hybrid structure which is divided into the north and south wings. Both wings are connected by a cylindrical shear wall to the east side, thus forming an atrium. The huge steel-support cross-hybrid structure is placed at the west side. The skirt building has reinforced concrete structures. The entire roofs of the main and skirt buildings are covered with large-span steel structures, and thus, the space underneath them becomes the indoor environment. The outer decoration of the curtain wall of the building comprises titanium zinc plates, glass, and composite aluminum plates.

In February 2009, the building caught fire after its main structure was completed. The fire spread to 21,333 m^2 of the building, and the total burned area was 8,490 m^2. The fire lasted for approximately six hours. It was caused by high-temperature firework sparks which ignited the combustible materials on the roof of the main building. The fire rapidly spread to the outer wall decoration and to the lower floors. This particular fire incident demonstrated several characteristics. First, the high-rise building had special structures, such as its large scale, complex layout, and multiple tortuous internal channels. Second, the curtain wall of the building was decorated with special materials, such as the glass curtain walls in the north and south, and the titanium zinc plates in the east and west. The melting point of titanium zinc plates is 418°C. Moreover, the inner parts of the plates were made of extruded sheets and ethylene propylene diene monomer rubber, which are flammable, thermally insulated, and waterproof materials. The fire melted the titanium zinc plates and ignited the materials beneath them, which produced huge amounts of toxic fumes. Third, the fire spread in an unusual direction. The fire was ignited at the top-middle part of the main building near the west. The combustion of the burning materials of the curtain wall decoration spread the fire in a vertical direction, thus causing it to spread rapidly and in a reverse manner (from top to bottom and from outside to inside). Given these characteristics, this fire incident was classified as rare in the history of the nation.

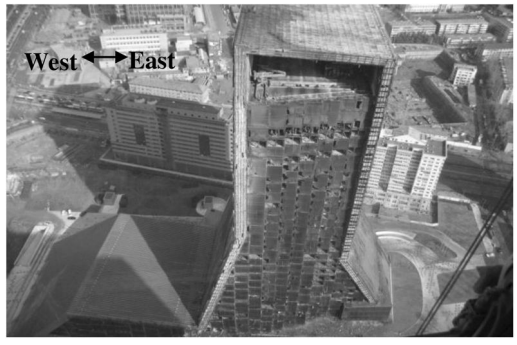

Figure 1. The south side of the high-rise building.

3 PROCEDURE FOR INSPECTION AND EVALUATION OF FIRE DAMAGE TO CONCRETE STRUCTURES

The flowchart of the inspection and evaluation procedure for the burnt concrete structures of the aforemetioned high-rise building is shown in Figure 2.

Several professionals conducted an emergency investigation and damaged zone division of the high-rise building after the fire incident. Their main objectives were as follows.

(1) Investigating the site. Each floor and room in the building was investigated, and all zones were documented through photographs and videos. Fire damage to the structures and decorations of the building were observed. The burned range, burned area, fire extinguishing materials, fuel types, and their placements were ascertained. The danger zones with falling debris were marked. The burned local zone of the building is shown in Figure 3.
(2) Determining the temperature of the fire. The duration of the fire was different in each floor, room, and structural component of the high-rise building. Therefore, the possible maximum temperature and the duration of the fire could be

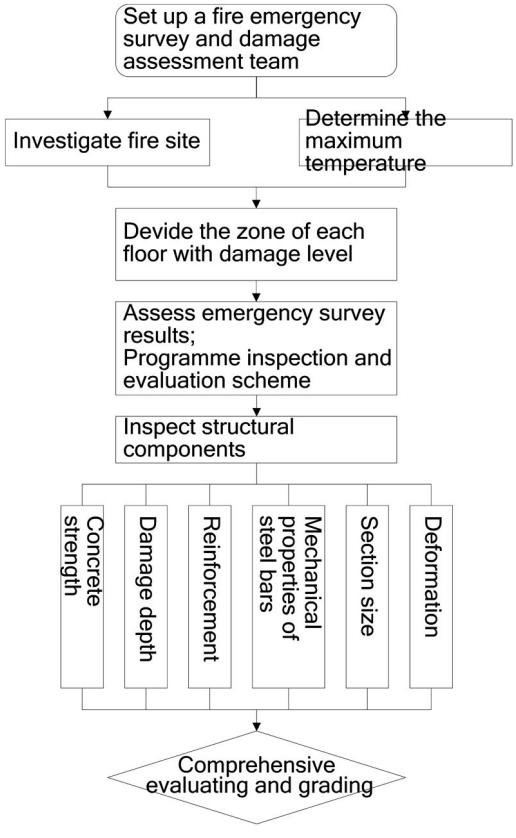

Figure 2. The inspection and evaluation procedure for the fire damage to the concrete structural components.

comprehensively analyzed and determined based on apparent damage (surface color, cracking and spalling), field-combustible residues, and the standard temperature–time curve set by the International Standardization Organization (ISO). The ISO 834 curve (ISO 843:2002), which is used frequently in China, is represented as follows:

$$T = T_0 + 345\lg(8t + 1) \quad (1)$$

where T(°C) is the average furnace air temperature at t minutes after the fire, and T_0 (°C) is the initial temperature in the testing furnace.

3.1 *Fire site emergency investigation and damaged zone division*

The maximum temperature of the fire was at approximately 1200°C, which was calculated based on Eq. (1).

(3) Dividing the building zones according to the degree of damage. The zones of each floor in the building were divided into three levels, which were preliminarily based on the results of the emergency investigation, the fire damage to the inner structures, and the maximum temperature of the fire. The primary characteristics of each level are shown in Table 1. The division according to the degree of damage is shown in Figure 4, with the 10th floor (where the cylindrical shear wall was located) as the main zone.

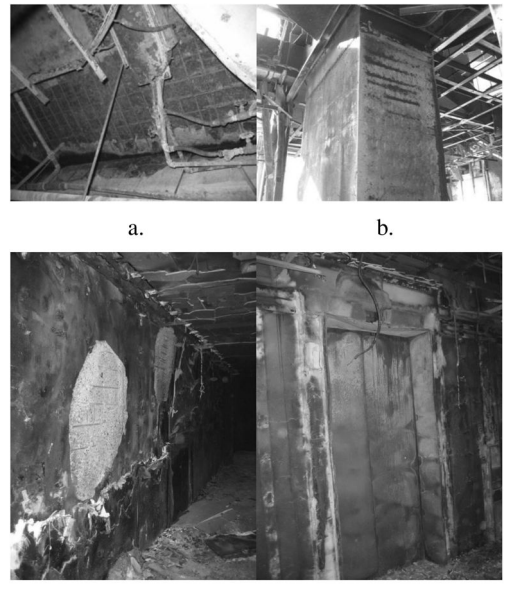

Figure 3. The damaged structures inside the building after the fire incident. a. The steel bars of the concrete roof slab were exposed. b. Cracks and map cracks were formed on the surface of the column. c. The concrete walls were spalled. d. The elevator doors were severely deformed.

Table 1. The characteristics of each zone based on the degree of damage.

Zone division	Zone characteristics
Undamaged zone (Zone A)	The concrete structures were not damaged by the fire, and only the exterior of local walls fell off. The surface of the structural components was blackened or had no obvious indicator of burns. The maximum temperature reached less than 300°C.
Slightly damaged zone (Zone B)	The structures around the elevator were not damaged by the fire. Spalled concrete covers were only observed on local walls. The steel bars were slightly exposed. The concrete had a pink color, and the maximum temperature ranged from 300°C to 600°C.
Seriously damaged zone (Zone C)	Fire damage near the elevator was serious, and the elevator doors were severely deformed (Fig. 3.d). Cracks were observed on the slab bottom and beam surface, and the steel bars in a large area of the concrete roof slab were exposed. The concrete cover of wall spalled, and the masonry burned down. The color of the concrete ranged from whitish gray to light yellow. The maximum temperature reached more than 600°C.

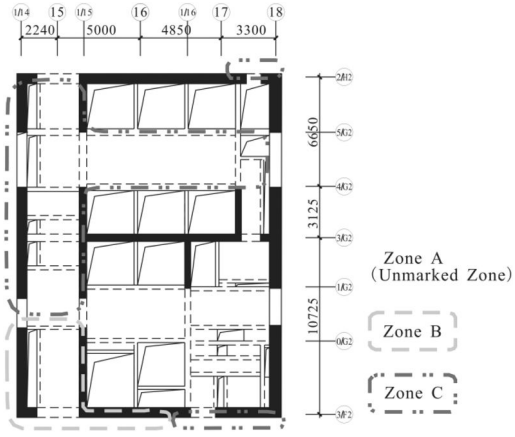

Figure 4. The main zone division of the 10th floor according to the degree of damage.

The preliminary division of the damaged areas was finished after the emergency investigation. The seriously damaged zones were found to be the floors above the 9th floor because the water cannons could only reach a height of approximately 55 m, which was located near the 9th floor of the building. This situation caused the fire to spread to the substructures of the building. Based on the results of the fire site emergency investigation and the preliminary fire damage evaluation, a conclusion was made that the main structures of the building were lightly damaged by the fire, but some of its local structures were seriously damaged. The state of the building after the fire posed no danger of overall collapse, but risks of falling objects were present in several local areas. Therefore, relevant precautions were recommended.

3.2 *Inspection of structural components*

The inspection plan was developed based on the damage assessment for each floor. The plan could be roughly divided into two parts: (1) the inspection of concrete strength and damage depth, and (2) the inspection of steel bars and the calculation of structural components. The lightly damaged zone (zone B) and the seriously damaged zone (zone C) were the main focus of the inspection.

3.2.1 *Inspection of concrete strength and damage depth*

Concrete structure appearance, concrete strength, and damage depth were inspected using the aforementioned plan. The loss of concrete strength was primarily influenced by factors such as temperature during heating, method of cooling, and duration of storage after the fire. Water cooling may further reduce the compressive strength of the concrete by 30% to 35% (Annerel & Taerwe 2012). The loss of concrete strength can be measured according to the maximum temperature reached by its surface. However, loss of concrete strength is extremely difficult to determine accurately by merely observing change in color because the interior and exterior of the concrete can reach different maximum temperature levels. Therefore, the use of devices and tests to measure concrete strength, rather than a simple observation of its appearance, is necessary. The rebound method and the drilling core sampling method were used in this study to determine concrete residual strength.

The inspection results show that the main structural components (beams, plates, columns, and walls) exhibited discoloration, crazing, cracking, and hollowing in different degrees; moreover, a few of these components demonstrated concrete spalling and reinforcement damage (Fig. 3.a). The strength of all undamaged concrete structural components satisfied the original design requirements, and the surface strength of the damaged structures was reduced to different degrees. The strength loss ratio of the seriously damaged structural components was between 13.8% and 31.1%. The damage depth of all burnt concrete structural components was between 5 mm and 100 mm, although in a few of them, damage was beyond the thickness of their protective cover.

The rebound hammer test combined with core sampling test were used to test the concrete strength for most burnt structural members of the building. And the test results for the components of the 10th floor show in Table 2 and Table 3. For this building, the concrete type of shear wall and column were C60 while the one of floor slab was C40 (according to Chinese code GB 50010:2010). The rebound hammer test was refer to Chinese code JGJ/T 23:2011, which provides the empirical value of concrete strength obtained from rebound hammer test.

3.2.2 *Inspection of steel bars and calculation of structural components*

The reinforcement of the structural components, the mechanical properties of the steel bars, the size of each section, and the deformation of the structures were inspected using the aforementioned plan. The strength of the steel bars was reduced after the concrete structures were exposed to the fire. The bond strength between concrete and steel also declined because of the differences in their expansion coefficients, which resulted in poor performance of the overall structure. Several inspection methods were adopted to determine the strength loss of the steel bars and the changes in bond strength and section size after the fire. A magnetic induction device was used to examine the structural reinforcement. The steel bars were sampled in the spalled and exposed zones, and a mechanical test was performed on the samples. The effect of the fire on the mechanical properties of the steel bars was also analyzed. A measuring tape was used to determine the dimension errors of the section size.

The results of the inspection showed that the number of beams, plates, columns, and walls in the main building satisfied the original design requirements. Moreover, the mechanical properties of the steel bars in the burnt zone satisfied the corresponding national

Table 2. The rebound hammer test result of concrete structural components in the 10th floor.

NO.	Structural type	Calculated strength (MPa) AVE	STDEV	Min	Empirical value (MPa)
12-13/E2-2.1/E2	floor slab	47.5	0.47	46.9	46.7
15-16/E2-3.2/E2	floor slab	48	0.92	46.2	46.5
11-12-1/D2-1.6/D2	floor slab	47.2	0.87	45.4	45.8
1/15-16-0/G2-1/G2	floor slab	48.9	0.92	48.1	47.4
1/15-16-4/G2-5/G2	floor slab	49.4	0.91	48	47.9
1/16-17-4/G2-5/G2	floor slab	42.9	1.09	40.1	41.1
17-18-2/H2	shear wall	65.5	0.65	64.8	64.4
1/14-2/H2-5/G2	wall	65.1	1	63.3	63.5
1/15-3/G2-4/G2	wall	66.4	0.52	65.6	65.5
16-1/16-3/F2	wall	65.3	0.51	64.6	64.5
3/F2-0/G2-1/15	wall	66.7	0.44	65.4	66
15-3/H2	column	66	1.69	63.6	63.2
13-3/H2	column	66	2.26	62.5	62.3
11-3/H2	column	67.9	2.2	65.2	64.3
15-3/E2	column	64.9	1.62	62.5	62.2
12-3/H2	column	64	1.42	62	61.7
12-13-2.1/E2	beam	46.6	1.16	44.1	44.7
16-1.3/E2-3/F2	beam	46.5	0.7	44.8	45.3
11-1/D2-1.6/D2	beam	52.3	2.56	48.7	48.1
12-1.1/E2-2.1/E2	beam	45.9	3.12	42.9	40.8
17-3.2/E2-2/F2	beam	47.6	1.03	46	45.9
16-17-2/F2	beam	47.3	1.4	44.5	45

Table 3. The core sampling test result of concrete structural components in the 10th floor.

NO.	Structural type	Condition	Strength (MPa)
16-17-4/G2-5/G2	floor slab	burnt	57.1
1/14-1/15-5/G2-2/H2	floor slab	burnt	48.2
1/15-1/G2-4/G2	shear wall (outward)	burnt	57
1/15-3/F2-0/G2	shear wall (outward)	burnt	64.6
17-18-3/F2	shear wall (outward)	burnt	57.5
1/15-1/G2-4/G2	shear wall (inner)	unburnt	61.1
1/15-3/F2-0/G2	shear wall (inner)	unburnt	72.4
17-18-3/F3	shear wall (inner)	unburnt	58.2
17-18-3/H2	shear wall	burnt	68
17-18-3/H2	shear wall	unburnt	82
16-3/H2	column	burnt	71.8
13-3/H2	column	burnt	65.3
16-3/H2	column	unburnt	82.2

standard in China (GB 50010:2010). The fire had no significant effect on the mechanical properties of the steel bars in the concrete structures and its effect on the mechanical properties of the steel bars in other structural components was not serious. The section size of the inspected structural components satisfied design requirements; however, the deflections of several structural components exceeded the maximum allowable value in the Chinese national standard (GB 50010:2010).

3.2.3 *Evaluation of fire damage to structural components*

The Shanghai City standard DBJ 08-291 (DBJ 08-291:1996) and the national technology standard CECS 252 (CECS 252:2009) are used in China for evaluating fire damage to concrete structures. The former classifies fire damage to concrete structural components into four grades primarily based on three aspects, namely, structural bearing capacity, cracks, and deformation. The latter provides a more comprehensive evaluation criteria based on concrete appearance, strength loss, cracks, bond strength between the concrete and the steel bars, deformation, and other factors. Both standards are divided into four grades. Several Chinese researchers also proposed their own evaluation criteria for assessing fire damage to concrete structures based on different projects and experiences (Yuan 1997; Min 2000; Zhai et al. 2009; Guo & Shi 2011). However, current evaluation criteria are mostly qualitative, and usually serve as guides in practical applications. Therefore, current standards, expert experiences, and project-specific conditions should be combined to evaluate damage in burnt buildings. Four fire damage grades are determined to evaluate damage on concrete structural components. The evaluation criteria for each damage grade are described in Table 4.

The concrete structural components in the burnt high-rise building were evaluated and graded based on the criteria described in Table 4. Based on the evaluation results, no grade IV damage on the concrete structural components in all floors of the building was observed. The 1st, 3rd, 4th, 6th, 26Eth, and 28th floors both suffered slight fire damage, and the highest grade of fire damage to their structural components was grade I. The 19th, 20nd, 24th, and 26Ath floors both suffered medium fire damage, the highest grade of their structural components was II. The 2nd, 5th, 7th to 13th, 15th, 17th, 26Dth, and 27th floors both suffered more serious fire damage, and the damage grades of structural components reached III.

4 SUGGESTIONS FOR REPAIRING AND REINFORCING DAMAGED CONCRETE STRUCTURES

The following measures are recommended for repairing and reinforcing damaged structures:

(1) For slightly damaged structural components (grade I), the dirt on the surface and the burnt paint layers should be cleaned first before the structures could be redecorated and repainted.
(2) For structural components with medium damage (grade II), the depths of damage and spalling are less than the thickness of the protective layer of the concrete, and no steel bar is exposed. Therefore,

Table 4. Fire damage grades and their evaluation criteria for concrete structural components.

Grade	Evaluation criteria
I (Slight)	The structural components have no obvious damage. The color of the concrete surface is either unchanged or is merely blackened by smoke. Loss of concrete strength is not apparent. The maximum temperature reaches less than 300°C.
II (Medium)	The structural components are slightly damaged. The color of the concrete surface ranges from pink to rusty red. Cracking and spalling occur on the local surface of the structural components. Loss of concrete strength is slight. None of the reinforcing bars are exposed, and the damage depth is less than 20 mm. The bond strength between the concrete and the steel bars is slightly damaged. The maximum temperature ranges from 300°C to 600°C.
III (Serious)	The structural components are obviously damaged. The color of the concrete surface ranges from white to grey. The structural components have numerous cracks. Loss of concrete strength is considerable. The steel bars are exposed in the local area, and the damage depth is greater than 20 mm. The bond strength between the concrete and the steel bars is seriously damaged. The maximum temperature ranges from 600°C to 900°C.
IV (Extreme)	The structural components are seriously damaged. The color of the concrete surface is light yellow. The structural components have numerous wide cracks in the vertical and horizontal directions. Loss of concrete strength is serious. The reinforcing bars are exposed in most areas, and the concrete covers have spalled off. The bond strength between the concrete and the steel bars is seriously damaged, and several steel bars are burned down or distorted. The maximum temperature reaches more than 900°C.

only the concrete cover needs to be repaired. However, loose, burnt concrete should be cleaned first and cracks in the structural components should be covered with better-quality concrete before repairs begin. The reinforcing bars should be rustproofed.

(3) For seriously damaged structural components (grade III), the increasing section method can be used to make repairs. The damaged concrete should be completely cleaned, and additional steel bars should be welded and anchored into a structure. Better-quality concrete should be used to repair the structure.

5 CONCLUSIONS

A procedure for inspecting and evaluating fire damage to concrete structures is proposed based on the case of a high-rise building in Beijing which caught fire in 2009. The procedure can be summarized as follows: emergency investigation of a fire site, determination of maximum temperature reached, division of fire-damaged zones, inspection of concrete structural components, and comprehensive evaluation of these components. A scientific and reasonable procedure for inspecting and evaluating fire damage to structures is generally more useful than a qualitative approach

Such a procedure enables accurate determination of the degree of damage to structural components, and consequently, proposes economical and reliable repair and reinforcement measures. A scientific and reasonable procedure also provides more efficient fire-resistant structure designs developed based on prior experiences with fire incidents. Given that no perfect procedure or standard for inspecting and evaluating fire damage to structures is yet available, existing methods are frequently combined, whether external or internal, qualitative or quantitative, or technology- or experience-based. However, the results of these methods are usually affected by subjective factors which may vary to a certain extent. Therefore, research on indicators and criteria for evaluating fire damage should be strengthened. Moreover, the theoretical system for inspecting and evaluating fire damage to concrete structures should be improved further.

REFERENCES

Annerel, E. & Taerwe, L. 2012. Innovative materials and techniques in concrete construction: Chapter 18 Assessment of the fire damage of concrete members after fire exposure: 283–290. New York:Springer.

ASCE 29-05:2007. 2007. Standard calculation methods for structural fire protection. American Society of Civil Engineers, Reston.

CECS 252:2009. 2009. China Standard: Standard for building structural assessment after fire. China Project Construction Association, Beijing: Plan Press of China.

DBJ 08-21:1996. 1996. Shanghai Standard: Criteria of assessment for concrete element after fire. Shanghai: Shanghai Construction Committee.

EN 1992-1-2:2004. 2004. Eurocode 2: design of concrete structures. Part 1-2: general rule – structural fire design. CEN, Brussels.

Fan, J., and Lv, Z. 1999. Essentials of fireproof research in concrete structure. *Architecture Technology* 30(05): 319–320.

Fang, C., Wei, Q. & Liang, H. 2010. A method of projection pursuit evaluation based on genetic algorithm on damage of high strength concrete after exposed to fire. *Sichuan Building Science* 36(4):84–86.

GB 50016:2012. 2012. China Standard: Code for fire protection design of buildings. Ministry of Housing and Urban-Rural Development of the People's Republic of China, Beijing: Plan Press of China.

GB 50010:2010. 2010. China Standard: Code for design of concrete structures. Ministry of Housing and Urban-Rural Development of the People's Republic of China, Beijing: China Architecture & Building Press.

Guo, Z. & Shi, X. 2011. Experiment and Calculation of Reinforced Concrete at Elevated Temperatures: Chapter 14 Fire

Resistance Analysis and Damage Grade Evaluation of a Structure. Beijing: Tsinghua University Press.
Han, L. & Song, T. 2012. Fire safety design theory of steel-concrete composite structures. Science Press, Beijing.
ISO 834:2002. 2008. Fire resistance tests – Elements of building construction. International Organization for Standardization, Geneva.
JGJ/T 23:2011. 2011. Technical specification for inspecting of concrete compressive strength by rebound method. Ministry of Housing and Urban-Rural Development of the People's Republic of China, Beijing: China Architecture & Building Press.
Li, G., Han, L., Lou, G. & Jiang, S. 2006. Fire protection design for steel and steel-concrete composite structures of buildings. Beijing: China Architecture & Building Press.
Li, M. 2005. The fire damadge of high strength concrete and its comprehensive evaluation. PHD Thesis, Southeast University, Nanjing.
Li, M., Kao, H. & Qian, C. 2008. Fuzzy comprehensive evaluation method on damage of high strength concrete after exposed to fire. *Concrete* 30(06):8–10.
Li, Y., Tang, Y. & Zeng, Z. 2008. Development and trend of the research on fire resistance of reinforced concrete structures. *Journal of Catastrophology* 23(01):102–107.
Min, M. 2000. A comprehensive method for evaluating structures after fire. *Architecture Technology* 31(6):403–404.
Wang, W., Su, J., Han, Y., Ma, D. & Yin, C. 2008. A matter element model for comprehensive evaluation on the degree of fire-damage concrete. *Concrete* 30(01):20–22.
Yang, X. 2010. The investigation of the fire accident in CCTV. *Journal of labor protection* 04:36–39.
Yuan, Q. 1997. Evaluation the fire damage to building structures based on a project. *Guangdong Civil and Architecture* 02:42–47.
Zhai, C., Dai, W., Wang, W. & Xiao, W. 2009. Safety appraisal and strengthening for a building after fire. *Construction Technology* 38(6):67–69.

This page intentionally left blank

Concrete Solutions – Grantham et al. (Eds)
© 2014 Taylor & Francis Group, London, ISBN 978-1-138-02708-4

Behaviour of High Strength Concrete (HSC) under high temperatures

H. Kew, T. Donchev, D. Petkova & I. Iliadis
Kingston University London, UK

ABSTRACT: The current study investigates the behaviour of high strength concrete (HSC) with strength class C45/55 and C60/75 under high temperatures and compares the test data with the results for a control mix with strength class of C30/37 (EN 1992-1-1:2004). Samples were heated up to temperatures of 100°C, 200°C, 300°C, 400°C, 500°C, 600°C and 700°C. Thermocouples of type K were inserted inside dummy samples to ensure that the specimens achieved the required temperature. The specimens were then tested for compression strength. The study discovered that all three concrete mixes exhibited critical changes when heated between 300°C and 500°C. However at temperatures between 300°C and 500°C, HSC exhibited more pronounced rates of strength loss as compared to other concrete mixes.

1 INTRODUCTION

In recent years, high strength concrete (HSC) classified as a "state of the art material" has been used widely in many types of structures due to its excellent performance and effectiveness. The beneficial factor for HSC development and its application is the availability of a significant variety of additives and admixtures needed for its production. Due to this, HSC provides many benefits such as high strength, better durability, high modulus of elasticity, reduced deformability and ease of manufacture (Nawy, 1996). The application of HSC in many diverse environments including high temperatures such as power plant stations, in the chemical industry as well as in aspect of fire protection of structures, demands an extensive knowledge of HSC behaviour. The purpose of the current study is to investigate and compare the residual strength of HSC when exposed to elevated temperatures.

2 BACKGROUND

Based on recent studies of the effects of elevated temperatures on the properties of high performance concrete, it has been concluded that the characteristics of high-strength concrete differ from that of normal performance concrete when subjected to temperatures above 50°C (Bazant and Kaplan, 1996). HSC can be classified as a material specially designed to provide many benefits in the construction of concrete infrastructure.

According to the American Concrete Institute Committee (1997), HSC is designed to have a specific strength of 42 MPa or more at 28 days. High performance concretes having strength of around 70 to 80 MPa, are often used in a broad range of applications. As Neville (2011) states, further research about HSC is essential in order to exploit the effect of its extraordinary high modulus of elasticity. Other factors, such as the increased strength, the lower permeability and its high resistance to the phenomenon of abrasion are of significant importance for its wider applications.

The length of exposure to high temperatures affects the loss of compressive strength considerably. When the duration of exposure is one hour or more, HSC loses its strength significantly. The most considerable loss appears when exposure is between 1 and 2 hours. After 2 hours or more, residual strength decreases to 70, 60 and 45% respectively at 200°C, 400°C and 600°C (Bazant & Kaplan, 1996). According to Phan (1996), three test methods usually known as stressed, unstressed and unstressed residual strength tests have been used in most experimental works on the fire performance of concrete under high temperatures.

Immediate heating can cause enormous volume changes as well as thermal shrinkage and creep connected with considerable loss of water. In extreme cases when fire is fast developing, explosive corner spalling of concrete might appear. As Khoury and Anderberg (2000) stated, HSC has a significantly higher tendency for explosive spalling than normal strength concrete. The main reason for this behaviour is that spalling is related to the low permeability.

Experiments conducted by Phan et al. (1996) on the behaviour of high strength concrete under high temperatures used steady state temperature test conditions. The cooling process has an effect on the residual strength. Several cooling techniques were tested by Peng et al. (2006) and it was found that when conventional concrete cools down with spraying water it faces severe damage. The cooling process will have an effect on residual strength as well. When concrete is exposed to high temperatures of 200°C and above and left to cool down under natural conditions its residual strength can be higher compared to samples that are exposed to water spraying conditions. The activation of additional hydration of residual cement in

Table 1. Concrete mix constituents.

Mix constituents	Mix 1: Mix C40 Control	Mix 2: Mix C60	Mix 3: Mix C80
Cement, kg	60.90	97.50	120.00
Water, l	29.25	25.25	22.25
Sand, kg	86.70	79.05	68.10
Thames Valley, kg	175.80	146.70	138.15
Superplasticizer*	–	0.97	1.20

*SIKA Viscocrete 25 PM

concrete happens at elevated temperatures. It develops to a lesser degree when there are rapid cooling regimes like water spraying.

As Bailey and Khoury (2011) stated, at temperatures between 100°C and 200°C water is driven off from high strength concrete and the hardening of cement paste is enhanced causing a steep increase in compressive strength, an effect known as curing. Some curing effects have been monitored during the experiments in this study as well.

According to the Concrete Society (2008), when concrete is exposed to temperatures up to 300°C the residual strength is not affected to a considerable extent. Having in mind the above mentioned publications for the current research, several limitations were accepted such as gradual increase of the temperature during heating, relatively slow cooling process and drying the samples before testing to avoid explosive spalling.

3 EXPERIMENTAL SET UP

The effect of high temperatures on HSC with different strengths C30/37, C45/55, and C60/75 was investigated in this research. Based on measured values of the average strengths further in this paper those 3 classes are indicated as C40, C60 and C80. The experimental program of the project included 3 phases. Phase 1 involved materials characterisation which includes sieve analysis, loose bulk density and particle density of aggregates. These were carried out in accordance with relevant British Standards. Phase 2 involved design of the concrete mixes (Table 1) and preliminary trial mixes in order to choose the correct superplasticizer and to achieve the desired compressive strength in each mix. Phase 3 involved heating of concrete specimens under high temperatures, cooling and testing for residual compressive strength.

3.1 *Materials*

Particle size distribution for Thames Valley natural aggregates was also conducted according to British Standards (BS EN 1097-3:1998). Loose bulk density and relative density was conducted according with BS EN 1097-3:1998. The loose bulk density for coarse aggregates was found to be 1.522 Mg/m^3 and for and for fine aggregates was 1.566 Mg/m^3.

Figure 1. Carbolite oven and position of the test samples.

Casting and compressive testing of the concrete specimens was carried out according to BS EN 12390-3:2009. The amount of water was adjusted to test fresh properties of concrete and get the required slump value. Cubes and mini- beams then were placed in the curing room for 28 days to achieve the required strength of the concrete. The curing room had a relative humidity of 95% and the samples were kept at 20°C. The slump value was recorded as 140 mm for control mix C40, 130 mm for mix C60 and 120 mm for mix C80.

3.2 *Heating and cooling down process*

Cubes and cylinders were heated in temperature increments of 100°C, 200°C, 300°C, 400°C, 500°C, 600°C and 700°C. For each temperature 3 cubes (150 × 150 × 150 mm) and 3 cylinders (150 × 300 mm) were used in order to measure the compressive strength. Therefore for each concrete mix, 24 cubes and 24 cylinders were cast. The total number of specimens used for testing was 144. 28 days after the casting and demoulding process was carried out, the three groups of concrete mixes were heated in a Carbolite Oven (Figure 1) to the required temperatures. The dimensions of the oven that was used for heating were 380 × 350 × 800 mm with a maximum heating ability of 800°C.

The specimens were placed in the oven carefully allowing the hot air to flow around the six specimens (three cubes and three cylinders) to allow even exposure to heat under the same conditions. The rate of heating of the samples was 5°C per minute. In order to control the temperature accurately, the heating process was controlled with the aid of thermocouples. The thermocouples were inserted in the centre of the dummy cubes and dummy cylinders. The thermocouples used were type K (Ni Cr/Ni Al) calibrated prior to the experiment.

Table 2. Compressive strength of cubes (N/mm^2).

Heating temperature	C40	C60	C80
20°C	48.3	66.7	82.6
100°C	41.9	64.1	85.2
200°C	39.1	73.7	95.1
300°C	36.0	61.8	90.6
400°C	31.3	62.0	53.0
500°C	9.2	36.6	19.6
600°C	3.6	14.2	17.2
700°C	1.2	11.2	10.9

Table 3. Compressive strength of cylinders (N/mm^2).

Heating temperature	C40	C60	C80
20°C	37.6	50.3	71.8
100°C	37.1	47.2	58.5
200°C	34.3	50.5	62.8
300°C	26.1	31.2	49.5
400°C	14.1	23.6	22.1
500°C	2.2	11.4	7.4
600°C	1.2	4.3	5.1
700°C	0.9	3.6	2.5

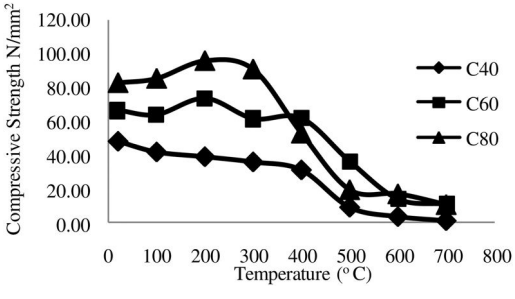

Figure 2. Compressive strength results of cubes (N/mm^2).

When uniform distribution of the temperature was achieved after a certain period of heating, the samples were kept in this condition for 10 minutes and a slow cooling process was adopted reducing the temperature to room conditions for 24 hours.

4 RESULTS AND ANALYSIS

4.1 *Compressive strength*

Compressive strength is tested and presented separately for cubes and cylinders as shown in Tables 2 and 3.

Figures 2 and 3 illustrate the results for the compressive strength of the tested samples from room temperature (20°C) to 700°C at 28 days for the three mixes (C40, C60 and C80). A gradual reduction in the compressive strength for C40 mix for cubes and cylinders was recorded. The cubic and

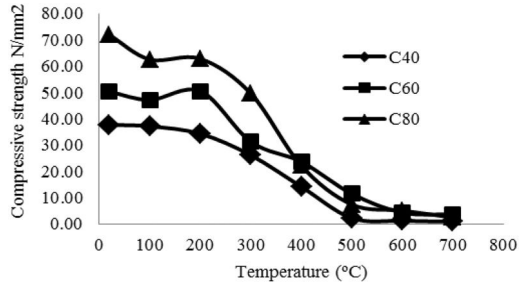

Figure 3. Compressive strength results cylinders (N/mm^2).

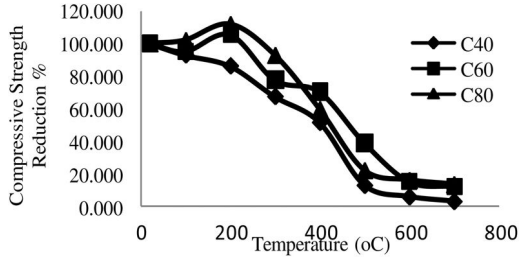

Figure 4. Combination of compressive strength reduction of cubes and cylinders in temperature range from 100°C to 700°C.

cylindrical average compressive strength were reduced from 48.3 to 1.2 N/mm^2 and from 37.6 to 0.9 N/mm^2 correspondingly.

The C60 mix had a minor reduction of strength up to 400°C for cubes and cylinders and more significant reduction between 400°C and 600°C. The total reduction was from 66.7 to 11.2 N/mm^2 for cubes and from 50.3 to 3.6 N/mm^2 for cylinders.

The C80 mix showed an increase of cube strength till 200°C probably due to curing effects, whereas a dramatic decrease was recorded between 300°C and 500°C. The values for strength above 600°C were approximately the same for the C60 and C80 mixes, while C40 mix showed much lower values.

The cubic and cylindrical average compressive strength were reduced from 82.6 to 10.9 N/mm^2 and from 71.8 to 2.5 N/mm^2 correspondingly. All 3 mixes exhibited similar significant reduction of the strength between 300 to 500°C but the reduction for samples with higher strength was more significant.

4.2 *Residual strength vs temperature increments*

Figure 4 shows the obtained results for the compressive strength reduction of the tested samples from 200°C to 600°C at 28 days for the three mixes (C40, C60 and C80). At a temperature range between 20°C to 200°C the strength of concrete increased gradually up to 10% for C60 and C80 mix because of the beneficial effect of the heating process on curing of the concrete (Figure 4).

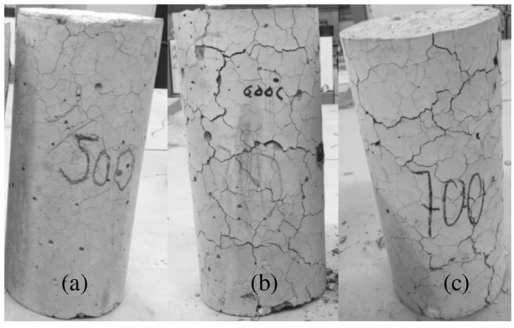

Figure 5. Appearance of cracks when concrete mix C80 samples were exposed to temperatures of (a) 500°C, (b) 600°C and (c) 700°C before compressive strength testing.

The heating process for the C80 mix started to affect the strength results above 200°C where the reduction percentage was very close to the results for the C60 mix. At 400°C the strength for the C80 concrete decreased by 40% where at 600°C, the C80 mix was able to sustain only 20% of its room temperature strength.

The C60 mix showed similar trends to the C80 mix as a slight increase in compressive strength at 200°C was recorded. At 400°C the strength for the C60 concrete started to decrease by 30% where at 600°C, the C60 mix was able to sustain only 20% of its room temperature strength.

A gradual reduction in the compressive strength for the C40 mix for cubes and cylinders was recorded in most temperatures.

The critical changes though are observed in the range of 400°C associated with change of $Ca(OH)_2$ to CaO. The results in the cubes and cylinders for C80 mix indicate a more rapid reduction in the interval 200°C to 500°C compared with other mixes (Figure 4).

4.3 *Crack appearance and development*

During the experiments, visible micro cracks on concrete samples were recorded when the temperature of exposure was above 400°C. A considerable increase in the number and size of cracks was recorded when specimens were exposed to temperatures of 500°C and above (see Figure 5).

The width of the cracks at 500°C for C80 mix was about 0.1–0.2 mm and the intensity was 1 crack per 5–10 cm^2 on the side surface of the specimens. For 600°C heating and cooling the intensity of the cracks was almost doubled and the crack widths were increased up to 1–2 mm. At 700°C the intensity of the cracks was approximately the same as per 600°C heated samples but the width of the cracks increased to 2–3 mm.

5 CONCLUSIONS

When HSC is exposed under elevated temperatures its material properties vary substantially with increased temperatures. The most significant changes in the behaviour of the three mixes were between 300°C and 500°C. Within this interval high strength concretes (HSC) had increased rates of strength loss in comparison with normal strength concrete. Several important conclusions concerning the behaviour of high performance concrete at high temperatures were revealed from the current project and are listed below:

- High strength concrete samples experienced a more significant increase of the initial strength due to curing effects.
- A significant reduction of strength for the C40 mix was recorded above 300°C with residual strength at 700°C of about 3%.
- Above 400°C the strength of C80 samples was generally less than the C60 samples at the same temperatures of heating.
- Above 600°C all mixes had strength below 20 MPa.
- The residual strength for C60 and C80 samples for temperature of heating 700°C was approximately 10% of initial strength.
- Reduction of the strength for the interval 200°C to 700°C was 97% for C40, 89% for C60 and 87% for C80 mix.

From investigating different types of mixes, high strength concretes experience a faster reduction of the compressive strength (both for cubes and cylinders) in comparison with lower strength concretes. As a result of the investigation it could be summarised that HSC is more heavily influenced at high temperatures than normal strength concrete.

REFERENCES

Albert, N., Rafat, S., Debicki, G. (2009) *Permeability of high performance concrete subjected to elevated temperature (600°C)*. Construction and Building Materials, Vol 23. pp. 1855–1861.

American Concrete Institute (1997) *State of the art report on high strength concrete.* ACI committee. Detroit: USA.

Bailey, C. and Khoury, G. (2011) *Guide to the performance of Concrete Structures in Fire*. The Concrete Society

Bazant, Z.P., Kaplan, M.F. (1996) *Concrete at High Temperatures. Material Properties and Mathematical Models.* Harlow: Longman Group Limited

BSI. *BS EN 1097-3:1998 Tests for mechanical and physical properties of aggregates – Part 3 an 6*. London

BSI. *BS EN 1992-1-1:2004 Design of concrete structures. General rules and rules for buildings.* London

BSI. *BS 8500-2:2006 Concrete – Complementary British Standard to BS EN 206-1 – Part 2: Specification for constituent materials and concrete*. London

BSI. *BS EN 12350-2:2009 Testing fresh concrete Part 2: Slump-test*. London

BSI. *BS EN 12390 3:2009 Testing Hardened Concrete. Part 3: Compressive Strength of Test Specimens*. London

Concrete Centre (2008) *Technical Report No.68. Assessment of fire-damaged structures*. The Concrete Society.

Kew, H., Donchev, T., Petkune, N. (2011). Behaviour of concrete containing lightweight expanded clay aggregates under high temperatures. *Concrete Solutions, Dresden,*

Germany, CRC Press, Taylor & Francis Group, September 2011. ISSN9780415616225; ISBN 978-0-415-61622-5.

Khoury, G.A. and Anderberg, Y. (2000) *Concrete Spalling Review.* Report Submitted to the Swedish National Road Administration.

Nawy, E.W. (1996) *Fundamentals of high strength high performance concrete*. Harlow. Longman Group Limited.

Neville, A. (2011) *Properties of concrete. 5th edition*. Pearson Education Limited

Peng, G.F., Bian, S.B., Guo, Z.Q., Zhao, J., Peng, X.L. and Jiang, Y.C. (2006) *Effect of thermal shock due to rapid cooling on residual mechanical properties of fibre concrete exposed to high temperature*.

Phan L.T. (1996) *Fire performance of High Strength Concrete: A report of the state- -of the Art.* Maryland: Gaithersburg.

Soutsos, M. (2010) *Concrete durability.* A practical guide to the design of durable concrete structures. London: Thomas Telford Limited.

This page intentionally left blank

Concrete Solutions – Grantham et al. (Eds)
© 2014 Taylor & Francis Group, London, ISBN 978-1-138-02708-4

Evaluation of geopolymer concrete for repair of rocket test facility flame deflectors

C. Montes
Louisiana Tech University, Ruston, LA, USA

D. Allgood
NASA Stennis Space Center, MS, USA

E. Allouche & R. Islam
Louisiana Tech University, Ruston, LA, USA

I. Tham
ML Smith, Ruston, LA, USA

ABSTRACT: A joint research effort by Louisiana Tech University (LTU) and NASA Stennis Space Center (SSC) was established to develop refractory geopolymer concrete. In preliminary tests, geopolymer was used to complete small repairs of the floors and walls of the refractory-lined flame trench at the SSC E-1 Cell 3 rocket engine testing facility. These repairs were then exposed to high temperature exhaust plumes of a 1780 kN class LOX/RP-1 engine. Subsequently, a controlled study was conducted of the geopolymer's performance under direct rocket plume impingement conditions. The NASA-SSC Diagnostic Test Facility (DTF) thruster, which is a 5.78 kN LOX/GH2 rocket engine, was used to generate the necessary supersonic plume environments to produce direct impingement on refractory test panels 30 cm wide × 60 cm × 15 cm deep. Various geopolymer and commercial grade formulations were tested. Data collected included surface profiles of the test panels giving localized erosion rates during the test.

1 INTRODUCTION

Geopolymer Concrete (GPC) is an emerging class of cementitious material, which offers a sustainable, low energy consuming, low carbon footprint, 100% substitute to Portland cement as a cementitious binder in construction applications (Davidovits, 2005). Geopolymer research at Louisiana Tech University is directed towards converting locally available Class F fly ash into a high performance refractory material that can be used as a monolithic refractory for applications under extreme conditions of temperature and pressure.

The term "geopolymers" refers to a 3D polymeric network of alumino-silicate binders. The polymerization process involves a rapid reaction of silico-aluminate minerals in the source material with the alkali metal hydroxide/silicate activator solution. The outcome of the polymerization reaction is a 3D polymeric chain/network structure of Si-O-Al-O bonds. (Davidovits, 1991). Due to the absence of water in the geopolymer molecule, these binders are capable of maintaining thermal stability at temperatures up to 1000°C without a significant change in their structure (Barbosa & MacKenzie, 2003).

The fly ash source is of extreme importance for the fire performance of the resulting geopolymer, which tends to remain amorphous after high temperature exposure (Rickard *et al*, 2012). However, some authors (Duxson & Lukey, 2007) have found crystallization at temperatures as low as 600°C, which suggests that the highly variable composition of geopolymer raw materials, especially fly ash, has a high impact on the type of crystallization. Heating and cooling conditions also play a role in this matter. Duxon also found that the choice of alkali is also of significant importance for thermal expansion. Unlike conventional refractories, some geopolymers have been found to have increased compressive strength after being exposed to elevated temperature (Kong, *et al*, 2007). This is especially important when comparing with Portland cement, which is highly susceptible to fire (Sanjayan & Stocks, 1993).

The development of robust monolithic refractory materials with improved physical properties for aerospace applications is directly in line with the missions of NASA. The application of a high performance refractory material to rocket engine flame deflectors will significantly improve support infrastructure at NASA launch and rocket propulsion test facilities.

The current paper describes the development and testing of a high temperature performance refractory geopolymer concrete that was performed at

Table 1. Fly ash characteristics.

Oxide	% wt.	Phase	%wt.
SiO_2	59.32	Quartz	12.2
Al_2O_3	19.72	Mullite	4.8
CaO	6.90	Amorphous	83.0
Fe_2O_3	7.22	(% >45 μm)	62.97
MgO	2.23	Specific gravity	2.23
SO_3	0.36		
Na_2O	1.11		
K_2O	1.27		
TiO_2	1.00		
Moisture	0.08		
LOI	0.15		

Table 2. Aggregate used to produce geopolymer concrete.

Aggregate type	Mullite-based	Alumina-based
Chemical composition	50% SiO_2, 46% Al_2O_3	99.7% Al_2O_3
Phase composition	65% Mullite, 20% Glass, 15% Cristobalite	99.7% Corundum
Specific gravity	2.6	3.7
Water absorption	3.6%	1.65%
Melting point	1650°C	2000°C

NASA Stennis. Geopolymer concrete was placed in the NASA-SSC E1 test stand and exposed to large-scale rocket exhaust plumes. Additionally, geopolymer concrete panels were tested during a 2-week comprehensive program, where the NASA-SSC Diagnostic Test Facility (DTF) thruster was used to generate supersonic plume environments on a 30 cm wide × 60 cm long × 15 cm deep refractory panels. The DTF operates on LOX/GH2 propellants producing a nominal thrust of 5.78 kN. The DTF operating conditions and facility configuration were selected to produce heating rates that were of the same magnitude as that of the full-scale engine tests.

2 LABORATORY TESTS

2.1 *Raw materials*

Fly ash from CLECO's Dolet Hills Power Station was used due to its proximity to the SSC and its high quality and consistency. The chemical and phase composition and other characteristics of the fly ash are summarized in Table 1.

For the activation, a liquid silicate with a SiO_2/Na_2O ratio of 3.22 in a 37.2 weight percent solution in water and a viscosity of 180 centipoises was utilized. Sodium hydroxide in pellets was used to obtain the desired Na:Al ratios in the final geopolymer. Table 2 summarizes the types of aggregate used for this project.

2.2 *Geopolymer formulation*

The reactive components of the fly ash were calculated based on its amorphous component. Then, an activation system was formulated to yield a Si:Al ratio between 2 and 3. A Na:Al ratio between 1 and 2.5 was kept throughout the experimentation.

2.3 *Test results*

Mechanical and thermal tests were conducted at Louisiana Tech to evaluate the quality of the geopolymer concrete.

Mass loss laboratory tests were conducted at Louisiana Tech University to evaluate the performance of geopolymer under flame exposure. A torch flame of 1300°C was directed at geopolymer cubes produced with Tabular Alumina and M47. The setup of the torch can be seen in Figure 1. Mass loss was evaluated for different geopolymer concrete formulations and it is shown in Table 3.

Figure 1. Geopolymer cube exposed to a flame of 1300°C.

Table 3. Summary of mass loss results after flame tests.

Formulation	Mass loss (%)
Geopolymer Paste	2.56
Geopolymer Coating	1.70
Geopolymer with Alumina Aggregate	0.70
Geopolymer with Mullite Aggregate	1.45
Geopolymer with Tabular Alumina Ambient Cured	1.22

3 PRELIMINARY EVALUATION OF GEOPOLYMER AT THE E-1 CELL 3 TEST STAND

Information from computational modeling, laboratory testing, and concrete guideline ACI 211.1 was incorporated in Louisiana Tech's geopolymer mix

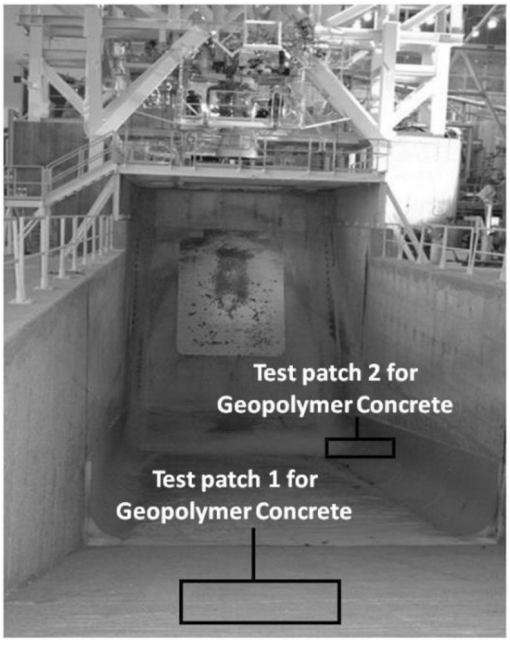

Figure 2. Location of the first two geopolymer repair sections at E-1 Cell 3.

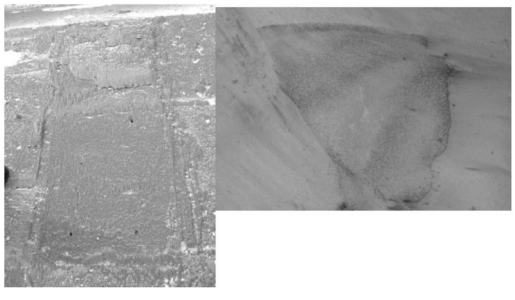

Figure 3. Geopolymer sections after rocket engine test.

design software to create a formulation to be tested at NASA-SSC Test Facility (E-1 Cell 3). This formulation was installed on a panel of dimensions 30 cm.–15 cm. horizontal × 120 cm.–0 cm. up slope × 120ft. thick = 56.53 lt. on top of the trench and an additional 10 cm × 10 cm × 10 cm. patch on the lower right hand side part of the trench (Figure 2). The slab was cured using a heating blanket for 24 hours. A smaller second patch was also casted with a slightly modified geopolymer formulation.

The geopolymer sections of the flame trench were examined after a nominal rocket engine test which lasted approximately 55 seconds producing temperatures as high as 2200°C. The appearance of both sections after the test is shown in Figure 3.

The geopolymer material was observed to erode/ablade at nearly identical rates as the surrounding commercial grade refractory material. There was no large-scale loss of geopolymer material and no indication of de-bonding of the geopolymer from the surrounding refractory of the concrete substrate. The geopolymer material has since undergone exposure to numerous subsequent engine tests with continued excellent performance.

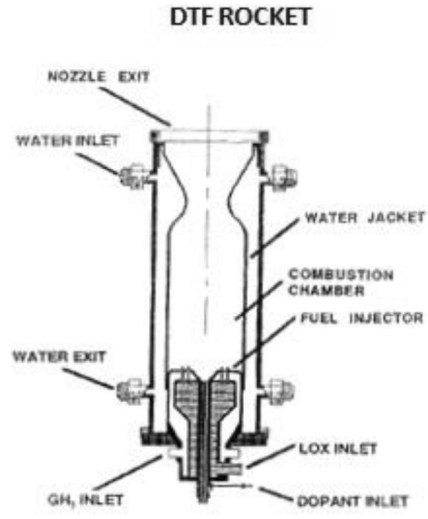

Figure 4. Schematic of the DTF rocket engine.

4 DIRECT PLUME IMPINGEMENT TESTING OF GEOPOLYMER

4.1 *Test setup*

The NASA Stennis Diagnostics Testbed Facility (DTF) rocket engine was used in this study. The DTF engine is a 5.78 kN gaseous-hydrogen/liquid-oxygen rocket engine that has been designed to produce plume properties (temperature and pressure at first mach diamond) that are very similar to the SSME (Tejwani et al, 1992). A schematic of the engine is given in Figure 4. Typical operating conditions of the engine are a chamber pressure of 3.45 MPa (relative to vacuum) and mixture ratio (O/F) of 5.0. For the current project, the chamber pressure was increased to approximately 4.33 MPa and O/F of 3.8, where the LOX and GH2 flow rates were on average 1 and 0.26 kg/sec respectively. The DTF engine was fitted with a bell nozzle that had an exit-to-throat area ratio of 6.15. These conditions were selected to produce dynamically similar data for the larger scale E-1 Cell 3 facility. Table 4 is a summary of the DTF nominal operating conditions and estimated plume properties. The plume properties are nominal predicted values obtained from the NASA Chemical Equilibrium Analysis Code (Gordon and McBride, 1994).

Test durations were limited to prevent excessive erosion of the test panels and subsequent plume detachment. A cumulative series of short duration (5 seconds) tests were conducted for each panel until a 55 second

Table 4. Nominal DTF engine parameters and corresponding estimations of Nozzle exit conditions.

Engine Parameters		
D_{NE}	Nozzle Exit Diameter	7.4 cm
AR_{NE}	Area Ratio of Diverging Nozzle	6.15
P_o	Combustion Chamber Pressure	4.3 MPa
O/F	Combustion Chamber Oxygen-to-Fuel Ratio	3.8
Nozzle Exit Conditions		
P_{NE}	Nozzle Exit Pressure	0.095 MPa
T_{NE}	Nozzle Exit Temperature	1234.4°C
M_{NE}	Nozzle Exit Mach Number	2.98
MW_{NE}	Nozzle Exit Molecular Weight	9.676
γ_{NE}	Nozzle Exit Ideal Gas Ratio of Specific Heats	1.27

total duration was achieved or the plume became too severely detached. Single long duration tests lasting up to 55 seconds were also planned to verify if the data was independent of test duration (i.e. thermal equilibrium is reached). Engine parameters and estimations of nozzle exit conditions can be seen in Table 4.

4.2 *Test panel configuration*

A steel structure was designed to support ablative refractory panels under direct plume impingement by the DTF engine. The panels were oriented at an angle (θ) of 30 degrees off plume axis as depicted in Figure 5. A 30-degree impingement angle was selected as most static test stands at NASA have such angles so as to produce a turning of the plume with an oblique shock. If the plume were to be deflected at a more aggressive angle (e.g. 75 degrees), a normal shock would form producing excessive heating and reverse flow up the deflector wall. By maintaining a consistent deflector angle, the flow profile over the subscale ablative panels would be dynamically similar to that of a full scale facility. In addition to deflector angle, the separation distance of the engine from the deflector panel was important as it would affect the level of heating to the test panels. In all tests, the engine was positioned such that the nozzle exit plane was an axial distance of 20.3 cm (or 2.74 DTF nozzle-exit diameters) away from the test panels. This distance was selected based on an a-priori knowledge that this would place the deflector panel just downstream of the first Mach disk in the plume. As such, the heating rate to the deflector would be maximized. The impingement pressure and heating rates for this test configuration were estimated using computational fluid dynamics (CFD) modeling.

Each test panel was 60 cm long by 30 cm wide by 10 or 15 cm thick, where the length of the test panel was oriented in-line with the primary flow direction of the impinged gases. The width and length of the test panels were selected to be sufficiently large to allow the entire plume to impinge on the panel. Also, it was critical for obtaining accurate erosion data that the deflector was a

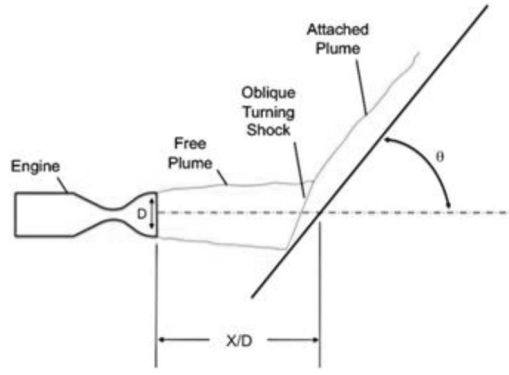

Figure 5. Engine-deflector geometry and orientation.

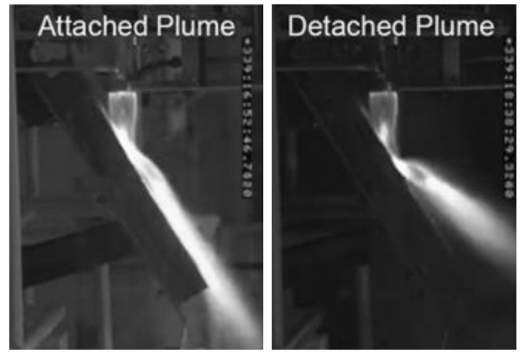

Figure 6. Example of plume detachment after excessive panel erosion.

sufficient size such that the primary impingement zone would not be influenced by the test panel dimensions. The refractory panel materials tested will be discussed in the next section.

The refractory test panels were evaluated by first performing a cumulative series of tests where each test consisted of a 5 second steady burn of the engine. The same test panel was then used during successive 5 second tests. Before and after each test, the surface profiles of the deflector panels were measured using a specially designed depth measuring gauge with an accuracy of +/−0.0254 cm. The surface profiles were measured across the panels on a 2.54 cm by 2.54 cm grid. Once the preliminary evaluation was completed, a single long duration test lasting up to 55 seconds was conducted using a new panel to obtain near steady-state erosion rate data (i.e. thermal equilibrium is reached). A 10 or 15 cm thickness for the test panel material was selected to avoid erosion thru the test panels during the maximum expected test duration. Total cumulative test durations were limited to prevent excessive erosion of the test panels and subsequent plume detachment (Figure 6).

4.3 *Test panel preparation*

All geopolymer test panels were prepared at the Geopolymer Laboratory at the Trenchless Technology

Table 5. Refractory panel designation and description.

Designation	Description
Test Panels Using Geopolymer	
GPM	Geopolymer mortar (trowable) with Tabular Alumina
GPC1	Geopolymer concrete grade 1 (Tabular Alumina)
GPC2	Geopolymer concrete grade 2 (Mulcoa 70)
GPC3	Geopolymer concrete grade 3 (Mulcoa 47)
UGPC1	Ambient cured GPC1
Test Panels Repaired with Geopolymer	
RGPM	GPM panel repaired with a new layer of GPM
RGPC	GPC1 panel repaired with GPM
RSEN	Sentinel RC panel repaired with GPM

Center of Louisiana Tech University. The concrete mix design for all of the samples was obtained using custom-developed software, developed at Louisiana Tech. The software utilizes user input such as raw materials' chemical composition, density, and absorption, together with the desirable properties of the application at hand to produce an initial geopolymer mix design. The initial mix design was then prepared in the laboratory and optimized as necessary.

Several samples of geopolymer concrete, mortar, and other commercial refractories were also repaired with geopolymer mortar (GPM) after the first plume test to evaluate adhesion to the parent material and reparability in general. Additionally, two samples had thermocouples installed with the intention of monitoring the heat evolution in the sample as the tests were being conducted. Two panels were manufactured for each geopolymer formulation. The control variables include type of refractory aggregates (Tabular Alumina, Mulcoa 70 and Mulcoa 47) and the grade of geopolymer product (concrete or trowable mortar). All the samples were subjected to standard geopolymer curing (60°C for 24 hours) with the exception of two specimens that were ambient cured for 28 days before testing.

Table 5 shows the samples that were tested during the two week program. Two repetitions (A, B) were used for each sample. In general, the samples were subjected to incremental 5-5-5-15-30 second flame exposure durations and to a 15 or 30 accumulated exposure, depending on the sample performance (e.g., if the plume became detached). The testing matrix shown below was developed to enable systematic evaluation of the performance of various formulations and grades of geopolymer as well as commercially available refractory products currently utilized by NASA SSC.

An attempt was made to measure the temperature profile of the geopolymer panels using embedded thermocouples. Ultimately, this proved to be unsuccessful. Most of the thermocouples melted before producing useful results, while others reached their upper range limit, which was below the actual temperature generated at the impingement zone. Future tests will incorporate thermocouples with higher temperature ranges.

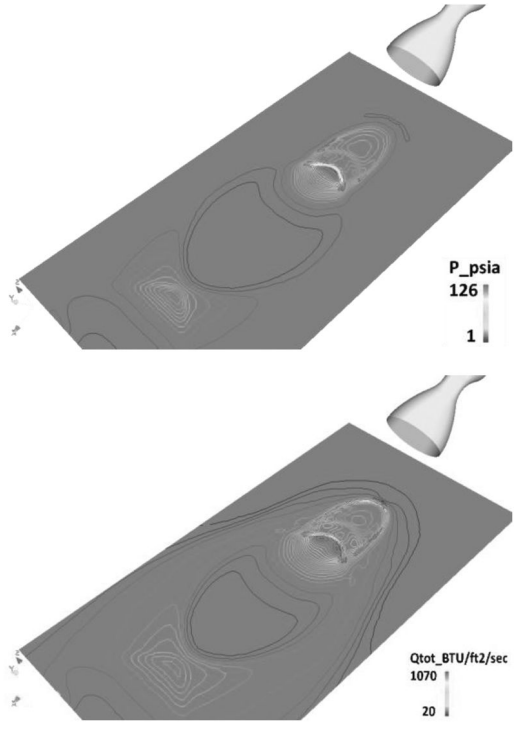

Figure 7. Predicted deflector panel contours of pressure (top) and cold wall heat flux (bottom).

5 RESULTS

Each refractory test panel was subjected to direct plume impingement from the DTF engine. The hot exhaust gases from the DTF engine impinged on the test panels at supersonic speeds, producing a complex pattern of intense shock induced heating and pressure loading as depicted in Figure 7. Figure 7 are results from NASA-SSC computational fluid dynamic (CFD) simulations of the plume induced loading on the 30 cm × 60 cm panel. The position of the DTF engine is also shown in the figures for reference. Due to 30-degree impingement angle of the plume to the panel (characteristic of rocket plume deflectors), the high heat-flux zone is elliptical in shape with maximum expected erosion in the downstream end of this elliptical impingement zone. This shape and distribution was confirmed for all test panels.

One of the critical parameters for a refractory-lined rocket deflector is the rate at which the materials will ablate/erode during a rocket test or launch. Based on previous testing of commercial grade refractories in this environment, it was of interest to obtain the erosion rate data for multiple short (5 seconds each) tests

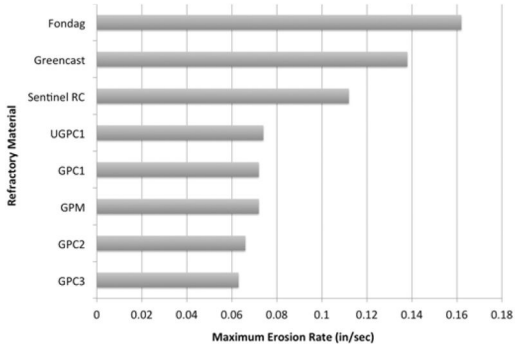

Figure 8. Maximum erosion rates when subjected to a 5-second DTF rocket firing.

on the same panel and for single long (15 second) duration tests. This classification of data would provide an understanding as to the material's sensitivity to transient thermal loads versus conditions where thermal equilibrium was reached in the heat-affected zone of the panel.

Comparing the maximum erosion (due to ablation and mechanical shearing) that was generated on each test panel provided a good overall indicator as to the relative performance of the refractory panels. Figure 8 shows the maximum erosion for all geopolymer formulations in comparison with some of the commercial refractories previously investigated by NASA. The data is for a single 5-second rocket firing on each panel. Under these short, transient conditions, all geopolymer formulations exhibited lower total erosion depths in comparison to the selected commercially available refractories. The data also indicated a relatively small sensitivity of the geopolymer ablative performance to the geopolymer formulations, namely GPC1-3 and GPM. The numeral values 1, 2 and 3 stand for aggregates with different refractory performance, with (1) being the material with higher chemical purity and (3) the material with lowest chemical purity. The GPM is a geopolymer mortar formulation. The letter "U" stands for ambient cured (other specimens were forced cured). Using the data from these tests, a cost-study could be performed to examine the most cost-effect approach for a particular application. These tests were also aimed at determining if the performance of the ambient cured grade geopolymer specimens matched that of their forced cured counterparts. Comparing UGPC1 to GPC1 showed only a small benefit in non-ambient curing of the material. This translates into significant savings in the installation costs of large-scale rocket deflectors.

While the above results provide an initial indication of the performance of the geopolymer materials, it does not provide any guidance on whether the material will continue to provide the same performance due to subsequence short firings or long-duration firings. Figure 9 shows the cumulative effect of rocket firings on the maximum erosion rates. Excluding GPC3, all

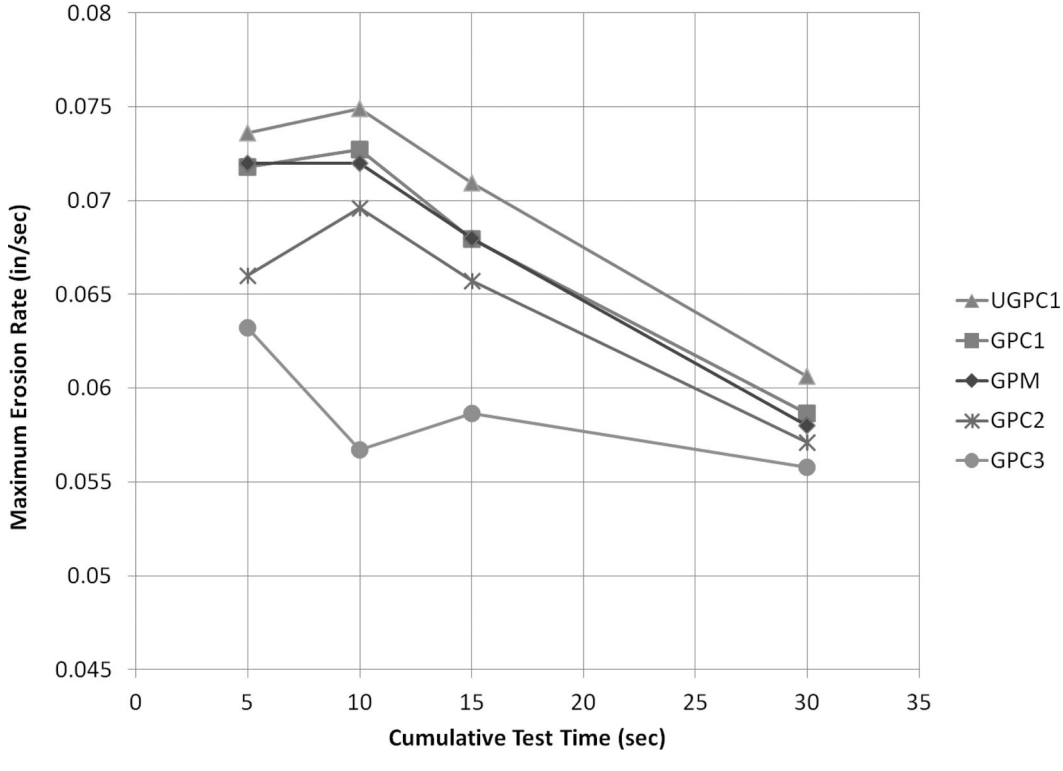

Figure 9. Geopolymer maximum erosion rates due to successive DTF rocket firings.

the other geopolymer formulations showed the same general trend in the maximum erosion rate with cumulative testing. Specifically, a near linear decrease in maximum erosion rate was observed as the overall exposure of the test panels to the rocket plume was increased. It is hypothesized that this behavior could be due to two factors: (1) the material was improving its resistance to erosion due to heat treatment or (2) the maximum heat rate was decreasing due to surface changes of the eroding test panel. In either case, the relative performance of each geopolymer formulation remained consistent over all cumulative testing. Namely, GPC3 showed the best performance while the ambient cured UGPC1 exhibited the poorest performance of the geopolymers. However, the UGPC1 performance is still quite competitive compared to commercial grade refractories as will be discussed in the next section.

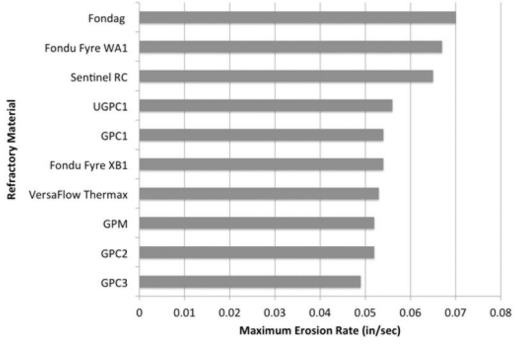

Figure 10. Maximum erosion rates after a single 15 second DTF rocket firing – geopolymer (branded "GP") and commercial products.

In most rocket engine test programs, the duration of the hot fire will not be of the order of a few seconds, but rather could occur over a significant period of time (minutes or even hours). Thus, it is critical that the material be able to withstand the thermal and shear loading of the rocket exhaust under long duration testing, i.e. where the material has reached some "steady-state" erosion behavior. To obtain this data, new refractory panels were fired upon for at least 15 seconds continuously. This provided enough time for a steady-state condition to be reached but not long enough to cause substantial erosion of the panel surface and thereby greatly affect the heating patterns. Figure 10 provides a direct comparison of all the geopolymer formulations to commercial grade refractories tested at NASA-SSC during this test program as well as earlier programs under similar conditions. The data shows that all geopolymer materials performed very well under these "steady-state" conditions. Their resistance to erosion by the rocket plume was greater than or comparable to the commercial grade refractory materials. This included the ambient cured geopolymer formulation UGPC1. Figure 11 is an example of the profiling images that were obtained after erosion measurements were taken.

Other tests were also conducted during the two-week program, including repaired geopolymer and Sentinel RC panels (Figure 12). All the panels were repaired with geopolymer mortar (GPM). One of the repaired Sentinel panels included an anchor to simulate the anchoring that takes place when repairing the NASA-SSC E-1 rocket flame deflector. Results showed that the adhesion of geopolymer to the parent surfaces was sufficient to withstand all the loads produced by direct rocket plume impingement, and that the use of mechanical anchors did not cause

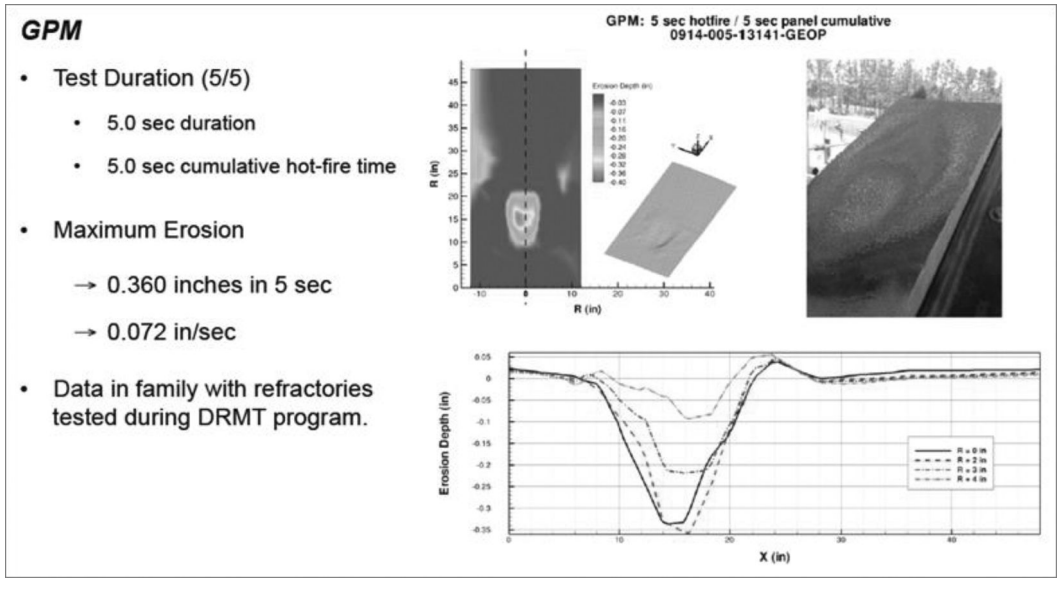

Figure 11. Profile of a GPM panel after the 5 second test.

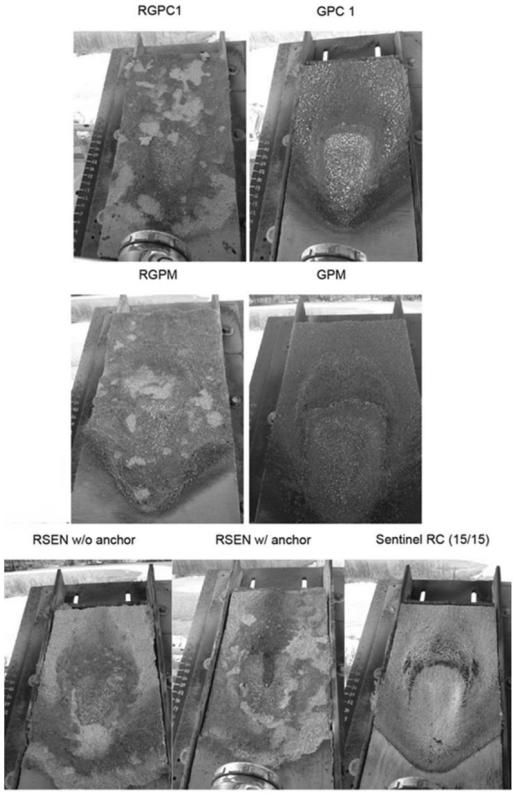

Figure 12. Repaired GPC1 panel (after 15/15 test) and original GPC1 panel (after 30/30 test). Repaired GPM with GPM panel (after 15/15) and original GPM panel (after 15/15) (middle). Repaired Sentinel panel without anchor after 15/15 test (bottom left), repaired Sentinel panel with anchor after 15/15 test (bottom middle) and original Sentinel panel after 15/15 test (bottom right).

any adverse effects. Specifically, the repaired panel behaved in a manner similar to the monolithic unit in spite of the fact the stainless steel anchor thermally ablated along with the Geopolymer material.

6 CONCLUSIONS

The current testing program showed that the LTU geopolymer products had an equivalent or in some cases superior resistance to rocket plume erosion compared to commercial refractories currently being tested by NASA Stennis Space Center.

Preliminary testing at Louisiana Tech demonstrated the geopolymer's ability to withstand thermal shock and exposure to flame. A computational model was created to find the optimal chemical ratios for geopolymer to be exposed to elevated temperatures. This information was incorporated in the geopolymer software to produce mix designs for field applications and panel construction.

Field testing at NASA Stennis demonstrated geopolymer's ability to withstand full-scale 55 second rocket engine testing in different sections of the flame trench.

Systematic testing of the geopolymer panels revealed erosion rates were lower in the majority of cases in comparison to commercial refractories for tests of the same duration. Geopolymer also proved to be a good candidate for the repair of existing commercial refractories due to its excellent adhesion to parent surfaces.

REFERENCES

Barbosa, V.F.F. and MacKenzie, K.J.D.Thermal behavior of inorganic geopolymers and composites derived from sodium polysialate. *Materials Research Bulletin*, 2003. **38**(2): p. 319–331.

Davidovits, J., Geopolymer chemistry and sustainable Development.The Poly(sialate) terminology : a very useful and simple model for the promotion and understanding of green-chemistry. *Proceedings World Congress Geopolymer 2005*, Saint-Quentin, France (Ed. J. Davidovits), p. 9–16. 2005.

Davidovits, J., Geopolymers: Inorganic Polymeric New Materials, *Journal of Thermal Analysis*. Vol. 37, p. 1633–1656. 1991.

Duxson, P., Lukey, G.C. and van Deventer, J.S.J. Thermal evolution of metakaolin geopolymers: Part 2 – Phase stability and structural development. *Journal of Non-Crystalline Solids*, 2006. **353**: p. 2186–2200.

Gordon, S. and McBride, B. J., "Computer Program for Calculation of Complex Chemical Equilibrium Compositions and Applications I. Analysis", NASA RP-1311, Oct. 1994.

Kong, D., Sanjayan, J. and Sagoe-Crentsil, K. Comparative performance of geopolymers made with metakaolin and fly ash after exposure to elevated temperatures. *Cement and Concrete Research*, 2007. **37**: p. 1583-1589.

Rickard, W.D.A., Temuujin, J., and A. van Riessen. Thermal analysis of geopolymer pastes synthesized from five fly ashes of variable composition. *Journal of Non-Crystalline Solids*, Vol. 358, 2012. p. 1830–1839.

Sanjayan, G. and Stocks, L. Spalling of High-Strength Silica Fume Concrete in Fire, *ACI Materials Journal,* American Concrete Institute, **90** (2), March–April, 1993, pp. 170–173.

Tejwani, G., Van Dyke, D. B., Bircher, F. E. and Gardner, D. G., "Emission Spectra of Selected SSME Elements and Materials", NASA Reference Publication, 1286, 1992.

NDT and diagnosis of problems

This page intentionally left blank

Concrete Solutions – Grantham et al. (Eds)
© 2014 Taylor & Francis Group, London, ISBN 978-1-138-02708-4

Combination of NDT techniques for studying external repair patches in concrete

D.G. Aggelis, S. Verbruggen, E. Tsangouri, T. Tysmans & D. Van Hemelrijck
Department of Mechanics of Materials and Constructions, Vrije Universiteit Brussel, Brussels, Belgium

ABSTRACT: One of the most commonly used techniques to strengthen steel reinforced concrete structures is the application of externally bonded patches in the form of Carbon Fiber Reinforced Polymers (CFRP) or recently, Textile Reinforced Cements (TRC). These external patches undertake the tensile stress of bending, constraining concrete cracking. Development of full-field inspection methodologies for fracture monitoring are important since the reinforcing layers are not transparent to allow visual observation of the material condition underneath. In the present study, Acoustic Emission (AE) and Digital Image Correlation (DIC) are applied during four-point bending of large beams to follow the damage accumulation. AE helps to determine the onset of fracture as well as the different damage stages through the registered shifts in AE rate, location of active sources and change in waveform parameters. Simultaneously, crucial information is supplied by DIC concerning the moments of stress release of the patches due to debonding and benchmarks the trends monitored by AE. Discussion is also done for the effect of acoustic wave propagation distance which in large components and in-situ can well mask the original information as emitted by the fracture incident. From the point of view of mechanics, conclusions on the reinforcing contribution of the different repair methodologies are also drawn.

1 INTRODUCTION

Classification of acoustic emission (AE) signals emitted during failure processes relative to the cracking mode enables assessment of the condition of a concrete structure. The reason is the sequence of fracture modes starts with concrete cracking due to moderate tensile stresses and leads to shearing phenomena before final failure. Therefore, reliable characterization of AE sources, may lead to warning before fracture reaches its final stage. The technique of AE uses piezoelectric sensors on the surface of the material to record the stress waves produced by the motion of the crack tips and transform them into electric waveforms, (Grosse & Ohtsu 2008). Basic waveform characteristics are; the maximum voltage of the waveform (amplitude, A in dB), the number of threshold crossings (counts), the duration (time between the first and last threshold crossings) and the rise time (RT in μs) which is the time between the first threshold crossing and the waveform peak amplitude, see Figure 1. A frequency indicator is the average frequency (AF in kHz), which is defined as the number of counts over the duration, while the central frequency, CF (centroid of the FFT spectrum in kHz) is also used. Additionally the "RA" value is the ratio of RT over A and is measured in μs/V. The number of recorded signals (hits) yields information on the active fracturing points and contributes to the monitoring of processes like fracture (Carpinteri et al. 2008, Karihaloo et al. 2013), creep (Verstrynge et al. 2009), corrosion (Uddin et al. 2006) and self-healing (Van Tittelboom et al. 2012). Localization of the sources is also possible in three dimensions if multiple sensors are used (Luo et al. 2006). In order to obtain qualitative information on the cracking mode several waveform shape parameters have been examined. In recent studies it is shown that frequency characteristics measured by AF, decrease for the shear mode of cracking relatively to the tensile. Additionally, RA increases substantially due to the different wave modes emitted. These trends have been exploited in laboratory conditions with quite successful characterization of the AE sources as to their mode (Aggelis 2011, Shahidan et al. 2013, Farhidzadeh et al. 2013). The classification is based on the AF-RA axes in which the tensile and shear cracking AE signal populations exhibit limited overlap in many laboratory cases so that they can be separated into clusters by a single line.

In this paper, the results of AE monitoring on externally reinforced concrete beams are presented. Three beam types are compared in a four point bending test: a reference beam, a beam with a Textile Reinforced Cementitious composite (TRC) as external reinforcement and a beam externally reinforced with a CFRP strip. The TRC consists of an Inorganic Phosphate Cement (IPC) matrix strengthened with 2D random glass fiber textiles.

The importance of this study is twofold. First the mechanical performance of the different reinforcing methods is evaluated compared to a reference beam

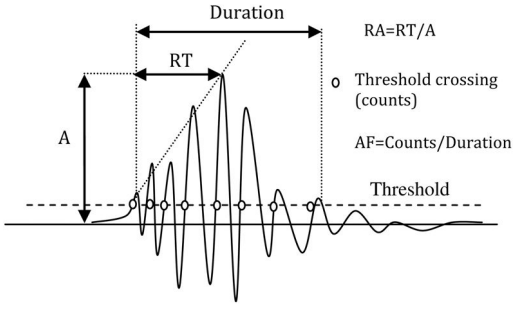

Figure 1. Typical AE signal and its main characteristics.

without external reinforcement. Additionally, since the external layers do not normally allow visual observation of the damage beneath, passive monitoring techniques are applied in order to build experience in evaluating the condition in a nonintrusive way. Acoustic emission is accompanied by digital image correlation (DIC) in order to confirm the damage in crucial loading moments. DIC is a non-contacting optical technique, capable of measuring and calculating displacements and strains by the comparison of subsequent pictures taken from 2 CCD cameras facing a speckle pattern applied on the specimen's surface. The combination of the DIC surface strain fields with the AE signals analysis benchmarks the bending/experimental results. Discussion is also done about the application of AE classification in large scale since the elastic waves are effectively attenuated and scattered by the heterogeneous nature of concrete.

2 EXPERIMENTAL DETAILS

2.1 *Materials and mechanical test*

Four-point bending tests with third point load were performed on the three beam types with a total length of 2.5 m (middle span length of 2.3 m) and height and width of 0.3 m and 0.2 m. The loading was displacement controlled by a servo-hydraulic actuator with an initial displacement rate of 0.2 mm/min. After the cracking moment of the beams was clearly surpassed (load of 60 kN), the displacement rate was increased to 2.0 mm/min.

The beams were cast with concrete of compressive strength of 35.0 MPa (Cube Strength), Young's modulus of 34.0 GPa and modulus of rupture of 5.3 MPa after 48 days.

The internal steel reinforcement (S500) consists of two longitudinal bars with a diameter of 16 mm and stirrups with a diameter of 6 mm placed every 100 mm in the shear zones of the beams. The material characteristics were not experimentally derived, so the standard values of 500 MPa for the yield stress and 200 GPa for the Young's Modulus are assumed.

The external TRC reinforcement covered the full bottom surface of the beam. It consisted of an IPC matrix reinforced with 16 randomly in-plane oriented

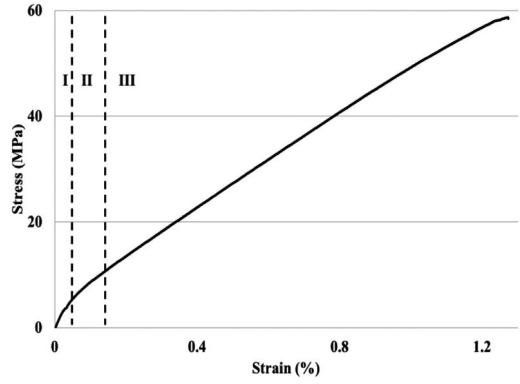

Figure 2. Stress strain relation of the TRC.

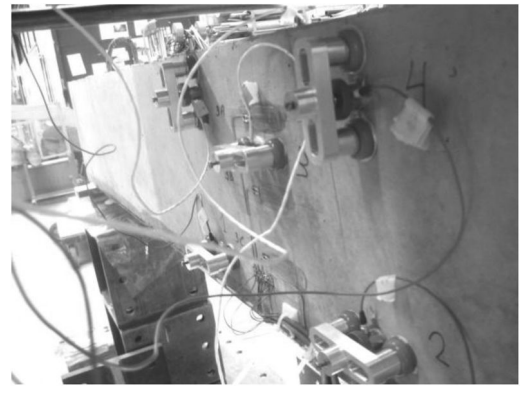

Figure 3. A snapshot during testing of the TRC reinforced beam with AE sensors. The magnetic clamping devices to support the sensors are also visible.

fibre textiles, being chopped strand mats Vetrotex M5, with a surface density of 300 g/m^2, resulting in a fibre volume fraction of 21%. These laminates have a tensile strength of 58.4 MPa, an ultimate strain of 1.2%, a Young's Modulus at the un-cracked stage (stage I) of 12.5 GPa and at the cracked stage (III) of 4.8 GPa. The tensile stress-strain behavior is depicted in Fig. 2.

The CFRP strip (TRADECC 2007) had a standard thickness of 1.2 mm and a width of 30 mm, so as to obtain the same ultimate load as the TRC reinforced beam, following the FIB bulletin 14 (CEB-FIB 2001). Only one tensile test was performed on a CFRP strip, resulting in a tensile strength of 2210 MPa and a Young's Modulus of 143 GPa.

In all the cases the external reinforcement was glued onto the concrete using a two-component epoxy glue (PC 5800/BL (TRADECC 2009)). Before attaching the reinforcement to the beams, the concrete surface was pretreated to remove the laitance layer.

2.2 *Acoustic emission*

Eight AE sensors were applied on the central part of the span. Five sensors were placed at one side, as shown in Fig. 3, and three at the top surface since the other

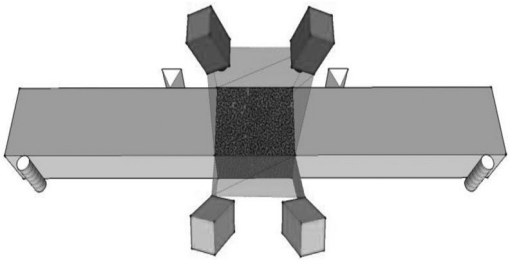

Figure 4. Schematic overview of the 2 DIC systems used.

two sides were covered by the DIC pattern. Three sensors were of the WD type with broadband response and center at 500 kHz while five were R15 (PAC) with resonance of 150 kHz. The sensors covered the center part of the beam spanning 30 cm, while the lowest were placed 50 mm above the bottom. There, two of the sensitive resonant sensors were placed since the damage was expected to start from the tensile side. Wideband sensors were placed at higher elevations. The threshold was set at 35 dB and the acquired signals were stored in a PAC micro-II 8 channel system. For the analysis in this paper the discussion is restricted to the broadband sensors in order to have a broader range of frequency values.

2.3 *DIC*

Two DIC systems were used to monitor the constant moment zone of the beams (central zone with a width of approximately 0.4 m). One pair of DIC cameras followed one vertical side of the beam and the second one the bottom side (Figure 4). Pictures were captured every 0.2 kN and every 5 seconds. The analysis was done using the VIC3D-2009 software package from Correlated Solutions where a subset size of 21 pixels, a step size of 5 pixels and a strain window size of 11 were used.

3 RESULTS

3.1 *Total activity and fracture mode*

Concerning the mechanical performance, the TRC reinforced beam exhibited a 37% higher maximum load compared to the reference (210 kN over 153 kN). The CFRP exhibited 190 kN, being in between. The externally reinforced beams exhibited some instantaneous load drops before reaching their maximum capacity which are results of partial delaminations of the CFRP strip and the TRC layer, see Figure 5.

The AE activity of the beams showed that the TRC layer was very effective in delaying the onset of cracking. This is evident in Figure 6 where the number of AE signals are shown for the three different beams. The reference beam exhibited its first AE "hit" at 4.8 kN and the CFRP reinforced one at 8.6 kN. However, the TRC started to register hits at the load of 11.3 kN. Additionally, for any sustained load the TRC registered less

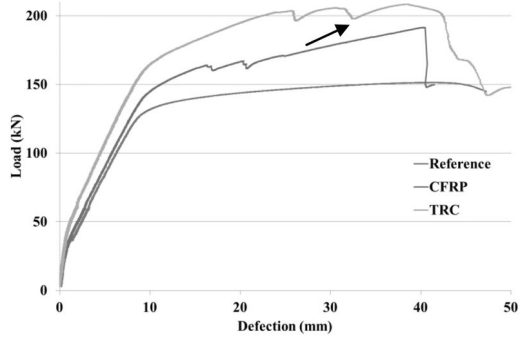

Figure 5. Load vs. deflection curves for the different beams.

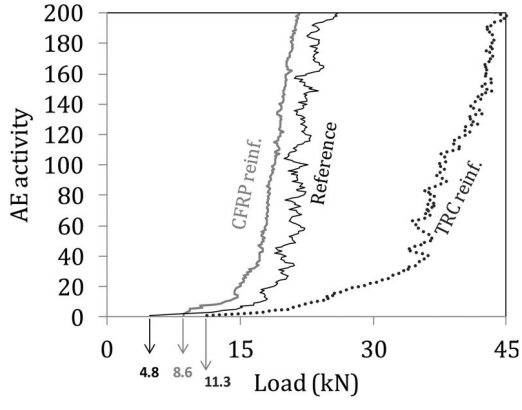

Figure 6. AE activity vs. load for different beams.

hits than any of the other two beams, which is again indicative of the restraining of cracking compared to the other beams. Indicatively, the AE activity recorded at 45 kN for the TRC Beam (200 hits) had already been recorded for the reference and CFRP beams at 20 and 25 kN respectively.

Apart from the overall number of AE activity it is worth studying the signal parameters that can reveal information on the original fracture pattern that created the specific failure incidents. Of particular interest is the comparison between the concrete cracking events and debonding of the external layer. This is because in similar cases of externally reinforced members, there is no visual contact in order to examine the damage that is developed beneath the reinforcing patch/layer. To study this case, the AE during debonding of the TRC layer was isolated and compared to a large population of matrix cracking events. The debonding signals were isolated based on their time and location. Specifically, they were registered at moments of temporary load drop (see arrow in Figure 5), at which DIC showed a release of strain on the patch (Aggelis et al. 2013) and at the lowest 50 mm of the height of the beam. The characteristics of these events (approximately 30 in total) are compared with a large population of events that occurred at the

Table 1. Average values of AE features for different processes.

	ENER (−)	AMP (dB)	AF (kHz)	CF (kHz)	RA (μs/V)
Matrix Cracking	10.2	50.0	87.5	130.9	4673.5
Debonding	4.1	47.0	81.7	113.1	7766.7

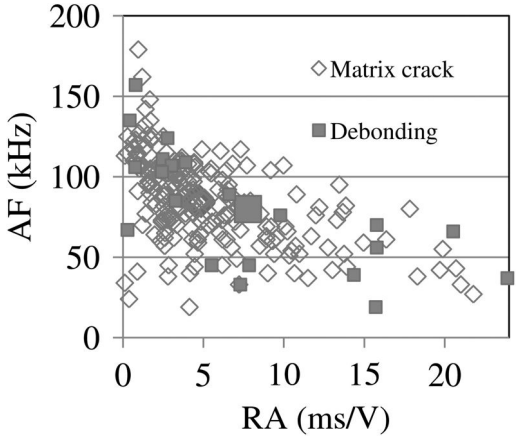

Figure 7. AF vs. RA for events of all the sensors for the TRC reinforced beam.

early loading stage when the load was increasing in a monotonic way.

Table 1 shows the average values of different AE parameters for concrete cracking and debonding of the TRC layer. A typical matrix cracking event occupies higher energy, amplitude and frequency characteristics in the form of the average or central frequency. On the other hand, lower RA values are obtained. These results showed that the different fracture processes can potentially be identified in large scale, despite the strong overlap between the different classes. Figure 7 shows the correlation plot between AF and RA, which is commonly used for classification purposes (Ohtsu 2010, Aggelis 2011). The populations of concrete cracking and TRC debonding are overlapping but the averages can be distinguished, especially in terms of RA. This overlap is mainly attributed to two reasons. One is the random nature of concrete bending fracture. Each event is not the same with the previous and therefore, any variability is transferred to the AE events which are the result of fracture. Additionally, another reason for the experimental scatter is the different propagation distance between the actual sources and the sensors in each incident. The elastic waves suffer strong attenuation and distortion due to the different excited modes and the heterogeneity of the medium. This distortion depends on the propagation distance; however, the different sensors are located at different points while the locations of the sources are also changing during the experiment. Therefore, a source may be located very close to a sensor (few mm away) as well as very far

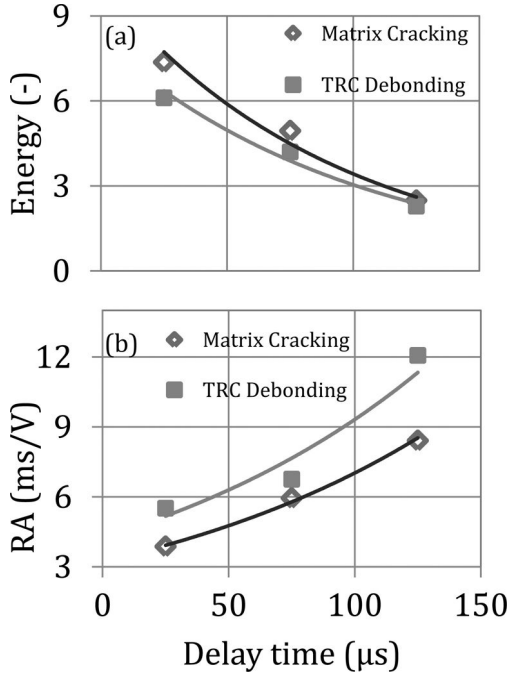

Figure 8. (a) AE Energy and (b) RA vs. the propagation time of the wave.

away (more than 400 mm). These phenomena render classification difficult in real structures as they cause a strong differential error factor in each of the AE hits, masking the original information of the crack tip movement.

3.2 *Effect of wave propagation on AE*

To elaborate on the propagation dependence of the AE signals, Figure 8a shows the trend of the energy of AE signals over the additional delay time after reception at the first sensor. The AE hits were divided in three different groups according to their acquisition delay; 0–50 μs (average 25 μs), 50–100 μs (average 75 μs) and more than 100 μs (average approximately 125 μs). Concrete cracking signals carry larger amount of energy (area under the waveform envelope) by more than 20% compared to the debonding ones for the same propagation distance range. However, due to attenuation the energy is reduced, and a matrix cracking signal propagating a few mm more may well carry less energy than a debonding one that is recorded close to its origin. The effect is quite similar for the RA but with inverse trend, see Figure 8b. In this case owing to the reducing amplitude and the stretching of the time domain waveforms due to scattering, the RA increases for longer distances. For incidents recorded by close-by sensors (up to 50 μs delay or approximately in the range of 20 cm) concrete cracking is characterized by an RA of approximately 3.8 ms/V, while the debonding by 5.5 ms/V. However, concrete cracking signals that propagate an additional distance of 20 cm exhibit

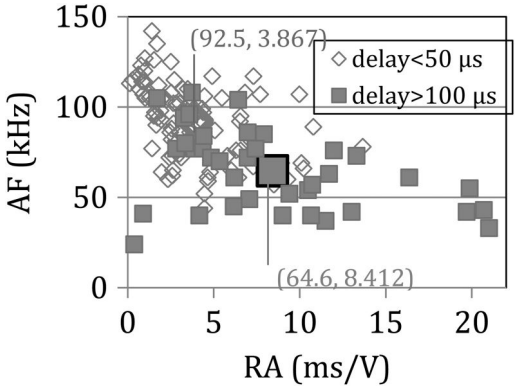

Figure 9. AF vs. RA for different groups of matrix cracking signals. Large symbols stand for the averages of the two populations and their exact values are in parentheses.

an average of 6 ms/V, while the ones that are recorded after longer propagation have an average of more than 8 ms/V and can certainly be mistaken for debonding ones that propagated shorter.

To illustrate the effect of propagation on the whole population of signals Figure 9 shows the correlation between AF and RA for two different groups of concrete cracking AE data. One consists of signals propagating for a short time (below 50 μs before reaching the sensor). The other consists of waves that propagated longer (more than 100 μs). It is obvious that the second group of hits exhibit a clear shift to lower AF and higher RA values. The differences in average values are strong: the drop of frequency is higher than 30% and the increase of RA is more than 200% for the long propagated group. It is stressed that the original AE events are the same and these changes arise only from the additional propagation of a few cm (20–30 cm). These changes, that are due to the heterogeneous texture of reinforced concrete, if not accounted for will certainly result in misclassification of concrete cracking events as debonding/shear which inherently exhibit lower frequency content and higher RA.

4 CONFIRMATION BY DIC

When an external reinforcing layer is debonded from the bottom concrete surface its strain is ocally decreased. Though debonding normally occurs at the moments of load drop, DIC confirms this assumption. Figure 10 shows the strain ε across the length of the beam before and after the 2nd load drop in the TRC beams (see arrow in Figure 5). The strain at the left of the monitored area is strongly reduced after the load drop.

This is also shown in Figure 11, where the quantitative strain evolution in the longitudinal direction of the beam is plotted. The strain at the first part of the monitored length (up to 300 mm) dropped by more than

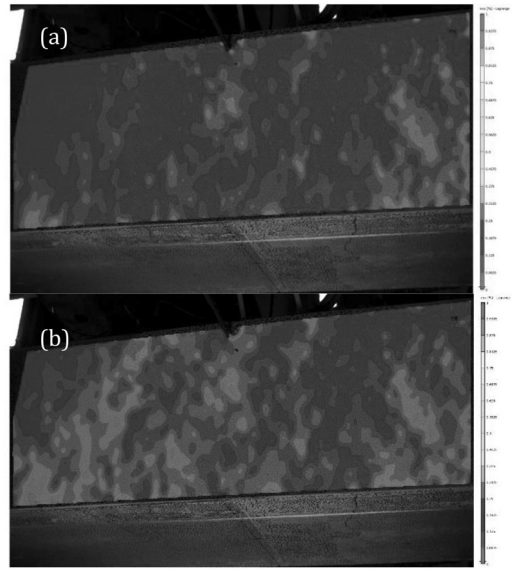

Figure 10. Strain field ε parallel to the axis of the beam (a) before and (b) after the 2nd load drop.

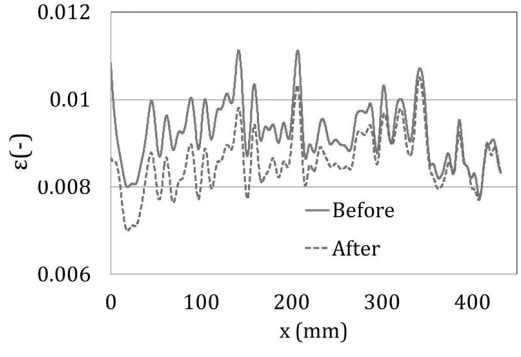

Figure 11. Strain field ε parallel to the axis of the beam (a) before and (b) after the 2nd load drop.

10% indicating that debonding occured at the moments of load drop.

The strain decrease for the 1st load drop of the TRC reinforced beam that is seen in Figure 5, is quite similar. Therefore, it is validated that the differences in AE characteristics recorded during the load drops and coming from the bottom of the beams actually originate from debonding events.

5 CONCLUSIONS

In the present study AE is used for monitoring of the fracture behavior of externally reinforced concrete beams under bending. The aim is twofold; to determine the onset of cracking for the different types of reinforcement as well as to characterize the dominant fracture mechanisms during loading. Reinforcement with the high performance TRC layer effectively restrained

the onset of cracking as shown by the negligible AE activity at early loadings compared to the CFRP strip and the plain beam. This enabled the TRC reinforced beam to withstand 10% higher load than the CFRP and 39% higher than the plain one. Apart from this, AE trends exhibit sensitivity in the different loading stages and failure mechanisms. Specifically, at the moments of load drop AE RA values are almost doubled in average. The load drops are triggered by debonding of the external patch as verified by release of strains in DIC measurements. This AE shift which is not exhibited in the plain concrete beam shows that certain parameters of AE can be used even in large size members for the determination of the nature of the fracture events. Complementary use of DIC and AE helps to minimize the assumptions in the interpretation of the AE trends in relation to the responsible damage mechanisms by revealing the fluctuation of the surface strain fields. The effect of the sensor separation distance is also discussed since strong changes in AE characteristics like AF and RA can be registered not only owing to the different type of source but also due to the different propagation distance travelled to the various sensors.

REFERENCES

Aggelis, D.G. 2011. Classification of cracking mode in concrete by acoustic emission parameters. *Mechanics Research Communications* 38: 153–157.

Aggelis, D.G., Verbruggen, S., Tsangouri, E., Tysmans, T., Van Hemelrijck, D. 2013. Characterization of mechanical performance of concrete beams with external reinforcement by acoustic emission and digital image correlation. *Construction and Building Materials* 47: 1037–1045.

Carpinteri, A., Lacidogna, G., Niccolini, G., Puzzi, S. 2008. Critical defect size distributions in concrete structures detected by the acoustic emission technique. *Meccanica* 43: 349–363.

CEB-FIB 2001 fib bulletin 14 Externally bonded FRP reinforcement for RC structures. Lausanne, Switzerland; ISBN 2-88394-054-1.

Farhidzadeh, A., Dehghan-Niri, E., Salamone, S., Luna, B., Whittaker, A. 2013. Monitoring Crack Propagation in Reinforced Concrete Shear Walls by Acoustic Emission, *Journal of Structural Engineering* 139(12), 04013010. doi:10.1061/(ASCE)ST.1943-541X.0000781

Grosse, C.U., Ohtsu, M. 2008. Acoustic emission testing. Heidelberg: Springer.

Karihaloo, B.L, Ramachandra Murthy, A., Iyer, N.R. 2013. Determination of size-independent specific fracture energy of concrete mixes by the tri-linear model. *Cement and Concrete Research* 49: 82–88.

Luo, X., Haya, H., Inaba, T., Shiotani, T. 2006. Seismic diagnosis of railway substructures by using secondary acoustic emission. *Soil Dynamics and Earthquake Engineering* 26: 1101–1110.

Ohtsu, M. 2010. Recommendation of RILEM TC 212-ACD: Acoustic emission and related NDE techniques for crack detection and damage evaluation in concrete: Test method for classification of active cracks in concrete structures by acoustic emission. *Materials and Structures* 43(9): 1187–1189.

Shahidan, S., Pulin, R., Muhamad Bunnori, N., Holford, K.M. 2013. Damage classification in reinforced concrete beam by acoustic emission signal analysis. *Construction and Building Materials* 45:78–86.

TRADECC 2007. Technical data sheet: PC®CARBOCOMP. pp.1–2.

TRADECC 2009. Technical data sheet: PC®5800/BL. pp.1–3.

Uddin, F.A.K.M., Shigeishi, M., Ohtsu, M. 2006. Fracture Mechanics of Corrosion Cracking in Concrete by Acoustic Emission, *Meccanica* 41: 425–442.

Van Tittelboom, K., De Belie, N., Lehmann, F., Grosse, C.U. 2012. Acoustic emission analysis for the quantification of autonomous crack healing in concrete. *Construction and Building Materials* 28: 333–341.

Verstrynge, E., Schueremans, L., Van Gemert, D., Wevers, M. 2009. Monitoring and predicting masonry's creep failure with the acoustic emission technique. *NDT&E International* 42:518–523

Concrete Solutions – Grantham et al. (Eds)
© 2014 Taylor & Francis Group, London, ISBN 978-1-138-02708-4

Determining bond strength of repair coatings on deformable substrates

D. Corbett
Proceq SA, Schwerzenbach, Switzerland

ABSTRACT: Determination of bond strength of repair coatings is traditionally carried out by the pull-off test. There are several standards dealing with this, for example EN 1542, ASTM C 1583 and ASTM D 7522. All specify maintaining a constant load rate to achieve repeatable results. This is not always easy to achieve in practice with conventional instruments. In particular difficulties arise when either the substrate or the coating is deformable. With such materials the coating tends to peel off, rather than providing a clean break that can be easily measured. Guidelines used in Germany (ZTV-ING) and Switzerland (SIA281-3) try to deal with this problem by specifying faster load rates in an attempt to identify a clear breaking load. Nevertheless the very nature of the materials used mean that it is very difficult to a) maintain a constant load rate as specified and b) determine the actual breaking load when the coating material pulls away from the surface. This paper shows how recent advances in pull-off technology have thrown new light on this issue and for the first time provide the engineer with a complete picture of what occurs during the test, making it possible to make an informed analysis.

1 INTRODUCTION

Pull-off testing is covered by more standards than any other non-destructive concrete test. The reason is due to the large number of applications and material types that are tested by this method. Nevertheless there are gaps in the standards that need to be addressed. As an equipment manufacturer Proceq are fully aware of standards compliance and this is a key factor when new instrument is released. In January 2013 a new instrument capable of recording and displaying the load rate during the test was introduced to the market. This new feature quickly brought to light unforeseen issues when testing on deformable materials.

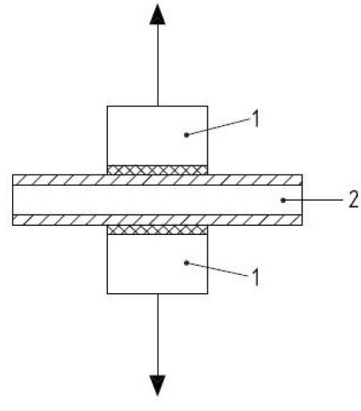

Figure 1. EN 4624 recommended test assembly for testing on deformable substrates. (1) dolly coated with adhesive, (2) substrate painted on one or both sides.

2 PULL-OFF TESTING ON ELASTIC OR DEFORMABLE MATERIALS – STANDARDS

Testing on elastic materials is not well handled by the current EN or ASTM standards. EN 4624 differentiates between testing on rigid substrates and deformable substrates. Two differing test set-ups are recommended.

The method prescribed for deformable substrates is only applicable for laboratory samples and could not be used on site. There is however a real need to carry out pull-off testing on elastic materials. In Germany the Federal Highway Research Institute published a document ZTV-ING (Additional technical contract conditions and guidelines for civil engineering) which contains a section on pull-off testing. This test is widely used for bitumen based sheeting. The main requirements of the test are:

The test is to be carried out in accordance with EN 1542

The applied load rate during the test should be:

100 N/s for concrete substrates and hard layers, or
300 N/s for elastic and thermoplastic layers.

The tolerance for the load rate is given in EN 1542 as +/− 20%. Also there is no limit as to how elastic or thermoplastic the material can be.

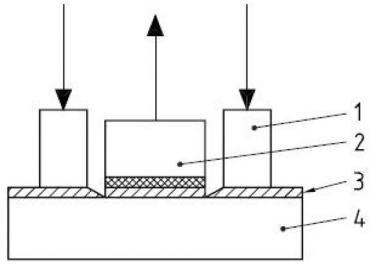

Figure 2. EN 4624 recommended test assembly for rigid substrates. (1) outer ring, (2) dolly coated with adhesive, (3) paint coating, (4) substrate.

In Switzerland the standard SIA 281/3 (Bituminous Sheeting – Tensile Bond Test) is widely used, not only for bituminous sheets, but also for testing the adhesion of plastic sheets and liquid plastic seals. A further standard SIA 273 (Waterproofing of trafficable surfaces in structures) gives the expected bond strengths of various materials.

The bond strength is carried out in accordance with SIA 281/3. SIA 281 also calls for a load rate of 300 N/s, and goes further than the ZTV-ING guideline in that it gives a tolerance of ±15 N/s. It also provides details of the number of pull-off tests to be carried out in a particular surface area, as follows.

Unless otherwise specified by the contract, for a complete sealed area of 250 m^2, at least one test location. (This is similar to the BS EN 14487 recommendation.)

- A minimum of three test locations per site.
- At least one test location when there is a change in the sealing system.
- At least one test location when there is a change in the substrate.
- At each test location, three single tests must be carried out.
- The single tests at each location should be within a 1 m × 1 m area.

Once again, however, there is no limit to the elasticity of the material under test.

3 IDENTIFICATION OF THE PROBLEM

The application in which the problem was first identified was for a test of a floor coating system used in multi-storey car park. Typically these are multi-layer systems.

The surface is prepared by shot blasting then a priming epoxy resin coat is applied. Uneven surfaces are smoothed out by using a layer of sand with a grain size of 0.4 – 0.8 mm and epoxy resin. Then a crack-bridging intermediate coat is applied which is typically a highly elastic material. Above this comes a wearing surface and finishing coat.

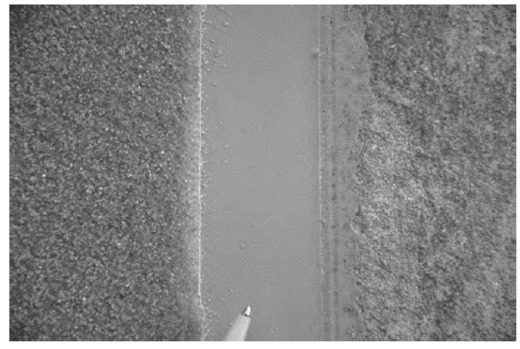

Figure 3. Left, wearing surface. Middle: Elastic membrane. Right: Epoxy resin/quartz sand smoothing layer.

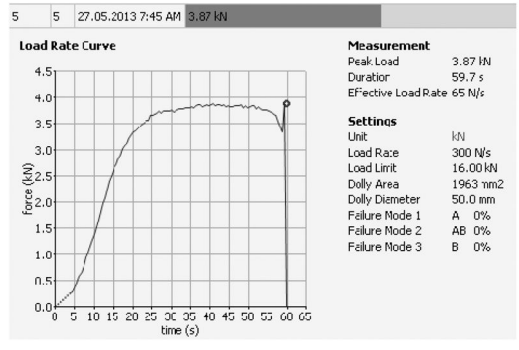

Figure 4. Pull-off test on StoPur EB400 material load development curve recorded with Proceq DY-216 pull-off tester.

A highly elastic membrane is then applied to the prepared surface. The material used in this particular case was StoPur EB 400.

Pull-off testing is required according to the SIA 281/3 standard. Initial tests carried out by the customer showed that the instrument being used Proceq DY-216 pull-off tester could not achieve the required 300 N/s load rate.

As can be seen, the programmed load rate is 300 N/s, whereas the effective load rate calculated from the beginning of the test to the final break point is only 65 N/s. Analyzing this curve we can see that a maximum load rate of about 230 N/s is achieved between the time at which the load rate control kicks in up to 2.5 kN. The load begins to taper off and remains constant for a long time until the break occurs after 60 s.

The explanation for this behaviour is that the material under test is too elastic to allow the programmed load rate to be achieved. Plastic deformation begins to occur after 3 kN. The load remains constant at 3.8 kN for a significant time as the test disc slowly pulls free of the substrate.

Following this test, modifications were made to the instrument to allow faster pulling rates and further tests were carried out using the same material under laboratory conditions.

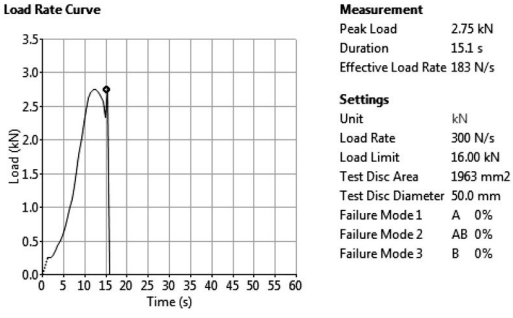

Figure 5. Pull-off test on StoPur EB400 material load development curve recorded with modified DY-216 pull-off tester.

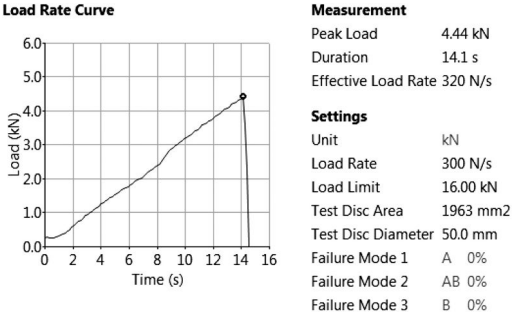

Figure 6. Pull-off test on StoPur EB400 material load development curve recorded with new DY-216 pull-off tester.

The conclusions reached from this testing were as follows:

- Tests with elastic/thermoplastic materials do not allow a clear breaking point to be recognized. The bonding slowly peels over a period of time with a constant force.
- The effect is independent of the load rate. A faster load rate only reduces the time required for the peeling.
- However a faster load rate is necessary to comply with the standards.
- The modified instrument was able to achieve the required load rate up until the point where the peeling process begins.

As a result of this test, further modifications to the instrument software were agreed:

Calculation of the effective load rate would no longer be from the start of the test up until the end of the test. It would begin at the point when load rate control takes place. And it would end at a point before the peeling off process begins. It could easily be argued that the pull-off force is the point at which the peel-off occurs.

4 THE FINAL SOLUTION

Further tests were carried out on materials with varying degrees of elasticity once the software modifications were made.

The peak load is the maximum load achieved during the test.

The effective load rate is calculated from the point at which load rate control begins (250 N) to the time at which 80% of the peak load is reached.

5 SUMMARY

Pull-off testing is also carried out in-situ on elastic materials. EN standards do not cover this sufficiently well and should be reviewed to accommodate this test.

In current guidelines that are available the amount of elasticity is not defined. This needs to be taken into consideration also, as there will always be a point at which due to the elasticity of the material under the test, the pull-off instrument being used will simply not be able to achieve the specified load rate.

It is recommended to review the way in which the load rate is calculated for pull-off tests on such materials from the point at which load rate control is applied up to a force below which the peeling of the test dolly begins.

A record of the load development allows precise analysis of what has really occurred during the test.

REFERENCES

British Standards Institution (2003) BS EN ISO 4624:2003. Paints and varnishes. Pull off test for adhesion. London, BSI.

Bundesanstalt für Strassenwesen ZTV-ING – Teil 1 Allgemeines – Abschnitt 3 Prüfung während der Ausführung. 3 Bestimmung der Abreissfestigkeit. Bergish Gladbach BAST.

Schweizerische Ingenieur- und Architektenverein SIA 281/3:2002 SN 573 281/3. Bitumenbahnen – Haftzugprüfung. Zurich SIA.

This page intentionally left blank

Concrete Solutions – Grantham et al. (Eds)
© 2014 Taylor & Francis Group, London, ISBN 978-1-138-02708-4

Prioritizing repairs to reinforced concrete water storage elevated tanks regarding seismic risk

H. Hammoum, K. Bouzelha & D. Slimani
Département de génie civil, Université Mouloud Mammeri, Tizi Ouzou, Algeria

ABSTRACT: The reinforced concrete water storage tanks are now very widespread across the Algerian park. Since these structures amount to heights much higher than the buildings to ensure adequate pressure in drinking water networks, and taking into account the hydrodynamic effect when tanks are fully or partially fulfilled, their failure can lead to catastrophic damage. In this paper, the concept of seismic vulnerability is used to predict the average level of damage that can occur at scale of an elevated tank under the earthquake action of known intensity. We propose, through our work, a simple and practical method allowing for a professional of civil engineering a quickly assess of the seismic vulnerability presumption of a storage elevated tank. The vulnerability scale is adapted from the Italian method called GNDT, where a retiming of weighting coefficients and the introduction of new parameters are made in order to better sticking with the seismic behavior of this kind of structure. Some parameters characterize the geometry of the tank, while others are associated with the supporting structure as defined by the design engineer and then the rest of the parameters are related to the location of the elevated tank. Vulnerability as it results from this scale is an abstract concept which provides information on the potential damage that may occur following a seism of known intensity. In this method, the level of vulnerability involves 12 parameters. From this index, we propose a tank classification scale in four levels of behavior, which are associated with different colors.

1 INTRODUCTION

The phenomenon of earthquakes is not new or specific to Algeria. It appears cyclically from one region to another causing sometimes immeasurable damage. Given that seismic prediction is still far from becoming a reality, it is necessary to improve the seismic behaviour of existing structures. Seismic design mainly focusses on ensuring an acceptable level of safety to reduce risks related to failures, disasters and loss of life. The need to improve the methodology of calculation of structures subjected to seismic action has been widely found in various seismic codes. In seismic codes, the study of the response of structures under seismic action is conducted by using methods depending on the nature of the structure and its intended end use.

Given the social importance of tanks and the role they play in the daily life of a country, they are sensitive structures to public opinion: the closure of a tank, even temporarily, for maintenance or repair causes strong reactions from subscribers, quick to denounce the laxity or negligence of public services.

This is the reason why studies of seismic vulnerability of structures have been developed to evaluate the expected damage in the different types of structures when there is a severe earthquake (Gent Franch et al. 2008).

The present paper focuses on the large-scale assessment of the seismic vulnerability of existing water storage elevated tanks. Section 2 of this paper focuses on seismic vulnerability of structures. Section 3 describes the Italian GNDT (Gruppo Nazionale per le Difesa dai Terremoti) method and their different applications to structures and urban centers. Section 4 contains a detailed assessment method of the seismic vulnerability of water storage elevated tanks, based on the calculation of a vulnerability index "Iv" to determine their seismic quality. This index allows the classification of tanks examined in four levels of behavior. Section 5 is dedicated to a practical example of a water storage elevated tank in order to test the reliability of the developed method. The tank chosen was a tank on piles in the Tizi-Ouzou area, classified as average seismicity. Finally, the main conclusions and the lessons learnt from the experience are given in Section 6.

2 SEISMIC VULNERABILITY

The seismic vulnerability of a structure is a quantity associated with its weakness in the case of earthquakes of given intensity, so that the value of this quantity and the knowledge of seismic hazard allows us to evaluate the expected damage from future earthquakes (Gavarini, 2001).

The evolution of the study of vulnerability in the world gave birth to several methods of assessing damage to the individual buildings, structures, buildings, urban and historical centers. They differ from one another in terms of cost, in used facilities and in precision. But there is, to our knowledge, no method of seismic evaluation of water tanks.

The systemization of these vulnerability assessment approaches has been developed by many researchers and therefore differs due to varying levels of dependence of the following factors: nature and objective of the assessment, quality and availability of information, characteristics of the structure stock inspected, scale of assessment, methodology criteria and degree of reliability of the expected results. Because of these differences, the coherence and consensus regarding the classification is always a contentious issue.

Various methods for seismic risk assessment have been implemented in countries with strong seismicity, such as that by the Federal Emergency Management Agency in the United States (ATC 1996; HAZUS 1999) and that by the Gruppo Nazionale per Difesa dai Terremoti in Italy (Benedetti and Petrini 1984).

We can also mention the RISK-UE project which is an advanced approach to earthquake risk scenarios with applications to different European towns, financed by the European Commission which is a major step toward the development of a European methodology to assess and mitigate the seismic risk ofcrucial and essential facilities in Europe. The RISK-UE project is based on the assessment of the vulnerability index for a given current building. This index is a function of the constructive typology and different factors that can change its behavior. The RISK-UE project was to treat the seismic vulnerability of seven pilot cities (Thessaloniki, Catania, Nice, Bucharest, Sofia, Barcelona and Bitola) (Pitilakis et al. 2006).

3 VULNERABILITY METHOD OF CNR-GNDT

In Italy the procedure to qualify the seismic vulnerability of buildings has been proposed for the first time by (Benedetti et al. 1984) then this method was developed by the Gruppo Nazionale per la Difesa dai Terremoti of the Italian Consiglio Nazionale delle Ricerche (CNR-GNDT). The method evaluates the seismic vulnerability of buildings, determining as a normalized index of vulnerability, which is obtained with the aid of survey forms which are filled in for one building or a group. The CNR-GNDT method was originally applied to stone rubblework buildings and reinforced concrete buildings, and a very detailed procedure exists for each one. The method is very easy to apply and it considers the structural characteristics of the buildings, such as: type of construction, building's use, quality of materials, structural system, geometric aspects of the structure, building's state of preservation, etc. These characteristics are quantified as parameters and are evaluated considering eleven factors, and a class, score and weight factor is assigned to each one. There are four classes for stone masonry buildings: A, B, C and D; and three for reinforced concrete buildings: A, B and C.

Several studies have been dedicated to the CNR - GNDT method, in some countries in South America, Europe and North Africa, such as: (Gent Franch et al. 2008). In their study, the Italian CNR-GNDT vulnerability index for masonry buildings was modified in order to obtain a vulnerability index I_{3GA} that considers the properties of confined masonry shear wall buildings. In Chile, the modified Italian method was applied considering a sample of twenty-four confined masonry buildings with three and four storeys built during the last twenty-five years for social housing programs. With this objective, new values of the weight factors and sub-factors were considered in order to obtain a logical relationship between I_{3GA} and the wall density per unit floor d/n. The scope of this work is restricted to regular four storey residential buildings with R.C. slabs at floor level.

(Vicente, 2011) applied methodology considered an hybrid technique in the evaluation of the vulnerability of the entire historic city centre of Coimbra (Portugal). The vulnerability index formulation proposed is based essentially on the GNDT II level approach, for the vulnerability assessment of residential masonry buildings. This methodology is based on post-seismic damage observation and survey data covering a vast area, focusing on the most important parameters affecting building damage which must be surveyed individually. Overall vulnerability is calculated as the weighted sum of 14 parameters used in the formulation of the seismic vulnerability index. This procedure has been used in Italy for the last 25 years, but has been adapted for use with Portuguese masonry buildings and improved by: (i) introducing a more detailed analysis, derived from the good level of building stock information; (ii) the discussion and redefinition of the criteria of some of the most important parameters; and (iii) the introduction of new parameters that take into account the interaction between buildings (structural aggregates) and other overlooked building features.

(Bezzazi et al. 2008) have adapted a scale of vulnerability from the CNR-GNDT method, where a retiming of the weighting coefficients is performed, to better match with architectural characteristics of local buildings in northern Morocco. The results of a survey in the field after the strong earthquake of magnitude 6.30 which hit Al Hoceima region (northern Morocco) showed that the proposed method can adequately assess the vulnerability. The authors have even proposed fragility curves for this typology building.

A large-scale vulnerability assessment using two methods was conducted for buildings of Tunis by (Mansour et al. 2013), for which few data were available. Vulnerability methods inspired by the EMS98 concepts and the Italian GNDT concepts were modified and applied to pilot-scale buildings located in the downtown zone (Habib Bourguiba Avenue) and in the old zone (Medina). The data analysis, through the application of the two methods, suggests that

(a) (b) (c)

Figure 1. Different forms of tanks.

the vulnerability of buildings surveyed in Tunis is significant and risk mitigation efforts are necessary.

4 PRESENTATION OF THE METHOD

This method is a simplified empirical method inspired by the CNR-GNDT method. Its goal is to allow for the establishment of a seismic inventory of water storage tanks on a large scale by the simple and rapid recording of structural parameters.

We have made some modifications to the methodology developed by (Benedetti et al. 1988), where a resetting of the weighting coefficients is performed in order to better fit to the geometric characteristics of elevated tanks. The main differences are the introduction of three new parameters called clashing, seismic zone and location of the reservoir. The detailed definition of each parameter is given bellow.

4.1 *The bracing system*

The bracing system of an elevated tank is constituted by the set of resistive elements ensuring its rigidity and stability to the horizontal forces caused by the earthquake. It constitutes one of the most important aspects of seismic design. The classification of this parameter is defined taking into account the capacity of energy dissipation to the seismic action and deformation. For this, there is currently interest to equip tanks with a regular structural mesh in order to avoid twisting of bracing elements. The bracing of the resistant system is divided into three classes defined below:

- Class A: includes structures resistant with constant stiffness, operating in vertical console with uniformly distributed mass (Fig. 1a).
- Class B: includes deformable structures with variable stiffness, assimilated to reverse pendulums where 50% or more of the mass is concentrated in the upper third of the structure (Fig. 1b).
- Class C: includes resistant structures with low stiffness where the distribution of the mass and stiffness change abruptly, such as tanks on piles (Fig. 1c).

4.2 *Qualities of the bracing system*

For this parameter, classification is done according to the quality control of materials, and quality control of execution. Systematic tests on the materials used must be made by the company on site during construction, in order to control the concrete strength. This task should include supervision of conducted tests on materials, in order to meet general terms and conditions of design, calculation and execution.

These quality controls are used to limit the problems of form stability, the ductility and the materials capacity to deform plastically during high loads without significant reduction of strength.

Thus, we define three classes for the quality of the bracing system:

- Class A: includes tanks having a good characteristic strength of concrete, greater than 25 MPa.
- Class B: includes tanks having an average characteristic strength of concrete, between 20 and 25 MPa.
- Class C: includes tanks with a bad characteristic strength of concrete, lower than 20 MPa.

Note that if the characteristic strength of concrete is not available at the archives, it is necessary to make ultrasound resistance tests or sclerometer tests during the investigation mission. Such tests must be calibrated against the concrete under investigation by comparison with core samples.

4.3 *Seismic behavior*

The seismic action results in an abrupt horizontal or vertical displacement of the soil, causing the deformation of the foundations and underground parts of the tank. In a partially filled tank, seismic excitation puts part of the fluid in motion, which leads to the formation of surface waves. This phenomenon is called the hydrodynamic effect, and its appreciation can be given by the Housner method (1963), which is based on the decomposition of the water action in impulse and oscillation action. Under the seismic action effect, the overall stability of the tank to collapse must be satisfied. The overall stability relating to rigid body behavior can be lost by sliding or overturning.

For this purpose, it is necessary to satisfy the following inequality: stabilizing moment $\geq$ overturning moment.

The classification of this parameter is done according to a safety factor "Fs" defined as the ratio of the stabilizing moment and overturning moment.

- Class A: includes tanks having a good stability against overturning under seismic action ($Fs > 3$).
- Class B: includes tanks having an average stability against overturning under seismic action ($1.5 < Fs < 3$).
- Class C: includes tanks having poor stability against overturning under seismic action ($1.5 < Fs$).

4.4 *Soil type*

Vulnerability due to the influence of soil can have two origins, the soil instability, due to its composition, its

liquefaction and to landslides, or then the resonance effect between the soil and the height of the structure.

The geological aspect is taken into account in analyzing the implementation category site which is based on mechanical properties of soil. The sites are classified into four categories by the Algerian seismic code (DTR BC 2-48, 2003) according to the average velocity of the shear wave Vs.

The classification of this parameter is as follows:

- Class A: includes the soil category type S1 (rocky soil).
- Class B: includes the soil category type S2 (firm soil).
- Class C: includes the soil category type S3 (loose soil) and type S4 (very loose soil). We find in this class, deposits of sand and gravel averagely dense or loose and clay deposits averagely stiff or soft.

4.5 *Regularity in plan*

Analysis of seismic damage, clearly shows that regular and symmetrical structures perform better than those whose geometric forms and the distribution of resistive elements are complex, even when the seismic rules were correctly applied. The calculations, as prescribed by these seismic codes, represent seismic stresses to structures of a fairly realistic way for regular structures whose seismic response is simpler than for irregular structures (J. Betbeder-Matibet et al.). The symmetry and regularity in plan have the function of providing better resistance to earthquakes. Structures should preferably have, on one hand, simple forms and on the other hand, distribution as regular as possible of masses and stiffness as in plan and elevation. The aim is to ensure the best possible distribution of forces through the structure, so as to involve all the resistant elements to the absorption and dissipation of the energy developed by the seismic action.

Taking inspiration of the seismic building rules (DTU PS92), applied to buildings, we can consider the following criteria:

- The tank should have a symmetrical configuration in both directions, both for the distribution of rigidities than those of the masses.
- The tank form should be compact, and the dimensions of the projecting parts shall not exceed 25% of the total tank size in the corresponding direction in accordance with this relationship:

$$\frac{D-d}{D} \leq 0.25 \qquad (1)$$

- The geometric slenderness ratio λg of the support, which defines the ratio between the buckling length and the minimum gyration radius of the cross section of the support, should be between the following values:

$$3 \leq \lambda g \leq 5$$

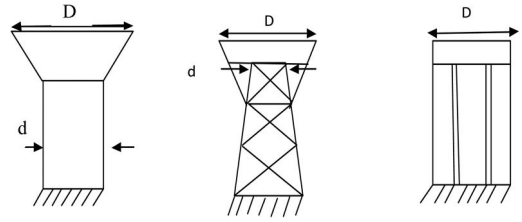

Figure 2. Different forms of elevated tanks.

- For each direction of calculation, the mass eccentricity should verify the following condition:

$$e \leq 0{,}20 \,.\, r$$
$$r^2 = \sum \frac{\text{torsional stiffness}}{\text{translational stiffness}} \qquad (2)$$

So, we define the three following classes:

- Class A: includes tanks with regular forms in plan, which responds to all the criteria raised.
- Class B: includes tanks with partially irregularly forms, and partially responds to the criteria raised.
- Class C: includes tanks with irregular forms, and doesn't respond to any of the criteria mentioned above.

4.6 *Regularity in elevation*

The principle of regularity in elevation is to avoid discontinuities or excessively fast changes in the distribution of inertias, stiffness and masses.

Taking inspiration from the seismic building rules (DTU PS92), applied to buildings, we can consider the following criteria:

Mass distribution between the vessel and the support must be substantially regular over the height of the structure, the mass ratio being between the following values

$$0.63 \leq {M_c}/{M_{tower}} \leq 1.33$$

Where, Mc means the mass of the container (cuve) and Mtower means the mass of the supporting tower.

The stiffness distribution should be substantially regular over the height of the structure.

In the case of a gradual narrowing of the height of the support, substantially preserving the symmetry of the tank, the difference in stiffness between the bottom and the top of the support should not exceed 25%.

So, we define the three following classes:

- Class A: includes tanks with regular forms in elevation, which respond to all the criteria raised.
- Class B: includes tanks with partially irregularly form in elevation, and partially respond to the criteria raised.
- Class C: includes tanks with partially irregularly form in elevation and doesn't respond to any criteria mentioned above.

Table 1. The seismic zones.

N°	Zone	Seismicity
1	Zone 0	Negligible
2	Zone I	Low
3	Zone IIa	Average
4	Zone IIb	Average
5	Zone III	High

4.7 *Quality of the nodes*

We define the nodes by the connection areas between the structural elements, such as the connecting zone "Foundation – support" and the connecting zone "support – tank". Among several reasons that are at the origin of failures and damage caused by earthquakes, we cite poor design and construction of the nodes in tanks between resistant elements. This observation has been demonstrated in previous studies (Masoudi et al. 2012).

Thus, we propose three categories of classification for this parameter:

- Class A: includes tanks in which the state of the connection areas of structural elements is good, without cracks.
- Class B: includes tanks in which the state of the connection areas of structural elements is average, where we can see cracks.
- Class C: includes tanks in which the state of the connection areas of structural elements is bad, where we can see deep cracks.

4.8 *Seismic zone*

The Algerian seismic code (DTR BC 2-48, 2003), divide the country into four seismic zones (Table 1).

- Class A: includes tanks located in regions with low seismicity such as Zone 0 and Zone I.
- Class B: includes tanks located in regions with average seismicity such as Zone IIa and Zone IIb.
- Class C: includes tanks located in regions with high seismicity such as Zone III.

4.9 *The clashing*

The clashing is the interaction between two or more adjacent tanks, whose effect of the seismic behavior one relative to the other, during the seismic occurrence is important. Figure 3 represents some adjacent tanks.

The classification of this parameter is a function of the minimum width of seismic joints, given by the following formula:

$$d_{min} = \delta + \delta_1 + \delta_2 \quad (3)$$

Where:

δ_1 and δ_2, are the maximum displacements of the two adjacent tanks (Fig. 4).

Figure 3. Example of group of adjacent elevated tanks.

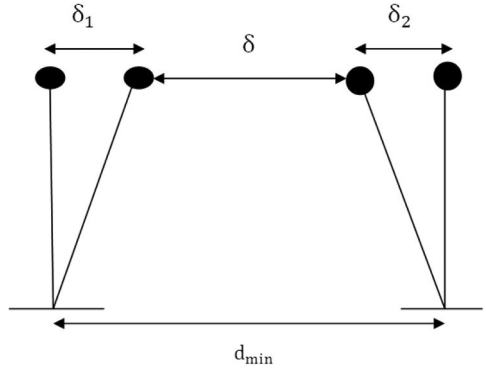

Figure 4. The minimum width of the joint.

δ, is the residual distance between the two adjacent tanks.

This leads us to define three classes for this parameter:

- Class A: includes tanks having no risk of clashing. These tanks are, either isolated, or separated by seismic joint whose residual distance is greater than 100 cm.
- Class B: includes tanks with an average risk of clashing. The residual distance is from 50 cm to 100 cm.
- Class C: includes reservoirs with a high risk of clashing. The residual distance is less than 50 cm.

4.10 *Site effect*

Tanks may be threatened by some effects of the implantation site (Liquefaction of sands, landslides, presence of surface faults and rockfalls) that can significantly amplify the oscillations of the soil and cause the loss of all engineering structure even paraseismic. Structures located there can sometimes undergo seismic loads up to five times higher than similar structures located

in a less dangerous Zone (Zacek, 2004). It is therefore imperative to take into account the site effect in a vulnerability study and the resort to a geotechnical engineer or geologist is desirable.

This leads us to define three classes for this parameter:

- Class A: includes tanks which are located in sites that present no risk.
- Class B: includes tanks located in the valleys, where the quality of the implantation site is average.
- Class C: includes tanks located in risk sites.

4.11 *Details*

We often hear about the detail parameter, the state and quality of non-structural elements that can influence the tank behavior during an earthquake and the status of various networks that are related to the functionality of the tank.

This parameter affects all the following elements:

- The state of hydraulic equipment (various distribution pipelines …).
- State of the cover roofing.
- State of the cornice.
- State of the stairs.

Thus, we propose three categories of classification for this parameter:

- Class A: includes tanks where all the non-structural elements are in good condition.
- Class B: includes tanks where a part of the non-structural elements are in good condition.
- Class C: includes tanks where all the non-structural elements are in bad condition.

4.12 *Maintenance*

Cracks on a the resistant components of the tank, shall result in the loss of stability and loss of the sealing function. Quantifying the cracking state is made according to the LPC method (Fasseu et al. 1997) a quick and easy way in order to characterize in conventional manner the state of damage at a given time a wall of reinforced concrete. This method concerns all existing cracks in a given area. The method consists of taking in an exhaustive manner all cracks intercepting four axes drawn in an area of one square meter on the part of the facing to study.

4.12.1 *Drawing of the landmark*

A landmark consisting of four axes graduated from 0.1 m to 0.1 m (a vertical axis of one meter length, a horizontal axis of one meter length and two axes arranged at 45° relative to the horizontal axis with 1.4 m length) is drawn on the facing using the jig (Fig. 5). The tracing is performed carefully to avoid altering the lips of the cracks.

4.12.2 *Measurement of cracks*

All the cracks with openings greater than 0.05 mm are searched and measured up to 2 mm opening. Each crack is measured with an accuracy of 0.1 mm just where it intersects with the axis of the landmark. A crack that intercepts the landmark several times, will be counted as many times as there are interceptions.

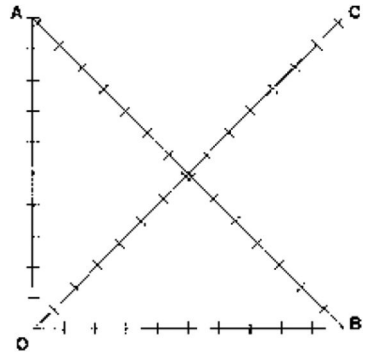

Figure 5. The four axes of the landmark.

Table 2. Characterization scale of cracking.

Value of crack index	Importance of cracking
0 to 0.5	Negligible
0.5 to 1	Low
1 to 2	Moderate
2 to 5	Strong
5 to10	Very strong
>10	Considerable

4.12.3 *Calculation of the cracks index*

For each of the four axes, we calculate the total accumulated of the opening, the average opening per crack and the average opening per meter length axis.

The cracking index is calculated by taking the average of the four openings per meter obtained on each axis.

The index obtained can be compared to the characterization scale of cracking given in Table 2.

Thus, we propose three categories of classification for this parameter:

- Class A: includes tanks whose cracking index is less than 1.
- Class B: includes tanks whose cracking index is between 1 and 5.
- Class C: includes tanks whose cracking index is greater than 5.

4.13 *Determination of the vulnerability index*

In Table 3, for each parameter, we define three classes of vulnerability. And for each class will correspond an elementary score K_i. Each parameter is affected by a weighting factor W_i. The elementary score K_i of each parameter can take three values (0, 5 or 15). The

Table 3. Classification of containers according to their vulnerability index "Iv".

N°	Parameters	Elementary score K_i			Weighting factor W_i
		Class A	Class B	Class C	
1	Seismic behavior	0	5	15	1,75
2	The clashing	0	5	15	1,75
3	The bracing system	0	5	15	1,50
4	Regularity in plan	0	5	15	1,50
5	Regularity in elevation	0	5	15	1,50
6	Soil Type	0	5	15	1,00
7	Site effect	0	5	15	1,00
8	Seismic zone	0	5	15	1,00
9	Quality of the nodes	0	5	15	0,75
10	Qualities of the bracing system	0	5	15	0,75
11	Maintenance	0	5	15	0,50
12	Details	0	5	15	0,25

Table 4. Classification of containers according to their vulnerability index "Iv".

Level	Green	Orange 1	Orange 2	Red
Iv	0–33	33–90	90–133	133–199

value of the weightings W_i varies from 0.25 to 1.75. The value of 0.25 corresponds to a minimum penalty of the parameter and 1.75 for a maximum penalty considering intermediate situations, as shown in Table 3. The partial score of a parameter is obtained by the product ($K_i.W_i$) and the vulnerability index "Iv" is expressed as the sum of the partial scores of different parameters:

$$Iv = \sum_{i=1}^{12} K_i.W_i \tag{4}$$

4.14 *Classification*

Considering all the twelve analysis criteria listed above, we propose the following classification, divided into four levels of vulnerability (Table 4).

- The green level, $0 \leq Iv \leq 33$: The tank examined is not vulnerable. It presents a good behavior to the earthquake and it doesn't require special repairs.
- The orange level 1: $39 \leq Iv \leq 90$: The tank has an average vulnerability to earthquake. It needs monitoring.
- The orange level 2: $90 \leq Iv \leq 133$: The tank has a fairly high earthquake vulnerability.
- The red level: $133 \leq Iv \leq 199$: The tank has a high earthquake vulnerability. Therefore, the tank must be decommissioned immediately.

5 PRACTICAL EXAMPLE

As a practical application (case study), we illustrate the method of vulnerability index in a water storage elevated tank of 200 m^3 capacity and located in average seismicity zone in Algeria. This tank, we studied here (shown in Fig. 1c) was built in 1986 and has been investigated and analyzed 27 years later. The vulnerability index value of the tank classes it in the Orange level 1 (Table 5). It has an average vulnerability to seismic risk. A repair program is necessary to increase its seismic strength.

6 CONCLUSION

The method developed is used to establish a hierarchy of tanks with risks from predefined safety criteria. The decision on the choice of maintenance, accrued to the manager of the tanks, consists in fact to estimate the limit vulnerability, which leads them to choose preventive maintenance (short-term repairs in order to prevent further deterioration to come) or consider a deferral of intervention if the tank does not represent high risk in terms of safety or cost, or without repairs.

According to the principles used for the vulnerability index evolution in the life cycle of the tank for the establishment of maintenance schemes, two terminals of vulnerability will be defined (I_{V1} and I_{V2}) segmenting all of the scale in three categories maintenance:

- Tanks whose vulnerability index is less than 33 (IV1): no maintenance is planned, only a regular monitoring (visual inspection, auscultation) is considered.
- Tanks whose vulnerability index is greater than 133 (IV2): the state of the tank is considered sufficiently degraded to justify short-term repair.
- Tanks whose vulnerability is between IV1 and IV2: additional studies and analysis of the potential risks of worsening defects must be engaged to decide on the nature and urgency of the repair work to be undertaken.
- In the hands of managers, this method allows us to fix the priorities for action in their rehabilitation

Table 5. The vulnerability index "Iv" calculated for the tank investigated.

N°	Parameter	Class	K_i	W_i	$K_i.W_i$
1	Seismic behavior	A	–	1,75	–
2	The clashing	A	–	1,75	–
3	The bracing system	C	15,00	1,50	22,50
4	Regularity in plan	B	5,00	1,50	7,50
5	Regularity in elevation	B	5,00	1,50	7,50
6	Soil Type	C	15,00	1,00	15,00
7	Site effect	B	5,00	1,00	5,00
8	Seismic zone	B	5,00	1,00	5,00
9	Quality of the nodes	A	–	0,75	–
10	Qualities of the bracing system	B	5,00	0,75	3,75
11	Maintenance	C	15,00	0,25	3,75
12	Details	B	5,00	0,25	1,25
				Iv	**71,25**

program or repair, in order to optimize its management under significant budgetary constraints.

REFERENCES

Applied Technology Council. 1996. *The seismic evaluation and retrofit of concrete building, ATC40*, volumes 1 and 2, Redwood, City, California.

Benedetti, D. Benzoni, G. Parisi, MA. 1988. Seismic vulnerability and risk evaluation for old urban nuclei. *Earthq Eng Struct Dyn* 16(2):183–201.

Betbeder-matibet & J. Doury, J.L. Constructions parasismiques. *Techniques de l'Ingénieur*.

Bezzazi, M., Khamlichi, A., Gonzalez, J.R.A. 2008. Vulnérabilité sismique des constructions de type béton armé aux Nord du Maroc, *revue canadienne de génie civil*, vol. 35.

DTR B-C 2-48. 2003. *Règles parasismiques algériennes (addenda 2003)*, CGS, Alger.

D.T.U. 1998. *Règles de construction parasismiques PS 92, applicables aux bâtiments*, Ed. Eyrolles, Paris, France.

Fasseu, P. & Michel, M. 1997. Détermination de l'indice de fissuration d'un parement de béton. Méthode d'essai LPC N°*47. Techniques et méthodes des Laboratoires des Ponts et Chaussées*.

Gavarini, C. 2001. Seismic risk in historical centers, *Soil Dynamics and Earthquake Engineering* 21: 459–466.

Gent Franch, K. A. Giuliano Morbelli, G. M. G. Inostroza, M. A. A. Gori, R. E. 2008. A seismic vulnerability index for confined masonry shear wall buildings and a relationship with the damage, *Engineering Structures* 30: 2605–2612.

Hammoum H., Bouzelha K., Hannachi N.E., Serre D. 2012. *Vulnerability assessment of the concrete tanks storage at natural hazards*, in : M. Grantham, V. Mechtcherine, U. Schnech (Eds.), Concrete solutions, Ed. Taylor and Francis Group CRC Press, London, United Kingdom.

HAZUS. 1999. *Earthquake loss estimation methodology–technical and user manuals*. Federal Emergency Management Agency (FEMA), National Institute of Building Sciences, Washington, DC.

Housner, G.W. 1963. *Dynamic analysis of fluids in containers subjected to acceleration, in Nuclear Reactors and Earthquakes*, Report No. TID 7024, U. S. Atomic Energy Commission, Washington DC.

Mansour, A. K. Romdhane, N. B. Boukadi, N. 2013. An inventory of buildings in the city of Tunis and an assessment of their vulnerability, *Bull Earthquake Eng* 11: 1563–1583.

Masoudi, M. Eshghi, S. Ghafory-Ashtiany, M. 2012. Evaluation of response modification factor (R) of elevated concrete tanks, *Engineering Structures* 39 : 199–209.

Pitilakis, K. Alexoudi, M. Argyroudis, S. Monge, O. Martin, C. 2006. Earthquake risk assessment of lifelines, *Bull Earthquake Eng* 4: 365–390 (DOI 10.1007/s10518-006-9022-1).

RISK-UE. 2003. *An advanced approach to earthquake risk scenarios with applications to different European towns, Projet Européen*. EVK4-CT-2000-00014.

Vicente, R. Parodi, S. Lagomarsino, S. Varum, H. Mendes Silva J. A. R. 2011. Seismic vulnerability and risk assessment: case study of the historic city centre of Coimbra, Portugal, *Bull Earthquake Eng* 9: 1067–1096.

Zacek, M. 2004. *Guide d'évaluation de la présomption de vulnérabilité aux séismes des bâtiments existants*, collection conception parasismique, France.

Concrete Solutions – Grantham et al. (Eds)
© 2014 Taylor & Francis Group, London, ISBN 978-1-138-02708-4

Estimation of the main factors influencing potential mapping

S. Kessler & C. Gehlen
Centre for Building Materials, Technische Universität München, Munich, Germany

ABSTRACT: Potential mapping is a widely used inspection method for detection of corrosion activity in reinforced concrete structures. The information coming from potential mapping is of vital importance, in particular for condition control and maintenance planning. The potential field, which is caused by an electrochemical macro-cell element, is influenced by a number of different factors. Some factors are influenced by the material resistance itself, some by the environmental condition or by a combination of both (e.g. the concrete resistivity and the oxygen level), others are influenced by the geometry of the tested member (e.g. concrete cover) or by geometric conditions caused by the procedure, e.g. grid size. These factors are well known in practice and literature, but the problem is, to analyze these influences separately. All influencing factors have to be evaluated with regard to the defect size; in the case of potential mapping: the anode area. However, in laboratory or on site the correct determination of the anode area during potential mapping is difficult to perform. The aim of this paper is the estimation of the main factors influencing potential mapping by means of numerical simulation. It is expected that some recommendations concerning the procedure and the interpretation of potential mapping data can be derived.

1 BACKGROUND

1.1 *Introduction*

In order to enable mobility of our modern civilization the maintenance of the ageing infrastructure requires knowledge, experience and professionalism of the judging engineer. In addition, the use of inspection data is needed to support decision-making and to reduce the inspection effort.

When a reinforced concrete structure is exposed to deicing salt or seawater the identification of corroding areas is one of the main tasks during inspection. If no maintenance is executed, corrosion can lead to local loss of cross section and subsequent cracking and spalling of the concrete cover.

The only measurement method which enables the detection of corrosion in reinforced concrete structures non-destructively is potential mapping. A lot of factors influence the potential field and therefore the interpretation of potential field data requires expertise of the engineer.

In practice it is difficult to separate and to quantify the input of each influencing factor. A large number of corroding specimens would be necessary. In this paper a numerical approach is pursued to estimate the main factors influencing potential fields to minimize these experimental efforts. This analysis leads to a deeper understanding of potential fields and can provide a helpful support for interpretation of potential fields.

1.2 *Potential mapping*

A lot of standards and guidelines (ASTM C876 (2009), RILEM (2003), DGZfP Merkblatt B3 (2014), Merkblatt SIA 2006 (2013)) describe potential mapping as a method for detecting the corrosion condition in reinforced concrete structures.

When corrosion is initiated, a potential field is established due to the flow of the corrosion current. This potential field can be measured by connecting an external reference electrode at the reinforcement and applying the electrode at the concrete surface. Corroding areas can be assumed mostly at the more negative potential values.

Potential mapping can only provide information about the current corrosion condition during the measurement. Statements about earlier or future corrosion processes are not possible.

But a lot of factors are influencing the extent of the potential field and impair the interpretability.

1.3 *Factors influencing potential fields*

The influencing factors of potential fields can be divided into different groups, Keßler et al. 2011, Reichling et al. 2013.

Group A considers all factors which determine the potential field behavior in an electrolyte, like concrete resistivity, concrete cover, macro-cell geometry, cracks, patch repair etc.. The second group B contains

electrokinetic effects like diffusion potential. Influencing group C includes the absolute value of the electrochemical potential of the reinforcement, which is ruled by the oxygen availability. The test procedure, e.g. grid size etc. is considered in group D.

This research focuses on the quantification of the influencing factors of groups A, C and D.

2 INVESTIGATION

2.1 *Numerical model*

The chosen numerical model reflects a standard geometry like a slab in a parking deck or in a bridge deck, Figure 1.

The quadratic model has a side length of 2 m. The slab contains four reinforcement layers with a diameter of 10 mm and a rod distance of 200 mm. The anode is placed in the middle.

The presented numerical calculations are realized with the Boundary Element Method software BEASY. The validation of the software is presented by Brem 2004, Keßler et. al. 2011 and Schießl et. al. 2012.

2.2 *Input parameters*

For the numerical estimation of the main factors influencing potential mapping several input parameters are varied, Tables 1 and 2.

The variation of the concrete cover corresponds to the range of concrete covers which can be found onsite. The concrete resistivity reflects values of CEM I and CEM III cement under different exposure conditions, Hornbostel et al. 2012, where corrosion processes can be expected. The anode area variation starts with very small spots. In connection with this statement often the question arises which is smallest detectable anode area.

Besides geometry and concrete resistivity the appropriate polarization curves for anodic and cathodic area has to be specified. These curves describe how much current is produced or consumed at the steel surface as a function of the electrochemical potential.

The cathodic polarization behavior can be approximated by the Butler–Volmer equation (1):

$$i = i_{corr}\left\{\exp\left[\frac{\ln(10)(\phi-\phi_{corr})}{b_a}\right]-\exp\left[-\frac{\ln(10)(\phi-\phi_{corr})}{b_c}\right]\right\} \quad (1)$$

where i = current density [A/m^2]; i_{corr} = corrosion current density [A/m^2]; ϕ = potential [V]; ϕ_{corr} = free corrosion potential [V]; b_a = anodic Tafel constant [V/dec]; b_c: cathodic Tafel constant [V/dec].

The anodic reaction (b_a) at the passive reinforcement can be neglected and so only the corrosion current density and the Tafel slope has to be determined for describing the cathodic reaction.

There is a lot of discussion concerning the cathodic polarization behavior in the literature. In this research

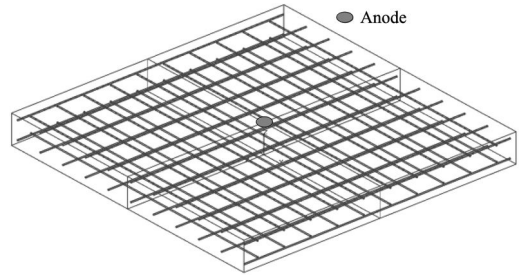

Figure 1. Sketch of the numerical model.

Table 1. Numerical input parameters.

Parameter	Unit	Variation
Concrete cover	mm	10, 20, 30, 40, 50
Resistivity	Ωm	100, 400, 700
Anode area	cm^2	0.8, 1.5, 2.3, 3.1, 3.9, 4.7, 5.5, 6.2, 7.0

Table 2. Electrochemical input parameters.

Parameter	Unit	Variation
R_a	Ω m^2	0.5, **1.3**, 2.0, 10
Driving potential	mV	325, **375**, 425
ϕ_{corr} anode	mV_{SCE}	−540, **−600**, −630
ϕ_{corr} cathode	mV_{SCE}	−175, **−225**, −255
b_c	V/dec	120, **285**
i_{corr}	μA/cm^2	0.003, **0.147**

the values $b_c = 285$ mV/dec and $i_{corr} = 0.145$ μA/cm^2 according to Brem 2004 and $b_c = 120$ mV/dec in combination with $i_{corr} = 0.003$ μA/cm^2 according to Warkus 2012 are selected. These values cover a wide range of cathodic polarization data in the literature, (Raupach 1992, Jäggi 2001).

The anodic polarization behavior can be simplified due to the linearity of the anodic polarization resistance R_a, (Warkus 2012) equation (2).

$$i = \frac{(\phi-\phi_{corr})}{R_a} \quad (2)$$

where i = current density [A/m^2]; R_a = anodic polarization resistance [Ωm^2]; ϕ = potential [V]; ϕ_{corr} = free corrosion potential [V].

The anodic polarization resistance is dependent on the cement type, concrete composition, the chloride content and temperature (Harnisch 2012). The chosen values are in the range of 0 Ωm^2 to 10 Ωm^2. The value of 0.5 Ωm^2 corresponds to a non-polarizable macro-cell anode whereas a very active macro-cell anode is characterized by a value of 10 Ωm^2.

Additionally the free corrosion potential of the anode and the cathode is an important input parameter

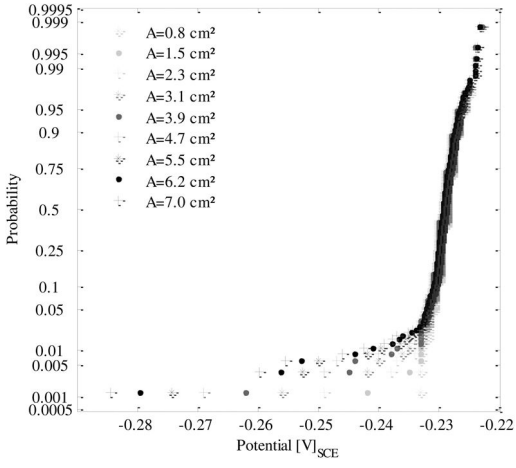

Figure 2. Probability plot with variation of the anode area: resistivity 400 Ωm, concrete cover 40 mm; driving potential 375 mV, R_a 1.3 Ωm^2, grid size 5 × 5 cm^2.

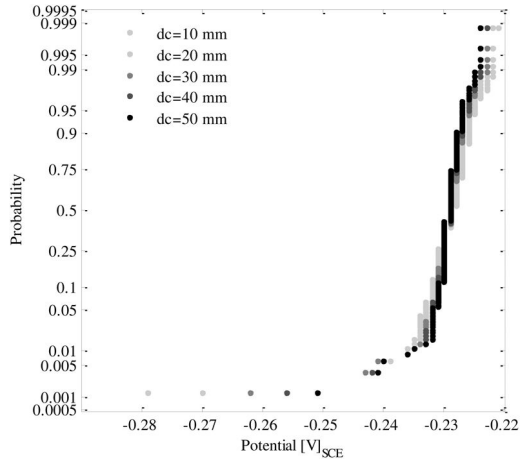

Figure 3. Probability plot with variation of the concrete cover: resistivity 400 Ωm, anode area 3.1 cm^2; driving potential 375 mV, R_a 1.3 Ωm^2, grid size 5 × 5 cm^2.

as well as the difference between them, the driving potential.

The driving potential values are in the range of 325 mV to 425 mV according to Warkus 2012.

The free corrosion potential ϕ_{corr} is influenced by the availability of oxygen. Therefore, different cement types or low water-binder ratio can lead to a denser concrete matrix and poor oxygen diffusion. Also increasing moisture content slows down the transport of oxygen. The concrete resistivity is also mainly affected by the cement type, the water-binder ratio and the moisture content. So, the changes in the free corrosion potential ϕ_{corr} can be expressed through the concrete resistivity.

The following ϕ_{corr} are selected:

$\phi_{corr,A} = -540\,mV_{SCE}$ and $\phi_{corr,K} = -175\,mV_{SCE}$ for R 700 Ωm;
$\phi_{corr,A} = -600\,mV_{SCE}$ and $\phi_{corr,K}$ = -225 mV_{SCE} for R 400 Ωm and
$\phi_{corr,A} = -630\,mV_{SCE}$ and $\phi_{corr,K} = -255\,mV_{SCE}$ for R 100 Ωm, according to Beck 2010 and Harnisch 2012.

The chosen electrochemical input parameters are summarized in Table 2.

If not specified otherwise, the marked values are the standard input parameters.

2.3 *Results*

The results of the numerical parameter study in the form of probability plots are given in the following section.

The standard setting is the cathodic polarization behavior according to Brem 2004 unless otherwise specified and for a better comparability a grid size of 5 × 5 cm^2.

The first plot, Figure 2, shows the potential data in dependency of the anode area.

A growing anode area leads to higher potential differences within a potential field, so the signal "corrosion" is amplified. But it is obvious that an anode area of 0.8 cm^2 is very difficult to detect. The distribution of the passive potentials is not as much polarized as the potential distribution of the active potentials.

Figure 3 presents the potential data with variation of the concrete cover.

The potential difference increases with decreasing concrete cover. This result may lead to the interpretation that smaller concrete cover improves potential mapping data. But with smaller concrete cover the polarizable cathodic area also decreases. So, the potential funnel is very small and as a consequence the detectability is limited, especially in combination with large grid sizes. In Figure 3 a small grid size of 5 × 5 cm^2 is presented.

In summary the concrete cover does have an impact on potential mapping data and the interpretation of potential mapping data has to be performed carefully, when a high spatial variability of concrete cover is measured.

Figure 4 summarizes the potential data dependency as a function of the concrete resistivity. The resistivity is considered as a constant value, so homogenous conditions are simulated in the whole reinforced component.

With increasing concrete resistivity the potentials become more positive and the potential difference within a potential distribution is larger. This effect is explained due to behavior of potential fields in an electrolyte. With low resistivity more cathodic areas are activated further away from the anode. As a conclusion the equipotential lines are very flat and the potential gradient on the concrete surface is relatively weak.

In consequence, high concrete resistivity leads to a better detectability but the resulting potential gradient is locally limited, so a small grid size is recommended.

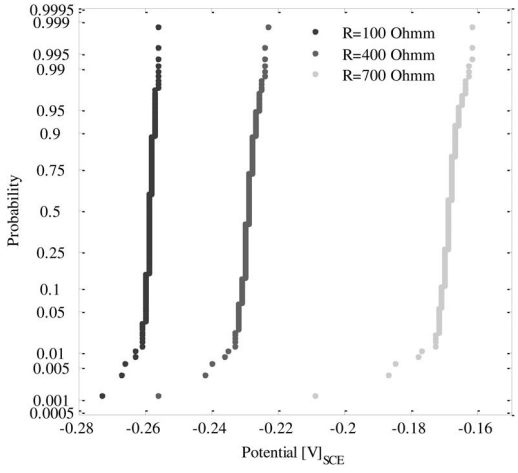

Figure 4. Probability plot with variation of the resistivity: anode area 3.1 cm^2, concrete cover 40 mm; driving potential 375 mV, R_a 1.3 Ωm^2, grid size 5 × 5cm^2.

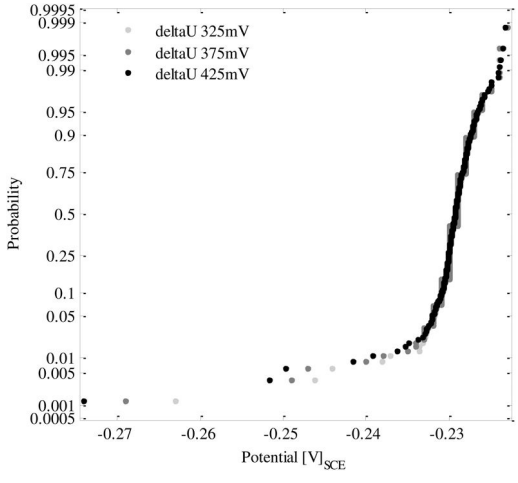

Figure 5. Probability plot with variation of the driving potential: resistivity 400 Ωm, concrete cover 40 mm, anode area 4.7 cm^2, R_a 1.3 Ωm^2, grid size 5 × 5 cm^2.

Additionally, it can be concluded that variations of moisture content in concrete during potential mapping can cause erroneous interpretation. It is recommended to interpret only potential mapping data of concrete surfaces with comparable resistivity, respectively moisture condition.

Figure 5 presents the probability plot with variation on the driving potential.

With increasing driving potential also the potential difference increases. But this effect is not very pronounced. Because a change in the driving potential of about 100 mV results only in a potential difference of ca. 20 mV for the most negative potentials.

The results of the variation of the anodic polarization resistance are plotted in Figure 6.

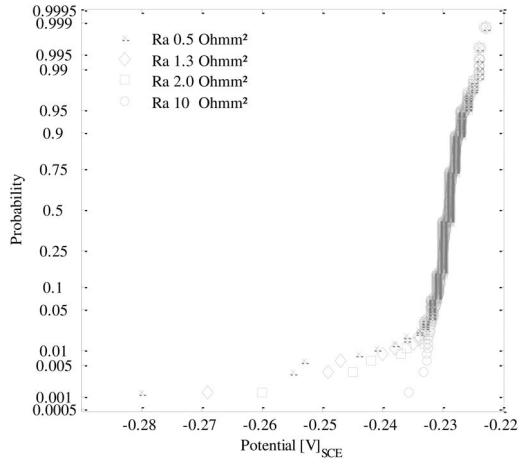

Figure 6. Probability plot with variation of the anodic polarization resistance: resistivity 400 Ωm, concrete cover 40 mm, anode area 4.7 cm^2, driving potential 375 mV, grid size 5 × 5 cm^2.

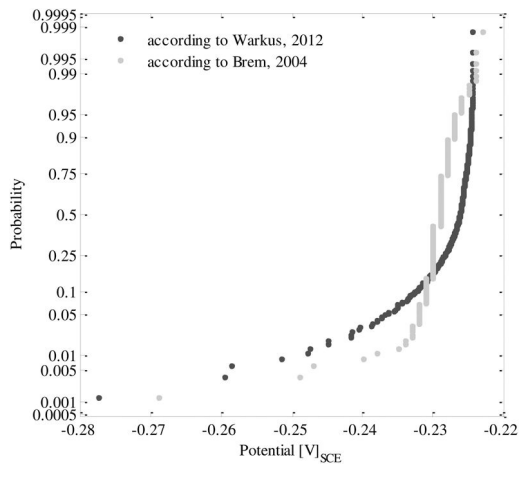

Figure 7. Probability plot with variation of the cathodic polarization curve: resistivity 400 Ωm, concrete cover 40 mm, anode area 4.7 cm^2, driving potential 375 mV, R_a 1.3 Ωm^2, grid size 5 × 5 cm^2.

The change in the anodic polarization behavior affects the potential difference within the potential field. With decreasing anodic polarization resistance the potential difference increases.

The anodic polarization resistance scatters in the case of chloride exposed concrete (XD3) lognormally with $\mu = 1.3\ \Omega m^2$ and $\sigma = 0.63\ \Omega m^2$ according to Osterminski 2013. In this range, the impact of the anodic polarization resistance on potentials fields is negligible.

Figure 7 shows the potential distribution with two different cathodic polarization curves.

The cathodic polarization behavior influences the potential distribution curve. The potential difference is higher with the cathodic curve according to Warkus

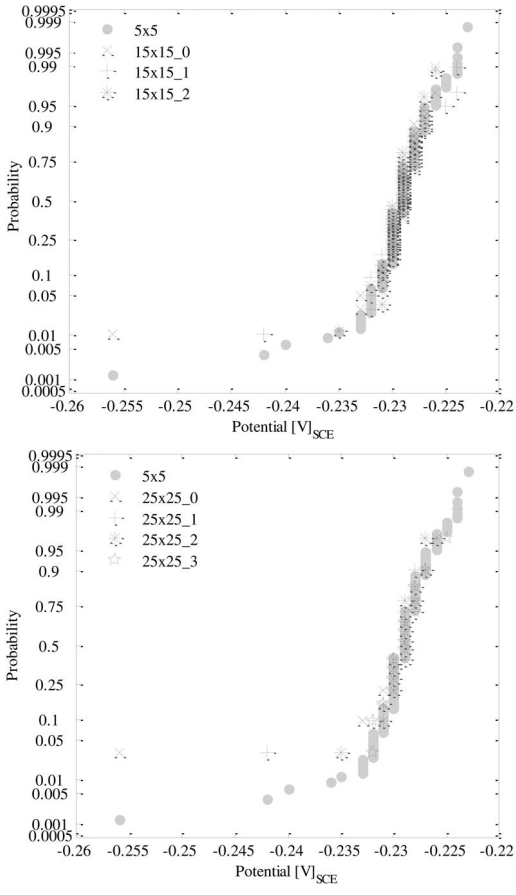

Figure 8. Probability plot with variation of the grid size $15 \times 15\,cm^2$ (above) $25 \times 25\,cm^2$ (below): resistivity 400 Ωm, concrete cover 40 mm, anode area 3.1 cm^2; driving potential 375 mV, R_a 1.3 Ωm^2.

and the potential distribution changes more constantly as the potential distribution according to Brem. But in general the changes are very small in comparison to other influencing factor like the concrete resistivity.

In the case of potential mapping the grid size is an important factor for the detectability of corroding areas. Therefore, numerically simulated potential fields were analyzed regarding the grid sizes $5 \times 5\,cm^2$, $15 \times 15\,cm^2$ and $25 \times 25\,cm^2$, Figure 8. With enlarging grid size the number of data is reduced. This is the reason for the changes in the probability.

Depending on the grid size and the starting point of the potential mapping different grid size combination are possible. The designation "0" means that the reference electrode is placed directly above the anode, "1" the reference electrode is placed 5 cm next to the anode, "2" 10 cm next to anode etc.

For a better comparability all figures contain the data of the grid size of $5 \times 5\,cm^2$ as a grey background.

Comparing the basis grid size $5 \times 5\,cm^2$ with the other grid sizes of $15 \times 15\,cm^2$ and $25 \times 25\,cm^2$ it is obvious that with increasing grid size it cannot be assured that the whole measuring range is covered. But the identification of the more negative potentials is of vital importance because they are the indication of corrosion.

With a denser grid size the probability of detecting the whole potential range increases. So, the grid size has an important impact on the detectability of corroding areas.

3 CONCLUSIONS

The numerical parameter study on potential mapping with the variation of numerous input parameters has shown that the potential field due to corrosion is affected by different factors.

Regarding the groups of influencing factors the most influencing one is group D, the measurement procedure, respectively the grid size. With a smaller grid size the probability of detecting corroding areas increases. Fortunately, this is the only parameter which can be influenced by the engineer. In connection with this an important question has to be answered "which is the smallest anode area to be detected?" Afterwards the chosen grid size can be adjusted.

Coming from the material and exposure side, the concrete resistivity is the main impact factor regarding potential mapping. The concrete resistivity is part of the influencing group A and due to the fact that the resistivity reflects the moisture condition and the availability of oxygen, the resistivity is also part of the influencing group C. Besides the extent of the potential field, the resistivity determines indirectly the free corrosion potential. Within the presented numerical study it is considered only homogenous resistivity condition.

Of particular importance is the resistivity when the structure is freely exposed to weathering. In these kind of structures heterogenic moisture conditions are expected, especially in the case of vertical components. This is the reason why in practice a wider range of potential values is measured (Keßler and Gehlen 2013).

It is recommended to evaluate only potential mapping data together, when the component is in a comparable moisture condition.

The influence of concrete cover and the electrochemical parameters like, driving potential and cathodic and anodic polarization behavior is negligible in comparison to grid size and concrete resistivity.

Obviously the anode area has an impact on potential mapping but based on this effect the success of potential mapping depends.

REFERENCES

ASTM C876, 2009. *Standards Test Method for Half Cell Potentials of Reinforcing Steel in Concrete* American Society for Testing and Materials

Beck, M. 2010. *Zur Entwicklung der Eigenkorrosion von Stahl in Beton*, Diss. RWTH Aachen (German)

Brem, M. 2004. *Numerische Simulation der Korrosion in Stahlbetonbauteilen*, Diss. ETH Nr. 15567, Zürich (German)

DGZfP Merkblatt B3 2014. *Elektrochemische Potentialmessungen zur Detektion von Bewehrungsstahlkorrosion* (German)

Harnisch, J. 2012. *Zeitabhängige Kenngrößen bei der chloridinduzierten Korrosion,* Diss. RWTH Aachen, (German)

Hornbostel, K., Larsen, C.K.; Geiker, M.R.. 2012. Relationship between concrete resistivity and corrosions rate – a literature review, In: *Proceedings International Conference on Durability of concrete*, Trondheim

Jäggi, S. 2001. *Experimentelle und numerische Modellierung der lokalen Korrosion von Stahl in Beton unter besonderer Berücksichtigung der Temperaturabhängigkeit.* Zürich, Eidgenössische Technische Hochschule, Diss.

Keßler, S.; Ebell, G.; Gehlen, C.; Burkert, A.: 2011. Die Aussagegenauigkeit der Potentialfeldmessung, *Beton- und Stahlbetonbau* Volume 106, Issue 7, p. 481–489, (German)

Keßler, S.; Gehlen, C. 2013. Studie zur Potentialfeldmessung an 40 Jahre alten Stahlbetonbauteilen vom Olympiastadion München – Einfluss des Elektrolytwiderstands und des Messrasters, *Beton- und Stahlbetonbau* 108 Heft 9

Merkblatt SIA 2006 2013. *Planung, Durchführung und Interpretation der Potenzialmessung an Stahlbetonbauten*, Zürich (German)

Osterminski, K. 2013. *Zur voll-probabilistischen Modellierung der Korrosion von Stahl in Beton – Ein Beitrag zur Dauerhaftigkeitsbemessung von Stahlbetonbauteilen*, TU München Diss.

Raupach, M. 1992. *Zur chloridinduzierten Makroelementkorrosion von Stahl in Beton. Berlin: Beuth.* Schriftenreihe des deutschen Ausschusses für Stahlbeton Nr. 433 = Diss.

Reichling K., Raupach M., Broomfield J., Gulikers J., L'Hostis V., Kessler S., Osterminski K., Pepenar I., Schneck U., Sergi G., and Tache G. 2013 Full surface inspection methods regarding reinforcement corrosion of concrete structures, In *Materials and Corrosion*, 64, No. 2

RILEM Technical Committees Elsener, B. Andrade, C. Gulikers, J. Polder R. and Raupach, M. 2003 Half-cell potential measurements – potential mapping on reinforced concrete structures. *Materials and Structures*, 36: 461–471

Schießl, P., Osterminski, K., Isecke, B., Beck, M., Burkert, A., Raupach, M., Harnisch, J., Warkus, J., Tian, W. 2012. Deterioration model and input parameters for reinforcement corrosion. *Structural Concrete*, Vol. 13, No. 3.

Warkus, J. 2012. *Einfluss der Bauteilgeometrie auf die Korrosionsgeschwindigkeit von Stahl in Beton bei Makroelementbildung*, Diss. RWTH Aachen, (German)

Concrete Solutions – Grantham et al. (Eds)
© 2014 Taylor & Francis Group, London, ISBN 978-1-138-02708-4

Freeze-thaw resistance testing of concrete railway sleepers

A. Köliö, T. Rantala, J. Lahdensivu & A. Nurmikolu
Tampere University of Technology, Tampere, Finland

ABSTRACT: Concrete samples taken from existing concrete railway sleepers were studied in the laboratory with methods that indirectly measure freeze-thaw durability and were also tested directly in a freeze-thaw chamber. The samples were monitored during the freeze-thaw tests with ultrasonic pulse velocity and gravimetric measurements. The residual strength of the specimens was measured by splitting the samples after the freeze-thaw test. As one of the results, fairly good consensus between the indirect and direct freeze-thaw resistance test methods was achieved.

1 INTRODUCTION

1.1 *TERA project – railway sleepers*

Owing to the need for better understanding in the life cycle of concrete sleepers installed in railway track during various decades, the Finnish Transport Agency (FTA) launched a comprehensive research programme at the Tampere University of Technology (TUT). The Department of Civil Engineering studied the failure mechanisms of concrete sleepers as a part of the Life Cycle Cost Efficient Track (TERA) research programme in 2009–2012.

The main objective of the project was to get an understanding of the determining factors in the failure of concrete sleepers based on domestic and foreign research findings and experiences. The scope of the project included the present situation pertaining to concrete sleepers including dimensioning, manufacturing, effects of the severe loading environment of the track and identified problems. The main focus was on prestressed monoblock concrete sleepers, which are practically the only concrete sleeper type of Finnish railways. Before the tests presented here, the researchers at TUT performed cyclic loading tests on concrete sleepers under varying ballast conditions (Nurmikolu et al. 2010) to estimate the soil-structure interaction of a railway track. Also loading tests were performed on decommissioned and unused sleepers. Loading tests were based on standards SFS-EN 13230 (Kerokoski et al. 2011).

1.2 *Objective*

The objective of the part of the study presented in this paper was to assess the long-term durability of concrete railway sleepers. Concrete samples taken from existing concrete railway sleepers were studied in the laboratory of Tampere University of Technology with various methods that indirectly measure freeze-thaw durability and tested in freeze-thaw chamber in accordance to national standard SFS 5447.

2 BACKGROUND

2.1 *Concrete railway sleepers*

The sleeper is one of the most important components of a railway track because of its behaviour under loading. The most important functions of sleepers are to transfer rail forces to the ballast layer, to serve as a support and mount for the rail foot and fastenings, and to preserve track gauge.

Concrete sleepers have been used in Finland since the early 1960s. Then, sleepers were post-tensioned and lighter than modern sleepers. The good experiences of concrete sleepers and their relatively competitive price increased production volumes significantly in the early 1990s. At present, concrete sleepers are manufactured in two plants in Finland. Parma Oy's plant in Forssa has manufactured a total of about five million and the Siilinjärvi plant of Lujabetoni Oy about three million sleepers in the past 23 years. At the end of the year 2013 about ten million concrete railway sleepers have been made in Finland and currently nearly 70% of the Finnish rail network is equipped with prestressed concrete monoblock sleepers. The minimum required concrete grade in these sleepers has been C50/60.

Sleeper production volumes vary annually. For example in 1997 about 700000 railway sleepers were manufactured and in 2012 less than 300000 sleepers were manufactured.

Despite mainly positive experiences, weathering problems have been detected in some sleeper types made in Finland between the 1960's to 1980's. The problems were caused by delayed ettringite formation

(DEF) but the problems have been brought under control by limiting the curing temperature of concrete. Currently the maximum curing temperature is 55 ^{o}C and the highest recommended temperature is 50 ^{o}C. Problems with DEF also occurred in Sweden. The problem was perceived in the late 1990s and after that hundreds of thousands of deteriorated concrete sleepers have been found (Thun, 2006). In Finland problems with DEF were not as significant as in Sweden.

Weathering problems are one of the reasons why the target for service life is about 30 years for sleepers made before the year 1982 and 40 years for sleepers made after that. Recent research findings by TUT have shown that the service life can actually be longer (Kerokoski et al. 2013).

2.2 *Degradation of concrete by freeze-thaw action*

Freeze-thaw attack due to a high moisture load is a common reason for the deterioration of concrete structures in the Nordic outdoor climate. Concrete is a porous material whose pore system may, depending on the conditions, hold varying amounts of water. If the level of water saturation of the system is high, the overpressure created during freezing cannot escape into air-filled pores and thus damages the internal structure of the concrete resulting in its degradation. More than 15 different theories or explanations for freeze-thaw attack on porous materials have been presented (Kuosa & Vesikari 2000).

The early phase of freeze-thaw damage is manifested as inner cracking of concrete or scaling of the concrete surface when the hydraulic pressure caused by freezing pore water exceeds the tensile strength of concrete. Cracking will decrease the strength of concrete and increase capillary water absorption. Continuing freeze-thaw cycles and a high moisture content of concrete will finally lead to freeze-thaw damage. (Neville 1995). Far advanced freeze-thaw damage is manifested as a reduction in strength of concrete, loss of adhesion, or crazing or chipping off of the surface due to internal expansion and subparallel cracking to the surface.

2.3 *Testing concrete by ultrasonic pulse velocity measurements*

The ultrasonic pulse velocity (UPV) in a solid medium is related to the density and elastic properties of the material. Degradation alters these properties in concrete and, therefore, can be observed as a change in the pulse velocity through damaged specimen. The relation of ultrasonic pulse velocity to the dynamic elastic modulus and density of a material is described by equation 1, where V is the UPV through material, E is the dynamic elastic modulus, ρ is density and υ is the Poisson's ratio. (Grantham 2003).

$$V = \sqrt{\frac{E}{\rho}} \cdot \frac{(1-\upsilon)}{(1+\upsilon)\cdot(1-2\upsilon)} \quad (1)$$

Degradation of a material can be studied by measuring the transit time of ultrasound through a material sample with certain intervals while it is being stressed by a degrading agent e.g. in this case freeze-thaw attack. When measurements are done in the initial stage and with certain intervals the equation 1 can be written as a relative equation 2 where the ratio of final and initial elastic dynamic modulus (E_N and E_I respectively) is directly proportional to the square of the ratio of final and initial ultrasonic pulse velocity (V_N and V_I respectively) through the material.

$$\frac{E_N}{E_I} = \left(\frac{V_N}{V_I}\right)^2 \quad (2)$$

As concrete is non-uniform and porous, the measurements are affected by concrete properties and the moisture of the specimens at the time of measurements. In various durability related cases, pulse velocities of 3500 – 4500 m/s (Qasrawi, 2000; Popovics & Popovics, 1991) or 3200–5500 m/s (Kewalramani & Gupta, 2006) have been measured from undamaged concrete samples. On the other hand, the influence of e. g. compressive strength on the ultrasonic pulse velocity through concrete has been shown to be quite clear (Grantham 2003). It would therefore be advisable to use relative measurements compared to the initial situation of the same sample rather than compare to literature values and to make the measurements always in the same moisture state.

3 RESEARCH METHODS AND MATERIAL

3.1 *Material*

In all 22 concrete railway sleepers were subjected to indirect and direct freeze-thaw durability tests during this study. The tested railway sleepers were removed from different parts of the Finnish railway network and those sleepers were manufactured 15 to 40 years ago. Also two new and unused sleepers were tested. Sleepers were extracted from the railway network in two batches. Batch 1 was distributed geographically (sleepers 1 to 12). Sleepers 13 and 14 in batch 1 were taken from storage as reference samples. Those sleepers were manufactured in 2009 and had been unused until the day of test. Batch 2 sleepers were all from the same Vartius railway section representing sleepers visually in different stages of degradation (sleepers V2, V3, V4, V5, V6, V8, V9 and V14). Cylindrical concrete specimens with the diameter of 50 mm were drilled from the studied railway sleepers in a vertical direction. In all, three specimens were drilled from each sleeper in batch 1 and five specimens from each sleeper in batch 2.

3.2 *Visual inspection*

All of the cylinder specimens were inspected visually. The quality of concrete was determined visually from

a scale 1 to 5 (very poor – poor – mediocre – good – very good, respectively) in regard of compaction, visible air voids and cracking. Maximum aggregate size was measured from particles visible on the cutting surface. After the visual inspection and carbonation depth measurements, the specimens were cut into 100 mm long cylinders and their diameter, length, weight and dry density were determined.

3.3 *Carbonation depth measurements*

Carbonation depth was measured from the fresh cutting surface of the concrete cylinders by spraying the surfaces with phenolphthalein solution. The phenolphthalein solution reacts in pH above 9 by changing the colour of concrete to fuchsia. The depth of carbonation from the upper and lower surface of the sleeper was measured as the thickness of the uncoloured layer. No significant carbonation was observed from these specimens.

3.4 *Porosity measurements*

The porosity of the concrete specimens was measured as the volume of capillary pores and the protective pore ratio, which describes the share of pores that stay air-filled in water immersion. The requirement for the protective pore ratio is 0.20 to ensure freeze-thaw resistance of concrete (BY 15, 1980). The properties were determined according to the Finnish standard SFS 4475.

The properties were determined by weighing the specimens in three moisture states: dry, capillary saturated and vacuum impregnated. Due to the test method, the porosity is given as the percent by weight. It was converted to % by volume with concrete density determined earlier by the Archimedes' principle. Capillary saturation was done by immersing the specimens in water. A container with the specimens was first filled half way with water and then after 8 hours filled up completely immersing the specimens. The specimens were weighed after a total time of 72 hours. The specimens were dried at a temperature of 105°C for 72 hours. Vacuum impregnation was done by placing the specimens in a vacuum container and filling the vacuum with water. The specimens were left in the vacuum for 72 hours and were then weighed.

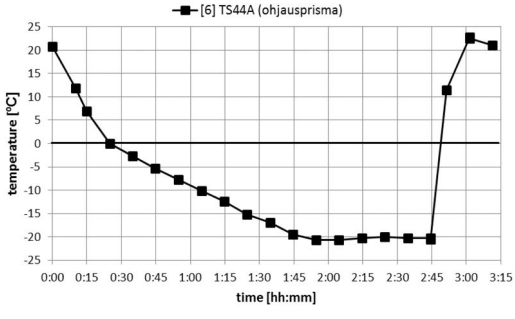

Figure 1. The temperature inside a control sample during one freeze thaw cycle.

3.5 *Freeze-thaw test*

The concrete specimens were exposed to automated freeze-thaw cycles in accordance to national standard SFS 5447. The freeze-thaw cycle used is shown in Figure 1. The number of cycles in the tests was 50 or 100 cycles. During the freeze thaw exposure the gravimetric changes (batch 1) and ultrasonic pulse velocity were measured and the specimens were inspected visually. The tensile splitting strength was measured after the completion of the freeze-thaw cycles as a residual indicator of the concrete strength. One series was stored in water immersion as a control group during the freeze-thaw test. Same measurements were done also from the control group. Table 1 shows the test schedule for the different specimen series.

The temperature of the freeze-thaw test was controlled with a monitoring prism made of highly freeze-thaw resistant concrete that contained a thermal sensor.

Table 1. Test schedule for the concrete samples.

Series	Freeze-thaw (SFS-5447)	Measurements
Batch 1		
Series A	100 cycles	ultrasonic pulse velocity and gravimetric changes every 25 cycles, tensile splitting strength after 100 cycles
Series B	control group (water immersion, no freeze-thaw)	ultrasonic pulse velocity and weighing in the beginning and at the end, tensile splitting strength at the end.
Batch 2		
Series A	50 cycles	ultrasonic pulse velocity every 25 cycles, tensile splitting strength after 50 cycles
Series B	control group (water immersion, no freeze-thaw)	ultrasonic pulse velocity in the beginning and at the end, tensile splitting strength at the end.
Series C	100 cycles	ultrasonic pulse velocity every 25 cycles, tensile splitting strength after 100 cycles

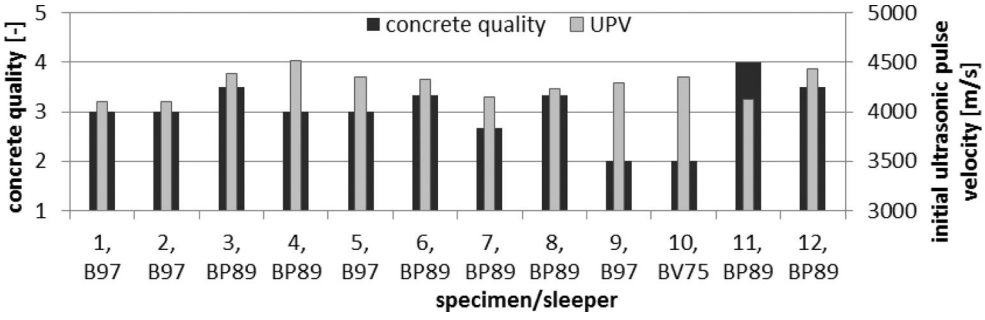

Figure 2. Visual rating of concrete quality and initial UPV measurements from batch 1 sleepers.

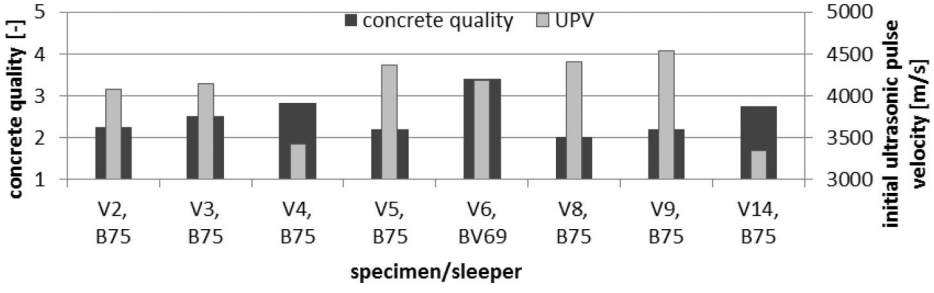

Figure 3. Visual rating of concrete quality and initial UPV measurements from batch 2 sleepers.

Also the air temperature in the freeze-thaw chamber was monitored 20 cm above the test specimens. The freeze-thaw cycle was composed of a freezing phase, where the temperature reached −20°C, a withhold phase to maintain the temperature for an hour and a thawing phase, where the temperature of the specimens was raised to +20°C by immersing them in warm water. During the three hour cycle, the temperature of the specimens was below 0°C approximately 2 h 10 min and above, approximately 50 min. The average freezing rate in the cycle was 0.36°C/min for 1 h and 45 min and the thawing rate was 2.5°C/min.

3.6 *Ultrasonic pulse velocity measurements*

The ultrasonic pulse velocity measurements were done using the transmission technique where pulsed waves were transmitted through the material sample to a receiver probe (SFS-EN 583-3). Ultrasonic pulse velocity through the concrete specimens was measured at the beginning of the freeze-thaw test and every 25 cycles. The measurements were done using a Maxi Tester Mod. PC91 Lucchi Elasticity tester. The penetration time of the ultrasonic pulse was measured in three different moisture states of the concrete specimens: immediately after the 25 cycles, dry and capillary saturated. Each measurement is an average of three readings. Drying and saturating of specimens was done in the same way than in porosity measurements.

3.7 *Gravimetric changes*

The specimens of batch 1 were also weighed in the beginning of the freeze-thaw test and every 25 cycles to compare the results of ultrasonic pulse velocity measurements.

3.8 *Residual strength*

In addition to the measurements done in between the freeze-thaw cycles, the residual tensile splitting strength was measured (SFS-EN 12390-6) at the end of the test schedule by compressing the cores horizontally with ELE AUTOTEST 25/250 –testing device. The diameter of the cores was 50 mm and length 100 mm. The loading speed in the test was 0.50 kN/s.

4 RESULTS AND DISCUSSION

4.1 *Freeze-thaw resistance properties prior to freeze-thaw cycles*

The concrete quality was graded visually with a grade from 1 to 5. The quality shown for batch 1 in Figure 2 is an average of three samples/sleeper and for batch 2 in Figure 3, an average of five samples/sleeper. The initial measured ultrasonic pulse velocity through the samples is illustrated in the narrow column in the figure. The initial (capillary saturated) UPV measured

Table 2. Results from the indirect frost resistance measurements and residual tensile splitting strength after the freeze-thaw test.

			Frost resistance parameters			Residual tensile splitting strength				
ID	Type of sleeper	Manufacture year	Capillary saturation content [% by wt.]	Capillary porosity [% by vol.]	Protective pore ratio	Reference sample [MPa]	50 cycles [MPa]	Change to reference [%]	100 cycles [MPa]	Change to reference [%]
Batch 1										
1	B 97	1998	4.1	9.9	0.11	5.05			1.10	−78%
2	B 97	1998	4.6	10.8	0.20	2.95			2.60	−12%
3	BP 89	1993	3.9	9.7	0.06	4.70			1.15	−76%
4	BP 89	1992	4.1	9.7	0.14	5.40			1.65	−69%
5	B 97	1998	5.0	11.7	0.16	3.85			3.45	−10%
6	BP 89	1993	4.2	10.0	0.05	3.60			1.15	−68%
7	BP 89	1994	4.4	10.5	0.02	3.45			0.75	−78%
8	BP 89	1994	4.1	9.8	0.14	3.00			0.60	−80%
9	B 97	1997	4.1	11.2	0.24	2.75			2.70	−2%
10	BV 75	1977	4.9	8.1	0.14	6.60			1.65	−75%
11	BP 89	1990	3.2	10.0	0.06	3.55			1.40	−61%
12	BP 89	1991	4.2	9.9	0.07	3.90			1.95	−50%
13	BP 99	2009	4.1	10.7	0.07	4.50			1.50	−67%
14	B 97	2009	4.4	7.8	0.22	4.70			2.70	−43%
Batch 2										
V2	B 75	1975	3.6	8.6	0.21	4.60	2.10	−54%	1.15	−75%
V3	B 75	1975	3.7	9.0	0.10	2.85	1.25	−56%	0.15	−95%
V4	B 75	1975	3.5	8.4	0.11	2.40	1.75	−27%	0.70	−71%
V5	B 75	1975	3.2	7.7	0.23	4.60	1.95	−58%	1.40	−70%
V6	BV 69	1975	4.7	11.2	0.02	4.00	0.25	−94%	0.00	−100%
V8	B 75	1975	2.9	7.0	0.23	5.10	4.35	−15%	2.50	−51%
V9	B 75	1975	2.9	7.1	0.16	5.15	2.85	−45%	1.95	−62%
V14	B 75	1975	3.7	9.1	0.05	1.90	1.25	−34%	0.65	−66%

was 4000–4500 m/s in batch 1 and 3300–4500 m/s in batch 2.

The concrete quality grade is a measure of the porosity and compaction of concrete. The grading indicates well the initial differences among the test specimens prior to the freeze-thaw test.

Porosity properties measured prior to the freeze-thaw test are presented in table 2. The capillary porosity of the concrete in batch 1 was by average 10.0% (range 7.8–11.7%). The protective pore ratio was by average 0.12 (range 0.02–0.24). Sleepers 2 and 9 fulfilled the national requirement for freeze-thaw resistant concrete (0.20). Thereby they were expected to withstand well also in the freeze-thaw test. On the other hand, sleepers 3, 6, 7 and 11 were expected to be the worst. The protective pore ratio was in general higher in B97 sleepers than in BP89 sleepers. The B97 sleepers are newer than BP89 sleepers.

In batch 2 the capillary porosity was by average 8.5% (range 7.0–11.2%). The protective pore ratio was by average 0.14 (range 0.02–0.23). In batch 2 sleepers V2, V5 and V8 fulfilled the national requirement for freeze-thaw resistant concrete.

4.2 *Ultrasonic pulse velocity and gravimetric measurements*

During the freeze-thaw test, the samples were monitored every 25 cycles by measuring the UPV and weight change. The samples were weighed capillary saturated and, therefore, an increase of weight was observed as cracking of concrete increased, increasing the amount of water able to be absorbed in pores and cracks in concrete. A good agreement was observed between the two methods as shown in Figures 4 and 5.

The ultrasonic pulse velocity decreased with the increase in weight of capillary saturated samples. The both methods indicated that samples 6, 7, 8 and 11 were degrading fast and samples 2, 5 and 9 were the most durable.

4.3 *Residual tensile splitting strength of concrete*

All of the specimens were split after either 100 or 50 freeze-thaw cycles and the tensile splitting strength was measured. The results are shown in table 2. All samples except numbers 2, 5 and 9 in batch 1 had a significant decrease in tensile splitting strength during the freeze thaw test compared to the reference sample. In batch 2, all of the sleepers were already damaged to various extent in the beginning of the tests. Therefore, all of the specimens were significantly degraded during the test.

Figure 6 shows the comparison between the residual tensile splitting strength measurements and the residual ultrasonic pulse velocity measured from saturated concrete samples after the freeze-thaw test.

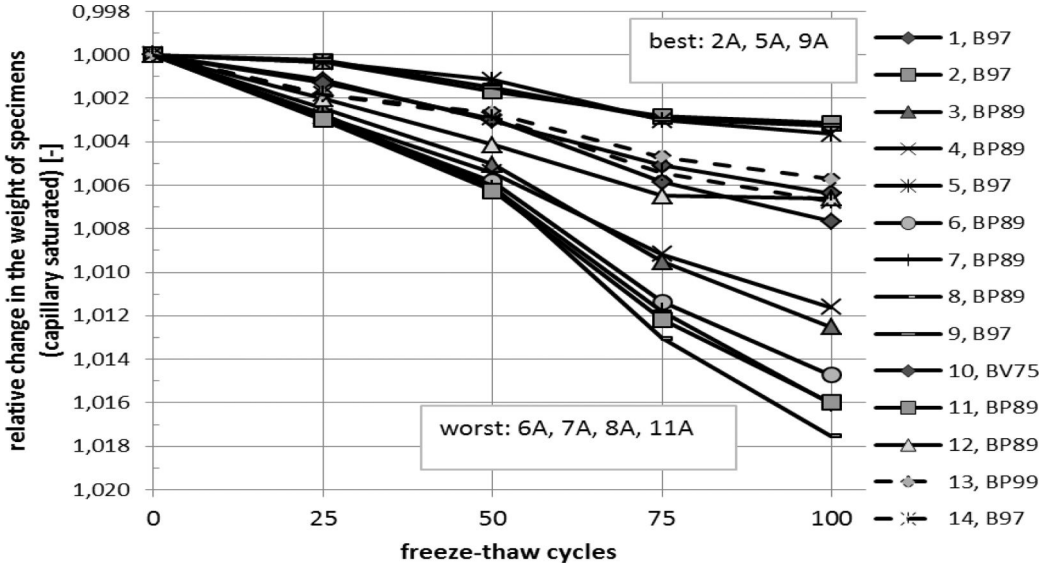

Figure 4. Weight changes of the specimen after each 25 cycles of freeze-thaw. The samples were capillary saturated before the weighing. Therefore, the specimens gained weight.

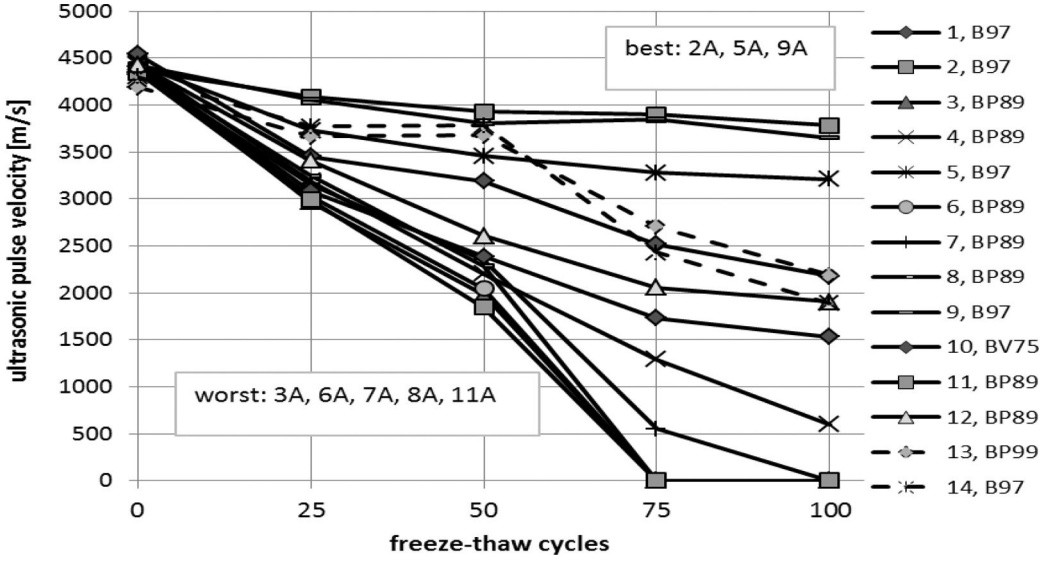

Figure 5. Changes in the ultrasonic pulse velocity through the samples during the freeze-thaw test. The samples were capillary saturated before the measurements of the UPV.

The level of residual tensile splitting strength correlates quite well with the level of residual ultrasonic pulse velocity.

However, in the lower strength range, the progression of the ultrasonic pulse was hindered already (unable to pass through the cracks) at the level of approximately 1 MPa of residual tensile splitting strength. Therefore, lower strengths than 1 MPa were not detected by the ultrasonic pulse velocity measurements.

5 CONCLUSIONS

In general, a fairly good consensus between the indirect and direct freeze-thaw resistance test methods was achieved. Although, little or no correlation was observed between the initial visual rating and the actual durability parameters of the concrete samples.

From the samples that had been categorized by the protective pore ratio as freeze-thaw resistant two out of three had the smallest reduction in the residual tensile

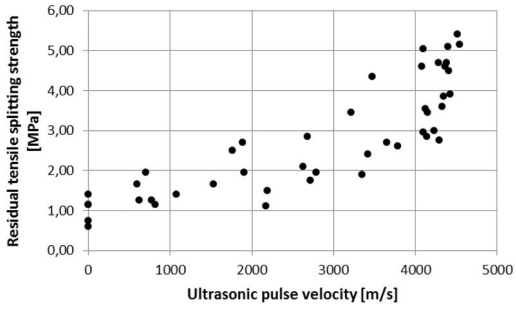

Figure 6. Correlation plot of the residual tensile splitting strength and ultrasonic pulse velocity in capillary saturated samples measured after the freeze-thaw test.

splitting strength. These samples that had the best durability in the freeze-thaw test were also identified by ultrasonic measurements and gravimetric measurements. The requirement of a protective pore ratio of 0.20 will lead to good freeze-thaw resistance in the direct freeze-thaw test, but if the value is even slightly below this requirement, the durability is unclear. Furthermore, samples with small (<0.10) protective pore ratio were degraded extensively in the direct freeze-thaw test. In the case of batch 2, all of the sleepers were initially damaged. Thus, the samples degraded extensively in the tests and agreement between the protective pore ratio and degradation could not be achieved.

The residual tensile splitting strength measurements and the residual ultrasonic pulse velocity measured from saturated concrete samples after the freeze-thaw test have a fairly good correlation as is also established in literature regarding compressive strength. This case has to be considered differently because the lower splitting tensile strength is here caused by cracks induced in freeze-thaw (not gained by hydration as in comparing different compressive strengths). The results indicate that ultrasonic pulse velocity measurements can reliably be used in estimating the progress of degradation by freeze-thaw attack. However, the residual performance level of concrete after far advanced freeze-thaw attack may not be accurately detected.

ACKNOWLEDGEMENTS

The study was funded as a part of TERA research programme by Finnish Transport Agency.

REFERENCES

BY 15. 1980. Finnish concrete code – RakMK B4. Finnish Concrete Association, Helsinki.

Grantham M. 2003. 6 – Diagnosis. inspection. testing and repair of reinforced concrete structures In: Newman J. (editor). Advanced Concrete Technology Set. Vol. 2. Oxford. Butterworth Heinemann. Ss. 6/1–6/54

Kerokoski, O., Nurmikolu, A., Rantala, T., Lilja, V. & Viitala, T. 2011. Structural behaviour and failure mechanisms of monoblock concrete railway sleepers. Proceedings of 9th International Congress on Railway Research, WCRR 2011, May 22–26, Lille, France.

Kerokoski, O., Rantala, T. Köliö, A. & Nurmikolu, A. 2013. Structural behaviour and failure mechanisms of concrete sleepers. Liikenneviraston tutkimuksia ja selvityksiä 37/2013. Liikennevirasto, Helsinki. ISBN 978-952-255-302-7. (In Finnish)

Kewalramani M.. Gupta R. 2006. Concrete Compressive Strength Prediction Using Ultrasonic Pulse Velocity Through Artificial Neural Networks. Automation in Construction 15 (2006). Ss. 374–379.

Kuosa, H., Vesikari, E. 2000. Ensuring of concrete frost resistance Part 1: Basic data and service life design. VTT Technical Research Centre of Finland. Research notes 2056. 141 p. (in Finnish)

Neville, A. 1995. Properties of concrete. Essex. Longman Group. 844 p.

Nurmikolu, A., Kerokoski, O., Rantala, T. & Viitala, T. 2010. Cyclic loading tests of concrete sleepers with varying ballast condition. JRC2010. Proceedings of the 2010 Joint Rail Conference. April 27–29, 2010, Urbana, Illinois, USA. 9 pages.

Popovics S. Popovics J. 1991. Effect of Stresses on the Ultrasonic Pulse Velocity in Concrete. Materials and Structures 24 (1991). Ss. 15–23.

Qasrawi H. 2000. Concrete Strength by Combined Nondestructive Methods Simply and Reliably Predicted. Cement and Concrete Research 30 (2000). Ss. 739–746.

SFS 4475. 1988. “Concrete. Frost resistance. Protective pore ratio”. Finnish Standards Association SFS, Helsinki.

SFS 5447. 1988. “Concrete. Durability. Freeze-thaw resistance”. Finnish Standards Association SFS, Helsinki.

SFS-EN 12390-6. 2010. Testing hardened concrete. Part 6: Tensile splitting strength of test specimens. Finnish Standards Association SFS, Helsinki.

SFS-EN 583-3. 1997. Non destructive testing. Ultrasonic examination. Part 3: Transmission technique. Finnish Standards Association SFS, Helsinki

Thun, H. 2006. Assessment of Fatique Resistance and Strength in Existing Concrete Structures, Doctoral thesis, Luleå University of Technology.

This page intentionally left blank

Concrete Solutions – Grantham et al. (Eds)
© 2014 Taylor & Francis Group, London, ISBN 978-1-138-02708-4

Importance of proper site evaluation and sample selection in non-destructive testing

Malcolm Lim & Paul Siwek
Proceq, Gurnee, Illinois, USA

ABSTRACT: Nondestructive testing has been successfully used globally in structural evaluation as a tool to identify underlying causes of deterioration or anomalies within the concrete structure, identifying both material and structural issues. In either case, using different nondestructive testing techniques helps to provide a more complete picture of the underlying cause of deterioration and obtaining results with limited openings and disruptions. As part of the investigation, understanding site conditions and obtaining information-filled core samples are the keys in determining the cause of the deterioration. In addition, it aids in finding the correct repair solution for the problem. These samples can also be used to correlate different nondestructive testing results to actual material properties. This paper will discuss the importance of custom curves correlating nondestructive testing results to material properties, thereby ensuring that the testing yield accurate results.

1 INTRODUCTION

It is very easy to walk onto a site and look at the different structural features facility without noticing the little details that may provide clues as to what has been happening over the last few years or even over the past few decades that have contributed to the deterioration of the structure. The clues to the cause of deterioration are always there, and to an experienced inspector, the clues tell a story of the events that have taken place over time to cause the deterioration.

The key to successfully evaluating a structure is to have a plan and to know what to look for. Many times, an engineer performs an evaluation with little or limited knowledge of the structure and its history. Not doing the homework to understand the different features of the structure will typically result in repair recommendations that address the symptom and not the cause. In this case, the repair recommendations typically will not last the desired timeframe and will need to be re-addressed in the not too distant future.

2 VISUAL INSPECTION

Initial on-site visual inspection should include an overall visual survey map showing the location of the deteriorations present. The size of each deteriorated surface should be indicated with the proper scale and color delineation of the deterioration. This will allow for the helicopter or top down view of the deteriorations that may be present in the structure[1]. Scaled base sheets with a legend showing the different common types of deterioration should be created so that the size, shape and location of each deteriorated area found will be consistent throughout all the sheets.

One of the key deteriorations in any structure evaluation is differentiating the many types of cracking that may be present in the structure. By recognizing and distinguishing the different types of cracks, it is possible to provide an indication as to the underlying cause associated with the cracking. Surface cracking or crazing is due to rapid evaporation of the moisture of the surface of the concrete or some other mechanism, for example Alkali-Silica Reaction (ASR), or Delayed Ettringite Formation (DEF). Structural cracking can be identified by understanding the load-carrying capacity and structural movement of the building. Typical types of cracking include:

- Pattern Cracking: Fine or minute cracking, regular in pattern. Due to volume change near the surface.
- Hairline Cracking: Small cracks that are usually randomly in location or pattern, in exposed areas.
- D-Cracking: Fine closely spaced cracks in a random pattern.
- Shrinkage cracking: A crack that occurs due to shrinkage of the concrete or restraint. Typically perpendicular to the longer orientation of the structure. Typically occurs after the concrete has hardened.
- Plastic cracking: Caused by rapid drying of the concrete surface after placement of the concrete. Most likely due to delays in curing operations. Occurs while the concrete is still "green."
- Structural cracking: Usually a result of movement of a structure in response to applied loads. This could be due to the structure not being designed adequately or the structure was not constructed correctly.

[1] Editor's note. In the UK, developed elevations are usually drawn with defects shown as if the reader were looking at that elevation, rather than "top down."

- Rust cracking: gradually develops over corroding reinforcing and appears at varying rates over time depending upon the degree of protection offered by the concrete cover. The concrete above the reinforcing bar provides a high pH environment, which protects the bar. The concrete cover can be compromised due to carbonation over time, or introduction of chlorides as marine or deicing salts. Once this protective layer has been compromised, the reinforcing bar will start to corrode, under ideal conditions. (ACI, 2008).

The mapping should include the crack width, length and the depth of the crack, and nondestructive testing can be used to estimate the depth of the crack. By mapping these types of deterioration, it can provide a roadmap to the evaluation of the structure.

Base sheets are a very important part of the field evaluation. Many times, base sheets are not created, and the deteriorations are just sketched out with little consideration in proportioning the amount of information present. Examination of the base sheets can provide some preliminary information such as whether the deteriorations are concentrated towards a certain area in the building. This information would be useful in the development of a testing plan. The testing plan might include nondestructive testing, sample selection and extraction, to determine the underlying cause of the deterioration. Having well-drawn base sheets can also serve as a checklist to ensure the objectives of the evaluation are completed.

3 UNDERSTANDING SAMPLE SIZE

There are many factors that influence the evaluation of a structure that are beyond the control of an engineer. Factors such as limited access to possible test areas, limited amount of time to perform the evaluation, or a small budget can limit the number of samples that can be obtained during the evaluation. As an engineer, it is important to weigh the amount of samples taken versus the limitations set forth by the project. These limitations are always negotiable, but in most situations, it is up to the engineer to figure out how to best serve the client and still adhere to the guidelines set forth. Taking samples from a structure is a critical step that can provide a great deal of information regarding potential causes of the deterioration. The information can include concrete compressive strength, amount of chlorides present at varying depths, concrete cover measurements etc. The number of samples that can be obtained is usually limited. Nondestructive testing can be used to provide additional information without damaging the structure.

When evaluating for concrete strength, there are many different nondestructive testing tools that have been accepted as an accurate means in determining the compressive strength of the concrete e.g (ASTM, 2013). One of the big advantages of utilizing nondestructive testing tools is that a great deal of information

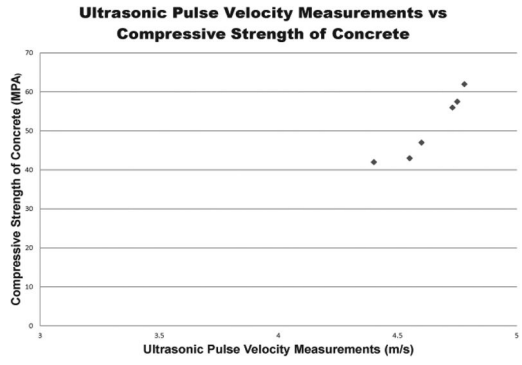

Figure 1. Data correlation from a limited set of data.

can be obtained with minimal or no damage to the structure. The conventional method of extracting cores and then sending the cores to a laboratory for conventional testing using a compression machine is labor intensive with a long turnaround time. Mishandling of the samples or inappropriate storage during transportation can affect the overall results. One advantage of utilizing nondestructive testing is that several tests can be performed even when there are limited test areas.

Statistically, obtaining a small number of samples is fine, but if the evaluation of a structure is based upon a limited number of samples, this can skew the data that is obtained. Also, with a small selection of samples, the distribution of the samples will be limited. ASTM C823 (ASTM, 2000) requires that the extracted samples be distributed throughout the structure. The distribution is based upon a designated size of test area, i.e. a certain amount of square meter/square footage. This allows for samples to be obtained throughout the structure and not confined to just a few specific areas.

With a small sample size, the results obtained are confined to the data set. In figure 1, the graph shows the correlation of ultrasonic pulse velocity measurements to compressive strength of concrete over a limited range. Five samples were obtained, and a trend line was added to the graph. The best-fit trend line was an exponential function, with a 0.9402 R-squared value. The data set show a good fit; however, one should keep in mind that the data set is only valid for that particular range of data, which would be 4,500 m/s to 4,750 m/s for this particular case.

Once a good correlation curve is established, nondestructive testing methods can then be used to evaluate the rest of the structure and correlate the data to determine the necessary information. It is important that the moisture content of the structure is similar to that of the samples used for calibration. Moisture affects both Schmidt hammer and ultrasound readings.

4 UNDERSTANDING SAMPLE SELECTION AND TESTING

Selecting samples to be tested in the field can be a very simple yet daunting task. Selection of the

samples should be based upon the primary objective that the samples will reveal information regarding the circumstances that led up to the deterioration. By obtaining samples in the wrong location, data will be provided on the structure that may not be relevant to the evaluation. It is relatively easy to select samples in convenient locations in order to complete the task. However, the criteria for selection cannot be based upon a convenient location but should be based on the following:

1. A control sample should be obtained away from any deterioration in order to establish baseline material properties.
2. If surface deterioration is present, such as scaling, the sample should be selected bridging across the deteriorated section and an apparently good section. Obtaining the sample in just the deteriorated section will not reveal the cause of the deterioration. Many times the cause of the deterioration, such as scaling, is due to a lack of air entrainment within the top surface of the concrete. By examining a portion of the intact concrete adjacent to the deteriorated section, it may become apparent that that section of concrete may been overworked during finishing procedures.
3. Sample selection to determine the compressive strength of the concrete should be done keeping in mind that compressive strength obtained from extracted concrete cores is approximately 85% to 90% of the cylinder strength. Samples should be selected in locations that are representative of the concrete.
4. If the samples that are taken with the intention of correlating to a nondestructive test method, the nondestructive testing should be done prior to the removal of the cores. This will allow for in-place data to be obtained. In testing, for example, with the rebound hammer, by taking the readings first would ensure that there is no loss of any energy that would affect the rebound reading.

Samples obtained from the site can serve several purposes. They can provide information on the nature of the deterioration, establish a correlation curve for nondestructive testing data or verify nondestructive testing results. Samples taken at a crack location can provide the crack depth, but it can also provide an indication as to the time of cracking, such as early age cracking or cracking after the setting of the concrete. Signs of early age cracking can be determined by examining the inside crack surfaces of the sample. Typically in early age cracking, cracks follow the aggregate periphery, which is an indication that the cracking occurred before the full development of the paste/aggregate bond. Later age cracking, such as drying shrinkage, often fractures the coarse aggregate. By analyzing all the information, the underlying cause can be determined, but more importantly, a cost effective repair strategy can be recommended to address the deterioration issues.

5 TAKING THE TIME TO UNDERSTAND DESIGN DRAWINGS

Many times, structural drawings of the building are available for review. When the structural drawings are available, it is very important to take the time to understand the construction details specified by the design engineer. The structural drawings or shop drawings provide a starting point as to where the reinforcing bar layout might be. The drawings also let you know the type of reinforcing system that was specified for the structure (i.e. prestressed, post-tensioned, or conventionally-reinforced concrete). Obviously, it is important to obtain a general idea of the reinforcing layout, in order to correlate the nondestructive testing to actual site conditions. An example of this would be in a conventional reinforced slab. If the structural drawings called for the reinforcing to be spaced at eight inches (20 cm) on-center, one would hope that the reinforcing bars would be laid out at the desired spacing. NDT can rapidly establish such details. If nondestructive testing indicates there is an additional object in between the detected reinforcing bars, or the survey indicates that an object is laid out in a diagonal direction, it is fairly safe to assume the indication is most likely something other than additional reinforcing bars placed in the slab. Reinforcing bars are typically placed in the positive and negative moment regions. Generally, structural defects may include improper bar placement, misplaced bars or missing bars and a lack of provision for movement.

An example of improper bar layout involved the development of cracks in a conventionally-reinforced concrete girder in an underground parking structure beneath a public library. The design drawings called for two layers of twenty-two (22) No. 11 bars (35mm) in the bottom of the girder. The problem lay in that the beam was thirty inches wide (762 mm) by thirty-six inches (915 mm) deep. However, twenty-two No 11 bars laid out side by side (30.25 inches or 768 mm total) exceeded the designed width of the girder and did not allow room for the concrete to be consolidated around the reinforcing bars! If the bars had been spaced so that the concrete could be consolidated around the bars, the overall width of the girder would have far exceeded the design width of the girder. The contractor took the initiative to stagger the bars so that there was sufficient side cover and spacing between the bars to allow for proper consolidation of the concrete. This however changed the designed layout of the bars and the overall load carrying capacity of the girder. Cracks were noted shortly after the forms and supports were removed. Nondestructive testing was performed on the beams to determine the number and layers of bars present. The testing noted that there were four to five rows of reinforcing bars with three to six bars in each row. Initial findings contradicted the design drawings and it was recommended that an inspection hole was made to confirm the testing results. The inspection hole confirmed the test results.

6 SUMMARY

In summary, consideration should be given to sampling selection and understanding how nondestructive testing can be used effectively. When used in conjunction with sampling, nondestructive testing has the advantage of being able to complete the structural evaluation with minimal damage to the structure. By using nondestructive testing data that is correlated to actual material properties in the field, it is possible to evaluate all the different elements of the structure. Understanding how the structure was constructed is an important element in determining how to repair the deterioration and recommending the most effective strategy for repair of the building.

REFERENCES

American Concrete Institute, 201.1R-08 Guide for Conducting a Visual Inspection of Concrete in Service, Reported by Technical Committee ACI Committee 201, 2008

ASTM C805 "Standard Test Method for Rebound Number of Hardened Concrete", ASTM International, West Conshohocken, PA, 2013

ASTM C823 "Standard Practice for Examination and Sampling of Hardened Concrete in Construction", ASTM International, West Conshohocken, PA, 2000

Concrete Solutions – Grantham et al. (Eds)
© 2014 Taylor & Francis Group, London, ISBN 978-1-138-02708-4

Diagnosis methodology in concrete structures reinforced with braided cable

A. Lozano, J.J. Del Coz, F. Alvarez & M. Alonso
Construction Engineering Area, University of Oviedo, Asturias, Spain

ABSTRACT: After the Spanish Civil War, lack of quality structural steel, especially as used in reinforcement bars, forced the use of alternative materials to substitute steel in housing construction and civil engineering. In this way, braided cables were frequently used for concrete slabs in cities near mining areas or seaports where those were easily available.

This context explains why many Spanish buildings, erected during the 40's and 50's in cities where docks or mines were the main source of income, were constructed using these materials.

This paper presents the preliminary studies and structural analysis applied to one of these buildings, halfway through a rehabilitation process as a residential building. In this case, the most remarkable issue is that the whole structure, including beams and pillars, had been constructed in braided cable. This paper may serve as a starting point for an analysis methodology proposal applicable to constructions using braided cable for reinforcement.

1 INTRODUCTION

In 1942 the construction in reinforced concrete of a residential building placed in Gijón (Asturias, Spain) was finished. Initially it consisted of a ground floor, four more floors and an attic.

In 1948, after successive enlargements, the entire fifth floor was completed and even one more floor was built. In this case the new roof was supported by a timber structure.

The building was permanently inhabited until 2003, when it was acquired by a large company in order to make various improvements and promote the sale of new homes.

Among the proposed changes, the replacement of the existing timber structure was defined. Furthermore, the removal of the structural elements on the top floor was planned in order to increase its volume.

Finally, their facilities should be adapted to current standards.

Prior to the design of these actions, the engineering firm, who was responsible for the structural calculations, needed to know the characteristics of the materials.

In this sense, two studies were developed. On the one hand, the strength of the concrete structures was evaluated through non destructive and destructive tests. On the other hand, the elasticity modulus of the reinforcement bars was obtained.

First, as expected, the results of the tests indicated a low resistance of the concrete, as well as a certain dispersion of the characteristic values.

However, steel wires were used as reinforcement in beams and pillars rather than smooth bars which were usually used.

For this reason, a detailed procedure of structural analysis was defined in order to analyze the behavior of the building with regards to the safety levels facing ultimate limit stages and both strength and usage.

2 DESCRIPTION OF THE STRUCTURE

The structure was a six storey building with concrete structure, clay blocks, and braided cable as reinforcement in every resistant element.

The slab was of a type called Río Cerámico, often used in Spain along the 60′–70′, with 160 mm of total thickness.

Its main façade, the floor plan type and a slab section is shown in Fig. 1.

In this particular case, the reinforcement consisted of one or two braided steel cables. The diameter of the cables ranged between 13.1 and 23.8 mm.

As was usual in this type of slab, there was no compression layer, and the floor consisted of clay tiles and 8 cm thick layer of mortar.

According to the general sketch which was raised for this purpose, the structure had been properly designed. Large edge beams (20×50) were used and the spans never exceeded 5.50 m.

3 CURRENT STATE OF THE BUILDING

Visual examination of the structure showed several areas of damage, more or less generalized. They can be grouped in the following sections.

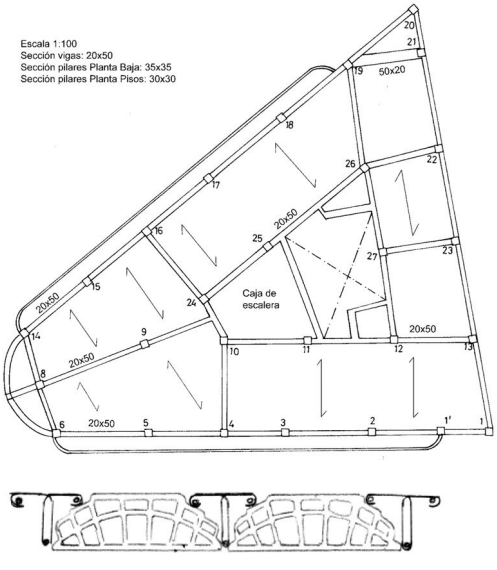

Figure 1. Main façade, floor type and slab cross section.

3.1 *Pillars*

According to the construction date of the building, most of the pillars had been cast using a small amount of cement and sand. This defect caused breakdown and material loss just when they were hit with a hammer.

On the contrary, the top slabs, built a few years later, seemed to have better mechanical properties. However, low quality of finish, deviations from verticality and voids were detected.

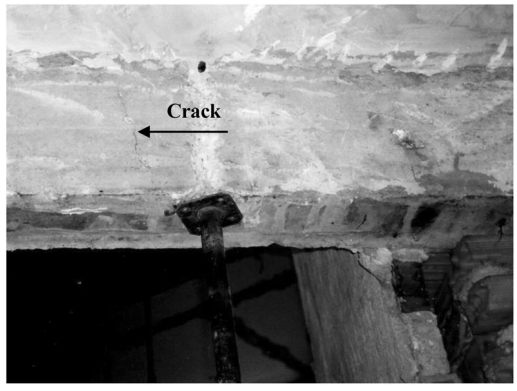

Figure 2. Typical damages in beams: passing cracks of constant width 1 mm.

3.2 *Beams*

As for the pillars, voids and defects of compaction and vibration of the concrete were appreciated in beams as well, especially in the bottom. Besides, a total absence of cover in these elements was observed.

However, the reinforcement bars showed only a very superficial oxidation, in spite of the low quality of the concrete coating, its thickness and the moist environment associated with the location of the building, pretty close of the sea.

Furthermore, almost all the beams had passing cracks of constant width of 1 mm, spaced at regular distances between 17 and 25 cm. This type of failure was also detected where the stress of the positive reinforcement was not close to its elastic limit. Even in beams with edges higher than 50 cm, visible fractures were clear, as can be seen in figure 2.

3.3 *Slabs*

There was no visual damage detected in these elements.

Only one wide crack on the overhanging slab was located in the first floor.

It was much wider than the others, and reached a width exceeding 10 mm.

Figure 3 shows this important crack, that crossed the whole slab.

As in the above members, some elements had been not well compacted, and voids and inclusions of small pieces of clay blocks were detected. However, there were neither significant deflections nor cracking defects, despite the minimum thickness of the slab and the lack of compression layer.

4 PATHOLOGICAL PROCESSES

Damage and defects listed in the previous section can be summarised in the following:

- Poor quality of the concrete members.
- Braided cable instead of reinforcement bars.

Figure 3. Large crack on the overhanging slab in the first floor.

- Insufficient cover in the resistant elements.
- Casting defects in some columns.
- Lack of compression layer in the floors.
- Cracking in the beams.
- One wide crack in the first floor overhanging slab.

Taking into account the date of construction of the building, it is obvious that the first two defects were caused by the difficulty of finding materials (cement and steel), and in the lack of current knowledge on the durability of concrete (carbonation, availability of separators and immersion vibrators, etc).

The lack of cover was also a common mistake in the constructions built at that time and in the following years.

The presence of voids, excessive cover and other faults performed throughout the execution of the concrete, were due to both, the ignorance of some aspects of this material and the few available resources. However, the lack of verticality of some pillars on the top floor had no justification.

The absence of a compression layer in the floors was a common practice at that time. It must be mentioned that in Spain the compression layer did not begin to be used until the publication of the first reinforced concrete standards, several years later.

Existing cracks in the beams, as already anticipated, were usually from a combination of the improper cover and the presence of transversal reinforcement. This issue could be checked using the rebar detector.

However, the cracking of the overhanging slab in the first floor (consequently the one with the biggest load), was probably due to an insufficient section of the negative moment reinforcement, as well as the possibility of an improper anchorage.

5 PROPOSED TESTS

Since the main purpose of the study was to analyze the quality of the structure and estimate an absolute value of its compression strength, the combined test method was proposed.

This method combines classic NDT readings (Schmidt hammer and ultrasonic tests) with the compression testing of cores extracted from the structure.

Of course, while these tests were carried out, as far as possible confirmation of the previous assumptions were attempted.

From all of the testing techniques which may be employed to evaluate the condition and strength of hardened concrete, those regarding the following stand out:

- Determination of carbonation front, due to its influence on the corrosion process of the reinforcement bars, and also on the increasing the surface strength of the concrete.
- In addition to the above issue, definition of the reinforcement cover.
- Once the previous factors were defined, execution of Schmidt hammer tests on the concrete structure.
- And after, evaluation of porosity and compaction of the concrete elements by means of ultrasonic pulse velocity testing.
- Once all of these tests were done, comparison of the results of previous NDT tests with those obtained through cores extracted from resistant elements.

In addition to this, the braided cables should be analyzed because there is not reliable data available.

In the case studied in this paper, this analysis was especially important for several reasons: the cables were the only reinforcement bar; the quality of the concrete was low; and for many years the building had been exposed to a humid and salty environment.

Therefore it was considered mandatory:

- To determine the mechanical characteristics and chemical composition of the wires.
- Finally, as it will be shown, according to the variability of the values obtained in these tests, it was considered compulsory to carry out several load tests on the slab floors.

In addition, the rebar detector allowed the discovery of longitudinal bars near the surface on the bottom of the beams. This was because of the low cable stiffness, and the absence of separators or wedges, as mentioned previously.

This method also provided confirmation of the presence of transversal reinforcement which was coincident with the position of the cracks in the beams.

Finally, the same procedure confirmed the insufficient anchorage of negative moment reinforcement in the overhanging slab of the first floor.

However, it was impossible to define accurately the diameter of the cables in any place of the structure, despite the use of equipment specifically developed for this purpose.

6 CORE EXTRACTION

Six cores from pillars of the five first floors were extracted in order to validate data obtained through

Table 1. NDT and DT related to concrete elements.

Concrete tests	Min. value	Max. value
Carbonation (mm)	14	33
Cover (mm)	5	36
Schmidt Hammer Rebound No	10.5	14.5
UPV m/s	2025	2560
Compression Test MPa	9.5	12.5

Table 2. Mechanical properties of braided cables.

Braided cables	Nº1	Nº2	Nº3	Nº4
Tensile stress kN	48.08	81.41	92.86	82.60
Outer diameter mm	23.00	17.50	23.00	23.00
Tensile strength MPa	115.72	338.46	223.49	287.40

DT tests and determine the statistical correlation of variables.

In this way, the combined method allowed the extrapolation of the results to the rest of the structural elements with a certain confidence level. Table 1 shows the most important results related to the concrete tests.

7 MECHANICAL AND CHEMICAL PROPERTIES OF THE BRAIDED CABLE

There was no doubt that some destructive tests must be performed on the cables due to the variability of their sections extracted from different floors.

In this sense, the cables were cleaned before their heads were embedded in resin so as to ensure grip during the test.

Then it was decided to carry out the tensile test according to the procedure described in UNE 7326 (1988), in order to define its mechanical properties.

Table 2 shows some of the results, while Figure 4 shows the chart obtained in one of the tests.

Figure 5 shows one of these cables after the test, and how the endings of the wires were prepared.

It is important to note that, as found in the tests, several cores of the braided cables consisted of one rope. Obviously, the lowest readings corresponded to this type of cable. This meant that the greatest outer diameter did not always correspond to higher mechanical characteristics. In other words: the structural analysis would be much more complex.

With respect to the chemical analysis, pieces were cleaned with acetone, placed in concentrated nitric acid, and then heated on a hotplate until they were completely dissolved with deionized distilled water.

The atomic emission spectrometer and the analyzer allowed determining, among other information, a high percentage of carbon which explained the low corrosion level of the wires.

The steel type corresponded to the one defined in DIN 1.0601 (designation C 60), as deduced from the values shown in Table 3.

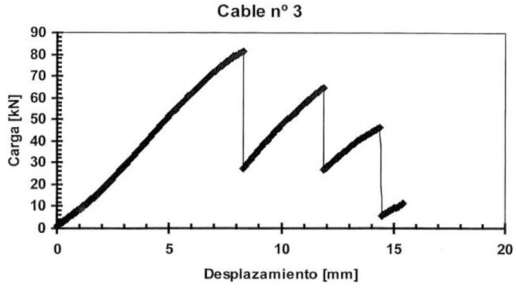

Figure 4. Tensile strength test performed on sample nº 3.

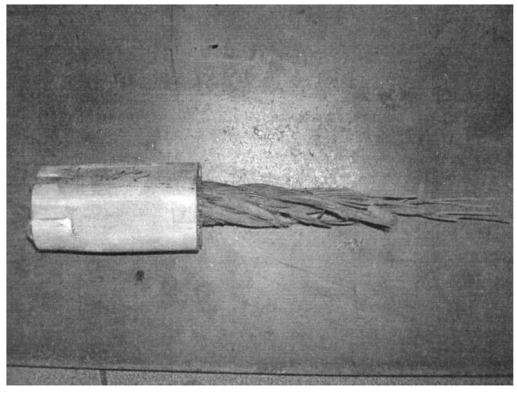

Figure 5. Cable Nº 2 after the test and ending preparation.

Table 3. Braided cable chemical composition.

% weight	C	S	Cr	Mn	Mo	Ni	P
Cable	0.60	0.043	0.043	0.70	0.01	0.03	0.027
DIN 1.0601	<0.65	<0.45	<0.4	<0.9	<0.1	<0.4	<0.45

Finally, according to the irregular surface of the braided cables, checking both adherence and anchorage were not considered.

8 LOAD TESTS

Owing to the results of the tests carried out so far, and especially those related to the chemical composition of the cables, load testing on all floors was strongly recommended. These tests provide more information about the behavior of the slabs, and guarantee its structural safety levels at both ultimate state limits and normal usage.

The most loaded pairs of joists were chosen in every floor. Furthermore, two tests per slab were carried out on each floor.

Three dial gauges with hundredth of a millimeter of precision were placed under each joist: two of them close to the pillars, and the other one in the middle of the span.

Table 4. Load tests results obtained in third floor.

	Deflection mm					
Load kN	1a	1b	2a	2b	3a	3b
0	11.00	20.00	21.00	5.00	10.00	16.00
11.2	11.32	20.31	21.61	5.13	10.11	16.05
22.4	11.44	20.45	21.74	5.27	10.21	16.22
39.0	11.72	20.70	22.02	6.44	10.43	16.51
31.5	12.26	20.91	22.22	6.59	11.16	16.76
24 h	12.32	20.73	22.62	6.96	11.18	16.76
Total	1.32	1.63	1.62	1.96	1.18	0.76

In order to analyze the overall behavior of each joist, the compression layer was cut by a radial saw.

Taking into account the complexity and variability of the reinforcement mechanical properties, it was decided to follow the requirements of standard ACI-437, slightly more restrictive than the one that is recommended in the Spanish standards (EHE).

Readings and maximum deflection were recorded after keeping the load during twenty four hours. The remainder deformation was not included because it was really low and the slabs recovered the deflection immediately after discharge.

This showed the optimal behavior of these slabs, despite their small width and the absence of compression layer.

Results for most requested members are included in Table 4. Numbers 1 and 3 correspond to measures taken at the ends of the joist, and number 2 corresponds to the one taken in the middle.

Letters a and b indicate left and right respectively. Deflections were measured twenty four hours after the last load was applied. Total deflection appears at the end of the table.

9 RESULTS ANALYSIS

From the combined method, it was verified that:

- This technique has higher accuracy than individual application of Schmidt hammer or ultrasonic pulse tests, specifically when concrete is advanced in age.
- Concrete quality was low. Evaluation of compressive strength of the concrete in situ suggested a low value around 10 N/mm^2.
- Yield strength of braided cables was always very high and brittle fracture was usual.
- Only the surface of the cables was rusted.
- Slabs had a very acceptable behavior, despite some of the joists showing voids and defects.
- Deflections measured through load tests were really small.
- The slabs had a perfect elastic behavior. According to our experience, this is not an isolated case, since all kinds of similar slabs were able to support very high loads, even higher than some of the most modern ones with joists of upper edge.

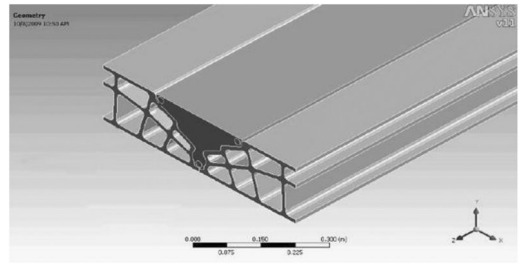

Figure 6. Cross section of the tested element.

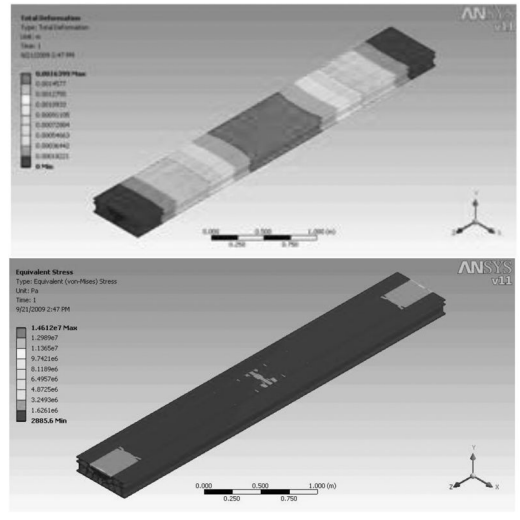

Figure 7. FEM model and strains and stresses in third floor.

- In our opinion, this is due to two different factors: the T section of the joist involves an important part of the hollow clay floor slab block; and the design of the block itself, which enables it to absorb a great amount of the compression stresses.

10 FEM ANALYSIS

A FEM model was developed using the experimental data obtained in the destructive and non destructive tests as well as those recorded in load testing measurements. Figure 6 shows a cross section of the element tested.

Stresses and strains obtained in one of the joists of the third floor appears in Figure 7.

11 CONCLUSIONS

The usual purpose of the insitu assessment of old concrete structures is to analyze its element's behavior with regards to its safety conditions.

Verification of the compressive strength of the concrete is often required in order to introduce said value in the calculation. Schmidt hammer and ultrasonic

techniques are suitable to be considered in such studies. Of course, both techniques need to be validated through core samples.

Sometimes dimensions of the elements, quality of the materials, and age of the building, loads and so on, do not allow so many tests to evaluate the whole structure.

However, if the reinforcement of an old concrete construction is composed by braided cable, tests should provide as much information as possible about the type of concrete and its resistance; and of course about the reinforcement as well. Therefore, it is highly recommended:

- To carry out a methodology of analysis based on combined methods, properly validated by the extraction of a significant number of cores. In this case NDT tests were performed on different concrete elements prior to extract the samples.
- To get as much information as possible about the type of reinforcement material used.
- Provide the number of destructive tests. Note that for many years concrete was batched by volume mixed on site, and compaction was carried out using bars instead of immersion vibrators. Consequently, the dispersion of the mechanical characteristic values of each element was often very wide.
- Above all, load tests should be performed with a proper procedure on the largest number of slabs, to check their behavior. It is especially important when it is impossible to define with accuracy the sections and the mechanical properties of the reinforcement, and the slabs are thin.
- With respect to this point, we consider it more convenient using the acceptance criteria defined in the standard ACI-437, as it is more restrictive than the one described in Spanish standards.

ACKNOWLEDGEMENTS

The authors wish to acknowledge support provided by the Spanish Ministry of Science and Innovation through the research project co-financed with FEDER funds BIA2012-31609.

REFERENCES

ACI 214-02 (2002). *Evaluation of strength test results of concrete.*

ACI 437-07 (2007). *Load Tests of Concrete Structures: Methods, magnitude, protocols, and acceptance criteria.*

Bathe, K. (1996) *Finite element procedures*. New York: Prentice-Hall.

Calavera, J. et al (2001). *Evaluación resistente de estructuras de hormigón armado.* Madrid: Intemac.

Chen, W. (1982). *Plasticity in reinforced concrete*. New York: McGraw-Hill Book Company.

Del Coz, J.J. et al (2007). *Non-linear analysis of a reinforced concrete sheet cover (umbrella) of 40 m diameter by the FEM method.* Applied mathematics and computation nº 184, 37–51. Elsevier.

Del Coz Diaz, J.J. et al (2011). *Nonlinear hygrothermal failure analysis of an external clay brick wall by FEM – Acase Study.* Construction and Building Materials, 25(12), 4454–4464. Elsevier.

Dirección General de Arquitectura (1947). *Sistemas especiales de forjados para la edificación.* Madrid: Vega Imp.

El-Reedi, M. (2013). *Concrete and steel construction: quality control and assurance*. Rotterdam: Balkema.

Heckroodt, R. (2002). *Guide to the deterioration and failure of building materials*. London: T. Thelford.

Hostalet, F. (1994). *Strength evaluation of in-situ hardened concrete.* Madrid: Intemac.

Lozano, A. et al (2003). *Diseño, cálculo, construcción y patología de los forjados según EFHE, EHE y EA 95*. Consultores técnicos de construcción: Gijón.

Ministerio de Fomento (2008). *Instrucción de hormigón estructural EHE.08*. Madrid: Servicio de publicaciones del Ministerio de fomento.

Mackenzie, W. (2013). Examples in structural analysis. Rotterdam: Balkema.

Moaveny, S. (2007). *Finite element analysis: theory and applications with ANSYS*. Prentice Hall; New York.

Petersons, N. (1980). *Recommendations for estimation of quality of concrete in finished structures.* Bulletin RILEM nº 24 November – December 1971.

Richardson, M. G. (2002). *Fundamentals of durable reinforced concrete*. London: Spon Press.

UNE 7326 (1988). *Determinación de la carga de rotura a tracción de cables y cordones de acero*. Madrid: AENOR.

Concrete Solutions – Grantham et al. (Eds)
© 2014 Taylor & Francis Group, London, ISBN 978-1-138-02708-4

Corrosion of steel in cracked concrete: A microscale study

J. Pacheco, B. Šavija & E. Schlangen
Delft University of Technology, Delft, The Netherlands
CiTG, Materials & Environment, Delft, The Netherlands

R.B. Polder
TNO Technical Sciences, Delft University of Technology, Delft, The Netherlands
CiTG, Materials & Environment, Delft, The Netherlands

ABSTRACT: The influence of concrete cracking upon reinforcement corrosion is complex. Cracks allow fast penetration of chlorides, potentially leading to a shorter initiation period of reinforcement corrosion. Structural regulations control acceptable crack width values based on the exposure class of the structure. These regulations are limited to crack width values at the concrete surface but do not account for the influence of cracks at the concrete-steel interface. Research studies on corrosion of reinforcement embedded in cracked concrete have shown that the correlation between cracks and corrosion is rather complex. Studying the condition of pitting in steel reinforcement embedded in cracked concrete from a microscopic approach could lead to insights on the mechanisms of corrosion under this condition. In this research, reinforced concrete specimens were subject to cracking. Subsequently, the specimens were exposed to salt-dry cycles with a chloride solution while continuously monitoring of open circuit potential (OCP), linear polarization resistance (LPR) and electrical resistance of concrete. Visual analysis of corrosion pits of steel bars showed that a correlation between crack width and pit dimensions was found.

Keywords: Corrosion, concrete cracking, pitting.

1 INTRODUCTION

Concrete infrastructure can be subject to cracking due to numerous causes. Current structural codes such as the fib and ACI 224 allow maximum crack width values according to the environmental conditions surrounding the structure. For a marine environment, fib and ACI 224 suggest values of 0.30 and 0.15 mm, respectively (ACI 224 2001; fib 2006).

Reinforcement corrosion is the most important deterioration mechanism in concrete infrastructure. Chlorides present in the marine environment or deicing salts penetrate through concrete pores and initiate steel corrosion. The presence of cracks in concrete cover allows a fast penetration of chlorides that can potentially lead to shorter initiation periods. Interestingly, results obtained from field studies and laboratory research shows that the influence of cracks on reinforcement corrosion is not well understood. The contradiction arises from differences in researchers opinion on: a) considering that cracks do not influence corrosion (Tremper 1947); b) they only affect the initiation period (François and Arliguie 1998); or c) that they also influence the propagation period (Ismail and Soleymani 2002; Otsuki et al. 2000).

Research studies have been focused on trying to establish a correlation between crack width and corrosion behavior (Castel et al. 2000; François et al. 1994; 2012; Otieno et al. 2010; Pease 2010; Scott and Alexander 2007; Vidal 2004). While most research publications have focused on correlating electrochemical measurements and cracking, this paper is focused on the influence of cracks on pit dimensions by performing a microscopic study on the steel surface of corroded bars.

2 EXPERIMENTAL DESIGN

Reinforced concrete 150 × 150 × 150 mm cubes were cast with ordinary Portland cement (CEM I 52.5R). The composition of the fabricated specimens was: w/c 0.45; cement content 380 kg/m^3; fine aggregate (<4 mm) 1027 kg/m^3; coarse aggregate (>4 up to 12 mm) 840 kg/m^3; superplasticizer 1.4% wt. cement. Two reinforcing bars of 120 mm in length and 12 mm in diameter were placed 50 mm from the bottom of the mould as shown in Figure 1a. The distance between reinforcing bars was 120 mm as shown in Figure 1b. In between reinforcing bars, activated titanium (Ti*) wires of 10 mm length with insulated copper wires were used as embedded reference electrodes. At the beginning, the potential of the Ti* electrodes was close to that of Ag/AgCl (saturated KCl). In all cases, steel

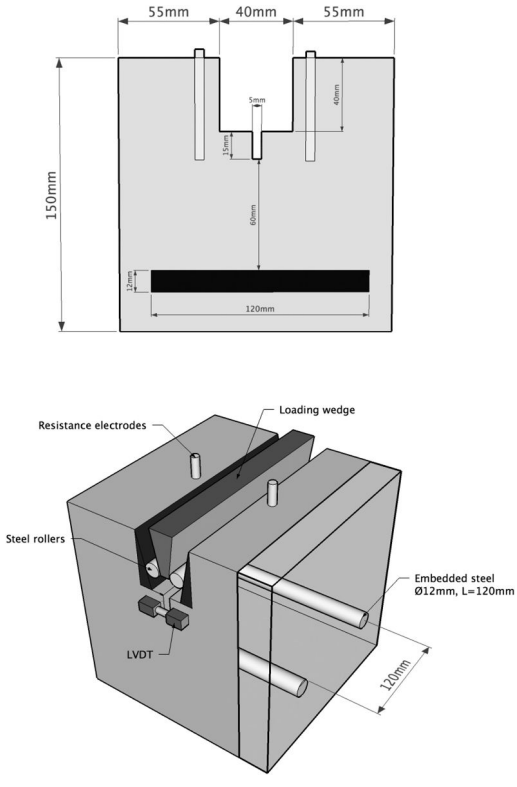

Figure 1. Top: a) geometry and bottom b) loading set-up of specimens.

reinforcement was embedded with a surface condition as-received. Before casting, a PVC profile with a cross section of 40×40 mm was mounted on the mould to obtain a recess. Two stainless steel electrodes (grade 316) were employed for electrical resistance measurements. They were attached to the sides of profile, with an embedded length of 50 mm and a diameter of 6 mm. The horizontal distance between the electrodes was 50 mm. The PVC profile was removed two hours after casting, leaving the electrodes embedded in the concrete.

After 24 hours, the specimens were demoulded and stored in a curing room with controlled conditions of 20°C, and over 95% RH for 27 days. At the end of the curing period, a notch (5mm wide, 15mm deep) was made at the bottom of the recess using a water-cooled diamond saw. Finally, the specimens were exposed to laboratory conditions of 20°C and approximately 50% RH for 7 days before the test (Šavija et al. 2012).

Cracking of concrete specimens was performed employing an INSTRON 8872 Testing System with a loading rate of 0.5 μm/s under displacement control. Two LVDTs (linear variable differential transformer) were placed on both front and back of the specimen at the bottom of the notch (Fig.1 bottom). Their average displacement was used as a feedback signal for the machine. The machine calculates the required load to continue at the prescribed displacement rate by using this signal. At the end, five specimens with final crack width values of 135, 165, 187, 217 and 396 μm were studied.

After cracking, the specimens were exposed to weekly salt-dry cycles consisting of 48 hr of 3.3% NaCl solution contained in the recess and 4 days of drying at 20°C and 50% RH. The electrochemical potential of each steel bar was measured continuously during exposure separately. At the end of the wet-period, linear polarization resistance (LPR) measurements were carried out with a Corr-Ocean Multicorr MKII device. The Rp test involved both bars as alternatively working and counter electrodes, and using the Ti* as reference electrode. In all measurements no correction for ohmic drop was performed. The exposed area of the bar (4521 mm^2) and B value ($B = 26$) were given as input for the test. As a result, the outcome of the Rp was reported as corrosion rate (μm/y). Electrical resistance measurements across the crack were carried out with an ESCORT resistance-meter at 120 Hz AC shortly after LPR measurements.

At the end of the exposure to chlorides, the specimens were cut into two pieces with each part containing a steel bar. The bar with higher corrosion rate was extracted by splitting. Subsequently, rust found on the steel surface was removed with an inhibited acid solution. Images of the steel surface condition were recorded with a calibrated Leica MZ6 stereomicroscope under normal light. For each pit, an elliptic shape was assumed. Pit dimensions were performed by assigning the longest distance within the pit as the long axis of the ellipse. The perpendicular length to the long axis was assigned to the short axis of the ellipse. Later, these lengths were converted to microns with a conversion value of 2.193 μm per pixel. Estimations of the pit volume were performed by assuming that the depth of the pit had the same length as the short axis of the ellipse. Finally, all pits bigger than 1 μm for each steel bar were accounted for and both accumulated area and volume of the pits were estimated.

3 RESULTS AND DISCUSSION

3.1 *Electrochemical measurements*

Results of open circuit potential values (OCP) of steel bars embedded in cracked concrete are shown in Figure 2. This figure shows that the OCP values of all specimens were around $0V_{Ti*}$ at the beginning of the experiment and decreased significantly during the first 10 weeks towards less noble values. During this period, OCP of bars embedded in specimens with large crack width values became less noble accordingly. For example, bars embedded in specimen 396 μm showed values between -0.7 to $-1.0V_{Ti*}$ whereas those embedded in specimen 217 μm were between -0.4 and $0.6V_{Ti*}$. Bars embedded in specimens with crack width values below 200 μm reported more noble values than $-0.3V_{Ti*}$. After 10 weeks, OCP for all bars

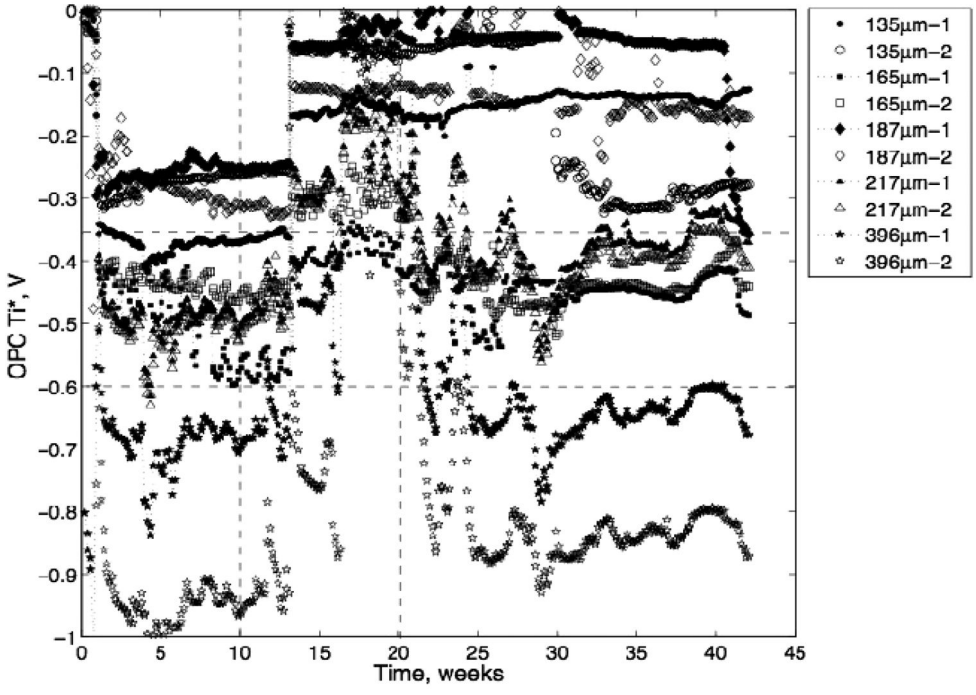

Figure 2. OCP values of bars embedded in cracked concrete specimens under salt-dry exposure.

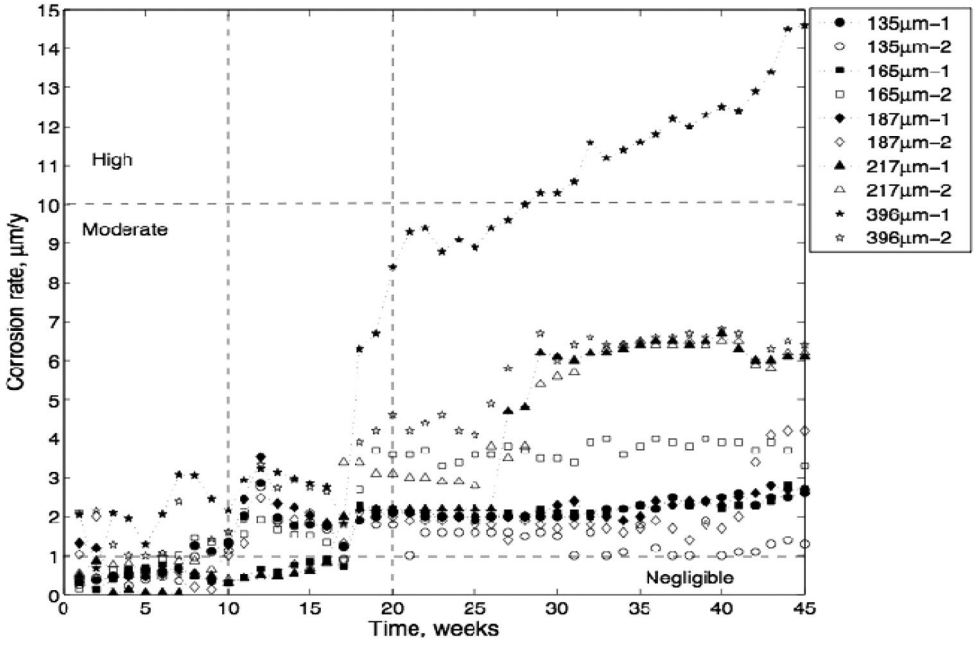

Figure 3. Corrosion rate values of bars embedded in cracked concrete specimens under salt-dry exposure.

were shifted towards more noble values. Those embedded in specimens, 135, 165 and 187 μm were more noble than $-0.1V_{Ti*}$ and those for specimens 217 and 396 were between -0.2 and $-0.4V_{Ti*}$. A third regime of OCP was observed after 20 weeks. While the OCP of bars embedded in specimens with crack width values under 200 μm remained at values similar to the previous period, those embedded in specimens 217 and

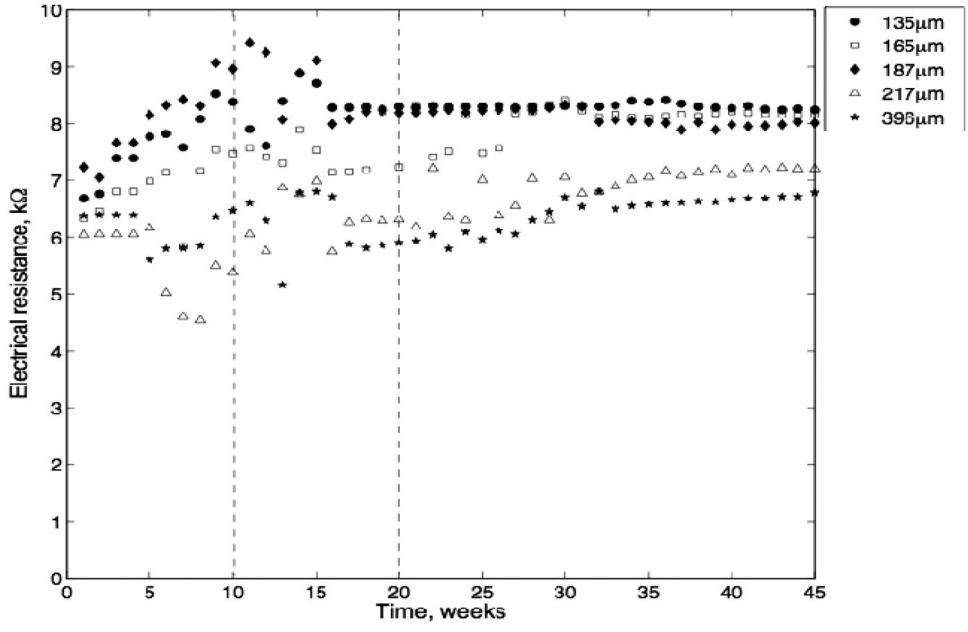

Figure 4. Electrical resistance of cracked concrete specimens under salt-dry exposure.

396 μm shifted to less noble values similar to those observed during the first 10 weeks.

Results of corrosion rate obtained from LPR measurements on cracked specimens are shown in Figure 3. Corrosion rate values of all specimens with crack width values under 200 μm were lower than 1 μm/y, which is considered as a negligible corrosion rate (Andrade 2004). These values showed a gradual increase in corrosion rate during the first 10 weeks. After 17 weeks, an increase in corrosion rate was observed in all bars, with those embedded in specimen 396 μm showing the most significant increase. The corrosion rate of one bar (396 μm^{-1}) embedded in this specimen was higher than 10 μm/y after 28 weeks. The remaining bars had corrosion rate values between 1 and 7 μm/y.

Finally, results of electrical resistance measurements on cracked concrete specimens are shown in Figure 4. Results show that initial resistance values are between 4 and 10 kΩ. During the first cycles, the electrical resistance of bars in specimens 217 and 396 μm decreased slightly. On the other hand, specimens with crack width values lower than 200 μm showed an increase in electrical resistance. This behavior was observed during the first 12 weeks. After 15 weeks, the values of electrical resistance in all specimens became stable.

3.2 *Pit size estimation*

Figure 5 shows a typical stereomicroscope image of pits found on the surface of a steel bar. The long axis of the ellipse was assigned to the longest distance in the pit perimeter whereas the short axis was perpendicular to the long axis. Each pit was measured independently and Table 1 shows the number of pits, the estimated area and volume of each pit and both accumulated area and accumulated volume of pits per bar.

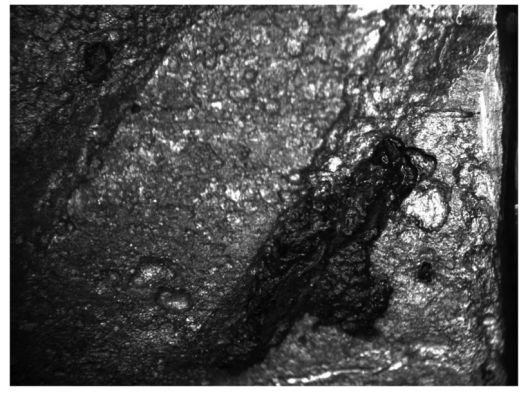

Figure 5. Visual inspection of corrosion pits.

Results from estimations of accumulated area and accumulated volume show a relationship with crack width. As the crack width was increased in concrete specimens, both area and pit volume increased accordingly. Values of accumulated area were 0.30, 0.72, 3.30, 4.12 and 8.97 mm^2 for specimens 135, 165, 187, 217 and 396 μm, respectively. In the case of pit volume, values of 0.03, 0.12, 1.40, 1.35 and 5.19 mm^3 were found. Interestingly, the number of pits also

Table 1. Area and volume estimation.

135 μm^{-1}		
Pit	Area, mm^2	Volume, mm^3
1	0.10	0.01
2	0.13	0.01
3	0.07	0.01
Accumulated	*0.30*	*0.03*
165 μm^{-2}		
Pit	Area, mm^2	Volume, mm^3
1	0.26	0.03
2	0.26	0.05
3	0.20	0.04
Accumulated	*0.72*	*0.12*
187 μm^{-2}		
Pit	Area, mm^2	Volume, mm^3
1	2.67	1.31
2	0.47	0.08
3	0.07	0.01
4	0.10	0.01
Accumulated	*3.30*	*1.40*
217 μm^{-1}		
Pit	Area, mm^2	Volume, mm^3
1	0.99	0.20
2	2.14	0.95
3	0.89	0.18
4	0.10	0.01
Accumulated	*4.12*	*1.35*
396 μm^{-1}		
Pit	Area, mm^2	Volume, mm^3
1	3.85	2.51
2	3.44	2.36
3	0.57	0.14
4	0.21	0.03
5	0.38	0.06
6	0.06	0.01
7	0.03	0.00
8	0.26	0.05
9	0.16	0.02
Accumulated	*8.97*	*5.19*

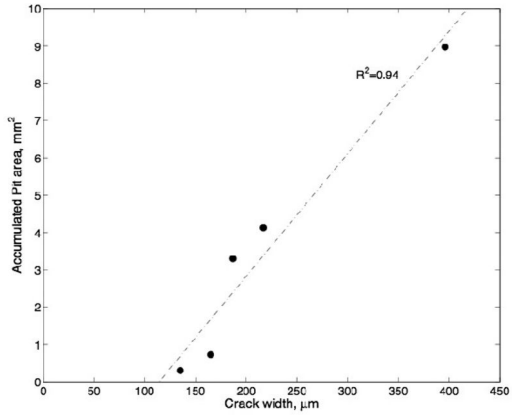

Figure 6. Estimated accumulated pit area of steel bars.

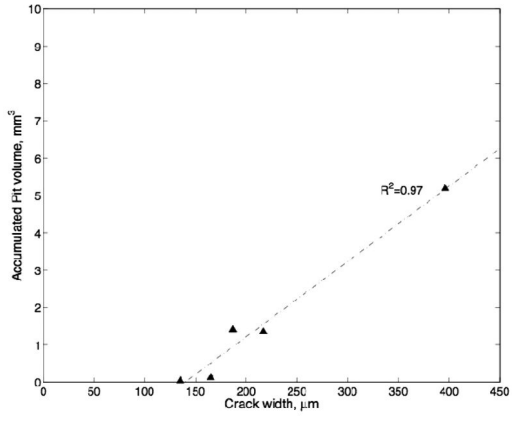

Figure 7. Estimated accumulated pit volume of steel bars.

increased when wider cracks were produced. Figure 6 shows the relationship between crack widths and the accumulated pit area and Figure 7 shows the relationship between crack widths and accumulated pit volume. Results show that in both cases, a strong correlation between crack width and pit dimensions was found.

3.3 *Discussion*

During the first 10 weeks, steel bars embedded in cracked concrete with wide cracks (217 and 396 μm) had OCP values shifted towards significantly negative values, whereas those embedded in specimens with cracks narrower than 200 μm seemed to be subject to a similar but rather milder shift. During this period, corrosion rate of steel bars remained at negligible values (except for 396 μm^{-1}). The combination of these two contradicting behaviors suggest that although corrosion pits of minuscule dimensions (probably at the μm range) could be formed, these pits represent a very low portion of the steel surface. Since the anodic area is required as an input parameter for performing LPR measurements, by accounting the whole bar surface resulted in very low corrosion rate values. These results are similar to those found by Otieno et al. (2010), who found that specimens cast with Portland cement and w/c ratio of 0.40 showed corrosion rate values around 0.2 μA/cm^2 (c.a. 2 μm/y) during the first 10 weeks for a specimen with 0.4 mm crack under Cl^- exposure. Scott and Alexander (2007) found a similar behavior for OCP and corrosion rate for crack width values of 0.2 and 0.7 mm. It is thus evident that although the penetration of chlorides could be fast during this period, the thermo-dynamic conditions of the concrete-steel interface might not be ideal for pit growth.

During the first 15 weeks, the electrical resistance of specimens with crack width values lower than 200 μm showed a slight increase during the first 15 weeks. On the other hand, specimens 217 and 396 μm showed decreasing values, which suggests that larger cracks allowed larger volumes of chloride solution to be

accommodated. After 15 weeks (105 days), the electrical resistance of specimens with cracks smaller than 200 μm entered a stable regime. Scott and Alexander (2007) also found stable behavior in concrete resistivity in specimens with different binders. The stabilization of electrical resistance may suggest that the cyclic nature of the exposure to chlorides is no longer relevant since the drying period is not long enough to completely remove the solution from the specimens. It seems that after 15 weeks, the specimens entered a steady regime of moisture content.

The behavior of OCP and corrosion rate of steel bars after 15 weeks, combined with the stabilization of electrical resistance, suggests that pits can grow to become a larger portion of the steel surface. The shift of potential towards less noble values and the increase in corrosion rate in bars embedded in specimens 217 and 396 μm confirms this hypothesis. On the other hand, bars embedded in specimens 135, 165 and 187 μm showed a gradual shift to less noble potential values and corrosion rates just above 1 μm/y. Results found by Otieno et al. (2010), after 30 weeks, showed corrosion rate values between 0.1 and 0.8 $\mu A/cm^2$ (c.a. 1 to 8 μm/y) for uncracked and 0.7 mm crack width specimens respectively. These results are comparable to those found in this research at 30 weeks with corrosion rate values between 1 and 10 μm/yr.

On corrosion pit size estimations, Angst et al. (2011) found that the area of pits was up to 0.04 mm^2 at early corrosion pits formed for 40 days. Results showed that the nucleation and size of corrosion pits are time dependent. Regarding the results found in this paper, the time dependency of corrosion pitting suggests that pits could have been formed during the first 10 weeks (less noble potentials) but their growth could not be sustained (low corrosion rates). Changes in moisture content (salt-dry cycles) prevented achieving stable thermo-dynamical conditions for pit growth. At the same time, the accumulated pit area to steel surface ratio remained low. When accounting for the whole bar surface as the electrode, pits must be large in order to represent an increase in corrosion rate as shown after 15 weeks in Figure 3. Due to the destructive nature of visually inspecting the size of pits, correlations between results found by Angst and those found in this paper are difficult. In any case, pits measured after 45 weeks are only up to two orders of magnitude higher than those found by Angst.

Measurements of pit dimensions and quantification of corrosion products have been recently performed by non-destructive techniques. Among them, computer tomography (CT) is a non-destructive technique that is able to locate and measure the size of pits. Česen et al. (2013) found pits of up to 130 μm deep in plain bars embedded in mortar exposed to carbonation and chloride penetration. Currently, this technique is limited to laboratory applications but new development could allow the study of ribbed bars embedded in larger concrete specimens.

Regarding estimations on the volume of corrosion pits, Polder et al. (2002) found pit volume values of up to 30 mm^3 for specimens in high corrosion deterioration. These estimations were performed visually and compared to analytical calculations based on LPR measurements. It should be noted that the results found by Polder et al. were obtained after 2.5 years of exposure, whereas those found in this research only consider 34% of that exposure period. The loss of material in probes obtained from measurements performed by Česen et al. (2013) was in the order of 1.7×10^5 to 7.1×10^6 μm^3 (1.7×10^{-4} and 7.1×10^{-3} mm^3 respectively). Each of these analyses faced a time constrain challenge in the order of weeks. Estimations of the volume of pits can be relevant for studies focused on modeling rust pressure on concrete due to reinforcement corrosion. Currently, corrosion cracking has been modeled as a general corrosion behavior (Andrade and Alonso 1993; Molina et al. 1993), although new research has been focused on modeling pitting corrosion of steel reinforcement (Michel et al. 2013; Šavija et al. 2013).

4 CONCLUSIONS

The influence of cracking on the behavior of reinforcement corrosion was assessed by monitoring the open circuit potential (OCP), corrosion rate and electrical resistance of concrete. Moisture content, measured indirectly by means of electrical resistance, was considered as the controlling parameter for corrosion propagation after 15 weeks. Results showed that steel reinforcement embedded in concrete specimens with cracks larger than 200 μm were seriously corroded, whereas the deterioration of bars embedded in concrete with cracks narrower than 200 μm was significantly lower. Visual analysis on the surface of steel bars showed that the accumulated pit area and volume were also dependent on the crack width.

REFERENCES

ACI 224. (2001). *Control of Cracking in Concrete Structures*. American Concrete Institute, 43.

Andrade, C. (2004). "Test methods for on-site corrosion rate measurement of steel reinforcement in concrete by means of the polarization resistance method." *Materials and Structures*, 37(9), 623–643.

Andrade, C., and Alonso, C. (1993). "Cover cracking as a function of bar corrosion: Part I-Experimental test." *Materials and Structures*, 26(8), 453–464.

Angst, U., Elsener, B., Larsen, C. K., and Vennesland, Ø. (2011). "Chloride induced reinforcement corrosion: Rate limiting step of early pitting corrosion." *Electrochimica Acta*, Elsevier Ltd, 56(17), 5877–5889.

Castel, A., François, R., and Arliguie, G. (2000). "Mechanical behaviour of corroded reinforced concrete beams—Part 1: experimental study of corroded beams." *Materials and Structures*, 33(9), 539–544.

Česen, A., Kosec, T., and Legat, A. (2013). "Characterization of Steel Corrosion in Mortar by Various Electrochemical and Physical Techniques." *Corrosion Science*, 75(October 2013), 47–57.

fib. (2006). *Model Code for Service Life Design*.

François, R., and Arliguie, G. (1998). "Influence of service cracking on reinforcement steel corrosion." *Journal of Materials in Civil Engineering*, 10(1).

François, R., Arliguie, G., and Maso, J. C. (1994). *Durabilité du betón armé soumis à l'action des chlorures*. Annales de l'Institut Technique du Batiment et des Travaux Publics, 1–24.

François, R., Khan, I., Vu, N. A., Mercado, H., and Castel, A. (2012). "Study of the impact of localised cracks on the corrosion mechanism." *European Journal of Environmental and Civil Engineering*, 16(3–4), 392–401.

Ismail, M. E., and Soleymani, H. R. (2002). "Monitoring corrosion rate for ordinary portland concrete (OPC) and high-performance concrete (HPC) specimens subjected to chloride attack." *Canadian Journal of Civil Engineering*, 29(6), 863–874.

Michel, A., Pease, B., Peterová, A., Geiker, M., Stang, H., and Thybo, A. A. (2013). "Penetration of corrosion products and corrosion-induced cracking in reinforced cementitious materials: Experimental investigations and numerical simulations." *Cement and Concrete Composites*, Elsevier Ltd, 1–12.

Molina, F., Alonso, C., and Andrade, C. (1993). "Cover cracking as a function of rebar corrosion: Part 2—Numerical model." *Materials and Structures*, 26(9), 532–548.

Otieno, M. B., Alexander, M., and Beushausen, H. (2010). "Corrosion in cracked and uncracked concrete – influence of crack width, concrete quality and crack reopening." *Magazine of Concrete Research*, 62(6), 393–404.

Otsuki, N., Miyazato, S., Diola, N., and Suzuki, H. (2000). "Influences of Bending Crack and Water-Cement Ratio on Chloride-Induced Corrosion of Main Reinforcing Bars and Stirrups ." *ACI Materials Journal*, 97(53), 454–464.

Pease, B. (2010). "Influence of concrete cracking on ingress and reinforcement corrosion." PhD Thesis, Denmark Technical University.

Polder R., Peelen W., Bertolini L., Guerrieri M., Corrosion rate of rebars from linear polarization resistance and destructive analysisin blended cement concrete after chloride loading, in: ICC 15th International Corrosion Congress, Granada, Spain, 2002: pp. 22–27.

Šavija, B., Lukoviæ, M., Pacheco, J., and Schlangen, E. (2013). "Cracking of the concrete cover due to reinforcement corrosion: A two-dimensional lattice model study." *Construction and Building Materials*, Elsevier Ltd, 44(C), 626–638.

Šavija, B., Schlangen, E., Pacheco, J., and Polder, R. (2012). "Modified wedge splitting test (MWST) – a simple tool for durability investigations of reinforcement corrosion in cracked concrete." Cape Town, South Africa, 1–6.

Scott, A., and Alexander, M. G. (2007). "The influence of binder type, cracking and cover on corrosion rates of steel in chloride-contaminated concrete." *Magazine of Concrete Research*, 59(7), 495–505.

Tremper, B. (1947). "The corrosion of reinforcing steel in cracked concrete." *ACI Journal Proceedings*, 18(10), 1137–1144.

Vidal, T. (2004). "Analyzing crack width to predict corrosion in reinforced concrete." *Cement and Concrete Research*, 34(1), 165–174.

This page intentionally left blank

Concrete Solutions – Grantham et al. (Eds)
© 2014 Taylor & Francis Group, London, ISBN 978-1-138-02708-4

Lock-in thermography approach to discriminate surface preparation in CFRP reinforced concrete

M.M. Rahman & H. Hamza
Brunel University, UK

D.A. Chamberlain
Epicuro Ltd, UK

ABSTRACT: The performance Carbon Fibre Reinforced Polymers (CFRP) in the form of plates and wrappings CFPR systems for stiffening and strengthening structural elements depends on the preparation of the concrete substrate. This research investigated the feasibility of Lock-in Infrared Thermography in assessing the surface preparation in bonded CFRP plating on concrete, for three different types of surface preparation-namely normal cast, disk abraded (using abrasive fabric) and needle gunned. CFRP sheets bonded to the prepared tension face of these beams whilst being suspended by a framed structure to simulate the application of CFRP in the field. Thermal modulations delivered to the test beam via two 500 W quartz lamps, with both transmission and reflective heat monitored for lock-in thermography analysis of five Regions Of Interest (ROI's). Thermal responses were recorded as a function of time in both heating and cooling cycles to assess the temperature variation due to bond integrity.

Whilst the subject of on-going investigation, experimentation indicates that the type of surface preparation may be discriminated through the use of lock-in thermography, raising the possibility of applying the method in the field assessment of installed CFRP systems. The different textures of the prepared concrete substrate, which is known to be a performance affecting factor for the installed CFRP systems, is detectable by the Lockin Thermography method employed in the investigation. This arises from characterisation of the different temperature variations under heating and cooling cycles.

Keywords: Fibre Reinforced Polymers (FRP), Carbon Fibre Reinforced Polymers (CFRP), Non-Destructive techniques (NDT), Non-Destructive Evaluation (NDE), IR Thermography (IR), Lock-in Thermography (LT) de-bonding, delamination, concrete.

1 BACKGROUND

In the UK alone, an approximate budget of £4 billion is required in strengthening or replacement work for the 160,000 bridges in the motorway and trunk road network. Similarly, in the US out of the 600,905 bridges, approximately 26.9% are categorised as being structurally deficient or functionally obsolete, hence a US $140 billion requirement for retrofitting. These figures cater for bridges and not all types of structures (Dirar, S., 2012). Demands for the use of buildings are also changing, resulting the need to increase the integrity of a structure long before the end of its service life. For example, many civil structures (i.e. bridges) need upgrading due to the requirements for traffic increase. These changes have led to a significant growth in the number of reinforced concrete strengthening projects worldwide.

The bonding of steel plates to reinforced concrete (RC) structures is a popular method for strengthening deficient RC structures. As technology has advanced, the use of carbon fibre reinforced polymers (also referred as fibre reinforced plastic) plates/sheets, as a replacement of steel plates in plate bonding, is gaining popularity. CFRP has also been used for column strengthening by external wrapping (Teng, J.G., 2002).

Reliable bonding of CFRP reinforcing components to the concrete surface is an important factor in achieving the design outcomes in CFRP strengthening of structures. Whilst the CFRP provides enhance properties in flexure and strength, lack of bonding or bonding failure under successive loading as an adverse effect on performance (Grinzato, et al., 1981, Chiang et al., 2008, Taillade et al., 2012) stress that the bond should be monitored with control procedures for assessing defects and imperfections. This issue has prompted considerable research activity in the effects of surface bonding with regards to de-bonding and delamination's of CFRP. Both destructive and non-destructive testing techniques (NDT) have been used in this. The

NDT methods include acoustic sounding through contact methods such as hammer tapping (Taillade, et al., 2012, Lai, et al., 2010) and destructive method such as the pull off test (Lai, et al., 2010). Both type of tests are localised and, therefore, not conducive to 100% coverage in the inspection of large scale structures.

Whilst destructive testing is a reliable method for assessing installed bond strength, non-destructive processes offer the advantages of detection without disturbing the function of the structure. Despite this obvious point, research into the bond integrity evaluation by non-destructive technique remains somewhat limited. Tashan & Al-mahaidi (2012) affirms that quality assurance of the bond through non-destructive testing (NDT) has received little attention.

2 THERMOGRAPHY FOR INTERNAL DEFECT DETECTION IN CONCRETE

Among other techniques, the application of Thermography, an emerging NDT method, for interface bonding and internal defect detection in FRP strengthening systems is very limited. In the past decades, the application of infrared thermography in civil engineering was mostly limited to passive investigations, to assess the quality of thermal insulation of building envelopes, for example. Recent advancements in infrared technology both in-terms of availability, price and functionality have made its use attractive for many industrial, scientific and medical applications. Active thermography has been applied with some success in the detection of defects in concrete and asphalt materials (Geyer et al., 1998, Mierhofer et al., 2002, Jean et al., 2009).

In 2002, Hu et al., used an active thermography approach to develop an inspection procedure for monitoring damage in structures, exploring occurrences and extent of air blisters at the bond interface of CFRP strengthened reinforced concrete elements. Using 500 mm long concrete beams, they introduced blisters using 16–30 mm pipes set 1 mm below the surface prior to commencement of the bonding processes. The air blisters were introduced by slight displacement of these tubes during the CFRP installation process. Detection of these artificial air pockets proved possible using IR (infrared) thermography, through thermal conductivity. These air pockets could be detected from a distance of 20 m.

Mierhofer et al., (2002), have researched the effectiveness of active impulse thermography in the detection of voids with different sizes and depths, using CFRP laminates with varying glue thickness, through the examination of thermal decay. This employed active pulse thermography, with thermal pulses varies from a few milliseconds to a few seconds duration. Analytical and semi-empirical methods were developed for quantitative analysis based on the Fourier Equation through a finite difference program. Results indicate shallow voids have good contrast in the cooling down process, while deeper voids are identified after the thermal heat flux has diffused from inside the specimen. Delaminations were observed after a short heating time. Several additional inhomogeneities were also detected in all the CFRP strips, these related to small unintentional delaminations rather than surface homogeneity. They also reported that active impulse thermography is effective in the detection of defects up to a 100 mm size, as well as quantifying the extend of delaminations in CFRP bonded to concrete. Differences in glue thickness could not be differentiated using this approach.

Bhalla (2011) and Tashan & Al-Mahaidi (2011) used active thermography and ultrasonic pulse velocity (USPV) to determine interface inhomogeneity's. The thermography technique involved placing artificial defects in known locations, with thermal transmission to heat specimens. Bhalla (2011) used wooden blocks to simulate defects, while Tashan & Al-Mahaidi (2011) used an application procedure, bonding layers of CFRP and insertion artificial delaminations between them. The USPV technique was used to provide a crude representation of void size and locality. Tashan & Al-Mahaidi (2011) applied water jetting and sand blasting for surface preparation, however, assessment of bond quality with respect to surface preparation is not relevant to the adopted experimental procedure.

Pronounced texture in the host substrate is understood to be extremely influential in achieving a well bonded CFRP installation. The epoxy-bonding agent needs to transfer flexural and shear stresses between the CFRP laminate and concrete, whilst eluding delamination due to long term creep. A suitably coarse texture, with removal of the potentially weak surface laitance layer, is a standard requirement from material manufacturers and suppliers. It is anticipated if the prepared surface is too rough, then excessive epoxy maybe required, to the possible detriment of the installation.

3 RESEARCH OBJECTIVES

The objective of this study is to investigate the potential role of a Lockin Thermography method in identifying and discriminating three different qualities of hidden substrate texture: normal cast, disk abraded and needle gunned. Both the heating and cooling cycles are utilised to extract the texture characteristics for CFRP bonded to unreinforced beams. The results are analysed in terms of temperature gain and loss during heating and cooling cycles, and include an attempt to identify air pockets in the bonded system. Practical considerations, such as the method of epoxy resins application, and issues associated with specimen heating processes are also considered.

Whilst there are has been mixed success in the detection of defects within the CFRP bond interface, no study has been reported on the application of Lockin thermography to identifying the prepared substrate texture in an installed CFRP system. This is

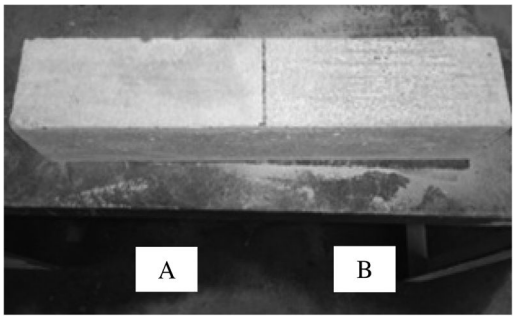

Figure 1. Beam 1 surface preparation: (A) normal-cast (B) needle gunned.

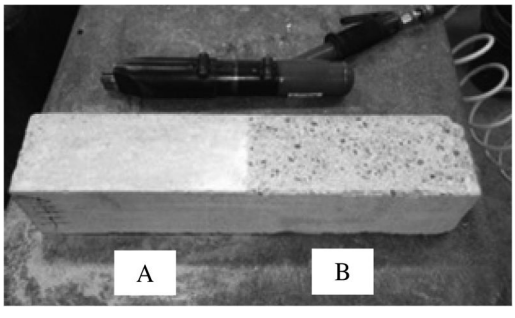

Figure 2. Beam 2 surface preparation: (A) normal cast (B) disk abraded.

an important installation 'quality control' issue that is decisive to the effectiveness and longevity of the structural enhancement. The Lockin Thermography method is an attractive proposition for this because, if successful, it could facilitate inspection of large-scale CFRP installations.

4 SPECIMEN PREPARATION

Under Stage 1 of testing, two C30 grade concrete beams ($100 \times 100 \times 500\,mm^3$), adhering to BS 1881-125: 1986 concrete mix design, where cast. To ensure similarity, they were cast in the same mix batch. After curing, the host face of each beam was prepared. One beam was prepared abraded to half its length and the other needle gunned to half its length. Figures 1 and 2 show the two prepared beams.

Preparation by needle gunning observes the technical guidance of CFRP material system manufacturers and suppliers, as one of the acceptable forms of substrate preparation. This gives a case texture, with aggregates stones exposed in the host substrate. The abrasion method represents partial preparation, with part of the weak cement paste laitance layer removed. The 'normal cast' texture has the complete laitance layer intact, this representing zero surface preparation, a completely unacceptable preparation.

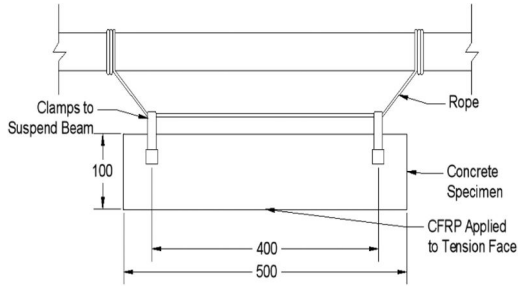

Figure 3. Schematic of suspended beam (all dimensions are mm).

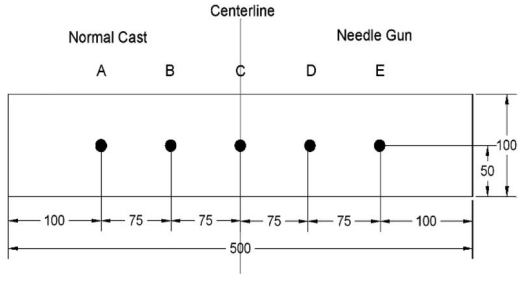

Figure 4a. Beam 1-target points.

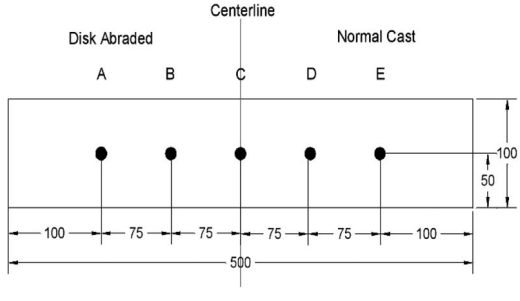

Figure 4b. Beam 2-target points.

Stage 2 involves bonding the CFRP sheets to concrete substrate. To ensure the method of application simulated real life practice, the beams were suspended from a frame structure, with access to tension face. The set-up is shown schematically in Figure 3. For the thermal investigation, the beams were rotated through 90° to present the CFRP overlay as a vertical plane.

5 EXPERIMENTAL RIG

For each beam, five target points were adopted for data collection, as shown in Figures 4a and 4b. This gave two target points for each surface preparation type. Reflective and transmitted heat processes heated the specimens. A schematic diagram for both methods is given in Figure 5.

In the reflective method, the heat was applied in front of the specimens, while in the transmitted method

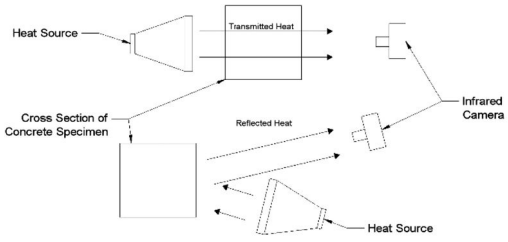

Figure 5. Experimental set up.

the heat was applied at back of the specimens. The lighting was applied by two quartz lamps (2 × 500 W), positioned at 500 mm during the transmitted heating and heat source is 700 mm during reflective heating to avoid rapid change in temperature. Thermal imaging camera was positioned at 1500 mm away from specimen in both cases the distance and source of lighting was adopted from the earlier research by Tashan and Al-Mahaidi's (2011).

Temperature recordings were taken every minute during the reflective heat process, as change in temperature (ΔT) was more rapid in both cycles. On the other hand, in the transmitted method, the temperature recordings were taken every 5 minutes. These measurements were derived through calibration tests (briefly explained in the testing programme section) that concluded that the temperature change was very slow in transmitted heat process hence using 5 minutes as a suitable time period.

6 TESTING PROGRAMME

6.1 *Calibration*

Calibration were carried out to ensure accurate temperature determination, an important issue because the variations in temperatures in the CFRP and concrete interface are expected to be small. The calibration process was done prior to the application of CFRP to the specimens. It should be noted that as the main criteria for this experiment is to replicate an application and procedure intended to be performed in the field. The emissivity ($\varepsilon = 0.92$) and reduce radiation of concrete and CFRP was used based on published literature (Infrared Thermography, 2013. Emissivity values of common materials).The calibration tests were performed using a calibrated Flir B-200 thermal camera (Flir Systems, 2013. Flir B-200 Infrared Camera)as follows:

- External temperature verification: the influences of external heat sources such as lights and nearby machinery were evaluated. Temperature was recorded with time whilst potential heat sources are switched on and after being switched off to evaluate if there is a fluctuation in temperature recordings. It was found that less than 0.1°C temperature difference was due to the lighting conditions in the laboratory environment.

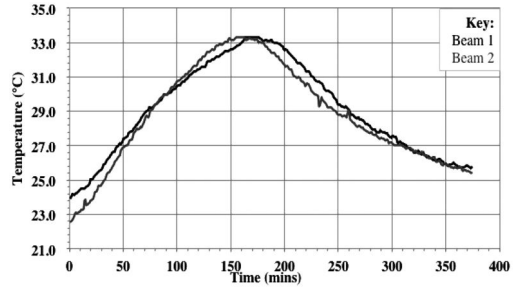

Figure 6. Heating and cooling curves for all beam specimens.

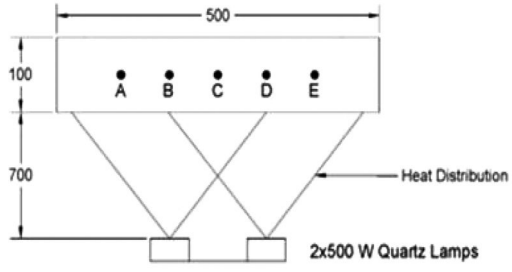

Figure 7. Heat distribution from quartz lamp (all dimensions in mm).

- Distance correction: The position of longitudinal spacing between specimen and camera was altered along with the on-board distance correction within the camera. Temperature was recorded with varying distance to find the optimum positioning for the thermal camera. The distance change is small during the experiments, giving an effect of less than 0.1°C. A similar result was reported by Hu et al., (2002) and Tashan and Al-Mahaidi's (2011).
- Homogeneity of concrete specimens: In addition, in order to evaluate the consistency of the concrete specimens, testing was performed through heating specimens using the transmitted heat process and recording temperature as a function of time. The temperature variations at the centre of the test beams for both heating and cooling cycles are shown in Figure 6. The temperature difference proved to be only marginally different in both cases of installed CFRP. Similar results were found at the left side and right side of all three specimens. These air pockets have a different thermal contrast due to the existence of air pockets, with an anticipated temperature difference of approximately 0.5°C.
- Influence of cross lighting: The possible influence of cross lighting as presented in Figure 7, was also investigated. It can be seen that position B, C and D appear to be influenced by the cross lighting, which may contribute to the marginally higher temperature at point A than E. This factor was taken into account during the analysis.

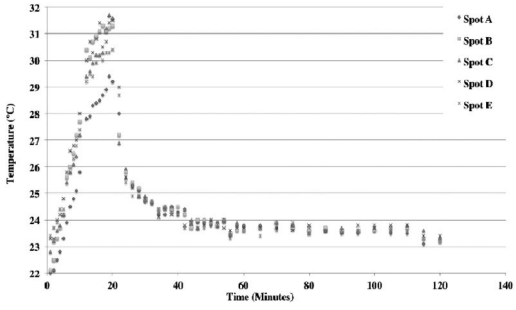

Figure 8a. Temperature/Time plot of reflective heat experiment: 'normal cast' (A & B) and 'needle gunned' (D & E).

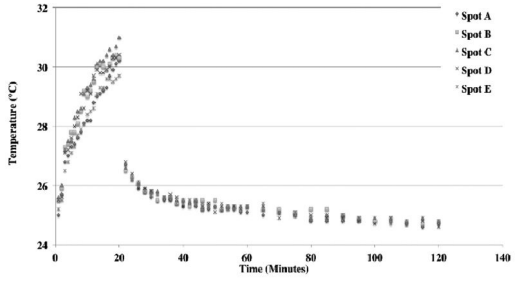

Figure 8b. Temperature/Time plot of reflective heat experiment: 'normal cast' (D & E) and 'disk abraded' (A & B).

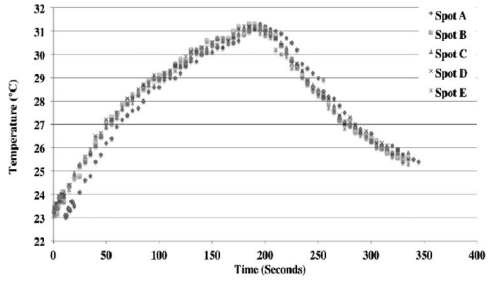

Figure 8c. Temperature/Time plot of transmitted heat experiment: 'normal cast' (A & B) and 'needle gunned' (D & E).

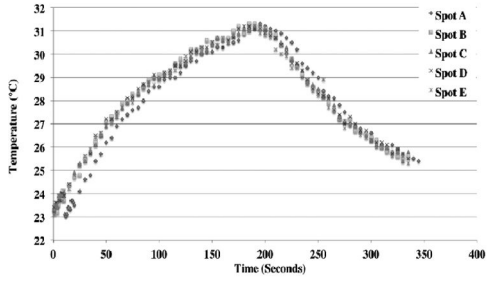

Figure 8d. Temperature/Time plot of transmitted heat experiment: 'normal cast' (D & E) and 'disk abraded' (A & B).

7 RESULTS AND ANALYSIS

The captured temperature distribution across a surface in a concrete element should be uniform other than edge effects and the existence of anomalies such as crack, voids and other defects. In the investigation, the texture of surfaces to which exterior reinforcement, in the form of a bonded CFRP plate, has been varied as 'normal cast', 'disk abraded' and 'needle gunned'. Disk abrasion of the surface results in a very smooth texture that is regarded as unsuitable for the application. By contrast, 'needle gunning', which is of the CFRP manufacturer's stipulated substrate preparation methods, delivers a pronounced texture.

7.1 *Temperature distribution using the reflective and transmitted method*

The temperature distributions for heating and cooling cycles of the reflective and transmitted methods, for the needle gunned and disk abraded surfaces are presented in Figures 8a to 8d.

It can be seen that in the case of the transmitted method, approximately 200 minutes were required to achieve an equilibrium temperature (same temperature at the back and at the front of the specimen). Contrastingly, the time was significantly less, only 20 minutes, to achieve equilibrium temperature (same temperature between two front adjacent surfaces) with the reflective method.

It can also be seen that, whilst the distribution of surface temperatures have similar trends in heating and cooling cycles, there are some variations in temperature at different points of measurement, in both cases. In addition, there was a sudden drop in temperature in the reflective method, as soon as the heating source was switched off, after 20 minutes and then a gradual decrease of the temperature. On the other hand, the temperature drop was gradual after switching off the heat source at 200 minutes, with the transmitted method. It is likely that the heat source has some effect on the heating process in the reflective method.

Due to the very slow temperature changes, the heat distribution is different in the transmission method. Defective areas in the heating process take longer to accumulate initial heat; therefore temperature change is slow (shown in Figures 8c and 8d), showing that areas with normal texture have a more progressive heat process. However after initial heating, poor texture preparation shows higher temperatures.

7.2 *Thermal image*

The thermal images taken at different stages of the experiments are shown in Figure 9. It can be seen that whilst the surface temperature changes with

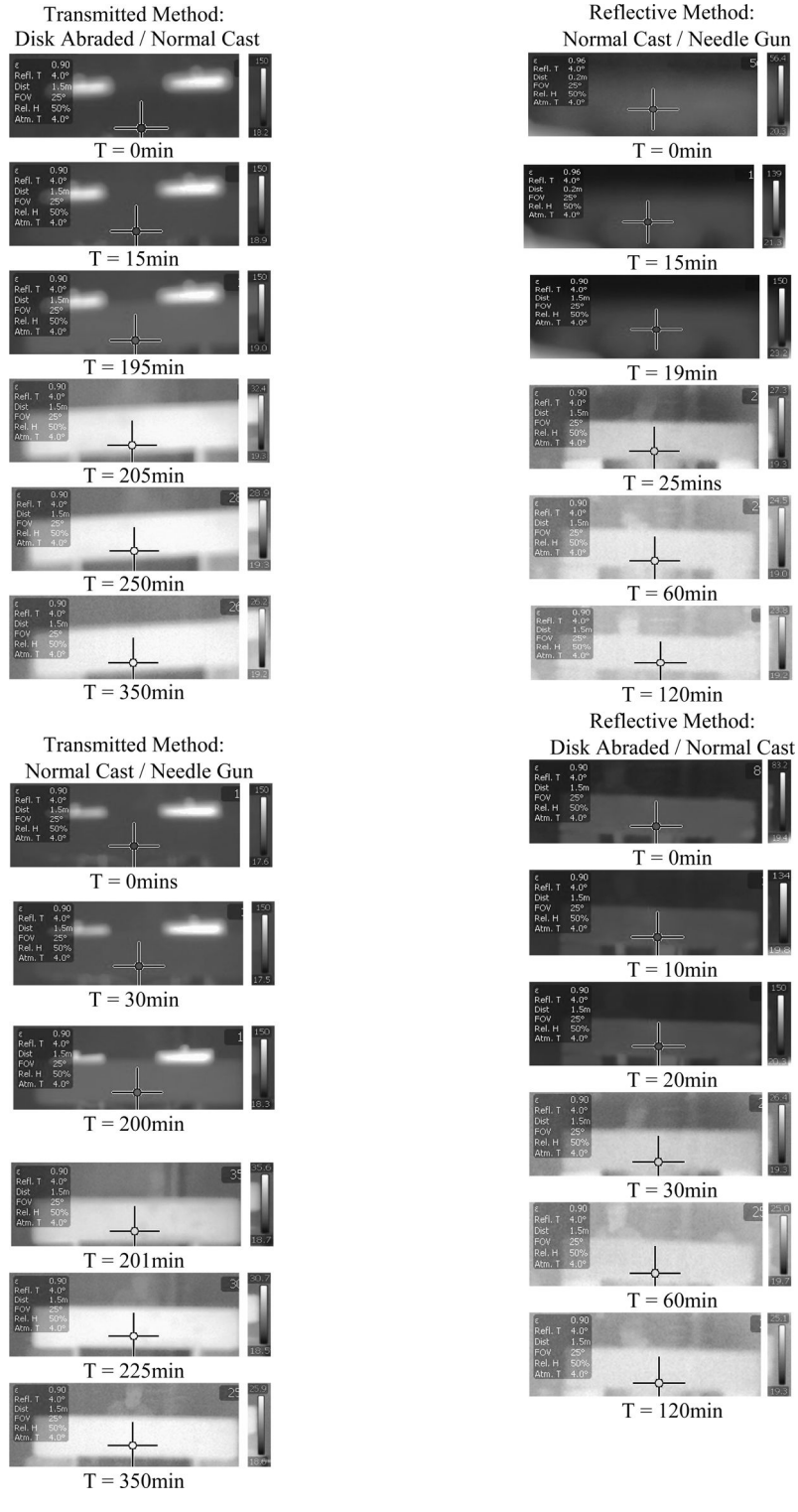

Figure 9. Thermal images at different stages of experiment.

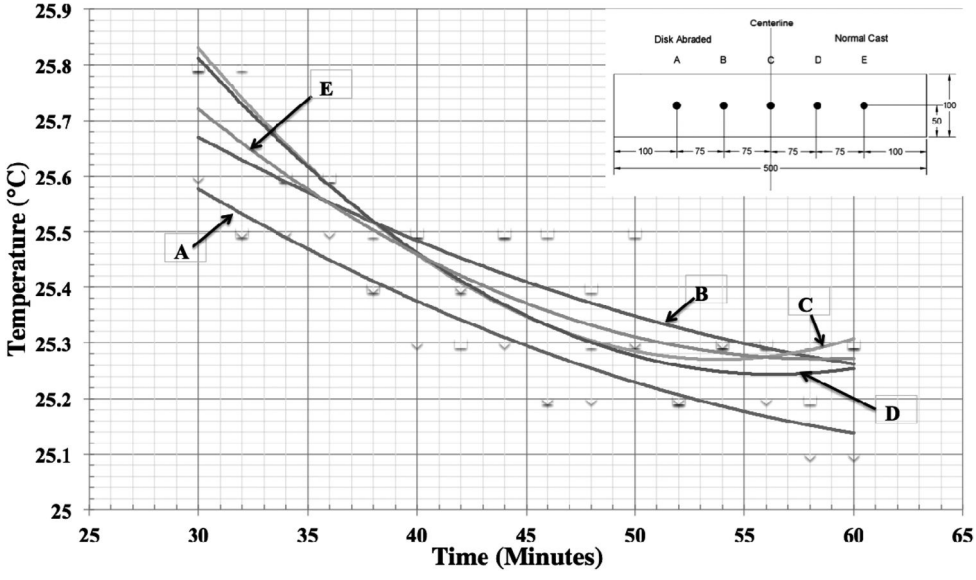

Figure 10a. Beam 1 temperature/time graph 30 minutes after heating stopped (average) – reflective method.

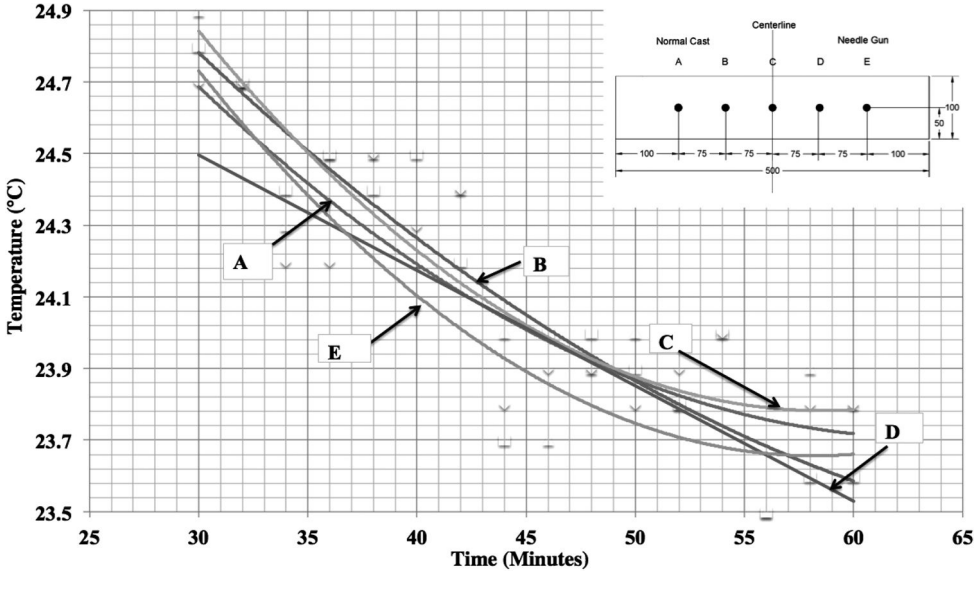

Figure 10b. Beam 2 temperature/time graph 30 minutes after heating stopped (average) – reflective method.

time, the contrast for different surface preparations is unclear. Whilst near surface defects such as large cracks or cavities are reported detectable by the previous researchers, the different textures in the surface preparations were found difficult to separate from the thermal images alone. This is likely to be the reason of close proximity of small voids creating an apparent uniform temperature distribution.

In an attempt to evaluate the temperature differences, the temperature distribution at different intervals were compared, to see whether there is any significant differences exist between adjacent surfaces.

7.3 *Temperature difference at different stages of experiments*

The temperature variation 30 minutes after switching off the heat sources in the reflective method is presented in Figure 10a and 10b, as best fit curves. It can be seen that the 'disk abraded' side of the beam (point A in Figure 10a) has a cooler temperature than

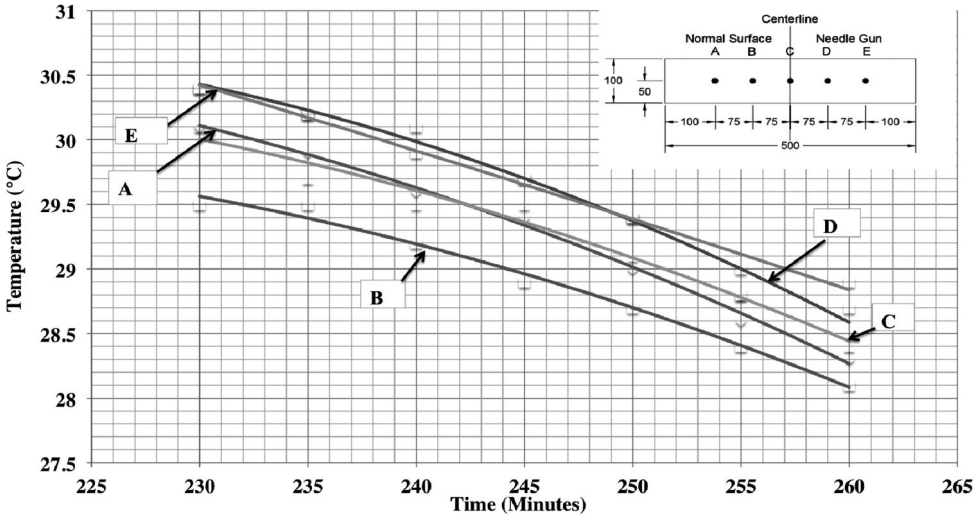

Figure 10c. Beam 2 temperature/time graph for 30 minute after lamp switch off (average) – transmitted method.

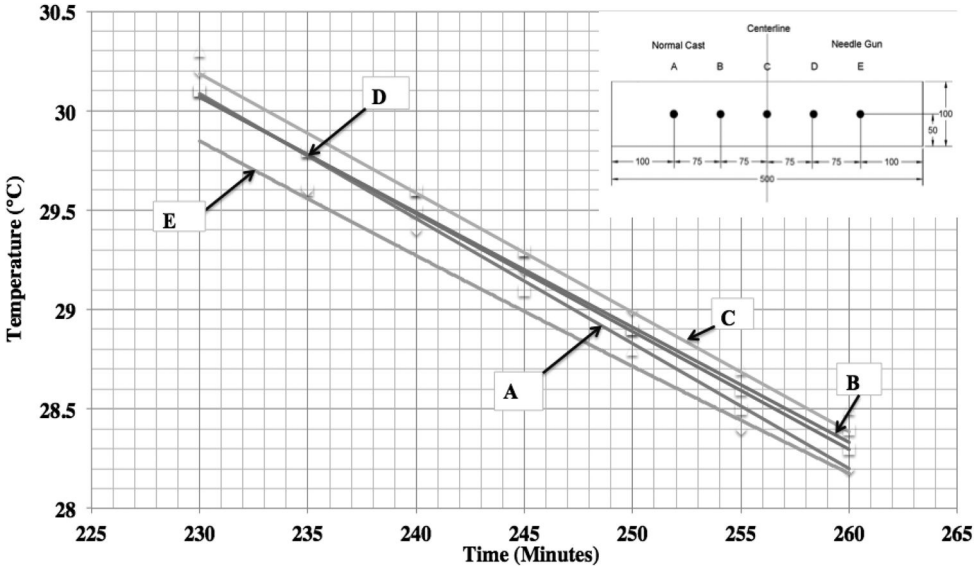

Figure 10d. Beam 1 temperature/time graph for 30 minutes after lamp switch off (averaged) – transmitted method.

the corresponding 'normal cast' point (point E). The highly textured area produced by 'needle gunning' (in Figure 10b), on the other hand, tends to cool to a lower temperature at 30 minutes after heating, indicating dissimilar thermal behaviour of the two surfaces points under heating and cooling.

Similar graphs were plotted as best fit curves for the transmitted method, where the range of heat distribution for spots B, C and D is greater. This occurs because the heat energy has to travel through the breadth of the beam section, distributing around the section, unless large anomalies are present. Nevertheless, during cooling cycle anomaly areas many take longer to cool as indicated by the gradient. For example, in Figures 10c and 10d, spot E has a lesser thermal gradient than spot A.

Figures 11a and 11b show the best-fit temperature variations for beams 1 and 2 with respect to the different surface preparations. It is clear that a disk abraded sanded surface provides a less fluctuating temperature variation The 'needle gunned' and 'normal cast' surface temperatures are consistently higher than the 'disk abraded' temperature.

Comparing the pairs of data capture points A & B and D & E in all cases, does not give a strong basis for discriminating the three hidden surface textures. At

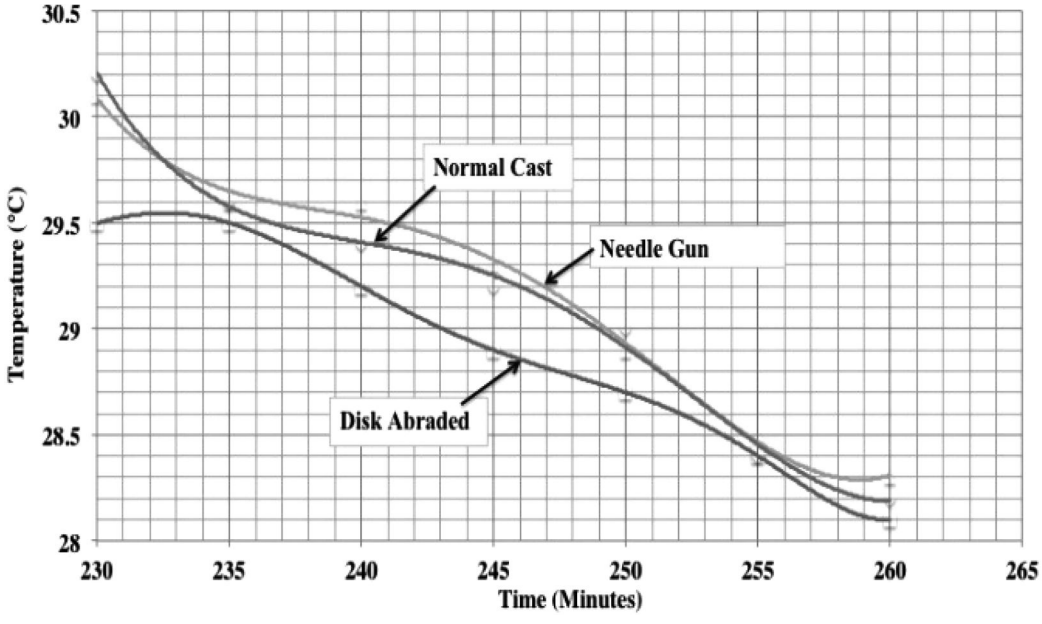

Figure 11a. Combined temperature/time graph 30 minutes after lamp switch off by transmitted heating method.

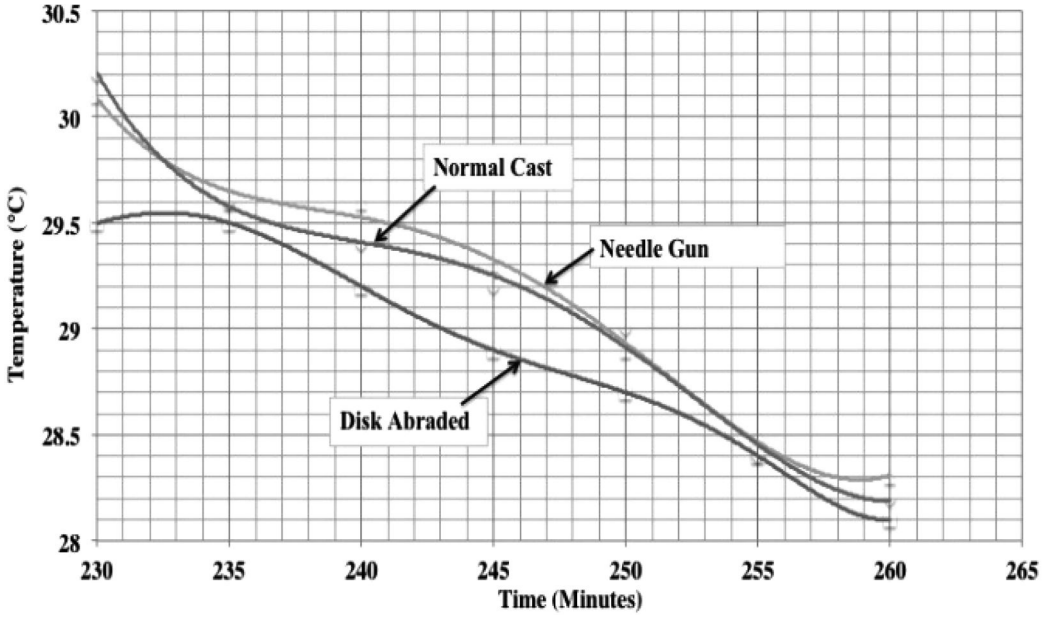

Figure 11b. Combined temperature/time graph for 30 minutes before lamp switch off by transmitted method.

the same time, the approach has been to use low order best fit curves to data point to reduce the influence of what is normally terms signal noise.

However, following the principles of Lock-in Thermography methodology, phase differences in the first order derivatives of temporal temperature variations in the raw data are also of interest. To this end.

Figure 12 plots the first derivative (dT/dt) of temperature raw data recoded at points A and E over 120 minute duration, for the case of reflective thermal loading. Features apparent in this are (i) the phase and wavelength differences between 'disk abraded' and 'smooth cast' surface preparations and (ii) the tendency for higher amplitudes and lower frequency

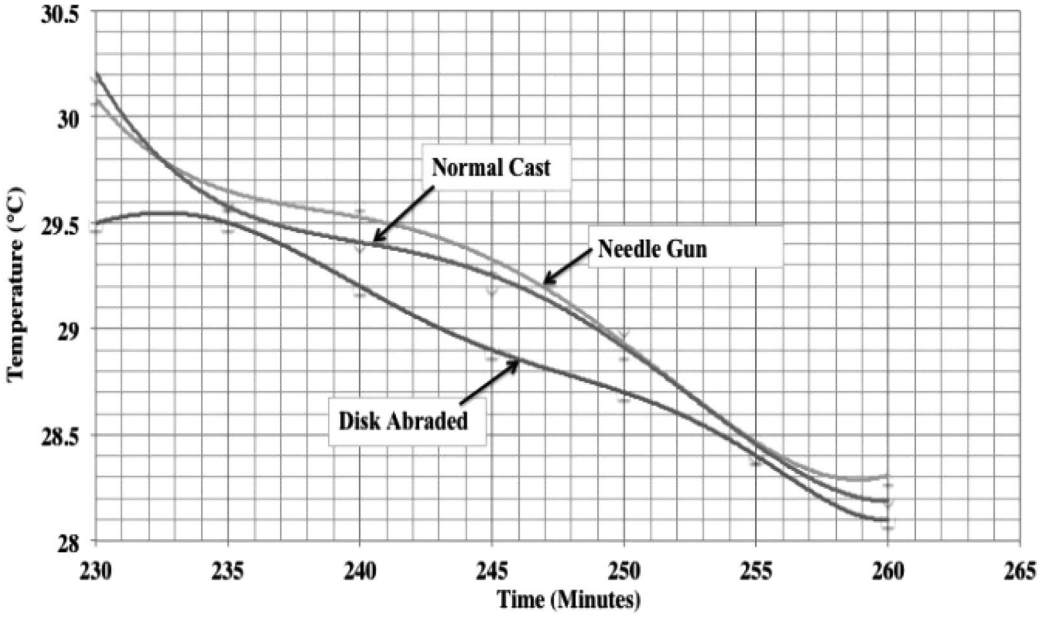

Figure 12. First derivative (dT/dt) for relective method for a duration of 120 mins.

oscillation with 'needle gunned' and (iii) the relatively small amplitude occurring in the case of 'normal cast'. It is also noted that the most useful data is confined to the first 60 minutes of data capture, which is useful because to shorten the time needed for investigation.

8 CONCLUSIONS

The conclusions that can be drawn from this study are:

- The reflective method of heating has shorter associated heating times than the transmission method with a maximum testing time requirement of 60 minutes indicated. This is a significant outcome because it will generally be more practical to use the reflective method in possible field applications.
- Temperature differences in the collected temperatures responses are typically less than 1°C and the thermal imager has a resolution of 0.08°C. Data needs to be collected at many more points for the reliability of the method to be tested.
- Acquiring data in pairs, by averaging at discrete target points, does not give high confidence for the discrimination of surface preparation features based on temperature variation only. Analysis, commencing on a pixel-by-pixel basis, might help in statistically eliminating possible influences of bond variations and defect anomalies in the CFRP system.
- The first derivative of temperature variation appears to have texture discriminating potential. Phase and wavelength differences occur between 'disk abraded' and 'smooth cast' surface preparations, amplitudes and lower frequency values with 'needle gunned' and amplitude in the case of 'normal cast'.
- This investigation offers a promising start to the possible role of a Locking Thermography method in discriminating substrate preparation in installed CFRP systems. Substantially more investigation and analysis, especially at individual pixel level, is necessary to give greater confidence.

REFERENCES

Bhalla, S. 2011. Experimental Techniques. *Defect Detection in Concrete Structures using Thermal Imaging Techniques*, 35(4), pp. 39–42.

British Standards Institution, 1986. BS 1881: 115. *Testing concrete. Methods of mixing and sampling fresh concrete in laboratory*

British Standards Institution, 1986. BS 1881: 115. *Testing concrete. Methods of mixing and sampling fresh concrete in laboratory*.

Chiang, C., Laio, Y. & Yu, W., 2008. *Thermography Inspection of Bond Quality of FRP Strengthened Concrete. Shanghai*, www.ndt.net.

Chiang, C., Laio, Y. & Yu, W., 2008. Thermographic Inspection of Bond Quality of FRP Strengthened Concrete. Shanghai, www.ndt.net.

Dirar, S., Lees, J., and Morley, C., 2012. ACI Structural Journal. *Pre-cracked reinforced concrete T-beams repaired in shear with bonded carbon fibre reinforced polymer sheets*, Issue: March–April 2012, pp. 215–224.

E. L. Klamer, 2009, *The Influence of Temperature on the Debonding of Externally Bonded CFRP*. Ph.D. thesis, University of Eindhoven.

Flir Systems, 2013: *Flir B-200 User Documentation* [online]. Flir System Co., LTD. Available at: http://www.flir.com/

uploadedFiles/Thermography_APAC/Products/Product_Literture/B200_Datasheet%20TW.pdf

Geyer E, Arndt D, Grüünder K, Roos A and Wiggenhauser H., 1998, Thermographic and shearographic investigations of carbon fiber laminates on concrete surfaces. In: Proceedings of 4th international workshop on advanced infrared technology and applications, vol. 93. Florence: Fondazione Giorgio Ronchi; p. 297–304.

Grinzato, E., Trentin, R., Bison, P. G. & Marinetti, S., 1981. Control of CFRP strengthening applied to civil structures by IR thermography. Thermosense, pp. 1–12.

Hu C W, Shih J K C, Delpak R and Tann D B, 2002. Inframation. *Detection of air blisters and crack propagation in FRP strengthened concrete elements using infrared thermography*, 1, pp. 1–8.

Infrared Thermography., 2013. *Emissivity of Common Materials* [online]. Infrared Thermography. Available at: http://www.infrared-thermography.com/material.htm.

Jean D, Ibos I, Marchetti M, Ludwig S and Mazioud A, 2009, Active Infrared Thermography applied to detection and characterization of non-emergent defects on asphalt pavement, NDTCE'09, Non-Destructive Testing in Civil Engineering Nantes, France, June 30th–July 3rd.

Maierhofer C, A. Brink, M. Rollig, H. Wiggenhauser, 2002, Transient thermography for structural investigation of concrete and composites in the near surface region, Journal of Infrared Physics & Technology 43, p. 271–278.

Tashan, J & Al-mahaidi, R. 2012. Composite Structures. *Investigation of the parameters that influence the accuracy of bond defect detection in CFRP specimens using IR thermography,* 94, pp. 519–531.

Teng, J.G, et al., 2002, *FRP Strengthened RC Structures*. 1st edition. Chichester: John Wiley & Sons Ltd.

T. Ullmann, Y. Shi and R. Aoki, 2012, Capabilities of Lock-in Thermography for Non-destructive Inspection of Fibre Reinforced Composites, 11th International Conference on Quantitative InfraRed Thermography, Naples, Italy.

Ullmann, T. Aoki, Shi & R., 2012: Capabilities of Lock-in thermography for Non-destructive inspection of Fibre Reinforced Composites, 11. pp. 1 – 11.

This page intentionally left blank

Concrete Solutions – Grantham et al. (Eds)
© 2014 Taylor & Francis Group, London, ISBN 978-1-138-02708-4

Stress wave velocity tests in early-stage of concrete piles

J. Rybak
Institute of Geotechnics and Hydrotechnics, Wroclaw University of Technology, Poland

ABSTRACT: During the pile quality inspection, the errors in velocity estimation may lead straight to proportional faults in the estimation of the pile's length. It is even more complicated to determine the wave velocity in the process of the young concrete setting (before the 15th day of concrete embedding). At the same time, site construction progress frequently forces the verification procedures to be made prior to the time suggested by testing equipment manufacturers and earlier than allowed by appropriate standards. To prove how vital is this problem, out of a total of 1000 tests for integrity for C20/C25 and C30/37 concrete Continuous Flight Auger (CFA) piles performed by Wroclaw University of Technology, as many as 393 piles were tested earlier than after 14 days from concreting. It meant that no fewer than 40% of tests were of "non-standard" nature. Research work outlined here on the relationship between acoustic wave velocity in young concrete and the time elapsed from pile concreting has been the response to the need for calibrating the non-standard tests (i.e. made at earlier time) of pile length and integrity. The research conducted at Wroclaw University of Technology showed that in the case of the concrete piles made with C25 concrete, examined between the 5th and 35th day after the concrete embedding, the measured elastic wave velocities ranged from 3000–4300 m/s. An important outcome of analyses carried out was also evaluation of the variability coefficient of acoustic wave velocity in concrete having been a peculiar measure of Pile Integrity Testing (PIT) method accuracy depending on the precision of wave velocity evaluation.

1 INTRODUCTION

Regarding the issue of the pile quality (continuity and length) tests by means of non-destructive methods, it seems essential to estimate the velocity of the elastic wave in the concrete. For example, considerable differences are observed in the measurement of the wave velocity before and after the pre-cast concrete piles are driven. For reinforced concrete piles made of C50 concrete, elastic wave velocity 'c', reported by Modl and Rybak (2009), measured before driving reaches 4500 m/s, and after the driving – oscillates around 4100 m/s. That is probably connected with the micro-cracking caused when driving the pile.

Very few publications on that subject (Niederleithinger and Taffe, 2006) show large changeability of the estimated velocity and suggest that each time at the construction site calibration should take place. Calibration, however, is possible only when the person who runs the tests is in possession of fully credible information about the length of the examined (controlled) piles.

2 PUBLICATIONS ABOUT WAVE VELOCITY

Measurements of acoustic wave velocity 'c' in concrete are generally related to searches for correlation between this velocity and the strength of concrete 'f_c' in concrete/ferroconcrete components or identification of defects in these elements. Exemplary correlations were presented in works of Yoo and Ryu (2008) where this relationship is given by the formula (1):

$$f_c = 0.0022c^{6.2893} \tag{1}$$

In the context of foundation pile concrete strength (quality), the problem is described by Amir et al., (2004) with empirical relation (2):

$$c = 2367f_c^{0.1482} \tag{2}$$

These examinations aim at evaluating the quality of the concrete itself while wave velocity is taken from the time the wave need to cover the segment of known length. Tests made on concrete samples in successive days elapsed from concrete work confirm that the relation of velocity versus time, until concrete attains its full strength, is of logarithmic type and it stabilizes after about 4 weeks at about 4,000 m/s. Final velocity depends on various factors such as: concrete grade, additives used, maturing conditions, etc. An extensive review of non-destructive diagnostic methods for concrete elements can be found in the publication of Hola and Schabowicz (2010).

As concerns foundation piles, estimation of acoustic wave velocity is attributable to their non-destructive

Table 1. Formerly published results for wave velocity.

Author	Proposal
Amir (1988)	$c = 3946 \cdot \sqrt[6]{\log(t+1) \cdot f_c/30}$ where f_c is concrete strength
Finno, Gassman, (1998)	$c = 217 \cdot \ln(t) + 3339$ for $1 < t \leq 14$ days
Finno, Gassman, (1998)	$c = 12 \cdot \ln(t) + 3887$ for $14 < t$ days
Thasnanipan et al., (2000)	$c = 204 \cdot \ln(t) + 3235$ for $5 < t \leq 62$ days
Niederleithinger, Taffe, (2006)	$c = 182 \cdot \ln(t) + 3497$ for $3 < t \leq 25$ days

diagnostics, both in the sense of pile load carrying capacity (high strain testing) and their quality (length and integrity) in low strain testing.

As concerns the dynamic testing of bearing capacity (high strain), it is justified, for analyzing the strain wave, to take the velocity determined for specific concrete strength class after complete concrete setting (testing is usually performed after 4 weeks from pile completion). However, for continuity testing with low strain method, the pile material it is not required to attain its full strength. Integrity testing is admitted as early as after 1 week from pile concreting as recommended by ASTM and equipment/software providers. In practice, this period is additionally shortened by the progress at construction site. Functional relations reported which describe changes in acoustic wave velocity in concrete are usually prepared for testing calibration for a single construction site. Hence, they are distinguished by small diversification of random sample resulting from small number of piles under testing, short testing time and – what could be the most important – pile homogeneity as concerns their length, diameter and grade of concrete.

The proposed velocity-versus-time relationships for bored foundation piles for time *t* elapsed from pile completion were published by various authors:

The results of author's experience, collected from the sample of about 140 bored piles made of C30/C37 concrete, as shown in Figure 1, are the closest to the findings of Thasnanipan et al., (2000) and are as follows (3):

$$c = 281 \cdot \ln(t) + 2891 \quad \text{for} \quad 12 < t \leq 33 \text{ days} \qquad (3)$$

These results confirm both the rising trend in time domain and relatively large variability of velocity for particular piles. Attention is attracted to large scatter of the results obtained. It is all the more striking that the measurements were taken from merely three construction sites and the piles were made with the same piling machine. It indicates that mistakes could be made in evaluating the length of piles, and – what is worse – in evaluating the quality of placed concrete. Independent testing for 131 concrete columns made in CFA (continuous flight auger) process with C20/25 concrete is

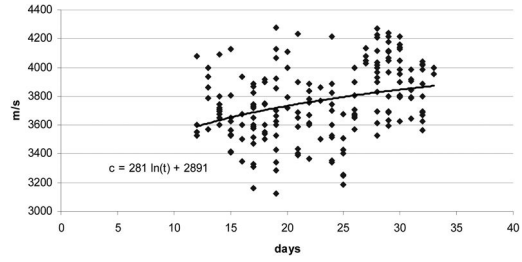

Figure 1. Increment in velocity over time for C30/C37 concrete bored piles.

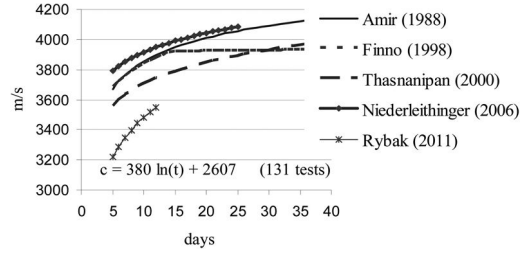

Figure 2. Increment in velocity over time for piles of C20/25-C30/37 concrete grades.

provided in the paper of Rybak and Schabowicz, 2011. The functional relationship were than in the form (4):

$$c = 380 \cdot \ln(t) + 2607 \quad \text{for} \quad 5 < t \leq 12 \text{ days} \qquad (4)$$

All publications confirm that velocity rises in time and stabilizes after some 4 weeks. It is necessary to stress that the testing results differ significantly due to various piling technologies, concrete recipes and, in general, different time of observations. Average values of acoustic wave velocity in CFA piles determined by the author in the second week from concreting were significantly lower that the remaining date found in literature and the author's own testing (for bored piles) summarized in Fig. 2. It could resulted from such factors as:

- an unique composition of concrete mixture (sand concrete in CFA piles),
- lower strength class of concrete (C25/30) than that in the remaining research works,
- testing was run in winter season which could affect the quality of concrete mixture and the conditions of its curing within the pile head zone,

Significant discrepancies of formulae describing the rise of acoustic wave velocity taken versus concrete ageing time justified more complex statistical analysis to find, for the statistical sample as broad as possible, both the relationship describing the increment in wave velocity and the variability coefficient for this feature. This coefficient could be an indication of possible scatter of results and in this way, it might define the accuracy of the method. The first attempts of such estimation were given in the work of

Table 2. Juxtaposition of the wave velocities for varying time.

Time [days]	Population [pcs]	Mean value [m/s]	Standard deviation [m/s]	Coefficient of variation [%]
5	29	3226.45	100.25	3.1%
6	19	3275.79	129.08	3.9%
7	13	3298.54	136.38	4.1%
8	19	3405.79	153.24	4.5%
10	16	3542.63	151.74	4.3%
11	16	3523.06	191.16	5.4%
12	19	3559.58	181.31	5.1%

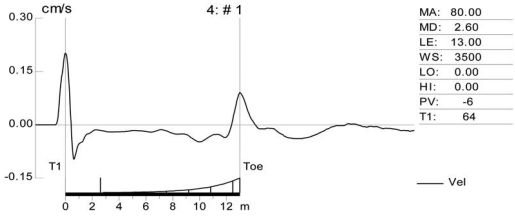

Figure 3. A sample PIT signal for a 13.00 m pile.

Amir (1988), where standard deviation was found at the level of 160 m/s which represented about 4% of the measured velocity value.

The results of wave velocity analyses in successive days of young concrete curing in CFA piles are shown in Table 1 from paper of Rybak and Schabowicz (2011). These results, in quality and quantity aspects, confirmed the conclusions of the Amir's paper (1988). Some anxiety could be however felt that the standard deviation values were rising in time, and as a consequence, the coefficients of variation went higher for the estimated velocity of acoustic wave in concrete. Due to small sizes of samples, an attempt was made to collect all the results of continuity testing with PIT (pile integrity test) method available to the author, which could be verified in pile records.

3 TEST DESCRIPTION

This paper presents the research programme carried out so far, as a part of which almost 1000 CFA piles were being screened in the course of 32 subsequent days – on 4th to 36th day after the concreting the piles. The signals were recorded by means of the PIT device (see Fig 5.). The tests were performed on CFA piles with the diameters of 600 and 800 mm and the length varying from 5 to over 20 m.

A sample signal (without noise reduction) was shown in Fig. 3. One may notice a distinct echo from the pile bottom at the depth of about 13.0 m below the pile head. Acoustic wave velocity corresponding with that pile length, in a pile tested on the 10th day after concreting, equaled app. 3500 m/s.

Figure 4. PIT equipment (hammer, accelerometer, main unit).

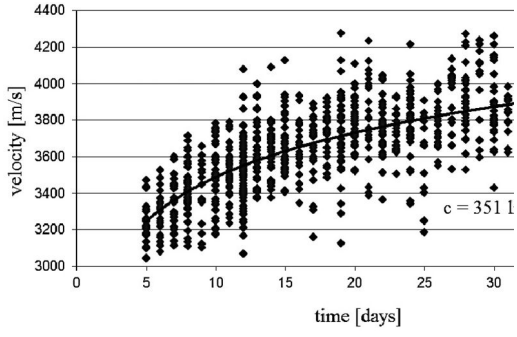

Figure 5. The increase of acoustic wave velocity over time.

Analogical analysis was carried out for app. 1000 signals from those piles, where the length could be confirmed by means of electronic piling report (from piling rig).

4 TEST RESULTS

4.1 *Cloud of velocity test results for CFA concrete*

The velocity test results, calculated on the basis of the PIT signals and the time elapsed since concreting, confirming the expected increase of velocity in time, have been juxtaposed in Fig. 5. Despite the visible variability in the observations on subsequent days, there is a distinct upward trend, and the results dispersion, measured by means of the coefficient of variation falls within the range of 3–4%.

Such variability can also be partially confirmed by the results of tests carried out in a laboratory conditions (Schabowicz, 2011). It must be stressed that the observed result dispersion may also arise to some extent from imperfection of piling works as far as the piling depth is concerned, as well as the absence of marking the level of hacking of the pile heads.

The functional relationship – formula (5), got from a cloud of results on Fig. 5, which describe wave velocity c versus time t can be used to evaluate the pile length

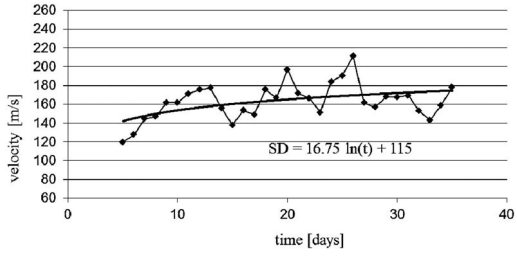

Figure 6. Standard deviation of wave velocity versus time.

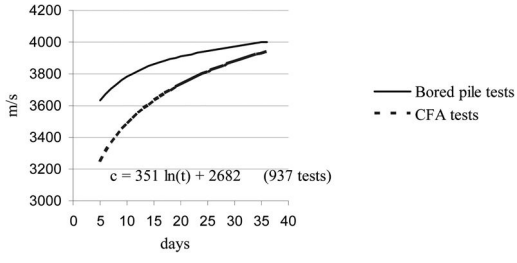

Figure 7. Comparison of results for bored and CFA piles.

with PIT method. This function can be also applied in sonic logging testing (type CHSL)

$$c = 351 \cdot \ln(t) + 2682 \quad \text{for} \quad 5 < t \le 36 \text{ days} \qquad (5)$$

As shown below on Fig. 6, the variation of standard deviation calculated for measurements of wave velocity in concrete, made in successive days, is very close to the value of 160 m/s presented by Amir (1988). Referring the relation which approximates the standard deviation to formerly proposed functional relationship describing variation of acoustic wave velocity during concrete curing, a virtually constant coefficient of variation at the level of 4.4% is attained.

4.2 *Bored piles vs. CFA piles*

The results obtained, compared with the once from bored piles investigation (see Fig. 7.) prove that special attention should be paid to CFA pile integrity and length testing especially at early stages of concrete maturing. The CFA concrete velocity test results are significantly lower.

Hence, examinations of C20/25 concrete CFA piles at construction site in Poland prove that specific composition of concrete mixture used in these piles affects significantly the evaluations of their length with PIT method over the first days after concreting. Also the conditions of concrete curing differ, in many cases, from typical laboratory environment, especially when constant temperature is considered. These factors influence the delay of concrete strength rise in the pile.

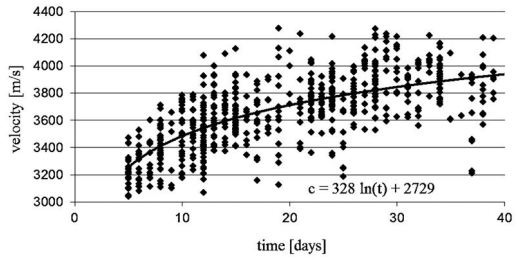

Figure 8. Results of 670 "short" pile's investigation.

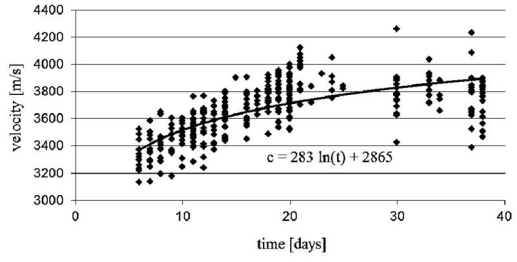

Figure 9. Results of 320 "long" (over 10 m) pile's investigation.

4.3 *Long piles vs. short piles*

Interesting observations about "quality" of foundation piles were presented by (Amir and Amir. 2008). They found that, in general, much less defects are recorded in projects where long piles are used as compared with those projects with short piles.

Such a regularity could be hardly explained rationally. In searching for positive answer, one can just suppose that "responsible" contracts are gained by companies with greater experience. Another, less optimistic explanation, is the equally feasible supposition that when concreting is made for more than one pile per batch supplied by one concrete mixer truck, the last pile is made from concrete weakened by adding some more water to maintain the consistency enabling concrete placing operation.

The statistic investigation of test results on Fig. 8 and Fig. 9. prove that (at least in Poland) the difference between long piles (over 10 m) and the shorter once is not significant.

4.4 *Histograms of acoustic wave velocity*

Figure 10 shows the histograms of wave velocity for the 7th, 21st and 35th day (the proportion of piles for which the wave velocity was calculated in every interval of 100 m/s within a range 3000–4000 m/s.

4.5 *Normal distribution tests*

It seems that the observed distributions of the identified velocities on subsequent days after concreting are similar to a normal distribution, and such thesis can be

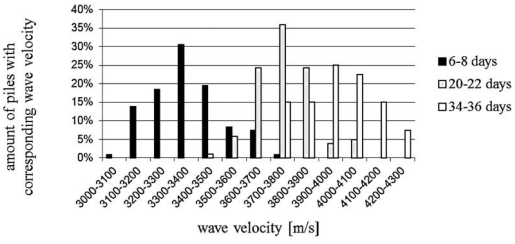

Figure 10. Histogram of velocity on selected days.

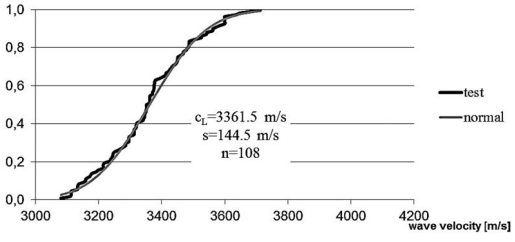

Figure 11. Test of normal distribution (6–8 days).

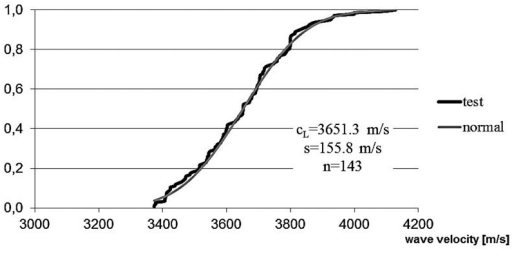

Figure 12. Test of normal distribution (13–15 days).

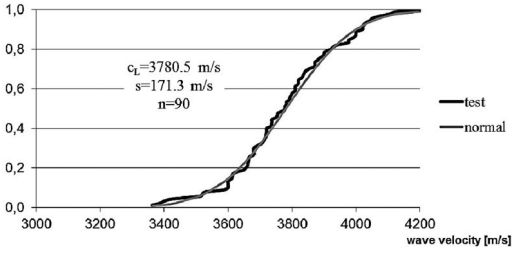

Figure 13. Test of normal distribution (20–22 days).

confirmed on a large statistic sample (Fig. 11, 12, 13, 14, 15) by cumulative distributions.

The consistency tests made for cumulated normal distribution starting from one-week to five-week piles gave satisfactory results as concerns technical applications. However, some differences can be observed. What seemed however important, it has no significant effect on final value of velocity determined after 5 weeks being in general somewhat over 4000 m/s. Figure 15 provides data based on review of almost

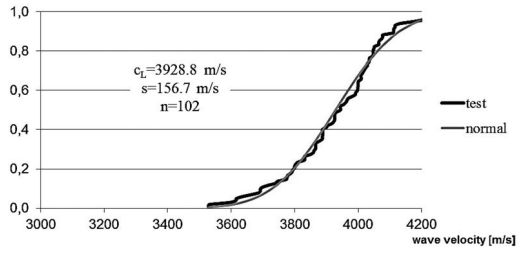

Figure 14. Test of normal distribution (27–29 days).

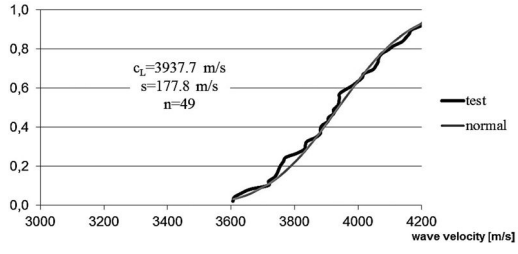

Figure 15. Test of normal distribution (34–36 days).

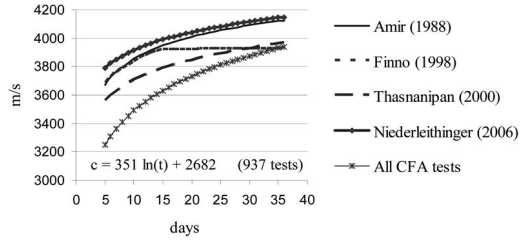

Figure 16. Results of concrete tests for CFA piles compared with those for bored piles .

1000 PIT tests for CFA piles compared with earlier relationships worked out mainly for bored piles.

5 SUMMARY AND CONCLUSIONS

The outcomes attained are of significant practical consequences because they mean that pile length evaluation with the PIT method (even when we consider unfinished process of concrete curing, and wave velocity in pile is estimated on the basis of earlier experience) is not worse than 4.4%. For piles under testing which lengths not infrequently reach up to 20 m, it means that the error which could be made is non-other than about 1 m.

It is not impossible to speed up the time of testing piles, in terms of both their load capacity and integrity. That, however, requires a certain amount of awareness of the processes which take place in the pile itself, as well as in its soil environment. It is possible to carry out necessary inspection procedures even before the time defined in the codes of practice, after consistent collecting data for different concrete types, with tests

starting on the 3rd-4th day after concreting (when the pile heads are uncovered) until the 28 day needed for its stabilization.

Rather conservative regulations in the codes are inconsistent with the construction practice, in which haste is often a crucial factor in decision making. It is moreover noteworthy that the documented tests under laboratory conditions (Schabowicz, 2011) end up with the results that differ (greater wave velocity values) from the field examinations. A simple "copying" of laboratory tests on the field tests may be the source of inaccuracy and errors.

Estimation of wave velocity in concrete for dynamic tests of piles must be made on the field tests and piling reports available and also through critical analysis or proposals from data base. Selection of velocities from laboratory tests of soil samples is risky because the curing conditions (temperature and moisture) are significantly dissimilar.

Concrete used for CFA piles is of specific nature (sand-cement grout and fine-grain concrete). Numerous points observed which diverge from the trend (outliers up and down the waveform) could be attributable to the unique conditions at given construction site.

ACKNOWLEDGMENTS

The author would like to express his gratitude to KELLER Polska Sp. z o.o and PPI CHROBOK S.A. for making available the results from the pile integrity tests.

REFERENCES

ASTM D5882–07 Standard Test Method for Low Strain Impact Integrity Testing of Deep Foundations

Amir J.M. 1988. Wave velocity in young concrete, In: *Proc 3rd Intl Conf on Application of Stress-wave Theory to Piles*, Ottawa, pp. 911–912

Amir J.M., Amir E.I. & Felice C.W., 2004 Acceptance criteria for bored piles by ultrasonic testing. In: *Proceedings of 7th International Conference on the Application of Stresswave Theory to Piles*, Kuala Lumpur 2004

Amir E.I. & Amir J.M. 2008. Statistical analysis of a large number of PEM tests on piles. In: *Proceedings of 6th Conference on the application of stress wave theory to Piles*, Lisbon, Portugal, IOS Press, pp. 671–675

Finno R. J. & Gassman S. L. 1998: Impulse response evaluation of drilled shafts. *Journal of Geotechnical and Geoenvironmental Engineering*, vol. 124, No. 10, pp. 965–975.

Hoła J. & Schabowicz K. 2010. State-of-the-art non-destructive methods for diagnostic testing of building structures – anticipated development trends. *Archives of Civil and Mechanical Engineering*. vol. 10, No. 3, pp. 5–18

Modl A. & Rybak J. 2009. Badania ciągłości pali prefabrykowanych. *Górnictwo i Geoinżynieria*. vol. 33, No. 1, pp. 443–451 (in Polish)

Niederleithinger E. & Taffe A. 2006. Early stage elastic wave velocity of concrete piles. *Cement & Concrete Composites* vol. 28, pp. 317–320

Restrepo, C. 2000. Stress wave propagation velocity at early ages. In: *Proceedings of 6th Conference on the application of stress wave theory to Piles*, Sao Paulo, Brazil, Balkema, Rotterdam

Rybak J. & Schabowicz K. 2011. Acoustic wave velocity tests in newly constructed concrete piles. *e-Journal of Nondestructive Testing & Ultrasonics*. vol. 16, nr 4 pp. 247–254

Schabowicz K. 2011. Empirical relations for nondestructively determined strength of concrete on different days of its maturing. *e-Journal of Nondestructive Testing & Ultrasonics*. vol. 16, nr 4. pp. 255–262

Thasnanipan N., Maung A.W., Navaneethan T. & Aye Z. Z. 2000. Non-destructive integrity testing on piles founded in Bangkok subsoil In: *Proceedings of 6th Conference on the application of stress wave theory to Pil*es, Sao Paulo, Brazil, Balkema, Rotterdam. pp. 171–177

Yoo J.K. & Ryu D.W. 2008. A study of the evaluation of strength development property of concrete ar early ages. In: *3rd ACF International conference-ACF/VCA*

Concrete Solutions – Grantham et al. (Eds)
© 2014 Taylor & Francis Group, London, ISBN 978-1-138-02708-4

Instant and solid corrosion diagnosis on reinforced concrete structures with galvanostatic pulse measurement

U. Schneck
CITec Concrete Improvement Technologies GmbH, Germany

ABSTRACT: The potential survey has established itself as the major NDT measurement for the assessment of rebar corrosion on concrete structures. Although it is easy to obtain the data, its correct interpretation is difficult and sometimes impossible, as the intended indicators for corrosion will be overlaid by varying concrete humidity, concrete cover and concrete composition to an unknown extent. Very often, a correlation with chloride values sampled from suspect areas will not result in a feasible pattern for the evaluation of the corrosion activity. With the help of enhanced corrosion measurement methods, such as impedance- and galvanostatic pulse measurements, these uncertainties can be eliminated safely in most cases. Furthermore, also carbonation induced corrosion – where potential mapping provides no access basically – can be evaluated securely.

1 INTRODUCTION

In the 4th Concrete Solutions Conference in Dresden 2011, a new Corrosion Measurement System was introduced which is able to run several electrochemical methods, among them also the galvanostatic pulse (GP) measurement. Starting with its application on long-term stored concrete specimen, where first indicators for the interpretation of the GP data came from, the device has been used increasingly during routine corrosion surveys. Within more than 15 projects, good experience has grown in how to use GP data for a solid understanding of corrosion behaviour of a structure.

It has shown that the polarisation curve has characteristic shapes depending on the respective state of corrosion (passive – passive like – active), although there are uncertainties about the possible spread of the pulse current across the reinforcement which influences the anodic current density and hence the change of polarisation. In a 3-step evaluation, GP data can be verified and interpreted quickly and reliably. This enables the user to pre-assess corrosion suspect areas which have been identified from a potential survey, and to focus dust sampling and inspection openings on proven hot spots. Another application is the determination of the individual chloride threshold value of a structural part.

2 ENHANCED ELECTROCHEMICAL MEASUREMENT METHODS

With electrochemical measurement methods the corrosion of reinforcement (and indirectly also of prestressing reinforcement) can be assessed as a process.

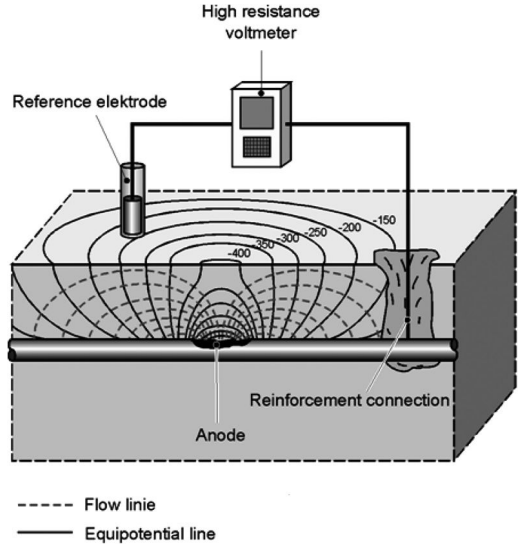

Figure 1. Potential survey and iso potential lines (source: ibac).

The condition of a rebar – blank or corroded surface, loss of cross-section – cannot be measured non-destructively. Potential mapping provides rough, qualitative information at rapid progress of the data collection and low technical effort (fig. 1).

On corrosion suspect areas it is not possible to distinguish between "real" chloride induced corrosion activity and effects coming from wet concrete and that are not associated with rebar corrosion (Schneck 2007, Schneck 2011). Furthermore, it is not possible to obtain information about corrosion currents and the

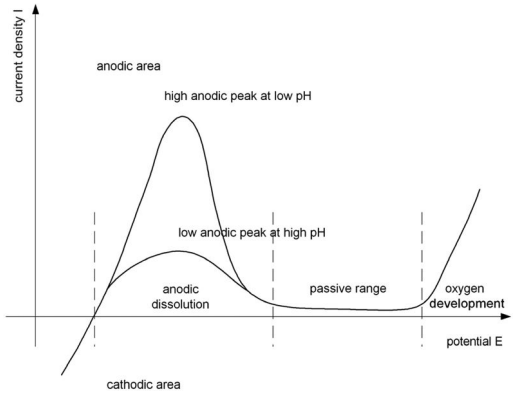

Figure 2. Current density – Potential plot of iron.

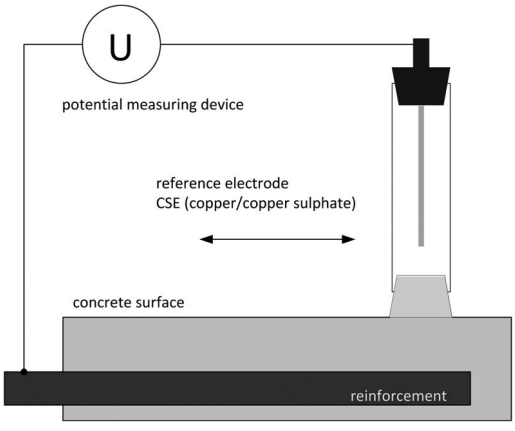

Figure 3. Principle of the open circuit potential measurement.

related corrosion progress. Fig. 2 illustrates this, as potentials only represent values on the ordinate of the diagram.

For running enhanced methods an electrochemical device is required – the potentiostat. It controls 3 electrodes as seen in fig. 4: the working electrode (WE – equals the reinforcement), the reference electrode (RE) and a counter electrode (CE). Depending on the method chosen, either a current between CE and WE is driven and the voltage at the RE (the potential) is measured, or according to defined signal movements at the RE, a voltage between CE and WE is controlled that corresponds to the recorded current. Contrary to this, potential mapping (fig. 4) is being done at the rest stage of the WE and being called "open circuit potential" (OCP) in electrochemistry.

The potentiostatic measurement setup (fig. 4) enables a substantially better evaluation of the corrosion behaviour, compared to potential mapping. Two methods of the various electrochemical standard methods are chosen that provide an internal verification on errors and can be done at reasonable effort of time.

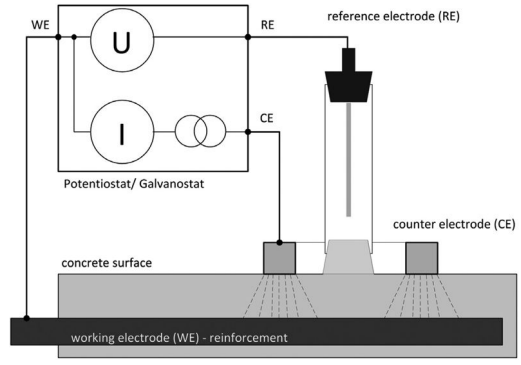

Figure 4. Principle of the polarization measurement using a potentiostat.

2.1 *Impedance measurement*

The impedance is the ohmic resistance of the concrete or the electrolyte resistance R_E of the measurement setup. It varies depending on concrete conductivity and concrete cover and influences the reaction between anode and cathode during corrosion. It results also in a signal distortion, a voltage shift during the potential measurement between RE and WE as soon as there's a current flow in the system. This voltage shift is called IR drop and will be calculated $\Delta E = I * R_E$. During potential mapping there is no external current flowing (OCP), and therefore no IR drop has to be considered.

The impedance is measured with AC at ca. 1 kHz between CE and WE. This frequency is considered to be characteristic for the electrolyte resistance as part of the total resistance in concrete, which consists furthermore of the transition- and depression resistances of the electrodes. In the electrode arrangement shown in fig. 4 the use of R_E (measured between CE and WE) for the correction of the potentials measured between RE and WE is possible because of the tolerable low geometric difference between RE and CE.

2.2 *Galvanostatic pulse measurement*

At this method, an anodic, constant current is driven between CE and WE, and the change of potential is measured at the RE (galvanostatic principle). According to fig. 5 the current pulse causes either a small potential shift if the system is in the steep, active range within the current-potential-plot, or a large potential shift if the system is in the shallow, passive range. The polarization resistance R_P can be calculated with $R_P = \Delta E/I$.

Immediately after applying the anodic pulse (within ca 1 to 3 ms) the IR drop, the instant shift of the potential in positive direction can be seen as shown in fig. 6, which may have some 100 mV.

After this initial potential shift, the polarization process itself starts. Depending on the composition of the cover layer on the rebar, this may take up to 100 s, until a stable potential value is reached.

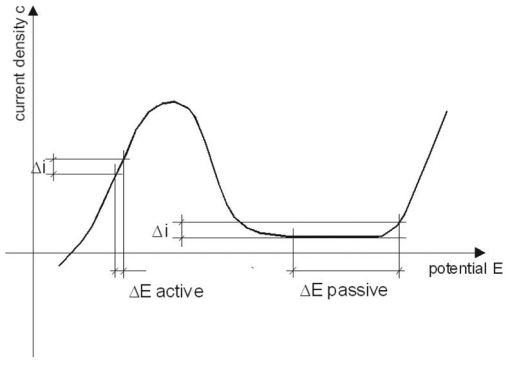

Figure 5. Resulting polarization of the reinforcement from an anodic, galvanostatic pulse.

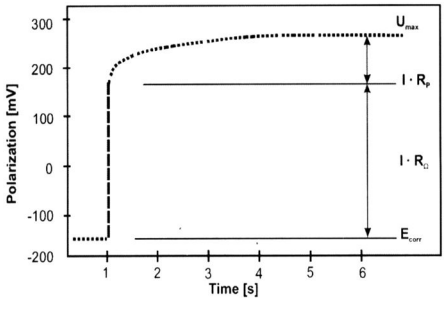

Figure 6. Parts of the galvanostatic polarization (from Bäßler et al 2007).

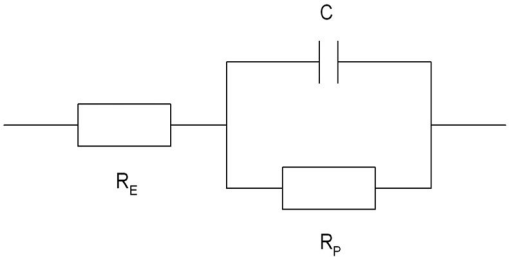

Figure 7. Electric circuit layout for the galvanostatic pulse measurement with $R_E = R_B$.

Simplified, polarization can be understood as a charging process of the capacitor as seen in the circuit of fig. 7. At an intact passive layer both depressing resistance and capacity are quite high, and a slowly increasing polarization and (positive) potential shift can be observed accordingly – see fig. 8. At an active stage of the reinforcement, R_P and the capacitor are small, and the final polarization will have met after a few seconds.

2.3 *Approaches for using and interpreting the measurements*

As being described, the total shift of potential during the galvanostatic pulse is determined by the IR

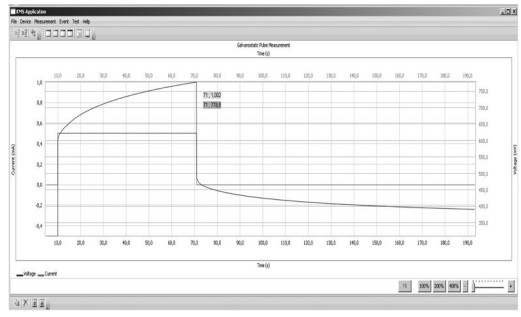

Figure 8. Polarization curve of a laboratory test on a specimen with zero chloride.

drop across the concrete and the "real", capacity influenced polarization following the anodic pulse. Concrete humidity and concrete cover control the spread of the pulse across the rebar surface in an unknown extent. Hence the polarized area is not known exactly, and only as an assumption the area directly under the CE is being considered as the WE area. The shielding effect of guard rings is not proven, and even the surface quality of the WE will influence its size.

This makes the determination of the related rebar (WE-) area very uncertain under practical circumstances, and attempts to calculate corrosion rates appear to be critical. This shall be mentioned not only because of the unknown polarized area, but also because the corrosion progress is not constant or linear; grown corrosion products on the rebar surface may limit corrosion after an initial high activity, and changes of environmental conditions (concrete resistivity, total anodic area) can alter the degree of corrosion activity as well.

However, under common test parameters (anodic pulse of 100 to 500 µA for about 60 s) R_P values can be evaluated on an empirical base, among others in accordance with (Böhni, Elsener 1991) as following:

- $R_P > 100\ \Omega$: passive behaviour
- $30\ \Omega < R_P < 100\ \Omega$: transition stage with uncertain evaluation of the corrosion activity
- $R_P < 30\ \Omega$: active behaviour, high corrosion progress

A verification of the feasibility of this evaluation guide has been done by the author's company at a large number of aged reinforced concrete specimens with different levels of mixed-in chloride, concrete cover, concrete admixture and during conditioning to various levels of humidity. During these experiments a special correlation between the state of corrosion and the shape of the polarization curve has been observed: in passive state, there is a permanent increase of the potential throughout the whole pulse application time, in highly active state no further potential shift will be seen after 5 s of pulse application, and in a passive-like state an increased R_P value will be measured (often on an uncritical level), but the continuing growth of polarization is missing.

These values are independent of the obtained open circuit potential. It can be assumed that R_P is being evaluated on the "safe side". In case of a good concrete conductivity the pulse can polarize a larger rebar surface than situated directly under the measurement cell or its CE. The current density on the rebar surface, resulting from the given anodic pulse, will be smaller – at the double surface only 50% of the assumed current density. A similar effect can be caused by highly fissured rebar surfaces. Hence, a lower polarization will be received, and a consequently less R_P value will be calculated. Contrary to this, it is most unlikely that the rebar surface directly located under the measurement electrode will be polarized only partly.

These influences on the spread of the current across the rebar do not permit to evaluate the corrosion behaviour in an explicit way and to find mathematical functions for it, even if laboratory tests showed very good correlation and measurement curves when varying a single parameter (chloride content, water content etc.). For a correct interpretation of the pulse data, a complex assessment of the final value of R_P after 60 s as well as the shape of the polarization curve between 10 s and 60 s of pulse application has to be done.

The R_B value coming from the impedance measurement is valuable for a check of plausibility of the pulse measurement. Ideally, it will be almost identical with $R_B = (E_{2ms} - E_{OCP})/I$. The AC resistivity measurement usually is very reliable, and deviations of $R_{B,Imp}$ from $R_{B,Pulse}$ give advice to check for more suitable points of "switching" between the IR-shift and begin of the polarization –such as at 3 ms. A very large difference between the R_B's shall raise doubt in the correctness of the measurements, and it is advised to repeat the tests after s certain time of recovery for the test location (Schneck 2013).

2.4 *Measurement tools*

A new system, consisting of an electrode, a potentiostat adopted for the conditions on reinforced concrete and a controlling software, has been developed to apply the methods as described previously (Ahlborn et al 2011). Its components can be seen in fig. 9. The CE is split into 8 single electrodes, which are spring suspended and can adopt to uneven surfaces or round shaped column surfaces. This technique is a result of a joint R + D project between the Kurt-Schwabe-Institut für Meß- und Sensortechnik Meinsberg e.V., Sensortechnik Meinsberg GmbH and CITec GmbH. It is acknowledged gratefully, that the project has been funded by the Sächsische Aufbaubank using resources of the European Fund for Regional Development (EFRE) and of the Free State of Saxony.

3 CASE STUDIES

The practical use of the above approaches shall be demonstrated with 2 case studies. In both projects the corrosion diagnosis started with the full-face sampling of NDT data (potential, surface resistivity, concrete cover) in a measurement grid of 60 × 60 cm, added by the visual inspection of the concrete surface on delamination, spalling and cracks. With a pre-evaluation of these data (cumulative frequency of potentials, correlation of the different measurements), corrosion suspect locations and areas have been identified for a closer inspection.

Figure 9. Components of the Corrosion Measurement System: measurement cell, potentiostat, controlling software on notebook.

Usually, core or dust samples will be taken now, and on the most suspicious coordinates the reinforcement will be uncovered for a visual inspection and carbonation testing. Since the amount of core/ dust samples should be limited for not only economic reasons, it is advised to use impedance- and galvanostatic pulse measurements after the full-face NDT survey for a non-destructive pre-evaluation of the suspect locations (and also for counter-checks on other locations). This way, a much larger number of tests can be made in a rapid way, and the core- or dust sampling can be focussed on the locations with proven activity.

3.1 *Walls of a highway tunnel*

3.1.1 *Description of the structure*

The tunnel has been 35 years in service at the time of survey. It has 2 tubes with 2 lanes each and a total length of ca. 900 m. There are 2 connecting structures between the tubes. The tube walls have an outer shotcrete shell (applied against rock) and an inner reinforced cast-in.place concrete shell with a sealing layer between both concrete shells. Due to given specifications, several wall sections have been surveyed on corrosion problems from the road surface up to 2.40 m height. Fig. 10 shows the tunnel entrance.

3.1.2 *Measurement results*

Following the approach mentioned above, impedance- and galvanostatic pulse measurements have been done on over 30 locations, and on 12 of these points dust samples were taken. Examples for the pulse measurement curves can be seen in figs. 22 to 24 that cover

Figure 10. View on the tunnel entrance.

Figure 11. Appearance of the rebar at 1.37% chloride, $R_P = 319\ \Omega$ – similar to the curve in fig. 23.

the whole range of obtained impedance- and polarization resistances. In fig. 11 a rebar in passive state can be seen at 1.37% chloride, and where an R_P of 319 Ω indicates no activity or even a well passive behaviour.

Figures 12 to 14 show the different R_P values over the respective free chloride content in rebar vicinity: first the total, IR-corrected R_P after 60 s pulse, second the increase of R_P (ΔR_P) between 10 and 60 s pulse, and third the percentage of ΔR_P to the total R_P. In all 3 diagrams a decrease of R_P at increasing chloride content can be seen.

Fig. 14 shall provide a more precise evaluation of the formally critical R_P values, and above 2% chloride, both total R_P and $\Delta R_P/R_P$ are in a critical low range, especially those at 4.32% chloride: The total R_P is in the formal transition stage (68 Ω), but the rise of the polarization curve is zero, as well as the ΔR_P value. The open circuit potential was −259 mV vs. CSE, which would not indicate a high likelihood of corrosion, but there were found delaminated concrete, heavy corrosion products and ca. 50% loss of cross-section. Apparently, the corrosion progress has been slowed down after a previous high intensity – concrete delamination and thick corrosion products have

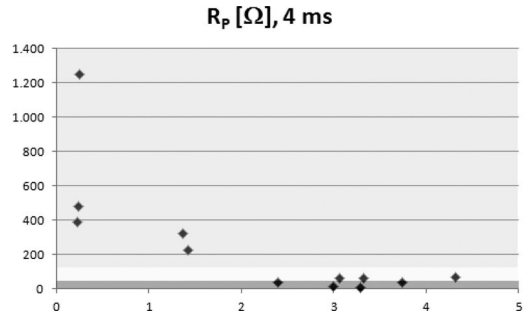

Figure 12. Total R_P values (after 60 s pulse) on sampling locations over the respective (free) chloride contents in rebar vicinity, related to cement mass.

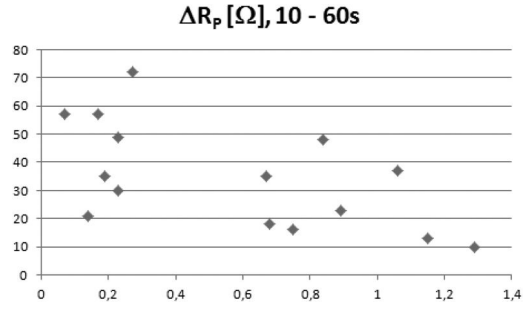

Figure 13. ΔR_P values (raise between 10 and 60 s pulse) over the respective (free) chloride contents in rebar vicinity.

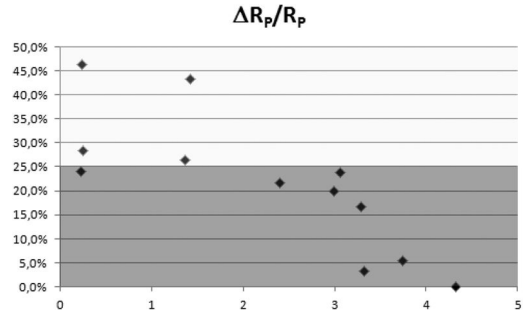

Figure 14. Percentage of ΔR_P on total R_P over the respective (free) chloride contents in rebar vicinity.

let the R_P increase, the corrosion current drop and the potential raise.

Fig. 15 shows how the open circuit potentials on the sampling locations have been in relationship to the chloride contents in rebar vicinity. It can be seen that there is much less correlation between the two parameters than in figs. 12 to 14.

3.1.3 *Conclusions from the project*

It was possible to conclude on an individual chloride threshold value of between 1.4 to 1.9%, related to the

cement mass by a formal interpretation of the galvanostatic pulse data. Visual inspections supported this evaluation. The potential survey has been less suitable for a direct data assessment, as the potentials have been influenced also by different concrete humidity (causing partly limited oxygen availability and thus negative potentials), pre-corrosion and concrete delamination.

3.2 *Floor slab of an underground car park*

3.2.1 *Description of the structure*

The introduced data have been collected on the second floor of a 3-storey underground car park with over 3,000 square meters per level. Slabs, columns, walls and beams have been made of cast-in-place reinforced concrete, and the parking areas were covered by a ca. 3 cm thick asphalt layer – see fig. 16. Some cracks close to joints have been visible on the soffit of the floor slabs with partly sintering. The car park was ca. 16 years old at the time of survey.

3.2.2 *Measurement results*

Similar to the tunnel project, on 27 of corrosion suspect locations (due to negative potentials and/or steep potential gradients of more than 150 mV) the enhanced electrochemical measurements have been done. Generally, they showed low R_B and R_P values, the latter ranging between 37 and 185 Ohm and being mostly in the transition or critical range. The related ΔR_P values were between 13 and 95 Ohm, so in almost all cases a sufficient raise of potential cloud be stated. Figs. 18 to 20 show the different R_P values in correlation to the chloride contents, which were not very high. Only at the maximum chloride value of 1.29% related to the cement mass some pitting corrosion could be observed as seen in fig. 17.

On other inspected locations, no signs of corrosion were visibly, such as at 1.15% chloride, $R_P = 37$ Ohm and $\Delta R_P = 13$ Ohm, which is a formally less critical coefficient $\Delta R_P/R_P$. So this observation supports the empirical evaluation of figs 15 and 19.

All locations for dust sampling have been selected on coordinates with very negative potentials of < -500 mV vs. CSE, as fig. 21 shows. Regardless the chloride contents (from zero to 1.3%), there is no difference in the obtained potentials. However, the concrete water contents were ranging in rebar vicinity between 4.30 and 7.63%, so the concrete has been very wet.

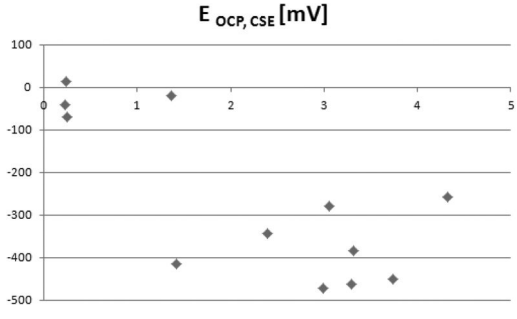

Figure 15. Open circuit potentials over the respective (free) chloride contents in rebar vicinity.

Figure 16. View on the car park after removal of the asphalt layer.

Figure 17. Appearance of the rebar at 1.29% chloride, $R_P = 41\ \Omega$, $\Delta R_P = 10\ \Omega$ – beginning pitting corrosion.

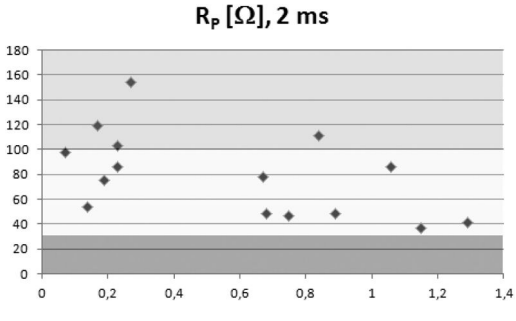

Figure 18. Total R_P values (after 60 s pulse) on sampling locations over the respective (free) chloride contents in rebar vicinity.

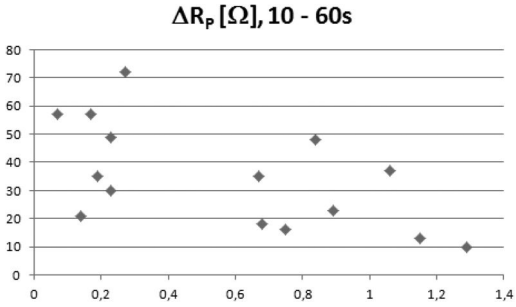

Figure 19. ΔR_P values (raise between 10 and 60 s pulse) over the respective (free) chloride contents in rebar vicinity.

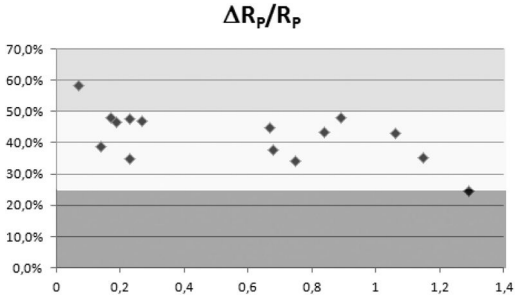

Figure 20. Percentage of ΔR_P on total R_P over the respective (free) chloride contents in rebar vicinity.

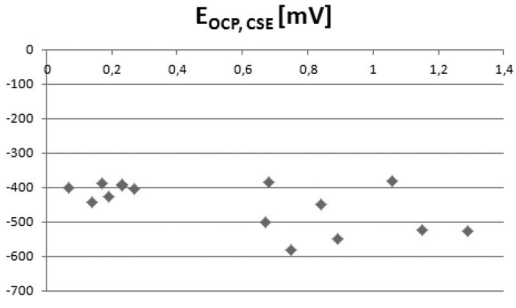

Figure 21. Open circuit potentials over the respective (free) chloride contents in rebar vicinity.

3.2.3 *Conclusions from the project*

The open circuit potentials have been much more influenced by wet concrete than by corrosion elements. This also shifted the R_B and R_P data down to rather small values, and gave principal concern of reinforcement corrosion. By considering the ΔR_P data – the increase of polarization resistance between 10 and 60 s of pulse application – it could be assumed that there is no considerable corrosion activity. The visual inspection of the reinforcement did prove this pre-evaluation.

3.3 *Imperfections*

Sometimes other than the intended polarization curves can be observed, where apparently no stable conditions have been effective during the measurements. Fig. 25 shows a drifting anodic current during the pulse application, which influences the value of the polarization accordingly and may be caused by internal control parameters of the potentiostat. Another effect is the drop of the potential curve after an initial raise, as seen in fig. 26. Very likely this has been caused by moistening water altering the conductivity of the concrete during the test and enlarging the polarized rebar surface. At the given constant anodic pulse this results in a decreasing current density. It has to be decided case by case, if those effects do still allow an evaluation or if the measurements should be repeated.

4 CONCLUSIONS

With innovative and practically applicable enhanced electrochemical measurement methods it is possible to obtain instant and very reliable information about the corrosion behaviour of the reinforcement. It is important to refer to the raw data and to check them on feasible measurement conditions. Another opportunity of evaluation is the determination of the critical, corrosion-triggering chloride threshold for an individual reinforced concrete structure/structural part. This approach could be demonstrated successfully in

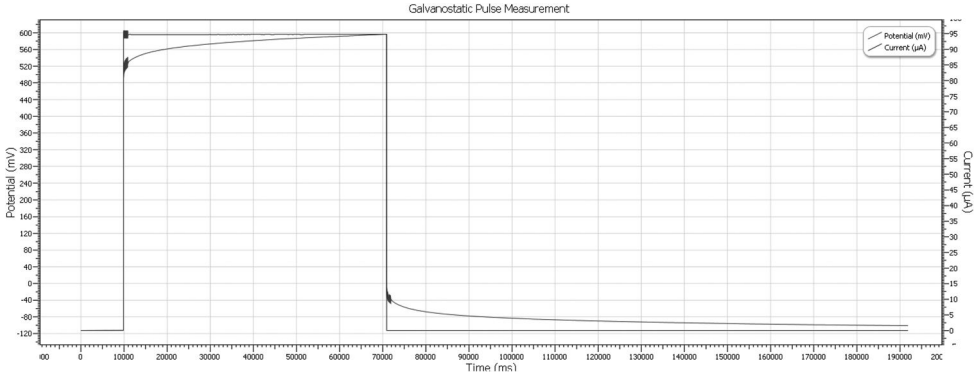

Figure 22. Development of pulse and polarization at 0.25% chloride in rebar vicinity: very high electrolyte resistance (5,848 Ω), very high polarization resistance (> 1,240 Ω), steep increase between 10 and 60 s (821 Ω) → passive behaviour.

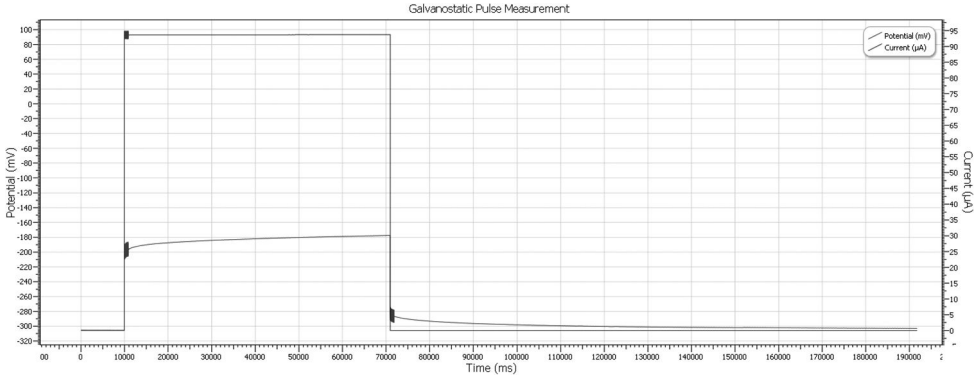

Figure 23. Development of pulse and polarization at 1.42% chloride in rebar vicinity: high electrolyte resistance (760 Ω), fairly high polarization resistance (>224 Ω), particular increase between 10 and 60 s (24 Ω) → passive behaviour.

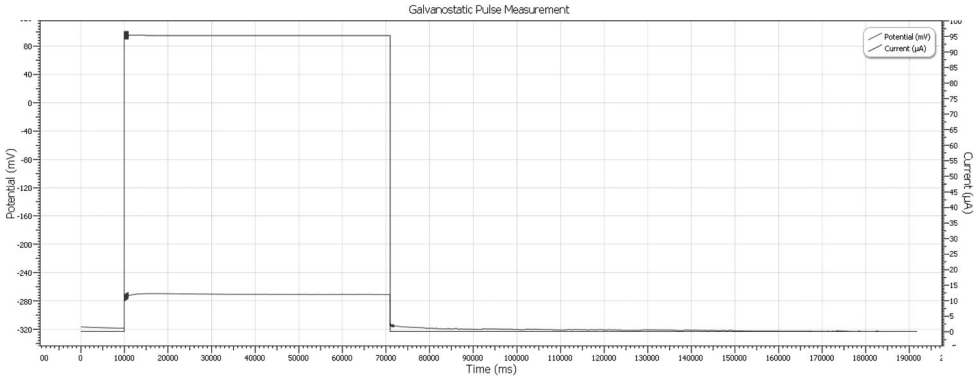

Figure 24. Development of pulse and polarization at 4.32% chloride in rebar vicinity; "normal" electrolyte resistance (440 Ω), polarization resistance in intermediate stage (68 Ω), almost no increase between 10 and 60 s (1 Ω) → active behaviour.

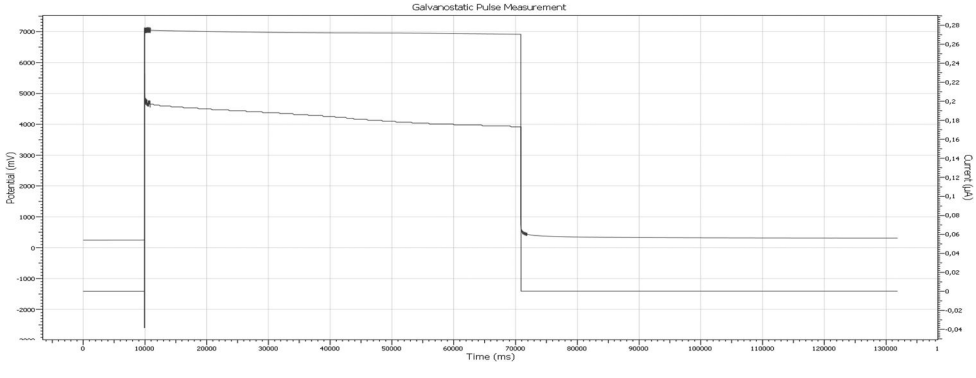

Figure 25. Dropping anodic current during polarization → uncertain evaluation of the zero polarization.

various projects and provides the following advantages:

- Corrosion suspect locations (from potential survey and/ or visual observations) can be tested on corrosion activity fast and very reliably; possible wrong interpretations of negative potentials on wet concrete cam be avoided.
- Concrete sampling locations for chloride and humidity analysis can be chosen more appropriately and at reduced total number with the knowledge of the R_P values.

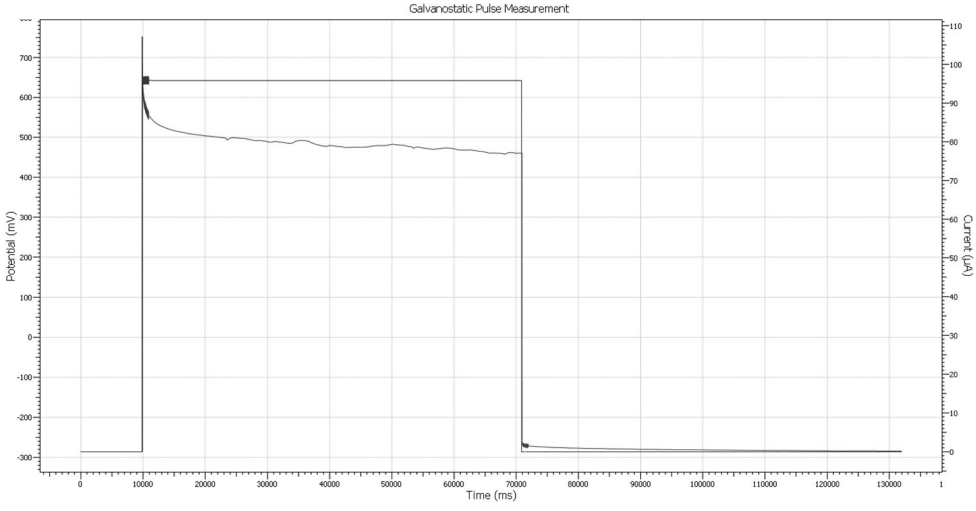

Figure 26. Dropping polarization curve at constant anodic pulse → possible increase of polarized rebar area and no useful evaluation of the galvanostatic pulse measurement.

- It is possible to conclude from the polarization curves on the intensity of the corrosion progress to be expected in areas of high chloride content.

REFERENCES

Ahlborn, K., Berthold, F., Vonau, W. Grünzig, H., Schneck, U., Jahn, H., Köhler, J. 2011. Modular Corrosion Measurement System (CMS) for electrochemical NDT. In M. Grantham, V. Mechtcherine, U. Schneck (eds.): *4th International Concrete Solutions Conference, Proc., Dresden, 2011.* Rotterdam: Balkema

Bäßler, R., Burkert, A., Frolund, T., Klinghoffer, O. 2007. Usage of portable equipment to determine the corrosion state of concrete structures. In M. Raupach, B. Elsener, R. Polder, J. Mietz (eds.): EFC-Publications Number 38 – Corrosion of reinforcement in concrete. 2007. Abington, Woodhead Publishing Ltd., 159–169

Böhni, H., Elsener, B. 1991. Früherkennung von Bewehrungskorrosion: Potentialmessung und galvanostatische Impulstechnik. In*: Symposium Zerstörungsfreie Prüfung im Bauwesen, Proc., Berlin, 1991.* Berlin: DGZFP

Schneck, U. 2007. Besonderheiten bei der Korrosionsmessung an Stahlbetonbauwerken. *Meßtechnik im Bauwesen 1 (2007), 62–66*

Schneck, U. 2011. Erweiterte elektrochemische Messungen zur objektbezogenen Beurteilung von Korrosion an Stahl- und Spannbetonbrücken. In M. Curbach, H. Opitz, S. Scheerer, T. Hampel (eds.): *6. Symposium Experimentelle Untersuchungen von Baukonstruktionen, Proc., Dresden, 2011*. Dresden: Technische Universität Dresden

Schneck, U. 2013. Nutzung erweiterter elektrochemischer Prüfungen zur Bestimmung des objektbezogenen, korrosionsauslösenden Chloridgehalts an Stahl- und Spannbetonbauwerken. In M. Curbach, H. Opitz, S. Scheerer, T. Hampel (eds.): *7. Symposium Experimentelle Untersuchungen von Baukonstruktionen, Proc., Dresden, 2013*. Dresden: Technische Universität Dresden

This page intentionally left blank

Concrete Solutions – Grantham et al. (Eds)
© 2014 Taylor & Francis Group, London, ISBN 978-1-138-02708-4

Ultrasonic non-destructive testing techniques for diagnosing concrete damage

A.A. Shah & S.-U.R. Rehman
Sarhad University of Science and Information Technology Peshawar, KPK, Pakistan

A. Naseer
University of Engineering and Technology Peshawar, KPK, Pakistan

ABSTRACT: In this research ultrasonic testing techniques of linear and nonlinear categories were applied to diagnose both initial and peak level damage in concrete. For this purpose standard cubic concrete specimens with different w/c were produced. The specimens were subjected to compression loading in several steps and ultrasonic evaluation of the test specimens at each loading step both in damaged and undamaged states was conducted. The induced concrete damages were diagnosed by analysing recorded waveform data in order to measure attenuation of the ultrasonic waveforms, harmonic generation and pulse velocity. From the test results analysis and comparison, ultrasonic attenuation and harmonic generation (non-linear ultrasonic) measurements were found more sensitive to early age cracking in concrete than pulse velocity (linear ultrasonic) measurements. The non-linear ultrasound technique has higher potential to be employed for in-situ diagnosing of damage in concrete structures.

1 INTRODUCTION

Concrete structures such as buildings, bridges, retaining walls etc. are often subjected to natural hazards or dangerous loading phenomena that lead to decreasing overall service life. Monitoring regularly the health or condition of existing/aging structures and diagnosing defects or damage, if any,are essential for assuring their safety and integrity. It is a known fact that concrete structures contain substantial nonlinearity as micro-cracks even well before reaching their maximum loading limit (Shah et al. 2013). This scenario is totally against the practice, commonly in use in developing countries, in which the integrity of a structure under stress is judged mainly by identifying major level defects. In this case, once a crack initiation has occurred near the end of the service life of a structure, it grows relatively quickly and if not controlled, leads to catastrophic failure (Shah and Ribakov 2010a). Hence, in order to ensure better performance in structures,it is essential to detect cracks at a very early stage or, even better, to detect changes in the microstructure before the crack initiation occurs (Nogueira and William 2001). For this purpose, the demand for inspection methods that can be used to perform effective non-destructive evaluation (NDE) of concrete structures is increased with the passage of time.

NDE of materials has several advantages when effectively used, as it provides early detection and warning for critical defects. Of all the variety of non-destructive inspection methods that are commercially very common in the construction industry, ultrasonic methods have been found more reliable in evaluating mechanical and environmental damage in concrete because of their relatively low cost, flexibility, and ability to reveal microscopic changes in the inspected material's structure (Tawie and Lee 2010).

However, there is a drawback of using conventional linear ultrasound methods such as pulse echo, pulse velocity etc. for flaw detection. In that case the information obtained may possess only surface properties whereas the interior properties cannot be obtained (Malhotra 1984). In addition, they can provide very little indication of the damage in concrete until it progresses to failure (Wu et al. 2000). Ultrasonic methods, considering non-linear response of concrete, allow property measurement more effectively than methods assuming linear behaviour (Chaix et al. 2003). The non-linear ultrasonic method is based on low to high-voltage ultrasonic measurements and monitors the occurrence of non-linearity in concrete at different loading stages (Shah and Ribakov 2010a).

Non-linear ultrasonic measurements often use the phenomenon of harmonic generation. It results from the non-linear interaction between the ultrasonic wave and the material (Shah and Ribakov 2010b). It is thus essential to use a non-linear ultrasonic test for effective assessment of a material's degradation when the damage in concrete appears under initial level of load applied.

It is also known that the decrease in the pulse amplitude (ultrasonic pulse attenuation) and shifts in the

peak frequency (harmonic generation) are more sensitive and more reliable measures to characterize distributed damage and diffuse cracking in the concrete than pulse velocity (Suaris and Fernando 1987). Ultrasonic longitudinal pulses were used to evaluate damage on concrete due to freeze–thaw cycles and salt scaling (Selleck et al. 1998). Changes in the pulse velocity, peak-to-peak attenuation and peak frequency were studied. It was observed that peak-to-peak amplitude and peak frequency were more sensitive to concrete damage induced by freeze–thaw cycles and salt scaling than pulse velocity. Both peak-to-peak amplitude and peak frequency, however, showed a large scatter during the experiments. Additionally, non-linear ultrasonic signals were used in order to detect concrete damage (Shah et al. 2009).

This research attempts to estimate the attenuation changes and harmonic generation in concrete using low to very high power input signals. Concrete specimens with different w/c ratios were evaluated by non-linear ultrasonic test method both in damaged and undamaged conditions. Frequency and normalized spectra of the received waveforms are obtained for different power and loading levels. It is demonstrated that attenuation and harmonic generation measurements are sensitive to change in power levels for a given frequency and damage level.

2 AIMS AND OBJECTIVES

This study is aimed at comparing the efficiencies of linear ultrasound (pulse velocity) and non-linear ultrasound techniques in the presence of compression induced damages in concrete. Using linear ultrasound techniques, concrete damage is assessed by measuring the changes in ultrasonic pulse velocity with increasing damage and output power level. Similarly, for non-linear ultrasound techniques, damage is evaluated by measuring changes in fundamental amplitude and generation of harmonic wave components for given damage and power levels. For this purpose, pulse velocity and nonlinear ultrasound measurements at different loading and power levels on cubic concrete specimens in damaged and undamaged states were performed. The influence of various w/c ratios on the changes in pulse velocity, signal attenuation and higher harmonic generation was also studied. Additionally, the non-linear ultrasound technique was examined to be applied as a measure of damage growth in concrete.

Non-linear ultrasonic with application of wave attenuation has earlier been used and the results obtained were compared with acoustic emission technique (Shah and Ribakov 2010b). In the present study harmonic generation of frequency components was additionally considered, as it can also provide information about occurrence of non-linearity in the damaged specimens both at initial and peak levels. Besides these calculations, pulse velocity measurements were separately made at each loading and power level. Since pulse velocity is an efficient linear ultrasound testing method, it was important to check its performance

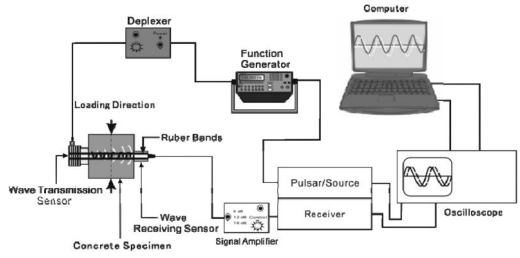

Figure 1. Ultrasonic test setup.

in detecting damage against wave attenuation and harmonic generation based non-linear ultrasonic. All these results are compared to evaluate sensitivity of non-linear ultrasound testing in detecting defects or damage relative to the pulse velocity based linear ultrasound method.

The outcomes of this research will allow easy understanding of concrete specimens' behaviour under axial compression loading. Damage of concrete in real structures could be readily estimated from wave attenuation and harmonic generation measurements without knowing the original state of the concrete at construction. Therefore the obtained results are expected to be very useful for proper structural health monitoring, allowing selection of the most suitable repair or rehabilitation activities.

3 TEST SETUP

The test setup used for linear or non-linear ultrasonic non-destructive evaluation is shown in Fig. 1. The entire test setup consists of a diplexer, a high power tone burst pulser, a broadband receiver, two piezoelectric broadband transducers (for pulse transmission and receiving), a function generator, a signal amplifier, a PC, and an oscilloscope.

To study the influence of w/c ratio 45 concrete cube specimens (150mm in size) were prepared with w/c of 0.40, 0.50, and 0.60 (15 specimens for each w/c ratio). Each specimen was loaded to failure under compression in various steps while the ultrasonic evaluation was performed simultaneously with the load application using five different output power levels. The wave attenuation and harmonic generation values were measured throughout the course of the test for non-linear damage evaluation, and pulse velocity was recorded for linear damage assessment. The non-linear ultrasonic measurements were then compared with the linear ones.

Fig. 2 illustrates time and frequency domain wave plots obtained by generating a 100 kHz frequency tone burst signal with six cycles.

4 TEST RESULTS AND DISCUSSION

The waveform data was analysed and plotted for each damage and output power level. The arrival time

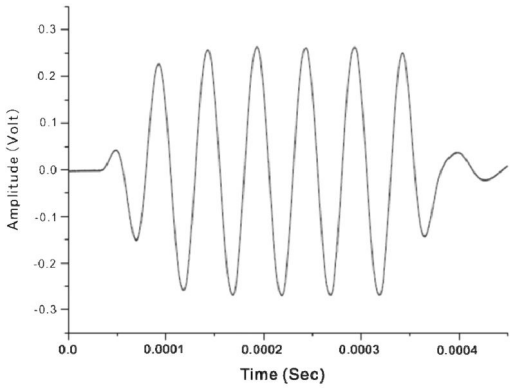

(a)

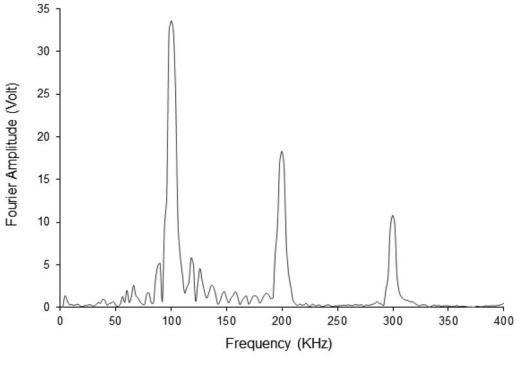

(b)

Figure 2. Typical six-cycle wave-plots (a) time domain (b) frequency domain.

and amplitude values were taken from the waveform graphs to measure the wave attenuation, harmonics generation, and pulse velocity.Fig. 3 shows the changes in fundamental amplitude (wave attenuation) for all frequency and power levels used for the specimens with w/c of 0.40, 0.50, and 0.60. The mean values of three tests with the best possible results as damage changes were plotted for comparison.

It is evident from the figure that fundamental amplitude smoothly decreases from the base line as damage increases. For damage level of 80% approximate reduction in amplitude of the waveform from the undamaged state, calculated for the specimens with w/c of 0.40, 0.50, and 0.60, were 35, 49, and 67% respectively (see Fig. 3). In addition, it can be seen in the figure that as damage progressed, the specimen with a w/c of 0.40 experienced a smaller loss in fundamental amplitude than the specimens with w/c of both 0.50 and 0.60. This illustrates that change in attenuation increases as w/c increases and vice versa.

Fig. 4 shows the changes in higher harmonic magnitude for all power and frequency levels used for the specimens with w/c of 0.40, 0.50, and 0.60 respectively.

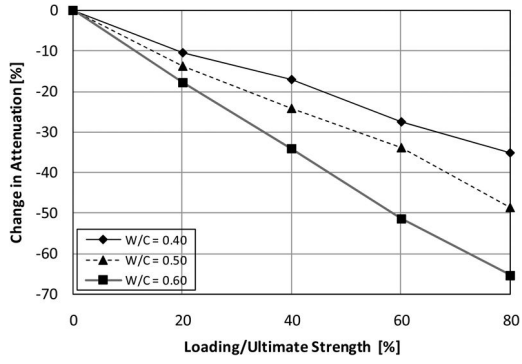

Figure 3. Average percent change in attenuation for all frequency and power levels.

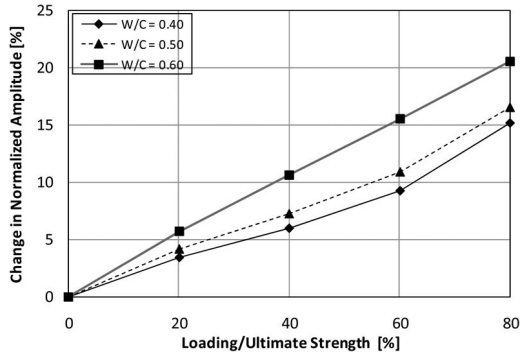

Figure 4. Average percent change in normalized amplitude for all frequency and power levels.

The trend is that harmonic generation increases as damage level increases. It was observed that at peak damage level, the generation of harmonic wave components for w/c of 0.40 increased from the undamaged state to the damaged state by about 15%.A similar tendency of increase in harmonic generation with respect to increasing damage wasevident for specimens with w/c of 0.50 and 0.60.

At the damage level of 80%, the normalized harmonic amplitude from the undamaged state for both w/c of 0.50 and 0.60 was increased by about 17, and 21% respectively. The figure demonstrates that as damage increased, the specimens with a w/c of 0.60 exhibited greater values of harmonic generation at all damage levels than the specimens with w/c of both 0.40 and 0.50. Following the experimental data, the non-linear ultrasonic effect, based on the phenomenon of higher harmonic generation, appeared greater in weaker concrete.

The ultrasonic pulse velocities for the same test specimens were additionally measured in order to investigate whether the traditional linear ultrasonic testing parameter had some correlation with damage progress. The pulse velocities were monitored during uni-axial compression testing of the concrete specimens in a direction perpendicular to the axis of loading. They were calculated by dividing the

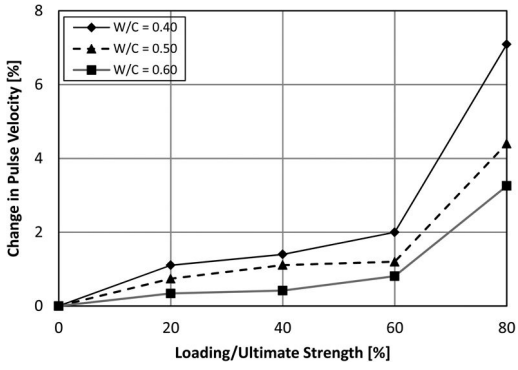

Figure 5. Average percent change in pulse velocity values for all power levels.

wave propagation distance by the arrival time of the ultrasonic signal.

Fig. 5 shows the pulse velocity values with change in damage level. The average values of three specimens for all power levels with w/c of 0.40, 0.50, and 0.60 respectively, were plotted. It was expected that the longitudinal cracks that developed under uni-axial compression would decrease the lateral pulse velocity significantly. However, it was evident that none of the case showed remarkable change in pulse velocity until about 60% of the peak compressive strength was reached.

Comparison of these results with those plotted using non-linear ultrasonic testing, reveals that the changes in attenuation and harmonic generation as the levels of damage and power changed were larger than those measured by the pulse velocity method.In general, this trend holds true regardless of damage level or w/c for the specimens tested. This observation shows that non-linear ultrasonic testing method is more sensitive to early damage diagnosing than standard linear ultrasonic testing, such as pulse velocity.Additionally, sensitivity of the non-linear ultrasonic testing method generally increased with increasing w/c.

5 CONCLUSIONS

In this study the performance comparison of linear and non-linear ultrasonic evaluation of concrete with distributed damage was investigated. Attenuation and harmonic generation were found quite sensitive to different damage levels. They were increased significantly as distributed damage increased. Additionally, for low w/c concrete smaller changes in attenuation and harmonic generation were observed than for high w/c concrete.

The sensitivity of a non-linear ultrasound method using wave attenuation and harmonic generation to detect early damage in concrete exceeded that of the standard linear ultrasonic testing method such as pulse velocity for all damage levels. Additionally, sensitivity of the non-linear ultrasonic testing method was influenced by the change in w/c. Pulse velocity measurements were observed sensitive to damage only when damage level exceeded 60% of the ultimate strength of the concrete.

The non-linear ultrasound technique has higher potential to be employed for in-situ diagnosis of damage in concrete structures.

REFERENCES

Chaix, J. F., Garnier, V. and Corneloup G. 2003. Concrete damage evolution analysis by backscattered ultrasonic waves. *NDT & E International* 36(7): 461–469.

Malhotra, V. M. 1984. In-Situ non-destructive testing of concrete-A Global Review. *American Institute of Concrete*, Detroit, SP-82: 1–16.

Nogueira, C. L. and William, K. J. 2001. Ultrasonic testing of damage in concrete under uni-axial compression. *ACI Materials Journal* 98(3): 265–275.

Selleck, S. F., Landis, E. N., Peterson, M. L., Shah, S. P. and Achenbach, J. G. 1998. Ultrasonic investigation of concrete with distributed damage. *ACI Mater J*. 95(1): 27–36.

Shah, A. A., Ribakov, Y. and Zhang, Ch. 2013. Efficiency and sensitivity of linear and non-linear ultrasonics to identifying micro and macro scale defects in concrete. *Materials and Design* 30(3): 775–82.

Shah, A. A. and Ribakov, Y. 2010a. Non-linear ultrasonic evaluation of damaged concrete based on higher order harmonic generation. *Materials and Design* 30(10): 4095–4102.

Shah, A. A. and Ribakov, Y. 2010b. Effectiveness of nonlinear ultrasonic and acoustic emission evaluation of concrete with distributed damages. *Materials and Design* 31(8): 3777–3784.

Shah, A. A., Ribakov, Y. and Hirose, S. 2009. Non-destructive evaluation of damaged concrete using non-linear ultrasonics. *Materials and Design* 30(3): 775–82.

Suaris, W. and Fernando, V. 1987. Ultrasonic pulse attenuation as a measure of damage growth during cyclic loading of concrete. *ACI Mater J*. 84(3): 185–93.

Tawie, R. and Lee, H. K. 2010. Piezoelectric-based non-destructive monitoring of hydration of reinforced concrete as an indicator of bond development at the steel–concrete interface. *Cement and Concrete Research* 40(12): 1697–1703.

Wu, T. T., Tong, J. H. and Lin, P. L. 2000. Measurements of in situ wave velocities of concrete using transient elastic waves. *Review of Progress in Quantitative Nondestructive Evaluation*: 1693–700.

Concrete Solutions – Grantham et al. (Eds)
© 2014 Taylor & Francis Group, London, ISBN 978-1-138-02708-4

Suitability of embedded RFID-sensors for concrete bridge structures

M. Stoppel
Federal Institute for Materials Research and Testing (BAM), Berlin, Germany

A. Fakhouri
Federal Highway Research Institute (BASt), Bergisch Gladbach, Germany

ABSTRACT: RFID (radio-frequency identification) is the wireless non-contact use of radio-frequency electromagnetic fields to transfer data for automatically identifying and tracking tags attached to objects and is well developed and known in commercial use. This technology has promise to be used within a monitoring system enabling a condition assessment for concrete bridge structures. The aim of the presented project, which was funded and supervised by the German Federal Highway Research Institute (BASt), was to investigate modular RFID-based sensor systems with respect to their basic suitability for the use in concrete (bridge) structures. The selected RFID tags have a sensor interface to be connected to sensors with low power consumption. The measured values of the embedded sensors can then be read wirelessly. After a literature and product research, the project focused on basic investigations, such as

- the selection of suitable sensors for humidity, temperature and corrosion activity,
- the application of the sensors to reinforced concrete structures and
- the determination of the maximum distance (cover), at which an RFID sensor tag can still be discovered and delivers correct data.

For this purpose, prototypes or RFID sensor tags were developed, assembled, encapsulated and embedded in concrete specimen. Measurements in climate chambers were carried out and showed useful results. The range measurement has shown that an effective range of up to 170 mm is reachable with the developed RFID UHF system in the undisturbed case. In addition, the developed RFID sensors were successfully embedded in a reinforced concrete slab with properties of a typical bridge superstructure. The laboratory experiments have confirmed the basic functional efficiency and reliability of the developed sensor system. Since the demand for embedded sensors in civil engineering is increasing, other measuring principles as a supplement to or a combination with the developed system are being investigated.

1 INTRODUCTION

Infrastructure is subject to continuous ageing. This has given life cycle management of infrastructure an important role. Therefore, an increasing demand for reliable inspection and monitoring tools is noticeable. The prediction of the service life of a new structure at the design stage or the diagnosis and the evaluation of the residual service life of existing structures is a key aspect of concrete structure management. Life-cycle analysis and risk evaluation methods can be beneficially used to assess existing structures: actions on structures, inspection-oriented design and construction, characteristics of components and structures, life-cycle costs, risk analysis and the environmental performance of a structure over its lifespan are important factors which have to be considered when the remaining service life of an infrastructure building is in question. An important pre-requisite for reliable assessment is the possibility of efficient inspections during construction, operation and maintenance, during the design phase.

Assessment of the safety of engineering works must be conducted by examining all aspects of their behavior and all possibilities for failure which can be manifested. Analyzing potential critical situations of structures in Europe is performed by identifying so-called limit states [Diamantidis, D., 2001]. A limit state is defined as a condition beyond which a structure is no longer able to satisfy the provisions for which it was designed. However, it has to be distinguished between ultimate and serviceability limit states. Primarily, the reactive maintenance approach has been implemented in Europe to manage the road infrastructure network with respect to deterioration. This approach may be valid for well-managed structures without deficits and exposition to unchanging loads. However, this approach is unsatisfactory to structures containing structural deficits and subjected to increasing loads, modifications or widening measures for

which they are not designed. Therefore, a paradigm change from reactive to proactive infrastructure management is required and non-destructive inspection methods play a key role here.

A reliable prognosis of the condition and behavior of a structure is an important basis for effective ser-vice life management. In order to determine the most economical point in time for repair measures in the life-time of a structure, a knowledge about the deterioration process at exposed regions as well as a detailed knowledge about the current condition of the whole structure is essential [Kurz, J. H. & Stoppel, M., 2009]. A combination of different non-destructive test methods is often necessary to receive reliable results for material characterization. Different concepts were developed depending on the type of infrastructure and the construction material. However, in general cracks and flaws, corrosion information, as well as the states of material degradation have to be retrieved. A combination of different non-destructive test methods is often necessary to receive reliable results for material characterization, flaw detection and the determination of component specific geometry parameters.

Embedded Sensors are meeting the demands for gathering more information from the inside of a structure. Wired Sensors are meanwhile well established but may have disadvantages in case of a subsequent installation in existing structures, due to cable installation or need for power supply.

Wireless sensors which can be embedded in concrete provide an attractive alternative solution. This paper summarizes the activities of a research project which dealt with the suitability of RFID sensor tags for concrete bridge structures.

2 EMBEDDED WIRELESS SENSORS

2.1 *Literature research*

A literature review and web research was carried out to determine the state of the art and state of research in the field of embedded RFID-based sensors.

2.1.1 *RFID components and manufacturers*

The vast majority of RFID manufacturers or suppliers develop or distribute RFID components that are used in logistics or in trade. Because of the huge demand, RFID electronics are very inexpensive. Active or passive sensors in RFID tags are a niche product that only few manufacturers have in their portfolio. Nevertheless, even in these areas there are sensor applications e.g. to monitor the temperature or humidity profile in the transport of sensitive goods (mainly food and medical devices).

2.1.2 *Research projects*

Most of the identified research projects related to RFID in construction report on the development and testing of RFID tags and their (mostly) successful use of the technique when embedded in building materials. However, in most cases, these developments are limited to a successful data transmission between RFID tag and reader (e.g. [Iowa State University, 2013], [Yi, X. et al. 2010]). The sensor or the evaluation of the measurement data collected plays a rather minor role in the reports. But it may also be that many approaches of data collecting are based on the principle of weakening of the transmission power and use the signal strength as a measurement variable [Ruhanen, A. et al. 2008], [Materer, N. 2011], [Watters, D, 2003].

In addition to RFID technology, the borders to other wireless technologies are fluent. Wi-Fi, Zigbee and other data communication protocols may also be applied to sensor systems [Liu, H. et al. 2008]. Here, larger transmission ranges and continuous measurements are possible because these components can be combined to form sensor nodes. A coupling for RFID systems may increase the possibilities here. These active tags are inapplicable for embedding in concrete due to their built-in battery and thus limited service lifetime.

Owing to these results, we decided to have a very different approach with our own sensors (section 3).

2.1.3 *System providers of RFID technology for construction trade*

The number of manufacturers that offer turnkey wireless sensor systems for installation in concrete structures is very limited. In Germany, only one manufacturer is known.

The company, BS2, provides a turnkey "early warning system of moisture in concrete". The sensor is likely based on a conductivity measurement with the indication of "normal" or "deviant," it does not provide quantitative information about the moisture content of concrete.

Another sensor tag of the company BS2 is used for corrosion detection. As shown in Figure 1, the sensor is fixed above the reinforcement rebars and detects the progression of a “corrosion Front” by means of two “sacrificial” wires which are no longer present if they are corroded completely; an actual corrosion of the reinforcement is not displayed.

In both types of sensors, passive RFID systems are used and the data acquisition is carried out through comparing the changes in signal strengths of the measurement tags in a sensor module in comparison to the reference tag.

2.2 *Suitable sensors*

For embedding in concrete, only those sensors come into consideration, which consume a very low power supply and observe the input voltage range of the selected RFID sensor tag. The input can be switched between the internal temperature sensor and an external sensor.

Within this research project it was decided to examine two sensor types in detail: A humidity sensor to determine the moisture content of the concrete in a

Figure 1. BS2 RFID corrosion Sensor tag [Website BS2, 2013].

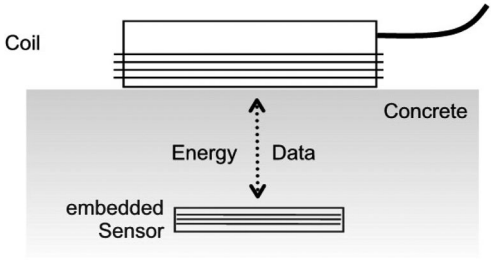

Figure 2. Scheme of the interaction between reader coil and embedded sensor in concrete.

cavity and a wire-shaped electrode along a reinforcing rebar to measures potentials caused by corrosion activity.

Therefore, several types of humidity sensors were tested and a special adaption circuit for the electrode wire was designed.

3 BAM RFID SENSOR TAG

3.1 *Design*

An RFID system consists of a transponder (so-called RFID tag) that is located on or in the object, and includes an identifying code and a reader for reading this code. The coupling is done by short-range high frequency radio waves. Not only can data be transferred, but also the transponder can be energized (Figure 2).

The transmitted power during the communication process is used as a power supply for the tag and for an optional sensor. In case of active tags, power is supplied by a built-in battery. In semi-active tags, the battery takes over only the supply of microchips.

For long-term installation in concrete structures, only passive tags come into consideration. It must also be ensured that the energy transferred is sufficient not only for the data transmission but also for the integrated signal processing and the associated sensors.

Currently, only two suppliers of RFID components offering solutions for the integration of sensors are known. Figure 3 shows the sensor tags integrated in signal processing units which were designed at BAM.

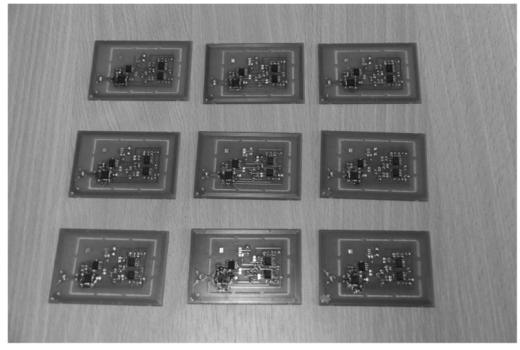

Figure 3. RFID sensor tags with signal processing designed at BAM.

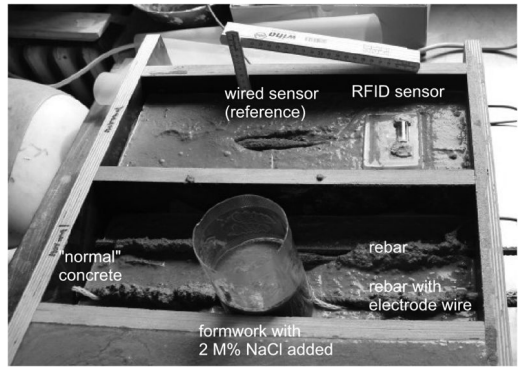

Figure 4. Concreting of small specimens with BAM RFID sensor tags.

After basic tests concerning the communication between the RFID tags and the reader device, a program for automatic data storage was designed. In addition to the stored measurement values, other parameters like signal strength are stored as well. These were used e.g. to determine the allowed maximum distance between transmitter and RFID tag.

The next step was to choose the right coating for sealing the RFID tags to enable embedding into concrete.

3.2 *Specimens*

For the first test, three small specimens were designed and tested in climate chambers. For long term tests, a reinforced concrete demonstrator plate with a bridge cap section and a pavement section was constructed.

3.2.1 *Small specimens*

The small specimens (Figure 4) were designed to test different sensor types and their behavior in concrete. Directly after concreting, a continuous collecting of data was carried out to monitor the curing process. After 30 days, the specimens were stored in a climate

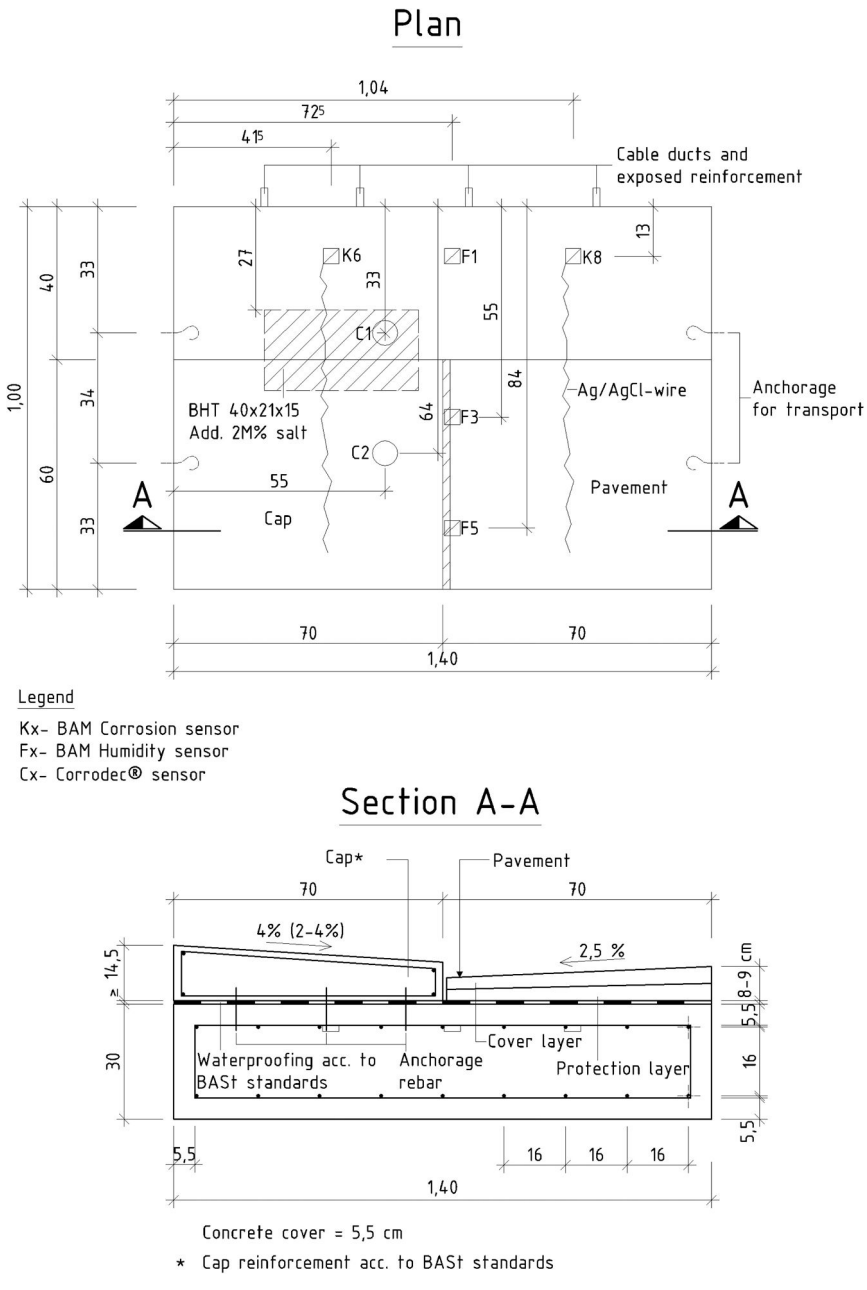

Figure 5. Design of demonstrator plate.

chamber with periodic cycles of temperature and humidity concentrations.

One of the specimens was equipped with an RFID sensor in addition to a wired sensor as a reference for moisture measurements. The other specimen was equipped with two rebars. One of them was wrapped with the electrode wire and salted concrete was added wet in wet while the making process (the formwork was pulled after one hour).

3.2.2 *Demonstrator plate with bridge cap*

The demonstrator plate (Figure 5 and Figure 6) had dimensions $1.4 \times 1.0 \times 0.3$ [m] and included embedded RFID-based humidity, corrosion and temperature sensors of the BAM type as well as two sensors of a commercially available system which indicate corrosion and moisture. At the top of the reinforced concrete plate, a pavement section according to the ZTV-ING specifications of the BASt [4] and a section of a

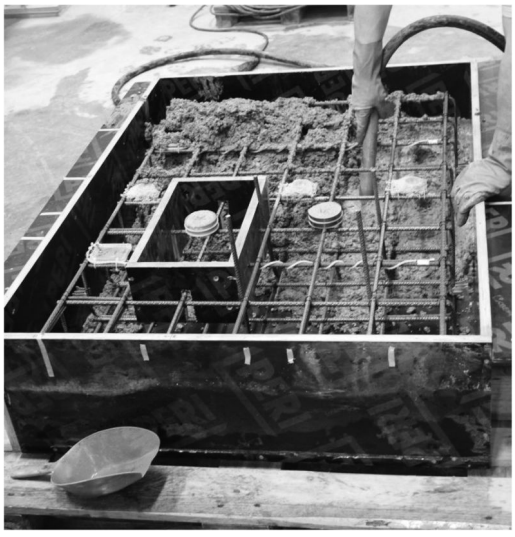

Figure 6. Concreting of demonstrator plate incl. RFID sensors.

standard bridge cap were added. This was to simulate a typical bridge superstructure and enable investigations of the reachable signal strengths in joint areas in a typical concrete bridge. As part of the standardized pavement system, a stainless-steel-coated strengthening strip has to be placed in joint areas between the bottoms of the cap construction and the asphalt pavement. The influence of this additional layer on the readings needed to be investigate.

3.3 *Measurement and results*

As an example, Figure 7 shows the results of the monitoring of a sensor tag in the demonstrator plate during the hardening process.

At the beginning, temperature and humidity increased as expected. After a few days, the values stabilized. The initial humidity values exceeded 100% because the sensor was saturated. After one week, the plate was installed in a climate chamber at a temperature of 50°C. The sensor temperature increased again with an expected delay, the values of the humidity sensor began to normalize and "move" toward realistic values.

The RFID sensor with the electrode wire – wrapped around one rebar section where salt was added to the concrete to initiate the corrosion process – showed potential values lower than 200 mV during the whole monitoring period. This means no active corrosion has occurred jet. Further investigations after moisten the demonstrator plate to initiate corrosion activities will be carried out; therefore they can not be presented jet. However figure 8 shows the results of a small specimen. 72 hours after moisten the surface area the potentials are decreasing to values smaller than −300 mV, which is high probability for corrosion activity.

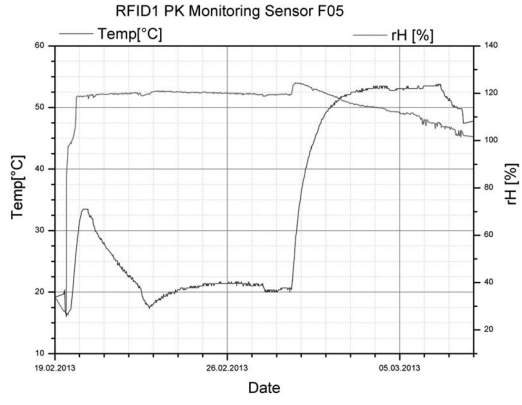

Figure 7. Monitoring values during hardening process of the demonstrator plate.

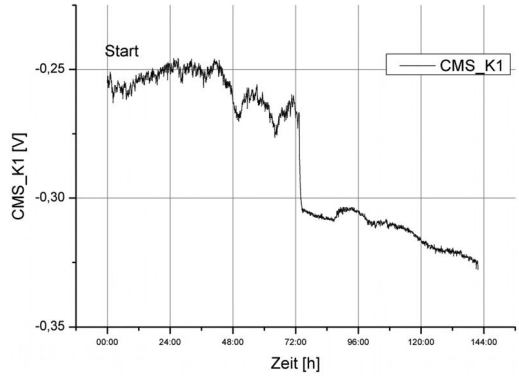

Figure 8. Monitoring RFID sensor with electrode wire (CMS) after moisten the surface of small specimen.

As a criterion for determining the maximum achievable working range the reference voltage for the measuring electronics, which is generated by the transmitter, was used. The range for reading the RFID-tag ID is much bigger, but for the use of sensors a stable reference has to be assured in order to achieve correct measurement values. As a result 17 cm distance are possible with the used equipment, without disturbances of surrounding rebars.

The analysis of all tests showed results with good reliability in general and confirmed the basic applicability of the developed wireless sensor system for concrete structures. Although the sensors give no information on absolute moisture content of the concrete or only presumptions of corrosion activities they represent the possibility of gathering data from the inside of the concrete wirelessly.

4 CONCLUSIONS AND OUTLOOK

This paper reports on the successful development of RFID sensor tags combined with two different types of sensors for humidity and corrosion measurement.

As a result of a currently completed research project, the basic operational capability of RFID-based sensor systems for concrete structures could be demonstrated.

The range measurement has shown that an effective range of up to 170 mm with the developed RFID system (UHF) is possible in the undisturbed case. A reduction by adjacent reinforcing steel or pavement joint strips may result due to an unfavorable positioning of the sensor tags to a reduction in range or even a complete blocking of the signals. The range may not be the maximum distance at which data communication is still possible to define, but must be determined from a (still) stable voltage reference for the sensor to avoid incorrect measurements. Here, the measured signal strength is used as a quality criterion. Thanks to the modular design of the sensor tags, it is possible to separate the sensor and antenna from each other, enabling a placement of the sensor deeper inside a structural component and to allow the reading process at/near the surface.

The results of the laboratory experiments have confirmed the quality of operation and capability of the selected sensors for humidity measurement and indication of active corrosion. A quantitative assessment of the correlation of the measured air humidity with the moisture content by means of the sorption isotherm could not be carried out within this project. A relevant study will be considered in future work. The robustness against direct water contact of the sensor during the concreting should be optimized. Other types of sensors, that are less sensitive to direct contact with water and high humidity but at the same time fulfill the low power requirements, are currently unknown. The electrode used as a sensor for corrosion activity has also proven to be compatible with the RFID system and its operation could be verified. The advantage of this sensor over measurement concepts involving corrosion reference wires is that the corrosion activity along the rebars themselves can be detected.

In numerous publications regarding RFID technology in civil engineering (e.g. [Luna Innovations, 2007], [Dauberschmidt, C. & Sodeikat, Ch., 2008], [Mohammad, I. et al. 2011], [Allianz Bau of Fraunhofer Society, 2011], [Iowa State University, 2013]), the importance and the future growing demand for embedded sensor systems in civil engineering are underlined. In this context, other measurement principles as a supplement or combination are feasible for a further development of the presented system. These include e.g. humidity sensors based on the measurement of material conductivity or corrosion sensors that can map the depth-dependent rate of corrosion based on electrode conductors.

In the design of the demonstrator plate, the findings of the preliminary tests have been considered. The sensors embedded in the demonstrator plate, which is a property of the Federal Highway Research Institute, will be subject to further long-term investigations.

ACKNOWLEDGEMENTS

The presented research project was funded and supervised by the German Federal Highway Research Institute (BASt) and carried out at the Federal Institute for Materials Research and Testing (BAM).

REFERENCES

Allianz Bau of Fraunhofer Society, 2011: Sensor-Transponder (RFID) für die Druck- und Temperaturüberwachung in Vakuum-Isolations-Paneelen (VIP) – Stand und Ausblick, 2011(in German).

Andrade, C. et al.: Non contacting corrosion method applied to the steel corrosion rate determination in different solutions an reinforced concrete specimens, NACE Corrosion, 2010.

Dauberschmidt, C. & Sodeikat, Ch., 2008: Innovative Zustandserfassung durch Korrosionsmonitoring und Ultraschallmessungen. In: Tiefbau; Heft 4/2008; Hrsg.: BG Bau - Baugenossenschaft der Bauwirtschaft; Erich Schmidt Verlag GmbH & Co; Berlin, 2008 (in German).

Diamantidis, D., 2001: Probabilistic Assessment of Existing Structures. RILEM Publications S.A.R.L

Iowa State University, 2013 Final Report "RFID Tags for detecting concrete degradation in bridge decks".

Kurz, J. H. & Stoppel, M., 2009: Control and Data Acquisition of Automated Multi-Sensor Systems in Civil Engineering. Proceedings of Non-Destructive Testing in Civil Engineering, NDT-CE, Paris, Laboratoire Central des Ponts et Chaussées (LCPC).

Lee, S.: Development of corrosion sensors for monitoring steel-corroding agents in reinforced concrete structures, Materials and Corrosion, 2003.

Liu, H. et al. 2008: Integration of RFID and Wireless Sensor Networks, University of Ottawa, Canada.

Luna Innovations, 2007, Presentation of Corrosion Sensor Development for Military Applications.

Materer, N. 2011: Passive, wireless corrosion sensors for transportation infrastructure, Oklahoma Transportation Center.

Mohammad, I. et al. 2011: Embedded Sensor for Detecting Corrosion of Reinforcement in Concrete, Advanced Materials Research Vols. 250–253 (2011) pp 1118–1123.

Ruhanen, A. et al. 2008.: Project report "BRIDGE: Sensor-enabled TFID tag handbook", European Commission contract No: IST-2005-033456.

Watters, D, 2003: SMART PEBBLES: Passive Embeddable Wireless Sensors for Chloride Ingress Monitoring in Bridge Decks, SRI Report No. 11071.

Website BS2, 2013 www.bs2-sicherheitssysteme.de, last access: October 2013

Yi, X. et al. 2010: Passive Wireless Smart-Skin Sensor using RFID-Based Folded Patch Antennas, Georgia Institute of Technology.

Concrete Solutions – Grantham et al. (Eds)
© 2014 Taylor & Francis Group, London, ISBN 978-1-138-02708-4

Detection of chloride and carbonation induced corrosion in reinforced concrete structures using piezo sensors via electro-mechanical impedance technique

T. Visalakshi
Department of Civil Engineering, Galgotia's University, Greater Noida, India

S. Bhalla & A. Gupta
Department of Civil Engineering, IIT Delhi, India

ABSTRACT: Rebar corrosion in Reinforced Concrete (RC) structures is recognized as the predominant factor that reduces the service life of RC structures exposed to aggressive environments. The two main causes of reinforcement corrosion are chloride attack and carbonation. These two mechanisms are unusual in that they do not attack the integrity of the concrete. Instead, they ingress through the pores and reduce the alkalinity or disrupt the passive oxide layer leading to corrosion. This paper presents a new technique to detect and quantify corrosion using piezo sensors via an electro-mechanical impedance technique.

1 INTRODUCTION

Steel is principally used as the reinforcing material in concrete as it is the time proven match for reinforced concrete (RC) structures, but the main problem with it is the occurrence of corrosion. Interest of the scientific community in corrosion problem has been increasing for several years because the wastage of precious metal, apart from endangering the structural performance and inducing failure. It is one of the main causes of damage and premature failure of RC structures, inflicting enormous costs for inspection, maintenance, restoration and replacement of the infrastructure worldwide. Rebar corrosion is generally accompanied by the loss of rebar cross-section and accumulation of corrosion products, which occupy much larger volume than the original steel (Broomfield, 2007), thereby generating tensile stresses which lead to cracking and spalling of concrete, commonly known as concrete cancer (Dehwah et al. 2002). This paper presents a new approach for assessment of corrosion in rebars, using piezo sensors via the electro-mechanical impedance (EMI) technique.

2 CORROSION IN RC STRUCTURES

Concrete normally provides a high degree of protection to the embedded steel reinforcement against corrosion by virtue of its high alkaline nature. But the chloride and carbonation penetration through the pores of concrete breaks down the passive film developed due to alkaline nature leading to corrosion. The main corrosive agents i.e. chlorides, can ingress from several sources, they can be cast into the concrete or they can diffuse in from the outside. While the carbon dioxide can ingress from the atmosphere.The chemical reactions are same for both types of corrosion as illustrated in Fig. 1. It may be noted that water and oxygen are needed at the cathode for corrosion to occur.

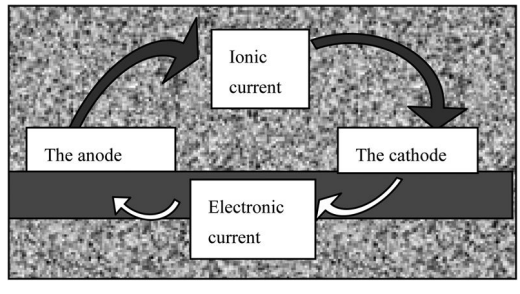

Figure 1. The anodic and cathodic reactions for corroding steel.

3 EMI TECHNIQUE USING PIEZO SENSORS

The recent developments in the area of smart materials and systems have ushered new openings for structural health monitoring (SHM) and nondestructive evaluation (NDE). Smart materials, such as the piezo-ceramics (PZT), and the fibre-optic materials can facilitate the development of non-obtrusive miniaturized systems with higher resolution and faster response. These smart materials possess immense

capabilities of damage diagnosis because of their inherent stimulus-response and energy transduction capabilities. The piezoelectric materials are categorized as 'smart' materials because of the 'stimulus-response' behaviour exhibited by them with reference to mechanical and electrical domains. When subjected to mechanical stresses, a piezo patch develops surface charges, known as the 'direct effect'. Conversely, when subjected to an electric field, it undergoes mechanical strain, which is called the 'converse effect'.

Recently through the measurement of parameters relating to the corrosion reaction of reinforcement, some corrosion sensors using optical fibers and piezo ceramics were investigated for corrosion assessment in RC structures. Gao et al. (2011) developed a fiber optic corrosion sensor comprising of one fiber bragg grating (FBG) sensor, twin steel rebar elements and some protectors to detect rebar corrosion. Fuhr and Huston (1998) presented a multiple-parameter sensing fiber optic sensors which may be embedded into roadway and bridge structures to provide an internal measurement and assessment of its health. Lalande et al. (1996) used the EMI technique to detect abrasive wear (a type of corrosion) in complex precision parts like those found in gear sets. Simmers (2005) reported the application of the EMI technique to detect corrosion induced damage in plates and beams. Thomas and Welter (2004) used "Lamb" waves to detect material loss through corrosion in thin plates representative of aircraft skins using piezoelectric wafer sensors in pitch-patch configurations. Park et al. (2007) employed the EMI technique using a miniaturized impedance measuring chip and a self-sensing macro fiber composite (MFC) patch to detect and quantify corrosion in aluminum structures. Park and Park (2010) conducted an experimental study involving wireless monitoring of corrosion damage in metallic structures. Bedekar et al. (2008) noted a systematic variation in the conductance of the PZT patch as corrosion progressed in aluminum specimen. Yang et al. (2013) conducted experimental study to monitor the local corrosion of a steel beam using the EMI technique and found that a quantitative relationship exists between the damage index and corrosion time, which can be used as a reference to the subsequent local corrosion monitoring.

The EMI technique is essentially a vibration based technique operating in the frequency range of 30–400 kHz excited by an impedance analyzer/LCR meter. Under external field excitation, the bonded patch induces deformations in the host structure (converse effect), whose response is transferred back to the patch (direct effect) in the form of admittance signature, consisting of conductance (the real part) and susceptance (the imaginary part). Any damage to the host structure affects the structural parameters, which in turn leads to change in the admittance spectrum. Hence a plot of conductance signature serves as a diagnosis of structural health.

The EMI technique was used in this paper for corrosion assessment, as it is a proven tool for structural health monitoring (SHM) of a wide variety of engineering structures, ranging from lab sized components to large prototype structures (Soh et al. 2000; Soh and Bhalla, 2005; Bhalla et al. 2012). Recently Talakokula et al. (2014) extended the application of EMI technique for chloride induce corrosion detection in RC structures through accelerated corrosion experiments performed for about four months and found that the EMI technique was effective in monitoring the changes caused during the exposure.

Table 1. Concrete mix design details.

Materials	Quantity
Water cement ratio	0.4
Cement (kg/m^3)	500
Fine aggregate (kg/m^3)	570.5
Coarse aggregate (kg/m^3)	1062.2
Slump	100 mm

4 SPECIMEN PREPARATION

In this investigative study, RC cylinders of M30 grade (as per IS 456, 2000), 100 × 60 mm in size, were cast along with 100 mm long, 16 mm diameter rebars of high yield deformed (HYD) steel of Fe415 grade (conforming to IS 1786, 1992). The rebars were thoroughly cleaned with a wire brush prior to bonding the PZT patch. A PZT patch measuring 10 × 10 × 0.3 mm, confirming to grade PIC 151 (PI Ceramic, 2012) was bonded to each rebar at the mid length, where a small flat surface was achieved through machining to allow for the bonding of the patch, as shown in Fig. 2. A thin layer of epoxy was applied on the machined rebar surface and then PZT patch was placed on it. The whole set up was kept undisturbed in this condition at room temperature for 24 hours to enable full curing of adhesive, after which wires were soldered to the electrodes of the PZT patch. The PZT patch was then covered with an additional thin layer of epoxy adhesive as a protective measure.

The concrete specimens were cast using ordinary portland cement, fine aggregate of Zone 1 grading (confirming to IS 383, 1970) and crushed coarse aggregate of nominal size 10 mm. Table. 1 presents the details of composition of the concrete mix. After 28 days curing period the wires soldered to the electrodes of the PZT patch were connected to LCR meter (model E4980A, Agilent. 2012) as shown in Fig. 2.In this manner, the electro mechanical admittance signature, consisting of real part (conductance G) and imaginary part (susceptance B) were acquired in a frequency range of 50–400 kHz (as shown in Fig. 3. for a typical specimen 1). A frequency interval of 100 Hz was used for each impedance measurement. All the tests were performed under controlled laboratory conditions so that the temperature fluctuations could be ruled out.

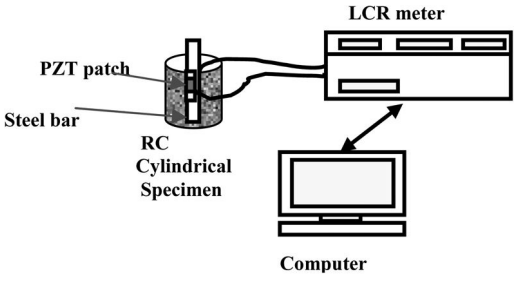

Figure 2. Data acquisition setup.

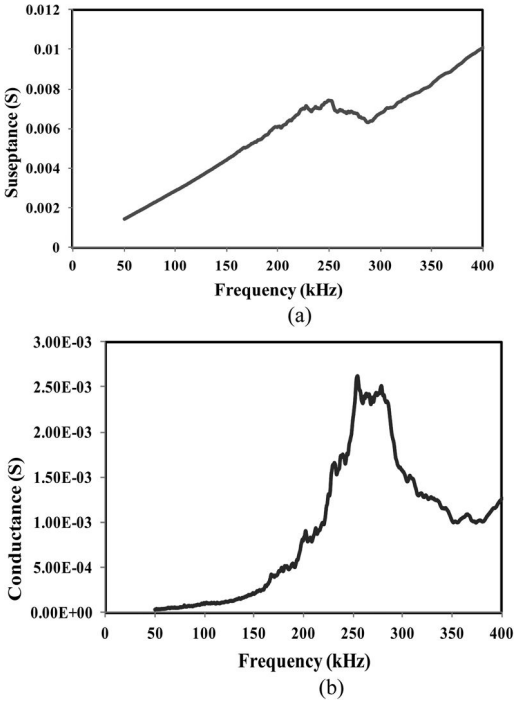

Figure 3. Experimental admittance signatures. (a) Susceptance (B) (b) Conductance (G).

5 ACCELERATED CORROSION TESTS

The variation of G (the real part of admittance) of the PZT patches, bonded to the steel bar specimens is considerable after corrosion and the signatures can be observed to change substantially with corrosion for all the specimens. Fig. 4 (a) and (b) shows the variation conductance signature during the accelerated chloride induced corrosion exposure as well as accelerated carbonation induced corrosion exposure for typical specimens. From the marked difference in the signature, it can be concluded that the mechanical impedance has changed due to corrosion. This happens because corrosion changes the mass, stiffness, and/or damping properties of the bar, which in turn causes the conductance signature to change. The next section focuses on quantification of the corrosion induced deterioration.

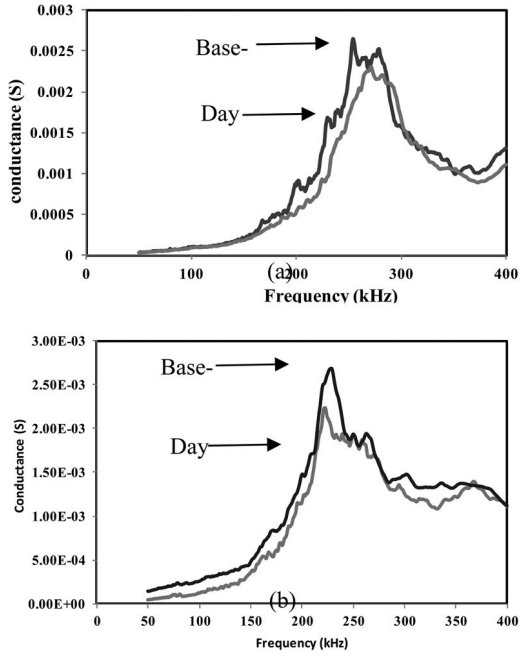

Figure 4. Variation of conductance signature. (a) During accelerated chloride induced corrosion (b) During accelerated carbonation corrosion.

5.1 *Damage quantification*

Described below are some of the computational techniques which can be used for the comparison of two signatures, one of which is the baseline signature of the healthy structure and the other one is the signature after an unknown damage.

5.1.1 *Root mean square deviation (RMSD)*

The RMSD index is defined as (Giurgiutiu and Rogers, 1998) as

$$RMSD = \sqrt{\frac{\sum_{1}^{N}\left(G_i - G_i^0\right)^2}{\sum_{1}^{N}\left(G_i^0\right)^2}} \times 100 \qquad (1)$$

where G_i is the conductance of the PZT patch at any stage during the test and G_i^0 is the baseline value (in pristine condition), i representing the frequency index (100 to 300 kHz).

5.1.2 *Signature assurance criteria (SAC)*

Let, $\mathbf{u} = [u_i], i = 1, 2, 3, \ldots, N$ be a reference signature obtained from an healthy structure, and

$\mathbf{v} = [v_i], i = 1, 2, 3, \ldots, N$ be the second signature obtained from the same structure after an unknown

level of degradation has occurred, then SAC value is given by

$$\text{SAC (u, v)} = \frac{\left|u^T . v\right|^2}{u^T . u \ . v^T . v} \tag{2}$$

$0 \leq \text{SAC} \leq 1.0$

SAC = 1.0 implies that u and v are identical and a value of SAC = 0 implies that the two are totally uncorrelated (Bhalla, 2001).

5.1.3 *Waveform chain code (WCC) technique (Bhalla, 2001)*

Let *u* and *v* be two signatures as defined above. WCC uses the summation of the absolute differences between two slopes and two curvatures (Samman and Biswas, 1994 a and b).

The slope at a point is given by

$$S_i = u_i - u_{i-1} \tag{3}$$

where i = 2, 3, 4, ….., N

The relative Slope can be expressed as,

$$S_i^r = \frac{S_i}{S_{\max}} \tag{4}$$

This can be converted to a scaled slope by scaled relative slope,

$$S_i^{sr} = 50 S_i^r \left(-50 \leq C_i^{sr} \leq 50\right) \tag{5}$$

Similarly, Scaled Relative Curvature, which is the derivative of slope, can be expressed as

$$C_i^{sr} = \frac{S_i^{sr} - S_{i-1}^{sr}}{2} \left(-50 \leq C_i^{sr} \leq 50\right) \tag{6}$$

The two signatures, *u* and v, as defined above, may be compared by calculating their Slope Differential Values (SDV) and Curvature Differential Values (CDV) as defined below

Slope Differential Value,

$$S_i^{dv} = \left|S_i^{rs,v} - S_i^{rs,u}\right| \tag{7}$$

Curvature Differential Value,

$$C_i^{dv} = \left|C_i^{rs,v} - C_i^{rs,u}\right| \tag{8}$$

A Larger value of SDV or CDV at a point implies a significant difference between the two signatures in the neighborhood of the point. Their values may range from 0 to 100%.

Four possible quantitative measures of identifying the change of a signature are

(i) maximum SDV (ii) area enclosed by SDV curve and frequency axis which is equivalent to summation of the values of SDV (iii) maximum CDV (iv) area enclosed by CDV curve and frequency axis which is equivalent to summation of values of CDV.

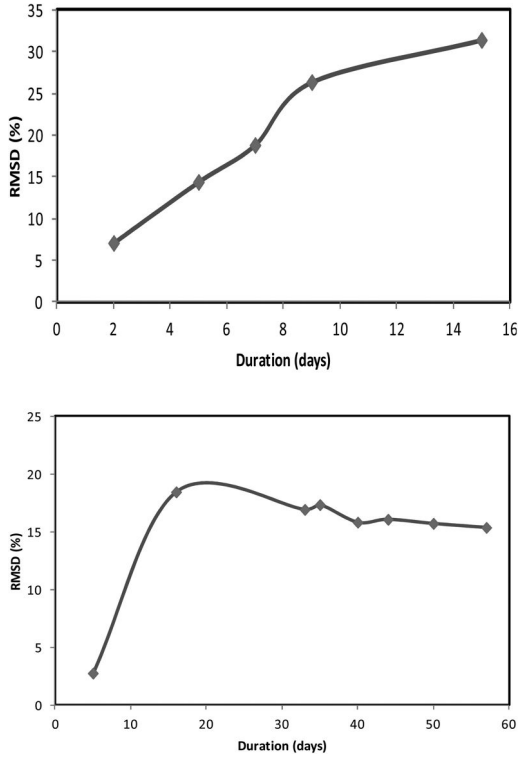

Figure 5. Variation of RMSD. (a) During accelerated chloride induced corrosion (b) During accelerated carbonation corrosion.

5.1.4 *Adaptive template matching (ATM)*

Two signatures *u* and *v* are considered identical if the following two criteria are satisfied (Samman and Biswas, 1994 a and b)

$$(1-\beta)\, u_i \leq v_i \leq (1+\beta)\, u_i \tag{9}$$
$$u_i > \Delta \text{ and } v_i > \Delta$$

in which, β is the percent tolerance on the magnitude and Δ is the threshold of the magnitude.

$$\Delta = \partial \ X \ \max (u_i, v_i) \ (i = 1, 2, 3, \ldots) \tag{10}$$
where $0 \leq \partial \leq 1$

Given *u*, *v*, and Δ, the technique calculates the minimum tolerance value β.

These damage metrics, as described above, can be used to mathematically quantify the damage while reducing the deviation in admittance data to single scalar value. In this investigations, the RMSD metric has been used because it is an established statistical metric to quantify damage (Giurgiutiu and Rogers, 1998). The variation of the RMSD index can be studied in light of the degradation of actual stiffness of the specimen with the increase in corrosion.

Fig. 5 (a) and (b) shows the variation of the RMSD index of typical specimens during the chloride and carbonation corrosion exposure respectively. From

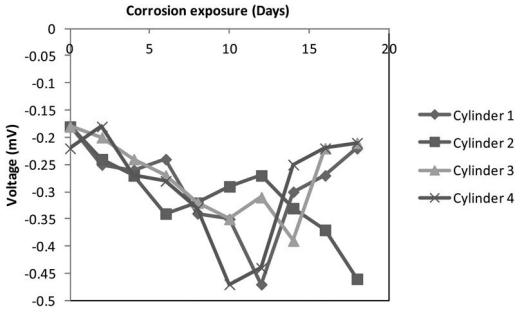

Figure 6. Variation of half cell potential values during corrosion.

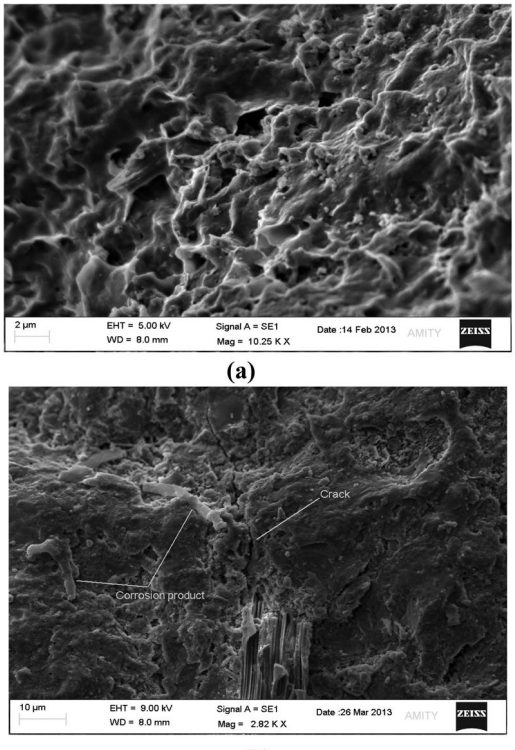

Figure 7. SEM image of concrete (a) In Pristine state (b) In corroded state showing cracks in C-S-H gel.

Fig. 5(a) it can be seen that the RMSD values increased throughout the chloride induced corrosion exposure whereas, for the carbonation corrosion exposure, the values increased up to the 19th day and after that they started decreasing. It can be observed from the Fig. 5(b) that the increase in RMSD values was steep up to a period of 40 days and once the carbonation front neutralizes the alkalinity of concrete, a slow increase in the values can be seen. Hence it can be concluded that the changes due to corrosion has been diagnosed well by the PZT sensor. The corrosion potential of reinforcing steels was also measured by means of half cell potential (HCP). The HCP values indicate the probability of

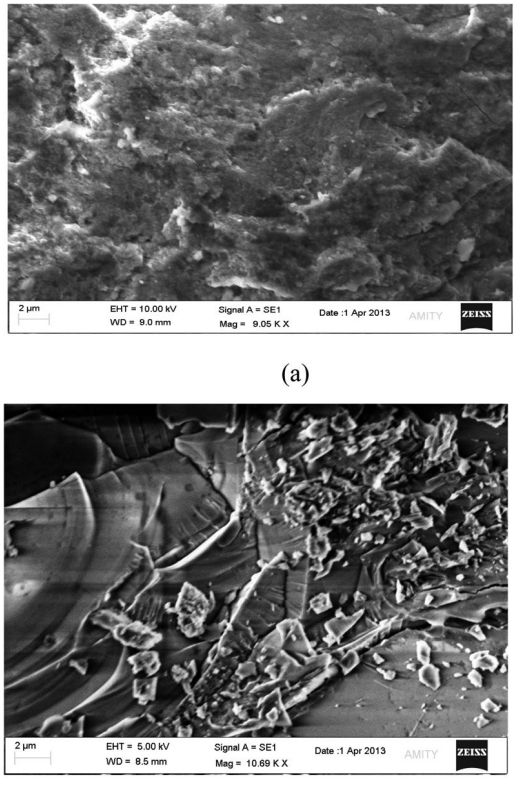

Figure 8. SEM image of steel. (a) In pristine stage (b) Corroded state.

occurrence of corrosion. Fig. 6 shows the variation of HCP reading during the accelerated chloride induced corrosion process.

From the figure it can be depicted that the HCP values ranged between 0.2 V to 0.45 mV. It is well known that potential values less than −350 mV indicate 90% probability of corrosion according to ASTM C876.

Fig. 7 (a) shows the scanning electron microscopic (SEM) images of the concrete in pristine stage, it can be observe that there is a flaky like appearance in the image which is $Ca(OH)_2$ and a uniform surface of C-S-H gel.7 (b) shows the concrete in corroded state, it can be observed in the figure that there is no flaky structure present at this stage and there are cracks in the C-S-H gel indicating the occurrence of corrosion inside the concrete due to the formation of rust. Prominent crack in the C-S-H gel with corrosion products can be seen.

Fig. 8 (a) and (b) shows the SEM image of steel rebar before and after corrosion process. Corrosion products can be clearly observed on the surface of steel in corroded state.

6 CONCLUSIONS

This paper has presented a new corrosion assessment approach using the EMI technique through the use of

surface bonded PZT patches. It is observed that both types of corrosion, chloride and carbonation corrosion induces well-defined change in conductance signatures clearly shows the corrosion. The HCP values indicated high probability of corrosion which can also be seen in the SEM images. The RMSD values calculated provides proof of concept validation that the EMI technique can be used to detect and quantify both types of corrosion.

REFERENCES

Agilent Technologies. (2011) www. Agilent technologies.com.

Agilent Technologies. (2012) www. *Home.agilent.com* ASTM C876. 1999. Standard test method for half-cell potentials of uncoated reinforcing steel in concrete, Annual Book of ASTM Standards, Vol.14.02.

Bedekar, V., Inman, D. and Priya, S. (2008), "Detection of Corrosion Using Impedance Spectroscope", Ferroelectrics letter section 35, 7–16.

Bhalla, S., Vittal, A. P. R. and Veljkovic, M. (2012), "Piezo-Impedance Transducers for Residual Fatigue Life Assessment of Bolted Steel Joints", Journal of Structural Health Monitoring, 11(6), 733–750.

Broomfield, J. P. (2007), "Corrosion of Steel in Concrete, Understanding, Investigation and Repair", Second edition, Taylor and Francis.

Dehwah, H. A. F., Maslehuddin, M and Austin, S. A. (2002), "Long-Term Effect Of Sulphate Ions And Associated Cation Type On Chloride Induced Reinforcement Corrosion In Portland Cement Concretes", Cement and Concrete Composites, 24, 17–25.

Fuhr, P. L and Huston, D. R. (1998), "Corrosion detection in reinforced concrete roadways and bridges via embedded fiber optic sensor", Smart Materials and Structures, 7, 217–228.

Gao, J., Wu, J., Li, J and Zhao, X. (2011), "Monitoring of Corrosion in Reinforced Concrete Structure using Bragg Grating Sensing", NDT & E International, 44, 202–205.

Giurgiutiu, V. and Rogers, C. A. (1998), "Recent Advancements in the Electro-Mechanical (E/M) Impedance Method for Structural Health Monitoring and NDE", Proceedings of SPIE Conference on Smart Structures and Integrated Systems, SanDiego, California, March, SPIE, 3329, 536–547.

IS 1786–1985 Indian Standard Specification for High Strength Deformed Steel Bars and Wires for Concrete Reinforcement, Bureau of Indian Standards, New Delhi.

IS: 456–2000 Indian Standard Plain and Reinforced Concrete-Code of Practice, Bureau of Indian Standards, New Delhi.

Lalande F, Childs B, Chaudhry Z, Rogers CA (1996) High Frequency Impedance Analysis for NDE of Complex Precision Parts. Conference on Smart Structures and Materials, Proceedings of SPIE 2717:237–245.

Park, S., Yun, C. B., Roh, Y., Lee, J. J. (2005), "Health monitoring of steel structures using impedance of thickness modes

Park, S., Benjamin, L. G., Inman, J. and Yun, C. B. (2007), "MFC-Based Structural Health Monitoring Using a Miniaturized Impedance Measuring Chip for Corrosion Detection", Research in Non-destructive Evaluation 18:139–150.

Park, S. and Park, S. K. (2010), "Quantitative Corrosion Monitoring Using Wireless Electromechanical Impedance Measurements", Research in Non Destructive Evaluation, 21, 184–192.

PI Ceramic, "Product Information Catalogue", Lindenstrabe, Germany, 2012 www.piceramic.de.

Samman, M. M. and Biswas, M. (1994a), "Vibration Testing for Non-Destructive Evaluation of Bridges. I: Theory", Journal of Structural Engineering, ASCE, 120 (1), 269–289.

Samman, M. M. and Biswas, M. (1994b), "Vibration Testing for Non-Destructive Evaluation of Bridges. II: Results", Journal of Structural Engineering, ASCE, 120 (1), 290–306.

Simmers, G. E. (2005), "Impedance-Based Structural Health Monitoring to Detect Corrosion", MS Thesis, Blacksburg, Virginia.

Soh, C. K., Tseng, K. K. H., Bhalla, S. and Gupta, A. (2000), "Performance of Smart Piezoceramic Patches in Health Monitoring of a RC Bridge", Smart Materials and Structures, 9(4), 533–542.

Talakokula. V, Bhalla. S and Gupta. A, (2014) "Corrosion Assessment of Reinforced Concrete Structures Based on Equivalent Parameters Using Electro-Mechanical Impedance Technique", Journal of Intelligent Material Systems and Structures, Volume 25 (4), pp 484–500.

Thomas D and Welter J (2004) Corrosion Damage Detection with Piezoelectric Wafer Active Sensors. SPIE's 11th Annual International Symposium on Smart Structures and Materials and 9th Annual International Symposium on NDE for Health Monitoring and Diagnostics, 14–18 March 2004, San Diego, CA:5394-2.

Yang, J., Zhu, H., Yu, J. and Wand, D. (2013), "Experimental Study on Monitoring Steel Beam Local Corrosion Based on EMI Technique", Applied Mechanics and Materials, 273, 623–627.

Concrete Solutions – Grantham et al. (Eds)
© 2014 Taylor & Francis Group, London, ISBN 978-1-138-02708-4

Monitoring the development of microcracks in reinforced concrete caused by sustained loading and chloride induced corrosion

Junjie Wang, P.A. Muhammed Basheer & Sreejith V. Nanukuttan
School of Planning, Architecture and Civil Engineering, Queen's University Belfast, Northern Ireland, UK.

Yun Bai
Department of Civil, Environmental & Geomatic Engineering, University College London, England, UK.

ABSTRACT: Chloride-induced corrosion of steel in reinforced concrete structures is one of the main problems affecting their durability and it has been studied for decades, but most of them have focused on concrete without cracking or not subjected to any structural load. In fact, concrete structures are subjected to various types of loads, which lead to cracking when the tensile stress in concrete exceeds its tensile strength. Cracking could increase transport properties of concrete and accelerate the ingress of harmful substances (Cl^-, O_2, H_2O, CO_2). This could initiate and accelerate different types of deterioration processes in concrete, including corrosion of steel reinforcement. The expansive products generated by the deterioration processes themselves can initiate cracking. The success of concrete patch repairs can also influence microcracking at the interface as well as the patch repair itself. Therefore, monitoring the development of microcracking in reinforced concrete members is extremely useful to assess the defects and deterioration in concrete structures. In this paper, concrete beams made using 4 different mixes were subjected to three levels of sustained lateral loading (0%, 50% and 100% of the load that can induce a crack with width of 0.1 mm on the tension surface of beams – $F_{0.1}$) and weekly cycles of wetting (1 day)/drying (6 days) with chloride solution. The development of microcracking on the surface of concrete was monitored using the Autoclam Permeability System at every two weeks for 60 weeks. The ultrasonic pulse velocity of the concrete was also measured along the beam by using the indirect method during the test period. The results indicated that the Autoclam Permeability System was able to detect the development of microcracks caused by both sustained loading and chloride induced corrosion of steel in concrete. However, this was not the case with the ultrasonic method used in the work (indirect method applied along the beam); it was sensitive to microcracking caused by sustained loading but not due to corrosion.

1 INTRODUCTION

Presence of microcracks can accelerate the chloride ingress into the concrete (Wang *et al.,* 2013b, Wang *et al.,* 2011), air permeability and sorptivity of concrete (Wang *et al.*, 2013a), and could accelerate the deterioration process of reinforced concrete structures. Detecting and monitoring cracks, especially the microcracks, is very important for the repair of reinforced concrete structures. Ultrasonic method can be used to detect microcracking caused by sustained loading (Wang *et al.,* 2013a, 2013b) and freezing/thawing cycles (Jacobsen *et al.*, 1996). In the work reported by Wang *et al.*, (Wang *et al.,* 2013b), ultrasonic pulse velocity measurements using different transducer orientations were related to cracking caused by sustained loading. Autoclam tests were also found to be able to detect the microcracking caused by loading (Wang *et al.,* 2013a). However, the effectiveness of these two methods for detecting and monitoring microcracks caused by corrosion of steel in concrete has rarely been studied. In this work, the ultrasonic pulse velocity measurements and Autoclam permeability tests were used to detect and monitor the development of cracks caused by the combined effects of sustained loading and corrosion of steel in concrete, and the results are compared.

2 EXPERIMENTAL PROGRAMME

Class 42.5N CEM I conforming to BS EN 197-1:2011 was used in the work. The coarse aggregate used was crushed and well graded basalt of size 5–20 mm (size 5–10 mm and 10–20 mm mixed in the ratio 1:2) and the fine aggregate was natural medium graded sand. Both aggregates were oven-dried at 100 (±5)°C for 24 hours to remove the initial moisture content, but the mix water content was adjusted by adding extra water to compensate for the aggregate absorption so as to ensure that the aggregates were in saturated surface dry condition at the time of mixing. Ground granulated blast-furnace (GGBS) complying with BS EN

Table 1. Concrete mix proportions (kg/m^3).

Mix ID	0.45–CEMI	0.45–35% GGBS	0.65–CEMI	0.65–35% GGBS
CEMI	360	234	300	105
GGBS	—	126	—	195
Water	162	162	195	195
Superplasticiser	0.47	0.42	—	—
Sand	776	772	761	754
5–10 mm	384	382	376	373
10–20 mm	780	776	764	758

6699: 1992 was used to replace CEM I by 35% in two mixes. Two different water-binder ratios (w/b), 0.45 and 0.65, were considered. The proportions for each mix are reported in Table 1.

Six beams (1200 × 250 × 200 mm in size) and six 100 mm size cubes were cast for each mix. The reinforcement drawing of the beams is shown in Figure 1. The required quantities of the mix constituents were batched by mass and then mixed using a pan mixer in accordance with BS 1881:125: 1986. The workability of the mixes was determined using the slump test and the slump of each mix is reported in Table 2. A vibrating table was used to compact concrete in the cubes and a poker vibrator was used to compact concrete in the beams. The top surface of the specimens was then finished with a trowel and a thick black polythene sheet was used to cover the surface. The cubes were demoulded after 24 hours and then placed in water bath at 20 (± 1)°C for the next 3 days, and then wrapped in wet hessian and thick polythene sheet. The beams were demoulded after 7 days and then wrapped in wet hessian and the thick polythene sheet. All specimens were then placed in a constant temperature room at 20 (± 1)°C. The compressive strength test was conducted on three cubes per mix at the age of 28 and 56 days and the results are reported in Table 2.

At the age of 56 days, two concrete beams of each mix were subjected to three loading levels (0%, 50% and 100% of the load that can induce crack with a width of 0.1 mm on the tension surface of the beam – $F_{0.1}$), as shown in Figures 1 and 2. The tension face of all beams was then subjected to weekly cycles of wetting (for 1 day) and drying (for 6 days) with chloride solution (10% NaCl by weight) for 60 weeks. The ponding setup is shown in Figure 3. All faces except the exposure faces were sealed with epoxy paint to ensure ingress of chloride ions through only the tension faces. The intensity of load was kept constant during the test period by topping up the level, if needed, at every 20 weeks. The experimental stages are illustrated in Figure 4. Ultrasonic pulse velocity (UPV), Autoclam air permeability and then water absorption tests were conducted on the exposure surface of beams every 2 weeks before wetting with the chloride solution.

Ultrasonic pulse velocity (UPV) test, with an indirect method of testing (Jacobsen *et al.*, 1996), was used to quantify the microcracking, as shown in Equation

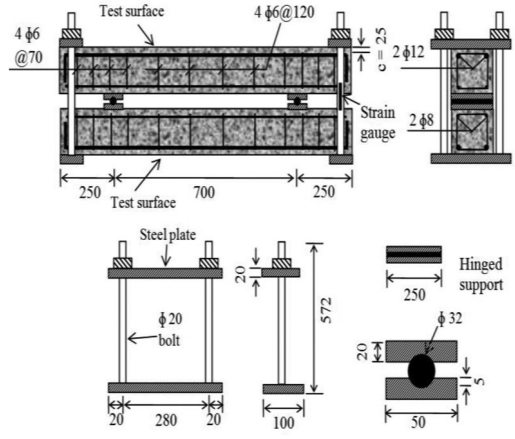

Figure 1. Schematic setup and reinforcement drawing.

Table 2. Physical properties of concrete.

Mix ID	0.45–CEMI	0.45–35% GGBS	0.65–CEMI	0.65–35% GGBS
Slump (mm)	120.0	95.0	95.0	100.0
f_c* 28d (MPa)	58.0	50.7	37.8	35.1
f_c 56d (MPa)	59.5	56.7	38.7	48.9

Figure 2. Test beams under sustained loading.

1. The change in UPV of concrete compared with the initial UPV of the concrete was described as a damage degree of the concrete surface, θ.

$$\theta = (V_0\text{-}V)/V_0 \quad (1)$$

where θ is the measured damage degree; V_0 is the UPV of the concrete at the initial state before loading; V is the UPV of the concrete during test period.

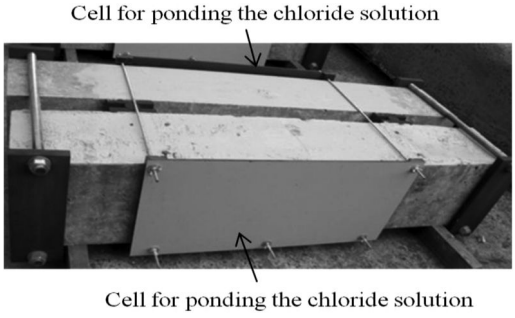

Figure 3. Setup for ponding cells.

There might be some error in measuring the exact length of the transmission path with the indirect transmission due to a significant contact area between the transducer and the concrete. Therefore, a series of measurements, in accordance with BS EN 12504-4: 2004 was made with the receiver transducers at different distances with fixed increments, as shown in Figure 5. The measurement points were kept to be the same each time. Vaseline petroleum jelly was used as a couplant between the transducer and the concrete surface. The transducers were pressed by hand to exert a constant force against the concrete surface to ensure good acoustic contact. Repeated readings at each location were taken and the minimum transit time was reported. After the test, the test locations were polished with sand paper to remove the jelly from concrete surface.

The *in situ* air permeability and water absorption were then measured using the Autoclam Permeability System (Basheer, 1991), and an air permeability index and a sorptivity index were determined for each of the test condition and the mix. In the air permeability test, compressed air (around 500 mbar) in the Autoclam was allowed to dissipate into the concrete and the pressure of air in the Autoclam was recorded every minute. A graph of natural logarithm of pressure monitored in the test from 5th minute to 15th minute was plotted on the Y-axis against the corresponding time in minutes on the X-axis. The absolute value of the slope of the straight line is reported as air permeability index (API) with units Ln(Pressure)/min. If a test did not last for 15 minutes, the available data were used to calculate the air permeability index.

The water absorption (sorptivity) test was conducted at least 60 minutes after the air permeability test at the same location in order to ensure that the pore pressure due to the air permeability test had dissipated. The water inside the chamber of Autoclam was allowed to ingress into the concrete by absorption

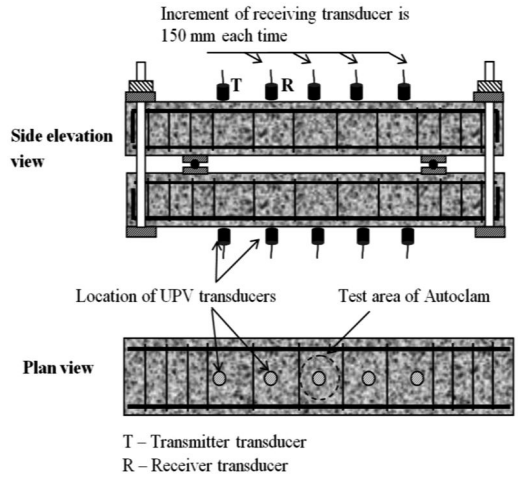

Figure 5. Location of testing points for UPV test and Autoclam test.
Note: The testing points and areas were chosen to avoid influence of rebar.

through the contact area, and the volume of the water leaving the chamber was recorded every minute. The quantity of water inflow in m^3 between the 5th and 15th minutes was plotted on the Y-axis against square root of the corresponding time in minutes on the X-axis, and the slope of the straight line graph was reported as the sorptivity index (SI), with units $m^3/min^{0.5}$. The same test locations were used each time when these tests were carried out.

3 RESULTS AND DISCUSSION

Results of the tests are shown in Figures 6 to 8. It can be seen from these figures that the damage degree, API and SI increased with an increase in loading level, but had different trends with increased duration of chloride ponding, w/b and type of binder. The effects on the damage degree determined from the UPV values and the Autoclam permeation indices (API and SI) of the beams with increasing load level are summarised in Table 3. Although the application of top up loads resulted in an increase of the damage degree and the Autoclam indices, these are ignored in the following discussion.

Although the trends in Figure 6 for the damage degree with increased test duration and load level are similar for both w/b and type of cement, there is a different trend in Figures 7 and 8 for the Autoclam permeation indices. Here, similar effects with increased

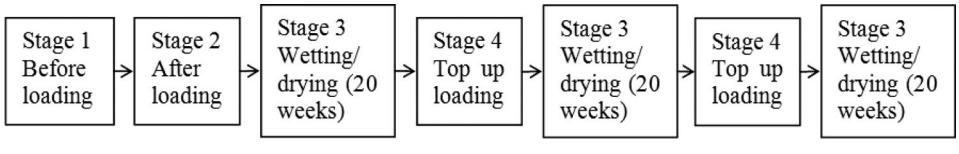

Figure 4. Diagram of test stages.

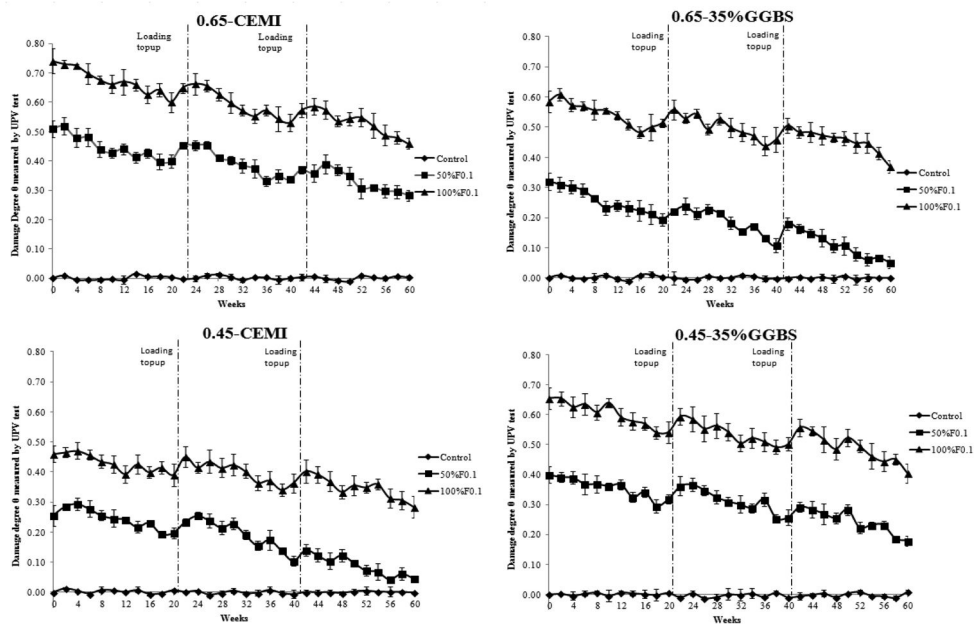

Figure 6. Damage degree θ of all beams measured by UPV test.

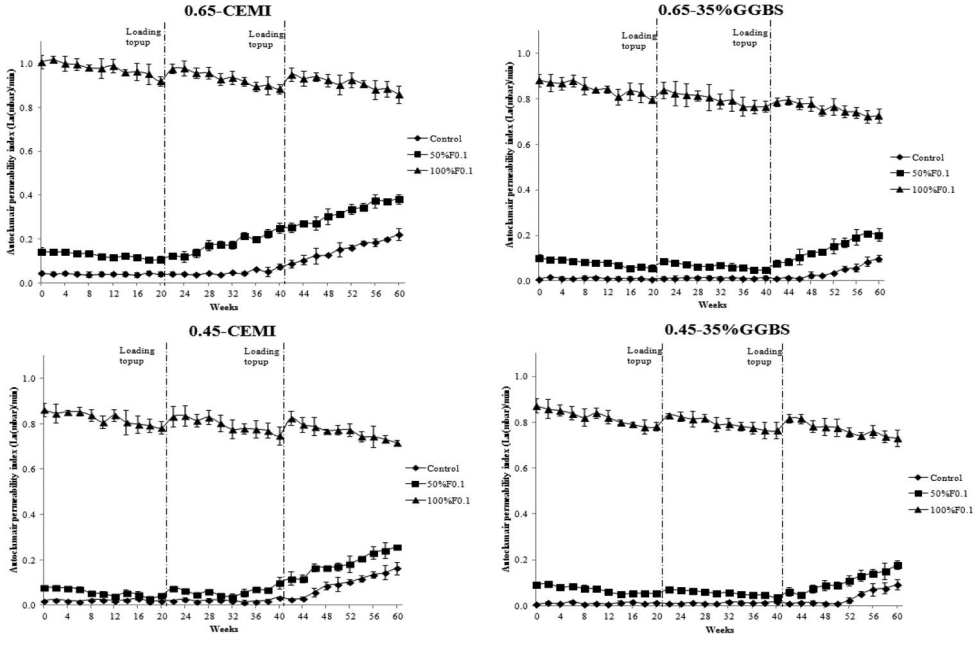

Figure 7. Autoclam air permeability indices of all beams.

test duration were obtained for no loading and 50% loading conditions, but a totally different trend is seen for the 100% loading condition. For both no loading and 50% loading conditions, the initial variations in API and SI for different mixes are small and this can be attributed to the influence of high level of moisture content in concretes (Basheer *et al.*, 2001). The measurement of relative humidity (RH) before conducting Autoclam tests indicated that the surface RH on all specimens was above 82%, which would suggest that the RH inside the concrete might have been even higher. As reported by Basheer *et al.*, (2001), the air permeability and sorptivity of 0.45 w/c and 0.65 w/c concretes cannot be differentiated if the internal RH is greater than 80%. Due to the particular test regime used in this research, it has not been possible

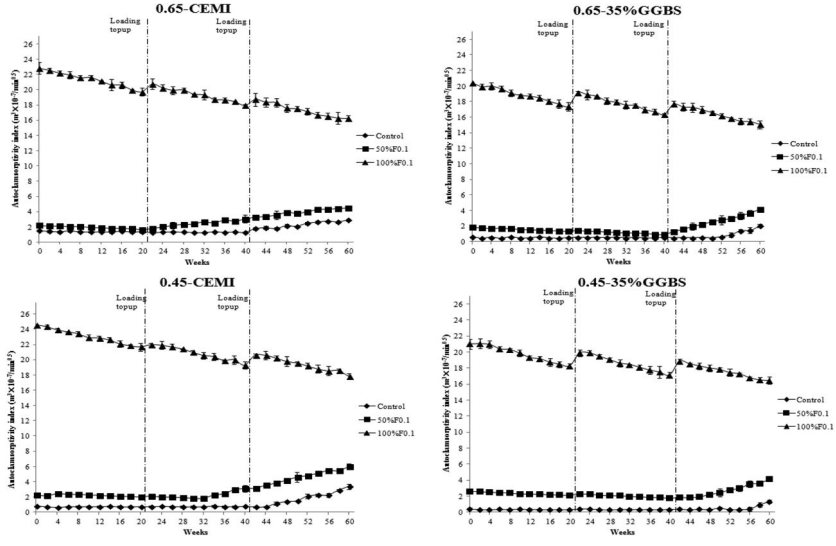

Figure 8. Autoclam sorptivity indices of all beams.

Table 3. Influence of duration of ponding, effect of w/b and type of binder on damage degree and Autoclam indices of beams at different load levels.

	Change in damage degree from UPV			Change in Autoclam indices		
Loading Level	Effect of duration of ponding	Effect of w/b	Effect of 35%GGBS	Effect of duration of ponding	Effect of w/b	Effect of 35%GGBS
No loading	Remained constant	No effect	No noticeable effect	Remained constant initially, then increased continuously	Both API and SI started increasing at an early period	Both API and SI started increasing at a later period
50% $F_{0.1}$	Decreased continuously	Higher at higher w/b	Increase at 0.45 w/b, but decrease at 0.65 w/b	Slightly decreased initially, then increased continuously	Same as above	Same as above
100% $F_{0.1}$	Same as above	Same as above	Same as above	Decreased continuously	No noticeable effect	No effect

to eliminate the effect of RH on both air permeability and sorptivity fully. Nevertheless, the data in Figures 7 and 8 could be used to discuss the effects of loading and corrosion induced microcracking on both the air permeability and sorptivity.

No loading specimens: From Figure 6, it can be seen that the damage degree measured by UPV test did not change with the increased duration of chloride ponding, but the Autoclam indices of beams (Figures 7 and 8) increased continuously after a certain duration of exposure. The effect of an decrease in w/b was to increase the time at which permeation indices increased. Similarly, with the use of 35% GGBS, there was a substantial increase in time before the permeation indices started to increase. Given that these specimens were not subjected to any loading, it can be concluded that any change in permeation indices is due to corrosion induced microcracking. That is, microcracks caused by the corrosion of steel in the beam have no influence on the damage degree obtained by the indirect UPV method, but could increase both the air permeability and the sorptivity, measured with the Autoclam Permeability System. So, by lowering the w/b and incorporating GGBS in concretes, it is possible to reduce corrosion and corrosion induced microcracking.

50% $F_{0.1}$ loading specimens: Both the damage degree and the Autoclam indices decreased initially with time, which could be due to either self-healing of micro-cracks, the modification of cement hydrates due to the penetration of chloride ions through the cracks (Suryavanshi *et al.,* 1995) or increased moisture content due to cracking. After a certain period of exposure, Autoclam permeation indices increased

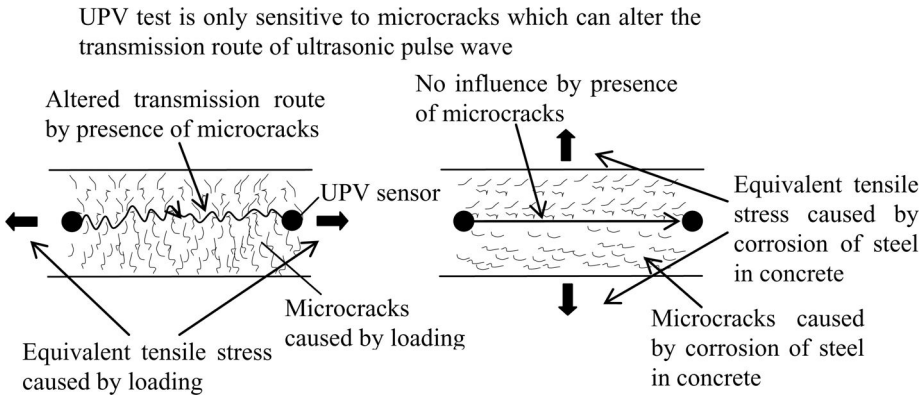

Figure 9. Influence of the orientation of microcracks on UPV test.

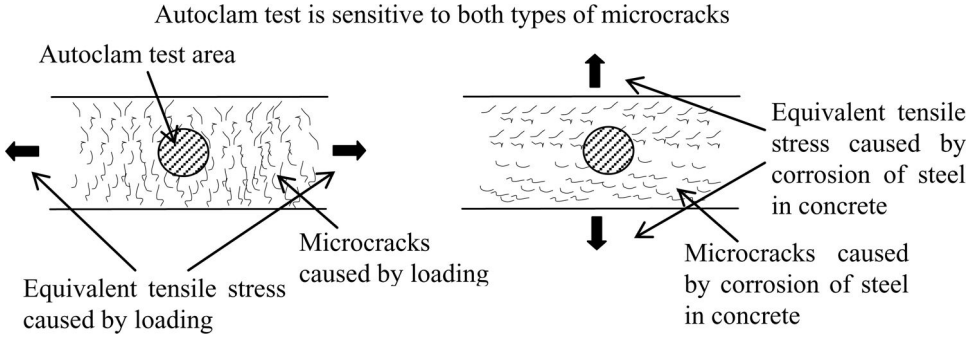

Figure 10. Influence of the orientation of microcracks on Autoclam tests.

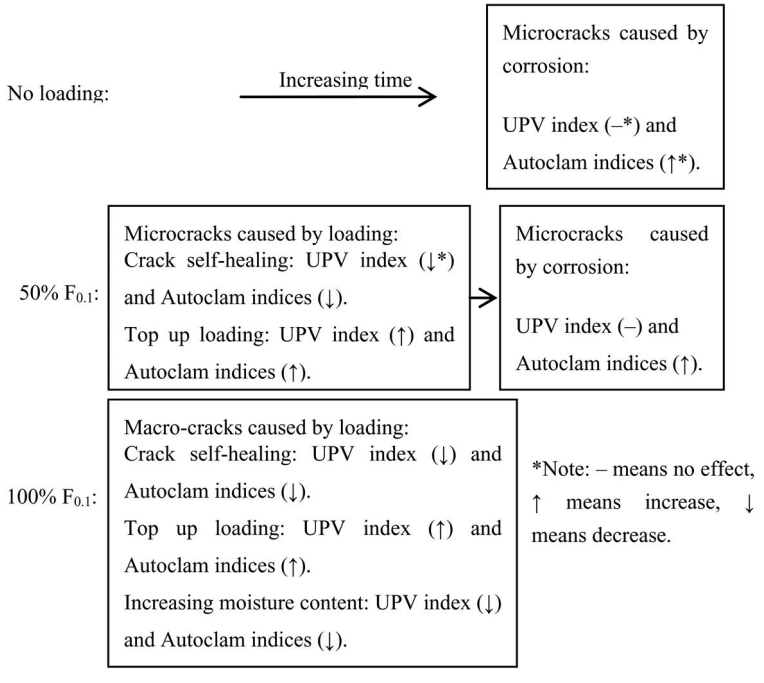

Figure 11. Effects of different types of cracks on UPV test and Autoclam tests with increasing time.

with time, but the damage degree calculated from the UPV decreased continuously. The continued decrease in damage degree is attributed to the increased moisture content of the concretes and/or self healing effect in large cracks (macro-cracks).

Figure 9 illustrates different directions of the different types of micro-cracks in the beams. As shown in this figure, only the cracks that can alter the transmission route of the ultrasonic pulse wave have an effect on the UPV test. However, as shown in Figure 10, cracks in any direction can have an effect on the Autoclam tests. This suggests that Autoclam test is better to detect the microcracks on the surface of concrete than the UPV test.

As shown in Figure 6, the microcracks caused by loading (50%$F_{0.1}$) can increase the damage degree quite significantly compared to no loading condition. However, a corresponding increase in permeation indices was not found. There are two reasons for this disparity in behaviour. It could be argued that there might have been substantial microcracking due to increased loading on the beams. This might increase the UPV and hence the damage degree. However, until the effect of microcracking exceeded the effect of moisture content in concrete, permeation measurements using the Autoclam might not have been influenced. Nevertheless, it can be seen that the time at which the permeation indices started to increase with increased duration of chloride ponding was earlier for 50% $F_{0.1}$ compared to the no loading condition. Therefore, the combined effects of loading and microcracking caused by corrosion could be detected with the Autoclam permeation tests.

100% $F_{0.1}$ loading condition: Both the damage degree and the Autoclam indices decreased continuously with time, as shown in Figures 6-8, but compared to other two loading conditions, there was a substantial increase in both the damage degree and the Autoclam permeation indices. It can be assumed that 100% $F_{0.1}$ loading might have resulted in substantial cracking (both micro and macro sized) of concrete. When these cracks are large in size and volume, it is possible that any damage caused by corrosion is not identified by both the UPV test and the Autoclam tests. Concretes with **macro**-cracks (high load level) can retain large quantities of water and the evaporation rate can be comparatively lower than concretes with **micro**-cracks or no cracks. As a result, there could be an improved self healing effect in their microstructure. Therefore, the decrease in both the damage degree and Autoclam indices could be attributed to a combination of increased moisture content and self healing effects/chemical modifications of the microstructure of concrete.

As summarised in Figure 11, cracks developed on the surfaces of the beams at different exposure time are different, and the related effects on damage degree and Autoclam indices are different.

4 CONCLUSIONS

By comparison of the results of the two different methods for detecting and monitoring the effect of loading and corrosion induced micro-cracking of concrete, the following conclusions have been made:

1) The indirect method using the UPV test was not able to detect the effects of micro-cracks in concrete caused by the corrosion of the steel. However, it could detect the effect of structural cracks caused by loading.
2) Autoclam permeation tests (air permeability and sorptivity) were sensitive to cracking caused by both structural loading and the corrosion of steel in concrete.
3) The influence of w/b and type of binder on corrosion-induced cracking could be detected using both the air permeability and sorptivity tests. However, if the structural cracking is extensive, there are limitations for detecting the effect of corrosion-induced cracking on permeation properties.

REFERENCES

Basheer, P.A.M., Nolan, E. and Long, A.E. 2001, Near surface moisture gradients and in-situ permeation tests, Construction and Building Materials, 15 (2–3), pp 105–114.

British Standards Institution 2011, BS EN 197-1:2011, Cement Part 1: Composition, specifications and conformity criteria for common cements.

British Standards Institution 2004, BS EN 12504-4:2004, Testing concrete – Part 4: Determination of ultrasonic pulse velocity.

British Standards Institution 1992, BS 6699:1992 Specification for ground granulated blastfurnace slag for use with Portland cement.

British Standards Institution 1989, BS 1881-125:1986 Testing concrete — Part 125: Methods for mixing and sampling fresh concrete in the laboratory.

Jacobsen, S., Marchand, J. & Boisvert, L. 1996, Effect of cracking and healing on chloride transport in OPC concrete, *Cement and Concrete Research,* vol. 26, no. 6, pp. 869–881.

Suryavanshi, A.K., Scantlebury, J.D. and Lyon, S.B. 1995, Pore size distribution of OPC & SRPC mortars in presence of chlorides, *Cement and Concrete Research,* vol. 25, no. 5, pp. 980–988.

Wang, J., Basheer, P.A.M., Nanukuttan, S.V. and Bai, Y. 2013a, Influence of microcracking on water transport into reinforced concrete beam under sustained bending. Water Transport in Cementitious Materials. November 3–6, Guildford, UK.

Wang, J., Basheer, P.A.M., Nanukuttan, S.V. and Bai, Y. 2013b, Influence of short-time and sustained compressive loading on chloride migration into concrete. Cement and Concrete Science Conference 2013, September 2–3, Portsmouth, United Kingdom.

Wang, H., Lu, C., Jin, W. and Bai, Y. 2011, Effect of External Loads on the Chloride Transport in Concrete, *Journal of Materials in Civil Engineering,* vol. 23, no. 7, pp. 1043–1049.

This page intentionally left blank

Concrete Solutions – Grantham et al. (Eds)
© 2014 Taylor & Francis Group, London, ISBN 978-1-138-02708-4

Laser Induced Breakdown Spectroscopy (LIBS) – alternative to wet chemistry and micro-XRF

G. Wilsch, T. Eichler, S. Millar & D. Schaurich
BAM – Federal Institute for Materials Research and Testing, Berlin, Germany

ABSTRACT: Laser Induced Breakdown Spectroscopy (LIBS) is a combination of laser ablation, plasma formation and optical emission spectroscopy. The possibility of direct measurements on the sample surface, the minimum of necessary sample preparation and the automated setup allows for fast investigations of building materials. In combination with a scanning technique (translation stage or scanning mirrors head) the element distribution can be evaluated in consideration of the material's heterogeneity. LIBS measurements are also time- and cost-saving. The ingress profile of chlorine on a 50 mm diameter concrete core up to a depth of 50 mm can be measured and evaluated in less than 10 minutes. The results are normally referred to the evaporated mass, which is approximately the cement mass of the specific concrete. As a completion to micro XRF measurements also light elements like sodium or hydrogen can be detected. The spatial resolution of the measurement may reach 50 μm at a maximum measurement frequency of up to 100 Hz. On the basis of calibration curves, results can be quantified.

1 INTRODUCTION

New concrete structures are generally dimensioned in consideration of a specific expected life time. For usual structures in civil engineering as e.g. multi-storey car parks a minimum life time of approximately 50 years is strived for. In some cases, the assessed life time is not attainable and ageing of specific structures happens far more quickly than expected. Environmental factors, influenced by weather, location or general exposition may cause the access of harmful species like SO_4^-, Na^+, CO_2 or Cl^-, etc. to the structure and accelerate the ageing process due to deterioration of concrete and/or reinforcement. Laser Induced Breakdown Spectroscopy (LIBS) can be applied as a fast and reliable method in order to identify harmful species and accompanying damage processes.

The LIBS method is a combination of material ablation, plasma formation and analysis of the emitted radiation by spectroscopic methods. For ablation and plasma formation usually a high energy pulsed NdYAG-laser is focused on the sample surface. Due to the high temperatures in early stage of the plasma all chemical bonds are broken and only elements can be detected. In a later stage of the plasma also molecules may be observed. Due to the excitation process all elements are detectable as a matter of principle, even light elements like hydrogen or sodium. The results can be quantified by calibration.

LIBS may be used on gases, liquids or solids. There are a lot of applications in different fields like environmental analysis, pharmaceutical investigation, biomedical investigation, forensic investigation or industrial applications like process control, recycling, sorting and quality control during manufacturing (Hahn & Omenetto 2012, Noll 2012).

The LIBS measurement on building materials is done without intensive sample preparation directly on the sample surface. A translation stage or a scanner is necessary when the heterogeneity of the material has to be taken into account.

The laser energy, pulse frequency, laser wavelength, surrounding atmosphere and the focus conditions are important for the sensitivity of the method. Also the spectrometer type, the spectrometer parameter, the fibre type and the CCD parameter are correlated with the elements under investigation. The spatial resolution of the measurement may reach 50 μm at a maximum measurement frequency of up to 100 Hz.

At BAM, LIBS has been successfully applied for the investigation of distribution and transport of different ions in building materials (Wilsch et al. 2005 & 2011, Weritz et al. 2005 & 2006 and Eichler et al. 2010). Quantitative measurements have been performed e.g. for chlorine, sodium, potassium, sulphur and lithium. Also the identification of substances and the evaluation of quantitative ratios by means of an integrated marker are possible.

The performance of LIBS is demonstrated by the investigation of a number of concrete cores to get the ingress profile of chlorides. A second example illustrates the advantage of LIBS for the spatial resolution of sodium profiles.

LIBS as a promising technique is currently on the step from pure laboratory applications to an in-situ on-site analysis technology. A validated

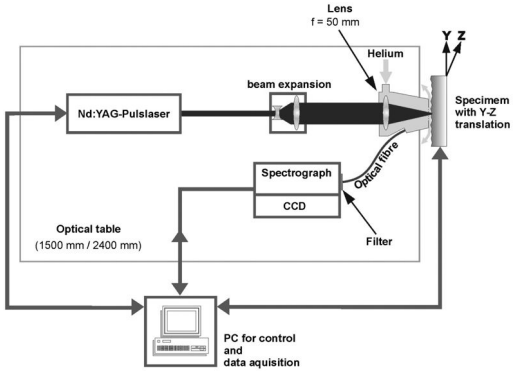

Figure 1. Experimental set-up.

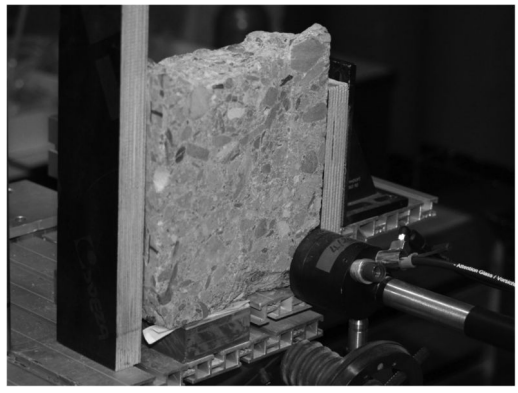

Figure 2. Translation stage with concrete core cut in the middle to do measurements on the cross section. During the measurement the specimen is moved line by line in the plane perpendicular to the laser beam.

Fibre-LIBS-System for the on-site application on building materials is under development at BAM in cooperation with system developers and companies which will use this technique for investigation on real structures.

2 LIBS

2.1 *Experimental set-up*

For our investigations the experimental set-up shown as schematic diagram in Figure 1 was used.

A pulsed NdYAG laser (Innolas Spitlight 600) with an output energy of 350 mJ per pulse is used at a undamental wavelength of 1064 nm at a frequency of 10 Hz. The beam is expanded by a beam expander and focused on the sample surface with a lens ($f = 50$ mm). The spot size at the surface is 0.2 mm. The light emitted from the plasma is guided by an optical fibre. The fibre is coupled to a Czerny-Turner type spectrometer (Shamrock 330i). In front of the entrance slit of the spectrometer an edge filter to supress light with wavelength below 550 nm is located. A CCD (Andor Idus DV420) is used as detector.

The specimen under investigation is located on a translation stage and may be moved in a plane perpendicular to the laser beam. To remove dust and to get a lower limit of detection the environment of the plasma is purged with helium.

The set-up is controlled by a laboratory-written Labview software. An automated measurement procedure minimizes the liability to errors and enables fast analysis of samples.

2.2 *Sample preparation*

For LIBS measurements only an optically accessible surface is necessary. To get volume information, a core has to be cut in the middle. This is done by dry cutting or by cutting cooled with petroleum. The measurements are performed on the cross section of the core (see figure 2).

2.3 *Measurement*

For a measurement the sample is placed on the translation stage at a constant distance to the lens. The measurements are performed line by line. The distance of the lines is of the order of 0.25 mm to 1.0 mm. The distance of subsequent measurements per line is also of the same order.

Using this scanning technique the heterogeneity of concrete is recorded.

2.4 *Resolution of measurement*

The resolution of a measurement is a compromise between exact reproduction of material heterogeneity and time for a measurement. In figure 3 the results measured on a specimen with constant chlorine content of 4% in the cement matrix are shown for different resolution of the measurement. The measurements of the 4 areas of 5 cm by 5 cm are done with a point distance of 0.25, 0.5, 0.75 and 1.0 mm. In comparison the time for the measurement is presented in the diagram in figure 3, right.

The time for a measurement increases from 8 minutes for a resolution of 1 mm to 128 minutes for a resolution of 0.25 mm.

2.5 *Evaluation and calibration*

The evaluation of LIBS data is done by a LABVIEW based software which calculates for every element under investigation and for every point measured, the peak maximum in correlation to the underground signal. The result is an element map over the measured area which represents the colour coded intensity values per point. The software allows for differentiation between measurements performed on coarse aggregates and on the cement matrix. For example by evaluation of calcium content for each point measured.

To get quantitative results, a calibration is necessary. This is done by measurements on a set of

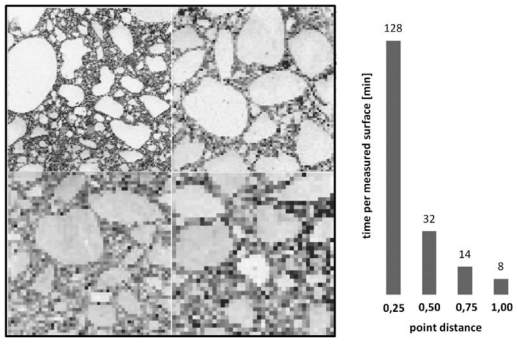

Figure 3. Left: Colour coded intensity of chlorine concentration measured on a concrete specimen (10 cm × 10 cm) with constant chlorine concentration of 4%. Darker grey means high chlorine concentration. There are for region of each 5 cm by 5 cm measured with 0.25, 0.5, 0.75 and 1.0 mm resolution. Right: Correlation between point distance and time for measurement.

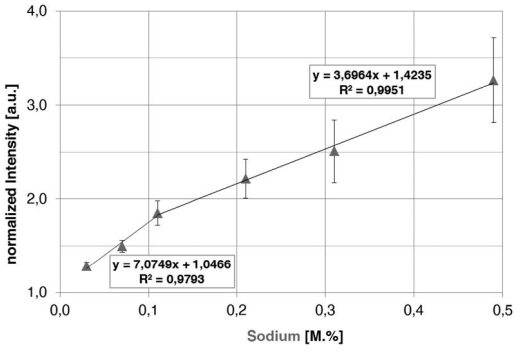

Figure 4. Calibration curve for sodium.

reference samples with known element content in a similar matrix. As an example the calibration curves for the evaluation of quantitative values of chlorine and sodium are shown in figure 4 & 5. It can be seen that the sensitivity for the evaluation of sodium is much higher compared to chlorine. There are linear correlations for chlorine concentration with different gradient in the region below and above 0.18%. For sodium there is a similar trend for the region below and above 0.11%.

3 RESULTS AN DISCUSSION

3.1 *ASR*

Alkali-silica reaction (ASR) may cause the degeneration of highway structures starting with crack formation and later spalling of the concrete surface.

In Germany, hundreds of kilometres of highways are potentially affected, which causes severe restriction in traffic and the need for extensive funds for reconstruction.

ASR is initiated if reactive aggregates, alkalis and water are present in the concrete. One source of alkalis,

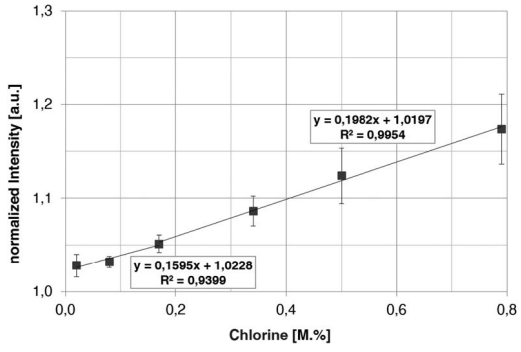

Figure 5. Calibration curve for chlorine.

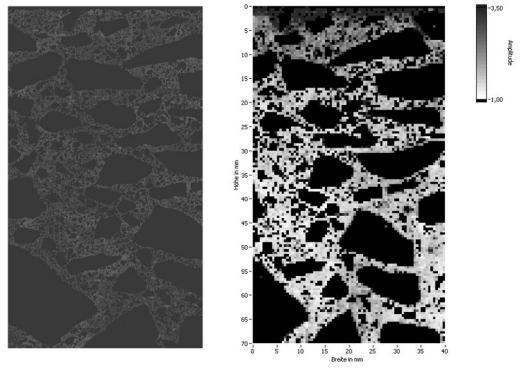

Figure 6. Comparison of evaluation of sodium concentration in a concrete core (40 mm × 70 mm) by μ XRF (left) and LIBS (right). The aggregates are excluded and marked by black colour. The sodium content is marked by grey colour. Darker grey means higher sodium concentration.

in most cases sodium, is the de-icing salt used extensively during winter time in the last decades. With LIBS it is possible to detect the ingress profiles of sodium. These can be used to estimate the endangering of highways and also to evaluate the effectivity of performance tests used to evaluate aggregates.

3.2 *Comparison μXRF – LIBS*

One technique available in laboratories to investigate building materials is μXRF. This technique works well to measure ingress profiles of chlorine. But for lighter elements starting with sodium the sensitivity is, due to the principle, limited. In contrast LIBS is sensitive for sodium detection (see figure 4). Both methods may in principle consider the heterogeneity of the material. In figure 6 a comparison of evaluation of sodium concentration in a concrete core by μXRF (left) and LIBS (right) is presented. The aggregates are excluded and marked by black colour. The sodium content is marked by grey colour. More intensive grey means higher sodium concentration.

Only in the LIBS results can the sodium ingress be seen. The sensitivity of μXRF is not sufficient.

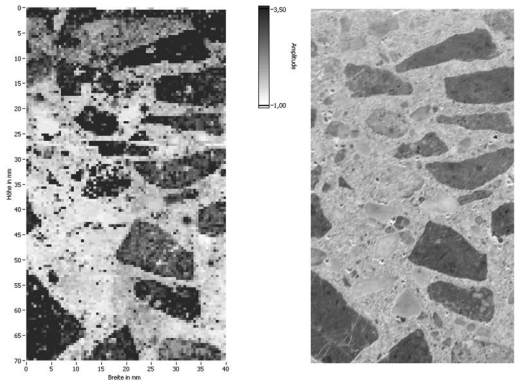

Figure 7. Left: Photo of measured cross section of concrete core. Right: Sodium concentration in a concrete core (40 mm × 70 mm) measured by LIBS (right). The sodium content is marked by grey colour. Darker grey means higher sodium concentration. The large aggregates are indicated by sodium concentration.

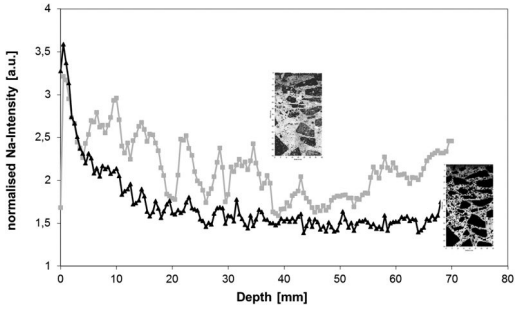

Figure 8. Comparison of ingress profile of sodium measured on the cross section of the concrete core shown in figure 7, left. Grey curve obtained by consideration of all measurements. Black curve obtained by excluding measurements on large aggregates.

3.3 *Considering Na – containing aggregates*

If all measurements, including those performed on large aggregates, are considered, the result shown in figure 7 (right) is obtained. The sodium content is marked by grey colour. More intensive grey means higher sodium concentration. Comparatively high sodium concentrations can be detected within the large aggregates. In figure 7 (left) a photo of the measured cross section of the concrete core is presented for comparison.

If the ingress of sodium through the pore structure of the cement matrix is to be evaluated the concentration of sodium in the large aggregates has to be excluded. Standard procedures which cut the core in slices of 1 cm thickness, mill it and investigate the powder are incomplete in such cases.

Only the exclusion of large aggregates (see figure 6, right) leads to an exact ingress profile of sodium. In figure 8 for both cases – consideration of all measurements and exclusion of measurements on large aggregates – the ingress profiles of sodium are presented.

The concentration values for a given depth are obtained by calculating a mean value for each line measured on the core. Simply the black curve in figure 8 is obtained by excluding the measurements on large aggregates and presents a clear ingress profile.

4 CONCLUSIONS

The following conclusions may be drawn from the investigations exemplarily shown above:

- LIBS is able to measure directly on the sample surface. An optimum sample drawing is given.
- The method is able to measure the heterogeneity of the material. The measured ingress profile of sodium is correlated with the cement matrix.
- LIBS is able to detect light elements which may be difficult by XRF.
- LIBS allows fast measurements with savings in time and manpower.

The LIBS technique is currently on the step from pure laboratory applications to an in-situ on-site analysis technology. At BAM a Fibre-LIBS-System in combination with a scanner for the on-site application on building materials is under development. Potential applications are the quality assurance of hydrophobic coatings or the quality assurance during removal of chloride contaminated concrete in parking garages. This can also lead to saving of the work force due to the fact that the polluted concrete is fully removed but not more.

The setup of rules and standards is the next step to establish LIBS as a standard procedure for chemical investigations of building materials.

ACKNOWLEDGEMENT

The presented results are partially obtained in collaboration between BAM and HTW Berlin, Fachbereich 2 – Civil engineering, Prof., Dr.-Ing. E. Genzel during supervision of a master thesis.

REFERENCES

Eichler, T., B. Isecke, et al. (2010). “Investigations on the chloride migration in consequence of cathodic polarisation.” Materials and Corrosion 61(6): 512–517.

Hahn, D. W. & N. Omenetto (2012). “Laser-Induced Breakdown Spectroscopy (LIBS), Part II: Review of Instrumental and Methodological Approaches to Material Analysis and Applications to Different Fields.” Appl. Spectrosc. 66(4): 347–419.

Noll, R., Laser-induced Breakdown Spectroscopy – Fundamentals and applications, 2012, Springer Verlag, Berlin Heidelberg.

Ralchenko, Yu., Kramida, A.E., Reader, J. and NIST ASD Team (2008). NIST Atomic Spectra Database (version 3.1.5), [Online]. Available: http://physics.nist.gov/asd3

[2009, April 29]. National Institute of Standards and Technology, Gaithersburg, MD.
Weritz, F., S. Ryahi, et al. (2005). "Quantitative determination of sulfur content in concrete with laser-induced breakdown spectroscopy." Spectrochimica Acta Part B-Atomic Spectroscopy 60(7–8): 1121–1131.
Weritz F, Schaurich D, Taffe A, and Wilsch G (2006) Effect of heterogeneity on the quantitative determination of trace elements in concrete, Anal Bioanal Chem 385: 248–255.
Wilsch G, Weritz F, Schaurich D, and Wiggenhauser H (2005) Determination of chloride content in concrete structureswith laser-induced breakdown spectroscopy, Constr Build Mater 19:724–730.
Wilsch, G., D. Schaurich, et al. (2011). Imaging Laser Analysis of Building Materials – Practical Examples. Review of Progress in Quantitative Nondestructive Evaluation, Vols 30a and 30b 1335: 1315–1322. References in the text: Figure 1, Figures 2–4, 6, 8a, b (not abbreviated).

This page intentionally left blank

Repair and preservation of heritage structures, roman cement

This page intentionally left blank

Concrete Solutions – Grantham et al. (Eds)
© 2014 Taylor & Francis Group, London, ISBN 978-1-138-02708-4

Wotruba Church and Cologne Opera: Aspects of concrete aging

M. Ban
Institute of Conservation and Restoration, University of Applied Arts Vienna, Austria

ABSTRACT: In the field of modern and contemporary heritage, the lack of knowledge particularly concerning the issue of aging concrete presents a new conservation challenge, requiring thorough analyses of stability and damage using non- and low-destructive examination methods. The comparison between the massive concrete blocks of Vienna's Church of the Holy Trinity (1974–1976), better known as the 'Wotruba Church', and the slender elements of the Opera house in Cologne (1954–1957) well illustrates the different aspects of preservation treatments. In the case of the Wotruba Church, the examination methods focus on academic research and the continually arising questions on how to approach conservation. In contrast, the Opera's condition analysis was adapted to define whether or not the concrete is worth being restored. The findings of both examples provide a basis for a well-founded discussion concerning further measures and development of a sustainable and durable treatment strategy.

1 OBJECTS OF EXAMINATION

1.1 *The Church of the Holy Trinity*

The two-storey church of the Holy Trinity, popularly known as the Wotruba Church, is a sacral sculpture built entirely of reinforced concrete (Fig. 1). The church is situated on a hilltop in Vienna's 23rd District, is 30 m long, 22 m wide and has a maximum height of 13 m. Designed and built by the sculptor Fritz Wotruba and the architect Fritz G. Mayr between 1974 and 1976 with its 152 massive concrete blocks cast in situ, it is an iconic example of modern Austrian heritage (Feuchtmüller 1977).

A multiphase construction was undertaken, which is visible in the three kinds of concrete used: dark grey at the base zone, yellowish in the middle section and light grey in the upper part of the building's structure.

A visual inspection of the concrete gave the following results regarding exposure to the elements: the cement skin was partly weathered, the edges were eroded, there was efflorescence at the underside of the concrete blocks, microbiological growth and consequent surface corrosion. Nevertheless, those occurrences can be described as effects of natural aging or the development of patina. Further visible damage included cracks, leaking joints, minor deformations and limited surface spalling.

Figure 1. Wotruba Church. View from north-east side.

The natural aging and development of patina is often taken as an indication of structural damage. Furthermore, 12 years after construction reports were published indicating the church's poor condition (BPV Test Report-PZG 88.068, unpubl.). To conclude the debate on the environmental impact on the building's structure the Vienna's archdiocese accepted a suggestion by the Institute of Conservation and Restoration of the University of Applied Arts to conduct a thorough stability and damage analysis using non- and low-destructive examination methods (Ban 2011). Concrete surface strength, the cover, position, depth and diameter of the reinforcement, capillary suction and air permeability were determined at representative locations inside and outside. Low invasive examinations like carbonation depth and concrete microscopy were analysed on cores drilled from areas both exposed to and protected from weathering. Additionally, the temperature and relative humidity inside and outside the structure were monitored and documented over a period of one year.

1.2 *The Cologne Opera*

The Colognes Opera designed by Wilhelm Riphahn, inaugurated in 1957 and a listed building since 1989, was built in the manner of Brutalism and therefore authentically composed of stone, brick veneer

Figure 2. Construction site of the Cologne Opera.

and concrete. The 35 m high pylon-like towers have approximately 3000 m^2 of concrete surface (Fig. 2).

The concrete was poured on site and shows the imprint of the formwork. Presumably it was originally roughly finished and exposed. Shortly after the construction it was covered with white emulsion paint. Regardless of the protective cover, extensive damage is visible on the structurally relevant columns and statically irrelevant walls. Damage on the façade has occurred where corrosion to steel reinforcement has caused spalling of the concrete cover, cracks of enormous lengths spreading vertically on the walls, opened construction joints, cavities as well as recent deterioration of former repair measures. Furthermore, large honeycombing in the concrete of the statically relevant columns is apparent.

The possibility of preservation of the concrete towers was questioned. The architect in charge HPP-Hentrich-Petschnigg & Partner and the restorer Götz-Lindlar BRB took the responsibility and risk for executing an intensive investigation of its surface condition from 2011 to 2012. Assessments of the concrete quality were determined through examinations of optical microscopy, carbonation depth, adhesive pull strength and localisation and colour mapping of reinforcement, cracks, secondary repairs as well as voids and flaws on 2900 m^2 concrete surface. Additionally micro chemical tests and binder analysis of the emulsion paint were made. The given material was also tested for its carbonation resistance in order to differentiate hydrophobic and exposed concrete carbonation depths.

In contrast to the Wotruba Church it was possible to work more invasively: therefore more measurements were undertaken in terms of the carbonation depth. The preparatory work of the future rehabilitation for the workers included marking the damage directly on the painted surfaces, which would anyway be removed necessarily for restoration. The structure is now being restored and renovated for the reopening of the Opera complex planned in 2015.

2 ANALYSIS AND INVESTIGATION PROGRAM

2.1 *Wotruba Church*

The following examination methods were used on the Wotruba Church to measure the yellow and the grey concrete:

- Water absorption tube test according to Karsten (Safeguard Europe Ltd.). In total 69 measurements were carried out on all four façades and the roof.
- Concrete surface strength with Schmidt Hammer NR in conformity with ON EN 12504-2. The final interpretation was carried out according to the average values of 61 samples, measured on all four facades and the roof.
- Micro structural analysis with optical-, polarised light-, incident light- and fluorescence microscopy with a Leica IM 500 and Leica ORTHOLUX II POL-BK conducted by Bruno Misteli (Holcim Group Support Ltd, CH) and Christine Merz (Consulting on Cement and Concrete TFB, CH). Four drilled cores where taken from the roof of the light grey concrete. Taking samples from the façade where the yellow concrete was applied was not permitted.
- The carbonation depth was measured with a 0.1% phenolphthalein indicator according to present standards of the ON EN 14630. The analysis was carried out on four cores drilled from the roof area; one protected from and three exposed to weathering. The same samples were afterward analysed by microscopy.
- Mapping and localisation of steel reinforcement with a Hilti PS 200 Ferroscan. In total 118 scans (60 x 60 cm) were carried out on all four outside façades and the roof area.
- Air Permeability in conformity with SIA 262/1, with the permeability tester from Torrent (Proceq SA). The concrete surface humidity was measured with a Tramex CME 4. The investigation was carried out with the support of Roberto Torrent (Materials Advanced Services, AR) and Frank Jacobs (Consulting on Cement and Concrete TFB, CH). 38 average values were performed on all four outside walls as well as on the roof area and in the interior.
- Climate analysis with relative humidity and temperature data logger (Rotronic HW3). The measuring interval was 60 minutes over a period of one year. The measuring sensors were positioned on 1 cm distance from the concrete surface.

2.2 *Cologne Opera*

The analysis and investigation program was measured on all weathering sides on the columns and the walls:

Colour mapping and localisation directly on the surface of steel reinforcement with a Proceq Profoscope Rebar Locator. Green stands for intact areas and a concrete cover >20 mm, orange marks potential area for damage and a concrete cover of 10 mm to 20 mm

and red classifies concrete cover <10 mm, mostly already damaged areas. Other damage like cracks, secondary repairs newly damaged, voids and flaws were visually located and mapped directly on the surface. Digital mapping and documentation was carried out with the software Metigo MAP, Fokus GmbH Leipzig Germany.

Petrographic microanalysis of thin sections of two concrete cores (method TI-B 5 modified) conducted by Peter Laugesen, report case no.: 12-073, Pelcon Materials & Testing Denmark. One core was taken from the walls and one from the statically important columns.

Petrographic microanalysis of thin sections of two concrete cores carried out by Farkas Pintér, report case no.: 356–357/12 National Heritage Agency, Natural Science Laboratory Vienna. Both cores were taken from the walls exposed to different weather sides.

Adhesive pull-off strength on site in conformity with Rili-SIB (German Committee for Structural Concrete) in cooperation with Wissbau Consulting Engineers. Disk diameter 50 mm, adhesive media MC Klebeset HF/MC Quicksolid from MC- Bauchemie (Temp. 15°C and 2 hours hardening time). A total of 12 tests were undertaken on the wall structure.

The carbonation depth was measured with a 0.1% phenolphthalein indicator according to present standards of the ON EN 14630. In total 83 measurements were undertaken all over the buildings structure.

Micro chemical tests and binder analysis of the emulsion paint with solubility and fire tests. Optical microscopy on cross sections with Nikon Eclipse ME 600 in cooperation with Lisa Gräber, University of Applied Arts Vienna. In total four samples were taken and analysed from the walls.

Test report case no.: 1-27346 of carbonation resistance of coated (hydrophobic treated) and exposed concrete in conformity with ON EN 13295 (2004) carried out by Materialprüfanstalt Hartl, state-accredited testing and inspection body in Seyring Austria. 56 days in a CO_2 incubator with a carbon dioxide of $1.0 \pm 0.1\%$, temperature of $20 \pm 2°C$ and relative humidity of $70 \pm 5\%$. Afterwards the carbonation depth was measured with a 0.1% phenolphthalein indicator.

3 RESULTS AND DISCUSSION

The investigation outcomes in case of the Wotruba Church have shown that the weathering was more pronounced on the north side of the buildings structure than on the other sides, which were protected by trees. The north façade stays humid longer, which results in a more extensive and faster development of all damage occurring in relation with humidity. The remaining sides show values comparable and acceptable for a historic concrete that was exposed to intensive weathering for about 40 years (Tab. 1).

Additionally the water adsorption showed strongly raised values on the north side with a water receptiveness of >2.0 kg/(m^2 h$^{0.5}$). The remaining sides showed analogue values from 0.5 to 1 kg/(m^2 h$^{0.5}$), which can be classified as water-resistant. Regarding historic concrete values up to 1 kg/(m^2 h$^{0.5}$) are satisfactory and there is no need for restoration or conservation (Holzinger 2005).

Table 1. Wotruba Church, examination methods and results.

Examination	Average results
Concrete cover	20–45 mm
Concrete strength	25–45 N/mm^2
Water adsorption	0.5–1.0 kg/(m^2 h$^{0.5}$)
East, south, west	1.7 – 3.7 kg/(m^2 h$^{0.5}$)
North	
Air permeability	–kT [$\times 10^{-16}$ m^2]
Climate analysis	60–80 (May-Sep.)% RH
Optical microscopy	5–10 Vol.-% air void
	0.50–0.60 w/c ratio
	350–400 kg cement/m^3
Carbonation depth after	15–18 mm exposed
38 years	05–20 mm exposed
	45–50 mm protected
	10–15 mm exposed

The concrete surface strength showed the lowest value of 25.5 N/mm^2 and the highest of 48.1 N/mm^2. Most values were between 30 to 35 N/mm^2, which can be classified as a present concrete strength class of C 25/30.

The micro structural analysis revealed a high quality concrete; well compressed, homogeneous and rich in binding material. The binding material appeared to be in the range from 350 to 400 kg of cement/m^3 concrete and was a sulphate-resistant, well-ground blast furnace cement and would now be classified as a B CEM III. The air void content reached from 5 to 10 Vol.-% and indicated the use of air-entraining admixtures and concrete plasticizers. The pore diameters lie between 20 and 300 µm. The given air void content is an indicator for a higher capillary porosity but besides that it implicates freeze-thaw durability. The w/c ratio lay in between 0.50 and 0.60; but tended towards 0.60.

The carbonation depth was up to 50 mm in weather-protected areas and up to 20 mm in exposed areas. A maximum of only 5% measured fields with critical depths of reinforcement (<10 mm) show that the construction was carefully planned and carried out by competent practitioners.

The reinforcement could be recognised as a TOR-Ribbed steel due to spalling. The measurements of the reinforcement localisation showed rebar diameters of 6 mm and 8 mm, and a mesh 20 cm x 20 cm wide.

The air permeability values were unfortunately unusable; the data gained showed extremely high kT [$\times 10^{-16}$ m^2] values, not comparable with standard values. However, the values received indicated that the yellowish concrete was more permeable than the grey concrete. Even though it was not possible to take examples from the façade, where the yellow concrete was

Table 2. Opera Cologne, examination methods and results.

Examination methods	Average values on columns	Average values on walls
Concrete cover	11% of	13% of
<10 mm	1100 m^2	1800 m^2
Concrete strength	35–55 N/mm^2	25–30 N/mm^2
Optical microscopy	0.50–0.55	~0.65
w/c ratio	2–3 %	3–4%
Air void content		
Pull-off strength	–	3.39 N/mm^2
Carbonation depth	1–3 mm	1–11 mm
after 57 years	max. 10 mm	max. 20 mm
Micro chemical test	emulsion paint, moderate bond	emulsion paint, good bonding

applied, it is known from the architect in charge Fritz G. Mayr that unintentionally different aggregates with high clay content were used. Nevertheless, the concrete cover of the yellow concrete had excellent values, not less then 2 cm, in most cases minimum 3 cm to 4 cm. While the grey concrete showed strong variation of the concrete cover ranging from 0.5 cm to 12 cm.

Three data loggers were positioned in the interior of the church and one on the roof. The outside climate analysis showed that the most critical period, where the carbonation process progresses rapidly (approximately 50–80% RH and higher temperature), occurs from mid May to early September (Hartl 1999). The values from the inside showed that the south side has critical values from May to October. This is due to direct exposure to sun, lack of air circulation and the absence of ventilation. The other sides shows critical values only in August.

Moreover, samples of materials commonly used in the preservation of historical-architectural heritage for crack and joint closure were artificially weathered. They were exposed to temperatures up to 100°C, UV- and infrared light, freeze-thaw cycles (−20°C/+20°C water saturated for 12 hours each) and determination of thermal compatibility (part 2: Thundershower cycling; thermal shock) based on ON EN 13687-2:2002. Materials used for filling joints were additionally tested for adhesive pull strength based on Rili-SIB-2001 (German Committee for Structural Concrete).

For crack closure, the product Oxal VP III (MC Bauchemie) was chosen, as it showed the best weathering resistance in the tests and a good condition by now. Unfortunately after the application, both chosen materials for joints Betofix R2 (Remmers) and Oxal SPM (MC Bauchemie) revealed flank cracks after the first winter.

In the condition analysis of the Opera in Cologne, all the obtained values needed to be differentiated between the statically relevant concrete columns and statically irrelevant walls (Tab. 2).

Throughout the colour mapping of 1800 m^2 surface of the walls, damage appeared in a range of ± 20 %. The same damage was seen on the concrete columns

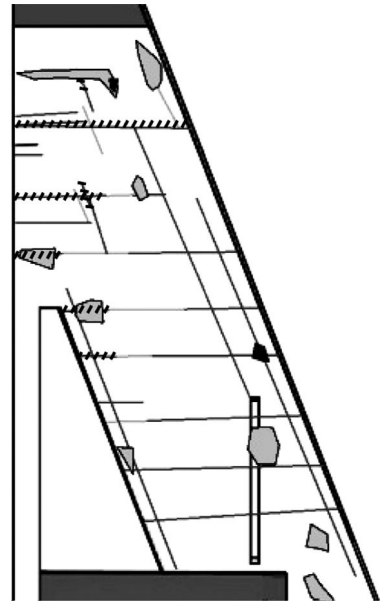

Figure 3. Example of the mapped column concrete surface.

with a measured surface of nearly 1100 m^2 and a ± 16% damaged area. These damaged areas involved insufficient concrete cover and other deterioration like cracks, secondary repairs newly damaged, voids and flaws. All of them were marked directly on the surface as a preparatory work for the restoration (Fig. 3).

Even though the damage was extensive it is argued that the building structure is worth being restored. Most damage occurs on spots with insufficient concrete cover (<10 mm) where the reinforcement was placed deficiently in the cast. Most of them were already restored during former renovations with local intervention. By now these secondary repairs have deteriorated and need to be restored again.

The original building plans showed a concrete compressive strength class of a B 300, today classified as C 25/30. Partially, the walls are made out of standard concrete C 20/25. The concrete had an average density of 2,20 [kg/dm^3] measured in hardened concrete. Higher compressive strength measured from cylindrical concrete on the columns showed an average threshold of 35 to 55 N/mm^2(Cologne University of Applied Sciences, unpubl.).The values gained show that a better concrete quality was achieved on the statically relevant columns.

The concrete of the walls and the columns, which had been analysed, was composed of a similar material: relatively coarse-grained Portland cement free of admixtures and additives and rounded natural sand and stone (Pintér, unpubl.). The sand (0–4 mm) consisted of quartz, feldspar, granite, sandstone, chert a.o. The aggregates (max. 20 mm Ø) consisted mainly of quartz, sandstone and claystone. The sample of the concrete columns analysed showed a w/c ratio from 0.50 to 0.55 with a carbonation depth from 1 mm to 3 mm. While the analysed concrete of the walls

showed a w/c ratio of ~0.65 with a carbonation depth of 10 mm. The columns had a 2 to 3% and the walls a 3 to 4% air void content. The alkali silica reaction did not cause any detoriation. No indications of frost damage, saturation or leaching were found (Laugesen, unpubl.).

The explanation for the higher w/c ratio could lie in the construction methods back in 1954 where the usage of admixtures and additives in concrete was rather unusual. To compensate the flow properties a higher amount of water was added.

The pull-off strength of 12 measurements showed an average value of 3.39 N/mm^2 (Ban & Auberg, unpubl.). These values are considered very good for a historical concrete and todays standard concrete repair systems, which need a minimum value of 1.5 N/mm^2 for structural and 0.8 N/mm^2 for non structural repair.

The carbonation depth of approximately 1 mm to 3 mm and a maximum of 10 mm were measured on 20 representative areas on the columns. The carbonation depth on the walls was highly uneven with a minimum of 1 mm to a maximum of 20 mm, which was tested on 63 areas. These results seem appropriate for a historical concrete with the given quality and w/c ratio. It's not clear what influence the emulsion paint has had on the carbonation depth. Still, it can be assumed that the carbonation process was slowed down. The values gained in the columns can be classified as optimal for a concrete that is exposed to weathering about 60 years. The carbonation depth of the walls appears rather usual.

The reinforcement diameter/mesh size of the walls structure showed a longitudinal reinforcement of a common 10 mm/15–20 cm and a transverse reinforcement of 8 mm/33 cm. The columns showed a transverse reinforcement of 10 mm/20 cm and approximately 3 to 4 diagonal main reinforcements, which had a diameter of 26 mm to 32 mm. The reinforcement was a BSt III S (Steel IIIb TOR-ribbed steel) and IVa Nori-Steel. This was identified on the areas where the reinforcement was visible and documented in original building plans.

The micro chemical tests showed a standard white emulsion paint with pigments of titanium dioxide. The paint was applied in four layers and two phases, which can be seen on the boundary (Fig. 4).

The first phase of appliance happened shortly after the construction while the second two layers were applied during the restoration work in 1980ies. The bonding on the covered surface of the walls is good as opposed to the one on the columns, which is moderate to partially poorly adhesive (Gräber & Ban, unpubl.).

The present concrete shows a relatively good carbonation resistance, exposed and as well hydrophobic, which can be seen in the extract from the test report in Table 3. The hydrophobic samples show slightly higher water ingresses (Hartl GmbH, unpubl.). These values differ from the theoretical grounding of a water-repellent coating and need to be further investigated.

It is still not decided if the concrete of the Opera will be covered with paint or left exposed with a hydrophobic treatment. It will be decided after the repair and depending on its resulting aesthetical appearance.

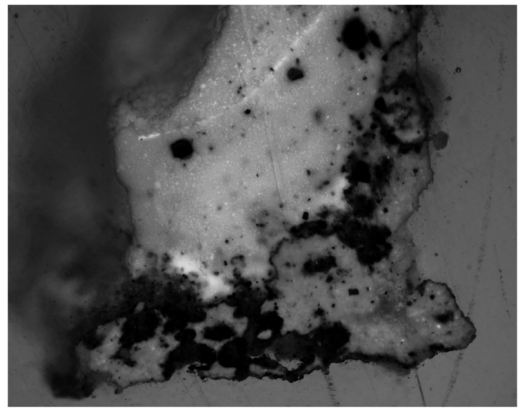

Figure 4. Optical microscopy at the magnification of 5 times showing the multi-layered emulsion paint with dirt particles.

Table 3. Extract from the report case no.: 1-27346 of carbonation resistance of cores taken from the wall.

Carbonation resistance	mm
Exposed concrete	from 2–8 to 5.9–9
Exposed concrete	from 5–9 to 8.2–13.3
Hydrophobic concrete	from 2–6 to 6.1–9.3
Hydrophobic concrete	from 4–10 to 5.4–13.5
Hydrophobic concrete	from 3–8 to 5.6–13.9

4 CONCLUSION

The chosen combination of non- and low destructive test methods provides useful values to determine the concrete's condition in both cases. One approach is designed for the practice to demonstrate and locate the damage that needs to be repaired with an additional result of an exactly calculated tender budget.

The other method of preservation is through an academic research with its less invasive examination methods meaning minimal interventions; this was conducted on the Wotruba Church.

In the abovementioned example, an argument arose whether the microbiological growth, found on the concrete, should be removed or not. The removal would only initiate a new settlement of microorganisms of a much more aggressive nature than the previous inactive ones. Furthermore, cleaning entails damaging the surface because it involves a removal of the remaining cement skin, which results in a more accelerated destructive process.

Selected care and maintenance procedures on a few problematic zones have to be favoured. Due to water seepage, the leaking joints need constant renewal due to persistent recurring damage and the closure as well

as monitoring of cracks. In 20 to 30 years an identical examination program should be carried out for an evaluation and comparison of values, especially the parts which have not been included in the present examination program.

After monitoring it was concluded that the weather-induced alteration of the concrete's surface, such as microbiological growth, colour changes, erosion of edges and corners, localised flaking of the concrete cover, surface cracks, etc., are not an indication of structural damage, but are merely evidence of concrete's natural aging and development of patina. Since the concrete analysed is homogeneous, well compressed and rich with binding material, a regular 10-year monitoring of the outside of the building, particularly of the north façade, should be conducted to prevent further unnecessary treatments. The structure did not require restoration nor conservation, despite the detection of two different concrete qualities, one having high clay content.

A continuation of research analysis is needed for a conclusion concerning the interactions between repair and historical materials, especially suitable for different historical concrete mix designs. The preservation strategy was possible due to the test results revealing the overall relatively good condition of the building. Serious damage is not expected in the near future, and can be avoided by preventive care and maintenance.

In the case of the Opera, the problem of localised treatments was never an issue, it was clear that here an all-over restoration and renovation was required. The concrete towers needed to be either restored or reconstructed even though the current concrete structure and its present condition could survive without any restoration; this particular aspect never stood to debate. The only question is whether it is possible to restore the structure without damage occurring in the near future. However, the quality of the restoration depends on the firms selected to undertake the work and the construction supervision. It was argued that a localised repair with the commonly used Polymer Cement Concrete II repair mortars with a bonding course according to ZTV-ING (additional technical terms of contract and guidelines for civil engineering works), can be performed. Premixed dry mortars are commonly used in restoration of architectural heritage despite the different material properties the ready-mixed mortars and the original material have. This is due to the liability risk one has to take by developing and implementing a special concrete composition.

Before a treatment strategy and tender were undertaken all preparatory measures like removing the paint, local repairs etc. were tested on sample surfaces.

A combination of condition analysis and preparatory tasks for the workers was in this case a cost and time effective approach to assessing aging concrete structures. Currently the concrete towers are being restored without any conclusions on whether or not a protective coating is necessary.

More research needs to be carried out in the field of protective coatings, especially the transparent coating systems that are suitable for visible concrete surfaces. Most of the transparent systems are not aging well and turn opaque with time. Also more studies in hydrophobic treatments for different concrete mixes design need to be made.

In the case of the Opera it was necessary to accept the fact that a historical surface, with its imperfections, would occasionally suffer from local damage despite restoration.

For the Wotruba Church it proved that restoration with minimal interference, which takes into consideration the artist's and architect's desire for a process of natural ageing of the surface, is a different but justifiable approach to preserving a structure.

ACKNOWLEDGEMENTS

The author wishes to express gratitude to following partners: Bruno Misteli (Holcim Group Support Ltd, CH) and Christine Merz (Consulting on Cement and Concrete TFB, CH) for executing and evaluating the microstructural analysis. Roberto Torrent (Materials Advanced Services, AR) and Frank Jacobs (TFB) for the support in performing and evaluating the air permeability measurements. Walter Strasser (TPA, STRABAG SE, AT) and Wolfgang Schwarz (CAS Composite Anode Systems GmbH, AT) who helped with my Master's thesis. Katja Sterflinger (University of Natural Resources and Life Sciences Vienna) for investigating the microbiology. After all I'm most grateful to my professor Gabriele Krist. The Institute of Conservation and Restoration, University of Applied Arts Vienna, carried out the work concerning the Wotruba Church.

HPP- Hentrich-Petschnigg & Partner Architects, Götz- Lindlar Büro für Restaurierungsberatung and Wissbau Consulting Engineers for the pleasant cooperation. Farkas Pintér (National Heritage Agency Austria) and Peter Laugesen (Pelcon Materials & Testing Søborg) for executing the petrographic microanalysis. Lisa Gräber (University of Applied Arts Vienna) and Materilalprüfanstalt Hartl (Seyring Austria) for executing the micro chemical tests and carbonation resistance. The condition analysis of the Opera in Cologne was accomplished in private commission.

Peter Urbanek, Luka Sola and Steffi Winkelbauer for proofreading and generally supporting this paper.

Parts of this publication have been previously published under the title: "Aspects of conserving exposed concrete architecture with Wotruba Church as an example", in print for PRO 89: RILEM International workshop on performance-based specification and control of concrete durability, held from 11 to 13 June 2014 in Zagreb, Croatia (RILEM Publications SARL).

REFERENCES

Ban, M. 2011. Aspekte zur Erhaltung von Sichtbetonarchitektur am Beispiel der Wotruba Kirche. Vienna: University of Applied Arts.

Ban, M. & Auberg, M. 2012. Adhesive pull-off strength on site. Cologne: unpublished report, Ban in cooperation with Wissbau Consulting Engineers.

Cologne University of Applied Sciences. 2009. Report case no.: 49/09. Cologne: unpublished report, Faculty 06- Civil and Environmental Engineering, Laboratory for building materials and materials testing.

Cologne University of Applied Sciences. 2010. Report case no.: 09/10. Cologne: unpublished report, Faculty 06- Civil and Environmental Engineering, Laboratory for building materials and materials testing.

Feuchtmüller, R. et al. 1977. *Wotruba: die Kirche in Wien Mauer*. Vienna: Herder.

Gräber, L. & Ban, M. Micro chemical tests and binder analysis of the emulsion paint with solubility and fire tests. Vienna: unpublished reports University of Applied Arts.

Hartl, G. 1999. Chlorid-Gehalt und Profil, Karbonatisierungstiefe. In Schwarz W. (ed.), *Korrosion von Bewehrungsstahl in Beto.* WTA-Schriftenreihe Heft Nr. 19: 18-31. Stuttgart: Aedificatio Verlag

Holzinger, F. 2005. *Behutsame Betonsanierung an historisch bedeutenden Bauwerken*: 140. Innsbruck: University of Innsbruck.

Laugesen, P. 2012. Report case no. 12-073, Petrographic microanalysis of thin section. Søborg: unpublished report, Pelcon Materials & Testing.

Materialprüfanstalt Hartl. 2012. Test Report (1-27346) of carbonation resistance in conformity with ON EN 13295 (2004). Seyring: unpublished report, Materialprüfanstalt Hartl.

Pintér, F. 2012. Report case no. 356–357/12, Petrographic microanalysis of thin section. Vienna: unpublished report, National Heritage Agency, Natural Science Laboratory.

Prüfbericht-PZG 88.068. 1988. *Erhebung des Ist-Zustandes – Sichtbetonflächen*. Bautechnische Prüf- und Versuchsanstalt (BPV) Lanzendorf. Wien: unpublished report, archive National Heritage Agency Vienna.

This page intentionally left blank

Concrete Solutions – Grantham et al. (Eds)
© 2014 Taylor & Francis Group, London, ISBN 978-1-138-02708-4

Corrosion condition evaluations of historic concrete icons

Gina Crevello
Echem Consultants LLC, New York, USA

Nancy Hudson
Robert Silman Associates, New York, USA

Paul Noyce
Axieom LLC, New York, USA

ABSTRACT: Corrosion condition assessments of historic concrete structures can provide the owner with invaluable information regarding the current condition of the structure, the factors contributing to the corrosion damage, and can also project when the structure may exhibit further material loss. This information is vital to be proactive in the repair process which is imperative to minimize loss to the structure. When dealing with a highly significant concrete structure, the investigative team is often faced with restrictive parameters limiting the amount of data which can be collected. This paper discusses challenges in preserving 'historic concrete' and provides four case studies of predictive corrosion condition assessments which were carried out to help in the decision making process.

1 INTRODUCTION

1.1 *Survey approach*

A corrosion condition evaluation of a concrete structure identifies the conditions which affect the long-term behavior of the concrete's performance over time within its given environment. The aim is to create a lifetime model of when the building will reach critical deterioration limit states and when the structure will require repairs. The analysis can also allow owners to plan for service life extension and obsolesce if necessary. With historic concrete buildings, the intended design life and desired service life are often many years apart. Historic buildings, defined in the United States as being 50 years or older (National Register of Historic Places), are almost always functioning beyond their intended service life.

A detailed Corrosion Condition Evaluation is a significant part of the evaluation process for aging concrete. The assessment procedure identifies deterioration factors, including physical, chemical, structural, mechanical and electrochemical damage, to incorporate into a risk matrix.

This holistic survey approach is multifaceted with a long term view on building performance. The final analysis includes the use of durability models to provide an understanding of future behavior, projected time frames to reach limit states and when the structure will see an increase in deterioration. This methodological approach allows owners to make informed decisions on the best repair choice for the life extension of the buildings.

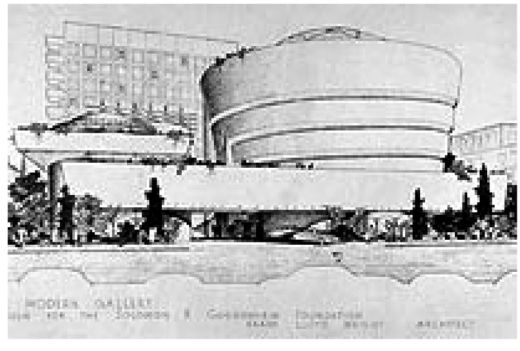

Figure 1. Rendering of the Guggenheim Museum, FLW. Credit Cohen.

Four case studies are used to illustrate the results of recent corrosion condition evaluations and durability models. Each structure assessed has historical relevance in American architectural history, each is a different form of construction, and designed by prominent American architects.

1.2 *"Preserving concrete"*

Reinforced concrete revolutionized construction of the 20th century. The material is ubiquitous and was at the forefront of modern technological advancements within the construction industry on an international platform. Structures once recognized as innovative and new, from beautiful in form, to brutalist and offensive, are now pending landmark designation.

As concrete buildings begin to age, structures greater than 50 years old which have been deemed architecturally significant now require conservation.

Particular challenges with historic buildings include landmark restrictions, such as minimizing interventions, preserving historic fabric, reversibility, and replacing materials in kind. This philosophy of minimal intervention is prevalent throughout the conservation community which is not in agreement with the general concrete repair industry. Industry professionals are challenged when treating landmark concrete as repairs do not follow a conservation philosophy.

Architectural concrete of the modern movement comprises individual structures to planned cities. The design, construction method, materials used and standards of workmanship employed in the creation of a concrete structure will vary enormously according to its date of construction. All these factors will affect the durability of the structure. (Macdonald 2003). Additionally, the location, climate, will play a part in the deterioration and subsequent repair. The ephemeral nature of the structure, the transitory attitude of the designer and the inextricable links between material, fabric, integrity and structure will need to be considered in the repair.

Current 'traditional repair' methods generally conflict with conservation standards. The attitude of treating 'historic' concrete structures as unimportant and disposable is all too prevalent. The requirements to provide interventions which may be invasive yet preserve the integrity of the structure create complex physical and philosophical challenges. The balance of conservation, authenticity of the original fabric, code compliance and minimizing deterioration must all be addressed. The final aim of an intervention should be to preserve the structure for future generations while minimizing impact and not compromising safety of the users or the stability of the structure.

Arguably the most detrimental mechanism of deterioration to concrete is corrosion of the reinforcing steel. It is not a question of if a concrete structure will corrode; it is a question of when it will corrode.

2 CORROSION CONDITION ASSESSMENTS

2.1 *Testing an icon*

Dealing with degradation and corrosion of concrete requires a multifaceted, holistic approach. Understanding concrete composition, material properties, additives, aggregates, types of reinforcing steel and construction details are key factors in the assessment. The corrosion evaluation process for historic, iconic concrete should embrace the tenets of the Secretary of the Interior Guidelines, English Heritage, Historic Scotland or the governing conservation body of the respective country. While standard practices outlined by the American Concrete Institute, the Corrosion Prevention Association, or the Concrete Society provide a baseline for surveys, they do not address the sensitivity required to assess historic concrete.

"The corrosion process for steel reinforced concrete can be simplified into a two-stage process namely, the 'initiation phase' and the 'propagation phase'. By definition the initiation phase is the time taken for conditions to become conducive to corrosion and the propagation phase is the period in which the accelerated corrosion of the steel reinforcement ultimately leads to rust staining, cracking and spalling of the cover concrete (BRE)." Once the structure has been evaluated and the team has an understanding on where the structure lies within a corrosion model, by ascertaining conditions prior to significant material loss, the architecture and engineering(A/E) team can determine root cause, modes of failure, time to failure, and a proactive approach to conservation versus a reactive repair of a failure. By approaching the subject building in a manner which looks at the overall pathology, one is required to assess the following topics while also understanding corrosion:

- History of construction materials
- Understanding the particular structures' building materials
- Type of construction
- Current conditions and
- Mechanisms of deterioration

In an historic structure, data collection may be limited. Often times the removal of concrete cores or the number of penetrations able to be made to the reinforcing steel during the test program is restricted. This provides a complex challenge to determine condition. Therefore, while the team is able to gather site data, the degradation models allow the team to forecast when interventions must be made.

Prior to choosing a repair option, best practices dictate that all factors of deterioration and current condition be analyzed.

2.2 *Deterioration models*

The models used by the authors to determine performance of the concrete are based upon the British Research Establishment's (BRE) "Residual Life Models for Concrete Repair. Chloride ingress and carbonation diffusion were utilized throughout the evaluation process when applicable to the structure and Crack Initiation Models were used in all instances. The authors further evaluated each structure with a customized risk matrix based on established industry thresholds. Thresholds conducive to corrosion were critically assessed, basing loss of material property being paramount to the evaluation process.

2.3 *Carbonation diffusion models*

Carbonation rates generally follow parabolic kinetics where the depth of the reaction on a sample or structure is proportional to the square root of time:

$$d = At^{0.5} \quad (1)$$

where d = carbonation depth, t = time and A is a constant, generally of the order 0.25 to 1.0 mm·year$^{-0.5}$ (Uhlig).

Where the investigation indicated that carbonation had not yet reached the depth of reinforcing steel, carbonation diffusion models were performed. The models were used to determine the time frame for carbonation to reach the embedded steel in good quality, sound concrete. As carbonation also occurs along cracks, the model was not applicable to locations where cracks, were present.

2.4 *Chloride profiles and chloride ingress models*

A model for predicting chloride ingress into concrete …aims at predicting the chloride profile C(x, t) after a certain exposure time t or at least the chloride content C at the depth of the reinforcement. The output is intended to be compared with a chloride threshold level which is relevant to reinforcement corrosion (Luping). The model assumes parameters which move the steel from corrosion initiation to propagation.

Chloride ingress models generally follow Fick's second law of diffusion, forming a chloride profile with depth into the concrete:

$$d[Cl^-]/dt = D_c . d^2[Cl^-]/dx^2 \quad (2)$$

where

[Cl-] is the chloride concentration, at depth x and time t and Dc is the diffusion coefficient (usually of the order of 10–8 cm2.s-1).

The solution to the differential equation for chlorides diffusing in from a surface is:

$$(C_{max} - C_{x,t})/(C_{mac} - C_{min}) = erf[(x)/(4D_c t)^{1/2}] \quad (3)$$

where Cmax is the surface or near surface concentration Cx,t is the chloride concentration at depth x at time t Cmin is the background chloride concentration erf is the error function.

Cmax must be constant which is why a near surface measurement is used, to avoid fluctuations in surface levels on wetted and dried surfaces.(Uhlig)

While the four structures presented are not at an obvious risk of environmental surface chloride attack testing for chlorides has allowed the team to determine if the structures is contaminated. Chloride profiles were taken from specific depths within the concrete cores and compared to the depth of the reinforcing steel. If the profiles follow typical diffusion patterns, time to reach chloride threshold at the reinforcing steel could be predicted.

2.5 *Crack initiation models*

Crack initiation models or "time to cracking" models presume that corrosion has initiated and the structure has moved into propagation. The models provide a time frame for micro-cracking failures. The actual corrosion rate is used and then the rate of section loss of the steel and subsequent the time to cracking is generated. The model presumes consistent and normal strength concrete cover without voids, porous or weak infill.

This model is solely concerned with modelling the effect of corrosion related cracking on the structure after corrosion initiation has begun.

The crack width at the surface up to 1mm is given by:

$$W = 0.05 + \beta(X - Xo) mm \quad (4)$$

Where:

β = 0.01 for top cast steel and 0.0125 for bottom cast steel

X = the steel decrease due to corrosion (microns) to produce crack width w

Xo = the steel decrease due to corrosion for crack initiation (microns)

And is given by

$$Xo = 83 + 7.4c/ø - 22.6fc,sp \quad (5)$$

Where

c = cover

ø = Steel width

fc,sp = tensile strength of the concrete

From this the time to cracking can be calculated if the corrosion rate and/or loss of section can be measured, determined or approximated. Ideally corrosion rate measurements over a period of time should be used to integrate the metal loss. For all test programs, the authors use the highest and average corrosion rates for each location tested.

2.6 *Risk matrix*

The risk matrix included the results of the half-cell potential, corrosion rate, electrical resistivity, depth of cover, depth of carbonation and percentage of chlorides by weight of cement in relation to the depth of reinforcing. The half-cell results were addressed in relation to ASTM C876 and also assessed with a ±25mV Δ between adjacent readings. Additional influencing material properties determined through laboratory analysis provided support to the concrete conditions. The categorization of the data was correlated with high, moderate, low and negligible corrosion risk. The matrix provides a comprehensive summary of all conditions that place the concrete structure at risk of further deterioration.

The overarching aim of the assessment is to determine:

- How the structure is performing,
- What are the key influences and modes of deterioration
- What is the current condition
- How will the structure continue to perform based on these conditions, and finally
- What are the available repair options

3 THE NEW YORK DOCK BUILDING

3.1 *History*

The New York Dock Buildings (160 Imlay and 162 Imlay) are located in Red Hook, Brooklyn, and were once key structures in the New York Dock Company's Atlantic Terminal (Brownstoner.com 2010). In 1912, the New York Dock Company began building two 460×80 foot (140.2 × 24.4 metre) concrete warehouses along Imlay Street, each six stories tall. The structures were built on the waterfront, placed alongside dock facilities and a rail terminal. These structures were one of the largest investments by the New York Dock Company at the time, and some of the largest concrete warehouses in the region.

The structures were designed by Maynicke & Franke, Maynicke was deemed a 'pioneer of the modern loft building' and designed many steel frame buildings listed as New York City landmarks today. The construction of the Dock Buildings took almost a year due to weather constraints, but was finally finished early in 1913 (Brownstoner.com 2010). The tenant, upon completion of 160 Imlay, was Montgomery Ward, founder of the first mail order retail business in the United States.

During World War I, the building became a government army base, as were many warehouses along the Brooklyn Waterfront. After the war, in 1919, the NY Dock Company leased the warehouse to the American Can Company. New York Dock consolidated its operations, but ceased functioning in 1983. The building has been unoccupied for decades.

Though not landmarked, the buildings represent early industrial concrete construction, were designed by a prominent New York firm, are relatively intact, and are associated with the pioneering figure of mail order commerce whose firm supported industrial concrete architecture. The change in use from abandoned warehouse to a deluxe mixed use 72 unit condominium complex instigated a condition survey prior to the repair and adaptive reuse project scheduled to begin in 2014.

3.2 *Construction*

160 Imlay is a reinforced concrete skeleton frame building with flat slab floors. The advantages of this construction type were 'repetitive layout, high ceilings, and high load capacity' (Friedman 2010). This building typology spread rapidly after 1905 and suited numerous requirements of warehouse and factory structures. The proliferation and speed of construction meant that the concrete warehouse is not often viewed as iconic.

The construction is similar to a Hennebique system. There is dense reinforcing at the base of the beams, with diagonal tie straps connecting upper and lower steel. The reinforcement utilized in the construction was square. The use of the concrete frame allowed for masonry or glass infill between the concrete spandrel beams and columns.

A Monument to the Vision of the Mail Order Pioneer

IT is part of the purpose of this advertisement to attract a high type of employees to our institution.

With the rapid expansion of Mail Order business comes the need for men and women with ambition and energy enough to step into the constantly increasing responsible positions.

What we ask is that employees make a study of mail order merchandising—from the bottom up.

Practically every executive of this institution was promoted from the ranks.

Forty-two years ago the late A. Montgomery Ward conceived the idea of Mail Order merchandise.

In those days such methods were unheard of. They were not considered practical—so he was laughed at—criticized—interfered with. But he hung on—persevered. George R. Thorne was an early associate and together they developed the first real Mail Order business in America.

From a few small rooms on a back street of Chicago, the business steadily grew into a national institution employing over six thousand people in five different distributing plants throughout the United States.

Our New York home is three years old—a fitting Eastern monument to the mark of the men who made it possible.

Like our various other plants it is a model of enthusiasm and loyalty. The well-being of every employee is given careful attention—and to this end we provide good wages, hours that are reasonable, and conditions that are pleasant. We provide generous vacations with pay, and the employees have a Mutual Benefit Association which pays sick benefits and death benefits and encourages thrift.

We believe an institution is merely the reflection of the men and women it employs. By standing our organization on RIGHT within, we make it satisfactory to our customers.

MONTGOMERY WARD & CO., Imlay and Bowne Streets

Ad from "Pictoral History Of Brooklyn", 1916. Published by Brooklyn Eagle.

Figure 2. New York Dock Building shortly after construction. "A Pictorial History of Brooklyn, 1916".

The slabs were constructed of a normal weight Portland cement concrete with no air entrainment and no supplementary additives. The coarse aggregate was fine grained natural gravel and the fine gravel was awell graded siliceous natural sand (Highbridge 2012). The concrete was highly permeable, with high capillary porosity. Poor compaction was identified at the base of the slabs.

The slabs were reinforced with a 1/4 inch diameter steel mesh near the base of the slabs. This mesh varied in depth, from no cover to 1 1/2 inches (38mm) of concrete cover, from the base up. The ground floor and roof slabs had additional square reinforcing bars. Reinforcing in the structural elements varied in diameter (1/2″ to 1″ – 13mm and 25mm) and spacing, but was consistent throughout the structure. The internal column steel radiated into the slabs, creating a 'mushroom' floor system at lower levels.

3.3 *Condition assessment*

The New York Dock building was constructed 101 years before the survey and was maintained for the majority of the years in service. The corrosion condition survey concentrated on the floor slabs and roof slabs for the installation of a roof-top pool, load capacity for change of use, and where lack of weather proofing led to ponding on the floor slabs.

With no weatherproofing since the 1990s and with waterfront exposure, corrosion initiation had begun long ago to the building envelope. While water had accumulated on the floor slabs, and the exterior envelope had visible losses, the majority of the inner structure was in fair condition for such an early example of concrete construction. Approximately 5% of the surface area was tested in-depth for corrosion rate, corrosion potential and resistivity. Of these selected test locations, the corrosion data revealed that 40% of the area was at a high risk of corrosion based on ASTM C876, and that 32% of the corrosion rate data was in the medium (28%) to high range (5%). Resistivity values varied greatly with readings correlating with high rates of corrosion (9KΩcm) to low rates of corrosion

Figure 3. New York Dock Building Today. Note thin polystyrene sheets as weatherproofing and standing water and the formation of plant growth at saturated slab. Author's photograph.

(96KΩcm), averaging at 36KΩcm or at moderate risk levels (Broomfield, 1997).

The test program indicated that carbonation induced corrosion was the root cause of the corrosion condition. All cores and in situ tests indicated that the depth of carbonation exceeded the depth of steel and was occurring from both base of the slabs upward and the top down. Chlorides were identified in all laboratory samples tested, at very low levels, indicative of cast in chlorides (PCA 1922).

Holistically, the data collected suggested that there was a corrosion risk throughout the structure, even in areas where there was little saturation and low corrosion activity. All slabs had a variation in condition, cover, and corrosion rates. The mesh within all slabs tested fell within the carbonated zone of the concrete. Therefore, as the mesh was within the carbonated zone it would be imperative that the structure be kept dry at all times to lessen the corrosion risk.

The building envelope is within the later stages of the corrosion deterioration process. Extensive repairs are required, and if the building is left derelict the cost of repair will increase exponentially within 15 years. The deterioration models suggest that damage will continue to be on-going at the building envelope if no repair is carried out in the near term. The slabs, which fared better, had between 10 and 15 years before significant damage would arise.

The lowest areas of corrosion activity indicated were from the roof level, where the pool is intended to be installed. It was recommended that this design feature not introduce chlorides into the existing concrete, which would increase the risk matrix. Based on the corrosion activity and carbonation front seen at the roof and the 6th floor (which will support the pool) it was recommended that the design team make efforts to isolate the existing concrete from the pool basin and supporting elements. Electrochemical repairs were not considered within the overall repair due to the lack of continuity between bars and the variation in concrete cover.

4 THE SOLOMON R. GUGGENHEIM MUSEUM

4.1 *History*

The Solomon R. Guggenheim Museum is arguably the most famous architectural masterpiece designed by Frank Lloyd Wright. It is an embodiment of Wright's philosophical and design achievements and "his attempts to render the inherent plasticity of organic forms in architecture." (Guggenheim.org). The building is located in New York City along the upper east side of Central Park, at 88th and Park Avenue. This location was chosen to provide interaction between the building and nature, though the realized design is very introspective.

In 1943 Wright was approached by Mr. Guggenheim and Ms. Rebay to design a building to house Guggenheim's four year old 'Non-Objective Art Museum.' The purpose was not only to showcase Guggenheims' growing art collection but to be an integral space from which the viewer would participate with the art. An initial design was formulated between the years of 1943-45 and based on the helical shape seen in Wright's contemporary work. During the next nine years the design was restudied and refined; construction began in 1956 and the building was dedicated in 1959, six months after Wrights death (Roth, 1979).

The WASA Architect, Engineers, and Planners. Historic Preservation Approach and Project Guidelines stated, "This historic property has retained its original use as a cultural institution for decades, and by doing so, the institution that it serves has gained worldwide recognition for promoting the understanding of art and architecture." (WASA 2005)

4.2 *Construction*

Since a smooth round concrete structure of such complexity had never before been constructed Wright was challenged through the entire construction process. The building features "a spiral ramp making six turns at an approximate grade of 3 percent, stiffened by exterior webs at 30-degree intervals, and an inner court covered by a glass dome. Reinforced concrete was used throughout, with lightweight "Lelite" aggregate for the superstructure.

All aspects of the concrete work were designed to eliminate cracking of all of the architectural concrete. Expansion joints were omitted to ensure a smooth surface. Three types of concrete were used in total on the building. These included lightweight expandable shale concrete in the ramp and floors, stone concrete at the interior walls, and the outer walls were 5 inch thick shotcrete walls, sprayed against curved plywood forms.

The five inch thick gunite walls were rigidly connected to the ramp slab and web. Original construction records indicate that the walls are reinforced with two layers of 2 by 2 (50 mm) mesh, plus 2 layers of No. 3 bars at 12-inch (30cm) centers horizontally, plus 2 layers of No. 4 bars vertically, plus top and bottom continuous No. 4 bars—all secured to a framework

Figure 4. The Architect, Owner, and Owner's Representative reviewing a model of the Solomon R. Guggenheim Museum. Guggenheim Foundation.

of 1 1/2-inch (38mm) tees which are in turn tied into the structure. The inside surfaces of these walls are furred, lathed and plastered. The outside surfaces were smoothed after the forms were removed, but while the gunite was still green (Cohen 1958).

4.3 *Condition assessment*

Already tasked with an established assessment approach, the corrosion condition assessment consisted of three distinct phases: a document review of earlier corrosion related reports, a corrosion assessment at two levels the 6th Floor Rotunda, and the 2nd Floor Tannhauser Gallery, and a polarization trial to determine the efficacy of impressed current cathodic protection (ICCP), to establish installation procedures, and to assess internal wiring logistics. The design for the ICCP work was halted after much debate between purists and practical interventionists.

Prior to the corrosion survey, an extensive condition assessment had been performed by the A/E team. The original protective coating (and subsequent layers) which normally graced the exterior had been removed for further investigations of the materials, documentation, and recording of conditions. There were a number of probe openings to verify construction details, and the interior walls had been stripped of all built out surfaces.

The document review, in situ testing, and visual verification of conditions revealed that carbonation had diffused between 1 and 6mm into the surface of sound concrete from the exterior and up to 17mm from the interior face of the gunite wall. The review revealed that corrosion had been documented along the cracks which were parallel with the reinforcing steel of the rotunda dating back to 1989, thirty years after completion. The RH values of the gunite wall were as high as 80%, which for an internal wall is very high. Reports up to 2006 confirmed visual observation between hairline cracking, reinforcement and minor corrosion activity.

A thorough analysis of half-cell potentials and mapping of potential gradients provided visual support of corrosion activity. The corrosion assessment indicated that 4% of the area tested exhibited corrosion rates greater than 2.2 microns per year. Though this is considered low to moderate (Broomfield 1997) in most structures, rates of 4 microns per year, combined with site specific details, indicated ongoing damage within 10 years. This level of degradation is significant based on a client's requirement of on-going and continued use of the space for an indefinite future.

In summary the restoration campaign sought to enhance overall performance of the building envelope, provide improved roofing and weather proofing, structurally strengthen the rotunda walls, reduce moisture within the exterior walls, re-coat the entire building and understand long term performance of the structure over time.

As a result of the corrosion survey, a long-term corrosion monitoring system was installed to better understand the performance of the structure. Fluctuations in activity have occurred, notably with seasonal changes, and at moderate to low rates. It was noted through this system that moisture within the gunite walls varied dramatically throughout the year but overall had decreased since the restoration was complete.

5 PAVILION ON THE POND

5.1 *History*

Philip Johnson's Pavilion on the Pond, built in 1962, is a unique, custom pavilion located at the edge of the pond at his Glass House Estate located in New Canaan, Connecticut. The neighbourhood is suburban, and the 47 acre estate lies on the outskirts of the North Stamford Reservoir. The historically significant folly is part of the National Trust for Historic Preservation's Glass House Estate, bequeathed to the Trust by Johnson himself. The Pavilion is just one of an ensemble of structures which makeup the Estate and is a one of the first structures in the United States to use the Schokbeton pre-cast concrete system.

In a condition assessment prepared by Cellini for the National Trust of Historic Preservation (Cellini 2009) it was stated, "Johnson wished to use his expanse of land to develop architectural "events of the landscape … Johnson developed two structures on site: a fort-like pond pavilion and a sculptural climbing tower. The former, the Pavilion on the Pond, is meant to foster a childlike spirit in both appearance and accessibility. Using his home and grounds as a canvas to test new ideas and materials, Johnson designed the pavilion out of precast concrete, which was becoming an important building material during the second half of the century. It was an experiment in form and material, a model." This folly was a precursor to Johnson's later assemblies and inspired the Sheldon Art Gallery, Lincoln NE and New York State Theatre at Lincoln Centre, New York City, home to the New York Ballet.

5.2 *Construction*

The structure is an articulated colonnade, with four rooms, and two patios. It is 6.5 foot (ca 2m) high on the

Figure 5. Pavilion on the Pond. Authors photograph.

outside, with an interior elevation of 5.3 feet. The prefabricated concrete arches and ziggurat roof panels were erected on a poured in place concrete base. This base is partially submerged within the pond beyond the Glass House. The Pavilion was constructed to have an interior pool with recessed lighting, while also concealing the pumps for the fountain located within the center of the pond.

The original architectural drawings reference mechanical and lighting schematics but 'no drawings can be located detailing the pavilion's individual pieces. However, Johnson was pleased that the contractor was able to assemble the pieces quickly, correctly and overnight, which he deemed a success with a "very difficult material" (Cellini 2009). At the time of construction, the pre-cast assembly was painted white, with gold leaf at the underside of the roof.

The precast system, called "Schokbeton" is a Dutch technique which used advanced machinery and vibration tables to mix the concrete in the form work. The components of the folly were constructed by the Eastern Schokbeton Company, located in New Jersey. The units were erected on the site, with craftsman like precision. Each column unit is a single column with half of an arch either side of the column. When two are connected, they complete a full arch. The columns have isolated reinforcing steel 1" (25 mm) in diameter; sit upon a metal plate; have 'z' shaped galvanized anchors between columns and brass bolts connecting the column configurations to the ziggurat roof.

5.3 *Condition assessment*

The corrosion survey was meant provide further evidence to the site directors that a repair campaign was imminent for the then 50 year Pavilion. Damage has increased exponentially since an extensive condition assessment was carried out in 2009, which laid the foundation for the corrosion survey. A comparison of documentation indicated that corrosion had been active since at least this time, if not before.

Prior to the investigation, it was established that no further concrete could be removed, no petrographic analysis had been carried out and that all testing had to be carried out at areas of exposed steel. Two columns and the base curb of the platform at the southwest corner were able to be tested.

Figure 6. Room 4 of the Pavilion, Glass House in background of hill. Authors photograph.

As this is a unique, experimental structure, any loss of material is significant. Where the concrete was sound, crack initiation models indicated approximately 8 years before cracking would be exhibited on the structure.

Corrosion activity was considered moderate for a structure with full exposure and no environmental shielding in accordance with general assessments, but like the Guggenheim Museum, the activity is determined to be high in a structure of architectural significance. Corrosion was identified as being active at the base of the structure and was identified as being significantly higher at the tops of two pre-cast columns tested.

Brass and zinc connectors were in close proximity of the embedded reinforcing steel. This connection detail lies between the roof and column capital where drainage failures caused the concrete to become saturated. The highest level of damage to the pre-cast concrete was occurring at this location.

The excessively damp conditions caused disintegration of the parent concrete. It was recommended that the moist and carbonated material be removed prior to repair, or repairs would presumably fail. A recommendation was made for an immediate waterproofing and a drainage solution as well as a petrographic analysis of the concrete. Removal of embedded conduit, and a well matched concrete patching campaign could provide the client with a 20 year repair. . Alternatively, and probably an unpopular choice would be to disassemble the entire pre-cast assembly, treat within a laboratory, as an objet d'art, and or replace full units which pose a safety risk.

6 THE NATIONAL GALLERY, EAST BUILDING

6.1 *History*

The National Gallery of Art, East Building, is located in Washington, DC on the block of 300 Constitution

Figure 7. National Gallery of Art.

NW off of Pennsylvania Avenue, near the Capital building. Designed by I.M. Pei, and constructed in 1974, the building, is not yet 50 years old, but is considered a national landmark. It houses the Nation's modern art collection. The East Building is situated on a very restrictive, trapezoidal shaped plot. By taking his cue from the plot, Pei crossed it with a 'diagonal reflecting that of Pennsylvania Avenue, dividing the plan into a long isosceles triangle and a right angle triangle. Once this was done, a logical system of related triangles was developed which gives the plan individual character and a clear sense of order, so that the building is classically simple and universal, while at the same time being particular and special" (Roth 1979). With bold line and sharp angles, it is an architectural contrast to the original building.

Contrarily the East Building pays homage to the original 1938 neoclassical gallery by Pope, which houses the older works of national art. As both structures were gifts of the Mellon Family, Paul Mellon stipulated that the same pink Tennessee marble that was used in the construction of John Russell Pope's Gallery be used by Pei.

6.2 *Construction*

The facade is a reinforced and post tensioned reinforced concrete frame, with brick wall cavities and marble cladding. The architectural concrete is comprised of a unique matrix of calcite and dolomitic marble, and acts both as a structural and aesthetic material. The building is clad with pink Tennessee Marble and the board form concrete finish is covered with a finely crushed marble

The focus of the limited corrosion survey was on two beams. One located at the 7th Floor Refectory Terrace, which is steel reinforced concrete with post tensioning and the 8th Floor Roof beam which is steel reinforced concrete. The reinforcing steel and ties were specified to be securely attached to one another in the original construction documents, as well as to have adequate cover of 2 inches (50mm) where the concrete was exposed to weathering. It was evident from the test program that the 2 inch cover requirement was not always adhered to.

Figure 8. National Gallery of Art, roof at the 8th floor. Authors photograph.

6.3 *Condition assessment*

The corrosion assessment of the National Gallery's East Building stemmed from opportunity rather than necessity. While the building was undergoing a restoration of the building envelope and re-anchoring of the marble panels, an opportunity to assess the corrosion condition in two locations was made possible. The locations assessed were the 7th Floor Terrace and 8th Floor Roof.

The concrete has intrinsic historic and architectural value; therefore the limitation in scope was based on areas with exposed reinforcing steel. Locations were chosen based on areas where a direct connection was able to be made to exposed rebar without additional concrete removal. One core and one sample of concrete were able to be removed in the investigative process. Continuity testing was limited, therefore original construction drawings, rebar identification, cover readings, and half-cell potential readings were required to determine continuity of the embedded components.

It was determined that the corrosion condition of the reinforcement to the National Gallery in the area of the testing program was fair. Corrosion activity was largely identified only in areas of spalling (2 areas) and along cracks. Corrosion activity was identified as being moderate to high in 8% of the area tested based on the significance of the building. The crushed marble surface finish of the concrete provided an excellent barrier to carbonation and deterioration. The carbonation front was identified both by laboratory and in situ testing as having penetrated no further than 1.5mm from the surface and at hairline cracks.

The electrical resistivity values of the concrete averaged 135KΩcm. In part this can be related to the concrete matrix and marble on the concrete surface, which provides a highly resistive surface layer. .

The crack initiation models indicated that the future cracking in areas of low corrosion activity, where the concrete was in good condition would be in excess of forty years. In areas where the corrosion rates were high, and cracks greater than 0.5 mm were present,

continued deterioration would be evident in five to six years.

The high quality concrete, with post-tensioning has retained its high pH throughout the majority of the concrete matrix. All conditions indicated that the reinforcing steel in areas without damage was in good condition.

As the concrete is highly unique in color and composition, little can be done to the surface of the material to enhance corrosion resistance (i.e. coatings or paints).

A repair option which was recommended at areas of low cover, cracking and carbonation was electrochemical or surface applied chemical realkalization. As this technique does not have a significant track record on historic buildings of high architectural significance in the US, the owners opted for an in-depth crack injection repair with a custom grout developed by an architectural conservator who was sensitive to the overall repair and cleaning campaign. In Europe and the UK there is a history of realkalization treatment on historic concrete, such as the Hoover Building and Uxbridge Station.

7 CONCLUSIONS

Corrosion condition assessments on historic concrete icons can have challenging parameters set forth prior to establishing testing protocols. Even though concrete is inexpensive and reproducible, the reasons for retaining as much material as possible during the investigation and subsequent repair must be balanced with safety and an understanding of the material conditions. An establishment of corrosion behavior can assist in understanding condition, deterioration, and future degradation. It is imperative to know condition prior to making repair decisions which may have lasting consequences.

Three of the four structures discussed in this paper have owners which are cognizant of the historic value of their buildings. Though landmark status created limitations within the corrosion conditions surveys, the forethought of the A/E team to address long-term performance was critical in determining the life cycle of the buildings. While each structure is unique in its construction type, each structure had evidence of corrosion activity. The levels varied based on a confluence of conditions, which were identified through the investigation and testing programs.

Understanding the conditions and developing degradation models in turn helped define the urgency and levels of intervention required for the repair. The corrosion investigations and subsequent recommendations provided the team with not only traditional repairs choices but the evaluation of an electrochemical treatment for each structure. In all instances, interventions which delay degradation of the historic material while keeping the parent concrete intact, thus delaying the loss of cultural heritage, must be considered.

REFERENCES

British Research Establishment (BRE), Client Report. Residual Life Models for Concrete Repair: Assessment of the Concrete Repair Process. October 2003.

Broomfield, J. 1997. *Corrosion of Steel in Concrete: Understanding, Investigation and Repair.* London: E& FN Spon.

Brownstoner.com

Celleni, J. 2009. "Existing Conditions Assessment of the Pre-Cast Concrete Structures at Philip Johnson's Glass House. Summer 2009." Prepared for the National Trust of Historic Preservation and the Philip Johnson Glass House.

Cohen, G. 1958. "Frank Lloyd Wright's Guggenheim Museum: He Adds New Dimensions to Use of Poured Concrete in Building Construction." The Aberdeen Group.

Friedman, D. 2010. *Historic Building Construction, 2nd Edition*. New York: Norton.

Guggenheim.com

Luping, S. L. Nilsson, and P. Basheer. 2012. *Resistance of Concrete to Chloride Ingress*. London: E&F Spon.

Macdonald, S (ed). 2003. *Concrete Building Pathology*. Oxford: Blackwell Science.

National Register for Historic Places. U.S. Department of the Interior and the National Park Service.

http://www.norcure.com/reportsedmonton.htm

The Portland Cement Association. 1922. "Concrete Work in Cold Weather" Trade Literature PCA.

Revie, W, (ed.). 2011. *Uhlig's Corrosion Handbook, Third Edition*. New Jersey: John Wiley & Sons, Inc.

Roth, L. 1979. A P*recise History of American Architecture*. New York: Harper and Row Publishers.

WASA Architect, Engineers, and Planners. Historic Preservation Approach and Project Guidelines: The Solomon R. Guggenheim Museum. November 8, 2005.

Endnote

All data presented within the case studies is from the authors' site investigations.

This page intentionally left blank

Concrete Solutions – Grantham et al. (Eds)
© 2014 Taylor & Francis Group, London, ISBN 978-1-138-02708-4

The role of material microstructure in the durability of historic buildings

A.J. Klemm & D.E. Wiggins
Glasgow Caledonian University, Scotland

ABSTRACT: This paper presents part of a larger research project focused on optimising the microstructure of lime repair mortar for compatibility with substrates. Preliminary results of a study into the change in microstructure of building sandstone under weathering are presented. Additionally, an overview of the primary degradation mechanisms (based on moisture movement) is given. Key findings of the study include that microstructural change due to weathering was observed in a localised, non-uniform manner. In the context of this present research, the change was on balance considered to be insignificant with respect to the selection of a compatible repair mortar.

1 INTRODUCTION

1.1 *Context for repair to heritage structures*

Moisture movement through building materials is a common feature to both modern and heritage structures and consequently it has an effect on their durability. Modern building designs typically focus on impermeable 'hi-tech', engineered materials designed to keep water out (concrete cover to steel reinforcement). Such structures tend to be less tolerant of design and/or construction defects (Dunbar-Nasmith 1997; Forsyth 2008) than old buildings, which adopt more natural 'low-tech' construction designs and materials.

The majority of all heritage repair work is as a direct result of inappropriate, damaging interventions using modern, typically impermeable, materials which disrupt buildings' operational mechanisms. It has been observed that it is the crossover of two opposing building technologies that inflicts the most harm on our stonework heritage (Gibbons 2003).

Moisture is widely accepted as the primary engine of decay in building stones. (Maxwell, 1995; Smith, 1995; Charola et al. 2011). It facilitates migration of any degradation agents to locations where they can best exploit any inherent weaknesses within the stonework mass. Consequently moisture movement is of primary importance with regard to the durability of heritage structures built of porous materials (Allen et al. 2003; Hughes 1986; Klemm & Wiggins 2013). The response to incident moisture is profoundly dependent on the microstructure in a porous material such as stone or lime (eg. Al-Mukhtar & Beck 2008; Benitez, D. *et al.* 2002.; Holmström 1996; Klemm & Wiggins 2013; Meng 1994; Thomson *et al.* 2004).

Repairing heritage structures requires that a difficult-to-define parameter is met; namely compatibility. Outwith technical aspects, it is affected by philosophical arguments and contemporary social and cultural ideals. Technical compatibility requires that the repair material should weather sacrificially to the substrate (Bell, 1997). In order for this to be realised, the agents of decay (water) must be drawn away from the substrate and the harmful evaporation stages promoted at the face of the repair material, rather than at the surface (or indeed deeper within) the substrate.

Owing to the concept that as it is the interaction between two material microstructures laden with water which governs capillary flow & corresponding evaporation regime through the collective porous mass, the microstructure can form the basis for selection of optimal repair material. For a compatible repair mortar to be designed/selected on the basis of its microstructure, however, it is imperative to build a firm picture of that of the substrate.

A firm understanding of the substrate's characteristics is identified as being the essential starting point for compatible repair, in addition to an understanding of the significance of the interacting microstructures of repair/mortar and substrate. This paper presents preliminary results from research where the focus is on the microstructural alterations in building sandstone due to prolonged weathering.

2 MOISTURE MOVEMENT IN POROUS MATERIALS

It is well known that microstructure governs the response of porous media to incident moisture. Yet to engineer compatibility (i.e. to coerce an anticipated moisture movement outcome) an understanding of the underlying processes, and the respectively relevant factions of the microstructure, is required as a starting point. An indicative spectrum of different microstructures is presented in Figure 1.

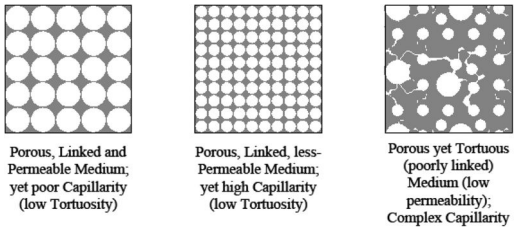

Figure 1. Conjectural microstructure models.

Heritage structures built of porous materials such as lime and stone function very differently in response to moisture from modern buildings. Attempts to *inhibit* water ingress to heritage structures invariably result in disrupting the underlying operational mechanisms and accelerating decay. Consequently the focus is on moisture handling characteristics of materials once water ingress has occurred; and in particular with its egress back into the environment. The latter aspect has the largest part to play concerning durability of structures due to salt deposition (Allen et al. 2003; Carter & Forster 2011; Hall & Hoff 2007; Hall & Hoff 2002).

Different ranges of pores (factions) serve different moisture movement purposes. Yet it is of primary importance to distinguish the mechanisms behind movement in the relevant pore ranges. Generally, movement in the vapour phase is most pronounced in larger pore regions and the liquid phase movement towards the smaller.

Regarding vapour phase movement, condensation problems in buildings have been demonstrated to be damaging to the health and wellbeing of occupants (Blackman 2008; Hens 2011) and the building fabric. If moisture in the vapour phase cannot traverse the porous mass walls quickly enough, it is liable to condense within the building, whereby it can support fungal growth. Similarly, it is important in the case of a plastic repair mortar that such moisture is not trapped to condense behind the repair, then becoming liable to frost/other crystallisation expansion. It is imperative, therefore, that any repair material must not retard the breathability of the substrate, but promote it.

Moisture vapour flux is driven by a function of pressure difference across a traverse length and the size (radius) of its pores – with the complication of interconnectivity to consider. The latter two variables (pore size and interconnectivity) are described by a material's vapour permeability, δp (kg/m^{2}s) – governed by the microstructure.

In consideration of the above, it is clear that in order to maintain compatibility, repair materials must not inhibit movement in either fluid phase. The repair materials should promote such movement, in order to best sacrificially protect the substrate (Figure 2).

Concerning liquid phase movement, the mechanism behind capillary movement in porous materials is the tendency of water to be drawn into small pores and throats, as the water body seeks to reduce the energy of the molecular system (Brown 1947; Chapin 1959; Sophocleous 2010; Walton 1972). The molecular activity around the meniscus is the driver behind capillary flow. The curvature of this air-water interface (descriptive of the capillarity strength) within the pore is largely governed by the radius of that pore (Hall & Hoff 2007), and thus the importance of microstructure for fluid phase movement in porous materials is starkly clarified.

The effect of the pore radius on capillarity is related to the wetted area, governing the surface energy interactions. Energy of the system is reduced by increasing the solid-liquid interface; this is a tendency for molecular systems (Shaw 1980; De Gennes et al. 2003). Capillary transport will therefore occur until sufficient area has been found to balance the energy. In the context of a simple capillary tube arrangement, this is a shorter height for a large radius and a substantial height for a capillary of small radius. This is because the energy of the solid-liquid interface is lower than that of the solid-vapour interface (Stone 2010).

From the above, having considered that the strength of capillarity is profoundly dependent upon the capillary radius, it would seem apparent that capillary flow would increase indefinitely with a falling pore diameter. Indeed, the strength of suction does increase, as the mathematical expressions for capillarity prove. However, the effects of viscous drag and surface roughness become increasingly prevalent with very small pore radii. It is for this reason that there are lower limits of pores relevant for capillary flow (Hall & Hoff 2002; Meng 1994).

2.1 *Optimal microstructure for moisture movement*

In light of the foregoing, optimisation credentials can be identified with which to select/design a compatible repair material. Consequently, in order to meet the breathability (vapour phase movement) criterion, the repair material should then have at least a similar volume of pores in the larger regions, so as not to retard vapour migration. In order to meet the liquid transport criteria, the repair material should have an abundance of pores in the smaller regions, reaching smaller pore factions than the substrate exhibits, to promote capillary suction to draw the water into the repair material.

Three microstructure characteristics of relevance are pore size distribution (PSD), tortuosity, and porosity (Figure 1). Tortuosity is a function of the length travelled by a fluid to the shortest distance through the medium, and is descriptive of the difficulty of direct fluid movement through a porous medium (Delgado *et al.* 2012). This helps characterise the internal pore geometry and interconnectivity (Ewing & Hunt 2009).

A compatible repair material should establish a wicking action, to draw the moisture (and hence soluble salts & other contaminants) into the repair material, from where the bulk of the harmful evaporation stage should take place; sacrificially protecting the substrate. This wicking mechanism is presented pictorially in Figure 2.

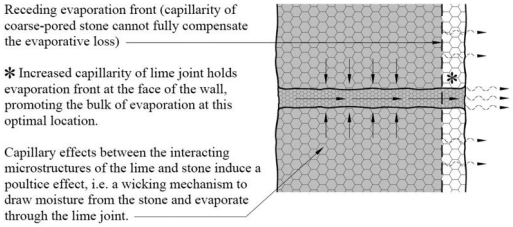

Figure 2. Wicking mechanism by capillary flow.

The above water movement through capillary flow can be engineered through selection of the right materials with known respective microstructures.

2.2 *Durability: Physico-chemical*

Decay processes in stone are exploitative in nature. Micro-cracking arising from settlement or thermal movement allows water to be drawn deep by capillary action, creating a deeper foothold from which to degrade the stonework mass. Micro-cracks eventually coalesce to form macro-cracks, which then hold structural significance, ultimately manifesting in failure of the stonework (Smith 1995; Gomez-Heras *et al.* 2008).

In view of the foregoing, the response of stonework to moisture holds engineering significance. Through a firm understanding of the mechanisms by which it occurs, intervention may be undertaken whilst decay remains at the micro-level – proactive, rather than reactive to the macro-level.

The response to moisture essentially dictates the durability of the stonework heritage material under the following degradation elements:

- Dissolution and leaching of mineral binder;
- Providing a receptive substrate of increased pollutant (contaminants and biological) uptake;
- Susceptibility to freeze-thaw cycles;
- Where the evaporation takes place (salt precipitation).

Stonework decay operates as a system, comprising parallel and/or sequential mechanisms (Smith, 1995). Sandstone as a building material is categorised by its cementing materials, which bind the sand grains (Akesson et al. 2007). The binder mineralogy, being a main control on durability, essentially forms a durability class system (Forsyth 2008). Incident moisture transports soluble contaminants to locations whereby it can be most exploitative; yet research has also shown that even pure water can serve to disaggregate stone, by dissolving the mineral binder over time (Cooke & Gibbs 1994).

The material's microstructure, determines the moisture movement mechanisms through its geometry and surface chemistry; and consequently the volume of water ingress, and the length of time that volume is held.

It follows that a porous medium that is receptive to water but which cannot readily shed, leaves itself open to increased pollutant uptake (wet deposition of soiling from the atmosphere has been found to be twice that on a dry substrate, Cooke & Gibbs 1994; Brimblecombe 2011). That wet substrate also finds itself a more receptive host to biological contaminants such as algae which can leach the minerals from the binder, weakening the material (Price 1975; Schaffer 1932). Further, the longer the porous mass remains wet, the longer it is at risk of damage through freeze-thaw cycles.

The factions of the microstructure most susceptible to freeze/thaw (F/T) attack remain the subject of debate, although it is generally agreed that they centre around the 250/300 – 1,400/3,000 nm range (Ravaglioli 1976; Lesniewska 1976).

A durable response to F/T attack is profoundly dependent upon the microstructure (Klemm & Klemm, 1997a). Because the phase change at the freezing point of water from liquid to solid is virtually instantaneous, the ~10% volume increase must stress the pore walls, unless those pores are only partially filled (Klemm & Klemm, 1997b). Engineering the microstructure (eg. air-entraining), an ancient practice (eg. Carran et al. 2011; Jasiczak & Zielinski 2005), attempts to address the (hydraulic) stress imposed upon the pore walls by the displaced water, rather than the ice.

The foregoing has briefly examined the damage by the prevalent moisture-related mechanisms of decay, which are closely interlinked, many serving to catalyse one another (Smith, 1995). Focussing on the expansion damage, if the location at which the bulk of the crystallisation phase occurs can be 'managed', an element of damage to the sensitive, historic stone units could be mitigated.

2.3 *Durability: Mechanical*

Modern masonry design typically relies upon materials of high strength and high stiffness (rigidity). Thermal expansion/contraction of these materials, given their geometrical arrangement, requires formal thermal movement joint provision. Where these are absent, frequently thermal stress builds up until brittle failure cracks are formed to a state of relief – essentially forming their own movement joints (Beckmann & Bowles 2004; IStructE 2008)

Historic stonework does not require such provision, principally due to the deformability (low modulus) of the lime mortar joints (Ferguson & Yates 2008). The lime also accommodates minor structural movement (small settlements, etc.) without cracking, maintaining an intimate bond with the stone units. The intimacy of the bond has a profound effect on the moisture handling characteristics of the collective mortar-substrate porous mass, principally in ensuring capillary continuity ancross the interface (Bakolas et al. 1999; Maurenbrecher 2012; Hughes & Valek 2003).

It follows that the plastic repair mortar should be deformable to accommodate the thermal movements of the substrate in order to maintain this intimate

bond. Application of brittle, cementitious mortars to stonework not only hinders moisture release, but separates from the substrate along the interface through differential expansion/contraction (often taking an extent of substrate with it, forming a deeper failure plane). This creates further pathways for moisture ingress and ultimately failing.

It is clear that for a compatible repair mortar for a stonework substrate, physico-chemical and mechanical aspects must be considered; both significant elements to the collective durability of the stonework.

3 EXPERIMENTAL WORK

3.1 *Analysing the substrate with a view to repair*

The study focussed on analysis of samples from a mid-1800s church building and samples of virgin stone cut freshly from a quarry (control set).

Reference samples were acclimatised for circa 1 year in the quarry's store yard prior to experimental investigation. The study aimed to indicate first the spread in microstructure characteristics (PSD, tortuosity and porosity) at the small scale, i.e. across a given block of virgin stone, indicating the ideal limits of what can be achieved in terms of sample uniformity/ reliability. Second, to examine the change in microstructure which may be expected from differential weathering of a c.175-yr-old block (sheltered vs. exposed).

This study examines how appropriate it may be to extrapolate microstructural characteristics obtained from representative sampling locations across a building façade. The view being to estimate a generalised 'average' microstructure for a defined area of given context. This would allow a repointing mortar which is technically compatible across that area to be designed.

A single block was abstracted from the south-west facing steeple tower in an exposure which may be regarded as moderate, in consideration of the rest of the structure (aspect, height) (Figure 3).

Local degradation mechanisms such as active water penetration from unprotected wall-heads or defective rainwater handling goods were identified and afforded due cognisance for their accelerating effect on building deterioration (Powys 1929) and consequent change in the microstructure of the material (Austrheim *et al.* 2011). Sample set B was selected as the outer arrise due to the accelerated weathering wet/dry cycles induced by locally turbulent wind. A control age of the sample set of greyey siliceous weathering sandstone was recorded as mid-1800s; such longevity has seen peaks and troughs of pollutants over the structure's lifetime.

An example of the effect of local exposure is found by comparing the following Figures, photographs of good condition stone, north west aspect (Figure 4) versus very weathered stone, south facing (Figure 5).

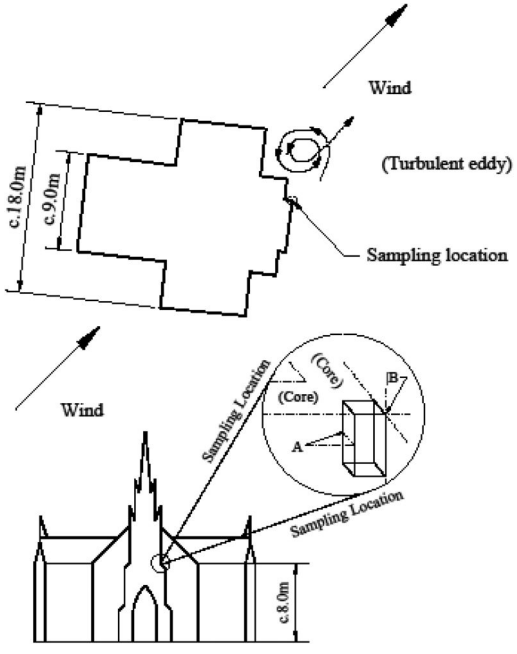

Figure 3. Sampling locations & exposure.

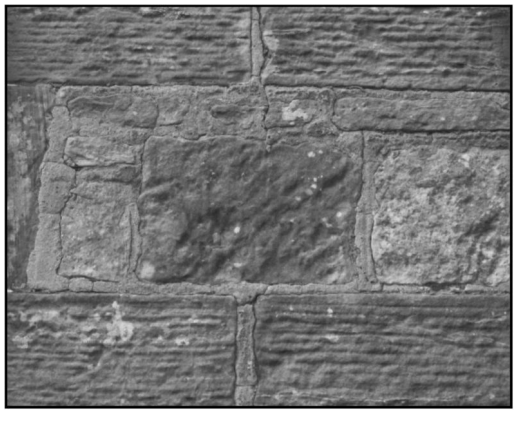

Figure 4. Good condition, durable stonework (NW).

3.2 *Result yield*

Given the significance of the microstructure for many of the behavioural phenomena exhibited by historic stonework, a method which examines a wide range of characteristics is invaluable. MIP meets this criterion, a powerful technique to aid in the characterisation of the microstructure of porous materials.

The method characterises the distribution of the pores, and indicates to what extent they may be interconnected through the Hager/Katz-Thompson tortuosity model. Whilst the latter function can risk indicating a link which would not otherwise be present through the ink-well phenomenon (where the results misrepresent such pores as the diameter of the connecting throats), this is mitigated using supplementary analyses to gauge representivity of the MIP data. Scanning

Figure 5. Poor condition, deteriorated stonework (S).

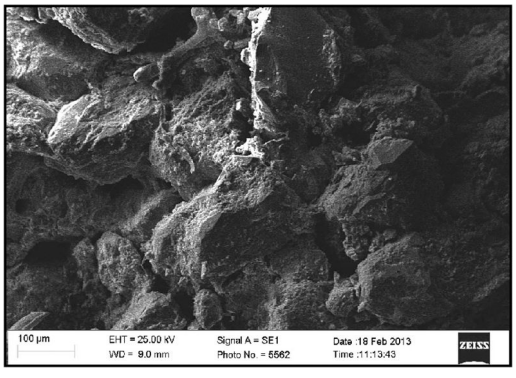

Figure 6. Sandstone microstructure: 'No-fines' cementing arrangement, thin smear of mineral binder. Large, interlinked, fairly uniform pores.

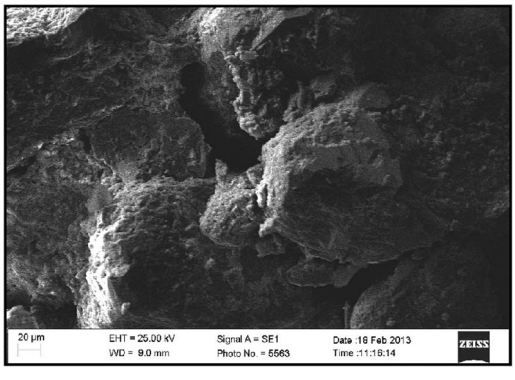

Figure 7. Sandstone microstructure: Bound grains @20µm, mineral binder smear (shown dappled).

Electron Microscopy (SEM) is an appropriate technique to validate the MIP results. Typical microstructures of the sandstone under investigation are validated by SEM in Figures 6 & 7.

It is a useful technique for qualitatively verifying typical pore geometry and interconnectivity. Combined, the methods cover the majority of the pore ranges responsible for moisture transport within

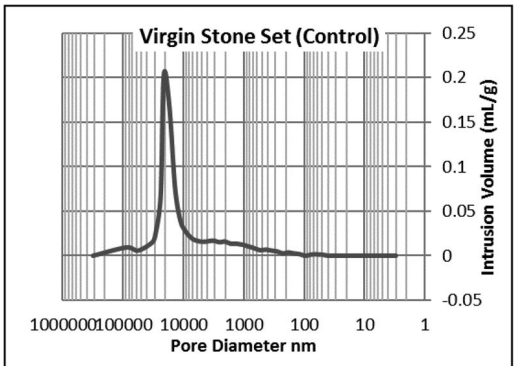

Characteristic (Control)	Avg. Value	Spread
Porosity	16.1%	2%
Permeability	82.7mD	10%
Tortuosity	7.1	6%

Figure 8. PSD & characteristics of virgin stone sample set.

porous media. As with any specialised analysis technique, SEM should be used on an objective basis; representivity has been observed as difficult to manage (eg. Ashall *et al.* 2004; Diamond & Kjellsen 2008; Hughes & Valek 2003).

4 RESULTS & DISCUSSION

The accuracy and weight of any conclusions drawn from analysis of historic substrates is profoundly dependent upon the representivity of the samples abstracted from the structure (Cizer et al. 2011; Hughes 2012). Indeed ultimately, the quality and compatibility of the repair with the substrate is governed by this (Van Hees 2012; Maurenbrecher 2012).

However a complication with the study of heritage structures is their sensitivity; the best-kept examples of optimal material are precisely the locations of most difficulty to sample. 'Less-destructive' techniques are therefore of primary importance for the study of historic buildings. Samples of weathering stone were first assessed in-situ, by means of qualitative visual inspection, on their respective degrees of pathology; this then formed the basis for designing further testing (Callebaut & Hughes 2002).

The virgin sandstone is a close geological match to that found in the church building under case study (grey siliceous; durable). The results on this control sample set demonstrate a high level of repeatability. Pore size distributions were near identical; a clear predominant pore size of c.12,500nm was evident. Further, the characteristics computed from the intrusion graph are closely repeatable, a 2% spread in porosity was found, and a c.5–10% spread in permeabilities and tortuosities. The results of MIP analysis are presented in Figures 8–10.

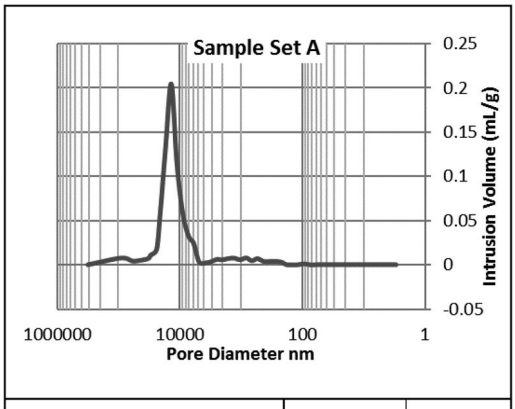

Characteristic (Set A)	Avg. Value	Spread
Porosity	16.7%	11%
Permeability	54.4mD	24%
Tortuosity	7.8	10%

Figure 9. PSD & characteristics of sheltered sample A set.

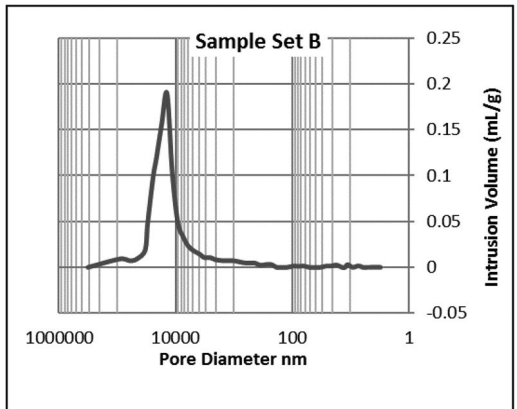

Characteristic (Set B)	Avg. Value	Spread
Porosity	17.5%	21%
Permeability	56.6mD	47%
Tortuosity	8.3	18%

Figure 10. PSD & characteristics of weathered sample B set.

The PSDs and porosity adhere closely to the base model underpinning the MIP analysis. A larger spread was experienced in the permeability and tortuosity characteristics; nevertheless, the collective results of the virgin sandstone study are considered very repeatable and hence reliable.

Sample set A was abstracted from the rear of an ashlar block from the steeple corner; set c.250mm back from the outer face (Figure 9), backed by a lime-bound rubble core. Analysis revealed characteristics in very close accordance with the control sample set. This adds strength to the comparison between set A and the weathered end, sample set B. PSDs recorded for set A were very repeatable. The characteristics computed exhibited a spread larger than for the virgin stone, but remained reasonably uniform.

Analysis of sample set B, abstracted from the outer arrise, demonstrates microstructural changes as a result of weathering. Porosity increased from 16.7% average (A) to an average of 17.5% (B); permeability slightly increased accordingly. Curiously, the tortuosity also increased, from a 7.8 to an 8.3 average value, indicating poorer interconnectivity. This is considered attributable to mineral redeposition and/or soiling blocking pore throats. Mineral redeposition/soiling lining the pore walls could also explain the drop in PSD peaks recorded.

The average microstrutural change from sheltered (set A) to weathered (set B) was small. This is promising for pointing towards representative sampling and extrapolating the results, within a similar context. This approach would appear to have promise in correcting/evening out the micro-scale fluctuations exhibited by weathered specimens.

Setting aside the relatively minor net average characteristic changes (which in this case may essentially be held as negligible for many purposes), the most prevalent result from this preliminary study is revealed in the difference in *spread* (uniformity). The spread exhibited by sample set B was double that of set A. In light of the rather negligible difference between sample sets A & B (average values), and considering the doubled spread, the results point towards a 'hot-spot-like' microstructural change under weathering.

It was previously observed (Klemm & Wiggins, 2013) that owing to the durability of the stone under study, the prevalence of deterioration mechanisms may be masked; so for a less durable sandstone, a more notable microstructural change may be expected.

5 CONCLUSIONS & RECOMMENDATIONS FOR FURTHER RESEARCH

A firm understanding of the durability-related mechanisms underlying the healthy operation of heritage structures is an essential starting point for the selection or design of a compatible repair.

It follows that a firm understanding of the given substrate – on a bespoke basis – is required in order to fully account for the context from which one is sampling, and hence imparting credible, reliable result upon which to base one's repair selection/design.

This short study indicates a good potential for reliably assessing the substrate microstructure using the above-described sampling techniques, for analysis under MIP to identify the target microstructure for the repair material to relate to in a compatible manner.

Microstructural changes in response to weathering were found to adopt a 'hot-spot'-like arrangement. On balance, for a durable stone and low-moderate exposure, the change in microstructure was found to be insignificant with regard to the material selection for repair.

Further research of most practical benefit would involve preparing a database of lime/repair mortar characteristics (resultant microstructures, in particular PSDs) for curing against a variety of substrates. Once such a database has been prepared for a variety of substrates, mortars, and interacting substrates & mortars, repairs may be optimised based on material selection. It then follows that perhaps by further engineering of the major lime classes currently available, repair mortars could be closer optimised towards their substrate.

ACKNOWLEDGEMENTS

The authors would like to thank Marcus Pein of Hutton Stone, who kindly afforded the control sample material and a tour of the quarrying/cutting/ dressing procedures involved.

REFERENCES

Åkesson, U., Lindqvist, J.E. & Malaga, K. 2007, "Microstructure and functional properties of rock materials", *Materials Characterization*, Vol. 58, pp. 1183–1188.

Allen, G., Allen, J., Elton, N., Farey, N., Holmes, S., Livesey, P. & Radonjic, M. 2003, *Hydraulic Lime mortar for stone, brick and block masonry*, Donhead, Shaftesbury.

Al-Mukhtar, M. & Beck, K. 2008, "Formulation and characterization of an appropriate lime-based mortar for use with a porous limestone", *Environmental Geology*, Vol. 56, pp. 715–727.

Ashall, G.J., Bartos, P.J.M., Groot, C. & Hughes, J.J. 2004, "Characterisation of old mortars with respect to their repair: A state of the art." in: *Characterisation of old mortars with respect to their repair - final report of RILEM TC 167-COM*, ed. G.J. Ashall, C. Groot & J.J. Hughes, RILEM, UK, pp. 1–10.

Austrheim, H., Jamtveit, B., Kobchenko, M., Malthe-Sørenssen, A., Røyne, A. & Svensen, H. 2011, "Porosity evolution and crystallization-driven fragmentation during weathering of andesite", *Journal of Geophysical Research*, Vol. 116, no. B12204,.

Bakolas, K., Bisbikou, A. & Moropoulou, A. 2000, "Physicochemical adhesion and cohesion bonds in joint mortars imparting durability to the historic structures", *Construction and Building Materials*, Vol. 14, pp. 35–46.

Barnes, G.T. & Gentle, I.R. 2005, *Interfacial science: An introduction*, 1st edn, Oxford University Press, Oxford.

Beckmann, P. & Bowles, R. 2004, *Structural aspects of building conservation*, 2nd edn, McGraw-Hill International, UK.

Bell, D. 1997, *The Historic Scotland guide to international conservation charters*, 1st edn, Historic Scotland, Edinburgh.

Benitez, D., Mosquera, M.J. & Perry, S.H. 2002, "Pore structure in mortars applied on restoration: Effect on properties relevant to decay of granite buildings", *Cement and Concrete Research*, Vol. 32, pp. 1883–1888.

Blackman, T. 2008, *Better homes, better health*, Care & Repair England and Housing LIN, York.

Brimblecombe, P. 2011, "Environment and architectural stone." in: *Stone in architecture*, ed. Siegesmund, S. & Snethlage, R., 4th edn, Springer, Berlin, pp. 317–346.

Callebaut, K. & Hughes, J.J. 2002, "In-situ visual analysis and practical sampling of historic mortars", *Materials and Structures*, Vol. 35, pp. 70–75.

Carran, D., Hughes, J., Kennedy, C. & Leslie, A. 2011, "A short history of the use of lime as a building material beyond europe and North america", *International Journal of Architectural Heritage*, Vol. 6, no. 2, pp. 117–146.

Carter, K. & Forster, A.M. 2011, "A framework for specifying natural hydraulic lime mortars for masonry construction", *Structural Survey*, Vol. 29, no. 5, pp. 373–396.

Charola, A.E., Steiger, M. & Sterflinger, M. 2011, "Weathering and deterioration." in: *Stone in architecture*, ed. Siegesmund, S. & Snethlage, R., 4th edn, Springer, Berlin, pp. 227–316.

Cizer, O., Janssens, E., Schueremans, L., Serré, G. & Van Balen, K. 2011, "Characterization of repair mortars for the assessment of their compatibility in restoration projects: Research and practice", *Construction and Building Materials*, Vol. 25, pp. 4338–4350.

Cooke, R.U. & Gibbs, G.B. 1994, *Crumbling heritage? studies of stone weathering in polluted atmospheres*, 1st edn, Creative Press, Reading.

Coutelieris, F.A. & Delgado, J. M. P. Q. 2012, "Transport phenomena in porous structures", *Transport Processes in Porous Media*, Vol. Advanced Structured Materials, no. 20, pp. 39–85.

De Gennes, P.G., Quere, D. & Brochard-Wyart, F. 2003, *Capillarity and wetting phenomena: Drops, bubbles, pearls, waves*, 1st edn, Springer, New York.

Diamond, S. & Kjellsen, K.O. 2008, "Scanning electron microscopic investigations of fresh mortars: Well-defined water-filled layers adjacent to sand grains", *Cement and Concrete Research*, Vol. 38, pp. 530–537.

Ewing, R. & Hunt, A. 2009, "Properties relevant for transport and transport applications." in: *Percolation theory for flow in porous media*, Springer, Berlin & London, pp. 37–55.

Ferguson, A. & Yates, T. 2008, *The use of lime-based mortars in new build*, 1st edn, IHS BRE Press, UK.

Forsyth, M. (ed) 2008, *Materials & skills for historic building conservation*, Blackwell Publishing Ltd, UK.

Gibbons, P 2003, *Preparation and use of lime mortars.* (Technical Advice Note 1), Historic Scotland, Edinburgh.

Hall, C. & Hoff, W.D. 2007, "Liquid movements", *Materials World*, Vol. 15, no. 1, pp. 24–26.

Hall, C. & Hoff, W.D. 2002, *Water transport in brick, stone and concrete,* 1st edn, Taylor & Hall, C. & Hoff, W.D. 2002, Water transport in brick, stone and concrete, 1st edn, Taylor & Francis, Oxford.Francis, Oxford.

Hens, H. 2011, *Applied building physics: Boundary conditions, building performance and material properties*, 1st edn, Wilhelm Ernst & Sohn, Berlin.

Holmström, I. 1996, "The use of lime", *The historic scotland international lime conference*, eds. J. Dorrington-Ward & I. Maxwell, Edinburgh, 1995, Historic Scotland, Scotland, pp. 60.

Hughes. P. 1986, *The need for old buildings to "breathe".* (Information Sheet 4), SPAB News, London

Hughes, J.J. & Valek, J. 2003, *Mortars in historic buildings*, Historic Scotland, Scotland.

Hughes, J.J. 2012, "The role of mortar in masonry: An introduction to requirements for the design of repair mortars", *Materials and Structures*, Vol. RILEM TC 203-RHM, no. 45, pp. 1287–1294.

IStructE 2008, *Manual for the design of plain masonry in building structures to eurocode 6*, 1st edn, The Institution of Structural Engineers, London.

Jasiczak, J. & Zielinski, K. 2006, “Effect of protein additive on properties of mortar”, *Cement & Concrete Composites*, Vol. 28, pp. 451–457.

Klemm, A. J. & Wiggins, D.E. 2013, “The dependence of lime mortar’s compatibility and behavioural phenomena upon its internal pore structure”, *3rd historic mortars conference*, ed. J.J. Hughes, Glasgow, 2013, University of the West of Scotland, Scotland, pp. 96.

Klemm, A.J. & Klemm, P. 1997, “The effects of the alternate freezing and thawing cycles on the pore structure of cementitious composites modified by MHEC and PVA”, *Building and Environment*, Vol. 32, no. 6, pp. 509–512.

Klemm, A.J. & Klemm, P. 1997, “Ice formation in pores in polymer modified concrete-II. the influence of the admixtures on the water to ice transition in cementitious composites subjected to freezing/thawing cycles”, *Building and Environment*, Vol. 32, no. 3, pp. 199–202.

Lesniewska, M. & Pogorzelski, J.A. 1976, “A study on the capillary movement of water in the selected building materials.”, *Arch. Inz. Lad.*, Vol. 2, pp. 333–343.

Maurenbrecher, P. 2012, “Repair mortars for historic masonry: Requirements for repointing mortars for historic masonry”, *Materials and Structures*, Vol. 45, pp. 1303–1309.

Maxwell, I. 1995, “Introduction to lime in scotland”, *The historic scotland international lime conference*, eds. J. Dorrington-Ward & I. Maxwell, Edinburgh, 1995, Historic Scotland; The Building Limes Forum, Scotland, pp. 5.

Meng, B. 1994, “Calculation of moisture transport coefficients on the basis of relevant pore structure parameters”, *Materials and Structures*, Vol. 27, no. 3, pp. 125–134.

Powys, A.R. 1929, *Repair of ancient buildings*, 3rd Edition edn, J.M. Dent & Sons Ltd., London, UK.

Price, C. 1975, “The decay and preservation of natural building stone”, *Chemistry in Britain*, Vol. 11, no. 10, pp. 350–353.

Ravaglioli, A. 1976, “Evaluation of the frost resistance of pressed ceramic products.”, *Transactions of the British Ceramic Society*, Vol. 75, no. 5, pp. 92–95.

Schaffer, R.J. 1932, *The weathering of natural building stones*, 1st edn, H. M. Stationery Office, London.

Shaw, D.J. 1980, *Introduction to colloid and surface chemistry*, 3rd edn, Butterworths, London.

Smith, B.J. & Warke, P.A. (eds) 1996, *Processes of urban stone decay*, Donhead, UK.

Sophocleous, M. 2010, “Understanding and explaining surface tension and capillarity: an introduction to fundamental physics for water professionals”, *Hydrogeology Journal*, Vol. 18, pp. 811–821.

Stone, H. 2010, “Interfaces: In fluid mechanics and across disciplines”, *Journal of Fluid Mechanics*, Vol. 645, pp. 1–25.

Thomson, M. 2004, “Porosity of mortars.” in: *Characterisation of old mortars with respect to their repair - final report of RILEM TC 167-COM*, ed. J. Elsen, C.J.W.P. Groot & J.E. Lindqvist, RILEM Publications SARL, UK, pp. 77–106.

Van Hees, R. 2012, “Repair mortars for historic masonry. from problem to intervention: A decision process”, *Materials and Structures*, Vol. 45, pp. 1295–1302.

Walton, A.J. 1972, “Surface tension and capillary rise”, *Physics Education*, Vol. 7, no. 8, pp. 491–498.

Concrete Solutions – Grantham et al. (Eds)
© 2014 Taylor & Francis Group, London, ISBN 978-1-138-02708-4

Realkalisation of a late 19th century bridge

E. Marie-Victoire & M. Bouichou
Laboratoire de Recherche des Monuments Historiques, LRM, CNRS-USR 3224, Champs-sur-Marne, France

V. Bouteiller & Y.Y. Tong
Laboratoire Sécurité et Durabilité des Ouvrages d'Art, Département Matériaux et Structures, UPE, IFSTTAR, Champs-sur-Marne, France

ABSTRACT: Camille de Hogues is a 3 arch reinforced concrete bridge, built at the dawn of the 20th century in Chatellerault (France). As the bridge was suffering from heavy corrosion of the rebars, largely due to carbonation of the concrete, in July 2006 a 3 year restoration program began. The architect opted for a combination of standard patch repairs and realkalisation. Within the frame of a larger project dedicated to realkalisation treatments, four series of both chemical and electrochemical tests were performed on two beams of one arch of the Bridge in parallel with the restoration. The analytical results evidenced an increase of pH above a value of ten, still measurable after one year. However, the conclusions based on the corrosion monitoring and in parallel tests as part of a larger project, were that corrosion was not likely to be stopped in the longer term. The issue of the durability of the efficiency of the realkalisation treatment couldn't be addressed through the experiments performed on the Bridge. Nevertheless additional results from the larger "realkalisation project" evidenced a lack of durability, working against the use of such treatments for cultural heritage applications.

1 INTRODUCTION

Carbonation is the main source of decay of reinforced concrete in the field of cultural Heritage (Marie-Victoire, 2006), and a major weathering factor for road infrastructures. The need for carbonation curing solutions, led the French ministries of Culture and Sustainable development to undertake a joint research project dedicated to realkalisation treatments. Three aspects were considered: efficiency, potential side-effects and durability of realkalisation treatments either by impressed current or sacrificial anodes. Tests were carried out on both artificially reinforced concrete slabs and on naturally aged concrete on site. The present papers deals with the field experiments on Camille de Hogues Bridge in Chatellerault (France) where an impressed current realkalisation was applied.

2 CAMILLE DE HOGUES BRIDGE

Camille de Hogues is one of the first examples of reinforced concrete bridges in France. It was erected between 1899 and 1900 in Chatellerault by the François Hennebique Company to cross the Vienne River. Consisting of 3 arches, it is 150 m long and 8 m wide. To build it, Hennebique used his well-known stirrups system for the reinforcing bars (Fig. 1) and a mix of siliceous aggregates (mainly quartz, feldspar, and mica) and Ordinary Portland Cement (380 ± 40 kg/m^3) for the concrete.

Figure 1. Hennebique Stirrups system was used to build Camille de Hogues Bridge.

As cracking appeared very rapidly on the concrete deck, a series of maintenance works was regularly performed (1902 to 1910, 1930, ….). Now, after almost 100 years of heavy traffic (2000 to 3000 vehicles per day), the bridge needed an extensive repair operation. Effectively it was suffering from generalized heavy corrosion of the rebars, cracking, spalling and leakage (Figs. 2–4).

Preliminary diagnosis evidenced a quite low quality concrete for a bridge by today's standards (compressive strength: 15 to 21 MPa, average open porosity:

Figure 2. Heavy corrosion was affecting rebars, sometimes up to complete loss of section.

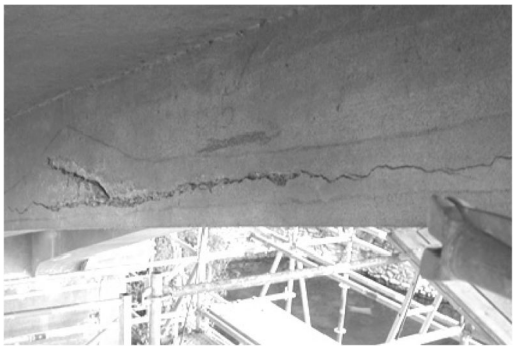

Figure 3. Some of the beams were deeply cracked.

Figure 4. Under the deck, evidence of leakage was observed, often associated with hollow "stalactites".

21%). This may have been linked to both the limited know-how and equipment available to build and compact concrete at the beginning of the 20th century. Numerous construction defects were also observed, such as honeycombing of the concrete, or absence of waterproofing of the deck.

Surprisingly, given the age of the bridge and the quality of the concrete, quite low carbonation depths were generally measured (10–20 mm), which may have resulted from the presence of a thin cement render on the surface. Nevertheless, as the concrete cover was also commonly quite thin (15 to 20 mm), carbonation had frequently reached rebar level. No evidence of chloride ion penetration, sulfate reaction, or ASR was found.

The conclusion was that the bridge was mainly suffering from heavy corrosion of the rebars due to carbonation, low concrete cover and an absence of deck waterproofing.

As a consequence, in July 2006, a restoration operation consisting of a combination of standard patch repair and an impressed current realkalisation treatment was selected by the architect in charge of the work.

3 REALKALISATION TREATMENT

Realkalisation treatments were specifically developed to cure reinforcement corrosion in carbonated concrete.

During the carbonation process, the gradual transformation of portlandite into calcite, due to a reaction with the carbon dioxide contained in the air, lowers the pH of the concrete from initial values close to 14 in a sound concrete, to values down to 9 in a carbonated concrete. This low pH environment, when oxygen and water are available, is favorable to the corrosion of steel rebars.

The idea of a realkalisation treatment is to electrochemically increase the pH of the concrete by promoting the ingress of an alkali from the surface towards the rebars and by generating water electrolysis around the rebars. To achieve this objective, the rebars are used as cathode and an anode is temporarily fixed on the concrete surface, in this case using a poultice soaked with an alkali-enriched water solution Then in the case of impressed current realkalisation, connections are made to a DC generator. For sacrificial anode realkalisation, specific anodes are used in order to deliver the current without a generator.

In Camille de Hogues Bridge, an impressed current treatment was applied. Due to an erratic network of bars and cages, a connection to the rebars had to be made every 1 m^2 as a minimum (Fig. 5) Then a steel anode (3 mm in diameter, 5 × 5 cm mesh) was embedded in a cellulose pulp soaked with a potassium carbonate solution (Fig. 6) Finally a 1 A/m^2 current was applied over a 15 day period.

It is to be noticed that due to permanent wind, the poultice had to be regularly moistened.

4 TESTING PROTOCOL

Apart from the renovation company self-evaluation, a one year research program was carried out on one of the arches, as part of a larger "realkalisation project" aiming at evaluating the efficiency, side effects and durability of such electrochemical treatments.

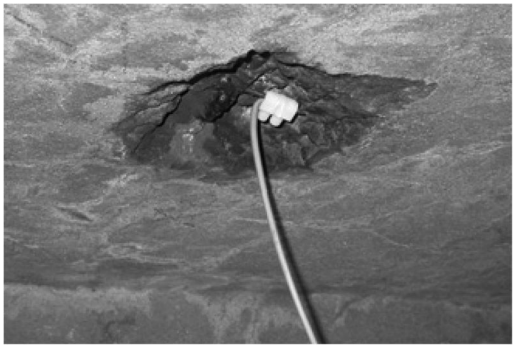

Figure 5. Due to an erratic rebar network, a connection every 1 m^2 had to be made.

Figure 6. A steel anode network was embedded in a paper pulp soaked with a potassium carbonate solution.

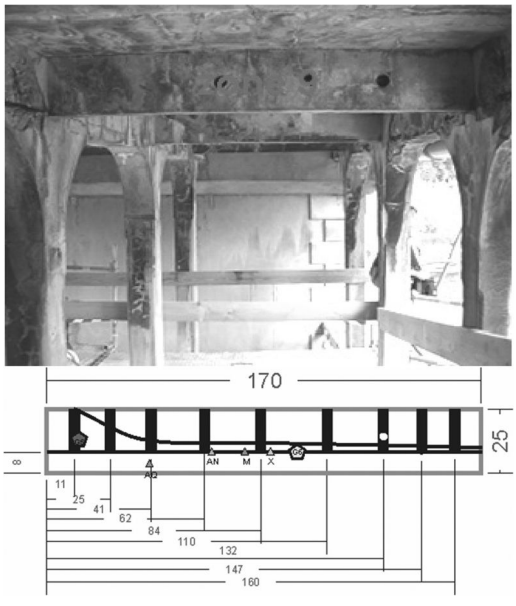

Figure 7. Atypical rebar network electromagnetically detected on zone 9, mixing 2 standard round shaped-rebars (one horizontal and one oblique, both 20 mm in diameter) and 9 flat Hennebique stirrups (4 to 4.5 cm large). On the scheme: the two pentagonal-shaped points refer to the Rp measurement spots, the white dot corresponding to the connecting point. The four triangular-shaped points refer to the powders drilled respectively before treatment (M), just after treatment (X), 2 months after (AN) and one year after (AQ).

In order to follow the pH of the concrete and the corrosion of the rebars, two types of experiments were considered:

Analytical experiments: phenolphthalein and thymolphthalein tests. Both color indicators are initially colorless and turn respectively pink for the phenolphthalein at a pH > 9 and blue for the thymolphthalein at a pH > 10 (Sergi, 2003). In this study, profiles were realized by collecting powders drilled at different depths (in order to preserve the original material) and spraying the indicator on the freshly drilled powders. It is to be mentioned that since 2013, phenolphthalein is declared carcinogenic and that its use should be safely controlled. Disregarding this new fact, phenolphthalein tests remain reliable.

Electrochemical experiments: potential mapping (with a CANIN© device equipped with a copper/copper sulfate reference electrode), resistivity mapping (with a Gecor6©, equipped with a copper/copper sulfate reference electrode, using the disc method), and polarization resistance measurements (with a Gecor6©, equipped with a copper/copper sulfate reference electrode).

Tests were carried out on two beams located under the deck (170 cm long, 25 cm wide), named zone 9 and zone 10. On both beams, two types of rebars were electromagnetically detected and then confirmed by coring: standard round shaped-rebars (one horizontal and one oblique, both 20 mm in diameter) and 9 Hennebique flat stirrups (4 to 4.5 cm large) (Figs. 7–8), creating an atypical rebar network. Dealing with concrete cover, its thickness varied from 4 cm for the flat stirrups up to 5–6 cm for the round-shaped rebars.

On those beams, four series of tests were performed respectively prior to the realkalisation treatment, just after treatment and then 2 months and one year after treatment.

5 RESULTS

5.1 *Preliminary characterization*

5.1.1 *Zone 9*

Phenolphthalein tests performed on powder sampled every centimeter up to a 7 cm depth on zone 9, evidenced a total carbonation of the concrete cover (5–6 cm for the round-shaped rebars), as the phenolphthalein remained uncolored (Fig. 9).

The potential mapping realized on zone 9 (Fig. 10) showed quite homogenous potential values (ranging from −425 mV to −518 mV). According to the RILEM recommendation (Elsener, 2003), corrosion was probable only on one spot on the bottom of the beam (potential gradient >100 mV).

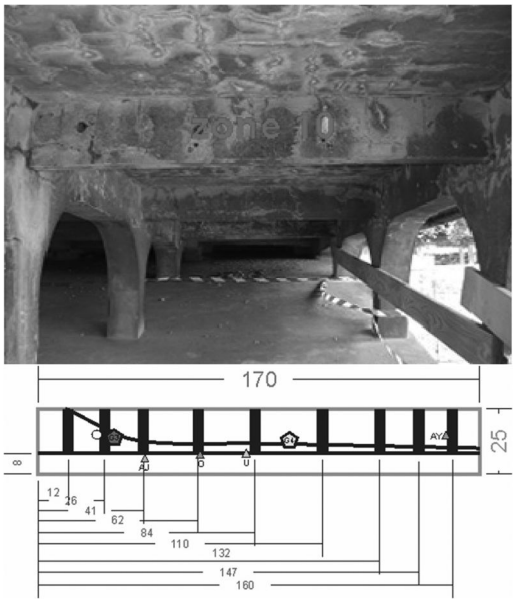

Figure 8. Atypical rebar network electromagnetically detected on zone 10, mixing 2 standard round shaped-rebars (one horizontal and one oblique, both 20 mm in diameter) and 9 flat Hennebique stirrups (4 to 4.5 cm large). On the scheme: the two pentagonal-shaped points refer to the Rp measurement spots, the white dot corresponding to the connecting point. The four triangular-shaped points refer to the powders drilled respectively before treatment (O), just after treatment (U), 2 months after (AJ) and one year after (AY).

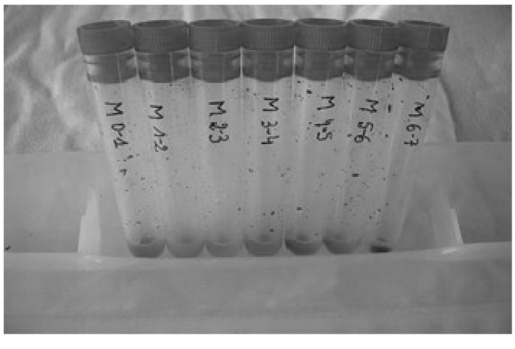

Figure 9. Zone 9. Phenolphthalein tests performed prior to the realkalisation, on powders sampled every centimeter up to a 7 cm depth, showing a total carbonation of the concrete cover of the round-shaped rebars.

Finally, polarization resistance (Rp) measurements were carried out on 2 points of the round-shaped rebars (on a single rebar and on a node), on the critical areas evidenced by the potential mapping (Fig. 7). In both cases the resulting corrosion current (respectively 0.082 ± 0.037 and $0.007 \pm 0.0017 \mu A/cm^2$) was below $0.1\ \mu A/cm^2$, which according to the RILEM Recommendation (Andrade, 2004), means that the corrosion level was negligible, which was consistent with the resistivity mapping.

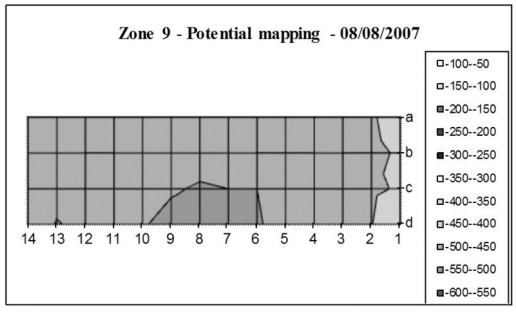

Figure 10. Potential mapping performed on zone 9 prior to the realkalisation treatment (T = 19°C, HR = 57%).

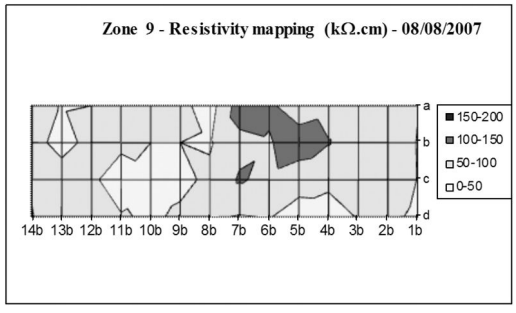

Figure 11. Resistivity mapping performed on zone 9 prior to the realkalisation treatment (T = 19°C, HR = 57%).

The resistivity mapping performed in zone 9 (Fig. 11) prior to the realkalisation treatment showed values ranging between 28 and 125 kΩ·cm, but generally higher than 50 kΩ·cm, indicating according to the RILEM recommendation (Polder, 2000) that the corrosion risk was weak to negligible.

So even if the carbonation had clearly reached the rebars, the corrosion activity was low, probably in correlation with the sheltered condition under the bridge and a permanent wind, inducing a drying process of the concrete.

5.1.2 *Zone 10*

Phenolphthalein tests performed on powders sampled every centimeter up to a 5 cm depth on zone 10, evidenced a total carbonation of the concrete cover (5–6 cm for the round-shaped rebars), as the phenolphthalein remained uncolored (Fig. 12).

As on zone 9, potentials measured on zone 10 were quite homogeneous (Fig. 13). They varied between −340 mV and −466 mV, indicating (Elsener, 2003) that corrosion was probable only on the left part of the beam (potential gradient > 100 mV).

On zone 10, resistivity values were a little lower than on zone 9 and ranged from 12 to 118 kΩ·cm (Fig. 14), which indicated a negligible to moderate corrosion risk (Polder, 2000).

Finally Rp measurements were performed on 2 points of the round-shaped rebars (on a single rebar and on a node), on the critical areas evidenced by the

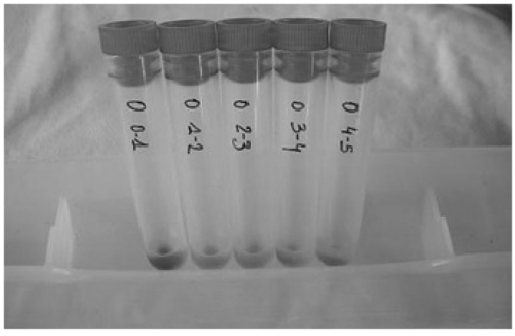

Figure 12. Zone 10. Phenolphthalein tests performed prior to the realkalisation treatment on powders sampled every cm up to a 5 cm depth, showing a total carbonation of the concrete cover.

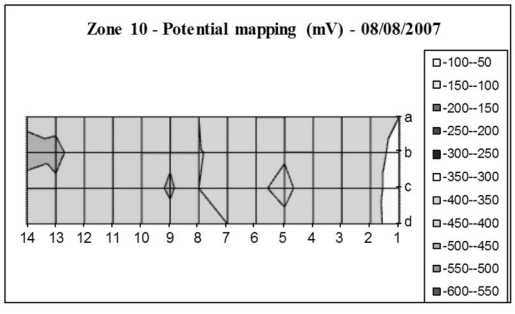

Figure 13. Potential mapping performed on zone 10 prior to the realkalisation treatment (T = 19°C, HR = 57%).

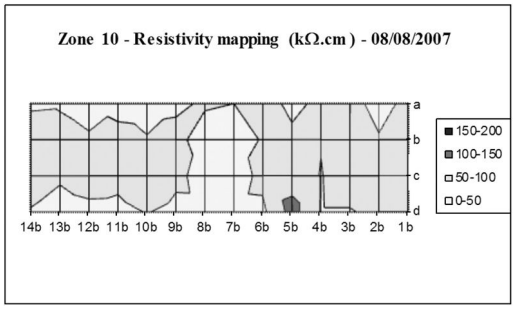

Figure 14. Resistivity mapping performed on zone 10 prior to the realkalisation treatment (T = 19°C, HR = 57%).

potential mapping (Fig. 8). Resulting corrosion current were very low (respectively $0.059 \pm 0.026 \mu A/cm^2$ and $0.012 \pm 0.006 \mu A/cm^2$), clearly below the $0.1 \mu A/cm^2$ threshold of the RILEM Recommendation (Andrade, 2004), revealing a negligible rate of corrosion.

So again the Rp measurements were consistent with the resistivity mapping and indicated a low corrosion activity, despite total carbonation of the concrete.

5.2 *Just after treatment*

5.2.1 *Zone 9*

Just after treatment, both phenolphthalein and thymolphthalein turned respectively pink and blue

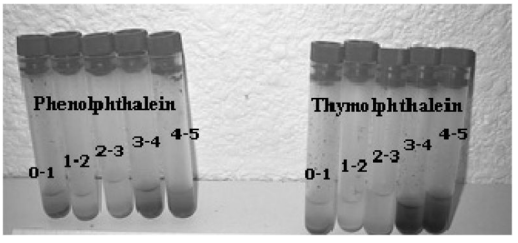

Figure 15. Zone 9. Phenolphthalein (left) and thymolphthalein (right) tests performed just after the realkalisation treatment showing an increase of pH around the rebars (3–5 cm depths).

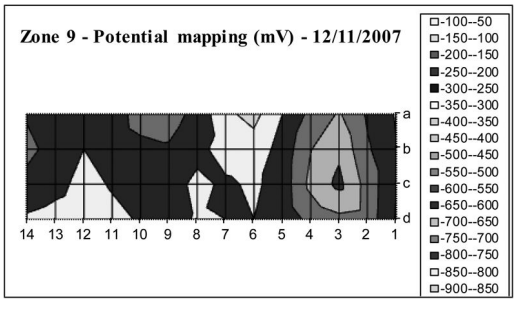

Figure 16. Potential mapping performed on zone 9 just after the realkalisation treatment, revealing a polarization of the rebars (T = 5°C, HR = 92%).

(Fig. 15) around the rebars (3–5 cm depth), indicating that the treatment succeeded in increasing the pH of the concrete around the rebars. This result is consistent with the criteria of efficiency indicated in specification FD CEN-TS 14038-1, Electrochemical realkalisation and chloride extraction treatments for reinforced concrete Part 1: Realkalisation.

Potential (Fig. 16) and resistivity (Fig. 17) mappings performed just after the realkalisation treatment indicated a lower resistivity of the concrete (probably linked to the dampening induced by the treatment) and a clear polarization of the rebars (−637 mV to −866 mV). Rp measurements were carried out on the same points as prior to the treatment, but the rebars were so polarized by the treatment that the measurement procedure was clearly disturbed.

5.2.2 *Zone 10*

As on zone 9, just after treatment, phenolphthalein and thymophthalein tests (Fig. 18) revealed an increase of pH around the rebars (5–6 cm depths), up to a value around 10.

As on zone 9, in consistency with both the moistening and the current flow generated by the treatment, potential (Fig. 19) and resistivity (Fig. 20) mappings were quite homogeneous and indicated a low resistivity and a polarization of the rebars (−965 mV to −966 mV). Rp measurements were performed on the same points as prior to the treatment, but again, the rebars were so polarized by the treatment that the measurement procedure was clearly disturbed.

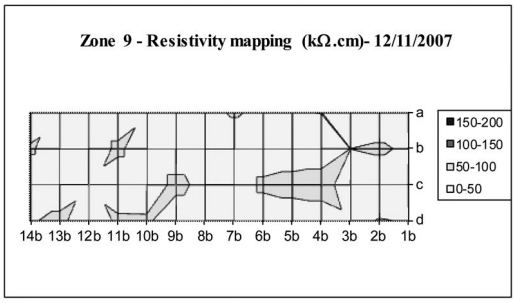

Figure 17. Resistivity mapping performed on zone 9 just after the realkalisation treatment (T = 5°C, HR = 92%).

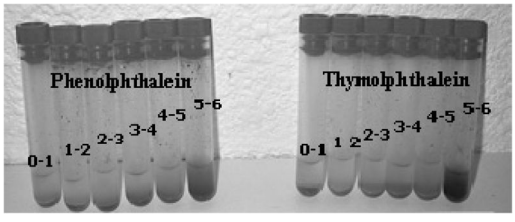

Figure 18. Zone 10. Phenolphthalein (left) and thymolphthalein (right) tests performed just after the realkalisation treatment showing an increase of pH around the rebars (5–6 cm depth).

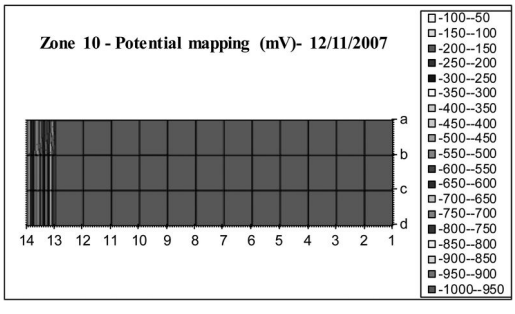

Figure 19. Potential mapping performed on zone 10 just after the realkalisation treatment, indicating a polarization of the rebars (T = 5°C, HR = 92%).

5.3 *Two months after treatment*

Two months after the realkalisation treatment, phenolphthalein and thymophthalein tests indicated that the pH had been maintained to values around 10 around the rebars in both zones 9 and 10.

On zone 9, the potential mapping (Fig. 21) evidenced that the rebars were still polarized (−508 mV to −772 mV). Resistivity values (Fig. 22) were a little higher than just after treatment (25 to 158 kΩ.cm), indicating that either a drying process was ongoing, or as suggested by Banfill (1997) and Yeih (2005) that, due to the treatment, the pore structure had been condensed, both phenomena possibly being intermingled.

On zone 10, the potential mapping (Fig. 23) also indicated a residual polarization of the rebars

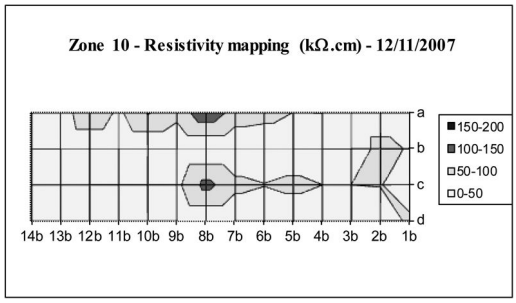

Figure 20. Resistivity mapping performed on zone 10 just after the realkalisation treatment (T = 5°C, HR = 92%).

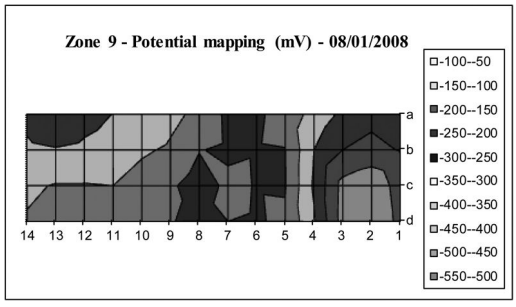

Figure 21. Potential mapping performed on zone 9 two months after the realkalisation treatment, indicating that the rebars were still polarized (T = 10°C, HR = 89%).

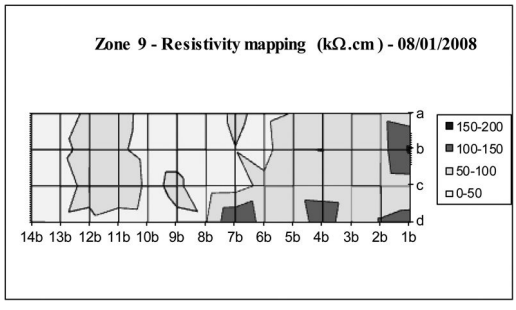

Figure 22. Resistivity mapping performed on zone 9 two months after the realkalisation treatment (T = 10°C, HR = 89%).

(−488 mV to −968 mV). The resistivity values measured two months after treatment were ranging between 34 to 673 kΩ·cm, the latest being representative of a quite resistive concrete. Again, either the concrete was drying or the pores structure had been densified by the treatment (Banfill, 1997; Yeih, 2005), both phenomena being possibly intermixed.

On both zones 9 and 10 Rp measurements were carried out. Resulting corrosion currents were comparable in the 2 zones, but also comparable with the values obtained just after treatment. However, as the rebars were still highly polarized two months after the treatment, again the measurement procedure was clearly disturbed.

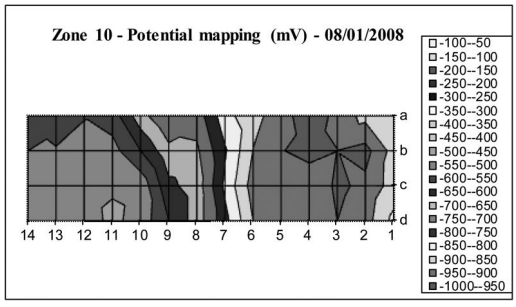

Figure 23. Potential mapping performed on zone 10 two months after the realkalisation treatment, indicating that the rebars were still polarized (T = 10°C, HR = 89%).

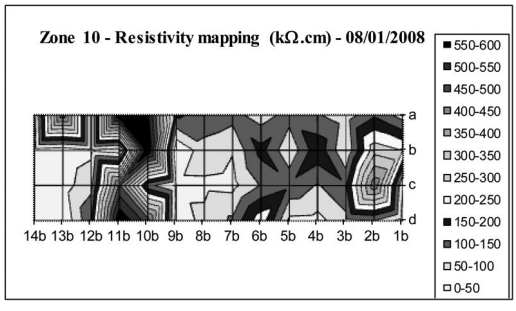

Figure 24. Resistivity mapping performed on zone 10 two months after the realkalisation treatment (T = 10°C, HR = 89%).

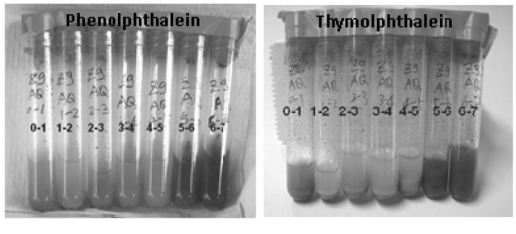

Figure 25. Zone 9. Phenolphthalein (left) and thymolphthalein (right) tests performed one year after the realkalisation treatment showing that the pH was still above 10 around the rebars (5–6 cm depth).

5.4 *One year after treatment*

One year after treatment a fourth series of tests has been carried out. However, it is to be noticed that the beams were covered with a render at the end of the restoration work. So for several months the testing areas were covered with a cement render, which has been eliminated a few days before this last series of measurements.

5.4.1 *Zone 9*

Phenolphthalein and thymolphthalein tests (Fig. 25) revealed that one year after the realkalisation treatment, the pH of the concrete was still above a value of 10 as both indicators turned respectively pink and blue at the rebars depth (5–6 cm), on zone 9.

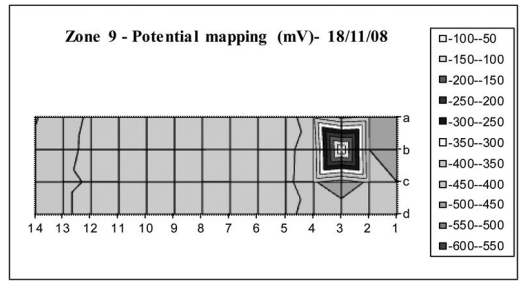

Figure 26. Potential mapping performed on zone 9 one year after the realkalisation treatment (T = 11°C, HR = 99%).

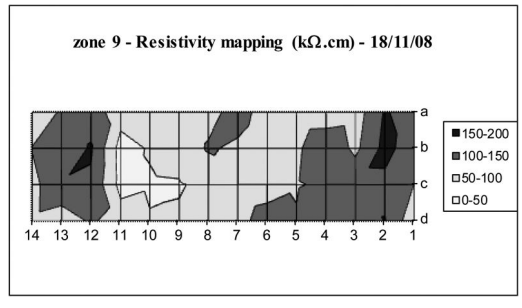

Figure 27. Resistivity mapping performed on zone 9 one year after the realkalisation treatment (T = 11°C, HR = 99%).

The potential map obtained one year after the realkalisation treatment in zone 9 (Fig. 26) indicated an increase of potential towards more positive values (−363 to −467 mV) than two months after treatment. However potential values were quite homogeneous (except on the connecting point located on b3), and indicative of a minor probability of corrosion (Elsener, 2003).

Resistivity values that were ranging between 30 and 165 kΩ.cm in zone 9 (Fig. 27), were consistent with the potential values and indicative of a negligible risk of corrosion (Polder, 2000).

Finally no Rp measurement could be achieved.

5.4.2 *Zone 10*

On zone 10, as on zone 9, phenolphthalein and thymolphthalein tests (Fig. 28) indicated that one year after the realkalisation treatment, the pH of the concrete was still above a value of 10 as both indicators turned respectively pink and blue at the rebars depth (4–5 cm).

Potential values measured on zone 10 (Fig 29) were ranging between −274 mV and −432 mV, but except around the connecting point (c9), no significant gradient was evidenced, the map being quite homogeneous. The corrosion probability was as a consequence quite low (Elsener, 2003).

The resistivity mapping obtained on zone 10 (Fig. 30) was almost a twin of the one of zone 9, and denoted that the concrete was quite resistive (4 to 166 kΩ.cm).

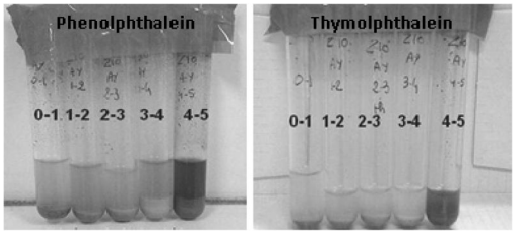

Figure 28. Zone 10. Phenolphthalein (left) and thymolphthalein (right) tests performed one year after the realkalisation treatment showing that the pH was still above 10 around the rebars (4–5 cm depth).

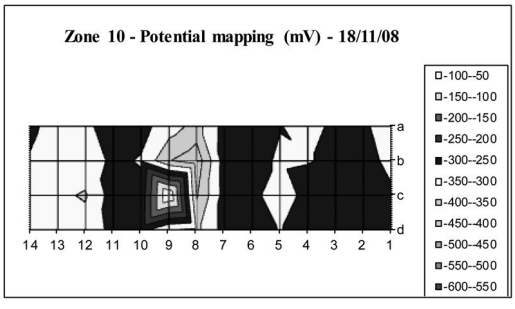

Figure 29. Potential mapping performed on zone 10 one year after the realkalisation treatment (T = 11°C, HR = 99%).

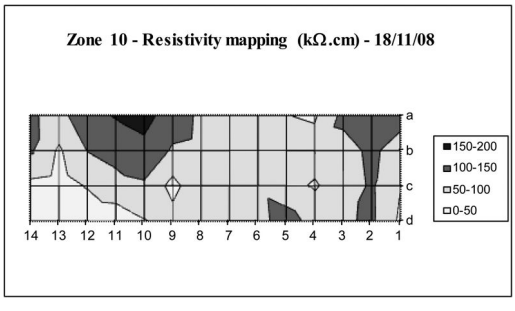

Figure 30. Resistivity mapping performed on zone 10 one year after the realkalisation treatment (T = 11°C, HR = 99%).

This result was consistent with the potential mapping and indicative of a low risk of corrosion (Polder, 2000).

Finally, as in zone 9 no Rp measurement could be achieved.

6 DISCUSSION

A first point to be stated is the great heterogeneity of this centenarian concrete which is common in ancient concretes, and that evidences the difficulty of representativeness of a diagnosis.

In ancient concrete, continuity of the rebar network constitutes another problem for both electrochemical measurements and treatments. Thus, as in the case of Camille de Hogues Bridge, where round shaped-rebars were mixed with rectangular-shaped Hennebique stirrups, in ancient concretes, the rebar network is often singular and disconnected. Subsequently, it can be necessary to ensure the connectivity of the rebars, indispensable for both a correct treatment and suitable electrochemical measurement conditions, and therefore to drill numerous holes, which is quite invasive for cultural heritage applications. Another consequence is that it can be tricky to precisely evaluate the polarized area when calculating corrosion rate, from Rp measurements.

Concerning the treatment itself, it is to be noticed that the rebars remained polarized more than two months after the treatment, which has to be taken into account in validation procedures. Now the ability of the treatment to increase the pH around the rebars was clearly highlighted. Yet, the pH of the surface in contact with the alkaline solution remained below 9, suggesting that under standard realkalisation conditions, the presence of alkalis was insufficient to increase enough the pH. Therefore, water electrolysis at the bar seemed to be the driving process, as found by Mietz (1995), Bertolini (2008) and Ribeiro (2013). Besides, as indicated by the thymolphthalein tests, after treatment pH values above 10 were reached around the rebars. Nevertheless, laboratory experiments (Tong, 2008; Sahal, 2011) performed in parallel to the Camille de Hogues Bridge tests, within the frame of the larger "realkalisation project", indicated that the pH hardly exceeds 10.5 around the rebars under standard impressed current realkalisation conditions, which could be insufficient to protect steel from corrosion. From literature data, a pH value of 11 is often considered as a threshold for re-passivation (Yeih, 2005). However, laboratory tests performed in the larger "realkalisation project" (Tong, 2008; Sahal, 2011) have shown that, even with a pH of 11, passivation is never recovered when corrosion has started. Several authors (Miranda, 2006; Bastidas, 2008) confirm that realkalisation can only be considered as a preventive treatment, as they have shown that when a substantial oxide layer is already formed, re-passivation cannot be achieved.

So, realkalisation treatments might slightly reduce the corrosion rate for a short period after treatment, but corrosion is never stopped (Miranda, 2006; Tong, 2008; Bastidas, 2008; Sahal, 2011). Moreover, some experiments have shown that after 30 months, the corrosion rate returns to its original level prior to the treatment, and corrosion layers expand again around the rebars (Tong, 2008, Sahal, 2011). So realkalisation treatment using impressed current can slow down corrosion just after treatment but this effect is not durable.

7 CONCLUSION

With carbonation being the first cause of degradation in ancient concrete in the field of historical monuments and a main degradation factor for road infrastructures, there is a strong need for dedicated restoration/repair

treatments. Realkalisation treatments which were developed to cure carbonation induced corrosion were consequently promising. Therefore, the French Ministries of Culture and of Sustainable development gathered to fund 10 years of research on realkalisation treatments (Marie-Victoire, 2003; Cailleux, 2003; Cailleux, 2006; Tong, 2008; Sahal, 2011).

In the field study carried out on Camille de Hogues Bridge, presented in this paper, both analytical and electrochemical tests were considered. The electrochemical characterizations performed on the bridge evidenced the difficulty of corrosion monitoring on site on ancient reinforced concrete, where the rebar network can be unusual in shape, erratic in distribution, and poorly connected. Those experiments did also evidence the complexity of the representativeness of diagnosis on ancient carbonated concrete, where compact zones can be neighbored by honey-combing or by very porous areas. Finally, as often in carbonated concrete, the more carbonated zones are also often the drier and therefore, represent areas where the corrosion activity is reduced due to the lack of water.

Analytical characterization performed on Camille de Hogues Bridge, was consistent with former field tests (Marie-Victoire, 2003; Cailleux, 2003; Cailleux, 2006) and laboratory tests (Tong, 2008; Sahal, 2011). All evidenced that realkalisation treatment using impressed current can increase the pH from lower than 9 to 10.5.

However, the ability of the treatment to stop corrosion could not be demonstrated. From former field trials and laboratory experiments, realkalisation reduces the corrosion rate for a while but then corrosion starts again. The more probable hypothesis is that the increase of pH generated by the treatment to reach values close to 10 or 11 is not sufficient to stop corrosion or prevent further corrosion in the long term.

As a consequence, the efficiency of such treatments is not sufficiently satisfactory compared to its invasiveness and potential side effects induced by the introduction of surplus alkali ions (Marie-Victoire, 2003; Cailleux, 2003; Cailleux, 2006).

Subsequently, on the basis of 10 years of research corroborated by these last experiments carried out on Camille de Hogues Bridge, realkalisation treatments should not be recommended on historical monuments.

AKNOWLEDGEMENTS

The authors would like to thank J. Dauthuille and A. Deman for their help on the field, but also the Renofors Company for their technical assistance and F. Jeanneau, the architect in charge of the restoration work.

REFERENCES

Andrade C. & Al., RILEM TC 154-EMC, Recommendations: Test methods for on-site corrosion rate measurement of steel reinforcement in concrete by means of the polarization resistance method, Materials and Structures, Vol. 37, November 2004, pp 623–643.

Banfill, P.F.G., 'Re-alkalisation of carbonated concrete-effect on concrete properties', Construction and Building Materials (1997),Vol. 11, pp. 255–258.

Bastidas D. M., Cobo A., Otero E. and Gonzalez J. A., Electrochemical rehabilitation methods for reinforced concrete structures: advantages and pitfalls, Corrosion Engineering, Science and Technology (2008) Vol. 43 No 3, 248–255.

Bertolini, L., Carsana, M. & Redaelli, E. 2008, 'Conservation of historical reinforced structures damaged by carbonation induced corrosion by means of electrochemical realkalisation', Journal of Cultural Heritage, Vol. 9, pp. 376–385.

Cailleux E., Marie-Victoire E., Texier A., MarcheseG., Experimental investigation of realkalisation treatments used for restoration of historical monuments made of reinforced concrete, Concrete solutions : 1st International conference on concrete repair, St-Malo, France, 15–17 July 2003, ed. by M. Grantham, F. Rendell, R. Jauberthie, C. Lanos, p. 527–534. London : GR technologie, cop. 2003.

Cailleux E. and Marie-Victoire E., Influence of the concrete composition on the efficiency and the durability of realkalisation treatment, Concrete solutions : proceedings of the 2nd international conference on concrete repair, St Malo, France, 27–29 June 2006, ed. by M. G. Grantham, R. M. Jauberthie and C. Lanos, p. 271–279. Watford: BRE Press, cop. 2006.

Elsener B. & Al., RILEM TC 154-EMC:Electrochemical Techniques for Measuring Metallic Corrosion – Recommendations – Half-cell potential measurements – Potential mapping on reinforced concrete structures, Materials and Structures, 36 (2003) 461–471.

Marie-Victoire E. and Texier a., Realkalisation and corrosion inhibitors, a conservation method for ancient buildings?, 6th CANMET/ACI International conference on durability of concrete, June 1–7, 2003, Thessaloniki, Greece, p. 615–629.

Marie-Victoire E., Cailleux E., Texier A., Journal de physique *IV*, vol. 136, November 2006, p. 305–318.

Mietz, J. 1995, 'Electrochemical realkalisation for rehabilitation of reinforced concrete structures', Materials and corrosion, Vol.46, 527–533.

Miranda J.M., Gonzalez J.A., Otero E., Several questions about electrochemical rehabilitation methods for reinforced concrete structures, Corrosion Science 48 (2006) 2172–2188.

Polder R & Al., RILEM TC 154-EMC, Recommendations: Test methods for on-site measurement of resistivity of concrete, Materials and Structures, Vol. 33, December 2000, pp 303–611.

Ribeiro P.H.L.C., Meira G.R., Ferreira P.R.R., Perazzo N., Electrochemical realkalisation of carbonated concretes – Influence of material characteristics and thickness of concrete reinforcement cover, Construction and Building Materials 40 (2013) 280–290.

Sahal M., Tong Y. Y., Sanz Merino B., Bouteiller V., Marie-Victoire E. and Joiret S., Durability of impressed current realkalization treatment applied on reinforced concrete slabs after 5 years, International conference on durability of building materials and components, proceedings of the XIIth DBMC, Porto, Portugal, April 12th–15th, 2011, 8p.

Sergi, G., Walker, R.J. & Page, C.L. 1996, 'Mechanisms and criteria for the realkalisation of concrete', Proceedings of the 4th international Symposium on corrosion

of reinforcement in concrete constructions, Cambridge, United Kingdom, pp. 491–500.

Tong Y. Y., Bouteiller V., Marie-Victoire E. and Joiret S., Durability evaluation of a realkalisation treatment using impressed current, Durability of buildings materials & components 11 : globality and locality in durability, Proceedings of the 11th International Conference, Istanbul, Turkey, 11–14 May 2008, ed. A. Nil Türkeri, Özkan Sengül, Istanbul : I.T.U., 2008, vol. 4, p. 1751–1762.

Yeih, W., Chang, J.J. 2005, 'A study on the efficiency of electrochemical realkalisation of carbonated concrete', Construction and Building Materials, Vol. 19, pp. 516–524.

Concrete Solutions – Grantham et al. (Eds)
© 2014 Taylor & Francis Group, London, ISBN 978-1-138-02708-4

Comparative analysis of the Transylvanian Jesuit churches from the XVIIIth century

C.G.R. Mircea & G. Orbán
Technical University of Cluj-Napoca, Romania

ABSTRACT: Under the patronage of the Catholic Church, several churches and minsters were built in Transylvania. These buildings still preserve their technical performance, cultural and aesthetical values. The paper presents a critical conception analysis and a numerical investigation of the masonry Jesuit churches built in the first half of the XVIIIth century. The research emphasizes the advances performed in the building practice brought by the expansion of the knowledge due to the clear definition of the inertia concept by Sir Isaac Newton in 1685. In this respect, 3D CAD models were assembled in order to quantify general and normalized parameters and indicators, used to justify the above conclusion. Next, Finite Element Analyses and Modal Analyses were considered to explain an unusual cracking pattern registered in the most rigid vault of all analyzed churches. It was concluded that cracks were generated by the frequently met surface earthquakes.

1 INTRODUCTION

According to etymology, the pilgrim (from the Latin peregrinus) is a person exiled or expatriated. This interpretation has undergone a gradual translation by definition that the faithful pilgrim is a traveler to a place of reverence, regarded as sacred in the tradition of his religion. The first evidence of the pilgrims, and consequently of the practice of religious pilgrimage, is the megalithic monument from Stonehenge, built between 2800 and 1100 BC, the transition from the Neolithic to the Bronze Age. Currently, the practice of pilgrimage and its definition have been adapted to the historical moment we are living now, the beginning of globalization. Thus, according to the Council of Europe, cultural pilgrimage materializes in practice the principles of the United Europe on diversity and cultural identity, dialogue and mutual development, beyond any borders. The first evidence of recognition of the cultural pilgrimage values is the cultural routes program launched in 1987 by the Council of Europe and the establishment in 1998 of the European Institute of Cultural Routes, as a tool for valuing European cultural routes. Currently, Romania secured funding for two cultural routes with governmental support. The movement, and later the association *Mary's Way* is a private European initiative, aiming to establish a network of pilgrimages in Central and Eastern Europe, following the example of Western pilgrimage routes. The proposed interconnection includes shrines dedicated to the Blessed Virgin Mary of Central and Eastern Europe along existing roads and practiced for pilgrimage for centuries or along tourist roads. This initiative is particularly important, leading to valuing many baroque monuments in Transylvania, to ensure the conservation of cultural heritage resources and spiritually in the area.

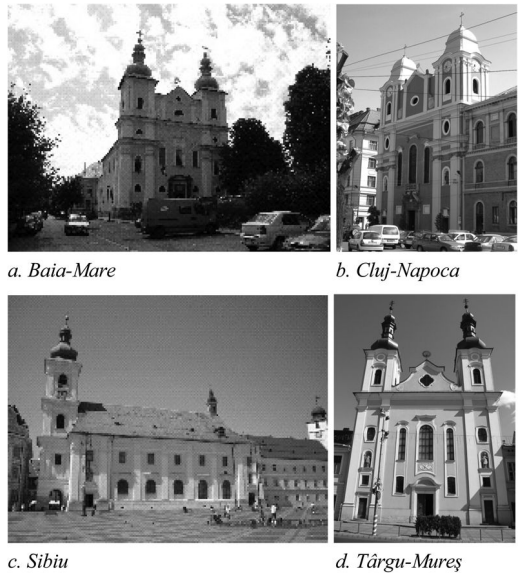

a. Baia-Mare *b. Cluj-Napoca*

c. Sibiu *d. Târgu-Mureş*

Figure 1. The Transylvanian Jesuit churches located on cities along the path of *Mary's Way*.

The paper presents research based on spiritual values of the proposed route, generating certain architectural and engineering technical values of universal jurisdiction, representing a fundamental step in the rebirth of the area of the proposed pilgrimage. More specifically, the investigation considers the four Transylvanian Jesuit churches (see Figure 1), spread along

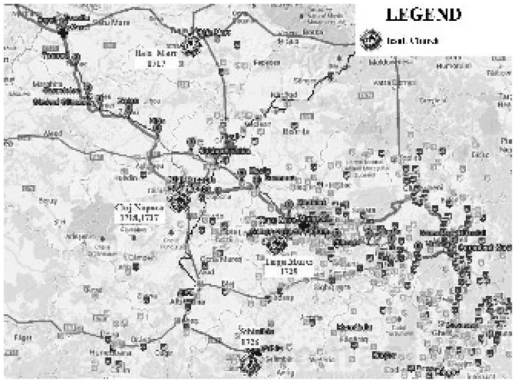

Figure 2. The Transylvanian routes of the *Mary's Way* and the five locations of the Jesuit churches.

the eastern routes of the *Mary's Way*, as shown in Figure 2.

2 ANALYSIS OF THE INTERIOR SPACE AND STRUCTURAL MATERIAL DISTRIBUTION

2.1 *Background concerns*

Even if the inertia concept (i.e., the resistance of a body to a change of its state of motion) was defined by Sir Isaac Newton as his first law only in 1685, its known background goes until the VIth century BC, when Aristotle stated his early motion theory. However, the laws of mechanics in physics were not entirely unknown for the architects and building practitioners up to Newton's publication.

While during ancient times the concept was embedded in empirical elementary mathematical formulations, regularly based on Pythagoras means and proportions, it seems that during the Renaissance more scientific evidence was considered in the design of the interior space and structural material distribution. Gravity and inertia concepts were decisive in the construction process of important buildings. Arguments will be presented considering four Transylvanian Jesuit churches built along the *Mary's Way* soon after the official definition of the inertia concept.

For a solid body, the mass inertia with respect to the mass centre represents one of the main features describing the body rigidity. If inside a parallelepipedal body, a hollow space occurs, the mass inertia changes. The larger the material dispersion in respect with its mass centre is, the higher the inertia is.

Assimilating the church with a parallelepipedal body, the hollow space represents the interior representative space (see Figure 3). The specific mass inertia represents an essential indicator with regard to the church structure rigidity, and consequently to its strength. Thus, the dimension and the ratios of the interior representative space determine decisively the church structure's inertia. The variation law of the

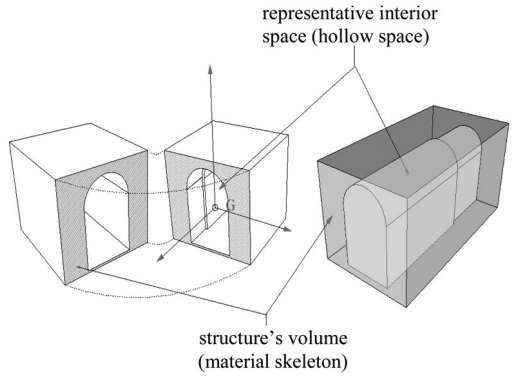

Figure 3. Basics of the modeling technique of the interior space for a given initial matrix.

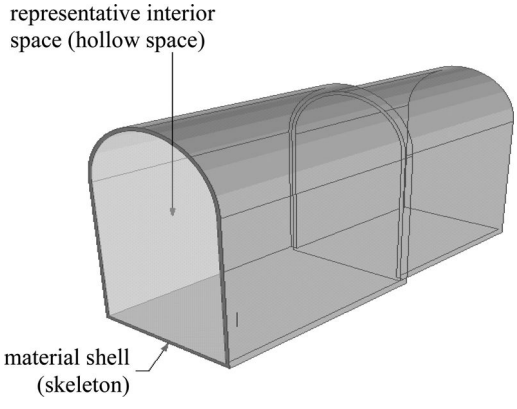

Figure 4. Scale modeling technique of the material distribution by covering the interior representative space with a shell.

interior representative space within the church body represents the creative act of the architects, sometimes artists. Besides aesthetical and functional reasons, it also has a major structural impact. Furthermore, at that time, the material distribution was controlled by 3D scale models built by embedding the interior representative space with the optimum shell (i.e., material skeleton), as shown in Figure 4.

Using such logical modeling techniques, the architects and carvers of the Jesuit building school could grow their experience and build more and more optimally, creating technical, aesthetical and historical values, lasting centuries, while facing extreme hazards and/or human ignorance. Nevertheless, today this patrimony ensures the background for the future sustainable development.

2.2 *Volumetric stiffness analysis*

At the beginning, Jesuit churches from Transylvania were built as replicas of *Church of the Gesù* (i.e., Baia-Mare and Cluj-Napoca). All four churches present similar conceptual features: massive brick and stone masonry walls, and cylindrical brick masonry vaults.

Table 1. Main characteristics of the masonry structures.

Church	Period of construction	Dimensions m × m	Built area Built area m^2	Wall heights m	Tower heights m	Masonry weight Masonry weight to	Masonry unitary consumption cm
Baia-Mare	1717–1724	43.24 × 23.10	998.05	20.100	28.100	10846.5	517.5
Cluj-Napoca	1718–1724	44.41 × 23.26	997.11	19.100	27.100	9677.7	510.8
Sibiu	1726–1738	41.91 × 22.15	968.03	15.400	35.000	9629,1	523.6
Târgu-Mureº	1728–1750	39.60 × 19.38	767.82	14.800	22.000	5739.3	393.4

Table 2. Volumetric inertia characteristic with regard to principal axes of the churches.

	Volumetric moments of inertia m^5			Radiuses of gyration m		
Church	Longitudinal axis – x	Transversal axis – y	Vertical axis – z	i_x	i_y	i_z
Baia-Mare	607779	1412031	149112	10.64	16.21	16.66
Cluj-Napoca	604746	1514501	1593279	10.57	16.73	17.16
Sibiu	518302	1332692	1405254	10.11	16.22	16.65
Târgu-Mureº	231924	518231	703200	8.50	13.87	14.79

Table 3. Results of the volumetric stiffness analysis.

Church	Masonry volume m^3	Interior representative volume m^3	Center mass inertia to × m^2	I_1 to/m	I_2 to/m	I_3 m^3/m^3
Baia-Mare	5165.0	7148.1	7372.9	1.03	1.43	1.38
Cluj-Napoca	5093.5	7352.7	7053.8	0.96	1.38	1.44
Sibiu	5068.6	7942.2	6186.9	0.78	1.22	1.57
Târgu-Mureº	3020.7	4761.6	2815.4	0.59	0.93	1.58

The main characteristics of the buildings are presented in Table 1. 3D CAD digital models were assembled on the ground of the field surveys (Orban 2013). The data was than digitalized, creating virtual solid objects as shown in Figure 5. Thus, the data could be processed for normalized analyses.

Besides the volumetric inertia and the associated gyradius (see Table 2), the following indicators are considered with regard to the rigidity assessment and global structural evaluation:

I_1 – the stiffness ensured for a cubic meter of internal representative space (i.e., mass inertia related to the interior volume);

I_2 – the stiffness ensured with a masonry cubic meter (i.e., mass inertia related to the masonry volume);

I_3 – the interior hollow space volume ensured by a masonry cubic meter (i.e., the interior volume related to the masonry volume).

Results and indicators are shown in Table 3. Figure 6 emphasizes that the chronological progress of the building concept for the churches was done by embedding a larger representative interior volume within a

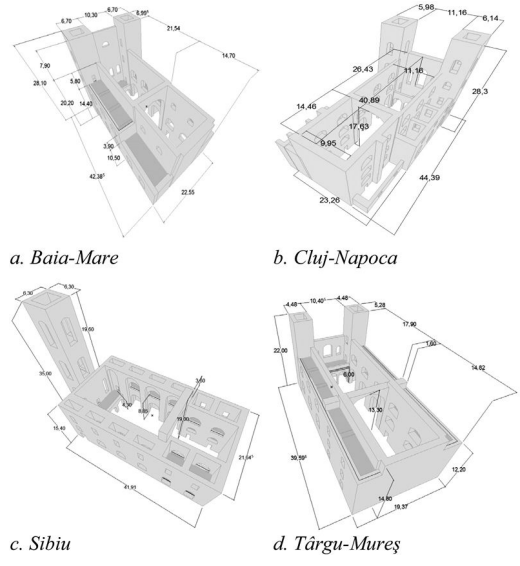

a. Baia-Mare *b. Cluj-Napoca*

c. Sibiu *d. Târgu-Mureş*

Figure 5. 3D CAD models.

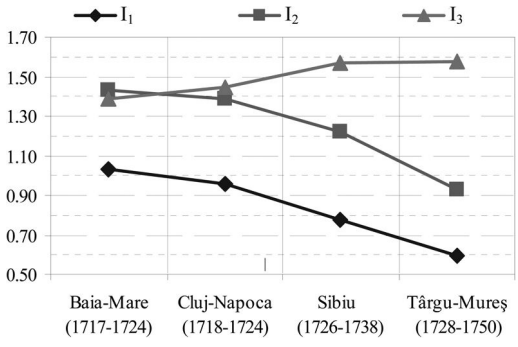

Figure 6. Progress indicators.

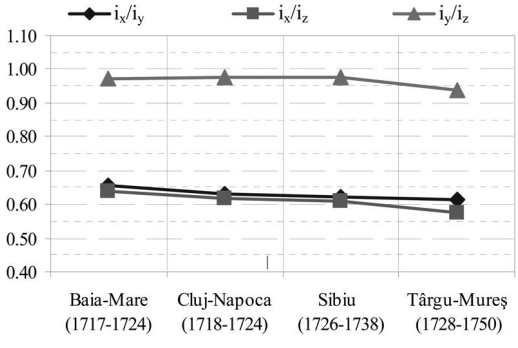

Figure 7. Normalized aspect ratios.

shell built with less material (i.e., indicator I_3), preserving the main aspect ratios shown in Figure 7. The aim was obtained by optimizing the inertial properties and costs of masonry.

2.3 *Vault analyses*

Some unexplained cracking has appeared over the centuries in the masonry vault of the Cluj-Napoca church (see Figure 8). It was quite an unexpected observation since is the most massive vault, with a thickness of 300 mm, double that the vault thickness of the other churches. The hazards investigation revealed as a possible cause the small surface earthquakes that happen in the area from time to time. The most severe was registered in 1786, with a magnitude of 5.2 on the Richter scale, and had the epicenter near Cluj-Napoca.

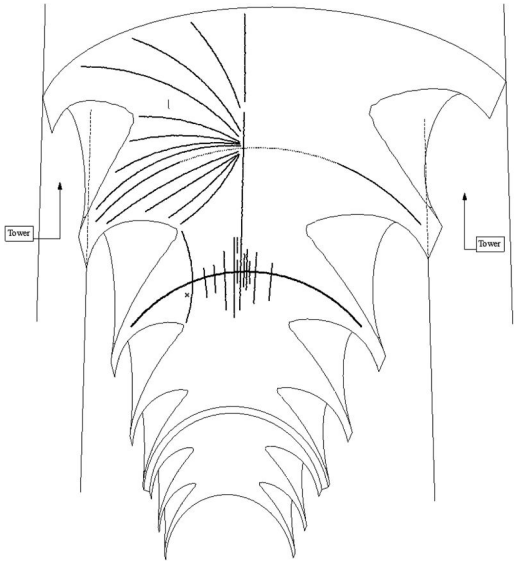

Figure 8. Cracking pattern of the vault from Cluj-Napoca.

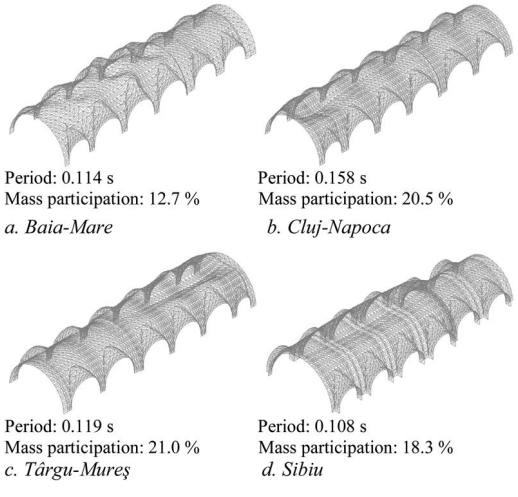

Figure 9. Fundamental vibration modes.

Table 4 presents the main characteristics of the vaults. Finite Element Analyses and Modal Analyses were performed with Risa 3D v9.2 in the elastic range of behavior, simulating the vault's behavior under a

Table 4. Main characteristics of the masonry vaults.

Church	Span m	Key height m	Key height/ span ratio	Thickness mm	Plan area m^2	Weight to	Material unitary Volume m^3	consumption cm
Baia-Mare	11.000	5.500	1/2	150	485.02	214.3	112.8	23.3
Cluj-Napoca	11.160	5.580	1/2	300	483.42	349.9	184.1	37.3
Sibiu	12.830	6.415	1.2	150	580.96	291.9	153.6	23.3
Târgu-Mureş	10.420	5.210	1/2	150	410.18	167.6	88.2	21.5

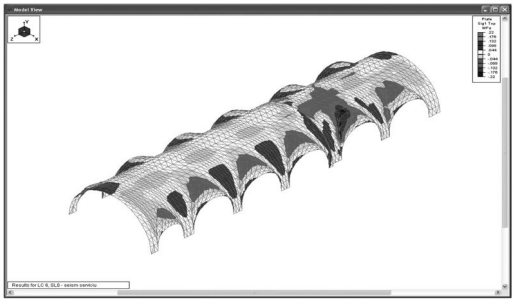

Figure 10. Principal stress in the vault from Cluj-Napoca under the service surface earthquake.

frequently met surface earthquake. Only the vertical vibrations were considered, and standard assumptions were considered with regard to the material properties and the elastic vertical spectrum.

Figure 10 presents the fundamental vibration modes and their characteristics, and Figure 10 the principal stresses in the vault from Cluj-Napoca under a service earthquake. In the case of the vault from Cluj-Napoca, the large mass engaged in the vibration resulted in a higher cracking vulnerability of the masonry. A second vibration mode also involved significant mass and suggests the same conclusion.

It seems that after an initial hesitation with regard to the optimal vault thickness, the practice returned to a slender solution, more compatible with the material properties. The heavy vault generates longitudinal splitting stresses during vertical vibration that are not present in the case of the slender vaults, which have the ability to adapt better to the vibration modes by membrane compressive stresses.

3 CONCLUSIONS

As shown above, the Jesuit building school improved its knowledge significantly during the construction process of the churches in Transylvania. Implementing modern ideas of inertia philosophies at that time, the reduction of the structural volume ensured the necessary rigidity and interior representative space. Initial doubts regarding the vaults stiffness were also surpassed by the 50 years of experience.

ACKNOWLEDGEMENT

This paper was supported by the project "Improvement of the doctoral studies quality in engineering science for development of the knowledge based society-QDOC" contract no. POSDRU/107/1.5/S /78534, project co-funded by the European Social Fund through the Sectorial Operational Program Human Resources 2007–2013.

REFERENCES

Orban, G. 2013. Analysis and capitalization of the built patrimony of the roman-catholique church from Transylvania, in the frame of the pilgrimage route Mary's Way. *PhD thesis* 65, Technical University of Cluj-Napoca, 246p.

This page intentionally left blank

Service life modelling

This page intentionally left blank

Concrete Solutions – Grantham et al. (Eds)
© 2014 Taylor & Francis Group, London, ISBN 978-1-138-02708-4

Study on autogenous shrinkage stress considering dependence on temperature in early age

Jun-ichi Arai, Takahiro Ajichi & Toshiaki Mizobuchi
Hosei University, Tokyo, Japan

ABSTRACT: The prediction formula of the autogenous shrinkage strain of concrete shows strain component deducted thermal strain from total strain in the temperature adjusted age of concrete. However, as thermal expansion coefficient should be assumed, the prediction formula of the autogenous shrinkage strain without thermal strain is desired. It is seemed that the formula which used the age further than the temperature adjusted age of concrete is practical. In this study, prediction formula of the autogenous shrinkage strain estimated using experimental results which measured the autogenous strain under conditions for fixing concrete temperature is reported.

1 INTRODUCTION

Recently, high durability and high strength concrete has been required for concrete structures in Japan. As the autogenous shrinkage strain is smaller than thermal strain and the drying shrinkage strain, the autogenous shrinkage strain has not been considered until now in the design. However, applications of high strength concrete and self-compacting concrete are increasing, since high performance concrete is more in demand for concrete structures recently. The autogenous shrinkage strain of concrete cannot be disregarded, since the cement contents used by the application of such concrete increases. Studies on the mechanism and control method of autogenous shrinkage strain of concrete are recently reported in great numbers.

For example, the prediction formula of autogenous shrinkage strain of concrete using Ordinary Portland cement and Portland blast furnace slag cement class B is shown in the Standard Specifications for Concrete Structures-2012 (Design) and Guidelines for Control of Cracking of Mass Concrete 2008 in Japan. In the prediction formula, autogenous shrinkage strain was defined as the value which removed thermal strain from the measured value. Thermal strain is calculated from the temperature change multiplied by thermal expansion coefficient. In past research, though the autogenous shrinkage strain of concrete rises quickly as the temperature rise with the hydration of cement increases, it is reported that it is possible to evaluate the effect of temperature in the autogenous shrinkage strain of concrete by using the temperature adjusted age of concrete. However, it is necessary to exclude the effect of thermal strain by the assumption of thermal expansion coefficient of concrete for measuring the autogenous shrinkage strain of concrete in existing structures. Therefore, prediction formula of the autogenous shrinkage strain exclude the effect of thermal strain as much as possible by correction. It seems that the prediction formula which can be evaluated using the age without using the temperature adjusted age of concrete is more applicable.

In this study, a method for evaluating the autogenous shrinkage strain from the relationship between the factors in terms of the rate of the autogenous shrinkage strain and age under the constant temperature conditions was examined.

2 EXPERIMENT SUMMARY

2.1 *Experiment standard and concrete composition*

The experiment was carried out at 20 degrees Celsius, 40 degrees Celsius, 50 degrees Celsius and 60 degrees Celsius.

All the tests were carried out at the same concrete composition as shown in Table-1. In addition, the type of cement was defined as Blast-Furnace Slag Cement type-B.

2.2 *Method for measurement of the autogenous-shrinkage strain*

The measurement of the autogenous-shrinkage strain of the concrete used a Temperature Stress Testing Machine (TSTM). The TSTM was comprised of two devices: a stress-testing-unit as shown in Fig-1, using a “dog-bone” type specimen. This device completely fixed one end of the Test Specimen and the other

was fixed in a controllable variable device. Therefore, results were based on the distortion measured in the Non-stress testing unit as shown in Fig-2. This device can control restriction degree freely. In addition, each device was covered with insulation material which had a heater built-in and can control temperature of the concrete. By this experiment, only temperature of the concrete was controlled with a device as shown in Fig-2. Dimensions of the Test Specimen were 150 × 150 × 850 mm as shown in Fig-3.

Table 1. Concrete Composition.

W/C (%)	Water (kg/m^3)	Cement (kg/m^3)	Gravel (kg/m^3)	Sand (kg/m^3)	Air (%)
50	154	308	1043	798	4.5

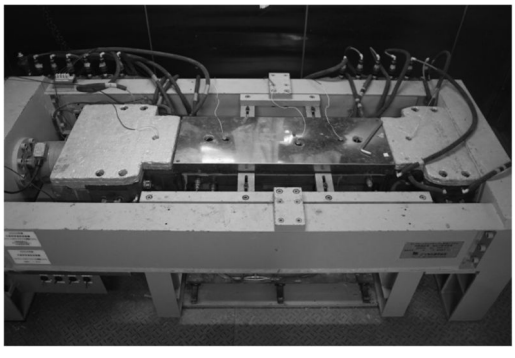

Figure 1. Stress testing unit (TSTM).

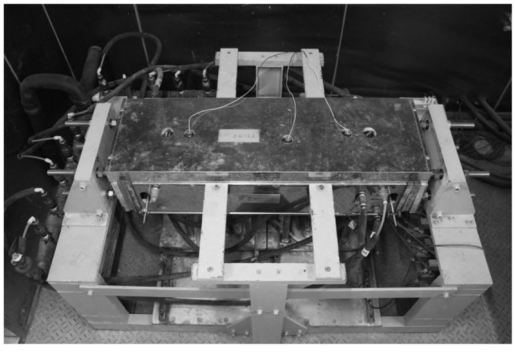

Figure 2. Non stress testing unit (TSTM).

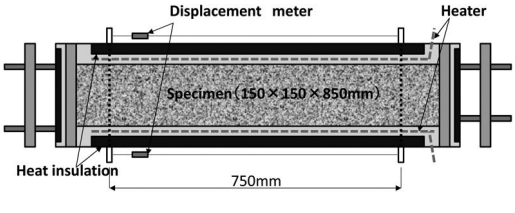

Figure 3. Test specimen.

2.3 *Method for measurement of a hydration product and the pore size distribution*

The observation of the hydration products using SEM were also carried out, as shown in Fig-4. In addition, the pore size distribution was measured using mercury porosimetry as shown in Fig-5.

Figure 4. Pore diameter.

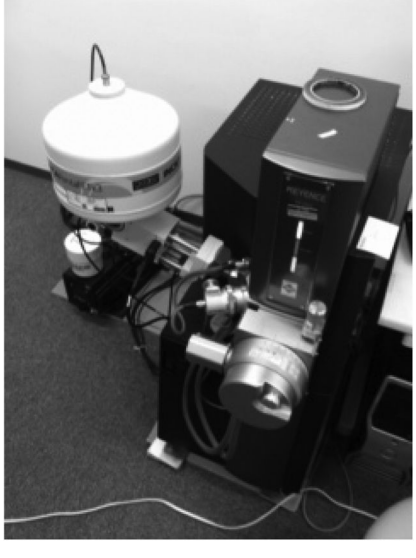

Figure 5. SEM.

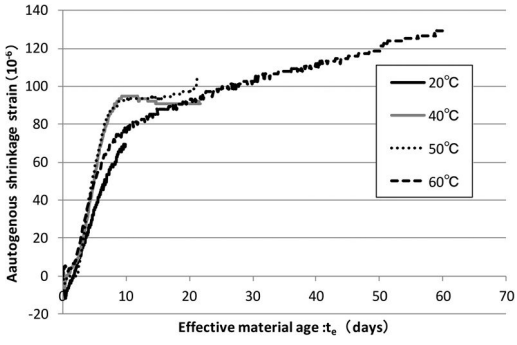

Figure 6. Effective material age and strain.

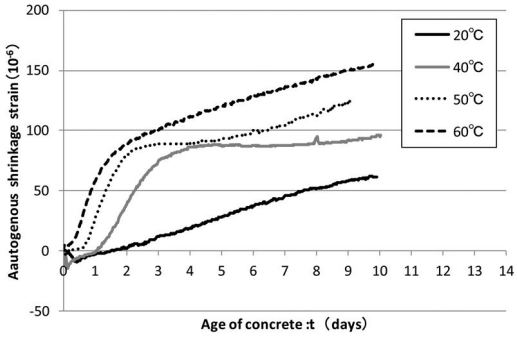

Figure 7. Age of concrete and strain.

3 RESULTS OF THE STUDY

3.1 *Result of the measurement of the autogenous-shrinkage strain*

The relation between the autogenous-shrinkage strain and the effective material age of concrete at temperatures of 20 degrees Celsius, 40 degrees Celsius, 50 degrees Celsius and 60 degrees Celsius by using TSTM is shown in Fig-6. Also, the relation between the autogenous-shrinkage strain and the age of concrete is shown in Fig-7.

From the relation between the autogenous-shrinkage strain and the effective materials age, only the concrete with controlled temperature at 20 degrees Celsius, showed slow development of the autogenous-shrinkage strain. However, in the case of 40 degrees Celsius, 50 degrees Celsius and 60 degrees Celsius, it became clear that there wasn't difference of the development speed of the autogenous-shrinkage strain.

Also, from the relation between the autogenous-shrinkage strain and the age of concrete, it was confirmed that the development speed of the autogenous-shrinkage strain became faster as the concrete temperature became higher.

3.2 *Result of observation of the hydration product*

The results of observations for the concrete at every temperature is shown in Fig-8. In the results in the case of 20 degrees Celsius, big hexagon board-formed

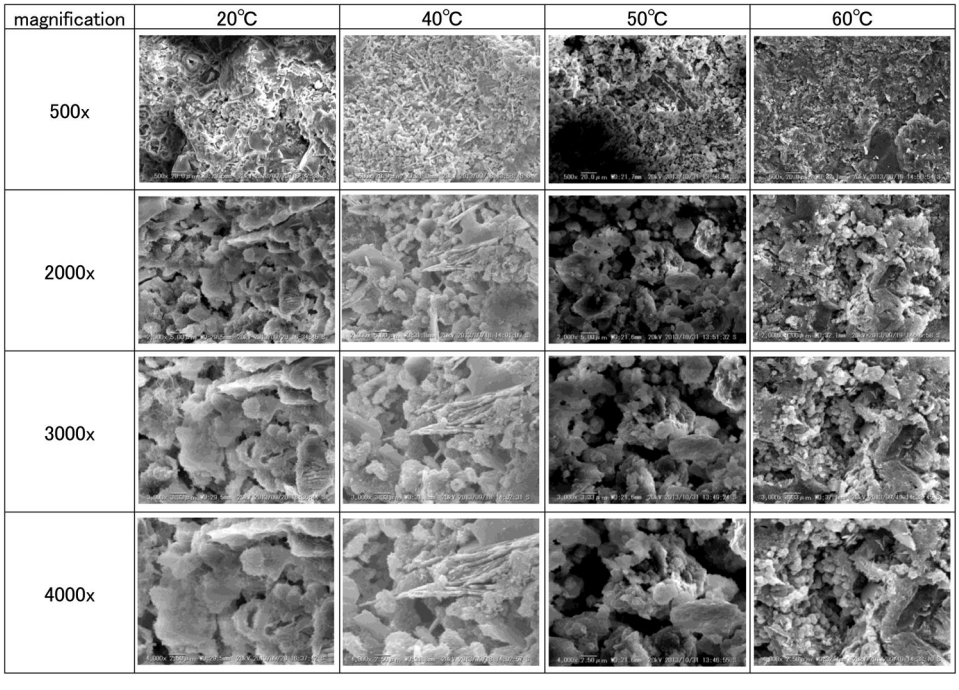

Figure 8. The image observed with SEM.

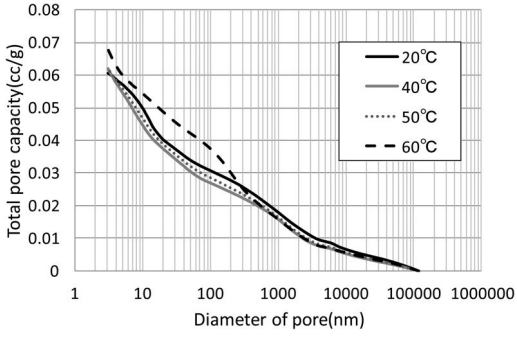

Figure 9. Total pore capacity.

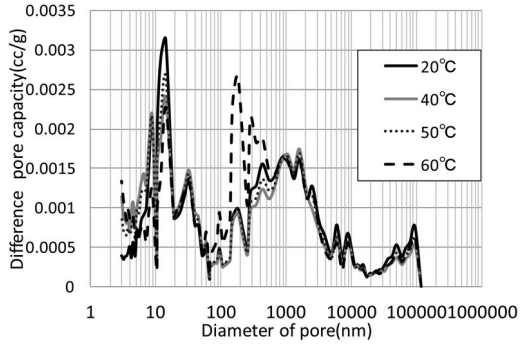

Figure 10. Difference pore capacity.

products were confirmed. In contrast, in the results in the case of 60 degrees Celsius, granular small products were confirmed. And in the 4,000 times extended image, big cavities were confirmed as setting temperature became high.

3.3 *Result of the measurement of the pore size distribution*

The accumulation pore capacity of the concrete at each temperature is shown in Fig-9. In the case of 20, 40 and 50 degrees Celsius, increase of pore volume is the same degrees, but only in the case of 60 degrees Celsius, pores with a diameter of about 200 nm and lower increased suddenly.

The relationship between pore capacity and pore diameter is shown in Fig-9.

It was confirmed that the development speed of the autogenous-shrinkage strain became fast as concrete temperature was high. In addition, it was confirmed that the pore structure of the hydration product was inclined to be coarse. So it was confirmed that difference of hydration temperature influences the pore structure of hydration product at the initial stage of the hydration reaction.

Because the development speed of the autogenous-shrinkage strain changes according to concrete temperature, it is considered that there is a correlation. Therefore, using the results of measurement and expression(1) of the autogenous-shrinkage strain, coefficient β about the dependence at each setting temperature at time, coefficient α about the progress speed of the autogenous-shrinkage strain, coefficient ε_∞ about end level of the autogenous-shrinkage strain were calculated. Just for information, the end level of the autogenous-shrinkage strain was set the same value regardless of setting temperature.

$$\epsilon_{(ti)} = \epsilon_\infty \{1 - \exp[-\alpha(t - t_0)^\beta]\} \quad (1)$$

$\varepsilon_{(ti)}$: shrinkage strain of concrete from t_0 to t ($*10^{-6}$)
ε_∞: final value of shrinkage strain ($*10^{-6}$)
α: Coefficient about the development speed of the autogenous-shrinkage strain
β: coefficient about the temperature dependence of the development speed of the autogenous-shrinkage strain

Table 2. Prediction-formulate coefficient.

$T_{(ti)}$	ε_∞	α	β	t_0
20	90	0.09	1.2	1.60
40	90	0.65	1.4	1.10
50	90	1.25	1.5	0.60
60	90	1.30	1.6	0.15

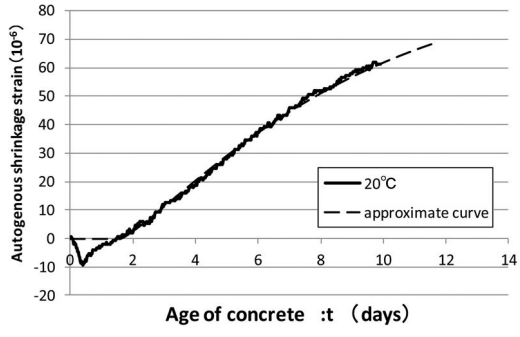

Figure 11. Approximate curve (20°C).

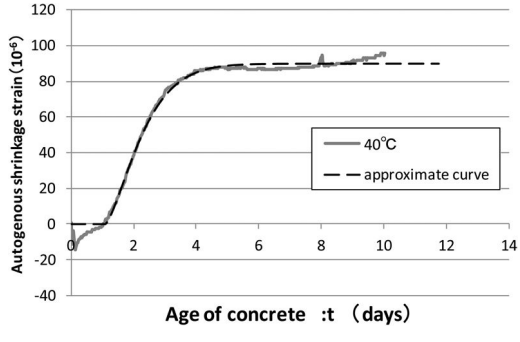

Figure 12. Approximate curve (40°C).

t_0: effective age(days) of concrete at the beginning of agregation.

The ε_∞, α, β and t_0 of each installed temperature are shown in table 2. In addition the results of the measured

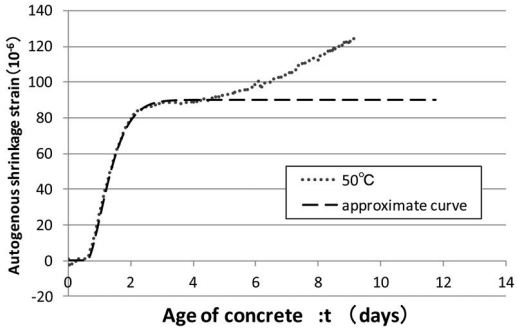

Figure 13. Approximate curve (50°C).

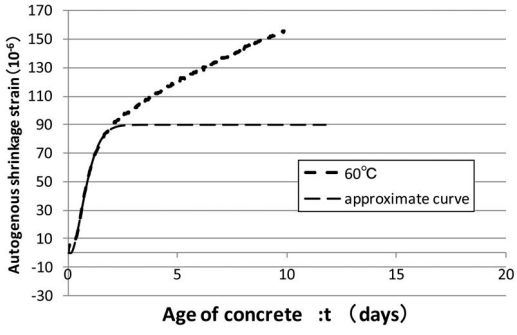

Figure 14. Approximate curve (60°C).

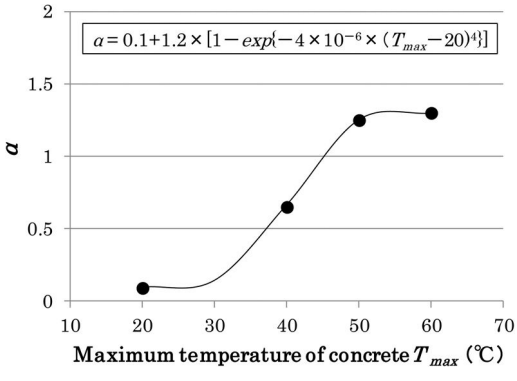

Figure 15. Approximate curve (α).

autogenous shrinkage strain and trendline are given in fig. 11 to fig. 14.

The coefficient α about the development speed of autogenous shrinkage strain became 1.30 at 60 degrees Celsius, 1.25 at 50 degrees Celsius, 0.65 at 40 degrees Celsius and 0.09 at concrete temperature 20 degrees Celsius.

From this result, the relation about concrete temperature and coefficient α is shown in expression (2) with the Fig. 15.

In addition, the coefficient β about temperature dependability of the development speed of autogenous shrinkage strain became 1.60 at 60 degrees Celsius,

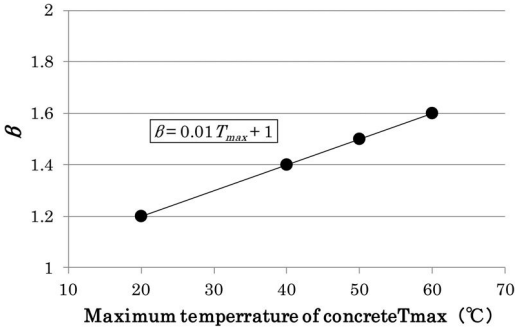

Figure 16. Approximate curve (β).

1.50 at 50 degrees Celsius, 1.40 at 40 degrees Celsius and 1.20 at concrete temperature 20 degrees Celsius.

From this result, the relation about concrete temperature and coefficient β is shown in expression (3) and with Fig. 16.

$$\alpha = 0.1 + 1.2 \times \{1 - \exp[-4 \times 10^{-6} \times (T_{max} - 20)^4]\} \quad (2)$$

$$\beta = 0.01 \times T_{max} + 1 \quad (3)$$

4 SUMMARY AND CONCLUSIONS

This experiment measured the autogenous shrinkage strain at controlled concrete temperatures of 20 degrees Celsius, 40 degrees Celsius, 50degrees Celsius and 60 degrees Celsius. As a result, it was confirmed that the speed to occur autogenous shrinkage of the concrete and concrete temperature had a high correlation. In addition, the more the concrete temperature increased, the more the hydration products of the concrete become coarse.

The expression to predict autogenous shrinkage strain of the concrete was made from the relation between concrete temperature and the autogenous shrinkage strain of the concrete. This prediction expression is applicable from 20 degrees Celsius to 60 degrees Celsius. In future, we will assume to increase the accuracy of it with the data of higher concrete temperature and confirm the duplicability with it.

REFERENCES

Tazwa E., Matsuoka Y., Miyazawa S., Okamoto S. (1994) Effect of autogenous shrinkage on self stress in hardening concrete, Proceeding of RILEM International Symposium on Thermal Cracking in Concrete at Early Ages, pp. 221–228.

Toshiaki M., Kousuke Y., Yoshinobu N. (2000). Control of Thermal Cracking by Pipe-Cooling System in Mass Concrete Structures, Control of Cracking in Early-Age Concrete. Swets & Zeitlinger Publishers, pp. 333–342.

Toshiaki M., Gorou S., Toshio O., Shinji M., (2006). Control of Thermal Cracking Using Heat of Cement Hydration in Massive Concrete Structures, Concrete Durability and Service Life Planning (Concrete Life '06).

This page intentionally left blank

Concrete Solutions – Grantham et al. (Eds)
© 2014 Taylor & Francis Group, London, ISBN 978-1-138-02708-4

Durability of fly ash concrete exposed to slow freeze-thaw cycles

A. Badr
Civil Engineering Department, MTC, Sultanate of Oman

ABSTRACT: Experimental research was carried out to investigate the effect of fly ash on the durability of concrete subjected to slow freeze-thaw cycles. Particular emphasis was given to the effect of fly ash replacement level (up to 65%) on the durability of air entrained concrete (AEC) and non-air entrained concrete (NAEC). Two groups of tests were conducted. In the first group, concrete specimens from all mixes were exposed to slow freeze-thaw cycles at an early age of 7 days. In the second group, the freeze-thaw cycles started after 28 days of curing. The deterioration, weight loss and residual strength of concrete specimens were assessed after cycles of slow freezing and thawing. The results showed that fly ash has a significant effect on the durability and residual strength of concrete exposed to freezing conditions. In addition, the initial curing period before exposing concrete specimens to freeze-thaw cycles was one of the most significant factors affecting the freeze-thaw durability of fly ash concrete. Compared to Portland cement concrete, air-entrainment is more vital for fly ash concrete if structures are expected to experience freeze-thaw cycles during their lifetime.

1 INTRODUCTION

The use of mineral admixtures such as fly ash (FA) to enhance properties of concrete has been researched for years. In well-designed concrete mixes, the replacement of a certain amount of Portland cement with FA modifies the microstructure of the cementitious paste and produces concrete with desirable characteristics and high performance with regard to rheological durability properties. (Badr 2012, Yu & Ye 2012, Badr & Platten 2006, Mazloom et al. 2004, Neville & Brooks 2010). Indeed, the utilization of these mineral admixtures, particularly fly ash, in concrete structures has dramatically increased due to the increase in environmental awareness. In addition, fly ash is significantly cheaper than Portland cement; thus, it contributes to reducing the cost of the concrete (Toutanji et al. 2004).

During the last few years, numerous concrete structures and concrete pavements have been exposed to very cold weather due to the record low temperatures reported in many parts of the world. For example, the UK experienced several spells of severe weather with extremely low temperatures and substantial snowfalls during the winter of 2009 to 2011. Temperatures generally fell below −10°C on several nights and on occasion below −20°C. Some snowfalls were considered amongst the most significant and widespread since 1965 (Met Office 2011). Concrete structures exposed to cold weather can be susceptible to degradation due to freeze-thaw cycles during such severe conditions. The deterioration of concrete due to freeze-thaw cycles is a very complex phenomenon. Many theories have been presented to explain the disintegration mechanisms. The prevailing mechanisms are generation of hydraulic pressure due to freezing in capillaries, osmotic pressures resulting from partial freezing in capillaries of solutions with a local salt concentration and differential strains due to localized shrinkage and swelling as well as thermal strains. However, the ease with which water can move within concrete depends on the microstructure and the pore size distribution (Penttala 2006, Basheer et al. 2001, Powers 1975, Fagerlund 1974).

Replacing a certain amount of Portland cement with FA is among many factors that can affect the microstructure characteristics of concrete (Badr & Platten 2006, Yu & Ye 2012). Other factors include using an air-entraining agent (Shang et al. 2009, Du & Folliard 2005) and drying of concrete using specific water removal techniques. (Badr 2011, Collier et al. 2008, Gallé 2004).

Each of these factors can modify the microstructure in such a way that it may either improve or degrade the ability of the concrete to resist deterioration due to freezing and thawing. For example, it is well established that air-entraining agents improve the freeze-thaw durability of most types of concretes (Shang et al. 2009, Bassuoni & Nehdi 2005).

The effect of fly ash on the freeze-thaw durability of concrete is debatable, particularly in air-entrained concrete. Nowak-Michta (2013) showed that research results are conflicting in this area, as much research shows that properly air-entrained fly ash concrete is resistant to cyclic freezing and thawing; but there is also research showing decreased freeze-thaw durability of fly ash concrete. Dhir et al. (1998) reported that pozzolans such as fly ash, could improve frost resistance, at least for concrete with water to binder

Table 1. Mix proportions (per m^3) and slump values.

Mixes	CEMM1 kg	FA kg	Limestone kg	Sand kg	SP litre	AEA litre	Air Content %	Slump mm
CEM-NA	450	–	720	1080	1.0	–	2.8	70
CEM-AE	450	–	720	1080	1.0	0.45	6.1	110
FA50-NA	225	225	720	1080	0.5	–	1.7	70
FA50-AE	225	225	720	1080	0.5	0.45	5.4	90
FA65-NA	158	292	720	1080	0.3	–	1.3	90
FA65-AE	158	292	720	1080	0.3	0.45	5.2	120

ratio above 0.40. Ten years later, Yazıcı (2008) studied the effect of silica fume and high-volume fly ash on freeze–thaw resistance of self-compacting concrete and concluded that all mixtures that contain fly ash showed greater residual compressive strength than a control mixture, particularly for replacement levels below 40%. However, Peng et al. (2007) showed that fly ash had little effect on frost resistance of concrete. Toutanji et al. (2004) concluded that using fly ash had a detrimental effect on the freeze-thaw resistance of concrete even at replacement levels below 30%.

Therefore, the effect of fly ash on the freeze-thaw durability of concrete is not well established and needs further investigation.

2 OBJECTIVES

The main aim of this research was to investigate the effect of fly ash on the freeze-thaw durability of concrete exposed to freezing conditions.

This aim has been achieved by studying the:

- Deterioration due to freeze thaw in concretes with and without fly ash (FA).
- Freeze-thaw resistance of air-entrained concrete and non-air-entrained concrete in the presence or absence of fly ash.
- Effect of initial curing period before exposing concrete to freeze-thaw cycles.

3 MATERIALS AND MIXES

3.1 *Materials*

The Portland cement used was CEM1 conforming to BS EN 197-1. Fly ash (FA) was used as a cement replacement material. The coarse aggregate was well graded limestone natural gravel of 10 mm nominal maximum size. Siliceous sand which complied with zone M of BS EN 12620 was used as a fine aggregate. Superplasticiser (SP) conforming to BS5075 Part 3 was used in all mixes. Air entraining agent (AEA) based on the salt of ether sulphate which complies with BS5075 Part 2 was used in the air-entrained mixes.

3.2 *Mixes*

Six mixes were initially optimised from laboratory tests. The composition of each of these mixes is given in Table 1. The name of every mix consists of two parts indicating the binder type and whether air is entrained. For example, CEM-NA is a control mix made with CEM1 as a sole binder and includes no entrained air. Similarly, FA50-AE is an air-entrained concrete mix with 50% of the CEM1 replaced by fly ash on a weight-to-weight basis.

The aggregate-to-binder and water-to-binder ratios were kept constant for all mixes at 4.0 and 0.40, respectively. The limestone was 40% of the total aggregate in all mixes. A target consistence class S2 (between 40 and 110 mm, BS EN13250-Part 1) was achieved for all mixes by changing the SP dosage. As would be expected, mixes with fly ash required lower SP dosages compared to counterpart mixes without fly ash, as can be seen in Table 1.

The dosage of the air-entraining agent was determined from trial mixes to achieve an air content of about 6% in the air-entrained mixes. About 0.45 litres of air entraining agent was required per cubic meter for all air-entrained mixes.

3.3 *Mixing*

The coarse and fine aggregates were mixed with the binder in a dry state for about one minute in a conventional rotary drum mixer of 50-liter capacity. Half of the mixing water was added and mixed for three minutes before adding the remaining mixing water and SP in addition to AEA where applicable. A further three minutes of mixing were needed to achieve a uniform mixture.

3.4 *Specimens*

Concrete cubes (150 and 100 mm) were cast and thermocouples were set within one of the 100 mm cubes during the casting in order to monitor the temperature profile inside the core of concrete specimens during the freeze-thaw cycles.

3.5 *Curing*

All specimens were covered with wet hessian and polyethylene sheets overnight. They were then demoulded after 24 hours and submerged in a water curing tank for 7 days, after which, the 150 mm cubes were cut into small cubes of 70 mm nominal dimension. The 100 mm cubes were kept intact. Enough

Figure 1. Reservoir on the top surface of each specimen.

specimens were then stored in the room conditions for 1 day to be prepared for the first group of freeze-thaw tests after 7 days moist curing. The rest of the specimens were then returned to the curing tank to complete the 28 days of curing before starting the second group of freeze-thaw tests. These specimens were then removed from the curing tank and stored in room conditions for 1 day to be prepared for the freeze-thaw tests.

4 FREEZE-THAW CYCLES AND TESTING

4.1 *Preparation of specimens*

Prior to starting the freeze-thaw cycles, control specimens were chosen randomly to be tested for compressive strength at room temperature to establish a control compressive strength for each mix.

Special aluminum adhesive tape was used to create a reservoir on the top surface of each specimen, as shown in Figure 1. In order to reduce the variability in the results, the top surface of each specimen was a cut face. Salt solution was prepared by adding 50 g of deicing salt per liter of distilled water. The salt solution was used to fill the reservoirs on top of each specimen before transferring the specimens to an environmental chamber to start the freeze-thaw test. The level of the salt solution was monitored daily during the thaw cycle and a top up was made if needed.

4.2 *Freeze-thaw tests*

The freeze-thaw tests were carried out according to RILEM recommendation (RILEM 4-CDC 1977). The specimens were exposed to freeze-thaw cycles inside an environmental chamber running at -20 ± 2. The nominal freezing cycle was 8 hours and the nominal thawing cycle was 16 hours. However, temperature monitored during the tests indicated that the specimens remained in the freezing state for about 16 hours and thawed for 8 hours only, during which the salt was in the solution state.

After certain numbers of freeze-thaw cycles (25, 50 and 100), the weight loss and residual compressive strength were determined to quantify the damage due to freeze-thaw.

Table 2. Weight loss after 25 cycles.

	Weight Loss (mg/mm^2)	
	7d curing	28d curing
CEM-NA	23.6	8.9
FA50-NA	35.8	29.7
FA65-NA	72.4	53.8
CEM-AE	1.7	0.8
FA50-AE	3.1	2.8
FA65-AE	6.9	6.7
Average	23.9	17.1

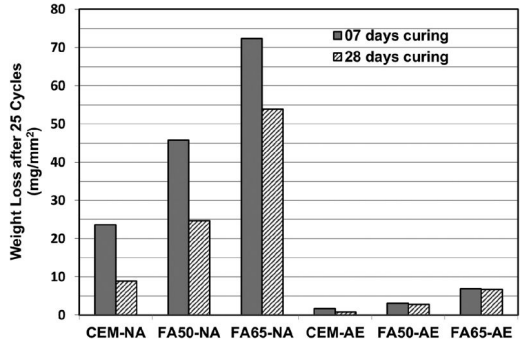

Figure 2. Weight loss after 25 cycles.

5 RESULTS AND DISCUSSION

5.1 *Effect of initial curing time*

Table 2 shows the weight loss of all specimens after 25 cycles of freeze-thaw. The first group of specimens were initially moist cured in a water-curing tank for 7 days before being exposed to freeze-thaw cycles, whereas the second group specimens were initially moist cured for 28 days.

The effect of a longer initial curing period was clear when comparing the weight loss from the top surface of the specimens. The average weight loss from group-two specimens after 25 cycles was 17.1 mg/mm^2 compared to an average of 23.9 mg/mm^2 from group-one specimens. This reduction in weight loss indicates an improvement of 28%. However, the level of improvement due to the longer initial curing period was dependent on the composition of the mix. The average improvement for the fly ash mixes was 21%; i.e. lower than the overall average of 28%. Nonetheless, the most significant reduction in weight loss was observed in the non-air-entrained concrete specimens, as can be seen from Figure 2. It can be seen that the reduction in the weight loss due to the longer initial curing period was almost unnoticeable in the air-entrained mixes; i.e. the improvement was less pronounced in air-entrained specimens, as the improvement was only 12%.

Table 3 shows the residual strength of the two groups of specimens after 25 cycles of freeze-thaw. The average residual strength of group-two specimens

Table 3. Residual compressive strength (MPa) after 25 cycles.

	Control @7 days	Control @28 days	Residual strength 7d curing	Residual strength 28d curing
CEM-NA	25.4	32.4	5.4	14.4
FA50-NA	17.3	25.3	1.0	2.4
FA65-NA	4.1	11.9	0.1	1.3
CEM-AE	22.9	30.2	27.5	31.3
FA50-AE	14.9	23.1	20.6	23.7
FA65-AE	3.6	10.2	7.9	12.8
Average	14.7	22.2	10.4	14.3

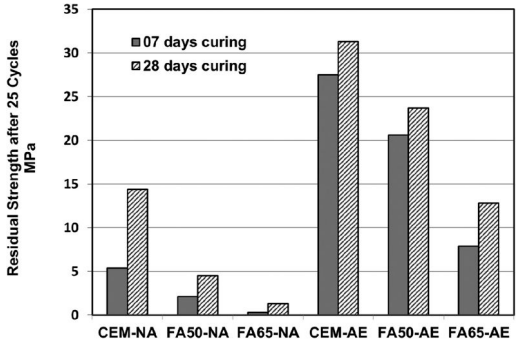

Figure 3. Residual strength after 25 cycles.

is 14.3 MPa, which is 37% higher than the 10.4 MPa average residual strength of group-one specimens.

As was the case with weight loss, the enhancement due to increasing the initial moist curing period was more pronounced in non-air-entrained specimens. This is evident from Figure 3. Increasing the initial curing period from 7 to 28 days before exposing air-entrained concrete to 25 freeze-thaw cycles increased the residual strength by 21%; a modest value compared to the overall average of 37%.

5.2 *Effect of entrained air in presence of fly ash*

Regardless of the length of initial curing period, the air entrained mixes showed improved resistance to degradation due to freeze-thaw cycles, as can be seen from Tables 2–3 and Figures 2–3. The use of air entraining agent resulted in a reduction in the weight loss by more than 90% in most cases in the presence or absence of fly ash, as can be seen from Figure 4.

The effect of air entrainment on the residual compressive strength is shown in Figure 5. The residual strength of the air-entrained mixes was on average more than 500% higher than that of the non-air-entrained mixes. The most significant increase in the residual strength was observed in FA concrete. This apparent enhancement was not due to better absolute values of the residual strength of the fly ash mixes compared to CEM mixes. Rather, it could be attributed to

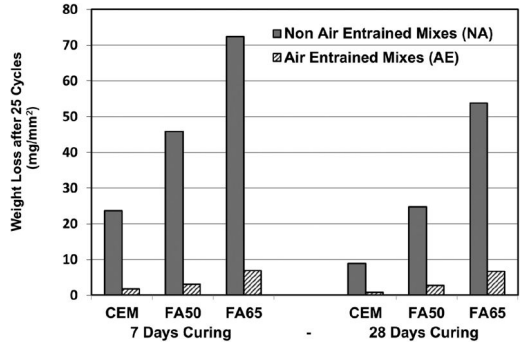

Figure 4. Entrained air on weight loss after 25 cycles.

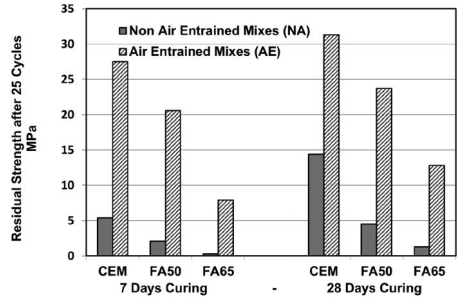

Figure 5. Entrained air on residual strength after 25 cycles.

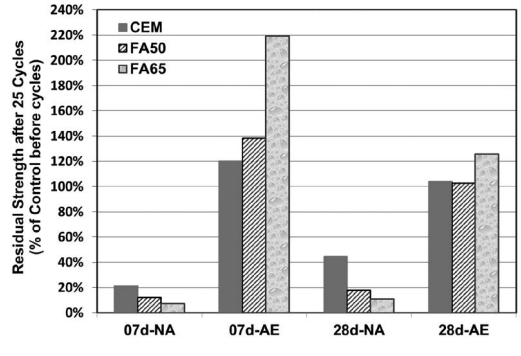

Figure 6. Relative residual strength after 25 cycles.

the very low residual strength of non-air-entrained fly ash mixes.

It was interesting to observe that the residual strength of the air-entrained concrete specimens subjected to 25 freeze-thaw cycles was in fact higher than their "start" strength, i.e. the strength of control specimens before starting the freeze-thaw cycles. This would be even clearer by presenting the residual strength as percentage of the strength of counterpart control specimens; i.e. "relative" residual strength, as shown in Figure 6.

The relative residual strength of all air-entrained specimens – with or without fly ash- was higher than

100% i.e. that of the control specimens, regardless of the initial curing period.

This increase can be attributed to the net effect of two factors. The first is negative due to the degradation in the strength caused by the freeze-thaw cycles. The second factor is positive due to strength development during the time of freeze-thaw cycles as a result of resuming the hydration process, as the water was available on top of specimens during the thawing cycle. In the air-entrained specimens, the net effect was positive and exhibited as an average increase of about 12%, 20% and 72% for CEM-AE, FA50-AE and FA65-AE, respectively. On the other hand, the degradation due to the freeze-thaw cycles outweighed the development in strength in the non-air-entrained concretes and, therefore, the net result was a reduction in the residual strength. The average reduction was, 67%, 85% and 91% for CEM-AE, FA50-AE and FA65-AE, respectively. Comparing these values would reveal that fly ash mixes reported the lowest relative residual strength for non-air-entrained specimens but the highest relative residual strength for air-entrained mixes. It could be, therefore, suggested that air-entrainment is more vital for fly ash concrete when exposed to freeze-thaw cycles.

The good resistance to deterioration by freeze-thaw cycles of the air entrained concrete used in this study suggests that the hardened concrete with and without fly ash had adequate systems of entrained air voids. This is in agreement with Hale et al. (2009). It can, therefore, be suggested that the dosages of the air entraining agent used in this study were adequate for mixes with and without fly ash.

It might be possible to explain the inferior freeze-thaw resistance of the specimens containing fly ash in the light of the hydraulic pressure theory. When water within the larger pores freezes, the created ice needs extra space to expand by about 9%. The empty or partially empty pores (if any) within the specimens should be able to provide this much-needed space. However, during the expansion of ice any excessive water could be pumped away from the freezing sites causing a buildup of hydraulic pressure. Yamashita et al. (1997) showed that the characteristics of the pore system would dictate the extent of the hydraulic pressure. The more the resistance to the movement of the unfrozen water, the higher the extent of the hydraulic pressure. Consequently, the hydraulic pressure could be intensified when the unfrozen water needs to travel for a long distance to reach an empty pore. Thus, it could be suggested that the unfrozen water within the pores of the fly ash concrete specimens either found it difficult to move within the pore structure or the next available empty pore was far from the freezing site. Therefore, it is likely that the generated hydraulic pressure was higher than the tensile strength of concrete. This could be mitigated by air-entraining agents that would provide the much needed pores to accommodate the excessive water and reduce the travel length. Therefore, it could be suggested the air-entrainment in fly ash concrete is more important than the case with Portland cement concrete.

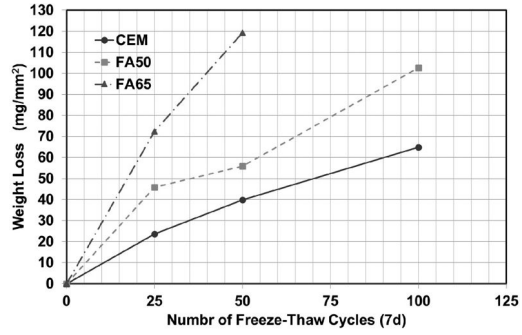

Figure 7. Weight loss up to 100 cycles following 7d curing.

5.3 *Effect of fly ash replacement level*

The absolute values of residual strength of mixes containing fly ash (FA50-NA, FA65-NA, FA50-AE, and FA65-AE) are significantly lower than those of the counterpart Portland cement mixes (CEM-NA and CEM-AE), as can be seen from Tables 2–3. However, this may be attributed to the fact that the original strength of these specimens was much lower than the strength of the Portland cement mixes before starting the freeze-thaw cycles.

Expressing the results of residual strength as a percentage of the strength of control specimens (Figure 6) showed that the effect of fly ash is dependent on the presence of air-entrainment. The non-air-entrained FA specimens (FA50 and FA65) exhibited the lowest "relative" residual strength. On the other hand, the air-entrained FA specimens showed the highest "relative" residual strength. However, this apparent enhancement was not due to better absolute values of the residual strength of the fly ash mixes compared to CEM mixes. Rather, it could be attributed to the low strength of the fly ash control mixes. Nonetheless, this finding is of significant importance because it confirms that air-entrainment could improve the freeze-thaw resistance of concrete containing FA compared to CEM mixes.

In terms of weight loss, specimens with fly ash showed more deterioration compared to specimens without fly ash, as can be seen from Figures 2 and 4. These figures demonstrate that fly ash had significantly impaired the freeze-thaw durability of concrete regardless of the length of initial curing (Figure 2) or air-entrainment (Figure 4). In order to ascertain this finding, the weight loss tests were continued to 100 freeze-thaw cycles. The results of these tests are presented in Figures 7 and 8 for specimens initially cured for 7 and 28 days, respectively. The increased weight loss of specimens containing fly ash was consistent and recorded throughout the entire period of the tests up to 100 cycles, at which the tests were terminated. The higher the replacement level of fly

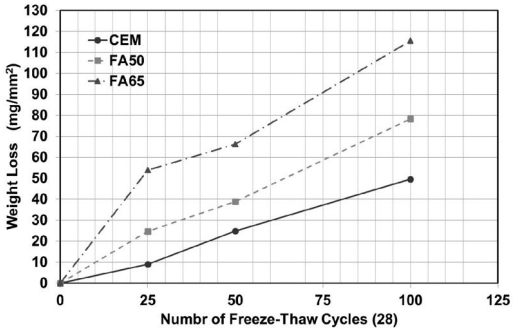

Figure 8. Weight loss up to 100 cycles following 28d curing.

ash the severer the damage. This is in agreement with results reported by Toutanji et al. (2004) using rapid freeze-thaw tests (ASTM C666). They reported that the greater the amount of fly ash, the lower the resistance to freeze-thaw exposure, albeit the maximum replacement level in their tests was 30% fly ash.

Figures 7 and 8 also show that increasing fly ash replacement level from 50 to 65% was more damaging compared to raising it from 0 to 50%. This could imply that a lower replacement level could have a less damaging effect. This is now under investigation by the author and further results will be published soon after they are available. As fly ash became an essential constituent of concrete used to cast large volume such as in dams, it is of particular importance that caution is exercised when deciding the fly ash replacement level if freezing temperatures are expected to be experienced during the lifetime of such structures.

6 CONCLUSIONS

For the concrete and test conditions used in this investigation, the following conclusions are made:

- The absolute values of residual strength of mixes containing fly ash were significantly lower than those made with Portland cement. The higher the replacement level of fly ash the severer the damage. Increasing fly ash replacement level from 50 to 65% was more damaging compared to raising it from 0 to 50%.
- Compared to Portland cement concrete, air-entrainment is more vital for fly ash concrete if structures are expected to experience freeze-thaw cycles. The air-entrained fly ash mixes had the highest "relative" residual strength (as % of strength of counterpart control specimens) but the lowest relative residual strength for non-air-entrained mixes.
- Increasing the initial moist curing period from 7 to 28 days resulted in enhancing the residual strength of concrete exposed to 25 freeze-thaw cycles by more than 37%. However, the improvement was more significant in the non air-entrained mixes. A similar effect of a longer initial curing period was observed when comparing the weight loss from the top surface of the specimens. The average weight loss after 25 cycles reduced by more than 28%.
- Air entrained concrete specimens showed a reduction in the weight loss by more than 90% compared to non-air-entrained specimens regardless of the number of cycles, binder type or the length of initial curing period.
- Caution should be exercised when deciding the fly ash replacement level if freezing temperatures are expected to be experienced during the lifetime of structures.

REFERENCES

Badr, A. 2012. Durability of PPFRC as Assessed by Oxygen & Water Permeability. *Durability of Cementitious Composites*. RILEM Proceeding, 83 (1): 1–8.

Badr, A. 2011. Preconditioning concrete for better freeze-thaw durability. *Concrete Solutions,* Grantham et al. (Editors), CRC Press, (1): 178–186.

Badr, A. & Platten, A. 2006. Effect of silica fume and fly ash on fatigue and impact strength of FRC. *Wastes & Secondary Materials in Pavement Engineering, 5th Inter. Conf., Liverpool, UK, 22-23 February*, 1(2): 1–12.

Basheer, L., Kroppb, J. & Clelandc, D.J. 2001. Assessment of the durability of concrete from its permeation properties: a review. *Construction and Building Materials,* 15(1): 93–103.

Bassuoni M.T. & Nehdi, M.L. 2005. The case for air-entrainment in high-performance concrete. *Structures & Buildings,* ICE, 158(5): 311–319.

Chatterji, C. 2003. Freezing of air-entrained cement-based materials and specific actions of air-entraining agents. *Cement & Concrete Composites,* 25(7): 759–765.

Collier, N., Sharp, J., Hill, J. & Godfrey, I. 2008. The influence of water removal techniques on the composition and microstructure of hardened cement pastes. *Cement and Concrete Research,* 38(6): 737–744.

Dhir, R.K., McCarthy, M.J. & Magee, B,J. 1998. Impact of BS EN 450 PFA on concrete construction in the UK. *Construction and Building Materials*, 12(1): 59–74.

Du, L. & Folliard, K.J. 2005. Mechanisms of air entrainment in concrete. *Cement and Concrete Research,* 35(8): 1463–1471.

Fagerlund, G. 1974. Critical moisture contents at freezing of porous materials. *CIB/RILEM 2nd Symposium on Moisture Problems in Buildings, Rotterdam, Netherlands*, 1(1): 1–17.

Gallé, C. 2004. Effect of drying on cement-based materials pore structure as identified by mercury intrusion porosimetry: A comparative study between oven-, vacuum-, and freeze-drying. *Cement and Concrete Research,* 31(10): 1467–1477.

Hale, W.M., Freyne, S. & Russell, B.W. 2009. Examining the frost resistance of high performance concrete. *Construction and Building Materials*, 23(2):878–888.

Met Office. 2011. Snow and low temperatures: December 2010. *UK Climate, Past Weather Events,* 3rd June 2011 at: http://www.metoffice.gov.uk/climate/uk/interesting/dec2010.

Neville, A.M. & Brooks, J.J. 2010. Concrete Technology, *5th ed. Longman Scientific & Technical, London, England.*

Nowak-Michta, A. 2013. Water-binder Ratio Influence on De-icing Salt Scaling of Fly Ash Concretes. *Procedia Engineering,* 57: 261–266.

Peng, G., Ma, Q., Hu, H., Gao, R., Yao, Q. & Liu, Y. 2007. The effects of air entrainment and pozzolans on frost resistance of 50–60 MPa grade concrete. *Construction & Building Materials*, 21(10): 1034–1039.

Penttala, V. 2006. Surface and internal deterioration of concrete due to saline and non-saline freeze–thaw loads. *Cement and Concrete Research,* 36(5): 921–928.

Powers, T.C. 1975. Freezing effects in concrete, Durability of concrete. *ACI SP-47*: 1–12.

RILEM 4-CDC. 1977. Methods of carrying out and reporting freeze-thaw tests on concrete with de-icing chemicals. *Materials and Structures,* 10 (58): 212–215.

Shang, H., Song, Y. & Ou, J. 2009. Behavior of air-entrained concrete after freeze-thaw cycles. *Acta Mechanica Solida Sinica,* 22(3): 261–266.

Toutanji, H., Delattec, N., Aggounb, S. & Dansona, A. 2004. Effect of supplementary cementitious materials on the compressive strength and durability of short-term cured concrete. *Cement and Concrete Research,* 34(2): 311–314.

Yamashita, H., Sakai, K. & Kita, T. 1997. Effect of Pore Structure in Concrete on Frost Resistance. *Durability of Concrete, 4th CANMET/ACI Inter. Conf., Sydney, Australia*: 919–931.

Yazıcı, H. 2008. The effect of silica fume and high-volume Class C fly ash on mechanical properties, chloride penetration and freeze–thaw resistance of self-compacting concrete. *Construction and Building Materials*, 22(5): 456–462.

Yu, Z. & Ye, G. 2012. Chloride penetration and microstructure development of fly ash concrete. *Durability of Cementitious Composites*. RILEM Proceeding, 83 (1): 101–108.

This page intentionally left blank

Concrete Solutions – Grantham et al. (Eds)
© 2014 Taylor & Francis Group, London, ISBN 978-1-138-02708-4

Correlation research on the electrical resistivity of concrete and its other electrical properties

Huajian Li, Lu Yang, Zhonglai Yi, Yanbin Tan & Yongjiang Xie
Beijing State Key Laboratory for Track Technology of High-Speed Railway, Research Institute of Railway Engineering, China Academy of Railway Sciences, Beijing, China

ABSTRACT: In order to rapidly evaluate the on site durability of concrete structure, some experiments on the correlation between the surface resistivity and the volume resistivity, electric charge and chloride diffusivity of different kinds concrete including concrete with mineral admixtures (fly ash, ground granulated blastfurnace slag, silica fume, limestone powder), air-entrained concrete and polymer concrete have been carried out. The volume resistivity and the surface resistivity were researched by the cyclic voltammetry method and the Wenner four-electrode measuring method. It was proved that the surface resistivity and volume resistivity can be used to quickly evaluate the durability of concrete. There was a good linear correlation between surface resistivity and volume resistivity of concrete, and the correlation coefficient (R^2) was 0.96. There was a good negative correlations between volume resistivity and electric charge, chloride diffusivity of concrete, and the correlation coefficients were 0.89 and 0.75 separately. The Wenner four-electrode measuring method proved fit for rapid evaluation of concrete structure durability.

1 INTRODUCTION

The structure and properties of concrete can be characterized by the electrical resistivity of concrete which is an electrical parameter and means the current impedance ability through unit length concrete. There are large numbers of connected and unconnected capillary pores which contain pore solution in concrete (David A et al. 2003, Gong Guo-jun et al. 2005). The pore solution is composed of a saturated solution of calcium hydroxide ($Ca(OH)_2$)and a variety of other ions (Zhao Tie-jun et al. 2000). Ions in the electrolyte solution migrate under a certain voltage, so that the concrete exhibits different electrical characteristics, that is, different electrical resistivity, conductivity, impedance and power saving constant (Sanchez et al. 2008). According to the relationship between electrical properties and properties of concrete structures, the electrical properties of concrete will be a new technology for rapid detection, online monitoring and effective evaluation of concrete microstructure formation and development (He Zhen et al. 2004, Hansson et al. 1983). To verify the feasibility of the surface resistivity test method used for the quick evaluation of concrete durability on site, the correlation between the volume resistivity and the surface resistivity, compressive strength, passed electric charge, chloride diffusion coefficient of concrete with different kinds mineral admixtures, air-entrained concrete and polymer concrete have been studied.

2 EXPERIMENTAL PROCEDURES

2.1 *Raw material*

All experiments were carried out using the same Jinyu brand P · O 42.5 Portland cement which was from Beijing Liulihe Cement Company. Grade I fly ash was from Qinhuangdao Power Plant and S95 Jiahua slag powder was from the Capital Steel Plant. Limestone of 5–20 mm continuous gradation was used as a coarse aggregate. The fineness modulus of the well graded sand was 2.4. Polycarboxylate water reducer and air-entraining agent were from Tianjin Yongyang Admixture Company. The properties of cement, fly ash, slag powder and silica fume are shown in Table 1.

2.2 *Mix proportions*

The basic water-binder ratio of the concrete was 0.31 and the basic dosage of cementitious materials was 480 kg/m^3. The slump of all the concretes was limited from 190 mm to 210 mm, and mineral admixtures were applied to replace equivalent cement. The slump and the air content of concrete were controlled by adjusting the dosage of the water reducer and air-entraining agent. The mix proportions of concrete are given in Table 2.

2.3 *Test method*

2.3.1 *Surface resistivity*

The four-electrode method was used in the concrete surface resistivity test with a Resipod concrete

Table 1. Physical mechanical properties and chemical compositions of cement and mineral admixtures.

Material type	Ignition loss %	SO_3 %	Cl^- %	Alkalis %	SiO_2 %	CaO %	MgO %	Fe_2O_3 %	Al_2O_3 %	Density g/cm^3	Specific surface m^2/Kg
Cement	1.76	2.55	0.008	0.6	32.25	59.02	1.07	2.89	5.46	3.12	327
Fly ash	1.16	0.38	0.006	1.46	59.65	4.71	1.46	7.58	19.6	2.35	–
Slag powder	0.96	0.29	0.015	0.52	20.82	36.71	12.98	0.72	14.22	2.89	442
Silica fume	0.96	0.5	0.007	1.11	94.63	0.82	1.29	–	0.33	–	17764

Table 2. Mix proportions of concrete (kg/m^3).

No.	Strength Grade	Consideration	Cement	Fly ash	Slag powder	Silica fume	Coarse aggregate (10–20 mm)	Coarse aggregate (5–10 mm)	Sand	Water
CIC1	C50	Mineral	288	192						
CIC2	C50	admixture	288		192		738	397	725	148.8
CIC3	C50	type	288	48		144				
CIC4	C50	Water to	480							
CIC5	C40	binder	400				706	380	754	152
CIC6	C30	ratio	360				751	371	688	151.2
CIC7	C50	Air content	288	192			738	397	725	148.8
CIC8										

Table 3. Experimental parameters of cyclic voltammetry (CV).

Init E	High E	Low E	Scan Rate	Sweep Segments	Sample Interval	Sensitivity
0.5 V	0.5 V	−0.5 V	0.1 V/s	2	0.01 V	1×10^{-6} A/V

Table 4. The experimental parameters of AC impedance.

Init E	High Frequency	Low Frequency	Amplitude	Quiet Time
0 V	100000 Hz	1 Hz	0.005 V	2 s

surface resistivity meter produced by the Proceq SA Company. The 100 mm × 100 mm × 300 mm concrete specimens were used for the experiment. There were three specimens each group, and the test result was the average of the three specimens.

2.3.2 *Volume resistivity*

The volume electrical resistivity of the concrete was measured with a Chenhua CHI660 Multifunctional Electrochemical Workstation (Figure 1). 100 mm × 100 mm × 100 mm concrete specimens were used for the experiment. Cyclic voltammetry with an electrical potential scanner over a very small voltage range was used on the concrete specimens for the test. The current-voltage curve is shown in Figure 2. The polarization resistance, R_p, was obtained by calculating the slope of linear regression of the open-circuit-potentials. The Polarization Resistance and the experimental parameters of the cyclic voltammetry are shown in Table 3.

2.3.3 *Concrete AC impedance test*

The AC impedance of the concrete was measured by Chenhua CHI660 Multifunctional workstation. The experimental parameters of the AC impedance are shown in Table 4. The equivalent circuit representing the concrete electrochemical properties is shown in Figure 3. The pore solution and pore characteristics of the concrete are characterized by Rs which is the electrical resistivity of the pore solution. The hydration degree of the concrete is characterized by Rp which is the gel resistance. C is the gel capacitance influenced by the hydration degree of the concrete. The influence of the electrodes was eliminated by using ZSimpWin impedance professional software, and then

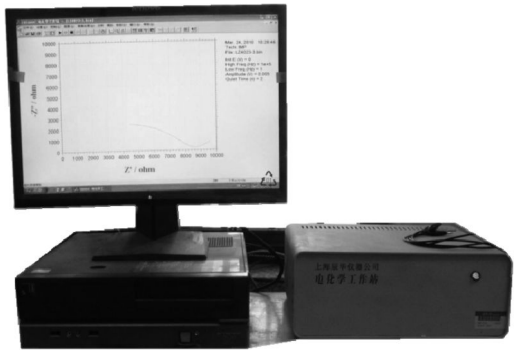

Figure 1. Electrochemistry workstation.

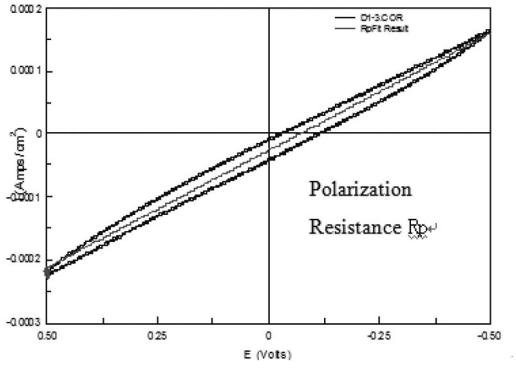

Figure 2. Polarization resistance fitting from cyclic voltammetry curve.

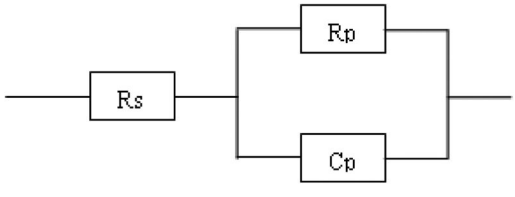

Figure 3. The equivalent circuit of concrete electrochemical properties.

these three electrochemical parameters were obtained through the fitted curve. The ion diffusion impedance ability of the concrete can be characterized by a diffusion impedance coefficient K which is obtained by linear processing of the data.

3 RESULTS AND DISCUSSION

3.1 *Correlation between concrete compressive strength and electrical resistivity*

Figure 4 shows the relationship between the compressive strength of concrete and its resistance. There is a linear correlation between the compressive strength and concrete electrical resistivity, but the correlation coefficient is not high. In contrast, the correlation

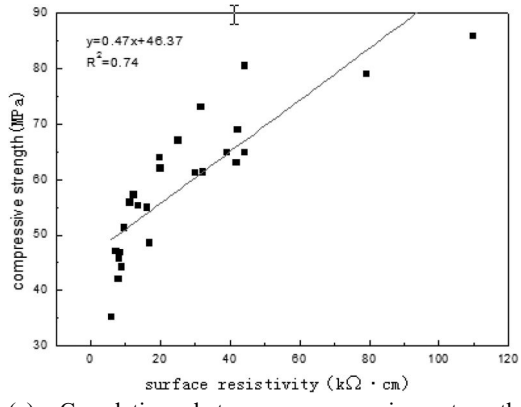

(a) Correlation between compressive strength and surface resistivity.

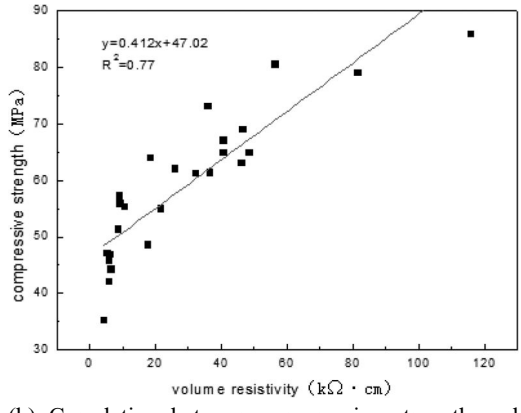

(b) Correlation between compressive strength and volume resistivity.

Figure 4. Correlation between compressive strength and electrical resistivity.

between volume resistivity and compressive strength is a little higher. That is because the overall performance of concrete is reflected by the volume resistivity and compressive strength, while the surface characteristics of concrete are mainly reflected by the surface resistivity. The correlation between late compressive strength and electrical resistivity is greater than that in the early age (Xiao Lianzhen et al. 2008). That is because the concrete structure at early age had not yet fully formed and the concrete electrical resistivity is affected by many factors.

3.2 *Correlation between electrical resistivity and passed electric charge*

Figure 5 shows the relationship between the electric current and time when testing the passed electric charge. In Figure 5, the electric current increased as the testing time increase at the age of 28 days. That is mainly because the electrical energy converted into heat energy during the test, so the temperature of the concrete increased. The activity of internal ions

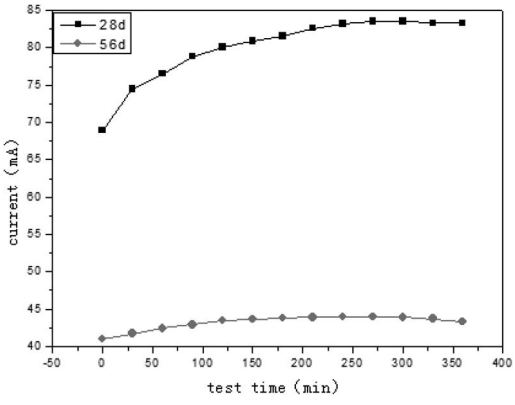

Figure 5. The relationship between current and time of test.

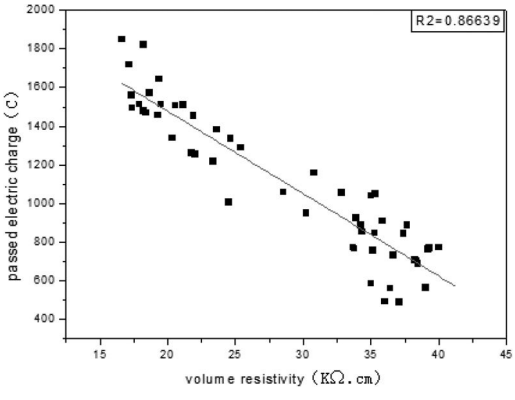

Figure 6. Correlation between passed electric charge and volume resistivity.

increased and the electrical resistance decreased which will have affected the measurement accuracy of the results. The concrete is less permeable at the age of 56 days, so the current was small and the temperature did not change significantly although the current changed a little. Figure 6 shows the correlation between the volume resistivity and passed electric charge of concrete. In Figure 6, there is a good negative correlation between the volume resistivity and passed electric charge of concrete and the correlation coefficient is 0.8976. So the passed electric charge of concrete can be characterized by volume resistivity of concrete.

3.3 *Correlation between impedance coefficient and volume resistivity*

Figure 7 shows the correlation between concrete diffusion impedance coefficient K and the volume resistivity of concrete. The ion diffusion impedance ability of concrete is characterized by a diffusion impedance coefficient K which is related to the concrete durability. The concrete is less permeable when the diffusion impedance coefficient K increases, so the ion diffusion impedance ability is greater and the durability is

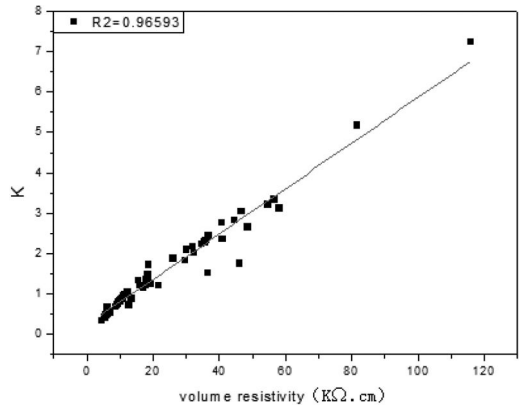

Figure 7. Correlation between diffusion impedance coefficient K and volume resistivity.

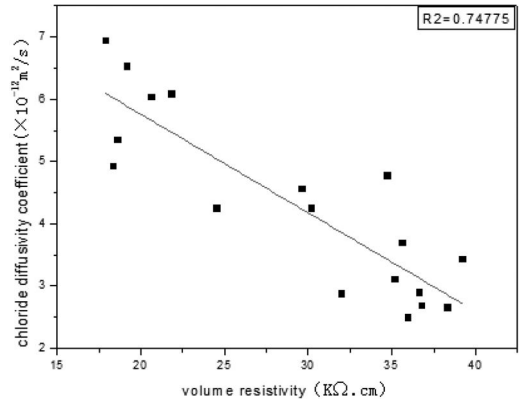

Figure 8. Correlation between chloride diffusion coefficient and volume resistivity.

better. In Figure 7, there is a good correlation between the diffusion impedance coefficient K and the volume resistivity of concrete, the correlation coefficient is 0.97. So the ion diffusion impedance ability of concrete can be characterized by electrical resistivity of concrete. Electrical resistivity of concrete increases as the increase of diffusion impedance coefficient K and the durability should be better with lower transport properties.

3.4 *Correlation between chloride diffusion coefficient and volume resistivity*

Figure 8 shows the correlation between chloride diffusion coefficient and volume resistivity. In Figure 8, there is a good negative correlation between volume resistivity and chloride diffusion coefficient of concrete, and the correlation coefficient is 0.75. The chloride diffusion coefficient of concrete can be characterized by the volume resistivity of concrete, so the impedance ability of chloride ion diffusion into concrete can be characterized by the volume resistivity

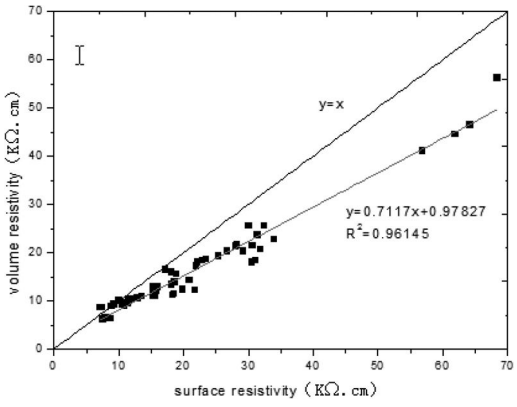

Figure 9. Correlation between volume resistivity and surface resistivity.

of concrete. In addition, the testing process of chloride diffusion coefficient is more cumbersome and test time is longer. The electrical resistivity of concrete can be tested quickly and easily.

3.5 *Correlation between volume resistivity and surface resistivity*

Figure 9 shows the correlation between volume resistivity and surface resistivity. In Figure 9, there is a good linear correlation between surface resistivity and volume resistivity of concrete, and the correlation coefficient is 0.96. Surface resistivity of concrete is greater than the volume resistivity of concrete under the same condition because of the shape factor of the specimen. The concrete is compacted, so the water inside cannot be lost easily and the surface water exchanges with the water around. The surface resistivity of concrete is obviously affected by the external environment. There are many advantages in surface resistivity testing technology, such as short test time (data can be obtained in 5 min), convenient test (device is simple), few influence factors, so it can be used for field durability test of concrete structures.

4 CONCLUSIONS

- Surface resistivity testing technology can be used for field durability testing of concrete structures. There is a good linear correlation between surface resistivity and volume resistivity of concrete, and the correlation coefficient is 0.96.
- Overall properties of concrete are characterized by the volume resistivity and the surface characteristics of concrete are mainly characterized by the surface resistivity. Correlation between the compressive strength and electrical resistivity of concrete is not high due to the unstable structure of concrete at early age.
- The passed electric charge of concrete can be characterized by volume resistivity of concrete. There is a good negative correlation between the volume resistivity and passed electric charge of concrete and the correlation coefficient is 0.8976.
- The ion diffusion impedance ability of concrete can be characterized by electrical resistivity of concrete. There is a good correlation between the diffusion impedance coefficient K and the volume resistivity of concrete, the correlation coefficient is 0.97.
- The chloride diffusion coefficient of concrete can be characterized by the volume resistivity of concrete. There is a good negative correlation between volume resistivity and chloride diffusion coefficient of concrete, and the correlation coefficient is 0.75.

ACKNOWLEDGEMENTS

Foundation item: Project (51378499) supported by National Natural Science Foundation of China; Project (2013yj118) supported by China Academy of Railway Sciences; Project (2014G004-R) supported by China Railway Corporation.

REFERENCES

David A, Mohamad A. 2003. Electrical Resistivity of Concrete–A Literature Review. *PCA R & D Serial* No. 2457.

Gong Guo-jun, Song Xiao-bing, Kong Qi-ming. 2005. The resisitivity of concrete contaminated by chloride. *Industrial Construction* 35(12):5–7.

Hansson I. L.H, Hansson C.M. 1983. Electrical resistivity measurements of Portland cement based materials *Cement and Concrete Research* 13(5):675–683.

He Zhen, Wang Xin-gang, Liang Wen-quan, Ye Qun-shan. 2004. Review of study on electrical property of cement-based materials. *Journal of Building Materials* 3:46–51.

Sanchez, I., Novoa, X.R. de Vera, G. et al. 2008. Microstructural modifications in Portland cement concrete due to forced ionic migration tests. Study by impedance spectroscopy. *Cement and Concrete Research* 38:1015–1025.

Xiao Lianzhen, Zongjin Li. 2008. Early-age hydration of fresh concrete monitored by non-contact electrical resistivity measurement, *Cement and Concrete Research* 38(3):312–319.

Zhao Tie-jun, Zhou zong-hui, Liu Jun-chang. 2000. Conductivity of pore solution and permeability of concrete evaluated by electric method. *Concrete* 13(2):12–15.

This page intentionally left blank

Concrete Solutions – Grantham et al. (Eds)
© 2014 Taylor & Francis Group, London, ISBN 978-1-138-02708-4

Effect of internal cracking on mass transfer resistance of cover concrete

S. Okazaki
Port and Airport Research Institute, Yokosuka, Japan

M. Kurumatani
Ibaraki University, Hitachi, Japan

I. Ujike & N. Takamoto
Ehime University, Matsuyama, Japan

ABSTRACT: A number of studies have shown that internal cracking of cover concrete around deformed bars degrades the tightness and mass transfer resistance of the concrete member and promotes the ingress of deformed bar corrosion factors such as water, air, and various ions. However, little attention has been given to the relation between cover deterioration from internal cracking and mass transfer resistance because quantifying invisible internal cracking in concrete is difficult. In this study, a novel specimen was developed that displays internal cracking on its surface; the proposed specimen was validated by finite element analysis. An air permeability test was carried out to evaluate the deterioration in the tightness of the cover concrete because of internal cracking.

1 INTRODUCTION

Goto et al. (1971) successfully visualized the internal crack distribution in a uniaxial tensile reinforced concrete (RC) member by placing red ink tubes next to the deformed bar. Once an internal crack occurs in the member under uniaxial tensile loading, the ink tubes split, and the red ink traces the presence of internal cracks. This concept enables internal cracks to be visualized even when there is no loading on the RC specimen. Because of their achievement, internal cracks near deformed bars are often called "Goto cracks"

Internal cracks in RC members are caused by dead loads and shrinkage stress; they are not at all visible on the surface of the member. Internal cracks cause the mass transfer resistance of cover concrete to deteriorate, but the extent of their effect has not yet been quantified. One of the reasons is that the above method can only obtain the crack position distribution and not the crack aperture distribution, which controls the mass transfer resistance, because the visualization takes place under the unloaded condition.

This method cannot visualize the internal crack apertures during loading, therefore associating the internal crack position and aperture distribution with the mass transfer resistance is difficult.

Otsuka et al. (2003) succeeded in visualizing the internal crack distribution in a tensioned RC member by using the radiographic visualization method. This method allows the aspects of invisible internal cracks to be obtained under loading conditions. However, with this method, measuring the aperture is difficult because of the blurry edges of the cracks, so obtaining the precise crack structure is impossible.

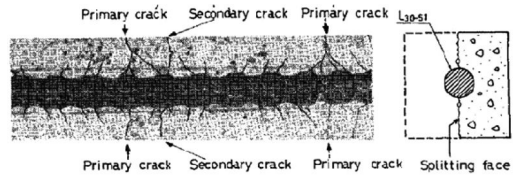

Figure 1. Internal crack distribution.

With this background, the aim of this study was to develop a direct visualization method for RC members; a novel specimen is proposed that can show not only the distribution of the crack positions but also the internal crack structure. The proposed model was validated by numerical simulation using a finite element (FE) model. With the validated method, mass transfer resistance parameters such as air permeability or chloride ion diffusion can be associated with the internal crack position and aperture distribution.

An air permeability test was carried out to evaluate the deterioration in the tightness of cover concrete because of internal cracking.

2 EXPERIMENTAL STUDY

2.1 *Summary of axial tension test method*

The aim of this research was to visualize internal cracks with the novel RC specimen: the deformed bar

is placed near the surface of the concrete in order to expose internal crack on the concrete surface.

An axial tension test was performed first to determine the specifications of the specimen.

Figure 2 shows the setup of the axial tension test. The specimen was set in the combined H steel frame (92 cm × 40 cm × 15 cm) to pull the deformed bar of the specimen. The center hole jack was set on one side of the exposed deformed bar of the specimen, and a center hole–type load cell was set on the jack. The exposed deformed bar was chucked in order to load the tensile force using the center hole jack.

2.2 *Materials, mix proportions, and curing of concrete*

All specimens used SD295-D25 deformed bars, and ordinary Portland cement was used to cast the concrete at a water–cement ratio of 0.50. Table 1 lists the concrete mix proportions. The coarse aggregate was crushed stone with a maximum nominal size of 20 mm and density of 2.61 g/cm^3. The fine aggregate was crushed sand with a density of 2.55 g/cm^3 and fineness modulus of 2.61.

The deformed reinforcing bar was set anywhere in the concrete form, and concrete was cast in the form. The cover depth of the proposed specimen was extremely thin; therefore, a wet film sheet was wrapped around the cover concrete in order to prevent corrosion of the reinforcing bar during the 28-day curing period. The concrete compressive strength at 28 days was 45.4 N/mm^2.

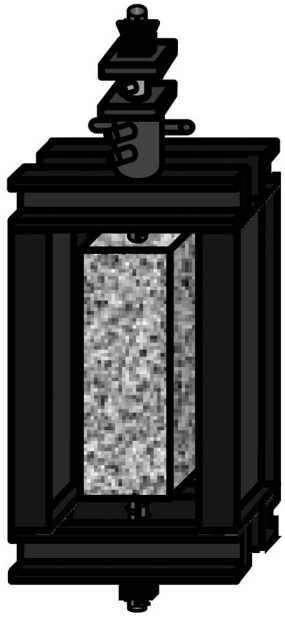

Figure 2. Experimental setup.

2.3 *Specimens*

The aim of this research was to visualize internal cracks around the deformed bar. The novel specimen was tested as shown in Fig. 3; one side of the cover concrete was extremely thin. We defined specimen A as having nodes (knots) of the deformed bar set extremely near to the surface, specimen B as having the rib of the deformed bar set extremely near to the surface, and the reference specimen as a normal uniaxial tensile specimen.

The way of deforming bar was to obtain the tensile strength by the center hole oil jack set on the bar shown in Figure 2. The uniaxial tensile load was equivalent to a stress of 125 N/mm^2 on the reinforcing bar.

2.4 *Experimental results*

Figure 4 shows the crack distribution of each specimen. For the reference specimen, a penetrating crack

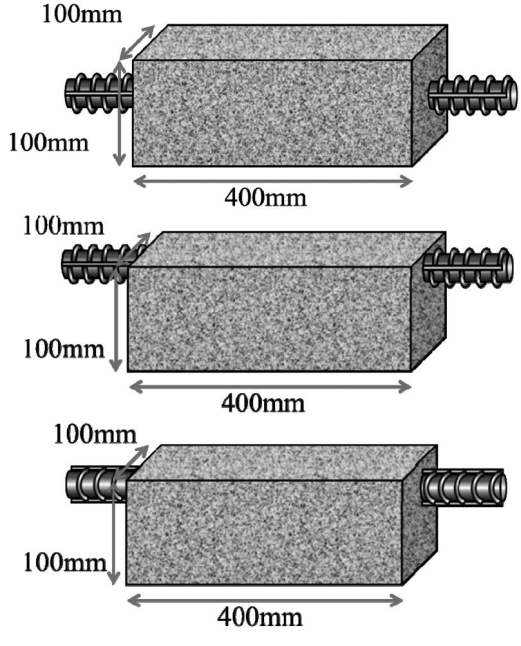

Figure 3. Specimen specifications: Reference (top), A (middle), and B (bottom).

Table 1. Mix proportions of concrete.

W/C (%)	Air (%)	Slump (cm)	s/a (%)	Unit weight (kg/m^3)				AE water-reducing agent (%)
				Water	Cement	Sand	Gravel	
50	3.5	7	50	175	350	825	922	1.2

occurred at the center of the longitudinal axis of the specimen. The internal crack around the deformed bar was not visible.

For specimen A, a penetrating crack similarly occurred; the cracks were in the axial direction near the deformed bar. However, almost no cracks were found with directions perpendicular to the longitudinal axis as in Fig. 1. In contrast, not only were there cracks in the same longitudinal direction as the penetrating cracks, but there were also vertical cracks that exposed the internal cracks. The longitudinal cracks made it difficult to discriminate between internal cracks, so a supplementary test was carried out on a specimen for which the deformed bar was exposed on the surface of the cover concrete. Figure 5 shows the overview of the proposed specimen. Specimen B′ was defined as specimen B with an exposed deformed bar, and specimen A′ was defined as specimen A with an exposed deformed bar.

2.5 *Results of supplementary test*

Figure 6 shows the crack distribution of specimens A′ and B′ under a tensile load equivalent to a stress of 125 N/mm^2 on the reinforcing bar.

For specimen A′, the penetrating crack was found on the exposed section of the deformed bar; no internal cracks were found there. This is because the node of the deformed bar was not near the surface of the cover concrete; the rib of the bar was exposed except for the node. For specimen B′, cracks formed diagonal to the longitudinal axis from the node of the deformed bar. This crack pattern was quite similar to the crack distribution shown in Fig. 1; thus, the internal crack distribution was successfully visualized on the exposed section of the deformed bar. The crack distribution on the proposed specimen differed from that for the normal uniaxial tensile test specimen in Fig. 1; however, being able to visualize the occurrence and development of internal cracks near the deformed bar during loading is very important.

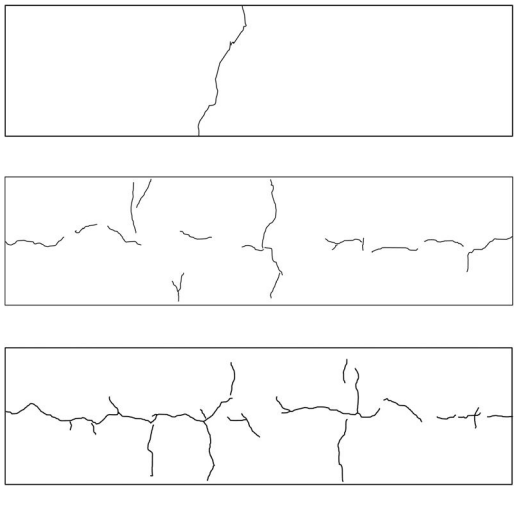

Figure 4. Experimental results: Reference (top), A (middle), and B (bottom).

2.6 *Loading value and crack occurrence development*

Using the proposed specimen, the relation between the loading value and the crack occurrence and development were obtained.

When the loading value was equal to 20, 100, 200, and 295 N/mm^2 the loading was maintained until a crack was observed on the specimen using acetone. Traces of cracks were marked with a marker, and the crack width was measured with a portable microscope having a precision of 1/1000 mm.

The crack width was not uniform even for the same crack; therefore, the crack width was defined in this

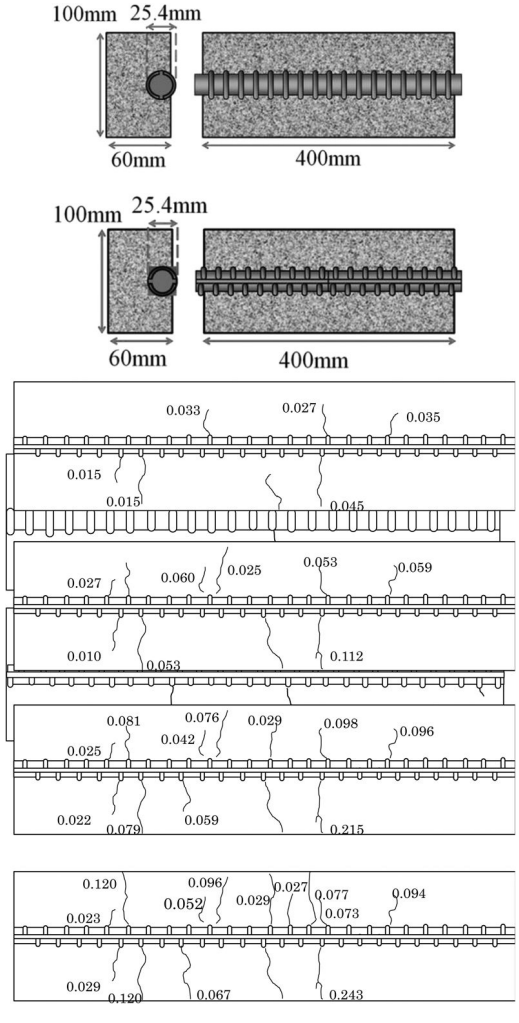

Figure 5. Crack distribution of proposed specimen. Bar stress (from top): 20, 100, 200, and 295 N/mm^2.

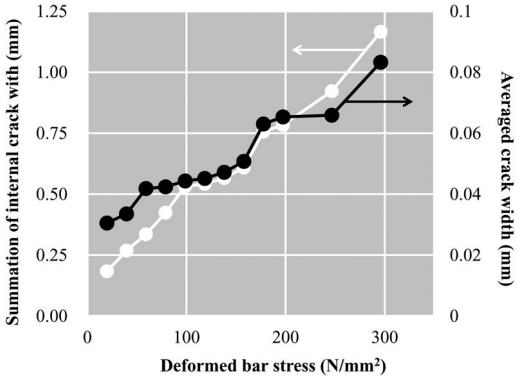

Figure 6. Relation between deformed bar stress and summation of internal crack and averaged crack width.

study as the average of about five points measured on the same crack.

Figure 7 shows the crack distribution and width under loading. Cracks that did not develop from a node of the deformed bar were not regarded as internal cracks; therefore, their crack widths were not described.

As the loading value was increased, new cracks occurred, and crack widths increased. Some of the cracks exceeded widths of 0.1 mm before the deformed bar yielded, and cracks developed up to the edge of the specimen. Therefore, internal cracks were inferred to have a large effect on the mass transfer resistance of the cover concrete.

Figure 8 shows the relation between stresses of the deformed bar and the sum of the crack widths of internal cracks; the sum of the crack widths was divided by the number of cracks.

The average crack width increased with the stress of the deformed bar. This tendency was the same as for the penetrating crack of the normal uniaxial tensile test specimen under tensile loading.

Sealing the exposed section of the deformed bar allowed corrosion from salt attack under tensile loading to be monitored; a tentative relationship was obtained between the mass transfer resistance, or deformed bar corrosion resistance, and internal cracks.

3 FE ANALYSIS BY DAMAGE MODEL

3.1 *Summary of damage model*

The proposed specimen was validated by comparing its exposed crack distribution with the internal crack distribution of the reference specimen. The internal crack distribution of the reference specimen cannot be visualized; therefore, the validation was carried out by numerical simulation.

FE analysis using an isotropy damage model based on the fracture mechanics of concrete was adopted for the numerical simulation.

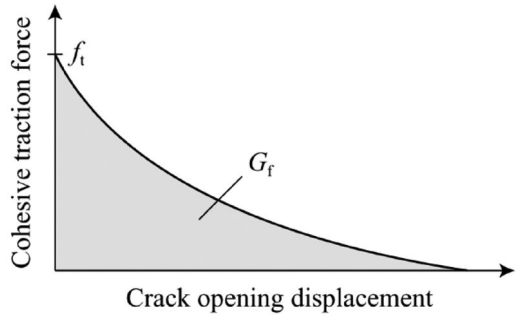

Figure 7. Relation between cohesive traction force and crack opening displacement.

The constitutive law of the isotropy damage model is based on Hooke's law and uses the scalar variable D, as shown in the following equation:

$$\boldsymbol{\sigma} = (1 - D)\boldsymbol{c} : \boldsymbol{\varepsilon} \tag{1}$$

Where $\boldsymbol{\sigma}$ is the Cauchy stress tensor, $\boldsymbol{\varepsilon}$ is the microstrain tensor, and $\boldsymbol{c}$ is the elastic modulus tensor. D is the damage index to show the degree of damage: $D = 0$ when the concrete is undamaged, and $D = 1.0$ when the concrete is completely collapsed.

Figure 9 shows the relation between the cohesive traction force and crack opening displacement. This relation was modeled by the stress and strain using FEs, and embedded in the constitutive law of the damage model. The damage index D is given in the following equation:

$$D(\kappa) = 1 - \frac{\kappa_0}{\kappa} \exp\left\{-\frac{E\kappa_0 h_e}{G_f}(\kappa - \kappa_0)\right\} \tag{2}$$

Where E is the elastic modulus of the material, G_f is the fracture energy, h_e is the characteristic length, κ is the maximum equivalent strain in the deformation history, and κ_0 is the equivalent strain at the start of damage. In the isotropic damage model of a multidimensional problem, the strain tensor is converted to the equivalent strain, which is a scalar value. In this study, the modified equivalent strain ε_{eq} proposed by de Vree et al. was adopted.

$$\varepsilon_{eq} = \frac{k-1}{2k(1-2\nu)} + \frac{1}{2k}\sqrt{\left(\frac{k-1}{1-2\nu}\right)^2 + \frac{12k}{(1+\nu)^2} J_2} \tag{3}$$

Where ν is Poisson's ratio and k is the ratio of the compressive strength to the tensile strength of material. $k \approx 10$ in the case of concrete. I_1 is the first invariant of the strain tensor $\boldsymbol{\varepsilon}$ and is shown in the following equation:

$$I_1 = \mathrm{tr}\boldsymbol{\varepsilon} = \varepsilon_{kk} \tag{4}$$

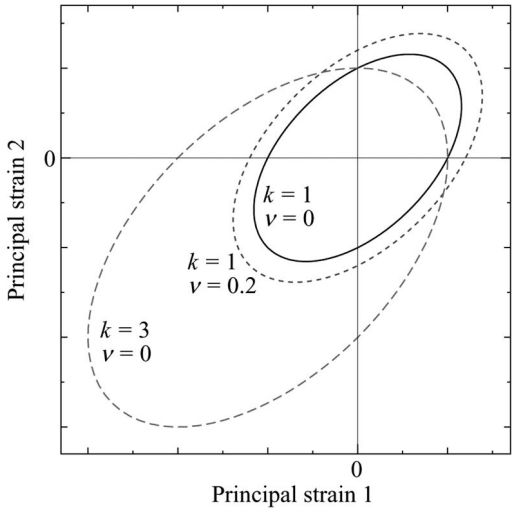

Figure 8. Relation between cohesive traction force and crack opening displacement.

J_2 is the second invariant of the deviatoric strain and is shown in the following equation:

$$J_2 = \frac{1}{2}\boldsymbol{e} : \boldsymbol{e} = \frac{1}{2} e_{kl} e_{kl} \tag{5}$$

Where $\boldsymbol{e}$ is given by the following equation:

$$\boldsymbol{e} = \boldsymbol{\varepsilon} - \frac{1}{3}\mathrm{tr}\boldsymbol{\varepsilon} \tag{6}$$

Figure 10 shows example plots of ε_{eq} on the two-dimensional main strain space. The relatively weak tensile strength and strong compressive strength are shown The damage model adopted in this research considered fracture energy; therefore the analysis could simulate damage and fracture behaviors that were resistant to the mesh size effect.

3.2 *Three-dimensional numerical simulation of internal cracks*

3.2.1 *Analysis model and conditions*

As shown in Fig. 11, an FE model of the proposed specimen, where a deformed D25 bar was embedded in concrete, was used to simulate the crack occurrence behavior around the deformed bar. This FE model had the same specifications as the specimen used in the experimental study, and the nodes and ribs of the deformed bar were precisely modeled. All FEs were linear, and about 1.16 million elements were used. The concrete model had dimensions of 60 mm × 100 mm × 400 mm. The boundary conditions were fixed on one side of the deformed bar and enforced an axial displacement of 0.6 mm on the other side.

Displacement in the off-plate direction was constrained on both ends of the deformed bar.

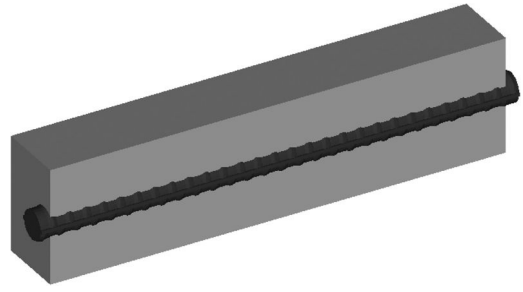

Figure 9. Model of proposed specimen.

The deformed bar was set as a linearly elastic material with an elastic modulus of 200 GPa and Poisson's ratio of 0.3. For the material parameters of the concrete, the elastic modulus was 20 GPa, Poisson's ratio was 0.2, the equivalent strain at the yielding was 0.0001, the fracture energy was 0.1 Nmm, and the ratio of the compressive strength to the tensile strength was 10.

3.2.2 *Analysis results and discussion*

Figure 12 shows the damage development in the concrete specimen. The distribution of damage index D was visualized with a detailed finite mesh; this figure shows an almost equivalent image to the visualized crack development.

First, damage developed from each side of the specimen; the simulated damage around the deformed bar increased with loading. Compared to the experimental results shown in Fig. 7, three-dimensional cone-shaped internal cracks formed. Although the number of cracks differed, the qualitative tendencies were almost concordant. Therefore, the results showed that the numerical simulation was dynamically appropriate. In an experimental study, the internal fracture behavior cannot be visualized; in contrast, a numerical simulation can visualize the fracture behavior in concrete, as shown in Figure 12.

3.2.3 *Comparison of proposed and reference specimen models*

Figure 13 shows the model used for numerical simulation of the reference specimen; the results were compared with the results of the proposed specimen model. The concrete had dimensions of 120 mm × 100 mm × 400 mm, and a deformed D25 bar was placed at the center of the concrete. The boundary conditions and material parameters were the same as those for the proposed specimen model.

Figure 14 shows the numerical results of the internal damage development in the reference specimen model. Similar to the proposed model, damage initially developed from each side of the specimen, and the simulated damage around the deformed bar increased with the loading. Subsequently, a penetrating crack occurred around the center of the member; furthermore, a penetrating crack occurred around the center of each divided area. The number of penetrating cracks and order of occurrence for the internal cracks differed

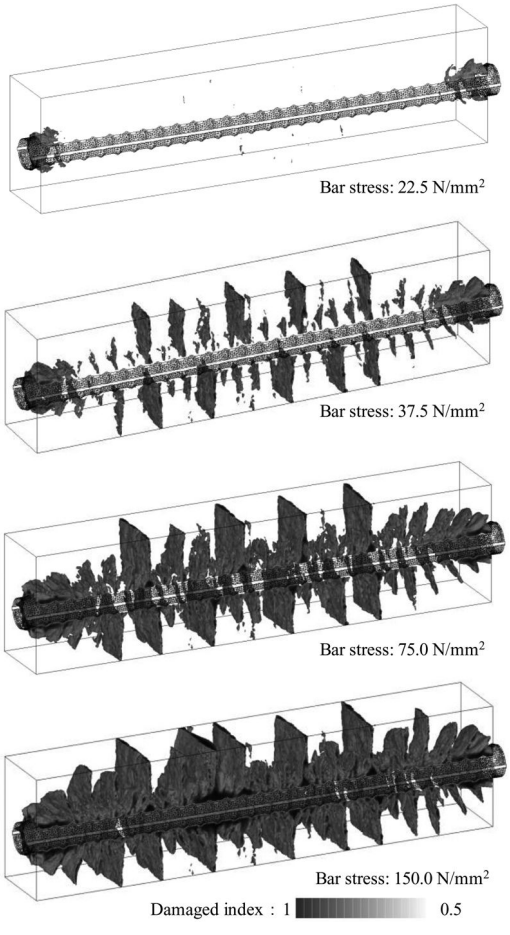

Figure 10. Damage development in proposed concrete specimen.

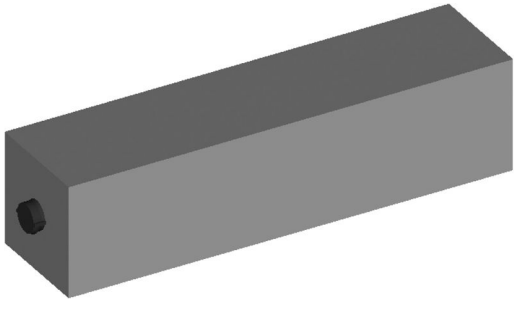

Figure 11. Model of reference specimen.

from those of the proposed model. However, three-dimensional cone-shaped internal cracks occurred in the specimen, and the damage behavior around the nodes of the deformed bar was similar to that of the proposed model. Therefore, the internal cracks of the proposed and reference models were almost the same, so the proposed specimen was determined to be appropriate.

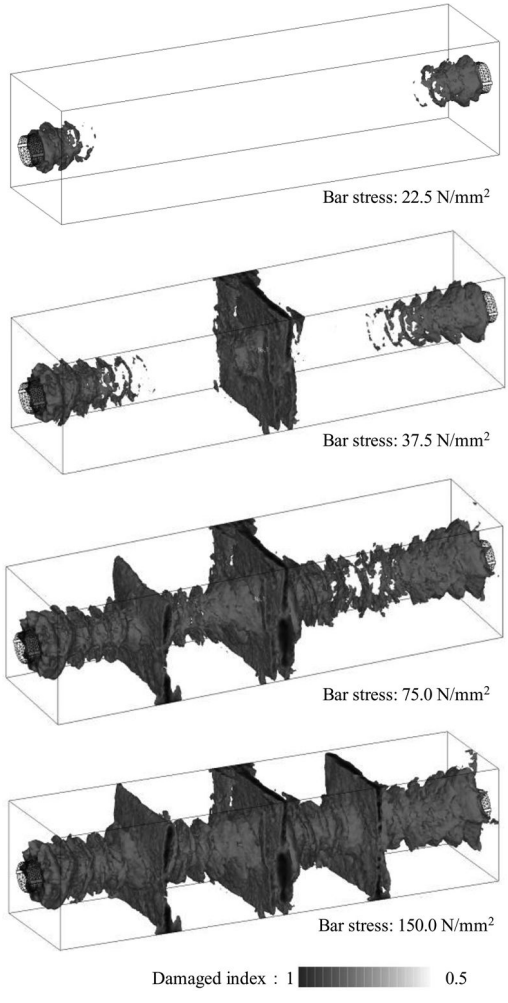

Figure 12. Damage development in proposed concrete specimen.

4 EFFECT OF INTERNAL CRACKS ON AIR PERMEATION

4.1 *Test setup and specimen*

Penetrating cracks often occurred at the center of the specimen; the air vacuum chamber for the air permeation test was thus placed elsewhere.

To obtain the effect of the crack distribution on concrete, other specimens with different concrete properties were used in this test. The mix proportions were almost the same as that for the previous specimens except for the inclusion of 1.2 vol % polyolefin fibers.

4.2 *Test results*

Figure 16 shows the relation between the deformed bar stress and the summation of crack widths, and Figure 17 shows the relation between the deformed bar

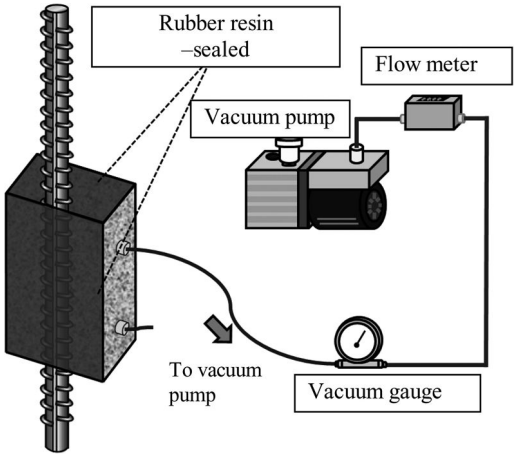

Figure 13. Air permeation setup.

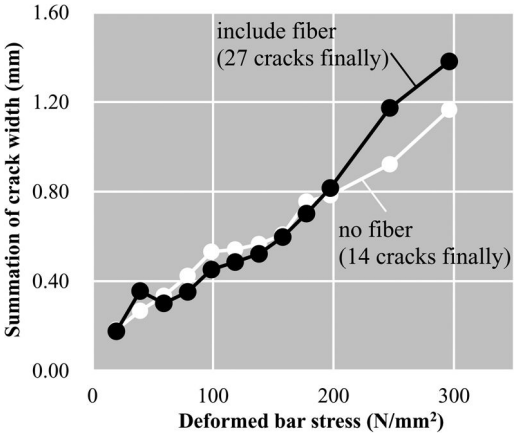

Figure 14. Relation between deformed bar stress and summation of crack width.

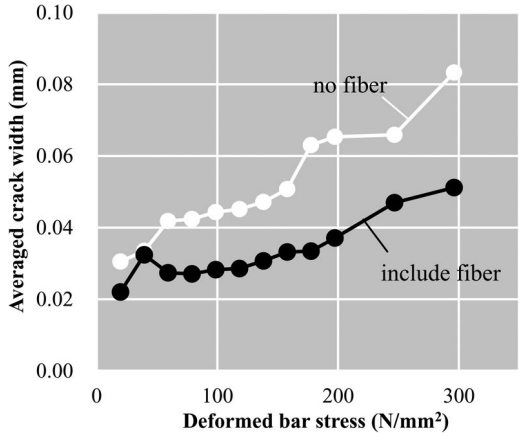

Figure 15. Relation between deformed bar stress and averaged crack width.

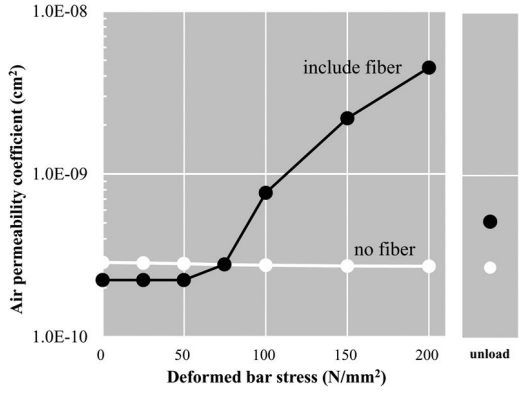

Figure 16. Air permeability coefficient (upward).

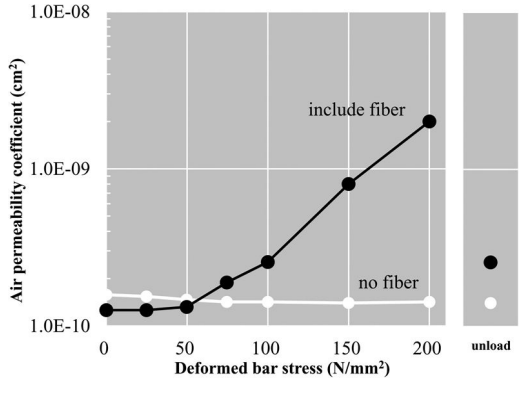

Figure 17. Air permeability coefficient (downward).

stress and averaged crack width. In figure 16, despite the fiber in the concrete, the summation of the crack widths did not differ. However, the numbers of cracks for each specimen were quite different. Because of this result, figure 17 shows that the averaged crack width of the five specimens with fiber was less than that of the specimens without fiber. This shows that including fiber increased the internal crack distribution of the RC member just like the penetrating cracks.

Figure 18 shows the relation between the deformed bar stress and the air permeability coefficient in the upward direction of the specimen, and figure 19 shows the relation in the downward direction.

Each figure shows the same tendency. Without fiber, the air permeability coefficient did not change despite the increasing stress of the deformed bar. On the other hand, with fiber, the air permeability coefficient increased when the deformed bar stress exceeded 50 N/mm^2. An air-permeable area formed in the shape of a half-sphere shape. Without fiber, no internal cracks occurred in the area, but they did occur with fiber because of the crack distribution.

With the proposed specimen, the effect of internal cracks on any kind of mass transfer resistance can be revealed. Future work will involve using the proposed

specimen to test the corrosion of the deformed bar due to salt attack.

5 CONCLUSION

In this study, the internal cracks around the deformed bar under uniaxial tensile loading were successfully visualized by means of a novel specimen that exposed the deformed bar under the cover concrete. The crack distribution was confirmed to be the same as the results of previous studies. The internal cracks were confirmed to be reproduced by numerical simulation. The effect of internal cracks on the air permeability coefficient was obtained. Especially the case in the concrete including fiber, there is some possibility of degrading the concrete cover protection performance due to the crack dispersion effect.

REFERENCES

Goto, Y.: Cracks formed in concrete around deformed tension bars, ACI Journal, No. 68-26, pp. 85–100, 1971.4.

Kurumatani, M., Terada, J. Kato, T. Kyoya, and K. Kashiyama: An isotropic damage model based on fracture mechanics for concrete and its evaluation, Transactions of JSCES Paper, Vol. 2013, pp. 20130015, 2013.8.

Otsuka, K. and M. Takeda: Detection of fine cracks by X-ray technique with contrast medium in concrete, Journal of JSCE, No. 725/V-58, pp. 143–156, 2003.2.

Vree, J.H.P. de, W.A.M Brekelmans, and M.A.J. van Gils: Comparison of nonlocal approaches in continuum damage mechanics, Comput. Struct., Vol. 55, pp. 581–588, 1995.

Concrete Solutions – Grantham et al. (Eds)
© 2014 Taylor & Francis Group, London, ISBN 978-1-138-02708-4

Study on effects of distribution of chloride ions by differences of pore structure with various conditions

R. Takatoku & T. Mizobuchi
HOSEI University, Koganei City, Tokyo, Japan

ABSTRACT: As the chloride ions permeate from pore voids in concrete and cause corrosion of reinforcing bars, it seems that the relationship between the pore voids and diffusion of chloride ions in concrete is concerned closely. However, research on that relationship has hardly been reported until now and the relationship has not yet been clarified. In this study, in order to investigate influences of differences of the pore structures on the diffusion of chloride ions with consideration of mix proportions, environmental condition, service life age and combined deterioration caused by chloride attack and carbonation and by chloride attack and leaching, experiments have been carried out to compare the distribution and content of chloride ions and the pore size distribution using several cores drawn from four marine existing structures.

1 INTRODUCTION

Chloride attack is one of the causes of deterioration in reinforced concrete structures. In reinforced concrete structure where chloride attack occurrs, cracks are resulted by corrosion expansion of the reinforcing bar by permeating chloride ions into the concrete. Generally, chloride diffusion in concrete is affected by external factors which are the environmental conditions of the structures like the air temperature and humidity, and by internal factors which are the materials characteristics like pore size distribution, the hydration of cement, and the air content. As chloride ions infiltrate from pore voids in concrete, and cause the corrosion of reinforcing bar, it seems that the relationship between the pore voids and diffusion of chloride ions in concrete is concerned closely. However, there have been few reports on the relationship between the pore structure and diffusion of chloride ions in concrete and both relationships have not yet been clarified.

In this study, in order to investigate influences of differences of the pore structures on the diffusion of chloride ions with the condition of mix proportion, environmental condition, service life age and combined deterioration caused by chloride attack and carbonation and by chloride attack and leaching, experiments have been carried out to compare the distribution of chloride ions and the pore size distribution using several cores drawn from four marine existing structures.

2 OUTLINE OF THIS STUDY

In this study, as shown Figure 1, the cores were drawn from four investigation places, and chemical analysis of the content of chloride ions and measurement of pore size distributions were carried out. As shown in Figure 2, the core was cut off at each 1 cm from the concrete surface, and samples for chemical analysis of chloride ion and pore size distribution measurement were collected at each depth. Figure 3 shows a Japanese map and each investigation structure position. Table 1 shows the mix proportion of the concrete and the service life of each structure.

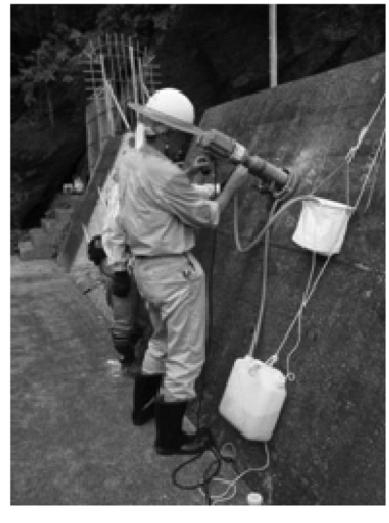

Figure 1. Situation of cutting of the core.

Each core was crushed to 150 μm or less. Chloride ion content on each sample was determined according to the testing method of potentiometric titration which is described in the "Standard Specifications for

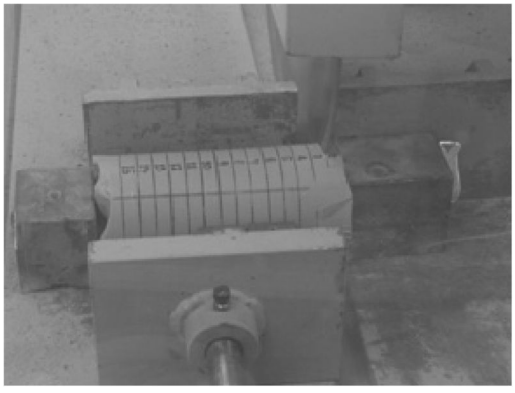

Figure 2. Situation of cutting of the core.

Concrete Structures" published by JSCE in Japan. Furthermore, the diffusion coefficient was calculated by using Fick's diffusion equation of equation (1) using the measured results.

$$C(x,t) = C_0\left(1 - erf\frac{0.1x}{2\sqrt{D \cdot t}}\right) \quad (1)$$

where x = distance from the surface (cm); t = progress number of years (year); C_0 = content of chloride ion of the surface (kg/m^3); D = diffusion coefficient (cm^2/year); erf = error function.

In order to measure the pore size distribution, the cores were sliced within 2.5 to 5.0 mm every depth. Before measuring the pore size distribution, the samples were freeze-dried for 1 week. The pore size

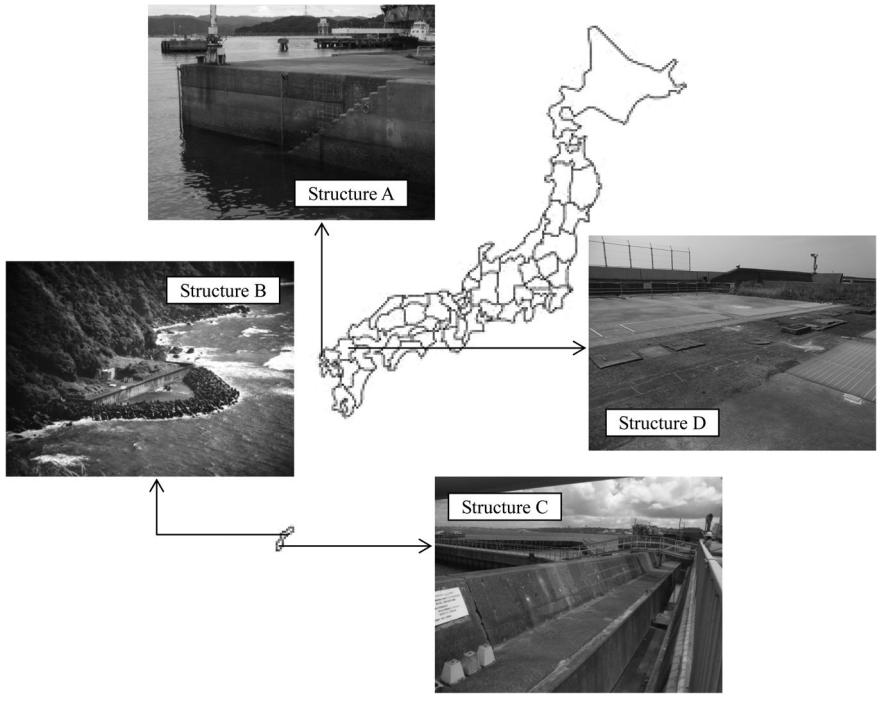

Figure 3. Location of each investigation places.

Table 1. Several conditions at investigation place.

Structure	Investigation place	Location	Water to cement ratio(%)	Type of cement	Service life (years)
A	Landing stage of coal-fired power plant	Nagasaki Prefecture	53	Fly ash type A	34
B	Outlet of seawater pumped storage power plant	Okinawa Prefecture	60	Ordinary Portland cement	16
C	Seawall in intake of coal-fired power plant	Okinawa Prefecture	53.7	Ordinary Portland cement	28 to 38
D	Seawall of coal-fired power plant	Fukuoka Prefecture	—	—	51

distribution of the samples was then measured by mercury intrusion porosimetry.

3 TEST RESULTS AND DISCUSSION

Figures 4 to 9 show the sampling point of the cores in each structure. Investigated places were the landing stage, the outlet, the seawall, and the sea deck. In the landing stage, the cores were drawn from the top surface and the sea side. The sampling position of the core in the sea side of landing stage was higher than sea surface at high-tide. Seven cores were drawn from four investigation places. Two cores were drawn from landing stage in a coal-fired power plant, two cores

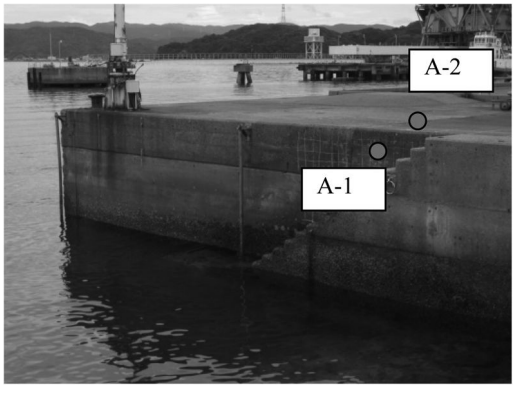

Figure 4. Landing stage of structure A.

Figure 5. Seawall in outlet of structure B.

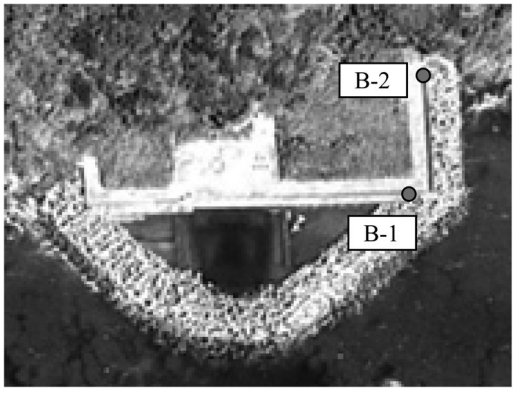

Figure 6. The outlet of structure B (Bird-eye view).

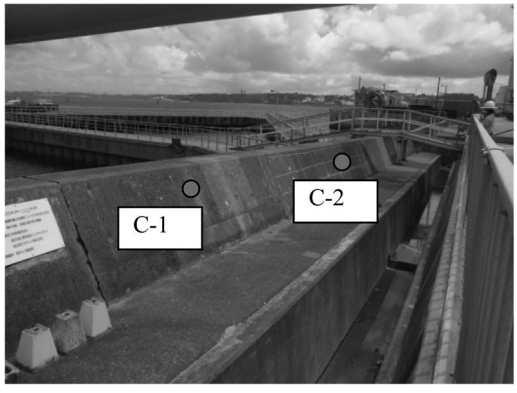

Figure 7. Seawall of structure C.

Figure 8. Intake of structure D.

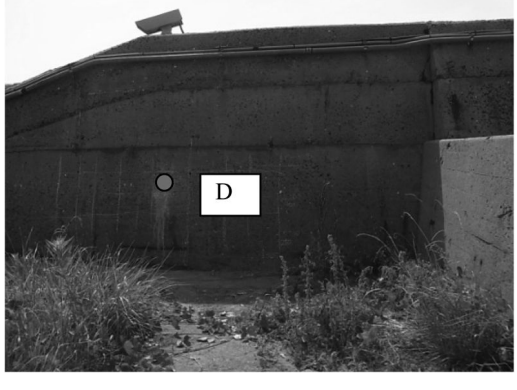

Figure 9. Seawall in intake of structure D.

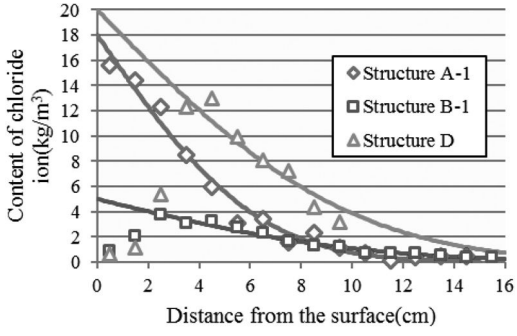

Figure 10. Comparison of content of chloride ion.

Table 2. Survey results of the cores.

Structure	Diffusion coefficient cm^2/year)	Carbonation depth (cm)
A-1	0.18	0.00
B-1	2.05	0.48
D	0.58	2.49

were drawn from the seawall of the outlet of a seawater pumped storage power station, two cores were drawn from the seawall in a coal-fired power plant, and one core was drawn from seawall in another coal-fired power plant.

Figure 10 shows the comparison with chloride ion penetration between structures A-1, B-1 and D. Table 2 shows the survey results of these cores. As shown in figure 10, content of chloride ions to the reinforcing bar in structure A-1 is higher than that in structure B-1 because structure A-1 is more exposed to tidal splashes than structure B-1 and the period of service life of structure A-1 is longer than that of structure B-1. In addition, though the carbonation depth of structure B-1 was 0.48 cm, the concentration phenomenon of chloride ions has reached the position which is more profound than the carbonation depth. It seems that this phenomenon is caused by the leaching. In both structures, large difference occurred in the diffusion coefficient because it seems that concrete of structure A-1 used fly ash and thus had lower diffusion properties than that of structure B-1. In structure D where the service life was longer than the other surveyed structures, the content of chloride ion was high and the carbonation was considerably deeper.

Figure 11, figure 12 and figure 13 show the relationship between pore diameter and the pore capacity in structure A-1, B-1 and D. As shown in figure 11, for the concrete away from the concrete surface, the pore capacity in the range from 0.1 to 1 μm decreases and pore capacity in the range from 0.01 to 0.1 μm increases. As shown in figure 12, the pore capacity in the range from 0.1 to 1 μm increases in the depth of 1.5 cm and is almost equivalent in the depth

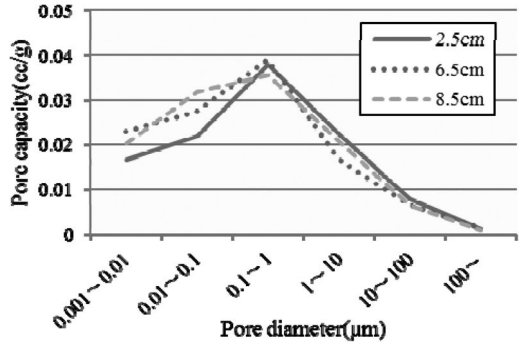

Figure 11. The relationship between pore diameter and pore capacity in structure A-1.

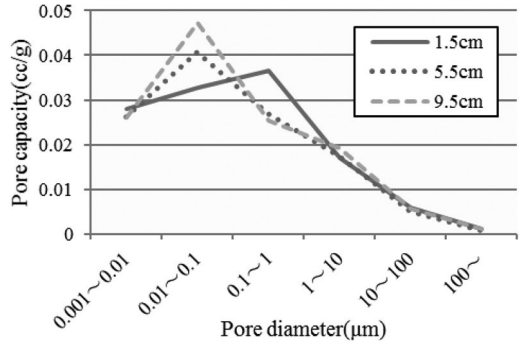

Figure 12. The relationship between pore diameter and pore capacity in structure B-1.

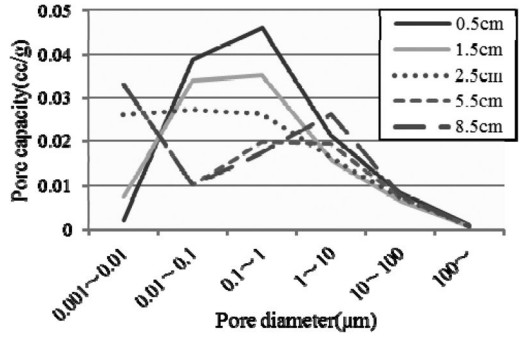

Figure 13. The relationship between pore diameter and pore capacity in structure D.

of 5.5 cm and 9.5 cm because it seems that from the effect of the leaching, the pore void in the range of 0.1 to 1 μm might increase by the sparseness of the pore structure. The pore capacity in the range from 0.01 to 0.1 μm showed the tendency which decreased as well as structure A-1 for the concrete inside. As shown in figure 13, it seems that the pore capacity tend to be different in the area in the depth from 0.5 to 2.5 cm where chloride ions concentrated in the effect of the

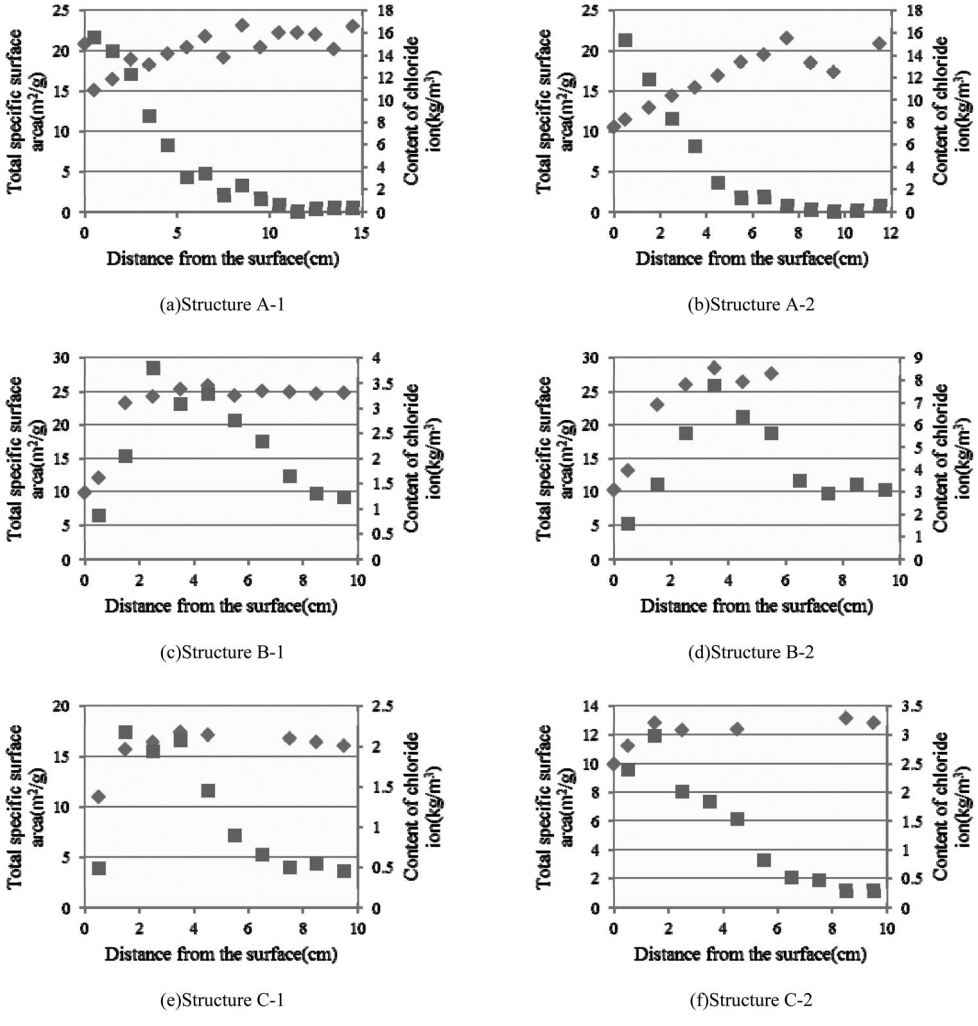

Figure 14. The relationship between diffusion of content of chloride ions and total specific area of the pore voids. (◇ = Total specific surface area; ■ = Content of chloride ion).

carbonation and in the soundness area. In the range from 0.01 to 0.1 μm, the pore capacity in carbonation area increases further than that in the soundness area. Therefore, it seems that the pore structure becomes sparse with the progress of carbonation.

Figure 14 show the relationship between diffusion of content of chloride ions and total specific area of the pore voids in each core. As shown in figure 14(a) and figure 14(b), total specific surface area becomes bigger with the decrease in chloride ions. As shown in figure 14(c) and figure 14(d), at the depth of concentration of the chloride ions, total specific surface area becomes bigger with the increase in chloride ions similarly and become constant in the soundness area. Therefore, it seems that the chloride ion distribution of each depth and total specific surface area are relevant.

4 CONCLUSIONS

- As the pore void in the range from 0.1 to 1 μm decreases with the decrease in content of chloride ions, it seems that the pore void in this range affects the diffusion of chloride ions.
- As the pore void in the range from 0.01 to 1 μm increases with the carbonation, it seems that the pore structure becomes sparse with the progress of carbonation.
- It seems that the chloride ion distribution of each depth and total specific surface area are relevant.

In this study, as the investigations were carried out only on existing structures, comparison and examination on the relationship between pore structure and diffusion of chloride ions using specimens in the

laboratory have to be carried out in future. From the results in this study, since there was no difference between test-pieces at the pore size over 10 μm, the investigation on the pore void at these diameters should be carried out by visualizing the pore void using the electron microscope in future.

REFERENCES

Takahashi, T., Inoue, S., Akiyama, H. and Kishi, T. 2010. The study that the influence of the materials age relates to at a salt penetration property and an investigation to fly ash concrete of true structures. Concrete engineering annual memoirs. Vol.32, No.1; 803–808.

Takeda, Y. & Sakoda, K. 1996. Secular variation of the steel reinforced concrete which came to light under marine environment for ten years. Concrete engineering annual memoirs. V0l.18, No.1; 753–758.

Takeda, Y. & Toga, S. 2004. Pore size distribution and salt osmosis of the concrete which became the neutrality. Society of Civil Engineering 59th annual academic lecture. 445–446.

Case studies

This page intentionally left blank

Concrete Solutions – Grantham et al. (Eds)
© 2014 Taylor & Francis Group, London, ISBN 978-1-138-02708-4

Examples of concrete structural elements in early 20th century buildings in Wrocław (Poland) – case studies

P. Berkowski & G. Dmochowski
Wrocław University of Technology, Wrocław, Poland

ABSTRACT: The aim of the paper, basing on selected real examples, is to present current technical state and general methodology of engineering actions dedicated to investigate the suitability of reinforced concrete structural elements from the turn of the 19th and 20th with aim to extend their service life for new functional aims. These innovative in their times structures can be found nowadays in historic buildings that are now under rehabilitation process and are very often situated in city centres of many Polish towns. The methodology of conducted actions is based on archival research, different *in situ* investigations, material testing, structural analysis and synthesis of adequacy of repair and strengthening methods and materials, both from a structural and conservation point of view.

1 INTRODUCTION

At the beginning of the 20th century, when reinforced concrete entered definitely our living environment as a structural material, it was considered to be a material which will last forever and not require any maintenance during a structures' exploitation. Nowadays, designed reinforced concrete structures should have a service life of about one hundred years under normal environmental conditions (e.g. Gulvanessian et al. 2012). This process takes into account life-cycle design and management of concrete structures relative to long-life exploitation, environmental influences, deterioration over time (Budelmann et al. 2012, Kumar et al. 2013), and also prediction of service repair work (Wachsmann & Budelmann 2012). Even though concrete structures can suffer deterioration after a very short period of time (e.g. Berkowski et al. 2013), they can also stay in a quite good structural and material condition after many years of use, which will be presented in this paper.

Problems with a lack of durability of many old concrete structures occur because designers in the past had no proper knowledge of the performance of the main structural materials (rebar steel and concrete) under the influence of different external and internal agents. Other factors negatively affecting the performance of reinforced concrete structures are poor quality of old material and workmanship, and also changes in load conditions.

Some structures built at the turn of the 19th and 20th century which are made of reinforced concrete elements and still survive now, are currently subjected to different processes of changing their functions or there is simply a need to prolong their service life. Some of them are now also considered to be structures of heritage value. Therefore, extending the lifetime of early RC structures is common and a current question arising in engineering practice.

In the case of historic concrete structures, their repair and/or strengthening poses a serious challenge to both structural engineers and conservation professionals. For concrete structures there is a European Standard EN 1504 (2010) in which requirements for quality performance of concrete repair are defined.

For historical buildings a general "restoration of serviceability" process was defined with recommendations consisting of a set of principles and guidelines for the analysis, conservation and restoration prepared by ICOMOS (2003). The rehabilitation process of concrete historic structures should not only take into account the structural needs but also the heritage value of buildings (Heinemann et al. 2012).

As an example of good practice in this field the renovation process of the Centennial Hall in Wrocław (UNESCO World Heritage Site) can be perfectly applied (Fig. 1). This spectacular reinforced concrete dome which has a diameter of 65.0 m (Fig. 2) was constructed in 1913 and in the years 2009–2011, after 100 hundred years of exploitation, including the 2nd World War period, underwent a major, successful rehabilitation (Czarniecki & Czerek 2012, Jasieńko et al. 2012, Jasieńko et al. 2013, Onysyk et al. 2013).

2 DIAGNOSIS AND REPAIR METHODOLOGY FOR OLD RC STRUCTURAL ELEMENTS

Both in contemporary and heritage reinforced concrete structures the external environmental (sometimes aggressive ones) and material internal influences

Figure 1. The Centennial Hall in Wrocław after renovation.

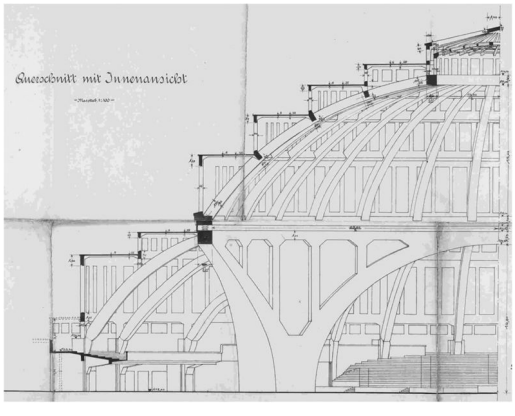

Figure 2. Dome of the Centennial Hall in Wrocław – archival drawing (City Building Archive).

can cause nearly the same durability and destructive problems. Common causes of defects in concrete structures are presented in Table 1.

However, the origins of damage may be different as used materials, design methods and execution technologies (Bertollini et al. 2011, Hellebois et al. 2010, Hellebois & Espion 2011) have changed extensively over the years since the first erection of RC elements.

Concluding, most of the material damage and structural deficiencies in old concrete structures have two main causes: the limited knowledge concerning design, material and construction matters, and the basic nature of the technological tools that designers and builders possessed at the beginning of the 20th century (Hellebois & Espion 2011, Gebregziabhier 2008).

Current guidelines for products and systems for the protection and repair of reinforced concrete structures are defined in the EN 1504 standard. General plan of the repair of concrete structures according to the rules described in this standard can be defined as follows (Raupach 2006, 2009):

- assessment of the structure technical condition (including reasons for causes of failures);
- selection of the repair strategy:
- do nothing for a definite time,
- re-analysis of structural bearing capacity, possibly leading to reduction of the structure function,
- prevention or reduction of further deterioration, without improvement of the concrete structure.
- improvement, strengthening or refurbishment of all or parts of the concrete structure,
- reconstruction of part or all of the concrete structure,
- demolition of all or part of the concrete structure;
- definition of the repair principles (protection against the ingress of media, strengthening etc.);
- decision on selection of repair method (impregnation, injection, patching etc.);
- determination of the requirements for repair materials (strength, adhesion etc.);
- adoption of the requirements for further maintenance and quality control.

Table 1. Common causes of defects in concrete structures (EN 1504-9).

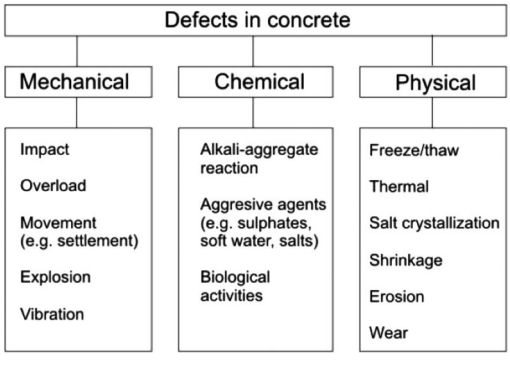

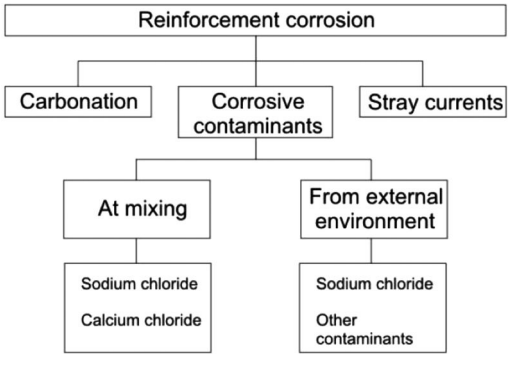

Generally, repair and strengthening methods used for modern reinforced concretes can be used for reinforced concrete heritage structures but with limitations being based on the principles of restoration of heritage structures. Also there are specific problems that may be encountered and specific actions that should be performed while preparing repair or rehabilitation project of historic concrete structures (Hellebois & Espion 2011):

A) Assessment of a structure's condition should begin with a review of all available documents related to original construction and earlier repairs – construction history. The design plans for old buildings may give information on the composition of the concrete mix or on the type and location of reinforcing bars, which sometimes can be wrong.
B) Materials used and workmanship in the construction of historic concrete structures, sometimes present potential sources of problems (low quality of aggregate susceptible to destruction when exposed to moisture and cyclic freeze/thaw, use of sand from seawater containing sodium chloride that accelerates rebar corrosion, etc.).

Poor consolidation of the concrete during its placement in forms, or in moulds in the case of precast elements which resulted in voids, can reduce the protective concrete cover over the reinforcing bars, entrap water, and reduce concrete strength.

3 BRIEF SYNTHESIS OF SELECTED CASE STUDIES

In the recent years, in connection with the ongoing activities related to the reconstruction, modernization and adaptation to the new functional purposes of existing old buildings located in the centre of many of Polish cities, building engineers are often faced with interesting structural solutions from the turn of the 19th and 20th century. In the course of research work aimed at diagnosing the technical condition of these old objects, including their safety, and the development of appropriate revitalization designs, there are discovered different concrete elements as, for example: prefabricated concrete slabs in apartment houses, different types of monolithic floor slabs in industrial or public buildings or even complete skeletal structures of factory halls or department stores. Studying them can give not only a good understanding of the knowledge and abilities of the engineers from the past, but also is absolutely necessary for the adequate design of repair interventions. However, sometimes it happens that old concrete structures withstand the passage of time and aging without significant loss of material and structural properties.

3.1 *Foundation structures*

Geotechnical and hydrotechnical foundation conditions, which are present in the area of Wroclaw are often very complex, due to, among others, the occurrence of numerous troughs and river channels and former areas of floodplain routes. Therefore, these conditions require the design and application of special methods of foundation work. In the course of carrying out various engineering activities, foundations of historic buildings dated from 100 years ago can be discovered and are interesting due to their construction and technology which use solutions modern for those times including the usage of reinforced concrete.

3.1.1 *Foundation slab with rigid reinforcement*

The building, which was subjected to a technical condition examination due to the anticipated execution of a deep trench nearby, consisted of two segments: the front part was a former German building dating from 1906, and the back part was built in the late twentieth century. The aboveground construction of the historic part of the building was traditional: the walls were built of solid brick, the slabs were monolithic and the roof was wooden. According to archival documentation (Fig. 3), the old part of the building was set on a reinforced concrete slab with a thickness of 0.5 m.

The slab was reinforced with double-layer rigid reinforcement in the form of a "grid" made of the I-shaped profiles NP10, located approximately every 1.0 m in both directions, locally below the projected wall columns and compacted to the mesh with dimensions of 0.5×0.5 m. The depth of foundation was specified from 1 m (at the back of the building) to

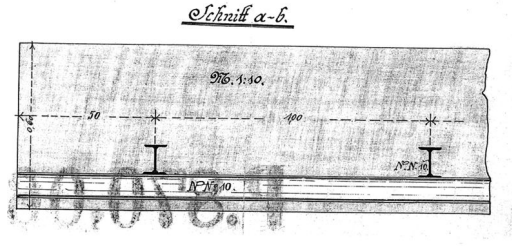

Figure 3. Cross-section of RC foundation slab with rigid reinforcement (City Building Archive).

Figure 4. Foundation examination pit.

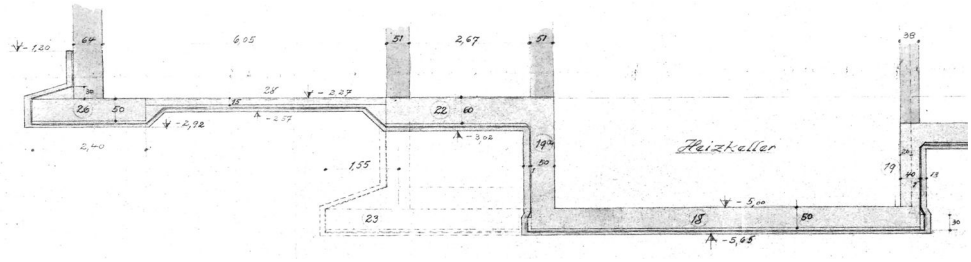

Figure 5. Foundation multi-level slab (City Building Archive).

1.5 m (at the front of the building) below ground level. The foundation method was determined by soil conditions which occurred in this place – loose scatter soil of low bearing capacity.

The foundation of the building was examined with the execution of foundation pits up to the foundation level. In the pits, the presence of a concrete slab was confirmed. The slab was located below groundwater level (Fig. 4) and the whole foundation was completely immersed in a layer of wet soil. The study did not show the aggressiveness of the groundwater in relation to the concrete.

Detailed inspections of the building, including the floor in the basement, confirmed the absence of any damage that might indicate bad functioning of the slab. The foundation did not require any building intervention in the form of construction strengthening, for example, the execution of additional piling.

3.1.2 *Multilevel foundation slab*

The main building of the theater was built around 1930. Based on analysis of archival documentation, it was found that the main building, basements of the courtyard and the office building were based on one shared RC foundation slab (Fig. 5).

The foundation slab varied in thickness – the thickness of the main part was equal to 0.5 m and possessed different levels of foundation. According to the original design there was a 5 cm lean concrete layer under the main foundation slab, and beneath it 1 cm thick insulation. Below the insulation, there was a 7.5 cm thick brick layer and below everything there was a 1.5 cm cement screed layer. Executed exposures inside the buildings confirmed that there was a RC slab at the foundation level. Exposures in the foundation slab were made to a depth of 35–40 cm (deeper exposures were not done because of the possibility of damaging the existing insulation, which according to archival documentation was under the slab). The top reinforcement was recognized to be made of smooth steel with a diameter of Ø14 mm, located approximately every 12.5 cm (Fig. 6).

The technical condition of the foundation slab was very good – there were no cracks, or groundwater infiltration found. There were only small cracks in one internal wall (Fig. 7). Static-strength calculations of the slab showed that such a foundation design solution would allow the introduction of all new functional solutions of the object without the need of strengthening the foundation.

Figure 6. RC slab reinforcement exposure.

Figure 7. RC foundation wall with cracks.

3.2 *Monolithic floor slabs*

In the historic center of Wroclaw, in addition to typical buildings in the form of tenements, there are also buildings which in the late nineteenth and early twentieth century were used as commercial premises or small industrial plants (textile, cigar factories or even mechanical plants). Due to their function, these objects required large functional areas, and therefore the need to construct floor slabs with a significant span, but also

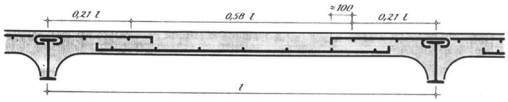

Figure 8. Cross-section of "Wolle'sche Konsoldecke" (Ahnert & Krause 1991).

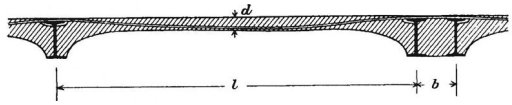

Figure 9. Cross-section of "Koennen'sche Voutenplatte" (Ahnert & Krause 1991).

with a sufficiently large bearing capacity. An excellent description of the typical solutions of reinforced concrete slab constructions was given, among others, in Ahnert & Krause (1991).

3.2.1 *RC slab floor in former industrial building*

In the past, inside the examined building, there was a factory which produced mechanical devices and at the time of inspection there was a pharmaceutical factory. The foundations of the building were brick, in the form of continuous footings along the walls and the spot footings below the columns. The load bearing construction of the building consisted of exterior brick walls and a system of steel columns. The exterior walls had a thickness of 77 up to 103 cm in the basement; from 64 up to 95 cm on the ground floor, 64 to 77 cm on the first floor, 51 to 64 cm on the second floor, 51 cm on the third floor and 38 cm on the fourth floor. The interior walls in the basement were 64 to 103 cm thick. Cast iron columns had a diameter of 36/30 cm on the ground floor, 29/23 cm on the first floor, 26/21 cm on the second floor and 20.5/15.5 cm on the third floor. Main steel beams were made of three I-beam profiles NPI380, 320 and 300 span between the walls and columns. The floor slabs above the basement and in localized areas on other floors were of Klein type. The attic slab was wooden with a concrete floor. The rafter was wooden. Slabs between floors were made in the form of 11 cm thick reinforced concrete panels, placed on steel NP I280 ribs and reinforced with Ø10 mm smooth steel rods anchored to the upper shelves of the steel beams. Visual inspections confirmed that the slab floors were of "Wolle'sche Konsoldecke" type (Fig. 8). The maximum span of these type of slabs reached 10.0 m.

Despite the long-term exploitation there was no visible damage in the form of cracks or scratches found. The floor slabs also had transverse reinforcement which protected them against the formation of cracks along the main reinforcement.

Verified structural calculations showed that the examined reinforced concrete slabs had a load capacity which enabled further exploitation of the object without the need of strengthening.

3.2.2 *RC slab floor in former department store*

The examined building was a five storey office and warehouse building with a basement and an attic. The building was erected in 1899 as commercial premises. The construction of the building varied. There were brick continuous footings under the walls, based approximately 1.5 m below the basement floor level. Beneath the cast-iron columns there were brick spot

Figure 10. Cracks in floor slab.

footings topped with granite blocks, based approximately 2.5 m below the basement floor level. The external load-bearing walls were made of solid brick. The wall thickness was: 77÷90 cm in the basements, 64 ÷ 77 cm on the ground floor, 64 cm on the first floor, 57 ÷ 64 cm on the second floor, 51 cm on the third floor and 38 cm on the fourth floor. The internal load-bearing structure was a system of circular cast-iron columns on which were based steel main beams made of I-profiles. These elements were based on walls and columns which were covered with concrete. The floor slab above the basement was monolithic and was based on steel beams. There was a wooden beam floor slab in the attic designed with tie rods in the floor level. The floor slabs above the ground, first, second and third floors were made of reinforced concrete panels with a thickness equal to 10, 12 and 14 cm, reinforced with ϕ10 mm rods every 10 cm. They were panel slabs called "Koennen'sche Voutenplatte" (Fig. 9). The maximum span of these type of floor slabs reached 10 m.

There were scratches, and in localized areas also cracks along the rods of the bottom main reinforcement (Fig. 10) found on the floor slabs of all levels. It was caused by the absence of transverse reinforcement. This is a common construction mistake. In order to ensure the further and safe use of the floor slabs, repair by injection of scratches and strengthening of the structure with the use of FRP tape on the bottom surfaces of the floor slabs was recommended. Implementation of the repair work was preceded by the strength analysis of concrete in the surface layers due to the need of ensuring the appropriate bearing capacity of joints between glued FRP tape and concrete from the floor slab.

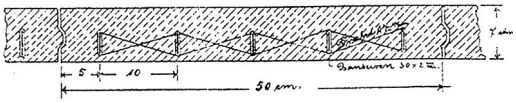

Figure 11. Cross-section of "Wygasch" precast RC plate (City Building Archive).

Figure 12. Destruction of "Wygasch" slab.

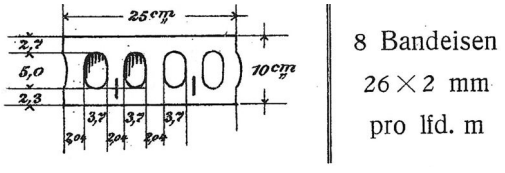

Figure 13. Cross-section of "Stolte" precast plate (City Building Archive).

3.2.3 *Precast balcony slabs*

The load bearing balcony slab consisted of prefabricated reinforced concrete slabs of "Wygasch" type. The thickness of the slabs was equal to 7 cm. They were reinforced with flat bar inserts with 30 × 2 mm dimensions, located in five rows, fastened transversally with wires with a diameter of 1.5 mm (Fig. 11). According to German projects, the weight of a single slab is equal to 129.25 kg, and the weight of leveling layers is equal to 120 kg. Slabs with a reach of up to 1.50 m were designed for operational loads up to 500 kg/m^2, and those with a reach of up to 1.20 m for operational loads up to 750 kg/m^2. In the structural layers of the balconies there was no evidence of any type of water insulation found.

"Stolte" cement balcony plates (Fig. 13), reinforced with flat bars 26 × 2 mm, had a span from 1.30 up to 2.50 m and corresponding total capacity from 1250 to 500 kg.

The prefabricated reinforced concrete slabs which are discussed in this chapter were directly exposed to the long-term impact of environmental influences, especially precipitation and processes related to the phenomena of freezing and thawing (Figs 12, 14). This mainly resulted in the destruction of their surface layers, however, it did not significantly reduce

Figure 14. Concrete destruction in "Stolte" slab.

their load-bearing capacity. Repair recommendations included the execution of typical surface repairs, and also protection of the entire balcony slabs by making waterproof insulation layers.

3.3 *Structural framing systems*

3.3.1 *Frame bearing structure of department store*

The building, dated from 1910, was used as a trade warehouse and had five floors, a basement and an attic. The construction of the load-bearing elements of the building was a combination of reinforced concrete and brick with ceramic beam-and-block floor slabs. The main load bearing elements were transverse, multi-storey, monolithic reinforced concrete frames, with Ackermann floor slabs between the main beams (girders). The main frames were located from the basements to the fourth floor of the building, and their span between the supports was equal to approximately 9.0 m. The cross-section of columns was composed of two rectangles with dimensions approximately equal to 62 × 30 cm and 60 × 50 cm. According to archival documentation, the reinforcement was as follows: the first part was reinforced with 7 rods of ϕ30 mm from the outer surface site and the inner part with an annular reinforcement of 10 rods of ϕ23 mm with winding rods of ϕ10 mm. The frame girders had T-shaped cross-sections with dimensions of 40/160 × 70 cm (with a floor slab 6 cm thick) and had slants. According to the archival documentation the reinforcement consisted of 8 rods of ϕ27 mm. Next to the girder supports curved rods were applied, and in slants 8 rods of ϕ27 mm which were located at the bottom (Fig. 15).

In order to diagnose the condition of the construction material, a series of exposures were executed which verified the strength of the concrete. It turned out that the concrete had a heterogeneous structure. It was a sand concrete with a low aggregate content (Fig. 16) and its strength was of the order of 12 MPa. Tensile tests of steel, made on samples which were taken from it, showd that their strength was equal to 100 MPa.

The general technical condition of the object and also the computationally confirmed load bearing

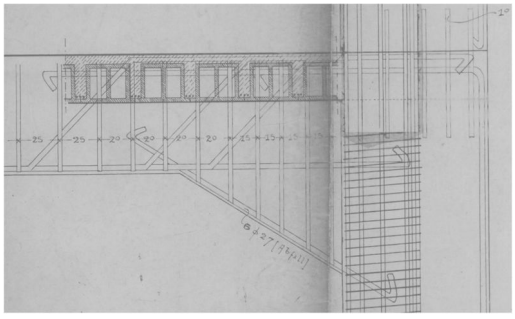

Figure 15. Archival drawing of rebar situation in frame corner (City Building Archive).

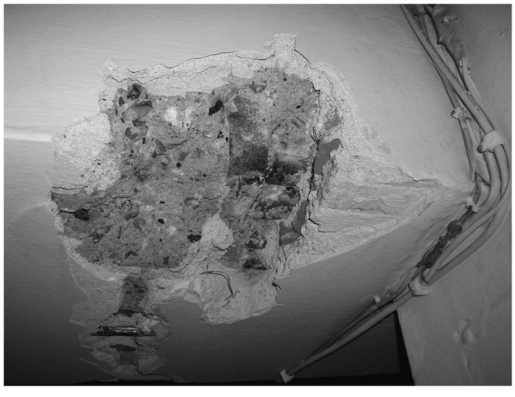

Figure 16. Concrete and rebar exposure.

Figure 17. General view of arch frame structure of market hall.

capacity of the reinforced concrete slabs and frames allowed for further exploitation of the object without the need of any repairs and strengthening.

3.3.2 *Arch framing structure of market hall*

Unusual, due to its construction, the reinforced concrete arch frame structure of the Market Hall (Gryglewska 1999) dated from 1906–1908. This was a three-nave building with a basement and galleries on the first floor which surrounded the main hall of

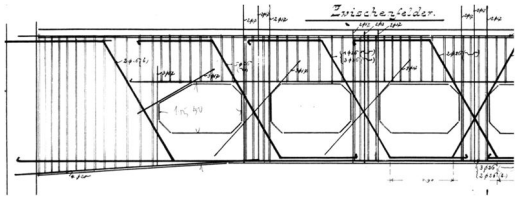

Figure 18. Archival drawing of rebar situation in the mid panel (City Building Archive).

the Market Hall. In the projection, the object had dimensions of 39.0 × 86.0 m and a total height equal to 20.0 m. The main load bearing hall construction consisted of parabolic arches (Fig. 17) with a span of 19.0 m, connected by transverse, openwork beams with a length of 12.0 m. The retained technical documentation contained both structural drawings (Fig. 18) and the detailed static calculation and dimensioning of reinforcement.

The technical condition of the construction, despite more than a hundred years of exploitation, was still very good. The only work that was performed, was maintenance renewal of the concrete surface on constructional elements.

4 CONCLUSIONS

In this paper, different reinforced concrete structural elements of buildings from the early twentieth century are described basing on selected examples. The presented solutions are found in historic buildings from the area of Wrocław, which are diagnosed due to their suitability for further exploitation. In all the described cases, apart from the prefabricated balcony slabs, reinforced concrete elements throughout the whole period of exploitation reaching almost 100 years were not exposed to any destructive external influences. This allowed for all their structural and operational characteristics to be kept and also the possibility of further usage, even in the case of functional changes. These elements provide an excellent example of both the quality of the design and executive work which were carried out more than a century ago, and also the properties of the "eternal" construction material, which is concrete that functions in conditions of suitable protection against environmental influences.

REFERENCES

Ahnert R., Krause K. H., 1991. Typische Baukonstruktionen von 1860 bis 1960. Zur Beaurteilung der vorhandenen Baussubstanz, Band 1. Berlin: Verlag für Bauwesen (in German).

Berkowski, P., Dmochowski, G., Kosior-Kazberuk, M. 2013. Analysis of structural and material degradation of a car-park's RC bearing structure due to city environmental influences. Procedia Engineering 57: 183–192.

Bertolini, L., Carsana, M., Gastaldi, M., Lollini, F. & Redaelli, E. 2011. Corrosion assessment and restoration

strategies of reinforced concrete buildings of the cultural heritage. *Materials and Corrosion*, 62(2): 146–154.

Budelmann, H., Holst, A., Wachsmann, A. 2012. Durability related life-cycle assessment of concrete structures: Mechanisms, models, implementation. In A. Strauss, D.M. Frangopol & K. Bergmeister (eds), Life-Cycle and Sustainability of Civil Infrastructure Systems; Proc. of Int. Symp., Vienna, 3–6 October 2012. Leiden: CRC Press/Balkema.

Czarniecki, M. & Czerek, D. 2012. Renovation of the Centennial Hall (UNESCO list, Wrocław). In J. Jasieńko (ed.), Structural Analysis of Historical Constructions, SAHC 2012; Proc. of Int. Conf., Wrocław, 15–17 October 2012. Wrocław: DWE.

EN 1504: 2010 Products and systems for the protection and repair of concrete structures – Definitions, requirements, quality control and evaluation of conformity. Part 1 to 10. European Committee for Standardization.

Gebregziabhier, T.T. 2008. Durability problems of 20th century reinforced concrete heritage structures and their restorations, Master's Thesis, SAHC 2007–2008, Technical University of Catalonia, Barcelona.

Gryglewska, A. 1999. Architecture in Wrocław in XIX-XX century in the works of Richard Plüddemann. Wrocław: Printing house of WrUT (in Polish).

Gulvanessian, H., Calgaro, J-A. & Holický, M. 2012. Designer's guide to Eurocode: Basis of structural design. 2nd ed. ICE Publishing Ltd.

Heinemann, H.A., Zijlstra, H. & van Hees, R.P.J. 2012. From concrete repair to concrete conservation: How to preserve the heritage values of historic concrete. In M. Grantham, V. Mechtcherine & U. Schneck (eds), Concrete solutions; Proc. of Int. Conf. on Concrete Repair, Dresden, 26–28 September 2012. Leiden: CRC Press/Balkema.

Hellebois, A., Germain, O., & Espion, B. 2010. Reinforcement assessment in early reinforced concrete constructions. In Forde, M. (ed.), Structural Faults and Repair, Proc. of the Int. Conf. Edinburgh: Engineering Technics Press.

Hellebois, A., Espion, B. 2011. Material properties of reinforced concrete at the turn of the 20th century: a review of primary literature. In Proc. of the 2nd WTA PhD Symp., Brno, 6–7 October 2011.

ICOMOS ISCARSAH. 2005. Recommendations for the Analysis, Conservation and Structural Restoration of Architectural Heritage.

Jasieńko, J., Moczko, M., Moczko, A., Wala, D. & Dżugaj, R. 2012. Centennial Hall in Wroclaw (Poland) – unique, hundred years old concrete structure of Max Berg. In J. Jasieńko (ed.), Structural Analysis of Historical Constructions, SAHC 2012; Proc. of Int. Conf., Wrocław, 15–17 October 2012. Wrocław: DWE.

Jasieńko, J., Moczko, A., Moczko, M., Dżugaj, R. 2013. Dome of the Centennial Hall in Wrocław. Mechanical and physical properties of hundred years old concrete. In J. Biliszczuk, J. Bień, P. Hawryszków & T. Kamiński (eds), Concrete Structures in Urban Areas; Proc. of Central European Congress on Concrete Engineering, Wrocław, 4–6 September 2013. Wrocław: DWE.

Kumar Verma S., Singh Bhadauria, S. & Akhtar, S. 2013. Estimating residual service life of deteriorated reinforced concrete structures. American Journal of Civil Engineering and Architecture, 1(5): 92–96.

Onysyk, J., Biliszczuk, J., Prabucki, P., Sadowski, K. & Toczkiewicz, R. 2013. Strengthening of a 100 year old reinforced concrete dome of the Centennial Hall in Wrocław, Structural Concrete Journal of the fib, DOI: 10.1002/suco.201300007.

Raupach, M. 2006. Concrete repair according to the new European Standard EN 1504. In Alexander M. et al. (eds), Concrete Repair, Rehabilitation and Retrofitting: 6–8. London: Taylor & Francis Group.

Raupach, M. 2009. Research in the field of repair – Actual approaches and future needs. In Alexander M. et al, (eds), Concrete Repair, Rehabilitation and Retrofitting II: 67–72. London: Taylor & Francis Group.

Wachsmann, A., Budelmann, H. 2012. Life time prediction for concrete repair measures In A. Strauss, D.M. Frangopol & K. Bergmeister (eds), Life-Cycle and Sustainability of Civil Infrastructure Systems; Proc. of Int. Symp., Vienna, 3–6 October 2012. Leiden: CRC Press/Balkema.

Concrete Solutions – Grantham et al. (Eds)
© 2014 Taylor & Francis Group, London, ISBN 978-1-138-02708-4

Repair of a reinforced concrete tower tank for water

C. Bywalski, M. Kamiński & M. Maszczak
Institute of Building Engineering, Wrocław University of Technology, Wrocław, Poland

ABSTRACT: An assessment of the technical condition of a reinforced concrete tower tank for water with a height of 36.94 m and a volume of 300 m^3 confirmed serious damage to the structure of carrying pillar and leakage from the conical shell. Damage to the carrying pillar included major cracking of the walls, corrosion of the exposed reinforcement and a bad condition of the concrete cover for reinforcing bars. Moreover a shortage of longitudinal and ring-shaped reinforcement was found in the lower part of the tower's carrying pillar, which required designing an additional structural strengthening. As a part of the technical condition assessment, the ultimate and service limit states were verified based on static and strength calculations of the reinforced concrete carrying pillar. The final step was to determine a type and a detailed technology of both repairing the damage to the structure and reinforcing the carrying pillar of the tower.

1 INTRODUCTION

Damage to concrete tanks usually manifest themselves in the form of leaks. Polish experiences show that the leaks are most often the result of design and construction errors as well as negligence while using a tank.

The typical design errors that affect the incorrect calculation of cross-section dimensions and the required reinforcement area, include (Buczkowski *et al.* 2003), (Dyduch & Płachecki 2003), (Estrada *et al.* 2006), (Halicka & Franczak 2013), (Podolski *et al.* 2009), (Runkiewicz & Rytwińska 1992):

- an erroneous assumption of a static scheme or the FEM model, which does not correspond to the actual work of the structure,
- an erroneous determination of loads and the adoption of improper sizing combinations,
- an incorrect inclusion of forced deformation values – shrinkage and thermal loads,
- an assumption of inappropriate or inadequate soil parameters for the actual model of the construction's interaction with the ground substrate,
- the lack or incorrect solution of dilatations and construction joints.

The most common construction errors include (Czarnecki & Emmons 2002):

- an improper placement of reinforcement, which does not allow fully for the transfer of tensile forces,
- reducing the thickness of bar coatings, which will not provide protection against corrosion of the reinforcement. This is especially important in a very aggressive environment,
- an inaccurate disassembling of the formwork, which may result in cracking and honeycombing on the concrete surface,
- weakening of the connection and leaks in the construction joints as a result of negligence in proper cleaning and preparation of the substrate,
- segregation of the concrete mix (Kamiński & Bywalski 2012),
- creation of a thinned concrete structure as a result of the lack of mortar in the spaces between the grains of coarse aggregate. Design errors in the form of a very congested reinforcement and too small cross-section areas, a leaky formwork, a wrong choice of the concrete mix recipe and improper technology to place it, are considered (among other factors) as possible causes of the structure thinning.

During the use as well as during the renovation and modernization of tanks the most common types of negligence were (Runkiewicz 2012):

- failure to perform periodic maintenance,
- insufficient maintenance and protection of the structure against a decrease in its durability,
- the formation of leaks and failure to remove them and their causes,
- repairs and improvements inconsistent with the construction rules.

This article presents an example of a technical condition assessment of a reinforced concrete water tower tank, which was used for over 30 years (Kamiński *et al*. 2006a), (Kamiński *et al*. 2006b). Conclusions from this evaluation were used to develop a project to strengthen the tank's pillar and a technology to repair it. (Kamiński, Bywalski 2006).

2 DESCRIPTION OF THE STRUCTURE

The monolithic reinforced concrete tower tank has a height of 36.94 m and is set on a concrete foundation

in the form of a circularly symmetric slab with a thickness of 1.40 m and an outer diameter of 9.60 m. It consists of a single tank with a capacity of 300 m^3, which is based on a carrying pillar (Kamiński *et al*. 2006a), (Kamiński *et al*. 2006b). A cross-section of the structure is presented in Figure 1.

The carrying pillar is a cylindrical shell with an outer diameter D = 3.0 m and a wall thickness of 25 cm in the underground part and 20 cm above the level of 0.20 m. The reinforcement of the pillar is made of vertical Ø12 mm bars with a spacing of about 19 cm in the 20 cm thick wall, Ø14 mm bars with a spacing of about 19 cm in the 25 cm thick wall and Ø10 mm annular rods spaced respectively 25 and 20 cm from each other. Inside the pillar, there are horizontal diaphragms in the form of circular and symmetric 8 cm thick slabs, reinforced with grids of Ø8 mm bars spaced 15 cm from each other.

In addition, the following monolithically connected elements of the structure can be distinguished:

– a top circular and symmetric 15 cm thick slab of a tank with manholes, reinforced at the top and bottom with Ø6 and Ø8 mm bars made of St0S steel,
– an upper 10 cm thick conical shell, reinforced with Ø6 and Ø8 mm vertical bars and Ø8 mm horizontal bars made of St0S steel,
– a lower shell in the form of a truncated 15 cm thick cone, reinforced with vertical and horizontal Ø8 mm and 10 mm bars made of 34GS steel, on its both surfaces,
– a bottom circular and symmetric slab, about 30 cm thick, with openings for installation cables and a manhole, reinforced with rectangular grids constructed of Ø10 mm rods placed 12 cm from each other, top and bottom, made of St0S steel,
– a vertical manhole pipe with an inner diameter of 80 cm and a wall thickness of 10 cm placed between the lower and upper slab,
– a partially hidden annular rim in the lower conical shell near the lower edge,
– a hidden annular rim at the junction of the tank and the carrying pillar.

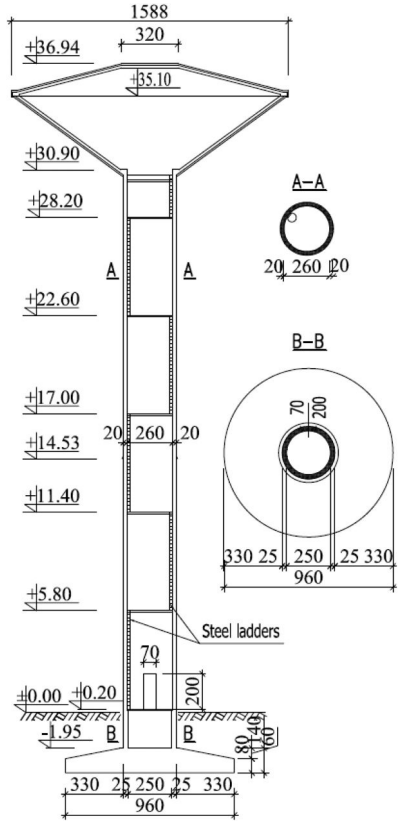

Figure 1. Schematic cross-section of the tower tank.

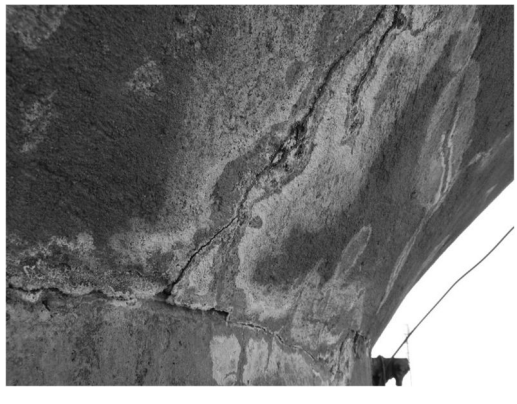

Figure 2. View of the lower conical shell with leakage.

3 DESCRIPTION OF TECHNICAL CONDITION

As a result of the structure inspection, Kamiński *et al*. (2006, 2007) assessed the technical condition of the tank as satisfactory, while the carrying pillar was in a very poor condition.

The leakage observed on the lower surface of the tank (Fig. 2), which alerted the owner, resulted from defectively implemented roof flashing works and mainly due to the partly hidden annular ring connecting the upper and lower conical shells.

The pillar walls were greatly cracked (Fig. 3) and the cracks most likely arose due to shrinkage deformations and thermal loads (temperature gradient), which had not been taken into account while dimensioning the structure at the designing phase.

At the same time, the pillar's longitudinal and circular reinforcing was corroded, in places to a great extent, that was mostly caused by cracks in the walls, through which the reinforcement was exposed to direct contact with atmospheric moisture and rainwater.

The poor state of concrete cover of rebars was caused by:

– marl presence in the aggregate (which was used in the concrete mix), leading, with time, to chipping,

Figure 3. View of the tank and cracked pillar.

Figure 4. View of the shaft with cracks, cover cavities and exposed corroded reinforcement.

– considerable cracks – rainwater filled the cracks and when the temperature dropped below 0°C it increased its volume bursting the concrete on the surface,
– the corrosion of reinforcing bars, which magnified in volume through corrosion, leading to the destruction of concrete. In the lower part of the pillar there was a 10%-shortage of the longitudinal reinforcement to the level of 5.80 m and the ring reinforcement to the level of 11.40 m.

The final assessment of the technical condition was based not only on the inspection inventory of the tank structure, but also on a detailed static strength analysis of the structure.

4 STATIC-STRENGTH ANALYSIS

4.1 *List of loads and combinations*

A detailed list of loads can be found in (Kamiński *et al*. 2006), (Kamiński & Bywalski 2006). The structure calculations were performed in accordance with Polish design standards.

The lists of self-weight loads included characteristic (G_k) and design values (G_d) according to PN-82/B-02001 for the manhole pipe and its insulation, the steel grate, finishing layers and, above all, the structural elements: the top slab, the upper and lower conical shell, the rim between conical shells, the rim at the joint of the tank with the pillar, and the bottom slab. The total self-weight loads of the tank chamber were $G_k = 2241.14\,\text{kN}$ i $G_d = 2576.26\,\text{kN}$.

According to PN-82/B-02003, characteristic and design imposed loads were determined respectively:

– $Q_{w,k} = 3{,}000\,\text{kN}$ and $Q_{w,d} = 3{,}300\,\text{kN}$ for the weight of the water in the tank,
– $p_{ls,k} = 42.00\,\text{kN/m}^2$ and $p_{ls,d} = 46.20\,\text{kN/m}^2$ for the water pressure exerted on the bottom of the conical shell,
– $p_{bp,k} = 42.00\,\text{kN/m}^2$ and $p_{bp,d} = 46.20\,\text{kN/m}^2$ for the water pressure exerted on the bottom slab.

In a similar way, characteristic $Q_{dp,k} = 15.93\,\text{kN}$ and design $Q_{dp,d} = 20.71\,\text{kN}$ operating loads were adopted for the diaphragm plates.

Snow characteristic and design loads, according to PN-80/B-02010 and PN-80/B-02010/Az1, projected onto the surfaces of the upper plate and the conical shell amounted to $s_k = 0.72\,\text{kN/m}^2$ and $s_d = 1.08\,\text{kN/m}^2$.

Increasing characteristic (w_k) and design loads (w_d) of wind on the structure were determined as for chimneys according to PN-88/B-03004. The diameter of the pillar was divided into 15 segments, each of which was perpendicularly loaded with a variable wind pressure throughout its whole height. The values of wind loads on the perimeter and the pillar height are shown in Table 1.

The difference, compared to the original design, was to change the coefficient of external pressure (C_e) from the previously assumed as for a bar with a diameter equal to the pillar's structure to a value closer to reality – as for the shell structure.

Furthermore, the temperature drop $\Delta t_s = -20°\text{C}$ equivalent to shrinkage deformations and thermal loads as temperature differences for the tank $\Delta T_c = 6.57°\text{C}$ and the pillar $\Delta T_{sh} = 30°\text{C}$, omitted in the original design, were included.

Subsequently, three dimensioning combinations of loads were defined in accordance with PN-82/B-02000:

– Combination 1: self-weight loads + the operating load of the diaphragm plates + the water load in the tank + wind + snow.
– Combination 2: self-weight loads + the operating load of the diaphragm plates + the operating load of the water in the tank chamber + wind + snow + the temperature gradient load + the difference between the highest listed temperature in the summer and the temperature of merging the structure.
– Combination 3: self-weight loads + the operating load of the diaphragm plates + the operating load of the water in the tank chamber + wind + snow + the temperature gradient load + the difference between

Table 1. Values of wind loads on the perimeter and the pillar height.

Height		w_k	w_d
m	Segment	kN/m^2	kN/m^2
0.00 ÷ 10.00	1	0.81	1.05
	2b*, 15e*	0.81	1.05
	2e, 15e	0.00	0.00
	3b, 14e	0.00	0.00
	3e, 14e	−1.10	−1.43
	4, 13	−1.17	−1.53
	5b, 12e	−1.17	−1.53
	5e, 12e	−0.39	−0.51
	6, 11	−0.35	−0.45
	7, 10	−0.37	−0.48
	8, 9	−0.37	−0.48
10.00 ÷ 20.00	1	0.97	1.26
	2b*, 15e*	0.97	1.26
	2e, 15e	0.00	0.00
	3b, 14e	0.00	0.00
	3e, 14e	−1.32	−1.72
	4, 13	−1.41	−1.83
	5b, 12e	−1.41	−1.83
	5e, 12e	−0.47	−0.61
	6, 11	−0.42	−0.54
	7, 10	−0.45	−0.58
	8, 9	−0.45	−0.58
20.00 ÷ 30.00	1	1.09	1.42
	2b*, 15e*	1.09	1.42
	2e, 15e	0.00	0.00
	3b, 14e	0.00	0.00
	3e, 14e	−1.49	−1.93
	4, 13	−1.59	−2.06
	5b, 12e	−1.59	−2.06
	5e, 12e	−0.52	−0.68
	6, 11	−0.47	−0.61
	7, 10	−0.50	−0.65
	8, 9	−0.50	−0.65
30.00 ÷ 37.00	1	1.18	1.54
	2b*, 15e*	1.18	1.54
	2e, 15e	0.00	0.00
	3b, 14e	0.00	0.00
	3e, 14e	−1.61	−2.09
	4, 13	−1.71	−2.23
	5b, 12e	−1.71	−2.23
	5e, 12e	−0.57	−0.74
	6, 11	−0.51	−0.66
	7, 10	−0.54	−0.71
	8, 9	−0.54	−0.71

*b – a beginning of a segment, e – an end of a segment.

the lowest listed temperature in the winter and the temperature of merging the structure.

4.2 *Results and analysis of the static calculations*

Calculations of the static construction work for the three load combinations were performed numerically with a computational software, based on the Finite Element Method. Taking into account the spatial work of the structure and the simultaneous modelling of its geometry with the use of shell and slab elements allowed an approximation of the numerical model to the real model. In the assumptions of the original design, the analysed model was simplified. The results of internal forces' calculations N and M from the various load combinations are shown in Table 2.

The strength of the cross-sections was tested in accordance with PN-B-03264:2002, both for the singly reinforced cross-sections and the doubly reinforced cross-sections with the use of, so called, simplified method, assuming a rectangular graph of the compression zone stresses.

The vertical reinforcement $A_{s,xx}$ and horizontal reinforcement $A_{s,yy}$ were calculated from the balance of internal forces in the cross-section with regard to the actual strength of concrete measured experimentally. The calculated reinforcement areas are given in Table 2.

Based on the archival design documentation, it has been concluded that the assumed reinforcement areas were $A_{s,xx} = 5.95\,\text{cm}^2$ i $A_{s,yy} = 3.14\,\text{cm}^2$.

The designed areas of reinforcement were reduced by the detected 10% loss, which allowed to approximate the actual surface area of the longitudinal reinforcement bars $A_{sxx,real} = 5.36\,\text{cm}^2$ and annular bars $A_{syy,real} = 2.83\,\text{cm}^2$.

Following comparison of the actual and maximum computational reinforcement areas at different levels, deficiencies in vertical reinforcement ($\Delta A_{s,xx}$) and horizontal reinforcement ($\Delta A_{s,yy}$) were determined:

- 2.20–5.80 m: $\Delta A_{s,xx} = 9.80\,\text{cm}^2$ i $\Delta A_{s,yy} = 0$,
- 5.80–11.40 m: $\Delta A_{s,xx} = 5.56\,\text{cm}^2$ i $\Delta A_{s,yy} = 0$,
- 11.40–22.60 m: $\Delta A_{s,xx} = 2.35\,\text{cm}^2$ i $\Delta A_{s,yy} = 0$,
- 22.60–28.20 m: $\Delta A_{s,xx} = 0$ i $\Delta A_{s,yy} = 0.97\,\text{cm}^2$.

At the same time, the minimum areas of reinforcement $A_{s,xx,min}$ and $A_{s,yy,min}$ for the three combinations were calculated according to PN-B-03264: 2002:

- ULS1: $A_{s,xx,min} = 8.22\,\text{cm}^2$ i $A_{s,yy,min} = 5.10\,\text{cm}^2$,
- ULS2: $A_{s,xx,min} = 8.18\,\text{cm}^2$ i $A_{s,yy,min} = 5.10\,\text{cm}^2$,
- ULS3: $A_{s,xx,min} = 8.16\,\text{cm}^2$ i $A_{s,yy,min} = 5.10\,\text{cm}^2$.

Static strength analysis showed that up to the level of 14.53 m it was necessary to strengthen the bearing pillar due to the scarcity of longitudinal reinforcement.

The authors skipped the need for a peripheral strengthening of the pillar at the 22.60–28.20 and 28.20–30.60 levels due to the rim, which will transfer tensile forces at the joint of the tank with the pillar.

5 REINFORCEMENT OF THE PILLAR

It was planned to strengthen the reinforced concrete pillar of the tank to the level of 14.53 m above ground level. The strengthening consisted in making an additional external shotcrete layer (reinforced with meshes) 80 mm thick from the level of 0.20 m to 14.53 m, and 110 mm thick from the level of −1.95 m to 0.20 m.

In order to ensure a proper interaction of the new reinforcement with the existing one, the proposed new

Table 2. Internal forces' calculations of different combinations ULS and calculated reinforcement areas.

Level	Internal forces				Reinforcement	
	N_{xx}	M_{xx}	N_{yy}	M_{yy}	$A_{s,xx}$	$A_{s,yy}$
m	kN/m	kNm/m	kN/m	kNm/m	cm^2	cm^2
2.20–5.80						
ULS1	−1917.84	3.87	−65.76	2.12	11.00	0.00
			28.46			0.81
ULS2	−1908.14	29.56	−93.46	33.72	15.16	0.00
			86.65			2.48
ULS3	−1904.80	3.83	−87.76	2.78	10.78	0.00
			94.70			2.71
5.80–11.40						
ULS1	−1740.15	4.58	−64.55	0.14	8.13	0.00
			23.51			0.67
ULS2	−1664.30	28.75	−93.94	34.43	10.92	0.00
			59.64			1.70
ULS3	−1731.31	2.76	−79.80	1.75	7.68	0.00
			45.44			1.30
11.40–22.60						
ULS1	−1495.59	4.13	−57.31	0.04	3.95	0.00
			18.72			0.53
ULS2	−1474.91	28.56	−92.40	31.00	7.71	0.00
			57.52			1.64
ULS3	−1489.44	2.01	−69.65	0.73	3.49	0.00
			49.48			1.41
22.60–28.20						
ULS1	−978.46	2.60	39.93	0.01	0.00	0.00
			8.00			0.23
ULS2	−973.85	32.69	−119.48	34.59	0.00	0.00
			132.97			3.80
ULS3	−985.25	0.98	−61.17	0.74	0.00	0.00
			13.60			0.39
28.20–30.60						
ULS1	−679.91	17.71	−396.15	3.16	0.00	0.00
			16.98			0.49
ULS2	−791.33	46.60	−1848.66[a]	43.04	0.00	3.79[b]
			296.62[a]			8.47[b]
ULS3	−769.90	38.88	−128.15[a]	15.57	0.00	0.00
			1633.63[a]			46.68[b]

[a] The value of N_{yy} directly under the rim (at the joint of the tank with the pillar).
[b] Reinforcement at the joint of the tank with the pillar.

bar diameters were chosen in relation to the spacing of existing longitudinal reinforcement bars and thus Ø14 mm bars, spaced in 190 mm intervals around the circumference, were selected. The existing bars were made of 34GS steel, which was not widely available in the market anymore. It was decided to select the RB 500W class of steel for the designed bars, since it was characterized by better parameters than those of 34GS steel. As a result of the change in the class of steel, a correction of actual reinforcement area was required and the new value was $A_{s,xx,real'} = 9.72$ cm^2/m.

The annular reinforcement was given structurally and comprised Ø10 mm bars made of 18G2-b steel or alternatively bars made of RB 500W steel spaced 200 mm from each other. When the RB 500W steel was used for annular bars, the reinforcement surface was not reduced, but Ø10 mm bars were additionally adopted, spaced 200 mm from each other. The connecting of reinforcement meshes was performed by lap welding over a length of 140 mm (for connecting Ø14 mm bars) and over a length of 100 mm (in the case of connecting Ø10 mm bars). The thickness of welds was 4 mm. The interaction between the additional reinforced concrete layer and the existing construction of the pillar was provided by "hooks" (anchor hooks) connecting the two layers. These hooks were made of Ø14 mm bars produced out of RB 500W steel and put into slots made in the existing pillar structure and filled with epoxy resin. The depth of the hooks' embedment was 100 mm. The length of the hooks provided an "embrace" for the annular bars while providing a 20 mm space for a concrete cover of the longitudinal bars from the inside. The hooks were arranged in a grid with a mesh size of 500x500 mm. For all the bars, including the hooks, the thickness of the concrete cover was 20 mm. Spacers bars between the pillar wall and the vertical Ø14 mm bars were used.

In order to safely transfer the vertical forces from the additional layer of the pillar (reinforcement) on the foundation, the vertical reinforcement Ø14 mm bars had to be anchored in the foundation slab. This was achieved by embedding the Ø14 mm bars made of RB 500W steel in the foundation slab at a depth of 400 mm with the use of epoxy resin and letting them extend 200 mm above the upper surface of the foundation slab. Spacing of these bars around the perimeter was the same as in the case of vertical bars placed in the reinforcing meshes, so that it was possible to connect these bars by lap welding. Accordingly, before drilling the holes for the bars, it was necessary to perform a preassembly of the meshes at the foundation in order to determine the location of the holes.

The door opening had to be reinforced with bars individually. For this reason, after having arranged the meshes, a door opening was cut out with an overmeasure, so that all the reinforcing bars had in each direction a concrete cover of 20 mm and 50 mm below the ground level from the outside. Similar steps were taken in the case of openings for water pipes. Additional reinforcement bars in the area of the holes was placed at a distance of 40 mm from each other.

The schematic structural solution of reinforcing the reinforced concrete pillar is presented in Fig. 5.

6 THE REPAIR TECHNOLOGY

The repair technology of the tower tank focused mainly on the technology of repair and protection measures of reinforced concrete, which required preparatory, refurbishment and protective works.

6.1 *Preparatory works*

Prior to the main refurbishment and protective works, the following preparatory works had to be carried out:

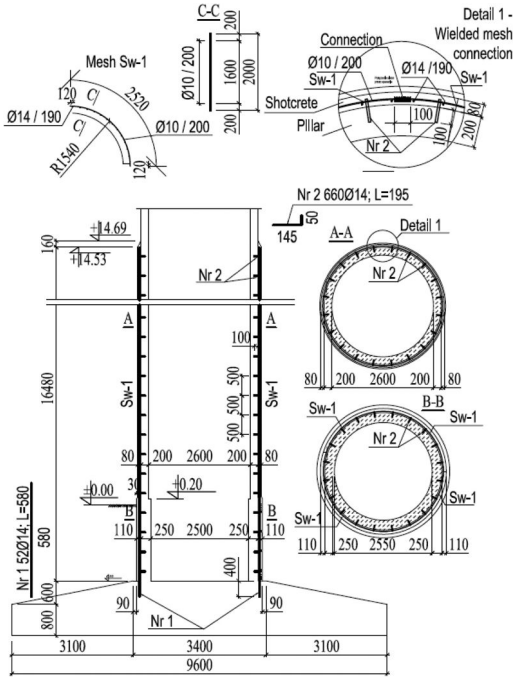

Figure 5. Schema of reinforcing the pillar.

– hammering off the cracked, loose and chemically polluted parts of the concrete and those under which corrosion of reinforcement was found, so that there was a space around the reinforcement of minimum 15 mm,
– cleaning the concrete surface by abrasive sandblasting to the 1st grade of cleanness and clean the exposed reinforcement from rust (to the Sa $2^1/_2$ degree, according to the PN-ISO 8501-1),
– inspecting the inner surface against a possible occurrence of cracks or other defects visible after cleaning the concrete surface.

6.2 *Refurbishment works*

Refurbishment works comprised a sealing-filling injection of cracks, anticorrosive protection of the reinforcing bars and filling of cavities in the concrete.

6.2.1 *A sealing-filling injection of cracks*

The existing cracks greater than 0.1 mm had to be filled with flexible polyurethane resin by pressure injection. Prior to the injection, the hammered off cracks should be closed with a fast swelling mortar. For the injection, it was recommended to use stretcher injection packers.

6.2.2 *Anticorrosive protection of the reinforcing bars*

The reinforcing bars had to be protected against corrosion and, immediately after cleaning them, an anticorrosion coating should be applied on the basis of cement slurry, improved with polymers (during a later filling of the cavities by hand or wet spraying) The material should be applied in two layers with the use of a small round brush with short, stiff bristles. In addition, the following requirements for mineral coatings designed for anti-corrosion protection of rebars had to be observed: the rebar surface temperature $\geq 5°C$ and the relative humidity below 95%.

6.2.3 *Filling of cavities in the concrete*

Prior to the filling of cavities in the concrete and in the concrete cover manually or by wet spraying, it was necessary to carry out the following operations:

– moistening the surface with water to a matt-damp state;
– applying a bonding layer (called a "linking bridge") on the surface of the cavity intended for re-profiling and letting extend about 1 cm out of the cavity. In the case of materials modified with plastics, the processing rules were the same as in the case of mineral materials, so that the ground layer should be correctly moistened and the slurry was applied in the right quantity and consistency. The bonding layer ("linking bridge") significantly increased the adhesion of repair mortar to the ground layer;
– applying the repair mortar on the bonding layer, active in terms of adhesion, using the "fresh on fresh" method.

6.3 *Protective works – levelling of the ground layer and protective coating*

A levelling material eliminated inequalities of the concrete surface and made a perfect primer beneath the main protective coating. Prior to applying it though, it was necessary to carry out the following operations:

– cleaning the ground layer by abrasive sandblasting or hydro-sandblasting. After cleaning the ground layer, its average peel strength had to be at least 1.5 MPa, but a minimum value of a single measurement could not be less than 1.0 MPa,
– moistening the surface with water to a matt-damp state,
– levelling the surface manually by spackling.

Only then a flexible protective paint coating could be applied.

6.4 *The scope and sequence of works depending on location*

Owing to the fact that the tower tank was damaged along its height the following parts were distinguished:

– the level from −1.95 m to 14.53 m – the area of the pillar reinforcement,
– the level above 14.53 m – the remaining upper part of the pillar above the reinforcement,
– the lower conical shell of the tank,
– the upper conical shell of the tank.

Then separately for each of these parts the technology of its repair was characterized in terms of the scope and sequence of work.

6.4.1 *The level from −1.95 m to 14.53 m*
The scope and sequence of work to the level of the reinforcement was as follows:

- carrying out preparatory works according to clause 6.1;
- performing repairs according to clause 6.2.1 involving only the sealing-filling injection of cracks (see 6.2.1);
- embedding hooks connecting the new reinforced concrete layer with the existing pillar structure with epoxy resin;
- carrying out reinforcement works, i.e. the embedding of longitudinal bars in the base slab with epoxy resin, installation of reinforcement meshes and welding them with each other as well as welding vertical bars embedded in the foundation slab with vertical mesh bars, linking the meshes with hooks embedded in the pillar and rebarring both the entrance hole and the holes for installation pipes;
- casting the concrete reinforcement layer through the shotcrete technology with several layers, each layer having a thickness of less than 30 mm; the concrete reinforcement layer thickness was 80 mm (equivalent to a 20 mm outer concrete cover) in the main part of the pillar being reinforced and 110 mm (which corresponded to the outer concrete cover of 50 mm) in the "ground";
- curing the shotcrete for a minimum of 7 days;
- carrying out protective works,
- and finally insulating the vertical walls of the pillar from the level of −1.95 m to 0.20 m by applying a bituminous sealing coating.

6.4.2 *The pillar above the level of reinforcement*
The pillar above the reinforcement level was repaired manually as follows:

- carrying out preparatory works according to clause 6.1,
- performing repairs according to clause 6.2 involving the sealing-filling injection of cracks (see 6.2.1), applying the anti-corrosion protection of reinforcing bars (see 6.2.2) and refilling cavities in the concrete (see 6.2.3),
- performing repairs according to clause 6.3, which involved levelling of the ground and the protective coating.

6.4.3 *The lower conical shell of the tank*
The scope of repair works in relation to the lower conical shell of the tank was as follows:

- cleaning the finishing coat surface by abrasive sandblasting to the 1st grade of cleanness,
- performing repairs according to clause 6.3, which involved levelling of the ground and the protective coating

6.4.4 *The upper conical shell of the tank – the roof*
The upper conical shell of the tank required a new roof covering with a single heat-sealable layer of tar paper, which had to be applied on the existing roofing with the replacement of all flashings.

6.5 *Other works*

In addition to the scope of repair works previously mentioned, more works had to be carried out, which included: anti-corrosion protection for all steel parts of the tank (including platforms), water installations, sealing or replacing the old valves (shutters) and installing a lightning protection system.

7 CONCLUSION

The article describes and analyzes the technical condition of the reinforced concrete tower water tank after 30 years of use. The conclusions drawn from the condition assessment unfortunately confirmed the universality of design, execution and operation errors in the case of tanks structures. The accumulation of errors led to the degradation of the supporting pillar. The design errors in this case were so serious that the progressive degradation of the structure and the shortage of longitudinal and ring-shaped reinforcement in the lower part of the tower could therefore lead not only to failure but also to disaster.

Finally, the authors described in detail the reinforcement of the pillar and the repair technology, which increased the reliability and durability of the structure.

REFERENCES

Buczkowski, W., Czajka S., Kowalski, J. 2003. O przyczynach awarii żelbetowego zbiornika prostopadłościennego [Reasons for failures of a rectangular reinforced concrete tank]. *Inżynieria i Budownictwo* (12): 683–685.

Dyduch, K., Płachecki, M. 2003. Błędy projektowe i wykonawcze w żelbetowych zbiornikach na wodę i ścieki [Errors in the design and construction of reinforced concrete tanks for water and wastewater]. *Materiały XII Konferencji Naukowo-Technicznej: Żelbetowe i sprężone zbiorniki na materiały sykie i ciecze.* Cracow.

Estrada, C.F., Godoy, L.A., Prato T. 2006. Thermomechanical behaviour of a thin concrete shell during its early age. *Thin-walled structures* (44): 483–495.

Kamiński, M., Bywalski, Cz. 2006. *Projekt budowlany żelbetowego zbiornika na wodę w mleczarni [The construction design of reinforced concrete water tank at the dairy]*.

Kamiński, M., Bywalski, Cz. 2012. Wybrane problemy projektowe i wykonawcze modułowych, prefabrykowanych zbiorników na ciecze [Selected design and realization problems of modular precast fluid tanks]. *Przegląd budowlany* (4): 104–107.

Kamiński, M., Trapko, T., Bywalski, Cz. 2006. *Ekspertyza stanu technicznego żelbetowego zbiornika wieżowego na wodę w mleczarni [The expertise of the technical condition of reinforced concrete water tower tank at the dairy]*.

Kamiński, M., Trapko T., Bywalski, Cz. 2007. Stan techniczny i naprawa żelbetowego zbiornika wieżowego na wodę [Technical state and repairing of the reinforced

concrete tower water container]. In M. Kamiński, J. Jasiczak, W. Buczkowski, T. Błaszczyński. (eds), *Trwałość i skuteczność napraw obiektów budowlanych [Durability and effectiveness of buildings repairs]*. Dolnośląskie Wydawnictwo Edukacyjne, Wrocław.

Czarnecki, L., Emmons, P., H. 2002. *Naprawa i ochrona konstrukcji betonowych* [Repair and protection of concrete structures]. Polski Cement, Cracow, 246–253.

Halicka, A., Franczak D. 2013 *Projektowanie zbiorników żelbetowych: zbiorniki na ciecze. T..2 [Design of reinforced concrete tanks. Vol. 2*. (in Polish). Wydawnictwo Naukowe PWN, Warsaw, 263–265.

PN-82/B-02001. Polish Standard. *Obciążenia budowli – Obciążenia stałe [Loads in static calculations – Dead loads]*.

PN-82/B-02003. Polish Standard. *Obciążenia budowli – Obciążenia zmienne technologiczne – obciążenia technologiczne i montażowe [Loads in static calculations – Imposed loads – Fundamental technological and execution loads]*.

PN-80/B-02010. Polish Standard. *Obciążenie śniegiem [Loads in static calculations – Snow loads]*.

PN-80/B-02010/Az1. Polish Standard. *Obciążenie śniegiem [Loads in static calculations – Snow loads]*.

PN-88/B-03004. Polish Standard. *Kominy murowane i żelbetowe – Obliczenia statyczne i projektowanie [Brick worked and reinforced concrete chimneys. Static calculation and design]*.

PN-82/B-02000. Polish Standard. *Obciążenia budowli. Zasady ustalania wartości [Loads in static calculations – General rules]*.

PN-B-03264:2002. 2002. Polish Standard. *Konstrukcje betonowe, żelbetowe i sprężone – Obliczenia statyczne i projektowanie* [Concrete, reinforced concrete and prestressed structures – calculations and design].

PN-EN ISO 8501-1. 2001. *Przygotowanie podłoży stalowych przed nakładaniem farb i podobnych produktów – Wzrokowa ocena czystości powierzchni – Część 1: Stopnie skorodowania i stopnie przygotowania niepokrytych podłoży stalowych oraz podłoży stalowych po całkowitym usunięciu wcześniej nałożonych powłok*.

Podolski, B., Podolski, M., Bartosik, T. 2009. Awaria oraz sposób wzmocnienia żelbetowego wielokomorowego zbiornika oczyszczalni ścieków. Przeciążenie zaprojektowanej z nadmiernym uproszczeniem niecki basenowej i sposób jej wzmocnienia [Failure and how to strengthen a reinforced concrete multi-chamber tank in a sewage treatment plant. Overload of a tank designed with an oversimplification and how to strengthen it]. *Materiały XXIV Konferencji Naukowo-Technicznej: Awarie budowlane. Szczecin-Świnoujście*, pp. 777–792.

Runkiewicz, L., Rytwińska, D. 1992. Przyczyny powstawania i sposoby usuwania zagrożeń zbiorników żelbetowych [Causes and ways to remove threats reinforced concrete tanks]. *Przegląd budowlany* (11): 471–474.

Runkiewicz, L. 2012. Analizy zagrożeń, awarii i katastrof żelbetowych zbiorników i silosów [Analysis of hazards, failures nad disasters involving reinforced concrete tanks and silos]. *Przegląd budowlany* (4): 75–79.

Concrete Solutions – Grantham et al. (Eds)
© 2014 Taylor & Francis Group, London, ISBN 978-1-138-02708-4

Maintenance and preservation of the Royal National Theatre, London

Stephen Douglas
Royal National Theatre, London, UK

ABSTRACT: The National Theatre was built between 1969 and 1976 by MacAlpines, to a design by Sir Denys Lasdun, one of the 20th Century's leading post modernist architects. It is a major UK public building of the post-war period and is an internationally significant example of late 20th century theatre architecture. The building was listed at Grade II* in 1994, and this paper looks at the challenges of maintaining and conserving a 20th Century reinforced concrete structure.

1 INTRODUCTION

The National Theatre is a spectacular and public example of a variety of visual concrete techniques. It is remarkable by both national and international standards for the quantity and quality of its in situ concrete work.

The distinctive board-marked finish to the reinforced concrete is of exceptionally high quality, the structural members and 'diagrid' soffits are visible on the exterior and throughout the interior front of house areas. This is materially contrasted by the more prosaic brick enclosure of the workshops to the southern part of the building.

The National Theatre front of house concrete was entirely produced on site and Douglas fir timber shuttering was formed using sawn elements, on a 6 inch module, some forms were used more than once on each section (if you examine them carefully you can spot the repetitions) Fibreglass moulds were used for the diagrid, which contrasts with the timber forms.

The predominance of board-marked béton brut (raw concrete) in the National recalls a number of other buildings of the period that have been popularly (and often inaccurately) grouped under the banner of Brutalism. Lasdun, however, would describe the architecture as "functional". The term 'Brutalism' has however been misappropriated to informally refer to a broad range of concrete buildings of the sixties and seventies, and the public's view of the National Theatre initially suffered as a result of this negative association.

The Prince of Wales famously attacked the National in 1988 as *'a clever way of building a nuclear power station in the middle of London without anyone objecting'.* In an article in The Independent on the 18th of May 2010, Jonathan Brown, said that the National (is) "*the result of a collision between and aircraft carrier and a Norman keep".*

The concrete is the dominant vessel for the architectural expression in the building and was almost entirely cast in-situ demonstrating an extremely high level of workmanship. In 1977, the National Theatre, Denys Lasdun, Flint & Neill and contractors Sir Robert McAlpine & Sons, received a Concrete Society Award for Outstanding Merit in the use of concrete. Lasdun later praised McAlpine for the '*extraordinarily important role'* played by the shuttering carpenters and those responsible for the concrete, both placing and mix design.

Figure 1. Aerial view of National Theatre.

The most striking treatment of the concrete is the board-marking used throughout the front of house areas internally and externally, the horizontally textured surface and raw concrete is remarkable and contrasts dramatically with the smooth finish of the coffered diagrid soffits.

The semi-circular stairs have vertical boarding which highlights the access routes, whilst contrasting with horizontal boarding used in the public areas. The Lyttelton Auditorium uses an unusual 45 degree boarding, which features a recessed board finish which

Figure 2. Showing typical concrete finishes.

helps to highlight the board marking and creates an interesting, almost explosive effect.

These concrete elements are applied in conjunction with the diagrid. This feature is often associated with car parks, where it is used to create the appearance of height. Here it is used to give a human scale to the foyers. Cast in purpose-made GRP moulds, the diagrid has a smooth surface that differs from the deep texture of the board finish. Along the edges of the workshop block, the rough, bush-hammered concrete plinth reinforces the sense of a robust, foundation layer to the brickwork and is entirely distinct from the board marked concrete elements of the public areas.

Away from the public, for the working areas (offices and workshops), brick is used to differentiate secondary and non-load bearing surfaces. Lasdun used a pale grey calcium silicate brick for these, set within a concrete structural framework. Brickwork can also be found in the foyer staircase from ground floor to basement level.

For the internal and external floors at ground level, a dark purple/blue brick paver compliments the dark mauve wool carpet used in the foyer areas. The contrasting tones of the raw concrete and dark wenge wood against the colours of the soft furnishings work together to emphasise and soften the public areas, whilst highlighting the hard textured concrete faces.

The National's three theatres have distinct spatial characteristics that recall three principal precedents:

The classical Greek theatre of Epidaurus, from which the Olivier is derived;
The proscenium theatres of the seventeenth, eighteenth and nineteenth centuries that provided a model for the Lyttelton;
The Tudor inn courtyards which formed the inspiration for the Cottesloe Theatre.

2 THE CHALLENGES

Whilst concrete is a resilient material, it does, despite earlier claims, deteriorate over time. At 2000 years old The Parthenon is unreinforced and of a high quality, however more modern reinforced concrete structures have failed. There have been a number of high profile demolitions of post war reinforced concrete buildings that have been required due to structural issues. The presence of steel in concrete, whilst offering benefits, can lead to premature failure if the alkalinity changes. Failings in 20th Century structures suggest that reinforced concrete structures deteriorate more rapidly than unreinforced structures. It is apparent that the effects of carbonation and other environmental factors on reinforcement can lead to destructive effects. Despite being constructed to a robust standard The National Theatre is beginning to show symptoms of deterioration. The bold initiative now is to commence a programme of concrete conservation and invest in a strategy which will prolong the life of the National Theatre.

The aim is to develop innovative methods of securing the life of concrete by preservation rather than repair.

In the past, repairs using proprietary materials were carried out. These materials have not always solved the problems they were meant to address and in some cases have caused further problems. The photos show some materials that have previously been used. It has been found that these repairs have not weathered, moved or been as stable as the surrounding material so that those repairs that initially seemed acceptable have proven to be exaserbating maintenance needs, sometimes introducing problems that would not have occured if proper repairs had been undertaken.

The NT is fortunate in that there are no significant structural defects with the concrete but some cracking, spalling and discolouration has developed over the years. A series of trials have been carried out to identify the efficacy of different techniques and it has been found that there is no one method suitable for addressing the different deterioration mechanisms.

The current architect, Paddy Dillon from Haworth Tompkins, and the 20th Century Society are of the opinion that, as far as practicable, the original mix should be used in any repair. The trials carried out so far show that even when using the same sources of constituent materials there is a significant colour variation, so a palette of mixes have been prepared to allow a close colour match to be chosen and used.

Moisture movement through the structure is a cause for concern as in a number of areas in the lower floors there is stalactite growth. Some of these are stained brown with rust, suggesting corrosion of reinforcement. In places displaying the worst stalactite formation there are small mounds of calcium materials at ground level as well. The presumption here is that the reduction of calcium in the concrete may affect the longevity or performance of the structure.

A number of specialist surveys have been commissioned and as a result, recent works have been carried out to replace aged or damaged waterproofing. These investigations have thus been useful in prioritising interventions and locating areas at risk.

Figure 3. Result of graffiti removal.

Figure 4. Stalactites forming due to water leakage.

Figure 5. Example of previous repair using proprietary system.

Figure 6. National Theatre from the Thames.

The moisture does not appear to have had a significant effect on the structure, probably due to the high quality of the original concrete, however there is a concern that the long term effects of moisture could be detrimental. Fortunately being in the urban area, next to the river and in constant use, the structure does not suffer from extreme low temperatures that may otherwise contribute to the deterioration of the structure.

As the NT continues to attract more and more attention from the popularity of the Southbank and Jubilee Walk it has been necessary to adapt the layout of the NT. This has brought into prominence some minor defects in the concrete façade that would have otherwise been less apparent. As a result some 'discrete' repairs and subtle maintenance have been carried out with the priority being aesthetic repair rather than 'conservation' in this instance.

The lack of skilled conservators for concrete has introduced challenges particularly in removing unwanted marks. Highlighting and preserving the quality of the board marking is another challenge. Some earlier cleaning activities were successful in not only removing the dirt/paint but also removing the board marking. Some cleaning processes also prevent the return of biological growth, which sometimes actually highlights the area where cleaning has taken place. In some areas removal of graffiti has been less than effective and some means of removing the marks without damaging the concrete or the board marking is proving to be a challenge for our maintenance team. A series of trials have been undertaken to investigate the effectiveness of the different cleaning methods and techniques. Being béton brut, the front of house areas collect marks, stains and wear, in those areas where people congregate. For example queuing areas near the bars are marked by a line of staining or marking where patrons lean against the concrete whilst waiting to be served.

Bearing in mind that this is a live theatre with a packed programme of performances, productions in rehearsal, construction of sets etc, the chance of finding a window of time to undertake maintenance is often difficult due to the demands placed by the business and artistic side of the Theatre.

Conserving and repairing concrete at the NT is big challenge. There are time, noise, and many other restrictions which prevent work being carried out as the Theatre and public areas are well used both day and night, and provide a strong revenue stream.

Figure 7. Anchor Staircase.

Given that the NT has a footfall past the building of millions of people each year the pressure of ensuring any type of works, including conservation, does not prevent any passers-by from enjoying the magnificence and beauty of the NT is a challenge that must be embraced and developed.

The building exists as a form of art in its own right, and attracts interest from architects and others who recognize the positive qualities of the building. Their requirements also need to be met.

There is a growing affection for this building and a real desire to conserve this important part of our heritage. Whilst the architecture may have a "marmite" effect, the use of the building continues to be popular and attracts tens of thousands of people a year to a wide range of performances, and it is significant as being the Nations Theatre.

The desire to conserve concrete structures is starting to become apparent and the previous disdain shown for this style of architecture is on the wane. It is likely that the conservation of concrete will become more important to society and the demolition of these structures will be the final option rather than the first. The challenge is to find a way of halting deterioration, whilst maintaining both the aesthetic and operation of the structure.

REFERENCE

Practical Building Conservation: Concrete by English Heritage (1 Aug 2012).

Concrete Solutions – Grantham et al. (Eds)
© 2014 Taylor & Francis Group, London, ISBN 978-1-138-02708-4

Natural draft cooling towers with flue gas inlet

Helena Eisenkrein
IBOS Institute of Concrete Technology and Surface Protection GmbH, Bochum, Germany

Christian Kotz-Pollkläsener
Zerna Baumanagement GmbH, Bochum, Germany

ABSTRACT: After nearly twenty years of flue gas inlet in cooling towers the formerly used epoxy-based coatings did not protect the interior concrete surfaces of cooling towers for as long as had been expected. Even on surfaces coated again in the last 10 years degradation took place and supplementary coatings were needed. Therefore certain analyses and considerations were undertaken to find new solutions to reinforce the surface protecting coatings of the cooling towers so they could be operated for another period of 25 years. The execution of this project needed new and optimized methods to plan and carry out the implementation.

1 INTRODUCTION

Although the (old) methods typically used until now to strengthen the interior of a cooling tower and/or to line the concrete with a protective system have provided limited protection, they have not maintained their effectiveness over the long term.

For this reason, the problem was considered and investigations were undertaken for the purposes of repairing – within a cooling tower's downtime, which can often be of short duration – the existing protective systems in a sustainable way such that a cooling tower could be expected to achieve a service life of 20 years or more following rework.

In this context, the altogether new idea was to fully treat the cooling tower no longer only above and/or below the throat, but rather to create stress-dependent repair concepts which are especially tailored to the object and specifically comprising separate zones with heavy, moderate and slight damage.

The classification into those zones depends, on the one hand, on the damage of the existing protective system and/or the concrete underneath it. At the same time, the intensive stress that weathering and flue gas feed exert on certain areas of the cooling tower shell must also be taken into account.

Over the past decade there has been a change in focus of quality assurance (QS) in executing protection measures to shell inside sections of natural draft cooling towers with flue gas discharge. For a long time it was normal to consider only execution monitoring of measures as part of quality assurance [Engelfried, 2013]. However, it often transpired that the time was already too late to guarantee quality of the measure. As a result, the idea developed that QS should be applied at a much earlier stage. Meanwhile the strategic weighting of QS has shifted to extension of long-term operational effectiveness. Figure 1 shows the strategic direction of planning focus, application of measures and the numerous elements of weighting involved. It is different to earlier executions by way of targeted and more detailed planning of measures by the professional planner and more extensive planning of the work process by the constructor and the relevant elements of such planning steps. The overall instrument of quality assurance of measures is optimized together with the professional implementation of measures by the contractor which must include working-target define measures of internal control as well as qualified external supervision of application.

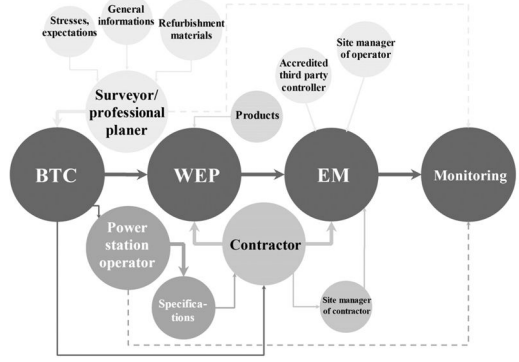

Figure 1. Strategic flow process chart of planning and execution of protection and refurbishment measures.

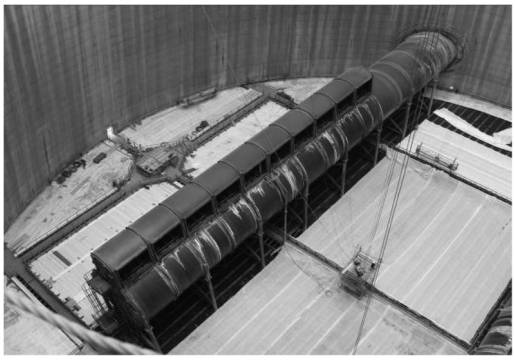

Figure 2. Protective netting and planking.

Figure 3. Chalking surface of epoxy coating due to photo-catalytic degradation process.

Figure 4. After degradation of protection coating cement stone will be attacked by acidified plume condensate.

2 EXECUTION OF PLANNING OF MEASURES

2.1 *Expert status analysis*

After clarifying and fulfilling general preconditions for planning [Eisenkrein, 2012], the next step is to create the basis for the individual item. This involves a status report or status analysis with regard to effects and resultant stress from operation and the environment.

The differentiation of meaning between effect and stress is an important pre-condition for planning action. When retrofitting flue gas desulfurization plant (FGD) operations and initially when constructing new so-called FGD cooling towers, the insides of shells were in the past coated from the cornice to the base with Epoxy coating systems in evenly spread coating thickness. Meanwhile it is known that this procedure was very inaccurate and partly under-dimensioned or exaggerated in terms of engineering and mistaken in terms of business.

Intensive examinations on insides of shells concerning effects from operations and the environment have identified wear-out and damage depending on respective stress levels, which should be counteracted by selectively targeted refurbishment measures [Engelfried, 1988] [Engelfried et al., 2009].

The main statement emerging from the status analysis must answer the question, which stress conditions from operations and the environment caused which wear-out and damage and with which rehabilitation and refurbishment measures the objective of long-term operative status can be achieved.

2.2 *Retrofitted cooling towers*

Retrofitting for flue gas discharge was executed in the 1980s to a fleet of 14 natural draft cooling towers. The flue gas discharge was installed horizontally in low level, refer to Fig. 2. All inside sections of the shell have been provided with a multi-coating of epoxy coating system as protection against acidic flue gas vapor condensate. Seven to ten years later, part surfaces of the inside sections of the shell had to be refurbished. After ten more years of operation there were again significant signs of wear-out and damage.

The inside of the shell was systematically inspected using suspended working platforms on ropes and a visual and technological examination was made. Two features were repeatedly identified in all items.

One feature involved the relatively extreme chalking of the surfaces of the epoxy coating, linked with an increasing reduction of coating thickness from half way up the cooling tower shell to the bottom side section. Fig. 3 illustrates a section of this weakening of the coating.

In addition, damage had been done to the cement stone at places with a weakened coating As an example of this type of damage is illustrated in Fig. 4.

Chalking and wear-out of the epoxy coating is caused by the photo-catalytic degradation effect from oxygen radicals from the symbiosis of UV radiation/NOx flue gas shares. The increasing coating wear up to the upper side section is to be associated with the extinction of UV radiation in the flue gas vapor.

Structural damage to the cement stone of the concrete was always linked to mechanical flow conditions of flue gas existent at the opening of the discharge duct (flow direction, distance to tower shell etc.) [Engelfried et al., 2009].

A display of positions of damage and the qualitative and quantitative refurbishment measures has been

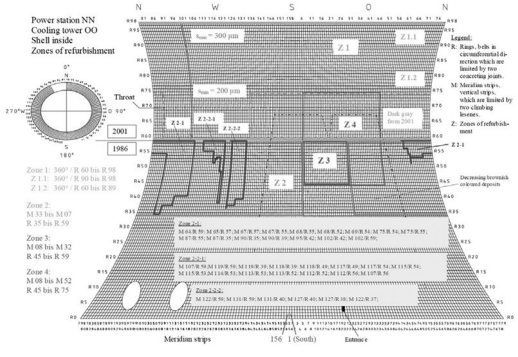

Figure 5. Face of a shell inside of retrofitting CT. Stress depending zones due to horizontal flue gas inlet and weathering influences especially the symbiosis of UV-radiation and NOX.

prepared based on the analysis of this and other stress conditions. Fig. 5 shows the respectively staggered zones which have been projected to the face of the shell inside using a coordinates system.

Zone 1, with its gradients 1.1. and 1.2., mainly involves the surface share of the inside of the shell with photo-catalytically degraded epoxy coating. On Zone 2, differentiated via Z 2-1, Z 2-2-1 and Z 2-2-2, as well as on Zones Z3 and Z4, chemically caused damage to the concrete with varying distribution has developed, depending on the aforementioned flow conditions of the horizontally discharged flue gas at the bottom left two ducts. These findings are included in the building protection technology concept (**BTC**) for planning refurbishment measures.

3 WORK EXECUTION PLAN **(WEP)**

In former times, test processes of quality assurance, derived from specifications standard processes such as, sand-blasting of the base surface concrete, sand-blasting of exposed reinforcing steels, reprofiling of concrete fractures, application of coatings' were examined and evaluated at the end of the respective process in accordance with sometimes vaguely described set standards.

The WEP has been developed from the practical finding and fact that the process of measures has to be planned much better if quality assurance is to be implemented more effectively.

It is the analogous to the planning of measures by surveyors respectively professional planners and this forms the second block of the VGB Guideline 612e. Consequently, this WEP is to be drawn up by the contractor, immediately after the order has been placed and with sufficient lead-time until commencement of measures. The WEP must include a plan and display of all activities required in order to be able to ensure coordinated implementation of all work assured and described in the specifications.

This WEP is prepared with regard to the building protection technology concept (BTC) and the specification (spec.) and it is made up of three parts, as

1. Working plan (WP)
Zone number (of BTC)
spec. pos.
- personal — qualification, quantity of people
- tools — equipment, machinery, devices etc.
- lifting technique — scaffolding, suspending platforms etc.
- materials — mortars and coating materials

2. Execution instruction (EI)
Zone number (of BTC)
spec. pos.
- materials
- working devices
- to fulfil working goals (adhesion, dft etc.)
- by target-performance-comparison

3. Timetable (TT)
Zone number (of BTC)
spec. pos. performance on time line

Figure 6. Work execution plan WEP by contractor.

illustrated in Figure 6: the working plan (WP) with mainly organizational content, the execution instruction (EI) with mainly quality-assurance statements and the time-table (TT) which specifies the time processes. The WEP is submitted to the client for release prior to commencement of execution.

3.1 *Working Plan (WP)*

The subsequent contractor has to deal with calculations involving staff, access technology, mortars, coatings and operating resources as well as tools, equipment and systems required for execution in the bidding phase.

After an order has been placed, he presents the dimensions required in terms of quality and quantity, in relation to the respective items of the specifications. With regard to staff, this includes:

The **Qualified Manager** (QF) (Project Manager)
The QF has extensive know-how regarding stress dimensions, materials and coating systems, their properties and certification requirements for application methods and for respective equipment, tools and systems. The QF is also responsible for internal control in terms of the work assured as well as verification of quality assurance tests. The QF of the contractor must set up the detailed work execution plan. The QF has overall responsibility for the project process.
The **Site Manager** (Bl)
He is familiar with planned organizational implementation of requirements of the building protection technology concept (BTC) and those of the specifications and the WEP.
Construction Site Staff (BFP)
Individual work which is partly allocated to different professional groups, must only be carried out by appropriately qualified and instructed staff. Qualification is confirmed after a course with a re-examination.

The staff to be employed at the construction site must be named together with their respective qualification in the WP.

The type and quantity or volume of access technology, type and order quantity of materials and operating resources required as well as the tools, equipment and systems required for application are listed, preferably in tabular form, in accordance with the respective type and quantity, and allocated to the respective specification items, the respective specification short texts and finally the different processing zones. In addition, the measurement methods used to calculate consumption quantities to achieve the dry film thickness (dft) limits of the coating specified are to be described, together with the parameters applied [VGB Standard, 2010].

The WP must also include detailed data on safety at work in connection with access facilities.

3.2 *Execution Instruction (EI)*

The EI is the actual work instruction of the Qualified Manager to the construction site staff with regard to individual work processes. These are to be coordinated and controlled by the Site Manager.

Each work position of the specifications is described via a short text of the work in accordance with a dual principle, with which material (name of manufacturer) or operating resource which work target (finely rough, rounded smin, β_{HZ} etc.) is to be achieved using which equipment or application method. Such descriptive texts should be short and coherent. They should not include texts from rules and standards or technical data sheets. Reference can be made to respective rules and standards and technical data sheets.

The EI is mainly intended as a source of information for construction site staff. Construction site staff must be able to inspect the EI at any time during execution of work.

3.3 *Time Table (TT)*

All specification items of the specifications are listed in the TT with their short texts and their respective sequence, e.g. displayed via bar sections above the time axis of execution time available. The TT is to be structured so that changes to sequences can be easily adjusted.

4 EXECUTION OF MEASURES (**EM**)

In principle, the awarding of contracts for the execution of protection and refurbishment measures to special structures such as cooling towers can only be made to a small group of professional, experienced service companies. Such companies must have relevant experience in working at height and have appropriately qualified staff and must be familiar with the special methods of application of measures required. This covers the qualitative side of service capability.

The second important condition involves the volume to be handled and the often restricted period of accessibility to the structure. For a new construction of a FGD cooling tower, the area of surface of the inside of the shell to be protected amounts to up to 45,000 m^2. Logistic work and expenditure for access and processing of protection measures are immense. However refurbishment to be executed during an overhaul period is always of less volume, but on account of its stress-oriented special feature mostly more complex and also involved with time pressure due to the overhaul. The uncertain weather conditions at most power plant locations are also of importance, since these require special flexibility during operative work.

Despite various measures particularly expressed in the stress-dependent building protection technology concept (BTC), refurbishment measures normally have a three-stage process:

- A component exists whose surface is not capable of permanently bearing a surface protection system, either due to manufacture, stress or for other reasons. The suitable condition is created by means of **base surface preparation**. This can cover a wide range with regard to equipment used. It ranges from sweeping the base surface through to compressed air blasting with solid blasting material and strongly abrasive high-pressure water-jet. Verification methods for suitability range from the trained eye through to a tensile bond test.
- The next stage is also dependent on the base surface, the **base surface pre-treatment**. This ranges from re-passivation and reprofiling of corroding reinforcing steel in concrete fractures through to the creation of a base surface ready for coating. The surface fine geometry required must ensure that, after application of a liquid coating material with the command variable of the minim coat thickness in the definition $s_{min} = 5\%$, an even and closed dry film thickness can be formed. The respective VGB R 612 e [VGB Standard, 2010] classification thereto is: finely rough rounded.
- Finally, the **coating** is applied. It is normally based on the binding agent basis of organic high polymers. It can be made up of individual layers or of a structure of functionally different individual layers. If bonding is required to the base surface, a **priming coat** is applied. The **intermediate** coat is applied if leveling, crack bridging, a specific diffusion resistance etc., is to be achieved. The **finishing coat** is provided as a functional barrier which protects against stress to be expected from operating and environmental influences.

During, production of individual measures by appropriately qualified staff the execution instruction (EI) described in the planning section of execution plays a central role. This instruction of the specified work target is regulated and controlled by the workman applying the material. This can only be executed after appropriate instruction from the QF. This is the first stage of **internal control** of the measure in accordance with the principle that quality first has to be produced before it can be verified by testing.

Internal control executes additional tests and verifies the actual status after hardening of the materials,

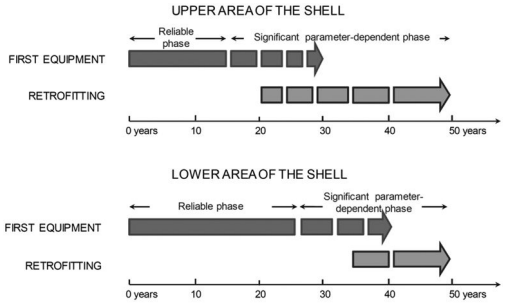

Figure 7. Long-term perspective for usage suitability of part areas of the inside of the shell subjected to stress.

and documents such accordingly. Continuous controlling of climatic conditions and their documentation and some other processes are also included in the self controlling duties of the executing company.

While internal controlling is a continuous process for the application of measures professional controlling by the power station operator, also referred to as **external supervisor** is executed sporadically depending on the respective type of sampling. Normally the client engages for such work specially qualified surveyors or test engineers.

Depending on the difficulty and complexity of measures to be applied it may be necessary to have expert opinions drawn up. This may also be necessary because unforeseen problems or irregularities occur during the process in achieving the defined work targets. These clarifications executed by third parties are also part of external supervision.

Based on a staggered long-term perspective, Figure 7 shows which long-term operational effectiveness of the surface protection system is to be expected on the inside of the shell of a new cooling tower construction with vertical flue gas discharge in high level, if commonly accepted rules of state of the art are redeemed, and which parameters influence the results.

Among the most important parameters for the durability of equipping the cooling tower shell with protection measures are the special structural and operating conditions of the cooling tower, the basic planning of measures with the respective building protection technology concept, planning of the process of measures by the contractor using WEP, quality of execution (high-skilled workmen) – escorted by internal and external controlling – and the adapted election of materials as well as the stress dimensions caused by operations and the environment. If all parameters are complied with and observed, optimum lifitime is possible with economic refurbishment expenditure.

In the case of optimum material selection (proved, highly-resistant polyurethane coating) and the usual corrosive gas concentration of lignite/hard coal combustion after absorber, a usage suitability expectacy for the upper shell half of up to 30 years results for the first equipment. Subsequent refurbishing executed would lead to protective effect until the planned conclusion of operating time of a further 20 years.

Under otherwise comparable conditions a maximum durability of almost 40 years can be expected for the lower shell half which means that the remaining period can be reliably covered by means of respective refurbishing.

It is assumed for both shell halves that in the final operating years there may be certain, justifiable substance wear-out of the surface zones of the inside of the shell.

5 IMPLEMENTATION OF THE UPGRADING MEASURES

For the repairs listed below, many different work procedures were required in order to achieve the planned objectives for the work. To illustrate the scope of the repairs, some numerical data should be provided at this point.

- Total surface area to be treated approx. 13,000 m^2
- Upper third, priorities 1 and 2 (+66.00 m to +94.00 m) approx. 4,800 m^2
- Middle third, priorities 1 and 2 (+30.00 m to +66.00 m) approx. 6,000 m^2
- Of that figure, concrete removal to a depth of approx. 50 mm approx. 2,400 m^2
- SPCC coating, including fine filler layer approx. 2,400 m^2
- Lower third, priorities 2 and 3 approx. 4,000 m^2
- Gaping deep cracks, priority 1 approx. 600 m
- Individual damage locations, priorities 1 to 3 approx. 6,000 locations
- Maximum treatment time 45 working days

After the relevant block at the power station was closed down in the spring of 2007, it was possible to start carrying out the prepared work, such as planking of the wire-mesh wet deck level (Fig. 2), setting up protective and covering sheets and the erection of access scaffolding.

After a ring of wooden planking was laid around the outer edge and two large working and protective platforms were installed, work started on the fitting of a circular rail. This consisted of an HEB steel profile, roughly matched to the curvature of the concrete shell at a height of about 1.50 m above the top edge of the drip collection tank. Steel beams, each about 2.50 m long were screwed onto their own dedicated brackets (Fig. 8).

During the course of the work, so-called undercarriage vehicles were to run along these rails. They were responsible for moving the cages suspended from them in a horizontal plane. Pre-stressed mechanisms could then draw the cages into the shell, making it possible to access any part of the cooling tower. A similar

Figure 8. Circular rail and undercarriage vehicle with pre-stressing mechanism.

Figure 9. Overcarriage vehicle for transport system.

construction runs around the top of the tower, with so-called overcarriage vehicles on it (Fig. 9). This system does not involve any pre-stressing though. Instead, it was often the case that special fittings were used in order to reach the last 1 or 2 metres up to the throat of the tower without difficulty. All in all, 5 separate transport wagons were used.

As soon as the first systems were ready for use, marking out of the improvement zones was begun. The zones were specified by the customer and the work planners and expressed as a coordinate system describing the shell of the tower. The axes of the system were mapped onto the shell of the tower and were termed meridians (vertical) and rings (horizontal) (Fig. 5).

To start with dry blasting work was carried out on the upper third of the tower. This involved spraying (sweeping) sharp-grained fine granules onto the coated surfaces at a pressure of 4 bars in order to carefully peel off the layer of existing epoxy coating, now crumbling due to ultra-violet exposure and other weathering effects. The object of this was to leave as much as possible of the old coating which was still intact in place and to render it into a state capable of supporting additional layers. At the same time, work started from the other cages on breaking up other spots of damage and intense blasting to completely

Figure 10. Deep cracks covered over by special coating.

remove the old coating to expose raw structure where necessary.

Also simultaneous with the work on the upper third, efforts began to remove concrete from areas where acidic concentrate had penetrated through to the concrete because the coating was no longer intact, thus destroying the hardened cement over a period of time (Fig. 4). Even on the very first day, two 11-hour shifts were completed, with 40 employees at work.

In addition to the substrate preparation work mentioned so far, preparation was carried out on very deep cracks up to 40 m in length, involving breaking work and intense dry blasting. This damage consisted of meridianal cracks approximately 0.5 mm in width. Chemical exposure to flue gases was the cause of these cavity-like cracks.

Once the breaking and blasting work had been completed, SPCC measures were taken to close the cracks and they were covered over with a crack-bridging coating (Fig. 10). Other measures involved preparation of those cracks which had penetrated all the way to the outside, their closure and in some cases reinforcements to maintain structural integrity.

Once a sufficiently large surface had been prepared in the middle third of the structure by means of high-pressure water blasting, with the concrete reinforcement there also being blasted and treated, then SPCC was started on these surfaces, too. The object of this work was to recreate the previous concrete profile of the tower's shell and ensure that the steel reinforcement was covered by at least 20 mm of concrete covering. In addition, the surface of the SPCC treatment also needed to be evened out, without using (too much) water for retrospective treatment and smoothing to ensure that no damage occurred to the microstructure of the SPCC mortar. The solution to this problem was to use a fine putty modified with plastic, which was applied close to when the SPCC material started to harden both for touching up purposes and to even out the surface and make it a suitable substrate for a coating to be applied on top. In addition, this PCC putty required no priming for the surface protection to be installed later.

In order to restore the previous profile of the shell as accurately as possible after removal of concrete, a large

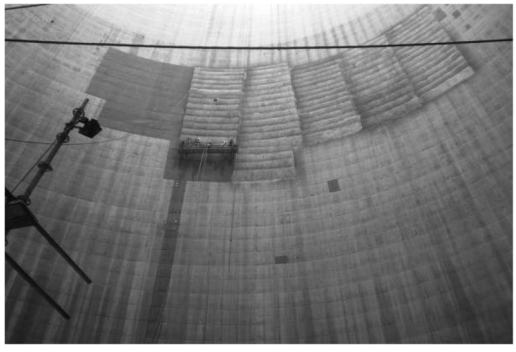

Figure 11. Application of SPCC material.

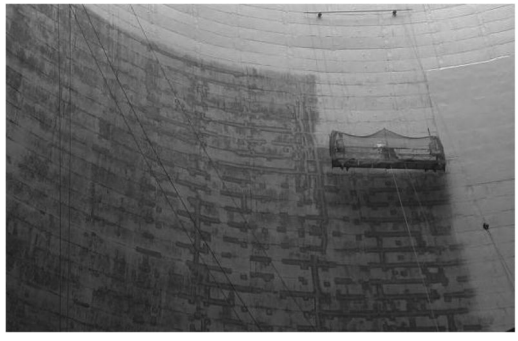

Figure 12. Individual areas of damage with PCC reprofiling.

number of spacer pins were positioned before high-pressure water blasting was begun. These enabled the personnel carrying out the work to gauge the minimum thickness for the SPCC treatment. Figure 11 shows the application of an SPCC layer from a cage platform at a height of some 45 to 50 m.

Once damaged concrete had been removed, calibrated sweep blasting of old coating had been finished and the deep cracks had been dealt with, work turned to a large quantity of individual areas of damage (Fig. 12), including some where the steel reinforcement had become exposed. In the course of this, some deeply embedded reinforcement rods (>20 mm) were treated with mineral corrosion protection ($s_{min} = 1{,}000\ \mu m$) and then sealed with PCC mortar, which included a bonding course. Where the reinforcement had been covered by too thin a layer of concrete or by no concrete at all, it was treated after blasting with an epoxy anti-corrosion coating with a thickness $s_{min} = 500\ \mu m$. This corrosion protection was applied in one or two layers and it was essential that it be made without spreading quartz sand or similar, since the coating was to be made exclusively using the surface treatment system and spreading with fine sand would have caused the protective system to become perforated.

Once all areas of the shell surface, all the individual areas of damage and the raw structure had been prepared and pre-treated, the individual coating procedures were carried out. This involved treating all the various zones with differing coating thicknesses in accordance with their exposure to ultra-violet radiation and flue gas.

This meant that the remaining intact surfaces in the upper third were treated with an additional epoxy coating ($s_{min} = 150\ \mu m$). Parts of the surfaces in this category, where the old coating had been totally removed by blasting, were then giving an extra layer of epoxy coating. The entire area of the upper third then had a final polyurethane coating applied (Fig. 13), which is highly resistant to photocatalytic degradation. The areas in the middle third, where large surfaces of SPCC material had been applied, were given both an epoxy ($s_{min} = 150\ \mu m$) and a polyurethane ($s_{min} = 150\ \mu m$) coating. Between the areas where concrete had been

Figure 13. Finished coating of upper third to the right of the picture.

Figure 14. View of all areas with finished coating.

removed, the same procedure was undertaken as in the top third.

From about 30.00 m down to a height of some 20.00 m the old coating was almost completely intact. Here, after preparation of the substrate, a single epoxy coating was applied ($s_{min} = 150\ \mu m$).

Finally the access facilities, the work platforms and the protective structures were dismantled and after a thorough final cleaning of the cooling fittings and the basin, it was possible to hand over a completed cooling tower back to the power station after a mere 44 days (Fig. 14).

6 MONITORING

For preservation reasons, structures with high requirements of availability should be subjected to systematic recording of their respective status via repeated tests and appraisals. This ensures that appropriate action can be taken if inadmissible reductions in characteristics of the protection system develop in the course of operations. This phase is also referred to as the chain of

Observation – Evaluation – Reaction.

Such developments in the surface protection system dealt with here almost always involve ageing. Therefore, the so-called Monitoring can also be seen as an ageing monitoring program.

REFERENCES

Eisenkrein H. 2012. Prognosis model on deterioration and damage of shell insides under FGD and about protection measures adapted to the local loadings. 6th International Symposium on Cooling Towers, Cologne, June 20–23.

Engelfried, R. 1988. Sichtbeton, Qualitätssicherung durch Ausführungsüberwachung, db Deutsche Bauzeitung, 122. Jahrgang, 4/88 (Exposed Concrete: Quality Assurance via Execution Monitoring).

Engelfried, R. & Scharf, H. & Eisenkrein, H. 2009. Konzeption von Ertüchtigungsmaßnahmen auf Schaleninnenseiten von Stahlbeton Naturzug-Nasskühltürmen im Betrieb mit Abgaseinleitung, Tagungsband "1. Kolloquium Erhaltung von Bauwerken", Technische Akademie Esslingen.

Engelfried, R. 2013. Strategic Direction of Protection and Refurbishment Measures on Standard Concrete Cooling Towers for FGD Operation with Consideration of VGB Guideline 612, Proceedings of the International Association for Shell and Spatial Structures (IASS) Symposium "BEYOND THE LIMITS OF MAN" 23–27 September, Wroclaw University of Technology, Poland.

VGB PowerTech: Guideline VGB-R612 e: Protection Measures on Reinforced Concrete Cooling Towers and Chimneys against Operational and Environmental Impacts, Essen/Germany, Third Edition 2010.

Concrete Solutions – Grantham et al. (Eds)
© 2014 Taylor & Francis Group, London, ISBN 978-1-138-02708-4

The strengthening and repair of the pierhead at Gorey in the Channel Island of Jersey

Steve Hold
Arup, Cardiff, UK

ABSTRACT: This paper describes how a long period of desk study and research, monitoring the structure over several years in conjunction with using new surveying technology using virtual modelling has enabled a very complicated and difficult marine structure to be saved. The use of these new technologies has also refined the focus, or costs, for repairs to be narrowed down to only one section of the breakwater at the pierhead. The original 400 year old Heritage structure had a partial collapse at the head in 1964 and in the past decade there has been an acceleration of the visible signs of damage reoccurring close to the original failure. Detailed investigation and modelling of the breakwater and pierhead has allowed an understanding of the behaviour of the structure and a concept for strengthening and repair to be achieved.

1 INTRODUCTION

1.1 *Location*

A shelter or haven at Gorey on the east cost of Jersey in the Channel Islands was first referred to in historic literature in 1243 as a location where fishermen would be able to shelter behind a small natural Breakwater of rocks in the lee of Mount Orgeil (Fig. 2). The surrounding seabed supports rich marine life, oyster bed cultivation and other marine harvests that were abundant close to this natural location for shelter. The development of a man made Breakwater in the engineering sense evolved over several centuries into the configuration we see today.

1.2 *History*

The first detailed historical records of a man made breakwater at Gorey are recorded in the naval military survey of 1640 which shows a straight breakwater at the foot of Mount Orgeil Castle. The survey was part of a military asset assessment of fortifications around the UK and English Channel harbours for Charles II (Fig. 3).

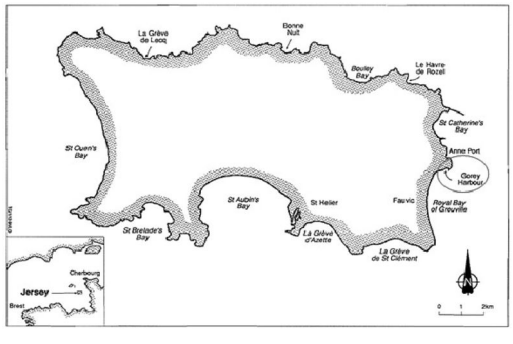

Figure 1. Jersey map – location of Gorey Pier.

1.3 *Function*

The settlement in Gorey has grown and thrived from not only seabed riches but also providing shelter for fishing as well as boat building and repairs in this part of the English Channel.

The breakwater evolved over 370 years from the 1640s (Fig. 3) using the traditional Jersey marine construction methods of forming the outer dressed masory

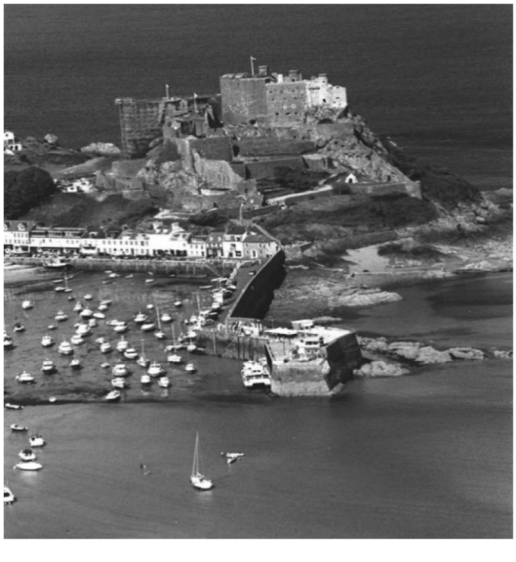

Figure 2. General view of Gorey Pier Breakwater and Mount Orguiel.

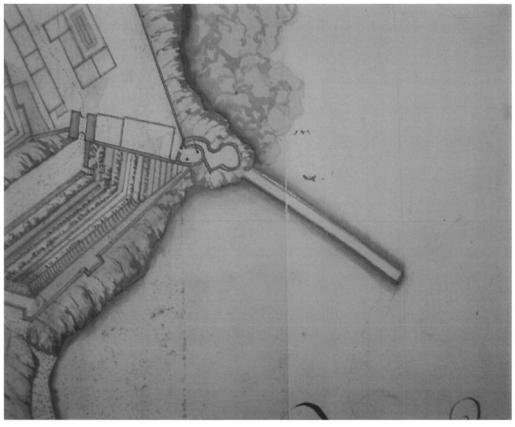

Figure 3. The Breakwater in 1640 known as the 'white pier'.

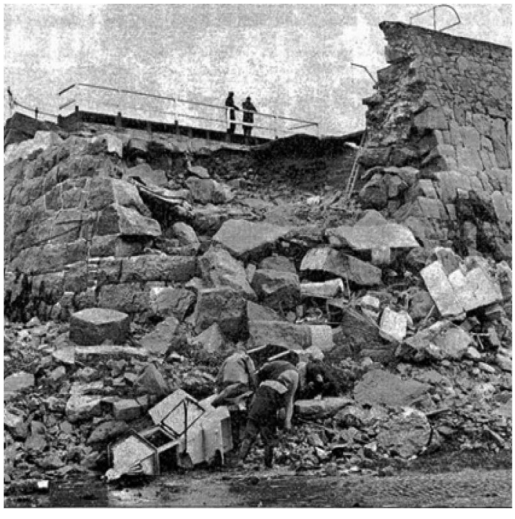

Figure 4. Catastrophic collapse of 1965 (the corner of monitoring point No. 5 in Fig. 5).

main walls with granite blocks with a secondary rock core infill built upon rock-outcrops. In the 1870s the parapet and upper walkway were added with a dog-leg providing further marine shelter at the pierhead. The further angled return of the dog-leg constructed out from the original straight spine was built around a rock outcrop which marks the current end of the pier (Fig. 2).

1.4 *Partial collapse in 1965*

This part of the extended breakwater pierhead suffered a partial collapse in 1964 after a severe storm. The failed sections of the pierhead were rebuilt using a mass concrete backing wall faced with the original masonry from the collapse and founded on sheet piles (Fig. 4).

A concrete landing jetty structure and a concrete deck slab over the end of the pier were also added.in the late sixties (Fig. 5).

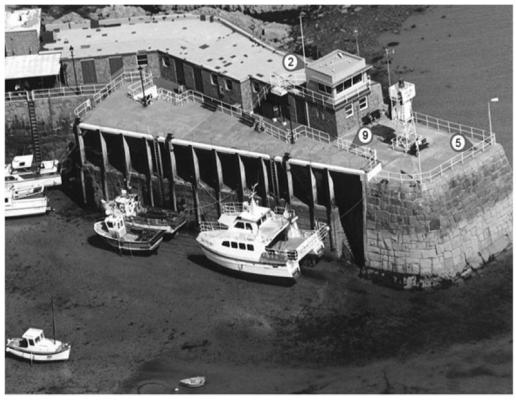

Figure 5. The Pierhead and concrete jetty with the main monitoring points. (The collapsed corner is at point 5).

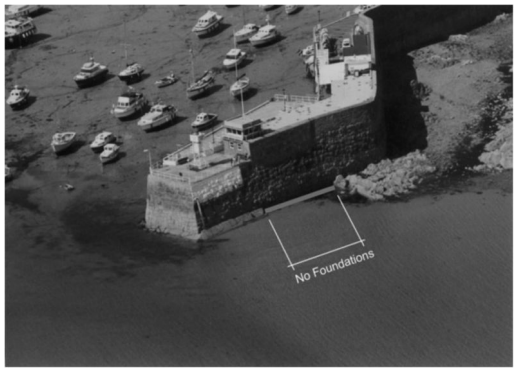

Figure 6. The vulnerable section of pier.

2 LATER DAY INVESTIGATIONS

2.1 *Initial intrusive investigations*

In 1999 an intrusive site investigation was carried out together with a crack pattern study that enabled a prognosis to be made that the pierhead was not, once again in danger of imminent collapse at that time. However, it was recommended that monitoring of crack widths should be regularly carried out and measured. The estimation in 2000 was that the major cracks on the deck were opening up some 3 mm each year; year on year. By 2005 the cracks had widened to the extent that a further detailed investigation was required. Fig. 7 shows the location of monitoring point No. 7a and Fig. 7b the opening up between the De-mec studs placed over the crack for monitoring these movements. The predicted amount of movement occurred over a five year period and was considered too significant just to monitor from then onwards.

2.2 *A second round of investigations*

Further boreholes were drilled through the deck, in 2006. In 2007 ground penetrating radar scans were used to identify if voids were present beneath the deck

Monitoring Point 9 in 2013

Monitoring Point 9

Monitoring Point 9 in 2015

Figure 7. Concrete and asphalt deck level photographs of monitoring point No. 9 and movement over 5 years, 2000 to 2005. Demec stud width of 32 mm (a) in 2000 and 49 mm (b) in 2005.

slabs. Little evidence of significant voiding beneath the Pierhead slabs was found at that time using this method due to the thickness of the slabs and the amount of reinforcement within them that prevented a good reflected signal.

2.3 *Recent 'virtual' modelling*

In 2009 a detailed feasibility study brought together past survey data and inserted the information into a 'virtual' model of the pier made possible using LiDAR (a laser scanning technique that produces 'point cloud' data) that when G.P.S. referenced enables a very accurate 3D model of the structure and its surroundings to be constructed. The 400 year old structure has very difficult, irregular geometry and conventional 2D drawings were not easy to produce to scale. A further recent intrusive survey in 2012 together with another LiDAR scan has now enabled the design of a strengthening remedial solution to protect this marine asset for the longer term.

3 UNDERSTANDING THE STRUCTURE

3.1 *Type of construction*

The structure originally was, as many other Heritage Marine structures in Jersey of that period, constructed from outer walls of dressed granite blocks with an inner core of secondary rock material. The original walls are founded directly upon the rock promontory which provides a good foundation. However, the site, as a breakwater suggests, is exposed and subject to harsh wind and wave combinations. The first intrusive testing in 1999 identified that a section of the outer wall is founded on the beach sands not the rock outcrop. This same section is not part of the 1965 rebuild in faced mass concrete and therefore has a higher permeability. Only recently in 2012 did information come to light that the original straight spine section of the breakwater on the rock outcrop had been pressure pointed and pressure grouted in 1969. This meant that like the rebuilt end of the pier the main section of the breakwater was also less susceptible to wash out as it is less permeable. The section with no pointing and no foundations however is more susceptible to 'wash out'. 'Wash out' is when the secondary core material is broken down, chemically or physically, and washed out through open unpointed joints in the outer facing wall masonry as the tide recedes.

3.2 *Behaviour of the structure*

This part of the pier with the original characteristics also behaves as a 'free draining' structure, i.e. the tide can flow freely into, then drain out of the external open jointed walls. It can be seen in Figs 6 and 7 that the flat, unprotected pierhead is more vulnerable to overtopping waves. However, in modern times (probably since the 1950s or 1960s) the exposed deck of this structure has been protected against wave overtopping

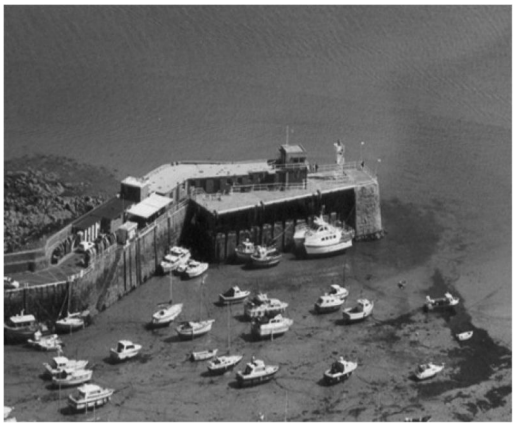

Figure 8. The end of the Pier with customs and police buildings.

and water draining down through the core by paving over the deck with asphalt on the main spine of the Breakwater and by providing a concrete deck slab upon the pierhead area rebuilt in the late 1960s (Fig. 8).

4 FUNCTION OF THE BREAKWATER AND PIERHEAD

4.1 *Protection in the harbour*

In its modern form, the breakwater and pierhead provides protection to Gorey Harbour where fishing and pleasure boats are moored. The breakwater and pierhead provide a significant tourist attraction in Jersey with the added use of the pierhead acting as a jetty for small ferries from France in the summer season. This use of the pierhead requires a police and customs post.

4.2 *Marine commerce*

There is also a fuel refuelling facility and storage tanks set within the end of the original breakwater beyond the first bend, thus making Gorey pier an important integral part of Jersey life and marine commerce.

5 RECENT HISTORICAL REPAIRS

5.1 *The original spine of the breakwater*

The inside face of the pierhead was provided with a two-stage reinforced concrete jetty after the 1964 reconstruction (Fig. 8). The spine or original part of the breakwater, founded on rock has shown historically little distress during the period of our monitoring from 2000 until the present time. Visual inspections during the monitoring periods found no evidence of movements at deck level or parapet walls during inspections after storm events. This indicates that not only has the main breakwater not been as susceptible to wash out because of its lack of permeability but wave impact being transmitted easier through a now 'solid' core has also not had a detrimental effect on the inner breakwater walls. The pier is externally pointed along the original breakwater length but the inner harbour wall is not. In 2009 and 2012 modern day LiDAR survey techniques have also not detected anomalies of pier movement in the spine as they have been able to do at the pierhead. The robustness and size of the original masonry and being constructed directly on the rock outcrop are thought to be the principle reasons why the spine of the breakwater remains undamaged. Only by chance in the latter part of 2012 was it anecdotally learned that the spine of the breakwater had been pressure grouted as well as pointed in 1969 despite extensive searches in maintenance records for information about the repair works carried out in the 1960's.

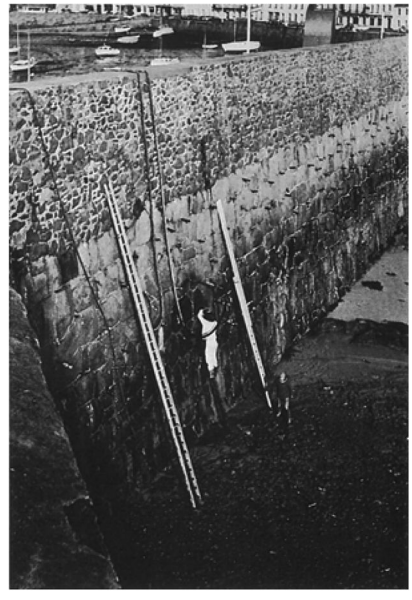

Figure 9. Pressure pointing in 1969.

5.2 *Importance of keeping contemporary records*

This demonstrates that owners or custodians of such important structures need to keep as much recorded information as possible on a date base and it was very fortunate that the contractor who carried out the work came forward after hearing about the 2012 study and investigation and provided a selection of record photographs of the 1969 work (see Fig. 9).

5.3 *Historically three different types of structure*

During the study period and the monitoring the intrusive investigation and measurements of movements indicated that the pierhead was acting as three independent structural elements butted together. The three different types of construction are; the original the mass block masonry stone outer walls and core partly founded on rock, the rebuilt pierhead founded on sheet

piles and backed with mass concrete, and the reinforced concrete jetty structure that all abut the original extended masonry section at the dogleg.

6 USE OF MODERN TECHNOLOGY TO UNDERSTAND THE STRUCTURE

6.1 *LiDAR to model and understand the structure*

In 2009 a first LiDAR survey accurately captured the superficial profile of the pier and breakwater at that time. A detailed feasibility study in 2012 discussed the problems and different forms of constructions of the pier. This work was brought together with the historical data and the previous investigation work so that a final detailed intrusive site survey to gain information still not known could be carried out in 2012 prior to being able to design strengthening works. The principle objective required both an understanding of the behaviour of the pier and its principal weaknesses. The wave loadings that will have to be resisted were calculated for 1 and 10 year return periods in order to design a remedial and strengthening scheme that can counteract the degradation mechanisms acting on the pierhead. This will enable the Ports of Jersey, the owner, to continue using the pier with a reduced risk of failure, increased design life, reduced on-going maintenance requirements and an improved visual condition.

6.2 *The use of super imposed LiDAR models for monitoring*

In 2001 the interpretive report identified that 'shunting' behaviour of the three separate pierhead types of structure (in a similar manner to stress propogation through a solid structure abutting another will tend to have a 'Newton Cradle' effect) and would continue year on year (Fig. 10). Traditional and modern techniques were used to survey and record the movements at the pierhead every six months (Fig. 5 shows some monitoring points) and this monitoring corroborated the theory of the abutting structures (refer back to Fig. 7) moving away from each other. A second LiDAR model was produced in 2012 which was then superimposed upon the 2009 model. Despite the difficult geometry an indication of which parts of the masonry was moving and by how much was detectable. Fig. 11 shows the two models superimposed, both are G.P.S. referenced in the same x, y, z co-ordinates. A movement outwards from the x, y, z co-ordinates between the two different models indicated a bulge in the masonry (difficult to see with the naked eye) and an inward movement is shown in Fig. 6 as the loss of concrete apron.

6.3 *Possible deterioration mechanisms*

The additional dogleg of the pierhead constructed in the 1870s, and then partly rebuilt at the end in 1964

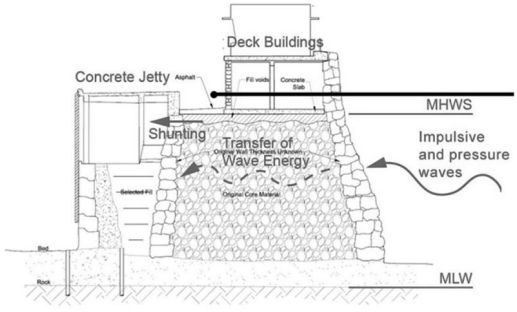

Figure 10. Pierhead cross section graphical indication of 'shunting' forces.

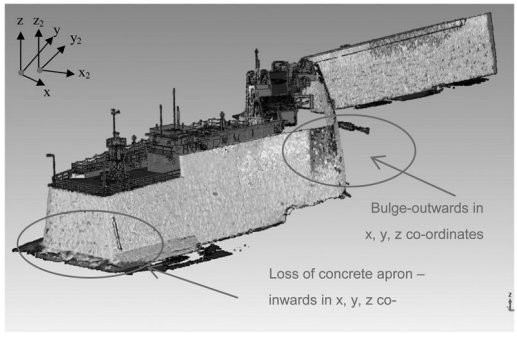

Figure 11. Pierhead cross section graphical indication of 'shunting' forces.

after the collapse, has been identified as the main troubled area of pier movements and current weaknesses. The main body of the breakwater and pier have shown little evidence of similar structural movements. The three different types of evolved structure at the pierhead act in different ways because of the different levels of robustness of the foundations as well as their construction. The main, original part of the breakwater is founded on rock, the dogleg is not founded on rock but on beach sands and the rebuilt end of the pier has been reconstructed on sheet piles founded on rock. The central section of the pierhead dog-leg between these two pier elements built upon beach sands is far less able to transfer wave loads to a robust foundation. At the same time it is the only section remaining which is semi-permeable to wave energy. The wave impulse forces are considered to be responsible for the 'Newton's Cradle' or 'shunting' mechanism and the stress damage seen between the old pier and the jetty at deck level (Fig. 7).

6.4 *Propagation of wave energy across the pierhead*

The transfer of energy by stress propagations from the old pier to the concrete jetty is also thought to be borne out by the damage at the small, narrow neck of the top deck of the reinforced concrete jetty. Similarly, the parallel lines of opening up of the adjacent

Figure 12. Removal of loose cover, repair and protection of concrete during full access survey and repairs.

asphalt deck structures to the jetty (Fig. 7) are another secondary result of the wave impact on the external surface, travelling across the structure.

LiDAR techniques also identified bulges in the masonry wall, a marked loss of concrete apron base at the end of the pierhead and a worrying loss of beach sand on the outside face of the pierhead.

6.5 *Types of waveload on the pier*

The idealised loads necessary to be resisted by a repaired and strengthened pierhead in conjunction with a sea state condition study of this area of the coast of Jersey using the MIKE21 modelling technology (Mike 21 by DHI, 2014) allowed predictions of wave heights and direction for both serviceability and ultimate limit states loads to be estimated.

Other degradation mechanisms in play include:

- Extensive wear of perimeter low level ring beam from wave action and scour.
- Washout of materials from under the pier between the section built on a rock outcrop and where the sheet piles commence.
- Ongoing lowering of bed level due to climate change and longitudinal drift of sands on the island.

For serviceability limits, a 10 in 1 to 1 in 10 year joint probability return period was used. For ultimate limits a 1 in 1000 year event was used.

7 REPAIR MAINTENANCE TO THE CONCRETE JETTY

7.1 *Originally protected by spray concrete*

The reinforced concrete jetty had experienced distress in the 1980s and was assessed by the States of Jersey engineers in 1997 as requiring concrete protection due to the onset of corrosion of the reinforcement. At that time spray concrete was applied and minor repairs carried out to the jetty.

Figure 13. Wave of 1.0 m passing.

Figure 14. Water flowing out of masonry after wave passes.

A patch concrete repair contract carried out in 2011 enabled a detailed assessment of the reinforced concrete integrity.

7.2 *Patch repairs allowed a full assessment of the jetty*

The full access study and the repairs enabled an engineering judgement to be made that with further protection the jetty can be rehabilitated again and built into the overall strengthening design of the joining together of the three different types of structure at the pierhead. The strengthened and repaired reinforced concrete jetty will reuse its buttressing effects and incorporating them with a 'tie-ing in' of the jetty to original loose masonry considerably improves the robustness of the whole structure.

8 REPAIR AND STRENGHTENING CONCEPTS

8.1 *Other weaknesses identified*

During 2012 a feasibility study was undertaken to produce ideas and concepts that would be appropriate for discreetly, strengthening and repairing the problems at the pierhead.

Some solutions were obvious in that a foundation support for the outer wall of masonry was required as well as a new concrete pile capping beam around

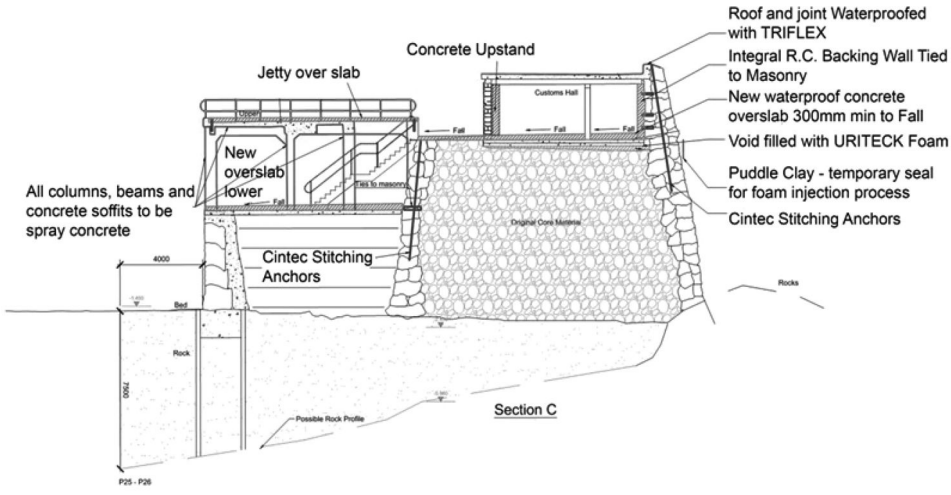

Figure 15. Scheme design remedial works – sheet piles, ring beam, deck over slab etc.

the end of the pierhead. The study also identified that there were voids beneath the concrete deck slabs in the troubled areas of the pier wall as well (Figs 13 and 14).

8.2 *Key remedial measures*

All of these observations and the questions raised during the feasibility study work provided a list of what still was not known. To address these unknowns a further intrusive site investigation was carried out in 2012 that provided the remaining further data necessary to formulate a design concept for repair and strengthening of the pierhead (Fig. 15).

The general principles are that the three abutting structures are physically 'tied' together to make one structural mass on a unified foundation to rock. In this way the combined structure will be better able to resist the overtopping and wave forces for the idealised design life of 50 years. This design criteria is compromised because the sea state analysis shows that the biggest threats to the structure are from overtopping waves. However, the engineering solution to raise the pierhead deck up to the level of the landing jetty was not acceptable to the Planning and Heritage bodies in Jersey.

New sheet piles are being installed where the pier is founded on beach sand rather than rock. This aims to limit migration of seabed material, prevent slip failure of the core material, resist sliding at the base of the wall and retain the finer core material.

The degraded concrete ring beam at the head of the existing piles at the end of the pier is to be replaced and linked to the new section of ring beam over the new sheet piles. This will extend the capping beam, unify the foundation capacity and make the three different parts of the pierhead have the same reaction to rock foundations.

The linking or tying together of the three different structural forms at the pierhead is provided by a series of new overlaid reinforced concrete deck slabs and reinforced concrete buttressing walls inside the customs hall. The loose masonry, mass granite parts of the structure are also joined and tied into the new concrete elements with Cintec 'stitching' anchors and mini ties.

The lost and deteriorating concrete apron at the base of the rebuilt pierhead wall is replaced with a new ring beam that ties into the new sheet pile foundation extension on the outside of the wall and the existing sheet piles under the rebuilt main concrete end wall. The design intent is to provide a uniform base support for the different elements of the pierhead now tied together above commonly responding foundations.

8.3 *Wave energy dissipation experiment*

An experiment is in place to try to identify the amount of energy that is dissipated by the existing secondary 'soft' core at the end of the pierhead in the troubled section. The 2012 S.I. showed that this part of the core was intact and not grouted. Pressure sensors have been installed on the inside face of the outer wall, centrally in the core and finally at the inside face of the inner stone wall at a depth to approximately 3m, Fig. 16. The number and spacing of Cintec ties on the inside face of the breakwater wall is related to the need to resist the forces propagated across the core to the inner wall and this study will, it is hoped, provide emperical data to verify the design assumptions. For the early design stages, the existing conservative theoretical dissipation factor of 60% has been used. The remedial and strengthening design although having to compromise in several key areas addresses the wave impact as well as overtopping distress. These forces for the future are now resisted by the three structures at the pierhead acting as one body. The strengthening aspects of the design intent is that conceptually with the use of deck diaphragms and vertical stitching the three

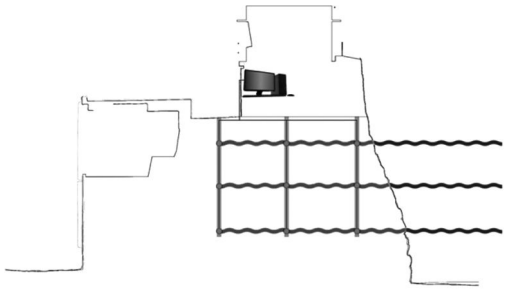

Figure 16. Wave energy transfer sensors.

joined together 'boxes' act as one on rock foundations (Fig. 15).

8.4 *Heritage and environmental aspects*

Much care and attention has had to be paid to the heritage, 'invisible' aspects of the repairs. The end of the Gorey Pierhead demarcates the start of Jersey's Ramsar site for the protection of wetland bird species, therefore particular attention has been paid to the Environmental Impact of the works. Not only this; the harbour of Gorey is a particularly sensitive and beautiful tourist attraction which provides leisure boating activities as well as the aforementioned fishing and seabed farming industries which have all had to be factored into the methods used for repair and the timing of the works.

9 CONCLUSION

The site work commenced in 2014 with a completion date of spring 2015. Through careful and respectful reasoning, the team has created a design solution that meets the client's aims providing a cost effective, reliable and minimally intrusive strengthening for such a challenging environment and an important structure.

ACKNOWLEDGEMENTS

The author acknowledges and thanks contributions from:

Bernard Reed – formerly Colcrete for the 1969 photographs of pressure grouting and pointing.

Ray Hine, Ports of Jersey

Dr Ian Statham and Dr. Gabe Treharne for identifying the 'shunting' of the pierhead in the 2000 Arup Interpretative Report to Jersey P.S.D

REFERENCE

Mike 21 2D modelling of Coast and Sea http://www.mikebydhi.com/Products/CoastAndSea/MIKE2 1.aspx, Accessed May 2014.

Concrete Solutions – Grantham et al. (Eds)
© 2014 Taylor & Francis Group, London, ISBN 978-1-138-02708-4

Technical diagnosis and recommendations for repair of RC tanks for water and liquid waste

M. Kosior-Kazberuk
Bialystok University of Technology, Bialystok, Poland

P. Berkowski
Wrocław University of Technology, Wrocław, Poland

ABSTRACT: The reinforced concrete tanks of different forms for water and liquid waste and the accompanying concrete infrastructure are subjected to the influence of physical, chemical and biological destructive factors. The variations in exploitation conditions and the diversity of harmful influence on the RC tanks in such objects as sewage-treatment plants or heat and power generating plants demand individual assessment of the need and the range of repairs as well as selection of suitable protection methods. The influence of specific destructive factors was analysed considering the selected cases of the RC tanks. The diagnosis of technical state of RC structures and the typical problems of construction quality were presented in the paper. The recommendations for the reconstruction and the methodology of repairs are described.

1 INTRODUCTION

The increase of regulations considering the environmental protection in last twenty five years have caused dynamic development in technologies and methods of sewage treatment and disposal in Europe. The main objective of the strategy of natural water resource protection against pollution is the adaptation of domestic regulations to the ecological legislation of the European Union. In addition, the requirements for the quality of the sewage treatment have increased. Formerly sufficient simple mechanical methods with a short period of sludge detention, were replaced by modern methods of effluent removal (e.g. biological, chemical methods) with long-term periods of sludge detention (Chetermisinoff 1995, Kosior-Kazberuk 2011). Moreover, the character of the sewage became more aggressive with civilization progress (Saricimen et al. 2003, Vipulanandan & Liu 2005). The increase in the ecological awareness in the society, the fact that particular states signed international agreements concerning the prevention of water pollution and conditions of the sewage disposal, the creation of sponsored domestic and foreign sources of the financial support of investments relating to the environmental protection have all caused dynamic development in the building and modernization of sewage treatment plants. Reinforced concrete is the most popular building material used in these structures. Concrete has proven its ability as a retaining material for liquids in structures such as tanks (Alexander & Fourie 2011, Reinhardt et al. 1998).

Reinforced concrete reservoirs in sewage treatment plants or in heat and power generating plants are exposed to the influence of the various destructive physical, chemical and biological factors (Chetermisinoff 1995, Davis et al. 1998). Analyses, carried out within the framework of the state programme of construction and modernization of sewage treatment plants, revealed that almost all structures suffer from corrosion related problems earlier than their expected service life time. The problem is particularly serious especially since it concerns the infrastructure necessary for the functioning of cities, industrial plants, etc. Total disasters of these kinds of structures are very rare, however they can suffer from quite complex damage. However, the damage concerns a significant number of structures and the mass nature of the problem should be highlighted.

Apart from the technological factors related to the sewage treatment process, the strong influence of other factors can be observed. In urban sewage treatment plants, where the contribution of industrial effluents is low in total amount of waste liquid, in the case of structures for pre-treated sewage, the chemical aggressiveness of sewage does not appear to be the dominant destructive factor (Rozière et al. 2009) but the external service conditions, errors in the design (Calderón et al. 2009) or errors during the elements construction, seem to be the most significant.

In the water supply and sewage disposal systems in which RC tanks for water and liquid waste are used, the following environments appear:

- the environment of surface waters (from rivers and lakes), seized by water-supply-installations for drinking water treatment,

- the environment of underground waters,
- the water-sewer environment; the wastewaters revealed considerable differences in the composition depending on their source; the domestic sewage, municipal sewage and industrial wastewater can be distinguished,
- the gaseous environment in the form of air directly above the water-level.

The chemically and biologically aggressive wastes, effluents, sewage, sludge and gases affect the concrete with various intensity. Additionally, the following factors connected with environmental conditions of the sewage treatment plant structures influence the intensity of concrete damage:

- the features of the local climate (changes in temperature of air, falls of the rain and snow, the humidity, the long-term influence of CO_2),
- the shape and the location of structure (e.g. horizontal and vertical elements partially hollow in the ground, which have direct contact with the ground water and the atmospheric air),
- the exposition of structural elements to the influence of solar radiation,
- the character of the moisture influence on concrete (the long-term, direct contact with water or moist air, constant sprinkle with water and sewage, the variable level of liquid, filtration of liquids through concrete elements),
- cyclic freezing and thawing, particularly in splash and tidal zones,
- mechanical influences in overflow and inflow zones with more intensive turbulence (abrasion, cavitation).

Structures in sewage treatment plants are much more exposed to destructive factors than other industrial facilities. The continuous action of the agents mentioned above, affects weak spots on the concrete surface and the reinforcing steel, rendering materials vulnerable to deteriorational defects with possible irreversible damage (Davis et al. 1998, Fernandes et al. 2012, O'Connell et al. 2010).

The variations in exploitation conditions and the diversity of harmful influences on the RC tanks in such structures as sewage-treatment plants or heat and power generating plants demand individual assessment of the need and the range of repairs as well as the choice of protection methods (Reinhardt et al. 1998, Vaysburd & Emmons 2000). The approach to ensure the durability of structures was proposed in a series of European standards EN 1504, for products and protection and repair systems of reinforced concrete structures. It should be noted that the damage to the concrete influences not only the safety of structure but also means a potential risk of environmental contamination.

The influence of factors mentioned above on the technical condition of RC tanks was analyzed on the basis of several structures as part of the programme of the facilities for sewage treatment modernization. Biochemical attack on concrete in sewage treatment facilities was described by Davis et al. (1998), O'Connell et al. (2010), thus the other significant factors were analyzed. The following examples were described in details:

– A twin-chamber sewage sludge reservoir in municipal sewage-treatment plant after 40 years of exploitation,
– A reinforced concrete oil-trap in the heat and power generating plant in a big city,
– The walls of the sewage pumping-station, subjected to water filtration.

The processes of structural degradation within their service life time were analyzed and some aspects of repairs with expected extending exploitation time were considered. Selected methods used in the structures diagnosis are presented.

2 ANALYSIS OF ENVIRONMENTAL THREAT

The mechanisms of carbonation and leaching corrosion, caused by underground waters and waters from rainfall, are comparatively well recognized (Balafas & Burgoyne 2010, Berkowski et al. 2013, Reinhardt et al. 1998). Usually underground waters show low aggressiveness to concrete. However, this *a priori* assumption in every situation is inadmissible, because the pH of underground waters can attain the value approx. 3.0 (e.g. in peaty grounds), and these waters can show strong corrosive activity to concrete.

The aggressiveness of the environment affecting the internal surface of RC objects in sewage treatment plant depends on the chemical composition of sewage and on the methods used in the treatment process performed in the structure considered. In the vast majority, municipal sewage with pH about 6.5–7.5 are discharged to the sewage treatment plant (Chetermisinoff 1995). They may contain dissolved carbon dioxide and hydrogen sulphid. These gases, in the effect of desorption to air, can exert an adverse influence on the concrete directly above the sewage surface. The substances aggressive to concrete and reinforced concrete in domestic sewage are mainly chloride ions, sulphate ions, ammonium ions and organic acids (Alexander & Fourie 2003, Fernandes et al. 2012). Mineral oils and organic solvents also occur in municipal sewage. Example of compositions of average sewage based on authors' tests are presented in Table 1.

According to the standard EN 206-1 (2003) there are three degrees of environmental chemical aggressiveness to concrete structures: XA1, XA2, XA3. However, the descriptions of exposure classes do not render the threat characteristics completely. In case of the RC tanks for water and wastewater the synergistic effect in various combinations of XA, XC, XD, XF and sometimes XM should be considered.

In the municipal sewage treatment plants the liquid and gaseous environments demonstrate a low or moderate degree of aggressiveness to concrete. Industrial effluents are the most dangerous, especially the

Table 1. Compositions of the untreated sewage (selected components based on authors' tests).

Anolyte	Domestic sewage	Sewage from tanning industry
pH	6.7–7.5	11.5–12.0
Chlorides [mg/dm^3]	145–153	3300–4600
Sulfates [mg/dm^3]	163–179	700–900
Sulfites [mg/dm^3]	–	50–150
Chromium [mg/dm^3]	–	700–850
Phenol	1.5–5.0	–

wastewater from chemical production plants which contain both inorganic and organic components – mainly acids, sulphur compounds and formaldehydes (Saricimen et al. 2003).

The efforts to maximize sewage treatment effectiveness is related with side reactions, which often have an adverse effect on the durability of concrete structures. Initially, typical untreated municipal sewage is not deleterious to concrete. However, in progress of the sewage effluent flow through the following degrees of the treatment and the phases of conditioning of sludge, secondary corrosion can occur, strongly affecting the concrete. There can appear hydrogen sulfide, sulftes, volatile fatty acids, biological films etc. (Alexander & Fourie 2011).

The untreated sewage discharged to the plant is much less aggressive to concrete and reinforcement than the chemical substances used in the process of their treatment. The media applied to the chemical sewage treatment, such as iron chloride, aluminium chloride, ammonia, calcium chloride, sulphates, hydrochloric acid are also aggressive. The treatment process is also associated with increased temperature. The acid dissolves calcium from the concrete. As a result, the concrete is gradually destroyed from the surface to the inside.

The classification of threats usually does not take into account the bioactivity of sludge and supernatant sludge and the processes of the anaerobic and aerobic digestion of organic substances which causes the chemical corrosive threats of concrete. The concrete can be also destroyed by sulfuric acid. As a result of bacteria activity the hydrogen sulfide contained in sewage can be oxidized, that causes the formation of sulfuric acid and the development of sulfate corrosion in concrete (Yuan et al. 2013).

An additional factor intensifying the process of degradation are mechanical damages of concrete during the treatment process, e.g. the abrasion in the channels supplying wastewater and sludge or the operation of equipment scraping the sand from the bottom of tanks.

The corrosion of steel reinforcement in concrete can occur as a result of neutralization (the carbonation process) of concrete, when the pH of liquid in pores is below 11.0, and the loss of protective properties of concrete cover of reinforcement. The deterioration of concrete makes the penetration of aggressive media towards the reinforcement easier (Berkowski et al. 2013).

Additionally, in the case of tanks and the accompanying infrastructure, the design and construction problems typical for other large-scale reinforced concrete structures occur, it means the defects due to inadequate structural design, defects due to inadequate construction or materials and defects revealed during service (Calderón et al. 2009). The designing of tank walls with regard to service loads only and omitting the influence of concrete shrinkage, changes in temperature and the behaviour of structure are often the major causes of damages of RC tanks apart from the aggressiveness of specific environment.

3 GENERAL PRINCIPLES IN THE PROCESS OF REPAIR OF RC STRUCTURES

The decision about the range of rehabilitation of the structure is preceded by the estimation of its technical condition and the possibilities of the repair work execution. The structure diagnosis should cover identification and estimation of damages and failures as well as their causes. The rate of structure degradation can be evaluated on the basis of the structural analysis, experimental investigation, previous experience or a combined approach (Bissonnette et al. 2013, Garbacz et al. 2006, Vaysburd & Emmons 2000). It is important to combine different testing methods and investigation operations. A good diagnosis requires overlapping information because of the variation of the site building material properties. Because of the complexity of destructive influences and their results, an individual approach, including an investigation programme, is necessary for every structure considered.

The intensive development of new methods and materials for protection and repair all over Europe, resulted in the need to develop the standards for this kind of works and products (Garbacz et al. 2006). A new approach to ensure the durability of structures was proposed in a series of European standards EN 1504, for products and protection and repair systems of reinforced concrete structures. The composition of the EN 1504 standards includes 10 fundamental standards and about 65 standards considering test methods. One of the achievements of EN 1504-9 (2008) is formulating the principles for the repair and protection of concrete and reinforcement and determining the methods for the technical implementation of these principles.

The stages of repair and the elements that should be taken into consideration in the particular phases of the project are specified in EN 1504-9. The sequent steps include well-known items such as technical diagnosis, planning, design and quality inspection. However, the systematization of planning is completely new in comparison to the existing recommendations for repair.

Planning of the repair according to EN 1504-9:

- Assessment of the structure's current condition (damage, their scope and causes);
- Developing a strategy for repair (choice of option: no action, repair, demolition);
- Defining the principles of repair (e.g. protection against the ingress of media, strengthening);
- Selection of repair method (e.g. impregnation, injection);
- Determination of the requirements for repair materials (e.g. strength, adhesion);
- Determination of the requirements for further inspection and maintenance.

Generally, the study of every tank or other structure consists of a site investigation and sampling and laboratory tests. The cause and type of defects are considered during close-up inspection. They included material deterioration as well as structural dysfunction. The results of the completed assessment are only valid at the time that the repair works are designed and carried out. The nature and the causes of defects, including potential combinations of causes are identified for every structure individually. The technical diagnosis of structures in sewage treatment plants and in heat and power generating plants need the application of various, sometimes atypical, test methods. This allows defining a repair strategy and selecting optimal repair techniques and products.

The important element is to link the protection and repair of the structure with the strategy of structure management. The structure management strategy should be chosen not only on the basis of technical reasons, but also taking into consideration economic, environmental and functional factors, and first of all the requirements of the structure owner. The basic premise for the design of the system of protection and repair is the expected lifetime of the concrete structure. The range of possible actions includes both the restoration of the expected lifetime in a single comprehensive operation, as well as simple actions, which may include cyclic treatment for maintenance or repeated application of repair system components, such as surface protection systems. The purpose of RC tanks and their importance in the infrastructure of plants makes it difficult to exclude them temporarily from operation. Thus, partial repairs are very often used, which do not eliminate the facility from work, but give a short-term solution only. Usually, the total exclusion of structure takes place in the case of a failure hazard.

4 TECHNICAL DIAGNOSIS OF SELECTED RC TANKS

4.1 *Twin-chamber reservoir in sewage treatment plant*

The sewage sludge reservoir and accompanying facilities (internal channels, service platforms, columns) of the municipal sewage-treatment plant in medium town were designed and constructed in the early seventies of the 20th century. The reservoir was designed as a monolithic reinforced concrete twin-chamber open tank with a common central wall. The horizontal section dimensions of each chamber in the light of walls were 15.00×28.00 m, and the height 6.00 m. The chambers were partially surrounded by the ground. Above the tank there were two platforms for mounting assembly and aerator installation.

The walls of the twin-chamber structure were inspected from the outside above the ground level and in trial pits in the ground, and also inside both to the level of wastewater and lower, after the decrease of the sewage level of about 1.50 m. Because of the high level of the groundwater around the object and the inability to empty completely the chambers, the examination of the bottom was carried out by divers.

The synergistic effects of physical, chemical and mechanical factors caused various damage to the concrete and also corrosion of the reinforcing steel. Especially, a lot of damage was found in a part of the structure placed above ground level and above the sewage level – exposed to cyclic wetting and drying. Cracking, scaling, and spalling of large parts of concrete and reinforcement without concrete cover were observed mainly on the upper edges of the chamber walls as well as in the technological channel walls. The thin walls of interior channels were cracked and deformed. The holes left after shuttering dowels in the walls (since the period of construction) made it possible to infiltrate the sewage into groundwater.

The water infiltration through the reinforced concrete walls left local efflorescence. High relative humidity, the biological character of the environment and the exposure to solar radiation created suitable conditions for the development of mosses, growths and larger plants on the surface of the concrete.

The bacteria found in ground water collected from the vicinity of the tank, indicated the penetration of wastewater from the tank to the groundwater and contamination of the environment.

The results of chemical analysis did not indicate the sewage or ground water to exhibit high aggressiveness to concrete (pH > 6.5). The structure degradation was caused by the accumulation of technological errors (inadequate composition of concrete and construction works, fresh concrete delamination), and specific service conditions of the structure. The examples of damage described are shown in Fig. 1.

The concrete was characterized by relatively high water absorption (up to 8.5% in the part of walls above ground level). The capillary suction of the liquid resulted in a significant moisture content inside the concrete walls. The bulk density of concrete was from 1870 to 2200 kg/m^3. The test results showed various compressive strengths of concrete in the range from C12/15 to C25/30. The concrete of better quality was found in the service platform structures and in the walls of chambers below the ground surface and below the level of sewage. The depth of the carbonated layer of concrete varied from 0.5 to 2.5 cm. This zone

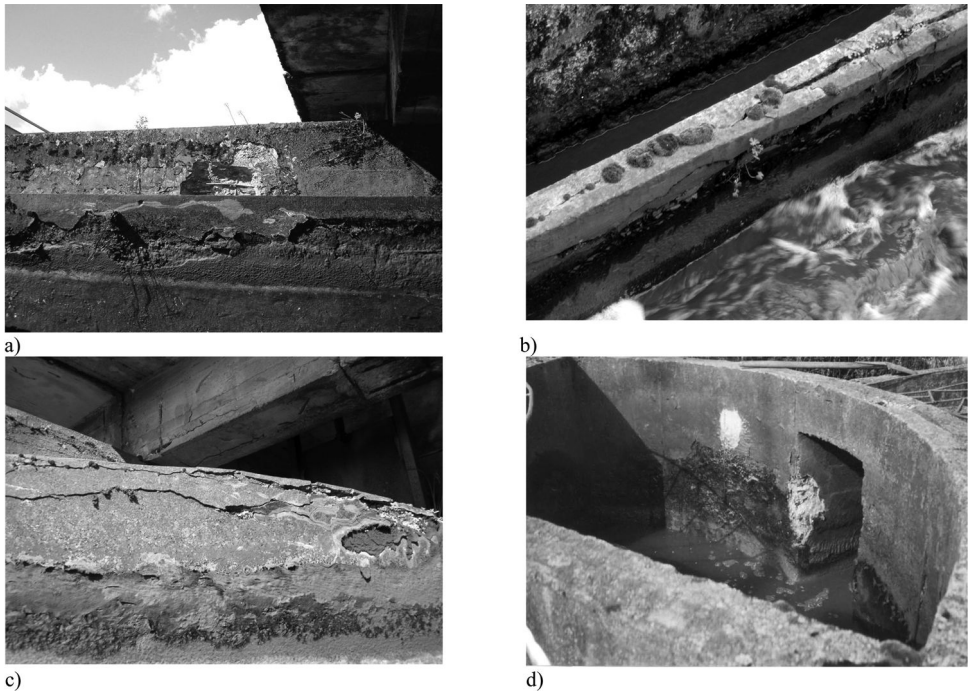

Figure 1. Typical damage of RC structures of sewage-treatment plant: a) wall and top edge; b) open channel (technological supply sewer); c) connection of platform with chambers; d) sludge well.

reached the reinforcement. The in-situ tests revealed the errors in the reinforcement disposition and wrong diameters of bars used during the construction of tank in comparison with the initial design.

The static calculations of chamber walls were conducted considering the following service life stages:

- exterior wall: the empty reservoir, surrounded by ground,
- exterior wall: the reservoir filled with sewage, no ground around,
- inner wall: only one chamber of reservoir filled with sewage.

Furthermore, the analysis of load bearing capacity and stability of the bottom slab considering the hydrostatic lift of ground water for the lower level of sewage (the tank almost empty) was made.

4.2 *Reinforced concrete oil-trap in heat and power plant*

One of the facilities for storm water and industrial wastewater treatment in heat and power plant is an oil-trap. The oil-trap is used for removing various kinds of fats and oils separated and collected on the surface of wastewater. The reinforced concrete structure has the form of a rectangular chamber flow tank, where the inflow and outflow of wastewater operate from the bottom. The wastewater contaminated with oils, derived from the area of the oil management, are fed into combined storm water and industrial wastewater drainage system, after treatment in the oil-trap. There was serious corrosion damages to the concrete and reinforcing steel caused by the influence of flowing sewage, especially in the lower part of the structure. The destruction of reinforced concrete walls was intensified by the break of the bituminous insulation, covering the inside of the tank. Improperly designed, the insulating layer was too thin and was not resistant to the mechanical action of flowing sewage and to the chemical compounds of sewage.

The damage was clearly visible, especially in the lower part of the walls where aggregate grains were exposed almost completely without the cement binder and, could be observed in large areas. Locally, deep pits occurred in the concrete. The heavily corroded reinforcing bars, without concrete cover were observed (Fig. 2).

The test results of the wastewater flowing through the oil-trap showed that, in accordance with the criteria of standard aggressive environment classification, it was aggressive to concrete in a moderate way. In the case of flowing water, which took place in the oil-trap, the concrete was washed by a constantly refreshed liquid, that increased the aggressiveness of the sewage.

The rate of dissolution and leaching of calcium from hardened cement paste depends on the water hardness and the presence of salts. The chloride and sulfate ions, which were found in the sewage, increased solubility. The oils, contained in the sewage, do not react with the concrete, but soaking in the concrete microstructure,

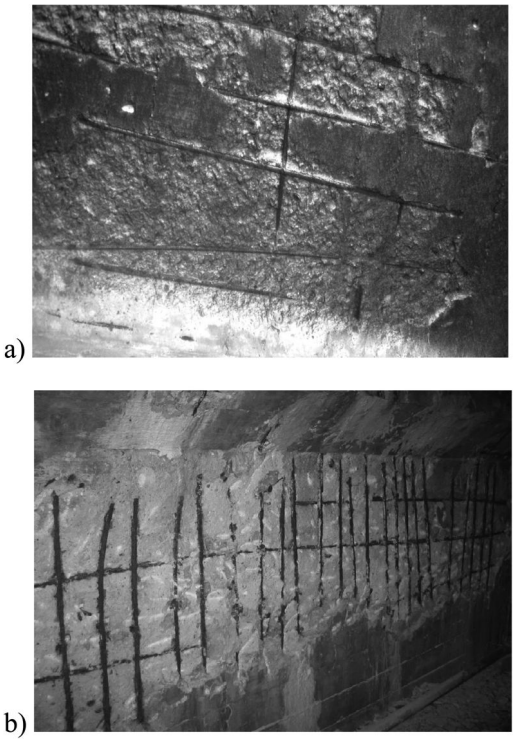

Figure 2. Bottom surface of oil-trap reservoir.

they reduce the inner friction, which leads to a loss of strength and concrete bond to the reinforcement.

4.3 *Analysis of the corrosion process due to water infiltration through concrete in pumping-station*

The reinforced concrete walls of the lowest level of the building of the sewage pumping-station, in the plant for storm water and industrial wastewater, were exposed to the destructive influence of water, causing leaching and carbonic acid corrosion of concrete. The room was located below the groundwater level, which caused hydrostatic pressure on the walls. Additionally, one of the walls adjoined the chamber of final settlement tank with effluents. The wastewater in the tank, with a depth of 2.50 m, put hydrostatic pressure on the wall of the lowest located room of the pumping-station. The deleterious effect of water on the concrete was observed on the walls inside the building.

The corrosion of hardened cement paste is related to the amount of calcium hydroxide and hydrated calcium silicates and aluminates contained in the paste. The corrosive destruction of concrete under the water influence means dissolving its ingredients. Removing the concrete paste components, as a result of contact with the liquid phase surrounding the concrete, could occur in two ways:

- washing out in the process of water infiltration through the paste under the influence of a pressure difference,

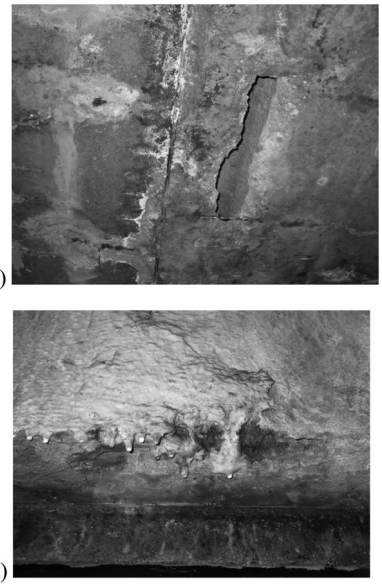

Figure 3. Calcium efflorescence on the concrete surface.

- diffusion of components in the liquid phase due to the difference in concentration between the liquid phase in the hardened cement paste and the surrounding aqueous medium.

In practice, the common case of acid corrosion, caused by the impact of industrial water and groundwater, is carbonic acid corrosion. This phenomenon accelerates considerably the process of leaching. The infiltration of water containing aggressive CO_2 through concrete causes calcium efflorescence due to leaching and decomposition of $Ca(HCO_3)_2$ on the concrete surface (Fig. 3).

Because of the complex structure of concrete the assessment of the course and rate of corrosion progress was very difficult. The laboratory tests only partially identified the destructive factors. When the corrosion process was already advanced its effects could be observed in the form of water percolations and salt coatings on the external surfaces.

The wet, white and brownish yellow coatings were visible on the inner surface of the walls (Fig. 3). The saline efflorescence formed a hardened crust (calcite), sometimes reaching a thickness of a few centimeters. The thicker layers were separated partially with the corroded concrete, indicating that the precipitation of calcium carbonate occurred not only on the surface but also inside of the concrete element. The concrete walls over the entire surface were wet, locally porous. In many places, such as the different types of holes for installation pipes, where the water leakages were more intense, stalactites formed.

The unilateral water pressure, the concrete microstructure not tight enough and inappropriate surface protection were the main factors for the corrosion initiation and development. The rate of dissolution and leaching of lime in concrete was affected by water

hardness and the presence of salts. The Ca^{2+}, OH^- ions reduce and Cl^-, SO_4^{2-}, Na^+, K^+ ions increase the solubility (Chetermisinoff 1995).

5 RECOMMENDATIONS FOR REPAIR

5.1 *Analysis of repair scope of sewage sludge reservoir*

The analysis of the technical state of the structure has shown that the repair is necessary primarily for RC elements and parts of structures located above the ground level and above the sewage level – it means the parts the most exposed to variable thermal and moisture conditions during operation.

The static calculations and analyses performed have shown that the current load bearing capacity of walls of the chambers was sufficient for its continued operation assuming the existing reinforcement, concrete strength class C16/20 and C20/25 and current loads. The situations possible during renovation were also analyzed, for example the case of one chamber emptied, while the exterior wall is loaded by the ground, and the inner wall being one-side loaded by the sewage filling the chamber. In this case, for low strength concrete, and locally reduced reinforcement, the present state of the structure did not guarantee the required load bearing capacity. The safety struts should be applied for keeping the sewage pressure in the fully-filled chamber as well as the earth pressure load. Another way to solve this problem can be reducing the sewage level of min. 0.50 m in the other chamber.

Due to moisture inside the walls of the porous concrete the chosen repair material should allow the drainage of moisture. It was a mineral system open to water vapor diffusion, which provided the required adhesion of coating to a wet surface. A silica mortar modified with polymer was used. In this protective system, the amorphous silica gel forms a tight, acid resistant, durable matrix integrated with the concrete. The overlay is resistant to mechanical and thermal impact as well as resistant to de-icing media. Due to the vulnerability of internal channels to deformation, the thickness of their walls needed to be increased to 15 cm. It was recommended to use steel fibre reinforced concrete (fibre length 13 mm, diameter 0.16 mm). Considering the improved strength properties as well as dynamic resistance, resistance to thermal shock, limited shrinkage and improved deformability, the fibre reinforced concrete is suitable material for objects in severe service life conditions.

5.2 *Repair of the oil-trap reservoir*

As a rehabilitation measur it was recommended that the deteriorated concrete and the bituminous lining were removed and replaced with new concrete. The reinforcing steel was repaired and concrete cover rebuilt. The smooth bottom of the reservoir was formed. Epoxy cement mortar containing synthetic microfibers was used for leveling and sealing the concrete surface. In the zone of variable levels of sewage table and above an epoxy protective coating was applied, resistant to fatty acids, floating on the surface of wastewater. The epoxy coating was also highly resistant to abrasion.

Measures were taken to decrease the velocity and turbulence of the inflow of wastewater in order to avoid mechanical corrosion of the concrete walls.

5.3 *Walls of the sewage pumping-station*

The damage to the concrete was mainly on the surface of walls, thus, after the elimination of the cause of water infiltration, surface repairs were carried out. The corrosion products and damaged layer of concrete (particularly, scaled concrete) were removed. The exposed concrete surface was thoroughly cleaned to remove the loose particles. After removing the thick layers of calcium carbonate coating, which scaled with the parts of porous concrete, the condition of the reinforcement of the walls was checked. The elimination of the corrosion effects consisted of the improvement of the concrete structure and then carrying out surface protection. The surface concrete defects were filled and the concrete cover was rebuilt. In areas of cracking, resin injections were applied and the leak-proofing of walls was made. The renovation of the drainage system in the ground around the pumping-station chamber was carried out.

6 CONCLUSIONS

Selected examples of RC tanks and accompanying infrastructure were presented and the frequently occurring durability problems were revealed. Apart from long-term environmental influence, the significant factor causing the deterioration of the structures considered was the use of concrete of low quality. Currently introduced advanced recommendations and international standards for design of concrete structures concerning durability and environmental impact are the concept for future approach.

The main aspects of the repair of RC tanks for water and wastewater can be formulated:

- the results of adequate analysis of the environment should be the basis for selection of the repair material solutions and protective coatings,
- the load-bearing behavior and the mechanical loads (hydrostatic pressure, ground pressure, friction of solid phase, aerodynamic effects in liquid phase) should be taken into consideration in structural analysis,
- in order to rehabilitate the structure, it is necessary to identify the main mechanism of deterioration and to understand the heterogeneous distribution of the damage,
- the repair strategy should be elaborated considering the real possibilities of temporary exclusion of the structure from operation,

- the repair process may be connected with the change in the method of sewage treatment (the change in the type or degree of aggressiveness).

REFERENCES

Alexander, M.G. & Fourie, C. 2011. Performance of sewer pipe concrete mixture with Portland and calcium aluminate cements subjected to mineral and biogenic acid attack. *Materials and Structures* 44: 313–330.

Balafas, I. & Burgoyne, C.J. 2010. Environmental effects on cover cracking due to corrosion. *Cement and Concrete Research* 40: 1429–1440.

Berkowski, P., Dmochowski, G., Kosior-Kazberuk, M. 2013. Analysis of structural and material degradation of a car-park's RC bearing structure due to city environmental influences. *Procedia Engineering* 57: 183–192.

Bissonnette, B., Courard, L., Beushausen, H., Fowler, D., Trevino, M. & Vaysburd, A. 2013. Recommendations for the repair, the lining or the strengthening of concrete slabs or pavements with bonded cement-based material overlays. *Materials and Structures* 46: 481–494.

Calderón, P.A., Adam, J.M. & Payá-Zaforteza I. 2009. Failure analysis and remedial measures applied to a RC water tank. *Engineering Failure Analysis* 16: 1674–1685.

Chetermisinoff, P.N. 1995. *Handbook of water and wastewater treatment technology*. New York: Marcel Dekker, Inc.

Davis J., Nica D., Shields K. & Roberts D.J. 1998. Analysis of concrete from corroded sewer pipe. *International Biodeterioration and Biodegradation* 42: 75–84.

EN 206-1: 2003 Concrete – Part 1: Specification, performance, production, and conformity. European Committee for Standardization.

EN 1504-9:2008 Products and systems for the protection and repair of concrete structures – Definitions, requirements, quality control and evaluation of conformity. *Part 9 – General principles for use of products and systems*. European Committee for Standardization.

Fernandes, I., Pericão, M., Hagelia, P., Noronha, F., Ribeiro, M.A. & Maia, J. 2012. Identification of acid attack on concrete of a sewage system. *Materials and Structures* 45: 337–350.

Garbacz, A., Courard, L. & Kostana, K. 2006. Characterization of concrete surface roughness and its relation to adhesion in repair systems. *Materials Characterization* 56: 281–289.

Kosior-Kazberuk, M. 2011. Application of SSA as partial replacement of aggregate in concrete, *Polish Journal of Environmental Studies* 20 (2): 365–370.

O'Connell, M., McNally, C. & Richardson, M.G. 2010. Biochemical attack on concrete in wastewater applications: A state of the art review. *Cement & Concrete Composites* 32: 479–485.

Reinhardt, H.-W., Sosoro, M. & Zhu, X. 1998. Cracked and repaired concrete subjected to fluid penetration. *Materials and Structures* 31: 74–83.

Rozière, E., Loukili, A., El Hachem, R. & Grondin, F. 2009. Durability of concrete exposed to leaching and external sulphate attacks. *Cement and Concrete Research* 39: 1188–1198.

Saricimen, H., Shameem, M., Barry, M.S., Ibrahim, M. & Abbasi, T.A. 2003. Durability of proprietary cementitious materials for use in wastewater transport systems. *Cement & Concrete Composites* 25: 421–427.

Vaysburd A.M., Emmons P.H. 2000. How to make today's repairs durable for tomorrow – corrosion protection in concrete repair. *Construction and Building Materials* 14: 189–197.

Vipulanandan, C. & Liu, J. 2005. Performance of polyurethane-coated concrete in sewer environment. *Cement and Concrete Research* 35: 1754–1763.

Yuan H., Dangla P., Chatellier P. & Chaussadent Th. 2013. Degradation modelling of concrete submitted to sulfuric acid attack. *Cement and Concrete Research* 53: 267–277.

Concrete Solutions – Grantham et al. (Eds)
© 2014 Taylor & Francis Group, London, ISBN 978-1-138-02708-4

Investigation of distress in a post-tensioned slab

Don Wimpenny & Richard Norwood-Grundy
CH2M Hill, London, UK

ABSTRACT: Cracking and spalling developed to the post-tensioned base slabs of an aeration tank to an effluent treatment works approximately a year after construction and prior to the plant entering service. The tank has an overall length of 210 m and was 110 m wide and was partitioned along its length into four bays. The base slab was divided into eight post-tensioned slabs, 110 m long and approximately 50 m wide, with a central conventionally reinforced infill strip to facilitate tensioning. The damage was principally around the movement joints between the central infill and adjacent post-tensioned slabs. Finer random cracking was also present elsewhere on the exposed upper surface of the slab. A comprehensive investigation involving non-destructive testing, finite element modeling and a review of construction records was carried out to systematically determine the cause and extent of the distress. A wide range of non-destructive test (NDT) methods was used to minimise damage to the structure, particularly at tendon locations, including radiography and strain relief. This paper describes the investigation and its findings and provides some important lessons for the design and construction of similar structures.

1 INTRODUCTION

Cracking and spalling developed to the post-tensioned base slabs of an aeration tank to an effluent treatment works in Australia approximately a year after construction of the slab and prior to the plant entering service.

The tank was approximately 5.4 m in height, 110 m wide and had an overall length of 210 m. It was partitioned along its length into four bays (Figure 1). Each of the four bays was further separated into four passes by precast internal walls. The tank had circulation channels running alongside the North, East and West perimeter walls. The tank is intended to have a 100-year design life.

The base slab was divided into eight post-tensioned slabs, 110 m long and approximately 50 m wide. The slabs were generally 200 mm in thickness, but thickened at the perimeter of the tank to a maximum of 500 mm.

The slabs had a central conventionally reinforced infill strip 1.5 m in width, running North-South, which accommodated tendon anchorages to facilitate post-tensioning. There were also 5 m wide infill strips running East-West under the internal walls between each bay.

An initial inspection found that the visible damage was principally around the movement joints between the central infill and adjacent post-tensioned slabs. There was occasional evidence of concrete within the joints near the surface. Finer random cracking as well as discrete areas of 'tearing' were also present elsewhere on the exposed upper surface of the slab. There was rectilinear cracking running north-south, which approximately aligned with the location where the slab began to thicken along the west perimeter wall.

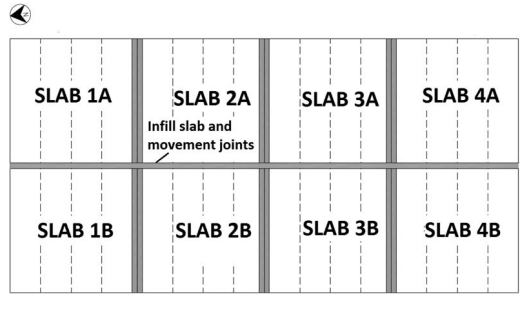

Figure 1. Plan of the aeration tank (passes are numbered 1 to 4 from left to right in each bay).

A comprehensive investigation involving non-destructive testing, finite element modelling and a review of construction records was carried out to systematically determine the cause and extent of the distress.

2 METHODOLOGY

The tank was being readied for service, so there was a desire for rapid investigation with minimal damage

Table 1. Investigation methods.

Method	Application
Hammer soundness	Locating hollowness
Crack mapping	Recording the pattern and width of cracking in selected passes
Ground Probing Radar (GPR)	Locating tendons and dowels
Radiography	Indentifying blockages in movement joints
Cores	Confirming the condition of the joints and the depth of cracking
Strain relief	Assessing stress from post-tensioning
Finite element analysis	Predicting temperature and stress in the slab
Temperature and movement monitoring	Confirming temperature and movement at joints

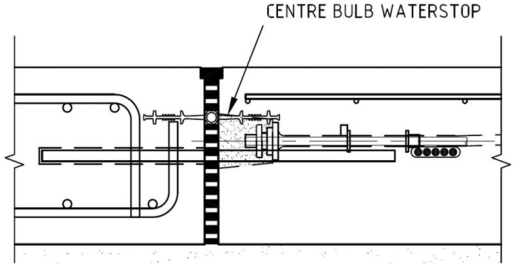

Figure 2. Cross-section through joint (reinforced infill slab to left and PT slab to right).

Figure 3. Measurement frame and core holes prior to forming the slot.

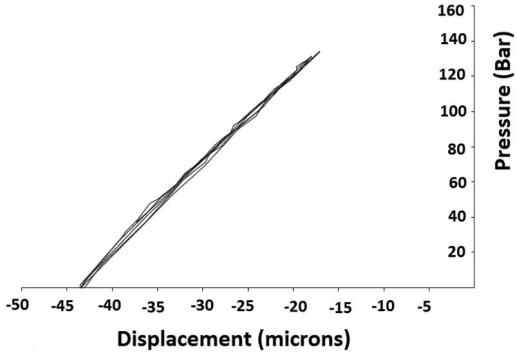

Figure 4. Typical pressure-displacement relationship.

to the structure. A wide range of non-destructive test (NDT) and other investigation methods were used, as summarised in Table 1.

Hammer soundness testing, using a 100 g hammer, and crack mapping using a crack ruler was used to assess the pattern of visible and underlying distress.

The joints had a design width of 25 mm wide and incorporated a bitumen impregnated fibre board above and below a central waterstop (Figure 2). A 40 mm wide rebate was saw cut at the surface to take an elastomeric sealant; which was never installed.

In order to assess the joint without disturbing the waterstop, a 25 mm diameter hole was cored at 45 degrees to the slab surface to intercept the joint beneath the waterstop. A hand-held miniature GPR (JRC model NJJ-105) was used to detect the stainless dowels at the joint before coring, as these could not be reliably detected using a normal covermeter.

Iridium 192 isotope, with an effective strength of 6 Curies, was inserted down the core hole to shine gamma radiation up through the joint to a radiographic plate at the slab surface. The plate used was Agfa D7 standard speed film, with a width of 100 mm and length of 400 mm.

The presence of cracking in the slab led to concerns that the post-tensioning may not have been working as intended. In order to assess the effectiveness of the post-tensioning, the residual stress in the tendons was assessed using the Slotstress® strain relief method (Hiroshi et al. 2003).

The hand-held GPR was first used to locate the tendons. A rectangular steel frame was bolted to the concrete surface. Two 35 mm core holes were drilled into the concrete to a nominal depth of 100 mm adjacent to the tendons. A slot was sawn perpendicular to the axis of the post-tensioning using a chain saw to link the two core hole (Figure 3).

During this operation the measurement frame was used to monitor the decrease in distance between points either side of the slot to an accuracy of approximately 40 microns. This contraction represents the strain relief resulting from the removal of concrete within the slot and cores. A calibrated flat jack was then inserted into the slot and pressure applied allowing the pressure and displacement to be monitored.

From the strain relief and the pressure-displacement relationship, the original stress in the concrete could be estimated (Figure 4). The difference between the measured stress and the actual stress measured independent tests is reported to be less than 0.5 MPa in more than 95% of the cases.

The temperature developed in the slab was monitored in a single pass using thermocouples at depths of 50 mm and 100 mm below the top surface. Measurements were taken hourly using a continuous data logger. The data was downloaded from the data logger each week. Tell-tales and Demec spots were also affixed across some of the joints to monitor movement.

3 FINDINGS

The hammer soundness identified extensive hollow areas in the slab, some over 1 m^2 in size, immediately adjacent to the movement joints alongside the central infill strip. The pattern of hollowness was consistent with areas of spalling and repair and suggested progressive damage to both the reinforced infill and the post-tensioned slab alongside the movement joints.

The random cracking and discrete areas of tearing were suggestive of plastic shrinkage and long term drying shrinkage (Concrete Society, 2010). In some cases the concrete surface in the areas of tearing had evidence of finishing using a power trowel, possibly in an attempt to close up the cracks. Rectilinear cracking in the North – South direction adjacent to the west wall was found to be typically 0.3 mm in width.

Petrographic examination of four cores taken vertically through the random cracking indicated that in three cases the cracks tapered to less than 0.1 mm width and penetrated less than 50 mm from the surface.

In eight out of the nine locations assessed using radiography, either one or both edges of the joint could not been seen on the plates. This suggests that the joint in these eight locations was fully or partially blocked by concrete.

Having established the possibility of a significant problem with the movement joints, four 100 mm diameter cores were taken vertically through the joints. Three of the four cores had evidence of concrete intruding into the joint below the waterstop, whilst the other core had evidence of concrete both above and below the waterstop. The intrusion occurred at the junction between the filler board and central bulb of the waterstop (Figure 5).

The strain relief method was used to assess the residual stress in the slab in areas with and without visible cracking. In four of thirty-one tests, the residual compressive stress in the slab was less than 0.5 MPa (Figure 6).

These low results were in the vicinity of the rectilinear cracking and suggest some loss of effectiveness in the post-tensioning. This was finding was consistent with a finite element analysis of the slab which identified a risk of low compressive stresses at the point where the slab began to thicken. This was probably due to a combination of long-term shrinkage and bending stresses induced by backfilling and the weight of the perimeter channels.

The compressive stresses were generally higher than the value of approximately 2MPa expected based on the post-tensioned design. Careful percussion drilling was carried out to determine the depth to the top of the tendon duct. These measurements suggest that these higher compressive stress values were due in part to the tendons being shallower than intended.

Figure 5. Example of concrete intrusion below filler board and above waterstop.

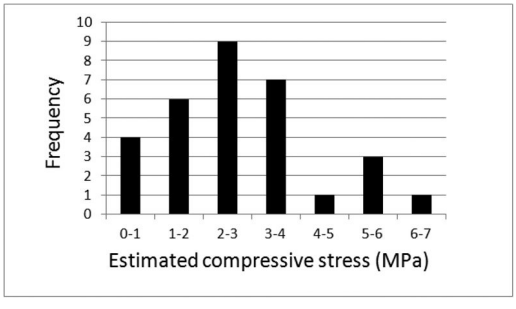

Figure 6. Histogram of estimated compressive stress values.

Temperature records from the local weather station showed that the slabs were generally cast during the cooler months when the median ambient temperature was approximately 15°C. Subsequently the slab was exposed to sustained ambient temperature values above 40°C and solar radiation after construction. An increase in the effective temperature of the slab in excess of 30°C was predicted using a finite element programme Femmasse developed by Intron bv. This programme had been used previously by the authors to assist in forensic engineering investigations (Wimpenny et al. 2008).

This increase in temperature would have generated over 15 mm expansion of the slab which would have been partially resisted by the concrete blocking the movement joint. Finite element analysis using Strand7® indicated that the stress induced in the post-tensioned slab and infill in combination with the horizontal waterstop and poorly anchored reinforcement would have been sufficient to promote tensile stresses sufficient to promote spalling in the slab.

Table 2. Comparison between measured and predicted temperature values in slab.

	Maximum diurnal temperature (°C)	
Depth in slab (mm)	Measured	Predicted
50	29.1	29.8
100	28.8	27.3

A connection between temperature and damage is consistent with the first reported incidence of spalling to the slab being shortly after a period of exceptionally high ambient temperatures.

The average diurnal range for the shade temperature during the temperature monitoring was 14 to 23°C. The maximum and minimum diurnal temperature values at 100 mm depth in the slab were on average approximately 6°C higher than the maximum and minimum shade air temperature illustrating the effect of solar gain and thermal inertia.

Table 2 shows a comparison between measured temperature values and the values predicted using finite element modeling. This indicates reasonable agreement for an assumed peak solar radiation value of 700 W/m^2.

The movement monitoring was not conclusive due to its short duration and the intermittent nature of the measurements. In hindsight it would have been better to have had continuous monitoring using a potentiometer which could have been correlated to the temperature measurements in the slab.

Following the discovery of concrete intrusion in the movement joints, the infill slabs were carefully removed by stitch coring to form blocks typically 1500 mm long, 750 mm wide and 300 mm deep.

All the blocks showed intact concrete, typically with a depth of 20 mm or more, both above and below the waterstop (Figure 7).

Figure 7. Block removed from infill slab showing concrete intrusion into movement joint above and below waterstop.

4 CONCLUSIONS

A wide range of NDT and analytical methods were used to systematically investigate the cause and extent of spalling and cracking to a post-tensioned slab within a newly constructed aeration tank.

Random cracking and tearing to the concrete surface was characteristic of plastic shrinkage and long-term drying shrinkage. Coring confirmed it was generally minor in nature.

Rectilinear cracking occurred in a location where low compressive stresses were expected based on finite element analysis of the slab. These low stresses were confirmed using the strain relief method.

Spalling of the slab was found to be associated with concrete intrusion into movement joints. The presence of intrusions was established using radiography and coring. It was subsequently confirmed by removal of infill portions of the slab.

The evidence indicates the slab was subject to a sustained period of high ambient temperatures promoting expansion and inducing stresses at blocked joints. Finite element analysis indicated that this stress in combination with the horizontal waterstop and poorly anchored reinforcement would have been sufficient to promote tensile stresses sufficient to propagate spalling in the slab.

Use of central waterstops in the slab compared to a rear waterstop increases the difficulty of successfully forming the movement joint. Extra care is needed to ensure gaps do not develop between the filler board and waterstop which could allow concrete intrusions to block the joint.

REFERENCES

Concrete Society. 2010. Technical Report 22, Non-structural cracks in concrete, Fourth Edition:4–5.

Hiroshi1A, Manabu F, Le Diouron T & Noriyuki M. 2003. Measurement of current release stress of concrete materials based on the releasing stress method using a flat jack, (English translation), Japanese Concrete Society.

Wimpenny, D E, Knights, J C & Slater D. 2008. Temperature simulation by FEA as a tool in forensic investigation. *From Failure to Understanding; Proc. Fourth International Conference on Forensic Engineering, London, UK, 3–5 December 2008.*

Concrete Solutions – Grantham et al. (Eds)
© 2014 Taylor & Francis Group, London, ISBN 978-1-138-02708-4

The current situation of concrete crash barrier walls on the city bridges of Harbin and the design concept of new fabricated protective plates

Xiangguo Wu
Key Lab of Structures Dynamic Behavior and Control (Harbin Institute of Technology), Ministry of Education, Heilongjiang, Harbin, China
School of Civil Engineering, Harbin Institute of Technology, Heilongjiang, Harbin, China

Jinkai Qiu & Sha Liu
School of Civil Engineering, Harbin Institute of Technology, Heilongjiang, Harbin, China

Ruofei Zou
Department of Civil and Environmental Engineering, University of Illinois at Urbana-Champaign, USA

ABSTRACT: In the code area, crash barrier walls on city bridges suffer from severe exposure to concrete aggressive substances such as de-icing salts, freezing and thawing cyclic action and impact like action. Such elements often show insufficient durability when built using conventional reinforced concrete. First, this article conducts an on-the-spot investigation of the current situation of reinforced concrete crash barrier walls on Harbin city bridges, which are of different ages, and puts forward a design concept of fabricated protective plate based on rapid repair of concrete crash barrier walls on city bridges. It gives the design size of protective plates, the basic requirements of performance target design, material mixing and the implementation of the installation technology for the protective plates. The new protection method will provide references for the high speed retrofitting of reinforced concrete crash barrier walls for city bridges in this code area.

1 INTRODUCTION

Recently, improving aging and deterioration of structures has become an important issue in the area of architecture and civil engineering. Crash barrier walls on new bridges and new concrete covers for the rehabilitation of existing bridges are usually cast on site. In recent years, the phenomenon of concrete cracking, spalling, and even corrosion of reinforcement has appeared on the crash barrier walls of city bridges. The concrete durability and the anti-collision grade of the crash barrier walls after performance deterioration has dropped. This paper first presents an on-the-spot investigation on the current situation of the main reinforced concrete crash barrier walls on Harbin city bridges, which are of different ages, and analyzes the main causes of the current situation of the concrete crash barrier walls' performance.

In order to repair concrete bridge crash barrier walls, some new high performance materials have been adopted. But they are all local reinforcement based on site application, and their durability and interfacial properties are difficult to guarantee, so the reinforcing effect is not ideal. In recent years, considerable effort to improve the durability of cementitious materials have led to the emergence of Ultra-High Performance Cementitious Composites (UHPCC) characterized by a very low water/binder ratio (<0.20), ultra high strength (>100 MPa), and high durability. These novel building materials provide extremely low permeability, high strength with significant tensile strain hardening, as well as excellent rheological properties in the fresh state(Reinhardt & Naaman 1991, Wu et al. 2008, Song & Hwang 2004, Wu et al. 2012, Wu & Han 2010). UHPCC is considered a promising construction and rehabilitation material due to its high ductility and durability (Kim et al. 2014). Rehabilitation and strengthening of various reinforced concrete structures (buildings and bridges) with a UHPCC layer are discussed by Moreillon&Menétrey (2013). The application of UHPCC in protective design of reinforced concrete crash barrier walls on bridges can effectively improve resistance to freeze thaw damage, salt erosion and impact to guarantee the long-term anti-collision grade of crash barrier walls. Oesterlee et al. (2007) conducted research on reinforced concrete by adopting the design method of UHPCC protective layers, the application background of which is reinforced concrete crash barrier walls on highway bridges. The scheme of formwork pouring on site is feasible because there are fewer vehicles. However, it will have serious effects on city traffic for city bridges with larger traffic flows. In order to meet the rapid repair target for concrete crash barrier walls on

city bridges, this paper puts forward a design concept of fabricated protective plates based on UHPCC and gives the basic size of the protective plates, the basic requirements of performance target design, material mixing, and the process of implementation of the installation technology of the protective plates.

2 THE DAMAGED CONDITION OF CRASH BARRIER WALLS ON EXISTING CITY BRIDGES IN HARBIN AND ANALYSIS OF THE MAIN CAUSES

Harbin city is located in the northeast of China, which has a relatively low temperature and large snowfall in winter. In the winter, in order to ensure the city traffic, a certain amount of deicing salt is often spread on partial areas of city bridges. Concrete damage is caused by the action of the deicing salts, such as concrete erosion, cracking, protection layer peeling, corrosion of reinforcement, and so on. Reinforced concrete crash barrier walls are the most vulnerable members of city bridges to frost and salt corrosion; in recent years; the phenomenon of damaged crash barrier walls has become common around the world, and this issue is also particularly prominent in Harbin city. According to an on-the-spot investigation into the current situation of the main reinforced concrete crash barrier walls on Harbin city bridges, which are of different ages, the current situation is shown in Figure 1. Among them, Figures 1 (a) and (b) are city bridges which have been in use for more than 20 years, while Figures (c)-(e) are city bridges which were built in the last 4 years. The Songhua River highway bridge was built in 1986. Certain carbonation and loosening has happened on the concrete surface, and the local protection layer has peeled off, aggregate has been exposed, and long cracks have appeared, shown in Figure (a). AnFa Bridge was built in the mid 1990's of last the century. For the reinforced concrete crash barrier wall's protective layer to peel off is common, and steel corrosion is very serious, as shown in Figure (b). Matsuura Bridge, built in 2010, has just been open for 3 years, and its concrete protective layer peeling off is serious, and there is generally exposed aggregate and multiple corrosion exposure, as shown in Figure (c). The "Wenchang" elevated overpass was built in 2010, and site inspection found that large area of the concrete protective layer is falling off, a large area of rebar in a partial region is exposed, and corrosion is serious, as shown in Figure (d). The Yangmingtan Bridge was built in 2011, and has just been in use for more than 2 years, a large area of the protective layer of concrete located at the mouth of the bridge has fallen off, and multiple re-bars are exposed to corrosion, as shown in Figure (e).

The field investigation found large areas of concrete cover having fallen off, honeycombing, aggregate exposure, exposed rebars, expansion appearing on most city bridge reinforced concrete crash barrier walls, and rebar corrosion that is very serious. The length of the concrete cover spalling zone stretches

(a) Reinforced concrete crash barrier walls on the Songhua River Highway Bridges (1986)

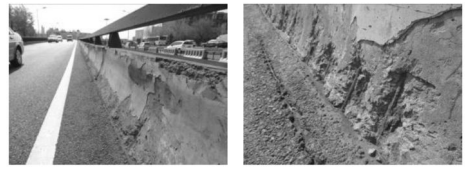

(b) Reinforced concrete crash barrier walls on An Fa Bridge (1990)

(c) Matsuura Bridge(2010)

(d) Wenchang elevated overpass(2010)

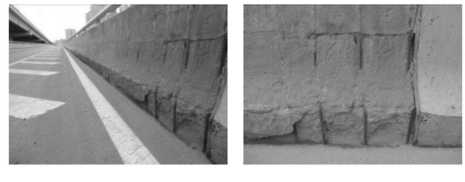

(e) Yangmingtan Bridge (2011)

Figure 1. The current situation of main reinforced concrete crash barrier walls on Harbin city bridges.

dozens of meters. The damaged situation of most reinforced concrete crash barrier walls on the city bridges appears at the entrance ramp position and the phenomenon of exposed tendons is serious. According to an appearance test, the main causes of the performance degradation of the reinforced concrete crash barrier walls on city bridges include the following three aspects: erosion due to deicing salts and the freezing and thawing of concrete, the lateral impact of snow clearing vehicles, and aggregate mortar segregation

Firstly, the erosion due to deicing salts and the freezing and thawing of concrete are the main causes of performance degradation. The snow-melting agent is a mix of chemicals, mainly divided into two class: potassium acetate and chloride according to its composition. The snow-melting effect of organic snow-melting agents that use potassium acetate as the main component is better and it has no corrosion damage. But the price is too high, so it generally used in such important places as airports. The price of inorganic snow-melting agents that uses "chloride salt" as the main ingredient is cheap for such products as sodium chloride, calcium chloride, magnesium chloride, potassium chloride and so on, which, only require the equivalent of 1/10 of organic deicer cost. Snow-melting agents applied to city bridges belong in this class and sodium chloride is predominantly used. But its corrosion on the infrastructure is very serious. Especially since the concrete currently in use on city bridges is generally ordinary performance concrete and their frost resistance performance is relatively low.

Secondly, the lateral impact of snow clearing vehicles leads to the premature loss of the concrete cover of the crash barrier walls. In 2006, in order to regulate the procedures of city road snow clearing, the Construction Department of Heilongjiang Province of China promulgated a local standard—the "city road snow specification," and the specification states clearly that the main effort of city road snow clearing should be focused on mechanized real-time snow clearing. At present, the general method of snow clearing work is that clearing vehicles clear the roads of snow rapidly to the base of the crash barrier walls on city bridges and shovel vehicles pile and remove it. In this process, impact friction between scraper buckets and the base of crash barrier walls cannot be avoided, and after the concrete of the crash barrier walls experiences some salt freezing cycles, its strength performance is degraded. This then leads to premature loss of the concrete cover due to this kind of impact friction effect.

Thirdly, according to the field survey, the aggregate accumulation in the lower region of concrete cash barrier walls is dense, causing the problem of the aggregate mortar segregation. This phenomenon is common in bridges which were built in the last 4 years. Aggregate accumulates at the base of crash barrier walls and is sparse at the top. Concrete segregation of crash barrier walls results in slurry insufficient in the lower area of the concrete, and the strength grade of concrete is reduced.

3 THE DESIGN OF REPAIR FOR REINFORCED CONCRETE CRASH BARRIER WALLS WITH FABRICATED UHPCC PROTECTIVE PLATES

3.1 *The basic conception of UHPCC protective plates*

In order to achieve the design goal of long-term protection and rapid repair for concrete crash barrier walls on city bridges, the repairing method of the tedious processes like maintenance and dismantling of formwork should be avoided, and a rapid repair plan of fabrication should be used. Ultra high performance cement-based composite material as a substrate to repair the collision wall shape and size as the benchmark, together with a preformed outsourcing plate, form the UHPCC protection plate. The protective plate is directly installed at the scene on the concrete crash barrier walls on bridges, and is fixed with expansion bolts. Its basic components are as shown in Figure 2.

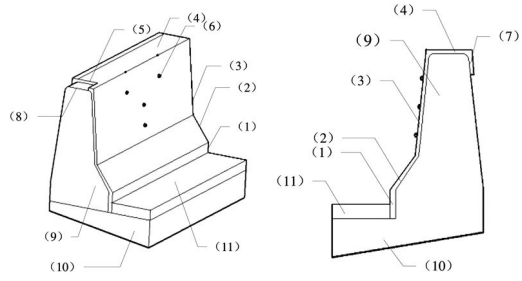

Figure 2. Schematic diagram of UHPCC protective plate.

The UHPCC protective plate geometry includes a vertical board (1), the slope plate (2) and (3), horizontal plate (4), reserved groove (5), reserved bolt holes (6), a vertical board (7), a reservation platform of upper arms or lighting (8), reinforced concrete crash barrier walls of the existing bridge (9), existing bridges load-bearing structure (10), and the bridge pavement surface layer (11). In order to meet the protective target, the design requirements of the size of beam section are that: the vertical section plate (1) thickness is not less than 25 mm, with a recommended thickness of 30 mm; the slope plate (2) using variable cross-section design, continuous uniform from the top at 15 mm to the bottom at 30mm; and the slope plate (3), horizontal plate (4), vertical board (7) have design thickness of 15 mm.

The lines of each component of the protective plate are determined according to the actual shape and anti-collision grade of the crash barrier walls. The anti-collision level is selected according to "highway traffic safety facilities code" (JTG D81) and "city bridge design code" (CJJ-2011). Take the F type reinforced concrete crash barrier walls used in project as an example, the geometric structure dimensions of the protective plate which corresponds to the anti-collision grade are shown in Figure 3 and Table 1.

3.2 *The aims and demands of UHPCC material performance*

In order to realize the protective requirements of the protective plates, the basic properties of the base material of UHPCC are proposed with the following design goals: a compressive strength of not less than 120 MPa,

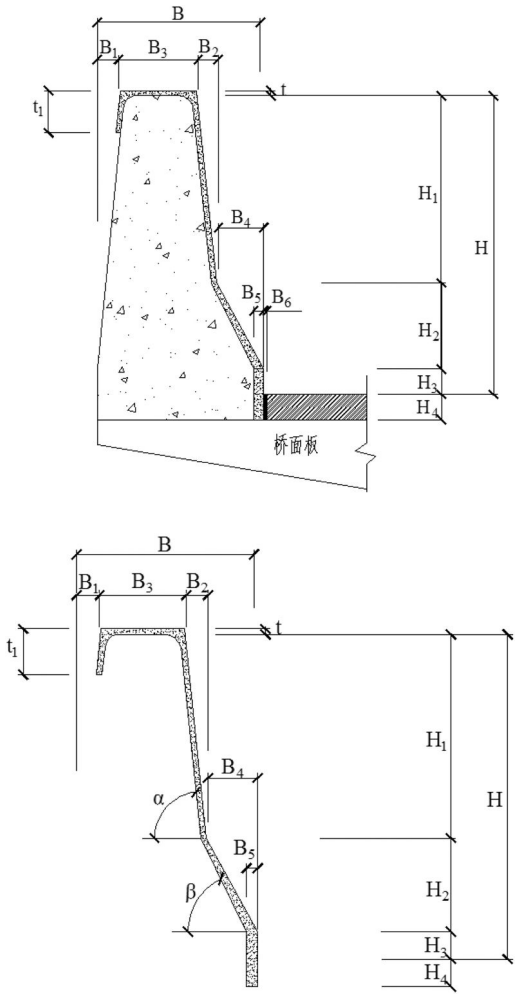

Figure 3. Geometry parameters of UHPCC protective plate.

Table 1. Geometry of UHPCC protective plate of F type concrete crash barrier walls (unit: mm).

Anti-collision grade	H	H_1	H_2	H_3	H_4	B	B_1
A, Am	810	555	180	75	75	464	81
SA, SAm	900	645	180	75	75	483	90
SB, SBm	1000	745	180	75	75	503	100

Anti-collision grade	B_2	B_3	B_4	B_5	t	t_1	t_2	α	β
A, Am	58	200	125	120	20	100	30	84	55
SA, SAm	68	200	125	120	20	100	30	84	55
SB, SBm	78	200	125	120	20	100	30	84	55

and flexural strength of not less than 18 MPa, modulus of elasticity of not less than 45 GPa, chloride ion penetration amount of not more than 40 Coul using the electric flux method, frost resistance of not less than F500, i.e. 500 freeze-thaw cycles. In order to achieve these performance objectives, the range of mix design is shown in Table 1; the raw materials include: cement, 425 Portland cement; silica fume, silica content, more than 90%; quartz powder , silica content more than 90%, fineness modulus of not less than 800 meshes; steel fiber with short fine steel fiber whose tensile strength shall not be less than 400 MPa, fiber length not less than 13 mm, diameter is not greater than 0.5 mm; water reducing agent, the solid content of the super plasticiser is more than 30%; and the water is tap water. According to the performance target, the basic mixing ratio design of materials are as shown in Table 2.

Table 2. Mix design of ultra high performance cement-based composite materials for protective plate (kg/m^3).

Cement	Silica fume	Quartz powder	Quartz sand	Steel fiber
750–800	150–250	200–250	800–900	50–100

Water reducing agent	Water	Antifoaming agents	Expanding agent
20–30	150–250	3.5–4	3.5–4

3.3 *The material mixing and the installation technology of protective plate*

In order to achieve the protective performance of the protective plates, material with special mixing curing process, site preparation and the installation process of the protective plates are shown in Figure 4. The size of the expansion bolts and preformed hole (6) diameter should be matched, with the diameter of expansion bolts being not less than 8 mm.

4 CONCLUSIONS

This paper conducts an on-the-spot investigation on the current situation of reinforced concrete crash barrier walls on Harbin city bridges, which are of different ages. The results of the investigation show that the concrete cover of reinforced concrete crash barrier walls peeling off is common and rebar corrosion is serious. Especially for bridges built in the last 4 years, the concrete cover of the reinforced concrete crash barrier walls falling off is very serious, significantly reducing their protection grade, and the prevalence of this phenomenon is increasing.

In order to meet the rapid repair target of concrete crash barrier walls on city bridges, this paper puts forward a design concept of fabricated protective plates based on UHPCC and gives their design. The basic requirements of performance target design, material mixing and the process of the installation

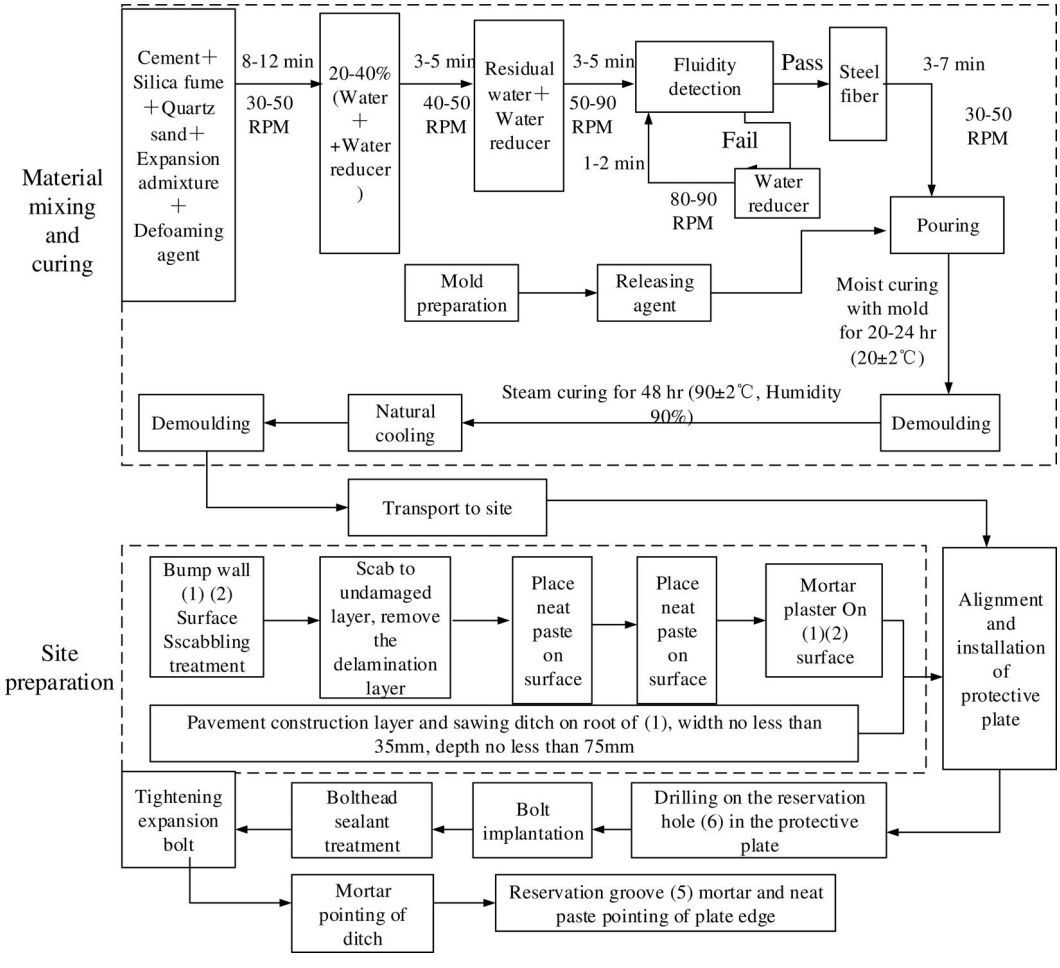

Figure 4. Material mixing and the process of the installation technology on protective plate.

technology of the protective plates is given. Compared with the current field reinforcing treatment with all kinds of composite material, the fabricated protective plate repair is faster and is not easy to disengage. Its long-term protective performance can be guaranteed.

ACKNOWLEDGEMENT

The authors would like to thank the China National Natural Science Fund (51008088), the fundamental Research Funds for the Central Universities (Grant No. HIT. NSRIF. 2013112), the project sponsored by Harbin city science and technology innovation talents special funds (2011RFLXG014), and Heilongjiang Province Natural Science Fund (E200911) for providing funding to this project, the Scientific Technical Plan of The Ministry of Housing and Urban-Rural Development of China (2010-K2-23), and the Science and Technology project of the Education Department of Heilongjiang Province for their support of the authors' work described herein.

REFERENCES

Kim, Y. Y.et al. 2014. Flexural performance of reinforced concrete beams strengthened with strain-hardening cementitious composite and high strength reinforcing steel bar. *Composites*: Part B 56: 512–519.

Moreillon, L & Menétrey, P. 2013. Rehabilitation and strengthening of existing RC structures with UHPFRC: various applications. *Proceedings of the RILEM-fib-AFGC International Symposium on Ultra-High Performance Fibre-Reinforced Concrete*: 127–136, Marseille, France, Oct. 1–3.

Oesterlee, C. et al. 2007. UHPFRC protection layer on the crash barrier walls of a bridge. *Advances in Construction Materials 2007*: 203–210, Springer Berlin Heidelberg New York.

Reinhardt, H.W. & Naaman, A.E. 1991. High performance fiber reinforced cement composites: workshop summary, evaluation, and recommendations. *Proceedings of the International Workshop 'High Performance*

Fiber Reinforced Cement Composites': 551–558. Mainz, June 23–26.

Song,P.S. &Hwang,S. 2004. Mechanical properties of high-strength steel fiber-reinforced concrete. *Constr. Build. Mater.* 18 (9): 669–673.

Wu, X.G. et al. 2008. Pseudo strain hardening model of ultra high performance cementitious composites under flexural loading. *Acta Materiae Compositae Sinica*, 25(2): 129–134.

Wu, X.G. et al. 2012. Structural analysis of circular UHPCC form hybrid pier under construction loads". Steel and Composite Structures.*An International Journal*, 12(2): 167–181.

Wu, X.G. & Han, S.M. 2010. Interface shear connection analysis of Ultrahigh-Performance fiber-Reinforced concrete composite girders.*J. of Bridge Engineering(ASCE)*, 15(5): 493–502.

Insitu strength assessment

This page intentionally left blank

Concrete Solutions – Grantham et al. (Eds)
© 2014 Taylor & Francis Group, London, ISBN 978-1-138-02708-4

Improved artificial neural network prediction of concrete strength based on non-destructive test results

O.V. Antonio & A. Jaurigue
University of the Philippines – Diliman, Quezon City, Philippines

ABSTRACT: Non-destructive tests have gained popularity in the testing of concrete strength because of their practicality and ease of use. However, modeling the correlation between them has remained inaccurate. A prediction system for the compressive strength of concrete from physical parameters and non-destructive test (NDT) results was made using artificial neural network (ANN) modeling. Tests for determining the ideal ANN properties and learning algorithms were done on different data sets with varying input parameters in order to determine the most accurate ANN model. These tests have shown that ANN modeling can be used as a prediction system for concrete strength. This study also investigated the effects of statistical processing such as data imputation and outlier removal to the ANN performance. It was shown that the use of these techniques improved the accuracy and robustness of the ANN model. The ANN model was also compared to traditional regression models and it demonstrated that ANN provided more accurate prediction of concrete strength.

1 INTRODUCTION

1.1 *Background of the study*

Compressive strength, the basis of design of concrete members in different structures, is the most important characteristic of concrete. Acquiring the value of strength is typically done using destructive tests. These tests, however, are difficult and costly to do in practice because of the need to destroy the sample (Cannas, 2007).

The traditional destructive strength of concrete is usually acquired using the uniaxial compressive strength (UCS) test which records the force that brings a sample to the point of crushing. It is a direct way of getting compressive strength and is the basis of concrete structure design (ACI, 2002).

Non-destructive tests (NDT) such as the Ultrasonic Pulse Velocity (UPV) and the Schmidt's Rebound Hammer (SRH) tests have been shown to have a strong correlation with compressive strength. Unlike destructive testing, NDTs can be done while keeping the concrete sample undamaged (Kou, 2009). However, results from these tests have not been accurate enough to make them the standard in determining concrete strength. In addition, calibration curves must be developed in order to use the results of the UPV and SRH tests. Multiple regression methods are then employed to relate all parameters of concrete strength. This involves restructuring whenever new data or parameters are added to the calibration data (Bilgehan, 2010).

Artificial neural networks (ANN) are data processing models that relate a set of output parameters to a set of input parameters. Unlike regression models, ANNs can be re-trained with the same model when new data or new parameters are added to it (Bilgehan, 2010). In addition, they give more accurate results and have a faster computation time.

This study mainly focused on making a system that predicts compressive strength using pulse velocity, rebound number, mix proportioning and age. The prediction system was created using ANNs. The best model was determined and subsequently compared with other published correlation curves from multiple regression analysis.

This study aimed to design an ANN model that can predict the compressive strength of concrete using the results of select published NDT results. ANN models with varying algorithms, architectures, activation functions, learning rates, and momentums were trained from the gathered data sets and were tested to determine the most accurate model.

The effect of different statistical pre-processing procedures to the data sets on the ANN performance was also investigated. The final ANN models were tested on how they performed in predicting concrete strength when different sets of input parameters were used. The final set of ANN systems were also compared to regression analysis and to the models of previously done researches.

NDTs, being more economical than destructive tests, have been used to approximate the compressive strength of concrete. However, they are not standard methods for measuring compressive strength because the results are not accurate enough (Basri, 2009). A more accurate model using ANN in the use of NDT for assessing concrete structures was then provided in this study.

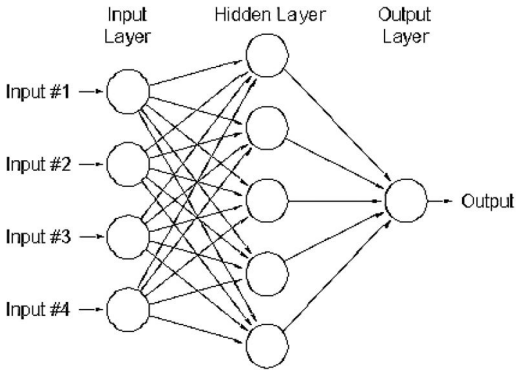

Figure 1. Schematic diagram of an ANN.

This study investigated the best ANN models that produced prediction systems capable of handling different sets of input parameters. Thus, compressive strength can now be determined even when certain data are unavailable to the evaluator. The effects of different learning algorithms and network properties to the performance of the ANN were also studied to determine the best model for future works. The effect of different statistical data pre-processing was also investigated to further improve the performance of the ANN.

1.2 *Artificial Neural Networks (ANN)*

Artificial neural networks are computer systems that simulate how the human brain works. This study used a multiple layer feed forward back-propagation network as shown in Figure 1. An ANN model is made up of Input Layer, Hidden Layer, and Output Layer. Each individual input parameter of the model is represented by a neuron in the Input Layer. These neurons are then individually connected to different neurons in the Hidden layer (this layer can be composed of several sublayers) where the computation of the model is done. In this layer, the neurons contain weights that are multiplied to the values that the neurons receive from the neurons of the previous layer. These neurons will continuously pass the value to the next layer until the output layer is reached. This layer contains the neuron associated to modeled compressive strength of the data set. If there is a large error between the model output and the actual results, the error is back propagated using a learning algorithm to adjust the weights of the network. This is repeated until an accurate model is created.

Several factors or parameters need to be considered when training an ANN model. One of these is the architecture of the network. This refers to the number of hidden layers and number of hidden neurons per layer. This provides the ability of the network to solve multi-dimensional problems. Another parameter is the activation function which is the function that the hidden neurons use to compute for their output. This provides the non-linearity of the ANN model. Learning rate and momentum are also ANN parameters used by the learning algorithms to determine the size of weight adjustment done from the error.

1.3 *Scope and limitations*

The data used in this study were from laboratory concrete samples that used ordinary Portland cement and normal weight aggregates without any admixtures. Cylindrical strength (150 × 300 mm) was used in this study, with the strengths of cubic samples converted using published conversion methods. This study only used data on compressive strength, rebound number and pulse velocity measured using ASTM standards.

The ANN only used the supervised back propagation algorithm for its training phase. The network parameters investigated were learning algorithms, architecture, learning rate and momentum. Different combinations of data sets and input parameters were used to train the ANN. This included a set containing zero values for missing data and another set that had its missing values assigned using multiple imputation statistical methods.

2 METHODOLOGY

2.1 *Data gathering*

The data for this study were acquired from previous studies with data sets relating the compressive strength, acquired from uniaxial compressive strength (UCS), to the results of rebound hammer and ultrasonic pulse velocity tests. Data for the age of curing and mix proportioning were also included. The data used contained missing data for some input parameters. The test specimens were standard laboratory concrete samples, either cylindrical (150 × 300 mm) or cubic (150 mm) in shape. The cubic compressive strength were normalized to their corresponding cylindrical counterpart using the L' Hermite equation. The destructive and non-destructive tests were also done using the standard procedures defined in ASTM. The final data set was divided into twelve (12) different data sets containing varying input parameters.

2.2 *Data pre-processing*

The first processing done was data imputation to determine the statistically correct guess for the missing parameters in the complete data set. Data imputation was done on the complete data set to acquire values for the missing data using the S-Plus software.

Each data set was randomly sub-grouped into their training, validation and testing data for the ANN model to be created. These sub-groups followed a 60:15:25 proportioning for the training, validation and test data respectively.

A multivariate outlier algorithm based on the Mahalanobis distance was used to remove the outliers from the data sets. This was done in Matlab using the Multivariate Outlier add-in function. The training,

validation and testing data of each data set was given to the outlier algorithm separately producing processed data sets.

The ANN requires values that are normalized to have values within the range of 0 to 1. This study used the minimum-maximum linear procedure to normalize the data sets. This means that the minimum and maximum of each parameter is acquired and used to scale down the values linearly.

2.3 *Programming of learning algorithms*

Eight learning algorithms were programmed in C language for the training of the ANN models. The algorithms were the Gradient Descent (Batch), Gradient Descent (Stochastic), Gradient Descent with Momentum (Batch), Gradient Descent with Momentum (Stochastic), Quick Propagation, Resilient Propagation, iResilient Propagation and Levenberg-Marquardt Algorithm.

The training starts with an ANN model with all of the ANN parameters given for the program. The program then ran the chosen learning algorithm on the training data for 5000 epochs while minimizing the mean square error (MSE) of the network. The validation data set was also inputted to the ANN but only to assess the performance of the network during each epoch. The resulting ANN model is the network with the minimum MSE for the validation data.

2.4 *Test for ANN parameters*

The activation function was the first to be tested to find which is ideal for each particular combination of data set (both processed and unprocessed) and algorithm. Seven different activation functions were tested namely: sigmoid, bi-sigmoid, tanh, Gaussian, bi-Gaussian, linear and logarithmic. The each data set was trained using each algorithm with varying activation functions but constant architecture, learning rate and momentum.

The ideal activation functions for each combination of data set (both processed and unprocessed) and algorithm was used for the test for the ideal architecture. The initial architectures for all runs were pre-determined with initial values for the weights as random values between -0.5 to 0.5.

3 – Layered Architecture
N [Input Layer] – M [1st Hidden Layer] – 1 [Output Layer]

4 – Layered Architecture
N [Input Layer] – M [1st Hidden Layer] – M [2nd Hidden Layer] – 1 [Output Layer]

where N = number of input parameters; M = number of neurons which varies from N to $(N+2)$ for Levenberg-Marquardt Algorithm, varies from N to $(N+4)$ for all other algorithms.

Tests for the learning rate and momentum were done on the algorithms that needed them. The learning rate was done first then the momentum. The values considered for this test were 0.05 to 0.95 for both learning rate and momentum at 0.05 steps.

2.5 *Statistical testing*

The final training of the ANN for each combination of processed and unprocessed data sets and algorithm were done using the ANN parameters acquired from the tests done earlier. The ANN model that resulted from this training was then ran with the test data to conduct statistical analysis on the performance of the ANN using the root mean square error (RMSE), average absolute error (AAE), average absolute relative error (AARE) and coefficient of determination (R^2). The results of the test data are then used to determine the most accurate algorithm.

2.6 *Sensitivity analysis*

Sensitivity analysis was done on the final ANN models of the data sets. This test was conducted on the imputed data set and the data set with missing values to see how the missing data affects the performance of the resulting ANN model. This was done on the data set with all parameters present to check if there are parameters that can be removed to simplify the ANN further. It was also done to see the relative strength of effect of each parameter to the ANN's output.

2.7 *Regression analysis*

The regression analysis was conducted using the software Minitab 16 with the confidence interval of 0.05. This was conducted on each of the data sets producing one equation per data set. These were then statistically tested using the RMSE, AAE, AARE and R^2. These values were then compared with that of the final ANN models produced to determine which fit the data sets better.

3 RESULT AND DISCUSSIONS

All of the raw data coming from the sources that complied with the standards previously discussed were compiled. These were then arranged and grouped together into twelve (12) clusters depending on the available input parameters as shown in Table 1. The original raw data set, labeled as "All w/o", was passed through data imputation process to replace the missing values for the different input parameters. This new data set is labeled as "All w/". The resulting unprocessed data sets were further divided into the training, validation and testing data.

The multivariate outlier removal algorithm using the Mahalanobis distance was used on each sub-group of the data sets. A confidence interval of 5% has been used for the outlier algorithm. The results of this algorithm were tabulated in Table 2.

Table 1. Groupings of unprocessed data.

	Input Parameters	# of Data	Code
1	UPV + RN + W/C + CA/C + FA/C + AGE UPV + RN + W/C + CA/C + FA/C + AGE	463	ALL Para
2	UPV + RN + AGE	481	URA
3	UPV + W/C + CA/C + FA/C + AGE	922	UAM
4	RN + W/C + CA/C + FA/C + AGE	463	RAM
5	UPV + AGE	940	UA
6	RN + AGE	481	RA
7	W/C + CA/C + FA/C + AGE	1180	MA
8	UPV + RN	481	UR
9	UPV	940	U
10	RN	481	R
11	All of data without Data Imputation	1198	All w/o
12	All of data with Data Imputation	1198	All w/

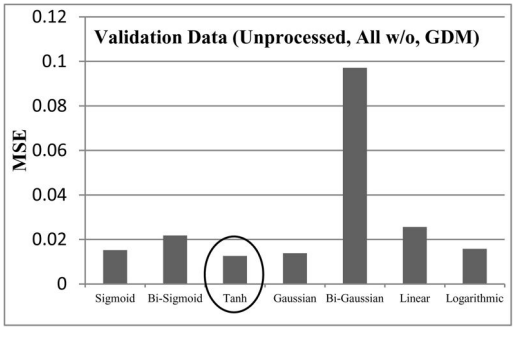

Figure 2. Sample test for ideal activation function.

The test for the ideal activation function was done first using both the processed and unprocessed data sets. An example of the results of these tests can be seen in Figure 2. These were results from unprocessed validation data of the "All w/o" data set using the gradient descent with momentum (GDM) algorithm. For this specific run, it can be seen that the ideal activation function was the "tanh". Also, the best architecture was found to be the "6-7-7-1" with the learning rate of 0.6 and momentum of 0.25.

The final training for the ANN with the unprocessed and processed data sets using all of the algorithms was done using the ideal ANN parameters determined in the tests. These values were then used to compare the algorithms for each data set to determine what algorithm performed best. The LMA was the generally the most accurate algorithm but there were times that the LMA was out-performed by other algorithms.

The removal of the outliers from the data sets have allowed for a better performing ANN model than the ones that had outliers in them (Figure 3). This was the expected results as intuitively, a data set that has outliers should perform worse than the ones without outliers. There were however a few data sets that the

Table 2. Training, validation and testing data of processed data.

Data Set	Train	Validation	Test	Total	No. of Outliers
ALL Para	253	105	63	421	42
URA	267	110	66	443	38
UAM	527	218	130	875	47
RAM	255	105	63	423	40
UA	541	224	135	900	40
RA	269	110	66	445	36
MA	680	283	165	1128	52
UR	266	109	66	441	40
U	540	226	134	900	40
R	268	110	66	444	37
All w/o	692	287	173	1152	46
All w/	688	287	172	1147	51

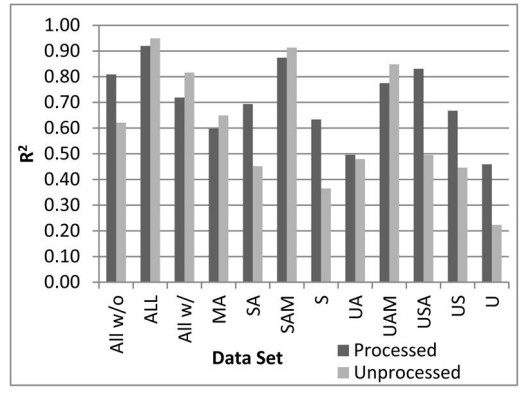

Figure 3. Resulting coefficient of determination of unprocessed vs. processed data sets.

Table 3. Most accurate ANN models.

Data Set	R^2	
ALL	0.949	Unprocessed
SAM	0.913	Unprocessed
UAM	0.848	Unprocessed
USA	0.821	Processed
All w/	0.816	Unprocessed
All w/o	0.812	Processed
US	0.796	Processed
MA	0.733	Processed
SA	0.680	Processed
S	0.663	Processed
UA	0.479	Unprocessed
U	0.457	Processed

ANN was able to learn better when the outliers were not removed. This can be explained by the existence of an ideal amount of algorithms to get the most accurate ANN model as seen in the paper of Jim et al. (1996). The final ANN models were compiled in Table 3.

Sensitivity analysis was conducted on the ALL, All w/o and All w/ data sets. The results for the ALL data set showed that the ANN model was sensitive to all of

Table 4. Results of regression analysis for processed data sets.

	θ_1	θ_2	θ_3	θ_4	θ_5	θ_6	θ_7
All w/o	−18.86	3.05E-07	−0.0018	13.19	−1.22	−1.57	4.05
ALL	−16.88	1.08E-06	0.0090	8.86	−12.66	−6.50	0.62
All w/	−11.26	−2.47E-08	0.0042	8.05	2.66	4.00	3.78
MA	−18.63	0	0	12.39	0.31	1.23	5.16
RA	7.26	0	0.0146	0	0	0	1.50
RAM	0.72	0	0.0116	5.86	−16.08	3.75	1.59
R	9.69	0	0.0174	0	0	0	0
UA	−6.51	1.27E-06	0	0	0	0	2.03
UAM	−26.12	8.67E-07	0	11.85	1.57	−2.52	3.39
URA	−6.03	9.28E-07	0.0125	0	0	0	0.65
UR	−5.66	9.75E-07	0.0134	0	0	0	0
U	0.16	1.26E-06	0	0	0	0	0

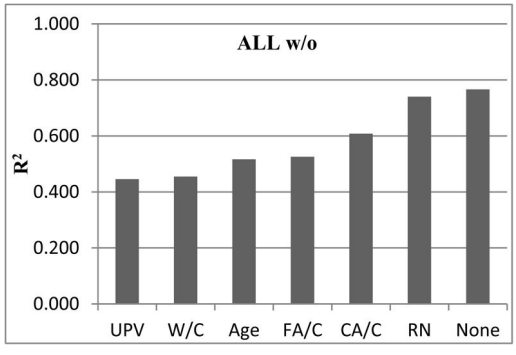

Figure 4. Results of sensitivity analysis on All w/o data set.

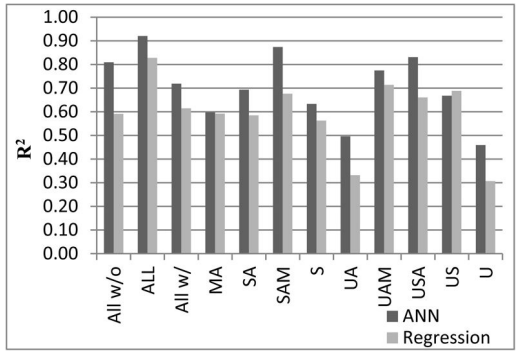

Figure 5. Comparison of ANN and Regression models for processed data.

the input parameters which meant that no parameter could be removed.

The sensitivity analysis of the All w/o data (Figure 4) showed that the ANN model was skewed being more sensitive to the UPV and mix proportioning with the rebound number having no effect to the ANN. The analysis of the imputed data showed a more robust ANN performance was sensitive to all input parameters. This means that the skewed ANN performance shown in All w/o was not seen in All w/ data set.

Regression analysis was done on the processed and unprocessed data sets. The general model used for the multivariate non-linear regression analysis can be seen in Equation 1. The values of the unknown coefficients were determined using the built-in function of Newton algorithm of Minitab 16.

$$UCS = \theta_1 + \theta_2 UPV^2 + \theta_3 RN^2 + \frac{\theta_4}{\frac{W}{C}} + \frac{\theta_5}{\frac{CA}{C}} + \frac{\theta_6}{\frac{FA}{C}} + \theta_7 \ln(Age)$$

Equation 1. General regression model.

The statistical analysis has shown that the ANN model generally performed better than the regression models. As shown in Figure 5, the processed data sets were modeled more accurately by the ANN model than the regression model.

4 CONCLUSIONS

This study has shown that ANN models can be used as a prediction system for the compressive strength of concrete from physical parameters and non-destructive tests results. It has also been demonstrated in this study that the function approximation problem warrants the investigation for the best ANN parameters for a specific problem. There exists an ideal set of activation function, architecture, learning rate and momentum for every different data set and learning algorithm. Arbitrary values and configurations for these parameters would not yield the most accurate ANN model.

This study has also confirmed that the best algorithm to be used for training of ANN models was the Levenberg-Marquardt algorithm. If the resulting network from this algorithm would not be sufficient, investigating the use of other algorithms would be suggested.

Another conclusion of this study was the effect of outliers to ANN performance. It has been shown that noise reduction generally increases the accuracy of the ANN. There were data sets that yielded better results when the outliers were kept. This paper has suggested

a possible explanation for this issue from the study of Jim et al. (1996).

It has also been shown that the data imputation provides a way of handling the case of missing data. Training the ANN model with imputed data set makes it an accurate and robust model. The basic case of training the network with missing data has been shown to provide misleading results as they produce more accurate prediction than the imputed data but having a skewed modeling of the problem.

Finally, this study confirms the works of other authors that the ANN modeling can be used as a more accurate alternative to the traditional regression method. The use of the ANN would be governed by the data that would be available to the user. It has been shown that when more parameters can be introduced to the ANN, the better its performance. The more practical method of using NDT results has also been shown to accurately predict concrete strength.

REFERENCES

American Concrete Institute (2002). *ACI C211.* Standard Practice for Selecting Proportions for Normal, Heavyweight and Mass Concrete. ACI.

Basri, H.B., Jamil, M., Zain, M.F.M. (2009). Neural network simulator model for optimization in high performance concrete mix design. European *Journal of Scientific Research***.** *Vol. 34.* January. EuroJournals Publishing Inc. Mahe, Seychelles. pp. 61–68.

Bilgehan, M., Turgut, P. (2010). Artificial neural network approach to predict compressive strength of concrete through ultrasonic pulse velocity. *Research in Nondestructive Evaluation. Vol. 21.* January. Taylor & Francis. London, UK. pp. 1–17.

Cannas B., Carcangiu S., Cau, F., Fanni, A., Montisci, A., Testoni, P., (2007). Artificial neural networks for non-destructive testing of concrete structures. Proc. of the 10th Int. Conf. on Engineering Applications of Neural Network. Vol 1. August. *Engineering Applications of Neural Networks.* Thessaloniki, Greece. pp. 29–31.

Giles, CL., Jim, KC., Horne, BG. (1995). Effects of noise on convergence and generalization in recurrent networks. *Neural Information Processing Systems. Vol 7.* pp. 649–660.

Greepala, V., Nimityongskul, P., Parichatprecha, R., Sayamipuk, S. (2007). Prediction of in situ concrete compressive strength using non-destructive test data and artificial neural networks. *3rd Annual Concrete Conference.* Pattaya, Thailand.

Kou, C. H., Liu, J. C., Sue, M. L. (2009). Estimating the Strength of Concrete using Surface Rebound Value and Design Parameters of Concrete Material. *Tamkang Journal of Science and Engineering. Vol. 12(1).* February. Tamkang University. New Taipei City, Taiwan. pp. 1–7.

Concrete Solutions – Grantham et al. (Eds)
© 2014 Taylor & Francis Group, London, ISBN 978-1-138-02708-4

Local concrete characterization assessment by the means of non-destructive tests (NDT) methods

L. Belagraa & A. Bouzid
Laboratory of Materials and Electronic Systems, Faculty of Sciences and Technology, B B Arreridj University, Algeria

N. Logzit & N. Badache
Department of civil Engineering, Faculty of Sciences and Technology, B B Arreridj University, Algeria

A. Belguendouz
Department of civil Engineering, Faculty of civil Engineering, Houari Boumedienne University, Algiers, Algeria

ABSTRACT: The physical and mechanical properties of concrete are depend mainly on the quality of materials, technologies and conditions of placement. The evaluation of the quality of concrete is fundamental in regard to the number and diversity of projects made by this material. Although it is not possible to make a direct measurement of the strength of concrete or other properties of a project by direct compressive test; several Non-Destructive Test methods (NDT) have been developed in order to assess and characterize the properties of concrete on site, including the ultrasonic velocity and rebound hammer tests.

The present work presents an experimental evaluation of the physical and mechanical properties of an ordinary concrete based on local materials from the region of Bordj Bou Arréridj (250 Km from Algiers). The parameters taken into account are the resistance of concrete beside the grading type, continuous (C_c) and gap graded (C_d) for based coarse aggregate concretes.

The results of this study provide correlations between the various measures and exhibit the impact of these parameters for the correlations observed, comparisons were made between the correlations proposed in this study with some existing correlations in the literature to see the placement conditions and local materials influence on measured values by such methods in the case of ordinary concrete with acceptable conventional strength less than 40 MPa at the age of 28 days.

Keywords: Concrete, physical and mechanical properties, Non-Destructive Testing (NDT), correlation.

1 INTRODUCTION

The method used so often to assess the quality of the concrete is the compression test: this is practiced on specimens made at the same time as the concrete is cast on the structure site. The results of this method are not obtained immediately because the concrete specimens might be different to the insitu concrete (sampling error), also the method of treatment, compaction and execution conditions in situ could not be compared to the carefully monitoring conditions mobilized at the laboratory. Further, the concrete strength also depends on the dimensions of the specimens, their shape and conditions for the conduct of testing (Toukal 2010; Hannachi & Guetteche 2012).

To avoid the drawbacks of direct test methods, in situ tests called non-destructive testing (NDT) have been developed, where the structure can be controlled without modifying either its performance or its appearance in a rapid and simple way. The NDT tests themselves are based on the fact that some measured physical properties of the concrete, can be related to the mechanical strength or other physical characteristics (Toukal 2010).

The combined testing techniques of NDT methods improve the reliability of assessment for the concrete mechanical strength property. The principle is based on correlations between the observed measurements and the desired property (Hannachi & Guetteche 2012; Fiesta & Dreux 2007; Bungey & Millard 1996; Breysse 2008).

In recent decades, numerous studies have developed theoretical models to observed relationships between NDT and physico-mechanical properties of concrete such as the strength, the dynamic elastic modulus, the density, the porosity and the permeability (Hannachi & Guetteche 2012; Kheder & al 2003; Nash't et al 2005; Turgut & Kucuk 2006; Rojas & al 2012). Some research works are based on the relationship between (NDT) and the characteristics of the cement paste, as

Table 1. Physical and mechanical characteristics of aggregates.

Fraction	γ (Kg/m^3)	ρ (Kg/m^3)	L_A (%)	A (%)
0/5	1558	2514	–	17,65
3/8	1338	2593	21	02,25
8/15	1419	2564	20,74	01,42
15/25	1437	2586	21	01,01

the W/C ratio, changes in hydration process and size of aggregates (Panzera et al 2011). In the same study framework, several correlations, linear and nonlinear, have been proposed by many authors based on statistical studies (Hannachi & Guetteche 2012; Kheder & al 2003; Nash & al 2005; Turgut & Kucuk 2006; Rojas & al 2012; Panzera et al 2011).

In light of these studies, the present research aims to assess the physical properties (density and rate of absorption) and mechanical ones (strength and dynamic modulus of elasticity) of a concrete made of local materials by the means of such NDT methods, as rebound hammer number (Is) and ultrasonic velocity (V) measured values. Further, the influence of the grading types (Continuous and gap graded) as well as the concrete grade on the correlations found are considered in the present study.

2 EXPERIMENTAL STUDY

2.1 *Materials*

The concrete is considered as an ordinary type prepared with CPJ Portland cement CEMII/B 42.5 MPa delivered by Hammam Dalaa cement factory wilaya M'sila (250 Km East of Algiers). Crushed limestone aggregates with a maximum size of 25 mm were used for this experimental program together with the siliceous sand of dune (0/5) as the granular fine aggregate fraction; having a fineness modulus $M_f = 1.94$ and the sand equivalent modulus E_{SV} equal to 65%. Table 1 presents some physical and mechanical properties of aggregates used in this experimental study.

2.2 *Mixtures and Testing*

The mixtures of continuously graded concretes (C_c) beside the gap graded (C_d) have been made under the following conditions. Concrete formulations studied were prepared by the method of absolute volumes; quantities of materials are presented in tables 2 & 3.

Five concrete grades 20, 25, 30, 35 and 40 MPa were chosen for the test program to treat the maximum possible situations encountered in the practice on site. A second parameter, also set along with the concrete grade was the type of grading. Sixty cylindrical specimens (100×200) mm^3 with granular fractions (8/15) and (15/25) for the case of the gap graded concretes (C_d) were cast (Table 2).

Table 2. Concrete mixtures of gap-graded types (C^d), quantities for 1 cubic meter in (Kg/m^3).

Grade	Cement	Water total	W/C eff	Coarse aggregate 8/15	Coarse aggregate 15/25	Sand
C_{d20}*	264	206	0.78	494	742	574
C_{d25}	305	206	0.68	487	730	558
C_{d30}	346	206	0.60	482	722	537
C_{d35}	386	206	0.53	478	717	513
C_{d40}	427	206	0.48	482	722	470

Table 3. Concrete mixtures of continuous graded types (Cc), quantities for 1 cubic meter in (Kg/m^3).

Grade	Cement	Water total	W/C eff	Coarse aggregate 3/18	Coarse aggregate 8/15	Coarse aggregate 15/25	Sand
C_{c20}**	264	206	0.78	371	284	581	574
C_{c25}	305	206	0.68	365	280	572	558
C_{c30}	346	206	0.60	361	277	566	537
C_{c35}	386	206	0.53	359	275	562	513
C_{c40}	427	206	0.48	361	277	566	470

* (d) Index indicates gap-graded type and (20) the grade of concrete.
** (c) Index indicates continuous graded type and (20) the grade of concrete.

A number of identical specimens were formulated based on granular fractions (3/8) (8/15) and (15/25) for the case of continuous grading mixtures (C_c) (Table 3).

Slump and air content tests were planned to determine the characteristics of fresh concrete according to European standards EN 12350-2 and EN 12350-7, respectively.

After calibrating the equipment, testing on hardened concrete (ultrasonic test, rebound test hammer and compression test) were performed on specimens at the age of 7, 14 and 28 days in respect of the European standards recommendations EN 12504-2, EN 12504-4 and EN 12390-4, respectively.

The absorption was taken into account at 28 days of age in accordance with the European standard EN 1097.

3 RESULTS ANALYSIS

The results of tests on cylindrical specimens of concrete (ultrasonic, rebound hammer and compressive test) are summarized in Tables 4 and 5.

3.1 *Mechanical properties correlations*

3.1.1 *Compressive strength (Rc) as a function of the velocity (V)*

The use of granular fraction (3/8) in the composition of the concrete gave favorable results for the resistance to compression. Concrete continuous grading

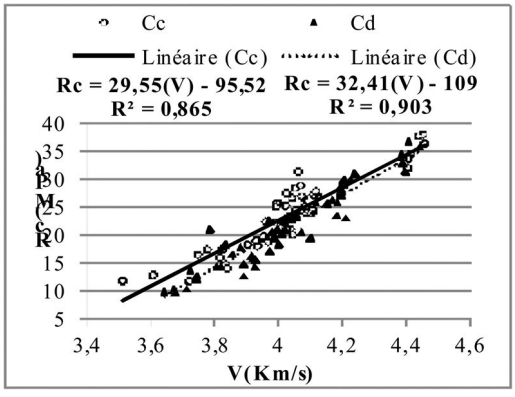

Figure 1. Correlation of compressive strength (Rc) and pulse velocity (V).

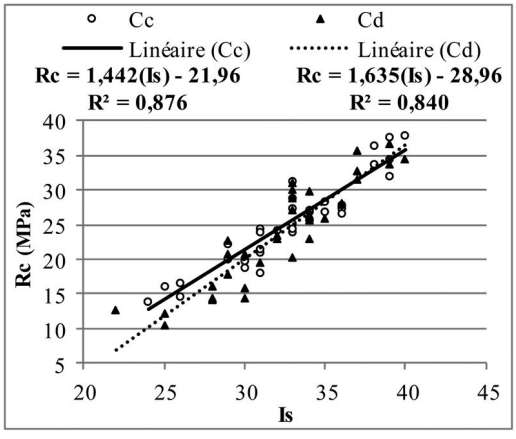

Figure 2. Correlation of compressive strength (Rc) and rebound hammer number (Is).

types (C_c) present a higher strengths than those of gap grading (C_d), which is justified by the speed recorded by ultrasonic velocity tests. Figure 1 also, shows the change in velocity depending on the strength values of the concrete where there is a proportional relationship between these two variables.

Previous research by Hannachi & Guetteche (2012); Boudina & Louradi (2012) proposed linear correlations between the compressive strength and the ultrasonic velocity as: $Rc = a\ (V) + b$). Other researchers propose an exponential correlations as : $Rc = Ae^{(bV)}$ (Nash & al 2005: Turgut & Kucuk 2006, Panzera et al 2011).

The results of experimental tests on (Cc) and (Cd) concrete mixtures of the present study allowed us to draw the regressions summarized in Figure 1 and establish the following linear correlation;

In the case of continuous grading (C_c):

$Rc = -95.52 + 29.55\ (V)$ (01)

With; $3.5 \leq V \leq 4.5$ (Km / s)

$R^2 = 0.865$

In the case of the gap grading (C_d):

$Rc = -109 + 32.41\ (V)$ (02)

With: $3.6 \leq V \leq 4.4$ (Km / s)

$R^2 = 0.903$

3.1.2 *Compression strength (Rc) as a function of the rebound hammer number (Is)*

According to table 4, while increasing the grade of concrete, one notices higher rebound number values (Is) as in the case of the indirect ultrasonic test. Figure 2., shows also that the granularity has an impact on the predicted results, where the regression results of the envelope fitting curve for continuous concretes grading types (C_c) is located upper to that of the gap graded concretes (C_d) and with a correlation coefficients of $R^2\ (C_c) = 0.876$ and $R^2\ (C_d) = 0.840$).

Research works conducted on the correlation between compressive strength and rebound hammer number exhibit a linear relationship (Bungey 1989; Neville 1976; Boudina & Louradi 2012). The European standard EN-13791 gives an expression of this relationship in the form,

$Rc = -34.5 + 1.73\ (Is)$ with: $24 \leq Is \leq 50$ (03)

Rc is the initial value of the compression strength in MPa obtained from the curve of the rebound hammer test in the horizontal position.

Correlations obtained for grading types (Cc) and (Cd) in this study are similar to those proposed by the European standard EN-13791 with;

In the case of continuous grading (Cc):

$Rc = -21.96 + 1.442\ (Is)$ (04)

$R^2 = 0.876$

With: $26 \leq Is \leq 40$.

In the case of the gap grading (Cd):

$Rc = -28.96 + 1.635\ (Is)$ (05)

$R^2 = 0.840$

With: $24 \leq Is \leq 40$.

3.1.3 *Rc as a function of (V, Is) [combined method]*

Several studies show that the composition of the concrete, technical measures of placement, petrologic and shape properties of aggregates, significantly influence the results of non-destructive testing. To reduce errors and the reliability of these tests, combining two or more methods could be advantageous.

Figure 3 & 4, present (Rc) as a function of the ultrasonic velocity and rebound hammer number for both types of grading (Cd) and (Cc), respectively.

The combined method gives good correlations between the compressive strength and non-destructive testing this is justified by the correlation coefficients close to the unity, $R^2\ (Cd) = 0.9428$ and $R^2\ (Cc) = 0.9176$.

The comparison between adjustments of concretes tested (Fig. 3 & Fig. 4) shows that continuous grading concretes (C_C) exhibit a wide dispersion of

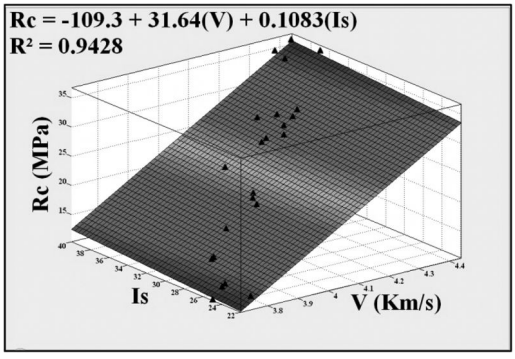

Figure 3. Correlation of compressive strength (Rc) ultrasonic velocity (V) and rebound hammer index (Ic) for concrete mixtures types (C_d).

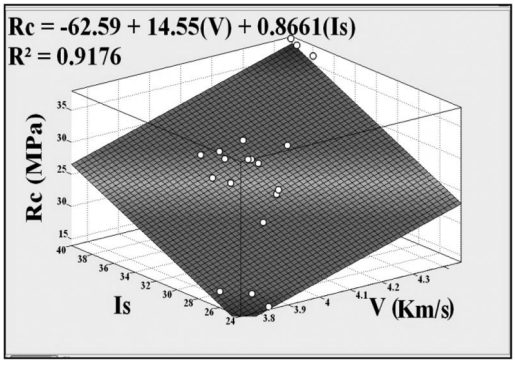

Figure 4. Correlation of compressive strength (Rc) ultrasonic velocity (v) and rebound hammer number (Ic) for (Cc) concrete mixtures types.

results compared to gap graded ones (C_d). Previous researches suggest polynomial correlations (Hannachi & Guetteche 2012) as:

$$Rc = a(V)b + (Is) + c$$

Correlations proposed for the present study case are:

(Cc): Rc = -62.59 + 14.55 (V) + 0.8861 (Is) (06)
$R^2 = 0.9176$

(Cd): Rc = -109.3 + 31.64 (V) + 0.1083 (Is) (07)
$R^2 = 0.9428$

3.1.4 *Elastic dynamic modulus(E_d) as a function of the velocity (V)*

The dynamic elastic modulus of concrete E_d depends on the specific modulus of its components (aggregates and cement paste).

The volume of aggregates is predominant, therefore the dynamic modulus of elasticity of the concrete is of advantage linked to the quality of the aggregates rather than the quality of cement paste (Bungey 1989; Munzer 1994).

It is observed according to Fig.5 that there is a strong correlation between (E_d) and ultrasonic velocity (V),

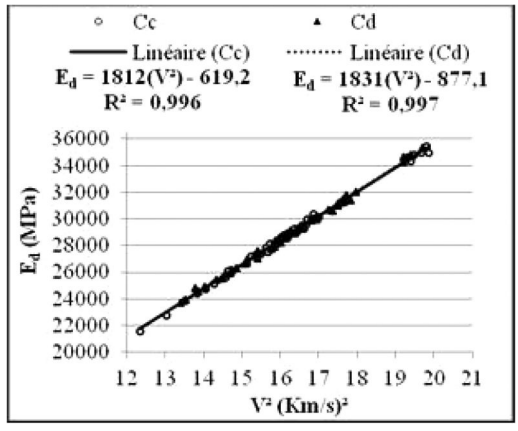

Figure 5. Correlation of elastic dynamic modulus (E_d) and ultrasonic velocity (V).

which is justified by the high correlation coefficients: (R^2 (Cc) = 0.996 and R^2 (Cd) = 0.997).

The grading type has not really a significant impact on the modulus E_d, the two regression lines for the two types of (C_c) and (C_d) are superimposed.

From the results obtained, the interrelation between the dynamic elasticity modulus of the concrete and the ultrasonic velocity offered to concretes (C_c) and (C_d) are of linear type, $E_d = a(V) + b$

For continuous grading (C_c):
$E_d = - 619.2 + 1812 (V^2)$ (09)
$R^2 = 0.996$

For gap grading (C_d):
$E_d = - 877.1 + 1831 (V^2)$ (10)
$R^2 = 0.997$

In the opposite side, many research works have found that the relationship between (E_d) and the ultrasonic velocity is not linear (Fiesta & Dreux 2007; Bungey 1989; Munzer 1994), the explanation of this contradiction is related to the extended class of resistance of concrete, while considering larger grades of the concrete they obtained correlation results showing non-linear relationships. However, the present work treated the case of ordinary concrete, with limited grades having strengths ranging from 20 to 40 MPa, only.

3.1.5 *Elastic dynamic modulus (E_d) as a function of rebound hammer number (Is)*

The rebound hammer is a test that provides information on local and superficial quality of concrete (Fiesta & Dreux 1998; Bungey 1989; Munzer 1994), the rebound number was compared to the dynamic elastic modulus of concrete, which is more evident in the case ultrasonic test.

Figure 6 shows the dynamic modulus of elasticity (E_d) as a function of the rebound hammer number. The scatter is slightly wider for rebound number, but it also gives us an indication of (E_d). According to

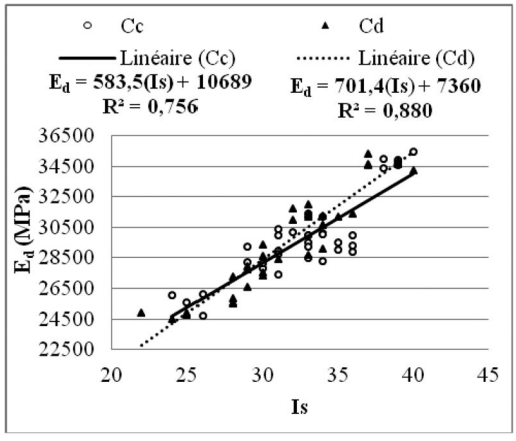

Figure 6. Correlation of elastic dynamic modulus and rebound hammer number (Is).

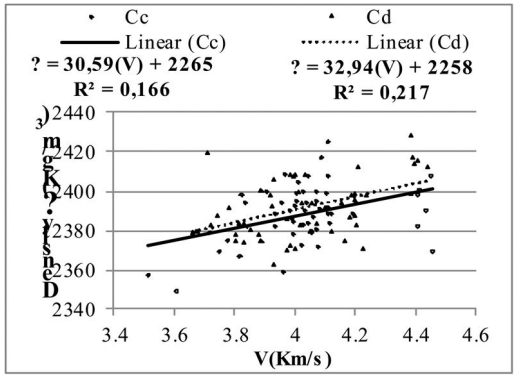

Figure 7. Correlation of density (γ) and ultrasonic velocity (V).

Figure 6 it can be seen that there is an impact of the grading type on the results of the rebound hammer test when evaluating the dynamic modulus of concrete. The concrete mixtures (C_c) give a wider dispersion than gap grading concretes (C_d), R^2 (C_c) = 0.756 and R^2 (Cd) = 0.880.

The correlations found from the experimental study gives linear relations for;

(C_c): Ed = 10689 + 583.5 (Is) (11)
R^2 = 0.756

(C_d): E_d = 7360 + 701.4 (Is) (12)
R^2 = 0.880

3.2 *Physical properties correlation*

3.2.1 *Density (γ) as a function of ultrasonic velocity (V)*

Density varies slightly from one plain concrete to another. In this study the values ranged from 2350 to 2430 Kg/m^3. So to determine the dynamic modulus of elasticity of concrete ultrasonic velocity must be firstly

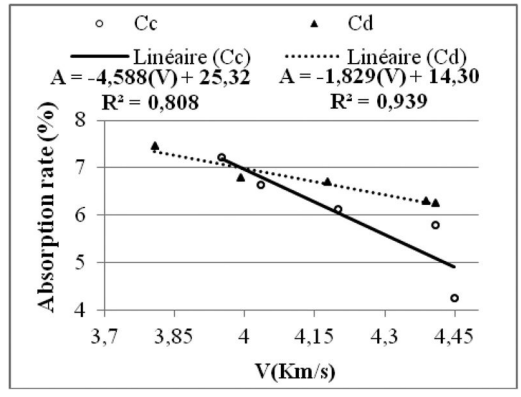

Figure 8. Correlations of adsorption (A) and ultrasonic velocity (V).

calculated. In the absence of a measured density, this leads us to suggest estimated values as a function of the ultrasonic velocity.

Wide dispersion is noted for both types of concrete (Figure 7). The correlation coefficients are very low (R^2 (Cc) = 0.166 and R^2 (Cd) = 0.217).

According to previous researches (Rojas & al 2012 ; Munzer 1994), one can see linear correlations for estimating the density (γ) as a function of the ultrasonic velocity like: $\gamma = a\,(V) + b$, With: a = 0.155 and b = 1.67, where:

γ is the concrete density (t/m^3) .
V is the ultrasonic velocity (Km/s).

The correlations proposed in this study for (C_c) and (C_d) are of linear forms:

(C_c): $\gamma = 2.265 + 0.030\,(V)$ (13)
$R^2 = 0.166$

(C_d): $\gamma = 2.258 + 0.032\,(V)$ (14)
$R^2 = 0.217$

It can be noted that the correlations observed for both types of concrete (Cc) and (Cd) are comparable. Moreover, previous research works on aggregates show that the type of aggregate can generate marked changes on concrete densities but not the grading type as treated in the case of this study (Maafi & Zemmit 2013; Topcu & Guncan 1995).

3.2.2 *The absorption (A) as a function of (V)*

It may be noted from the figure 8, that the rate of absorption of concrete and ultrasonic velocity are inversely proportional, the same observation as for higher concrete grades gave lower absorption rate. This is due to the concrete granular skeleton of continuous grading concretes with better compaction resulting in a lower absorption.

One can notice a large dispersion of the results of concrete (C_c) compared to concretes types (C_d) due to the irregularity of the absorption rate among the concrete grades types (C_c). The proposed correlations for

Table 4. Mechanical properties test results for the different concrete types.

	7 days			14 days				28 days			
grade	V (Km/s)	E_d (MPa)	Rc (MPa)	Is	V (Km/s)	E_d (MPa)	Rc (MPa)	Is	V (Km/s)	E_d (MPa)	Rc (MPa)
$C_{d20}^{(*)}$	3,67	23728	9,96	24	3,74	24859	12,21	28	3,81	25638	14,11
C_{d25}	3,89	26712	14,89	29	3,92	27355	16,03	31	3,99	28341	20,10
C_{d30}	3,86	26346	18,67	31	4,01	28556	21,72	34	4,18	31054	26,73
C_{d35}	4,09	29758	23,42	33	4,22	31669	29,54	38	4,39	34573	32,67
C_{d40}	4,04	28917	20,30	34	4,22	31510	28,25	39	4,41	34701	35,66
$C_{c20}^{(**)}$	3,61	22896	12,25	25	3,82	25737	15,29	30	3,95	27669	18,82
C_{c25}	3,85	26371	17,98	30	4,02	28845	21,18	33	4,03	28940	24,55
C_{c30}	3,98	28121	20,97	32	4,09	29923	24,17	35	4,20	31384	27,31
C_{c35}	4,02	28599	22,70	34	4,09	29662	28,45	38	4,41	34541	33,35
C_{c40}	4,02	28563	26,23	35	4,09	29637	27,14	39	4,45	35112	37,30

Table 5. Physical properties test results for the different concrete types.

	7 days	14 days	28 days	
Grade	(γ) Bulk density (Kg/m^3)			Adsorption$^{(***)}$ (%)
$C_{d20}^{(*)}$	2378	2395	2380	7,46
C_{d25}	2380	2394	2394	6,80
C_{d30}	2384	2393	2396	6,70
C_{d35}	2390	2395	2416	6,30
C_{d40}	2385	2383	2403	6,25
$C_{c20}^{(**)}$	2365	2378	2386	7,23
C_{c25}	2390	2398	2394	6,65
C_{c30}	2385	2408	2395	6,12
C_{c35}	2387	2387	2393	5,80
C_{c40}	2384	2385	2389	4,25

(*): (d) Index indicates gap graded type and (20) the grade of concrete.
(**): (c) Index indicates continuous graded type and (20) the grade of concrete.
(***): Adsorption measured at 28 days of age.

estimating the rate of absorption by using ultrasonic measurements are linear.

$$A = 25.32 - 4.588\ (V) \quad (15)$$
$$R^2 = 0.808.$$

$$(Cd):\ A = 14.30 - 1.829\ (V) \quad (16)$$
$$R^2 = 0.939.$$

4 COMPARISON OF RESULTS

The table 7 above shows some formulas used to estimate correlations of (Rc) and (γ) as a function of the ultrasonic velocity (V), the rebound hammer number (Is) or the combined method. To see the impact of local conditions and materials on the test results, a comparison between the proposed correlations in this work and some existing correlations is considered.

4.1 *Mechanical characteristics (Rc)*

Figure 9–11, show the ratio of the resistances estimated as proposed in this study and other existing correlations in literature in relation with the actual results obtained for compressive test method values Rc on cylindrical specimens (100 × 200) mm^3.

4.1.1 *Rc as a function of (Is)*

Figure 9, shows the differences of ratios (Rs/Rc) for the results of different correlations relatively to the actual (Rc) value ranging from 3% to 33.5%.

The formulas proposed in this experiment are acceptable and comparable to that proposed by the European standard EN 13791 with a difference of compressive strength ranging from 9.9% to12.5%.

The values obtained by the correlation (C_C) and (C_d) are very close with a difference of (2.6%), so we see that the type of grading does not really have an impact on the estimation of (Rc) depending on (Is), because the hardness test provides a local and superficial idea about the quality of concrete.

4.1.2 *(Rc) as a function of (V)*

According to Figure 10, It can be noted that sometimes a significant variation of strength (Ru) is observed using the ultrasonic velocity (V). The ratio of the actual value (Rc) of the compressive test sometimes reaches

Table 6. Formulas of correlations proposed for physical and mechanical concrete properties assessment.

Property	Method	Continuous graded type (Cc)	Gap graded type (C_d)
Mechanical strength (MPa)	Ultrasonic	$Rc = -95.52 + 29.55(V)$ $R^2 = 0.865$	$Rc = -109 + 32.41(V)$ $R^2 = 0.903$
	Reb hammer	$Rc = -21.96 + 1.442(Is)$ $R^2 = 0.876$	$Rc = -28.96 + 1.635(Is)$ $R^2 = 0.840$
	Combined	$Rc = -62.59 + 14.55(V) + 0.8861(Is)$ $R^2 = 0.9176$	$Rc = -109.3 + 31.64(V) + 0.1083(Is)$ $R^2 = 0.9428$
Elastic dynamic modulus (MPa)	Ultrasonic	$E_d = -619.2 + 1812(V^2)$ $R^2 = 0.996$	$E_d = -877.1 + 1831(V^2)$ $R^2 = 0.997$
	Reb hammer	$E_d = 10689 + 583.5(Is)$ $R^2 = 0.756$	$E_d = 7360 + 701.4(Is)$ $R^2 = 0.880$
Adsorption (%)	Ultrasonic	$A = 25.32 - 4.588(V)$ $R^2 = 0.808$	$A = 14.30 - 1.829(V)$ $R^2 = 0.939$
Density (Kg/m^3)	Ultrasonic	$\gamma = 2265 + 30.59$ (V) $R^2 = 0.166$	$\gamma = 2258 + 32.94$ (V) $R^2 = 0.217$

Table 7. Formula's correlations from literature for the assessment of strength (Rc) and the density (γ) for concrete.

References [corresponding Number for graphs]	Method	R^2	Formula
Hannachi, S & Guetteche, N(2012) [2]	Ultrasonic	0.5213	$Rc = 97.5409 - 0.0162(V)$
	Reb-hammer	0.3983	$Rc = 54.6389 - 0.7708(I_S)$
	Combined	0.5452	$Rc = 121.2976 - 0.0261(I_S) + 0.5452(V)$
Boudin & Louradi (2012) [15]	Ultrasonic	0.950	$Rc = -110.28 + 31.289(V)$
	Reb-hammer	0.4976	$Rc = -9.5105 + 1.1843(I_S)$
	Combined	0.7230	$Rc = -25.467\ 7.401(I_S/V)$
Rojas & al (2012) [11]	Ultrasonic	0.7560	$Rc = 0.35\ e^{(1.12V)}$
EN 13791 (2007)	Reb-hammer	–	$Rc = -34{,}5 + 1.73(Is)$
Nash't et al (2005) [9]	Ultrasonic	0.5900	$Rc = 1.19\ e^{(0.715V)}$
Turgut (2004) [10]	Ultrasonic	0.8000	$Rc = 1.146\ e^{(0.77V)}$
Feret	Combined	–	$Rc = (Is/\ (3.64 + 0.0235(Is) - 0.56(V))^2$
Panzera et al (2008) [12]	Ultrasonic	0.886	$\gamma = -0.3596 + 6.64 \times 10^{-4}(V)$
Munzer (1994) [17]	Ultrasonic	–	$\gamma = 1.67 + 0.155(V)$

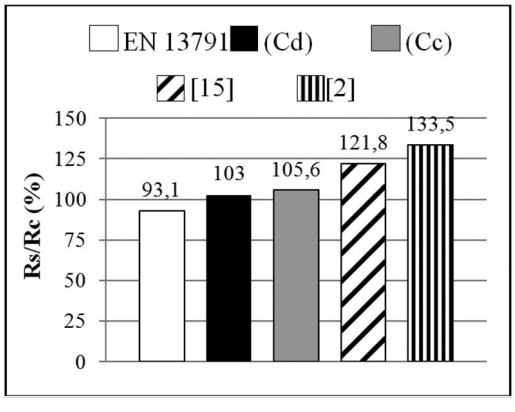

Figure 9. Comparison of results for compressive strength with assessed values for the different correlations as a function of rebound hammer number.

(48.5%), however, the remaining results of assessed strength results still comparables.

Previous work (Fiesta & Dreux 1998; Bungey 1989; Khatib 2005) found that may have an uncertainty of ±10 to 25% in the estimate based on conditions of practice and materials used; such factors may explain the range of variation shown in Figure 10.

It is also noted that the formulas proposed in this study to estimate (Rc) are very similar, thus acceptable with a differences that varies from 3.5% to 10.3% compared to the actual value, and about (6.8%) between the correlation of the two grading type (C_C) and (C_d).

A difference of 4.2% is observed between the assessed values of ultrasonic and rebound hammer test, this can be explained by the sensitivity of the ultrasonic testing method due to changes in composition and homogeneity of the concrete as compared with the former rebound hammer test.

It can be said that the grading type is a factor that has a slight influence on the estimation of (Rc) as a function of (V).

4.1.3 *(Rc) using combined method (V, Is)*

Very satisfactory results are obtained for the different correlations in the estimation of the mechanical strength by the combined method, which shows the reliability of the method except for the proposed formulas by Boudina & Louradi (2012), where the difference up to 38.3% was recorded. The correlations proposed in this work are satisfactory, very close

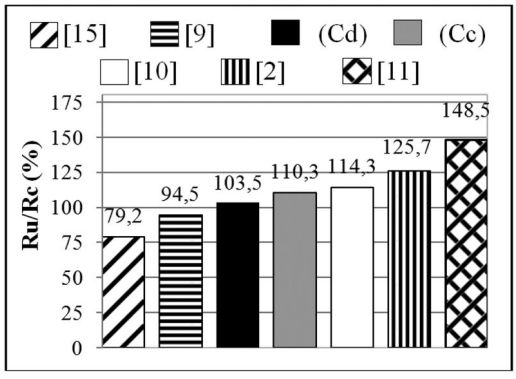

Figure 10. Comparison of result of compressive strength with assessed values using different correlations (ultrasonic velocity method).

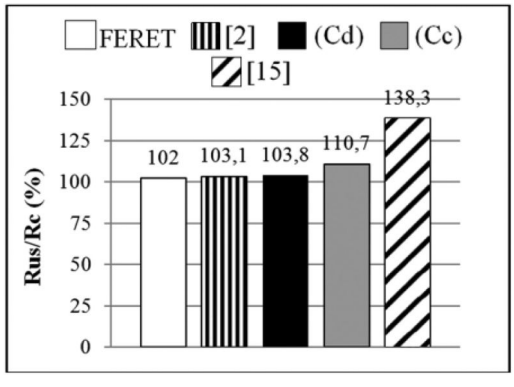

Figure 11. Comparison of results of compression with assessed values using the different correlations (combined method).

and consistent with the proposed formulas and (Feret 2001); including the correlation in the case of the gap-grading type (C_d).

The difference of (8.7%) has been shown between the correlation (C_C) of FERET and (6.9%) with that of (C_d).

It can be considered that the grading type is slightly influencing the assessment of the strength by the combined method.

4.2 *Physical properties (γ)*

Figure 12, shows the relationship of the densities estimated using the correlations proposed in this study and other previous suggested in literature with the actual density measured at 28 days of age.

4.2.1 *(γ) as a function of the velocity (V)*

According to Figure 12, it can be seen that all ratios are very satisfactory, because the values estimated from the correlation formulas proposed in this study are similar to the actual measured values by the direct test of compression.

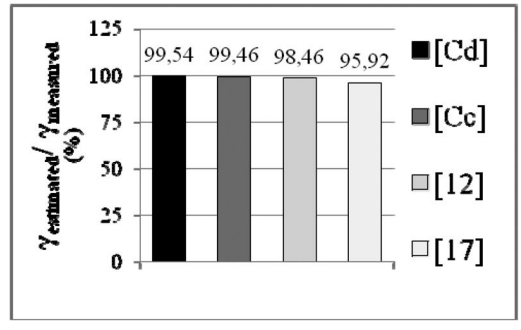

Figure 12. Comparison of the measured density (γ) and estimated values for the different correlations in function of ultrasonic velocity (V).

In addition, the results for the density (γ) remain comparable with the correlations proposed by other researchers (Panzera et al 2008; Munzer 1994).

The correlations proposed in this work are convenient and give similar results, so it is estimated that the grading does not really affect these correlations. Moreover, the research work of on the aggregates shows that the type of aggregate that is critical and can result in important variations in the density (Maafi & Zemmit 2013; Topcu & Guncan 1995).

5 CONCLUSION

This study has investigated correlations of compressive test and non-destructive methods (NDT) in order to physically and mechanically characterize a normal concrete. The influence of parameters on the observed correlations, were taken into account such as the concrete grade and grading type (continuous C_c and gaped C_d); the following conclusions could be drawn.

The proposed correlations are applicable only for the specific concrete treated in this study limited to ordinary concrete where concrete grades are ranging from 20 to 40 MPa.

The study shows that the results of testing (NDT) are significantly influenced by the grade of concrete and its composition and correlations of linear type are obtained.

The grading type does not have really a great impact on the correlations observed and especially for correlations based on rebound hammer test.

The comparison between the different approaches used to estimate the strength of concrete has shown differences more or less important, the thing that makes the use of these approaches for the evaluation of strength for concrete made in our local conditions or even specific climate conditions require some corrections to be considered regarding the difference between the materials, the composition, placement conditions once compared to the proper data implemented of these methods.

We note that the formulas proposed in this study to estimate Rc are acceptable and very close with a standard ranging from 3% to 10% of the actual value.

The difference of about 3% is found between the correlations (C_c) and (C_d) for rebound hammer and 7% for ultrasonic and combined method. The formulas given to assess the density are judged very satisfactory.

Through this experimental work, the recommended physical formulas and mechanical characterization of a concrete made using local materials are mainly accepted for gap graded concrete (C_d). In general, we can conclude that the use of non-destructive methods for the characterization of the properties of concrete is of great interest, and become an industrial alternative, in regards to the ease, rapidity and economy that can offer in terms of resources, time and materials.

REFERENCES

Boudina, R & Louradi A, 2012. *Proposition d'un modèle de corrélation entre les essais non destructifs et les essais d'écrasement d'un béton fabriqué dans les conditions locales.* Mémoire de Master, Centre Universitaire de B. B. Arreridj, Algérie.

Breysse, D. 2008. *Combining information, reliability and maintenance.* Diagnosis of NEC Works.

Bungey, J.H, Millard, S.G. 1989. *Testing of concrete in structures.* 2nd Edition, London: Surrey University Press UK: 229.

Bungey, J.H & Millard, S.G 1996. *Testing of concrete in structures.* 3rd Edition, London: Blackie Academic and Professional.

C.N.E.R.I.B, 2004. Cycle de formation, Algérie.

Contrôle technique des constructions (CTC), 2001. *Formule de Feret pour l'estimation de la résistance du béton par la méthode combinée.* Lettre circulaire, Algérie.

Fiesta, F & Dreux, G. 2007. *Nouveau guide des bétons*, Huitième édition, Troisième tirage, Paris :Eyrolles

Hannachi, S & Guetteche 2012. Application of the combined method for evaluating the compressive strength of concrete on site. *Journal of Civil Engineering, Scientific Research,* 2: 16–21.

Hobbs, B & Tchoketch, K. 2007 Non-destructive testing techniques for the forensic engineering investigation of reinforced concrete buildings. *Forensic Science International,* 67(23): 167–172.

Khatib, J.M, 2005. Properties of concrete incorporating fine recycled aggregate. *Cement and Concrete Research* 35: 763–769.

Kheder, G.F, A.M. Al Gabban, A.M & Abid, S.M. 2003. Mathematical model for the prediction of cement compressive strength at the ages of 7 and 28 days within 24 hours. *Materials and Structures*, 36: 693–701.

Maafi, N & Zemmit, A. 2013. *Etude de l'effet de type d'agrégats sur le comportement mécanique d'un béton.* Mémoire de Master, université de Bordj Bou Arreridj, Algérie.

Munzer, H. 1994. Critè*res découlant d'essais de charge pour l'évaluation du comportement des ponts en béton et pour le choix de la précontrainte*. Thèse de Doctorat, Ecole polytechnique fédérale de Lausanne, France.

Nash't, I.H, A'bour, S.H & Sadoon, A.A. 2005. Finding a united relationship between crushing strength of concrete and non-destructive tests. *Proceedings of Middle East nondestructive testing conference and exhibition,* Bahrain.

Neville, A, 1985. Properties of concrete. London :Addison-Wesley Longman, UK: 844.

Panzera, T.H & al. 2011. *Ultrasonic pulse velocity evaluation of cementitious materials*. Department of Mechanical Engineering, Federal University of São JoãodelRei – UFSJ, PraçaFrei Orlando, 170 São João Del Rei – MG.

Rojas-Henao, L, Fernández, J.G & López-Agüí, J.C. 2012.Rebound hammer, pulse velocity, and core tests in self-consolidating concrete. *ACI Materials Journal*, 109(02): 235–243.

Topcu, B.I & Guncan, F.N 1995. Using waste concrete as aggregate. *Cement and Concrete Research* 25(7): 1385–90.

Toukal, A. 2010. *Influence du taux de chargement sur la caractérisation non destructif du béton par ultrason. Mémoire de Master,* Université M'HAMED BOUGARA BOUMERDES, algérie.

Turgut, P. & Kucuk, O.F. Comparative relationships of direct, indirect and semidirect ultrasonic pulse velocity measurements in concrete. *Russian Journal of non-destructive Testing*, 42(11): 745–751.

This page intentionally left blank

Concrete Solutions – Grantham et al. (Eds)
© 2014 Taylor & Francis Group, London, ISBN 978-1-138-02708-4

Concrete Strength Evaluation through indirect UPV

S. Biondi, C. Valente & L. Zuccarino
inGeo Engineering and Geology Department, "Gabriele d'Annunzio" University of Chieti-Pescara, Pescara, Italy

ABSTRACT: The assessment of concrete properties in existing r/c buildings is a topic of fundamental importance to get reliable safety checks in structural retrofitting or seismic rehabilitation. Among other techniques, the ultrasonic pulse velocity test (UPV) is largely employed to estimate the concrete strength. This is because UPV is a non destructive method, easy to perform and provides reliable results. Several formulas are available in technical literature to relate the UPV measurements to concrete strength. These formulas are robust and reliable above all for direct measurements. Unfortunately these direct measures are a problem for existing buildings where, for a number of reasons, it is often necessary to perform indirect or, at most, semi-direct tests. In these cases relations available in the literature are not definitive. The present paper aims to contribute to develop a correlation between direct and indirect (or semi-direct) measures in order to use this latter kind of measure for reliable concrete strength estimations.

1 INTRODUCTION

1.1 *Research objective*

The real insitu strength characteristic of a structural concrete is a fundamental datum for the assessment of capacity of existing structures. Generally the designer involved in structural retrofitting has not at his disposal the original results obtained, via destructive tests, on specimens (cubes or cylinders) at the construction time, or it is not possible to guarantee that the original specimen strength is the same as the actual building strength due to construction difficulties, to environmental actions or to material degradation.

For these reasons the investigation of in situ concrete strength is an important research topic. Accurate strength predictions are possible via semi-destructive procedures i.e. via concrete core drilling and laboratory compressive tests. Unfortunately this approach is limited by its "local" nature and, above all, by the structural weakness caused on specimens (concrete cores) by the drilling procedure and specimen extraction. So it is very important to get refined non destructive testing procedures on in-situ structures. These procedures are different to each other and use different physical criteria in order to determine concrete strength.

One of the most efficient procedures is using ultrasonic pulse velocity (UPV) in order to determine dynamical elastic modulus of concrete. This dynamical elastic modulus can be related to static elastic modulus and then to compressive strength. These measures are generally combined with the rebound index in order to carry out the so-called Son-Reb tests. The procedure is robust and efficient if it is integrated with complementary compression laboratory tests on sampled cores.

It is noted (Biondi, 2008) that direct UPV tests provide reasonably estimates of the concrete strength, whereas both semi-direct and indirect ultrasonic tests can underestimate concrete strength.

Also changes in humidity content of the medium, caused by environmental conditions, can have great influence on material response to ultrasonic wave.

Owing to this problem, a comprehensive research activity that first of all considers the influence of the casting direction for pulse velocity measurements and then different humidity and temperature (seasonal) conditions has been planned by a research team at the Laboratory of Structures of Chieti-Pescara University. Some previous results of this activity were discussed in the past (Biondi et al., 2013) regarding casting direction. In this paper the seasonal variability is discussed.

Although the UPV technique is well-known and standardized (e.g. European Standard EN 12504-4:2004), at the present time no systematic studies concerning the correlation between direct, semi-direct and indirect measures appear to have been carried out. The UPV state of the art is sufficiently consolidated in terms of the dependence of UPV on chemical-physical characteristics, (Panzera et al., 2011), and on reinforcement influence in the in-situ case, (Naik et al., 2004).

More recently some authors, (Qixian & Bungey, 1996), (Lawson et al., 2011), (Mahure et al., 2011), focused their attention on direct, semi-direct or indirect tests. Among these literature contributions, Qixian & Bungey (1996) observed that a smaller pulse velocity is detected in case of indirect measures as compared to direct measures. This difference is explained in terms of differences both in concrete composition and

humidity content between concrete cover and concrete nucleus. These velocity differences are significantly lower than those detected on existing structures in previous studies by one of the authors of this paper, (Biondi & Candigliota, 2008), (Biondi, 2008).

A statistical analysis of direct and indirect measures, performed by Yaman et al., (2001) shows that both measures can be considered statistically similar (T test) and can be represented by a normal distribution (i.e. they are defined by average and standard deviation values). In the same paper, as a complementary result, it was also pointed out that the statistical aspect of the data depended on the uniformity and humidity characteristics of the concrete.

The in-situ casting direction is considered too in order to evaluate the influence on direct, semi-direct and indirect UPV results, (Turgut et al., 2006). The casting direction enhances the difference between direct and indirect measures where the higher the concrete strength, the lower is this difference.

Also in that paper, considering laboratory specimens having known casting age, curing conditions, concrete composition and compressive strength, the difference between direct and indirect measures is lower than those differences that have been detected on in-situ structures, above all in the case of low quality structures, i.e. structures having low quality strength (see again Biondi, 2008).

In consideration of all those reasons, an experimental campaign was carried out on different concrete specimens. In order to be comparable with actual on site conditions, these specimens have been selected having unknown characteristics in terms of both aging and curing.

The specimens were collected from different construction sites and only the casting direction can be determined via a visual inspection. It is to be noted, however, that the influence of this parameter should be carefully evaluated when considering a structural element (beam, slab, column) instead of a specimen.

The geometrical difference between a specimen and a real structural element seems to be very significant in order to permit a real understanding of casting direction influence. Obviously segregation and bleeding phenomena or reinforcement influence are much more significant for a column having a dimension of some meters than in the case of a specimen having a dimension of some centimeters.

1.2 *Research activities*

A large experimental campaign was designed to fulfill the research purposes. The experimental activities were replicated in different seasonal conditions. At this time results for summer and winter conditions are available and are discussed in order to complete previous discussions (Biondi et al., 2013).

A certain number of concrete samples were tested in the laboratory in different environmental conditions. The samples were collected from different construction sites and they could have different (unknown) mix design. On the other hand, the specimens showed an identical geometry.

The curing conditions were identical to those of concrete of a building during the construction period and the age was approximately 5 years for each specimen at the time of test. Direct, semi-direct and indirect UPV tests were performed and replicated in two opposite seasonal conditions (Summer and Winter) according to an average temperature variation of 20°C. The same apparatus was used throughout.

In both cases, three different humidity conditions were considered for the specimens: a natural humidity condition, a fully wet condition and an intermediate humidity condition.

The natural humidity condition, for simplicity herein referred to as "dry" condition, corresponds to an average humidity condition that one can find inside a building. Obviously, these humidity conditions are susceptible to change depending on the season even if for a lower extent than the outside humidity. One therefore should expect that "dry" conditions in summer and winter correspond to different humidity rates (i.e. to different specimen masses). In the present paper, natural humidity conditions refer to as storing in the laboratory without any particular curing or heating provisions. On the contrary, the "full wet" conditions were artificially obtained. The specimen were immersed in water for sufficient time until they were completely saturated, i.e. until no weight changes could be detected on each specimen for successive measures. Intermediate humidity conditions are those that reveal a mass density for a specimen that is an average value between "dry" and "full wet". For these reasons the intermediate condition is different with respect to winter or summer.

Finally, dependence on the path length of the UPV impulse and the influence of casting direction on transmission velocity have been also considered. The results show that it is possible to obtain a clear relationship between direct and indirect UPV tests and that this relationship is strongly dependent upon the humidity content. This dependence appears as a seasonal dependence and has to be confirmed in real in-situ structures. This relationship can help in obtaining reliable concrete strength evaluations even when using indirect UPV tests; other factors are less influencing the pulse velocity.

2 EXPERIMENTAL PROGRAM

2.1 *Specimen geometry*

The experimental campaign was conducted on concrete prisms of identical nominal geometry: $480 \times 150 \times 150$ mm, see Table 1, collected from different construction sites with different unknown mix designs. The curing, after an initial period at the construction sites, was carried out in the laboratory (in a closed and unheated store room). The curing conditions can be considered as identical to those of a r.c.

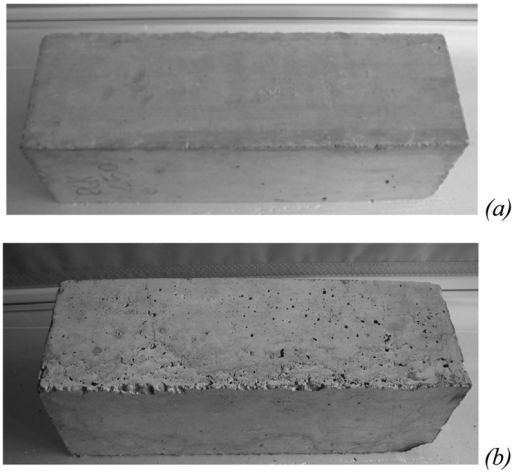

Figure 1. Concrete specimens: (a) P_2, (b) P_4.

Table 1. Geometric characteristics of the specimens.

Specimen	Geometry mm	Volume m^3
P_1	483 × 153 × 153	0.0113
P_2	480 × 150 × 148	0.0107
P_3	483 × 153 × 153	0.0112
P_4	480 × 151 × 152	0.0110
P_5	478 × 152 × 152	0.0110
P_6	480 × 150 × 150	0.0108
P_7	480 × 150 × 150	0.0108
P_8	480 × 150 × 150	0.0108
P_9	481 × 150 × 150	0.0108
P_10	480 × 151 × 150	0.0109

infilled frame, while the specimen age was about five years at the time of tests.

The water content is the parameter that simulates maturation of the material. In particular, the saturated "full wet" specimen can be taken as representative of the condition of the material at 28 days (reference time for design strength), while the "dry" specimen could be considered as the condition of the material during service life. Figure 1. shows the two specimens that showed maximum (specimen P_2) and minimum (specimen P_4) specific mass. A significant difference in superficial porosity is evident.

The geometric characteristics of the concrete specimens are summarized in Table 1, while Figure 2 and Figure 3. show the variation of bulk density ρ_b and porosity φ in the concrete specimens. In order to understand correctly the data, some comments have to be made.

In particular we need to define the condition assumed as the reference condition. We defined two reference conditions: minimum humidity content (called 0% humidity in following figures and tables) and maximum humidity content (called 100% humidity in following figures and tables).

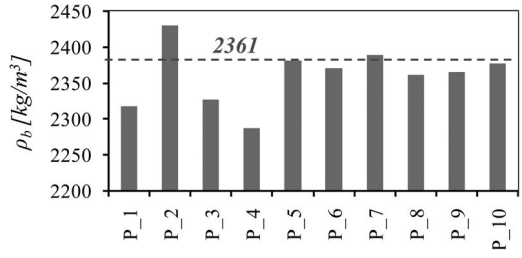

Figure 2. Bulk density of concrete specimens (0% humidity, summer "dry" condition).

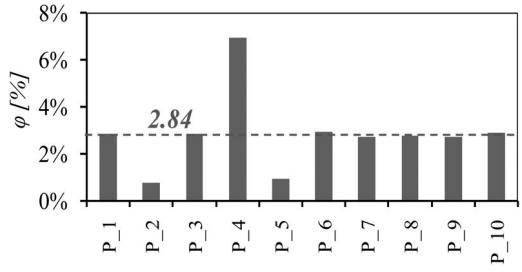

Figure 3. Porosity of concrete specimens (weight difference between winter "full wet" condition [100% humidity] and summer "dry" condition [0% humidity]).

The minimum humidity content corresponds to the "dry" condition measured during the summer season. On the contrary, the maximum humidity content corresponds to the "full wet" conditions artificially obtained via water immersion of specimens. Theoretically, the "full wet" conditions should not change from summer to winter. Indeed small differences are however observed: a bulk density greater in winter than in summer was detected.

These differences are insignificant from a practical point of view, however they are reported as measured in Table 2. The bulk density of Figure 2 was computed using data for summer "dry" conditions; whereas the porosity of Figure 3 was computed considering the mass difference between winter "full wet" conditions and summer "dry" conditions.

These latter two limits were used throughout the paper to represent the maximum range of measures performed.

For the sake of conciseness and simplicity these two limits have been normalized to 0% ("dry" summer conditions) and 100% ("full wet" winter conditions). All other measures falling inside this range are normalized accordingly.

In this manner the average bulk density of the concrete specimens, in "dry" conditions, was equal to 2361 kg/m^3 (2287 ÷ 2431 kg/m^3); while the average porosity, computed as a weight percentage, was equal to 2.84. As shown in Figure 2 and Figure 3, two specimens, P2 & P4 respectively, presented values that deviated from average values (minimum and maximum density). Those specimens are shown in Figure 1.

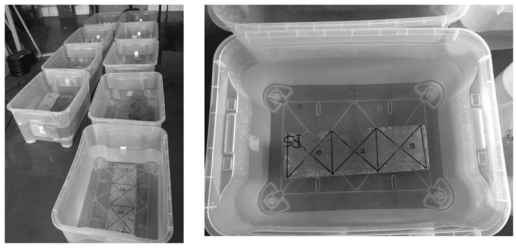

Figure 4. Specimens immersed in water for obtaining the "full wet" condition.

Table 2. Measured masses for different conditions.

	Summer (T > 30°C)		Winter (T < 10°C)	
	"dry"	"full wet"	"dry"	"full wet"
Specimen	mass kg			
P_1	26.20	27.00	26.25	26.95
P_2	25.90	26.05	25.30	26.10
P_3	26.15	26.80	26.30	26.90
P_4	25.20	27.00	26.45	26.95
P_5	26.30	26.55	26.15	26.55
P_6	25.60	26.35	25.90	26.35
P_7	25.80	26.50	26.10	26.50
P_8	25.50	26.15	25.80	26.20
P_9	25.60	26.20	25.80	26.30
P_10	25.85	26.50	26.10	26.60
min.	*25.20*	*26.05*	*25.30*	*26.10*
max.	*26.30*	*27.00*	*26.45*	*26.95*
average	*25.81*	*26.51*	*26.02*	*26.54*

2.2 *Humidity conditions*

The experimental investigation consisted of different measurements on the same specimens according to two different conditions: seasonal temperature and humidity content variation. The UPV tests were performed and replicated in summer and winter with an average temperature respectively of 30°C and 10°C. In both cases, three different humidity conditions were considered: "dry", "intermediate" and "full wet". As mentioned above, the summer "dry" condition is the so-called 0% humidity while the winter "full wet" condition is the so-called 100% humidity.

The parameter that allows the monitoring of water content is the specimen mass both in summer and winter. Specimens were weighed in each humidity condition before the UPV tests. At first the samples were tested in dry conditions, then immersed in water until complete saturation and then tested again, Figure 4. Finally, saturated specimens were exposed to the external environment until an intermediate humidity condition in terms of weight was achieved and then tested again via the ultrasonic apparatus.

Table 2 shows the comparison, in terms of masses, between wet samples (maximum saturation) and dry samples (minimum saturation). These categories are season dependent. In fact from the data, it is possible to observe that if the same "full wet" conditions are not obtained in different seasons (summer "full wet" is 95.9% of winter "full wet") and a not negligible difference was detected for "dry" condition between summer and winter (winter mass percentage was 28.1%).

This is due to the adopted "natural" humidity condition, i.e. the condition of a specimen in the lab without the use of any curing and heating apparatus in order to obtain the lower "dry" condition.

At the end of this campaign, each specimen will be subdivided in three cubic specimens in order to perform compressive tests. Before these crushing tests it will be interesting to control the mass variation in dry and wet conditions due to lower geometrical dimensions or to the use of a heating apparatus.

2.3 *Ultrasonic apparatus and test procedure*

The UPV measurement equipment (Ultrasonic concrete tester Controls Mod. 58-E0046 – E0046/Z) consisted of two 54 kHz transducers, with a diameter of 50 mm: one transducer for producing ultrasound pulses and the other for receiving the transmitted pulses. The system used is based on the piezoelectric principle of trans-conduction: ultrasonic waves are generated by exciting the piezoelectric element in one transducer by an alternating electrical voltage, which causes it to vibrate at its resonant frequency.

Any kind of sound can only be propagated in a material medium and it is strongly influenced by that medium. For this reason the velocity of sound, as well as its attenuation, depends in a characteristic way on the nature of the medium. So the UPV can be assumed as a fundamental parameter of medium characteristics and time and distance are test data to be collected for this scope.

In the present activity, ultrasonic tests were performed in three different manners: direct, semi-direct and indirect. The tests were performed on each side of specimen in order to evaluate the influence of concrete casting direction on the ultrasonic pulse velocity. Three directions were considered: one parallel (150 mm length) and two orthogonal (150 and 480 mm lengths) to the casting direction.

The UPV tests carried out on each specimen were direct, VD, semi-direct, VS, and indirect, VI, tests.

The direct VD tests included tests along the longitudinal axis of the specimen VD_{48} (path length equal to 480 mm, orthogonal to casting direction) and along transversal axes VD_{15} (path length equal to 150 mm, both orthogonal and parallel to the casting direction). The indirect VI tests included path lengths equal to 75, 150, 225 and 300 mm on each specimen face (both orthogonal and parallel to the casting direction). Direct, indirect and semi-direct UPV measurements schemes are shown in Figure 5.

Direct, indirect and semi-direct UPV measurements were collected at each measuring station for each sample. The average values were calculated. In Figure 5. it is possible to observe that each specimen is ideally

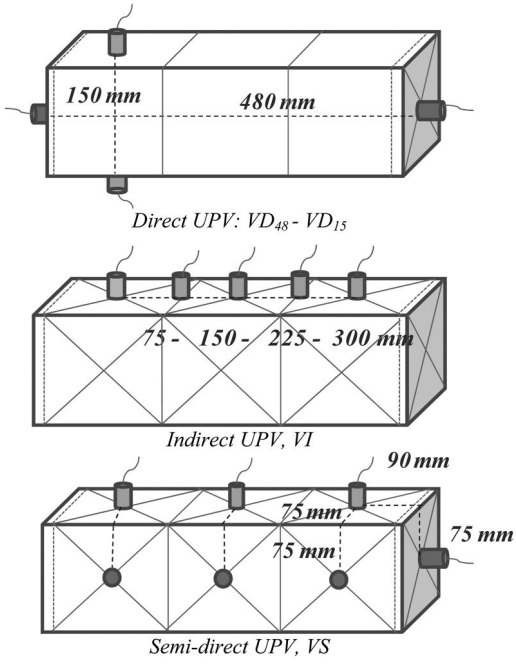

Figure 5. UPV measurements schemes for different classes of ultrasonic tests: direct, indirect and semi-direct tests.

subdivided into three parts of 150 mm length (three ideal cubes).

For direct and semi-direct UPV tests the transducers (transmitter and receiver) were applied at the intersections of diagonals of each cube face while for indirect UPV tests the transmitter-receiver configuration was that with the transmitter fixed on the axis of an ideal cube and measurements taken by progressively shifting the receiver by 75 mm steps with the center-to-center distance from the transmitter increasing from 75–300 mm. For each test gel was used as the coupling medium.

The influence of concrete casting direction, parallel (//) or orthogonal ($\perp$), on ultrasonic pulse velocity was evaluated using the direct UPV (VD_{15}) and indirect UPV (VI) methods.

For each test 1 to 4 measuring points were adopted. The tests were repeated up to a maximum of 3 times. In total 15 tests for VD_{48}, $30 + 30$ tests for VD_{15} (//) and VD_{15} ($\perp$), $24 + 24$ for VI (//) and VI ($\perp$) were performed.

3 TEST RESULTS

The results of tests were analyzed and compared in order to evaluate the possibility to point out possible relationships between direct, indirect, and semi-direct UPV measurements according to the various humidity levels and seasonal temperature variations. The testing program had three principal goals.

The first goal was to compare direct, semi-direct and indirect UPV measurements according to concrete casting direction. The second goal was to evaluate humidity and temperature dependence.

Last but not least, the third purpose was to compare direct, indirect and semi-direct UP velocities and to develop relationships to be used in the case of a difficulty to carry out direct measurement due to the in-situ conditions.

In order to assess the accuracy of the collected data, several repetitions for the same test were carried out. The results showed a stable aspect regardless of type of measure (direct, indirect or semi-direct), test conditions (humidity and temperature) and test apparatus use. Regarding the latter aspect it is to point out that the ultrasonic apparatus that was used was a common apparatus, extensively used in the past for in-situ test on existing structures.

3.1 *Casting direction dependence*

The dependence of the UPV on the casting direction was first considered. From the results of the experimental campaign it was observed that there was no significant relationship between direct UPV, indirect UPV, semi-direct UPV and the concrete casting direction. Average values, coefficient of variation and standard deviation were computed and regression models adopted to compare the data.

A sample result referring to specimen P_6 is shown in Figure 6, where the two cases of "dry" and "full wet" summer conditions were considered for indirect tests. The high similarity between the UPV recorded in the two directions is well assessed by the linear regressions of the data that estimates the pulse velocities. The differences between the angular coefficients are very modest and in any case less than 3%, thus confirming the low influence of the casting direction on pulse velocity.

The European Standard (EN 12504-4:2004) that suggests the use of the angular coefficient in order to determine pulse velocity has to be assumed as a correct procedure in common practice.

3.2 *Humidity and temperature dependence*

As said previously, different humidity and temperature conditions were taken into account. The UPV tests were performed and replicated in summer ($T = 30°C$) and winter ($T = 10°C$) according to an average temperature variation of 20°C. In both cases 3 different humidity conditions were considered: "dry", "intermediate" and "full wet". For each season, each condition was different in terms of humidity ratio. So the "dry" winter condition revealed a 28,1% humidity in respect to "dry" summer condition.

The main results for the whole set of specimens are summarized in Figure 7. Four histograms: two for direct UPV, VD_{15}, and two for indirect UPV, VI. In each case both low humidity ("dry") and high humidity ("full wet") results are reported.

If the seasonal variation is assumed dependent on temperature, it is possible to detect an almost uniform

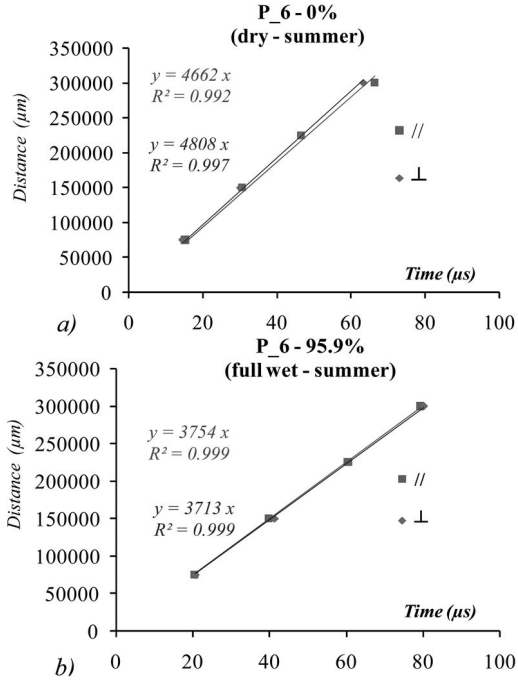

Figure 6. Casting direction dependence – P_6 VI tests for summer minimum ("dry" – 0% humidity) and maximum ("full wet" – 95.9% humidity) humidity conditions. Top equation in each graph is for // direction.

increase of UPV equal to 5% in winter conditions as compared to summer conditions. Particularly interesting is that the same ratios are shown by single specimens. This aspect underlines the stability of the results. An exception is for the case VD_{15} "dry" tests where only 1% increase is observed and the behavior is less stable with some fluctuations for the single specimen: water tends to uniform the medium response to the ultrasonic pulsing signal.

Concerning humidity, an expected result is pointed out in Figure 7: the UPV increases with the humidity level. The increase is greater in the VI case than in the direct measurement, VD_{15}. Specifically, the increase is about 15% for VD_{15} and 30% for VI and it does not appear to be related to seasonal conditions. But an unexpected result is pointed out too: a 28.1% humidity (i.e. weight) difference in "dry" condition (winter to summer) is less relevant than a 4.1% humidity difference in "full wet" condition (summer to winter). This aspect has to be investigated deeply.

3.3 *Direct, semi-direct, indirect dependence*

In Figure 8 direct (VD_{48} and VD_{15}) and indirect (VI) ultrasonic pulse velocities are reported for winter conditions considering defined boundary humidity ratios ("dry", 28.1%, and "full wet", 100%).

In Figure 9 and Table 3, the whole set of results is shown in terms of average values. In particular in Table 3 the percentage ratio between a current value and the

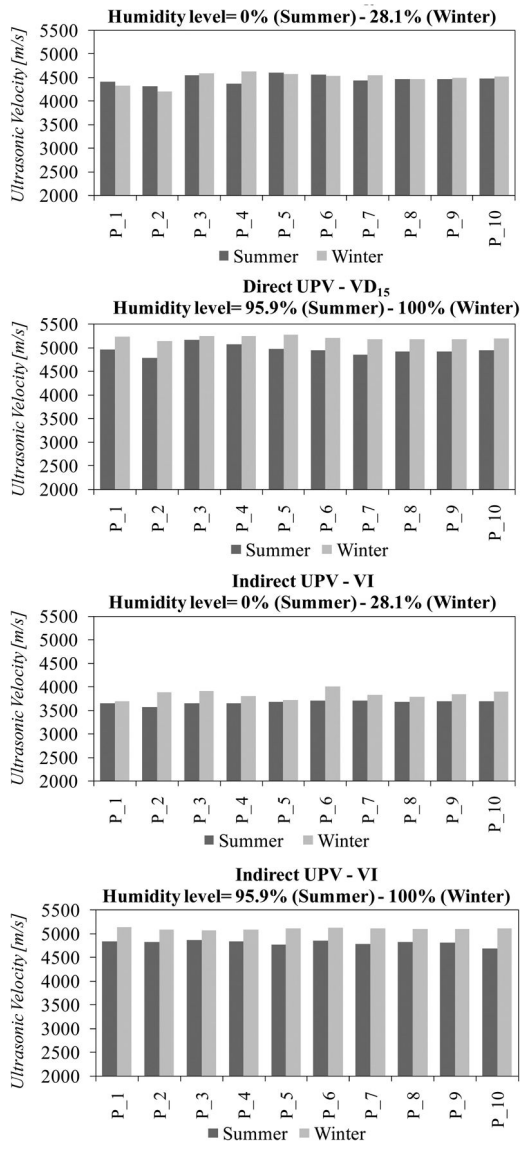

Figure 7. UPV: Humidity and temperature dependence for each specimen in both summer and winter condition.

VD_{15} "dry" or "full wet" value is calculated. From these data it is possible to point out some interesting observations.

It is possible to observe that VD_{48} velocities are generally lower than VD_{15} ones. The ratio between the two cases is stable and approximately equal to 0.97. This value is observed regardless of the humidity level. However VD_{48} tests are characterized by a greater uncertainty than VD_{15} ones. In the first case, the standard deviation is about 2.0% whereas in the second case it reduces to about 0.7%. This fact could be due to irregularity in the concrete specimens. This aspect will be investigated when the specimens are subdivided into three identical concrete cubes.

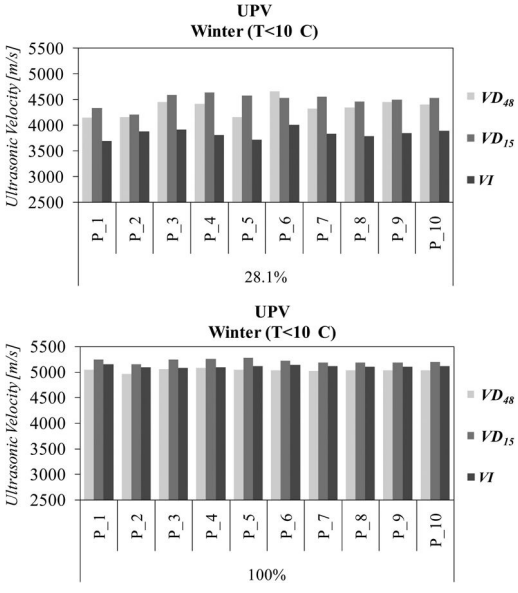

Figure 8. Direct to indirect UPV comparison for winter tests on each specimen.

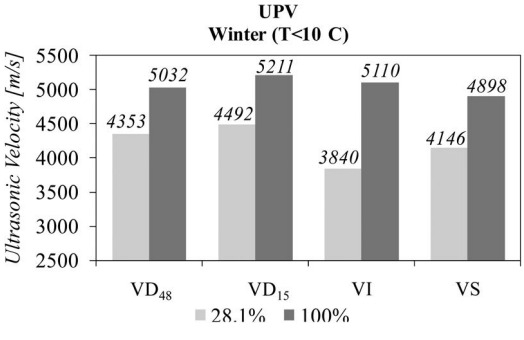

Figure 9. Direct, semi-direct and indirect average values for winter "dry" (28.1%) and "full wet" (100%) conditions.

Table 3. UPV average values for different testing conditions.

	Summer				Winter		
Humidity	VD_{48}	VD_{15}	VI	VD_{48}	VD_{15}	VI	VS
"dry"	4333	4468	3670	4353	4492	3840	4146
"full wet"	4768	4958	4812	5032	5211	5110	4898
"dry"	3%	–	22%	3%	–	17%	8%
"full wet"	4%	–	3%	4%	–	2%	6%

The VI tests produce results systematically lower than the direct tests and the relationship between direct and indirect UPV is influenced by humidity level. In "dry" conditions the VD_{15}/VI ratio is equal to 17% for winter. This ratio decreases at about 11% in the intermediate conditions and reduces to 2% in "full wet" conditions. A similar comparison is observed for semi-direct tests. In this case the UPV reduction is lesser and

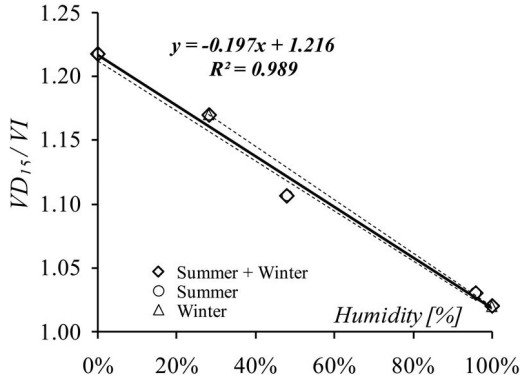

Figure 10. VD_{15} direct to VI indirect UPV correlation for different humidity level (0% summer "dry" condition).

Table 4. Linear regression coefficients (S summer, W winter).

$y = ax + b$	S	W	S + W
a	−0,195	−0,208	−0,197
b	1,211	1,228	1,216

almost constant in the range 8%-6%: so the "full wet" VI average value (5110 m/s) is greater than the corresponding VS average value (4898 m/s) while in "dry" condition the VS average value is greater than the VI average value.

Similar conclusions can be observed in the case of summer conditions.

One topic to be better investigated is the relationship between direct and indirect UPV for different humidity levels. The ratio VD_{15}/VI is shown in Figure 10. For the sake of correctness we have to reaffirm that the humidity level, as we define it, is a conventional one. In fact it ranges from "dry" summer conditions (conventionally 0%) and "full wet" winter conditions (conventionally 100%).

In Figure 10. it is possible to observe that the ratio VD_{15}/VI reduces as long as the humidity level increases.

The reduction can be modeled by a linear regression. Three linear regressions are considered, Table 4, one for summer conditions, one for winter conditions and one for both cases. In any case similar regression coefficients are detected. Clearly those coefficients have to be refined if different humidity levels would be considered.

4 CONCLUSIONS

The present experimental activity was carried out with the aim to contribute to development of a correlation between direct and indirect (or semi-direct) UPV to be used for in-situ tests on existing RC structures. For this purpose, ultrasonic pulse velocities were measured, using direct and indirect tests, on ten concrete

specimens. On the one hand, the results showed that it is possible to obtain a good correlation between direct and indirect UPV tests; on the other hand this correlation was strongly dependent on the humidity level.

In the paper three conditions have been studied: the so-called "dry", "intermediate" and "full wet" conditions. The reference condition for minimum humidity content was assumed to be the "dry" condition in the summer season. On the contrary, the reference condition for maximum humidity content was assumed to be the "full wet" condition in the winter season. The "full wet" conditions were obtained, in each season, via water immersion of specimens.

Direct, semi-direct and indirect UPV tests were performed and replicated in two opposite seasonal conditions (summer and winter) according to an average temperature range of about 20°C. In order to assess the degree of accuracy of the results, several readings and repetitions for the same test were carried out. The results were stable and repeatable regardless of the type of measure (direct, indirect, semi-direct), temperature and humidity conditions of the tests. In order to evaluate the test impact on common practice, a "normal" pulse velocity apparatus was used.

First of all it was detected that the concrete casting direction was quite irrelevant on different UPV tests: the difference between perpendicular casting directions did not exceed 1%. This result was clear and stable for specimen geometry. It is possible that a different result could be obtained if a structural element is considered, due to macro phenomena in the concrete (segregation, bleeding, rebar interaction).

Considering different measure distances, the average direct UPV, VD_{15}, was 3% higher than the average direct UPV, VD_{48} for "dry" conditions, while it increased to 1% for "full wet" conditions, regardless of the temperature. The center-to-center transmitter-receiver distance was quite irrelevant in indirect tests. The ratio between direct UPV, VD_{15} and indirect UPV, VI, was equal to 1.22 in summer ($T > 30°C$) for the minimum humidity content ("dry"), while it reduced to 1.17 in winter ($T < 10°C$).

On the contrary, for the maximum humidity content of the specimens ("full wet") this ratio tended to unity both in summer (1.03) and in winter (1.02). The indirect UPV tests were more dependent on humidity, particularly in the case of the winter test ($T < 10°C$).

Finally a relationship between direct and indirect UPV for different humidity levels was apparent. A simple linear regression model can be used in order to define the ratio between direct UPV, VD_{15} and indirect UPV, VI, results.

Correlation coefficients were quite similar for both summer and winter condition. A linear model can be assumed as efficient for indirect to direct velocity dependence on humidity.

REFERENCES

Biondi, S. & Candigliota, E. 2008. Non destructive tests for existing r.c. structures assessment. *Fib 2008 Symposium*. Amsterdam, Cd-Rom Paper: 1037–1039.

Biondi, S. 2008. The Knowledge Level in existing buildings assessment. *14th World Conference on Earthquake Engineering*, *Beijing, October 12–17, 2008*. CAEE-IAEE, Digital Paper ID 05-01-0462, Mira Digital Publishing.

Biondi, S., Valente, C., Zuccarino, L. 2013. La prova ultrasonica indiretta nella valutazione della resistenza meccanica del calcestruzzo in opera. *15° Congresso AIPnD, Trieste, 23–26 Ottobre 2013.* ISBN: 978-88-89758-14-4.

Breysse, D. 2012. Non destructive assessment of concrete structures: usual combinations of techniques. In D. Breysse (ed). *Non-Destructive Assessment of Concrete Structures: Reliability and Limits of Single and Combined Techniques*. Springer Netherlands. ISBN: 978-94-007-2735-9

Lawson, I., Danso, K.A., Odoi, H.C., Adjei, F.K., Quashie F.K., Mumuni, I.I., Ibrahim, I.S. 2011. Non-Destructive Evaluation of Concrete using Ultrasonic Pulse Velocity. *Research Journal of Applied Sciences, Engineering and Technology* 3(6): 499–504.

Mahure, N.V., Vijh, G.K., Sharma, P., Sivakumar, N., Ratnam, M. 2011. Correlation between Pulse Velocity and Compressive Strength of Concrete. *International Journal of Earth Sciences and Engineering* 4(6): 871–874.

Naik, T.R., Malhotra, V.M., Popovics, J.S. 2004. The Ultrasonic Pulse Velocity Method. In V.M. Malhotra & N.J. Carino (eds), *CRC Handbook on nondestructive testing of concrete*. Boca Raton: CRC Press.

Panzera, T.H., Christoforo, A.L., Cota, F.P., Borges, P.H.R., Bowen, C.R. 2011. Ultrasonic Pulse Velocity Evaluation of Cementitious Materials. In Dr. Pavla Tesinova (ed) *Advances in Composite Materials-Analysis of Natural and Man-Made Materials*. Rijeka: InTech. ISBN: 978-953-307-449-8.

Qixan, L. & Bungey, J.H. 1996. Using compression wave ultrasonic transducers to measure the velocity of surface waves and hence determine dynamic modulus of elasticity for concrete. *Construction and Building Materials* 10(4): 237–242.

Turgut, P. & Kucuk, O.F. 2006. Comparative relationship of direct, indirect and semi-direct ultrasonic pulse velocity measurements in concrete. *Russian Journal of Nondestructive Testing* 42(11): 745–751.

Yaman, I.O., Inci, G., Yesiller, N., Aktan H.M. 2001. Ultrasonic pulse velocity in concrete using direct and indirect transmission. *ACI Materials Journal* 98(6): 450–457.

Concrete Solutions – Grantham et al. (Eds)
© 2014 Taylor & Francis Group, London, ISBN 978-1-138-02708-4

Assessment of insitu structural capacity of aged buildings

S.T. Chan, Danny K.C. Chung, Bosco L.K. Au & Stanley T.K. Ng
Hong Kong Housing Authority, Hong Kong

ABSTRACT: With the first public rental housing (PRH) development 60 years ago, the Hong Kong Housing Authority (HKHA) now provides home to two million people in Hong Kong. With over 30% of the PRH stock over 30 years old, structural degradation becomes inevitable for the older buildings. Faced with an aging PRH stock, the HKHA has been utilizing the Comprehensive Structural Investigation Programme (CSIP) since 2005 to evaluate the insitu structural capacity of the aged PRH buildings and based on which establish effective solutions to better sustain them. This paper describes the probabilistic approach used by the HKHA in appraising the current and predicting the future structural performance of the aged buildings. In particular, this paper elaborates the statistical techniques used to determine the estimated insitu characteristic strength (EIChS) of concrete, and the methodology developed for the corrosion evaluation of steel reinforcement under the CSIP.

1 INTRODUCTION

Hong Kong is a densely populated city with over seven million people living in an area of 1,100 km^2. With a limited supply of land, private home ownership is often beyond the reach of low-income families. To help those families with housing needs, the Hong Kong government has been providing affordable public rental housing (PRH) since the 1950s. Today, about two million people live in about 1,150 PRH buildings maintained by the Hong Kong Housing Authority (HKHA). Over the last six decades, the design and construction of PRH buildings have continuously evolved and improved. From low-rise to high-rise and from cast-in-situ to precast, new PRH buildings are now often praised for their quality, sustainability and innovativeness. Yet, with a long history of public housing in Hong Kong, structural degradation becomes inevitable for the older buildings. Faced with an aging PRH stock (Figure 1), the HKHA has been utilizing the Comprehensive Structural Investigation Programme (CSIP) since 2005 to evaluate the insitu structural capacity of the aged buildings and based on this establish effective solutions to better sustain them. This paper describes the probabilistic approach used by the HKHA in appraising the current and predicting the future structural performance of the aged PRH buildings. In particular, this paper elaborates the statistical techniques used to determine the estimated insitu characteristic strength (EIChS) of concrete, and how a comprehensive structural investigation (CSI) statistically evaluates the corrosion conditions of different groups of steel reinforcement for a PRH building.

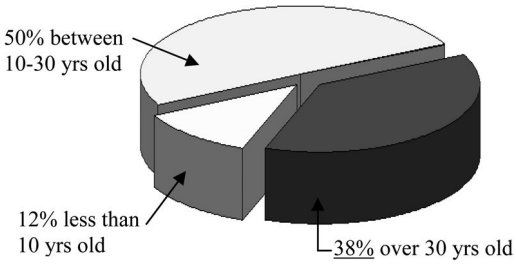

Figure 1. Age distribution of PRH stock as of 2013. (Total number of PRH Flats ≈ 730000 units).

2 BACKGROUND OF CSIP

Launched in 2005, the CSIP aims to determine the sustainability for the next 15 years of PRH buildings approaching 40 years of age. The CSIP systematically and thoroughly probes into the structural conditions of the aged PRH buildings and evaluates whether these buildings are structurally and economically viable to maintain. The six major steps of a typical CSI are illustrated in the flowchart below (Figure 2):

The first step of a CSI is to carry out a desktop study, which includes reviewing record drawings, design calculations, past repair/strengthening history, and previous structural appraisals. A visual survey is then conducted to cover the entire common area and a representative number of flats in a PRH building. Based on the information gathered from the desktop study and visual survey, a test programme is devised to diagnose in-depth structural conditions. Test results are then reviewed and analyzed statistically (to be further elaborated in later sections) to obtain the necessary data for a physical service life assessment. To structurally maintain an aged building effectively,

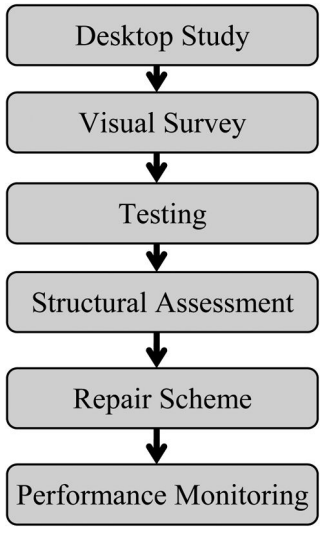

Figure 2. Flowchart of the CSIP methodology.

the repair scheme developed under a CSI is tailor-designed and focuses on addressing the root causes of defects. In addition, long-term performance monitoring is implemented so that continuous enhancement can be made to future investigation methodology and repair solutions.

3 CONCRETE

A typical 40-year-old PRH building is a cast-in-situ reinforced concrete structure (Figure 3, 4). The earlier buildings are six to seven storeys high but those completed in the 1960s are up to 20 storeys. While these aged PRH buildings are considered to be constructed with quality in their era, the concrete control and workmanship are nevertheless inferior when compared with today's standards. As concrete strength is critical for the integrity and stability of a reinforced concrete structure, it is important to determine the existing insitu concrete strength with confidence to appraise the existing structural adequacy and future sustainability of a PRH building.

3.1 *Destructive vs non-destructive tests*

A number of in-place concrete test methods are available to estimate the existing insitu strength of concrete (ACI Committee 228, 2003). From non-destructive tests such as the rebound hammer test and ultrasonic test to destructive tests such as the break-off test and the conventional compression test on core samples, the selection of suitable method(s) for an application should be based on the needed accuracy, budget, site conditions, and the risk of damage due to testing. It should be noted that even if "non-destructive" test methods are adopted, sufficient compression tests on core samples are required to establish and calibrate the relationship between non-destructive test results and

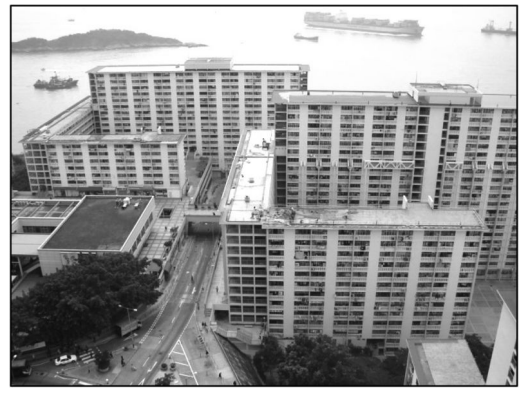

Figure 3. General view of 40-year-old PRH buildings.

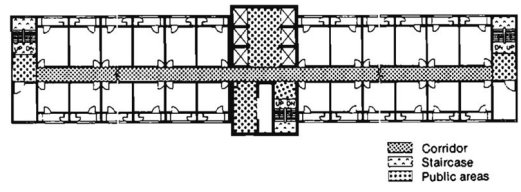

Figure 4. A common structural layout plan for an aged PRH building.

the associated concrete strength values. In an attempt to identify a non-destructive method that could provide a good correlation with the strength determined from the compression test method, various non-destructive test methods were experimented and evaluated for old PRH buildings (Stubbings et al., 1990). Unfortunately, no single test method could give a satisfactory correlation for the relatively low-strength concrete existed in the old PRH buildings. As CSIP results are crucial in determining whether a structure is structurally and economically viable to sustain for a further 15-year period, the conventional compression test on core samples is used in the CSIP for evaluating concrete strength due to its greater accuracy and reliability.

3.2 *Testing and sampling for concrete*

Concrete is a heterogeneous material with strength that inherently varies in nature. For the same design mix, strength varies in different batches due to differences in materials, batching, handling, curing, and external environmental factors. Even for the same concrete batch, strength variations could be a result of fluctuations in compaction and curing within a single member. For example, the lower region of a member tends to be better compacted than the higher region due to hydrostatic effects. The tendency for moisture to rise and aggregates to settle during construction also affects the density and strength of concrete. Minor differences in sampling and testing procedures further add to the variations in strength. While these different types of variations are difficult to isolate and measure in an as-built environment, a thorough understanding

of these variations is essential in the planning of an effective test programme and interpretation of the associated test results.

Before carrying out any test, due consideration should be given to the choice of sample locations both in terms of the representativeness of cores and appropriateness for coring. The most appropriate number of samples for a CSI is a balance among accuracy, cost, duration and damage to structure. A building can be globally divided into test regions in which concrete in each region may be assumed to belong to the same population. Since the methods of placing, compaction, and curing of concrete for horizontal members are different from vertical members, a good starting point is to divide test regions into horizontal elements and vertical elements for a PRH building. Within each test region, individual test locations are sampled at random so that samples obtained are representative of the general quality of a population. Statistical tests are required to validate the assumption that only a single population exists in each test region. To strike a balance among reliability, resources and potential damage to an existing PRH building, one core sample for every 50 m^3 of concrete is generally appropriate for the CSI of a typical aged building. More samples will be obtained if further analysis is needed for a particular region.

3.3 *Statistical analysis for EIChS*

Most modern limit state design codes adopt the precept that concrete strength values exhibit a normal distribution for the same design mix. For example, in Hong Kong Code of Practice for Structural Use of Concrete 2013 (2013) and BS EN 206 (2000), the characteristic strength of concrete is defined as the value of the cube strength at 28 days below which 5% of all compressive test results are expected to fall based on a normal distribution. A normal distribution can be assumed because quality control in making concrete cube samples for characteristic strength determination is high. On the other hand, for as-built concrete in an aged PRH building, the control of placing, handling, compacting, and curing in actual construction 40 years ago might be inconsistent. Instead of assuming a normal distribution, concrete strength values for core samples could exhibit a positively skewed log-normal distribution (Figure 5) (Watkins and McNicholl, 1990).

To determine the underlying distribution for a concrete population, various statistical tools such as the natural/logarithmic probability plot, the Epps-Pulley test, and the Kolmogorov-Smirnoff test are utilized. Based on the best fitting curve, the characteristic concrete strength can be determined from test data according to the level of confidence required. Without knowing the true mean or true standard deviation of an entire population, the EIChS, which is defined in the CSIP as the lower statistical tolerance limit for a proportion of 95% of the population at the 95% confidence level, is given by

$$EIChS = m - k_2 \times s$$

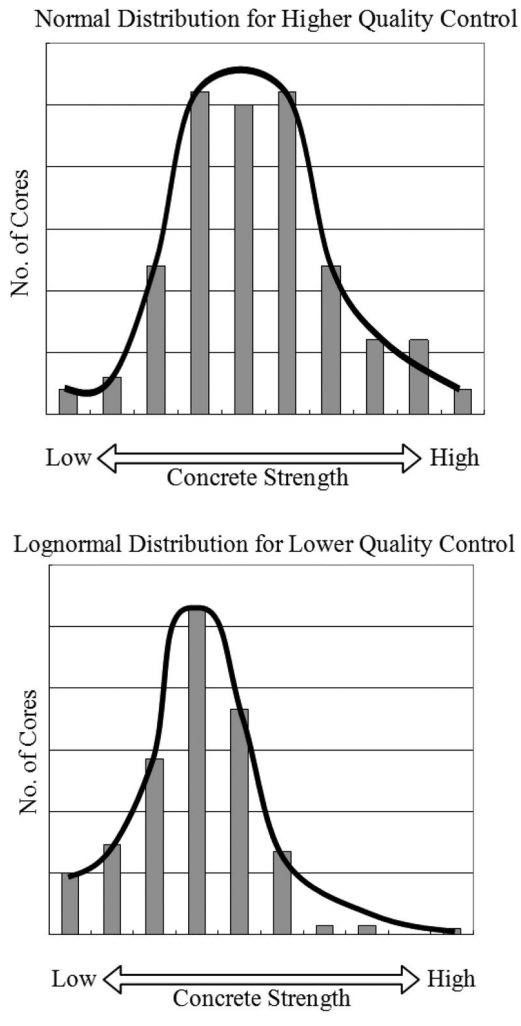

Figure 5. Normal distribution vs log-normal distribution for concrete strength in aged PRH buildings.

where m = the mean value of concrete strength within the same population; s = the standard deviation of the sample data; and k_2 = a factor derived from Table D.4 in Annex D of BS ISO 16269-6 (2005), which depends on the number of available samples, the required proportion of the population in the statistical tolerance interval, and the required confidence level.

3.4 *Verification of past concrete data*

As the CSIP is for PRH buildings approaching 40 years of age, extensive core data are available for some buildings through previous investigations done at different times long before the launch of the CSIP in 2005. If there is no loss of concrete strength with time under a typical PRH environment, a full coring programme could be avoided to minimize the risk of damaging an existing structure already with sufficient core data. To ensure that the historical data are not invalid,

a null-hypothesis can be made and tested under a 2-tailed condition as follows:

1. Determine the mean strength (m) and standard deviation (s) of concrete core test results based on previous investigations. Different batches of previous results should only be combined if they can demonstrate their homogeneity through statistical tests such as the "F-test" and "t-test".
2. Extract a minimum of 5 (n_1) cores from the building and determine the mean value (m_1).
3. Determine the interval (E) that the null hypothesis can be rejected based on the following equation:

   $$E = z \times s \Big/ \sqrt{n_1}$$

   where $z = 1.96$ for 5% level of significance.
4. If $|m_1 - m| < E$, it fails to reject the null hypothesis. In other words, the concrete strength as determined in the past structural appraisal can still be used for the new investigation.
5. If $|m_1 - m| > E$, the hypothesis has to be rejected and further investigation into the concrete strength is required.
6. If $m_1 > m$, the concrete strength based on the past data can still be used for an initial assessment as a lower bound value, which might only need to be refined when a structurally deficient member is identified.
7. If $m_1 < m$, extract a minimum of 5 additional cores (n_2) and repeat Step 3 to 6 with the number of cores equal to $n_1 + n_2$. If the hypothesis is still rejected and $m_1 < m$, the past data should be disregarded and a new concrete strength should be established based on a reasonable sample size with new cores only. An investigation on the possible chemical and other deleterious process influencing the concrete strength with time should also be carried out.

3.5 *Refined evaluation of concrete strength*

Existing concrete strength is a key element that determines the structural capacity of a building. When an EIChS is evaluated to be structurally inadequate for a PRH building, a comprehensive strengthening scheme, which could be costly, time-consuming, and tenant-disturbing, might be required. To minimize public disturbance and utilize public funds efficiently, refined concrete strength assessments described below are warranted before any strengthening proposal is recommended:

1. If concrete strength is marginally below the required values in various parts of a building, additional concrete cores throughout the building may be obtained to increase the available sample size for a more accurate EIChS determination.
2. If concrete strength is marginally below the required values for elements concentrated on a specific floor, additional concrete cores may be obtained to establish a revised EIChS for the specific floor. In a PRH setting, 1 core per 20 m^3 of concrete is generally desirable for evaluating the concrete strength on a floor-by-floor basis. In addition, a revised EIChS for the entire building could also be established if the additional concrete cores are tested statistically to be homogenous (i.e. from a single population) with the previous data from other floors.
3. To make a local assessment of concrete strength for a particular location, the Worst Credible Strength approach as described in BA44/96 (1996) and BS 6089 (2010) can be adopted:

   $$WCS = \frac{\sum f_c}{n}\left(1 - \frac{0.2}{n^{0.5}}\right)$$

   where WCS = the worst credible strength at a location; Σf_c = sum of estimated insitu cube strength of concrete cores; and n = number of cores at a particular location, normally not less than 3.

A particular location in the WCS approach should normally be confined to a particular element, but could be extended to a test region or a particular category of structural members where materials, workmanship, quality control, and other factors are considered to be the same resulting in concrete strength values with no more than a normal random variation. The applicability extent of the WCS is largely a matter of engineering judgment and care must be taken to avoid over-extending the validity of local test results.

4 STEEL REINFORCEMENT

The introduction of reinforcing steel, with its high tensile strength and good ductility to complement concrete, is the main reason why reinforced concrete has become one of the most common construction materials in the world since the last century. Ironically, the presence of reinforcing steel is also the main reason why aged reinforced concrete buildings today are facing the major challenge of structural degradation from corrosion. PRH buildings in Hong Kong, a place with a subtropical climate and a coastal environment, are no exception. In fact, the open-building design (Figure 6) adopted in aged PRH buildings for better natural lighting and ventilation makes them vulnerable to ingress of chemicals, moisture, and other contaminants. Coupled with a relatively low concrete grade and thin concrete cover, corrosion of steel has become the major factor in deciding the sustainability of aged PRH buildings.

4.1 *Testing and sampling for steel reinforcement*

With billions of dollars being spent on corrosion problems worldwide every year (NACE, 2002), corrosion of steel reinforcement is an on-going research topic that has attracted a vast amount of research effort. Below is a non-exhaustive list that illustrates some of the factors that would influence the corrosion process of steel reinforcement embedded in concrete:

- Thickness of concrete cover
- Quality of concrete cover (generally reflected by concrete strength)

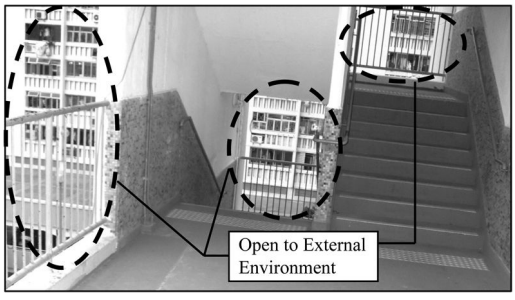

Figure 6. Open-building design in aged PRH building.

- Chloride level in concrete
- Depth of carbonation front
- Presence and quality of surface finish
- Age
- Maintenance history
- Member specific micro environment (e.g. temperature, relative humidity, air flow)
- Whether air is salt laden (near a coastal zone)
- Whether air is particularly contaminated
- Dry or exposure to rain / wet and dry

Understanding these factors is essential in developing and implementing a test programme for evaluating the existing condition of steel reinforcement. Before establishing a test programme, visual inspection should be carried out to assess the general condition of a structure. Besides documenting visible defects on structural elements, a visual survey is to identify symptoms and clues which would characterize the underlying structural degradation process. Destructive and non-destructive tests can be used to confirm findings of a visual survey and provide insights into the condition of steel reinforcement. Information such as concrete moisture levels, chloride profiles, and carbonation depths is invaluable in understanding the causes of corrosion. Corrosion risk can be quantified by a half-cell potential survey, which measures the voltage difference between steel reinforcement and a reference electrode in contact with the concrete surface. Corrosion rates can be deduced through the conversion of polarization resistance measurements using Stern-Geary equation and Faraday's Law (ASTM G102, 2010). Yet, even with these state-of-the-art testing techniques, the only method to determine the actual corrosion level of steel reinforcement is through concrete breakout (Figure 7).

4.2 *Corrosion measurement*

With steel reinforcement exposed by concrete breakout, a length of steel bar can be cut and the mass can be weighed to determine the degree of corrosion. However, this procedure is very disruptive as the load path will be altered and the concrete breakout will need to be significantly extended for lapping of steel bars in repair. In addition, this method cannot properly assess the steel area loss caused by pitting corrosion that concentrates at local points. As a result, the CSIP

Figure 7. Concrete breakout for inspection of corroded steel reinforcement.

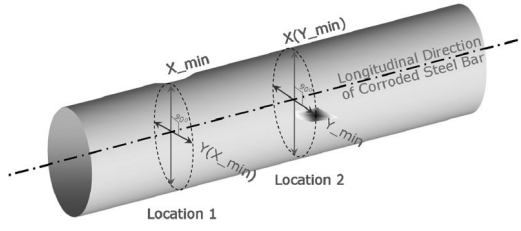

Figure 8. CSIP corrosion measurement for steel reinforcement.
Location 1: Locate and measure the least sectional dimension of a steel bar and record it as X_min. To account for the fact that the cross-section of a corroded bar is unlikely to be circular, measure the sectional dimension 90^o from X_min and record it as Y(X_min)
Location 2: Locate and measure the least sectional dimension along the axis 90^o from X_min and record it as Y_min. Then measure the sectional dimension 90^o from Y_min and record it as X(Y_min)

adopted a less disruptive method for measuring the steel corrosion level. Through opening up of concrete at randomly selected locations, the corrosion level within an exposed length of steel bar is best represented by the lesser area (i.e. πxy/4) of the 2 locations determined as follows (Figure 8):

4.3 *Statistical analysis for reinforcement corrosion level*

In accordance with ASTM G16 (2010), "corrosion test results often show more scattered than many other types of tests because of a variety of factors including the fact that minor impurities often play a decisive role in controlling corrosion rates". In view of this, statistical techniques are essential for interpreting these scattered test results and deducing reliable conclusions. The data grouping and categorization in a CSI require consideration of the following factors:

- Element types
- Environmental conditions (including local usage, exposure conditions, surface protection and maintenance quality)
- Bar types, sizes and covers
- Modes of corrosion, i.e. corrosion caused by chloride or carbonation

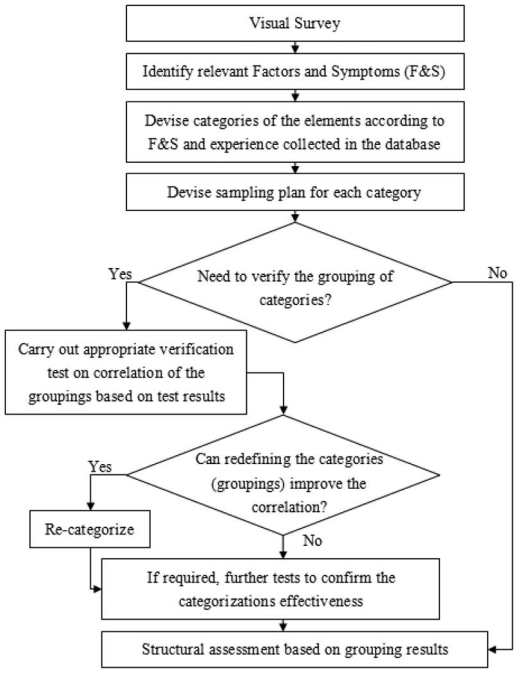

Figure 9. Statistical analysis for corrosion of steel reinforcement.

Based on the factors listed above and past CSI experience in a similar setting, different grouping of categories can be hypothesized and tested statistically. Depending on the degree of correlation between different categories, refinement of grouping and additional testing may be required to confirm the grouping effectiveness. With a dependable grouping of categories, the characteristic values of the measured average steel diameter loss for different groups at 95% confidence level can be evaluated statistically (Figure 9).

5 STRUCTURAL APPRAISAL

With a well devised test programme and a proper statistical analysis, the EIChS and corrosion levels for various groups of structural elements can be determined with confidence. The corresponding structural capacity of different elements in a building can then be evaluated reliably and compared against the intended loading. In addition to assessing the current condition, a CSI needs to predict whether a PRH building is structurally competent for the next 15 years. While concrete does not usually lose its strength with time, corrosion of steel reinforcement results in structural degradation. Based on a number of references (BRE, 2004; BRE/CRC; BD, 2003), the CSIP typically adopts a corrosion rate of 15 μm in loss of steel bar radius per year for intact or lightly cracked sections. A review (Pang et al., 2011) of the CSIP corrosion rate measurements conducted in the period from 2009 to 2011 in a number of aged PRH buildings confirmed the variable nature of corrosion rates. Nonetheless, the 15 μm/year corrosion rate was found to be a reasonable figure for general assessment considering that PRH buildings today are under good maintenance and care. However, if a building element is subject to adverse conditions, such as exposure to wet and dry condition or the presence of a high chloride content level, a refined analysis is necessary and a corrosion rate greater than 15 μm/year should be adopted if representative corrosion rate measurements confirm a higher value. In summary, the structural assessment of a CSI is carried out as follows:

1. Confirm the structural configuration and assess loading;
2. Determine the causes, mechanisms, severity and extent of deteriorations;
3. Evaluate the current capacity of structural elements;
4. Estimate future corrosion rates for various groups of structural elements based on concrete cover depths, screed thicknesses, existing chloride contents, carbonation depths, and current corrosion rates;
5. Assess the residual capacity of structural elements before the next investigation in 15 years.

6 CONCLUSIONS

Faced with the challenge of an aging PRH stock, the HKHA launched the CSIP in 2005 to determine the structural and economic sustainability of PRH buildings approaching 40 years of age. Based on the various established documents and CSIP experience, the methodology in assessing the insitu concrete strength and reinforcement corrosion level has been established and proved to be invaluable in assessing the residual structural capacity of aged PRH buildings. The extensive use of statistics in the analysis of concrete core results and corrosion measurements has undoubtedly led to higher reliability and greater confidence in conclusions of the CSIP. While the appraisal techniques developed were mainly based on aged PRH buildings unique in Hong Kong, many of the underlying principles could be extended for use in reinforced concrete structures in other parts of the world.

REFERENCES

ACI Committee 228, 2003. *ACI 228.1R-03 – In-place Methods to Estimate Concrete Strength*. American Concrete Institute. US.

ASTM G102, 2010. *ASTM G102-89(2010) Standard Practice for Calculation of Corrosion Rates and Related Information from Electrochemical Measurements*. ASTM International. US.

ASTM G16, 2010. *ASTM G16-95(2010) – Standard Guide for Applying Statistics to Analysis of Corrosion Data*. ASTM International. US.

BA, 1996. *BA 44/96 - The Assessment of Concrete Highway Bridges and Structures*. The Highways Agency. UK.

BD, 2003. *Internal Reference Document*. Buildings Department. Hong Kong.

BD, 2013. *Code of Practice for Structural Use of Concrete 2013*. Hong Kong Building Department. Hong Kong.

BRE, Digest 491, 2004. *Corrosion of steel in concrete – A review of the effect of humidity*. BRE Press. UK.

BRE/CRC DME Final Report Deliverable 45. *Corrosion Measurement*. BRE Press. UK.

BSI, 2000. *BS EN 206-1:2000 – Concrete Part 1: Specification, performance, production and conformity*. British Standards Institute. UK.

BSI, 2005. *BS ISO 16269-6:2005 – Determination of statistical tolerance intervals*. British Standards Institute. UK.

BSI, 2010. *BS 6089:2010 – Assessment of insitu compressive strength in structures and precast concrete components – Complementary guidance to that given in BS EN 13791*. British Standards Institute. UK.

NACE, 2002. *Corrosion Costs and Preventive Strategies in the United States*. U.S. Federal Highway Administration. US.

Pang, H.W., Au, B.L.K., Chan, W.B., 2011. *Classification of Environmental Exposure of Building Elements by Tests*. Proceedings of the International Conference on Advances in Construction Materials through Science and Engineering. Hong Kong.

Stubbings, B.J., Ainsworth, P.R., Crane, R., and Watkins, R.A.M., 1990. *Appraisal of the Structural Adequacy of High-rise Reinforced Concrete Domestic Buildings in Hong Kong*. The Structural Engineer, 68, No.16, 21 August 1990. The Institution of Structural Engineers. UK.

Watkins, R.A.M., McNicholl, D.P., 1990. *Statistics Applied to the Analysis of Test Data from Low-Strength Concrete Cores*. The Structural Engineer, 68, No.16, 21 August 1990. The Institution of Structural Engineers. UK.

This page intentionally left blank

Concrete Solutions – Grantham et al. (Eds)
© 2014 Taylor & Francis Group, London, ISBN 978-1-138-02708-4

Evaluation of the mechanical integrity of a concrete surface by means of combined destructive methods

L. Courard
GeMMe Building Materials, ArGEnCo Department, University of Liège, Belgium

B. Bissonnette
CRIB, Civil Engineering Department, Laval University, Québec (QC), Canada

A. Vaysburd
Vaycon Consulting, Baltimore, MD, USA

A. Garbacz
Warsaw University of Technology, Poland

ABSTRACT: As a good bond between the repair and the old concrete is required, the soundness of the prepared surface has to be carefully assessed. This paper presents the results of an investigation intended to assess and compare quantitatively different test methods, namely the rebound hammer and the pull-off test, to evaluate superficial mechanical integrity of a prepared substrate. Although it does not yield a precise evaluation of compressive strength, the rebound hammer test is recognized as a useful tool for performing quick surveys to assess concrete uniformity. The pull-off test is very well correlated with the splitting-tensile test, but it is not suited for vertical and overhead surfaces. It appears from the results generated in this study that the combination rebound hammer / pull-off test could very well fill the needs for the evaluation of prepared horizontal surfaces.

1 INTRODUCTION

As part of the concrete repair process, in order to promote optimal adhesion of the repair material, the concrete substrate must be prepared to yield a rough surface that is free from defects and contaminants (Bissonnette *et al*. 2006; Courard *et al*. 2009). Depending on the technique being used, the concrete removal operation can be harmful to the residual concrete substrate. Whenever bond is key to the success of a repair, the soundness of the prepared surface should be assessed after surface preparation (Vaysburd *et al*. 2000; Garbacz *et al*. 2005). This issue could become even more critical than the condition evaluation carried out before undertaking the repair project (Courard *et al.* 2012).

Although the effect of substrate condition on bond is widely recognized (Silfwerbrand 1990; Courard *et al*. 2011), there is still no standard method intended for characterizing the integrity of a concrete substrate after concrete removal. For one, Belgian guidelines (2007) explicitly recommend performing a pull off test (EN1542, 1999) directly on the substrate, especially if doubt exists about the quality of surface preparation; a minimum value of 2 MPa is usually recommended. This must be seen as a guiding value. For low strength concrete, a lower value could be specified.

An experimental program has been conducted by the authors (Bissonnette *et al*. 2004) to evaluate the influence of various parameters on the measured cohesion of a concrete surface by means of pull off test. The test method shows good potential for a sound quantitative evaluation of a concrete surface mechanical integrity prior to repair, provided that the test parameters are selected properly.

Test location and interpretation of test results (Bungey 2000) must consider the possible variations of material properties within structural members and differences between in-situ and standard specimen strengths. The proper testing layout actually depends on whether it is intended to determine average values for a member (for specification compliance) or to assess the substrate condition in critical areas (for structural adequacy assessment). Furthermore, the number of test locations would vary with the objectives of the test and the expected level of confidence for the overall strength estimates. Typically, between 5 and 8 locations are tested.

This paper presents the results of an investigation intended to assess and compare quantitatively different test methods, namely the rebound hammer and the pull

Figure 1. The Schmidt rebound hammer.

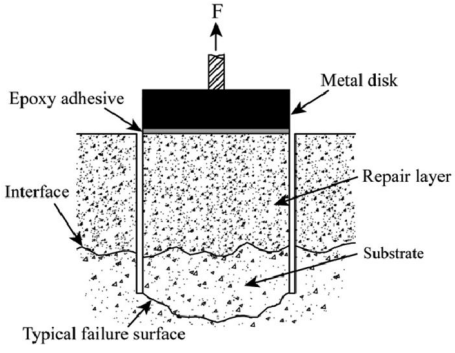

Figure 2. Pull off test.

off test, to evaluate the integrity of a substrate after concrete removal operations.

2 TEST METHODS AND MATERIALS

2.1 *Schmidt rebound hammer (ASTM C 805 and) EN 12504-2 determination of rebound number*

Due to its simplicity of use and low cost, the rebound hammer is a most widely used device for non-destructive testing of concrete (Figure 1). It operates as follows: a spring-loaded hammer impacts, with a given amount of energy, a steel plunger in contact with the concrete surface, and the distance that the hammer rebounds is recorded. The rebound value is primarily influenced by the elastic modulus and strength of the concrete near the surface (Carino 2003). While the test may be simple to perform, the relationship between measured rebound number and in-place concrete strength is sensitive to a number of parameters. In particular, the results are influenced by the moisture condition, carbonation and surface texture of the concrete, as well as hammer inclination (Courard *et al*. 2011; Carino 2003). Since the plunger's rebound depends on the energy being restituted from the substrate, it is expected that incidence of bruising and cracking in the surface layer will reflect in the recorded values. Although the evaluation of strength is not an issue in the present study, the test results are expressed in terms of strength.

2.2 *Pull off test (EN 1542-4,)*

The pull off test is commonly used to assess the adhesion of repair systems to concrete.

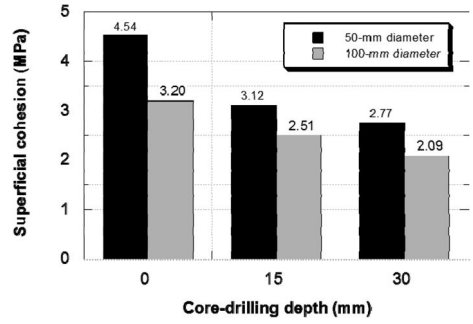

Figure 3. Effects of core-drilling depth and metal disk diameter on surface concrete cohesion (loading rate < 0.05 MPa/s).

It measures the direct tensile force required to pull off a metallic disk, together with a layer of concrete, from the surface to which it has been epoxy-glued (Figure 2).

The pull off test can also be used to evaluate the cohesion and integrity of a concrete surface to be repaired (Bungey *et al*. 2001; Hindo 1990; Emberson *et al.* 1990; Austin *et al*. 1995). An experimental program was conducted in a previous study (Bissonnette *et al*. 2004) to evaluate the influence of various test parameters—metal disk thickness and diameter, core drilling depth, loading rate, adhesive type and thickness, and number of tests—to measure the cohesion of a reference concrete surface. A statistical results analysis revealed that disk diameter and core-drilling depth are the most significant parameters, presumably with threshold values (Figure 2), which actually depend on the maximum aggregate size.

In order to yield low standard deviation and satisfactory level of confidence in the results (maximum coefficient of variation of 12 %), a minimum of 5 tests is recommended. Other authors (Bungey 2000) recommend a minimum of 6 pull off tests in a specific area to be assessed.

It was proved that up to a certain misalignment limit angle (about 5°), load and coring misalignments were not found to yield significantly value of pull-off strength (Courard *et al.* 2014).

After testing, and depending on the failure mode or value, concrete integrity may need to be assessed further to examine the presence of cracks near the failure surface (mostly parallel to the surface) as a result of surface preparation operations (Bissonnette *et al.* 2006).

2.3 *Materials*

Experiments have first been performed on untreated concrete surfaces in order to study the significance and sensitivity of test parameters. Then, test series intended to evaluate the cohesion of concrete after various surface treatments were carried out.

Slab test specimens were cast using concrete with 0.40 and 0.48 water/cement ratios, respectively. The former was made using 10-mm crushed granite as

Table 1. Concrete mixture composition and properties.

Mixture design	S1	S2
Cement CSA type 10 (kg/m^3)	384	383
Water (l/m^3)	156	187
Sand (kg/m^3)	736	734
Coarse aggregate 10 mm (kg/m^3)	–	916
Coarse aggregate 20 mm (kg/m^3)	918	–
Air-entraining (ml/m^3)	78	76
Superplasticizer (ml/m^3)	980	1269
W/C	0.40	0.48
Slump (mm)	145	75
Compressive strength (MPa)	32.3	46
Splitting tensile strength (MPa)	3.3	4.0

coarse aggregates, while the latter used 20-mm aggregates from the same source. Table 1 presents the concrete mixture designs, which had been used as reference materials in other related research projects devoted to repair and rehabilitation issues.

Three concrete batches were prepared for the fabrication of 13 concrete slabs. Two different slab configurations were cast: type S1 (500 × 500 × 90 mm) and type S2 (730 × 730 × 90 mm). After casting, the slabs were covered with wet burlap and a polyethylene sheet for 48 hours. They were then stored in the laboratory at 23°C and 50–70% RH for 26 days. A relatively good quality of concrete was obtained due to compaction and low w/c ratio: an even higher w/c ratio (S2 *vs* S1) but smaller aggregates offered a good resistance to splitting.

3 EXPERIMENTAL PROGRAM

3.1 *Rebound hammer test*

The rebound hammer tests were performed on cast surfaces, before any treatment. To estimate the required number of data for statistical significance, a large number of tests were carried out. Based on the results summarized in Table 2, it seems that the average compressive strength estimated with the rebound hammer is not significantly influenced by the number of tests, at least beyond 25 replicas. It thus appears that 25 tests are sufficient (but also necessary) for the surface investigated.

The rebound hammer results obtained for all concrete slabs are presented in Figure 4. The differences between S1-3 and S1-3* appear to be mostly related to the nature of the support provided underneath the test slabs, either continuous (wooden platform) or discontinuous (2 wood lumbers), which offer different rigidities.

Variability, which was evaluated with the coefficient of variation (CV), was lower when the concrete specimen was placed on a continuous support.

3.2 *Pull off test*

The pull-off tests were performed on the S1- and S2-series slabs using a core-drilling depth of 20 mm. The test results are summarized in Table 3. The aggregate size appears to have a limited influence on cohesion strength and variability. Nonetheless, the location and shape of the failure surface were more variable for the larger size aggregate concrete.

Overall, the recorded values are very close to the corresponding splitting tensile strength data (Table 1). This is consistent with the results of a previous program (Bissonnette *et al.* 2004), where pull off testing was shown to be an effective technique for evaluating the mechanical integrity of horizontal surfaces after concrete removal. For quality control purposes,

Table 2. Schmidt rebound hammer test results: influence of the number of tests performed upon statistical parameters (S2 slab specimens).

Statistical parameter	S2-5 slab			S2-6 slab		
	Number of tests					
	61	36	25	61	36	25
Ave. value (MPa)	32.3	32.1	32.5	30.9	30.9	30.8
Coefft. of var. (%)	10.1	10.8	9	8.3	9.3	6.8

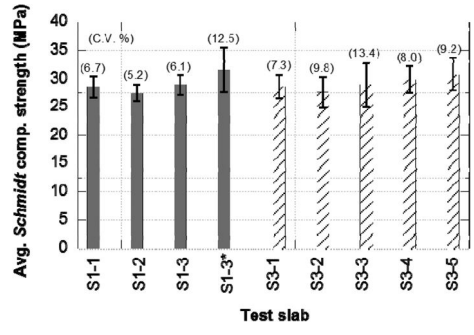

Figure 4. Average compressive strength values estimated from the rebound hammer tests on flat finished slab specimens.

Table 3. Pull off test results (S1- and S2-series test slabs).

Test nr.	Pull off stress (MPa)	
	S1-series slabs	S2-series slabs
1	3.42	3.92
2	3.06	3.60
3	3.35	4.19
4	3.24	4.10
5	3.30	3.92
6	3.30	3.67
7	3.12	4.05
8	3.40	4.01
Average value	3.27	3.93
Coefficient of Variation (%)	3.91	5.12

an acceptance criterion corresponding to a fraction of the average splitting-tensile strength (f_{st}) result could be specified.

4 CONCLUSIONS

Surface preparation is often a critical step in concrete repairs. While it is well acknowledged that the concrete removal operation can induce bruising and cracking in the substrate, there are still no simple practical means available to assess the integrity of a concrete surface. The investigation reported in this paper intended to evaluate different test methods for that purpose: the rebound hammer and the pull off test.

Although the rebound hammer test cannot systematically yield a reliable evaluation of the in-place compressive strength of concrete, it was shown to provide valuable comparative data for detecting superficial defects on a concrete surface. The rebound hammer method is thus recognized as a useful tool for performing quick surveys to assess concrete uniformity and mechanical integrity over substrates.

The pull off test provided results that are very close to the actual splitting-tensile strength of the material. Moreover, it was shown in a previous study (Bissonnette *et al*. 2006) that it can effectively capture the presence of bruising. Still, it is difficult to perform adequately on vertical or overhead surfaces and, in practice; its use is essentially limited to horizontal surfaces.

Finally, it appears from the results generated in this study that the combination rebound hammer/pull off tests can fulfill the needs for the evaluation of horizontal surfaces. For quality control purposes, acceptance criteria could be specified for both the hammer soundings (ex. C.V. $< 20\%$) and cohesion strength test results (ex. pull off test: cohesion strength > 0.75 fst.

ACKNOWLEDGMENTS

This project has been financially supported by the Natural Sciences and Engineering Research Council of Canada (NSERC), the Québec FQRNT Research Fund and the industrial partners of the Industrial Chair on Durable Repair and Optimized Maintenance of Concrete Infrastructures at Laval University (BASF Building Systems, City of Montreal, City of Québec, Euclid, Hydro-Québec, King Packaged Materials, Lafarge, Ministry of Transportation of Québec, St-Lawrence Cement, W.R. Grace & Co. Support was also provided by the Belgium (Wallonia Brussels International) and Quebec governments through the Wallonie-Bruxelles-Québec Scientific Cooperation Program as well as Belgium – Poland (MNiSW) Scientific Cooperation Program.

REFERENCES

Austin, S.; Robins, P.; and Pan, Y., "Tensile Bond Testing of Concrete Repair," Materials and Structures, V. 28, No. 179, 1995, pp. 249–259.

Belgian Construction Certification Association, "Technical Prescriptions for Concrete Repair Mortars," Belgian Guidelines PTV 563, Brussels, Belgium, 2007.

Bissonnette, B.; Courard, L.; Vaysburd A.; and Bélair, N., "Concrete Removal Techniques: Influence on Residual Cracking and Bond Strength," Concrete International, V. 28, No. 12, 2006, pp. 49–55.

Bissonnette, B., and Courard, L., "Pull Off Test for the Evaluation of the Superficial Cohesion of Concrete Substrates in Repair Works: Analysis of the Test Parameters (in French)," Materials and Structures, V. 37, 2004, pp. 342–350.

Bungey, J.H., "Assessment of In-Situ Concrete Strength: Overview of Test Procedures," University of Liverpool, 2000.

Bungey, J.H., and Soutsos, M.N., "Reliability of Partially-Destructive Tests to Assess the Strength of Concrete on Site," Construction and Building Materials, V. 15, 2001, pp. 81–92.

Carino, N.J., "Non Destructive Test Methods to Evaluate Concrete Structures," Sixth CANMET/ACI International Conference on the Durability of Concrete, Special Seminar, Thessaloniki, Greece, 2003, 75 pp.

Courard, L.; Bissonnette, B.; Garbacz A., Vaysburd A.; von Fay K., Moczulski G., Morency M., "Effect of Misalignment on Pulloff Test Results: Numerical and Experimental Assess-ments", ACI Materials Journal, 2014, 111 (1–6).

Courard L.; Bissonnette B.; Vaysburd A.; Belair N.; Lebeau F., "Comparison of destructive methods to appraise the mechanical integrity of a concrete surface". Concrete Repair Bulletin 25(4) (July–August 2012), 22–30.

Courard, L.; Michel, F.; Schwall, D.; Van der Wielen, A.; Garbacz, A.; Piotrowski, T., Perez, F.; and Bissonnette, B., "Surfology: Concrete Substrate Evaluation prior to Repair," Materials Characterization: Computational Methods and Experiments IV, A. Mammoli and C.A. Brebbia eds., Wessex Institute of Technology Press, The New Forest (U.K.), June 17–19, 2009, pp. 407–416.

Courard, L.; Bissonnette, B.; and Trevino M., "Condition Evaluation of the Existing Structure prior to Overlay," Bonded cement-based material overlays for the repair, the lining or the strengthening of slabs or pavements, Report of RILEM TC 193-RLS, 2011, pp. 17–50.

Emberson, N.K., and Mays, G.C., "Significance of Property Mismatch in the Patch Repair of Structural Concrete Part 1: Properties of Repair Systems," Magazine of Concrete Research, V. 42, No. 152, 1990, pp. 147–160.

EN 1542 CEN European Committee for Standardization, "Products and systems for the protection and repair of concrete structures – Test methods – Measurement of bond strength by pull-off", Brussels, Belgium, 1999.

Garbacz, A.; Gorka, M.; and Courard L., "Effect of Concrete Surface Treatment on Adhesion in Repair Systems," Magazine of Concrete Research, V. 57, No. 1, 2005, pp. 49–60.

Hindo, K.L., "In-Place Bond Testing and Surface Preparation of Concrete," Concrete International, V. 12, No. 4, 1990, pp. 46–48.

Silfwerbrand, J., "Improving Concrete Bond in Repaired Bridge Decks," Concrete International, V. 12, No. 9, 1990, pp. 61–66.

Vaysburd, A. M., and Emmons, P.H., "How to Make Today's Repairs Durable for Tomorrow – Corrosion Protection in Concrete Repair," Construction and Building Materials, V. 14, No. 4, 2000, pp. 189–197.

Structural modelling/finite element analysis

This page intentionally left blank

Concrete Solutions – Grantham et al. (Eds)
© 2014 Taylor & Francis Group, London, ISBN 978-1-138-02708-4

Damage model for the analysis of structural response of RC columns subjected to corrosion phenomena

I. Finozzi & A. Saetta
Department of Architecture Construction Conservation, University IUAV of Venice, Venice, Italy

ABSTRACT: The problem of durability of Reinforced Concrete (RC) structures represents an evolving research topic in the assessment of existing structures. The corrosion of reinforcing bars is one of the most critical consequences of aging of RC members subjected to chloride and carbonation attack, because it can lead to an early and intense deterioration of such structures, reducing drastically their service life. Therefore, it is necessary to develop operative and reliable tools able to analyze the structural response of RC elements, both in sound and degraded conditions. In this paper, a numerical model based on damage mechanics, is presented and applied to simulate the behaviour of a number of experimentally tested RC columns, subjected to different level of corrosion. Both the residual load carrying capacity and the behavior of reinforced concrete elements observed in the experimental tests are well represented by the numerical model.

1 INTRODUCTION

The problem of durability of reinforced concrete (RC) elements, exposed to both physical and chemical actions, represents an evolving research topic in the assessment of existing structures: actually, due to aggressive environments and poor construction, nowadays an increasing number of existing RC constructions exhibit high levels of deterioration. The corrosion of reinforcing bars is one of the most important and widely encountered causes of degradation, which can lead to serious structural consequences, as loss of serviceability and load carrying capacity. The corrosion of steel reinforcement in concrete may also influence the seismic response of the RC structures, leading to a more brittle behavior and to a loss of ductility, particularly required in seismic conditions. In recent years, a number of models have been proposed to study of the local effects of corrosion, but relatively little attention has been paid on the assessment of the performance of corroded RC elements. In this work, a numerical model based on damage mechanics, e.g. Saetta et al 1999, is presented and applied to simulate the structural response of RC columns subject to different level of corrosion. In particular, the concrete is modelled with an isotropic coupled environmental-mechanical damage model, whose mechanical feature has been based on the work of Faria (Faria et al. 1998) and then extended to environmental damage by one of the authors, e.g. (Saetta et al 1999, Berto et al. 2013). Then, all the main local effects of corrosion are included in the proposed model, i.e. the reduction of cross sectional area of the corroded reinforcements, the change of the mechanical properties of both steel and concrete materials, the cracking and the spalling of the concrete cover. In this way the actual behaviour of both sound and corroded RC elements can be profitably modelled.

As a validation of the proposed approach, the data obtained during the experimental campaign carried out by Rodriguez et al. 1996 on sound and corroded RC columns are compared with the results of the numerical analyses. The good agreement demonstrates the effectiveness of the proposed formulation and the possibility to apply the numerical approach also to real RC structures.

2 NUMERICAL SIMULATION

2.1 *Coupled damage model for concrete*

The concrete material is modelled with the coupled environmental-mechanical damage model described e.g. in Berto et al 2013. Such a model, couples the mechanical variables d^+ and d^-, with the environmental damage parameter d_{env}, as following reported:

$$\boldsymbol{\sigma} = (1-d_{env})[(1-d^+)\bar{\boldsymbol{\sigma}}^+ + (1-d^-)\bar{\boldsymbol{\sigma}}^-] = (1-d^{*+})\bar{\boldsymbol{\sigma}}^+ + (1-d^{*-})\bar{\boldsymbol{\sigma}}^- = (1-D^*)\bar{\boldsymbol{\sigma}} \quad (1)$$

where $\bar{\boldsymbol{\sigma}}^+$ and $\bar{\boldsymbol{\sigma}}^-$ are the tensile and the compressive components of the effective stress tensor.

This approach, is adopted in order to simulate the evolution of the deterioration in the concrete, due also to environmental attack. The stress-strain curve of the isotropic damage model is able to well reproduce the softening branches of the concrete under tensile

and compressive stresses, and also the reduction of stiffness and strength due to environmental damage.

As well known, continuum damage models suffer from strain localization and mesh dependency of the numerical results. Regarding the tensile behaviour, the mesh dependency associated with the strain softening branch is overcome for the energy aspect by adopting the "enhanced local method" (Saetta et al. 1999) which considers the specific fracture energy as a function of the mesh element size *h*:

$$g_f = \frac{G_F}{h} \tag{2}$$

In the proposed model, a characteristic internal length, related to *h*, is introduced to avoid dependency of the dissipated energy on the width of the band.

A similar approach could be adopted for the softening behavior of concrete loaded in compression. In this work the numerical law is firstly calibrated on the one suggested by Model Code 1990 (CEB-FIP, 1993) and then the softening branch is amplified with a *mesh size factor*, which corresponds to the ratio between the 200 mm length of the specimen on which the Model Code law is based, and the mesh size of the adopted numerical model:

$$mesh\ size\ factor = \frac{200mm}{mesh\ length} \tag{3}$$

More details about the compressive fracture energy criteria can be found in (Finozzi & Saetta 2014).

Concerning the different behavior of confined and unconfined concrete in the compression state, it is worth noting that it is particularly evident in columns, for which confinement has a high influence on the structural response: i.e. well-confined columns show high ductility behaviour, especially under seismic actions. For this reason, in the following numerical analyses specifically aimed at analyzing the columns response, two different constitutive laws are considered for the concrete cover and the concrete core.

Among the numerous models which have been proposed to take into account the effect of confinement, the model of Scott (Scott et al. 1982) is here considered. In this model, an increase of the compressive strength of the concrete is introduced as a function of the effect of confinement of the transverse reinforcement. The uniaxial constitutive law is a parabola for the ascending branch of the curve, and a straight line for the post-peak behaviour.

As declared by Claeson (Claeson, 1999) the structural behaviour of a column depends on the load eccentricity. Actually, for a small load eccentricity, the compressive behaviour of the concrete is dominant and it is necessary to accurately model the phenomena associated with compression, such as gradual spalling of the concrete cover and the confining action of the stirrups. Otherwise, as the load eccentricity increases, cracking phenomena gradually dominates and the properties of the reinforcing steel become more and more important.

In this research the proposed model is used to simulate the experimental tests carried out by Rodriguez (Rodriguez et al. 1996) on sound and corroded RC columns. In particular type 2 columns are analysed due to the low value of the load eccentricity that they present, with the aim of considering situations which are dominated by the compressive behaviour. Therefore, in these cases, the constitutive laws considered for the concrete assume particularly relevance, and the confinement effect must be considered.

For the sake of brevity, in this paper only the results obtained for columns n°21–22 and n°28, respectively non-corroded and corroded, with the smaller values of load eccentricity, are reported.

2.2 *Corrosion effects on concrete*

Corrosion of reinforcement bars induces cracking of concrete cover; indeed, when iron becomes rust, the oxides products occupy a greater volume than the original steel. The development of cracks on the cover concrete has important consequences on the structural response, in particular, as declared by Rodriguez (Rodriguez et al. 1996) the damage of the concrete cover is the most relevant form of deterioration for the column strength

The deterioration of the concrete cover can be taken into account by reducing the compressive strength of the concrete, as proposed by Coronelli (Coronelli et al. 2004) according to the following relationship:

$$fc^* = \frac{f_c}{1+k\frac{\varepsilon_1}{\varepsilon_{co}}} \tag{4}$$

where *k* is a coefficient (a typical value is 0,1) depending on bar roughness and diameter, ε_{c0} is the strain at the compressive stress peak *fc* and ε_1 is the average tensile strain in the cracked concrete, which can be calculated as:

$$\varepsilon_1 = \frac{n_{bars} \cdot w_{cr}}{b_o} \tag{5}$$

with w_{cr} the average width of crack of each bar (which can be calculated with the formula proposed by Molina et al. 1993), n_{bars} the number of bars and b_0 the original section width.

Due to the development of micro-cracks and cracks in the concrete cover, the mechanical properties of the material change: the concrete becomes weaker and less ductile. To take into account this second effect, a reduction of the ductility of concrete in compression as the level of corrosion increases, is introduced. In particular a linear relationship between the percentage reduction of the area of the reinforcements and the reduction of the ductility is proposed:

$$\varepsilon_u' = \varepsilon_u \left[1 - f\left(1 - \frac{A_{s,tot}'}{A_{s,tot}}\right)\right] \tag{6}$$

where $A_{s,tot}$ and $A_{s,tot}'$ are respectively the initial and the residual area of all the reinforcement bars, ε_u is

the ultimate strain of the sound concrete and ε'_u is the ultimate strain of the deteriorated concrete, f is a coefficient which can be assumed equal to 2. For more detail, refer to Finozzi & Saetta, 2014.

2.3 *Constitutive laws for steel reinforcement bars*

The behaviour of the longitudinal bars and stirrups is simulated using a linear elastic-plastic material model with linear strain hardening. This constitutive law is used for the reinforcement of sound columns, i.e. the tested columns n°21 and 22.

For the corroded columns, a different constitutive law for the longitudinal bars is adopted in the numerical simulation. Indeed, a premature buckling of the main bars can occur, as proved by a number of evidences in experimental tests. In case of high levels of corrosion penetration, some stirrups can fail, so the spacing between the stirrups increases and at the same time the diameter of the main bars decreases, due to the effect of cross-section reduction provoked by the corrosion. Therefore, the ratio between the stirrup spacing and the diameter of the longitudinal bars exceeds the critical value of the geometrical slenderness ratio λ_{crit} and buckling phenomena can occur. To estimate the reduction of the reinforcement strength, Rodriguez et al. 1996 have suggested to consider the theoretical stress value corresponding to the critical load of the main bars:

$$\sigma_{crit} = \frac{\pi^2 E\,[0.25\,\Phi]^2}{[0.75\,s]^2} \tag{7}$$

where E is the modulus of elasticity, Φ is the main bar diameter and s is the stirrups spacing.

The behavior of the reinforcement under axial load has been the subject of various studies; in particular, Monti (Monti et al. 1992) developed an analytical model for simulating the bar behaviour in the presence of buckling over the elastic threshold. In this model, when the critical load (always greater than the yield stress) is reached, a softening branch in compression which tends to an asymptotic value, starts.

In the present work, a new constitutive law based on the one of Monti et al. 1992 is proposed, in order to consider the premature buckling phenomena described by Rodriguez et al. 1996. As reported in Figure 1, the following monotonic stress-strain relation in tension, consisting of two linear branches, is assumed:

$$\begin{aligned} &\sigma_s = E_0 \cdot \varepsilon_s \qquad 0 \le \varepsilon_s \le \varepsilon_{crit} \\ &\sigma_s = E_0 \cdot b \cdot \varepsilon_s \;\; \varepsilon_{crit} \le \varepsilon_s \le \varepsilon_u \end{aligned} \tag{8}$$

where $E_n = b \cdot E_0$ is the slope of the softening branch which depends on the initial elastic modulus E_0 and on the factor $b = \alpha\,(\lambda_{crit} - \lambda)$ with $\lambda_{crit} = 5$ and a is a parameter (can be assumed equal to 0,006), while the factor b is equal to the one suggested by Monti et al. 1992 for the slope of the tangent of the softening branch.

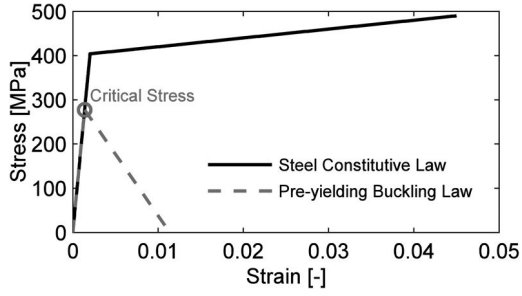

Figure 1. Pre-yielding law for longitudinal reinforcement bars.

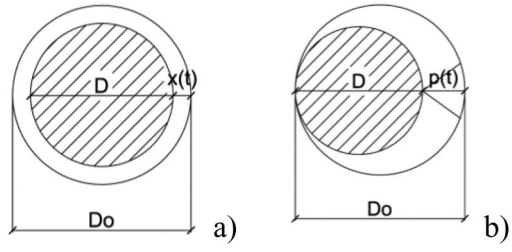

Figure 2. Reduction of cross-sectional steel area a) uniform corrosion b) pitting and uniform corrosion.

2.4 *Corrosion of reinforcement*

As well known, in case of carbonation, once the depassivation phenomenon occurs, the corrosion develops uniformly over the reinforcing bars. In this case, the remaining cross-sectional area, function of the depth of corrosion $x(t)$, may be calculated as:

$$A_s(t) = \pi \cdot \left(\frac{D_0}{2} - x(t)\right)^2 \tag{9}$$

where $A_s(t)$ is the cross-sectional area of a reinforcing bar at time t, D_0 is the initial diameter of the bar.

Instead, in the presence of localized corrosion (e.g. chloride attack), the loss of area is not uniformly distributed, but is concentrated in localized "pits" in the bars. The reduction of the cross-section must be evaluated in a different way than the case of uniform corrosion (e.g Stewart 2009). One way to consider the concurrence of uniform and localized corrosion, which often happens in accelerated corrosion tests, is the model proposed by Rodriguez et al.1996:

$$\Delta A_s = \tfrac{\pi}{4} \cdot (2 \cdot x(t) \cdot D_0 - x(t)^2) \tag{10}$$

In the present work, the two equations are used, in order to consider the case of only uniform corrosion and the case of high reduction of steel area due to both pitting and uniform attack (see Figure 2).

Furthermore, in case of high levels of pitting attack, the cross section of the bars may greatly reduce and failure can occur. This consequence of steel corrosion can be particularly important, indeed if stirrups fail, buckling of the longitudinal bars can take place and

Table 1. Summary of experimental results.

Column no.	no. of days	Max crack width (mm)	Attack penetration (mm) (*)		Delamination load (+)			Ultimate load		Eccentricity [mm]	
			Main bars	Stirrups	Axial force (KN)	mean strain (.)	Axial force (KN)	Mean strain (.)	no. of broken stirrups	ex	ey
22	–	–	–	–	–	–	1702	2.6	–	2.1	5.4
28	204	2.5	0.63	0,50 (4.7)	975	1.4	997	1.8	4	1.9	5.5

* Maximum values of pitting are reported in bracket. +Load value when initiation of delamination of concrete cover was observed.
. Mean strain at the midspan zone, in %, on the four sides of the column.

provoke the failure of the columns. For this reason, in the numerical model, the failure of stirrups will be considered and analysed together with the buckling of the main bars. In particular, due to the non-effective contribution of the stirrups subjected to the highest level of pitting penetration (reduction of 95% of the cross section), two different hypotheses of stirrup failure are considered: the loss of two consecutive stirrups and the loss of alternate stirrups.

3 EXPERIMENTAL SETUP

Rodriguez et al. 1996 have tested 24 columns of three different types, to investigate the effects of accelerated corrosion on column structural response. The type 2 columns, had 200 × 200 mm cross section and were 2000 mm high with end stiffening. For the 2 × 2Φ16 longitudinal bars and Φ6/150 stirrups reinforcement, AEH 500S steel type were used. To accelerate the corrosion of steel bars, 3% of calcium chloride by weight of cement was added to the mixing water and a current of 0.1 mA/cm^2 has been applied to all of the reinforcement in the 1200 mm central test section, for a number of days between 100 to 200. The compressive strength of concrete was respectively 34 MPa and 35.6 MPa for concrete without and with chloride, while yield stress and ultimate strength of the steel were in the following range: 550–590 MPa and 600–670 MPa.

The columns were tested under axial load and four displacement transducers (one for each side of the columns) were located to measure the average compressive strain. During the loading test, some eccentricities of relevant value were detected in the measurement of the strains on the four sides in most of the corroded columns, due to the non-uniformity of the corrosion, geometrical and testing imperfections and spalling phenomena, which showed up at later stages. In the numerical analysis, the eccentricity is not considered, indeed, as said, only the simulation of the columns with smaller eccentricity values are presented, in which the eccentricity effects are negligible. A future development of this research will consider also this aspect, that, as explained by different authors (Rodriguez et al. 1996, Claeson 1999) has a great influence on the column strength, especially in presence of corrosion that amplify the eccentricity values.

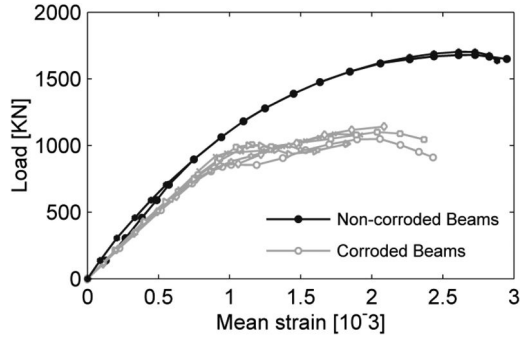

Figure 3. Load versus mean strain in column type 2.

Table 1 summarizes the main results of the experimental work, for corroded and uncorroded type 2 columns. The mean value of the attack penetration was obtained by a gravimetric method, while the maximum values of pitting were determined by geometrical measurement. During the test, delamination phenomena of the concrete cover was observed and the level of the load at which spalling of the concrete cover firstly occurred on one side, was named the Delamination Load. The Ultimate Load corresponds to the maximum load measured in the tests; close to this level of load, stirrup failures were observed. Finally, in Figure 3 the load-strain curves of the type 2 column are reported.

4 NUMERICAL SIMULATIONS

4.1 *Sound columns*

Type 2 Columns as used in the Rodriguez et al. 1996 test campaign, were taken as a benchmark for the numerical analysis carried out. The Type 2 column's geometry is shown in Figure 4. The concrete was modelled using four-node plane stress elements with thickness equal to the beam width and a regular mesh of 25x25mm was adopted. Regarding the constitutive law for the concrete material, refer to Figure 5; a detailed description is given in paragraph 2.1. The following values for the mechanical properties of

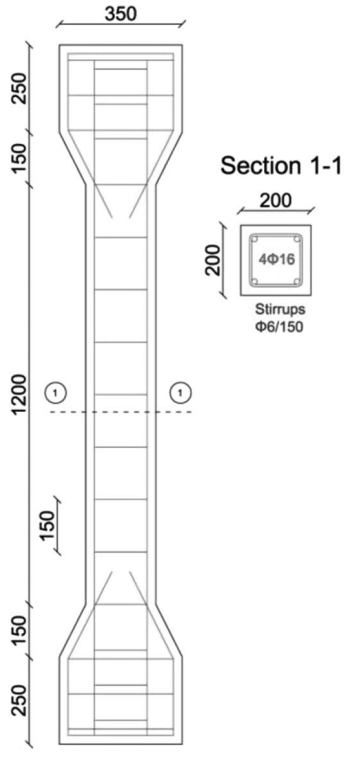

Figure 4. Scheme of columns type 2 (dimensions in mm).

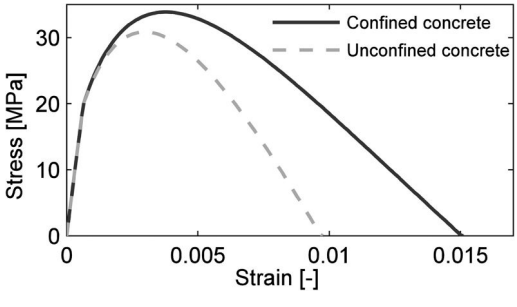

Figure 5. Stress-strain curves for confined and unconfined concrete.

the concrete material were adopted in the numerical simulation:

– Confined compressive strength = 33.86 MPa
– Unconfined compressive strength = 30.83 MPa
– Confined Tensile strength = 2.6 MPa
– Unconfined Tensile strength = 2.4 MPa
– Tension fracture energy = 66 N/m

The steel reinforcement bars were modelled with truss elements and connected directly with the concrete material, in order to reproduce a perfect adherence condition. The elasto–plastic constitutive law for

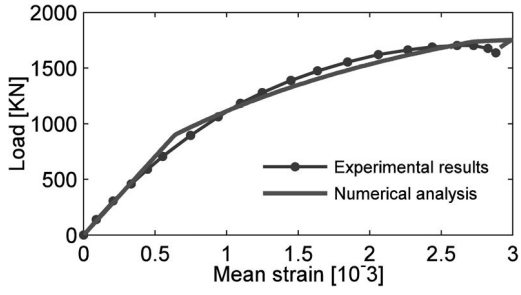

Figure 6. Load-mean strain in column type 2, n°22: numerical and experimental results.

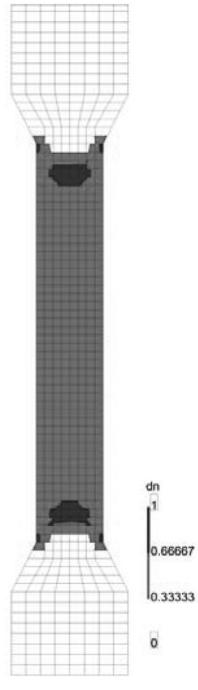

Figure 7. Compressive damage contour at the failure step.

the un-corroded bars was adopted for all the reinforcement. The yield strength and the ultimate strength of the reinforcement bars was based on the experimental data and were respectively:

Longitudinal bars:
Yield strength = 550 MPa
Ultimate strength = 600 MPa
Stirrups:
Yield strength = 590 MPa
Ultimate strength = 670 MPa

The comparison between numerical and experimental load-mean strain curves are shown in Figure 6 for which a good agreement is found in term of both ultimate axial load and mean strain. The mode of failure is shown in Figure 7 by the compressive damage contour.

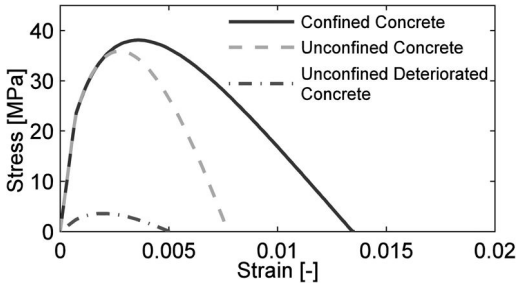

Figure 8. Constitutive laws for concrete cover and core.

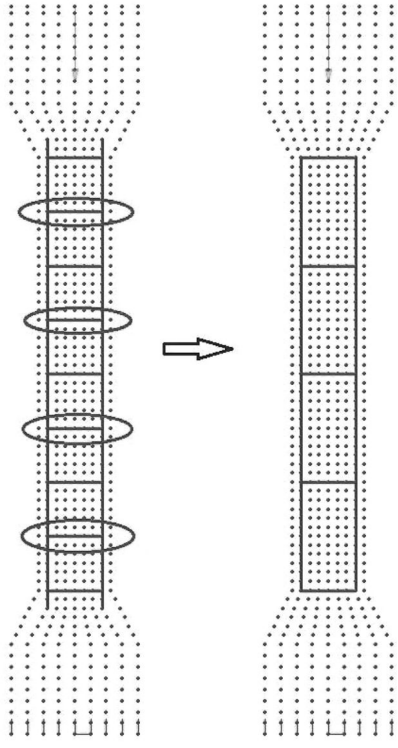

Figure 9. Alternate stirrups failure.

4.2 *Columns subjected to corrosion*

As previously stated, the corroded column n°28 was simulated, since it was the one that presented the smallest value of eccentricities. The concrete of the corroded columns was different from that of the sound columns. Two different constitutive laws were used for simulating column n°28: for the confined concrete core and the concrete cover, as shown in Figure 8 (blue lines). However, as described in paragraph paragraph 2.2, a degraded constitutive law for the concrete cover was adopted in the numerical analysis. For the simulation of the deterioration of the concrete cover, a reduction of the compressive strength and of the ductility of the concrete was considered. The stress-strain law for the deteriorated concrete cover is represented by the red line of Figure 8.

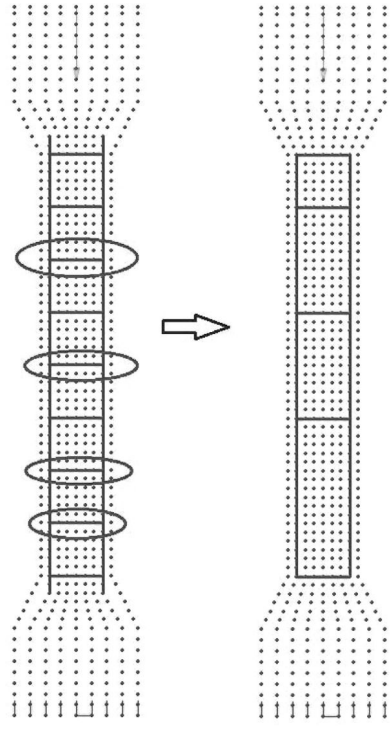

Figure 10. Two consecutive stirrups failure.

The following values for the mechanical properties of the concrete material were adopted in the numerical simulation:

- Confined compressive strength = 38.12 MPa
- Unconf. deteriorated compr. strength = 3.6 MPa
- Confined tensile strength = 2.9 MPa
- Unconf. deteriorated tensile strength = 0.1 MPa
- Tension fracture energy = 73 N/m

For the longitudinal steel reinforcement, a value of 0,63 mm of uniform corrosion was reported by the experimental test. The total value of the residual area of the bars, assumed in the numerical analysis, was equal to 682.56 mm^2. A stress-strain curve with pre-yielding buckling was adopted for these bars, as described in paragraph 2.3. Regarding the stirrups, the experimental test showed a penetration value of uniform corrosion of 0.50 mm and a maximum value of pitting of 4.7 mm. Due to the high level of pitting attack, the cross-section of stirrups was strongly reduced: the residual area was 1.33 mm^2. The experimental test demonstrated also that 4 stirrups failed shortly before the ultimate load. However it is not reported if the bars failed consequentially or if the stirrups that failed were located in different position. Due to this fact, both cases were considered in the numerical analyses. The elasto–plastic law with linear hardening was adopted for all the stirrups that did not fail.

Instead, the pre-yielding law was adopted for the longitudinal bars. The numerical load-mean strain curve is reported, for both the case of alternate stirrups

Table 2. Critical buckling loads.

		1 stirrup fail	2 consecutive stirrups fail
Residual bar diameter (mm)	$\Phi=$	14.74	14.74
Stirrups spacing (mm)	s=	300	450
Critical buckling stress (MPa)	$\sigma_{cri}=$	529.47	235.32

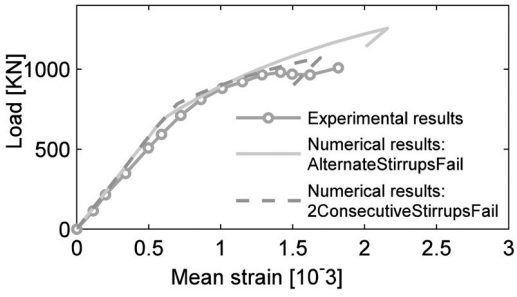

Figure 11. Load-mean strain curve for corroded column n°28.

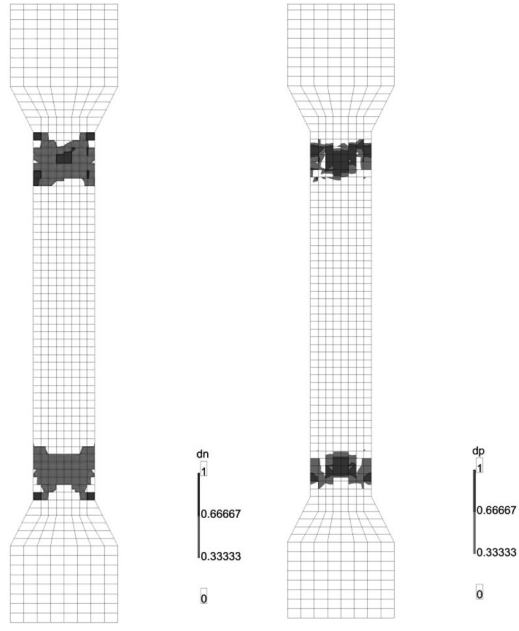

Figure 12. Tensile and Compressive damage contours at the failure step.

that failed (Figure 9) and for two consecutive stirrups that failed (Figure 10).

Clearly, the geometrical slenderness ratio increased in the case of two consecutive stirrups failure, and the critical buckling loads are reported in Table 2.

The load-mean strain curves obtained from the numerical simulation are reported in Figure 11. As can be observed, the result of the analysis with two consecutive stirrups is closer to the experimental curve. The mean strain at the failure step obtained with the numerical analysis, was smaller than the experimental one, probably due to the type of constitutive law for buckling considered for the longitudinal bars (linear post-buckling branch).

Figure 12 shows the tensile and compressive damage contours, which evidence the failure mode of the corroded column by tension damage.

5 CONCLUSIONS

A number of experimental tests carried out on sound and corroded RC columns, e.g. Rodriguez et al. 1996, Uomoto & Misra 1990, demonstrate that the main effects of corrosion are the reduction of the load carrying capacity, the reduction of the strain at the maximum load and the reduction of the compressive stiffness (slope of the first part of the force-mean strain graph). In this work, the tests performed by Rodriguez are simulated with a proposed numerical model. The results show that the model is able to well capture the structural response of the columns and in particular the effect of the concrete cover cracking, the failure of the stirrups as well as the buckling phenomena of longitudinal bars, that play the main role in structural collapse. The reduction of the longitudinal bar section has instead a negligible influence, as proved by both the experimental tests and the numerical analyses. Finally, it is worth noting that both the number and the position of failed stirrups have a significant influence, especially when buckling phenomena occur.

Starting from this study, further aspects may be investigated, such as the corrosion effect on the P-Δ response of eccentrically loaded columns, since the asymmetric deterioration of the columns due to corrosion might lead to an increase of the eccentricity, particularly dangerous when bending is present.

In conclusion, the good results obtained by the simulation of the experimental structural response of RC corroded columns, carried out with the proposed numerical model, demonstrate its capacity to capture the main effects of corrosion well and also the possibility to apply such a model to assess the residual strength and the mode of failure of existing degraded structures.

ACKNOWLEDGMENTS

Thanks are due to prof. Renato Vitaliani and prof. Harald Budelmann for their profitable collaboration in the progress of the research and for valuable discussions.

REFERENCES

Berto, L., Saetta, A. & Talledo, D. 2013. A coupled damage model for r.c. structures: proposal for a frost deterioration

model and enhancement of mixed tension domain. *Submitted.*

CEB-FIP, 1993. *Ceb-fip model code 1990*. Lausanne, Switzerland: Bulletin d'Information 213/214.

Claeson, C. 1999. Finite element analysis of confined concrete columns. *Nordic Concrete research publications* 22: 1–20.

Coronelli, D. & Gambarova, P. 2004. Structural assessment of corroded reinforced concrete beams: Modeling guidelines. *Journal of Structural Engineering – ASCE* 130 (8): 1214–1224.

Faria, R., Oliver, J. & Cervera, M. 1998. A strain-based plastic viscous-damage model for massive concrete structures. *International Journal of Solids and Structures* 35: 1533–1558.

Finozzi, I. & Saetta, A. 2014. Structural assessment of rc beams with different level of corroded reinforcement. *Submitted.*

McLeish 1987. *Structural assessment, Manual for life cycle aspects of concrete in buildings and structures.* UK: Taywood Engineering Limited: B4.1-B4.22.

Molina, F. J., Andrade, C. & Alonso, C. 1993. Cover cracking as a function of bar corrosion: Part II – Numerical model. *Materials and structures* 26: 532–548.

Monti, G. & Nuti, C. 1992. Nonlinear cyclic behaviour of reinforcing bars including buckling. *Journal of Structural Engineering, ASCE* 118 (12): 3268–3284.

Rodriguez, J., Ortega, L. M. & Casal, J. 1996. Load carrying capacity of concrete columns with corroded reinforcement. *Fourth international symposium on the corrosion of reinforcement in concrete structures*: 220–23. Cambridge, UK.

Saetta, A., Scotta, R. & Vitaliani R. 1999. Coupled Environmental-Mechanical Damage Model of RC Structures. *J. of Eng. Mech.* (125)8: 930–940.

Scott, B.D., Park, R., & Priestley M.J.N. 1982. Stress-strain behaviour of concrete confined by overlapping hoops at low and high strain rates. J. *of the American Concrete Institute* 79(1): 13–27.

Stewart, M.G. 2009. Mechanical behaviour of pitting corrosion of flexural and shear reinforcement and its effect on structural reliability of corroding RC beams. *Structural Safety* 31: 19–30.

Tschegg, E.K., Tritthart, J., Bohner, E. & Müller, H.S. 2011. Investigations into fracture of carbonated concrete. *Magazine of Concrete Research* 63(1): 21–30.

Uomoto, T. & Misra, S. 1990. Behaviour of concrete beams and columns in marine environment when corrosion of reinforcing bars takes place. *Concrete in marine environments, ACI SP* 109(6): 127–146.

Concrete Solutions – Grantham et al. (Eds)
© 2014 Taylor & Francis Group, London, ISBN 978-1-138-02708-4

Mechanical properties of corroded rebar in deteriorated reinforced concrete members

Y. Kitsutaka
Tokyo Metropolitan University, Tokyo, Japan

Y. Uchida
Japan Testing Center for Construction Materials, Tokyo, Japan

K. Matsuzawa
Tokyo Metropolitan University, Tokyo, Japan

ABSTRACT: In this paper, the mechanical properties of corroded rebars in deteriorated reinforced concrete structures were investigated. Since reinforcing bars in concrete members bear tensile forces, their corrosion greatly damages the load-bearing capacity of reinforced concrete members. This study aims to investigate changes in the mechanical properties of deformed reinforcing bars of different types and sizes when they were subjected to salt spray testing. As a reinforcing bar is corroded and the cross-sectional area is reduced, the yield point linearly decreases. The rate of such reduction is common to all types, being independent of the strength and diameter of the bar. The apparent Young's modulus linearly decreases as corrosion proceeds. The rate of such reduction is common to all types, being independent of the strength and diameter of the bar.

1 INTRODUCTION

Concrete structures in offshore facilities or segments in contact with seawater are particularly prone to reinforcing steel corrosion. Reinforcing steel in general concrete structures is also subject to the risk of corrosion by carbonation, the effect of chloride-laden air, etc. Corroded reinforcing bars cause cracking in the concrete cover, which contributes to further steel corrosion. Since reinforcing bars in concrete members bear tensile forces, their corrosion greatly damages the load-bearing capacity of reinforced concrete members. However, there has not been sufficient data in the research literature as to losses in the strength of corroded reinforcing bars. Changes in the mechanical properties of electrically corroded reinforcing bars were, however, investigated by Kitsutaka (2012).

In view of the importance of evaluating the degree of deterioration of reinforced concrete structures, the relationships of the deterioration factor and year (*F-t* diagram), the material deterioration and deterioration factor (*D-F* diagram) and the structural performance and material deterioration (*P-D* diagram) should be cleared. Relationships between these diagrams are independent. The combined diagram of these relationships, the so called *PDFt* diagram, may be effective to evaluate the deterioration of concrete structures (Kitsutaka 2010). In order to evaluate the performance of the concrete structure caused by reinforcing bar corrosion by using the *PDFt* diagrams. The relationships between the degree of reinforcing bar corrosion and strength performance of the reinforcing bar should be indicated.

This study aims to investigate the changes in the mechanical properties of deformed reinforcing bars of different types and sizes when they are corroded by salt spray testing.

2 EXPERIMENT OVERVIEW

2.1 *Specimens*

Table 1 gives the factors and levels of experiments. Table 2 gives and major mechanical properties of reinforcing bars such as the dimensions and mass of reinforcing bars.

Table 1. Factors and levels.

Factor	Levels
Strength of rebar *1	SD295A, SD345, SD390, SD490
Diameter of rebar *2	D13, D19, D29, D41
Method of corrosion	Salt spray test (35°C, NaCl 5%)
Length of corroded bar 50 (mm)	
Target of corrosion	0, 2.5, 5, 10(%)

*1 Number is a minimum yield strength (N/mm^2), *2 Number is a nominal diameter (mm).

Table 2. Properties of reinforcing bar.

Name	Nominal dimension			External diameter (mm)
	Diameter (mm)	Cross section area (mm^2)	Unit weight (kg/m)	
D13	12.7	126.7	1.0	14.0
D19	19.1	286.5	2.3	21.5
D29	28.6	642.4	5.0	32.1
D41	41.3	1340.0	10.5	46.3

Photo 1. Reinforcing bar specimen (Center is corroded area).

The types of reinforcing bar include the following deformed bars specified in JIS G 3112: SD295A, SD345, SD390, and SD490. D13 bars were tested in regard to SD295A; D13 and D19 in regard to SD345 and SD390; and D19 in regard to SD490. Corrosion was induced to a length of 50 mm by the salt spray testing. The target losses in the cross-sectional area were in some levels from 0 to 10%. Specimens were threaded bars 600 mm in length. All areas other than the corrosion surface were sealed with silicone and PVC tape (Photo 1).

2.2 *Method of accelerating the corrosion of reinforcing bar*

Reinforcing bars were subjected to the salt spray testing and corrosion was accelerated. Photo 2 shows the salt spray testing apparatus. Fig. 2 shows the outline of the accelerated corrosion test. The test zone of reinforcing bar was immersed in a 5% NaCl solution by continuous spraying with the temperature condition of 35 degrees Celsius. Corrosion periods were selected to attain the target cross-sectional losses of reinforcing bars of 2.5, 5, 7.5, and 10%. Photo 3 shows the appearance of the corrosion accelerated specimens. After the specified corrosion periods, specimens were immersed in a 10% diammonium hydrogen citrate solution to remove rust and subjected to tension tests after measuring the cross-sectional areas.

2.3 *Method of measuring cross-sections*

Figure 2 shows the equipment for measuring the cross-sections of a specimen. This equipment is capable of

Photo 2. Salt spray testing apparatus.

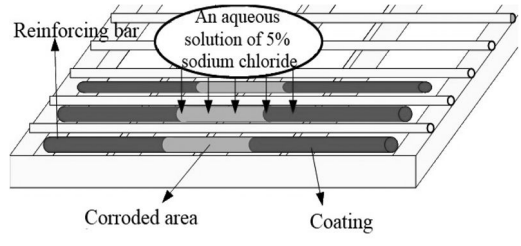

Figure 1. Outline of the corrosion accelerating test by the salt spray testing.

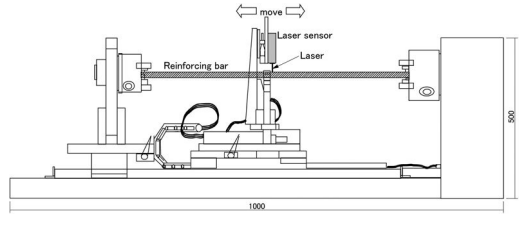

Figure 2. The equipment for measuring the cross-sections of a specimen (unit: mm).

measuring the cross-sections of reinforcing bars with a diameter of up to around 50 mm over a span of 100 mm at 0.1 mm intervals using a laser displacement meter. Note that the radial displacement was measured at 0.36 degree intervals. In this study, the cross-sections were measured at 1 mm intervals in the longitudinal direction.

2.4 *Tensile test*

After the measurement of cross sections, specimens were subjected to tensile tests using a universal testing machine with a capacity of 1,000 kN. Gauge marks were dented in the coated area using a punch before testing, with the distance between the gauge marks and

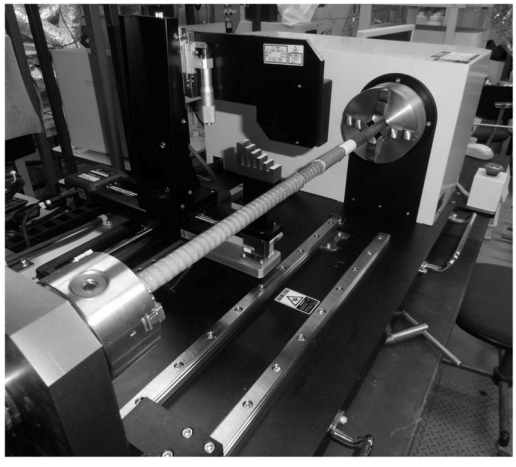

Photo 3. The equipment for measuring the cross-sections of a specimen.

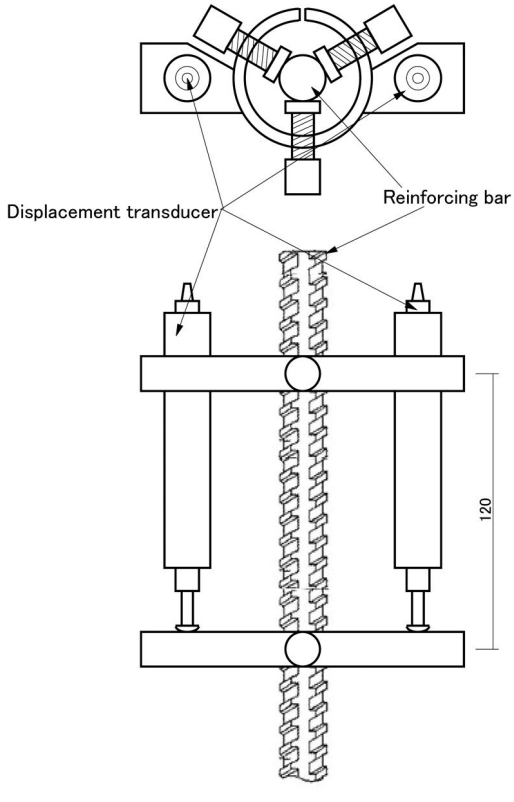

Figure 3. Detail of the jig used for a tensile test.

longitudinal length of the corrosion test zone being measured using a jig (Figure 3 and Photo 4). The distance between the gauge marks was set at 120 mm. Prior to testing, PVC tape and silicone wound around the specimens for waterproofing were removed to prevent slipping between the chuck of the jig and the bar. Note that the displacement was also measured during

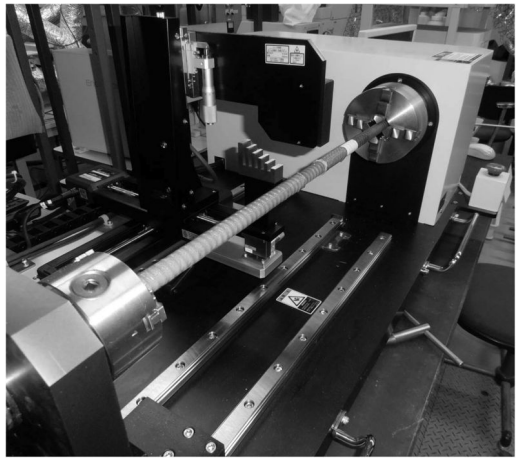

Photo 4. Jig used for a tensile test.

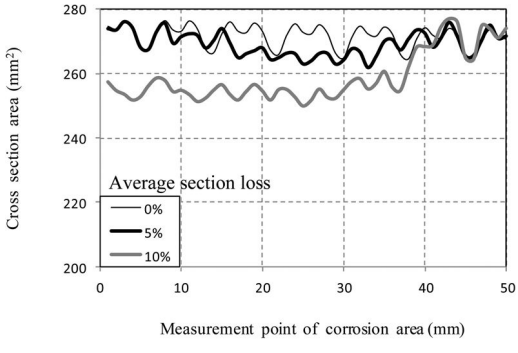

Figure 4. An example of the measurement about the cross section of a reinforcing bar (SD345-D19).

testing using a displacement measuring jig and LVDTs as shown in Figure 3.

3 RESULTS AND DISCUSSION

3.1 *Loss in the cross-section due to corrosion*

Figure 4 shows a typical result of cross-section measurement. The average cross-sectional area represents the average of the cross-sectional areas measured at 1 mm intervals. The minimum cross-sectional area is the minimum of the measurements. The average corrosion loss ratio is the quotient of the average corroded cross-sectional area divided by the nominal cross-sectional area. The maximum corrosion loss ratio is the quotient of the minimum corroded cross-sectional area divided by the nominal cross-sectional area.

As shown in Figure 4, the cross section area is decreased with the increase of the target losses set in the accelerated test. Because of the reinforcing bar used in this test is the deformed bar, so the distribution of the cross section area is rugged. With the increase of the accelerated test, the distribution of the cross section area becomes uniform.

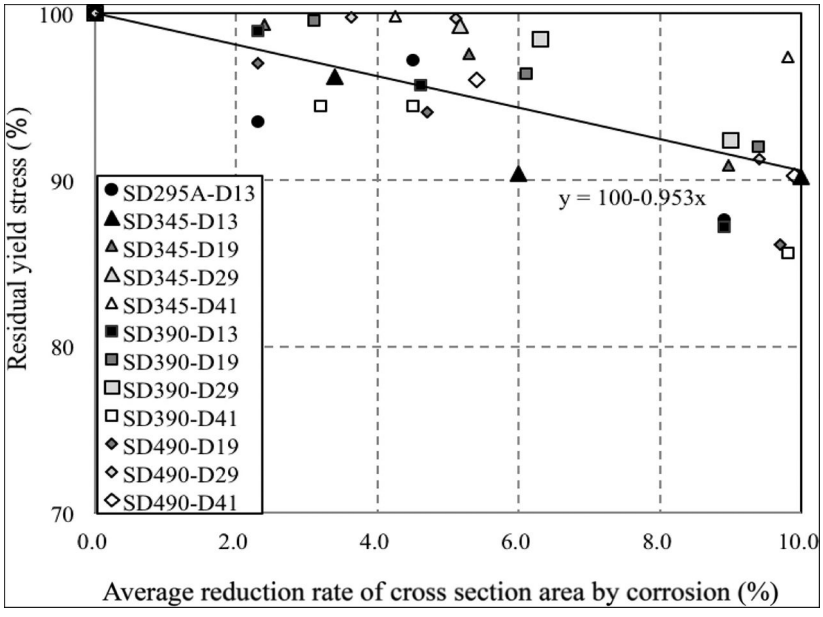

Figure 5. Relationship between the average corrosion loss ratio and the residual yield stress.

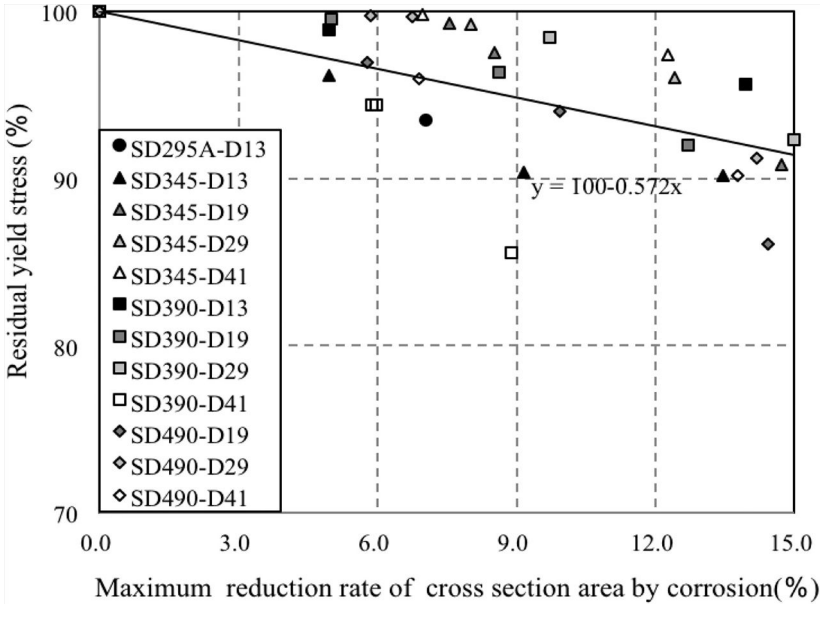

Figure 6. Relationship between the maximum corrosion loss ratio and the residual yield stress.

3.2 *Load-displacement curve*

The maximum load and yield point decrease as the corrosion-induced loss in the cross-sectional area of reinforcing bar increases. The displacement at the maximum load also tends to decrease as corrosion proceeds. Strength is correlated with elongation. The yield strength of the reinforcing bar decreases as the degree of corrosion increases, with the maximum tensile load decreasing as well.

3.3 *Residual yield stress*

Figure 5 shows the relationship between the average corrosion loss ratio and the residual yield stress. Note that the yield points in this figure are apparent values determined by dividing the tensile load by the nominal cross sectional area. A residual yield stress is the value determined by dividing the yield point of the corroded reinforcing bar by the yield point of a sound reinforcing bar. When a reinforcing bar is corroded, with the

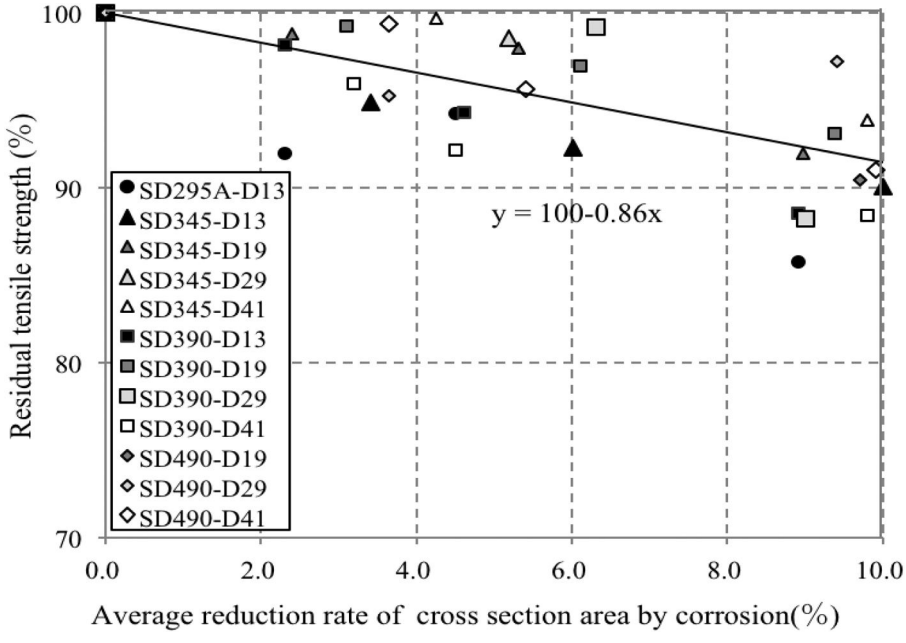

Figure 7. Relationship between the average corrosion loss ratio and the residual tensile strength.

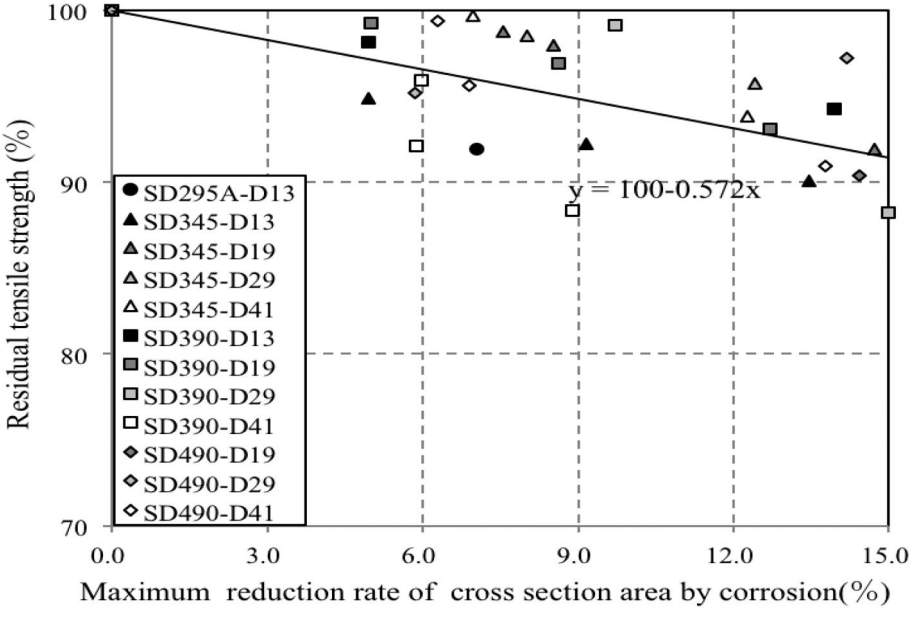

Figure 8. Relationship between the maximum corrosion loss ratio and the residual tensile strength.

cross-sectional area being reduced, its yield point linearly decreases regardless of the type and diameter of the bar. Also, the ratio of such reduction is nearly equal to the ratio of cross-sectional loss. Figure 6 shows the relationship between the maximum corrosion loss ratio and the residual yield stress.

Residual yield stress linearly decreases regardless of the type and diameter of the bar. The coefficient of the linear line is −0.572 and this value is smaller than that of the average corrosion loss case of −0.953 as shown in Figure 5.

3.4 *Residual tensile strength*

Figure 7 shows the relationship between the average corrosion loss ratio and the residual tensile strength. The residual tensile strength is determined by dividing

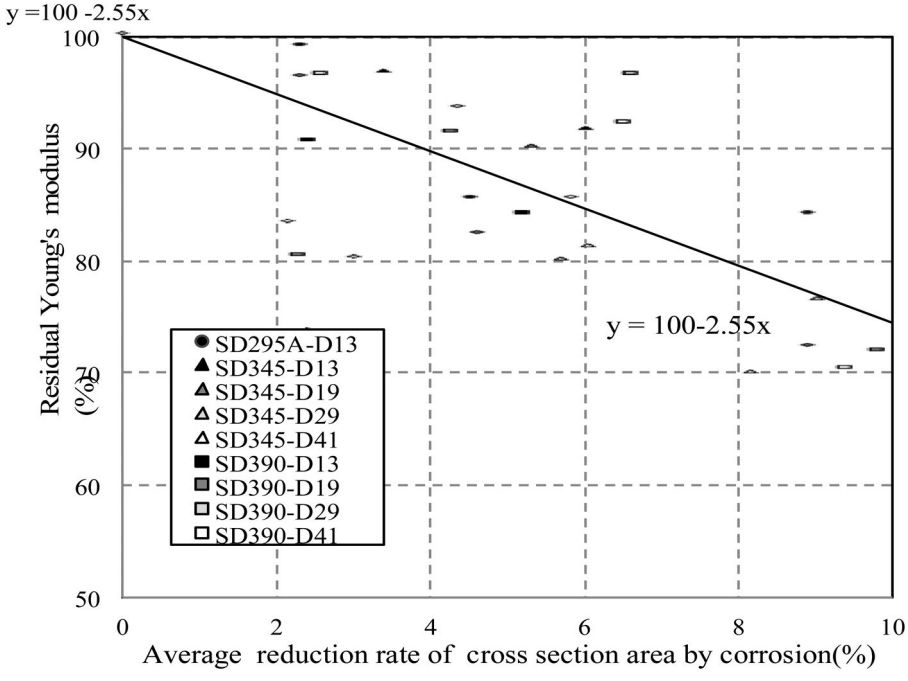

Figure 9. Relationship between the average corrosion loss ratio and the residual yield stress.

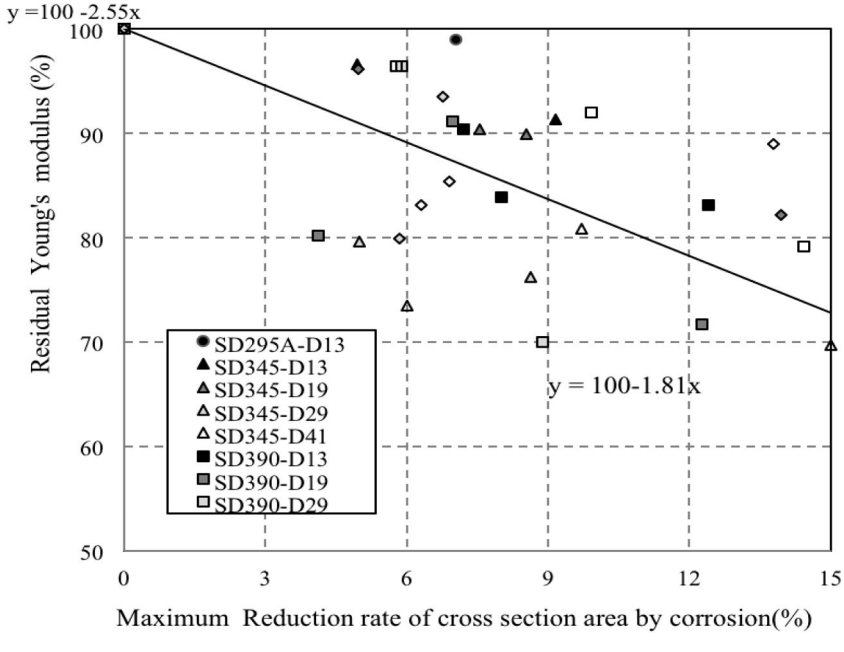

Figure 10. Relationship between the maximum corrosion loss ratio and the residual yield stress.

the maximum tensile load by the nominal cross sectional area of sound reinforcing bar. When a reinforcing bar is corroded, with the cross-sectional area being reduced, its tensile strength linearly decreases regardless of the type and diameter of the bar.

Figure 8 shows the relationship between the maximum corrosion loss ratio and the residual tensile strength. The residual tensile strength linearly decreases regardless of the type and diameter of the bar. The coefficient of the linear line is −0.572 and

this value is smaller than that of the average corrosion loss case of −0.86 as shown in Figure 7.

3.5 *Young's modulus*

Figure 9 shows the relationship between the average corrosion loss ratio and the residual Young's modulus ratio. In the present tests, the corrosion zone spans 50 mm in the test zone of 120 mm. Therefore, the apparent Young's modulus of the corrosion zone was determined from the equation below based on the load-displacement relationship obtained from the tests. Young's modulus of the sound zones with no corrosion was assumed to be 191.8 kN/mm^2, which is the average of the measured Young's moduli.

$$E_2 = l_2/(S \times \Delta l/\Delta P - l_1/E_1) \quad (1)$$

where E_1 and E_2 denote Young's modulus of the sound zones and the apparent Young's modulus of the corrosion zone, respectively; l_1 and l_2 denote the lengths of the bars in the sound and corrosion zones, respectively, in the test zone; ΔP denotes the difference between the loads at 1/3 and 2/3 of the yield point; and Δl denotes the difference in the displacements at 1/3 and 2/3 of the yield point.

This figure reveals that the apparent Young's modulus linearly decreases as the corrosion proceeds. The Young's modulus of the reinforcing bar is generally assumed to be 20.5 kN/mm^2 regardless of the bar type. However, the total elongation of corroded bars is small due to the non-uniform cross-sectional areas, which causes stress concentration as stated above. It is therefore considered that the load necessary for causing deformation similar to sound bars becomes lower in corroded bars, leading to a smaller apparent Young's modulus. Therefore, the greater the corrosion loss ratio, the smaller the Young's modulus, and the lower the bar strength, the greater the rate of reduction in the Young's modulus.

Figure 10 shows the relationship between the maximum corrosion loss ratio and the residual Young's modulus. Residual Young's modulus linearly decreases regardless of the type and diameter of the bar. The coefficient of the linear line is −1.81 and this value is smaller than that of the average corrosion loss case of −2.55 as shown in Figure 9.

4 CONCLUSIONS

Findings obtained in this study include the following:

- As a reinforcing bar is corroded by the salt spray testing and the cross-sectional area is reduced, the mechanical properties of a reinforcing bar such as yield stress, tensile strength and Young's modulus linearly decreases. The rate of such reduction is common to all types, being independent of the strength and diameter of the bar.
- The coefficient of the linear regression for the relation between the maximum corrosion loss ratio and the mechanical properties of a reinforcing bar is smaller than that of the relation between the average corrosion loss ratio and the mechanical properties.

ACKNOWLEDGEMENT

A part of this study was supported by a grant from the Japanese Ministry of Economy, Trade and Industry.

REFERENCES

Kitsutaka, Y. 2010. Methodology on the Integrity Evaluation of Reinforced Concrete Structures by Extrapolation, CIB World Congress 2010, CD 1095, 2010.5

Kitsutaka, Y., Matsuzawa, K. and Uchida, Y. 2013. Integrity Evaluation of Corroded Reinforcing Bar Used for Reinforced Concrete Structures, Transactions, SMiRT-22 San Francisco, California, USA – Division IX, August 18–23, 2013.

This page intentionally left blank

Concrete Solutions – Grantham et al. (Eds)
© 2014 Taylor & Francis Group, London, ISBN 978-1-138-02708-4

Effect of corrosion cracks in the compression zone on the bending performance of deteriorated RC members

M. Oyado
Railway Technical Research Institute, Tokyo, Japan

T. Kanakubo & A. Yasojima
University of Tsukuba, Ibaraki, Japan

ABSTRACT: In order to evaluate the effect of material degradation of not only tensile rebar but also compressive concrete, the static bending test was carried out using the RC beam specimen deteriorated by long-term weathering, and the influence of corrosion of compressive rebar and corrosion cracks in the compression zone was studied. According to the test results, it is clarified that the damage of compression zone of the RC beam specimen brings not only reduction of loading capacity but also degradation of displacement ductility. According to the digital photoimage analysis for three dimentional location tracking, it was clarified that collapse of the specimen is mainly governed by side leanout of side-surface in spite of uplift of compressive-surface.

1 INTRODUCTION

It is important to confirm the safety performance of existing reinforced concrete (RC) structures, especially when they are damaged by corrosion. It is considered that bending performance of RC member decreases due to corrosion of reinforcing bars. It is naturally considered that the load bearing performance of RC members will appear when internal tensile force and compressive force properly work together, therefore, it is essential to evaluate not only tensile performance of rebar but also compressive performance of concrete when they are damaged by corrosion. However, in previous studies, deterioration in the compression zone is hardly taken into account when evaluating mechanical performance of deteriorated RC members. It is because there are very few experimental results which indicate the effect of compression failure on mechanical performance.

On the other hand, the authors have conducted the bending tests using the RC beam specimens subjected to long-term (over ten years) weathering, in order to investigate the relationship between deterioration and mechanical performance (Oyado et al 2010). In the series of these experiments, a certain specimen showed severe reduction of ductility in addition to reduction of bending strength. It could be supposed that the load carrying behavior of this specimen was brought by the reduction of compressive performance of concrete. The same series of specimens were subsequently exposed to long term weathering, – in 2013 26 years were attained. It was presumed that these specimens would show the effect of corrosion cracks on the bending performance of deteriorated RC members.

In this paper, the bending test on this long-term exposed beam was carried out in order to investigate the effect of corrosion cracks in the compression zone on the bending performance of deteriorated RC members. In order to clarify the process of compressive failure of the deteriorated RC beam, local behavior of the concrete surface in the compression zone should be investigated in detail. However, it is speculated that conventional displacement transducers (DT) are not suitable for measuring three dimensional deformation of concrete surfaces. Therefore the authors took the method of the digital Photoimage Analysis for three Dimensional location tracking (3DPA) in order to measure the local deformation of the concrete surface in the compression zone. This paper also describes the applicability of the 3DPA as a measuring method for concrete structural experiment.

2 STATIC BENDING TEST

2.1 *Details of test specimen*

In this study, a bending test was carried out for one RC beam specimen, which was subjected to long-term weathering for 26 years. Fig.1 shows the details of this specimen. The specimen was designed to fail in bending. Concrete composition and strength test results are shown in Tables 1 and 2 respectively.

The history of the long-term weathering is shown in Fig. 2, and the method and the status of the weathering are shown in Figures 3 and 4 respectively. The weathering was conducted near an urban (not coastal) area in Tokyo. The specimen was combined together

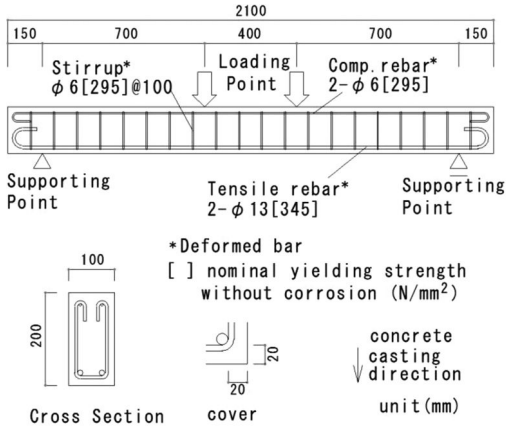

Figure 1. Details of specimen.

Table 1. Concrete composition.

			Unit amount (kg/m^3)			
Air (%)	W/C (%)	S/(S + G) (%)	Water	Cement	Sand	Gravel
4 ± 1	65	50	165	245	932	953

Design Strength: 24(N/mm^2)

Table 2. Concrete strength test result.

Specimen	Elastic modulus	Concrete strength
A	19700	28.5
B	31900	42.4
C	31800	38.6

Measured by cylindrical core = 50 mm extracted from 2nd stage specimen Unit :N/mm^2

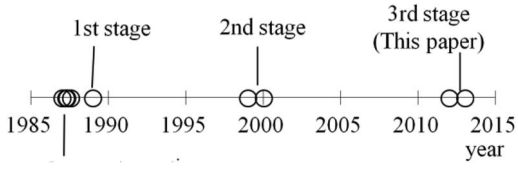

Figure 2. History of exposition.

with the other specimens by using sandwiched rollers and stainless steel bars, and then preliminary induced bending cracks were kept open. Sodium chloride solution was sprayed periodically (three times a day except on rainy days) for 17 months after starting exposure, in an attempt to accelerate corrosion. In this study, a specimen which continued to be exposed to weathering after the 2nd stage test (13 years of exposure) was subjected to the bending test. The total duration of exposure was 26 years. The experiment of this time is named the 3rd stage.

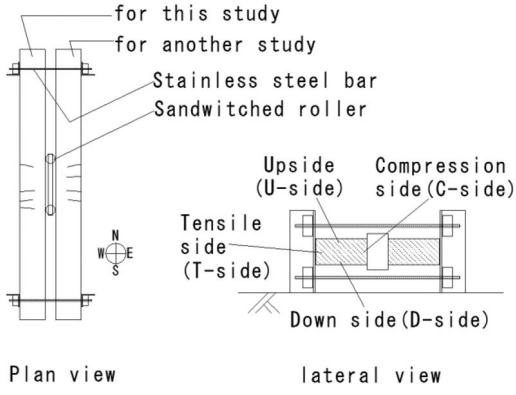

Figure 3. Weathering method.

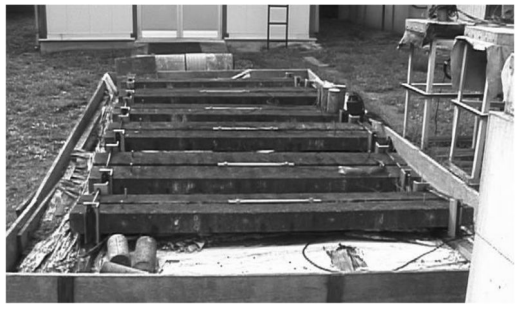

Figure 4. Status of weathering (at 2nd stage).

2.2 *Loading test and material inspection*

In this experiment, visual inspection of the specimen was firstly conducted. After this inspection, a bending test was carried out. Fig. 1 also shows the loading and supporting points of the bending test. In accordance with the former (2nd) stage test result, unexpected sudden collapse was not presumed to take place, therefore, monotonic increase of displacement up to failure was simply imposed to the specimen using the Amsler universal testing machine. Measurement items were the applied load, the deflection and the local displacements. The local displacements were obtained by using the 3DPA, which is to be mentioned in the following section.

After the loading test, small concrete blocks of $100 \times 50 \times 100$(mm) were taken out from the specimen, and cut into five small layers. Every layer of the concrete blocks was examined, and in-depth distribution of the amount of the chloride ion was investigated in accordance with the prescribed Japanese test code of JCI-SC4.

3 TEST RESULT

3.1 *Visual inspection before loading test*

Fig. 5 shows the result of visual inspection of the test specimen before the loading test. Very wide corrosion

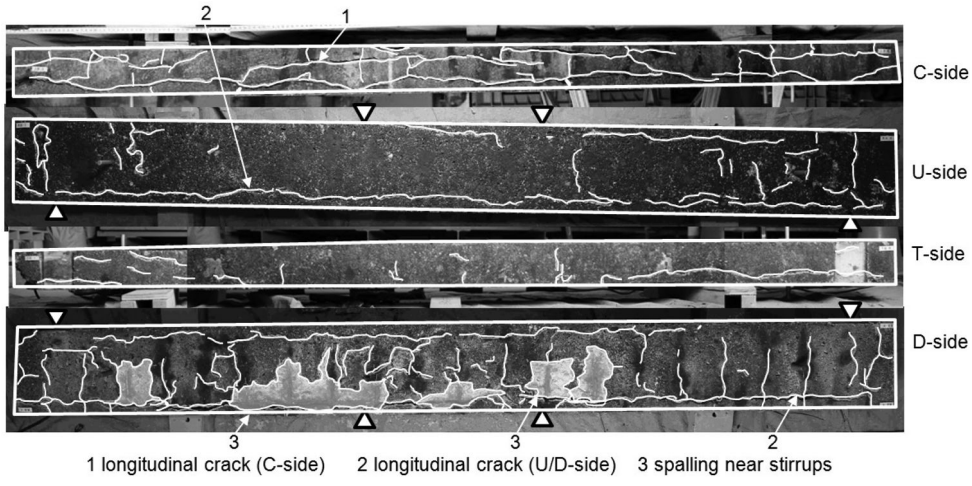

Figure 5. Visual appearance of specimen before loading test.

cracks could be recognized along the longitudinal reinforcement, especially on the C-side, U-side and D-side (Name of surface: see Fig. 3). Corrosion crack widths estimated by visual inspection were over 5 mm. The cover concrete in some areas was about to spall or had already spalled off due to the corrosion cracking. Corrosion crack widths along the stirrups observed on the D-side were relatively small in comparison with the longitudinal cracks, but the scaling of the cover concrete around the stirrups was observed in many areas. The results of the 3rd stage in comparison with the 2nd stage show that long-term weathering causes severe deterioration of specimens.

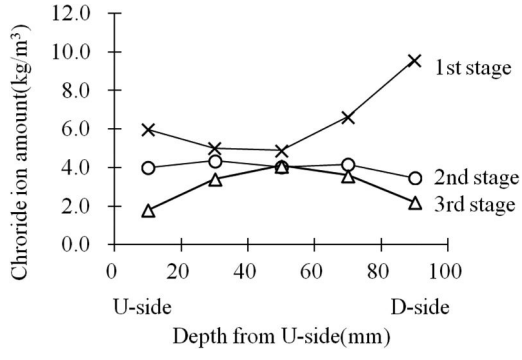

Figure 6. Test result of chloride ion amount.

3.2 *Chloride ion amount*

Fig. 6 shows the investigation result of the chloride ion amount in concrete. The amount of the chloride ion in concrete was lower than the 2nd stage specimens, especially near the U-side and the D-side surface. It is supposed that the chloride ion was washout after the long-term weathering. However, large amount of the chlorides (2–4 kg/m^3) remained in the concrete in a depth of about 50 mm resulting in severe deterioration of the concrete due to salt ingress.

3.3 *Test result*

The load-displacement relationship of the loading test is shown in Fig. 7, including those of the 2nd stage specimens. The concrete material strength of specimen A was lower than that of the other specimens B and C referring to Table 2; which shows summarized test results of the 2nd stage. The bending strength of this 3rd stage specimen was lower than that of the other specimen A, B and C in the 2nd stage. Furthermore, the ductility of this 3rd stage specimen was also lower than that of the 2nd stage specimens, referring that the applied load indicated a remarkable decrease from around the displacement of 20 mm. The decrease of

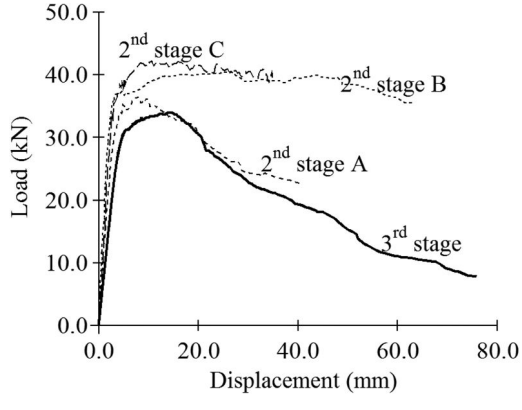

Figure 7. Load-displacement relationships.

ductility must be due to the degradation of the compressive performance of the concrete, considering that the failure of the tensile bar didn't occur.

Visual appearance of the specimen after failure is shown in Fig. 8. The pure bending region around not only the C-side but also the U/D-side had almost fallen.

(a) U-side of pure bending region

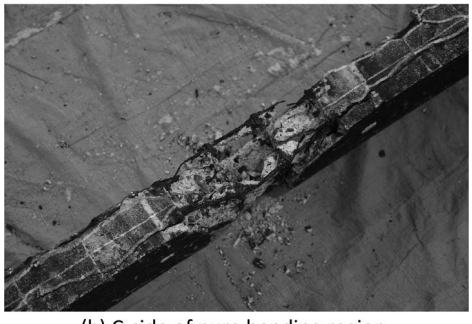

(b) C-side of pure bending region

Figure 8. Visual appearance after failure.

From the viewpoint of the C-side, compressive bars were severely deformed due to buckling. On the other hand, less damage could be observed in the shear span regions (between the loading point and supporting point), so that only the midspan area (pure bending span) of the exact loading position had suffered mechanical damage due to the loading test. From the standpoint of Fig. 5, there are many severe corrosion cracks before the loading test on the C-side along with the specimen. It can be presumed that concrete damage of the compression zone due to corrosion crack affects the bending performance of RC members.

In addition according to the internal crack (see Fig. 8(a)), the internal concrete of the pure bending region, as well as near surface, was severely damaged due to loading, so that the internal concrete was divided into some small portions that could be removed easily by hand.

4 THREE DIMENTIONAL IMAGE ANALYSIS

4.1 *Inspection method*

According to the ailure status of this specimen, the effect of not only the rebar corrosion but also the reduction of compressive performance of the concrete should be considered when discussing the failure behavior of deteriorated RC beams subjected to bending force. It is important to trace the history of the local displacement precisely if the failure was caused by bar buckling or concrete crushing. Unfortunately,

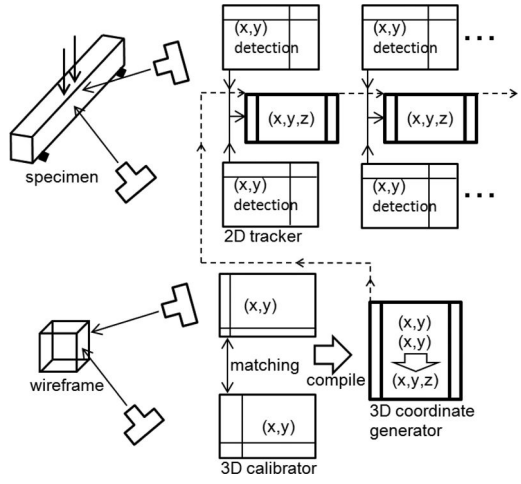

Figure 9. Flowchart of 3DPA.

conventional measuring methods are difficult to solve this challenge, because conventional DT is, in essence, not applicable for measuring three dimensional deformation of concrete surfaces, owing to the fact that they are too large to place on many target points, and they are not suitable for multiaxial measurement in arbitrary spatial direction. Therefore in order to measure the three dimensional behavior of the concrete surface, the method of 3DPA was adopted in this experiment.

The flowchart of the 3DPA is shown in Fig. 9. In some previous studies, two dimensional displacement analysis method using digital photo-imaging was already applied in order to investigate the concrete structural performance, for instance, as reported by Matsuo et al (2002). The 3DPA applied to this study was developed from the conventional 2D method to 3D. Several target points were marked in advance on the objective specimen as shown in Fig. 10(a), then photos of them were captured periodically in some seconds intervals by plural digital cameras from the different viewpoints during the loading test as shown in Fig. 10(b). After the loading test, a 2D image tracker was activated and photo-image analyses were independently conducted to achieve tracking of the target points. On the other hand, after removing the tested specimen, a readymade cubic wireframe as shown in Fig. 10(c) was placed at the exact position at which the tested specimen was once placed, and a pair of photo-images of the wireframe were captured by the same digital cameras from the same viewpoints of the case of the loading test. Then the 3D calibrator was activated and 3D referential axes were fixed through photo-image matching. The 3D coordinate generator was compiled together with calibrating parameters to transform from plural 2D detected coordinates into the corresponding 3D position. Finally the 3D coordinate generator was activated, and photo-image analyses were executed. Through these processes time-dependent transitions of the 3D position of targetpoints were calculated.

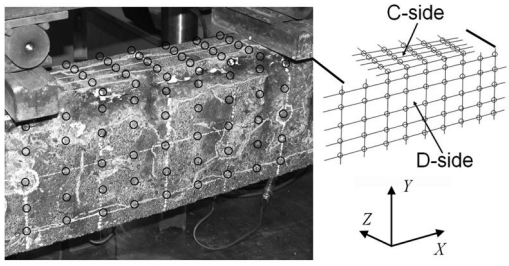

(a)Targetpoint (black circular mark)

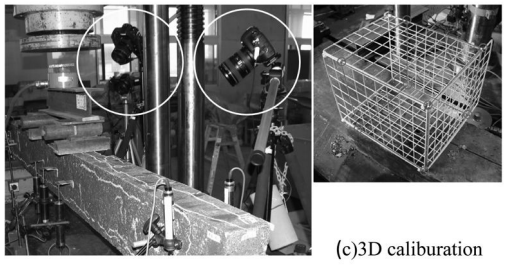

(b) Digitalcameras (c)3D caliburation cubic wireframe

Figure 10. Photo capturing for 3DPA.

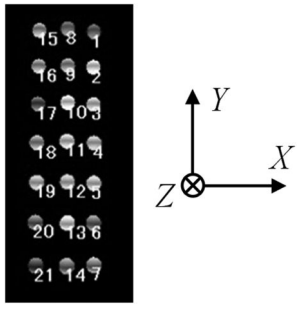

Figure 11. Coordinate and axis.

In this experiment, digital cameras whose image sensors were 35.8 × 23.9 mm sized with an image resolution of 5472 × 3648 pixels were applied. Automatic interval timers were equipped to the digital cameras to set time intervals of photo-image capture to be 20 seconds. In addition, measuring values such as the applied load via load-cell were also acquired in the same intervals as the digital cameras in order to get into synchronization.

4.2 *Preliminary test*

Preliminary tests of the 3DPA was carried out in order to confirm applicability for this photo-image analysis.

An uniaxial compressive loading test using cylindrical (100 mm in dia. and 200 mm in height) normal strength concrete without reinforcement was carried out in this study. Target points were marked with the

Figure 12. Targetpoints and failure status.

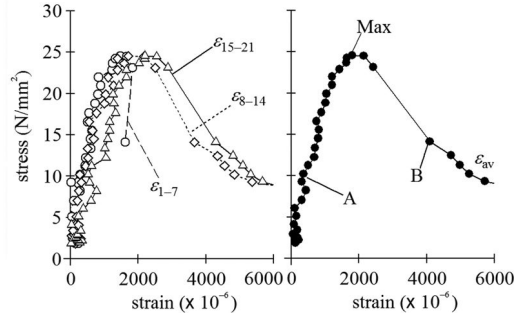

Figure 13. Preliminary test result.

spacing which was 20 mm in the circumferential (in approximate X) direction and 30 mm in the vertical (Y) direction as depicted in Fig. 11. Target points effectively captured by two digital cameras shown in Fig. 12 were taken into the analysis. In this measurement, the distance between the digital camera and the specimen was decided to be about 500 mm, and the focus length of the lens was decided to be 60 mm. Totally, 45 pairs of photo-images were collected during the preliminary test using above mentioned photo-image acquisition setups. Stress-strain relationships of the cylindrical specimen obtained by the 3DPA are shown in Fig. 13. In this figure, the coordinates and target points are defined as shown in Fig. 11. $\varepsilon_{1\text{-}7}$ shows the average of ε_{12}, ε_{23}, ε_{34}, ε_{45}, ε_{56} and ε_{67}, where, ε_{ij} is the strain between the points i and j. (Strain is calculated by the change of distance divided by the original distance). Similarly, $\varepsilon_{8\text{-}14}$ and $\varepsilon_{15\text{-}21}$ are calculated. According to the left of Fig. 13, the strain $\varepsilon_{1\text{-}7}$, $\varepsilon_{8\text{-}14}$ and $\varepsilon_{15\text{-}21}$ shows a considerable scatter especially in the early loading phase, for example, $\varepsilon_{15\text{-}21}$ is twice as large as $\varepsilon_{1\text{-}7}$ or $\varepsilon_{8\text{-}14}$ when the stress is 15 N/mm^2.

The stress-ε_{av} relationship is shown on the right of Fig. 13, where ε_{av} is the average of $\varepsilon_{1\text{-}7}$, $\varepsilon_{8\text{-}14}$ and $\varepsilon_{15\text{-}21}$. Compared with similar concrete strength tests, the strain showed a large variation, although, the general stress-strain relationship can be sufficiently observed, and the observed strain at the peak stress showed a reasonable value of 2000×10^{-6}.

The bubble chart of Fig.14 shows the strain in the circumferential (X) and vertical (Y) direction. Gray

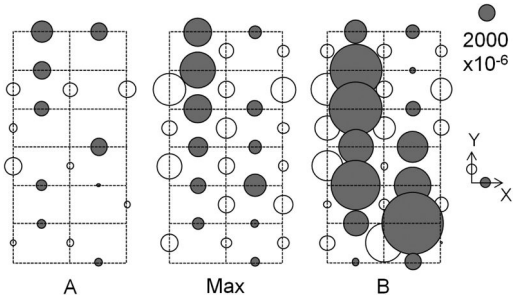

Figure 14. Bubble chart of local strain.

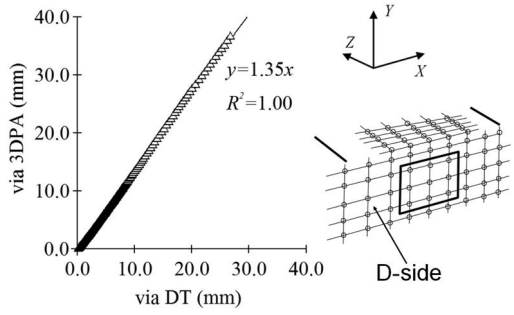

Figure 15. Comparison between measuring methods.

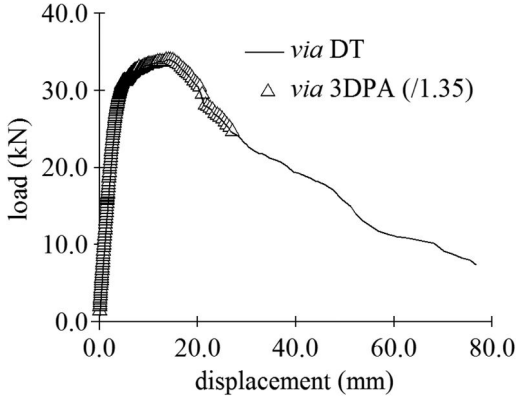

Figure 16. Load-displacement relationships.

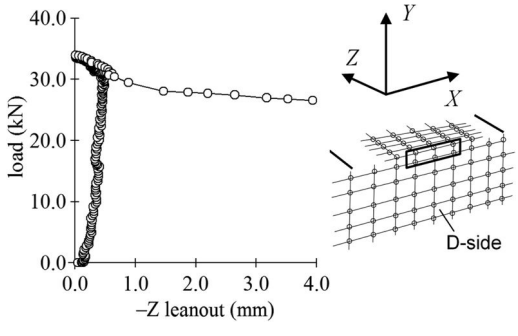

Figure 17. −Z leanout of D-side.

bubbles show tensile strain in the X direction and white bubbles show compressive strain in the Y direction. According to this figure, developing local strain with the approach to failure can be observed, corresponding to the vertical crack at the failure shown in Fig. 12.

4.3 *3DPA for beam specimen*

As shown in the previous section, the concluding preliminary test result should demonstrate the possibilities for the 3DPA to be adoptable for the concrete loading test. The 3DPA result of the long-term exposed RC beam specimen is shown in this section.

As shown in Fig. 10(a), the target points were marked on the C- and D-side. The spacing of the target points of the D-side was 40 mm in the vertical (Y) direction and 50 mm in the horizontal (X) direction, and that of the C-side was 25mm in the depth (Z) direction and 50 mm in the horizontal (X) direction. In this measurement, distance between the digital-camera and the specimen was decided to be about 700 mm, and the focus length of the lens was decided to be 24 mm. Totally, 261 pairs of photo-images were collected during the bending test.

Fig. 15 shows the vertical (−Y) displacement obtained by the 3DPA versus the bending displacement obtained by the DT, where the former is the average of the Y displacements of nine target points shown in the right of Fig. 15. The vertical displacement obtained by the 3DPA was 1.35 times as large as the bending displacement obtained by the DT. It can be supposed that one reason of this result is due to the mismatch of the vertical axis of the 3DPA with the measuring axis of the DT, though further discussion will be needed. However, an almost perfect proportional relationship can be found between these two kinds of displacement, and this result conclusively demonstrates that the 3DPA provides a good reference for the evaluation of displacement.

The load-displacement relationship is shown in Fig. 16, in which two kinds of displacement are applied as the X-value; one is the displacement obtained by the DT, and the other is that obtained by the 3DPA. The latter value is divided by 1.35, which is the gradient of the fitting line described in Fig. 15. Fig. 16 shows that the curve of the 3DPA is terminated at the displacement about 30 mm, because the 2D image tracker lost the positions of several targetpoints and couldn't follow their movement owing to the change of their appearance due to concrete cracking or spalling. However, it can be recognized that the 3DPA gave sufficient information about the loading test in respect to the displacement range from 0 to 30 mm.

Fig.17 shows the relationship between the applied load and −Z leanout of the D-side obtained by the 3DPA, where −Z leanout was the average of the (in the counter-direction of depth) Z movement of the six target points shown in the right of Fig.17. At the beginning, the D-side of the specimen slightly (0.5 mm at the maximum) leant outward as the load increased, it next

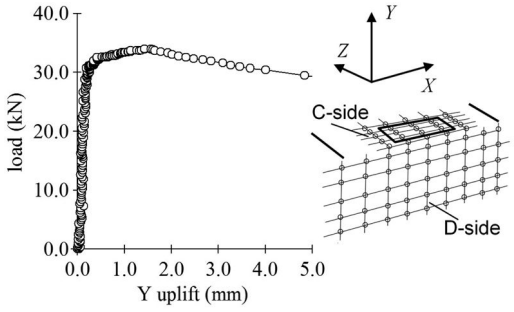

Figure 18. Y uplift of C-side.

turned to decrease to zero after yielding, and finally went back to a one-way increase after the maximum load. In that way, the −Z leanout acted in concert with the major event, such as the yielding point or maximum loading point of the member. Its tendency was very distinctive.

Fig. 18 shows the relationship between the applied load and Y uplift of the C-side obtained by the 3DPA, where the Y uplift is defined as the difference between the Y displacement of the D-side and that of the C-side. The former is defined by the average of six target points as shown in Fig. 17, and the latter is also defined by the average of nine target points as shown in Fig. 18. The Y uplift of the C-side shows monotonic increase. Before the yielding point the value of the Y uplift is very small, and after the yielding point the increasing rate be-comes larger. There is no relationship between the applied load and the Y uplift such as in the case of the –Z leanout of the D-side shown in Fig. 17. These two figures would imply that collapse of the specimen was mainly governed by the –Z leanout of the D-side, in spite of the Y uplift of the C-side.

Besides these discussions, compressive strain in the X (horizontal) direction was calculated and examined. Unfortunately, the calculated value of strain was not applicable because too much strain scatter from about minus 2000×10^{-6} to plus 2000×10^{-6} was observed. There is a possibility that resolution degradation of the photo image had actually occurred in the bending test by taking a wide angle shot in comparison with the preliminary test. In order to use this method of 3DPA for strain analysis, strain fluctuations should be evened out and further consideration about the local strain will be needed.

5 CONCLUSIONS

In this paper, the bending test using a long-term exposed beam specimen was carried out in order to investigate the effect of the deterioration of the compression zone on bending performance of deteriorated RC members. In order to investigate the three dimensional behavior of the concrete in the compression zone, the authors took the method of 3DPA. The following information was obtained through the loading test and analysis.

- The RC specimen suffered severe deterioration through the long-term weathering for over 20 years due to the effect of chloride induced rebar corrosion.
- It is possible for severely deteriorated RC members to show degradation of ductility in addition to degradation of strength. When considering the effect of deterioration to the bending performance of RC members, not only degradation of tensile performance of the reinforcing bars but also compression failure and buckling of the concrete due to corrosion cracking should be taken into account.
- It is possible for the measurement method by means of the 3DPA to contain errors, for example, the strain obtained by the 3DPA has large variation, and the displacement obtained by the 3DPA is larger than that by the DT. However, it can be recognized that the 3DPA gives sufficient information about the loading test.
- It was clarified that collapse of the specimen is mainly governed by side leanout of the side-surface (–Z leanout of D-side) in spite of uplift of the compressive-surface (Y uplift of C-side).

ACKNOWLEDGMENT

This work is financially supported by JSPS KAKENHI grant Number 24560593.

REFERENCES

Matsuo, T., Sakai, M., Matsumura, T. and Kanazu, T., 2002. Fatigue Property of Reinforced Concrete Beam with Corroded Reinforcement, *Proceedings of the Japan Concrete Institute*, Vol. 24, No. 1: 783–788. (in Japanese)

Oyado, M., Kanakubo, T., Sato, T. and Yamamoto, Y., 2010. Bending performance of reinforced concrete member deteriorated by Corrosion, *Structure and Infrastructure Engineering*, 1–10, iFirst article, Taylor & Francis.

This page intentionally left blank

The Concrete Solutions series of International Conferences on Concrete Repair began in 2003 with a conference held in St. Malo, France in association with INSA Rennes. Subsequent conferences have seen us partnering with the University of Padua in 2009 and with TU Dresden in 2011. This conference is being held for the first time in the UK, in association with Queen's University Belfast and brings together delegates from 36 countries to discuss the latest advances and technologies in concrete repair.

Earlier conferences were dominated by electrochemical repair, but there has been an interesting shift to more unusual methods, such as bacterial repair of concrete plus an increased focus on service life design aspects and modelling, with debate and discussion on the best techniques and the validity of existing methods. Repair of heritage structures is also growing in importance and a number of the papers have focused on the importance of getting this right, so that we may preserve our rich cultural heritage of historic structures.

This book is an essential reference work for those working in the concrete repair field, from Engineers to Architects and from Students to Clients.

ISBN 978-1-138-02708-4

9 781138 027084

an **informa** business

CRC Press
Taylor & Francis Group
an **informa** business
www.crcpress.com

6000 Broken Sound Parkway, NW
Suite 300, Boca Raton, FL 33487

Schipholweg 107C
2316 XC Leiden, NL

2 Park Square, Milton Park
Abingdon, Oxon OX14 4RN, UK